Cover Page, Journal of the Turkish Chemical Society, Section A: Chemistry (JOTCSA)

ETHICAL GUIDELINES

Guidelines for the Editors

An editor (editors, associate editors, *etc*.) should provide impartial consideration to all manuscripts offered for publication, judging each on its particular feature without regard to race, religion, nationality, sex, seniority, or institutional affiliation of the author(s). An editor should review and treat a manuscript submitted for publication with all reasonable speed. An editor takes the sole responsibility for accepting or rejecting a manuscript for publication. An editor may seek assistance on a manuscript from specialists chosen for their expertise and fair judgment. An editor should not reveal any information about the manuscript under consideration to anyone other than the author and designated reviewers until after the evaluation process is complete. An editor should respect the intellectual independence of authors.

Authors

Our journal considers a person as an author who is responsible at least for a part of the work. Authors should be able to explain the problem in study in a deep manner. For our journal, all authors are responsible for the content they submitted. The corresponding author is responsible for the agreement of all the authors and to keep them informed about the submission process since first submission of their manuscript. He/she is responsible for providing the license to publish, in case of acceptance, on behalf of all the authors. Our journal assumes that submitting the paper implies in total agreement from all the authors. For manuscripts with more than 8 authors, all the authors should provide a declaration specifying what was their contribution to the manuscript. It is not acceptable for JOTCSA to consider for publication anything that was previously published, neither entirely nor partly in other journals. Anything sent to our journal must not be under analysis by anywhere else. Simultaneous submissions to JOTCSA and any other journal, is considered a major conduct flaw, and all the authors will be definitely banned, and all their previous publications in JOTCSA will be publicly retracted. Plagiarism and self-plagiarism will be treated in the same way. Multiple manuscripts, dealing with closely related subjects and/or variables are discouraged as long as they could figure in a single paper.

Reviewers

JOTCSA invites peers to review its submissions, relying on their expertise, curricula, and their will to review them as volunteers. By accepting to review a manuscript, the reviewer commits himself to do so in due time. Delays are extremely negative to the review process and makes it last much longer than it should. When a reviewer is requested, he/she is gently asked to answer the invitation e-mail, informing if he/she is willing or not willing to review the manuscript. It is a gesture of politeness, and it avoids delays too. By accepting to review a manuscript, the reviewer declares that no conflicts of interests do exist, and he/she is doing his/her revision for the wealth and progress of Science. Those reviewers who answer our requests, agreeing or not, and those who respect the deadlines, are scored positively, and eventual submissions they could send to JOTCSA will be treated with priority.

Hint: The online version of this declaration can be viewed on http://dergipark.ulakbim.gov.tr/public/journals/5106/ethical_guidelines.pdf.

Synthesis and Characterization of N-((6-methylpyridin-2-yl)carbamothioyl)thiophene-2-carboxamide and its Co(II), Ni(II) and Cu(II) Complexes: Calculation of the Molecular Orbitals and Antioxidant and Antitumor Activities

Tuncay Yeşilkaynak

Department of Chemistry Technology, Afsin Vocational School,
Sütcü İmam University, TR46500, Kahramanmaras, Turkey

Abstract: N-((6-methylpyridin-2-yl)carbamothioyl)thiophene-2-carboxamide, $C_{12}H_{11}N_3OS_2$ (HL) and its Co(II), Ni(II) and Cu(II) complexes (ML_2 type) have been synthesized and characterized by elemental analysis, FT-IR ,^{1}H-NMR and HR-MS methods. Moreover, HL was characterized by single crystal X-ray diffraction method. The HL crystallizes in the monoclinic crystal system with *P* 1 2$_1$/*c* 1 space group, *Z*=4, a=7.2326(8) Å, b=18.3492(16) Å, c=9.7724(9) Å. The [ML$_2$] complex structures were optimized by using B97D/TZVP level. Molecular orbitals of HL ligand were calculated at the same level. Antioxidant activities of the complexes were determined via DPPH and ABTS assays. Anticancer activity of the complex was studied via MTT assay in MCF-7 breast cancer cells.

INTRODUCTION

Thiourea derivatives are important compounds due to their wide range of applications. They have a long history as functional ligands in coordination chemistry and they coordinate to metals via both O and S atoms [1]. Benzoylthioureas have been reported as extractants for various valuable metals such as Ni, Co, Ag, Pd and Au [2–4]. In previous studies, metal complexes of benzoylthiourea derivatives were synthesized and their properties were reported [5–7]. It is known that thiourea derivatives show antibacterial, antifungal, antitubercular, antithyroid, and insecticidal properties [8].

Therefore, this study is focused on the synthesis, characterization, and crystal structure of new thiourea derivatives (Figure 1) and their metal complexes. Quantum chemical computations were performed to investigate molecular orbitals of HL ligand and optimized geometries of ML_2 complexes. Also, antioxidant and anticancer activity of all complexes and electrochemical behavior of the Cu complex were investigated.
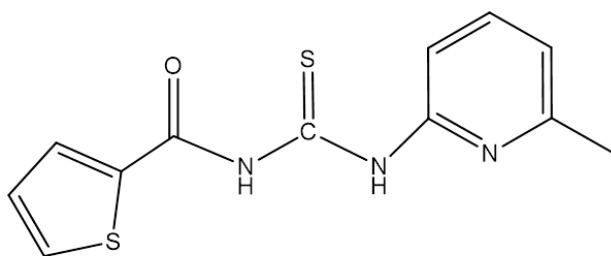
Figure 1 Molecular structures of the HL.

MATERIAL and METHODS

Experimental

Synthesis of the ligand

All chemical reagents used for the synthesis were analytical purity. A solution of an appropriately substituted thiophenecarboxylic acid chloride (0.01 mole) in acetone (50 cm^3) was dropwise added to a solution of KSCN (0.01 mole) in acetone (30 cm^3). The reaction mixtures were heated under reflux for 30 min. Then they were cooled to room temperature. Solutions of 2-amino-6-methylpyridine (0.01 mole) in acetone (10 cm^3) were added and the resulting mixtures were stirred for 2 h. The resulting mixture was poured into HCl (0.1 N, 300 cm^3) solution and was filtered. The obtained solid product was washed with H_2O and was purified by recrystallization from EtOH/CH_2Cl_2 [9].

N-((6-methylpyridin-2-yl)carbamothioyl)thiophene-2-carboxamide,   HL: Light Yellow. Yield: 88%, m.p. 155–157 °C. (*Anal.*:   C, 51.5; H, 3.9; N, 15.0; S, 22.9; $C_{12}H_{11}N_3OS_2$ *calc.*: C, 52.0; H, 4.0; N, 15.2; S, 23.1%.). FT-IR (ATR, cm^{-1}): υ(N-H) 3181, υ(C-H *aro.*) 3013, υ(CH$_3$) 2810,1354, υ(C=O) 1695 (s), υ(C=S) 1155. ^{1}H-NMR (400 MHz, CDCl$_3$, ppm): 8.37 (s, 1H, NH), 7.25–6.96 (m, 6H, Ar-H.).

Synthesis of the complexes, [ML$_2$]

Complexes were synthesized according to the following method: MCl$_2$.xH$_2$O (0.001 mole) (M:Co^{2+}, Ni^{2+} and Cu^{2+}) in ethanol (10 cm^3) were added drop wise to into the solution containing the ligand (0.002 mole) dissolved in ethanol (40 cm^3) in the presence of a few drops of Et$_3$N under constant stirring for 30 min. The sediment was filtered, washed with a small amount of cold ethanol and was dried in desiccator [10].

L   [ML$_2$]
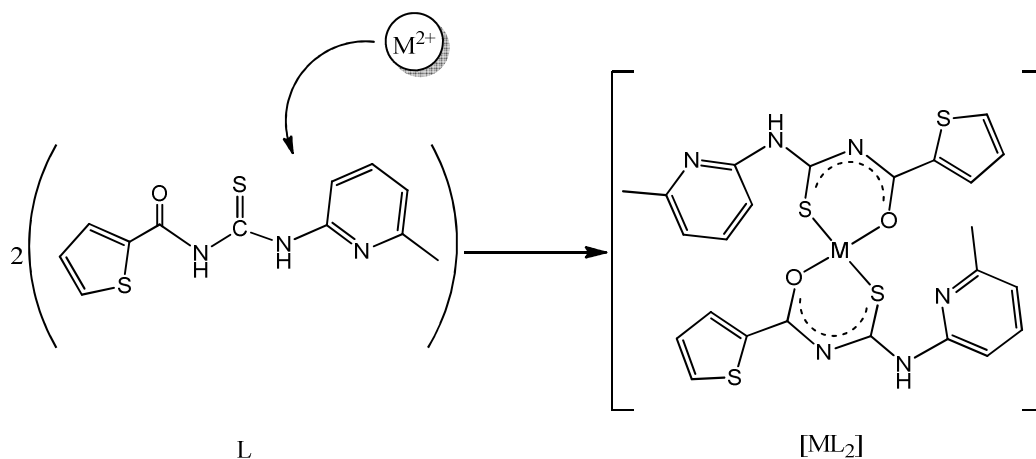
Bis(N-((6-methylpyridin-2-yl)carbamothioyl)thiophene-2-carboxamide)cobalt(II), [CoL$_2$]: Pale green. Yield: 89%, *Anal.*: C, 46.9; H, 3.1; N, 13.2; S, 21.3; $C_{24}H_{20}N_6O_2S_4Co$, *calc.*: C, 47.1; H, 3.3; N, 13.7; S, 21.0%. FT-IR (ATR, cm^{-1}): υ(C=N) 1567 (s). HR-MS (ES$^+$), *m/z* (calc./found): 611.6478/611.6589.

Bis(N-((6-methylpyridin-2-yl)carbamothioyl)thiophene-2-carboxamide)nickel(II), [NiL$_2$]: Green. Yield: 77%, *Anal.*: C, C, 47.3; H, 3.4; N, 13.3; S, 21.5; $C_{24}H_{20}N_6O_2S_4Ni$, *calc.*: C, 47.2; H, 3.3; N, 13.8; S, 21.0%. FT-IR (ATR, cm^{-1}): υ(C=N) 1536 (s). ^{1}H-NMR (400 MHz, CDCl$_3$, ppm): 7.21–6.87 (m, 12H, Ar-H), 4.34 (m, 1H, N-H). HR-MS (ES$^+$), *m/z* (calc./found): 611.4080/611.4164.

Bis(N-((6-methylpyridin-2-yl)carbamothioyl)thiophene-2-carboxamide)copper(II),[CuL$_2$]: Brown. Yield: 82%, *Anal.*: C, 46.0; H, 3.5; N, 13.3; S, 20.3, $C_{24}H_{20}N_6O_2S_4Cu$, *calc.*: C,

46.8; H, 3.3; N, 13.6; S, 20.8%. FT-IR (ATR, cm^{-1}): υ(C=N) 1520 (s). HR-MS (ES$^+$), *m/z* (calc./found): 616.2606/616.2690.

Instrumental

FT-IR measurements were performed via a Perkin Elmer LX-125000B FT-IR spectrometer with an ATR component (4000–30 cm^{-1}). ^{1}H-NMR spectra were recorded on a Bruker Avance III 400 MHz NMR spectrometer, using CDCl$_3$ as solvent and TMS as internal standard. ^{1}H-NMR signals were recorded with the aid of 2D COSY spectra where necessary. Elemental analyses were performed on a Costech ECS 4010 instrument. Melting point of the ligand was determined by Stuart model SMT30 instrument. The mass spectra were obtained by using Waters SYNAPT G1 MS instrument. The exact mass analyses were made in positive mode (ES+) with HR-MS (Da 50-1000, ESI-TOF-MS). X-ray data of the HL were collected on a Bruker D8 Venture diffractometer using monochromated MoK$_\alpha$ radiation. The structure was solved and refined using the Bruker SHELXTL Software. The voltammetric measurements were made via BAS 100 W (Bioanalytical System, USA) electrochemical analyzer. The standard one-compartment three electrode cell of 10 mL capacity contained glassy carbon working electrode (BAS; *Φ*: 3 mm diameter), a Ag/AgCl reference electrode (BAS; 3 M KCl) and platinum wire counter electrode.

Computations

Computations were made by using G09 [11] program package. HOMO and LUMO orbitals of the ligands were computed as single point calculation using B97D/TZVP [12,13] level on the X-ray structure. DOS (density of state) spectrum was obtained using Gaussian [14] program package. The proposed [ML$_2$] complex structures were optimized using the same computational level. The optimized bond distances and angles were visualized by using CYLView[15] program package. Frequency calculations were also made to verify that optimized structures are stationary points (no imaginary frequency).

RESULTS and DISCUSSION

^{1}H-NMR

The ^{1}H-NMR spectra of the ligand there is a single peak at 8.37 ppm which corresponds to the N-H group. The aromatic C-H bonds are shown as multiple peaks at 7.28-7.14 ppm for HL. The N-H peaks, which are observed at 8.37 ppm, would not appear in the metal complexes. These data agree with the complexation reaction and structure of the metal complexes. The aromatic C-H protons are shown at 7.21-6.87 ppm for [NiL$_2$]. The

N-H protons are shown at 4.34 ppm for [NiL$_2$]. ^{1}H-NMR spectra of [CoL$_2$] and [CuL$_2$] complexes could not be obtained because of their paramagnetic properties.

X-Ray Crystallography

The single crystals suitable for X-ray diffraction analysis were grown from ethanol solutions. The structures were solved via direct methods and were refined on F^2 by full matrix least-squares using SHELXL 2013[16]. All non-hydrogen atoms were refined via anisotropic displacement parameters. The molecular structure plots were obtained by using Mercury CSD 2.4 software [17]. The crystal and instrumental parameters were summarized in the supporting information. Molecular structure with the atom-numbering scheme of the HL is given in Figure 2.
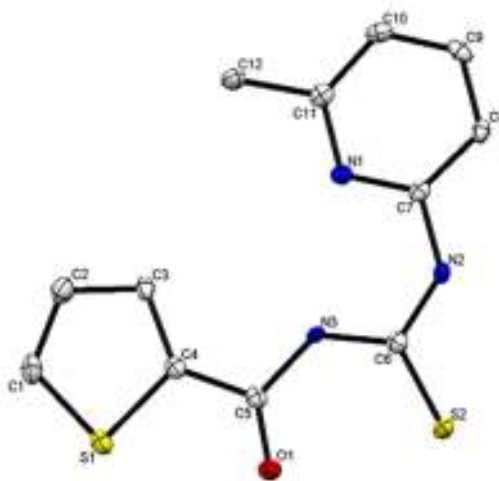
Figure 2 ORTEP view of the HL, thermal ellipsoids are shown at the 50% probability level.

Crystal data parameters of HL and some experimental parameters are given in the supplementary material file.

Packing scheme of the HL is given in Figure 3.
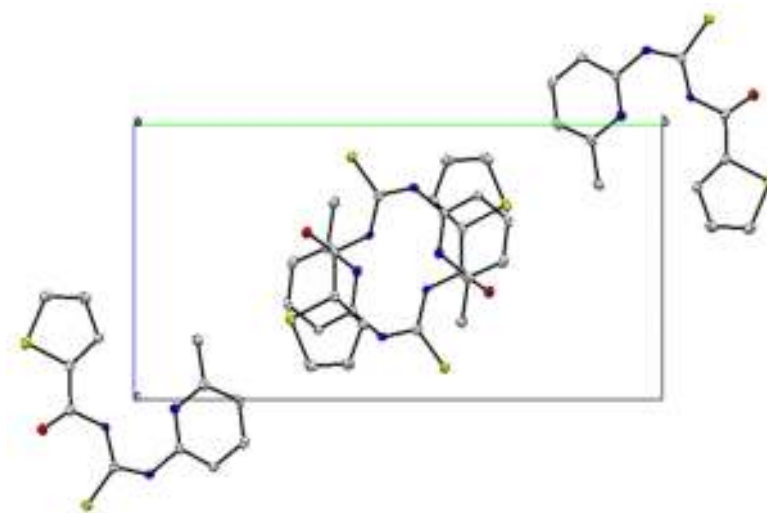
Figure 3 Crystal packing scheme of the HL in *P* 1 2$_1$/*c* 1.

The structures were solved and refined using the Bruker SHELXTL Software Package. Selected bond lengths and angles of the HL are presented in supplementary material file. The bond lengths and angles in the HL are typical for thiourea derivatives; C6-S2 and C5-O1 bonds show a typical double-bond character with 1,672(18) and 1,212(2) Å, respectively. The bond lengths of the N2-C6, N3-C6, N3-C5, and N2-C7 were determined as 1,359(2), 1.368(2), 1.400(2) and 1,409(2) Å respectively. These results show that the bonds have partial double bond character. The carbonyl and thiocarbonyl part bound angles are N2-C6-S2, 119.3(14); N3-C6-S2, 125.7(14); N3-C5-O1, 124.4(17) and O1-C5-C4, 122.1(17)°[14,18-22]. The crystal packing is determined by intermolecular N-H…S hydrogen bonds [23,24]. Orbital diagrams of the HL were given in Figure 4. For HL molecule, HOMO are dominantly made up of π orbital of sulfur atom. On the other hand, LUMO are mainly delocalized over amide and thioamide moiety and thiophene ring of the HL molecule.
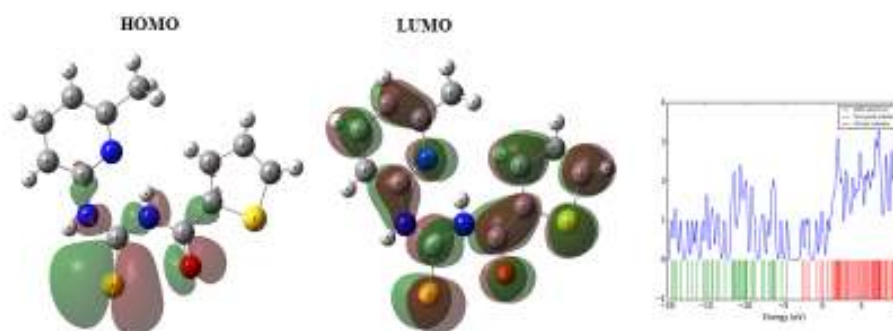
Figure 4 Orbital diagrams of the HL computed using B97D/TZVP level on the X-ray structure.

Complex Structure

The [ML$_2$] (M: Ni, Co, Cu) structures were proposed based on the reported cis-bis(*N,N*-dimethyl-*N'*-2-chlorobenzoylthioureato)Ni(II) crystal structure[25] and were optimized by using B97D/TZVP computational level. Figure 5 show optimized bond distances and O-M-S bond angles of the [ML$_2$] structures, respectively.
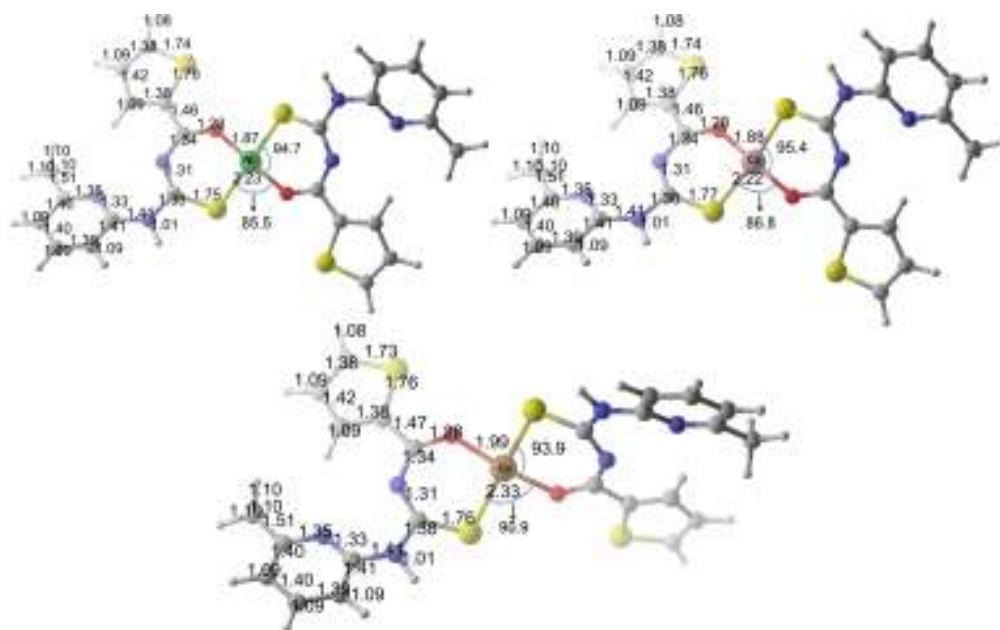
Figure 5 Optimized the [ML$_2$] structure using B97D/TZVP level.

The O-Ni-S bond angles in the [NiL$_2$] and [CoL$_2$] structures are very similar but in the [CuL$_2$] they slightly differ from those of Ni and Co complexes. The M-O distance for complexes follows the order; Cu-O (1.99 Å) >Co-O (1.88 Å) >Ni-O (1.87 Å). The M-O distance values for complexes agree with literature values which are 1.94 Å, 1.92 Å and 1.86 Å, respectively [26-28]. The M-S distance order for complexes is Co-S < Ni-S < Cu-S. It can be said that the bond lengths for the rest of the bond types (the C-H, C-C, C-N, C-S and C-O bonds) are almost the same in all complex structures since the largest difference is only 0.02 Å. The C6-S2 bond distance elongates from 1.672 Å in the HL structure to 1.75 – 1.77 Å in the [ML$_2$] structure. Similarly, the C5-O1 bond length also stretches from 1.212 Å to 1.28 Å for the [ML$_2$]. Due to leaving proton from N3 atom, C6-N3 and C5-N3 bond lengths changed to 1.31 and 1.34 Å in the [ML$_2$], respectively.

Antioxidant and Antitumor Activity of the Complexes

In vitro antioxidant and antitumor properties of all complexes were studied in cell culture systems. The antioxidant activity of metal complexes was studied by using the DPPH and ABTS assays. The anticancer activity of complex was studied via MTT assay in MCF-7

breast cancer cells. MTT assay is fast, easy and with high accuracy. The amount of living cells will be determined depending on the amount of binding via spectrophotometric analysis. The DPPH, ABTS, Reduction power and IC_{50} values are presented in supplementary material file. Natural or synthetic antioxidants are important in the management of severe oxidative stress conditions. Synthetic antioxidants are currently being developed as therapeutic agents against oxidative stress. The antioxidant activity is related to DPPH, ABTS and reduction power values. The [CoL$_2$] shows good antioxidant properties. These results show that antioxidant properties of [CoL$_2$] is better than those of propyl gallate and worse than those of vitamin E. Both propyl gallate and vitamin E are important antioxidant materials [29]. The [CuL$_2$] complex shows good antitumor activity. The IC_{50} value of the [CuL$_2$] complex is comparable with that of Fluorouracil (5-FU) which is widely used in cancer treatment. Other compounds (IC_{50} values, >40 ppm) were less active against the tumor cells [30]. Similarly, the researchers examined the antitumor properties of the Cu complex. They observed that the Cu complexes show good antitumor properties [31,32].

Electrochemical Behavior of the [CuL$_2$]

The cyclic voltammetric (CV) studies were carried out to understand the electrochemical behavior of the [CuL$_2$]. In cyclic voltammogram of the [CuL$_2$], there are two peaks. One of these peaks is at about +0.52 V, which is an oxidation peak, and the other one is at about -1.40 V which is a reduction peak. By the help of the pH measurements, optimum pH of the medium was found to be pH=2, where the sharpest and best results were obtained. To understand whether the process was under control of diffusion or absorption, scanning rate studies were carried out between 25 mV/s and 750 mV/s. Studies were carried out in Britton-Robinson buffer solution at pH=2, where the best oxidation and reduction results were obtained. The characteristic scan rate curves of the [CuL$_2$] are given in Figure 6.
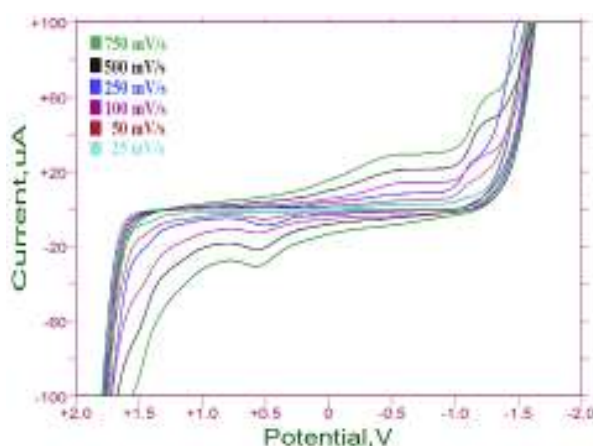
Figure 6 Cyclic Voltammograms of [CuL$_2$] compound with different scan rates.

Scan rates were investigated between the 25-750 mV/s and at 1×10^{-5} M concentration. The linear dependence of peak current Ip (µ) on the square root of the scan rate $v^{1/2}$ (mVs^{-1}) was found by GCE, demonstrating diffusional behavior. The equations about scan rate studies for the $[Cu(L)_2]$ is noted via the equation below (1);

$$Log\ I_p\ (\mu A) = 0,\ 2607\ \sqrt{v}\ (mVs^{-1}) - 0,\ 5439\ (r^2 = 0,\ 9501) \tag{1}$$

The linear relationship between Log I_p and Log v was also investigated and the equations about these relationships are given via the equation below (2);

$$Log\ I_p\ (\mu A) = 0,\ 4455\ Log\ v\ (mVs^{-1}) - 0,\ 3970\ (r^2 = 0,\ 9940) \tag{2}$$

The slope of the relationships fit with the theoretically expected values for an ideal diffusion controlled reaction (0.5) [33]. The Cu(II) complexes could be studied because they are stable in this pH range.

CONCLUSIONS

N-((6-methylpyridin-2-yl)carbamothioyl)thiophene-2-carboxamide, $C_{12}H_{11}N_3OS_2$ (HL), and its Co(II), Ni(II) and Cu(II) complexes have been synthesized. Characterization of the compounds were made by elemental analysis, FT-IR, ^{1}H-NMR and HR-MS methods. In addition, HL was characterized by single crystal X-ray diffraction method. The HL crystallizes in the monoclinic crystal system with $P1\ 2_1/c\ 1$ space group, Z=4, a=7.2326(8) Å, b=18.3492(16) Å, c=9.7724(9) Å. Molecular orbitals of both HL calculated and the $[ML_2]$ structures were optimized by B97D/TZVP level. The anticancer and antioxidant activities of the complexes were also investigated. Antioxidant activities of the complexes were determined by using DPPH and ABTS assays. The $[CoL_2]$ shows good antioxidant properties. Anticancer activity of the complex was investigated via MTT assay in MCF-7 breast cancer cells. The IC_{50} values of complexes are 111, 79 and 31 ppm for $[CoL_2]$, $[NiL_2]$ and $[CuL_2]$, respectively. The $[CuL_2]$ complexes were found to have better antitumor activities. Cyclic voltammograms of the complexes show oxidation and reduction peaks at +0.52 V and -1.40 V for the $[CuL_2]$.

Appendix A. Supplementary material

Crystallographic data for the HL structure have been deposited at the Cambridge Crystallographic Data Centre (CCDC), CCDC 1055243 (HL). This data can be obtained free of charge from The Cambridge Crystallographic Data Centre via

www.ccdc.cam.ac.uk/data_request/cif. Cartesian coordinates of optimized geometries are also available. The tables in the text were also combined in the Supplementary Material.

REFERENCES

1. Burrows AD, Coleman MD, Mahon MF. Platinum thiosemicarbazide and thiourea complexes: the crystal structure of [PtCl(dppe){SC(NHMe)NHNMe2-S}](PF6) and the influence of intramolecular hydrogen bonding on ligand co-ordination mode. Polyhedron. 1999 Aug;18(20):2665–71.

2. Domínguez M, Anticó E, Beyer L, Aguirre A, García-Granda S, Salvadó V. Liquid–liquid extraction of palladium(II) and gold(III) with N-benzoyl-N',N'-diethylthiourea and the synthesis of a palladium benzoylthiourea complex. Polyhedron. 2002 Jun;21(14–15):1429–37.

3. König K-H, Schuster M, Schneeweis G, Steinbrech B. Zur Chromatographie von Metallchelaten: XIV. Dünnschicht-Chromatographie von N,N-Dialkyl-N?-benzoylthioharnstoff-Chelaten. Fresenius' Zeitschrift für Analytische Chemie. 1984;319(1):66–9.

4. König K-H, Schuster M, Steinbrech B, Schneeweis G, Schlodder R. N,N-Dialkyl-N?-benzoylthioharnstoffe als selektive Extraktionsmittel zur Abtrennung und Anreicherung von Platinmetallen. Fresenius' Zeitschrift für Analytische Chemie. 1985;321(5):457–60.

5. Ozpozan N, Ozpozan T, Arslan H, Karipçin F, Külcü N. Thermal behaviours of Co(II), Ni(II), Cu(II)), and Pb(II) complexes of N,N-dipropyl-N'-benzoylthiourea. Thermochimica Acta. 1999 Sep;336(1–2):97–103.

6. Özpozan N, Arslan H, Özpozan T, Özdeş N, Külcü N. Thermal studies of Ni(II), Pd(II), Pt(II) and Ru(III) complexes of N,N-dihexyl-N'-benzoylthiourea. Thermochimica Acta. 2000 Jan;343(1–2):127–33.

7. Özpozan N, Arslan H, Özpozan T, Merdivan M, Külcü N. Thermal Decomposition Kinetics of Some Metal Complexes of N,N-diethyl-n '-benzoylthiourea. Journal of Thermal Analysis and Calorimetry. 2000;61(3):955–65.

8. Madan V, Taneja A, Kudesia V. SYNTHESIS AN SPECTRAL STUDIES OF SOME PYRIMIDYL AND THIAZOLYL SUBSTITUTED THIOUREAS AS POTENTIAL FUNGICIDES AND NEMATICIDES. J Ind Chem Soc. 1991;68(8):471–2.

9. Arslan H, Flörke U, Külcü N. Synthesis, characterization, and crystal structure of 1-(4-chloro-benzoyl)-3-naphthalen-1-yl-thiourea. J Chem Crystallog. 203AD;33(12):919–24.

10. Gunasekaran N, Jerome P, Ng SW, Tiekink ERT, Karvembu R. Tris-chelate complexes of cobalt(III) with N-[di(alkyl/aryl)carbamothioyl] benzamide derivatives: Synthesis, crystallography and catalytic activity in TBHP oxidation of alcohols. Journal of Molecular Catalysis A: Chemical. 2012 Feb;353–354:156–62.

11. Frisch M, Trucks G, Schlegel H, Scuseria G, Robb M, Cheeseman J, et al. Gaussian [Internet]. Gaussian, Inc.; 2009. Available from: http://www.gaussian.com/

12. Grimme S. Semiempirical GGA-type density functional constructed with a long-range dispersion correction. Journal of Computational Chemistry. 2006 Nov 30;27(15):1787–99.

13. Schäfer A, Huber C, Ahlrichs R. Fully optimized contracted Gaussian basis sets of triple zeta valence quality for atoms Li to Kr. The Journal of Chemical Physics. 1994;100(8):5829.

14. O'boyle NM, Tenderholt AL, Langner KM. cclib: A library for package-independent computational chemistry algorithms. Journal of Computational Chemistry. 2008 Apr 15;29(5):839–45.

15. Legault C. CYLview, 1.0b [Internet]. Université de Sherbrooke; 2009. Available from: http://www.cylview.org

16. Sheldrick GM. A short history of *SHELX*. Acta Crystallographica Section A Foundations of Crystallography. 2008 Jan 1;64(1):112–22.

17. Macrae CF, Bruno IJ, Chisholm JA, Edgington PR, McCabe P, Pidcock E, et al. *Mercury CSD 2.0* – new features for the visualization and investigation of crystal structures. Journal of Applied Crystallography. 2008 Apr 1;41(2):466–70.

18. Arslan H, Külcü N, Flörke U. Synthesis and characterization of copper(II), nickel(II) and cobalt(II) complexes with novel thiourea derivatives. Trans Met Chem. 2003;28(7):816–9.

19. Binzet G, Arslan H, Flörke U, Külcü N, Duran N. Synthesis, characterization and antimicrobial activities of transition metal complexes of **N,N** -dialkyl- **N'** -(2-chlorobenzoyl)thiourea derivatives. Journal of Coordination Chemistry. 2006 Aug 5;59(12):1395–406.

20. Arslan H, Flörke U, Külcü N, Emen MF. Crystal structure and thermal behaviour of copper(II) and zinc(II) complexes with *N* -pyrrolidine- *N* '-(2-chloro-benzoyl)thiourea. Journal of Coordination Chemistry. 2006 Jan 20;59(2):223–8.

21. Ugur D, Arslan H, Külcü N. Synthesis, characterization and thermal behavior of 1,1-dialkyl-3-(4-(3,3-dialkylthioureidocarbonyl)-benzoyl)thiourea and its Cu(II), Ni(II), and Co(II) complexes. Russian Journal of Coordination Chemistry. 2006 Sep;32(9):669–75.

22. Emen M, Arslan H, Külcü N, Flörke U, Duran N. Synthesis, characterization and antimicrobial activities of some metal complexes with N'-(2-chloro-benzoyl)thiourea ligands : The crystal structure of fac-[CoL3] and cis-[PdL2]. Pol J Chem. 2005;79(10):1615–26.

23. Binzet G, Emen FM, Flörke U, Yeşilkaynak T, Külcü N, Arslan H. 4-Chloro- *N* -[*N* -(6-methyl-2-pyridyl)carbamothioyl]benzamide. Acta Crystallographica Section E Structure Reports Online. 2009 Jan 15;65(1):o81–2.

24. Yesilkaynak T, Flörke U, Külcü N, Arslan H. 1-Benzoyl-3-(4-methylpyridin-2-yl)thiourea. Acta Crystallographica Section E Structure Reports Online. 2006 Sep 15;62(9):o3934–5.

25. Emen FM, Flörke U, Külcü N, Arslan H. *cis* -Bis(*N* , *N* -dimethyl- *N* '-2-chlorobenzoylthioureato)nickel(II). Acta Crystallographica Section E Structure Reports Online. 2003 Aug 15;59(8):m582–3.

26. Ozer CK, Arslan H, Vanderveer D, Binzet G. Synthesis and characterization of N -(alky(aryl)carbamothioyl)cyclohexanecarboxamide derivatives and their Ni(II) and Cu(II) complexes. Journal of Coordination Chemistry. 2009 Jan;62(2):266–76.

27. Hernández W, Spodine E, Vega A, Richter R, Griebel J, Kirmse R, et al. Cis-trans Isomerism in Copper(II) Complexes with N-acyl Thiourea Ligands. Zeitschrift für anorganische und allgemeine Chemie. 2004 Aug;630(10):1381–6.

28. Binzet G, Arslan H, Külcü N. Synthesis and Thermal Behaviour of Co(II), Ni(II) and Cu(II) Complexes of N,N-di-n-propyl-N?- (2-chlorobenzoyl)thiourea. Asian Journal of Chemistry. 2007;19(7):5711–7.

29. Dong Y, Venkatachalam T., Narla RK, Trieu VN, Sudbeck EA, Uckun FM. Antioxidant function of phenethyl-5-bromo-pyridyl thiourea compounds with potent anti-HIV activity. Bioorganic & Medicinal Chemistry Letters. 2000 Jan;10(1):87–90.

30. Liu W, Zhou J, Zhang T, Zhu H, Qian H, Zhang H, et al. Design and synthesis of thiourea derivatives containing a benzo[5,6]cyclohepta[1,2-b]pyridine moiety as potential antitumor and anti-inflammatory agents. Bioorganic & Medicinal Chemistry Letters. 2012 Apr;22(8):2701–4.

31. Kumar R, Obrai S, Jassal AK, Hundal MS, Mitra J, Sharma S. Synthesis, structure, computational, antimicrobial and *in vitro* anticancer studies of copper(II) complexes with N,N,N',N'-tetrakis(2-hydroxyethyl)ethylenediamine and tris(2-hydroxyethyl)amine. Journal of Coordination Chemistry. 2015 Jun 18;68(12):2130–46.

32. Zhang X-T, Ma Z-Y, Zhao C, Zhou Q-J, Xie C-Z, Xu J-Y. Synthesis, crystal structures, DNA binding, and cytotoxicity activities of two copper(II) complexes based on unsymmetrical tripodal ligands. Journal of Coordination Chemistry. 2015 Jul 3;68(13):2307–23.

33. Muslu H, Golcu A, Tumer M, Ozsoz M. Electrochemical investigation and DNA-binding studies of pefloxacin–metal(II/III) complexes. Journal of Coordination Chemistry. 2011 Oct 10;64(19):3393–407.

Türkçe Öz ve Anahtar Kelimeler

N-((6-metilpiridin-2-il)karbamotioil)tiyofen-2-karboksamid ve Co(II) Ni(II) ve Cu(II) komplekslerinin sentezi ve karakterizasyonu: Molekül Orbitallerin Hesaplanması, Antioksidan ve Antitümör Aktiviteleri

Tuncay Yeşilkaynak

Kimya Teknolojisi Bölümü, Afşin Meslek Yüksek Okulu, Sütçü İmam Üniversitesi, TR46500 Kahramanmaraş

Öz: N-((6-metilpiridin-2-il)karbamotioiltiyofen-2-karboksamid, $C_{12}H_{11}N_3OS_2$ (HL) ve Co(II), Ni(II) ve Cu(II) kompleksleri (ML_2 türü) sentezlenmiş ve elementel analiz, FT-IR, ^{1}H-NMR HR-MS yöntemleriyle karakterize edilmiştir. Bunun dışında, HL tek kristal X-ışını saçılması yöntemi ile karakterize edilmiştir. HL monoklinik kristal sisteminde P 1 21/c 1 uzay grubunda kristallenir ve Z = 4 a=7.2326(8) Å, b=18.3492(16) Å, c=9.7724(9) Å.olarak bulunmuştur. [ML_2] kompleks yapıları B97D/TZVP seviyesinde optimize edilmiştir. HL ligandının moleküler orbitalleri de aynı seviyede hesaplanmıştır. Komplekslerin antioksidan aktiviteleri DPPH ve ABTS deneyleri ile belirlenmiştir. Kompleksin antikanser aktivitesi MTT deneyi ile MCF-7 meme kanser hücrelerinde çalışılmıştır.

Anahtar kelimeler: Tiyoüre; tiyofen; antikanser aktivitesi, kristal yapısı; moleküler orbital.

Sunulma: June 27, 2016. **Kabul:** July 9, 2016.

Green Synthesis of New Amino Acid Schiff Bases and Their Biological Activities

Cigdem Yorur-Goreci[1*], Zulal Demir[1], Nilay Altas[1]

[1]Yildiz Technical University, Faculty of Arts and Sciences, Department of Chemistry, 34210

Istanbul, Turkey

Abstract: In this study, four new and two known amino acid Schiff base compounds derived from the condensation reaction of benzaldehyde, salicylaldehyde, pyrrole-2-carbaldehyde, pyridine-2-carbaldehyde, fluorene-2-carbaldehyde and terephthalaldehyde with 2-phenylglycine methyl ester hydrochloride have been synthesized by both conventional method and microwave irradiation protocol. The new compounds were characterized by FTIR, ^{1}H-NMR, LC-MS and electronic spectral studies. A comparative study between conventional heating and microwave irradiation has also been reported. Based on these results, with the microwave synthesis, the yield of the products was increased from 37% up to 96% as compared to conventional method. By microwave, reactions were completed within 5.5-8.5 minutes and the products were obtained in good to high yields, with reduced time, waste, and formation byproduct. DPPH (2,2-diphenyl-1-picrylhydrazyl) radical scavenging effect were performed to determine antioxidant activities of the new compounds. All of the compounds exhibited significant activities in DPPH radical scavenging.

INTRODUCTION

Amino acids are an important class of organic chemistry which can improve pharmacological and biological properties of molecules as enhancing the lipophilicity, easing toxicity, and increasing bioavailability when these compounds are esterified and introduced to the molecular structure. Additionally, amino acids and combining molecules with them play an important role in elucidating the mechanism of transamination reaction in biological systems [1-3].

In response to the increasing industrial and biological importance of amino acid Schiff bases, many researches are directed toward the development of different methods for their preparation [4-10]. Also, the microwave synthesis of amino acid Schiff bases is of great importance in this area [11, 12].

As a green chemistry approach, microwave-assisted synthesis has been highly intriguing since last few decades by the chemists. Microwave irradiation methods used for carrying out chemical transformations are pollution free, eco-friendly, low cost, and offer high yields together with simplicity in processing and handling. The important area of green chemistry is to use non-conventional approaches of synthesis because of less or no solvent requirements, easy isolation, eco-friendly nature, less reaction time with good yield and purity of target molecules [13-15].

In this work, the synthesis of the four new and two known amino acid Schiff bases by conventional and microwave methods was aimed for the first time. Additionally, the antioxidant activities as DPPH (2,2-diphenyl-1-picrylhydrazyl) radical scavenging effect of synthesized compounds were aimed to investigate in this study.

MATERIALS AND METHODS

All reactions in the conventional method were carried out under the inert atmosphere of nitrogen. The solvents were purified and dried according to the standard procedures. All reagents were obtained commercially and used without further purification. The aromatic aldehydes (benzaldehyde, salicylaldehyde, pyrrole-2-carbaldehyde, pyridine-2-carbaldehyde,

fluorene-2-carbaldehyde) were purchased from Merck Chemicals. 2-Phenylglycine methyl ester hydrochloride was provided from Aldrich, Sigma Chem.

UV-Vis spectra were recorded with a PU 8740 spectrophotometer in $CHCl_3$. The FT-IR spectra were measured on a Perkin Elmer, Spectrum One Bv 5.0 spectrometer. ^1H NMR spectra were recorded on an Agilent-NMR-vnmrs400 MHz and Varian UNITY INOVA 500 MHz spectrometers, using $CDCl_3$ as solvent and TMS as an internal standard. Mass spectra (LC-MS) were determined on an Agilent 1200 Infinity HPLC and Agilent 6460 Jet-Stream TripleQuad spectrometer (350 ^{o}C and 11 L/min). Column chromatography was conducted on silica gel 60. TLC was carried out on aluminum sheets precoated with silica gel 60_{F254} (Merck). Melting points were obtained with Gallenkamp Melting Point Apparatus (350 ^{o}C) in open capillaries with no correction.

Microwave irradiation experiments using simultaneous IR/FO temperature monitoring were performed using a Monowave 300 single-mode microwave reactor from Anton Paar GmbH (Graz, Austria). The instrument uses a maximum of 850 W magnetron output power and can be operated at 300 °C reaction temperature and 30 bar pressure.

Synthesis

The Schiff base derivatives (**1a-f)** were synthesized by the reaction of appropriate starting materials with two different methods (Scheme 1).
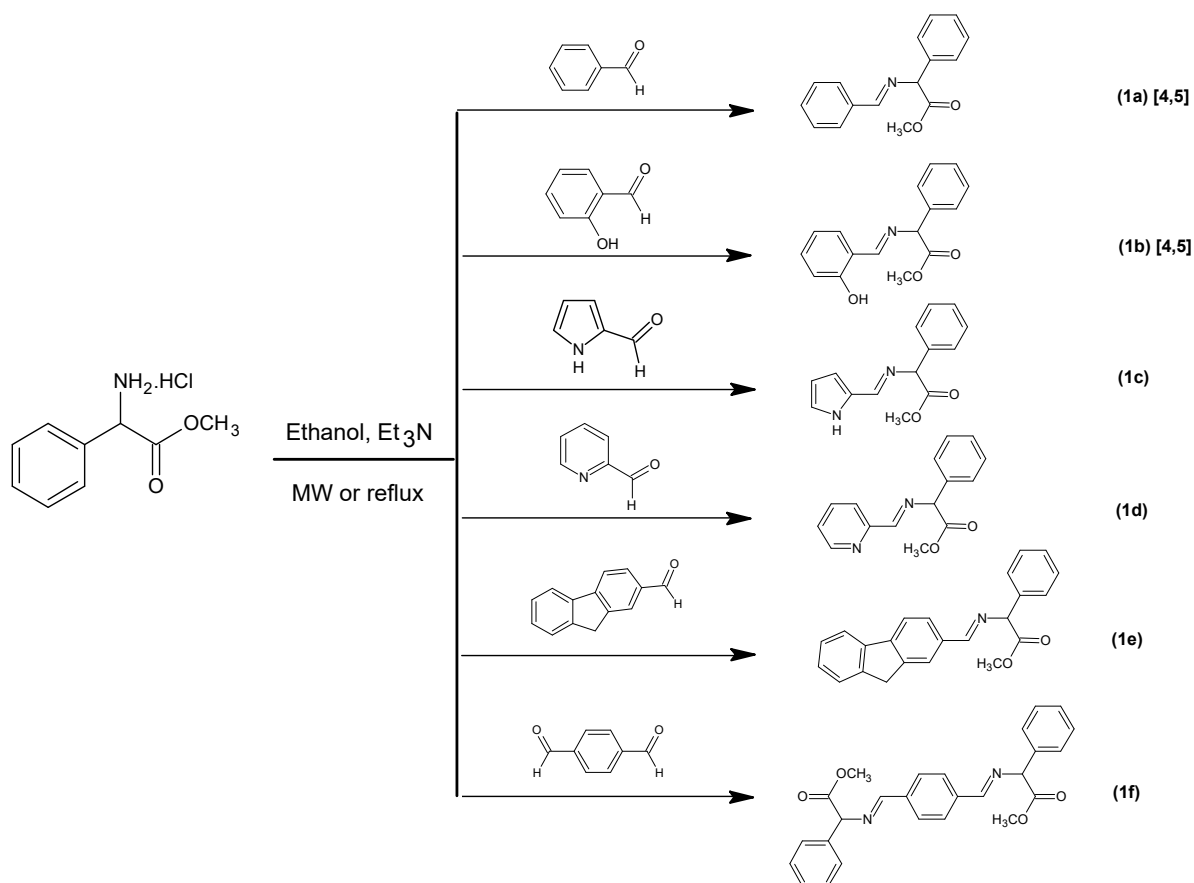
Scheme 1. Synthetic process of compounds (**1a-f**).

Method 1: *Conventional Method for the Synthesis of Methyl 2-[substituted methyleneamino]-2-phenylacetate (**1a-f**)*

The Schiff bases (**1a-f**) were synthesized by the condensation of appropriate aromatic aldehydes (1 mmol) and 2-phenylglycine methyl ester hydrochloride (1 mmol, in case of **1f** 2 mmol, after stirring for half an hour with Et_3N) dissolved in dry ethanol (10 mL). The resulting reaction mixture was stirred and refluxed from 4-8.5h and then allowed to cool overnight. The precipitated Schiff base was filtered, washed with cold ethanol several times, and dried in air at room temperature. The solid product was then recrystallized with ethanol [4, 11, 12].

Method 2: *Microwave Method for the Synthesis of Methyl 2-[substituted methyleneamino]-2-phenylacetate (**1a-f**)*

The suitable ratio (1:1 or 1:2) of appropriate aromatic aldehydes and 2-phenylglycine methyl ester hydrochloride (after stirring for half an hour with Et_3N) were mixed thoroughly in a grinder (Figure 1).

(a)   (b)   (c)   (d)
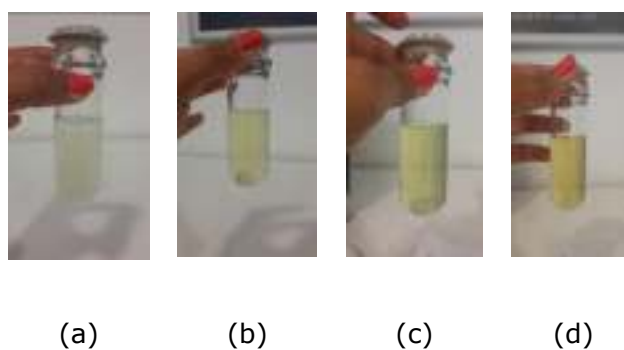
Figure 1. a) Reaction mixture without MW, b) 2 min, c) 6 min, d) 8 min, at 1200 rpm and 100 °C for compound **1f**.

The reaction mixture was then irradiated by the microwave reactor after adding 3-4 mL of dry ethanol at 850 watts and 100°C. The reaction was completed in a short time (5.5-8.5 min) with higher yields. After completion of reaction, the mixture was cooled and the separated solid was filtered and washed with cold ethanol. The resulting product was then recrystallized from ethanol [5, 16, 17].

Characterizations

The physical properties of Schiff base compounds are given in Table 1 (see Supplementary file).

The structures were characterized by using UV, FTIR, ^{1}H NMR, LC-MS spectral data. All data supported the structures of target molecules (Table 2; see Supplementary file).

LC-MS spectra confirmed the molecular weight of all the structures. The LC-MS spectrum for compound **1c** is given in Figure 2.
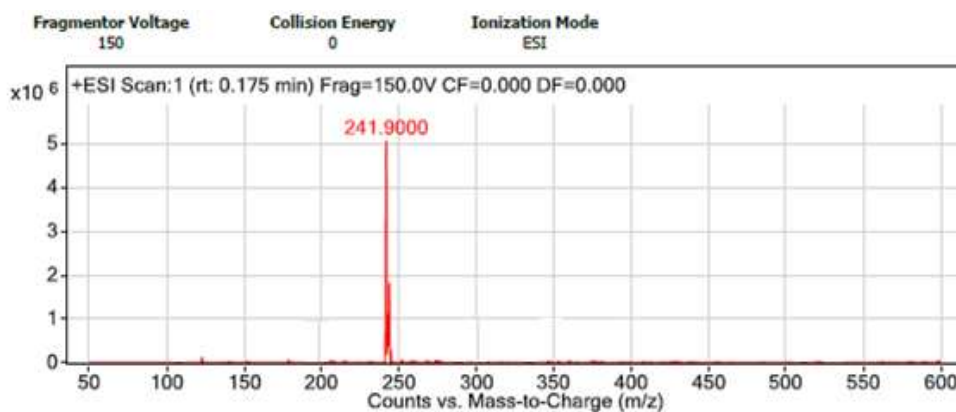
Figure 2. LC-MS spectrum for compound **1c**.

DPPH Radical Scavenging Studies

1,1-diphenyl-2-picryhyrazyl radical (DPPH•) is a stable free radical which surveys the antioxidant potential of pure compounds by an easy colorimetric method. The method is based on the guideline that accepting a hydrogen atom from the antioxidant scavenger compound DPPH• turns DPPH and the change in the color of purple to yellow is screened by spectrophotometric means at 517 nm. Higher free radical scavenging activity is designated by lower absorbance of DPPH$^{•+}$ sample mixture measured at the concerned wavelength [11, 18].

According to the DPPH radical scavenging protocol, a 1-mL aliquot of the samples at determined concentration (50 µg\mL) were added to 2 mL of DPPH solution and the absorbance of DPPH reagent was determined at 517 nm after 30 min. of incubation at the dark [19].

RESULTS AND DISCUSSION

Schiff bases **1a-f** were synthesized by the condensation reaction of 2-phenylglycine methyl ester with different aromatic aldehydes under microwave assisted method as well as conventional method.

Compounds **1a-f** were completed by heating at reflux temperature in conventional method. These reactions were continued longer time than microwave method.

All reactions under microwave irradiation were performed successfully at 850 watts and 100 °C. As a result of microwave-assisted synthesis, it was observed that the reaction was completed in a short time with higher yields as compared to the conventional method.

Based on these results, with the help of microwave synthesis, the yield of product increased from 37% up to 96% as compared to conventional method. By microwave, reactions were completed within 5.5-8.5 minutes and the products were obtained in good to high yields, with reduced time, waste, and formation byproduct. The microwave assisted reactions were seen in the reaction period and yields improved significantly. The comparison study data of microwave and conventional methods are given in the Table 3 (see Supplementary file).

Synthesized compounds **1a-f** were characterized by UV, FTIR, ^{1}H NMR and LC-MS spectral data. The UV-Vis electronic spectra of the Schiff bases showed absorption bands that could be attributed to π-π* and n-π* electronic transitions. Maximum wavelength values of Schiff bases have been shown in Table 2 (see Supplementary file). The FTIR spectra showed that the band of C=N imine stretching vibration appeared for the Schiff bases in the range of 1608-1653 cm^{-1}. The ^{1}H-NMR spectra of **1a-f** showed the characteristic chemical shifts in CDCl$_3$. The singlet signals at 2.11-2.18 ppm were attributed to the protons of the OCH$_3$ moiety, the multiplet signals at 6.58 to 7.98 ppm showed aromatic protons. The most important singlet signals at 8.51-8.65 ppm were attributed to protons of the CH=N groups.

All the compounds **(1a-f)** showed good free radical scavenging activity by inhibiting DPPH radical in a concentration-dependent manner. Figure 3 depicts the percentage for antioxidant activity of the synthesized compounds at the concentration of 50 µg/mL.
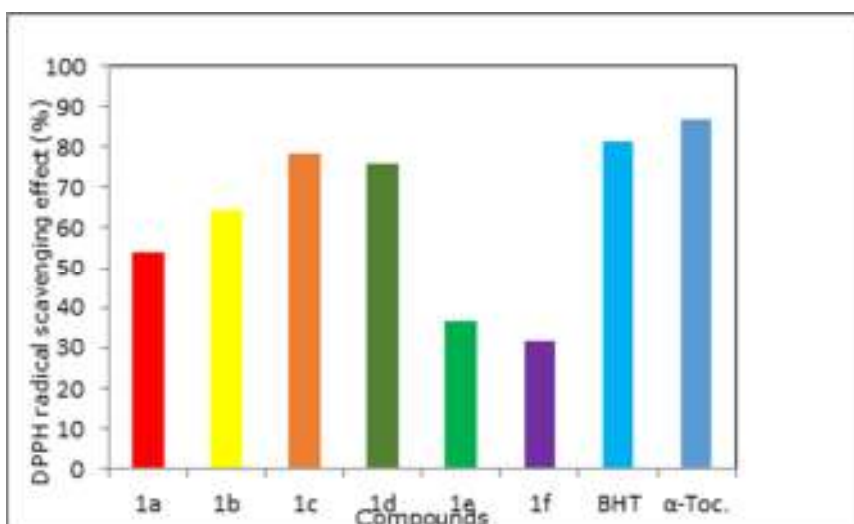
Figure 3 DPPH· scavenging effect (%) of the Schiff bases (**1a-f**).

Compound **1c,** with pyrrole ring, exhibited the best antioxidant activity of 78.27% which is similar to that of reference antioxidants, butylated hydroxytoluene (BHT) and α-tocopherol. Several positive correlations were observed among the structure and antioxidant activities.

ACKNOWLEDGEMENT

REFERENCES

1.   Sari N, Gurkan P. Some Novel Amino Acid-Schiff Bases and their Complexes Synthesis, Characterization, Solid State Conductivity Behaviors and Potentiometric Studies. Z Naturforsch B. 2014 Jun;59(6):692–8. DOI: 10.1515/znb-2004-0610.

2.   Fei-Ran L, Xin Z, Dong-Dong W, Zhi-Na X, Ying-Ke M. Syntheses, Crystal Structures and Antibacterial Activities of Schiff Base Ligand and Its Nickel (II) Complex. CHINESE JOURNAL OF STRUCTURAL CHEMISTRY. 2014;33(9):1367–1374. URL: http://manu30.magtech.com.cn/jghx/EN.

3.   Al-Salami B, Abd Ul-Saheb R, Asker K. Synthesis spectral, thermal stability and antibacterial activity of schiff bases derived from alanine and threonine and their complexes. Journal of Chemical and Pharmaceutical Research. 2015;7(8):792–803. URL : http://jocpr.com/vol7-iss8-2015/JCPR-2015-7-8-792-803.pdf.

4.   Alavi H, Taheri M, Daryani M. Enantio Selective Synthesis of Chairal Alfa Amino Acids by Phase Transfer Catalysts. Orient J Chem. 2013;29(1):135–43. URL:

http://www.orientjchem.org/dnload/Haniyeh-Alavi-Milad-Taheri3CSUP3E-3C2FSUP3E-and-Mehdi-Daryani/OJCV029I01P135-143.pdf.

5.   Kaid Slimane R, Djafri A, Djafri F. The use of bentonite in heterogeneous medium as an efficient recyclable catalyst in the synthesis of iminoesters. Mediterranean Journal of Chemistry. 2011 Apr 20;1(1):1–7. DOI: 10.13171/mjc.1.1.2011.20.04.20

6.   Bashiardes G, Cano C, Mauze B. Regio- and Enantioselective Synthesis of Novel Functionalized Pyranopyrrolidines by 1,3-Dipolar Cycloaddition of Carbohydrates. ChemInform [Internet]. 2005 Aug 9 [cited 2016 Jul 20];36(32). DOI: 10.1002/chin.200532134.

7.   Padwa A, Verlag T. Science of synthesis: Houben-Weyl methods of molecular transformations. 5th ed. Stuttgart ; New York: Thieme; 2000. 48 p. First volume ISBN: 978-3-13-112131-8.

8.   Zheng Y, Jiang A. Asymmetric Synthesis of 2, 4-Dihydroxymethylpyrrolidine Derivatives and Their Inducing Ability for Epoxidation of Olefins. Chinese Journal of Organic Chemistry. 2003;23(10):1114–1119. URL: http://sioc-journal.cn/Jwk_yjhx/EN/Y2003/V23/I10/1114.

9. Márquez A, Rodríguez H, Morales E, Quintanar C, Chuaqui C. SYNTHESIS AND STEREOCHEMISTRY OF BICYCLIC PYRROLIDINES OBTAINED BY 1, 3-DIPOLAR CYCLOADDITION BETWEEN ALPHA-AMINO-ACID ARYLESTERS AND MALEIMIDES. BOLETIN DE LA SOCIEDAD CHILENA DE QUIMICA. 1991;36(1):43–55. URL: http://hdl.handle.net/10533/54505.

10. Sharma P, Dubey S. SYNTHESIS AND STRUCTURAL STUDIES OF IRON (II) COMPLEXES WITH N-SALICYLIDENE-(2-HYDROXY-1-NAPHTHYLIDENE) AMINO AND N-(2-HYDROXY-1-NAPHTHYLIDENE) AMINO ACIDS. Vol. 33. COUNCIL SCIENTIFIC INDUSTRIAL RESEARCH PUBL & INFO DIRECTORATE, NEW DELHI 110012, INDIA; 1994. 1113–1115 p.

11. Wei Q-Y, Xiong J-J, Jiang H, Zhang C, Ye W. The antimicrobial activities of the cinnamaldehyde adducts with amino acids. International journal of food microbiology. 2011;150(2):164–170. URL: http://www.ncbi.nlm.nih.gov/pubmed/21856030.

12. Ando R, Inden H, Sugino M, Ono H, Sakaeda D, Yagyu T, et al. Spectroscopic characterization of amino acid and amino acid ester–Schiff-base complexes of oxovanadium and their catalysis in sulfide oxidation. Inorganica Chimica Acta. 2004 Mar;357(5):1337–44. DOI: 10.1016/j.ica.2003.10.030.

13. Panda J, Sahoo BM, Mishra NK, Padhi SK, Mishra J. Microwave Mediated Organic Reaction: A Convenient Approach for Rapid and Efficient Synthesis of Biologically Active Substituted 1,3-Dihydro-2H-indol-2-one Derivatives. Journal of Nanomaterials. 2013;2013:1–8. DOI: 10.1155/2013/272598.

14. Abirami M, Nadaraj V. Synthesis of Schiff Base under Solvent-free Condition: As a Green Approach. Int J ChemTech Res. 2014;6(4):2534–2538. URL: http://www.academia.edu/download/34362507/In_J_chem_tech.pdf.

15. Naglah AM, Awad HM, Bhat MA, Al-Omar MA, Amr AE-GE. Microwave-Assisted Synthesis and Antimicrobial Activity of Some Novel Isatin Schiff Bases Linked to Nicotinic Acid via Certain Amino Acid Bridge. Journal of Chemistry. 2015;2015:1–8. DOI: 10.1155/2015/364841.

16. Mishra AP. Microwave induced synthesis and characterization of semiconducting 2-thiophenecarboxaldehyde metal complexes. Advanced Materials Letters. 2012 Jul 1;3(3):213–9. DOI: 10.5185/amlett.2011.9307.

17. Sharma K, Singh R, Fahmi N, Singh RV. Microwave assisted synthesis, characterization and biological evaluation of palladium and platinum complexes with azomethines. Spectrochimica Acta Part A: Molecular and Biomolecular Spectroscopy. 2010 Jan;75(1):422–7. DOI: 10.1016/j.saa.2009.10.052.

18. Peksel A. Evaluation of antioxidant and antifungal potential of Asphodelus aestivus Brot. growing in Turkey. Journal of Medicinal Plants Research [Internet]. 2012 Jan 16 [cited 2016 Jul 20];6(2). DOI: 10.5897/JMPR11.1229.

19. Amarowicz R, Estrella I, Hernández T, Robredo S, Troszyńska A, Kosińska A, et al. Free radical-scavenging capacity, antioxidant activity, and phenolic composition of green lentil (Lens culinaris). Food Chemistry. 2010 Aug;121(3):705–11. DOI: 10.1016/j.foodchem.2010.01.009.

Yeni Amino Asit Schiff Bazlarının Yeşil Yöntemle Sentezi ve Biyolojik Aktiviteleri

Cigdem Yorur-Goreci[1*], Zulal Demir[1], Nilay Altas[1]

[1]Yıldız Teknik Üniversitesi, Fen-Edebiyat Fakültesi, Kimya Bölümü, 34210 Istanbul.

Öz: Bu çalışmada, dört yeni ve iki bilinen amino asit Schiff bazı bileşikleri benzaldehit, salisilaldehit, pirol-2-karbaldehit, piridin-2-karbaldehit, fluoren-2-karbaldehit ve tereftalaldehit ile 2-fenilglisin metil ester hidroklorürü arasındaki kondensasyon reaksiyonundan geleneksel ve mikrodalga yöntemleriyle sentezlenmiştir. Yeni bileşikler FTIR, ^{1}H-NMR, LC-MS ve elektronik spektral çalışmalarla karakterize edilmiştir. Geleneksel ısıtma ve mikrodalga uyarması arasında karşılaştırma yapılmış ve bildirilmiştir. Bu sonuçlara göre, mikrodalga sentezi ile ürünlerin verimi %37'den %96'ya yükselmiştir Mikrodalga ile, tepkimeler 5,5-8,5 dakika arasında tamamlanmış ve ürünler iyi ve yüksek verimlerle, azalmış durumdaki reaksiyon süresi, atık ve yan ürünler ile ele geçmiştir. DPPH (2,2-difenil-1-pikrilhidrazil) radikal süpürme etkisi de yeni bileşiklerin antioksidan aktivitesi belirlenmiştir. Bütün bileşikler etkili bir biçimde DPPH radikal süpürme özelliği göstermektedir.

Anahtar Kelimeler: Antioksidan aktivite, yeşil sentez, mikrodalga, Schiff bazları.

Sunulma: 01 Temmuz 2016. **Düzeltme:** 19 Temmuz 2016. **Kabul:** 19 Temmuz 2016.

(This article was presented to the 28th National Chemistry Congress and submitted to JOTCSA as a full manuscript)

The Syntheses and Structural Characterizations, Antimicrobial Activity, and *in vitro* DNA Binding of 4-Fluorobenzylspiro(N/O)Cyclotriphosphazenes and their Phosphazenium Salts

Gamze Elmas[1,*], Aytuğ Okumuş[1], Zeynel Kılıç[1], L. Yasemin Gönder[2], Leyla Açık[3], Tuncer Hökelek[4]

[1]Ankara University, 06100, Ankara, Turkey
[2]The Turkish Sugar Authority, 06510, Ankara, Turkey
[3]Gazi University, 06500, Ankara, Turkey
[4]Hacettepe University, 06800, Ankara, Turkey

Abstract: In the present study, the condensation reaction of $N_3P_3Cl_6$ (**1**) with sodium 3-(4-fluorobenzylamino)-1-propanoxide gave partly substituted 4-fluorobenzylspirocyclotriphosphazene (**2**). The Cl replacement reactions of **2** with excess benzylamine, n-hexylamine, n-butylamine and n-propylamine led to the formation of the corresponding 4-fluorobenzylspiro(N/O)tetrabenzylamino (**3a**), tetrahexylamino (**3b**), tetrabutylamino (**3c**) and tetrapropylamino (**3d**) cyclotriphosphazenes. With the protic ionic liquids (PILs), phosphazenium salts (**4a-4d**), were obtained from the reactions of the corresponding phosphazene bases (**3a**-**3d**) with gentisic acid in dry THF. The structures of all the isolated cyclotriphosphazene derivatives were determined by elemental analyses, FTIR and ^1H, $^{13}C\{^1H\}$, $^{31}P\{^1H\}$ NMR techniques. The crystal structure of **4d** was verified by X-ray diffraction analysis. All the compounds were screened for antibacterial and antifungal activities against bacteria and yeast strains. The interactions of the compounds with supercoiled pUC18 plasmid DNA were investigated.

*Corresponding author: Gamze Elmas. E-mail: gegemen@ankara.edu.tr, tel: +90 0312 2126720/1195.

INTRODUCTION

Hexachlorocyclotriphosphazene, $N_3P_3Cl_6$, is one of the best known and studied one as the starting compound in the family of inorganic heterocyclic ring systems [1]. Various cyclotriphosphazene derivatives have been prepared from the Cl replacement reactions of $N_3P_3Cl_6$ with the different nucleophiles [2]. The condensation reactions of $N_3P_3Cl_6$ with excess monodentate and bidentate ligands resulted in the formation of fully substituted cyclotriphosphazenes [3]. For instance, there are several studies in the literature on the reactions of cyclotriphosphazenes with NO donor type difunctional reagents [4-6]. Some of the cyclotriphosphazene derivatives are used as liquid crystals [7,8], rechargeable lithium-ion batteries [9,10], OLEDs [11,12], and lubricants [13,14]. It is found that aminocyclophosphazene derivatives have antimicrobial activity against bacteria and fungi [15-17]. The interactions between DNA and the phosphazene derivatives have also been investigated in the two last decades [18,19].

On the other hand, the oldest protic ionic liquids (PILs), *e.g.* ethanolammonium nitrate and ethylammonium nitrate were reported in 1888 and 1914 by Gabriel and Walden, respectively [20]. The amine-based PILs were also reported by Bicak [21] and by Karadag [22]. Nevertheless, there is only one paper about the PILs based on cyclotriphosphazene with salicylic acid in the literature [23].

The present study is focused on the preparation of the partly substituted 4-fluorobenzylspirocyclotriphosphazene (**2**), and the fully substituted phosphazene ligands (**3a**-**3d**) for the goal of the preparation of the PILs (**4a-4d**) of the phosphazene ligands with gentisic acid. In addition, this paper also describes features of spectroscopic crystallographic properties, the evaluation of antimicrobial activity, and DNA interactions of all the compounds.

EXPERIMENTAL SECTION

Materials and Methods: $N_3P_3Cl_6$ (Aldrich), 4-fluorobenzaldehyde, 3-amino-1-propanol, benzylamine, n-hexylamine, n-butylamine, n-propylamine and 2,5-dihydroxybenzoic acid (Merck) were purchased. The solvents were distilled by standard methods before use. All the Cl replacement reactions were carried out under argon atmosphere and the reactions were monitored using thin-layer chromatography (TLC) on Merck DC Alufolien Kiesegel 60 B254 sheets in different solvents. Column chromatography was performed on Merck Kiesegel 60 (230-400 mesh ATSM) silica gel. The melting points were determined on a Gallenkamp apparatus using a capillary tube and are uncorrected. The FTIR spectra of all the phosphazenes were recorded on a Jasco FT/IR-430 spectrometer in KBr discs and reported in cm^{-1} units. The mass spectra (ESI-MS) of the phosphazenes were recorded on the Waters 2695 Alliance Micromass ZQ spectrometer. Elemental analyses were carried out by using a Leco CHNS-932 instrument (microanalytical service of Ankara University). ^{1}H and $^{13}C\{^{1}H\}$ NMR spectra were recorded on a Varian Mercury FT-NMR (400 MHz) spectrometer (SiMe$_4$ as an internal standard), operating at 400.13 and 100.62 MHz, respectively. The spectrometer was equipped with a 5 mm PABBO BB inverse-gradient probe, and standard Bruker pulse programs [24] were used. The $^{31}P\{^{1}H\}$ NMR spectra of the cyclotriphosphazenes were obtained on a Bruker Ascend^{TM} 600 ULH spectrometer (85% H_3PO_4 as an external standard), operating at 242.93 MHz.

Synthesis of 3-(4-fluorobenzylamino)-1-propanol: A solution of 3-amino-1-propanol (1.20 g, 16.0 mmol) in ethanol (25 mL) was added into the solution of 4-fluorobenzaldehyde (2.00 g, 16.0 mmol) in ethanol (25 mL) with stirring at -5°C. The mixture was stirred for three days at room temperature. The solvent was evaporated at reduced pressure and the Schiff base (oily product) was obtained. NaBH$_4$ (2.92 g, 76.50 mmol) in a small portion was added into the solution of the Schiff base (2.80 g, 15.30 mmol) in ethanol (150 mL). The mixture was stirred for 24 h, and then the solvent was evaporated at reduced pressure. The crude product was extracted with CHCl$_3$ (3 x 100 mL), and dried over Na$_2$SO$_4$. The colorless oily product was dried overnight *in vacuo*. Yield: 2.60 g (89%). FTIR (KBr, cm^{-1}): v3402 (N-H), 3065 (asymm.), 3028 (symm.) (C-H arom.),1030 (C-F). ^{1}H NMR (400 MHz, CDCl$_3$, ppm): δ 7.25(dd, 2H, $^3J_{FH}$=5.4 Hz, $^3J_{HH}$=8.6 Hz, $H_3$and H_5), 6.98(dd, 2H, $^3J_{FH}$=8.8 Hz, $^3J_{HH}$=8.6 Hz, $H_2$and H_6), 3.71 (s, 2H, Ar-CH_2-N), 3.70 (t, 2H, $^3J_{HH}$=6.4 Hz, O-CH_2), 3.61 (b, 2H, NH and OH),2.80 (t, 2H, $^3J_{HH}$=6.0 Hz, N-CH_2), 1.70 (m, 2H, $^3J_{HH}$=6.4 Hz, $^3J_{HH}$=6.0 Hz, N-CH$_2$-CH_2). ^{13}C NMR (100 MHz, CDCl$_3$, ppm): δ 161.94 (d, $^1J_{FC}$=244.5 Hz, C_1), 135.12(d, $^4J_{FC}$=2.5 Hz, C_4), 129.77 (d, $^3J_{FC}$=7.8 Hz, C_3 and C_5), 115.19 (d, $^2J_{FC}$=21.2 Hz, C_2 and C_6), 62.81 (s, O-CH$_2$), 52.98 (s, Ar-CH$_2$-N), 48.17 (s, N-CH$_2$), 31.04 (s, N-CH$_2$-CH$_2$).

Synthesis of compound 2: A total of 4.42 g of N$_3$P$_3$Cl$_6$ (**1**) (12.70 mmol) in dry THF (150 mL) was added into the solution of sodium (3-amino-1-propanoxide) (3.13 g, 15.0 mmol) and triethylamine (7.10 mL, 50.8 mmol) at -10 °C. The mixture was stirred for three days at room temperature. The precipitated triethylammonium hydrochloride and sodium chloride were filtered off and the solvent was evaporated completely. The product was eluted by column chromatography using toluene, and it was crystallized from toluene. Yield: 3.96 g (68%). mp: 71 °C. Anal. Calcd. for C$_{10}$H$_{12}$FCl$_4$N$_4$OP$_3$: C, 26.23; H, 2.64; N, 12.23. Found: C, 26.18; H, 3.05; N, 11.73. ESI-MS (fragments are based on ^{35}Cl, Ir %, Ir designates the fragment abundance percentage): *m/z* 459 ([M+H]$^+$, 100). FTIR (KBr, cm^{-1}): v 3067 (asymm.), 3025 (symm.) (C-H arom.), 2927, 2855(C-H aliph.), 1243 (asymm.), 1198 (symm.) (P=N), 1046 (C-F), 575 (asymm.), 531 (symm.) (PCl). ^{1}H NMR (400 MHz, CDCl$_3$, ppm): δ 7.35 (dd, 2H, $^3J_{FH}$=5.6 Hz, $^3J_{HH}$=8.4 Hz, H_3 and H_5), 7.03 (dd, 2H, $^3J_{FH}$=8.8 Hz, $^3J_{HH}$=8.4 Hz, H_2 and H_6), 4.41 (m, 2H, $^3J_{PH}$=13.6 Hz, $^3J_{HH}$=5.6 Hz, O-CH_2), 3.94 (d, 2H, $^3J_{PH}$=9.6 Hz, Ar-CH_2-N), 3.04 (m, 2H, $^3J_{PH}$=14.0 Hz, $^3J_{HH}$=6.3 Hz, N-CH_2), 1.92 (m, 2H, $^3J_{HH}$=6.3 Hz, $^3J_{HH}$=5.6 Hz, N-CH$_2$-CH_2). ^{13}C NMR (100 MHz, CDCl$_3$, ppm): δ 162.43 (d, $^1J_{FC}$=245.8 Hz, C_1), 131.92 (dd, $^3J_{PC}$=9.6 Hz, $^4J_{FC}$=3.2 Hz, C_4), 130.13 (d, $^3J_{FC}$=8.4 Hz, C_3 and C_5), 115.48 (d, $^2J_{FC}$=21.2 Hz, C_2 and C_6), 62.18 (d, $^2J_{PC}$=7.1 Hz, O-CH$_2$), 50.34 (d, $^2J_{PC}$=3.2 Hz, Ar-CH$_2$-N), 45.43 (s, N-CH$_2$), 25.85 (d, $^3J_{PC}$=4.5 Hz, N-CH$_2$-CH$_2$).

Synthesis of compound 3a: A solution of benzylamine (2.30 mL, 21.0 mmol) in dry THF (50 mL) was slowly added into a stirred solution of triethylamine (0.97 mL, 7.00 mmol) and **2** (0.80 g, 1.80 mmol) in dry THF (100 mL) at room temperature. The mixture was refluxed for over 72 h. The precipitated triethylammonium hydrochloride was filtered off and the solvent was evaporated. The product was purified by column chromatography using toluene-THF (3:2), and the light yellow powder was crystallized from toluene. Yield: 0.80 g (62%). mp: 91 °C. Anal. Calcd. for C$_{38}$H$_{44}$FN$_8$OP$_3$.H$_2$O: C, 60.19; H, 6.11; N, 14.78. Found: C, 60.31; H, 5.73; N, 14.68. ESI-MS (Ir %, Ir designates the fragment abundance percentage): *m/z* 741 ([M+H]$^+$, 100). FTIR (KBr, cm^{-1}): v3374, 3200 (b, N-H), 3063 (asymm.), 3028 (symm.) (C-H arom.), 2954, 2850 (C-H aliph.), 1198 (b, P=N), 1052 (C-F).^{1}H NMR (400 MHz, CDCl$_3$, ppm): δ 7.35 (dd, 2H, $^3J_{FH}$=5.2 Hz, $^3J_{HH}$=8.8 Hz, H_3 and H_5), 7.31 (m, 4H, H_{10} and $H_{10'}$), 7.25 (m, 8H, H_8 and $H_{8'}$), 7.19 (m, 8H, H_9 and $H_{9'}$), 6.96(dd, 2H, $^3J_{FH}$=9.2 Hz, $^3J_{HH}$=8.4 Hz, H_2 and H_6), 4.34 (m, 2H, $^3J_{PH}$=13.2 Hz, $^3J_{HH}$=5.6 Hz, O-CH_2), 4.15 (m, 8H, NH-CH_2), 3.82 (d, 2H, $^3J_{PH}$=7.6 Hz, Ar-CH_2-N), 2.97 (m, 2H, $^3J_{PH}$=13.2 Hz, $^3J_{HH}$=5.2 Hz, N-CH_2), 2.56 (b, 4H, NH), 1.85 (m, 2H, $^3J_{HH}$=5.6 Hz, $^3J_{HH}$=5.2 Hz, N-CH$_2$-CH_2). ^{13}C NMR (100 MHz, CDCl$_3$, ppm): δ

162.02 (d, $^1J_{FC}$=244.6 Hz, C_1), 140.87 (t, $^3J_{PC}$=7.8 Hz, C_7), 140.71 (t, $^3J_{PC}$=7.7 Hz, $C_{7'}$), 134.17 (dd, $^3J_{PC}$=7.7 Hz, $^4J_{FC}$=2.9 Hz, C_4), 129.73 (d, $^3J_{FC}$=7.7 Hz, C_3 and C_5), 128.31 (s, C_8 and $C_{8'}$), 127.44 and 127.31 (s, C_9 and $C_{9'}$), 126.85 and 126.82 (s, C_{10} and $C_{10'}$), 115.00 (d, $^2J_{FC}$=20.7 Hz, C_2 and C_6), 66.36 (d, $^2J_{PC}$=6.9 Hz, O-CH_2), 50.83 (d, $^2J_{PC}$=2.1 Hz, Ar-CH_2-N), 45.95 (s, N-CH_2), 45.09 and 45.00 (s, Ar-CH_2-NH), 26.62 (d, $^3J_{PC}$=3.8 Hz, N-CH$_2$-CH_2).

Synthesis of compound 3b: The work-up procedure was similar to that of compound **3a**, using **2** (0.80 g, 1.80 mmol), n-hexylamine (2.78 mL, 21.0 mmol) and triethylamine (0.97 mL, 7.00 mmol). The product was purified by column chromatography using toluene-THF (3:2), and the yellow oily product was crystallized from toluene. Yield: 0.65 g (52%). Anal. Calcd. for $C_{34}H_{68}FN_8OP_3$: C, 57.00; H, 7.94; N, 14.01. Found: C, 56.23; H, 7.36; N, 13.42. ESI-MS (Ir %): m/z 717 ([M+H]$^+$, 100). FTIR (KBr, cm^{-1}): v 3377, 3244(b, N-H), 3068 (asymm.), 3037 (symm.) (C-H arom.), 2956, 2856(C-H aliph.), 1198 (b, P=N), 1052 (C-F). ^{1}H NMR (400 MHz, CDCl$_3$, ppm): δ 7.39(dd, 2H, $^3J_{FH}$=5.6 Hz, $^3J_{HH}$=8.4 Hz, H_3 and H_5), 6.98(dd, 2H, $^3J_{FH}$=8.8 Hz, $^3J_{HH}$=8.8 Hz, H_2 and H_6), 4.30 (m, 2H, $^3J_{PH}$=12.4 Hz, $^3J_{HH}$=5.2 Hz, O-CH_2), 3.93 (d, 2H, $^3J_{PH}$=7.6 Hz, Ar-CH_2-N), 2.98 (m, 2H, $^3J_{PH}$=13.2 Hz, $^3J_{HH}$=5.2 Hz, N-CH_2), 2.90 (b, 8H, NH-CH_2), 2.24 (b, 4H, NH), 1.82 (m, 2H, $^3J_{HH}$=5.2 Hz, $^3J_{HH}$=4.8 Hz, N-CH$_2$-CH_2), 1.48 (m, 8H, NH-CH$_2$-CH_2), 1.27 (m, 24H, NH-CH$_2$-CH$_2$-(CH_2)$_3$), 0.88 (t, 6H, $^3J_{HH}$=7.2 Hz, CH_3), 0.84 (t, 6H, $^3J_{HH}$=7.2 Hz, CH_3). ^{13}C NMR (100 MHz, CDCl$_3$, ppm): δ 161.91 (d, $^1J_{FC}$=244.5 Hz, C_1), 134.25 (dd, $^3J_{PC}$=10.4 Hz, $^4J_{FC}$=2.6 Hz, C_4), 129.68 (d, $^3J_{FC}$=7.7 Hz, C_3 and C_5), 114.82 (d, $^2J_{FC}$=21.5 Hz, C_2 and C_6), 65.51 (d, $^2J_{PC}$=6.9 Hz, O-CH_2), 50.78 (s, Ar-CH_2-N), 45.74 (s, N-CH_2), 40.97 and 40.85 (s, NH-CH_2), 31.92 (d, $^3J_{PC}$=7.7 Hz,NH-CH$_2$-CH_2), 31.79 (d, $^3J_{PC}$=7.7 Hz,NH-CH$_2$-CH_2), 26.57 (s,N-CH$_2$-CH_2), 22.51 and 22.47 (s, NH-CH$_2$-CH$_2$-(CH_2)$_3$), 13.90 and 13.85 (s, CH_3).

Synthesis of compound 3c: The work-up procedure was similar to that of compound **3a**, using **2** (0.80 g, 1.80 mmol), n-butylamine (2.10 mL, 21.0 mmol) and triethylamine (0.97 mL, 7.00 mmol). The product was eluted by column chromatography using toluene-THF (3:2), and the light yellow powder was crystallized from toluene. Yield: 0.75 g (71%). mp: 53 °C. Anal. Calcd. for $C_{26}H_{52}FN_8OP_3 \cdot H_2O$: C, 50.18; H, 8.75; N, 18.00. Found: C, 50.74; H, 8.26; N, 17.96. ESI-MS (Ir %): m/z 607 ([M+H]$^+$, 100). FTIR (KBr, cm^{-1}): v 3386, 3243(b, N-H), 3068 (asymm.), 3040 (symm.) (C-H arom.), 2958, 2869(C-H aliph.), 1202(b, P=N), 1053(C-F). ^{1}H NMR (400 MHz, CDCl$_3$, ppm): δ 7.40(dd, 2H, $^3J_{FH}$=5.2 Hz, $^3J_{HH}$=8.4 Hz, H_3 and H_5), 6.99(dd, 2H, $^3J_{FH}$=8.8 Hz, $^3J_{HH}$=8.4 Hz, H_2 and H_6), 4.30 (m, 2H, $^3J_{PH}$=12.4 Hz, $^3J_{HH}$=5.6 Hz, O-CH_2), 3.92 (d, 2H, $^3J_{PH}$=7.2 Hz, Ar-CH_2-N), 2.96 (m, 2H, $^3J_{PH}$=13.6 Hz, $^3J_{HH}$=5.6 Hz, N-CH_2), 2.89 (b, 8H, NH-CH_2), 2.13 (b, 4H, NH), 1.80 (m, 2H, $^3J_{HH}$=5.6 Hz, $^3J_{HH}$=5.2 Hz, N-CH$_2$-CH_2), 1.47 (m, 8H, NH-CH$_2$-CH_2), 1.33 (m, 8H, NH-CH$_2$-CH$_2$-CH_2), 0.90 (t, 6H, $^3J_{HH}$=7.6 Hz, CH_3), 0.83 (t, 6H, $^3J_{HH}$=7.6 Hz, CH_3). ^{13}C NMR (100 MHz, CDCl$_3$, ppm): δ 161.97 (d, $^1J_{FC}$=244.6 Hz, C_1), 134.38 (dd, $^3J_{PC}$=10.4 Hz, $^4J_{FC}$=2.7 Hz, C_4), 129.78 (d, $^3J_{FC}$=7.8 Hz, C_3 and C_5), 114.90 (d, $^2J_{FC}$=20.6 Hz, C_2 and C_6), 66.09 (d, $^2J_{PC}$=6.9 Hz, O-CH_2), 50.88 (d, $^2J_{PC}$=2.3 Hz,Ar-CH_2-N), 45.85 (s, N-CH_2), 40.70 and 40.59 (s, NH-CH_2), 34.09 (d, $^3J_{PC}$=8.5 Hz,NH-CH$_2$-CH_2), 34.00 (d, $^3J_{PC}$=8.5 Hz,NH-CH$_2$-CH_2), 26.57 (d,$^3J_{PC}$=3.0 Hz,N-CH$_2$-CH_2), 20.07 and 20.04 (s, NH-CH$_2$-CH_2-CH$_2$), 13.82 and 13.74 (s, CH_3).

Synthesis of compound 3d: The work-up procedure was similar to that of compound **3a**, using **2** (0.80 g, 1.80 mmol), n-propylamine (1.73 mL, 21.0 mmol) and triethylamine (0.97 mL, 7.00 mmol). The product was purified by column chromatography using toluene-THF (3:2), and and the light yellow powder was crystallized from toluene. Yield: 0.73 g (76%). mp: 77 °C. Anal. Calcd. for $C_{22}H_{44}FN_8OP_3$: C, 57.00; H, 8.01; N, 13.99.

Found: C, 56.23; H, 7.36; N, 13.42. ESI-MS (Ir %): m/z 549 ([M+H]$^+$, 100). FTIR (KBr, cm^{-1}): v 3371, 3237(b, N-H), 3068 (asymm.), 3033 (symm.) (C-H arom.), 2957, 2853(C-H aliph.), 1204(b, P=N), 1051(C-F). ^{1}H NMR (400 MHz, CDCl$_3$, ppm): δ 7.37(dd, 2H, $^3J_{FH}$=5.6 Hz, $^3J_{HH}$=8.8 Hz, H_3 and H_5), 6.96(dd, 2H, $^3J_{FH}$=8.8 Hz, $^3J_{HH}$=8.8 Hz, H_2 and H_6), 4.28 (m, 2H, $^3J_{PH}$=12.4 Hz, $^3J_{HH}$=5.6 Hz, O-CH_2), 3.89 (d, 2H, $^3J_{PH}$=7.6 Hz, Ar-CH_2-N), 2.92 (m, 2H, $^3J_{PH}$=13.2 Hz, $^3J_{HH}$=5.6 Hz, N-CH_2), 2.84 (b, 8H, NH-CH_2), 2.14 (b, 4H, NH), 1.78 (m, 2H, $^3J_{HH}$=5.6 Hz, $^3J_{HH}$=5.2 Hz, N-CH$_2$-CH_2), 1.46 (m, 8H, NH-CH$_2$-CH_2), 0.88 (t, 6H, $^3J_{HH}$=7.2 Hz, CH_3), 0.81 (t, 6H, $^3J_{HH}$=7.6 Hz, CH_3). ^{13}C NMR (100 MHz, CDCl$_3$, ppm): δ 161.99 (d, $^1J_{FC}$=244.6 Hz, C_1), 134.41 (dd, $^3J_{PC}$=10.0 Hz, $^4J_{FC}$=2.8 Hz, C_4), 129.82 (d, $^3J_{FC}$=7.7 Hz, C_3 and C_5), 114.92 (d, $^2J_{FC}$=21.5 Hz, C_2 and C_6), 66.11 (d, $^2J_{PC}$=6.9 Hz, O-CH$_2$), 50.89 (d, $^2J_{PC}$=3.0 Hz,Ar-CH$_2$-N), 45.87 (s, N-CH$_2$), 42.81 and 42.73 (s, NH-CH$_2$), 26.58 (d, $^3J_{PC}$=3.0 Hz,N-CH$_2$-CH$_2$), 25.07 (d, $^3J_{PC}$=6.9 Hz,NH-CH$_2$-CH$_2$), 24.99 (d, $^3J_{PC}$=8.4 Hz,NH-CH$_2$-CH$_2$), 11.44 and 11.35 (s, CH$_3$).

Synthesis of compound 4a: A solution of **3a** (0.50 g, 0.67 mmol) in dry THF (30 mL) was slowly added by the dropwise addition of gentisic acid (0.10 g, 0.67 mmol) in dry THF (10 mL) at room temperature. The reaction mixtures were refluxed for over 30 h. Afterwards, the solvent was evaporated under vacuum, and the light yellow oily crude product was crystallized from toluene. Yield: 0.45 g (75%). mp: 62 °C. Anal. Calcd. for C$_{45}$H$_{50}$FN$_8$O$_5$P$_3$.H$_2$O: C, 59.27; H, 5.75; N, 12.28. Found: C, 58.81; H, 5.05; N, 11.82. FTIR (KBr, cm^{-1}): v 3277 (b, N-H), 3062 (asymm.), 3029 (symm.) (C-H arom.), 2923, 2858 (C-H aliph.), 2668 (N$^+$-H), 1571 (asymm.), 1377 (symm.) (COO$^-$), 1260 (b, P=N), 1050 (C-F). ^{1}H NMR (400 MHz, CDCl$_3$, ppm): δ 7.70 (b, 1H, H_b), 7.26-7.03 (m, 24H, H_3, H_5, H_8, $H_{8'}$, H_9, $H_{9'}$, H_{10}, $H_{10'}$, H_d and H_e), 6.93(dd, 2H, $^3J_{FH}$=8.8 Hz, $^3J_{HH}$=8.4 Hz, H_2 and H_6), 4.24 (m, 2H, $^3J_{PH}$=12.4 Hz, $^3J_{HH}$=6.0 Hz, O-CH_2), 3.98 (m, 8H, NH-CH_2), 3.80 (b, 4H, NH), 3.61 (d, 2H, $^3J_{PH}$=7.6 Hz, Ar-CH_2-N), 2.89 (m, 2H, $^3J_{PH}$=12.8 Hz, $^3J_{HH}$=6.0 Hz, N-CH_2), 2.34 (s, 1H, NH), 1.80 (m, 2H, $^3J_{HH}$=5.2 Hz, $^3J_{HH}$=4.4 Hz, N-CH$_2$-CH_2). ^{13}C NMR (100 MHz, CDCl$_3$, ppm): δ 175.05 (s, COO$^-$), 162.17 (d, $^1J_{FC}$=245.3 Hz, C_1), 155.26 (s, C_f), 148.09 (s, C_c), 139.44 (t, $^3J_{PC}$=6.0 Hz, C_7), 139.31 (t, $^3J_{PC}$=6.0 Hz, $C_{7'}$), 132.92 (dd, $^3J_{PC}$=7.6 Hz, $^4J_{FC}$=2.8 Hz, C_4), 129.64 (d, $^3J_{FC}$=7.7 Hz, C_3 and C_5), 128.46 and 128.42 (s, C_8 and $C_{8'}$), 127.44 and 127.23 (s, C_9 and $C_{9'}$), 127.16 and 127.10 (s, C_{10} and $C_{10'}$), 121.70 (s, C_a), 117.55 (s, C_d), 117.32 (s, C_e), 116.32 (s, C_b), 115.22 (d, $^2J_{FC}$=21.5 Hz, C_2 and C_6), 67.49 (d, $^2J_{PC}$=6.1 Hz, O-CH$_2$), 50.17 (s, Ar-CH$_2$-N), 45.64 (s, N-CH$_2$), 44.77 and 44.76 (s, Ar-CH$_2$-NH), 26.18 (s, N-CH$_2$-CH$_2$).

Synthesis of compound 4b: The work-up procedure was similar to that of compound **4a**, using **3b** (0.50 g, 0.70 mmol) and gentisic acid (0.11 g, 0.70 mmol). The reaction mixture was refluxed for over 30 h. Afterwards, the solvent was evaporated under reduced pressure, and the light yellow oily crude product was crystallized from toluene. Yield: 0.49 g (80%). mp: 90 °C. Anal. Calcd. for C$_{41}$H$_{74}$FN$_8$O$_5$P$_3$.H$_2$O: C, 54.32; H, 8.67; N, 12.36. Found: C, 54.21; H, 7.84; N, 11.95. FTIR (KBr, cm^{-1}): v 3263(b, N-H), 3065 (asymm.), 3040 (symm.) (C-H arom.), 2956, 2857(C-H aliph.), 2667 (N$^+$-H), 1579(asymm.), 1381 (symm.) (COO$^-$), 1257(asymm.), 1193 (symm.) (P=N), 1055(C-F). ^{1}H NMR (400 MHz, CDCl$_3$, ppm): δ 7.59 (b, 1H, $^4J_{HH}$=3.1 Hz, H_b), 7.33 (dd, 2H, $^3J_{FH}$=5.2 Hz, $^3J_{HH}$=8.4 Hz, H_3 and H_5), 7.00 (dd, 2H, $^3J_{FH}$=8.4 Hz, $^3J_{HH}$=8.4 Hz, H_2 and H_6), 6.93 (dd, 1H, $^3J_{HH}$=8.5 Hz, $^4J_{HH}$=3.1 Hz, H_d), 6.77 (d, 1H, $^3J_{HH}$=8.5 Hz, H_e), 4.36 (m, 2H, $^3J_{PH}$=11.6 Hz, $^3J_{HH}$=5.2 Hz, O-CH_2), 3.94 (d, 2H, $^3J_{PH}$=6.0 Hz, Ar-CH_2-N), 3.02 (m, 2H, N-CH_2), 2.86 (b, 8H, NH-CH_2), 2.84 (b, 4H, NH), 2.28 (s, 1H, NH), 1.73 (m, 2H, $^3J_{HH}$=5.2 Hz, N-CH$_2$-CH_2), 1.40 (m, 8H, NH-CH$_2$-CH_2), 1.18 (m, 24H, NH-CH$_2$-CH$_2$-(CH_2)$_3$), 0.85 (t, 6H, $^3J_{HH}$=6.8 Hz, CH_3), 0.78 (t, 6H, $^3J_{HH}$=7.6 Hz, CH_3). ^{13}C NMR (100 MHz, CDCl$_3$, ppm): δ 174.03 (s, COO$^-$), 162.23 (d, $^1J_{FC}$=245.4 Hz, C_1), 155.45 (s, C_f), 148.22 (s, C_c), 132.93 (dd, $^3J_{PC}$=10.0 Hz, $^4J_{FC}$=2.6 Hz, C_4), 129.65 (d, $^3J_{FC}$=7.8 Hz, C_3 and C_5), 122.63 (s, C_a), 117.52 (s, C_d), 115.94 (s, C_b), 115.43 (s, C_e), 115.27 (d, $^2J_{FC}$=21.4 Hz, C_2 and C_6), 67.40 (d, $^2J_{PC}$=4.6 Hz, O-CH$_2$), 50.40 (s, Ar-CH$_2$-N), 45.73 (s, N-CH$_2$), 41.21 and 41.08 (s, NH-

CH_2), 31.64 (d, $^3J_{PC}$=7.0 Hz,NH-CH$_2$-CH_2), 31.53 (d, $^3J_{PC}$=7.8 Hz,NH-CH$_2$-CH_2), 26.45 (s,N-CH$_2$-CH_2), 22.56 and 22.50 (s, NH-CH$_2$-CH$_2$-(CH_2)$_3$), 14.00 and 13.94 (s, CH_3).

Synthesis of compound 4c: The work-up procedure was similar to that of compound **4a**, using **3c** (0.50 g, 0.83 mmol) and gentisic acid (0.13 g, 0.83 mmol). The reaction mixtures were refluxed for over 30 h. Afterwards, the solvent was evaporated under vacuum, and the light yellow oily crude product was crystallized from toluene. Yield: 0.53 g (84%). mp: 87 °C. Anal. Calcd. for C$_{33}$H$_{58}$FN$_8$O$_5$P$_3$: C, 52.27; H, 6.46; N, 14.78. Found: C, 52.40; H, 6.54; N, 14.50.FTIR (KBr, cm^{-1}): v 3361, 3314, 3209 (b, N-H), 3072 (asymm.), 3040 (symm.) (C-H arom.), 2959, 2873 (C-H aliph.), 2667 (N$^+$-H), 1579 (asymm.), 1382 (symm.) (COO$^-$), 1255 (asymm.), 1189 (symm.) (P=N), 1057 (C-F). ^{1}H NMR (400 MHz, CDCl$_3$, ppm): δ 7.69 (b, 1H, $^4J_{HH}$=2.9 Hz, H_b), 7.34 (dd, 2H, $^3J_{FH}$=5.2 Hz, $^3J_{HH}$=8.4 Hz, H_3 and H_5), 6.99 (dd, 2H, $^3J_{FH}$=8.8 Hz, $^3J_{HH}$=8.8 Hz, H_2 and H_6), 6.83 (dd, 1H, $^3J_{HH}$=8.7 Hz, $^4J_{HH}$=2.9 Hz, H_d), 6.73 (d, 1H, $^3J_{HH}$=8.7 Hz, H_e), 4.34 (m, 2H, $^3J_{PH}$=12.0 Hz, $^3J_{HH}$=6.4 Hz, O-CH_2), 3.94 (d, 2H, $^3J_{PH}$=6.0 Hz, Ar-CH_2-N), 3.01 (m, 2H, N-CH_2), 2.86 (b, 8H, NH-CH_2), 2.85 (b, 4H, NH), 2.35 (s, 1H, NH), 1.86 (m, 2H, $^3J_{HH}$=6.4 Hz, N-CH$_2$-CH_2), 1.46 (m, 4H, NH-CH$_2$-CH_2), 1.38 (m, 4H, NH-CH$_2$-CH_2), 1.32 (m, 4H, NH-CH$_2$-CH$_2$-CH_2), 1.18 (m, 4H, NH-CH$_2$-CH$_2$-CH_2), 0.85 (t, 6H, $^3J_{HH}$=7.4 Hz, CH_3), 0.73 (t, 6H, $^3J_{HH}$=7.4 Hz, CH_3). ^{13}C NMR (100 MHz, CDCl$_3$, ppm): δ 174.91 (s, COO$^-$), 162.20 (d, $^1J_{FC}$=244.6 Hz, C_1), 155.20 (s, C_f), 148.09 (s, C_c), 133.03 (dd, $^3J_{PC}$=6.7 Hz, $^4J_{FC}$=2.7 Hz, C_4), 129.67 (d, $^3J_{FC}$=8.4 Hz, C_3 and C_5), 121.43 (s, C_a), 117.53 (s, C_d), 117.10 (s, C_e), 116.36 (s, C_b), 115.24 (d, $^2J_{FC}$=21.5 Hz, C_2 and C_6), 67.21 (d, $^2J_{PC}$=4.6 Hz, O-CH_2), 50.43 (s, Ar-CH_2-N), 45.75 (s, N-CH_2), 40.81 and 40.73 (s, NH-CH_2), 33.62 (d, $^3J_{PC}$=6.1 Hz,NH-CH$_2$-CH_2), 33.58 (d, $^3J_{PC}$=6.2 Hz,NH-CH$_2$-CH_2), 26.21 (d, $^3J_{PC}$=3.2 Hz,N-CH$_2$-CH_2), 19.87 and 19.83 (s, NH-CH$_2$-CH$_2$-CH$_2$), 13.70 and 13.57 (s, CH_3).

Synthesis of compound 4d: The work-up procedure was similar to that of compound **4a**, using **3d** (0.50 g, 0.90 mmol) and gentisic acid (0.14 g, 0.90 mmol). The reaction mixtures were refluxed for over 30 h. Afterwards, the solvent was evaporated under vacuum, and the light yellow oily crude product was crystallized from toluene. Yield: 0.55 g (86%). mp: 114 °C. Anal. Calcd. for C$_{29}$H$_{50}$FN$_8$O$_5$P$_3$.H$_2$O: C, 48.36; H, 7.28; N, 15.56. Found: C, 48.88; H, 6.81; N, 15.37. FTIR (KBr, cm^{-1}): v3373, 3289(b, N-H), 3062 (asymm.), 3033 (symm.) (C-H arom.), 2962, 2875 (C-H aliph.), 2669 (N$^+$-H), 1580(asymm.), 1372 (symm.) (COO$^-$), 1256 (asymm.), 1218 (symm.) (P=N), 1046(C-F). ^{1}H NMR (400 MHz, CDCl$_3$, ppm): δ 7.70 (b, 1H, $^4J_{HH}$=3.1 Hz, H_b), 7.33(dd, 2H, $^3J_{FH}$=5.6 Hz, $^3J_{HH}$=8.8 Hz, H_3 and H_5), 6.99(dd, 2H, $^3J_{FH}$=8.8 Hz, $^3J_{HH}$=8.8 Hz, H_2 and H_6), 6.82 (dd, 1H, $^3J_{HH}$=8.9 Hz, $^4J_{HH}$=3.1 Hz, H_d), 6.73 (d, 1H, $^3J_{HH}$=8.9 Hz, H_e), 4.33 (m, 2H, $^3J_{PH}$=11.6 Hz, $^3J_{HH}$=6.4 Hz, O-CH_2), 3.93 (d, 2H, $^3J_{PH}$=6.0 Hz, Ar-CH_2-N), 2.99 (m, 2H, N-CH_2), 2.83 (b, 8H, NH-CH_2), 2.80 (b, 4H, NH), 2.35 (s, 1H, NH), 1.86 (m, 2H, $^3J_{HH}$=6.4 Hz, N-CH$_2$-CH_2), 1.48 (m, 4H, NH-CH$_2$-CH_2), 1.41 (m, 4H, NH-CH$_2$-CH_2), 0.86 (t, 6H, $^3J_{HH}$=7.4 Hz, CH_3), 0.74 (t, 6H, $^3J_{HH}$=7.5 Hz, CH_3).^{13}C NMR (100 MHz, CDCl$_3$, ppm): δ 175.02 (s, COO$^-$), 162.18 (d, $^1J_{FC}$=245.3 Hz, C_1), 155.12 (s, C_f), 148.10 (s, C_c), 133.07 (dd, $^3J_{PC}$=7.3 Hz, $^4J_{FC}$=2.8 Hz, C_4), 129.70 (d, $^3J_{FC}$=8.5 Hz, C_3 and C_5), 121.23 (s, C_a), 117.93 (s, C_d), 117.02 (s, C_e), 116.42 (s, C_b), 115.21 (d, $^2J_{FC}$=21.4 Hz, C_2 and C_6), 67.18 (d, $^2J_{PC}$=4.5 Hz, O-CH_2), 50.46 (s, Ar-CH_2-N), 45.79 (s, N-CH_2), 42.82 and 42.76 (s, NH-CH_2), 26.20 (d, $^3J_{PC}$=3.0 Hz,N-CH$_2$-CH_2), 24.71 (d, $^3J_{PC}$=6.7 Hz,NH-CH$_2$-CH_2), 24.68 (d, $^3J_{PC}$=6.7 Hz,NH-CH$_2$-CH_2), 11.23 and 11.14 (s, CH_3).

X-Ray Crystal Structure Determinations: The light yellow crystals **4d** were obtained from toluene at ambient temperature. The crystallographic data (Table 1) and the selected bond lengths and angles (Table 2) were given. Crystallographic data were recorded on a Bruker Kappa APEXII CCD area-detector diffractometer using MoK$_\alpha$

radiation (λ=0.71073 Å) at T=173(2) K. Absorption correction by multi-scan was applied [25]. The structure was solved by direct methods and refined by full-matrix least squares against F^2 using all data [26,27]. All non-H atoms were refined anisotropically. Atoms H2A (for N2), H51 (for N5), H61 (for N6), H71 (for N7), H81 (for N8) and H5A (for O5) were located in a difference Fourier map and refined isotropically. The remaining H atoms were positioned geometrically at distances of 0.82 Å (OH), 0.93 Å (CH), 0.97 Å (CH_2) and 0.96 Å (CH_3) from the parent C and O atoms; a riding model was used during the refinement process and the $U_{iso}(H)$ values were constrained to be $1.2U_{eq}$ (for methine and methylene carrier atoms) and $1.5U_{eq}$ (for hydroxyl and methyl carrier atoms).

Determination of antimicrobial activity: The antimicrobial susceptibility testing was performed by the BACTEC MGIT 960 (Becton Dickinson, Sparks, MD) system. The antimicrobial efficacy of the compounds (**3a-3d** and **4a-4d**) was examined using the standard broth dilution method [28]. The microorganisms used in antimicrobial screening included three bacteria {*Escherichia coli* ATCC 25922 (G-), *Klebsiella pneumoniae* ATCC 13883 (G) and *Enterobacter faecalis* ATCC 29212 (G+)} and a fungus (*Candida albicans* ATCC 10231). The MIC values were determined in benzo-(1,2,3)-thiadiazole-7-carbothioic acid S-methyl ester (BTH) broth using serial dilution of the compounds ranging from 3000-15,63 µM with adjusted bacterial and fungal concentration ($1x10^6$ CFU/mL, 0,5 McFarland's standard). Bacterial strains were grown in nutrient agar medium and incubated at 37 ºC for 24 h. The yeast cells were cultured on Sabouraud dextrose agar (SDA) medium and incubated at 30 ºC for 48 h. Ampicillin (Amp, 10 µg/mL) and Chloramphenicol (C, 30 µg/mL) (antibacterial), and Ketoconazole (K, 50 µg/mL) (antifungal) were used as controls. The solutions (4000 µM) of the compounds were obtained in DMF. All the experiments were repeated three times, and the mean values were used. The MIC is the lowest concentration of compounds that inhibits 90% growth. The MBC and MFC are determined by inoculating previous culture which showed no growth in agar plates. The MBC and MFC are the lowest concentration of the compound that kills 99,9% of the initial microorganism concentration.

Table 1: Crystallographic data for **4d**.

Empirical Formula	$C_{29}H_{50}O_5N_8P_3F$	Z	4
Fw	702.68	μ(MoKα) (cm^{-1})	2.172
Crystal System	monoclinic	ρ(calcd) (g cm^{-1})	1.289
Space Group	P 2_1/n	Number of Reflections Total	22308
a (Å)	11.9537(3)	Number of Reflections Unique	6402
b (Å)	24.0902(5)	R_{int}	0.094
c (Å)	12.7785(3)	$2\theta_{max}$ (°)	50.1
α (°)	90.00	T_{min} / T_{max}	0.80/0.90
β (°)	100.331(3)	Number of Parameters	443
γ (°)	90.00	R [$F^2 > 2\sigma(F^2)$]	0.079
V (Å^3)	3620.1(2)	wR	0.199

Table 2: The selected bond lengths and angles for **4d**.

Bond Lengths (Å)		Bond Angles (°)	
P1-N1	1.589(4)	α_1	115.3(2)
P1-N3	1.585(4)	α_2	102.3(2)
P2-N1	1.579(4)	β_1	123.5(2)
P2-N2	1.655(4)	β_1'	128.5(3)
P3-N2	1.666(4)	γ_1	111.6(2)
P3-N3	1.575(4)	γ_1'	108.5(2)
P1-N4	1.649(4)	γ_2	105.9(3)
P1-O1	1.581(4)	γ_2'	104.0(2)
P2-N7	1.626 (5)	δ_1	126.7(3)
P2-N8	1.598(5)		
P3-N5	1.610(4)		
P3-N6	1.610(5)		
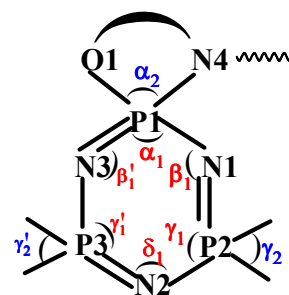
Determination of the pUC18 plasmid DNA interaction with the compounds: The interactions of the cyclotriphosphazenes and the PILs with the pUC18 plasmid DNA were evaluated using agarose gel electrophoresis [29]. The compounds were incubated with pUC18 plasmid DNA in an incubator at 37 ºC for 24 h in the dark. The compound/DNA mixtures were loaded onto the 1% agarose gel with a loading buffer (0.1% bromophenol blue, 0.1% xylene cyanol). Electrophoresis was made in 0.05 M Tris base, 0.05 M glacial acetic acid, and 1 mM EDTA (TAE buffer, pH = 8.0) for 3 h at 60V [30]. Subsequently, the gel was stained with ethidium bromide (0.5 µg/mL), visualized under UV light using a transilluminator (BioDoc Analyzer, Biometra), photographed with a video camera, and saved as a TIFF file. The experiments were repeated three times.

Determination of *BamH*I and *Hind*III restriction enzyme digestion of the compounds-pUC18 plasmid DNA: In order to assess whether the compounds **3a-3d** and **4a-4d** show affinity towards adenine-adenine (AA) and/or guanine-guanine (GG) regions of DNA, the restriction analyses of the compound-pUC18 plasmid DNA adducts by *BamH*Iand *Hind*III enzymes are performed. The compound/pUC18 plasmid DNA mixtures were incubated for 24 h,and then restricted with *BamH*I or *Hind*III enzymes at 37 ºC for 2 h. The restricted DNA was run in 1% agarose gel electrophoresis for 1 h at 70 V in TAE buffer. Consequently, the gel was stained with ethidium bromide (0.5 µg/mL), and it was viewed using a transilluminator, and the image was photographed using a video-camera, and saved as a TIFF file[20].

RESULTS and DISCUSSION

Syntheses and Characterizations. The intermediate Schiff base, "N-[(E)-(4-fluorophenyl)methylidene]-3-(hydroxy)propan-1-amine", was prepared from the condensation reaction of 4-fluorobenzaldehyde with 3-amino-1-propanol. Subsequently, this compound was reduced with $NaBH_4$ in methanol to give the starting compound 3-(4-fluorobenzylamino)-1-propanol. The total reaction yield was 89%. In the literature, the latter compound was also prepared from the reaction of 4-fluorobenzyl chloride with 3-amino-1-propanol in moderate yield 64%, and patented [31].

The condensation reaction of $N_3P_3Cl_6$ (**1**) with an equimolar amount of sodium 3-(4-fluorobenzylamino)-1-propanoxide gave 4-fluorobenzylspiro(N/O)cyclotriphosphazene (**2**) in a high yield (68%). The reactions of partly substituted **2** with excess benzylamine, n-hexylamine, n-butylamine and n-propylamine led to the formation of the corresponding 4-fluorobenzylspiro(N/O)tetrabenzylamino (**3a**), tetrahexylamino (**3b**), tetrabutylamino (**3c**) and tetrapropylamino (**3d**) cyclotriphosphazenes. The calculated yields of these compounds were found to be 62, 52, 71 and 76%, respectively. The PILs (**4a-4d**) of phosphazene bases (**3a-3d**) with gentisic acid were obtained in a high yield in dry THF (Figure 1). The crystal structure of **4d** was verified by X-ray diffraction analysis. The results indicate that compound **4d** was monoprotonated with the nitrogen of phosphazene ring non-adjacent to the NO spiro ring. However, in the literature the protonation was observed from the nitrogen atom of phosphazene ring adjacent to the NN spiro ring [23]. The NMR results exhibit that all the compounds are likely to be protonated in the same fashion. All the PILs were highly soluble in the common organic polar and apolar solvents. However, they are dissolved slightly in water. The solubilities of these PILs increased with the increasing temperature.
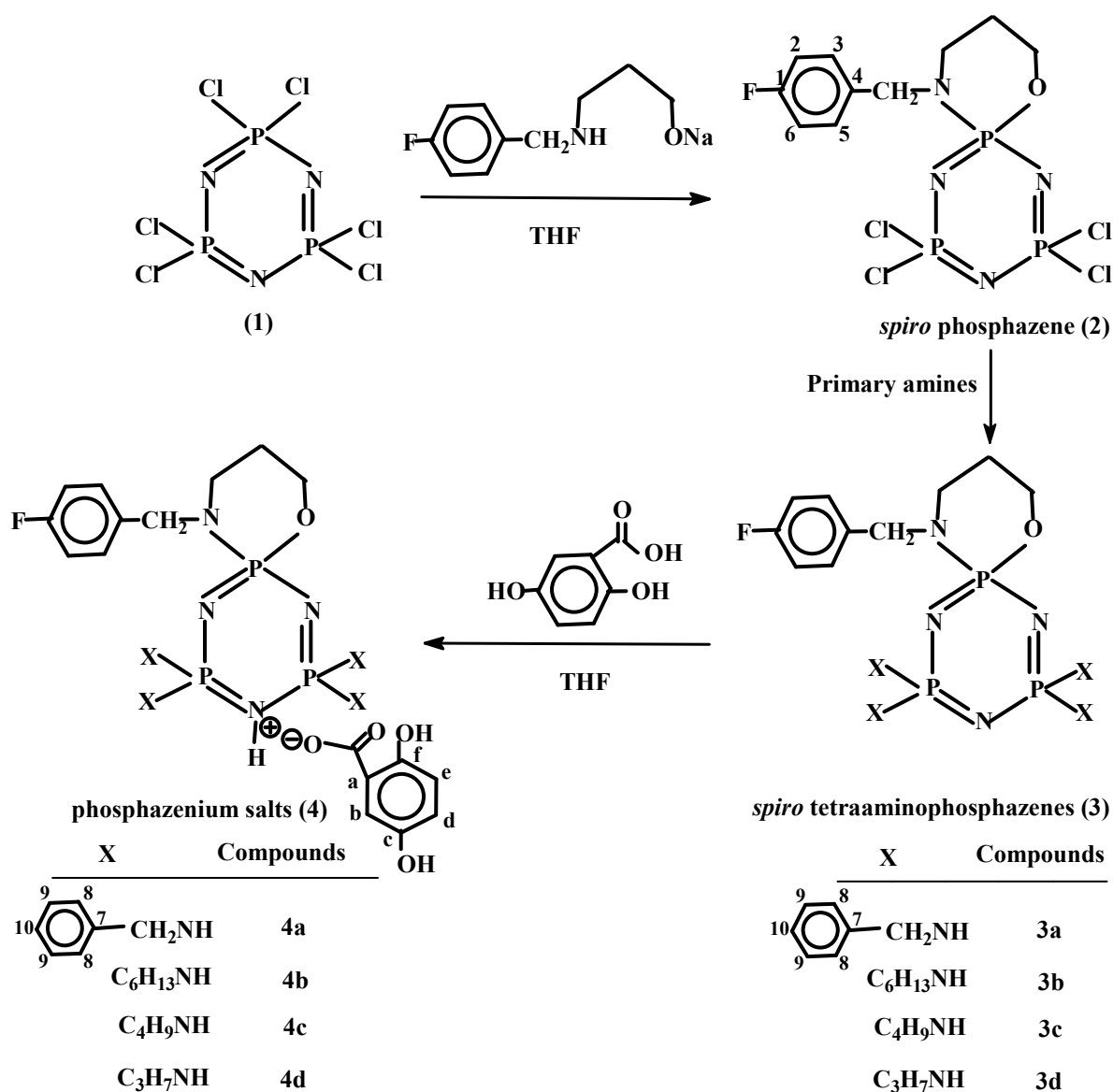
Figure 1. The cyclotriphosphazene derivatives obtained from the reactions of 4-fluorobenzylspiro(N/O)cyclotriphosphazene with primary amines and their phosphazenium salts.

The structures of all the isolated cyclotriphosphazene derivatives were determined by elemental analyses, FTIR and ^{1}H, ^{13}C{^{1}H}, ^{31}P{^{1}H} NMR techniques. All the compounds were screened for antibacterial and antifungal activities against bacteria and yeast strains. The interactions of the compounds with supercoiled pUC18 plasmid DNA were investigated.

The microanalyses, FTIR and ^{1}H, ^{13}C{^{1}H}, ^{31}P{^{1}H}, and NMR results were confirmed the suggested structure of the compounds with one mole of water for **3a**, **3c, 4a, 4b** and **4d**. The protonated molecular [MH]$^+$ ion peaks were observed in the mass spectra of the free phosphazene bases (**3a-3d**). The analytical data and NMR results are given in the "Experimental Section".

The spin systems and the ^{31}P-NMR spectral data of the cyclotriphosphazenes are given in Table 3. The starting compound **2** has AX$_2$ spin system. It gives rise to one triplet (P$_{spiro}$, P$_A$) and one doublet (P$_X$). Compound **3a** has an ABC spin system and displays a total of twelve signals for the expected ABC spin system. The fully substituted phosphazenes; **3b**, **3c** and **3d** have AB$_2$ spin systems and exhibit a total of eight signals. The ^{2}J$_{PP}$/Δv

values of these compounds are calculated and listed in Table 3. The $\delta P_{(spiro)}$-shifts of the phosphazene bases (**3a-3d**) are considerably larger than that of the starting compound (**2**). However, when the Cl atoms exchanged with amine groups, the δP-shifts of the free bases were decreasing. The spin systems of the PILs are found to be as AB_2 for **4a** and A_3 for **4b**, **4c** and **4d**. The chemical shifts of these salts were smaller than those of the corresponding free bases, depending on the salt formation with bulky organic acid.

Table 3: ^{31}P NMR parameters of compounds.[a]

X: Cl, $PhCH_2NH$, $C_6H_{13}NH$, C_4H_9NH, C_3H_7NH

AX₂ (2)
AB₂ (3b, 3c and 3d)

ABC (3a)

AB₂ (4a)
A₃ (4b, 4c and 4d)

	Spin System	$\delta PNO_{(spiro)}$	δPCl_2	δPN_2	$^2J_{PP}$ (Hz)	$^2J_{PP}/\Delta v$
2	AX_2	P_A 9.06	P_X 23.32	-	$^2J_{AX}$ 50.2	-
3a	ABC	P_A 21.20		P_B 20.22	$^2J_{AB}$ 53.4	-
				P_C 18.83	$^2J_{BC}$ 53.2	
					$^2J_{AC}$ 51.0	
3b	AB_2	P_A 19.90		P_B 18.75	$^2J_{AB}$ 48.6	0.17
3c	AB_2	P_A 20.04	-	P_B 18.88	$^2J_{AB}$ 46.2	0.15
3d	AB_2	P_A 20.04	-	P_B 18.80	$^2J_{AB}$ 48.6	0.16
4a	AB_2	P_A 14.84	-	P_B 14.35	$^2J_{AB}$ 56.7	0.48
4b	A_3	P_A 14.70	-	P_A 14.70	-	Broad singlet
4c	A_3	P_A 14.75	-	P_A 14.75	-	Broad singlet
4d	A_3	P_A 14.74	-	P_A 14.74	-	Broad singlet

[a]242.93 MHz ^{31}P NMR measurements in $CDCl_3$ solutions at 298 K. Chemical shifts referenced to external H_3PO_4.

The assignments of the chemical shifts, multiplicities, and coupling constants were elucidated from the ^{13}C and ^1H-NMR spectra of all the cyclotriphoshazenes (**2** and **3a-3d**) and their salts (**4a-4d**), and given in "Experimental Section". In the ^{13}C NMR spectra of the cyclotriphosphazene bases (**3a-3d**) and the PILs (**4a-4d**), the geminal substituents display two small separated peaks for $NHCH_2$, $NHCH_2CH_2$, CH_3, and $ArCH_2NH$ and *ipso-C_7* carbons (for **3a** and **4a**), implying that the two geminal groups are not equivalent. The average coupling constants of the free bases (**3a-3d**), $^2J_{POC}$=6.9 Hz, is very higher than that of the PILs ($^2J_{POC}$=5.0 Hz). The coupling constants, $^3J_{PNCC}$, of the free bases (**3a-3d**) and the PILs (**4a-4d**) emerge to triplets of the $NHCH_2CH_2$ and $NHCH_2C_7$ carbons depending on the second-order effects (Figure 2). The $^3J_{PNCC}$ values are calculated using the external transitions of the triplets as it is estimated in the literature [32]. In addition, the coupling constants of $^1J_{FC}$, $^2J_{FC}$, $^3J_{FC}$ and $^4J_{FC}$ are also assigned for the cyclotriphosphazene and the PILs.
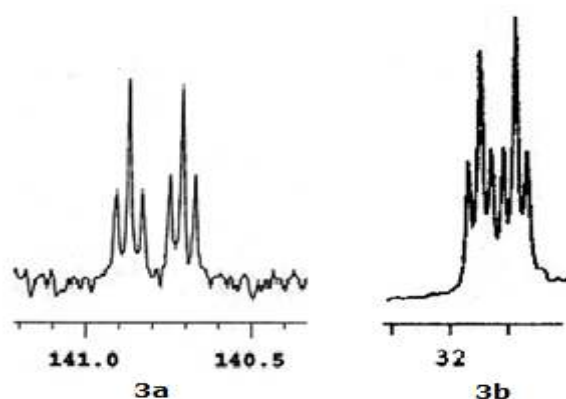
Figure 2. The second order effects in ^{13}C NMR spectra of **3a** and **3b**.

The interpretations of the free bases (**3a-3d**) and the PILs (**4a-4d**) were made using the coupling constants of $^3J_{FH}$ and $^4J_{FH}$, and the multiplicities. The results were presented in "Experimental Section". The average values of $^3J_{FH}$ and $^4J_{FH}$ were found to be at 8.8 Hz and 5.4 Hz, respectively. The protons of ArCH_2N were observed asa doublet. The average values of $^3J_{PH}$ of ArCH_2N protons in the free bases and the PILs were found to be at 7.5 and 6.4 Hz, respectively. The δ_H-shifts of OCH_2 spiro protons of the cyclotriphosphazenes and the PILs were observed in the range of 4.24-4.34 ppm, and the average $^3J_{PH}$ value, 12.3 Hz, was very large.

The characteristic stretching band (ν_{N-H}, 3402 cm^{-1}, broad) was observed for 3-(4-fluorobenzylamino)-1-propanol disappeared in the FTIR spectra of the compound **2**. Whereas, in the FTIR spectra of the free bases and the PILs exhibit the broad ν_{N-H} peaks. They are observed in the ranges of 3200-3289 cm^{-1} and 3361-3389 cm^{-1}. All the salts display ν_{+N-H} (ca. 2668 cm^{-1}), ν_{coo-}(asymm.) (*ca*. 1578 cm^{-1}) and ν_{coo-} (symm.) (*ca*. 1377 cm^{-1}) absorption frequencies clearly indicating the salt formation. The cyclotriphosphazenes and the PILs show intense stretching vibrations between 1202-1257 cm^{-1} and 1193-1218 cm^{-1}, attributed to the $\nu_{P=N}$ bonds of the phosphazene skeletons [33,34].

The crystal structure of 4d: The molecular and the solid state structure of **4d** were verified by X-ray crystallography. Figure 3 depicts the molecular structure of **4d** along with the atom-numbering scheme. The phosphazene ring of **4d** is in twisted boat conformation [Figure 3b: φ_2 =-84.6(6)°, θ_2 =100.0(6)°(P1/N1/P2/N2/P3/N3)] with a total puckering amplitude, Q_T of 0.270(4)Å] [35]. The six-membered *spiro* ring (P1/N4/C8/C9/C10/O1) is in the chair conformation [Figure 3c: φ_2 =34.7(4)°, θ_2 =88.1(5)°] with a total puckering amplitude, Q_T of 0.673(5)Å]. Moreover, the torsion angles of N$_3$P$_3$ ring of **4d** exhibit that the cyclotriphosphazene ring does not have any pseudo-mirror plane (Figure 3d).

In PILs **4d**, the endocyclic PN bond lengths of the phosphazene ring were found to be in the range of 1.575(4)–1.666(4) Å (average value is 1.608(2) Å), compared with the corresponding values [1.588(1)–1.599(1) Å, average value is 1.595(1) Å] of the analogues phosphazene free bases [23]. In addition, the exocyclic PN bond lengths of **4d** are in the range of 1.581(4)–1.649(4) Å (average value is 1.612(5) Å). The corresponding values of analogues phosphazene free bases and its salts are in the ranges of 1.652(1)–1.674(1) Å (average value is 1.663(1) Å) and 1.625(2)–1.647(2) Å (average value is 1.639(2) Å) [23] (Table 2). In **4d**, the P2N2 (1.655(4) Å) and P3N2 (1.666(4) Å) bond lengths are considerably larger than those of other PN bond lengths, depending on the protonation of N2 atom.

The considerable narrowings of the endocylic α_1 [115.3(2)º] and γ_1 [111.6(2)º and 108.5(2)º] angles and the considerable expanding of the endocylic β_1 [123.5(2)º], $\beta_1{}'$ [128.5(3)º] and δ_1 [126.7(3)º] angles may indicate the electron delocalization in the phosphazene ring (Table 2). These findings may be compared with the corresponding values of analogues phosphazene free bases and its salts reported in the literature [23]. In addition, it was observed that the great changes are observed at around the N2 atom indicating HN^+ bond formation.

Hydrogen-bond geometries of **4d** were listed in Table 4. It was observed that the strong intramolecular hydrogen bonds (O–H … O) were present in the gentisic acid anion. Furthermore, the strong intramolecular N–H … O hydrogen bond links the gentisic acid anion to the phosphazene molecule [36].

Crystallographic data for the structural analysis have been deposited with the Cambridge Crystallographic Data Centre, CCDC1487569 Copies of this information may be obtained free of charge from The Director, CCDC, 12 Union Road, Cambridge CB2 1EZ, UK (fax: 44-1223-336033; e-mail: deposit@ccdc.cam.ac.uk or www: http://www.ccdc.cam.ac.uk).

Table 4: Hydrogen-bond geometries (Å, º) for **4d.**

D-H …A	D-H	H …A	D …A	D-H …A
N2-H2A … O3^{iv}	0.84(5)	2.83(1)	2.01(5)	166.9(4.0)
C8-H8A … O4	0.97(1)	3.41(1)	2.59(1)	142.3(3.0)
N5-H51 … O5^{iii}	0.86(5)	2.95(1)	2.09(5)	172.7(4.0)
N8-H81 … N1^{ii}	0.86(5)	3.12(1)	2.30(4)	156.8(4.0)
O4-H4A … O2	0.82(1)	2.52(1)	1.81(1)	146.1(3.0)
N6-H61 … O4^{i}	0.85(1)	2.99(1)	2.31(1)	137.4(4.0)
O5-H5A … O2^{i}	0.82(1)	2.56(1)	1.74(1)	170.3(3.0)
N7-H71 … O5^{iii}	0.87(1)	3.09(1)	2.27(1)	157.3(2.0)

Symmetry codes (i) x + ½, -y + ½, z + ½, (ii) −x, -y, -z +1, (iii) x − ½, -y + ½, z + ½, (iv) x, y, z + 1.

(**a**)

(**b**)   (**c**)   (**d**)
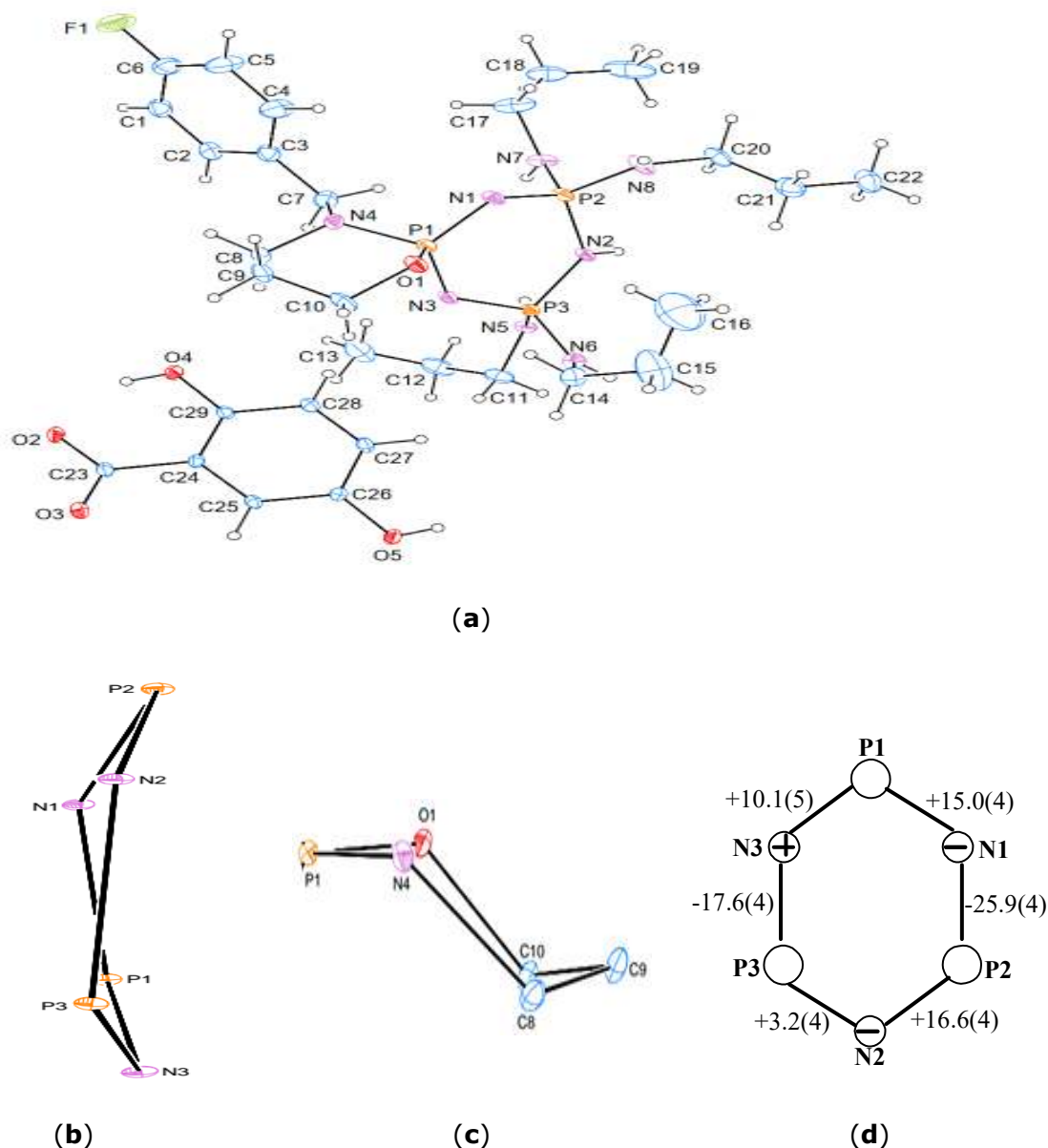
Figure 3. (**a**) An ORTEP-3 [37] drawing of **4d** with the atom-numbering scheme. Displacement ellipsoids are drawn at the 30% probability level. The conformations of (**b**) the trimer ring and (**c**) the six-membered spiro-ring of **4d,** and (**d**) the shape of the phosphazene ring in **4d** with torsion angles (deg) given.

Antimicrobial activity evaluation: In this paper, the antimicrobial activity of the cyclotriphosphazene bases and the PILs have been investigated for discovering the new antimicrobial agents against some (G−) and (G+) bacteria and fungi. Table 5 illustrates *in vitro* antimicrobial activity of cyclotriphosphazene bases (**3a-3d**) and the PILs (**4a-4d**) against three types of bacteria and one type of fungus. The MIC, MBC and MFC values of the compounds have ranges of 15.63-1000 µM, 31.25-2500 µM and 15.63-250µM, respectively. Compounds **3c** and **4c** are strongly active against *E. faecalis* (G+). As known, *E. faecalis*, is a facultative anaerobic Gram-positive coccus and causes root canal failure and persistent apical periodontitis [38]. In addition, the free base **3d**, and the PILs, **4a**, **4c** and **4d,** are very active against *C. albicans.* On the other hand, compared to the salts with the corresponding free bases, the salts (**4a** and **4c**) and (**4b** and **4d**) are found to be more effective than corresponding free bases (**3a** and **3c**) and (**3b** and **3d**), respectively, against *C. albicans* and *K. pneumoniae,* indicating that the salt formation considerably increases antimicrobial activity. This situation may attribute to the strong

hydrogen bond formation of the anion and/or cation of the saltswith the DNA of microorganisms.

Interactions of pUC18 plasmid DNA with the compounds: The interactions of pUC18 plasmid DNA with the free bases (**3a-3d**) and the PILs (**4a-4d**) were studied using agarose gel electrophoresis (Figure 4). In the electrophoretograms, in all the cases run with untreated pUC18 plasmid DNA was included as a control, while lanes 1 to 4 contained plasmid DNA interacted with decreasing concentrations of the compounds (from 4000 µM to 500 µM). It appears that all of the compounds, exhibit similar effects against plasmid DNA except **3d**. As the concentrations of the compounds decrease, the mobility of Form I DNA increases slightly. In the case of **3d**, two bands co-migrate for the concentration of the compound at the highest concentration (4000 µM). In the lower concentrations, the seperated two bands are observed,indicating that compound **3d** is binding to DNA.
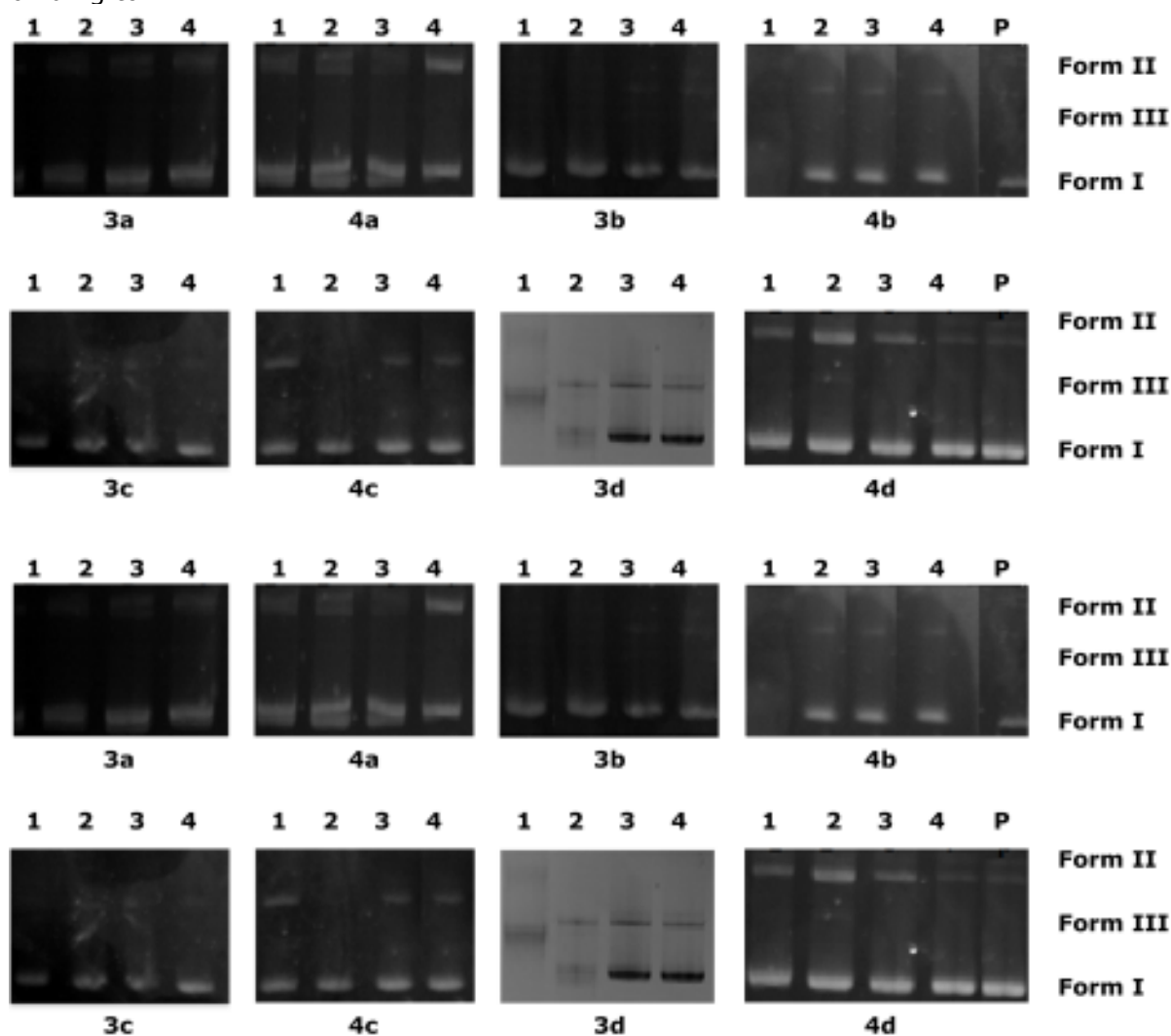
Figure 4. Interaction of pUC18 plasmid DNA with decreasing concentrations of the compounds (lanes 1–4; 1: 4000 µM; 2: 2000 µM; 3: 1000 µM; 4: 500 µM, and P: untreated pUC18 plasmid DNA as a control).

Table 5: The *in vitro* antimicrobial activities of compounds **3a-3d**and **4a-4d**against test strains (MIC: Minimum Inhibitory Concentration, MBC: Minimum Bactericidal Concentration, and MFC: Minimum Fungicidal Concentration. MIC, MBC and MFC values are reported in µM).

Compounds	*E. coli ATCC 25922*		*K. pneumoniae ATCC 13883*		*E. faecalis ATCC 29212*		*C. albicansATCC 10231*	
	MIC	**MBC**	**MIC**	**MBC**	**MIC**	**MBC**	**MIC**	**MFC**
3a	250	500	125	125	250	500	125	125
4a	250	500	250	250	500	1000	<15.63	<15.63
3b	250	1000	250	500	250	250	125	125
4b	125	125	125	125	250	250	125	250
3c	125	125	62.5	62.5	<15.63	<15.63	62.5	125
4c	125	125	62.5	62.5	<15.63	<15.63	31.25	62.5
3d	250	500	250	250	500	1000	31.25	31.25
4d	250	500	125	125	500	1000	62.50	62.50
Amp	<19.5	NS	1250	NS	312.5	NS	NS	NS
C	1250	NS	2500	NS	625	NS	NS	NS
Keto	NS	NS	NS	NS	NS	NS	1250	NS

Amp: Ampicillin, C: Chloramphenicol, Keto: Ketoconazole (NS: Not studied).

***BamH*I and *Hind*III digestion of compounds-pUC18 plasmid DNA:** DNA–compound mixture was digested with *BamH*I and *Hind*III restriction enzymes in order to understand DNA-compound binding. Figure 5 displays the electrophoretograms for the incubated mixtures of pUC18 plasmid DNA with the compounds followed by *BamH*I and *Hind*III digestion. In the absence of the compounds, when untreated plasmid DNA is digested with the enzymes, only the linear Form III band is observed, indicating that two strands of pUC18 plasmid DNA arecut by *BamH*I at the specific GG site and *Hind*III enzymes at the specific AA site. For *BamH*I digestion, a mixture of Form I and Form II bands are observed for all the compounds, **3a-3d** and **4a-4d**. Form III band is also detected for *BamH*I digestion for **3d**, **4a** and **4c**. On the other hand, for *Hind*III digestion, only one band is determined for **3a**, **3c**, **3d**, **4c** and **4d**. Whereas two bands, Form I and Form II, were observed for **3b**, **4a** and **4b**. Eventually, the prevention of *BamH*I digestion by **3b**, **4a** and **4b**, disclosed binding with GG nucleotides in DNA.
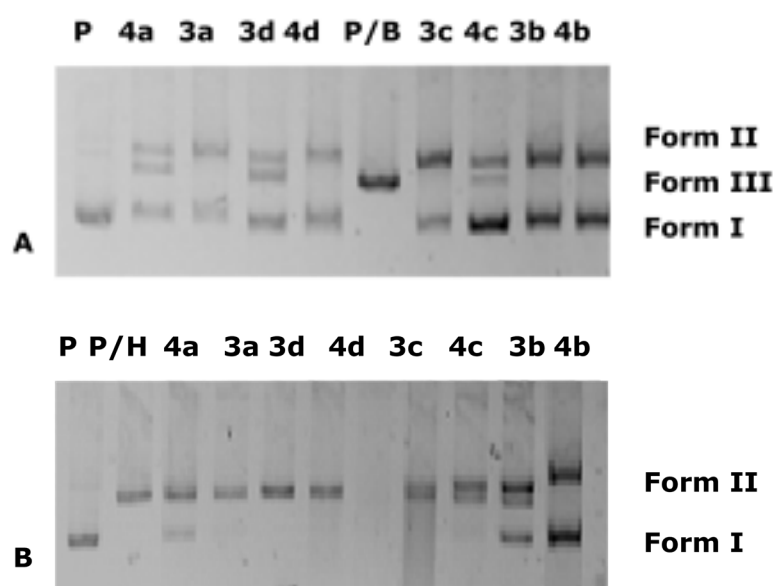
Figure 5. Electrophoretogram for the incubated mixtures of pUC18 plasmid DNA followed by digestion with (**A**) *BamH*I and (**B**) *Hind*III. Lane P applies to untreated DNA, P/B and P/H, untreated, but digested pUC18 plasmid DNA.

CONCLUSIONS

The structures of the cyclotriphosphazenes (**3a-3d**) and the PILs (**4a-4d**) were elucidated using NMR data in $CDCl_3$ solution. The crystallographic results of **4d** unambiguously indicate that the nitrogen of the phosphazene ring is monoprotonated. The fully substituted cyclotriphosphazenes (**3a-3d**) appear to be the ligating agents for transition metal cations. The antimicrobial activities of all the compounds were scrutinized against bacteria and fungi. Compounds **3c** and **4c** are the most active compounds against *E. faecalis* (G+). In addition, the phosphazene base, **3d**, and the PILs, **4a**, **4c** and **4d,** are found to be considerably active against *C. albicans.* The gel electrophoretic data demonstrate that compound **3d** is binding to pUC18 plasmid DNA.

ACKNOWLEDGMENTS

REFERENCES

1.   Chandrasekhar V, Thilagar P, Pandian B.M. Cyclophosphazene-based multi-site coordination ligands. Coord. Chem. Rev. 2007;251:1045-74. DOI: 10.1016/j.ccr.2006.07.005.

2.   Allen W.C. Regio- and stereochemical control in substitution reactions of cyclophosphazenes. Chem. Rev. 1991 Mar;91:119-35. DOI: 10.1021/cr00002a002.

3.   Okumuş A, Kılıç Z, Hökelek T, Dal H, Açık L, Öner Y, Koç L.Y. Phosphorus–nitrogen compounds part 22. syntheses, structural investigations,biological activities and DNA interactions of new mono and bis (4-fluorobenzyl)spirocyclophosphazenes. Polyhedron. 2011 Nov;30:2896-2907. DOI: 10.1016/j.poly.2011.08.035.

4.   Işıklan M, Asmafiliz N, Özalp E.E, İlter E.E, Kılıç Z, Çoşut B, Yeşilot S, Kılıç A, Öztürk A, Hökelek T,Koç L.Y, Açık L,Akyüz E. Phosphorus−nitrogen compounds. 21. syntheses, structural investigations, biological activities, and DNA interactions of new N/O spirocyclic phosphazene derivatives. The NMR behaviors of chiral phosphazenes with stereogenic centers upon the addition of chiral solvating agents. Inorg. Chem. 2010 Jun;49:7057-71. DOI: 10.1021/ic100781v.

5.   Asmafiliz N, Kılıç Z, Hayvalı Z, Açık L, Hökelek T, Dal H, Öner Y.Phosphorus-nitrogen compounds. Part 23: syntheses, structural investigations, biological activities, and DNA interactions of new N/O spirocyclotriphosphazenes. Spectrochimica Acta Part A.2012 Feb;86:214-23. DOI: 10.1016/j.saa.2011.10.027.

6.   İlter E.E, Asmafiliz N, Kılıç Z, Işıklan M, Hökelek T, Çaylak N, Şahin E. Phosphorus−nitrogen compounds. 14. synthesis, stereogenism, and structural investigations of novel N/O spirocyclic phosphazene derivatives. Inorg. Chem. 2007 Oct; 46:9931-44. DOI: 10.1021/ic701216f.

7.   Jimenez J, Laguna A, Gascon E, Sanz J.A, Serrano J.L, Barbera J, Oriol L.New liquid crystalline materials based on two generations of dendronised cyclophosphazenes. Chem. Eur. J. 2012 Nov;18:16801-14. DOI: 10.1002/chem.201202748.

8.   Jimenez J, Pintre I, Gascon E, Sanchez-Somolinos C, Alcala R, Cavero E, Serrano J.L, Oriol L.Photoresponsive liquid-crystalline dendrimers based on a cyclotriphosphazene core. Macromol. Chem. Phys. 2014 Jun;215:1551-62. DOI:10.1002/macp.201400190.

9.   Ahn S, Kim H.S, Yang S, Do J.Y, Kim B.H, Kim K.Thermal stability and performance studies of $LiCo_{1/3}Ni_{1/3}Mn_{1/3}O_2$ with phosphazene additives for Li-ion batteries. J. Electroceram. 2009;23:289-94. DOI: 10.1007/s10832-008-9437-y.

10.   Harrup M.K, Gering K.L, Rollins H.W, Sazhin S.V, Benson M.T, Jamison D.K, Michelbacher C.J, Luther T.A.Phosphazene based additives for ımprovement of safety and battery lifetimes in lithium-ion batteries. ESC Trans. 2012 May;41(39):13-25. DOI:10.1149/1.3703065.

11.   Nishimoto T, Yasuda T, Lee S.Y, Kondo R, Adachi C.A six-carbazole-decorated cyclophosphazene as a host with high triplet energy to realize efficient delayed-fluorescence OLEDs. Mater. Horiz. 2014 Sep;1:264-69. DOI: 10.1039/C3MH00079F.

12.   Schrogel P, Hoping M, Kowalsky W, Hunze A, Wagenblast G, Lennartz C, Strohriegl P.Phosphazene-based host materials for the use in blue phosphorescent organic light-emitting diodes. Chem. Mater. 2011 Oct;23:4947-53. DOI: 10.1021/cm201940f.

13.   Zhu J, Liu W, Chu R, Meng X.Tribological properties of linear phosphazene oligomers as lubricants. Tribology Int. 2007 Mar;40:10-14. DOI: 10.1016/j.triboint.2006.01.014.

14.   Wang X, Tan A.Y.X, Cho C.M, Ye Q, He C, Ji R, Xie H.Q, Tsai J.W.H, Xu J. Highly thermally stable cyclotriphosphazene based perfluoropolyether lubricant oil. Tribology Int. 2015 Apr;90:257–62. DOI: 10.1016/j.triboint.2015.04.018.

15.   Tümer Y, Koç L.Y, Asmafliz N, Kılıç Z, Hökelek T, Soltanzade H, Açık L, Yola M.L, Solak A.O.Phosphorus–nitrogen compounds: part 30. syntheses and structural investigations,

antimicrobial and cytotoxic activities and DNA interactions of vanillinato-substituted NN or NO spirocyclic monoferrocenyl cyclotriphosphazenes. J. Biol. Inorg. Chem. 2015 Dec;20:165-78. DOI: 10.1007/s00775-014-1223-5.

16.   Başterzi N.S, Bilge Koçak S, Okumuş A, Kılıç Z, Hökelek T, Çelik Ö, Türk M, Koç L. Y, Açık L, Aydın B, Dal H.Syntheses, structural characterization and biological activities of spiro-ansa-spiro-cyclotriphosphazenes. New J. Chem. 2015 Sep;39:8825-39. DOI: 10.1039/C5NJ01530H.

17.   Mutlu G, Elmas G, Kılıç Z, Hökelek T, Koç L.Y, Türk M, Açık L, Aydın B, Dal H. Phosphorus-nitrogen compounds: part 31. syntheses, structural and stereogenic properties, in vitro cytotoxic and antimicrobial activities, DNA interactions of novel bicyclotetraphosphazenes containing bulky side group. Inorganica Chimica Acta. 2015 July;436:69-81. DOI: 10.1016/j.ica.2015.07.027.

18.   Akbaş H, Okumuş A, Kılıç Z, Hökelek T, Süzen Y, Koç L.Y, Açık L, Çelik Z.B.Phosphorus-nitrogen compounds: part 27. syntheses, structural characterizations, antimicrobial and cytotoxic activities, and DNA interactions of new phosphazenes bearing secondary amino and pendant (4-fluorobenzyl)spiro groups. EuropeanJournal of MedicinalChemistry. 2013 Dec;70:294-307.DOI: 10.1016/j.ejmech.2013.09.046.

19.   Okumuş A, Elmas G, Cemaloğlu R, Aydın B, Binici A, Şimşek H, Açık L, Türk M, Güzel R, Kılıç Z, Hökelek T. Phosphorus-nitrogen compounds. part 35. syntheses, spectroscopic and electrochemical properties, antituberculosis, antimicrobial and cytotoxic activities of mono-ferrocenyl-spirocyclotetraphosphazenes. New J. Chem. 2016 Apr;40:5588-603. DOI: 10.1039/C6NJ00204H.

20.   Greaves T.L, Drummond C.J.Protic ionic liquids: properties and applications. Chem. Rev. 2008 Dec;108:206-37. DOI: 10.1021/cr068040u.

21.   Bicak N.A new ionic liquid: 2-hydroxy ethylammonium formate. Journal of Molecular Liquids. 2005 Jan;116:15-8. DOI: 10.1016/j.molliq.2004.03.006.

22.   Karadağ A, Destegül A.N-(2-hydroxyethyl)-ethylenediamine-based ionic liquids: synthesis, structural characterization, thermal, dielectric and catalytic properties. Journal of Molecular Liquids. 2013;177:369-75. DOI: 10.1016/j.molliq.2012.10.040.

23.   Akbaş H, Okumuş A, Karadağ A, Kılıç Z, Hökelek T, Süzen Y, Koç L.Y, Açık L, Aydın B, Türk M.Phosphorus–nitrogen compounds: part 32. structural and thermal characterizations, antimicrobial and cytotoxic activities, and in vitro DNA binding of the phosphazenium salts. J. Therm. Anal. Calorim. 2016 Sep;123:1627-41. DOI: 10.1007/s10973-015-5001-6.

24.   Bruker program 1D WIN-NMR (release 6.0) and 2D WIN-NMR (release 6.1).

25.   Bruker, SADABS, Bruker AXS Inc., Madison, Wisconsin, USA,(2005).

26.   Sheldrick G.M. SHELXS-97, SHELXL-97 University of Gottingen, Gottingen, Germany, (1997).

27.   Sheldrick G.M. A short history of SHELXL. Acta Crystallogr. Sect. A. 2008 Jan;64: 112-22. DOI: 10.1107/S0108767307043930.

28.   Clinical and Laboratory Standards Institute, Performance Standards for Antimicrobial Susceptibility Testing Sixteenth Informational Supplement, CLSI document M100eS16, Pennsylvania, (2006).

29.   Elmas G, Okumuş A, Koç L.Y, Soltanzade H, Kılıç Z, Hökelek T, Dal H, Açık L, Üstündağ Z, Dündar D, Yavuz M. Phosphorus-nitrogen compounds. part 29. syntheses, crystal structures, spectroscopic and stereogenic properties, electrochemical investigations, antituberculosis, antimicrobial and cytotoxic activities and DNA interactions of ansa-spiro-ansa cyclotetraphosphazenes. European Journal of Medicinal Chemistry. 2014 Oct;87:662-76. DOI: 10.1016/j.ejmech.2014.10.005.

30.	Elmas (nee Egemen) G, Okumuş A, Kılıç Z, Hökelek T, Açık L, Dal H, Ramazanoğlu N, Koç L.Y. Phosphorus−nitrogen compounds. part 24. syntheses, crystal structures, spectroscopic and stereogenic properties, biological activities, and dna ınteractions of novel spiro-ansa-spiro- and ansa-spiro-ansa-cyclotetraphosphazenes. Inorg. Chem. 2012 Nov;51:12841-56. DOI: 10.1021/ic3017134.

31.	Seto S, Tanioka A, Ikeda M, Izawa S. European Patent Office, Bulletin, 2004, EP 1 473 295 A 1 [0100].

32.	Koçak S.B, Koçoğlu S, Okumuş A, Kılıç Z, Öztürk A, Hökelek T, Öner Y, Açık L. Syntheses, spectroscopic properties, crystal structures, biological activities, and dna interactions of heterocyclic amine substituted spiro-ansa-spiro- and spiro-bino-spiro-phosphazenes. Inorganica Chimica Acta. 2013 Sep;406:160-70. DOI: 10.1016/j.ica.2013.07.023.

33.	Carriedo G.A, Alonso F.G, Gonzalez P.A, Menendez J.R.Infrared and Raman spectra of the phosphazene high polymer $[NP(O_2C_{12}H_8)]_n$. J. Raman Spectrosc. 1998 Dec;29:327-30. DOI: 10.1002/(SICI)1097-4555(199804)29:4.

34.	Egemen G, Hayvalı M, Kılıç Z, Solak A.O, Üstündağ Z. Phosphorus-nitrogen compounds. part 17. the synthesis, spectral and electrochemical investigations of porphyrinophosphazenes. J. Porphyrins Phthalocyanines. 2010;14:1-8. DOI: 10.1142/.

35.	Cremer D, Pople J.A, General definition of ring puckering coordinates. J. Am. Chem. Soc. 1975 Mar;97:1354-8. DOI: 10.1021/ja00839a011.

36.	Okumuş A, Bilge S, Kılıç Z, Öztürk A, Hökelek T, Yılmaz F. Phosphorus−nitrogen compounds. part 20: fully substituted spiro-cyclotriphosphazenic lariat (PNP-pivot) ether derivatives. Spectrochimica Acta Part A. 2010 Apr;76:401-9. DOI: 10.1016/j.saa.2010.04.007.

37.	Farrugia L.J.ORTEP-3 for Windows- a version of ORTEP-III with a Graphical User Interface (GUI). J. Appl. Crystallogr. 1997 Feb;30:565-6. DOI: 10.1107/S0021889897003117.

38.	Haapasalo M, Ranta H, Ranta K.T. Facultative gram-negative enteric rods in persistent periapical infections. Acta OdontolScand. 1983;41:19-22. DOI: 10.3109/00016358309162299.

Türkçe Öz ve Anahtar Kelimeler

4-FLOROBENZİLSPİRO(N/O) TRİMERİK HALKALI FOSFAZENLERİN VE TUZLARININ SENTEZİ, YAPILARININ KARAKTERİZASYONU, ANTİMİKROBİYAL AKTİVİTELERİ VE DNA İLE ETKİLEŞİMLERİ

Gamze Elmas[1,*], Aytuğ Okumuş[1], Zeynel Kılıç[1], L. Yasemin Gönder[2], Leyla Açık[3], Tuncer Hökelek[4]

[1]Ankara Üniversitesi, 06100, Ankara, Türkiye
[2]Türkiye Şeker Fabrikası, 06510, Ankara, Türkiye
[3]Gazi Üniversitesi, 06500, Ankara, Türkiye
[4]Hacettepe Üniversitesi, 06800, Ankara, Türkiye

*Gamze Elmas. E-mail: gegemen@ankara.edu.tr, tel: +90 0312 2126720/1195.

Özet: Bu makalede, $N_3P_3Cl_6$ (**1**) bileşiğinin sodyum 3-(4-florobenzilamino)-1-propanoksit ile kondenzasyon tepkimesinden kısmen sübstitüe 4-florobenzilspiro(N/O) trimerik halkalı fosfazen (**2**) bileşiği elde edildi. Bu bileşiğin klorlarının aşırı miktarda benzilamin, n-hekzilamin, n-bütilamin ve n-propilamin ile yer değiştirme tepkimelerinden 4-florobenzilspiro(N/O)tetrabenzilamino (**3a**), tetrahekzilamino (**3b**), tetrabütilamino (**3c**) and tetrapropilamino (**3d**) halkalı trifosfazen bileşikleri oluştu. Oluşan bu bazların (**3a-3d**), kuru THF'de gentisik asit ile etkileştirilmesinden fosfazenyum tuzları (**4a-4d**), protik iyonik sıvılar (protic ionic liquids; PILs), sentezlendi. Elde edilen tüm bileşiklerin yapıları; element analizleri, FTIR ve ^1H, $^{13}C\{^1H\}$, $^{31}P\{^1H\}$ NMR verileri kullanılarak belirlendi. Bileşik **4d**'nin kristal yapısı X-ışını kırınımmetre yöntemi ile aydınlatıldı. Tüm bileşiklerin bakteri ve mayalara karşı antibakteriyal ve antifungal aktiviteleri incelendi. Ayrıca, bu bileşiklerin süper sarmal plasmid pUC18 DNA ile etkileşimleri araştırıldı.

Anahtar Kelimeler: Spirosiklotrifosfazenler, kristallografi, spektroskopi, antimikrobiyal aktivite, DNA'ya bağlanma.

RESEARCH ARTICLE

(This article was presented to the 28th National Chemistry Congress and submitted to JOTCSA as a full manuscript)

Production and Investigation of Controlled Drug Release Properties of Tamoxifen Loaded Alginate-Gum Arabic Microbeads

Onur Korkmaz[1], Bernis Girgin[1], Çağdaş Sunna[1], Rukiye Yavaşer*[1], Arife Alev Karagözler[1]
[1]Adnan Menderes University, 09010, Aydın, Turkey

Abstract: The entrapment of tamoxifen onto alginate-gum arabic beads and the production of controlled drug release was investigated in this study. The polymeric system that would provide the controlled release of tamoxifen was formed using alginate and gum arabic. In the first phase of the study, the optimization of the alginate-gum arabic beads production was conducted; then the study continued with drug entrapment experiments. Tamoxifen entrapment yield was found to be approximately 90% of initial tamoxifen concentration. *In vitro* drug release experiments were performed in simulated gastric juice and intestinal fluid where the tamoxifen release was 20% and 53% of the initial drug present, respectively. As a result of this study, it is expected that a valuable contribution to the field of controlled drug release system production is realized.

Keywords: Tamoxifen, alginate, gum arabic, bead, controlled drug release.

*Corresponding author: E-mail: ryavaser@gmail.com, tel: +902562128498.

INTRODUCTION

Controlled drug release systems have a significant role in medicine. They are considered as useful systems that enable the drug to be more efficient. These systems have advantages such as decreasing the risk of harmful effects that may come from the drug and increasing the efficiency and availability of the drug compared to conventional drug applications (1). In controlled drug release systems, the drug is entrapped by the carrier. The carrier is required to release the drug in a desired manner during its voyage to the defined part of the body or when it reaches there.

Natural polymers have gained attention as suitable materials to produce controlled drug release systems (2). Alginate (Figure 1a) is a natural polysaccharide composed of α-1,4-guluronic acid and β-D-mannuronic acid blocks. Guluronic acid residues are responsible for the gelation properties of alginate. Alginate is a water-soluble, linear, and polyanionic biopolymer obtained from brown algae and it is employed in numerous applications such as food, textile, pharmaceutical, cosmetic industries as stabilizers, thickening and gelling agents, and adhesives. Alginate is reported to be safe when it is taken by the oral route since it is nontoxic and biodegradable (3). Alginate can be gelled with Ca^{2+} anions easily. Gel beads, microparticles and nanoparticles can be synthesized from alginate alone or together with other polymers like chitosan, gelatin, and albumin. Gum arabic (Figure 1b) is a polysaccharide obtained from acacia tree. Similar to alginate, gum arabic finds usage in food and other industries.

(a)   (b)
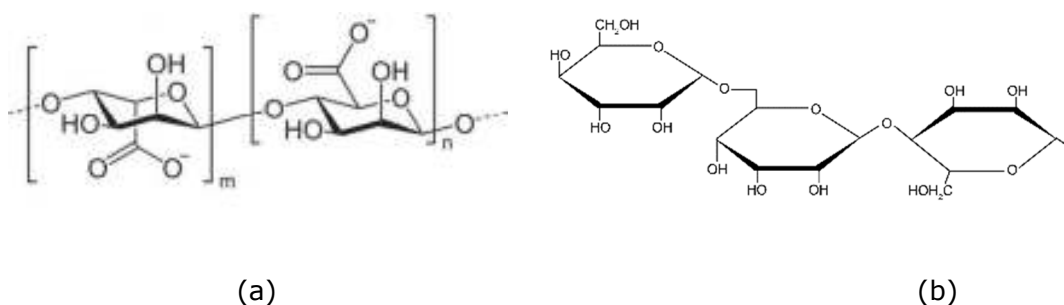
Figure 1. Molecular structures of alginate (a) (4) and gum arabic (b) (5).

Tamoxifen [(*Z*)-2-[4-(1,2-diphenylbut-1-enyl)phenoxy]-*N*,*N*-dimethyl-ethanamine, TMX] (Figure 2) is a synthetic drug used for cancer therapy. It is an antagonist for estrogen receptors in mammary tissue via its active metabolite hydroxytamoxifen (6). Antagonists attach to the cell receptor and act as a natural stimulator and prevent the natural response (7). TMX is being administrated to patients with different stages of breast cancer and although it is a very effective drug, in high doses it may lead some harmful developments such as endometrial cancer and tumor progression (8-9). Entrapment materials were synthesized for minimizing these disadvantageous effects to capture tamoxifen and deliver

it to the tumor site. Polymeric micelles (10), nanoparticles (11-12), alginate/chitosan microparticles (13), and hydrogels (14) are examples of tamoxifen carriers.
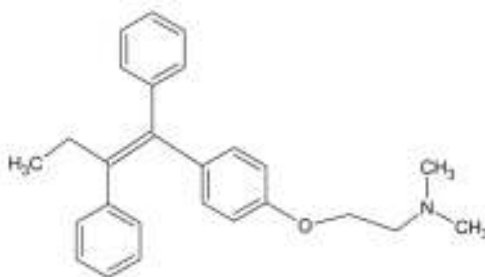
Figure 2. Chemical structure of tamoxifen molecule (15).

In this study, the entrapment of tamoxifen into alginate/gum arabic beads and *in vitro* controlled tamoxifen release was investigated. The aim of the study was to develop a new carrier for tamoxifen with a high entrapment yield and good carrier properties.

MATERIALS AND METHODS

Materials

Tamoxifen citrate, alginic acid sodium salt from brown algae (medium viscosity), $CaCl_2$, gum arabic, ethanol, and HCl were purchased from Sigma (Steinheim, Germany). Tween 80 was obtained from Merck (Darmstadt, Germany) and KCl was obtained from Carlo Erba (Ronado, Italy). Phosphate buffer tablets (PBS) were purchased from Oxoid (Hampshire, England). All chemicals used were of analytical grade.

Production of plain alginate-gum arabic beads

Plain beads were prepared by ionic crosslinking method (16). Two hundred milligrams of alginic acid sodium salt was dissolved by stirring the solution at 200 rpm at room temperature for 30 min in 20 mL distilled water. Gum arabic (100 mg) was added slowly and mixture was stirred for 30 min at 200 rpm and sonicated for 5 min. Alginate-gum arabic solution was added dropwise into continuously stirred (100 rpm) 5% $CaCl_2$ solution. The resulting beads were maturated for 1 h, filtered, and washed with distilled water.

Preparation of TMX entrapped alginate-gum arabic beads

TMX entrapped beads were produced by adding 1.0 mL of TMX solution (3 mg/mL in ethanol) into 20 mL of alginate solution (1%, w/v) containing 100 mg gum arabic. The

solution was mixed at 200 rpm for 30 min. The resulting solution was added dropwise into the crosslinker solution (5% CaCl$_2$) and the drug-entrapped beads were obtained (Figure 3). The beads were maturated for 1 hour, then filtered. All experiments were employed triplicate.
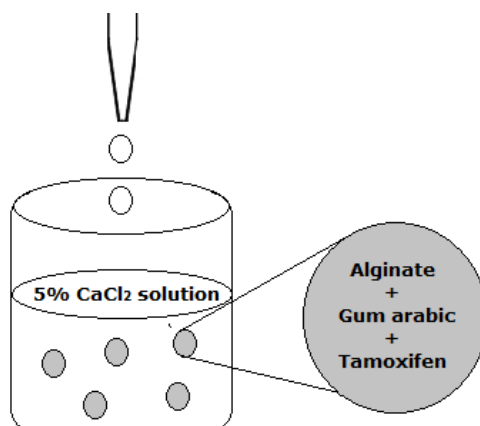
Figure 3. Production of TMX entrapped alginate-gum arabic beads.

Entrapment efficiency (EE%)

Entrapment efficiency was calculated evaluating the drug content in the filtrate that indicates the untrapped TMX. Two mL of the filtrate was centrifuged at 18000 rpm at 4 ºC for 30 min in order to remove any suspended molecules and the absorbance of the supernatant was recorded at 276 nm. The EE% of beads was calculated from the formula given below:

$$EE = \frac{\text{Total TMX added (mg)} - \text{Untrapped TMX (mg)}}{\text{Total TMX added (mg)}} \times 100$$

***In vitro* release studies**

I*n vitro* release of TMX from alginate-gum arabic beads was carried out at 37±1 °C in 50 mL of simulated gastric fluid (SGF) (mixture of 100 mL 0.2 M HCl and 82.8 mL 0.2 M KCl, pH 1.5) and 103 mL of simulated intestinal fluid (SIF) (100 mL PBS solution containing 3.0 mL of 1% Tween 80, pH 7.4) separately. At 30 min intervals, 2.0 mL aliquots were sampled out. Prior to absorbance measurements at 276 nm, the samples were centrifuged at 18000 rpm at 4ºC for 30 min to remove any suspended particles. The percent of TMX released was calculated and plotted versus time.

The release profile of TMX was also evaluated in SGF and SIF consecutively. Beads were transferred into 100.0 mL of SGF and allowed to stir at 150 rpm for 2 h. At each 30 min intervals, 2.0 mL of the medium was sampled and centrifuged at 18000 rpm at 4 ºC for 30 min and the absorbance was recorded at 276 nm. Then, beads were removed from SGF and transferred into 103 mL of SIF and stirred for another 3 h. The release procedure was followed in intestinal medium for 22 hours. Release experiments were conducted at 37 ºC in triplicate. The amount of released tamoxifen was calculated from TMX standard curve.

RESULTS AND DISCUSSION

In this study, an anticancer agent, Tamoxifen, was selected as the model drug which was further entrapped by ionic crosslinking method in alginate and gum arabic natural polymers. Alginate-gum arabic beads were produced and their abilities to release the anticancer drug Tamoxifen in a controlled manner were investigated. A polysaccharide blend was prepared composed of alginate and gum arabic. Spherical beads were obtained about 3 mm size (Figure 4).

Figure 4. TMX entrapped alginate-gum arabic beads.

TMX entrapment efficiency was calculated using the TMX standard curve which is demonstrated in Figure 5. According to the results from entrapment studies, approximately 90% of TMX was entrapped in the beads.
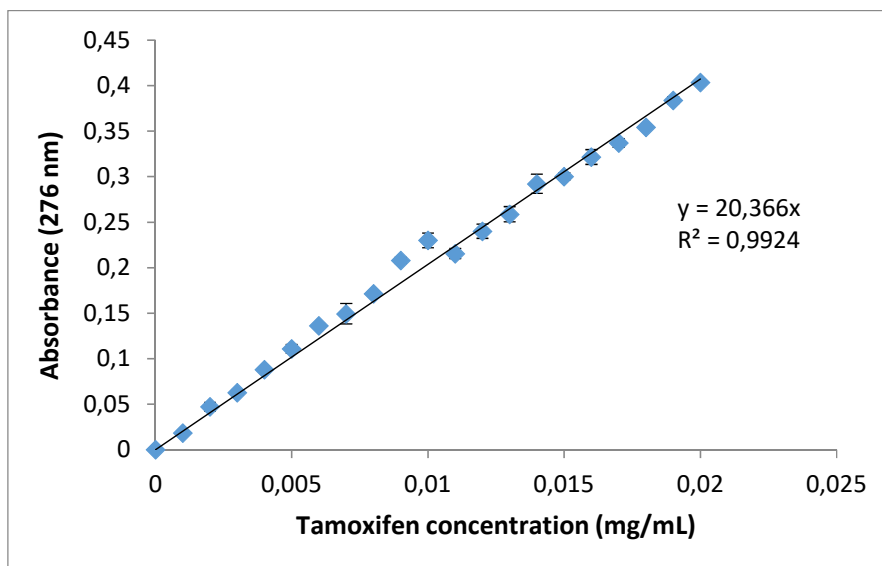
Figure 5. TMX standard curve.

The extend of drug release in *in vitro* stomach (gastric) and small intestine (intestinal) media were measured using pH 1.5 and pH 7.4 for 24 hours. The results revealed that the release of the initial TMX present in beads was 20% at pH 1.5 whereas it was 53% at pH 7.4. The release ratio did not change significantly after five hours. The release profiles in SGF and SIF are shown in Figures 6 and 7.
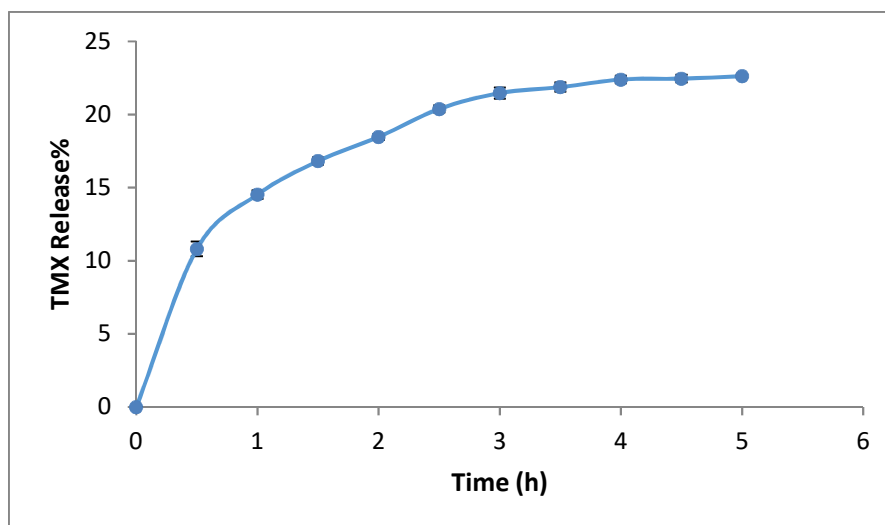
Figure 6. The release profile of TMX entrapped alginate-gum arabic beads in SGF.

For *in vitro* drug release studies, the physiological conditions such as pH and temperature are important. Simulated gastric fluid (pH 1.5) and simulated intestinal fluid (pH 7.4) are usually preferred as drug release media. The temperature of the release medium is generally chosen as 37 °C since it is the temperature of the human body. By this way, the results reflect the behavior of drug carrier particle in the body.
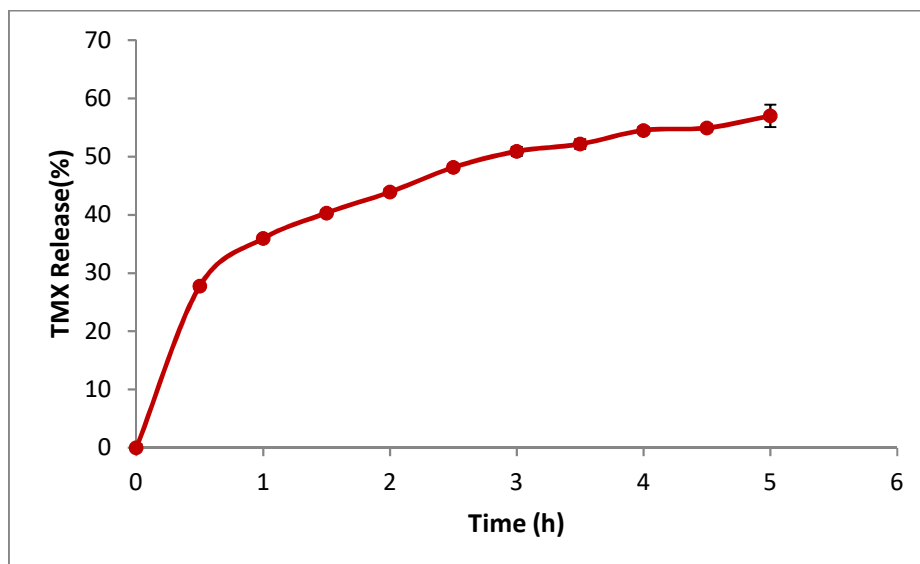
Figure 7. The release profile of TMX entrapped alginate-gum arabic beads in SIF.

The release percentage in SGF was lower compared to SIF. This may be explained by the swelling behaviors of beads in these media. Alginate-gum arabic beads might have the capability to swell and release the drug entrapped slightly in gastric medium. However, they might swell more in intestinal media and also disintegrate and allow the drug to become free (17). Disintegration may be the major reason of higher release profile since calcium favors to form calcium phosphate (18), as it is observable that the release medium was turbid during the studies in SIF.

The consecutive TMX release in SGF and SIF was also studied and was illustrated in Figure 8. The results were similar to individual procedures applied in SGF and SIF alone. However, this treatment was assumed to be more convenient to mimic the stages that a drug passes in the human body. As seen in Figure 8, 30% of TMX was released in SGF and when the beads were transferred into SIF, with a shift of 10% in 30 min, 60% of cumulative TMX release was observed after 5 h.
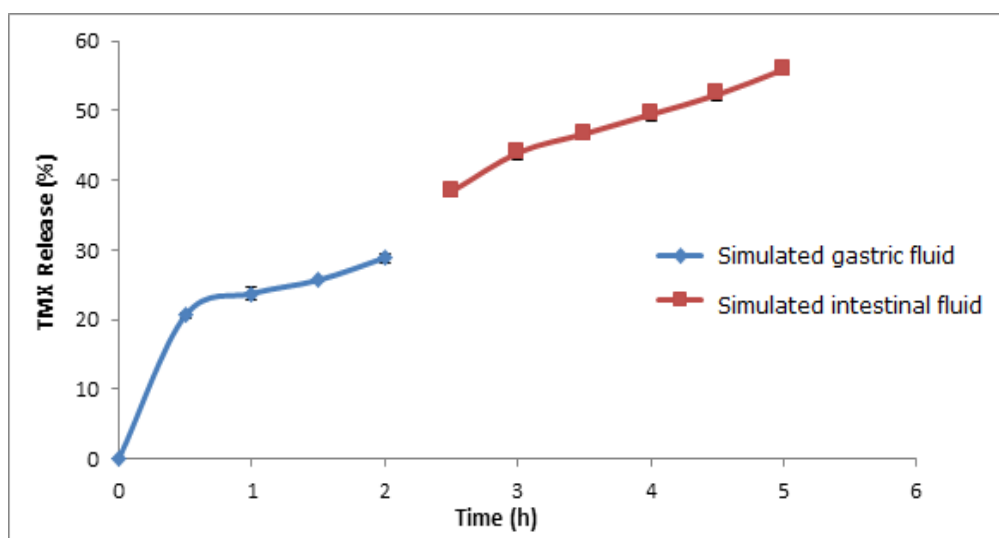
Figure 8. Consecutive TMX release from alginate-gum arabic beads in SGF and SIF.

CONCLUSION

The polymeric system that provided the controlled release of Tamoxifen was built using alginate and gum arabic natural polymers. *In vitro* drug release experiments were conducted in simulated gastric juice and intestinal fluid using the tamoxifen entrapped beads. It may be concluded that results presented here indicates that it is possible to manufacture a working drug carrier and release system for Tamoxifen using alginate and gum arabic natural polymers. The study needs further investigation for production of the drug carrier in real time manufacturing plants.

ACKNOWLEDGEMENTS

REFERENCES

1. Kumar R, Majeti NV. Nano and microparticles as controlled drug delivery devices. Journal of Pharmaceutical Sciences. 2000; 3(2):234-258. http://www.ncbi.nlm.nih.gov/pubmed/10994037.

2. Jana S, Ghandi A, Sen KK, Basu SK. Natural Polymers and their application in drug delivery and biomedical field. 2011; 1(1):16-27. http://www.pharmascitech.in/admin/php/uploads/6_pdf.pdf.

3. Kalia S., Averous L. Biopolymers: Biomedical and Environmental Applications. Scriven Publishing LLC., Massachusetts. 2011. ISBN: 978-0-470-63923-8.

4. Guarino V, Caputo T, Altobelli R, Ambrosio L. Degradation properties and metabolic activity of alginate and chitosan polyelectrolytes for drug delivery and tissue engineering applications. AIMS Materials Science. 2015; 2(4): 497-502. DOI: 10.3934/matersci.2015.4.497.

5. http://www.justpaint.org/the-science-behind-qor/

6. Ogura K, Ishikawa Y, Kaku T, Nishiyama T, Ohnuma T, Muro K, Hiratsuka A. Quaternary ammonium-linked glucuronidation of trans-4-hydroxytamoxifen, an active metabolite of tamoxifen, by human liver microsomes and UDP-glucuronosyltransferase 1A4. Biochemical Pharmacology. 2006; 71(9): 1358-1369. DOI: 10.1016/j.bcp.2006.01.004.

7. Jensen, SC, Peppers, MP. Pharmacology and drug administration for imaging technologists. Elsevier Health Sciences, 2013. ISBN: 978-0-323-03075-5.

8. MacGregor JI, Jordan VC. Basic guide to the mechanisms of antiestrogen action. Pharmacological Reviews. 1998; 50(2): 151–196. PMID: 9647865.

9. Brigger I, Chaminade P, Marsaud V, Appel M, Besnard M, Gurny R, Couvreur P. Tamoxifen encapsulation within polyethyleneglycol-coated nanospheres. A new antiestrogen formulation. International Journal of Pharmaceutics. 2001; 214(1): 37-42. DOI:10.1016/S0378-5173(00)00628-1.

10. Cavallaro G, Maniscalco L, Licciardi M, Giammona G. Tamoxifen-loaded polymeric micelles: preparation, physico-chemical characterization and in vitro evaluation studies. Macromolecular Bioscience. 2004; 4(11): 1028-1038. DOI: 10.1002/mabi.200400089.

11. Chawla JS, Amiji MM. Biodegradable poly (ε-caprolactone) nanoparticles for tumor-targeted delivery of tamoxifen. International Journal of Pharmaceutics. 2002; 249(1):127-138. DOI:10.1016/S0378-5173(02)00483-0.

12. Maji R, Dey NS, Satapathy B., Mukherjee B, Mondal S. Preparation and characterization of Tamoxifen citrate loaded nanoparticles for breast cancer therapy. International Journal of Nanomedicine. 2014; 9, 3107. DOI:10.2147/IJN.S63535.

13. Coppi G, Iannuccelli V. Alginate/chitosan microparticles for tamoxifen delivery to the lymphatic system. International Journal of Pharmaceutics. 2009; 367(1): 127-132. DOI:10.1016/j.ijpharm. 2008.09.040.

14. Shaker DS, Shaker MA, Klingner A, Hanafy MS. In situ thermosensitive Tamoxifen citrate loaded hydrogels: an effective tool in breast cancer loco-regional therapy. Journal of Drug Delivery Science and Technology. 2016; 35:155-164. DOI:10.1016/j.jddst.2016.05.007.

15. Yarman A, Scheller FW. The first electrochemical MIP sensor for tamoxifen. Sensors. 2014; 14(5): 7647-7654. DOI: 10.3390/s140507647.

16. Malakar M,Nayak AK, Pal D, Jana P. Potato starch-blended alginate beads for prolonged release of tolbutamide: Development by statistical optimization and *in vitro* characterization. Asian Journal of Pharmaceutics. 2013; 7: 43-51. DOI: 10.4103/0973-8398.110935.

17. Nayak AK, Das B, Maji R. Calcium alginate/gum arabic beads containing glibenclamide: Development and in vitro characterization. International Journal of Biological Macromolecules. 2012; 51(5): 1070-1078. DOI:10.1016/j.ijbiomac.2012.08.021.

18. Lee, B. J., Min, G. H., & Kim, T. W. Preparation and in vitro release of melatonin-loaded multivalent cationic alginate beads. Archives of Pharmacal Research. 1996; 19(4): 280-285. DOI:10.1007/BF02976241.

Tamoksifen Yüklü Aljinat-Gam Arabik Mikroboncukların Üretimi ve Kontrollü İlaç Salımı Özelliklerinin İncelenmesi

Onur Korkmaz, Bernis Girgin, Çağdaş Sunna, Rukiye Yavaşer, Arife Alev Karagözler

Öz: Bu çalışmada aljinat-gam arabik boncuklarına tamoksifenin tutturulması ve kontrollü ilaç salımının üretilmesi araştırılmıştır. Tamoksifenin kontrollü salımını sağlayacak polimerik sistem aljinat ve gam arabik kullanılarak oluşturulmuştur. Çalışmanın ilk kısmında, aljinat-gam arabik boncuklarının en uygun şartlarda elde edilmesi sağlanmıştır; ardından çalışma ilaç tutuklama deneyleriyle devam etmiştir. Tamoksifen tutuklaması ilk tamoksifen derişiminin yaklaşık %90'ı kadar tespit edilmiştir. *In vitro* ilaç salım deneyleri yapay mide ve bağırsak ortamına benzer ortamlarda gerçekleştirilmiştir ve tamoksifen salımı baştaki ilaç derişiminin sırayla %20'si ve %53'ü olarak bulunmuştur. Bu çalışmanın sonucu olarak, kontrollü ilaç salımı sistem üretimine değerli bir katkıda bulunulması beklenmektedir.

A Study on the Sensitivity and Selectivity Properties of Polymer-Based Gas-Vapor Sensors

Hüsnü Cankurtaran[1,*], Özlem Yazıcı[1], Ferdane Karaman[1]

[1]Yıldız Technical University, Faculty of Science and Letters, Department of Chemistry, 34220, İstanbul, Turkey

Abstract: In this study, the water soluble poly (diphenylaminesulfonic acid) (PSDA) and the diblock copolymer of PSDA with poly(ethylene glycol) (PEG) were used to construct the interdigitated film electrodes (IDEs). Their responses against humidity and various solvent vapors were investigated by impedance measurements. Sorption and desorption behaviors of the solvents were determined by simultaneous registration of the impedance (Z) and the resistive (R, resistance) and capacitive (X, reactance) components of the Z under different potential bias and alternating current (ac) frequencies. The sensor responses were discussed considering the polar/non-polar and polarizability properties of the polymers and solvents. The effect of ac frequency and potential bias on the sensitivity and selectivity of the sensors were discussed. It was found that the solvent polarity is the primary effect on the electrical conductance and capacitance of both PSDA homopolymer and PSDA-b-PEG block copolymer. The results supported that the dipolarity-polarizability properties of solvents have also a critical role on sensor response at low ac frequencies. The more polarizable solvents gave higher sensor responses at lower ac frequencies. The equilibrium response of the PSDA based sensor was correlated with the dielectric constant of the solvents. The values of Z and R of PSDA film under saturated solvent vapors at 1 kHz ac frequency were linearly correlated (R^2 was 0.955, 0.993 and 0.957 for Z, R and X, respectively, in semi-logarithmic scale) with the values of the dielectric constants of the solvents, except water. A similar correlation (R^2= 0.996) was obtained by using the R values of the PSDA film at 100 kHz ac frequency. In the case of PSDA-b-PEG polymer film, it was also possible to establish an almost linear correlation (R^2=0.943) between the R at 100 kHz ac frequency and the values of the dielectric constants of the solvents, except acetone and water. Consequently, it was found that the applied ac frequency was distinctive on both the sensitivity and selectivity of the studied sensor.

INTRODUCTION

Some thermodynamic parameters have been extensively used to explore the polymer-solvent interactions and recognition patterns of the polymer based sensor devices [1-9]. Many transduction mechanisms have been proposed to explore sensing characteristic of the various type of sensors. Electrical resistivity measurement is one of the most practical transduction methods in gas sensor technology. The sensitivity and selectivity of each individual sensor is controlled by tailoring the chemical and physical properties of the coating material to maximize particular solubility interactions. The interactions between gas or vapor molecules and polymeric sensing material are mainly based on solubility interactions, which have been modeled and systematically investigated using linear solvation energy relationships (LSERs) for non-polar systems [10-12]. Solubility properties are characterized and quantified by solvation parameters related to polarizability, dipolarity, acidity, basicity, and dispersion interactions. Some physical properties such as porosities of sensing elements and molar mass, molar volume and vapor pressure of analytes have been also taken into consideration to predict the polymer-solvent interactions and recognition pattern of the sensor devices [5, 7, 8]. The crucial problem with the use of such parameters is, in fact, a complex quantity.

In general, some electrical conductive materials, such as carbon black and graphite, have been used as probes in polymer composites to measure the electrical resistance response of sensors to various solvent vapors [3, 7-9, 13]. Different response mechanisms have been described for carbon black (or graphite)/polymer composites. When the sensor was exposed to a solvent vapor, swelling of the polymer matrix decreases the electrical connectivity between the conductive particles within the composite, and cause an increase in electrical resistance [18, 19]. For crystalline polymers, it was also considered that the polymer matrix within the composite is dissolved by solvent absorption, and the movement of carbon black particles in the amorphous regions causes the destruction of conductive networks, which results in the increase in electrical resistance consequently [13,14]. In some cases, the decreasing of resistance has been observed for polar solvent vapors due to the increasing the mobility of polar analytes, ionizable hydrophilic functional groups and/or doped ions in the sensing material if the hydrophilic polymers, polyelectrolytes and ion doped conductive polymers are used as sensing element [15-18]. Capacitance measurements (impedimetric sensors) have been also widely used in gas-vapor sensors, if the insulating polymers are used as sensing element and there is a significant difference between the dielectric permittivity of sensing material and vapor analyte. For example, capacitive insulating polymer based sensors have been extensively used for humidity

measurement because of the high dielectric permittivity of water, compare to insulating polymers [19-22]. Consequently, the chemical properties of the sensing material and analyte are important for the resistive/capacitive type of sensors, which determines the transduction method, sensitivity and selectivity.

Apart from the above findings, one of the other determining factors on the sensitivity and selectivity of the resistive/capacitive type of sensors is the induced polarization and the other one is the orientational polarization of solvent vapors under electrical field. It is known that if the frequency of the electric field is increased, the orientational polarization is decreased because the permanent dipoles need some time to rotate or reorient for polarization [10]. Empirical solvent polarity/polarizability parameters have been also proposed to correlate the solute-solvent interactions with these parameters [11]. In numerous studies, the effect of ac frequency and the polarization of water on the sensitivity and response/recovery time of the humidity sensors have been discussed [16, 17, 23]. It is well known that the polymer-based humidity sensors have low sensitivity for low humidity levels due to the lower polarization of water at high ac frequencies compare to that of the lower ac frequencies or dc current. The chemical properties of humidity sensing films and gas/solvent vapors have been also discussed in terms of sensitivity and selectivity. Literature survey shows that the selectivity of the humidity sensors was rarely studied [24-27]. However, to the best of our knowledge, the effect of ac frequency on the selectivity of humidity sensors has not studied to date. It is well known that the most of the hydrophobic polymers, such as polyacrylates, polystyrenes, and hydrophilic polymers such as polyelectrolytes, used in humidity sensors are soluble in many conventional solvents. Thus, in order to predict the sensitivity and selectivity of the polymeric humidity sensor elements to various solvents, it is required to investigate the sensor responses to organic vapors which are known as weak solvents or non-solvents for sensing polymer.

In our previous study, PSDA and PSDA-b-PEG based impedimetric sensors were studied to investigate the effect of applied potential bias, ac frequency and film thickness on the sensitivity and response kinetic in humidity measurements [16]. Nanohybrid composite of EPSDA (electrochemically synthesized PSDA) with nano-ZnO and 3-mercaptopropyltrimethoxysilane was also studied for impedimetric humidity measurement [17]. In this study, the effect of the applied potential and frequency on the selectivity and sensitivity of PSDA and PSDA-b-PEG based impedimetric sensors against water and other common solvents were studied. It was proposed that the selectivity and sensitivity of impedimetric gas/vapor sensors could be tailored via not only use of a suitable polymeric material but also choosing a suitable ac frequency.

EXPERIMENTAL

Apparatus

A Radiometer PST050 potentiostat was used in electrochemical polymerization of PSDA. A Pt sheet (2x3 cm), Ag/AgCl (3 M KCl) and Pt wire were used as working, reference and auxiliary electrode, respectively. A HIOKI 3522-50 model LCR meter was used for four point probe electrical measurements. Measurements were carried out at constant temperature (21±1 °C).

SEM images were obtained by using a Philips XL 30-ESEM-FEG/EDAX instrument. ATR-IR spectra of the thin polymer films were registered using a Perkin Elmer Spectrum One FT-IR spectrometer. UV-visible spectra were recorded using an Agilent-8453 spectrometer.

Materials

The sodium salt of diphenylaminesulfonic acid, polyethylene glycol (M_w: 750), tosyl chloride, ammonium hydroxide, hexane (Hx), heptane (Hp), acetone (Ac), ethylacetate (EA), chloroform (Ch), dichloromethane (DCM), tetrahydrofuran (THF) were of analytical grade. Hydrochloric acid and water were of ultra-pure grade.

Synthesis of Polymers

The electrochemical polymerization of diphenylaminesulfonic acid and the characterization of PSDA and PSDA-b-PEG block copolymer have been carried out as reported previously [16, 28] and not given here again. The chemical structure of the PSDA and PSDA-b-PEG are shown in Figure 1.

Fabrication of Humidity Sensor and Impedance Measurements

Appropriate amounts of aqueous polymer solutions of PSDA (10% w/v) and PSDA-b-PEG (11% w/v) were drop-casted onto the home-made Ag-coated copper IDEs [16, 17] which were constructed by using an epoxy-based circuit board. Then the as-coated substrates were dried at room temperature. Their electrical responses were measured upon exposure of saturated concentration of the solvents in a closed flask of 250 mL capacity. Dry atmosphere was obtained by passing the air through silica desiccant spheres in a column with 2 m in length and 0.7 cm in diameter, and used for the regeneration of the sensor. Impedance spectra were recorded in the frequency range of 100 kHz–10 Hz with a bias potential between 0.2-1.5 V after the steady state response of the sensor was obtained.

The electrical parameters (Z, R and X) were recorded every 5 seconds in the time interval measurement of sensor responses.

PSDA   **PSDA-b-PEG**
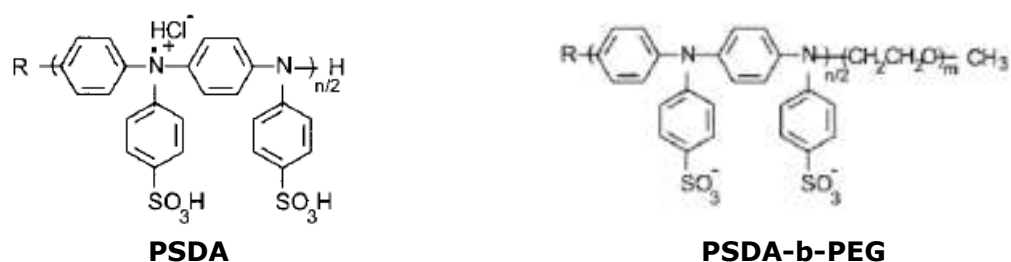
Figure 1. Chemical structure of the polymers.

RESULTS and DISCUSSION

Morphology of the Films

The electrical and sensing behaviors were expected to be related to the morphological arrangement and composition of the films. SEM images of the PSDA homopolymer and PSDA-b-PEG copolymer have been shown in Fig. 2. While the PSDA-b-PEG copolymer films have uniform morphology and stability against cracking, PSDA films may have non-uniform and relatively less stable structure in dry atmosphere [16]. Fortunately, the thinner PSDA films prepared by using 10 μL aliquot of PSDA solution were more stable against cracking and used for further studies. In addition, the sorption of the non-polar solvents by PSDA film was less than that of the PSDA-b-PEG films. Therefore, the impedance change upon exposure of non-polar solvents for thicker PSDA films was rather low. To obtain a higher impedance change and a higher sensitivity, the thinner PSDA films were more suitable in the comparative experiments. No cracks were observed for both thin and thick PSDA-b-PEG films in dry atmosphere. However, 150 μL of polymer solution was chosen to prepare the PSDA-b-PEG based sensor. This was done to make a thicker diffusion barrier and to protect the epoxy substrate against the deteriorative effect of some of the solvents which may act as good solvents for both substrate and sensing film.
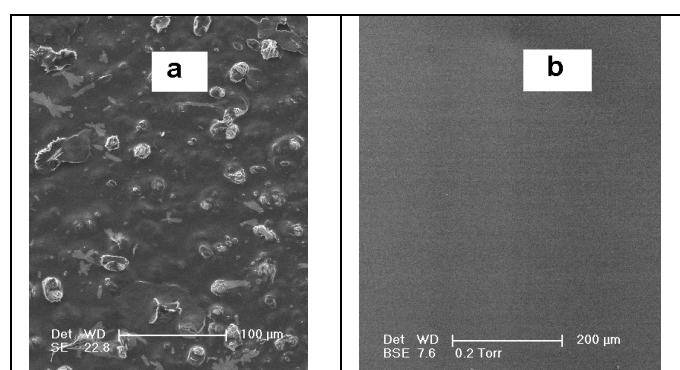
Figure 2. SEM images of a) PSDA, b) PSDA-b-PEG.

Frequency and Voltage Characteristics of the Sensor Responses

The electrical behavior of the polymer films were investigated at different constant voltage and ac frequencies. Figures 3.a-c show the impedance spectrum of the PSDA and PSDA-b-PEG based sensors in dry atmosphere. The spectrum shape for dry PSDA film has only a line slightly divergent from the ordinate at higher ac frequencies. Some difficulties were observed in measuring the impedance of dry PSDA film especially at a frequency lower than 1 kHz. This might be due to the destroying of the PSDA film at low ac or dc mode or its low dc conductance [16]. Despite the fact that the bulk PSDA-b-PEG film contains PEG polymer as a dielectric material, its electrical conductivity in dry atmosphere were not significantly lower than that of PSDA. As shown from SEM images, the PSDA-b-PEG film has a denser, rigid, and uniformly ordered structure and it should be well adhered onto the electrode enhancing the electronic conduction pathways between the digits of the electrode. At saturated vapor pressure of less polar and non-polar solvents, this line became a semicircle for both PSDA and PSDA-b-PEG films. It was presented for PSDA-b-PEG film in Figure 4.This is due to the decrease in capacitive reactance *i.e.*, increase in capacitance by sorption of solvents. It is expected that the adsorption of organic solvents, which have higher relative permittivities than oxygen and nitrogen in air [29], causes to increase in the capacitance of the films. It is important to note here that the resistive components of the impedances of the films exposed to non-polar solvent were higher than their dry film resistances at high frequencies. These results indicate to the distortion of the conductive pathways upon exposure of solvents, consequently, to the presence of electronic conductivity of dry PSDA film. At saturated or high vapor pressure of polar solvents such as acetone and water, the Warburg impedance was observed at low ac frequencies with or without a semicircle. This was demonstrated for acetone in Figure 5. The negative slope at high frequency section of the spectrum in Figure 5 is probably due to the increase in the sorption of acetone by decreasing in frequency during the registration of the impedance spectrum. In contrast with the PSDA-based film, the steady state resistance of the PSDA-b-PEG film in acetone atmosphere was lower than its dry film resistance even at high ac frequencies. This might be related with the higher solubility of PEG moiety of the block copolymer in acetone. As a result, doped ions from hydrochloric acid medium and/or ionizable functional groups of PSDA can move easily, resulting in a decrease of the resistance of the PSDA-b-PEG polymer [16, 17]. The same conduction mechanism was also observed for PSDA film at 1 kHz ac frequency.

The voltage dependency of the impedance spectrum of the dry films was insignificant. However, as shown in Figure 6 for PSDA-b-PEG film in saturated hexane atmosphere, the resistive component of the impedance in solvent atmosphere slightly changed with the

change in applied potential bias at lower ac frequencies. This is due to the polarizability of the sensor at higher voltages at dc or low ac mode [30]. It was considered that the polarization effect causes the formation of the electrolysis products and alter the electrical nature of the electro-active PSDA polymer and the film morphology [31]. This effect was more pronounced in the case of more polar solvents. Therefore, the applied potential bias was not higher than 0.5 V in the impedance measurements.
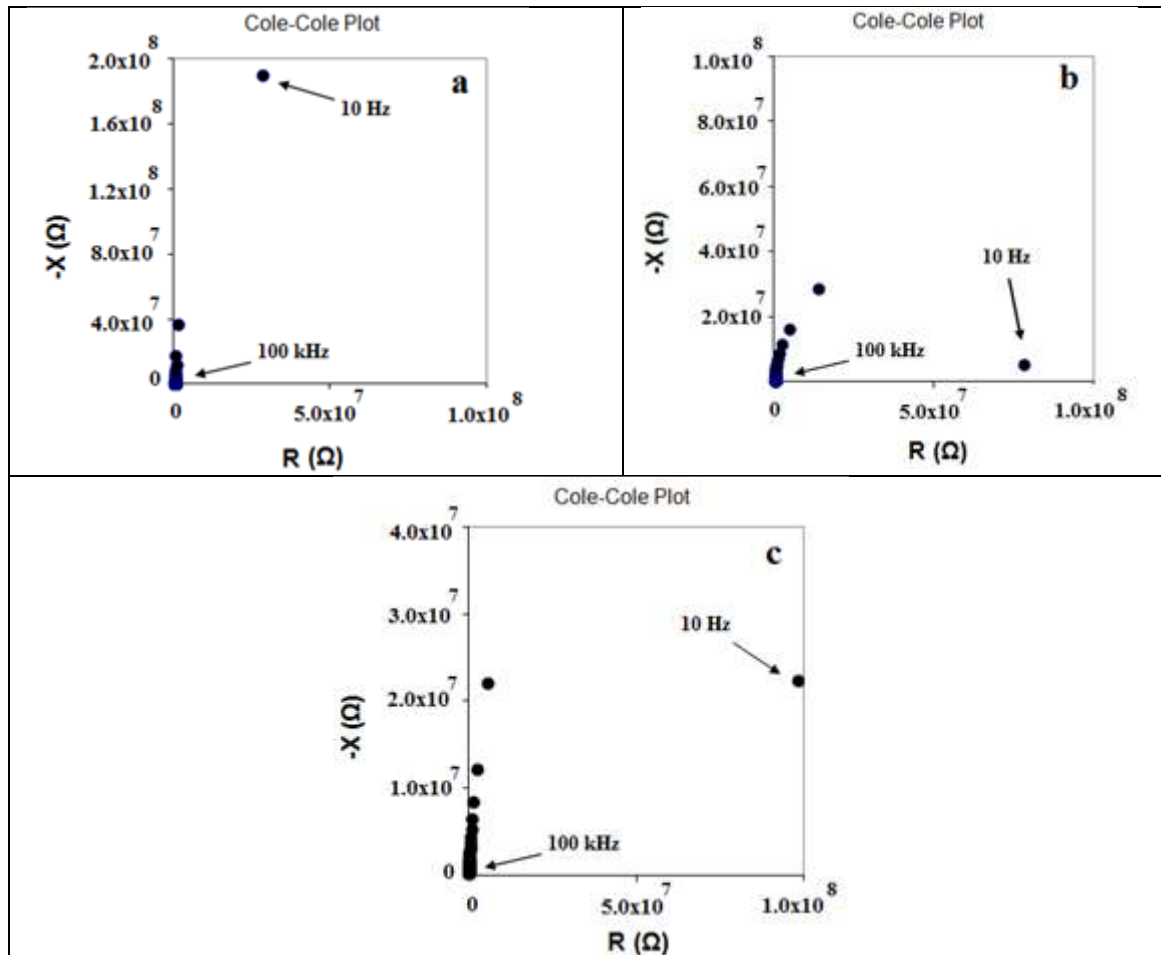
Figure 3. Impedance spectrum of the sensors coated with the solutions of a) 10 μL of PSDA, b) 10 μL PSDA-b-PEG and c) 150 μL of PSDA-b-PEG in dry atmosphere. Potential bias: 0.5 V.
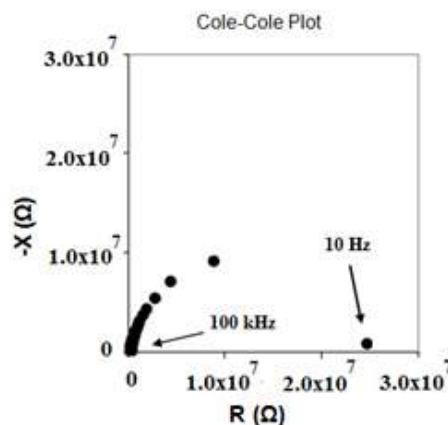
Figure 4. Impedance spectrum of the sensor coated with the solution of 150 μL of PSDA-b-PEG in saturated hexane atmosphere.
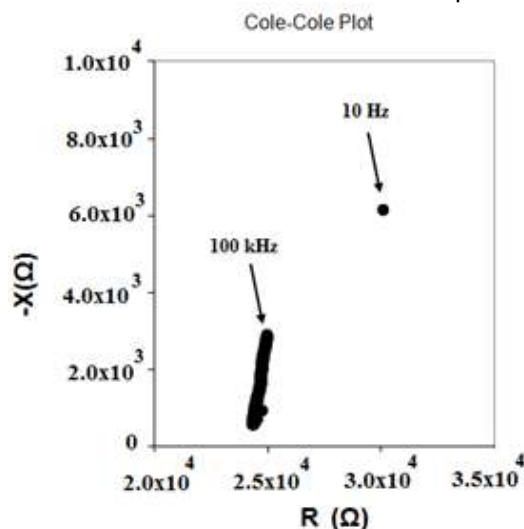
Figure 5. Impedance spectrum of the sensor coated with the solution of 150 μL of PSDA-b-PEG in saturated acetone atmosphere.
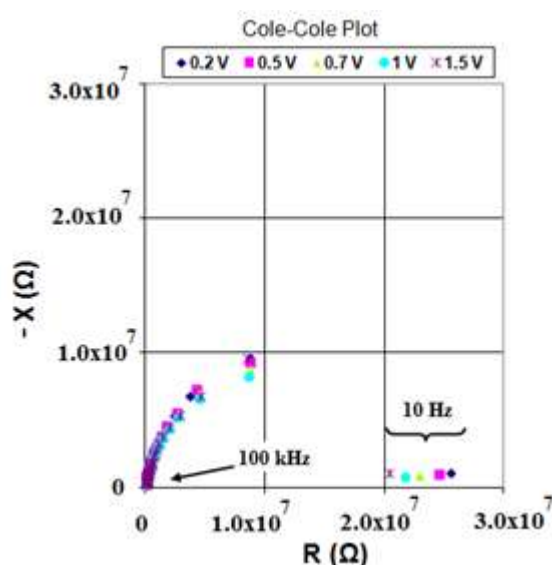
Figure 6. Applied potential bias dependency of impedance spectrum of PSDA-b-PEG sensor coated with the solution of 150 μL of PSDA-b-PEG in saturated hexane atmosphere.

The Effect of Solvent Properties on Sensor Response

The time dependent changes in the electrical properties of the polymer films of PSDA and PSDA-b-PEG upon successive exposure of solvents and dry air are given in Figures 7 and 8, respectively. It is clearly seen that the resistive component of impedance increases continuously with the exposure time of the non-polar solvents. In the case of the response of PSDA based sensor to acetone, the resistance increases firstly at initial time period of

solvent exposure and then decreases. Water exhibits a similar response behavior with that of acetone but the impedance and resistance of PSDA based sensor were much lower as close to 930 ohm at saturated humidity. The response to water was not shown in Figures 7 and 8 to show the low responses of the other solvents clearly. It can be seen from Figure 7, while the reactance determines the impedance of the dry film, the impedance of the acetone exposed film almost equals to the resistive component of impedance. Similar behavior can be seen for PSDA-b-PEG film in Figure 8. As inferred from Figures 7 and 8, compare with the PSDA film, the impedance change for the block copolymer film was higher between the exposure cycles of dry air and solvents.

The effect of ac frequency on the sensor responses was studied for both PSDA and PSDA-b-PEG film. The magnitude of the changes in electrical parameters upon exposure of solvents was higher at 1 kHz ac frequency. This was demonstrated for PSDA-b-PEG film in Figure 9.
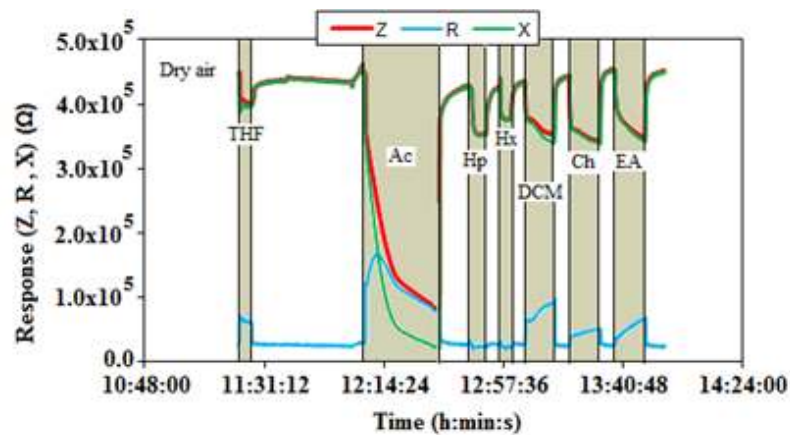
Figure 7. Time-dependent changes in impedance (Z) and resistive (R) and capacitive (X) components of the Z of PSDA based sensor upon exposure of solvents. Potential bias: 0.2 V, ac frequency: 100 kHz.
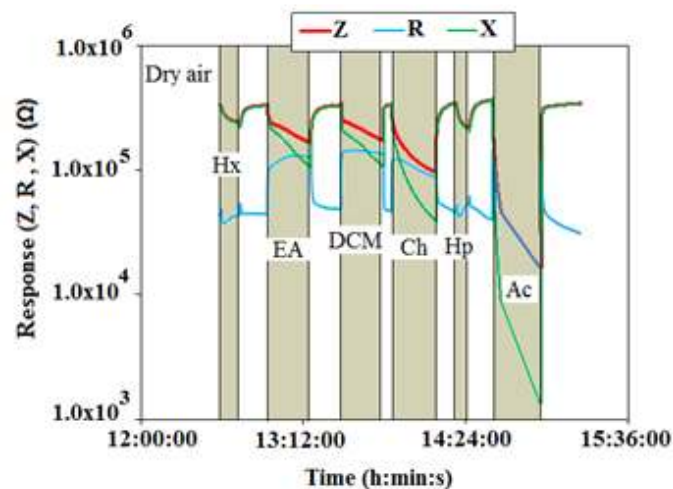
Figure 8. Time-dependent changes in impedance (Z) and resistive (R) and capacitive (X) components of the Z of PSDA-b-PEG based sensor upon exposure of solvents. Potential bias: 0.5 V, ac frequency: 100 kHz.
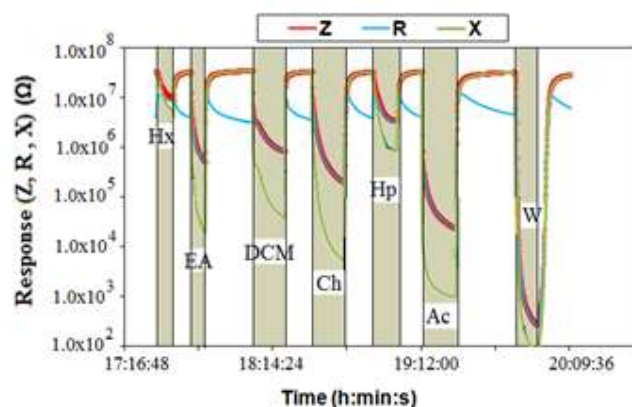
Figure 9. Time-dependent changes in impedance (Z) and resistive (R) and capacitive (X) components of the Z of PSDA-b-PEG based sensor upon exposure of solvents. Potential bias: 0.5 V, ac frequency: 1 kHz.

It was found that the saturated response of the PSDA based sensor was correlated with the dielectric constant of solvents. The dielectric constants of solvents are given in Table 1[32]. Both the Z and R of PSDA film decrease under exposure of solvents at 1 kHz frequency. The linear correlations (in semi-logarithmic scale) were found between the equilibrium Z (R^2=0.955), R (R^2=0.9926) and X (R^2=0.9569, not shown) values of PSDA film at 1 kHz ac frequency and the values of the dielectric constant of the solvents (Figure 10a). It can be concluded that the polarity of the sorbed solvent affects the electrical properties of the PSDA polymer. As shown in Figure10a, non-polarizable aliphatic solvents such as hexane and heptane (Table 1) have extremely lower resistance response on PSDA film than those of polar and less polar solvents at 1 kHz ac frequency. The relationship between their resistance and the dielectric constants of these solvents is not fitted with the linear correlation. It seems that the polarizability of solvents is definitely important on sensor responses at low ac frequencies. However, the resistance of the film under exposure of the polarizable solvents varies linearly with the dielectric constant of solvents regardless with their dipolarity/polarizability degree (π^*) given in Table 1. In addition, it was determined that the R value in saturated water atmosphere was very low (1.7 kohm at 1 kHz) and dropped to the out of the linearity range. Under high ac frequency of 100 kHz, a similar linear correlation (R^2= 0.9961) was obtained by using only the R values of the PSDA film (Figure 10b). It is noticeable that the resistance of PSDA film increases upon exposure of whole solvents studied, except water. It can be concluded that the changes in R at high ac frequency might be purely related with the change in electronic conduction and dielectric properties of solvents. In the case of PSDA-b-PEG polymer film, it was also possible to establish an almost linear correlation (R^2=0.943) between the R at 100 kHz ac frequency and the values of the dielectric constants of the solvents, except acetone and water (Figure

10c). It is also interesting to note here that the contribution of the acid-base behavior of the solvents and the applied ac frequency plays an important role on the sensor response. For example, while the resistance of PSDA-b-PEG sensor at 100 kHz ac frequency is higher in dichloromethane than that in chloroform, the case is *vice versa* at 1 kHz. This might be due to the higher acidic behavior of chloroform, compare with dichloromethane, and the basic PEG moiety of block copolymer [33]. As a result, the interaction between PSDA—b-PEG polymer and chloroform is expected to be stronger via acid-base interaction process, especially at low ac frequencies. It is worth to mention here again that the change in Z or R of PSDA-b-PEG film in water and acetone atmosphere is composed of changes in both electronic and ionic mobility of the charges even at high frequencies. Also, as mentioned above, the high solubility of PEG moiety in highly polar acetone and water enhance the possible ionic transport pathways of the ionic charges. On the other side, the data in Figures 10b and c are considered to be related with the electronic conductivity of charges. Therefore, no data point for acetone and water could be used for PSDA-b-PEG based sensor in Figure 10c to fit them with the linear correlation. It is because PEG is soluble in most of the solvents studied, except aliphatic hydrocarbons such as hexane and heptane, and the segmental and/or ionic mobility of the charge carriers in the film is enhanced under exposure of high and moderate polar solvents.

In conclusion, we have revealed that the sensor responses are greatly dependent on the nature of the solvent. The polarity of solvent is the primary effect on the electrical conductance and capacitance of both PSDA and PSDA-b-PEG based sensors. This effect promises be most useful in promoting selectivity of the given polymers. We confirmed that the interaction of the analyte molecule with the polymer and/or its attendant dopant anion, induces significant changes in the degree of pi conjugation and ionic mobility in the polymer back-bone, with concomitant changes in its conductivity. PSDA is a water-soluble and electronically conductive polymer. It is almost not soluble in common polar and non-polar solvents including alcohols. Although PEG is also soluble in many conventional solvents, it has a high humidity selectivity and sensitivity. On the other side, the humidity sensitivity and selectivity of the studied sensors was determined to be dependent on the applied ac frequency. Although the sensitivity of the sensors against polar solvents was higher at low frequencies, their humidity selectivity in the presence of the other solvent vapors, which have lower polarity/polarizability, could be increased by applying higher frequencies and choosing a suitable electrical parameter among the impedance, resistance and capacitive reactance.

Table 1. Dielectric constant and polarizability (π^*) of solvents studied [32].

Solvent	Dielectric constant	Scale of dipolarity-polarizability π^*
Water	78.39 (25°C)*	1.09*
Dichloromethane	9.02 (20°C)	0.82
Chloroform	4.89 (20 °C)	0.58
Acetone	21.36 (20°C)	0.71
Tetrahydrofuran	7.47 (20°C)	0.58
Ethylacetate	6.03 (20°C)	0.55
Hexane	1.89 (20°C)	-0.008
Heptane	1.94 (20 °C)	-0.008

*: Values taken from [10].
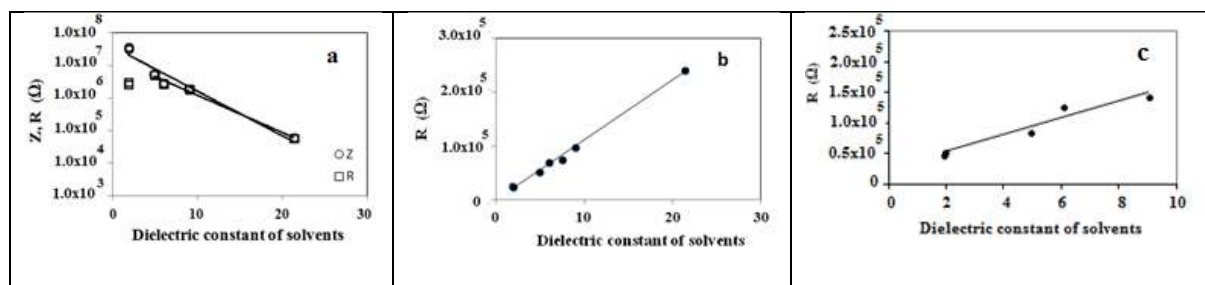
Figure 10. Relationship between the values of dielectric constant of solvents, and
a) ●: Z, □: R of PSDA film at 1 kHz,
b) R of PSDA film at 100 kHz and
c) R of PSDA-b-PEG film at 100 kHz.

ACKNOWLEDGEMENT

REFERENCES

[1] Mayer U, A semiempirical model for the description of solvent effects on chemical reactions, Pure Appl. Chem. 1979; 51: 1697-1712.

[2] Shevade AV, Ryan MA, Homer ML, Manfreda AM, Zhou H, Manatt KS, Molecular modelling of polymer composite–analyte interactions in electronic nose sensors, Sens. Actuators B. 2003 Sep; 93: 84-91.DOI: 10.1016/S0925-4005(03)00245-4.

[3] Li JR, Xu JR, Zhang MQ, Rong MZ, Carbon black/polystyrene composites as candidates for gas sensing materials, Carbon. 2003 Dec; 41 (12): 2353-60.DOI: 10.1016/S0008-6223(03)00273-2.

[4] Bouvree A, Feller JF, Castro M, Grohens Y, Rinaudo M, Conductive Polymer nano-bio Composites (CPC): Chitosan-carbon nanoparticle a good candidate to design polar vapor sensors, Sensors and Actuators B.2009 Apr; 138 (1): 138-47.DOI: 10.1016/j.snb.2009.02.022.

[5] Zeng W, Zhang MQ, Rong MZ, Zheng G, Conductive polymer composites as gas sensors with size-related molecular discrimination capability, Sensors and Actuators B. 2007 Jun; 124: 118-26.DOI: 10.1016/j.snb.2006.12.021.

[6] Vercelli B, Zecchin S, Comisso N, Zotti G, Berlin A, Dalcanale E, Groenendaal LB, Solvoconductivity of polyconjugated polymers: the roles of polymer oxidation degree and solvent electrical permittivity, Chem. Mater. 2002 Oct; 14 (11): 4768-74.DOI: 10.1021/cm0205938.

[7] Chen SG, Hu JW, Zhang MQ, Rong MZ, Effects of temperature and vapor pressure on the gas sensing behavior of carbon black filled polyurethane composites, Sensors and Actuators B. 2005 Mar; 105 (2): 187-93.DOI: 10.1016/j.snb.2004.05.060.

[8] Hu JW, Cheng GS, Zhang MQ, Li MW, Xiao DS, Chen SG, Rong MZ, Zheng Q, Electrical Response of Poly(ethylene Oxide)-Based Conductive Composites to Organic Vapors: Effect of Filler Content, Vapor Species, and Temperature, Journal of Applied Polymer Science. 2005 Nov; 98 (4): 1517-23.DOI: 10.1002/app.21973.

[9] Cakar F, Moroglu MR, Cankurtaran H, Karaman F, Conducting poly(ether imide)–graphite composite for some solvent vapors sensing application, Sensors and Actuators B. 2010 Mar; 145 (1): 126-32.DOI: 10.1016/j.snb.2009.11.045.

[10] Izutsu K, Electrochemistry in Nonaqueous Solutions, Part One: Fundamentals of Chemistry in Nonaqueous Solutions. Weinheim: WILEY-VCH; 2009. P. 10. ISBN: 978-3-527-32390-6.

[11] Kamlet MJ, Taft RW, Linear Solvation Energy Relationships. Local Empirical Rules or Fundamental Laws of Chemistry? A reply to Chemometricians. Acta Chem. Scand. 1985 Jan; B39: 611-28. DOI: 10.3891/acta.chem.scand.39b-0611.

[12] Hierlemann A, Zellers ET, Ricco AJ, Use of linear salvation energy relationships for modeling responses from polymer-coated acoustic-wave vapor sensors, Anal. Chem. 2001 Jun; 73 (14): 3458-66. DOI: 10.1021/ac010083h.

[13] Chen J, Tsubokawa N, Novel Gas Sensor from Polymer-Grafted Carbon Black: Vapor Response of Electric R of Conducting Composites Prepared from poly(ethylene-block-ethylene oxide)-Grafted Carbon Black, J. Appl. Poly. Sci. 2000 Sep; 77 (11): 2437-47. DOI: 10.1002/1097-4628(20000912)77:11<2437::AID-APP12>3.0.CO;2-F.

[14] Dong XM, Fu RW, Zhang MQ, Zhang B, Rong MZ, Electrical R response of carbon black filled amorphous polymer composite sensors to organic vapors at low vapor concentrations, Carbon. 2004 Jan; 42 (12-13): 2551-59. DOI:10.1016/j.carbon.2004.05.034.

[15] Sun A, Li Z, Wei T, Li Y, Cui P, Highly sensitive humidity sensor at low humidity based on the quaternized polypyrrole composite film, Sensors and Actuators B. 2009 Oct; 142 (1): 197-203.DOI: 10.1016/j.snb.2009.08.028.

[16] Cankurtaran H, Yazici O, Dinc S, Karaman F, Humidity Sensitive Properties of Electronically Conductive Poly(diphenylamine sulfonic acid) and Its Block Copolymer and Blends, Int. J. Electrochem.Sci. 2013 Mar; 8 (3): 3265-78.URL:http://www.electrochemsci.org/papers/vol8/80303265.pdf

[17] Zor ŞD, Cankurtaran H, Impedimetric Humidity Sensor Based on Nanohybrid Composite of Conducting Poly(diphenylamine sulfonic acid), Journal of Sensors. 2016; Article ID 5479092, 9 pages http://dx.doi.org/10.1155/2016/5479092.

[18] Lee CW, SW J, Gong MS, Polymeric humidity sensor using polyelectrolytes derived from alkoxysilane cross-linker, Sensors Actuators B. 2005 Mar; 105 (2): 150-58. DOI: 10.1016/j.snb.2004.05.037.

[19] Casalini R, Kilitziraki D, Wood D, Petty M, Sensitivity of the electrical admittance of a polysiloxane film to organic vapours, Sensors and Actuators B. 1999 Jul; 56 (1): 37-44.DOI: 10.1016/S0925-4005(99)00039-8.

[20] Harrey PM, Ramsey BJ, Evans PSA, Harrison DJ, Capacitive-type humidity sensors fabricated using the offset lithographic printing process, Sensors and Actuators B. 2002 Dec; 87 (2): 226-32.DOI: 10.1016/S0925-4005(02)00240-X.

[21] Kim JH, Hong SM, Moon BM, Kim K, High-performance capacitive humiditysensor with novel electrode and polyimide layer basedon MEMS technology,Microsystem Technologies Micro and Nanosystems Information Storage andProcessing Systems. 2010 Dec; 16 (12): 2017-21.DOI: 10.1007/s00542-010-1139-0.

[22] Lee MJ, Min NK, Yoo KP, Microhotplate-based high-speed polyimide capacitivehumidity sensors, Sensor Letters. 2009 Aug; 7 (4): 517-22.DOI: 10.1166/sl.2009.1102.

[23] Wang Y,Park S, Yeow JTW,, Langner A, Müller F, A capacitive humidity sensor based on ordered macroporous silicon with thin film surface coating, Sensors and Actuators B. 2010 Aug; 149 (1): 136-42.DOI:10.1016/j.snb.2010.06.010.

[24] Oikonomou P, Manoli K, Goustouridis D, Raptis I, Sanopoulou M, Polymer/BaTiO3 nanocomposites based chemocapacitive sensors, Microelectronic Engineering. 2009 Apr; 86 (4): 1286-8.DOI: 10.1016/j.mee.2008.11.081.

[25] Bearzotti A,Fratoddi I,Palummo L,Petrocco S,Furlani A,Lo Sterzo C,Russo MV, Highly ethynylated polymers: synthesis and applications for humidity sensors, Sensors and Actuators B. 2001 Jun; 76 (1-3): 316-21.DOI: 10.1016/S0925-4005(01)00607-4.

[26] Mohr GJ,Spichiger-Keller UE, Development of an optical membrane for humidity, Microchim. Acta. 1998 Mar; 130 (1-2): 29-34.DOI: 10.1007/BF01254587.

[27] Sakai Y, Sadaoka Y, Matsuguchi M, Humidity sensors based on polymer thin films, Sensors and Actuators B. 1996 Sep; 35 (1-3): 85-90.DOI: 10.1016/S0925-4005(96)02019-9.

[28] Hua FJ, Ruckenstein E, Synthesis of a water-soluble diblock copolymer of polysulfonic diphenyl aniline and poly(ethylene oxide), J. Poly. Sci., Part A: Polymer Chemistry. 2004 May; 42 (9): 2179-91.DOI: 10.1002/pola.20042.

[29] Schmidt JW, Moldover MR, Dielectric Permittivity of Eight Gases Measured with Cross Capacitors, Int. J. Thermophys.2003 Feb; 24 (2): 375-403.DOI: 10.1023/A:1022963720063.

[30] Gong MS, Kim JU, Kim JG, Preparation of water durable humidity sensor by attachment of polyelectrolyte membrane to electrode substrate by photochemical crosslinking reaction, Sensors and Actuators B. 2010 Jun; 147 (2): 539-47.DOI: 10.1016/j.snb.2010.04.017.

[31] Anderson JH, Parks GA, Electrical Conductivity of Silica Gel in the Presence of Adsorbed Water, The Journal of Physical Chemistry. 1968 Oct; 72 (10): 3662-68.DOI: 10.1021/j100856a051.

[32] Abboud JLM, Notario R, Critical compilation of scales of solvent parameters. Part I. Pure, non-hydrogen bond donor solvents, Pure Appl. Chem. 1999 Jan; 71 (4): 645-718.DOI: 10.1351/pac199971040645.

[33] Stuart BH, Williams DR, A study of the absorption of chlorinated organic solvents by poly(ether ether ketone) using vibrational spectroscopy, Polymer. 1995 Oct; 36 (22): 4209-13. DOI: 10.1016/0032-3861(95)92215-Z.

Polimer Esaslı Gaz-Buhar Sensörlerinin Hassasiyet ve Seçimlilik Özellikleri üzerine bir Çalışma

Hüsnü Cankurtaran[1,*], Özlem Yazıcı[1], Ferdane Karaman[1]

Öz: Bu çalışmada, suda çözünür poli(difenilaminosülfonik asit) (PSDA) ve PSDA'nın poli(etilen glikol) (PEG) ile diblok kopolimeri birbiri içine geçen film elektrotları (IDE'ler) yapmak için kullanılmıştır. Neme ve çeşitli çözücü buharlarına karşı tepkileri impedans ölçümleriyle araştırılmıştır. Çözücülerin sorpsiyon ve desorpsiyon davranışları farklı potansiyel sapması ve alternative akım (ac) frekanslarında impedansın (Z) altındaki resistif (R, rezistans), kapasitif (X, reaktans) bileşenlerinin eş zamanlı kayıt edilmesinden bulunmuştur. Sensör cevapları, polimerlerin ve çözücülerin polar/non-polar ve polarizlenebilirlik özellikleri düşünülerek tartışılmıştır. Ac frekansı ve potansiyel sapmasının, sensörlerin hassasiyet ve seçimliliği üzerindeki etkisi tartışılmıştır. Çözücü polarlığının PSDA homopolimer ve PSDA-b-PEG blok kopolimerlerinin elektriksel iletkenlik ve kapasitansı üzerine birincil derecede etkili olduğu bulunmuştur. Sonuçlar, çözücülerin dipolarite-polarizlenebilirlik özelliklerinin de düşük ac frekanslarında sensör cevabı üzerine kritik bir rol oynadığını göstermiştir. Daha çok polarize olabilen çözücülerin düşük ac frekanslarında daha yüksek sensör tepkisi verdiği bulunmuştur. PSDA esaslı sensörün denge cevabı, çözücülerin dielektrik sabitleri ile uyumludur. PSDA filmin doygun çözücü buharı altında 1 kHz ac frekansı altında Z ve R değerleri, su hariç olmak üzere çözücülerin dielektrik sabitlerinin değerleri ile doğrusal olarak ilişkili bulunmuştur (R^2 yarı logaritmik ölçekte Z, R ve X için sırası ile 0,955, 0,993 ve 0,957 bulunmuştur. Benzer bir korelasyon (R^2=0,996), 100 kHz frekansta PSDA filminin R değerleri kullanılarak elde edilmiştir. PSDA-b-PEG polimer filminde, 100 kHz ac frekansta R ile aseton ve su hariç olmak üzere çözücülerin dielektrik sabiti değerleri arasında neredeyse doğrusal bir ilişki bulunmuştur (R^2=0,943). Bunun sonucu olarak, uygulanan ac frekansının sensöre ait hassasiyet ve seçimlilik parametreleri üzerinde belirleyici rol oynadığı bulunmuştur.

Anahtar kelimeler: İletken polimer, poli(difenilaminosülfonik asit), polietilen glikol, polimer-çözücü etkileşimi, impedimetrik buhar sensörü.

Gönderme: 28 Haziran 2016. **Düzeltme:** 15 Ağustos 2016. **Kabul:** 20 Ağustos 2016.

RESEARCH ARTICLE

Evaluation of Energy Consumption in Electrochemical Oxidation of Acid Violet 7 Textile Dye Using Pt/Ir Electrodes

Bahadır K. Körbahti[1]* and Kezban Meltem Turan[1]

[1]*Faculty of Engineering, Chemical Engineering Department, Mersin University, Çiftlikköy 33343 Mersin, Turkey*

Abstract: The effects of processing parameters were investigated on the electrochemical oxidation of textile dyeing wastewater containing Acid Violet 7 (AV7) at Pt/Ir electrodes in the presence of 75% NaCl + 25% Na_2CO_3 (w/w) supporting electrolyte mixture in a batch electrochemical reactor. Experimental parameters were operated in the range of 300-1500 mg/L textile dye concentration, 4-20 g/L electrolyte concentration, 5-15 mA/cm^2 current density, and 20-60 °C reaction temperature. Energy consumption decreased with increasing textile dye concentration and electrolyte concentration, and decreasing the current density. In the study, energy consumption values were evaluated for textile dye decolorization (t=15 min) and chemical oxygen demand (COD) removal (t=120 min) as 2.7-23.3 kWh/kg dye decolorization and 50.9-317.9 kWh/kg COD removal, respectively.

INTRODUCTION

Textile wastewater is a hard-to-treat one due to its strong color, large amount of suspended solids, high chemical oxygen demand (COD), variable pH, salt content, and high temperature. salt, auxiliary chemicals, and temperature-controlled dye bath conditions enhance and optimize the efficiency of the dyeing process (1). Typical dyeing processes use sodium chloride and sodium carbonate as common salts (2). Decolorization and removal of pollutants are major problems in dyeing process with salt elimination and water-use reduction as well (2). The main source of dyeing wastewater is rinsing processes and spent dye bath which typically contains auxiliary chemicals, salt, and residual dye (2). Wastewater from textile processes that can cause damage if not treated before discharging to the environment (3).

In the literature, treatment methods such as adsorption, biosorption, biodegradation, chemical oxidation, ozonization, coagulation, advanced oxidation, photocatalytic oxidation, electrocoagulation, and electrochemical oxidation have been investigated in order to remove various types of textile dyes, mainly photocatalytic degradation of Acid Violet 7 (AV7) dye was reported using Fe^{3+}-Al_2O_3 (4,5), ZnO (6), Fe^{3+}-fire clay (7), CdS-SnO_2 (8), TiO_2 (9), and AgBr-ZnO (10) photocatalysts.

Muthuvel and Swaminathan (4) stated that Fe^{3+}-Al_2O_3 catalyst was efficient in the photoassisted Fenton mineralization of Acid Violet 7 dye in the presence of H_2O_2 and UV light. The authors determined the optimal conditions for the highest efficiency with 5×10^{-4} M dye, 1 g/L Fe^{3+}-Al_2O_3, 10 mmol/L H_2O_2 and pH 3. In their following study, Muthuvel and Swaminathan (5) achieved 99% COD reduction in UV process at 90 min and 99% COD reduction in solar process at 60 min with 5×10^{-4} M dye, 1 g/L 25% Fe^{3+}-Al_2O_3 catalyst, 10 mmol H_2O_2, and 8.1 mL/s airflow rate. Krishnakumar and Swaminathan (6) used ZnO catalyst and they obtained 94.4% COD removal with 5×10^{-4} M dye at 2 g/L ZnO catalyst, 8.1 mL/s airflow rate and pH 9. In another study, the authors indicated that AgBr-ZnO was found to be more efficient than commercial ZnO and prepared ZnO at pH 12 for the mineralization of AV7 (10). Krishnakumar and Swaminathan (10) obtained 94.4% dye degradation with 5×10^{-4} M dye at 3 g/L AgBr-ZnO catalyst, 8.1 mL/s airflow rate and pH 12. Muthuvel *et al.* (7) found that 26% Fe^{3+}-fire clay (Fe-FC) catalyst exhibited the best photocatalytic activity at an initial pH 3 in the degradation of AV7 and its activity is significant up to pH 7. The authors

achieved 77% AV7 dye degradation at 60 min with 20 mmol H_2O_2 at pH 7 in solar light (7). Ghugal *et al.* (8) reported the photocatalytic activity of CdS–SnO_2 composite for the degradation of Acid Violet 7 dye. The authors obtained complete degradation and mineralization with 50 mg/L dye, 49CdS-SnO_2 composite by irradiation for 150 min (8). Fabbri *et al.,* (9) investigated the photocatalytic degradation of Acid Violet 7 using TiO_2 photocatalyst. The authors obtained complete AV7 degradation and mineralization at 120 min with 20 mg/L dye and 200 mg/L TiO_2 (9).

It is known that textile dyeing processes contribute very high amount of salt, auxiliary chemicals, and textile dye in wastewater effluent that conventional treatment systems may be inefficient for the effective treatment of industrial textile wastewater in removing both salt and color in order to meet discharge limits (2).

Electrochemical oxidation is a promising wastewater treatment method and replacing conventional processes in order to treat wastewater from industrial processes which are not easily biodegradable (2). Electrolysis reactions involve electrical charges moving between the electrolyte and the electrodes. The process depends on the use of direct electric current for the chemical changes in non-spontaneous oxidation/reduction reactions. The minimum amount of electrical energy that must be provided should be equal to the change in Gibbs free energy of the reaction and the losses in the system. In most cases, direct electrical input is larger than the enthalpic change of the reaction, so excess energy is released in the form of heat. Therefore, energy consumption in electrochemical processes should be optimized for its minimum use.

In this study, the electrochemical oxidation of Acid Violet 7 (AV7) textile dye using Pt/Ir electrodes was investigated, and the effects of process variables such as current density, electrolyte concentration, initial dye concentration, and reaction temperature on electrochemical oxidation were analyzed for optimum energy consumption.

MATERIALS AND METHODS

Chemicals and Materials
Acid Violet 7 (AV7) textile dye (Sigma Aldrich) (Figure 1), Na_2CO_3 and NaCl (Merck) were purchased as extra pure grade. Textile dyeing wastewater was prepared synthetically using double distilled water. Double distilled water was obtained using

ultrapure water system (Millipore Simplicity® UV) and water still (GFL-2008) with the resistivity of 18.2 MΩ·cm@25°C, TOC < 5 ppb.

Figure 1. Molecular structure of Acid Violet 7 textile dye ($C_{20}H_{16}N_4Na_2O_9S_2$)

EXPERIMENTAL

The electrochemical reactor (DURAN® glass) used in this study has a heating and cooling jacket (Rettberg, Germany) as shown in Figure 2. Iron cathodes and Pt/Ir anodes were used as four pairs with 5 mm anode/cathode spacing. Total electrode surface area was 172 cm^2. Pt/Ir anodes (Dr. Wieland, Germany) were in spiral shape with 90% Pt and 10% Ir composition (w=150 mm, $\phi_{internal}$=10 mm, ϕ_{wire}=1.10 mm). Iron electrodes were in cylindrical shape (ϕ=12.0 mm) and purchased from local sources. Pt/Ir and iron electrodes were used as received without further preparation and treatment. Batch electrochemical system was equipped with programmable DC power supply (Goodwill PST-3201), heating/cooling tank (Lauda RE 630 S), mechanical mixer (Heidolph RZR 2021), and peristaltic pump (Cole Parmer Masterflex® RZ-77924-60). The reaction medium was mixed at 500 rpm. Influence of experimental parameters were operated as textile dye concentration, 300-1500 mg/L; electrolyte concentration, 4-20 g/L; current density, 5-15 mA/cm^2; and reaction temperature, 20-

60°C.

Figure 2. Batch electrochemical reactor system (1. programmable DC power supply, 2. heating/cooling tank, 3. batch electrochemical reactor, 4. reactor lid, 5. electrodes, 6. sampling cell, 7. thermometer, 8. heating/cooling pump, 9. mechanical mixer).

Samples in 10 mL volume were withdrawn from the reaction medium at 5 min time intervals for the analysis. Decolorization yield was analyzed using UNICO 4802 model UV/Vis double beam spectrophotometer at 490 nm wavelength. Merck Spectroquant® 14541 COD cell tests used for the COD analysis.

RESULTS AND DISCUSSION

Textile dye concentration, current density, electrolyte (75% NaCl + 25% Na_2CO_3) concentration, and reaction temperature parameters were investigated on energy consumption in electrochemical oxidation of Acid Violet 7 (AV7) textile dye using Pt/Ir anodes. In this study, 75% NaCl + 25% Na_2CO_3 (w/w) mixture was used as a supporting electrolyte in order to increase the ionic conductivity of the reaction medium which are also main components in real textile industry wastewater (11).

Experimental results were analyzed using Design-Expert® 10 software. Energy consumption values were calculated using Equations 1 and 2 (12).

$$E_{D\%} = \frac{iV_m \Delta t}{C_o(0.01d\%)V_R} \qquad \text{(Eq. 1)}$$

$$E_{COD\%} = \frac{iV_m\Delta t}{(COD_o - COD_t)V_R}$$
(Eq. 2)

In Equations 1 and 2, $E_{D\%}$, $E_{COD\%}$, V_m, i, Δt, C_o, COD, $d\%$, and V_R are energy consumption for dye decolorization (kWh/kg dye decolorization), energy consumption for COD removal (kWh/kg COD removal), mean cell voltage (volt), current (ampere), reaction time (h), dye concentration (g/L), chemical oxygen demand (g O_2/L), dye decolorization percent, and electrolyte volume (L), respectively.

In the study depending on electrochemical reaction conditions, energy consumption values were outlined in Table 1 for Acid Violet 7 textile dye decolorization (t = 15 min) and COD removal (t=120 min) as 2.7-18.9 kWh/kg dye decolorization and 51.0-190.7 kWh/kg COD removal, respectively. Energy consumption for dye decolorization was obtained as much lower than COD removal due to the degradation of azo bond is the first step of the electrochemical degradation of the textile dyes (2,13).

Table 1. The influence of process parameters on energy consumption in electrochemical oxidation of textile dyeing wastewater containing Acid Violet 7 (AV7) using Pt/Ir electrodes.

Parameter	Reaction Conditions	$E_{D\%}$ (kWh/kg dye decolorization) (t = 15 min)	$E_{COD\%}$ (kWh/kg COD removal) (t = 120 min)
Textile dye concentration	300-1500 mg/L (Electrolyte=12 g/L, J=10 mA/cm^2, T=40°C)	4.5 - 18.9	83.5 - 169.8
Electrolyte concentration	4-20 g/L (AV7=900 mg/L, J=10 mA/cm^2, T=40°C)	5.9 - 15.0	94.2 - 177.3
Current density	5-15 mA/cm^2 (AV7=900 mg/L, Electrolyte=12 g/L, T=40°C)	2.7 - 13. 8	51.0 - 190.7
Reaction temperature	20-60°C (AV7=900 mg/L, Electrolyte=12 g/L, J=10 mA/cm^2)	6.4 - 9.3	97.7 - 113.3

In electrochemical treatment processes, organic pollutants could be removed from wastewater by indirect and direct mechanisms (13–17). Indirect oxidation occurs in the liquid bulk phase by the mediated oxidants, and direct oxidation at the anode surface (13–17). Most electrochemical processes are based on indirect oxidation because direct oxidation of organic pollutants are very slow on inert anodes due to limiting reactions and reaction kinetics (18,19).

Hydroxyl radicals are produced by the anodic discharge of water in indirect electrochemical oxidation of organic pollutants at Pt/Ir anodes. Hydroxyl radicals are adsorbed on the anode surface [S], and oxidize the organic material (20,21). This reaction could also occur in acidic medium at high current densities (21). Oxidation process continues by the formation of hydroxyl radicals with anodic discharge of water molecules (20,21).

$$H_2O + S \rightarrow S[OH^\bullet] + H^+ + e^- \qquad\qquad\qquad (Eq. 3)$$

$$R + S[OH^\bullet] \rightarrow S + RO + H^+ + e^- \qquad\qquad\qquad (Eq. 4)$$

Chlorohydroxyl radicals are also produced with the presence of chloride ions, and adsorb on the active sites of the anode surface [S], and then oxidize the organic material (20,21).

$$H_2O + S + Cl^- \rightarrow S[ClOH^\bullet] + H^+ + 2e^- \qquad\qquad (Eq. 5)$$

$$R + S[ClOH^\bullet] \rightarrow S + RO + H^+ + 2e^- \qquad\qquad (Eq. 6)$$

Therefore, electrochemical oxidation of textile dyeing wastewater results in decolorization with the formation of chlorohydroxyl and hydroxyl radicals. The reactions can also yield O_2, H_2O_2, and Cl_2 (20,21).

$$H_2O + S[OH^\bullet] \rightarrow S + O_2 + 3H^+ + 3e^- \qquad\qquad (Eq. 7)$$

$$H_2O + S[OH^\bullet] \rightarrow S + H_2O_2 + H^+ + e^- \qquad\qquad (Eq. 8)$$

$$H_2O + S[ClOH^\bullet] + Cl^- \rightarrow Cl_2 + S + O_2 + 3H^+ + 4e^- \qquad (Eq. 9)$$
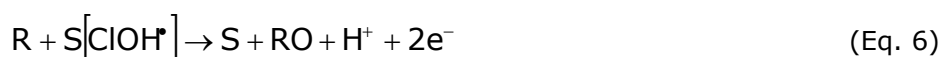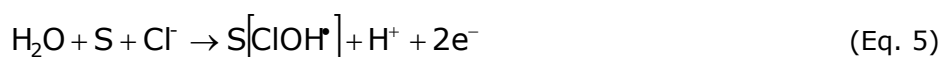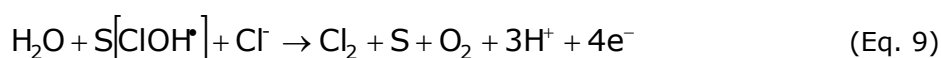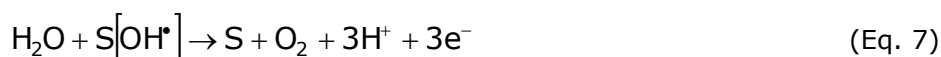
Indirect oxidation also occurs with the formation of HOCl/OCl⁻ redox mediators by the presence of NaCl which provides the anodic evolution of Cl_2 (20–24). The percentage distribution of HOCl/OCl⁻ depends on the solution pH (24). Chloride-chlorine-hypochlorite-chloride cycle occurs in neutral to moderate pH solutions which maintain the initial concentration of chlorides stable (21).

$$2Cl^- \rightarrow Cl_2 + 2e^- \qquad\qquad\qquad\qquad (Eq. 10)$$

$$Cl_2 + H_2O \Leftrightarrow HOCl + H^+ + Cl^-$$ (Eq. 11)

$$HOCl \Leftrightarrow H^+ + OCl^-$$ (Eq. 12)

$$6OCl^- + 3H_2O \rightarrow 2ClO_3^- + 4Cl^- + 6H^+ + \tfrac{3}{2}O_2 + 6e^-$$ (Eq. 13)

$$OCl^- + H_2O + 2e^- \rightarrow Cl^- + 2OH^-$$ (Eq. 14)
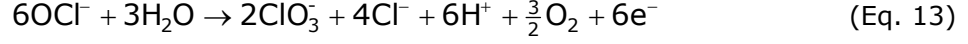
Figures 3-5 show the effect of process parameters on energy consumption in electrochemical oxidation of Acid Violet 7 textile dye that obtained by the quadratic models in Equations 15 and 16 using Design-Expert® 10. Energy consumption model for dye decolorization evaluated using Equation 15 with R^2=0.971, R_{adj}^2=0.947 and signal/noise ratio=26.553 ($\geq$4); and energy consumption model for COD removal evaluated using Equation 16 with R^2=0.981, R_{adj}^2=0.935 and signal/noise ratio=18.273 ($\geq$4). These model coefficients indicating that the models are adequate and can be used for the mathematical analysis. In Equations 15 and 16, $E_{D\%}$, $E_{COD\%}$, x_1, x_2, x_3, and x_4 are energy consumption for dye decolorization (kWh/kg dye decolorization), energy consumption for COD removal (kWh/kg COD removal), Acid Violet 7 concentration (mg/L), 75% NaCl + 25% Na_2CO_3 electrolyte concentration (w/w) (g/L), current density (mA/cm^2), and reaction temperature (°C), respectively.

$$
\begin{aligned}
E_{D\%} = &-0.021760x_1 - 0.53535x_2 + 4.84365x_3 + 0.69701x_4 + 4.32165 \times 10^{-4}x_1x_2 \\
&-1.87807 \times 10^{-3}x_1x_3 - 1.10883 \times 10^{-4}x_1x_4 - 0.086221x_2x_3 - 0.028898x_2x_4 \\
&-0.040203x_3x_4 + 1.51628 \times 10^{-5}x_1^2 + 0.064540x_2^2 + 0.042631x_3^2 \\
&+9.51469 \times 10^{-4}x_4^2 - 14.07577
\end{aligned}
$$

(Eq. 15)

$$
\begin{aligned}
E_{COD\%} = &-0.17811x_1 - 33.09568x_2 + 70.30423x_3 - 0.33819x_4 + 0.014291x_1x_2 \\
&-0.028618x_1x_3 + 2.95185 \times 10^{-3}x_1x_4 - 1.02395x_2x_3 + 0.35414x_2x_4 \\
&-0.68232x_3x_4 + 5.71180 \times 10^{-5}x_1^2 + 0.46313x_2^2 + 0.59078x_3^2 \\
&-1.63474 \times 10^{-3}x_4^2 + 33.19238
\end{aligned}
$$

(Eq. 16)

In Figure 3, energy consumption values were obtained as 3.7-31.1 kWh/kg dye decolorization and 83.3-314.7 kWh/kg COD removal between 300-1500 mg/L Acid Violet 7 concentration and 4-20 g/L 75% NaCl + 25% Na_2CO_3 (w/w) electrolyte mixture. Energy consumption decreased with increasing Acid Violet 7 concentration

and electrolyte concentration as shown in Figure 3. Ionic conductivity of the reaction medium is a very important parameter in electrochemical cells for energy saving processes. Solution conductivity influences current efficiency, applied cell voltage, and electrical energy consumption. More energy is required for overcoming high ohmic resistance between anode and cathode when the ionic conductivity of the solution is low (25). The most common method used to increase the conductivity of the solution is by adding a small amount of supporting electrolyte that reduces the energy consumption during electrochemical treatment (25–27). Increasing electrolyte concentration decreases energy consumption (2). This behavior could be attributed to the increase of ionic conductivity of the reaction medium, and decrease of electrical resistance and applied cell voltage as well (2,28–30). Dalvand *et al.* (2011) studied the efficiency of electrocoagulation process using aluminum electrodes to treat synthetic wastewater containing Reactive Red 198. The authors reported that energy consumption strongly increases with increasing applied cell voltage. Petrović *et al*. (28) investigated the effect of Na_2SO_4 electrolyte concentration on the removal of crystal violet dye by electrochemical oxidation using platinum anode. The authors also found that the decolorization rate increased and the process energy consumption decreased with the increase of Na_2SO_4 concentration.

In Figure 3, the optimum region of lower than 10 kWh/kg dye decolorization and 95 kWh/kg COD removal energy consumption was determined at above 1200 mg/L Acid Violet 7 and between 5.5-13.9 g/L 75%NaCl+25%Na_2CO_3 electrolyte mixture.
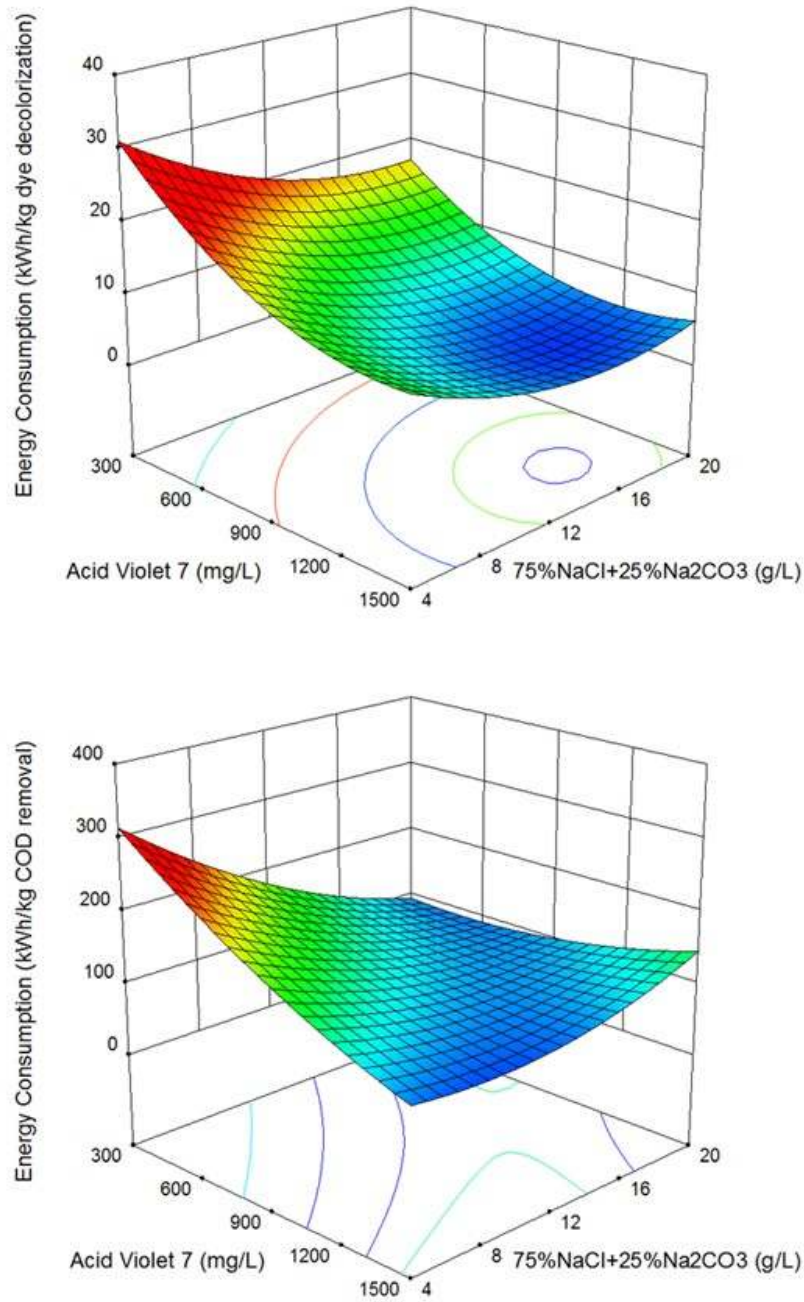
Figure 3. Effect of textile dye concentration and electrolyte concentration on energy consumption in electrochemical oxidation of Acid Violet 7 textile dye using Pt/Ir electrodes (J=10 mA/cm^2, T=40°C, t_{dye}=15 min, t_{COD}=120 min).

84
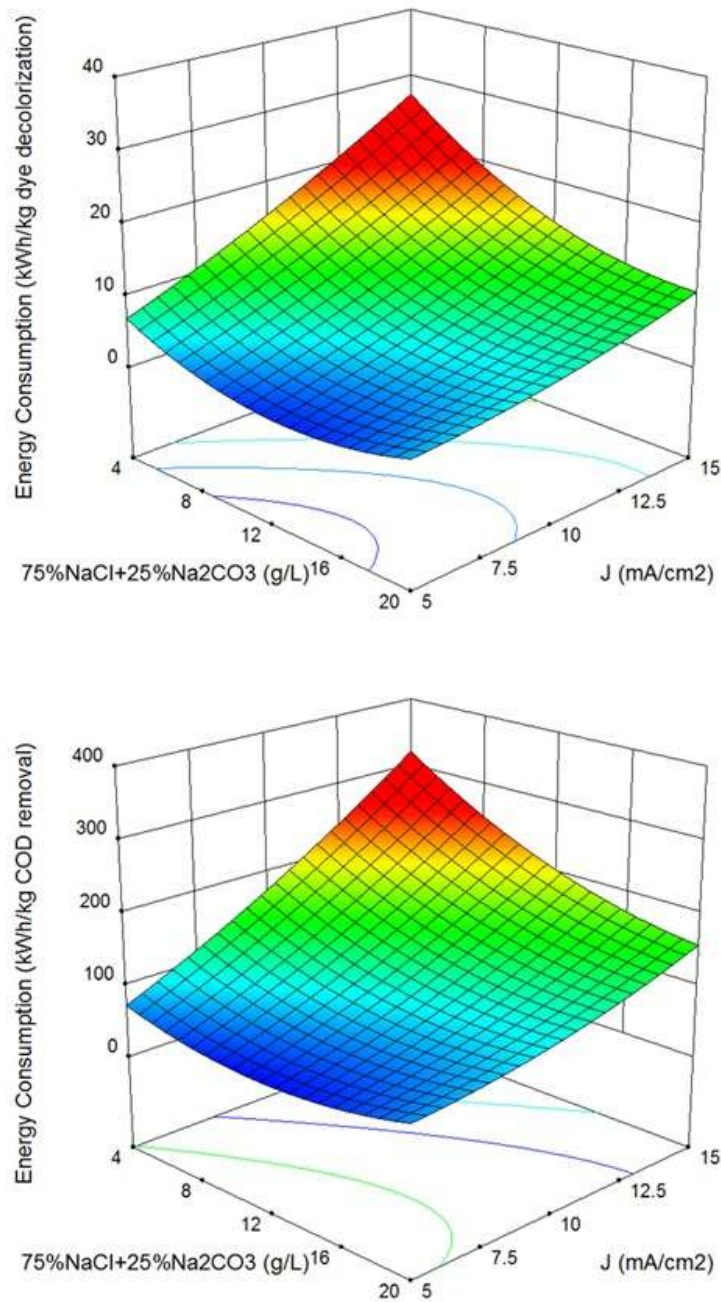
Figure 4. Effect of electrolyte concentration and current density on energy consumption in electrochemical oxidation of Acid Violet 7 textile dye using Pt/Ir electrodes (AV7=900 mg/L, T=40°C, t_{dye}=15 min, t_{COD}=120 min).

In Figure 4, energy consumption values were obtained as 1.3-27.4 kWh/kg dye decolorization and 43.7-312.2 kWh/kg COD removal between 5-15 mA/cm^2 current density and 4-20 g/L 75% NaCl + 25% Na$_2$CO$_3$ (w/w) electrolyte mixture. Energy

consumption decreased with decreasing current density as shown in Figures 4 and 5. Although increasing current density increases electrochemical oxidation efficiency, increasing current density causes an increase in the energy consumption according to Equations 1 and 2. In addition, applied current may be consumed by secondary reactions at very high cell voltages (16,31). In Figure 4, the optimum region lower than 10 kWh/kg dye decolorization and 95 kWh/kg COD removal energy consumption was determined at below 10.5 mA/cm^2 current density and between 10.1-14.6 g/L 75% NaCl + 25% Na$_2$CO$_3$ electrolyte mixture.

Energy consumption values were obtained as 1.3-20.8 kWh/kg dye decolorization and 2.4-284.9 kWh/kg COD removal between 5-15 mA/cm^2 current density and 20-60°C reaction temperature in Figure 5. Energy consumption decreased by decreasing the reaction temperature below 10.5 mA/cm^2 current density values as shown in Figure 5, in which the optimum region of lower than 10 kWh/kg dye decolorization and 95 kWh/kg COD removal energy consumption was determined below 10.5 mA/cm^2 current density and between 20-60°C reaction temperature. Therefore, optimum reaction temperature was determined in the mid of the experimental conditions as 40°C.

The optimum region was determined for the energy consumption in electrochemical oxidation of Acid Violet 7 textile dye using Pt/Ir electrodes in Figure 6. The shaded region in Figure 6 shows energy consumption of lower than 10 kWh/kg dye decolorization and 95 kWh/kg COD removal at optimum operating values of 40 °C reaction temperature and 1200 mg/L textile dye concentration. In this study, energy consumption values were obtained in a good agreement with the data previously reported in the literature for electrochemical wastewater treatment such as 2.6-90.0 kWh/kg dye decolorization and 1.2-253.3 kWh/kg COD removal (12,15,28). The optimum operating region was found to be applicable for the electrochemical treatment of industrial textile wastewater.
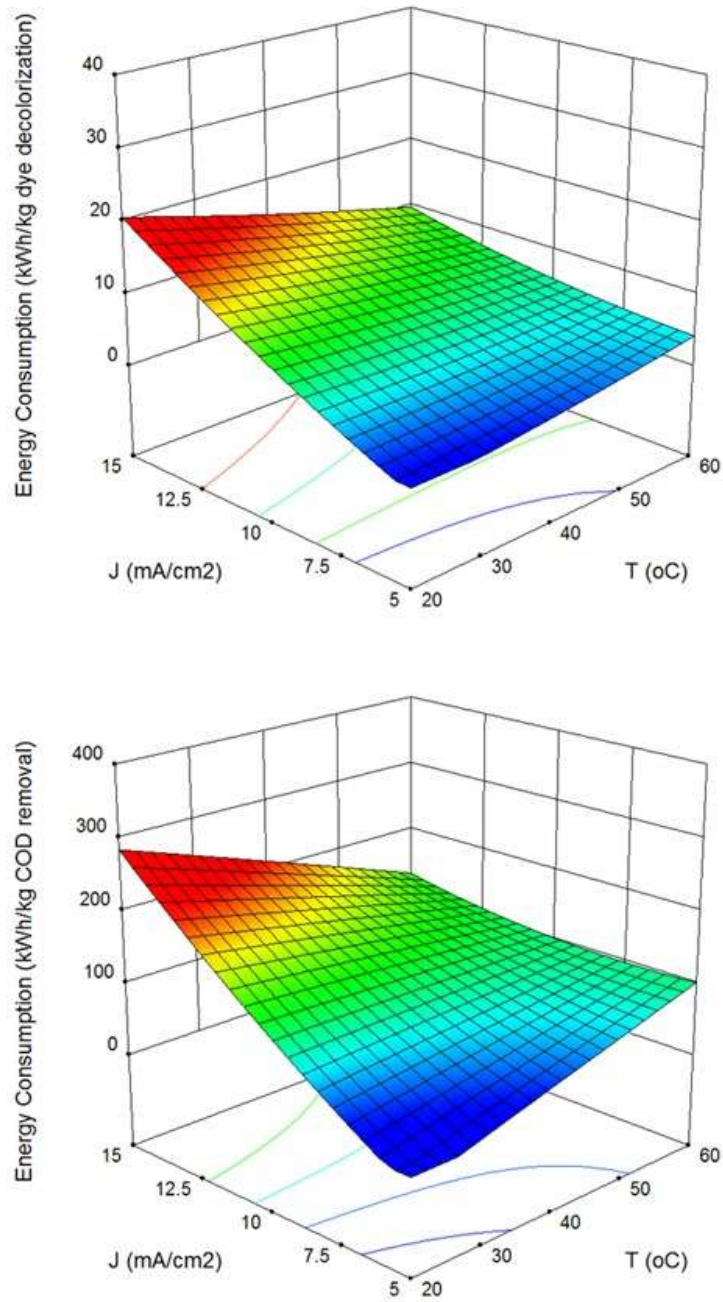
Figure 5. Effect of current density and reaction temperature on energy consumption in electrochemical oxidation of Acid Violet 7 textile dye using Pt/Ir electrodes (AV7=900 mg/L, Electrolyte=12 g/L, t_{dye}=15 min, t_{COD}=120 min).
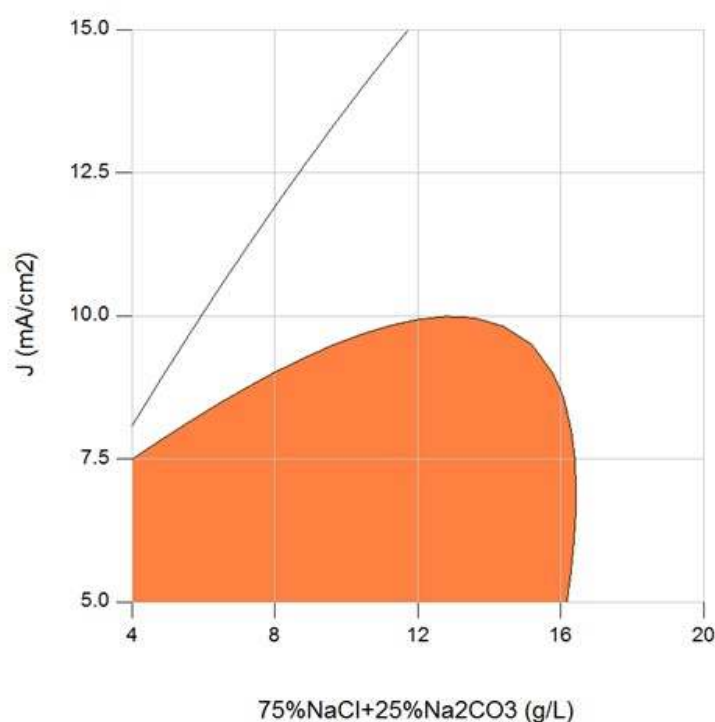
Figure 6. Optimum region for energy consumption in electrochemical oxidation of Acid Violet 7 textile dye using Pt/Ir electrodes (AV7=1200 mg/L, T=40°C, t_{dye}=15 min, t_{COD}=120 min).

CONCLUSIONS

The evaluation of energy consumption in electrochemical oxidation of Acid Violet 7 textile dye was investigated using Pt/Ir anodes in the presence of 75% NaCl +25% Na_2CO_3 supporting electrolyte mixture. Energy consumption decreased with increasing textile dye concentration and electrolyte concentration, and decreasing the current density. Depending on electrochemical reaction conditions, energy consumption values were evaluated for textile dye decolorization (t=15 min) and COD removal (t=120 min) as 2.7-18.9 kWh/kg dye decolorization and 51.0-190.7 kWh/kg COD removal, respectively. The optimum region was determined for the energy consumption in electrochemical oxidation of Acid Violet 7 textile dye using Pt/Ir electrodes at lower than 10 kWh/kg dye decolorization and 95 kWh/kg COD removal. In this study, energy consumption values were obtained in a good agreement with the data reported in the literature. Experimental findings showed that electrochemical oxidation could be an alternative as a treatment method for textile wastewater effluent.

ACKNOWLEDGEMENTS

REFERENCES

1.   US EPA. EPA Office of Compliance Sector Notebook Project : Profile of the Textile Industry. 1997. EPA310R97009.

2.   Körbahti BK. Response surface optimization of electrochemical treatment of textile dye wastewater. Journal of Hazardous Materials. 2007;145(1-2):277–86. DOI: 10.1016/j.jhazmat.2006.11.031.

3.   US EPA. Best Management Practices for Pollution Prevention in the Textile Industry. 1996. EPA625R96004.

4.   Muthuvel I, Swaminathan M. Photoassisted Fenton mineralisation of Acid Violet 7 by heterogeneous Fe(III)–Al2O3 catalyst. Catalysis Communications 8 (2007) 981–6. DOI: 10.1016/j.catcom.2006.10.015.

5.   Muthuvel I, Swaminathan M. Highly solar active Fe(III) immobilised alumina for the degradation of Acid Violet 7. Solar Energy Materials & Solar Cells. 2008;92:857–63. DOI: 10.1016/j.solmat.2008.02.007.

6.   Krishnakumar B, Swaminathan M. Influence of operational parameters on photocatalytic degradation of a genotoxic azo dye Acid Violet 7 in aqueous ZnO suspensions. Spectrochimica Acta Part A. 2011; 81:739– 44. DOI: 10.1016/j.saa.2011.07.019.

7.   Muthuvel I, Krishnakumar B, Swaminathan M. Solar active fire clay based hetero-Fenton catalyst over a wide pH range for degradation of Acid Violet 7. Journal of Environmental Sciences. 2012;24(3):529–35. DOI: 10.1016/S1001-0742(11)60754-7.

8.   Ghugal SG, Umare SS, Sasikala R. A stable, efficient and reusable CdS–SnO2 heterostructured photocatalyst for the mineralization of Acid Violet 7 dye. Applied Catalysis A: General. 2015;496:25–31. DOI: 10.1016/j.apcata.2015.02.035.

9.   Fabbri D, Calza P, Prevot AB. Photoinduced transformations of Acid Violet 7 and Acid Green 25 in the presence of TiO2 suspension. Journal of Photochemistry and Photobiology A: Chemistry. 2010;213:14–22. DOI: 10.1016/j.jphotochem.2010.04.014.

10.   Krishnakumar B, Swaminathan M. Photodegradation of Acid Violet 7 with AgBr-ZnO under highly alkaline conditions. Spectrochimica Acta Part A: Molecular and Biomolecular Spectroscopy. 2012;99:160–5. DOI: 10.1016/j.saa.2012.08.077.

11.   Körbahti BK, Tanyolaç A. Electrochemical treatment of simulated textile wastewater with industrial components and Levafix Blue CA reactive dye: Optimization through response surface methodology. Journal of Hazardous Materials. 2008;151(2-3):422–31.

12.   Körbahti BK, Artut K, Geçgel C, Özer A. Electrochemical decolorization of textile dyes and removal of metal ions from textile dye and metal ion binary mixtures. Chemical Engineering Journal. 2011;173(3):677–88. DOI: 10.1016/j.cej.2011.02.018.

13.   Comninellis C, Chen G. Electrochemistry for the environment. Springer; 2010. ISBN:

9780387369228.

14.   Brillas E, Martínez-Huitle CA. Decontamination of wastewaters containing synthetic organic dyes by electrochemical methods. An updated review. Applied Catalysis B: Environmental. 2015;166:603–43. DOI: 10.1016/j.apcatb.2014.11.016.

15.   Körbahti BK, Artut K. Electrochemical oil/water demulsification and purification of bilge water using Pt/Ir electrodes. Desalination. 2010;258(1-3):219–28. DOI: 10.1016/j.desal.2010.03.008.

16.   Körbahti BK, Taşyürek S. Electrochemical oxidation of ampicillin antibiotic at boron-doped diamond electrodes and process optimization using response surface methodology. Environmental Science and Pollution Research. 2015;22(5):3265–78. DOI: 10.1007/s11356-014-3101-7.

17.   Panizza M, Cerisola G. Direct And Mediated Anodic Oxidation of Organic Pollutants. Chemical Reviews. 2009;109(12):6541–69. DOI: 10.1021/cr9001319.

18.   Tarr MA. Chemical Degradation Methods for Wastes and Pollutants. CRC Press; 2003. ISBN: 9780824743079.

19.   Rajeshwar K, Ibanez JG. Environmental Electrochemistry. Academic Press; 1997. ISBN: 9780123887320.

20.   Vlyssides AG, Israilides CJ, Loizidou M, Karvouni G, Mourafeti V. Electrochemical treatment of vinasse from beet molasses. Water Science and Technology. 1997;36(2-3):271–8. DOI: 10.1016/S0273-1223(97)00398-3.

21.   Israilides C, Vlyssides A, Mourafeti V, Karvouni G. Olive oil wastewater treatment with the use of an electrolysis system. Bioresource Technology. 1997;61(2):163–70. DOI: 10.1016/S0960-8524(97)00023-0.

22.   Do J-S, Yeh W-C. Paired electrooxidative degradation of phenol with in situ electrogenerated hydrogen peroxide and hypochlorite. Journal of Applied Electrochemistry. 1996;26(6):673–8. DOI: 10.1007/BF00253467.

23.   Lin SH, Shyu CT, Sun MC. Saline wastewater treatment by electrochemical method. Water Research. 1998;32(4):1059–66. DOI: 10.1016/S0043-1354(97)00327-8.

24.   Tchobanoglous G, Burton FL, Stensel HD. Wastewater Engineering: Treatment and Reuse. McGraw-Hill, 2004. ISBN: 9780071241403.

25.   Chou WL, Wang CT, Chang SY. Study of COD and turbidity removal from real oxide-CMP wastewater by iron electrocoagulation and the evaluation of specific energy consumption. Journal of Hazardous Materials. 2009;168:1200–7. DOI: 10.1016/j.jhazmat.2009.02.163.

26.   Lin SH, Chang CC. Treatment of landfill leachate by combined electro-Fenton oxidation and sequencing batch reactor method. Water Research. 2000;34(17):4243–9. DOI: 10.1016/S0043-1354(00)00185-8.

27.   Wang C-T. Decolorization of Congo Red with Three-Dimensional Flow-By Packed-Bed Electrodes. Journal of Environmental Science and Health Part A—Toxic/Hazardous Substances & Environmental Engineering. 2003;A38(2):399–413. DOI: 10.1081/ESE-120016903.

28.   Petrovi M, Miljkovi M, Boji A, Stepanovi J, Stamenkovi M. The Influence of the Background Electrolyte Concentration on the Removal of Crystal Violet by Electrochemical Oxidation on the Platinum Anode. Advanced technologies. 2013;2(1):41-4.

29.   İrdemez Ş, Tosunoglu NDV. The effects of supporting electrolyte type and concentration

on the phosphate removal from wastewater by electrocoagulation with aluminum plate electrodes. Iğdır University Journal of the Institute of Science and Technology. 2011;1(2):35-40.

30.   Dalvand A, Gholami M, Joneidi A, Mahmoodi NM. Dye Removal, Energy Consumption and Operating Cost of Electrocoagulation of Textile Wastewater as a Clean Process. CLEAN - Soil, Air, Water. 2011;39 (7):665–72. DOI: 10.1002/clen.201000233.

31.   Shen ZM, Wu D, Yang J, Yuan T, Wang WH, Jia JP. Methods to improve electrochemical treatment effect of dye wastewater. Journal of Hazardous Materials. 2006;131(1-3):90–7. DOI: 10.1016/j.jhazmat.2005.09.010.

Türkçe Öz ve Anahtar Kelimeler

Pt/Ir Elektrotlar Kullanarak Asit Viyole 7 Tekstil Boyasının Elektrokimyasal Yükseltgenmesinde Enerji Tüketiminin Değerlendirilmesi

Bahadır K. Körbahti[1]* and Kezban Meltem Turan[1]

Öz: %75 NaCl + %25 Na_2CO_3 (w/w) varlığında Pt/Ir elektrotlarda Asit Viyole 7 (AV7) içeren tekstil boyama atık suyunun elektrokimyasal yükseltgenmesinde proses parametreleri kesikli elektrokimyasal reaktörde incelenmiştir. Deneysel parametreler 300-1500 mg/L tekstil boya derişimi, 4-20 g/L elektrolit derişimi, 5-15 mA/cm^2 akım yoğunluğu ve 20-60 °C tepkime sıcaklığı kullanılarak yürütülmüştür. Enerji tüketimi artan tekstil boyar madde derişimi, elektrolit derişimi ve ve azalan akım yoğunluğu ile artmıştır. Çalışmada, tekstil boya giderimi (t = 15 dak) ve kimyasal oksijen ihtiyacı (KOİ) giderimi (t = 120 dak) için enerji tüketim değerleri sırasıyla 2,7 – 23,3 kWh-kg boya derişimi ve 50,9 – 317,9 kWh/kg KOİ giderimi olarak bulunmuştur.

Anahtar kelimeler: Asit Viyole 7, Elektrokimyasal Atık Su Islahı, Enerji Tüketimi, Pt/Ir Elektrotlar, Tekstil Boyarmaddesi.

Sunulma: 29 Haziran 2016. **Düzeltme:** 04 Ağustos 2016. **Kabul:** 17 Ağustos 2016.

N-Butyl Substituted N-Heterocyclic Carbene-Pd(II)-Pyridine (PEPPSI) Complexes: Synthesis, Characterization, and Catalytic Activity in the Suzuki-Miyaura Reaction

Rukiye Fırıncı[1*]
[1]Adnan Menderes University, 09100, Aydın, Turkey

Abstract: A series of N-butyl substituted imidazolium salts, (**1a-c**) and their pyridine enhanced precatalyst preparation stabilization and initiation (**PEPPSI**) themed palladium *N*-heterocyclic carbene complexes (**2a-c**) were synthesized and characterized. Pd-NHC complexes were fully determined by elemental analysis and spectroscopic methods. The synthesized complexes were tested in Suzuki-Miyaura cross-coupling reaction. These complexes were found to be efficient catalysts for the Suzuki-Miyaura reaction of phenylboronic acid with aryl bromides.

INTRODUCTION

N-Heterocyclic carbenes (NHCs) have become a significant class of ligands in organometallic chemistry [1]. Stable *N*-heterocyclic carbenes (NHCs) have attracted much attention, due to being a strong *σ*-donor for transition metals [2, 3]. NHC complexes have some advantages over phosphine complexes such as their stability, being ease-to-handle, and lower toxicity [4]. Many NHC transition metal complexes have been generated in homogeneous catalysis as catalysts [5, 6] after the first isolation of free NHC by Arduengo [7]. Since the electronic and steric features of NHCs are tunable, the bearing NHC ligand metal complexes have become valuable reagents for homogeneous/heterogeneous catalysis [8-12].

Pd-NHC complexes have proved to be efficient catalysts in catalytic formation of carbon-carbon and carbon-heteroatom bonds [13-19]. Since the first example PEPPSI type (PEPPSI= Pyridine-Enhanced Precatalyst Preparation, Stabilization, and Initiation) Pd-NHC complexes were reported by Organ *et al*. in 2006, considerable efforts have been undertaken to develop these type of complexes because they are easy to prepare, air- and moisture-stable [20]. After Organ's work, Doucet and Matt exhibited monoligated NHC-based palladium pyridine complexes [21, 22].

In this context, this study was reported that the synthesis and characterization of three novel PEPPSI type N-butyl functionalized N-heterocyclic carbenes (NHC) complexes. Moreover, the catalytic activity of Pd(II) complexes were examined in Suzuki-Miyaura reaction.

MATERIALS and METHODS

All manipulations for the preparations of (**2a-c**) were performed under a dry argon atmosphere using standard Schlenk techniques. All glassware was flame-dried before use. Solvents were purified by distillation from an appropriate drying agent. Unless otherwise specified, chemicals were used as received without further purification. ^{1}H- and ^{13}C-NMR spectra were recorded on a Varian Mercury AS 400 spectrometer. A HP Agilant-6890N gas chromatograph was used in catalytic studies. Chemical shifts (δ) are referenced to external TMS. An electrothermal-9200 melting point apparatus was used to record the melting points. Elemental analyses were obtained by ODTU Microlab (Ankara, Turkey).

Syntheses of Imidazolium Salts (1a-c): To a solution of *N*-butylimidazole (10.0 mmol) in toluene (10.0 mL) was added aryl halides slowly (10.0 mmol) at 25°C for 24 h. Diethyl ether (15.0 mL) was added to obtain a white precipitate, which was collected on a Gooch crucible and washed with Et_2O (3×15.0 mL), and dried under vacuum. Recrystallization of the crude product from $EtOH/Et_2O$ solution obtained white crystals of the salt (Scheme 1).

1a: Yield: 84%. m.p.: 100 °C. ^{1}H-NMR (δ, 400 MHz, $CDCl_3$): 0.83 [t, *J* = 7.2 Hz, 3H, $CH_3CH_2CH_2CH_2N$]; 1.26 [m, 2H, $CH_3CH_2CH_2CH_2N$]; 1.81 [m, 2H, $CH_3CH_2CH_2CH_2N$]; 2.16 [s, 9H, $NCH_2-Ar-(CH_3)_3-o,p-CH_3$]; 4.27 [t, *J* = 7.2 Hz, 2H, $CH_3CH_2CH_2CH_2N$]; 5.49 [s, 2H, $NCH_2-Ar-(CH_3)_3$]; 6.80 [s, 2H, $NCH_2-ArH_2-(CH_3)_3$]; 6.80 [s, 2H, NCHCHN]; 7.60 [s, 2H, NCHCHN]; 10.26 [s, 1H, NCHN]. ^{13}C-NMR (δ, 100 MHz, $CDCl_3$): 13.4 [$CH_3CH_2CH_2CH_2N$]; 19.4 [$CH_3CH_2CH_2CH_2N$]; 19.8 [$NCH_2-Ar-(CH_3)_3-o-CH_3$]; 21.0 [$NCH_2-Ar-(CH_3)_3-p-CH_3$]; 32.1 [$CH_3CH_2CH_2CH_2N$]; 47.8 [$CH_3CH_2CH_2CH_2N$]; 50.0 [$NCH_2C_6H_2(CH_3)_3$]; 120.6 [NCHCHN]; 122.3 [NCHCHN]; 125.3 [$NCH_2-ArC-(CH_3)_3$]; 130.0 [$NCH_2-ArC-(CH_3)_3$]; 136.7 [$NCH_2-ArC-(CH_3)_3$]; 138.0 [$NCH_2-ArC-(CH_3)_3$]; 139.9 [NCHN].

1b: Yield: 81%. m.p.: 110 °C. ^{1}H-NMR (δ, 400 MHz, $CDCl_3$): 0.85 [t, *J* = 7.4 Hz, 3H, $CH_3CH_2CH_2CH_2N$]; 1.30 [m, 2H, $CH_3CH_2CH_2CH_2N$]; 1.84 [m, 2H, $CH_3CH_2CH_2CH_2N$]; 2.09 [s, 6H, $NCH_2-Ar-(CH_3)_4-o-CH_3$]; 2.14 [s, 6H, $NCH_2-Ar-(CH_3)_4-m-CH_3$]; 4.29 [t, *J* = 7.4 Hz, 2H, $CH_3CH_2CH_2CH_2N$]; 5.57 [s, 2H, $NCH_2-Ar-(CH_3)_4$]; 6.81 [s, 1H, NCHCHN]; 6.95 [s, 1H, $NCH_2-ArH-(CH_3)_4$]; 7.59 [s, 1H, NCHCHN]; 10.27 [s, 1H, NCHN]. ^{13}C-NMR (δ, 100 MHz, $CDCl_3$): 13.4 [$CH_3CH_2CH_2CH_2N$]; 15.8 [$CH_3CH_2CH_2CH_2N$]; 19.4 [$NCH_2-Ar-(CH_3)_4-o-CH_3$]; 20.4 [$NCH_2-Ar-(CH_3)_4-p-CH_3$]; 32.1 [$CH_3CH_2CH_2CH_2N$]; 48.5 [$CH_3CH_2CH_2CH_2N$]; 50.0 [$NCH_2-Ar-(CH_3)_4$]; 120.8 [NCHCHN]; 122.4 [NCHCHN]; 128.0 [$NCH_2-ArC-(CH_3)_4$]; 129.7 [$NCH_2-ArC-(CH_3)_4$]; 133.4 [$NCH_2-ArC-(CH_3)_4$]; 134.0 [$NCH_2-ArC-(CH_3)_4$]; 135.0 [$NCH_2-ArC-(CH_3)_4$]; 135.8 [$NCH_2-ArC-(CH_3)_4$]; 136.4 [NCHN].

1c: Yield: 89%. m.p.: 117 °C. ^{1}H-NMR (δ, 400 MHz, $CDCl_3$): 0.86 [t, *J* = 7.4 Hz, 3H, $CH_3CH_2CH_2CH_2N$]; 1.29 [m, 2H, $CH_3CH_2CH_2CH_2N$]; 1.83 [m, 2H, $CH_3CH_2CH_2CH_2N$]; 2.13 [s, 6H, $NCH_2-Ar-(CH_3)_5-o-CH_3$]; 2.14 [s, 6H, $NCH_2-Ar-(CH_3)_5-m-CH_3$]; 2.17 [s, 3H, $NCH_2-Ar-(CH_3)_5-p-CH_3$]; 4.29 [t, *J* = 7.2 Hz, 2H, $CH_3CH_2CH_2CH_2N$]; 5.57 [s, 2H, $NCH_2-Ar-(CH_3)_5$]; 6.83 [t, *J* = 1.7 Hz, 1H, NCHCHN]; 7.54 [t, *J* = 1.7 Hz, 1H, NCHCHN]; 10.14 [s, 1H, NCHN]. ^{13}C-NMR (δ, 100 MHz, $CDCl_3$): 13.4 [$CH_3CH_2CH_2CH_2N$]; 16.8 [$CH_3CH_2CH_2CH_2N$]; 16.9 [$NCH_2-Ar-(CH_3)_5-o-CH_3$]; 17.2 [$NCH_2-Ar-(CH_3)_5-m-CH_3$]; 19.4 [$NCH_2-Ar-(CH_3)_5-p-CH_3$]; 32.1 [$CH_3CH_2CH_2CH_2N$]; 49.0 [$CH_3CH_2CH_2CH_2N$]; 50.0 [$NCH_2-Ar-(CH_3)_5$]; 120.8 [NCHCHN]; 122.2 [NCHCHN]; 125.3 [$NCH_2-ArC-(CH_3)_5$]; 133.5 [$NCH_2-ArC-(CH_3)_5$]; 133.7 [$NCH_2-ArC-(CH_3)_5$]; 136.4 [$NCH_2-ArC-(CH_3)_5$]; 137.2 [NCHN].

Syntheses of Pd-NHC Complexes (2a–c): Imidazolium bromide salts (**1a-c**, 1.0 mmol), $PdCl_2$ (1.1 mmol), KBr (5.0 mmol) and K_2CO_3 (5.0 mmol) were mixed in pyridine (5.0 mL). After the mixture was refluxed in for 18h, it was cooled down to room temperature. The mixture was then filtered by cannula and the solution was removed under vacuum. The residue was dissolved with CH_2Cl_2 (20.0 mL) and subsequently treated with saturated aqueous $CuSO_4$ solution (2 x 20.0 mL). After separation of the organic and the aqueous layer, the organic layer was dried over anhydrous $MgSO_4$ and then filtered. The filtrate was concentrated under vacuum to give the product (**2a-c**) as a yellow solid.

2a: Yield: 56%. m.p.: 172 °C. Anal. Calc. for $C_{22}H_{29}Br_2N_3Pd$: C, 43.91; H, 4.86; N, 6.98. Found: C, 44.34; H, 5.11; N, 6.92%. ^{1}H-NMR (δ, 400 MHz, $CDCl_3$): 1.02 [t, J = 7.4 Hz, 3H, CH_3CH$_2$CH$_2$CH$_2$N]; 1.44-1.54 [m, 2H, CH$_3$CH_2CH$_2$CH$_2$N]; 2.03-2.11 [m, 2H, CH$_3$CH$_2$CH_2CH$_2$N]; 2.30 [s, 3H, NCH$_2$-Ar-(CH$_3$)$_3$-p-CH_3]; 2.31 [s, 6H, NCH$_2$-Ar-(CH$_3$)$_3$-o-CH_3]; 4.49-4.53 [m, 2H, CH$_3$CH$_2$CH$_2$CH_2N]; 5.70 [s, 2H, NCH_2-Ar-(CH$_3$)$_3$]; 6.27 [d, J = 2.4 Hz, 1H, NCHCHN]; 6.78 [d, J = 2.4 Hz, 1H, NCHCHN]; 6.92 [s, 2H, NCH$_2$-ArH_2-(CH$_3$)$_3$]; 7.32-7.35 [m, 2H, pyridyl-CH]; 7.75 [tt, J = 7.7 Hz, J = 1.8 Hz, J = 1.6 Hz, 1H, pyridyl-CH]; 9.09 [dt, J = 4.8 Hz, J = 1.5 Hz, 2H, pyridyl-CH]. ^{13}C-NMR (δ, 100 MHz, $CDCl_3$): 13.8 [CH$_3$CH$_2$CH$_2$CH$_2$N]; 20.0 [CH$_3$$CH_2CH_2CH_2$N]; 20.1 [NCH$_2$-Ar-(CH$_3$)$_3$-$o$-$CH_3$]; 21.0 [NCH$_2$-Ar-(CH$_3$)$_3$-$p$-$CH_3$]; 32.2 [CH$_3CH_2$$CH_2CH_2$N]; 49.5 [CH$_3CH_2CH_2$$CH_2$N]; 51.2 [N$CH_2$-Ar-(CH$_3$)$_3$]; 119.9 [N$C$HCHN]; 120.8 [NCH$_2$-Ar$C$-(CH$_3$)$_3$]; 124.5 [pyridyl-$C$]; 127.4 [NCHC$H$N]; 129.3 [NCH$_2$-Ar$C$-(CH$_3$)$_3$]; 137.8 [NCH$_2$-Ar$C$-(CH$_3$)$_3$]; 138.7 [pyridyl-$C$]; 138.8 [NCH$_2$-Ar$C$-(CH$_3$)$_3$]; 146.5 [Pd-$C_{carbene}$]; 152.6 [pyridyl-$C$].

2b: Yield: 67%. m.p.: 187 °C. Anal. Calc. for $C_{23}H_{31}Br_2N_3Pd$: C, 44.86; H, 5.07; N, 6.82. Found: C, 44.38; H, 5.46; N, 7.59%. ^{1}H-NMR (δ, 400 MHz, $CDCl_3$): 1.03 [t, J = 7.4 Hz, 3H, CH_3CH$_2$CH$_2$CH$_2$N]; 1.46-1.52 [m, 2H, CH$_3$CH_2CH$_2$CH$_2$N]; 2.05-2.10 [m, 2H, CH$_3$CH$_2$CH_2CH$_2$N]; 2.21 [s, 6H, NCH$_2$-Ar-(CH$_3$)$_4$-o-CH_3]; 2.25 [s, 6H, NCH$_2$-Ar-(CH$_3$)$_4$-m-CH_3]; 4.49-4.53 [m, 2H, CH$_3$CH$_2$CH$_2$CH_2N]; 5.76 [s, 2H, NCH_2-Ar-(CH$_3$)$_4$]; 6.27 [d, J = 2.4 Hz, 1H, NCHCHN]; 6.78 [d, J = 2.4 Hz, 1H, NCHCHN]; 7.02 [s, 1H, NCH$_2$-ArH-(CH$_3$)$_4$]; 7.32-7.36 [m, 2H, pyridyl-CH]; 7.73-7.77 [tt, J = 7.7 Hz, J = 1.8 Hz, J = 1.6 Hz, 1H, pyridyl-CH]; 9.08-9.10 [dt, J = 4.8 Hz, J = 1.5 Hz, 2H, pyridyl-CH]. ^{13}C-NMR (δ, 100 MHz, $CDCl_3$): 13.8 [CH$_3$CH$_2$CH$_2$CH$_2$N]; 16.0 [CH$_3$$CH_2CH_2CH_2$N]; 20.0 [NCH$_2C_6$H(CH$_3$)$_4$-$o$-$CH_3$]; 20.4 [NCH$_2$-Ar-(CH$_3$)$_4$-$m$-$CH_3$]; 32.2 [CH$_3CH_2$$CH_2CH_2$N]; 50.2 [CH$_3CH_2CH_2$$CH_2$N]; 51.2 [N$CH_2$-Ar-(CH$_3$)$_4$]; 120.2 [N$C$HCHN]; 120.7 [NCH$_2$-Ar$C$-(CH$_3$)$_4$]; 124.5 [pyridyl-$C$]; 130.2 [NCHC$H$N]; 132.4 [NCH$_2$-Ar$C$-(CH$_3$)$_4$]; 134.3 [NCH$_2$-Ar$C$-(CH$_3$)$_4$]; 134.8 [pyridyl-$C$]; 137.8 [NCH$_2$-Ar$C$-(CH$_3$)$_4$]; 146.4 [Pd-$C_{carbene}$]; 152.6 [pyridyl-$C$].

2c: Yield: 71%. m.p.: 193 °C. Anal. Calc. for $C_{24}H_{33}Br_2N_3Pd$: C, 45.77; H, 5.28; N, 6.67. Found: C, 45.79; H, 5.64; N, 7.78%. ^{1}H-NMR (δ, 400 MHz, CDCl$_3$): 1.03 [t, J = 7.2 Hz, 3H, CH_3CH$_2$CH$_2$CH$_2$N]; 1.44-1.54 [m, 2H, CH$_3$CH_2CH$_2$CH$_2$N]; 2.04-2.11 [m, 2H, CH$_3$CH$_2$CH_2CH$_2$N]; 2.24 [s, 6H, NCH$_2$-Ar-(CH$_3$)$_5$-o-CH_3]; 2.25 [s, 6H, NCH$_2$-Ar-(CH$_3$)$_5$-m-CH_3]; 2.27 [s, 3H, NCH$_2$-Ar-(CH$_3$)$_5$-p-CH_3]; 4.49-4.53 [m, 2H, CH$_3$CH$_2$CH$_2$CH_2N]; 5.77 [m, 2H, NCH_2-Ar-(CH$_3$)$_5$]; 6.31 [d, J = 2.0 Hz, 1H, NCHCHN]; 6.77 [d, J = 2.0 Hz, 1H, NCHCHN]; 7.32-7.35 [m, 2H, pyridyl-CH]; 7.73-7.77 [tt, J = 7.7 Hz, J = 1.8 Hz, J = 1.6 Hz, 1H, pyridyl-CH]; 9.08-9.10 [dt, J = 4.8 Hz, J = 1.5 Hz, 2H, pyridyl-CH]. ^{13}C-NMR (δ, 100 MHz, CDCl$_3$): 13.8 [CH$_3$CH$_2$CH$_2$CH$_2$N]; 16.8 [CH$_3$$CH_2CH_2CH_2$N]; 17.0 [NCH$_2$-Ar-(CH$_3$)$_5$-o-$CH_3$]; 17.1 [NCH$_2$-Ar-(CH$_3$)$_5$-m-$CH_3$]; 20.0 [NCH$_2$-Ar-(CH$_3$)$_5$-p-$CH_3$]; 32.0 [CH$_3CH_2$$CH_2CH_2$N]; 50.7 [CH$_3CH_2CH_2$$CH_2$N]; 51.1 [N$CH_2$-Ar-(CH$_3$)$_5$]; 120.3 [N$C$HCHN]; 120.6 [NCH$_2$-Ar$C$-(CH$_3$)$_5$]; 124.4 [pyridyl-$C$]; 127.5 [NCH$C$HN]; 133.1 [NCH$_2$-Ar$C$-(CH$_3$)$_5$]; 134.3 [NCH$_2$-Ar$C$-(CH$_3$)$_5$]; 136.0 [pyridyl-$C$]; 137.7 [NCH$_2$-Ar$C$-(CH$_3$)$_5$]; 146.2 [Pd-$C_{carbene}$]; 152.6 [pyridyl-$C$].

General procedure for Suzuki–Miyaura cross-coupling reactions: In a typical procedure, a mixture of aryl halide (0.5 mmol), phenylboronic acid (0.75 mmol), Cs$_2$CO$_3$ (1.5 mmol), diethylene glycol di-n-butyl ether (0.3 mmol, as an internal standard) and palladium(II) catalyst (1 mol%) was added to a two-necked 25.0 mL flask containing 3.0 mL of 2-propanol. The flask was placed in a pre-heated oil bath (25 °C and 80 °C) under an argon atmosphere. After completion of the reaction, the mixture was cooled down to room temperature and 2-propanol was added. The mixture was filtered through a pad of silica gel with copious washing. The solution was concentrated and purified by flash chromatography on silica gel. The reactions were followed by GC and the yields were based on aryl bromide.

Table 1: Performance of the **2c** in the Suzuki-Miyaura of 4-bromoacetophenone in the presence of different bases (Temperature = 80 °C).

Entry	Base	Solvent	Time (min.)	Yield (%)[b,c]
1	NaOH	IPA	30	41
2	KOH	IPA	30	47
3	K$_2$CO$_3$	IPA	15	73
4	Cs$_2$CO$_3$	IPA	15	99

RESULTS and DISCUSSION

Preparation of the imidazolium salts: The asymmetrically substituted imidazolium salts (**1a-c**) were synthesized by reaction of N-butylimidazole and benzyl bromide derivative in toluene at room temperature (see the scheme). The imidazolium salts were

obtained as white solids, which have been observed to be air-stable. The imidazolium salts were characterized by ^{1}H- and ^{13}C-NMR spectroscopy. ^{1}H- and ^{13}C-NMR chemical shifts complied with the expected structures. The resonances for NC*H*N protons give as a sharp singlet between at δ 10.14 and 10.27 ppm. According to ^{13}C-NMR spectrum of these salts, the C2 carbon atoms appeared between at δ 136.4 and 137.2 ppm.

Preparation of NHC-Pd-pyridine complexes: PEPPSI type Pd-NHC complexes (**2a-c**) were synthesized from the reaction of 1,3-dialkylimidazolium salts with $PdCl_2$, KBr and K_2CO_3 as base in pyridine (Scheme 1). The characterization of the NHC-Pd-pyridine complexes were confirmed by ^{1}H- and ^{13}C-NMR spectroscopy and elemental analysis. The chemical shifts for the carbene carbon atom, **2a-c**, fall in the range δ 146.2–146.5 ppm.

Table 2: The Suzuki–Miyaura cross-coupling reaction of aryl bromide with phenylboronic acid catalyzed by Pd-NHC (PEPPSI) complexes (**2a-c**). Optimization of reaction parameters[a].
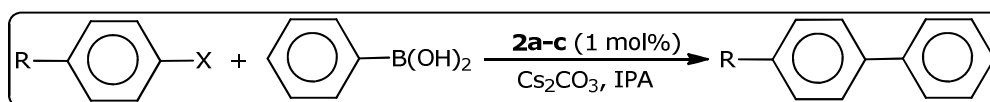
Entry	[Cat.]	[Pd](%)	Ar-X	T (°C)	t (min)	Yield (%)[b,c]
1	**2a**	1	Ph-Br	25/80	120/15	67/94
2	**2a**	1	Me-C_6H_4-4-Br	25/80	120/15	29/90
3	**2a**	1	$CH_3(O)C$-C_6H_4-4-Br	25/80	30/15	89/99
4	**2b**	1	Ph-Br	25/80	120/15	65/75
5	**2b**	1	Me-C_6H_4-4-Br	25/80	120/15	32/91
6	**2b**	1	$CH_3(O)C$-C_6H_4-4-Br	25/80	30/15	87/99
7	**2c**	1	Ph-Br	25/80	120/15	69/94
8	**2c**	1	Me-C_6H_4-4-Br	25/80	120/15	34/72
9	**2c**	1	$CH_3(O)C$-C_6H_4-4-Br	25/80	30/15	97/99
10	**$PdCl_2$**	1	$CH_3(O)C$-C_6H_4-4-Br	80	240	1
11	**2a**	1	$CH_3(O)C$-C_6H_4-4-Cl	80	240	37
12	**2b**	1	$CH_3(O)C$-C_6H_4-4-Cl	80	240	30
13	**2c**	1	$CH_3(O)C$-C_6H_4-4-Cl	80	240	36

[a] Reagents: an aryl halide (0.50 mmol), $PhB(OH)_2$ (0.75 mmol), Cs_2CO_3 (1.50 mmol), diethylene glycol di-*n*-butyl ether (0.3 mmol, internal standard), Pd-NHC catalyst (1 mol%), and 2-propanol (3.0 mL).
[b] Yields based on the aryl halide and average of two runs.
[c] All reactions were followed by GC.
[d] Referred to the reaction time indicated in column.
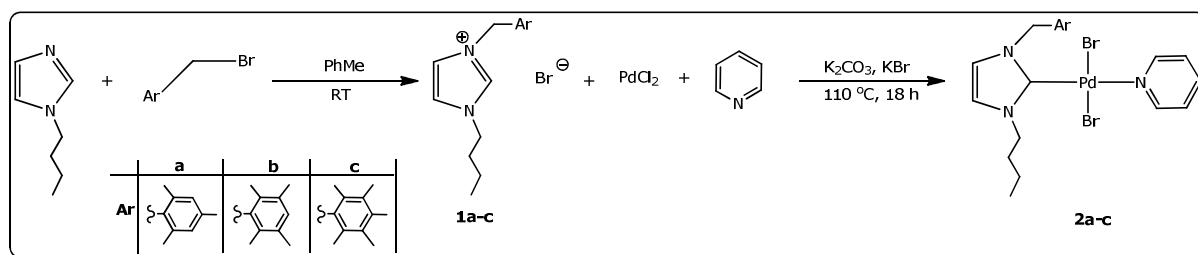
Scheme 1: Synthesis of imidazolium salts and PEPPSI type Pd-NHC complexes.

Suzuki-Miyaura Coupling Reaction: A series of studies were performed to determine a suitable base for the catalytic system in Suzuki-Miyaura coupling reaction (Table 1). In the catalytic studies, complexes (**2a-c**) were employed in 2-propanol with 1 mol% catalyst loading, Suzuki-Miyaura coupling reactions (Table 2). The works were initiated with the investigation of coupling of *p*-bromoacetophenone and phenylboronic acid in the presence of Pd-NHC catalyst at 25°C. The results indicated that the complexes (**2a-c**) displayed the best catalytic activity, giving excellent yield for 30 min. Under these conditions, *p*-bromobenzene and *p*-bromotoluene reacted with phenylboronic acid. The three complexes (**2a-c**) showed the lowest coupling yields for *p*-bromotoluene, and moderate yields for *p*-bromobenzene within 2h. In order to examine the influence of temperature on the yields, same reactions were performed for *p*-bromoacetophenone, *p*-bromobenzene, and *p*-bromotoluene reacting with phenylboronic acid at 80 °C instead of 25 °C. The results indicated that the complexes (**2a**-**c**) could also be converted to corresponding desired coupling products in good to excellent yields at 80 °C within 15 min (Table 2). After good results from bromo derivatives, the catalytic activities were investigated for the coupling of *p*-chloroacetophenone and phenylboronic acid, in the presence of **2a-c** at 80 °C. The results are summarized in Table 2. It indicates that the complexes exhibited low activity when *p*-chloroacetophenone was used as substrates within 4 h. Also, the catalytic activity of $PdCl_2$ was studied (Entry 10) which the coupling yield is 1% for *p*-bromoacetophenone as a substrate at 80 °C. The low activity of aryl chloride in Suzuki-Miyaura cross coupling reaction has also been reported in the previous studies [23-24].

In this work, several new air- and moisture-stable, convenient to handle, and easily synthesized PEPPSI-type Pd-NHC complexes have been designed. A series of NHC precursors (**1a-c**) were synthesized by the alkylation reaction of *N*-butylimidazole. The Pd-NHC complexes (**2a-c**) were prepared from their respective imidazolium halide salts by the reaction with KBr and $PdCl_2$ in pyridine in presence of K_2CO_3 as a base. All complexes are stable toward light and air both in the solid state and in solution. The molecular structures of the imidazolium bromide salt (**1a-c**) and the Pd–NHC complexes (**2a-c**) have been characterized by elemental analysis and ^{1}H- and ^{13}C-NMR spectra.

These novel imidazolium based NHC-palladium(II)-pyridine complexes have high catalytic activity in the Suzuki-Miyaura coupling reactions of aryl bromides. Reactions reach completion in short reaction time for *p*-bromoacetophenone as a substrate at 25°C. The catalytic activities of **2a-c** were compared with $PdCl_2$ for *p*-bromoacetophenone as a substrate at 80°C. Synthesized complexes have significantly better activity than $PdCl_2$. Furthermore, the complex **2c** shows the most noticeable activity and a maximum yield of 97% was achieved after 30 min. The complexes (**2a**-**c**) exhibit good catalytic activity at 80°C within 15 min.

ACKNOWLEDGEMENTS

REFERENCES

1. Jacobsen H, Correa A, Poater A, Costabile C, Cavallo L. Understanding the M(NHC) (NHC=N-heterocyclic carbene) bond. Coordination Chemistry Reviews. 2009 Mar;253:687-703. DOI: 10.1016/j.ccr.2008.06.006.

2. Boehme C, Frenking G. Electronic structure of stable carbenes, silylenes, and germylenes. Journal of the American Chemical Society. 1996 Feb;118:2039-46. DOI: 10.1021/ja9527075.

3. Viciu M. S, Navarro O, Germaneau R. F, Kelly R. A, Sommer W, Marion N, Stevens E. D, Cavallo L, Nolan S. P. Synthetic and structural studies of (NHC)Pd(allyl)Cl complexes (NHC = N-heterocyclic carbene). Organometallics. 2004 Feb;23:1629-35. DOI: 10.1021/om034319e.

4. a. Diez C, Nagel U. Chiral iridium(I) bis(NHC) complexes as catalysts for asymmetric transfer hydrogenation. Applied Organometallic Chemistry. 2010 Apr;24:509-516. DOI: 10.1002/aoc.1650. b. Crudden C. M, Allen D. P. Stability and reactivity of N-heterocyclic carbene complexes. Coordination Chemistry Reviews. 2004 Dec;248:2247-73. DOI: 10.1016/j.ccr.2004.05.013. c. Crabtree R. H. NHC ligands versus cyclopentadienyls and phosphines as spectator ligands in organometallic catalysis. Journal of Organometallic Chemistry. 2005 Dec;690:5451-57. DOI: 10.1016/j.jorganchem.2005.07.099.

5. Herrmann W. A. N-Heterocyclic Carbenes: A new concept in organometallic catalysis. Angewandte Chemie International Edition. 2002 Apr;41:1290-1309. DOI: 10.1002/1521-3773(20020415)41:8<1290::AID-ANIE1290>3.0.CO;2-Y.

6. Hahn F. E. Heterocyclic carbenes. Angewandte Chemie International Edition. 2006 Jan;45:1348-52. DOI: 10.1002/anie.200503858.

7. ArduengoIII A. J, Harlow R. L, Kline M. A stable crystalline carbene. Journal of the American Chemical Society. 1991 Jan;113:361-63. DOI: 10.1021/ja00001a054.

8. Mangalum A, McMillen C. D, Tennyson A. G. Synthesis, coordination chemistry and reactivity of transition metal complexes supported by a chelating benzimidazolylidene carboxylate ligand. Inorganica Chimica Acta. 2015 Feb;426:29-38. DOI: 10.1016/j.ica.2014.11.003.

9. Akkoç S, Gök Y, Akkurt M, Tahir M. N. Catalytic activities in the direct C5 arylation of novel palladium N-heterocyclic carbene complexes containing benzimidazol-2-ylidene nucleus. Inorganica Chimica Acta. 2014 Mar;413:221-30. DOI: 10.1016/j.ica.2014.01.015.

10. Serrano J. L, Pérez J, García L, Sánchez G, García J, Lozano P, Zende V, Kapdi A. N-Heterocyclic-Carbene complexes readily prepared from di-μ-hydroxopalladacycles catalyze the Suzuki Arylation of 9-bromophenanthrene. Organometallics. 2015 Jan;34:522-33. DOI: 10.1021/om501160n.

11. Lee J. Y, Ghosh D, Lee J. Y, Wu S. S, Hu C. H, Liu S. D, Lee H. M. Zwitterionic palladium complexes: Room-temperature Suzuki–Miyaura Cross-Coupling of sterically hindered substrates in an aqueous medium. Organometallics. 2014 Oct;33:6481-92. DOI: 10.1021/om500834y.

12. Hashmi A. S. K, Lothschütz C, Böhling C, Hengst T, Hubbert C, Rominger F. Carbenes made easy: Formation of unsymmetrically substituted N-heterocyclic carbene complexes of palladium(II), platinum(II) and gold(I) from coordinated isonitriles and their catalytic activity. Advanced Synthesis & Catalysis. 2010 Nov;352:3001-12. DOI: 10.1002/adsc.201000472.

13. Kong Y, Wen L, Song H, Xu S, Yang M, Liu B, Wang B. Synthesis, structures, and norbornene polymerization behavior of aryloxide-N-heterocyclic carbene ligated palladacycles. Organometallics. 2011 Dec;30:153-59. DOI: 10.1021/om100994s.

14. a. Doucet H. Suzuki–Miyaura Cross-Coupling Reactions of alkylboronic acid derivatives or alkyltrifluoroborates with aryl, alkenyl or alkyl halides and triflates. European Journal of Organic Chemistry. 2008 Feb;2008:2013-30. DOI: 10.1002/ejoc.200700984. b. Budarin V. L, Clark J. H, Luque R, Macquarrie D. J, White R. J. Palladium nanoparticles on polysaccharide-derived mesoporous materials and their catalytic performance in C–C coupling reactions. Green Chemistry. 2008 Oct;10:382-87. DOI: 10.1039/B715508E. c. Kotha S, Lahiri K, Kashinath D. Recent applications of the Suzuki—Miyaura Cross-Coupling Reaction in organic synthesis. Tetrahedron. 2002 Nov;58:9633-65. DOI:10.1016/S0040-4020(02)01188-2.

15. Miyaura N, Suzuki A. Palladium-catalyzed cross-coupling reactions of organoboron compounds. Chemical Reviews. 1995 Nov;95:2457-83. DOI: 10.1021/cr00039a007.

16. Suzuki A. ChemInform Abstract: Recent Advances in the Cross-Coupling Reactions of Organoboron Derivatives with Organic Electrophiles. Journal of Organometallic Chemistry. 1999 Mar;576:147-68. DOI: 10.1016/S0022-328X(98)01055-9.

17. Stanforth S. P. Catalytic cross-coupling reactions in biaryl synthesis. Tetrahedron. 1998 Jan;54:263-303. DOI: 10.1016/S0040-4020(97)10233-2.

18. Whitcombe N. J, Hii K. K, Gibson S. E. Advances in the Heck chemistry of aryl bromides and chlorides. Tetrahedron. 2001 Aug;57:7449-76. DOI: 10.1016/S0040-4020(01)00665-2.

19. Crisp G.T. Variations on a theme—recent developments on the mechanism of the Heck reaction and their implications for synthesis. Chemical Society Reviews. 1998; 27:427-36. DOI: 10.1039/A827427Z.

20. O'Brien C. J, Kantchev E. A. B, Valente C, Hadei N, Chass G. A, Lough A, Hopkinson A. C, Organ M. G. Easily prepared air- and moisture-stable Pd–NHC (NHC=N-Heterocyclic Carbene) complexes: A reliable, user-friendly, highly active palladium precatalyst for the Suzuki–Miyaura Reaction. Chemistry A European Journal. 2006 Mar;12:4743-48. DOI: 10.1002/chem.200600251.

21. Ozdemir I, Gok Y, Ozeroglu O, Kaloglu M, Doucet H, Bruneau C. N-Heterocyclic Carbenes: Useful ligands for the palladium-catalysed direct C5 arylation of heteroaromatics with aryl bromides or electron-deficient aryl chlorides. European Journal of Inorganic Chemistry. 2010 Apr;2010:1798-1805. DOI: 10.1002/ejic.200901195.

22. Teci M, Brenner E, Matt D, Toupet L. N-Heterocyclic Carbenes Functioning as Monoligating Clamps. European Journal of Inorganic Chemistry. 2013 Mar;2013:2841-48. DOI: 10.1002/ejic.201300087.

23. Yılmaz Ü, Küçükbay H, Şireci N, Akkurt M, Günal S, Durmaz R, Tahir M.N. Synthesis, microwave-promoted catalytic activity in Suzuki-Miyaura cross-coupling reactions and antimicrobial properties of nıvel benzimidazole salts bearing trimethylsilyl group. Applied Organometallic Chemistry. 2011, 25, 366-373. DOI: 10.1002/aoc.1772.

24. Küçükbay H, Yılmaz Ü, Yavuz K, Buğday N. Synthesis, characterization, and microwave-assisted catalytic activity in Heck, Suzuki, Sonogashira, and Buchwald-Hartwig cross-coupling reactions of novel benzimidazole salts bearing N-ohtalimidoethyl and benzyl moieties. Turkish Journal of Chemistry. 2015, 39, 1265-1278. DOI: 10.3906/kim-1505-34.

Türkçe Öz ve Anahtar Kelimeler

N-Butyl Substituted N-Heterocyclic Carbene-Pd(II)-Pyridine (PEPPSI) Complexes: Synthesis, Characterization, and Catalytic Activity in the Suzuki-Miyaura Reaction

Rukiye Fırıncı[1*]

Öz: Bir seri N-butil sübstitüe imidazolyum tuzu (**1a-c**) ve piridinle kuvvetlendirilen ön katalizör hazırlama, kararlılaştırma ve başlatma (PEPPSI) yöntemiyle üretilen paladyum *N*-heterosiklik karben kompleksleri (**2a-c**) sentezlenmiş ve karakterizasyonları yapılmıştır. Pd-NHC kompleksleri elementel analiz ve spektroskopik yöntemlerle tam olarak tayin edilmiştir. Sentezlenen kompleksler Suzuki-Miyaura çapraz eşleşme tepkimesinde test edilmiştir. Bu kompleksler Suzuki-Miyaura tepkimesinde kullanılan fenilboronik asit ve aril bromürler için etkili katalizörler olarak bulunmuştur.

Anahtar kelimeler: Suzuki-Miyaura eşleşme tepkimesi, *N*-heterosiklik karben, PEPPSI paladyum kompleksleri.

Synthesis, Characterization, and Antioxidant Activities of Novel 1-(Morpholine-4-yl-Methyl)-3-Alkyl(Aryl)-4-[4-(Dimethylamino)-Benzylidenamino]-4,5-Dihydro-1H-1,2,4-Triazol-5-Ones

Özlem Gürsoy-Kol[1*], Haydar Yüksek[1], Sevda Manap[1], Feyzi S. Tokalı[1]

[1]Department of Chemistry, Kafkas University, Kars, Turkey

Abstract: In this paper, eight novel 1-(morpholine-4-yl-methyl)-3-alkyl(aryl)-4-[4-(dimethylamino)-benzylidenamino]-4,5-dihydro-1H-1,2,4-triazol-5-ones (**2**) were obtained by the reactions of 3-alkyl(aryl)-4-[4-(dimethylamino)-benzylidenamino]-4,5-dihydro-1H-1,2,4-triazol-5-ones (**1**) with formaldehyde and morpholine. The novel synthesized compounds were identified by FT-IR, ^{1}H NMR, and ^{13}C NMR spectral data. Besides, the newly synthesized compounds were analyzed for their *in vitro* potential antioxidant capacities in three different assays. All of the compounds demonstrated significant activity for metal chelating effect.

Keywords: 4,5-Dihydro-1*H*-1,2,4-triazol-5-one; synthesis; mannich base; antioxidant capacity.

INTRODUCTION

Mannich bases have applications the field medicinal chemistry, the product synthetic polymers, the petroleum industry, as products used in water treatment, cosmetics, the dyes industry, *etc.* (1). Moreover, Mannich bases have some biological activities such as anticancer (2,3), antibacterial (4,5), antimycobacterial (6), anti-HIV (7), anti-inflammatory (8,9), analgesic (10,11), antifungal (12,13), antitumor (14,15), antiviral (16), antidepressant (17), antiulcer (18), anticonvulsant (19), antimalaria (20), and antioxidant activities (21).

Antioxidants are extensively studied for their capacity to protect organisms and cells from damage that is induced by the oxidative stress. A great deal of research has been devoted to the study of different types of natural and synthetic antioxidant. A large number of heterocyclic compounds, containing the 1,2,4-triazole ring, are associated with diverse biological properties such as antioxidant, anti-inflammatory, antimicrobial, and antiviral activity. External chemicals and internal metabolic processes in human body or in food system might produce highly reactive free radicals, especially oxygen-derived radicals, which are capable of oxidizing biomolecules by resulting in cell death and tissue damage. Oxidative damages play a significantly pathological role in human diseases. Cancer, emphysema, cirrhosis, atherosclerosis, and arthritis have all been correlated with oxidative damage. Also, excessive generation of reactive oxygen species (ROS) induced by various stimuli and which exceeds the antioxidant ability of the organism leads to variety of pathophysiological processes like inflammation, diabetes, genotoxicity and cancer (22).

Triazoles are heterocyclic compounds that contain three nitrogen atoms. 1,2,4-Triazole and 4,5-dihydro-1H-1,2,4-triazol-5-one derivatives are reported to possess a broad spectrum of biological activities such as analgesic, antibacterial, antioxidant, and antiparasitic properties (23–26). Considering about the development of new hetero moieties by combining potential biological active scaffolds, an attempt was made here to obtain 1,2,4-triazoles bearing morpholine ring and to evaluate their antioxidant activity.

In this regard, eight new 1-(morpholine-4-yl-methyl)-3-alkyl(aryl)-4-[4-(dimethylamino)-benzylidenamino]-4,5-dihydro-1H-1,2,4-triazol-5-ones (**2**) were synthesized and investigated by using different antioxidant methodologies like reducing

power, 1,1-diphenyl-2-picryl-hydrazyl (DPPH) free radical scavenging activity, and iron binding effect.

MATERIALS AND METHODS

Chemicals and Apparatus

Chemical reagents used in this paper were bought from Merck AG, Aldrich, and Fluka. Melting points were recorded in open glass capillaries using an Electrothermal melting point apparatus and were not corrected. The infrared spectra were recorded on an Alpha-P Bruker FT-IR Spectrometer. ^{1}H and ^{13}C NMR spectra were determined in deuteriated dimethyl sulfoxide with TMS as internal standard using a Bruker Ultrashield spectrometer at 400 MHz and 100 MHz, respectively.

Synthesis of Compounds 2: General Procedure

3-Alkyl(Aryl)-4-[4-(dimethylamino)-benzylidenamino]-4,5-dihydro-1H-1,2,4-triazol-5-ones (**1**) were obtained according to the literature (27). To the solution of this compound (**1**) (5 mmol) in absolute ethanol was added formaldehyde (% 37, 10 mmol) and morpholine (6 mmol). The reaction mixture was refluxed for 4 hours. The mixture was left at room temperature overnight. After cooling the mixture in the refrigerator, the solid formed was obtained by filtration, washed with cold ethanol, and recrystallized from ethanol.

Physical data of the new compounds are presented in Table 1. IR, ^{1}H-NMR and ^{13}C-NMR spectral data are given in Tables 2, 3, and 4, respectively.

ANTIOXIDANT ACTIVITY

Chemicals

Butylated hydroxytoluene (BHT), iron(II) chloride, DPPH·, α-tocopherol, 3-butylated hydroxyanisole (BHA), (2-pyridyl)-5,6-bis(phenylsulfonic acid)-1,2,4-triazine (ferrozine), and trichloroacetic acid (TCA) were obtained from E. Merck or Sigma.

Reducing power

The reducing power of the compounds **2a-h** was determined using the method of Oyaizu (28). Different concentrations of the samples (50-250 µg/mL) in DMSO (1 mL) were mixed with phosphate buffer (2.5 mL, 0.2 M, pH = 6.6) and potassium ferricyanide (2.5 mL, 1%). The mixture was incubated at 50 °C for 20 min. after which a portion (2.5 mL) of trichloroacetic acid (10%) was added to the mixture, which was then centrifuged for 10 min at 1000 x g. The upper layer of solution (2.5 mL) was mixed with distilled water (2.5 mL) and $FeCl_3$ (0.5 mL, 0.1%), and then the absorbance at 700 nm was measured in a spectrophometer. Higher absorbance of the reaction mixture indicated greater reducing power.

Free radical scavenging activity

Free radical scavenging effect of the compounds **2a-h** was estimated by DPPH·, by the method of Blois (29). Briefly, 0.1 mM solution of DPPH. in ethanol was prepared, and this solution (1 mL) was added to sample solutions in DMSO (3 mL) at different concentrations (50-250 µg/mL). The mixture was shaken vigorously and allowed to stand at room temperature for 30 min. Then the absorbance was measured at 517 nm in a spectrophometer. Lower absorbance of the reaction mixture indicated higher free radical scavenging activity. The DPPH. concentration (mM) in the reaction medium was calculated from the following calibration curve and determined by linear regression (R: 0.997):

$$Absorbance = 0.0003 \text{ x DPPH. } - 0.0174$$

The capability to scavenge the DPPH radical was calculated using the following equation:

$$DPPH. \text{ scavenging effect (\%)} = (A_0 - A_1/A_0) \text{ x } 100$$

where A_0 is the absorbance of the control reaction and A_1 is the absorbance in the presence of the samples or standards.

Table 1. Physical data of the compounds **2a-h.**

Compound No	R	Yield (%)	m.p. (°C) (Crystallized from)
2a	CH_3	67	135 (Ethanol)
2b	CH_2CH_3	66	108 (Ethanol)
2c	$CH_2C_6H_5$	64	148 (Ethanol)
2d	$CH_2C_6H_4.CH_3$ (*p*-)	70	152 (Ethanol)
2e	$CH_2C_6H_4.OCH_3$ (*p*-)	95	194 (Ethanol)
2f	$CH_2C_6H_4.Cl$ (*p*-)	66	148 (Ethanol)
2g	$CH_2C_6H_4.Cl$ (*m*-)	66	184 (Ethanol)
2h	C_6H_5	75	155 (Ethanol)

Table 2. FTIR data of the compounds **2** (cm^{-1})

Compound No	$\nu_{C=O}$	$\nu_{C=N}$	$\nu_{1,4\text{-}disubstituted\ benzenoid\ ring}$	$\nu_{monosubstituted\ benzenoid\ ring}$
2a	1682	1596	857	-
2b	1702	1610, 1589	814	-
2c	1692	1592	816	775 and 693
2d	1702	1590	**813**	-
2e	1705	1608, 1587	816	-
2f	1707	1609, 1584	811	-
2g	1701	1588	811	-
2h	1696	1613, 1586	814	777 and 692

Metal chelating activity

The chelating of ferrous ions by the compounds **2a-h** and references was measured according to the method of Dinis *et al.* (30). Briefly, the synthesized compounds (30–60 µg/mL) were added to a 2 mM solution of $FeCl_2 \cdot 4H_2O$ (0.05 mL). The reaction was initiated by the addition of 5 mM ferrozine (0.2 mL), and then the mixture was shaken vigorously and left to stand at room temperature for 10 min. After the mixture had reached equilibrium, the absorbance of the solution was measured at 562 nm in a spectrophotometer. All tests and analyses were run in triplicate and averaged. The percentage of inhibition of ferrozine–Fe^{2+} complex formation was given by the formula: % inhibition = $(A_0 − A_1 / A_0) × 100$, where A_0 is the absorbance of the control, and A_1 is the absorbance in the presence of the samples or standards. The control did not contain compound or standard.

RESULTS and DISCUSSION

In the current paper, eight new 1-(morpholine-4-yl-methyl)-3-alkyl(aryl)-4-[4-(dimethylamino)-benzylidenamino]-4,5-dihydro-1H-1,2,4-triazol-5-ones (**2a-h**) were synthesized. The starting compounds **1a-h** were prepared as explained in the literature (27). Compounds **2a-h** were obtained by the reactions of 3-alkyl(aryl)-4-[4-(dimethylamino)-benzylidenamino]-4,5-dihydro-1H-1,2,4-triazol-5-ones (1) with formaldehyde and morpholine (**Scheme 1**). The novel 3-alkyl(aryl)-4-(3-benzoxy-4-methoxy-benzylidenamino)-4,5-dihydro-1*H*-1,2,4-triazol-5-ones (**2a-h**) were characterized with FT-IR, ^{1}H NMR and ^{13}C NMR and spectral data.

1, 2	R
a	CH$_3$
b	CH$_2$CH$_3$
c	CH$_2$C$_6$H$_5$
d	CH$_2$C$_6$H$_4$.CH$_3$ (*p*-)
e	CH$_2$C$_6$H$_4$.OCH$_3$ (*p*-)
f	CH$_2$C$_6$H$_4$.Cl (*p*-)
g	CH$_2$C$_6$H$_4$.Cl (*m*-)
h	C$_6$H$_5$
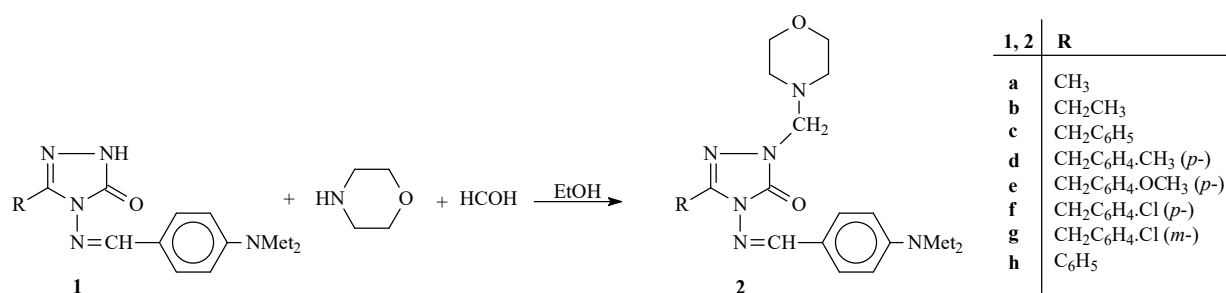
Scheme 1 Synthetic pathway of compounds **2**.

Table 3. ^{1}H-NMR data of the compounds **2** (DMSO-d_6, δ/ppm)

Comp.No	CH$_3$	CH$_2$NCH$_2$	CH$_2$	2CH$_3$	CH$_2$OCH$_2$	OCH$_3$	CH$_2$Ph	NCH$_2$	Aromatic H	N=CH
2a	2.27 (s)	2.56-2.59 (m)	-	2.99 (s)	3.54-3.57 (m)	-	-	4,51 (s)	6.77 (d,2H,*J*=8.8 Hz); 7.64 (d,2H,*J*=8.8 Hz	9.41 (s)
2b	1.21 (t, *J*=7.60Hz)	2.56-2.58 (m)	2.68 (q, *J*=7.60Hz)	2.99 (s)	3.55-3.57 (m)	-	-	4.52 (s)	6.78 (d,2H,*J*=8.8 Hz); 7.63 (d,2H,*J*=8.8 Hz	9.40 (s)
2c	-	2.57-2.59 (m)	-	3.00 (s)	3.56-3.57 (m)	-	4.05 (s)	4.55 (s)	6.76 (d,2H,*J*=8.8Hz); 7.22-7.24 (m,1H); 7.31-732 (m,4H); 7.60 (d,2H,*J*=8.8 Hz)	9.37 (s)
2d	2.24 (s)	2.57-2.58 (m)	-	3.00 (s)	3.56-3.57 (m)	-	3.99 (s)	4.55(s)	6.77 (d,2H,*J*=8.8 Hz); 7.11 (d,2H,*J*=7.6 Hz); 7.20 (d,2H,*J*=8.8 Hz); 7.61 (d,2H,*J*=8.8 Hz)	9.36 (s)
2e	-	2.54-2.57 (m)	-	3.00 (s)	3.56 (m)	3.65 (s)	3.97 (s)	4.54 (s)	6.77 (d,2H,*J*=8.8 Hz); 6.87 (d,2H,*J*=8.4 Hz); 7.23 (d,2H,*J*=8.4 Hz); 7.61 (d,2H,*J*=8.8 Hz)	9.37 (s)
2f	-	2.56-2.58 (m)	-	3.00 (s)	3.55-3.57 (m)	-	4.06 (s)	4.54 (s)	6.77 (d,2H,*J*=8.4 Hz); 7.33-7.39 (m,4H); 7.6 (d,2H,*J*=9.2 Hz)	9.38 (s)
2g	-	2.57 (m)	-	3.00 (s)	3.56 (m)	-	4.08 (s)	4.55 (s)	6.76 (d,2H,*J*=8.4 Hz); 7.29-7.37 (m,3H); 7.42 (s,1H); 7.60 (d,2H,*J*=8.0 Hz)	9.38 (s)

Table 4. ^{13}C-NMR data of the compounds **2** (DMSO-d_6, δ/ppm)

Comp.No	Triazole C_5	N=CH	Triazole C_3	Aromatic C	Aliphatic C
2a	152.49	150.50	142.92	156.02; 132.23(2C); 120.13; 111.06(2C)	66.04(CH_2OCH_2); 65.85(NCH_2N); 50.00(CH_2NCH_2); 38.95(2CH_3); 11.03(CH_3)
2b	152.50	150.63	146.70	156.03; 129.29(2C); 120.16; 111.65(2C)	66.04(CH_2OCH_2); 65.88(NCH_2N); 50.01(CH_2NCH_2); 38.94(2CH_3); 18.50($\underline{CH_2}CH_3$); 10.06($CH_2\underline{CH_3}$)
2c	152.50	150.51	144.81	155.66; 135.79; 129.32 (2C); 128.70 (2C); 128.45 (2C); 126.72; 120.10; 111.65 (2C)	66.04(CH_2OCH_2); 65.97(NCH_2N); 50.02(CH_2NCH_2); 38.95(2CH_3); 30.99(CH_2Ph)
2d	152.49	150.51	144.97	155.62; 135.79; 132.66; 129.31 (2C); 129.01 (2C); 128.59 (2C); 120.13; 111.66 (2C)	66.04(CH_2OCH_2); 65.95(NCH_2N); 50.02(CH_2NCH_2); 38.96(2CH_3); 30.58(CH_2Ph); 20.37($PhCH_3$)
2e	152.49	150.51	145.12	158.09; 155.62; 129.77 (2C); 129.33 (2C); 127.54; 120.13; 113.89 (2C); 111.63 (2C)	66.03(CH_2OCH_2); 65.95(NCH_2N); 55.01(OCH_3); 50.02(CH_2NCH_2); 38.94(2CH_3); 30.13(CH_2Ph)
2f	152.51	150.50	144.49	155.74; 134.76; 131.43; 130.65 (2C); 129.35 (2C); 128.39 (2C); 120.04; 111.66 (2C)	66.04(CH_2OCH_2 + NCH_2N); 50.00(CH_2NCH_2); 38.95(2CH_3); 30.34(CH_2Ph)
2g	152.53	150.49	144.31	155.75; 138.21; 132.96; 130.28; 129.36 (2C); 128.85; 127.51; 126.77; 120.04; 111.64 (2C)	66.04(CH_2OCH_2 + NCH_2N); 50.02(CH_2NCH_2); 38.96(2CH_3); 30.58(CH_2Ph)

Antioxidant activity

The antioxidant capacities of ten newly synthesized compounds **2a-h** were determined. Different processes have been used to identify the antioxidant capacities. The processes used in the paper are clarified below:

Reducing power

The reducing power of the compounds **2** was determined. The reducing capacity of a compound may serve as a significant indicator of its potential antioxidant activity. The presence of reductants such as antioxidant substances in the samples causes the reduction of the Fe^{3+} / ferricyanide complex to the ferrous form. Therefore, the Fe^{2+} can be monitored by measuring the formation of Perl's Prussian blue at 700 nm (31). The antioxidant activity of putative antioxidant has been attributed to various mechanisms such as prevention chain initiation, binding of transition metal ion catalyst, decomposition of peroxides, prevention of continued hydrogen abstraction, reductive capacity and radical scavenging (32). In the paper, all of the concentrations of the compounds showed lower absorbance than reference antioxidants as seen in Figure **1**. Hereby, any reductive activities were not observed.
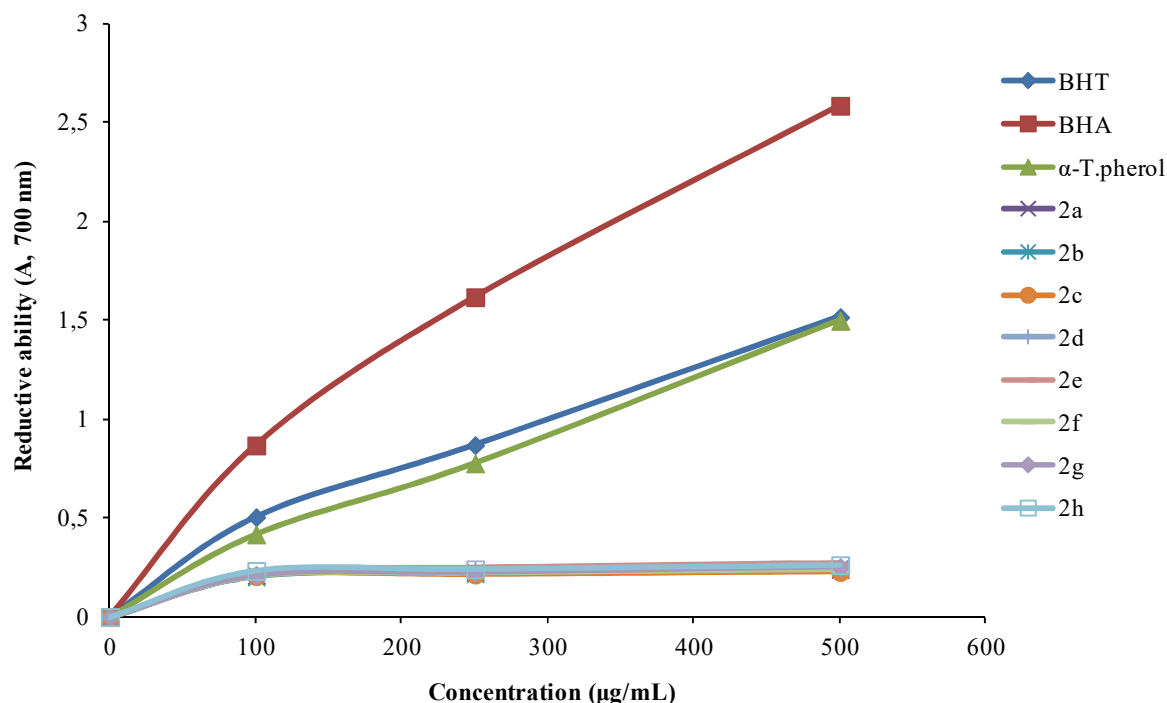
Figure 1. Total reductive potential of different concentrations of compound **2a-h**, BHT, BHA and α-tocopherol.

DPPH radical scavenging activity

Free radical scavenging effect of the compounds **2** was estimated by DPPH radical model. The effect of antioxidants on DPPH radical scavenging was thought to be due to their hydrogen donating ability (33). DPPH is a stable free radical and accepts an electron or hydrogen radical to become a stable diamagnetic molecule (34). The reduction capability of DPPH radicals was determined by decrease in its absorbance at 517 nm induced by antioxidants. In the study, antiradical capacities of the compounds **2a-h** and reference antioxidants for instance α-tocopherol, BHA and BHT were detected by using DPPH· method. Scavenging effect values of compounds **2** with BHT, BHA and α-tocopherol at different concentrations are given in Figure 2. All of the compounds tested with this method exhibited very low DPPH free radical scavenging activity in a concentration-dependent manner. In other words the newly synthesized compounds did not show any ability like a radical scavenger.
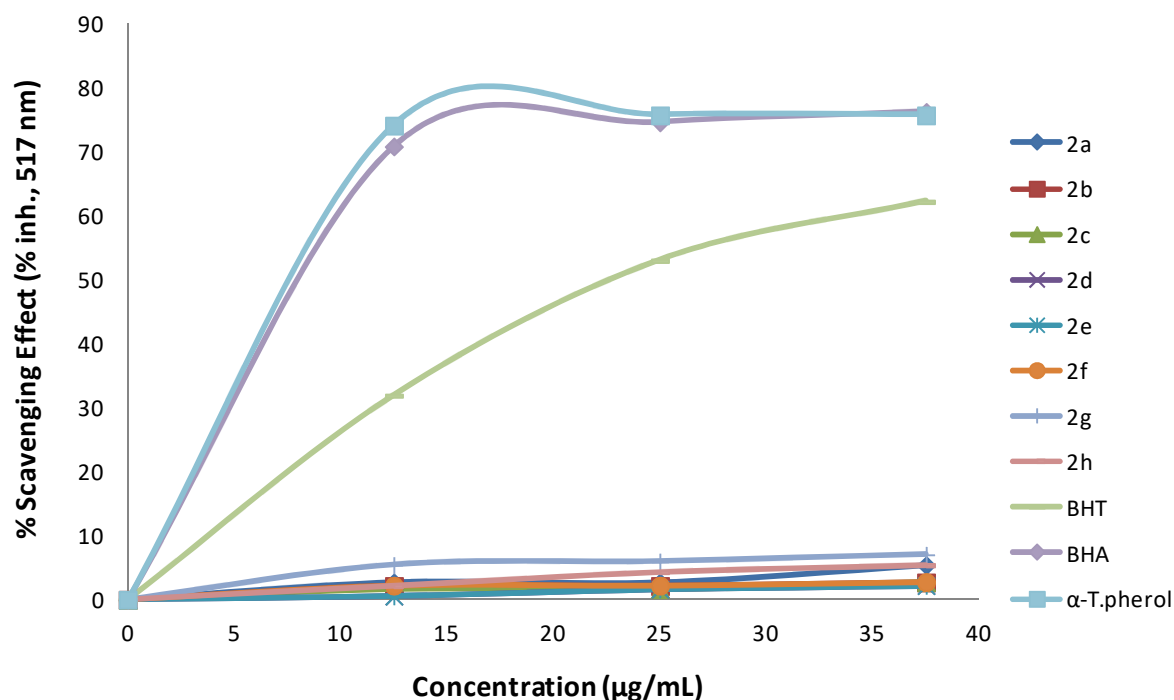
Iron binding capacity

The chelating of ferrous ions by the compounds **2** and references was measured. Ferrozine can quantitatively form complexes with Fe^{2+}. In the presence of chelating agents, the complex formation is disrupted with the result that the red color of the complex is decreased. Measurement of color reduction therefore allows estimation of the chelating activity of the coexisting chelator (35). The transition metals ions play an important role as catalysts of oxidative process, leading to formation of hydroxyl radicals and hydroperoxide decomposition reaction via Fenton chemistry (36). The production of

these radicals may lead to lipid peroxidation, protein modification, and DNA damage. Chelating agents are effective as secondary antioxidants because they potentially inhibit the metal-dependent processes thereby stabilizing the oxidized form of the metal ion (37). Iron binding activities of the compounds **2**, α-tocopherol and EDTA are shown in Figure 3. In the current paper, high iron binding capacity of synthesized compounds would be beneficial in retarding metal-chelating oxidation. The data acquired from Figure 3 discloses that the metal chelating effects of the compounds **2** were significant and concentration-dependent. The metal chelating effect of the compounds and references decreased in order of EDTA > **2g** ≈ **2b** > **2a** ≈ **2h** > **2c** ≈ **2d** > **2f** ≈ **2e** > α-tocopherol, which were 85.4, 84.5, 84.0, 82.5, 82.0, 60.3 (%), at the highest concentration, respectively.
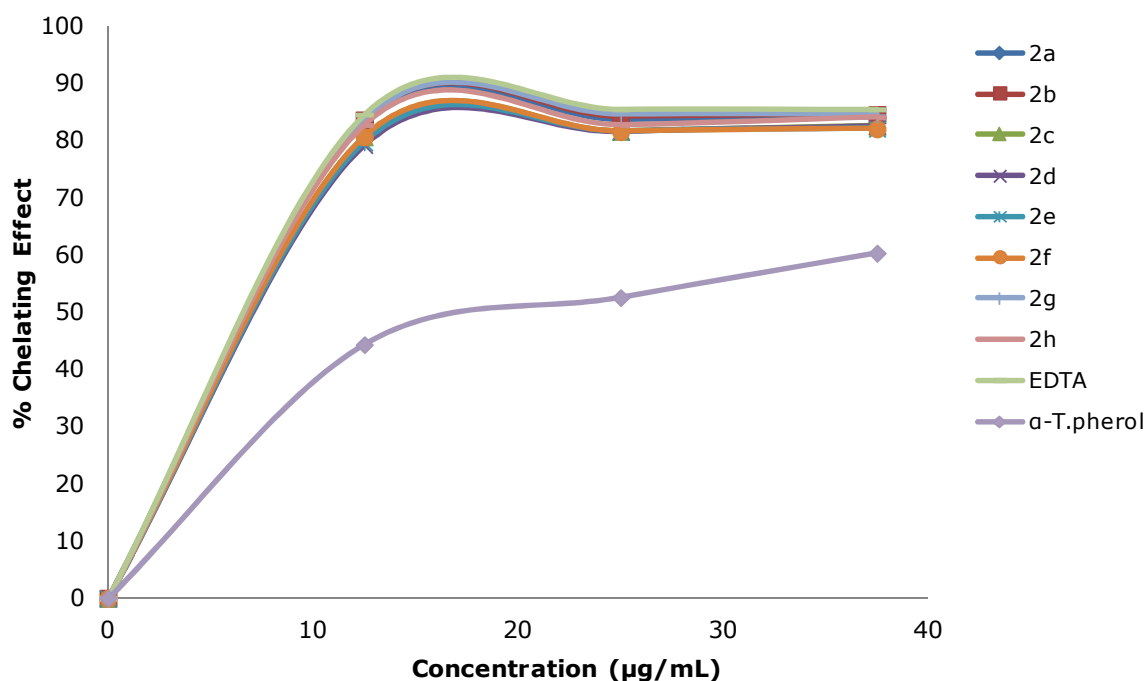
Figure 3. Iron binding effect of diverse amount of the compounds **2a-h**, and reference antioxidants.

CONCLUSION

New 4,5-dihydro-1*H*-1,2,4-triazol-5-one derivatives were obtained and evaluated for their *in-vitro* antioxidant capacity. All of the compounds demonstrate a marked ability for metal chelating activity. The data reported with regard to the observed metal chelating activities of the studied compounds could prevent redox cycling. The results may also give several advices for the improvement of new triazole-based therapeutic target.

REFERENCES

1.   Tramontini M, Angiolini L. Mannich Bases: Chemistry and Uses. CRC Press; 1994. 289 p.

2.   Savariz FC, Formagio ASN, Barbosa VA, Foglio MA, Carvalho JE de, Duarte MCT, et al. Synthesis, antitumor and antimicrobial activity of novel 1-substituted phenyl-3-[3-alkylamino(methyl)-2-thioxo-1,3,4-oxadiazol-5-yl] β-carboline derivatives. J Braz Chem Soc. Sociedade Brasileira de Quimica; 2010;21(2):288–98.

3.   CHEN Y, WANG G, DUAN N, CAO T, WEN X, YIN J, et al. Synthesis and Antitumor Activity of Fluoroquinolone C3-Isostere Derivatives: Oxadiazole Mannich Base Derivatives. Chinese J Appl Chem. 2012;29(11):1246–50. DOI: 10.3724/SP.J.1095.2012.00537.

4.   El-Emam AA, Al-Tamimi A-MS, Al-Omar MA, Alrashood KA, Habib EE. Synthesis and antimicrobial activity of novel 5-(1-adamantyl)-2-aminomethyl-4-substituted-1,2,4-triazoline-3-thiones. Eur J Med Chem. 2013 Oct;68:96–102.

5.   Maddila S, Jonnalagadda SB. New Class of Triazole Derivatives and Their Antimicrobial Activity. Lett Drug Des Discov. 2012;9(7):687-93.

6.   Das S, Das U, Bandy B, Gorecki DKJ, Dimmock JR. 2-[4-(4-Methoxyphenylcarbonyloxy)benzylidene]-6-dimethylaminomethyl cyclohexanone hydrochloride: a Mannich base which inhibits the growth of some drug-resistant strains of Mycobacterium tuberculosis. Pharmazie. 2010 Nov;65(11):849–50.

7.   Sriram D, Yogeeswari P, Gopal G. Synthesis, anti-HIV and antitubercular activities of lamivudine prodrugs. Eur J Med Chem. 2005 Dec;40(12):1373-6.

8.   Liu D, Yu W, Li J, Pang C, Zhao L. Novel 2-(E)-substituted benzylidene-6-(N-substituted aminomethyl)cyclohexanones and cyclohexanols as analgesic and anti-inflammatory agents. Med Chem Res. 2013 Aug;22(8):3779–86. DOI: 10.1007/s00044-012-0362-x.

9.   Köksal M, Gökhan N, Küpeli E, Yesilada E, Erdoğan H. Synthesis, analgesic and antiinflammatory properties of certain 5-/6-acyl-3-(4-substituted-1-piperazinylmethyl)-2-benzoxazolinones derivatives. Arch Pharm (Weinheim). 2005 Mar;338(2-3):117–25.

10.   Nithinchandra, Kalluraya B, Aamir S, Shabaraya AR. Regioselective reaction: Synthesis, characterization and pharmacological activity of some new Mannich and Schiff bases containing sydnone. Eur J Med Chem. 2012;54:597–604.

11.   Manjunatha K, Poojary B, Lobo PL, Fernandes J, Kumari NS. Synthesis and biological evaluation of some 1,3,4-oxadiazole derivatives. Eur J Med Chem. 2010;45(11):5225–33.

12.   Ozkan-Daguyan I, Sahin F, Koksal M. Synthesis, Characterization and Antimicrobial Activity of Novel 3,5-Disubstituted-1,3,4-oxadiazole-2-ones. Rev Chim -Bucharest- Orig Ed. 2013;64(5):534–9.

13.   Frank P V, Manjunatha Poojary M, Damodara N, Chikkanna C. Synthesis and antimicrobial studies of some Mannich bases carrying imidazole moiety. Acta Pharm. 2013 Jun;63(2):231–9.

14.   Pati HN, Das U, Kawase M, Sakagami H, Balzarini J, De Clercq E, et al. 1-Aryl-2-dimethylaminomethyl-2-propen-1-one hydrochlorides and related adducts: A quest for selective cytotoxicity for malignant cells. Bioorg Med Chem. 2008 May;16(10):5747–53.

15.   Pau A, Murineddu G, Asproni B, Murruzzu C, Grella GE, Pinna G a, et al. Synthesis and cytotoxicity of novel hexahydrothienocycloheptapyridazinone derivatives. Molecules. 2009;14(9):3494–508.

16.   Chen D, Zhai X, Yuan QH, Luo J, Xie SC, Gong P. Synthesis and in vitro anti-hepatitis B virus activity of 1H-benzimidazol-5-ol derivatives. Chin Chem Lett. 2010 Nov; 21(11):1326-9.

17.   Köksal M, Bilge SS. Synthesis and Antidepressant-Like Profile of Novel 1-Aryl-3-[(4-benzyl)piperidine-1-yl]propane Derivatives. Arch Pharm (Weinheim). 2007 Jun;340(6):299–303. DOI: 10.1002/ardp.200700028.

18.   Kodhati V, Vanga MR, Yellu NR. Synthesis and Anti Bacterial and Anti-ulcer Evaluation of New S-mannich Bases of 4,6-diaryl-3,4-dihydropyrimidin-2(1H)-thiones. J Korean Chem Soc. 2013 Apr;57(2):234–40.

19.   Rajasekaran A, Rajamanickam V, Darlinquine S. Synthesis of some new thioxoquinazolinone derivatives and a study on their anticonvulsant and antimicrobial activities. Eur Rev Med Pharmacol Sci. 2013 Jan;17(1):95–104.

20.   Görlitzer K, Meyer H, Walter RD, Jomaa H, Wiesner J. [1]Benzothieno[3,2-b]pyridin-4-yl-amine – Synthese und Prűfung auf Wirksamkeit gegen Malaria. Pharmazie. 2004;59:506–12.

21.   Hamama WS, Zoorob HH, Gouda MA, Afsah EM. Synthesis and antimicrobial and antioxidant activities of simple saccharin derivatives with N-basic side chains. Pharm Chem J. Springer US; 2011 May;45(2):118–24. DOI: 10.1007/s11094-011-0573-3.

22.   McClements D, Decker E. Lipid oxidation in oil-in-water emulsions: Impact of molecular environment on chemical reactions in heterogeneous food systems. J Food Sci. 2000;65(8):1270–82. DOI: 10.1111/j.1365-2621.2000.tb10596.x.

23.   Yüksek H, Akyıldırım O, Yola ML, Gürsoy-Kol Ö, Çelebier M, Kart D. Synthesis, In Vitro Antimicrobial and Antioxidant Activities of Some New 4,5-Dihydro-1 H -1,2,4-triazol-5-one Derivatives. Arch Pharm (Weinheim). 2013;346(6):470–80. DOI: 10.1002/ardp.201300048.

24.   Aktas-Yokus O, Yuksek H, Gursoy-Kol O, Alpay-Karaoglu S. Synthesis and biological evaluation of new 1,2,4-triazole derivatives with their potentiometric titrations. Med Chem Res. Springer US; 2015;24(7):2813–24. DOI: 10.1007/s00044-015-1334-8.

25.   Chidananda N, Poojary B, Sumangala V, Kumari NS, Shetty P, Arulmoli T. Facile synthesis, characterization and pharmacological activities of 3,6-disubstituted 1,2,4-triazolo[3,4-b][1,3,4]thiadiazoles and 5,6-dihydro-3,6-disubstituted-1,2,4-triazolo[3,4-b][1,3,4]thiadiazoles. Eur J Med Chem. 2012;51:124–36. DOI: 10.1016/j.ejmech.2012.02.030.

26.   Saadeh HA, Mosleh IM, Al-Bakri AG, Mubarak MS. Synthesis and antimicrobial activity of new 1,2,4-triazole-3-thiol metronidazole derivatives. Monatshefte fur Chemie. 2010;141(4):471–8. DOI: 10.1007/s00706-010-0281-9.

27.   Bahçeci Ş, Yüksek H, Ocak Z, Azakli I, Alkan M, Özdemir M. Synthesis and Potentiometric Titrations of Some New 4-(Benzylideneamino)-4,5-dihydro-1H-1,2,4-triazol-5-one Derivatives in Non-Aqueous Media. Collect Czechoslov Chem Commun. 2002;67(8):1215–22.

28.   Oyaizu M. Studies on products of browning reaction. Antioxidative activities of products of browning reaction prepared from glucosamine. JapaneseJ Nutr Diet. 1986;44(17):307–15. DOI: 10.5264/eiyogakuzashi.44.307.

29.   Blois M. Antioxidant Determinations by the Use of a Stable Free Radical. Nature. 1958 Apr;181(4617):1199–200. DOI: 10.1038/1811199a0.

30.   Dinis TCP, Madeira VMC, Almeida LM. Action of Phenolic Derivatives (Acetaminophen, Salicylate, and 5-Aminosalicylate) as Inhibitors of Membrane Lipid Peroxidation and as Peroxyl Radical Scavengers. Arch Biochem Biophys. 1994;315(1):161–9. DOI: 10.1006/abbi.1994.1485

31.   Chung YC, Chang CT, Chao WW, Lin CF, Chou ST. Antioxidative activity and safety of the 50% ethanolic extract from red bean fermented by Bacillus subtilis IMR-NK1. J Agric Food Chem. 2002 Apr;50(8):2454–8. DOI: 10.1021/jf011369q

32.   Yildirim A, Mavi A, Kara AA. Determination of antioxidant and antimicrobial activities of Rumex crispus L. extracts. J Agric Food Chem. 2001;49(8):4083–9. DOI: 10.1021/jf0103572

33.   Baumann J, Wurn G, Bruchlausen V. Prostaglandin synthetase inhibiting O2 – radical scavenging properties of some flavonoids and related phenolic compounds. Naunyn-Schmiedebergs Arch Pharmacol. 1979;308:R27.

34.   Soares JR, Dinis TCP, Cunha AP, Almeida LM. Antioxidant activities of some extracts of Thymus zygis. Free Radic Res. 1997;26(5):469–78. DOI: 10.3109/10715769709084484

35.   Yamaguchi F, Ariga T, Yoshimura Y, Nakazawa H. Antioxidative and anti-glycation activity of garcinol from Garcinia indica fruit rind. J Agric Food Chem. 2000;48(2):180–5. DOI: 10.1021/jf990845y.

36.   Halliwell B. Antioxidants: The Basics-what they are and how to Evaluate them. Adv Pharmacol. 1996;38(C):3–20.

37.   Finefrock AE, Bush AI, Doraiswamy PM. Current status of metals as therapeutic targets in Alzheimer's disease. J Am Geriatr Soc. 2003 Aug;51(8):1143–8. DOI: 10.1046/j.1532-5415.2003.51368.x

Türkçe Öz ve Anahtar Kelimeler

Yeni 1-(Morfolin-4-il-Metil)-3-Alkil(Aril)-4-[4-(Dimetilamino)-Benzilidenamino]4,5-dihidro-1H-1,2,4-Triazol-5-On'ların Sentezi, Karakterizasyonu ve Antioksidan Aktiviteleri

Özlem Gürsoy-Kol[*], Haydar Yüksek, Sevda Manap, Feyzi S. Tokalı

Öz: Bu yayında sekiz adet yeni 1-(morfolin-4-il-metil)-3-alkil(aril)-4-[4-(dimetilamino)-benzilidenamino]-4,5-dihidro-1H-1,2,4-triazol-5-on'lar (**2**), 3-alkil(aril)-4-[4-(dimetilamino)-benzilidenamino]-4,5-dihidro-1H-1,2,4-triazol-5-on'ların (**1**) formaldehit ve morfolin ile tepkimesinden elde edildi. Yeni sentezlenen bileşikler IR, ^{1}H HMR ve ^{13}C NMR spektral verileri ile tanımlandı. Bunun yanında, yeni bileşikler üç farklı ölçüm türüyle *in vitro* potansiyel antioksidan kapasiteleri açısından analiz edildi. Bütün bileşiklerin metal kelatlama etkisi olarak belirgin aktiviteye sahip olduğu görüldü.

Anahtar kelimeler: 4,5-Dihidro-1*H*-1,2,4-triazol-5-on, Sentez, Mannich bazı, Antioksidan kapasitesi.

Electrorheological Properties of Biodegradable Chitosan/Expanded Perlite Composites

Mehmet Cabuk[1]*

[1]Süleyman Demirel University, 32260, Isparta, Turkey.

Abstract: In this study, chitosan (CS)/expanded perlite (EP) composites with different chitosan fractions (10%, 20% and 50%) were prepared by absorbing chitosan into porous networks of expanded perlite, as a new hybrid smart electrorheological (ER) material. Structural and morphological characterizations of the composites were carried out by FTIR and SEM-EDS techniques. Also, apparent density, particle size, and conductivity of the CS/EP composites were determined. Finally, the effects of electric field strength (E), shear rate, shear stress, and temperature onto ER behavior of the CS/EP/silicone oil (SO) system were investigated. The CS/EP/SO ER system showed reversible ER activity when subjected to E by showing shear thinning non-Newtonian viscoelastic behavior. The yield stress value reached to 1250 Pa under E = 3 kV/mm for CS/EP3 composite.

INTRODUCTION

Electrorheological (ER) fluids are composed of semiconducting or polarizable particles dispersed in a non-conducting liquid and regarded as smart materials because their flow behaviors can be tuned by externally applied *E*. These smart particles are polarized and formed fibrous structures when subjected to *E* by increasing their viscosities reversibly due to the interparticle interactions. ER fluids have been extensively studied because of their potential applications in many industrial areas such as control systems, human muscle stimulators, robotic arms, seismic controlling frame structures, and photonic crystals [1-3].

Natural polymers such as cellulose, starch, and chitosan have been widely used in ER studies. Chitosan is N-deacetylated derivative of chitin. Its structure is β-(1→4)-linked 2-amino-2-deoxy-D-glucose and 2-acetamido-2-deoxy-D-glucose. Chitosan obtained from the shells of crustaceans like crabs and shrimps. The main properties of chitosan are biodegradability, solubility in organic acids, chemical inertness, biocompatibility, low density and low cost [4]. On the other hand, its low mechanical and thermal stability is a barrier for chitosan's applications. Preparation of chitosan/clay composite is one of the attractive techniques to improve its weak features [5]. ER active properties of Chitosan/Silicone oil suspension was reported in the literature and attributed to the presence of polarizable amino polar groups onto chitosan backbone [6]. Chitosan adipate which is a chitosan derivative, was used as ER material [7].

About 70% of the world's known perlite reserves are located in Turkey. Perlite is a naturally occurring dense glassy volcanic rock which consists mainly of fused sodium, potassium, aluminum silicate (greater than 70%) and 3–5% water. When it is heated at temperatures in the range of 850–1100 °C, it expands 4–35 times of its original volume and is named as 'expanded perlite' [8]. Expanded perlite (EP) is an excellent thermal and acoustical insulator, resists fire, and is an ultralight weight material. EP is chemically inert in many environmental areas. Therefore, they are excellent filter aids and fillers in various processes and materials [9].

The benefit of using biodegradable CS/EP composites as a dispersed phase in ER applications is important both from industrial and environmental point of views. The aim of the present study was to reveal the preparation, characterization, and investigation of the ER properties of biodegradable CS/EP composites which have not hitherto been reported in the literature. The composite structures were characterized via FTIR, and SEM-EDS analyzes. Then, CS/EP dispersions were prepared in SO at 10% volume fraction and the effects of E, shear rate and temperature on ER performance of these dispersions were investigated.

MATERIALS AND METHODS

Materials

The EP particles were obtained from AKPER Company (Çankırı, Turkey). The chemical composition of the EP is given in Table 1. CS, $\overline{Mw}$ = 3.0 × 10^5 gmol^{-1} and with 82% degree of deacetylation, was purchased from Aldrich with analytical grade. SO ($\eta = 1$ Pa s, $\rho = 0.965$ g cm^{-3}, $\varepsilon = 2.61$ at 25 ºC) was obtained from Aldrich and used in ER measurements. NaOH, acetic acid (HAc) and all the other chemicals were purchased from E. Merck and used as received.

Synthesis of CS/EP composites

Before the experiments, EP samples were washed with distilled water to remove any impurities. Then the EP particles were ground milled (Retsch MM400, Germany) and vacuum dried before subjecting to particle size measurements. For the synthesis of CS/EP composites; 5 g EP was stirred in 300 mL distilled water for 2 h. Then, CS (0.5 g) was dissolved (10% (w/w) of EP) in 100 mL of 2%(w/w) HAc solution and added into the EP/water dispersion at room temperature. The white dispersion was stirred at room temperature for 4 h. And then, the reaction mixture was treated with 1 M aqueous NaOH solution by dropwise addition of NaOH to provide the precipitation of CS chains (pH=7-8). CS biopolymer is only soluble in acidic medium of pH below 6.5. Then the precipitates were washed with distilled water until the particles were neutral and dried in a vacuum oven at 60 °C for 48 h. The same method was applied for the other CS fractions (20% and 50%). Synthesized CS/EP composites containing 10, 20 and 50 wt.% of CS were obtained nearly 88% yield and coded as CS/EP1, CS/EP2 and CS/EP3, respectively. Thus, three different CS/EP composites were prepared and used in characterization and ER studies.

Table 1. Chemical composition of perlite [10].

Component	%
SiO_2	72-76
Al_2O_3	11-17
K_2O	4-5
Na_2O	3-4
CaO	0.5-2
MgO	0.1-0.5
Fe_2O_3	0.5-1.5
TiO_2	0.03-0.2
MnO_2	0.03-0.1
SO_3	0-0.2
H_2O	2-7

Characterizations

Perkin Elmer Spectrometer BX model (England) was used to record the FTIR spectra as KBr discs. The surface morphology of the samples was performed using a scanning electron microscope (SEM) with an energy-dispersive X-ray spectrometer (EDS) (SEM/EDS, XL 30S FEG, Phillips). The particle sizes of the composites were performed via a Malvern Mastersizer E, version 1.2b particle size analyzer by dispersing in distilled water and stirring at 20ºC. The samples were turned into pellets and these pellets were used for apparent density and electrical conductivity measurements. Conductivities of the samples were measured via four-probe technique and calculated with the equation of $\sigma = d/AR$, where σ is conductivity, d is the thickness, A is the surface area, and R is the resistance of the samples.

ER studies: Dispersions of the samples were prepared in SO at a constant volume fraction (φ =10% V/V). To investigate the ER properties of the suspensions, Thermo-Haake RS600 parallel plate torque Electro-Rheometer (Germany) was used with a 35 mm plate to plate geometry by altering the shear rate between 1-1000 s^{-1} and keeping the gap between the upper and lower plates as 1.0 mm. To determine the electric field viscosity, electric field was created in the fluid perpendicular to the plates, and the rotor was forced to rotate. The voltage used in the ER experiments was supplied by a 0–12.5 kV (with 0.5 kV increments) dc external electric field generator (FUG electronics, Germany) The CS/EP/SO dispersions were mechanically stirred against sedimentation before each measurement.

RESULTS AND DISCUSSION

Characterization results

Figure 1 presents the FTIR spectra of CS/EP composites (inset shows CS). CS shows distinctive peaks of typical saccharide absorptions as mentioned in the literature [11]. The broad peak at 3200–3600 cm^{-1} is attributed to O-H stretching and N–H stretching, the peak at 2900 is due to C–H stretching, the peak at 1700 cm^{-1} is due to C=O stretching; also, the broad peak at 1050 cm^{-1} is attributed to C-C stretching of saccharide structure of chitosan. EP shows typical clay peaks [9]. The peaks at 3430 cm^{-1}, 1050 cm^{-1} and 800-530 cm^{-1} are assigned to stretching vibrations of structural hydroxyl (-OH), Si–O stretching vibrations and stretching vibrations of Al–O, respectively. As shown in Figure 1, The CS/EP1, CS/EP2 and CS/EP3 composites showed all the expected characteristic peaks arising from the CS and EP structures. It is shown that there are differences in the intensities and values of peaks. It can be attributed to electrostatic interactions between the polycationic CS and negatively charged EP units.
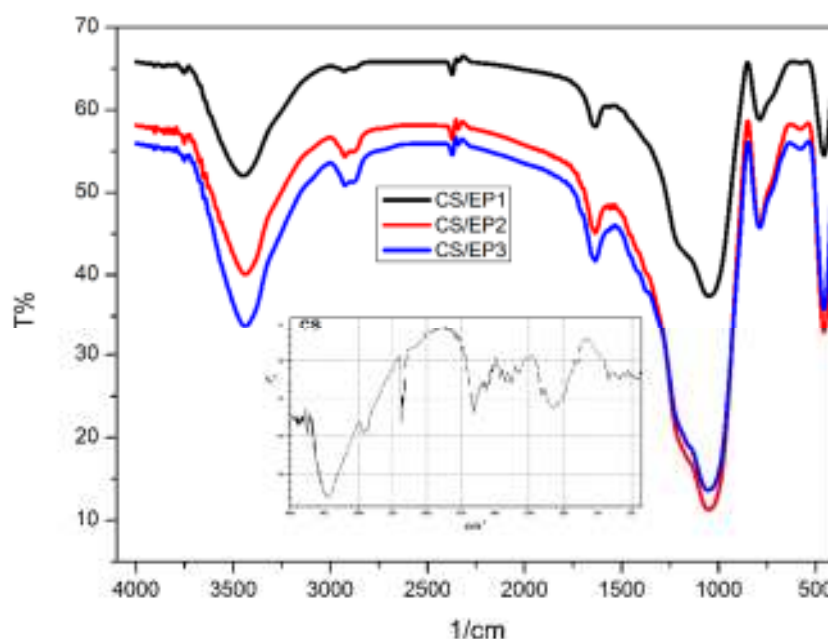
Figure 1. FTIR spectra of CS/EP composites. Inset shows CS.

Figure 2(a-c) shows the SEM-EDS images of CS/EP composites. It was observed that CS/EP composites have splintery and porous morphology. With the increasing CS percentage in the composite structure, EP particles were more surrounded by CS biopolymer and then the morphology was turned to less porous particle structure, as expected. Note that SEM shows the shape of the surfaces, while Energy Dispersive Spectroscopy (EDS) gives the composition of the surfaces. The elemental analysis data of the EDS analysis was given in

Table 2. According to EDS results, the presence of both CS and EP components in the composite structures were proved. The CS structure was characterized with N and C atoms. It was observed that the percentage of these atoms increased with increasing CS content in the composite formation. The wt.% values of N atoms in the CS/EP composites were found as 0.95%, 2.44% and 3.80% with the increasing CS content (from 10% to 20% and 50%), respectively.

Table 2. Elemental analysis values (wt.%) of the samples according to EDS results.

Samples	C	N	O	Na	Al	Si	K
CS/EP1	5.08	0.95	46.89	2.75	7.28	32.41	4.66
CS/EP2	13.65	2.44	45.71	2.36	6.32	26.13	3.42
CS/EP3	28.45	3.80	43.36	1.45	3.70	16.62	2.63
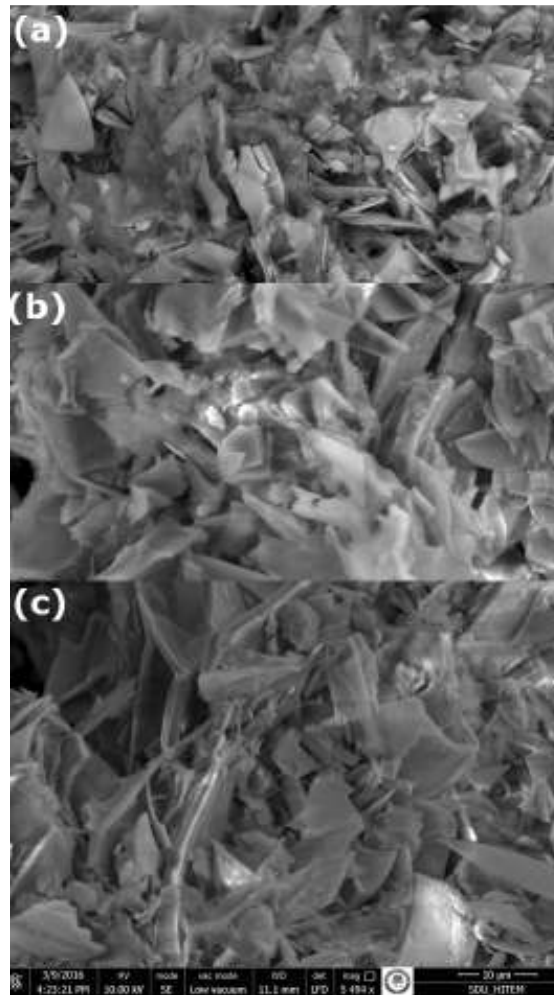
Figure 2. SEM images of a) CS/EP1, b) CS/EP2, c) CS/EP3 composites.

Hydrodynamic average particle diameters, apparent densities, and conductivities of the composites were given in Table 3. The hydrodynamic average diameters of the particles increased with increasing CS content. As expected, the hydrodynamic average particle

sizes of the composites obtained from dynamic light scattering experiments were bigger than the ones obtained from SEM images (~10 μm). Densities of the composites observed to increase with increasing CS content due to the high density of the CS (0.86 gcm^{-3}) compared with that of EP (0.44 gcm^{-3}). The conductivities of the CS/EP composites were found in semiconducting range and slightly increased with increasing CS content. These characterization results of the composites are very suitable for their potential and industrial applicability as new ER materials.

Table 3. Some physical properties of the samples (T = 25 °C).

Samples	Average hydrodynamic diameters (nm)	Electrical conductivity (σ, Scm^{-1})	Apparent density (ρ, gcm^{-3})
CS/EP1	32	2.0×10^{-4}	0.52
CS/EP2	37	2.3×10^{-4}	0.67
CS/EP3	44	2.9×10^{-4}	0.80

ER results: The ER properties are attributed to the chaining of micron-sized polarizable particles with applied E, electro-rheometer studies are conducted to observe the electric field induced viscosity change and ER behaviors of CS/EP composite dispersions, and results obtained are discussed below.

ER efficiencies of the CS/EP/SO fluids

The dependence of the viscosity on the E was given in Figure 3. As shown that the viscosity of all the CS/EP composites increased with applied E, which confirms that the ER fluids are solid-like under E. It is known that CS is responsible component for the CS/EP composites to show ER effect. The viscosity values were observed to increase with rising CS content which has polarizable amino groups in the composite structure. CS enhances the particle polarization by increasing the particle surface conductivity of CS/EP composites via enhanced interfacial polarization and the attractive interactions of particles, which would lead to the enhanced ER response. ER efficiencies of the samples as a function of the composite composition were determined using eq. (1):

$$ER_{efficiency} = \frac{\eta_{E \neq 0} - \eta_{E=0}}{\eta_{E=0}} \qquad (1)$$

where $\eta_{E=0}$ and $\eta_{E\neq0}$ show the non-electric field- and electric field- induced viscosities of the dispersions, respectively. ER efficiencies of the samples were calculated from Figure 3 under constant conditions (φ=10%, E=0-3kV/mm) and results were found as follows: 0.11< 0.21<0.26 for CS/EP1, CS/EP2 and CS/EP3 composites, respectively. As shown, the highest ER efficiency was determined for CS/EP3/SO composite dispersion which has the

highest CS content and that is why, for the rest of the ER experiments, CS/EP3/SO ER fluid was used.
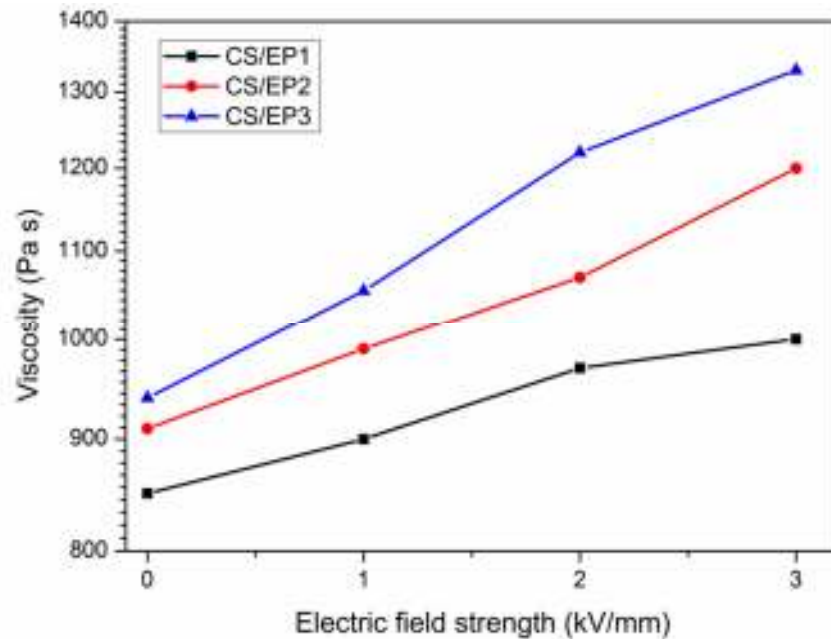
Figure 3. The effect of E on viscosity. $\varphi = 10\%$, T = 25 ºC.

Effect of shear rate on viscosity

The change of viscosity with shear rate was presented in Figure 4. Electric field induced viscosity of CS/EP3/SO ER fluid sharply decreased with increasing shear rate and showed a typical shear thinning non-Newtonian viscoelastic behavior. This behavior may be attributed to the distortion and breakage of fibrillar structures between the perlite particles. Similar behavior was reported for chitosan phosphate suspensions [12].
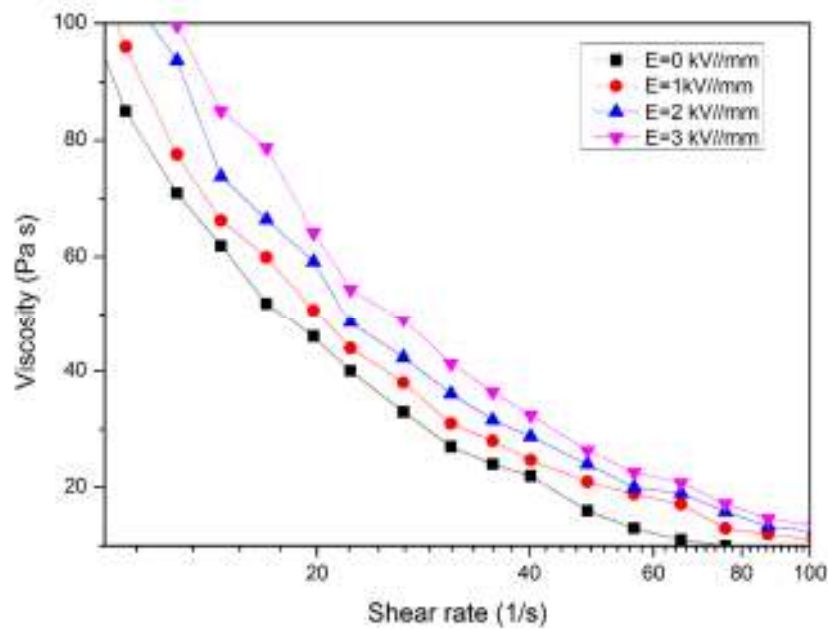
Figure 4. Change in viscosity with shear rate. φ = 10%, T = 25 ºC.

Effect of shear rate on shear stress

Figure 5 shows the change of shear stress with shear rate. It was observed that shear stress increased with rising shear rate and with the applied *E*, the ER fluid showed typical non-Newtonian Bingham-like flow behavior. Under an applied *E*, the curves of the samples first showed yield stresses and then wide plateau regions [13] which may be attributed to the polarization mechanism of the EP particles.
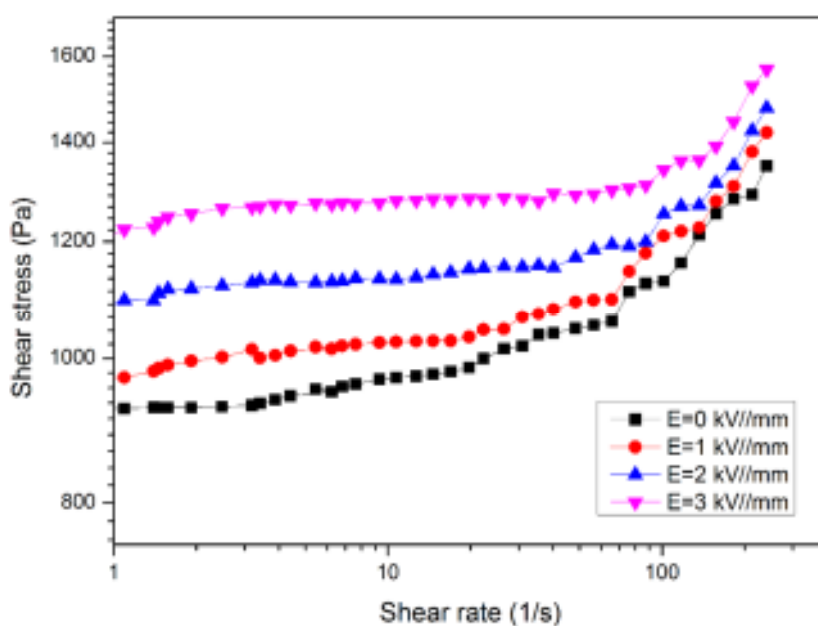
Figure 5. Change in shear stress with shear rate. φ = 10%, T = 25 ºC.

Yield stress (τ_y) values of the composites were obtained from the initial slops of the shear rate-shear stress graphs [14]. The yield stress values of the CS/EP3/SO ER fluid were observed to increase with rising E and the results obtained are as following: τ_y=1250 Pa (E = 3 kV/mm)> τ_y=1100 Pa (E = 2 kV/mm)> τ_y=980 Pa (E = 1 kV/mm)> τ_y=920 Pa (E = 0 kV/mm). It can be attributed to the formations of stronger solid-like fibrous structures between the electrodes with the influence of dipole-dipole interactions of the semiconducting particles.

Effect of temperature on shear stress

To test whether the CS/EP3 composite shows ER weakening or loss of power between 30-80 °C, shear stress measurements were carried out under E=3 kV/mm (Figure 6). As shown, slight shear stress increments were observed with increasing temperature. The increasing temperature can be caused to the increase of polarization forces between the particles due to the increasing current density, dielectric constant and conductivity with rising temperature. Thus, the increasing polarization forces cause a stronger fibrous structure and the ER effect increases. On the other hand, the viscosity of the SO media decreases with the temperature and this may also be caused the fibrous chain formation relatively easy and thus leads to improved ER performance [15, 16].
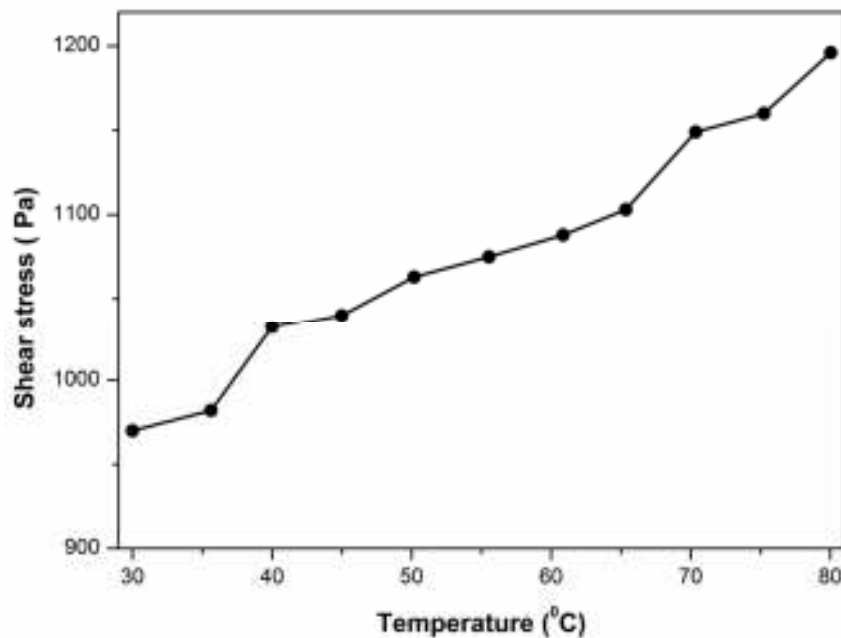
Figure 6. Change in shear stress with temperature. φ = 10%, E=3 kV/mm, $\dot{\gamma}$ = 0.2 s^{1-}.

CONCLUSION

Biodegradable CS/EP composites with different CS fractions were successfully prepared and their structures and morphologies were confirmed by FTIR and SEM-EDS analyses. Conductivities of the composites were found in semiconducting range which is suitable for ER measurements. The CS/EP/SO system were observed to sensitive to external E by showing reversible viscosity enhancements. ER efficiencies and yield stresses of the ER fluids increased with increasing CS content having polar amino groups. Shear stress values of the ER fluids were slightly affected with temperature.

ACKNOWLEDGMENTS

REFERENCES

[1] Lin, KF, Hsu CY, Huang TS, Chiu WY, Lee YH, Young TH. A novel method to prepare chitosan/montmorillonite nanocomposites. Journal of Applied Polymer Science. 2005 SEP; 98: 2042-47. DOI: DOI: 10.1002/app.22401.

[2] Zhang WL, Liu YD, Choi HJ, Kim SG. Electrorheology of Graphene Oxide. ACS Appl. Mater. Inter. 2012 APR; 4: 2267-72. DOI: 10.1021/am300267f.

[3] Cabuk M, Yavuz M, Unal HI. Colloidal, electrorheological, and viscoelastic properties of polypyrrole-graft-chitosan biodegradable copolymer. *J. Intel. Mat. Syst. Str.* 2015 MAR; 26: 1799-810. DOI: 0.1177/1045389X15577652.

[4] Kittur FS, Prashanth KVH, Sankar KU, Tharanathan RN. Characterization of chitin, chitosan and their carboxymethyl derivatives by differential scanning calorimetry. Carbohydrate Polymers. 2002 APR; 49: 185-93. DOI: doi:10.1016/S0144-8617(01)00320-4.

[5] Hong CH, Sung JH, Choi HJ. Effects of medium oil on electroresponsive characteristics of chitosan suspensions. Colloid and Polymer Science. 2009 MAY; 287: 583-89. DOI: 10.1007/s00396-009-2006-3.

[6] Jang WH, Cho YH, Kim JW, Choi HJ, Sohn JI, Jhon MS. Electrorheological fluids based on chitosan particles. Journal of Material Science Letters. 2001; 20: 1029-31. DOI: 10.1023/A:1010960424567.

[7] Choi US, Park YS. Electrorheological behavior of chitosan adipicate suspension as anhydrous ER fluid. Journal of Industrial and Engineering Chemistry. 2001 JUL; 7: 281-4. DOI:10.1016/j.polymer.2005.10.133.

[8] Dogan M, Alkan M. Removal of methyl violet from aqueous solution by perlite. J. Colloid Interface Sci. 2003 OCT; 267: 32–41. DOI: doi:10.1016/S0021-9797(03)00579-4.

[9] Dogan M, Alkan M. Some physicochemical properties of perlite as a adsorbent, Fresenius Environ. Bull. 2004 JAN; 13: 251–7.

[10] Alkan M, Dogan M. Surface titrations of perlite suspensions, J. Colloid Interface Sci. 1998 APR; 207: 90–6. DOI: 10.1006/jcis.1998.5694.

[11] Tiwari A, Sen V. Dhakate SR, Mishra AP, Singh V. Synthesis, characterization, and hoping transport properties of HCl doped conducting biopolymer-*co*-polyaniline zwitterion hybrids. Polym. Advan. Technol. 2008 MAR; 19: 909-14. DOI: 10.1002/pat.1058.

[12] Li H, Yunling J, Shuzhen M, Fuhui L. Synthesis and electrorheological property of chitosan phosphate and its rare earth complex. Journal of Rare Earths. 2007 JUN; 25: 15-9. DOI: 10.1016/S1002-0721(07)60514-6.

[13] Marins, JA, Giulieri F, Soares BG, Bossis G. Hybrid polyaniline-coated sepiolite nanofibers for electrorheological fluid applications. Synth. Met. 2013 DEC; 185: 9-16. DOI: 10.1016/j.synthmet.2013.09.037.

[14] Cho MS, Choi HJ, Jhon MS. Shear stress analysis of a semiconducting polymer based electrorheological fluid system. Polymer. 2005; 46: 11484–8. DOI: 10.1016/j.polymer.2005.10.029.

[15] Cabuk M, Yavuz M, Unal HI, Erol O. Synthesis, characterization and investigation of electrorheological properties of biodegradable chitosan/bentonite nanocomposites. Clay Minerals. 2013 MAR; 48; 129-41. DOI: 10.1180/claymin.2013.048.4.09.

[16] Koyuncu K, Unal HI, Gumus OY, Erol O, Sari B, Ergin T. Electrokinetic and electrorheological properties of poly(vinyl chloride)/polyindole conducting composites, Polym. Advanc. Technol. 2011 OCT; 23: 1464-72. DOI: 10.1002/pat.2068.

Türkçe Öz ve Anahtar Kelimeler

Biyobozunur Kitosan/Genleşmiş Perlit Kompozitlerinin Elektroreolojik Özellikleri

Öz: Bu çalışmada, kitosan (CS)/genleşmiş perlit (EP) kompozitleri farklı kitosan oranlarına (%10, %20 ve %50) göre yeni bir hibrid akıllı elektroreolojik (ER) malzeme olarak, genleşmiş perlitin gözenekli ağ sistemi içine kitosanın adsorplanması ile hazırlandı. Kompozitlerin yapısal ve morfolojik karakterizasyonları FTIR ve SEM-EDS teknikleri ile gerçekleştirildi. Bunun dışında, CS/EP kompozitlerin görünür yoğunluğu, tanecik boyutu ve iletkenlikleri belirlendi. Son olarak, CS/EP/Silikon yağı (SO) sisteminin ER davranışı üzerine elektrik alan kuvveti (E), kayma hızı, kayma gerilimi ve sıcaklığın etkileri incelendi. CS/EP/SO ER sistemi E'ye maruz bırakıldığında kayma incelmesi türünden Newtoniyen olmayan viskoelastik davranış göstererek tersinir ER aktivite göstermiştir. CS/EP3 kompozitinin akma gerilimi değeri, E = 3 kV/mm'de 1250 Pa değerine ulaşmıştır.

Anahtar kelimeler: Elektroreolojik akışkanlar, genleşmiş perlit, kitosan, kompozit, silikon yağı, akma gerilimi.

Sunulma: 1 Temmuz 2016, **Düzeltme:** 15 Ağustos 2016, **Kabul:** 22 Ağustos 2016.

RESEARCH ARTICLE

Extraction and Characterization of Chitin and Chitosan from Blue Crab and Synthesis of Chitosan Cryogel Scaffolds

Didem Demir[1], Fatma Öfkeli[1], Seda Ceylan[1,2], Nimet Bölgen Karagülle[1,*]

[1]Mersin University, Engineering Faculty, Chemical Engineering Department, 33343, Mersin, Turkey

[2]Adana Science and Technology University, Bioengineering Department, Adana, Turkey

Abstract: Polymeric scaffolds produced by cryogelation technique have attracted increasing attention for tissue engineering applications. Cryogelation is a technique which enables to produce interconnected porous matrices from the frozen reaction mixtures of polymers or monomeric precursors. Chitosan is a biocompatible, biodegradable, nontoxic, antibacterial, antioxidant, and antifungal natural polymer that is obtained by deacetylation of chitin, which is mostly found in the exoskeleton of many crustaceans. In this study, chitin was chemically isolated from the exoskeleton of blue crab (*Callinectes sapidus*). *Callinectes sapidus* samples were collected from a market, as a waste material after it has been consumed as food. Demineralization, deproteinization, and decolorization steps were applied to the samples to obtain chitin. Chitosan was prepared from isolated chitin by deacetylation at high temperatures. The chemical composition of crab shell, extracted chitin and chitosan were characterized with FTIR analysis. Moreover, in order to determine the physicochemical and functional properties of the produced chitosan, solubility, water uptake, and oil uptake analysis were performed. Chitosan cryogel scaffolds were prepared by crosslinking reaction at cryogenic conditions at constant amount of chitosan (1%, w/v) with different ratios of glutaraldehyde (1, 3, and 6%, v/v) as crosslinker. The chemical structure of the scaffolds were examined by FTIR. Also, the water uptake capacity of scaffolds have been determined. Collectively, the results suggested that the characterized chitosan cryogels can be potential scaffolds to be used in tissue engineering applications.

INTRODUCTION

Tissue engineering is one of the topics in biomedical engineering that can provide many alternatives for the repair of damaged tissues [1]. By applying the principles of tissue engineering, characteristic properties of the original tissues can be mimicked by scaffolds. An ideal scaffold should be biocompatible, biodegradable and does not induce an immune reaction or inflammation. These scaffolds can be obtained from natural or synthetic polymers [2-5].

Chitin is a a naturally abundant mucopolysaccharide which can be obtained from crab shells [6,7]. It is a nitrogenous polysaccharide that is white, rigid, with inelastic structure. Chitin contains 2-acetamido-2-deoxy-b-D-glucose groups by (1→4) linkage which named as *N*-acetylglucosamine [7, 8]. After the cellulose, chitin is the second most abundant biopolymer over the world. Invertebrates, insects, marine diatoms, algae, fungi and crustaceans like crabs, shrimps, and lobsters are the source of chitin [9].

Chitosan is one of the chitin derivatived products that can be obtained by N-deacetylation [6,10]. Moreover, it has also biological properties including biocompatibility, biodegradability and non-toxicity for living cells [10].

Blue crab, called *Callinectes sapidus,* contains chitin in its shell, lives in North America, Mersin-Silifke area lagoons, İskenderun coasts and Adana-Yumurtalık lagoon in Turkey [11].

In this study, we aimed to extract chitin from shells of blue crab and produce chitosan from extracted chitin by deacetylation at high temperatures. The chemical compositon of extracted chitin and chitosan were characterized by FTIR analyses. In addition to this, solubility, water uptake and oil uptake analysis were performed to determine the physicochemical and functional properties of the produced chitosan. Chitosan-based cyrogels were produced by using gluteraldehyde as a crosslinking agent. Characteristic properties of the produced cryogels were demonstrated in order to be used in tissue engineering applications.

MATERIALS AND METHODS

Materials

Blue crab (*Callinectes sapidus*) shell wastes were collected from a local market in Mersin, Turkey after it has been consumed as food. The samples were transferred to the laboratory as soon as possible and stored in a freezer at -16˚C, until starting the extraction procedure. Hydrochloric acid was obtained from Merck, Germany, sodium hydroxide and acetone were purchased from Emir Kimya, Turkey for use in experimental steps of extracting chitin and chitosan. Glutaraldeyde (GA) solution 25% in water as a crosslinking agent and 100% (v/v) glacial acetic acid as a solvent were both obtained from Merck for the preparation of cryogel scaffolds.

Chitin and chitosan extraction from crab shells

Extraction of chitin from crab shells: Crab shells were washed several times with distilled water and then dried at 40 °C in an oven. Dried shells were powdered by a grinder. First step of extraction of chitin was demineralization. 40 g of powdered sample was treated with 2 M HCl solution for 24 h at 80 °C to remove all minerals from the sample. The second step of extraction was deproteinization in which the sample was treated in 2 M NaOH solution at 110 ºC for 20 h at a solid to solution ratio of 1:10 (w/v) to remove all proteins of the sample. After deproteinization, sample was treated with acetone for decolorization of extracted chitin. Chitin was obtained after applying these three steps respectively. At the end of each step, the sample was filtered, washed several times with distilled water, and dried in an oven at 40 °C.

Production of chitosan from extracted chitin

Extracted chitin was treated with 50% concentrated NaOH (w/v) solution at 150 °C for 4 h at a solid to solution ratio of 1:10 (w/v) to remove the acetyl groups of chitin. This process is called as deacetylation. After deacetylation, the sample was filtered and washed several times with distilled water until pH was neutral. The obtained chitosan was then dried before using for production of chitosan cryogel scaffolds. Schematic illustration of extraction steps of chitin and production of chitosan is demonstrated in Figure 1.
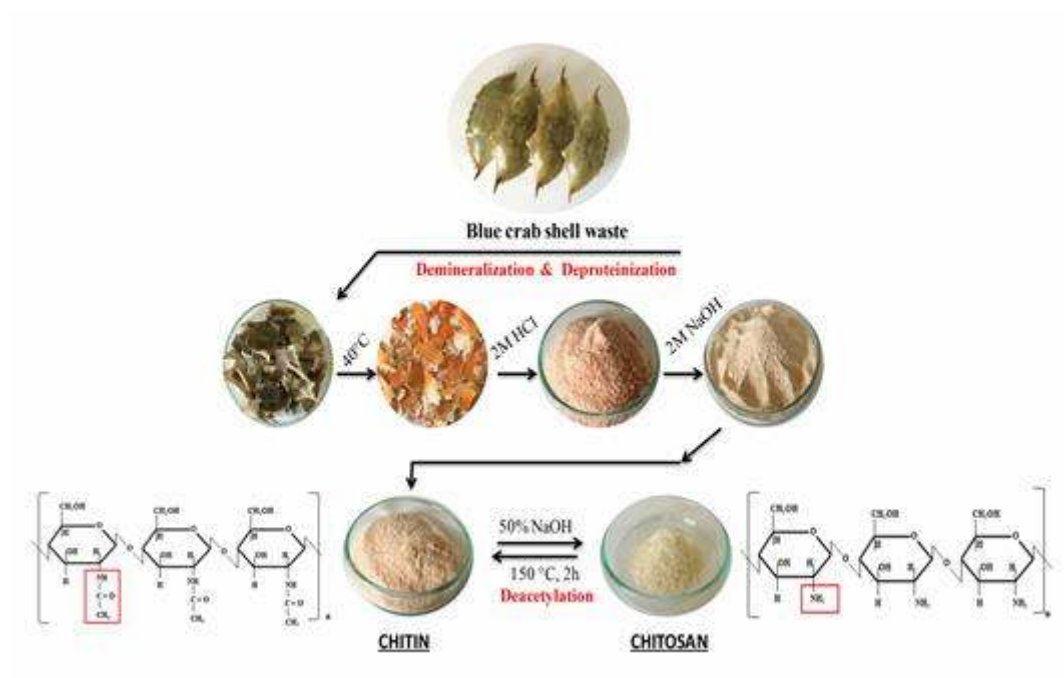
Figure 1. Schematic illustration of extraction steps of chitin and production of chitosan.

Production of chitosan cryogels

The chitosan cryogels were synthesized at three different concentrations of GA. 2 mL of chitosan solution was prepared in (6%, v/v) acetic acid solution and mixed until the solution was homogenous and clear. 1 mL of GA solution (1, 3 and 6%, v/v) was poured to the prepared chitosan solutions. The polymer and crosslinker mixture was immediately poured into a plastic syringe and placed into the cryostat. The mixture was incubated in the cryostat at -16 °C for 2 h and stored in the freezer at the same temperature for 24 h. The reaction mixture was thawed to room temperature and the formed blocks were washed in distilled water until the unreacted polymer and crosslinker was removed.

Characterization of chitin and chitosan

Yield of chitin and chitosan: The percantage of the yield of chitin was calculated by dividing the weight of extracted chitin to initial dry crab shell weight and the percentage of the yield of chitosan was calculated by dividing the weight of produced chitosan to dry chitin weight before deacetylation. Yields were calculated as follows:

$$\text{Yield of chitin (\%)} = [\text{Extracted chitin (g)/Crab shells (g)}] \times 100 \qquad \text{(Eq. 1)}$$

$$\text{Yield of chitosan (\%)} = [\text{Produced chitosan (g)/Chitin (g)}] \times 100 \qquad \text{(Eq. 2)}$$

FTIR analysis of chitin and chitosan

The infrared spectral analysis of the crab shell, extracted chitin, and produced chitosan samples was measured by Fourier Transform Infrared Spectrometry, FTIR (Frontier Spectrometer, Perkin Elmer, USA) in the wavelength range of 450 - 4000 cm^{-1} at a resolution of 4 cm^{-1}.

Solubility

10 mL of 1% acetic acid solution was put in a centrifuge tube containing 0.1 g of produced chitosan. The sample was centrifuged at 10,000 rpm for 30 min. After the supernatant was poured away, the undissolved part of chitosan was washed with 25 mL of distilled water and then centrifuged at 6,000 rpm. The supernatant liquid was poured away and the undissolved solid was dried at 60 °C for 24 h in an oven. Lastly, the amount of the dried solid was weighed and the percentage of solubility was determined [12].

Water uptake capacity (WUC)

10 mL of distilled water was put in a centrifuge tube containing 0.5 g of produced chitosan. The sample was mixed on a vortex about 5 min until the sample was dispersed. Then, the dispersed sample was vortexed for 5 s every 10 min (for a total of 30 min) and centrifuged at 3500 rpm for 30 min. After centrifugation, supernatant was poured off and the sample was weighed. WUC was calculated as follows [12]:

$$WUC\ (\%) = [Bound\ water\ (g)/Initial\ chitosan\ weight\ (g)] \times 100 \qquad (Eq.\ 3)$$

Oil uptake capacity (OUC)

10 mL of sunflower oil was put in a centrifuge tube containing 0.5 g of produced chitosan. The sample was mixed on a vortex about 5 min until the sample was dispersed. Then, the dispersed sample was vortexed for 5 s every 10 min (for a total of 30 min) and centrifuged at 3500 rpm for 30 min. After centrifugation, supernatant was poured away and the sample was weighed. OUC was calculated as follows [12]:

$$OUC\ (\%) = [Bound\ oil\ (g)/Initial\ chitosan\ weight\ (g)] \times 100 \qquad (Eq.\ 4)$$

Characterization of Chitosan Cryogels

FTIR analysis of cryogels: Chemical surface analysis of the produced chitosan cryogels was performed by Fourier Transform Infrared Spectrometry, FTIR (Perkin Elmer, FT-IR/FIR/NIR Spectrometer Frontier, ATR, USA) with the range of 450 - 4000 cm^{-1} at a resolution of 4 cm^{-1}.

Water uptake capacity: Water uptake capacity of chitosan cryogels was measured by a gravimetric analysis. The chitosan cryogels of about 50 mg weight (the surface bound water was removed by filter paper) were incubated in 10 mL of distilled water at room temperature. After specified time intervals (5, 15 30, 60 and 90 min) the wet weight of cryogels was determined and the water uptake capacity calculated according to the following equation:

$$WUC\ (\%) = [(Ws - W_w)\ /\ Ww]*100 \qquad (Eq.\ 5)$$

Where WUC is water uptake capacity, Ws is weight of cryogel and Wd is weight of swollen cryogel.

RESULTS AND DISCUSSION

Chitin extraction and chitosan production

Yield of extracted chitin and produced chitosan: The yields have been calculated for extracted chitin and produced chitosan. The yield of chitin extraction from dry crab shells was 11.73%. The yield of chitosan produced from extracted chitin was 77.78%, which was similar to the results that was reported in the literature by Kaya *et al.* (76% yield of chitosan from *Callinectes sapidus* from İskenderun, Turkey) and Odote *et al.* (74.6% yield of chitosan of *Sylla cerrata* from Mombasa, Kenya) [13, 14]. The yields were above average in these studies and our study indicated that crabs are one of the major resources of chitin and chitosan among the other crustacean group of organisms.

FTIR spectra of chitin and chitosan

Figure 2 demonstrates the FTIR spectra of the crab shell, chitin, and chitosan. The FTIR spectra shows the characteristic bands of $-NH_2$ at 3447 cm^{-1} and carbonyl group band at 1477 cm^{-1} [15]. The band at 3448 cm^{-1} could be assigned to (N-H), (O-H) and (NH_2) groups. The band at 3267 cm^{-1} is associated with (N-H) in secondary amides only with trans-configuration and usually is due to the formation of linear associates [16]. Additionally, the lower intensity

band at 3110 cm^{-1} confirmed trans-configuration of NH-CO group in chitin. The presence of methine group in pyranose ring and methyl group in methylene group was proved by the corresponding stretching vibrations of these groups in the range of 2892-2961 cm^{-1} [17]. The only one intense peak at 626 cm^{-1} indicate crystalline state of chitin [18]. Furthermore, the spectra of the samples indicated the presence of two bands, one at 1626 cm^{-1} and another at 1657 cm^{-1}, probably indicating an amorphous state. The peak at 1626 cm^{-1} could be based on to the stretching of C–N vibration, linked to OH group by bonding [19,20]. The characteristic bands for chitosan can be observed in Figure 2. The spectra showing the amine peak at 2923.88 cm^{-1} indicates the presence of CH stretch and the peak at 3400 cm^{-1} indicates symmetric stretching vibration of OH. In addition to this, the peak at 1650.95 cm^{-1} was due to C=O stretching (amide I) the peaks at 1095.49 cm^{-1} and 1033.77 cm^{-1} show C-O stretching [15]. The wavelength at 894.91 cm^{-1} represent a ring stretching, a characteristic bond for β-1-4 glycosidic linkage.
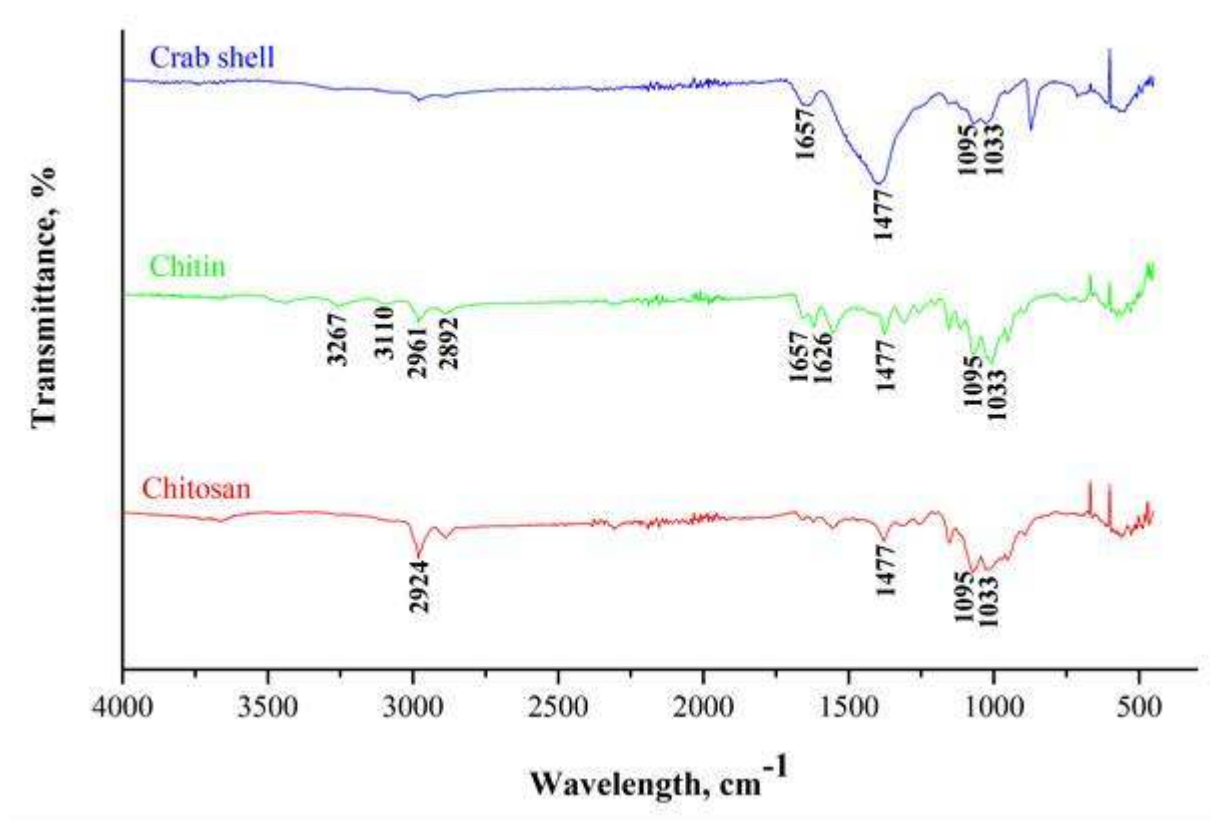
Figure 2. FTIR spectrum of crab shell, extracted chitin and produced chitosan.

137

Solubility

Chitosan had an excellent solubility of 99.29% ± 0.001 in 1% acetic acid solution. The high solubility of produced chitosan was due to the process conditions in deacetylation step. The temperature was 150 °C, period of deacetylation was 2 h, and alkaline concentration was 50% NaOH. The high solubility of chitosan in acetic acid indicates that the deacetylation degree is at least 85% [21].

Water uptake capacity

Water uptake capacity of produced chitosan was 582.59% ± 58.67. The chitosan showed similar WUC compared with the results of Özbay *et al.* (650.51% ±18.55 WUC, blue crab) [22].

Oil uptake capacity

Oil uptake capacity of produced chitosan was 372.21% ± 9.29. The percentage OUC of chitosan is in agreement with the result (437.82 % ± 21.48 OUC, blue crab) reported by Özbay *et al.* [22].

Production of chitosan cryogels

Cryogelation process: The concentration of GA as a crosslinking agent was varied in this study. The concentration of GA affects the chemical, physical, mechanical, morphological, and porous structure of cryogels. Cryogelation technique was used in the synthesis of chitosan cryogels. Figure 3 shows the image of GA crosslinked chitosan cryogels after cryogelation reaction is completed (Figure 3A) and behavior of cryogels before, under, and after force (Figure 3B). The chitosan cryogels showed a yellowish color with increasing the GA ratio, which can be due to the double bonds resulting after GA crosslinking [23]. Chitosan cryogels which were crosslinked with 1% and 3% GA did not show a significant deformation after applying force. However, although the cryogels prepared with 6% GA were elastic, when the applied force was increased they were deformed.
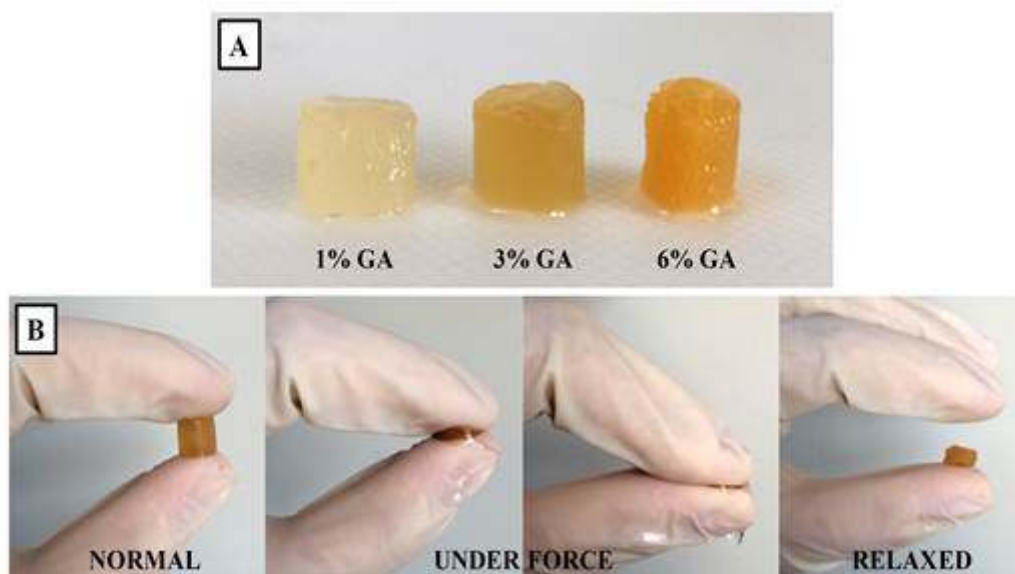
Figure 3. The image of prepared chitosan cryogels: (A) cryogels after cryogelation reaction is completed, (B) behavior of cryogels (crosslinked with 3% GA) before, under, and after applying force.

FTIR spectra of cryogels

Figure 4 demonstrates the FTIR spectra of crosslinked cyrogels with GA (1, 3, and 6%, v/v). As a result of the imine bonds N=C, the crosslinking of the scaffolds with GA shows the main absorption peak at 1646 cm^{-1} [24]. Shoulders at 1587 cm^{-1} appeared due to the ethylenic bonds [24, 25]. Increasing gluteraldehyde (crosslinker) concentration, caused increase in the intensity of ethylenic bond frequency at 1562 cm^{-1}. For the C-H stretching vibration frequency at 2936 cm^{-1} was observed. In addition, the peak at 1100 cm^{-1} demonstrated the aliphatic amino groups [25,26].

Water uptake capacity

WUC is releated with the highly porous and spongy structure of the cryogels. The WUC results of the synthesized cryogels are demonstrated in Figure 5. WUC of all chitosan cryogels was higher than 120% in the first 15 min. It was observed that the WUC of cryogels decreased as the concentration of crosslinker (GA) increased. Mirzaei *et al.* reported a similar trend related to the effect of different glutaraldehyde concentrations on the swelling behavior of freeze-dried chitosan hydrogels [25]. Cryogels crosslinked with 1% GA showed the highest WUC (514.51% ± 31.91) compared to the ones prepared with 3% and 6% GA which showed a WUC of 257.14% ± 29.28 and 154.18% ± 24.17, respectively.
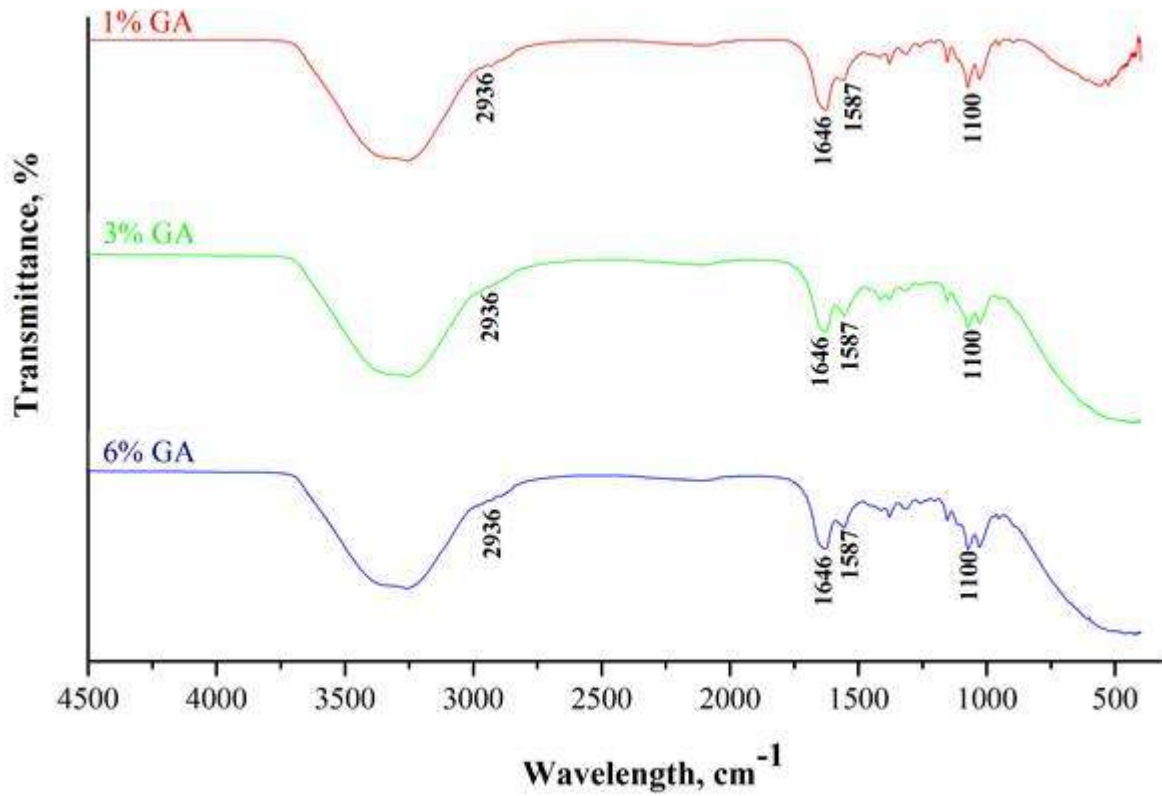
Figure 4. FTIR spectrum of synthesized chitosan cryogels.
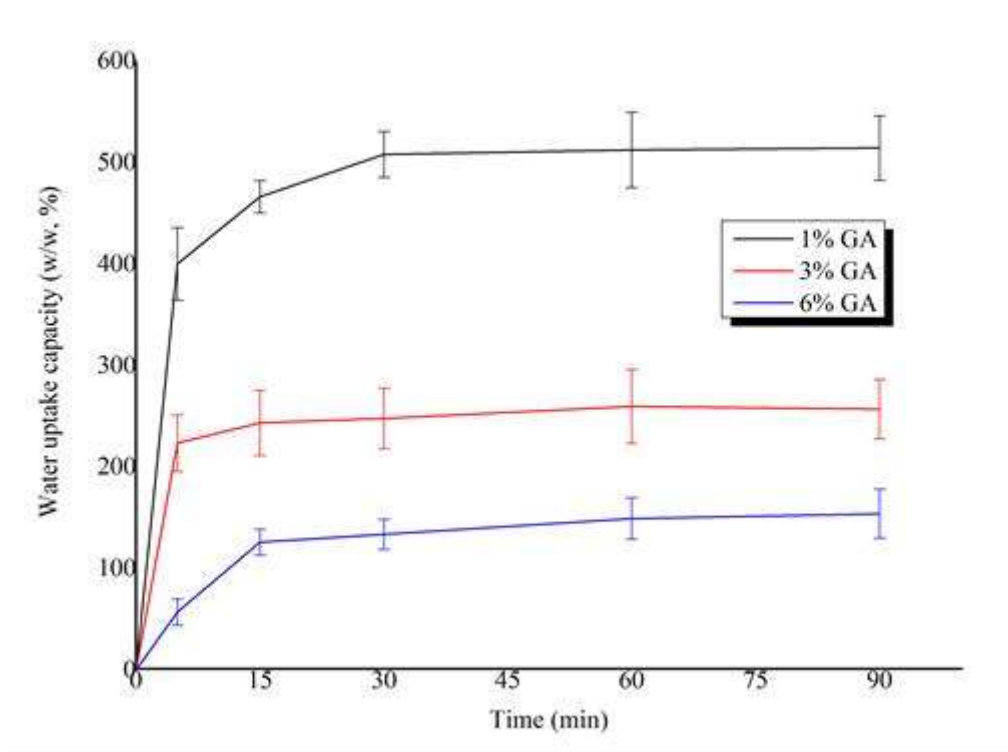
Figure 5. Water uptake profiles of the synthesized cryogels.

CONCLUSION

Chitin was extracted from the waste of blue crab shells (*Callinectes sapidus*) and chitosan was produced from extracted chitin by deacetylation. The chemical composition of crab shell, extracted chitin, and chitosan were characterized with FTIR. In addition to this, physicochemical properties of obtained chitosan was determined by solubility, water uptake and oil uptake capacity analysis. According to these results, obtained chitosan can be used as a biomaterial in tissue enginnering applications. For this purpose, chitosan scaffolds were synthesized by cryogelation technique and characterized by FTIR and water uptake capacity tests. Increasing the crosslinker (GA) concentration affected the properties of cryogels. The cryogel scaffolds were mechanicaly stable and had water uptake ability. The cryogels synthesized in this study have potential to be used as tissue engineering scaffolds in biomedical applications.

CONFLICT OF INTEREST

The authors declare that no conflict of interests exist in relation to the writing of this article.

REFERENCES

1. Yang S, Leong KF, Du Z, Chua CK. The design of scaffolds for use in tissue engineering. Part I. Traditional factors. Tissue Engineering. 2001 Dec;7(6):679-89. DOI: 10.1089/107632701753337645.

2. Eisenbarth E. Biomaterials for tissue engineering. Advanced Engineering Materials. 2007 Dec;9(12):1051-60. DOI: 10.1002/adem.200700287.

3. Kim BS, Baez CE, Atala A. Biomaterials for tissue engineering. World Journal of Urology. 2000 Feb;18(1):2-9. http://www.ncbi.nlm.nih.gov/pubmed/10766037.

4. Ma Z, Kotaki M, Inai R, Ramakrishna S. Potential of nanofiber matrix as tissue-engineering scaffolds. Tissue Engineering. 2005 Feb;11(1-2):101-9. DOI: 10.1089/ten.2005.11.101.

5. Gualandi C. Porous polymeric bioresorbable scaffolds for tissue engineering. Doctoral Thesis University of Bologna, Italy. 2011. DOI: 10.1007/978-3-642-19272-2.

6. Dutta PK, Dutta J, Tripathi VS. Chitin and chitosan: Chemistry, properties and applications. Journal of Scientific and Industrial Research. 2004 Jan;63:20-31. http://nopr.niscair.res.in/bitstream/123456789/5397/1/JSIR%2063(1)%2020-31.pdf.

7. Majeti NV, Kumar R. A review of chitin and chitosan applications. Reactive and functional polymers. 2000 Nov;46(1):1-27. DOI: 10.1016/S1381-5148(00)00038-9.

8. Bolat Y, Bilgin Ş, Günlü A, Izci L, Bahadır Koca S, Çetinkaya S, Koca HU. Chitin-chitosan yield of freshwater crab (Potamon potamios, Olivier 1804) shell. Pakistan Veterinary Journal. 2010; 30 (4);227-31. http://www.pvj.com.pk/abstract/30_4/9.htm.

9. Kumari S, Rath PK. Extraction and characterization of chitin and chitosan from (Labeo rohit) fish scales. Procedia Materials Science. 2014;6:482-9. DOI:10.1016/j.mspro.2014.07.062.

10. Lertsutthiwong P, HOW NC, Suwalee C, Stevens WF. Effect of chemical treatment on the characteristics of shrimp chitosan. Journal of Metals, Materials and Minerals. 2002 Jan;12(1):11-8. http://www.material.chula.ac.th/Journal/V12-1/11-18%20LERTSUTTHIWONG.pdf

11. Türeli C, Celik M, Unal E. Comparison of meat composition and yield of blue crab (Callinectes sapidus RATHBUN, 1896) and sand crab (Portunus pelagicus LINNE, 1758) caught in İskenderun Bay, North-East Mediterranean. Turkish Journal of Veterinary and Animal Sciences. 2000 May;24(3):195-03. http://dergipark.ulakbim.gov.tr/tbtkveterinary/article/view/5000032294.

12. Nessa F, Masum SM, Asaduzzaman M, Roya SK, Hossain MM, Jahan MS. A process for the preparation of chitin and chitosan from prawn shell waste. Bangladesh Journal of Scientific and Industrial Research. 2010;45(4):323-30. DOI: 10.3329/bjsir.v45i4.7330.

13. Kaya M, Dudakli F, Asan Ozusaglam M, Cakmak YS, Baran T, Mentes A, Erdogan S. Porous and nanofiber a-chitosan obtained from blue crab (Callinectes sapidus) tested for antimicrobial and antioxidant activities. LWT - Food Science and Technology. 2016 Jan;65:1109-17. DOI: 10.1016/j.lwt.2015.10.001.

14. Oduor-Odote PM, Struszczyk MH, Peter MG, Characterisation of chitosan from blowfly larvae and some crustacean species from kenyan marine waters prepared under different conditions. Western Indian Ocean Journal of Marine Science. 2005;4(1):99-107. DOI: 10.4314/wiojms.v4i1.28478.

15. Wanule D, Balkhande JV, Ratnakar PU, Kulkarni AN, Bhowate CS. Extraction and FTIR analysis of chitosan from American cockroach, Periplaneta americana. International Journal of Engineering Science and Innovative Technology. 2014 May;3(3):299-04. http://www.ijesit.com/Volume%203/Issue%203/IJESIT201403_39.pdf.

16. Zhang Y, Xue C, Xue Y, Gao R, Zhang X. Determination of the degree of deacetylation of chitin and chitosan by X-ray powder diffraction. Carbohydrate Research. 2012 Aug;340(11):85-9. DOI:10.1016/j.carres.2005.05.005.

17. Zvezdova D. Investigation of some physicochemical properties of chitin from crab shells. Proceedings of University of Ruse, 2010;36-40. http://conf.uni-ruse.bg/bg/docs/cp10/9.1/9.1-6.pdf.

18. Abdulwadud A, Muhammed TI, Surajudeen A. Abubakar JM, Alewo OA. Extraction and characterisation of chitin and chitosan from mussel shell. Civil and Environmental Research. 2013;3(2):108-14. http://www.iiste.org/Journals/index.php/CER/article/view/4237.

19. Rinaudo M. Chitin and chitosan: properties and applications. Progress in Polymer Science. 2006 July;31(7):603-32. DOI:10.1016/j.progpolymsci.2006.06.001.

20. Brugnerotto J, Lizardi J, Goycoole FM, Argüelles-Monal J, Desbrières J, Rinaudo M. An infrared investigation in relation with chitin and chitosan characterization. Polymer. 2001 Apr;42:3569-80. DOI:10.1016/S0032-3861(00)00713-8.

21. Hossain MS, Iqbal A. Production and characterization of chitosan from shrimp waste. Journal of the Bangladesh Agricultural University. 2014;12(1):153-60. http://ageconsearch.umn.edu/bitstream/209911/2/21405-76710-1-PB.pdf.

22. Özbay T, Bastürk Ö, Sungur MA. Physicochemical characterization of chitin and chitosan extracted from shell waste of mantis shrimp (Squilla sp.) and blue crab (Callinectes sapidus, Rathbun, 1896). Journal of Eğirdir Fisheries Faculty, 2011;7(2):1-10. http://edergi.sdu.edu.tr/index.php/esufd/article/viewFile/3235/3210.

23. Yuan Y, Chesnutt BM, Utturkar G. Haggard WO, Yang Y, Ong JL, Bumgardner JD. The effect of cross-linking of chitosan microspheres with genipin on protein release. Carbohydrate Polymers. 2007 Oct;68:561-67. DOI: 10.1016/j.carbpol.2006.10.023.

24. Nazemi K, Moztarzadeh F, Jalali N, Asgari FS, Mozafari M. Synthesis and characterization of poly(lactic co-glycolic) acid nanoparticles-loaded chitosan/bioactive glass scaffolds as a localized delivery system in the bone defects. BioMed Research International. 2014 May;2014:1-9. DOI: 10.1155/2014/898930.

25. Mirzaei BE, Ramazani SA, Shafiee M, Danaei M. Studies on glutaraldehyde crosslinked chitosan hydrogel properties for drug delivery systems, International Journal of Polymeric Materials and Polymeric Biomaterials, 2013 Jun;62(11):605-11. DOI: 10.1080/00914037.2013.769165.

26. Beppu MM, Vieira RS, Aimoli CG, Santana CC, Vieira RS, Aimoli CG. Crosslinking of chitosan membranes using glutaraldehyde: Effect on ion permeability and water absorption. Journal of Membrane Science. 2007 Jun;301:126-30. DOI: 10.1016/j.memsci.2007.06.015.

Türkçe Öz ve Anahtar Kelimeler

Mavi Yengeçten Kitin ve Kitosanın Ekstraksiyonu ve Karakterizasyonu, ve Kitosan Kriyojel Doku İskelelerinin Sentezi

Didem Demir, Fatma Öfkeli, Seda Ceylan, Nimet Bölgen Karagülle[*]

Öz: Kriyojelleşme tekniği ile elde edilen polimerik doku iskeleleri, doku mühendisliği uygulamaları için artan ilgi konusu olmaktadır. Kriyojelleşme, polimerler veya monomerik öncül maddelerin donmuş tepkime karışımlarından birbiri ile bağlantılı gözenekli matrisler elde edilmesine imkân tanıyan bir tekniktir. Kitosan, biyo-uyumlu, biyo-bozunur, toksik olmayan, antibakteriyel, antioksidan ve antifungal olan bir doğal polimerdir ve pek çok kabuklu hayvanın dış iskeletinde bulunan kitinin deasetilasyonu ile elde edilir. Bu çalışmada, kitin mavi yengeç (*Callinectes sapidus*) dış iskeletinden kimyasal olarak izole edilmiştir. *Callinectes sapidus* örnekleri bir marketten gıda olarak tüketilen yerleri bitirildikten sonra çöpe atılan alandan toplanmıştır. Kitini elde etmek için örneklere demineralizasyon, deproteinizasyon ve renksizleştirme adımları uygulanmıştır. Kitosan, yüksek sıcaklıklarda kitinin deasetilasyonu ile hazırlanmıştır. Yengecin kabuğu, ekstrakte edilen kitin ve kitosana ait kimyasal bileşim FTIR analizi ile karakterize edilmiştir. Bunun dışında, üretilen kitosanın fizikokimyasal ve işlevsel özelliklerini belirlemek için, çözünürlük, su alımı ve yağ alımı analizleri gerçekleştirilmiştir. Kitosan kriyojel doku iskeleleri, kriyojenik koşullarda sabit miktarda kitosan (%1, w/v) ile çapraz bağlayıcı olarak farklı oranlarda glutaraldehit (%1, 3 ve 6) karışımının çapraz bağlanma tepkimesinden elde edilmiştir. Doku iskelelerinin kimyasal yapıları FTIR ile incelenmiştir. Ayrıca, doku iskelelerinin su alma kapasiteleri de ölçülmüştür. Sonuç olarak, elde edilen neticeler karakterize edilmiş kitosan kriyojellerinin doku mühendisliği uygulamalarında potansiyel doku iskeleleri olarak kullanılabileceğini göstermiştir.

Al(III), Cu(II), Co(II), Pb(II), Mn(II), and Fe(III) Determinations in

Various Samples by FAAS after Solid Phase Extraction

Şule Dinç Zor[1*], Güzin Alpdoğan[1]

[1]Department of Chemistry, Faculty of Science and Arts, Yildiz Technical University,

34210 Davutpasa-Istanbul, Turkey

Abstract: In this study, a novel method for the preconcentration of Al(III), Cu(II), Co(II), Pb(II), Mn(II), and Fe(III) in the form of their hematoxylin chelates using a column filled with Amberlite XAD-16 resin was proposed. Metal chelates collected on the resin were eluted and their determinations were carried out by flame atomic absorption spectrometry (FAAS). The influences of some analytical parameters including pH, flow rate, sample volume, and the type and concentration of eluent on the preconcentration efficiency were examined. The effects of some interfering ions on the recovery values of analytes were also investigated. While the optimum pH value was 8.5 for Cu(II), Co(II), Mn(II), and Fe(III) ions, it was 6.5 for Al(III) and Pb(II) ions. The appropriate eluent for quantitative elution was 8.0 mL of 1 mol/L nitric acid in acetone. Sample and eluent flow rates were found to be 2.0 mL/min. The maximum sample volume was established by changing it from 50 mL to 2500 mL. The sample volume does not significantly affect recovery within the range of 50-2000 mL of the sample volume for the investigated metal ions. The obtained preconcentration factor was 400. At optimum conditions, the detection limits found as concentration which is threefold of the standard deviation of the blank solution were 0.053 µg/L, 0.080 µg/L, 0.620 µg/L, 1.310 µg/L, 0.330 µg/L and 0.120 µg/L for Al(III), Cu(II), Co(II), Pb(II), Mn(II), and Fe(III) ions, respectively, and the adsorption capacities for these ions were 0.47 ± 0.02 mg/g, 0.81 ± 0.01 mg/g, 0.66 ± 0.01 mg/g, 0.58 ± 0.01 mg/g, 0.91 ± 0.01 mg/g, and 0.73 ± 0.02 mg/g, respectively. By using the certified reference materials, the accuracy of the method was verified. The proposed method was successfully applied to cigarette, hair, and some vegetable species.

Keywords: Metal chelates, hematoxylin, preconcentration, FAAS.

***Corresponding author. E-mail: sule_dinc@yahoo.com.

INTRODUCTION

Heavy metal pollution is a major issue in all around the world. It occurs by means of air, water, soil, and food as a carrier of heavy metals. Particularly, heavy metals can easily enter and accumulate in living organisms through food chain and they have threatened human health. Therefore, the monitoring of the level of trace metals in food and environmental samples is an important task. Some analytical methods such as flame atomic absorption spectrometry (FAAS), electrothermal atomic absorption spectrometry (ETAAS), inductively couple plasma optical emission spectrometry (ICP-OES), and inductively couple plasma mass spectroscopy (ICP-MS) are employed for fast, accurate, and repeatable analysis of heavy metals in various samples [1, 2]. FAAS is widely used due to its good precision, selectivity, low cost, and simplicity. However the direct analysis of heavy metals in complex matrices by FAAS is a challenging matter owing to low concentration of trace metals and matrix effects. Hence, separation/preconcentration techniques such as solid phase extraction (SPE), solvent extraction, ion extraction, cloud point extraction and co-precipitation prior to instrumental measurements are an important requirement in order to achieve accurate and reliable results [3]. Among them, SPE is extensively used due to its simplicity, high preconcentration factor, short extraction time, low consumption of organic solvents, and low cost [4]. Amberlite XAD resins, silica gel, activated carbon, nanomaterials, biological microorganisms, chelating polymers are the most widely employed adsorbents for SPE procedure [5-11].

In particular, Amberlite XAD resins which have satisfied physical properties including porosity, high surface area, and uniform pore size distribution have been widely used as supports for preconcentration of metal chelates. Amberlite XAD-16 is a hydrophobic polyaromatic resin (polystyrene-divinyl benzene copolymer) with a higher surface area (800 m^2/g) and sorption capacity; and has been utilized for separation and preconcentration of many metal ions in different matrices with or without derivatization by various ligands [12].

Hematoxylin is a phenolic chromogenic reagent for the spectrophotometric analysis of some certain metal ions such as Fe(III) and Al(III) [13]. When oxidized, it transforms to haematein which forms strongly colored complexes with some transition metal ions [14]. However, hematoxylin has not yet been used in separation and preconcentration of trace heavy metal ions prior to their determination by FAAS.

In this study, a new preconcentration method has been proposed for FAAS determination of Al(III), Cu(II), Co(II), Pb(II), Mn(II), and Fe(III) on Amberlite XAD-16 as hematoxylin chelates. The effects of some analytical parameters including pH, flow rate, sample volume, and the type and concentration of eluent on the preconcentration efficiency were examined. The optimized method was applied for the determination of target metal ions in various real samples including potato, tomato, hair and cigarette.

MATERIALS and METHODS

Instruments

A Perkin Elmer Analyst 700 FAAS instrument (Waltham, MA, USA) was used for the determination of Al(III), Cu(II), Co(II), Pb(II), Mn(II), and Fe(III). The analytes were determined under the optimized measurement conditions presented in Table 1. For pH measurements, a Metrohm 780 pH meter (Herisau, Switzerland) was used. Ultrapure water was obtained using a Milli-Q Water Purification System (Millipore, Bedford, MA, USA).

Table 1. Measurement parameters for determination of the analyte ions by FAAS.

Metal ion	Wavelength (nm)	Slit width (nm)	Lamp current (mA)	Air flow rate (L/min)	Acetylene flow rate (L/min)	Burner height (cm)	Acetylene flow pressure (kg/cm²)
Al(III)	309.2	0.5	2.0	8.0	2.0	3.25	0.4
Cu(II)	324.8	0.5	2.0	10.0	2.0	10.5	0.3
Mn(II)	279.5	1.0	10.0	10.0	2.0	10.5	0.3
Pb(II)	217.0	0.7	12.5	10.0	2.0	10.5	0.3
Fe(III)	248.3	0.7	11.0	10.0	2.0	10.5	0.3
Co(II)	240.7	0.8	6.0	10.0	2.0	10.5	0.3

Reagents and Solutions

In this study, all chemicals were of analytical reagent grade and used without further purification. Ultra pure water was employed for all dilutions. The metallic standard solutions used for calibration were prepared by diluting a stock solution of 1000 mg/L of the given metal salt purchased by Sigma–Aldrich (Milwaukee, USA). The proposed preconcentration procedure was not applied to standard calibration solutions. Working standard solutions were prepared by suitable dilution of the stock solutions. Amberlite XAD-16 (non-ionic divinyl polystyrene; specific area 800 m²/g and bead size; 20-60 mesh) was procured from Sigma–Aldrich (Milwaukee, USA).

A hematoxylin solution (6.0×10^{-3} mol/L, Sigma–Aldrich, USA) was prepared daily by dissolving the requisite amounts of hematoxylin in water/ethanol (1/1, v/v).

Certified reference materials (NIES CRM No.13 Human Hair, Virginia Tobaco Leaves (CTA-VTL-2), and NIST SRM 1515 Apple Leaves) were used in order to check the accuracy of the method.

In order to adjust pH, HCl/KCl buffer solution were prepared by mixing of appropriate volume of 0.1 mol/L hydrochloric acid and potassium chloride solutions for pH between 2.0-3.0. CH_3COO^-/CH_3COOH buffer solution were prepared by mixing appropriate volumes of 0.1 mol/L acetic acid and 0.1 mol/L sodium acetate solutions for pH between 4.0-7.0. NH_4^+/NH_3 buffer solution was prepared by mixing of appropriate amounts of 0.1 mol/L ammonia and 0.1 mol/L ammonium chloride solution for pH between 8.0-10.0.

Preparation of the Column

0.6 g of Amberlite XAD-16 was loaded after washing with methanol, 1 mol/L HNO_3 solution and water, respectively, into a 10 mm x 200 mm glass column with a glass frit resin support. The resin bed was approximately 1.5 cm. The column was preconditioned by the blank solution prior to each use. After the elution, the resin in the column was washed with a 10-15 mL of the elution solution and of water in a subsequent manner.

General Preconcentration Procedure

The proposed method was tested with model standard solutions containing analyte ions (8 μg Al(III), 10 μg Cu(II), 30 μg Co(II), 40 μg Pb(II), 25 μg Mn(II), and 10 μg of Fe(III)) before application. 10.0 mL of buffer solution (to give the desired pH between 2.0-10.0) and 1.2 mL of 6.0×10^{-3} mol/L hematoxylin solution were added to 50-60 mL of solution. 0.6 g Amberlite XAD-16 column was preconditioned with the relevant buffer solution. Metal-hematoxylin solution was passed through the Amberlite XAD-16 column at a flow rate of 1.0-10.0 mL/min. After passing of this solution, the column was washed twice with 10.0 mL of water. The metal chelates adsorbed on the column were eluted with 8.0 mL of 1.0 mol/L HNO_3 in acetone. The eluted solution was evaporated to near dryness and then diluted to 5.0 mL with 0.01 mol/L HNO_3. The eluent was analyzed by FAAS for the determination of metal concentration.

Sampling

Hair samples were collected from male subjects who especially work in battery production and soldering in Kocaeli, Turkey. The hair samples (approximately 2 mm) were cut with sterilized stainless steel scissors from the nape of the scalp. All hair samples were sealed in plastic bags prior to analysis. Samples collected were weighed about 1.0 g.

In spring and summer of 2015, the vegetables including potato and tomato were collected from production sites in Adapazarı, Turkey. The vegetables were washed with distilled water, air-dried for 72 h, crushed, passed through a 2 mm mesh sieve and stored at ambient temperature until analysis.

The test samples for cigarettes are brands of commonly smoked in Istanbul. These samples were purchased in packet with seals from a retailer at local market in Bahçelievler, Turkey. The samples were stored in a cool and dry place before analysis.

Digestion Procedures

Hair samples were treated with a 10.0-mL mixture of HNO_3 and $HClO_4$ (6:1, v/v) and consequently heated at 200 ^{o}C until obtaining a clear solution. It was diluted to 25 mL with 0.01 mol/L HNO_3.

For digestion of the vegetables, from each dried sample, 1.0 g ground fine particles were added to a flask containing concentrated HNO_3 (5.0 mL) and concentrated HCl (15.0 mL; *aqua regia*). The flask was covered with a watch glass and then was allowed to stand for at least 16 h. Afterwards, the mixture was heated gradually and boiled under reflux for 2 h. After cooling and rinsing with 20 mL of ultra pure water, the rinse water was recovered in the digestion flask. After filtration, filtrates were used to make a volume of up to 100 mL using 0.01 mol/L

HNO_3. The samples were refrigerated in acid-washed polyethylene bottles at 4 °C before final analysis of metal ions.

For cigarettes, sample mineralization with a mixture of HNO_3 and H_2O_2 included the following stages:

a) 0.5 g from the sample dried to a constant weight were initially placed in borosilicate test tubes. Then the Teflon collector for removal of the discharged gases was fixed. 6.0 mL HNO_3 (65%) were added to each test tube through the openings of the collector, and the heating block was heated to 40 °C for 30 min. Consequently, the temperature was increased to 100 °C. The temperature was kept constant until the abatement of the reaction.

b) 1.0 mL H_2O_2 (30%) was added through the collector openings dropwise after cooling, then the thermos block was heated again to 15 °C for 30 min. In case of need, H_2O_2 addition was continued till the solution was clear enough. Consequently, the solution was quantitatively placed in a measuring flask, which was filled with 0.01 mol/L HNO_3 to the 25 mL. Blank digestions were also performed in the same way.

RESULTS and DISCUSSION

Influences of pH

The pH study was performed to find its effect on the degree of metal sorption using the column process and the pH effect was evaluated in the pH range 2.0-10.0 by using different buffer solutions. The effect of pH on the recovery of target metal ions is shown in Figure 1. The optimum pH value is 8.5 for Cu(II), Co(II), Mn(II), and Fe(III), and 6.5 for Al(III), and Pb(II).

The studies were also carried out at the same pH range without hematoxylin. The recoveries of related metal ions were below 20%. It can be concluded that hematoxylin as a chelating reagent increases the efficiency for preconcentration on Amberlite XAD-16 resin column.
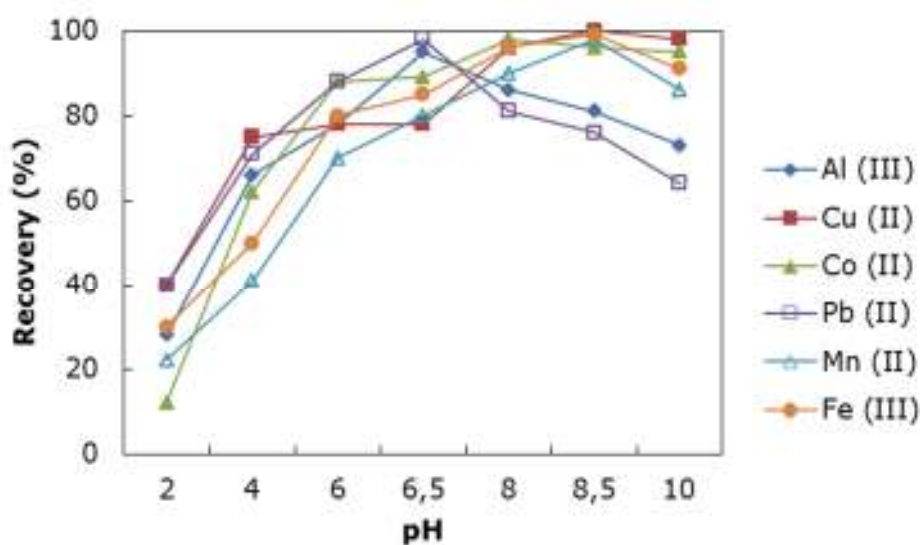
Figure 1. Effect of pH on recovery of investigated metal ions.

Effect of Amounts of Hematoxylin

The effect of the amount of hematoxylin on the quantitative recoveries of the metal ions studied was also investigated. 0.2-1.6 mL portion of a 6.0×10^{-3} mol/L hematoxylin solution

was added to a model solution containing 5-20 µg of each analyte ion. The amounts of analyte ions adsorbed on Amberlite XAD-16 resin were determined by the proposed method. Over 1.0 mL of 6.0×10^{-3} mol/L hematoxylin solution, Al(III), Cu(II), Co(II), Pb(II), Mn(II), and Fe(III) were quantitatively adsorbed. Hence all further studies were performed by using 1.2 mL of 6.0×10^{-3} mol/L hematoxylin.

Effect of the Type of Elution Solution

The effect of the various eluents on the recoveries of Al(III), Cu(II), Co(II), Pb(II), Mn(II), and Fe(III) ions from the Amberlite XAD-16 resin column was examined by using 8.0 mL of each eluent solution. This volume was determined according to previous studies in the literature and from our experiences. Recoveries obtained with all eluent solutions for each analyte ion are given in Table 2. According to these results, 8.0 mL of 1.0 mol/L HNO_3 in acetone was used as an eluent for further applications.

Table 2. Effect of the eluent type on recoveries (N=3).

Eluent type	Recovery (%)					
	Al(III)	Cu(II)	Co(II)	Pb(II)	Mn(II)	Fe(III)
Acetone	71 ± 1	96 ± 2	85 ± 2	24 ± 2	100 ± 3	66 ± 2
0.5 mol/L HNO_3	81 ± 1	86 ± 2	90 ± 1	87 ± 3	88 ± 2	76 ± 2
1.0 mol/L HNO_3	95 ± 2	92 ± 1	89 ± 2	99 ± 2	90 ± 3	88 ± 3
0.5 mol/L HCl	46 ± 3	89 ± 2	71 ± 3	86 ± 1	78 ± 1	84 ± 2
1.0 mol/L HCl	61 ± 1	92 ± 3	83 ± 1	92 ± 3	85 ± 1	88 ± 1
1.0 mol/L HNO_3 in acetone	95 ± 3	99 ± 2	96 ± 2	98 ± 1	100 ± 1	96 ± 1

Effect of Flow Rate and Sample Volume

The effect of flow rate on the sorption was investigated by varying the flow rate from 1.0 to 10.0 mL/min at optimum conditions. It was observed that the best results were reached at 2.0 mL/min for retention and elution steps.

In order to investigate the possibility of enriching low concentration of the analyte ions from large sample volumes, the effects of the sample solution volume on the recoveries of the metal ions were also tested in the range of 50-2500 mL. The results are given in Fig. 2. According to these results, the recoveries of analyte ions were not affected until 2000 mL. Above 2000 mL, the recoveries of the target ions decrease probably owing to the excess analytes loaded over the the column capacity with increasing sample volume. In the light of this result found, preconcentration factor was calculated to be 400 for the analyte ions when the final volume was 5.0 mL.
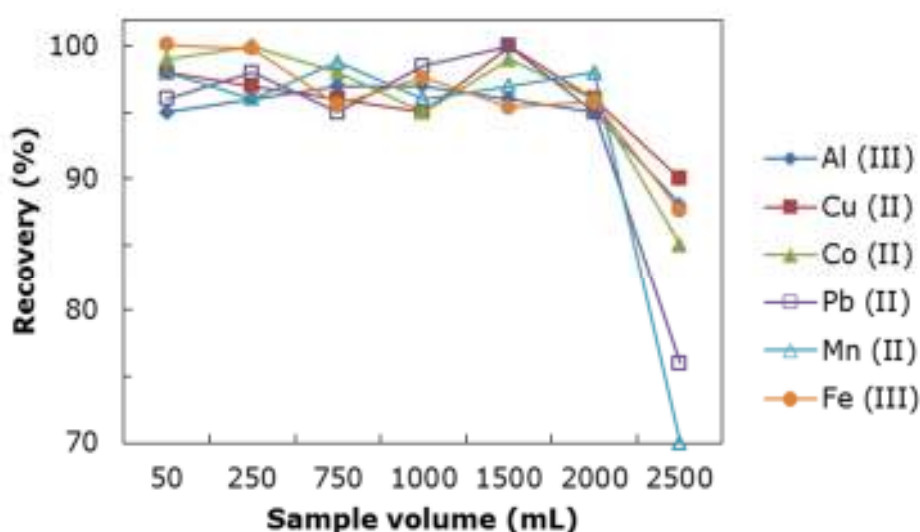
Figure 2. The effect of sample volume on the recoveries of metal ions.

Effect of Coexisting Ions

The influences of possible matrix ions on the recoveries of analytes were also examined by a generic procedure. The obtained experimental results are showed in Table 3. The tolerance limit is defined as the ion concentration inducing a relative error smaller than ± 3% related to the preconcentration and determination of the analyte ions. The results given in Table 2 showed that the existence of high concentrations of some cations and anions has no obvious influence on the metal ions adsorption at optimum conditions.

Total Sorption Capacity

The sorption capacity of the resin is described as the amount of metal adsorbed by 1.0 g of resin. A suitable aliquot of metal ion chelate at appropriate pH value was loaded onto the column filled with 1.0 g of resin. The eluate was determined by FAAS as described in the general procedure until the resin was saturated. This procedure was repeated for each analyte ions. The sorption capacity for each analyte ion on the sorbent was calculated from the difference between the metal ion concentration before and after desorption. The obtained results are presented in Table 4.

Resin Reusability Study

In order to determine the potential reusability of the resin, the resin was subjected to several adsorption-elution cycles at optimum conditions. Ten runs were performed on the same day and the next ten runs were made the following day. According to the obtained results, a small decrease in the recoveries occured after 50 cycles. The resin could be utilized up to 70 runs in succession without any appreciable loss in the sorption efficiency.

Detection Limits

The detection limits based on the concentration corresponding to three times the standard deviation of blank signal were found to be 0.053 µg/mL for Al(III), 0.08 µg/mL for Cu(II), 0.62 µg/mL for Co(II), 1.31 µg/mL for Pb(II), 0.33 µg/mL for Mn(II) and 0.12 µg/mL for Fe(III) using a synthetic sample volume as blank.

Accuracy of the Results

The accuracy of the proposed method was checked by determination of the metal ions in the certified reference materials, NIES CRM No.13 Human Hair, Virginia Tobaco Leaves (CTA-VTL-2), and NIST SRM 1515 Apple Leaves. The results in Table 5 show that developed method was

in a good agreement with the certified values and is free from interferences of the various constituents.

Application to Real Samples

The presented method was applied to the determination of Al(III), Cu(II), Co(II), Pb(II), Mn(II), and Fe(III) ions in potato, tomato, hair, and cigarette. The results are summarized in Table 6. Accordingly, relative standard deviations (RSDs) of the method were lower than 8%, showing that the developed method has good precision for the analysis of trace metal ions studied from different samples.

Table 3. Influences of some foreign ions on the recoveries of metal ions (N=3).

Cations/ Anions	Added as	C (mg/L)	Al(III)	Cu(II)	Co(II)	Pb(II)	Mn(II)	Fe(III)
					Recovery (%)			
Na^+	NaCl	500	95 ± 1[a]	96 ± 1	97 ± 3	97 ± 2	96 ± 1	95 ± 2
K^+	KCl	500	97 ± 2	95 ± 1	95 ± 2	98 ± 3	98 ± 2	96 ± 1
Ca^{2+}	$CaCl_2$	400	96 ± 2	98 ± 3	96 ± 2	97 ± 1	100 ± 1	97 ± 2
Mg^{2+}	$MgCl_2$	200	95 ± 1	95 ± 1	97 ± 1	95 ± 2	95 ± 2	96 ± 3
Ni^{2+}	$Ni(NO_3)_2$	100	96 ± 3	96 ± 2	95 ± 3	96 ± 3	97 ± 3	98 ± 1
Cd^{2+}	$Cd(NO_3)_2$	100	95 ± 2	98 ± 2	97 ± 2	97 ± 2	98 ± 2	95 ± 2
Sn^{2+}	$SnCl_2$	300	96 ± 2	96 ± 3	97 ± 3	95 ± 1	99 ± 1	98 ± 1
Cr^{3+}	$Cr(NO_3)_3$	600	99 ± 1	98 ± 2	96 ± 2	97 ± 2	100 ± 1	96 ± 1
Ag^+	$AgNO_3$	150	98 ± 1	96 ± 1	97 ± 1	96 ± 3	95 ± 3	97 ± 1
V^{5+}	V_2O_5	50	96 ± 3	95 ± 2	96 ± 2	98 ± 2	97 ± 3	97 ± 3
Bi^{3+}	$Bi(NO_3)_3$	50	96 ± 1	96 ± 3	95 ± 1	95 ± 3	96 ± 1	95 ± 2
PO_4^{3-}	Na_3PO_4	5000	96 ± 2	96 ± 2	99 ± 2	99 ± 2	96 ± 2	96 ± 3
Cl^-	NaCl	4000	97 ± 2	97 ± 1	98 ± 1	95 ± 3	98 ± 1	97 ± 2
SO_4^{2-}	Na_2SO_4	3000	97 ± 3	95 ± 2	96 ± 3	97 ± 3	99 ± 2	96 ± 1

[a] Mean ± standard deviation.

Table 4. Total sorption capacity of the metal ions on Amberlite XAD-16 (Experimental conditions: Amberlite XAD-16: 1.0 g; Al(III): 50-800 μg, pH 6.5; Cu(II): 50-1400 μg, pH 8.5; Co(II): 60-1100 μg, pH 8.5; Pb(II): 70-1000 μg, pH 6.5; Mn(II):50-600 μg, pH 8.5; Fe(III): 80-900 μg, pH 8.5; flow rate: 2.0 mL/min for each element).

Metal ion	Capacity (mg/g)
Al(III)	4.7 ± 0.2
Cu(II)	8.1 ± 0.1
Co(II)	6.6 ± 0.1
Pb(II)	5.8 ± 0.1
Mn(II)	9.1 ± 0.1
Fe(III)	7.3 ± 0.2

Table 5. The results for reference standard materials (N=5).

Metal ion	SRM 515 Apple Leaves (µg/g)		CRM 13 Human Hair (µg/g)		CTA-VTL-2 Virginia Tobacco Leaves (µg/g)	
	Certified value	Found value	Certified value	Found value	Certified value	Found value
Al(III)	289 ± 9	284 ± 4	120[a]	118 ± 2	1682[a]	1679 ± 18
Cu(II)	5.64 ± 0.24	5.61 ± 0.10	15.3 ± 1.3	14.9 ± 0.7	18.2 ± 0.9	17.9 ± 0.7
Co(II)	0.09[a]	0.08 ± 0.01	0.07[a]	0.06 ± 0.01	0.429 ± 0.026	0.424 ± 0.03
Pb(II)	0.470 ± 0.024	0.468 ± 0.08	4.6 ± 0.4	4.5 ± 0.3	22.1 ± 1.2	20.8 ± 1.1
Mn(II)	54 ± 3	53.42 ± 0.7	3.9[a]	3.8 ± 0.3	79.7 ± 2.6	77.6 ± 1.3
Fe(III)	83 ± 5	81 ± 0.9	140[a]	138 ± 3	1083 ± 33	1080 ± 24

[a]:informative value.

Except for Pb, there is no information about maximum Al, Cu, Co, Mn, and Fe levels in foodstuff in the Turkish Food Codex (TFC, regulation no 2011/28157) [15]. When the results of samples in terms of Pb contents are examined, it is seen that Pb levels in potato and tomato samples are higher than their maximum permissible limit (0.10 mg/kg) of the TFC.

Additionally, Pb average concentration in the hair samples was found to be 6.43 ± 0.6 mg/kg and a similar observation (8.67 ± 13.83 mg/kg) were also reported by Li *et al.* in case of lead content for the scalp hair of residents living in the mining areas in China [16]. Moreover this value is higher than Pb levels of another study (≤ 4.60 ± 0.57 mg/kg) based on ETAAS in literature [17]. Consequently, these results obtained for lead determination show that people in the battery and soldering work areas are more susceptible to lead pollution and thus, it should be paid more attention to the monitoring of their lead levels.

Cigarette samples presented the highest Al, Cu, Mn, and Fe values according to other samples, while they gave the lowest Pb value. These results are almost comparable with some studies done in literature [18-20].

Table 6. The results of Al(III), Cu(II), Co(II), Pb(II), Mn(II), and Fe(III) ions in potato, tomato, hair, and cigarette samples by the proposed method.

Metal ion	Potato (mg/kg)	Tomato (mg/kg)	Hair (mg/kg)	Cigarette (mg/kg)
Al(III)	9.42 ±0.3	1.31 ±0.2	85 ± 3.4	835 ± 8
Cu(II)	3.67 ±0.1	2.48 ± 0.4	21 ± 2.7	41 ± 2
Co(II)	0.098 ± 0.01	0.85 ± 0.1	0.85 ± 0.3	0.75 ± 0.09
Pb(II)	2.14 ± 0.2	1.21 ± 0.2	6.43 ± 0.6	0.641 ± 0.2
Mn(II)	11.45 ± 0.3	96 ± 2.1	31.4 ± 0.9	109 ± 3
Fe(III)	82.5 ± 2.0	2.17 ± 0.3	140 ± 4.4	540 ± 6

Comparison with the other SPE methods

The new method was compared with other SPE methods based on Amberlite XAD resins in terms of preconcentration factor, limit of detection, sorption capacity, and relative standard deviation (Table 7). The preconcentration factor of the analyte ions is superior to those of SPE methods described in Table 7. The obtained results related to sorption capacity, LOD and RSD are also comparable to those of other preconcentration studies in Table 7.

Table 7. Comparison of the developed method with the other some SPE methods.

Chelating agent	Studied metal ions	PF	LOD (µg/L)	Sorption capacity (mg/g)	RSD (%)	Reference
Amberlite XAD-4/SAB	Cu, Ni, Co, Fe	240	0.40-0.90	8.14-11.13	< 5	5
Amberlite XAD-4/PAN	Cd, Co, Ni, Mn, Zn, Pb, Cu	160-400	0.09-1.30	0.030-0.050*	< 5	21
Amberlite XAD-7/MDTC	Pb, Cu, Co, Fe, Ni, Cd, Zn	-	2.10-4.19	9.14-10.43	< 5	22
Amberlite XAD-1180/PV	Fe, Pb	100	0.37, 0.20	-	< 10	23
Amberlite XAD-16/PAN	Ni, Cd, Co, Cu, Pb, Cr	200	0.056-0.268	4.7-5.0	< 8	24
Amberlite XAD-1180/ EBBR	Cu	60	1.3	0.90	3.3	25
Amberlite XAD-7/PAR	Co	200	0.1	-	13	26
Amberlite XAD-4/DPKT	Co, Ni, Fe, Cu	200-300	30-50	2.0	< 2	27
Amberlite XAD-2010/Na-DDTC	Mn, Co, Ni, Cu, Cd, Pb	100	0.08–0.26	5.7-6.3	< 5.1	28
Amberlite XAD-1180/TAN	Cu, Ni, Pb, Cd Mn	50-200	0.03-1.19	0.30-0.77	< 5.1	29
Amberlite XAD-4/DDTP	Cd, Pb	6-13	0.02-2.0	-	< 13	30
Amberlite XAD-8/AMOTACTA	Cu	200	0.20	2.37	< 4.1	31
Amberlite XAD-7/PAR	Cu, Ni, Zn	200-400	0.013-0.027	-	< 3.2	32
Amberlite XAD-16/ 8-hydroxyquinoline	Cu, Zn	80, 147	0.16, 0.2		1.2, 2.2	33
Amberlite XAD-16/Hematoxylin	Al, Cu, Co, Pb, Mn, Fe	400	0.053-1.310	0.47-0.91	< 5	Present study

PF: Preconcentration factor, LOD: Limit of detection, RSD: Relative standard deviation, PAN: 1-(2-pyridylazo)-2-naphtol, MDTC: Morpholine dithiocarbamate, Na-DDTC: Sodium diethyldithiocarbamate, PV: Pyrocatechol violet, EBBR: Eriochrome blue black R, PAR: 4-(2-pyridylazo) resorcinol, SAB: Salicylaldehyde benzoylhydrazone, DPKT: Di-2-pyridylketone thiosemicarbazone, TAN: 1-(2-thiazolylazo)-2-naphthol, DDTP: O,O-diethyldithiophosphate, and AMOTACTA: Carbothioamide derivative. *mmol/g.

CONCLUSION

In the present study, a new method for solid phase extraction of trace metals, Al(III), Cu(II), Co(II), Pb(II), Mn(II), and Fe(III) prior to their determinations by FAAS was developed. The conditions of preconcentration and elution were investigated and optimized. At optimum conditions, the method has high preconcentration factor, and low RSD and LOD values. In addition, the proposed method is not influenced by many foreign ions present together with analyte ions. Certified reference materials were also used for method validation and the results showed that the developed method was in good agreement with certified values and it is suitable for the analysis of metal ions studied in real samples. This method based on the sorption of hematoxylin-metal chelates on Amberlite XAD-16 provides simple, fast, and low-cost preconcentration procedure for accurate and precise quantification of target analyte ions in some vegetable, human hair and cigarette samples.

REFERENCES

1.   Jorhem L, Engman J. Determination of lead, cadmium, zinc, copper, and iron in foods by atomic absorption spectrometry after microwave digestion: NMKL1 collaborative study. Journal of AOAC International. 2000 Sept; 83, 5:1189-1203.

2.   Sardans J, Montes F, Penuelas J. Determination of As, Cd, Cu, Hg and Pb in biological samples by modern electrothermal atomic absorption spectrometry. Spectrochimica Acta Part B, Atomic Spectroscopy. 2010 Feb;65, 2: 97–112. DOI: 10.1016/j.sab.2009.11.009.

3.   de Godoi Pereira M, Arruda MAZ. Trends in preconcentration procedures for metal determination using atomic spectrometry techniques. Microchimica Acta. 2003 Mar; 141:115-31. DOI: 10.1007/s00604-002-0941-5.

4.   Türker AR. Separation, preconcentration and speciation of metal ions by solid phase extraction. Separation & Purification Reviews. 2012 Feb; 41:169–206. DOI: 10.1080/15422119.2011.585682.

5.   Alpdogan G. Solid phase extraction of Cu(II), Ni(II), Co(II), and Fe(III) ions in water samples using salicylaldehyde benzoylhydrazone on amberlite XAD-4 and their

determinations by flame atomic absorption spectrometry. Toxicology Environmental Chemistry. 2015 Dec; 98(2):179-88. DOI: 10.1080/02772248.2015.1115508.

6.   Berber H, Alpdogan G, Asci B, Yildirim H, Sungur S. Preparation and metal sorption properties of GMA-MMA-DVB microspheres functionalized with 2-aminothiazole. Analytical Letters. 2010 Oct; 43(15):2331-39. DOI: 10.1080/00032711003725557.

7.   Er Ç, Şenkal B.F., Yaman M. Determination of lead in milk and yoghurt samples by solid phase extraction using a novel aminothioazole-polymeric resin. M. Food Chemistry: 2013 Apr; 137:55-61. DOI: 10.1016/j.foodchem.2012.10.013.

8.   Bakircioglu Y, Bakircioglu D, Akman S. Biosorption of lead by filamentous fungal biomass-loaded TiO2 nanoparticles. Journal of Hazardeous Materials. 2010 June; 178:1015–20. DOI: 10.1016/j.jhazmat.2010.02.040.

9.   Jufang C, Xiaoguo M, Yuguang W. Silica gel chemically modified with ionic liquid as novel sorbent for solid-Phase extraction and preconcentration of lead from beer and tea drink samples followed by flame atomic absorption spectrometric determination. Food Analytical Methods. 2014 Sept; 7:1083–89. DOI: 10.1007/s12161-013-9716-3.

10.   Imyim A, Daorattanachai P, Unob F. Determination of cadmium, nickel, lead, and zinc in fish tissue by flame and graphite furnace atomic absorption after extraction with pyrrolidine dithiocarbamate and activated carbon. Analytical Letters. 2013 Apr; 46: 2101-10. DOI: 10.1080/00032719.2013.784913.

11.   Ramesh A, Devi B.A., Hasegawa H, Maki T, Ueda K. Nanometer-sized alumina coated with chromotropic acid as solid phase metal extractant from environmental samples and determination by inductively coupled plasma atomic emission spectrometry. Microchemical Journal. 2007 Jun; 86:124–30. DOI: 10.1016/j.microc.2007.01.002.

12.   Ahmad A, Siddique JA, Laskar MA, Kumar R, Mohd-Setapar SH, Khatoon A, Shiekh RA New generation Amberlite XAD resin for the removal of metal ions: A review. Journal of Environmental Sciences. 2015 May; 31:104-23. DOI: 10.1016/j.jes.2014.12.008.

13.   El-Sayed AY. Simultaneous determination of aluminium and iron in glasses, phosphate rocks and cement using first-and second-derivative spectrophotometry. Fresenius Journal of Analytical Chemistry. 1996 May; 355:29-33. DOI: 10.1007/s0021663550029.

14.   Shirai K, Matsuoka M. Structure and properties of hematein derivatives. Dyes and Pigments. 1999 Feb; 32(3):159-69. DOI: 10.1016/0143-7208(96)00022-8.

15.   Türk Gıda Kodeksi Bulaşanlar Yönetmeliği. URL: http: //www. faolex.fao.org/docs/texts/tur110178.doc.

16.   Li Y, Zhang X, Yang L, Li H. Levels of Cd, Pb, As, Hg, and Se in hair of residents living in villages around Fenghuang polymetallic mine, southwestern China. Bulletin of environmental contamination and toxicology. July 2012;89(1):125-28. DOI 10.1007/s00128-012-0650-7.

17.   Baysal A, Akman S. Determination of lead in hair and its segmental analysis by solid sampling electrothermal atomic absorption spectrometry. Spectrochimica Acta Part B: Atomic Spectroscopy. Apr 2010; 65(4):340-344. DOI: 10.1016/j.sab.2010.02.016.

18.   Kazi TG, Jalbani N, Arain MB, Jamali MK, Afridi HI, Sarfraz RA, Shah AQ. Toxic metals distribution in different components of Pakistani and imported cigarettes by electrothermal atomic absorption spectrometer. Journal of Hazardous Materials. Apr 2009; 163(1):302-307. DOI:10.1016/j.jhazmat.2008.06.088.

19.   Ashraf MW. Levels of heavy metals in popular cigarette brands and exposure to these metals via smoking. The Scientific World Journal, 2012 http://dx.doi.org/10.1100/2012/729430.

20.   Andrade FP, Nascentes CC, Costa LM. Cadmium and lead cloud point preconcentration and determination in tobacco samples by thermospray flame furnace atomic absorption spectrometry. Journal of the Brazilian Chemical Society, Aug 2009; 20(8):1460-1466. DOI: 10.1590/S0103-50532009000800011.

21.   Islam A, Asaduddin M, Ahmad A. The efficiency of Amberlite XAD-4 resin loaded with 1-(2-pyridylazo)-2-naphthol in preconcentration and separation of some toxic metal ions by flame atomic absorption spectrometry. Environmental Monitoring and Assessment. 2011 Apr; 175:201-12. DOI: 10.1007/s10661-010-1506-4.

22.   Purna Chandra Rao, G, Satya Veni S, Madhava Rao M, Pratap K, Wang MC, Seshaiah K. Amberlite XAD-7 impregnated with morpholine dithiocarbamate as trace metal extractant. Toxicological Environmental Chemistry. 2007 Feb;88(1):65-76. DOI: 10.1080/02772240500504919.

23.   Soylak M, Tuzen M, Narin I. Solid phase extraction of iron and lead in environmental matrices on amberlite XAD-1180/PV. Química Nova. 2006 Jan;29(2):203-7. DOI: 10.1590/S0100-40422006000200005.

24.   Narin I, Soylak M, Kayakirilmaz K, Elci L, Dogan M. Preparation of a chelating resin by immobilizing 1-(2-pyridylazo) 2-naphtol on amberlite XAD-16 and its application of solid phase extraction of Ni(II), Cd(II), Co(II), Cu(II), Pb(II), and Cr(III) in natural water samples. Analytical Letters. 2003 Jan;36(3):641-58. DOI: 10.1081/AL-120018254.

25.   Şahan S, Şahin U. Determination of copper (II) using atomic absorption spectrometry and eriochrome blue black R loaded Amberlite XAD-1180 resin. Clean–Soil, Air, Water, 2010 Jun;38(5-6):485-91. DOI: 10.1002/clen.200900303.

26.   Ince M, Kaya G, Yaman M. Solid phase extraction and preconcentration of cobalt in mineral waters with PAR-loaded Amberlite XAD-7 and flame atomic absorption spectrometry. Environmental Chemistry Letters. 2009 Apr;8(3):283-88. DOI: 10.1007/s10311-009-0218-x.

27.   Aşçı B, Alpdoğan G, Sungur S. Preconcentration of Some Trace Metal Ions from Drinking and Tap Water Samples by Sorption on Amberlite XAD-4 after Complexation with Di-2-Pyridyl Ketone Thiosemicarbazone. Analytical Letters. 2007 Feb; 39(5):997-1007. DOI: 10.1080/00032710600614263.

28.   Duran C, Gundogdu A, Bulut VN, Soylak M, Elci L, Sentürk HB, Tüfekci M. Solid-phase extraction of Mn (II), Co (II), Ni (II), Cu (II), Cd (II) and Pb (II) ions from environmental samples by flame atomic absorption spectrometry (FAAS). Journal of Hazardous Materials. 2007 Aug;146(1):347-55. DOI: 10.1016/j.jhazmat.2006.12.029.

29.   Tokalıoğlu Ş, Yılmaz V, Kartal Ş. Solid phase extraction of Cu (II), Ni (II), Pb (II), Cd (II) and Mn (II) ions with 1-(2-thiazolylazo)-2-naphthol loaded Amberlite XAD-1180. Environmental Monitoring and Assessment. 2009 May;152(1-4):369-77. DOI: 10.1007/s10661-008-0322-6.

30.   Santos ÉJD, Santos ABD, Herrmann AB, Kulik S, Baika LM, Tormen L, Curtius AJ. Simultaneous determination of Pb and Cd in seafood by ICP OES with on-line pre-concentration by solid phase extraction with amberlite XAD-4 after complex formation with DDTP. Brazilian Archives of Biology and Technology. 2013 Jan-Feb;56(1):127-34. DOI: 10.1590/S1516-89132013000100017.

31.   Elvan H, Ozdes D, Duran C, Sahin D, Tufekci M, Bahadir Z. Separation and preconcentration of copper in environmental samples on Amberlite XAD-8 resin after complexation with a carbothioamide derivative. Química Nova. 2013 May;36(6):831-35. DOI: 10.1590/S0100-40422013000600016.

32.   Sert R, Höl A, Kartal AA, Akdoğan A, Elçi A, Baig JA, Elçi L. Simultaneous solid phase chelate extraction for ultratrace determination of copper, nickel, and zinc by microsample injection system coupled flame atomic absorption spectrometry. Analytical Letters. 2013 Aug;46(16):2570-82. DOI: 10.1080/00032719.2013.803249.

33.   Saxena R, Meena PL. Flow injection online solid phase extraction system using Amberlite XAD-16 functionalized with 8-hydroxyquinoline for copper and zinc determination by flame atomic absorption spectrometry. RSC Advances.2014 Apr;4(39): 20216-25. DOI: 10.1039/C4RA01260G.

Katı Faz Ekstraksiyonu Sonrası FAAS ile Çeşitli Örneklerde Al(III), Cu(II), Co(II), Pb(II), Mn(II) ve Fe(III) Tayini

Şule Dinç Zor[*], Güzin Alpdoğan

Öz: Bu çalışmada, Amberlite XAD-16 reçinesi ile doldurulmuş bir kolon kullanarak hematoksilin kelatları şeklinde Al(III), Cu(II), Co(II), Pb(II), Mn(II) ve Fe(III) iyonlarının ön derişiklendirilmesi için yeni bir yöntem önerilmiştir. Reçinede toplanan metal kelatları elüe edilmiş ve tayinleri alev atomik absorpsiyon spektrometrisi (FAAS) ile yapılmıştır. Ön derişiklendirme etkinliğine pH, akış hızı, örnek hacmi ve elüentin konsantrasyonu gibi bazı analitik parametrelerin etkisi incelenmiştir. Analitlerin geri kazanım değerlerine girişim yapan bazı iyonların etkisi de incelenmiştir. Cu(II), Co(II), Mn(II) ve Fe(III) iyonları için en uygun pH değeri 8,5 iken Al(III) ve Pb(II) iyonları için en uygun değer 6,5 olarak tespit edilmiştir. Kantitatif elüsyon için en uygun elüentin, aseton içindeki 8,0 mL 1 mol/L nitrik asidin çözeltisi olduğu belirlenmiştir. Örnek ve elüent akış hızları 2,0 mL/dak olduğu bulunmuştur. En yüksek örnek hacmi, bu değerin 50 mL'den 2500 mL'ye değiştirilmesi ile bulunmuştur. Örnek hacmi, geri kazanıma 50-2000 mL örnek hacmi aralığında çalışılan metal iyonları için belirgin şekilde etki etmemektedir. Elde edilen ön derişiklendirme faktörü 400'dür. En uygun koşullarda, kör çözeltinin standart sapmasının üç katı olarak bulunan ve konsantrasyon cinsinden tayin sınırları Al(III), Cu(II), Co(II), Pb(II), Mn(II) ve Fe(III) iyonları için sırasıyla 0,053 µg/L, 0,080 µg/L, 0,620 µg/L, 1,310 µg/L, 0,330 µg/L and 0.120 µg/L olarak bulunmuştur. Söz konusu iyonlar için adsorpsiyon kapasiteleri de 0,47 ± 0,02 mg/g, 0,81 ± 0,01 mg/g, 0,66 ± 0,01 mg/g, 0,58 ± 0,01 mg/g, 0,91 ± 0,01 mg/g, and 0,73 ± 0,02 mg/g olarak bulunmuştur. Onaylı referans malzemeleri kullanarak yöntemin kesinliği doğrulandı. Önerilen yöntem sigara, saç ve bazı sebze türlerine başarıyla uygulanmıştır.

Keywords: Metal kelatları, hematoksilin, ön derişiklendirme, FAAS.

(This article was presented to the 28th National Chemistry Congress and submitted to JOTCSA as a full manuscript)

Determination of Bisphenol A in Thermal Paper Receipts

M. Serkan Yalcin[1,*], Cihan Gecgel[1], Dilek Battal[1,2]

[1]Mersin University, Advanced Technology Education, Research and Application Center, 33343, Mersin, Turkey.
[2]Mersin University, Faculty of Pharmacy, Department of Toxicology, 33169, Mersin, Turkey.

Abstract: Bisphenol A (BPA) is a chemical substance which is produced in great quantities globally and of which serious negative effects on endocrine system are suspected. It is a commonly used color developer in thermal papers. BPA used for this purpose is in free, unbound form and is one of the potential sources for BPA exposure of humans. In this study, 12 thermal paper receipt samples were collected from various workplaces selected randomly and analyzed. BPA was determined in all samples. Average value of high BPA concentrations obtained from 10 samples was found as 13.83±0.69 mg BPA/g paper. At the same time, low values being 0.40±0.11 mg BPA/g paper and 0.11±0.05 mg BPA/g paper respectively were found in two samples as compared to others.

*Corresponding author. M. Serkan Yalçın. E-mail: serkanyalcin@mersin.edu.tr.

INTRODUCTION

Bisphenol A (BPA, 2,2-bis(4-hydroxyphenyl) propane) (Figure 1) is one of the chemical substances produced mostly in the world. It has generally been used in great quantities in manufacturing polycarbonate plastic, epoxy resin, dental materials as well as paper industry [1].

BPA is the subject of hot debates regarding "low dose" toxicological effects, *i.e.,* effects at doses clearly below the present tolerable daily intake (TDI) of 0.05 µg/kg body weight [2-4]. A great number of studies where BPA's effects on human health and especially on its destructive side effects are investigated were made and have continued to be made [5, 6]. BPA exposure of humans is basically through food and beverage. This is because epoxy resin used in producing containers where food and beverage are packed contains BPA. In addition, air, dust, and water are other sources of exposure. Furthermore, manual contact with thermal paper receipts received at the end of shopping is another source for BPA exposure [7, 8].

Thermal papers have been used as shopping mall receipts, public transportation tickets, lottery tickets, cinema tickets, airline tickets, *etc.* [9]. European Union's risk assessment report of BPA states that 168.000 tons of thermal paper is used per year in European Community and these papers contain 1890 tons of BPA [10]. BPA acts as a color developer in thermal papers [11]. It is present in its free, non-polymerized form and is thus easily available for uptake [12]. If a person who comes in contact with thermal paper receipts mentioned above in his-her daily life takes nourishment by direct contact of unwashed hands or by dermal contact, he/she has the BPA exposure. Furthermore, reusing these papers which were sent to recycling after usage in producing food and beverage containers by processing again has caused BPA contamination [13, 14].

In this study, BPA quantities of thermal paper receipts collected from different shops were determined and compared with other international studies.
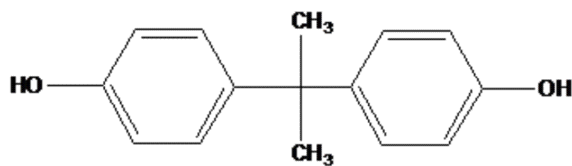
Figure 1: Molecular structure of BPA.

MATERIALS and METHODS

12 thermal paper receipt samples used in this study were collected from various workplaces randomly. We collected a fax paper, a bank account receipt, a bank card receipt, an ATM receipt, a lottery ticket, a gift store receipt, a gas station receipt, a restaurant receipt, and four shopping mall receipts (Table 1). Thermal printing paper was identified by its ability to darken upon heating. The samples were analyzed as soon as they were collected. The average BPA levels of samples were calculated by three parallel studies. The chemical substances were used of high purity.

20 mg of thermal paper receipt samples were cut into small pieces and extracted for 60 minutes in 50 mL of pure water in room temperature. After this extraction process, the BPA quantity passed into water was analyzed through high performance liquid chromatography (HPLC). All the HPLC analyses were carried out on a Agilent 1200 Series HPLC system equipped with an Supelco C_{18} column (100 x 2.1 mm, particle size 2.7 μm) using a mobile phase composed of water/acetonitrile (60:40, v/v) at a flow rate of 0.4 mL/min; the column temperature was 30 °C. Fluorescence excitation and emission wavelengths for BPA detection were 225 and 310 nm, respectively. Calibration line was formed between 25 and 200 μg BPA/L (R^2=0,999). Detection limit was calculated as 3.3 μg/L and relative standard deviations 1.1% for 6 measurements made in 30 μg/L.

RESULTS and DISCUSSION

The results of 12 thermal paper samples where BPA concentration was determined are shown in Table 1. BPA was found in all thermal paper receipts which were analyzed.

Average value of ten thermal paper receipts having high concentration ratios was calculated as 13.83 ± 0.69 mg BPA/g paper. This average value we obtained is compatible with the literature [15-20]. As seen in Table 1, the highest BPA concentration were determined in supermarket samples No: 2, 3, and 4. The results are 19.52 ± 0.71 mg BPA/g paper, 20.14 ± 1.23 mg BPA/g paper and 21.65 ± 0.83 mg BPA/g paper, respectively. When considering these results and excessiveness of customer circulation, supermarket cashiers may be the persons who have the highest risk of undergoing BPA exposure [21]. However, rather low values were determined as 0.40±0.11 mg BPA/g paper and 0.11±0.05 mg BPA/g paper respectively in one bank account receipt and one lottery receipt, comparing to other samples. In some thermal paper receipts, low BPA concentrations were determined also by Geens *et al*. (2012) (22). This situation can be described with the use of alternative chemical substances instead of BPA because of its bad name in recent years. Goldinger *et al.* (2015) (15) investigated some alternatives of BPA, namely bisphenol S (BPS), bisphenol F (BPF), Pergafast® 201 and D-8. Their study showed that D-8 and Pergafast® 201 could be good alternatives for the replacement of BPA. Recently some Swiss retailers announced stopping the use of thermal papers containing BPA. In addition, cross contamination can occur while BPA-free thermal papers are being processed along with high BPA content papers which are reprocessed in recycling plants [23]. In similar studies made with thermal paper samples in Belgium, Switzerland and U.S.A., the results of 15.00 mg BPA/g paper, 13.50 mg BPA/g paper and 12.50 mg BPA/g paper respectively were reported. However, the BPA values obtained in studies carried out in countries like Japan, Korea, and Vietnam were calculated between <LOD and 10.00 mg BPA/g paper. These values have been observed as low values when compared with other country's results. Reason of this situation may be tight control onto materials containing BPA applied by Japan [24].

CONCLUSION

According to the results we achieved, BPA concentration in 10 out of 12 thermal paper receipts analyzed is between 7.26 ± 0.58 and 21.65 ± 0.83 mg BPA/g paper. Similar results have also been reported in the literature. High BPA content ratio of thermal papers can cause contamination risk for "BPA-free" papers during reprocessing in recycling plants. Furthermore, waste waters containing BPA of these plants can give hazardous effects to environment. And the most important risk is thermal paper sourced BPA exposure of humans. According to Genns *et al.,* 2012; an estimation of human exposure through thermal paper results in a median intake of 445 ng BPA/day for the general population, which corresponds to an exposure of 6.4 ng/kg bw/day for a person of 70 kg. The exposure of those people who come occupationally in contact with thermal

paper can be much higher. Biomonitoring studies shall be required in the future so that influences of BPA on human health can be revealed completely.

Table 1.BPA concentrations in 12 thermal paper receipts according to the type of store (n=3).

Type of store	BPA (mg/g paper±SD)
Fax paper	7.26±0.58
Bank account receipt	0.40±0.11
Bank card receipt	14.96±0.54
ATM receipt	15.00±0.72
Lottery ticket	0.11±0.05
Gift store receipt	12.94±0.66
Gas station receipt	8.47±0.33
Restaurant receipt	10.78±0.67
Supermarket 1	7.59±0.61
Supermarket 2	19.52±0.71
Supermarket 3	20.14±1.23
Supermarket 4	21.65±0.83

REFERENCES

1. Geens T, Aerts D, Berthot C, Bourguignon J.P, Goeyens L, Lecomte P, Maghuin-Rogisterg G, Pironnet A.M, Pussemier L, Scippo M.L, Van Loco J, Covacia A. A review of dietary and non-dietary exposure to bisphenol-A. Food Chem. Toxicol.2012a;50(10):3725-3740. DOI:10.1016/j.fct.2012.07.059.

2. European Food Safety Authority (EFSA) Opinion of the Scientific Panel on Food Additives, Flavourings,   Processing Aids and Materials in Contact with Food on a request from the Commission related to 2,2-bis(4-hydroxphenyl)propane (bisphenol A) question number EFSA-Q-2005–100, adopted on 29 November 2006. The EFSA Journal.2006; 428:1–75. DOI: 10.2903/j.efsa.2007.428

3. NTP (2008) NTP-CERHR monograph on the potential human reproductive and developmental effects of bisphenol   A, September 2008, NIH Publication No. 08 – 5994. URL:http://cerhr.niehs.nih.gov/chemicals/bisphenol/bisphenol.pdf

4.EFSA (2008) Opinion on the toxicokinetics of bisphenol A. The EFSA Journal 759:1–10.URL:http://www.efsa.europa.eu/sites/default/files/scientific_output/files/main_documents/759.pdf

5.Christiansen S, Axelstad M, Boberg J, Vinggaard A.M, Pedersen G.A, Hass U. Low-dose effects of bisphenol A on early sexual development in male and female rats. Reproduction.2014;147: 477–487. DOI:10.1530/REP-13-0377.

6.Frederick V, Hughes C.An Extensive New Literature Concerning Low-Dose Effects of Bisphenol A Shows the Need for a New Risk Assessment.Environ. Health Perspect. 2005;113:926–933. DOI: 10.1289/ehp.7713.

7.Mielkea H,Partoschb F, Gundert-Remya U.The contribution of dermal exposure to the internal exposure of bisphenol A in man.Toxicology Letters.2011; 204:190–198.DOI:10.1016/j.toxlet.2011.04.032

8.URL: https://www.niehs.nih.gov/health/topics/agents/sya-bpa/

9.Baily A.B, Hoekstra E.J. Background paper on sources and occurrence of bisphenol A relevant for exposure of consumers. FAO/WHO expert meeting on bisphenol A (BPA) Ottawa, Canada, 2–5 November 2010. Available at: http://www.who.int/foodsafety/chem/ chemicals/2_source_and_occurrence.pdf.

10.JRC-IHCP, 2008. European Union Risk Assessment Report: 4, 4′-isopropylidenediphenol (Bisphenol-A). Eur. Union 2008, 201–245.   DOI:10.2788/40195.

11.PlasticsEurope, 2007. Applications of Bisphenol A. Polycarbonate/Bisphenol A (BPA) group of the industry association PlasticsEurope. URL:http://www.bisphenol-aeurope.org/uploads/applications%20of%20BPA%20Sept%2008.pdf.

12.Terasaki M, Shiraishi F, Fukazawa H.I, Makino M. Occurrence and estrogenicity ofphenolics in paper-recycling process water: pollutants originating from thermalpaper in waste paper. Environ Toxicol Chem. 2007;26:2356–66. DOI: 10.1897/06-642R.1.

13.Takahashi Y, Shirai A, Segawa T, Takahashi T, Sakakibara K. Why does a colordevelopingphenomenon occur on thermal paper comprising of a fluoran dye and a color developer molecule? Bull Chem Soc Jpn. 2002;75:2225–31. DOI:10.1246/bcsj.75.2225.

14.Petersen H, Schaefer A, Buckow C.A, Simat T.J, Steinhart H. Determination of bisphenol A diglycidyl ether (BADGE) and its derivatives in food: identification and quantification by internal Standard. Eur Food Res Technol.2003; 216:355–364. DOI: 10.1007/s00217-002-0648-1.

15.Goldinger D.M,Demierre A.L,Zoller O,Rupp H, Reinhard H,Magnin R, Becker T.W, Bourqui-Pittet M. Endocrine activity of alternatives to BPA found in thermal paperin Switzerland. Regul Toxicol Pharmacol.2015;71(3):453-62. DOI:10.1016/j.yrtph.2015.01.002.

16.Lu S.Y,Chang W.J,Sojinu S.O,Ni H.G.Bisphenol A in supermarket receipts and its exposure to human in Shenzhen, China.Chemosphere.2013;92(9):1190–1194. DOI: 10.1016/j.chemosphere.2013.01.096

17.Lassen C,Mikkelsen S.H,Brandt U.K.Migration of Bisphenol A from Cash Register Receipts and Baby Dummies.Environmental Protection Agency. (2011);1–67. URL:http://www2.mst.dk/udgiv/publications/2011/04/978-87-92708-93-9.pdf.

18.Liao C,Kannan K.Widespread occurrence of bisphenol A in paper and paper products: implications for human exposure.Environ. Sci. Technol.2011;45 (21):9372–9379. DOI: 10.1021/es202507f.

19.Mendum T,Stoler E,VanBenschoten H,Warner J.C. Concentration of bisphenol A in thermal paper.Green Chem. Lett. Rev.2011;4(1):81–86.DOI: 10.1080/17518253.2010.502908.

20. Biedermann S, Tschudin P, Grob K. Transfer of bisphenol A from thermal printer paper to the skin.2010;398:571-576. DOI 10.1007/s00216-010-3936-9.

21. Porras S, Heinälä M, Santonen T. Bisphenol A exposure via thermal paper receipts.Toxicol Lett.2014 Nov 4;230(3):413-20. DOI: 10.1016/j.toxlet.2014.08.020.

22. Geens T,Goeyens L,Kannan K,Neels H,Covaci A. Levels of bisphenol-A in thermal paper receipts from Belgium and estimation of human exposure.Sci Total Environ.2012; 435-436:30-3. DOI: 10.1016/j.scitotenv.2012.07.00.

23. Liao C,Kannan K.High levels of bisphenol A in paper currencies from several countries, and implications for dermal exposure.Environ Sci Technol.2011b;45: 6761–6768. DOI: 10.1021/es200977t.

24. Pivnenko K,Pedersen G.A,Eriksson E,Astrup T.F.Bisphenol A and its structural analogues in household waste paper.Waste Management.2015;44:39-47.DOI:10.1016/j.wasman.2015.07.017.

Türkçe Öz ve Anahtar Kelimeler

Termal Kâğıt Fişlerde Bisfenol A'nın Tayini

M.Serkan Yalcin*, Cihan Gecgel, Dilek Battal

*Corresponding author: M.SerkanYalcin. E-mail: serkanyalcin@mersin.edu.tr.

Öz: Bisfenol A (BPA) dünya çapında büyük miktarlarda üretilen ve bağışıklık sistemine ciddi negatif etkide bulunduğundan şüphelenilen bir kimyasal maddedir. Bu madde termal kâğıtlarda renk geliştirici olarak yaygın şekilde kullanılmaktadır. Bu amaçla kullanılan BPA serbest ve bağlanmamış bir haldedir ve insanlardaki BPA maruziyetinin potansiyel kaynaklarından biridir. Bu çalışmada, 12 termal kâğıt örneği, rasgele seçilen çeşitli çalışma yerlerinden toplanmış ve analiz edilmiştir. BPA bütün örneklerde bulunmuştur. 10 örnekten elde edilen yüksek BPA derişimlerinin ortalama değeri 13,83±0,69 mg BPA/g kâğıt olarak tespit edilmiştir. Aynı zamanda, diğerleriyle karşılaştırıldığı zaman iki örnekte sırasıyla 0,40±0,11 mg BPA/g kâğıt ve 0,11±0,05 mg BPA/g kâğıt olarak düşük değerler bulunmuştur.

Anahtar kelimeler: Bisfenol A, BPA, Termal kâğıt, insanda maruziyet.

Optical Properties of Al:ZnO Thin Film Deposited by Different Sol-Gel Techniques: Ultrasonic Spray Pyrolysis and Dip-Coating

Ebru Gungor[1]* and Tayyar Gungor[1]

[1]Mehmet Akif Ersoy University, 15030 Burdur, Turkey

Abstract: Undoped and Al-doped ZnO polycrystalline thin films have been fabricated on glass substrates by using a computer-controlled dip coating (DC) and ultrasonic spray pyrolysis (USP) systems. The film deposition parameters of DC process were optimized for the samples. In this technique, the substrate was exposed to temperature gradient using a tube furnace. In the study, the other solvent-based technique was conventional USP. The zinc salt and Al salt concentrations in the solution were kept constant as 0.1 M and 2% of Zn salt's molarity, respectively. The optical properties were compared for the films deposited two different techniques. The optical transmission of Al:ZnO/Glass/Al:ZnO sample dip coated and the optical transmission of Al:ZnO/Glass sample ultrasonically sprayed were determined higher than 80% in the visible and near infrared region. Experimental optical transmittance spectra of the films in the forms of FilmA/Glass/FilmA and FilmA/Glass were used to determine the optical constants. It was observed that the optical band gaps of Al doped ZnO films onto glass substrate were increased with increase of Al content and the absorption edge shifted to the shorter wavelength (blue shift) compared with the undoped ZnO thin film.

INTRODUCTION

In 1742, a method of coating iron by dipping it in molten zinc was described by Malouin [1]. Nowadays, this technique has different applications fields such as coating the surface of the materials with protective agents or coloring materials. Materials in almost any geometry can be coated using this technique. In addition to coating of large-scale material, this technique was used to deposit to the metal oxide semiconductors (ZnO, TiO_2, SnO_2 and WO_3). Investigation of compound semiconductor-focused work has gained momentum [2]. It is possible to coat the surface of the material using the liquid phase growth techniques. These techniques are generally divided into three groups such as sol-gel, chemical baths, and electrochemical methods. The sol-gel method is widely used in thin film coating. In the sol-gel process, the precursor solution can be coated on the substrate by dip coating, spray pyrolysis, and spin coating techniques. In recent years, ZnO, prepared by various deposition methods such as reactive evaporation [3], RF sputtering [4], chemical vapor deposition [5], ultrasonic spray pyrolysis [6-8], sol-gel method [9], and dip coating method [10], have found very different application areas for optoelectronics and sensor technology applications. In addition to changes of the optical constants, the change in the band gap may be advantageous in the technological use of the films. While the increase in the band gap can be useful in poly-crystalline solar cells, the decrease in the band gap can be applicable for gas detection such as CO [11]. The number of studies that examined the changes in the optical and electrical properties due to the elements to be incorporated into the ZnO lattice is increasing. The substrate temperature is an important parameter for the formation of the thin film. For example, the substrate temperature is kept at a given temperature in USP technique. However, substrate is kept at room temperature and dip number is increased for the formation of the film for the DC technique. However, during DC process pre-heating or after the deposition-post heating can be done. The samples were exposed to temperature gradient from the room temperature to set temperature then subject to post heating using DC system.

In this study, using the *modified dip coating system (MDC)* pre-heating and post-heating features are added using the tube furnace, which was used in the vertical geometry. Undoped and Al-doped ZnO polycrystalline thin films have been fabricated on glass substrates using dip coating (DC) and ultrasonic spray pyrolysis (USP) systems. In this way, although a small number of dip process to be done the film formation on the substrate becomes more prominent. Substrate temperature was kept at 400 °C for USP

system. In order to compare the samples deposited by DC, post heating temperature set at 400 °C. Moreover, the changes in optical transmittance of Al doped ZnO thin films were examined.

MATERIALS and METHODS

Experimental details

The home-made computer-controlled dip coating system was modified by adding the heating facilities after the withdrawing process (Figure 1). In this system, the tube furnace which was used in the vertically was added to the system for pre-heating and post-heating up to 400 °C for the dipping process. The details of the previous dip coating system are given in the reference [10]. The vertical movement distance is also expanded about up to 40 cm using the modified mechanical unit. Stepper motor and threaded spindle is provided with a 5 μm precision movement. Another modification is changing the home-made stepper motors driver unit with a commercial one (Leadshine step motor drive unit M542 model). This unit has a micro-step feature. Thus, a number of steps for one revolution can vary from 400 to 25000 steps. The step control is made by means of the computer's printer port. M542 stepper motor drive unit can be controlled by two data bits such as D1 and D0. Using a suitable computer program such as LabView, dipping time, dwell time, withdrawal rate, and pre-heating time of the substrate can be adjusted to the desired value.
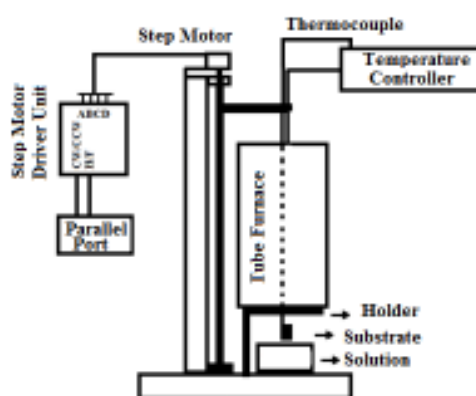
Figure 1. The schematic diagram of modified dip coating (MDC) system.

The salts zinc acetate dehydrate ($Zn(CH_3COO)_2.2H_2O$, 99.9%-Merck) and Al chloride hexahydrate ($AlCl_3.6H_2O$, 99.9%-Merck) as the metal sources were dissolved in methanol. In order to produce a clear and homogeneous solution, monoethanolamine (MEA) was added into the precursor solution which was stirred at 60°C at a moderate

speed for 1 h. Al and Zn concentrations were kept at 0.002 M and 0.1 M in the starting solutions, respectively. This precursor solution was used to deposit ZnO and Al:ZnO (AZO) thin films on to ultrasonically cleaned glass substrates using the conventional USP and MDC systems.

The ZnO and AZO thin films (2 layers) were deposited on both sides of the glass substrate, withdrawal speed fixed at 1 cm/min and the deposition time at 30 s. In USP method, the position of substrates was fixed and precursor solution was sprayed over a hot substrate. The substrate temperature was kept at 400°C. The solution flow rate was held constant at 5 mL/min. The nozzle (100 kHz oscillator frequency) used in this study was in a downward vertical configuration. A more detailed description of the USP system was reported in previous papers [8]. X-ray diffraction (XRD) spectra were collected with a D-Max X-ray diffractometer (Rigaku International Corp. Japan) with CuK$_\alpha$ (λ=1.5405Å) to obtain the structural information of the films. The optical measurements of the Al:ZnO thin films were carried out at room temperature using T70 Model Spectrophotometer (PG Instrument) in the wavelength range 300–900 nm.

Table 1. Calculated film thickness of the single sided (t) and double sided (t_1 and t_2) thin films deposited by DC. Calculated refractive index n for 700nm wavelength and optical band gap values E_g (eV).

Thin film profile	Dip number	t_1 (nm)	t_2 (nm)	n (700nm)	E_g (eV)
ZnO/Glass/ZnO	2	138	120	1.66	3.29
Al:ZnO/Glass/Al:ZnO	2	95	133	1.46	3.33

Table 2. Calculated film thickness of the single sided (t) thin films deposited by USP. Calculated refractive index n for 700nm wavelength and optical band gap values E_g (eV).

Thin film profile	t_1 (nm)	n (700nm)	E_g (eV)
Al:ZnO/Glass	104	1.67	3.32
ZnO/Glass	602	2.00	3.23

RESULTS and DISCUSSION

Structural Characterization

The X-ray patterns for ZnO and Al:ZnO thin films deposited by USP and DC films at room temperature are presented in Figures 2 and 3, respectively. The hexagonal wurtzite structure of ZnO seems to be protected for both samples group. It was observed that the

(002) peak indicating a strong orientation along the *c*-axis for USP type undoped ZnO film. For the USP type Al:ZnO film (200) and (101) as well as (110) and (103) peaks were observed. But the intensities of peaks are decreased when a small amount of Al was inserted into the ZnO lattice structure. There was no impurity and/or unreacted phase of Zn and Al for the DC type ZnO and Al:ZnO thin film. The peaks (100), (200), (101), (102), (110) and (103) were observed. But there are no dominant peaks considering (100), (002) and (101). In addition, detection of (102), (110) and (103) peaks were hard for the DC type Al:ZnO thin film.
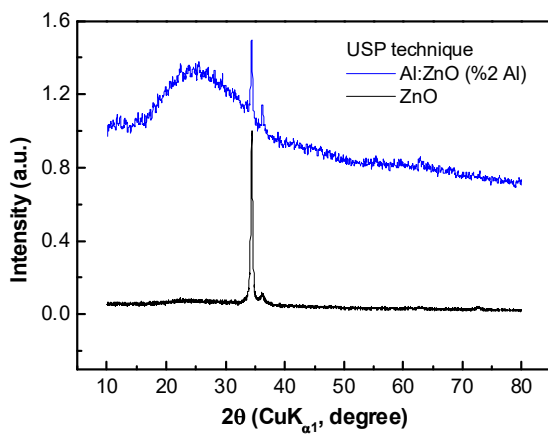
Figure 2. XRD patterns of Al:ZnO and ZnO thin films deposited by USP technique.
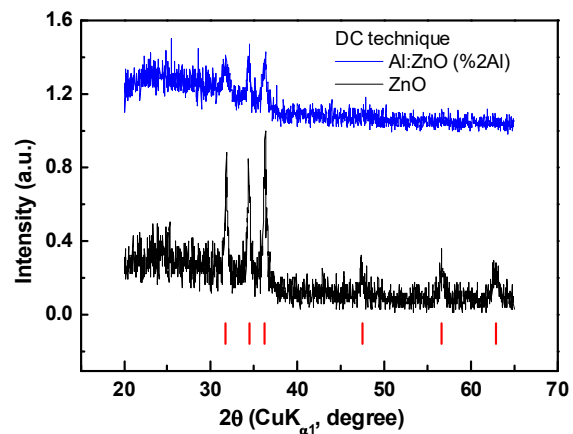
Figure 3. XRD patterns of Al:ZnO and ZnO thin films deposited by DC technique. "|"indicates the reference peaks for ZnO (JCPDS file no. 03-065-3411).

Optical characterization

The optical transmission spectra of undoped ZnO and Al-doped ZnO thin films are shown in Figure 4. The effects of Al doping into the ZnO lattice is clearly observed in the optical transmission spectra. First, optical transmittance increased rapidly due to the incorporation of Al. Because Al incorporation decreases the refractive index that can cause increases for the transmittance. This result is clearly observed in the optical transmission spectrum. Optical band gaps of the thin films can be determined using this wavelength with the relation, $E_g(eV) = 1240.8/\lambda_{inf}$. Where λ_{inf} is the defined as the inflexion wavelength where the second derivative of the transmission curve is zero. The optical band gap (E_g), was estimated from the second derivative of the $T(\lambda)$ (Table 1). The optical band gaps of Al doped ZnO films onto glass substrate are increases with increase of Al content and the absorption edge shifted to a shorter wavelength (blue shift) compared with the undoped ZnO thin film.
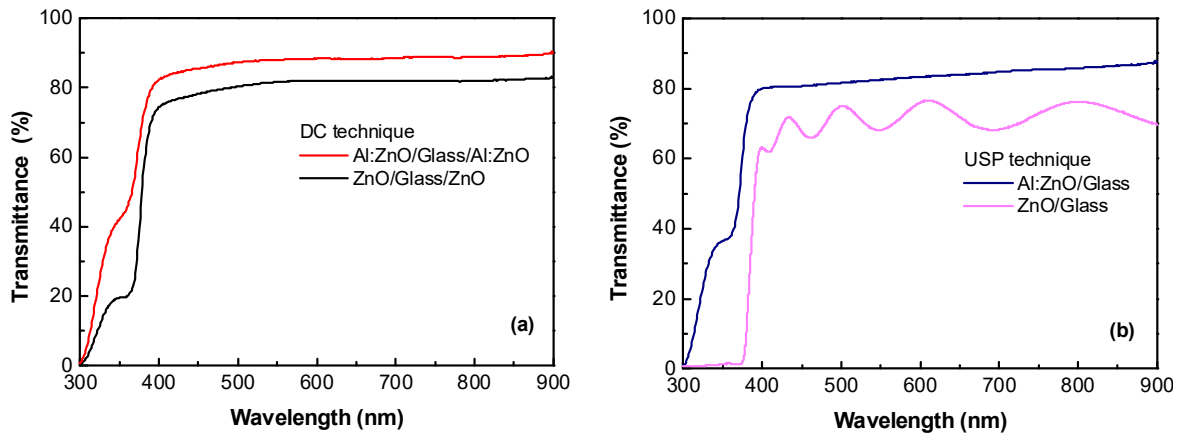
Figure 4. Transmittance spectra of Al:ZnO and ZnO films deposited by **(a)** DC technique and **(b)** USP technique.
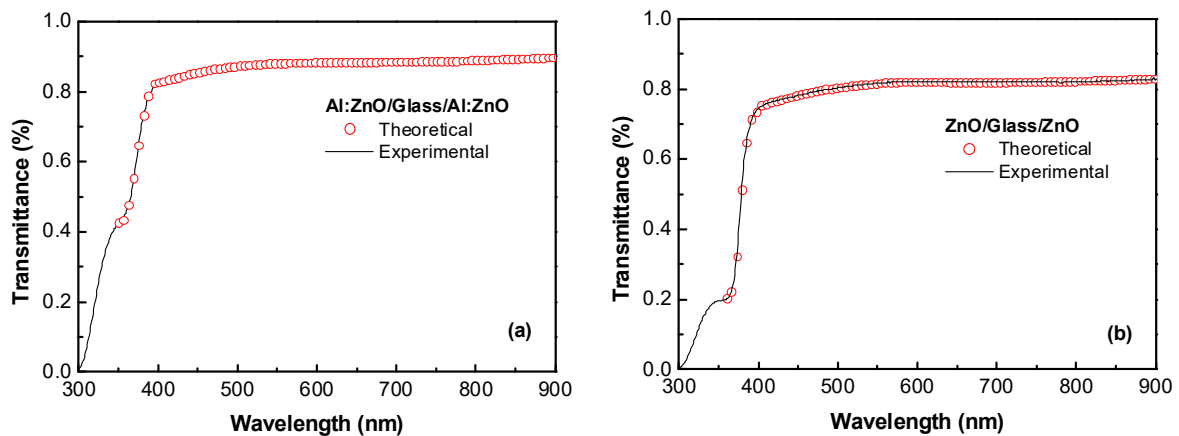
Figure 5. Experimental and calculated optical transmittance spectra of **(a)** double sided Al:ZnO and **(b)** double sided ZnO films deposited by dip coated technique.

The estimated thicknesses of thin films were obtained using the optical transmittance spectra in the range 300-900 nm. The optical constants such as thickness and refractive indexes of thin films in the form of Film A/Glass/Film A or Film A/Glass can be obtained using a method called *Pointwise Unconstrained Minimization Algorithm (PUMA)* developed by Birgin [12]. The main advantage of this method is that it does not need the interference fringes in the optical transmission spectrum. There is excellent agreement between the experimental spectra and theoretical spectra for all the Al:ZnO/Glass/Al:ZnO, ZnO/Glass/ZnO and Al:ZnO/Glass and ZnO/Glass samples. Two of the experimental and computed optical transmission spectra for the Al:ZnO/Glass/Al:ZnO and ZnO/Glass/ZnO thin films are shown in Figure 5. Calculated film thickness and refractive index for 700 nm are given in Tables 1 and 2. Decreasing the refractive index that is indicates the band gap shift and increase in transmittance.

CONCLUSION

We have demonstrated an effective dip-coating method for synthesis of undoped ZnO and Al:ZnO thin films. In this method, although a small number of dip process to be done, the film formation on the substrate becomes more prominent. It is because the samples were exposed to temperature gradient between the dipping periods. As a result, considerable changes were observed in the optical transmission spectra of the films. Optical transmittance spectra of the films in the form of Film A/Glass/Film A were used to determine the film thickness and optical band gaps. The optical transmission of Al:ZnO/Glass/Al:ZnO samples was higher than 80% in the visible and near infrared region. The optical band gaps of Al doped ZnO films onto glass substrate are increases with increase of Al content and the absorption edge shifted to a shorter wavelength (blue shift) compared with the undoped ZnO thin film. According to the results an increases of the band gap for AZO films prepared by both DC and USP techniques. The hexagonal wurtzite structure of ZnO seems to be protected for Al:ZnO thin film. However, there is no preferential orientation such as (002). In addition, the peaks intensities are decreased when a small amount of Al was inserted into the ZnO lattice structure.

ACKNOWLEDGMENTS

REFERENCES

[1] http://en.wikipedia.org/wiki/Hot-dip_galvanizing

[2] Ignjatovic N, Brankovic Z, Dramicanin M, Nedeljkovic J. M, and Uskokovic D. P, Preperation of TiO2 and ZnO Thin Films by Dip-Coating Method. Materials Sciences Forum. 1998; 282-283:147-152. DOI:10.4028/www.scientific.net/MSF.282-283.147.

[3] Jin M, Ying L. S, Preperation of ZnO films by reactive evaporation. Thin Solid Films. 1994; 237: 16-18. DOI:10.1016/0040-6090(94)90230-5.

[4] Aktaruzzaman A. F, Sharma G. L, Malhotra L.K, Electrical and Optical Properties of Germanium-Doped Zinc Oxide Thin Films. Thin Solid Films. 1991; 198: 67-74. DOI:10.1016/0040-6090(91)90325-R.

[5] Chen Z, Shum K, Salagai T, Zhang W, Strobl K, ZnO thin films synthesized by chemical vapor deposition. Applications and Technology Conference (LISAT), 7 May 2010; 1-6. DOI: 10.1109/LISAT.2010.5478331.

[6] Erarslan N, Güngör T, The determination of the thickness and optical constants of the ZnO crystalline thin film by using pointwise unconstrained minimization algorithm. Journal of Graduate School of Natural and Applied Sciences of Mehmet Akif Ersoy University. 2010; 2: 181-193.

[7] Gungor E, Gungor T, Effect of the substrate movement on the optical properties of ZnO thin films deposited by ultrasonic spray pyrolysis, Advances in Materials Science and Engineering. 2012;1-7 Article ID 594971. DOI: 10.1155/2012/594971.

[8] E. Gungor, T. Gungor, D. Caliskan, A, Ceylan, and E. Ozbay, Applied Surface Science, 2014; 318; 309–313. DOI:10.1016/j.apsusc.2014.06.132.

[9] Lee J. H, Park B. O, Transparent conducting ZnO:Al, In and Sn thin films deposited by the sol–gel method. Thin Solid Films. 2002; 426: 94-99. DOI: 10.1016/0040-6090(91)90325-R.

[10] Gungor T, Gungor E, Computer Controlled Dip Coating System Design. Journal of Graduate School of Natural and Applied Sciences of Mehmet Akif Ersoy University. 2012; 3:1-4.

[11] Hadipour N. L, Peyghan A. A, and Soleymanabadi H, Theoretical Study on the Al-Doped ZnO Nanoclusters for CO Chemical Sensors. The journal of Physical Chemistry C. 2015; 119; 6398-6904. DOI:10.1021/jp5130192.

[12] Birgin E. G, Chambouleyron I, and Martinez J. M, Estimation of optical constants of thin films using unconstrained optimization. Journal of Computational Physics. 1999; 151: 862-888.

Türkçe Öz ve Anahtar Kelimeler

Farklı Son-Gel Teknikleri ile Biriktirilmiş Al:ZnO İnce Filmlerinin Optik Özellikleri: Ultrasonik Sprey Pirolizi ve Daldırmalı Kaplama

Ebru Gungor* and Tayyar Gungor

Öz: Aşılanmamış ve Al ile aşılanmış çok kristalli ince filmler cam substratlar üzerinde bilgisayarla kumanda edilen daldırmalı kaplama (DC) ve ultrasonik püskürtmeli piroliz (USP) sistemleriyle üretilmiştir. DC sürecinin film biriktirme parametreleri örnekler için en uygun hale getirilmiştir. Bu teknikte, substrat bir tüp fırını kullanılarak sıcaklık gradyanına maruz bırakılmıştır. Çalışmada, diğer çözücü esaslı teknik ise geleneksel USP'dir. Çözeltide çinko tuzunun ve alüminyum tuzunun derişimleri sırasıyla 0,1 M ve çinko tuzunun molaritesinin %2'si olarak sabit tutulmuştur. Optik özellikler iki farklı teknikle biriktirilen filmler için karşılaştırılmıştır. Daldırmayla kaplanmış Al:ZnO/Cam/Al:ZnO örneğinin ve ultrasonik yöntemle püskürtülmüş Al:ZnO/Cam örneğinin optik geçirgenliği görünür alanda ve yakın kızılötesi alanda %80 daha yüksek bulunmuştur. Optik sabitleri belirlemek için FilmA/Cam/FilmA ve FilmA/Cam biçimlerinde filmlerin deneysel optik geçirgenlik spektrumları kullanılmıştır. Cam üstüne Al ile aşılanmış ZnO filmlerinin kaplandığı örneklerde optik band aralıkları Al içeriğinin artması ile yükselmiştir ve aşılanmamış ZnO ince filmleriyle karşılaştırıldığı zaman soğurma eşiği daha düşük dalgaboyuna (maviye) kaymıştır.

Anahtar kelimeler: Sol-jel, daldırmalı kaplama, ultrasonik püskürtmeli piroliz, Al aşılı çinko oksit, optik sabitler.

Sunulma: 9 Temmuz 2016. **Düzeltme:** 15 Ağustos 2016. **Kabul:** 23 Ağustos 2016.

RESEARCH ARTICLE

Characterization of Magnetic Polymeric Microparticles

Kazım Köse

Hitit University, Scientific Technical Research and Application Center, Çorum, Turkey.

Abstract: The separation process is very important in a variety of scientific fields, especially in biochemistry and biotechnology. The separation performance of a method can be determined by the separation time and the purity of the separated molecule, which is directly proportional with the ligand chosen for the target molecule. The separation time is actually a very important step for the cost and the time-dependent analysis, especially in medical applications. Magnetic separation is a very advantageous technique because it eliminates the time-consuming sample preparation and centrifugation steps. However, the magnetic performance of adsorbent may not be strong enough to respond the magnetic force applied externally. Therefore, in nanoparticle studies, magnetic performance of nanoparticles is highly important. In this study, the magnetic performance of polymeric microparticles synthesized using different magnetic cores (Fe_2O_3 & Fe_3O_4, Fe & Ni, Ni & Co, Fe & Ni & Co) with a solid support, HEMA (2-hydroxyethylmethacrylate), and a functional monomer, AdeM (adenine methacrylate), were compared. Some other properties such as size, zeta potential, surface morphology, *etc*. were also studied.

*Corresponding author. E-mail: kazimkos1903@gmail.com. GSM: +905535478078.

INTRODUCTION

There are a variety of applications in the fields such as high-density data storage, ferro-liquids, magnetic resonance imaging, wastewater treatment, protein purification, biomedical (1-7), and especially clinical (8, 9) areas (10, 11). The classical separation and purification techniques have been replaced by magnetic separation methods in terms of the removal of the long steps, including filtration and centrifugation (12, 13) or disadvantages like decomposition, inactivation, or deformation of biomolecules (14). The magnetic separation techniques, as expected, requires magnetic particles to satisfy some vital features such as colloidal sustainability, equality in size, low poly dispersity index, the high and equal amount of magnetite content, superparamagnetic behavior, and effective surface functional groups to interact with active biological ligands (15). There is a variety of methods to synthesize magnetic polymeric spheres like emulsion (16) and multistep swelling polymerization (17), solvent evaporation (18), *etc*. In contrast to these methods, providing very complex or broad polydispersity index, the dispersion polymerization has been suggested as an alternative method to synthesize micron-sized magnetic particles (19). The most crucial advantage of this method is being simple: It is a single-step technique providing mono-size particles under desired conditions (20). The polymeric magnetic particles are quite available candidates in terms of and due to the high mechanical resistance, insolubility and wonderful shelf-life (21), having a variety of surface functional groups, (22-26), good mechanical features, easy preparation, and biocompatibility developed for bio-friendly components (27). Poly(2-hydroxyethyl methacrylate) [Poly(HEMA)] has been considered as a suitable matrix for enzyme immobilization due to being a biocompatible synthetic polymer with a good mechanical strength for several biomedical and biotechnological applications (28). Magnetic separation techniques have a number of applications in biosciences especially in laboratory scale (29). The magnetic separation is very fast and simple with the requirement only a simple apparatus, namely magnetite (30). The magnetic carriers also decrease the cost of operation and supply (31-34). Beside the providing solution for diffusion limitation, nanoparticles providing the increase of the adsorption capacity of the solid support are alternative for the macroporous microparticles (3, 21, 35, 36). High surface area and lack of carrying limitations make the magnetic nanoparticles the desired choice for the purification of biomolecules (37). However, the main problem in the use of nanoparticles is agglomeration. In this aspect, researchers should be very careful while using nanoparticles.

Spinel ferrite (SF) magnetic materials are an important class of metal oxide composites including iron ions with the structural formula of $M^{2+}Fe_2^{3+}O_4$ (M = Mg^{2+}, Co^{2+}, Ni^{2+}, Zn^{2+}, Fe^{2+}, Mn^{2+}, *etc*.). SFs have unique properties such as perfect magnetic characteristic, high surface area, surface active sites, surface chemical stability, controllable size, and easy functionalization and modification. Because of multi-functionality, being cost effective, and high capacity of magnetic separation, SF adsorbents are the first as a choice for the purification process with the requirement of high adsorption effectivity and fast kinetics (38).

Iron-oxide based materials are at the center for the nanostructured magnetic materials and because of the being naturally abundant, cost-effective and environmentally friendly, they are studied in a large spectrum of research (38).

Iron(III) oxide (Fe_2O_3) or iron(II-III) oxide (Fe_3O_4) (39) and also Fe & Ni (40) and Fe & Co (41, 42) double salts were used to get magnetic polymeric materials in some studies up to now. There is almost not yet any research with the double salt in the literature. In this study, the salts of Fe_2O_3 and Fe_3O_4, Fe & Ni, Fe & Co, Ni & Co and Fe & Ni & Cu structures were synthesized and the polymeric particles with these salts were compared in terms of size, magnetism, *etc*.

MATERIAL AND METHODS

Material

The chemicals [cobalt(II) nitrate hexahydrate, iron(II) nitrate nonahydrate, toluene, sodium nitrite and potassium carbonate] needed for the double salt synthesis process were obtained from Sigma-Aldrich (St. Louis, MO, USA). The polymerization of microparticles was run using polyvinyl alcohol (PVA) (cold water soluble, MW 31,000–50,000), ethylene glycol dimethacrylate (EGDMA), 2-hydroxyethyl methacrylate (HEMA), and methacryloyl chloride obtained from Aldrich (Munich, Germany). The initiator [azobis(isobutyronitrile) (AIBN)] used in this experiment obtained from Fluka (St. Gallen, Switzerland). Fe_2O_3 and Fe_3O_4 N-methacryloyl adenine (43) and double and triple salts [Fe(II)-Co(II), Fe(II)-Ni(II), Ni(II)-Co(II), Fe(II)-Co(II)-Ni(II)] (44) used were synthesized in the laboratory according to the literature (42). Monomers were maintained in a refrigerator at 4 ºC until use. The remaining chemicals not mentioned above are of analytical grade.

Methods

First step, synthetic process of poly(HEMA-AdeM) microparticles with magnetic core: The suspension polymerization technique was used to obtain m-poly(HEMA-AdeM) microparticles (45). 50 mg of adenine methacrylate (AdeM) was added to the mixture of 2 mL of 2-hydroxyethyl methacrylate and 4 mL of ethylene glycol dimethacrylate. After AdeM was totally dissolved, toluene (6 mL) was added as a diluent. 200 mg of polyvinyl alcohol and 50 mL of distilled water were mixed to have dispersion medium. Before treatment with nitrogen gas, the two media were mixed with each other. The polymerization process was started with the addition of 50 mg azobis(isobutyronitrile) and also 1 g of the magnetic core (Fe_2O_3 and Fe_3O_4 for mc-Fe_2O_3 & Fe_3O_4-poly(HEMA-AdeM), Fe-Ni double salt for mc-Fe & Ni-poly(HEMA-AdeM), Fe-Co double salt for mc-Fe & Co-poly(HEMA-AdeM), Ni-Co double salt for mc-Ni & Co-poly(HEMA-AdeM) and Fe-Ni-Co triple salt for mc-Fe & Ni & Co-poly(HEMA-AdeM)). The polymerization process was completed at the end of stirring (the conditions; 500 rpm, 65°C, 6 h and 650 rpm, 85°C, 2 h) for 8 hours. All microparticles were washed to get rid of the unreacted chemicals and other contaminants, and they were remained under vacuum at 45–50 °C for a day.

Second step, characterization process: The magnetic properties owned by the microparticles were determined using vibrating sample magnetometer (VSM) (Quantum Design, Physical Properties Measurement System (PPMS), USA). The hysteresis curves for all particles were obtained under the external magnetic field of 20,000/+20,000 G at room temperature. The surface morphology of microparticles was determined using scanning electron microscopy (SEM; Carl Zeiss AG - EVOR 50 Series, Germany). The microparticles were dried at 50 °C overnight before the analysis. The Fourier transform infrared spectroscopy (FT-IR, Thermo Scientific Nicolet 6700 FT-IR spectrometer, USA) was used in the wavenumber range of 400–4000 cm^{-1} to identify the characteristic peaks obtained from structures, especially nitrogen containing AdeM molecules. 98 mg of IR-grade KBr was mixed with the microparticles of approximately 1 g. The Brunauer-Emmett-Teller (BET), (Quantachrome Autosorb® iQ-Chemi, USA) analysis was performed to investigate the specific surface area of microparticles. Carefully dried microparticles using vacuum oven under the conditions of 20 mbar, 6 h were run the adsorption of nitrogen gas at 200°C, but the desorption process at room temperature.

RESULTS AND DISCUSSION

Characterization Data

The structure of microparticles synthesized in this study was assumed as given in Figure 1. As can be understood from the figure, there is a magnetic core in the center and the polymerization of HEMA and the monomer form of adenine were polymerized by surrounding of the magnetic core. As a result of this polymerization, spherical microparticles were obtained.
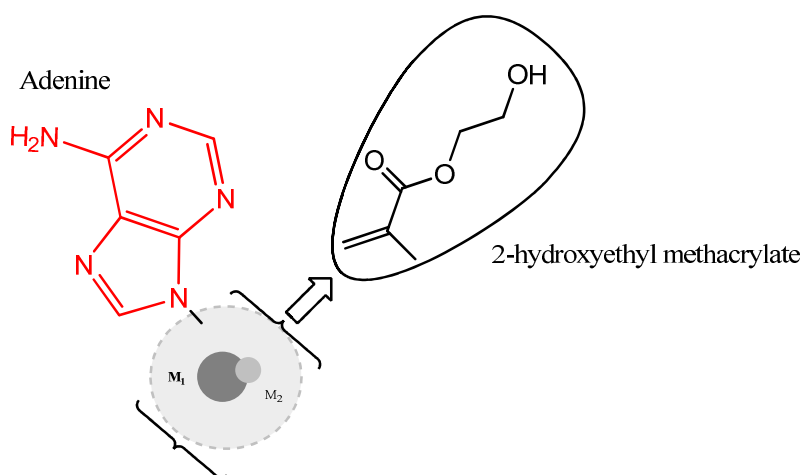
Figure 1. Expected polymeric structure of mc-M1&M2-poly(HEMA-AdeM) microparticles.

From the FTIR spectral data, the synthesis of m-poly(HEMA-AdeM) microparticles was proved by the bands obtained especially at 1636.03 cm^{-1} for amide (I and II), at 1558.17 cm^{-1} and 1456.44 cm^{-1} for ester, at 1730.94 cm^{-1} for carbonyl (C=O) stretching and at 1071.84 cm^{-1} for C-N=C stretching (Figure 2).

Figure 2. FTIR spectra of microparticles.

The perfect spherical structure and rough surface of microparticles can be seen in the SEM images of the m-poly(HEMA-AdeM) microparticles (Figure 3). The roughness is actually advantageous in terms of the existence of functional groups and the attachment of target molecules. Moreover, some of the microparticles like in Figure 3.b are equidimensional, but some are not. The reason for this may be the slight daily changes in environmental conditions, personal error or the characteristics of the magnetic core. After all, the polydispersity indexes of all microparticles obtained are almost <0.5.

Figure 3. SEM images of microparticles: a) mc–Fe$_2$O$_3$ & Fe$_3$O$_4$-poly(HEMA-AdeM), b) mc–Fe & Ni-poly(HEMA-AdeM), c) mc–Fe & Co-poly(HEMA-AdeM), d) mc–Ni & Co-poly(HEMA-AdeM), e) mc–Fe & Ni & Co-poly(HEMA-AdeM).

The theoretical sizes of the magnetic core were calculated as given in Table 1. The polymeric microparticles with Fe & Co magnetic core have the lowest ionic radii, in parallel with this the highest is Fe & Ni & Co magnetic core as expected due to the number of the metallic cores which is one more than the former. However, in the light of Brunauer-Emmett-Teller (BET) analyses (the specific surface areas given in Table 2), it is obvious that the molecular size and also the double salt character affect the size construction of microparticles and thus specific surface area. From the data, the lowest particle size and thus the highest surface area are owned by the mc-Fe & Ni-poly(HEMA-AdeM) microparticles. The reason for this contradiction may be attributed to the interaction between the metals and the polymeric structure, *i.e.* the interaction between Fe & Ni is somewhat higher than that of Fe & Co or the polymerization process around the metallic core. Moreover, the microparticles with the large surface area will have a high amount of adsorption capacity. This is also proof of a thin polymer layer surrounded over magnetic core.

Another useful data given in Table 2 is the zeta potential, providing the degree of intermolecular interaction. As can be seen from the table, all microparticles have good zeta potential values indicating the existence of almost no intermolecular interaction microparticles have.

Table 1. The theoretical size of magnetic cores formed by double and triple salts.

	Fe	Ni	Co	Total
Ionic radius				
Fe-Ni	0.55	0.69		1.24
Fe-Co	0.55		0.65	1.20
Ni-Co		0.69	0.65	1.34
Fe-Ni-Co	0.55	0.69	0.65	1.89

RESEARCH ARTICLE

Table 2. Some specific properties of microparticles.

Microparticles	Size (μ)	S. Area (m²/g)	BJH S. Area (m²/g)	Pore Volume (cc/g)	Pore Radius Dv (r) (Å)	Zeta Pot. (mV)	Ligand Incorp. (N%)
1) mc-Fe2O3 & Fe3O4-poly(HEMA-AdeM)	2.745	39.178	35.647	0.155	17.078	-24.9	1.08
2) mc-Fe & Ni-poly(HEMA-AdeM)	1.534	113.478	91.376	0.380	21.566	8.06	1.08
3) mc-Fe&Co-poly(HEMA-AdeM)	2.545	51.216	36.687	0.084	17.063	-24.1	0.79
4) mc-Ni&Co-poly(HEMA-AdeM)	3.452	6.884	5.367	0.040	15.280	-23.8	0.82
5) mc-Fe & Ni&Co-poly(HEMA-AdeM)	4.446	4.103	3.248	0.026	17.082	-22.9	0.53

The hysteresis curves of m-poly(HEMA-AdeM) microparticles are given in Figure 4. According to these curves, it is obvious that all microparticles have significant paramagnetic character. There was a loss observed in the magnetic behavior, which may be because of the oxidation during the process causing the iron oxide, nickel oxide, and cobalt oxide molecules, actually nonmagnetic, in the chain of polymeric materials. The main reason for this phenomenon is the oxidizing initiator fragment. In the light of the Mrs/Ms values of microparticles (0.1-0.3), it can be concluded that the microparticles synthesized in the scope of this study all have almost natural magnetism due to the pseudo-single-domain grains (46). These particles are irregularly-shaped and thus they have domain imbalance resulting in stability to thermal demagnetization and alternating field. Consequently, as can be seen from the figure, the mc-Fe & Ni-poly(HEMA-AdeM) microparticles have the highest and regular magnetism. However, the magnetism of Fe & Co double salt incorporated polymeric material should be higher than that of Fe & Ni because of smaller size and higher electron delocalization resulting higher magnetic field, but it is not. The explanation may be the negative effect of Co(II), d^7 metal with 3 paramagnetic d orbitals but Ni(II), a d^8 metal, has two paramagnetic orbitals diminishing the magnetic power of iron, on the d orbitals of the Fe which is the source of Fe magnetism, and thus the magnetic power of iron may be diminished but less for the nickel case. As a conclusion, the magnetism of Fe & Ni is a little bit higher than that of Fe & Co double salt incorporated polymeric material.
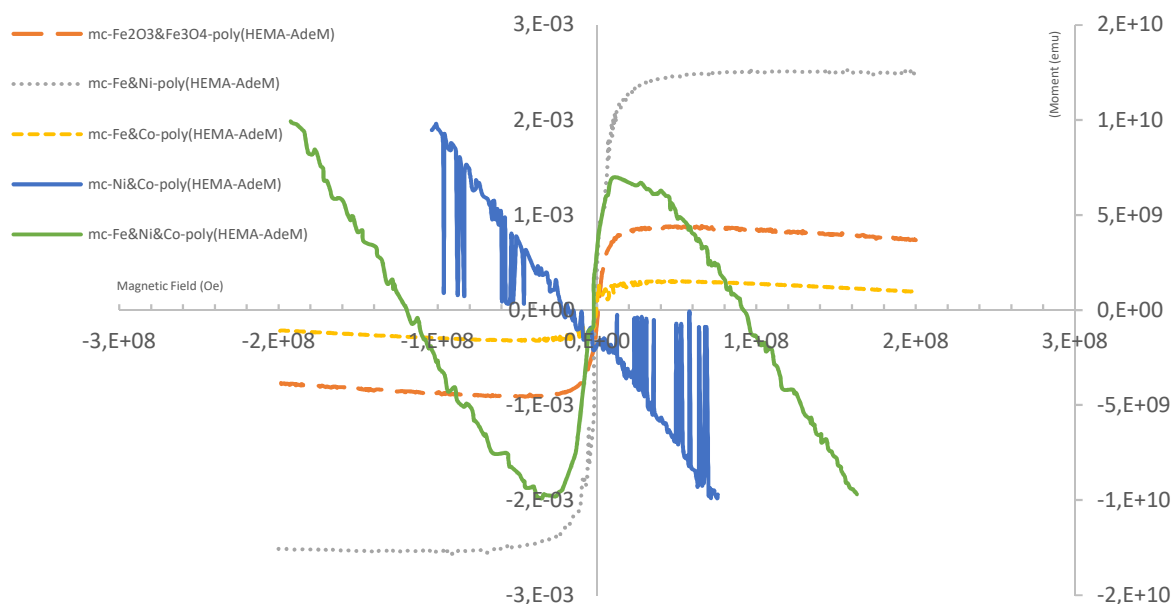
Figure 4. The magnetic hysteresis curves for microparticles.

The application of an external field to the sample may create an internal field which may be added to or subtracted from external field. To produce local magnetic effective field ($H_{effective}$) produced by electronic magnetic moment, it should be done vector addition to the external magnetic field ($H_{external}$).

$$H_{effective} = H_{external} + H_{local} \qquad \text{(Eq. 1)}$$

The molecules with an unpaired electron can be analyzed using an electron spin resonance device (ESR, Bruker ELEXSYS E580, Germany), indicating whether these molecules have a magnetic feature or not. This method also proves the incorporation of magnetic double salts into the polymeric structure.

An external magnetic field applied to a material with an unpaired electron pair produces energy levels with the energy difference known as ΔE depending on magnetic moments. The difference between these energy levels is equal to $\Delta E = g.\beta.H$. The magnetic field at the time of equivalence of the energy difference to the microwave energy is defined as the resonance field (H_r). The resonance field is the value of magnetic field at the point that the signal intensity in the ESR spectrum is zero, *i.e.*, the maximum microwave energy was absorbed. The g factor indicates the characteristic amount of molecules on which the unpaired electron pairs are located. For example, the g values for iron, nickel, and cobalt are 2.09, 2.21, and 2.18 (47). For the identification of an unknown signal, it is better to determine the g factor. The g factors for the mc-Fe & Ni-poly(HEMA-AdeM) and mc-Fe_2O_3 & Fe_3O_4-poly(HEMA-AdeM) microparticles were calculated as 2.3 and 2.68, respectively, according to the formula given. Moreover, the magnetic field value, H_r, obtained from the graph was 3023 and 2582 gauss for the mc-Fe & Ni-poly(HEMA-AdeM) and mc-Fe_2O_3 & Fe_3O_4-poly(HEMA-AdeM) microparticles, respectively, which are the sufficient values for the stimulation of all dipole moments in the mc-Fe & Ni-poly(HEMA-AdeM) and mc-Fe_2O_3 & Fe_3O_4-poly(HEMA-AdeM) microparticle samples of 1 g each (Figure 5).

$$g = \frac{h.\vartheta}{\beta.H_r} \qquad \text{(Eq. 2)}$$

Wherein h is the Planck's constant (6.626×10^{-27} erg x s^{-1}), ϑ is the frequency (9.707×10^9 Hz), β is the universal constant (9.274×10^{-21} erg x G^{-1}) and the H_r is the magnetic field resonance (G).
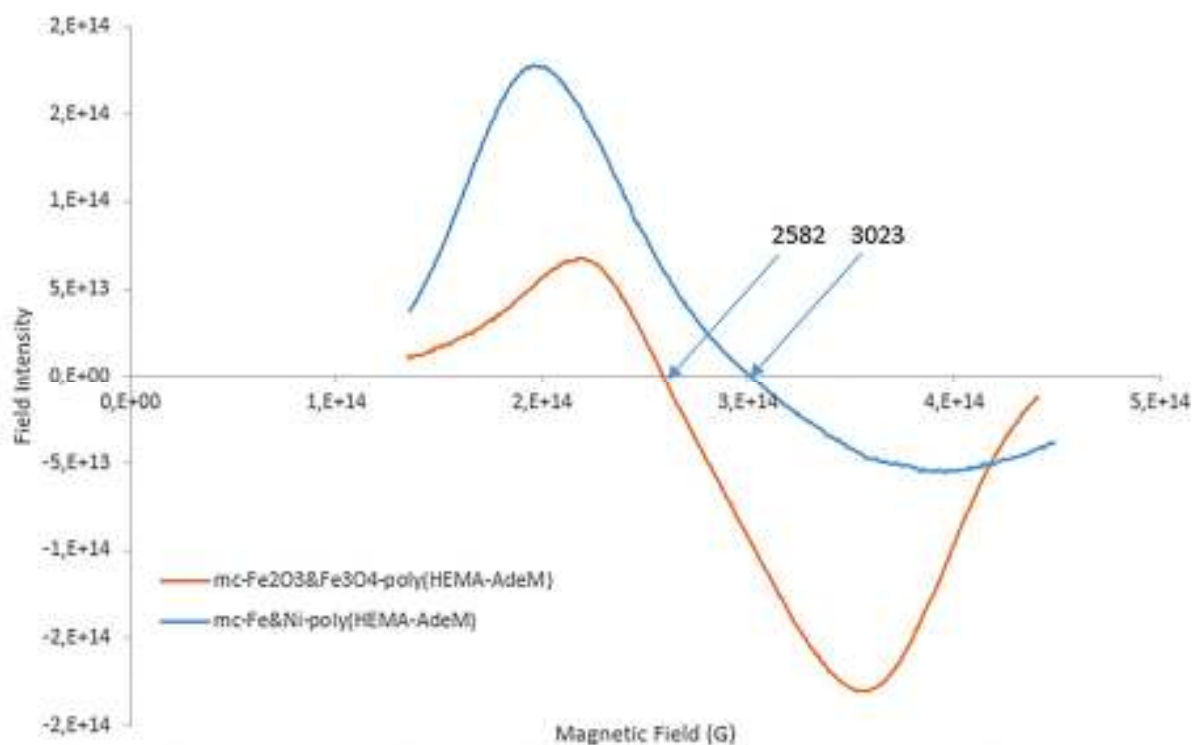
Figure 5. The ESR spectra of mc-Fe & Ni-poly(HEMA-AdeM) and mc-Fe$_2$O$_3$ & Fe$_3$O$_4$-poly(HEMA-AdeM) microparticles.

On the contrary to mc-Fe & Ni-poly(HEMA-AdeM) and mc-Fe$_2$O$_3$ & Fe$_3$O$_4$-poly(HEMA-AdeM) microparticles, there were no H$_r$ points observed for other microparticles synthesized in this study. The reason for this result may be the same with the cause given above about the d orbitals and overlapping of energies. This result does not mean that other microparticles have no magnetic behavior but very minor as compared to the both of mc-Fe & Ni-poly(HEMA-AdeM) and mc-Fe$_2$O$_3$ & Fe$_3$O$_4$-poly(HEMA-AdeM) microparticles.

The microparticles synthesized in this study have also significant water swelling ability. The porous structure of microparticles is very convenient to uptake water. In the adsorption process, the water swelling ratio is very important; because of that, the more water diffuses to the pores, the more interaction between ligand and target molecules occurs. According to Figure 6, the water uptake ability of mc-Fe & Ni-poly(HEMA-AdeM) microparticles is almost the same with that of the mc-Fe & Ni-Co-poly(HEMA-AdeM) microparticles, which is the highest in the group. If these data are compared with those in Table 2, it can be inferred that the mc-Fe & Ni-poly(HEMA-AdeM) microparticles are also highly adequate for water swelling.
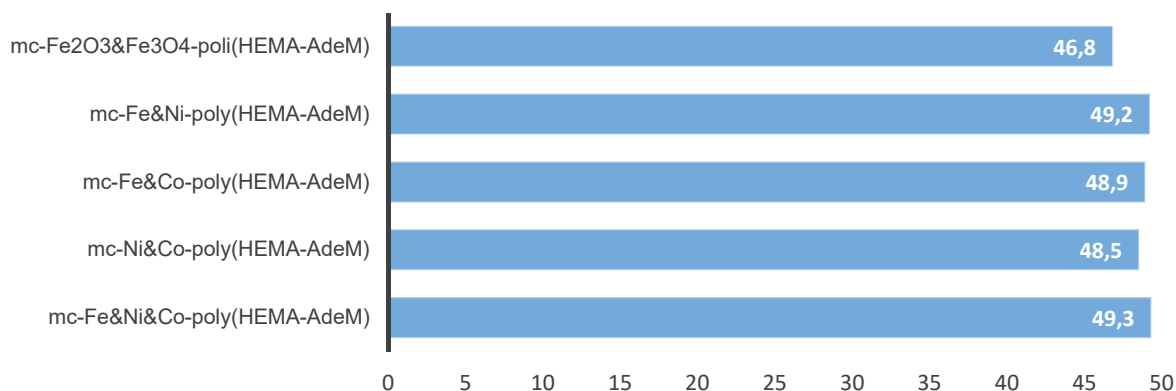
Figure 6. The water swelling ability of microparticles.

It can be concluded as a summary of all characterization steps that the mc-Fe & Ni-poly(HEMA-AdeM) microparticles are almost equidimensional with the lowest size (which is important for the surface area and effectivity) and thus the highest surface area (important for the interaction number and thus the amount to be adsorbed) as compared to other microparticles according to the SEM images. According to the theoretical size of double salts, the lowest theoretical size belongs to the Fe-Co magnetic core, but this does not mean the polymeric material in which the Fe-Co magnetic core was incorporated will have the lowest particles size; actually the size of polymeric microparticles is directly related with the polymerization conditions which are all the same for all polymeric microparticles and also the interaction of the magnetic core with the monomers and other chemicals needed in polymerization step. This interaction, according to the results, was happened as highly effective for Fe-Ni magnetic core and thus mc-Fe & Ni-poly(HEMA-AdeM) microparticles. Moreover, the pore volume and also the water swelling ability obtained as a result of polymerization step is the highest for mc-Fe & Ni-poly(HEMA-AdeM) microparticles meaning that the diffusion of the matrix into the pores of mc-Fe & Ni-poly(HEMA-AdeM) microparticles will be the highest and thus interaction and adsorption. In this point, the water swelling of mc-Fe & Ni & Co-poly(HEMA-AdeM) microparticles is a tiny little bigger than the mc-Fe & Ni-poly(HEMA-AdeM) microparticles, but it does not make sense because of other characterization results. With respect to the results, all polymeric microparticles have ideal zeta potentials, meaning the lowest inter- and intra-molecular interactions with each other are present. In the light of the characterization of magnetism, the mc-Fe & Ni-poly(HEMA-AdeM) microparticles have the highest magnetic moments as compared to even mc-Fe$_2$O$_3$ & Fe$_3$O$_4$-poly(HEMA-AdeM) microparticles which is the only structure having the H_r value other that mc-Fe & Ni-poly(HEMA-AdeM) microparticles. Therefore, one should compare these to structure in terms of magnetism and also applicability. As seen, the magnetic hysteresis curve of mc-Fe$_2$O$_3$ & Fe$_3$O$_4$-

poly(HEMA-AdeM) microparticles is very low as compared to mc-Fe & Ni-poly(HEMA-AdeM) meaning the magnetic moment of former is very low as compared to latter, *i.e.*, magnetism. As given above, The ESR spectrum was obtained only for both mc-Fe_2O_3 & Fe_3O_4-poly(HEMA-AdeM) and mc-Fe & Ni-poly(HEMA-AdeM) microparticles and thus H_r value needed for the stimulation of dipole moments in the molecule which is bigger for mc-Fe & Ni-poly(HEMA-AdeM) microparticles (better if it is low). Overall, a researcher may choose the Fe-Ni magnetic core for the synthesis of magnetic polymeric micro- or nanoparticles for a separation process due to the promising features of this double salt core.

CONCLUSION

The polymeric microparticles are very good materials used in a wide variety of fields from the cleaning of wastewater to isolation of DNA as indicated above. Therefore, in this respect, the efficiency of microparticles is very important. Up to date, there are so many studies about the improvements of the functionality of microparticles and also there have been lots of ligands developed to interact with these microparticles. Especially, magnetic microparticles are very good at the magnetic separation of biomolecules in almost single or double steps. The double salts or microparticles containing double salts are very new in the literature and also very effective. The magnetism of these double salts or other features affects the microparticle formation, composition, and also the structure. Which double salt or which magnetic core is promising for the isolation, removal or purification of biomolecules is very vital in terms of time, efficiency, labor or purity of biomolecules obtained. In this study, some double salts and iron oxide structure were used to synthesize microparticles for the investigation of the effect of double salt on the functionality or performance of microparticles obtained. As noted in the text, mc-Fe & Ni-poly(HEMA-AdeM) microparticles passed all steps in success. The reason for this may be attributed to the Fe & Ni ionic radius, Fe & Ni magnetism, and the efficient interaction with polymeric structure because of their useful orbitals pulling negatively charged structures of polymeric material around them. The researchers studying polymeric materials for the removal, isolation, or purification of biomolecules may consult these data prior to their studies.

ACKNOWLEDGMENTS

The author thanks Assoc. Prof. Dr. D. Ali Köse from Hitit University (Çorum, Turkey) for his very kind help and permission to use the available devices.

REFERENCES

1.   Josephson L, Tung C-H, Moore A, Weissleder R. High-efficiency intracellular magnetic labeling with novel superparamagnetic-Tat peptide conjugates. Bioconjugate chemistry. 1999;10(2):186-91.

2.   Partington KM, Jenkinson EJ, Anderson G. A novel method of cell separation based on dual parameter immunomagnetic cell selection. Journal of immunological methods. 1999;223(2):195-205.

3.   Türkmen D, Yavuz H, Denizli A. Synthesis of tentacle type magnetic beads as immobilized metal chelate affinity support for cytochrome c adsorption. International journal of biological macromolecules. 2006;38(2):126-33.

4.   Park J-H, Im K-H, Lee S-H, Kim D-H, Lee D-Y, Lee Y-K, et al. Preparation and characterization of magnetic chitosan particles for hyperthermia application. Journal of Magnetism and Magnetic Materials. 2005;293(1):328-33.

5.   Lübbe AS, Alexiou C, Bergemann C. Clinical applications of magnetic drug targeting. Journal of Surgical Research. 2001;95(2):200-6.

6.   Hinds KA, Hill JM, Shapiro EM, Laukkanen MO, Silva AC, Combs CA, et al. Highly efficient endosomal labeling of progenitor and stem cells with large magnetic particles allows magnetic resonance imaging of single cells. Blood. 2003;102(3):867-72.

7.   Mornet S, Vasseur S, Grasset F, Duguet E. Magnetic nanoparticle design for medical diagnosis and therapy. Journal of Materials Chemistry. 2004;14(14):2161-75.

8.   Serda RE, Adolphi NL, Bisoffi M, Sillerud LO. Targeting and cellular trafficking of magnetic nanoparticles for prostate cancer imaging. Molecular imaging. 2007;6(4):277.

9.   Ranzoni A, Sabatte G, van IJzendoorn LJ, Prins MW. One-step homogeneous magnetic nanoparticle immunoassay for biomarker detection directly in blood plasma. Acs Nano. 2012;6(4):3134-41.

10.   Fee CJ. Stability of the liquid-fluidized magnetically stabilized fluidized bed. AIChE journal. 1996;42(5):1213-9.

11.   Graves D. Bioseparations in the Magnetically Stabilized Fluidized Bed, Chapter 9, 187 207 Barker and Ganetsos, Eds., Preparative and Production Scale Chromatography. Marcel Dekker, Inc., NY; 1993.

12.   Sawakami-Kobayashi K, Segawa O, Obata K, Hornes E, Yohda M, Tajima H, et al. Multipurpose robot for automated cycle sequencing. Biotechniques. 2003;34(3):634-7.

13.   Tanaka T, Matsunaga T. Fully automated chemiluminescence immunoassay of insulin using antibody-protein A-bacterial magnetic particle complexes. Analytical chemistry. 2000;72(15):3518-22.

14.   Idil N, Perçin I, Karakoç V, Yavuz H, Aksöz N, Denizli A. Concanavalin A immobilized magnetic poly (glycidyl methacrylate) beads for prostate specific antigen binding. Colloids and Surfaces B: Biointerfaces. 2015;134:461-8.

15.   Zheng W, Gao F, Gu H. Carboxylated magnetic polymer nanolatexes: preparation, characterization and biomedical applications. Journal of magnetism and magnetic materials. 2005;293(1):199-205.

16.   Pollert E, Knížek K, Maryško M, Závěta K, Lančok A, Boháček J, et al. Magnetic poly (glycidyl methacrylate) microspheres containing maghemite prepared by emulsion polymerization. Journal of magnetism and magnetic materials. 2006;306(2):241-7.

17.   Lea T, Vartdal F, Davies C, Ugelstad J. Magnetic monosized polymer particles for fast and specific fractionation of human mononuclear cells. Scandinavian journal of immunology. 1985;22(2):207-16.

18.   Ramanujan R, Chong W. The synthesis and characterization of polymer coated iron oxide microspheres. Journal of Materials Science: Materials in Medicine. 2004;15(8):901-8.

19.   Jayachandran KNN, Chatterji PR. Preparation of linear and crosslinked polymer microspheres by dispersion polymerization. Journal of Macromolecular Science, Part C: Polymer Reviews. 2001;41(1-2):79-94.

20.   Horak D, Lednický F, Petrovský E, Kapička A. Magnetic characteristics of ferrimagnetic microspheres prepared by dispersion polymerization. Macromolecular Materials and Engineering. 2004;289(4):341-8.

21.   Uygun DA, Karagözler AA, Akgöl S, Denizli A. Magnetic hydrophobic affinity nanobeads for lysozyme separation. Materials Science and Engineering: C. 2009;29(7):2165-73.

22.   Safarik I, Safarikova M. Magnetic techniques for the isolation and purification of proteins and peptides. BioMagnetic Research and Technology. 2004;2(1):1.

23.   Özkara S, Akgöl S, Çanak Y, Denizli A. A Novel Magnetic Adsorbent for Immunoglobulin-G Purification in a Magnetically Stabilized Fluidized Bed. Biotechnology progress. 2004;20(4):1169-75.

24.   Takahashi K, Hiwada K, Kokubu T. Occurrence of anti-gizzard P34K antibody cross-reactive components in bovine smooth muscles and non-smooth muscle tissues. Life sciences. 1987;41(3):291-6.

25.   Hu T-T, Wu J-Y. Study on the characteristics of a biological fluidized bed in a magnetic field. Chemical engineering research & design. 1987;65(3):238-42.

26.   Burns MA, Graves DJ. Continuous affinity chromatography using a magnetically stabilized fluidized bed. Biotechnology progress. 1985;1(2):95-103.

27.   Rebroš M, Rosenberg M, Mlichova Z, Krištofíková Ľ. Hydrolysis of sucrose by invertase entrapped in polyvinyl alcohol hydrogel capsules. Food Chemistry. 2007;102(3):784-7.

28.   Denizli A, Özkan G, Arica MY. Preparation and characterization of magnetic polymethylmethacrylate microbeads carrying ethylene diamine for removal of Cu (II), Cd (II), Pb (II), and Hg (II) from aqueous solutions. Journal of applied polymer science. 2000;78(1):81-9.

29.   Xue B, Sun Y. Protein adsorption equilibria and kinetics to a poly (vinyl alcohol)-based magnetic affinity support. Journal of Chromatography A. 2001;921(2):109-19.

30.   Tüzmen N, Kalburcu T, Denizli A. α-Amylase immobilization onto dye attached magnetic beads: Optimization and characterization. Journal of Molecular Catalysis B: Enzymatic. 2012;78:16-23.

31.   Martin C, Cuellar J. Synthesis of a novel magnetic resin and the study of equilibrium in cation exchange with amino acids. Industrial & engineering chemistry research. 2004;43(2):475-85.

32.   Akgöl S, Türkmen D, Denizli A. Cu (II)-incorporated, histidine-containing, magnetic-metal-complexing beads as specific sorbents for the metal chelate affinity of albumin. Journal of applied polymer science. 2004;93(6):2669-77.

33.   Altıntaş EB, Uzun L, Denizli A. Synthesis and characterization of monosize magnetic poly (glycidyl methacrylate) beads. China Part. 2007;5(1):174-9.

34.   Tong XD, Sun Y. Application of magnetic agarose support in liquid magnetically stabilized fluidized bed for protein adsorption. Biotechnology progress. 2003;19(6):1721-7.

35.   Çorman ME, Öztürk N, Tüzmen N, Akgöl S, Denizli A. Magnetic polymeric nanospheres as an immobilized metal affinity chromatography (IMAC) support for catalase. Biochemical Engineering Journal. 2010;49(2):159-64.

36.   Shan Z, Wu Q, Wang X, Zhou Z, Oakes KD, Zhang X, et al. Bacteria capture, lysate clearance, and plasmid DNA extraction using pH-sensitive multifunctional magnetic nanoparticles. Analytical biochemistry. 2010;398(1):120-2.

37.   Nie L, Gao L, Yan X, Wang T. Functionalized tetrapod-like ZnO nanostructures for plasmid DNA purification, polymerase chain reaction and delivery. Nanotechnology. 2006;18(1):015101.

38.   Reddy DHK, Yun Y-S. Spinel ferrite magnetic adsorbents: Alternative future materials for water purification? Coordination Chemistry Reviews. 2016;315:90-111.

39.   Kose K, Denizli A. Poly(hydroxyethyl methacrylate) based magnetic nanoparticles for lysozyme purification from chicken egg white. Artif Cell Nanomed B. 2013;41(1):13-20.

40.   Köse K. Nucleotide incorporated magnetic microparticles for isolation of DNA. Process Biochemistry.

41.   Köse K, Erol K, Emniyet AA, Köse DA, Avcı GA, Uzun L. Fe(II)-Co(II) Double Salt Incorporated Magnetic Hydrophobic Microparticles for Invertase Adsorption. Applied Biochemistry and Biotechnology. 2015;177(5):1025-39.

42.   Erol K, Kose K, Kose DA, Sizir U, Satir IT, Uzun L. Adsorption of Victoria Blue R (VBR) dye on magnetic microparticles containing Fe(II)-Co(II) double salt. Desalination and Water Treatment. 2016;57(20):9307-17.

43.   Hur D, Ekti SF, Say R. N-Acylbenzotriazole mediated synthesis of some methacrylamido amino acids. Letters in Organic Chemistry. 2007;4(8):585-7.

44.   Erol K, Köse K, Köse DA, Sızır Ü, Tosun Satır İ, Uzun L. Adsorption of Victoria Blue R (VBR) dye on magnetic microparticles containing Fe (II)–Co (II) double salt. Desalination and Water Treatment. 2016;57(20):9307-17.

45.   Kara A, Osman B, Yavuz H, Beşirli N, Denizli A. Immobilization of α-amylase on Cu 2+ chelated poly (ethylene glycol dimethacrylate-n-vinyl imidazole) matrix via adsorption. Reactive and Functional Polymers. 2005;62(1):61-8.

46.   Fabian K, Hubert A. Shape-induced pseudo-single-domain remanence. Geophysical Journal International. 1999;138(3):717-26.

47.   Baberschke K. Anisotropy in Magnetism. In: Baberschke K, Nolting W, Donath M,. Band-Ferromagnetism: Ground-State and Finite-Temperature Phenomena. Berlin, Heidelberg: Springer Berlin Heidelberg; 2001. p. 27-45.

Türkçe Öz ve Anahtar Kelimeler

Characterization of Magnetic Polymeric Microparticles

Kazım Köse

Öz: Ayırma işlemi, özellikle biyokimya ve biyoteknolojide olmak üzere, bir çok bilim dalında çok önemli bir işlemdir. Bir yöntemin ayırma performansı ayırma zamanı ve hedef molekül için seçilen ligandla doğrudan ilişkili olan, ayrılacak molekülün saflığı ile belirlenebilir. Ayırma zamanı,özellikle tıbbi uygulamalarda olmak üzere zamana bağlı analizlerin ve maliyetin çok önemli bir bileşeni olmaktadır. Manyetik ayırma çok avantajlı bir tekniktir, çünkü zaman alan örnek hazırlama ve santrifüjleme adımlarını ortadan kaldırır. Ancak, adsorbanın manyetik performansı, dışarıdan uygulanan manyetik kuvvete cevap verecek kadar kuvvetli olmayabilir. Bu sebepten ötürü, nanoparçacık çalışmalarında nanoparçacıkların manyetik performansı son derece önemlidir. Bu çalışmada, farklı manyetik çekirdeklerin (Fe2O3 & Fe3O4, Fe & Ni, Ni&Co, Fe & Ni&Co) HEMA (2-hidroksil etilmetakrilat) ve fonksiyonel bir monomer olan AdeM (adenin metakrilat) kullanılarak sentezlenen polimerik mikroparçacıkların manyetik performansı karşılaştırılmıştır. Boyut, zeta potansiyeli, yüzey morfolojisi gibi diğer bazı özellikler de çalışılmıştır.

Anahtar kelimeler: Mikroparçacıklar, manyetik mikroparçacıklar, polimer malzemeler.

Gönderme: 16 Ağustos 2016. **Düzeltme:** 25 Ağustos 2016. **Kabul:** 27 Ağustos 2016.

Production and Drug Release Assessment of Melatonin-Loaded Alginate/Gum Arabic Beads

Bernis Girgin[1], Onur Korkmaz[1], Rukiye Yavaşer[1], A. Alev Karagözler[1]

[1]Adnan Menderes University, 09010, Aydın, Turkey

Abstract: Melatonin containing alginate-gum arabic beads were produced by ionotropic gelation. The most suitable alginate-gum arabic ratio for bead production was optimized. To the optimized beads the loading of changing amounts of melatonin was conducted to produce the beads with the best melatonin entrapment and release. Entrapment efficiency of the beads as melatonin carrier was calculated to be approximately 70%. Release profiles of melatonin from the beads were generated using *in vitro* gastric fluid (pH 1.5) and intestinal fluid (pH 7.4). According to results obtained, following a burst in the first half hour, melatonin release from the beads in pH 1.5 medium was approximately 45% in the first 5 hours whereas the release was approximately 50% in pH 7.4 medium. The results indicate that the beads manufactured may be used as carriers for controlled release of melatonin.

Keywords: Melatonin, alginate, gum arabic, bead, controlled drug release.

INTRODUCTION

Conventional application of drug doses for treatment of diseases involves repetitive introduction of the medicine with equal intervals (1). However, this method may cause fluctuation of the drug concentration and this may lead to low non-treating or high toxic levels. Controlled drug release systems aim to balance this fluctuation and provide a constant level of drug for a certain period of time (2). Controlled drug release systems are accepted as more reliable and high therapeutic carriers compared to conventional drug pills. Polymeric beads are regarded as good candidates for controlled drug release systems since they serve high bioavailability and stability. They also offer advantages such as limited fluctuation in the therapeutic range, reduced side effects, decreased dosing frequency and improved patient compliance (3).

Natural polymers have been widely used in controlled drug release formulations in view of their abundance and biocompatibility (3). Biopolymers are natural, biodegradable, and generally nontoxic materials. Due to these properties, they are often used in applications of pharmacology and food industry. Alginate is a natural polysaccharide which is mainly obtained from brown algae and is easily gelled when contacts with multivalent cations, especially Ca^{2+}, forming small pores which enable to entrap and release the desired molecule. The gelling and release profile of alginate beads differ depending on the conditions like the type and concentration of gelling agents, curing time, release medium, and the drug itself (4). Gums are naturally occurring polysaccharides which increase the viscosity of the solutions in which they are added even at very low concentrations. Gum arabic is the most frequently used one among them. It is also known as acacia gum since it is the leakage of acacia tree. Alginate and gum arabic are used in drug release formulations in several studies (5).

Melatonin (N-acetyl-5-methoxy tryptamine) (Figure 1) is a tryptophan-derived hormone which is synthesized and secreted from pineolacites of pineal gland during night in human body. The most important task of melatonin molecule is to regulate circadian rhythm and sleep-wake cycle in humans. Melatonin also provides positive effects on immune system, reduction of tumor growth, antioxidative protection, and homeostasis (6). Low melatonin release may cause sleep disorder, tiredness, and memory impairment. In order to restore these disorders melatonin is available as over the counter supplement drug. Melatonin is excreted in urine as 6-sulphatoxymelatonin after metabolized by the liver (7).
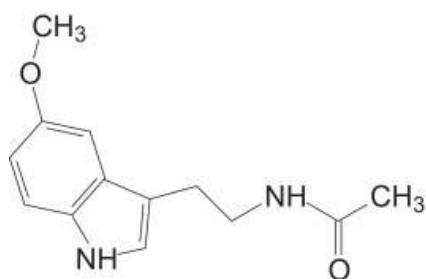
Figure 1. Molecular structure of melatonin (8).

In this work, entrapment of melatonin molecule in alginate-gum arabic beads (AG) and their melatonin release properties were investigated. In order to achieve this, first, the most suitable alginate/gum arabic ratio was optimized. Then, using the optimal combination loading of changing amounts of melatonin was conducted to produce the beads with the best melatonin entrapment and release. Release profiles of the melatonin loaded beads (AGM) in simulated gastric (SGF) and intestinal (SIF) fluids were obtained.

MATERIALS AND METHODS

Materials

Melatonin, alginic acid sodium salt from brown algae (low viscosity), $CaCl_2$, gum arabic, ethanol, and HCl were purchased from Sigma (Steinheim, Germany). Tween 80 was obtained from Merck (Darmstadt, Germany) and KCl was obtained from Carlo Erba (Ronado, Italy). Phosphate buffer tablets (PBS) were purchased from Oxoid (Hampshire, England). All chemicals were of analytical grade.

Production of alginate-gum arabic beads and melatonin-loaded beads

AG beads were prepared by ionic crosslinking method reported by Malakar *et al.* (9). Briefly, 10.0 mL of aqueous alginate solution (1.5%, w/v) was prepared by stirring the solution gently at 200 rpm at room temperature for 1 h. Fifty milligrams of gum arabic was added slowly and mixture was stirred for 30 min at 200 rpm and sonicated for 5 min. Alginate-gum arabic solution was added dropwise into continuously stirred (100 rpm) 5% $CaCl_2$ solution. The resulting maturated beads were filtered and washed with distilled water. To produce AGM beads, 1.0 mL of melatonin solution (3 mg/mL in ethanol) was added slowly into alginate solution in order to achieve a homogenous mixture. Other steps

were employed as the same for production of AG beads (Figure 2). Optimization studies to determine the best bead formation were conducted using different alginate/gum arabic ratios. Also, the effect of initial melatonin concentration on entrapment efficiency was investigated at various drug quantities (1-10 mg). All experiments were employed in triplicate.
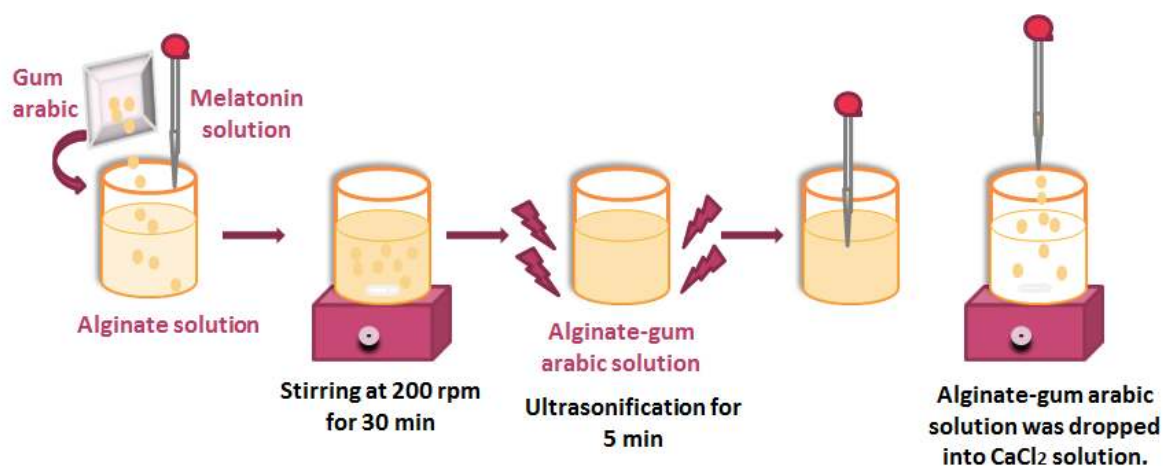
Figure 2. Preparation of melatonin loaded alginate-gum arabic beads.

Determination of melatonin entrapment efficiency of AG beads

Entrapment efficiency (EE) of AG beads was calculated by measuring the absorbance of the supernatant obtained from the entrapment medium after centrifugation (Sigma 3-30KS, Germany) at 18000 rpm for 30 min employing a UV spectrophotometer (Shimadzu UV-1601, Japan) at 278 nm and calculating the % EE from the equation below.

Melatonin concentration was determined from the melatonin standard plot.

$$EE = \frac{Total\ amount\ of\ melatonin\ added - Amount\ of\ free\ melatonin\ after\ entrapment}{Total\ amount\ of\ melatonin\ added} \times 100 \qquad \text{(Eq. 1)}$$

***In vitro* release of melatonin**

In order to determine the release profile of melatonin from AGM, beads were transferred into 50.0 mL of SGF (mixture of 100 mL 0.2 M HCL and 82.8 mL 0.2 M KCl, pH 1.5) and allowed to stir at 150 rpm for 2 h. At each 30 min intervals, 2.0 mL of the medium was collected and centrifuged at 18000 rpm at 4°C for 30 min and the absorbance was recorded at 278 nm. Then, beads were removed and transferred into 51.5 mL of SIF (50 mL PBS solution containing 1.5 mL of 1% Tween 80, pH 7.4) and stirred for 22 h more. The release

procedure was employed in intestinal medium for 22 hours. Release experiments were conducted at 37°C in triplicate. The amount of released melatonin was calculated from melatonin concentration curve.

RESULTS AND DISCUSSION

Production of alginate-gum arabic beads and melatonin loaded beads

There are few studies concerning on synthesis of alginate-gum arabic beads and their usage in controlled drug release studies. Alginate and gum arabic are anionic polysaccharides. When they are exposed to calcium ions, carboxylate groups of both polymers interact with positively charged calcium ions by electrostatic interactions (10). AG and AGM beads produced in this study were spherical, semi-opaque, and their sizes were approximately 3 mm (Figure 3).

Figure 3. Melatonin loaded alginate-gum arabic beads.

In order to study the best bead formation, ionically crosslinked alginate-gum arabic beads were produced using different amounts of alginate (0.5-2.0 w/v %) and gum arabic (0-100 mg). The most suitable combination was chosen as 1.5 % alginate solution containing 50 mg of gum arabic regarding to the stability, shape, and intensity of the beads.

Melatonin concentrations in entrapment and release media were measured spectrophotometrically. The UV spectrum (Figure 4) of melatonin solution (dissolved in ethanol) was obtained in order to determine the wavelength at which the measurements would be performed. All spectrophotometric measurements were recorded at 278 nm.
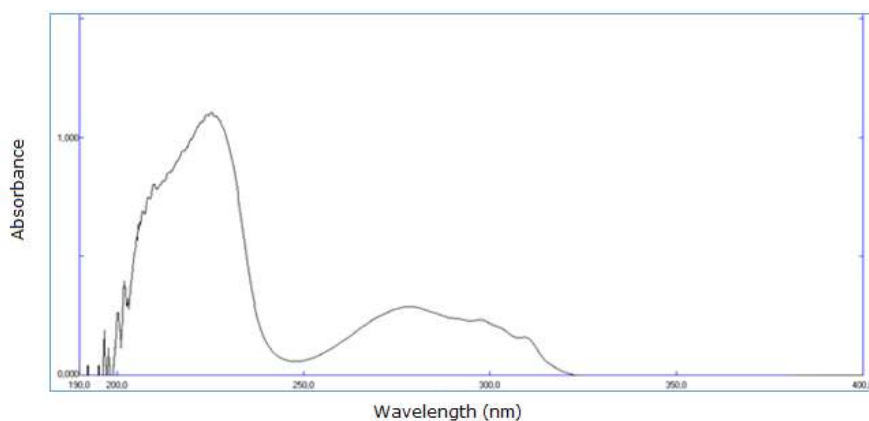
Figure 4. UV spectrum of melatonin solution.

Melatonin concentrations in the entrapment and release media were calculated using the plot (Figure 5) constructed with concentration dependent absorbance values at 278 nm.
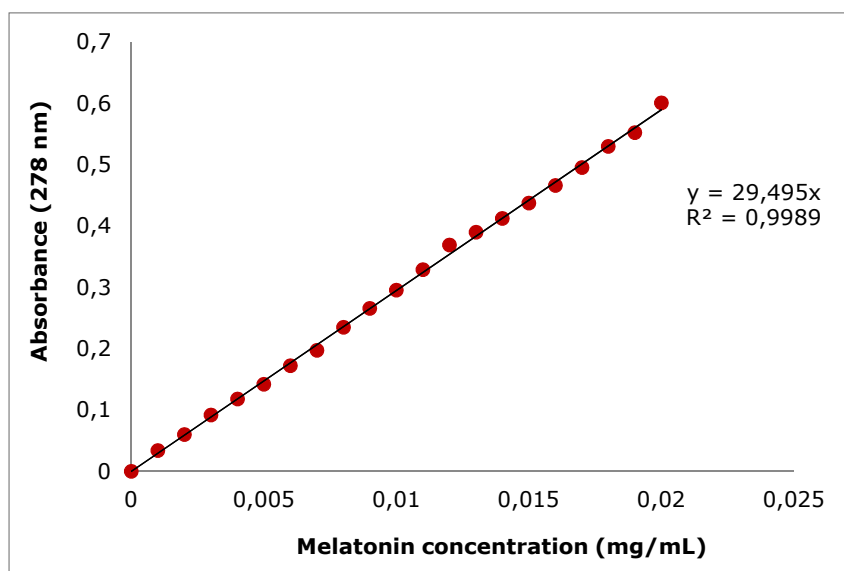
Figure 5. Melatonin standard curve.

Melatonin entrapment efficiency of AG beads

The effect of melatonin concentration on entrapment efficiency was evaluated and maximum EE% was calculated to be 77.82±4.47% with the optimized bead formulation (1.5 mg alginate-50 mg gum arabic) at the drug concentration of 3.0 mg in the entrapment medium (Table 1). Entrapment efficiency increased in the range of 1-3 mg melatonin and decreased beyond probably due to the saturation of the beads. Findings of Dubey *et al.* (2006) were consistent with our results where they loaded different amounts of melatonin into elastic liposomes (11).

Table 1. Effect of melatonin concentration on EE%.

Alginate-Gum Arabic (% / mg)	Melatonin concentration (mg)	Entrapment (%)
1.5 - 50	1.0	58.45 ± 2.56
1.5 - 50	2.0	70.70 ± 5.41
1.5 - 50	3.0	77.82 ± 4.47
1.5 - 50	4.0	60.41 ± 4.60
1.5 - 50	5.0	60.73 ± 6.36
1.5 - 50	6.0	59.44 ± 3.62
1.5 - 50	7.0	62.58 ± 6.34
1.5 - 50	8.0	64.52 ± 3.63

In vitro release of melatonin from alginate-gum arabic beads

The solubility and stability of drugs as well as increased pharmacologic efficiency can be enhanced by entrapping them in drug carriers (6). Melatonin has a short half-life, therefore, developing a controlled release system may be useful (12). Controlled release systems should release melatonin over 8-10 h to mimic the endogenous release of melatonin. Lee and Min (1995) have reported alginate beads for sustained release of melatonin for oral administration (13).

In this work, release experiments were carried out exposing the AGM beads to SGF for 2 h and SIF for 3 h consecutively to simulate the way that drugs pass in the human body. In SGF, totally 45.6% of the entrapped melatonin was release in 2 hours with a burst in the first 30 min. The cumulative percentage shifted to 51% when the beads were transferred to SIF (Figure 6). This increase may be explained by the tendency of alginate to erode and disintegrate in SIF. A burst release was also reported for melatonin loaded into stearyl alcohol microspheres. Drug release was retarded by coating the spheres with chitosan and alginate (14).
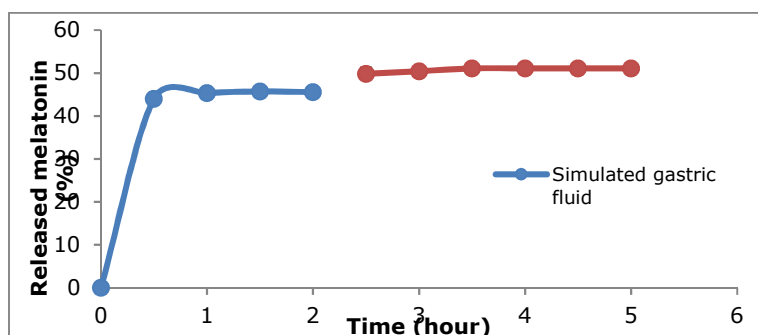
Figure 6. Consecutive melatonin release in SGF and SIF, respectively. (37°C, stirring rate: 100 rpm).

It was stated that melatonin had a solubility of 3.11±0.90 mgmL^{-1} and 2.76 mgmL^{-1} in gastric and intestinal fluids, respectively. Entrapment efficiency was 60.6±4.5%. Approximately 80% of melatonin was released in gastric medium whereas 90% in intestinal medium (4).

Generally, relatively low release is observed in gastric fluid compared to intestinal fluid due to the stability and low swelling of alginate beads in acidic conditions. Solubility, passive diffusion, and hydrogen bonding properties of the drug were suggested as the major factors that influence the drug release (4, 15, 16).

CONCLUSION

Entrapment efficiency of melatonin in beads was calculated to be approximately 70%. Release of melatonin from the beads was measured using *in vitro* gastric fluid and intestinal fluid (pH 1.5 and pH 7.4; respectively) and release profiles were plotted. According to results obtained, melatonin release from the beads in pH 1.5 medium was approximately 45% in the first 5 hours whereas the release was approximately 40% in pH 7.4 medium. Melatonin release from alginate-gum arabic beads demonstrated an initial burst profile since the drug on the outer surface of the beads were able to be released easily. The results indicate that the beads manufactured may be used as carriers for melatonin.

ACKNOWLEDGEMENTS

REFERENCES

1. Bruschi, ML.. Strategies to modify the drug release from pharmaceutical systems. Woodhead Publishing. 2015. ISBN: 978-0-08-100112-7.

2. Siegel RA., Rathbone MJ. Overview of controlled release mechanisms. Fundamentals and Applications of Controlled Release Drug Delivery. Springer US, 2012; 19-43. DOI:10.1007/978-1-4614-0881-9_2.

3. Şanlı O, Ay N, Işıklan N. Release characteristics of diclofenac sodium from poly (vinyl alcohol)/sodium alginate and poly (vinyl alcohol)-grafted-poly (acrylamide)/sodium alginate blend beads. European Journal of Pharmaceutics and Biopharmaceutics. 2007; 65(2), 204-214. DOI:10.1016/j.ejpb.2006.08.004.

4. Lee B-J, Min G-H, Cui J-H. Correlation of drug solubility with trapping efficiency and release characteristics of alginate beads. Pharmacy and Pharmacology Communications. 1999; 5(2): 85-89. DOI: 10.1211/146080899128734505.

5. Nizam El-Din HM, Khafaga MR, El-Naggar, AWM. Physico-Chemical and Drug Release Properties of Poly (Vinyl Alcohol)/Gum Arabic/TiO$_2$ Nanocomposite Hydrogels Formed by Gamma Radiation. Journal of Macromolecular Science, Part A. 2015; 52(10): 821-829. DOI: 10.1080/10601325.2015.1067040.

6. Altındal DÇ, Gümüşderelioğlu M. Melatonin releasing PLGA micro/nanoparticles and their effect on osteosarcoma cells. Journal of Microencapsulation. 2016; 33(1): 53-63. http://dx.doi.org/10.3109/02652048.2015.1115901.

7. Garfinkel D, Laudon M, Nof D, Zisapel N. Improvement of sleep quality in elderly people by controlled-release melatonin. The Lancet. 1995; 346(8974): 541-544. DOI:10.1016/S0140-6736(95)91382-3.

8. Mihailiasa M, Caldera F, Li J, Peila R, Ferri A, Trotta F. Preparation of functionalized cotton fabrics by means of melatonin loaded β-cyclodextrin nanosponges. Carbohydrate polymers, 2016;142: 24-30. DOI:10.1016/j.carbpol.2016.01.024.

9. Malakar M,Nayak AK, Pal D, Jana P. Potato starch-blended alginate beads for prolonged release of tolbutamide: Development by statistical optimization and *in vitro* characterization. Asian Journal of Pharmaceutics. 2013; 7: 43-51. DOI: 10.4103/0973-8398.110935.

10. Nayak AK, Das B, Maji R. Calcium alginate/gum arabic beads containing glibenclamide: Development and *in vitro* characterization. International Journal of Biological Macromolecules. 2012; 51(5): 1070-1078. DOI:10.1016/j.ijbiomac.2012.08.021.

11. Dubey V, Mishra D, Asthana A, Jain, NK. Transdermal delivery of a pineal hormone: melatonin via elastic liposomes. Biomaterials. 2006; 27(18): 3491-3496. DOI:10.1016/j.biomaterials.2006.01.060.

12. Schaffazick SR, Pohlmann AR, Mezzaliraa G, Guterres SS. Development of nanocapsule suspensions and nanocapsule spray-dried powders containing melatonin. Journal of The Brazilian Chemical Society, 2006. 17(3):562–569. http://dx.doi.org/10.1590/S0103-50532006000300020.

13. Lee, B. J., Min, G. H., & Kim, T. W. Preparation and *in vitro* release of melatonin-loaded multivalent cationic alginate beads. Archives of Pharmacal Research. 1996; 19(4): 280-285. DOI:10.1007/BF02976241.

14. Lee BJ, Choe JS, Kim CK. Preparation and characterization of melatonin-loaded stearyl alcohol microspheres. Journal of Microencapsulation. 1998; 15(6): 775-787. DOI:10.3109/02652049809008260.

15. Østberg T, Lund EM, Graffner C. Calcium alginate matrices for oral multiple unit administration: IV. Release characteristics in different media. International Journal of Pharmaceutics. 1994; 112(3): 241-248. DOI:10.1016/0378-5173(94)90360-3.

16. Fathy M, Safwat SM, El-Shanawany SM, Tous SS, Otagiri M. Preparation and evaluation of beads made of different calcium alginate compositions for oral sustained release of tiaramide. Pharmaceutical Development and Technology. 1998; 3(3): 355-364. DOI:10.3109/10837459809009863.

Türkçe Öz ve Anahtar Kelimeler

Melatonin Yüklü Aljinat/Gam Arabik Boncukların Üretimi ve İlaç Salım Özelliklerinin Değerlendirilmesi

Bernis Girgin, Onur Korkmaz, Rukiye Yavaşer, A. Alev Karagözler

Öz: Melatonin içeren aljinat-gam arabik boncuklar iyonotropik jelleşme ile üretilmiştir. Boncuk üretimi için en uygun aljinat - gam arabik oranı tespit edilmiştir. En iyi melatonin tutuklama ve salım özelliğine sahip boncukları üretebilmek için, değişen miktarlarda melatonin yüklenmiştir. Melatonin taşıyıcısı olarak boncukların tutuklama etkinliği yaklaşık %70 olarak hesaplanmıştır. Melatoninin boncuklardan salım profilleri *in vitro* mide özütü (pH 1,5) ve bağırsak özütü (pH 7,4) kullanılarak oluşturulmuştur. Elde edilen sonuçlara göre, ilk yarım saatte ani bir yükselmeyi takiben, boncuklardan melatonin salımı pH 1,5 ortamında ilk 5 saat için yaklaşık %45 olmuştur ve pH 7,4 ortamında ise salım yaklaşık %50 olarak tespit edilmiştir. Sonuçlara göre melatoninin kontrollü salım için, üretilen boncukların taşıyıcı olarak kullanılabileceği anlaşılmaktadır.

Anahtar kelimeler: Melatonin, aljinat, gam arabik, boncuk, kontrollü ilaç salınımı.

Antiproliferative effect of Cherry laurel

Ali Aydın*[1], Ramazan Erenler[2], Bülent Yılmaz[2], Şaban Tekin[1]

[1] *Faculty of Art and Science, Department of Molecular Biology and Genetics, Gaziosmanpaşa University, 60240, Tokat, Turkey*

[2] *Faculty of Art and Science, Department of Chemistry, Gaziosmanpaşa University, 60240, Tokat, Turkey*

Abstract: Cherry laurel (*Prunus laurocerasus*) fruits including phenolic and flavonoid contents are consumed as fresh, dried or prepared in marmalade and its leaves containing cyanogenic glycosides have healing activity of a well-known Anatolian folkloric remedy. Herein, Cherry laurel fruits were boiled in water for 2 h, then extracted with hexane, EtOAc, and BuOH successively. Antiproliferative activities of extracts were evaluated on HeLa (Human Cervix Carcinoma), HT29 (Human Colorectal Adenocarcinoma), C6 (Rat Brain Tumor Cells), and Vero (African Green Monkey Kidney) cell lines. All extracts exhibited slightly antiproliferative effects on various cancer cell lines at high concentration. We assessed the ability of extracts of cherry laurel fruit to devastate the membrane of cells. Results indicated that cherry laurel fruit extracts slightly destroys the cellular membrane in tumor cell lines at merely high concentrations. The results of this study does not support the efficacy of cherry laurel fruit extracts as an anticancer agent for cancer cells, but it suggests that cherry laurel fruit extracts may be used through reducing cytotoxicity, a potential adjuvant therapy to current chemotherapeutic agents. Fatty acids of hexane extract were also determined by GC-MS analysis and found out that linoleic acid, palmitic acid, and oleic acid were the major products.

INTRODUCTION

Plants have been used for treatment of various diseases from ancient times. Drug discovery and development process from natural products for confronting cancer has taken in the reasonable opportunity to achieve most new clinical applications of plant secondary metabolites and their derivatives (1, 2). Cancer, occurring from heterogeneous diseases, is an excruciating illness and constitutes a significant medical problem. Despite promising progress in cancer epidemiology, cancer treatments are still not a good medicine without serious side effects, persistent drug resistance, and limited effect due to their ADME properties. Because of the need for more effective anticancer agents, natural products can be considered as suitable anticancer drug candidates. The natural products acquiring significance in the treatment of malady have contributed to health care worldwide through the isolation of bioactive compounds. Nearly 60% of drugs approved for cancer treatment are of natural source represent more than 50% of all the drugs in clinical use of the world (3, 4). Several of them, namely taxol, camptothecin, and etoposide, are in clinical use all over the world. Many cancer research studies have been currently performed using extracts or isolate from plants in an effort to discover new therapeutic agents. *Prunus laurocerasus* (cherry laurel) is an evergreen species of cherry (Prunus), a shrub, which grows in southwestern Asia, and the Balkans. Ethanolic extraction of the fresh leaves of cherry laurel has a long traditional use as a homeopathic mother tincture. In Anatolian folk medicine, the leave extract is used in the therapy of coughs, hemorrhoids, eczemas, asthma, digestive system complaints as well as in the treatment of stomach ulcers (5-13). Traditionally it is also used in analgesic, antispasmodic, and sedative effects and furthermore, according to latest research, its aqueous and ethanolic extracts showed antifungal, antinociceptive and antiinflammatory activity without inducing any gastric lesions (5-13). Overall, leaves, fruit, and seed of cherry laurel are a valuable herbal medicine and used for various health complaints. However, cherry laurel containing cyanogenic glycosides and amygdalin (Laetrile) can be toxic due to using dosage. According to our knowledge, there are no literature data on fruit of cherry laurel biological activities, especially the antiproliferative effect, to date. The topic of this study was to assess pharmacological activity, cell cytotoxicity, and morphological alteration of valuable extracts from cherry laurel used traditionally in Anatolia. The antiproliferative activity of the extracts was conducted following the European Pharmacopoeia 8.0 protocol. According to this protocol, we investigated the antiproliferative and cytotoxic activity of fruits of cherry laurel in various solvent systems. Aqueous (WEPL), hexane (HEPL), n-butanol (NBEPL) and ethyl acetate (EAEPL) extracts of cherry laurel (25 to 500 µg/mL) were investigated for their antiproliferative and cytotoxic activity against HT29, HeLa and C6 cancer cells and nontumorigenic Vero cells

using ELISA BrdU Cell Proliferation assay and LDH cytotoxicity assay as well as morphological analysis.

MATERIALS and METHODS

Extraction

Cherry laurel fruits were boiled in water for 2 h then extracted with hexane, EtOAc, and n-butanol. After filtration and evaporation process, water, hexane, ethyl acetate, and n-butanol extracts were acquired to execute the antiproliferative activities (Table 1).

Table 1. Cherry laurel fruits extracts.

Solvent system	Fruits
Water	WEPL
Hexane	HEPL
EtOAc	EAPL
n-butanol	NBEPL

Preparation of cell culture

The anticancer potential of cherry laurel extracts was investigated on cancerous HT29 (ATCC® HTB-38™), HeLa (ATCC® CCL-2™), and C6 cells (ATCC® CCL-107™) and nontumorigenic Vero cells (ATCC® CCL-81™). The cell lines were cultured in a cell medium (Dulbecco's modified eagle's) enriched with 10% (v/v) fetal bovine serum and 2% (v/v) Penicillin-Streptomycin (10,000 U/mL). First, old medium was removed out of the flask while cells had reached approximately 80% confluence. Next, cells were taken from the flasks surface using 4-5 mL of trypsin-EDTA solution and then subjected to centrifugation. Following, the cell pellet was suspended with 4 mL of DMEM working solution and was counted to obtain a final concentration of 5×10^4 cells/mL, and inoculated into wells (100 μL cells/well).

Cell proliferation assay (CPA)

A cell suspension containing approximately 5×10^3 cells in 100 μL was seeded into the wells of 96-well culture plates. The cells were treated with cherry laurel extracts and control drug, 5-fluorouracil (5FU), dissolved in sterile DMSO (max 0.5% of DMSO) at final concentrations of 25, 50, 100, 150, 200, 250, 375, and 500 μg/mL at 37°C with 5% CO_2 overnight. The final volume of the wells was set to 200 μL by medium. Cell proliferation assay was evaluated by ELISA BrdU methods as described previously (14).

Calculation of IC$_{50}$ and % inhibition

IC$_{50}$ value is a concentration that inhibits half of the cells in vitro. The half maximal inhibitory concentration (IC$_{50}$) of the test and control compounds was calculated using XLfit5 or excel spreadsheet and represent in μM at 95% confidence intervals. The

proliferation assay results were expressed as the percent inhibition according to the following formula:

$$Inhibition\ (\%) = 1 - \left(\frac{Absorbance\ of\ Treatments}{Absorbance\ of\ DMSO}\right) x100 \qquad (Eq.1)$$

Cytotoxic activity assay

The cytotoxicity of the compounds and of 5 fluorouracil on HeLa, C6, HT29, and Vero cells was determined through a Lactate Dehydrogenase Assay Kit according to the manufacturer's instructions. Approximately 5×10^3 cells in 100 µL were placed into 96-well plates as triplicate and treated with IC_{50} (µg/mL) concentrations of test compounds at 37°C with 5% CO_2 for 24 h. LDH activity was obtained by determining absorbance at 492 - 630 nm using a microplate reader. The cytotoxicity assay results were noted as the percent cytotoxicity according to the following formula:

$$Cytotoxicity\ (\%) = \left[\frac{(Experimental\ Value - Low\ Control)}{High\ Control - Low\ Control} x100\right] \qquad (Eq.\ 2)$$

Cell imaging

Cells were plated in 96-well plates at a density of 5.000 cells per well and allowed 24 h. IC_{50} values of the test compounds were administered and morphology alters of the cells were screened by phase contrast microscopy for 24 h every 6 h. Images of control and test compounds treated cells were photographed at the end of the process using a digital camera attached to an inverted microscope.

GC-MS analysis

A Perkin Elmer Clarus 500 instrument with FID flame ionizing detector (Rtx-2330) and column (30 m × 0.25 mm × 0.2 µm) was used for fatty acid analysis. Methyl esters of 37 fatty acids were applied for standards. Temperature of the detector was 250°C and injection temperature was 250°C. Injection splitting was 50/1 and carriage gas flow was 1 mL/min.

RESULTS and DISCUSSION

Antiproliferative effect of the Prunus laurocerasus extracts

Here, different extracts of cherry laurel were conducted for their antiproliferative activity against cancer and normal cell lines using 5FU as a control anticancer drug. The medicines from natural sources such as plant, algae or fungi are used in the management and treatment of various diseases including cancer (15). For example, the fresh leaves of *Prunus laurocerasus* (*British Pharmaceutical Codex*, 1949) have been used as a flavoring agent (Cherry Pits, Extract (*Prunus* spp.)) in bad odor drugs and as a sedative for nausea or vomiting. With regard to the antiproliferative potential of cherry

laurel, the data suggest that the growth of the cell lines was slightly inhibited by using cherry laurel extracts and among different extracts were not found any difference (Figure 1). The IC_{50} values of cherry laurel extracts could not be calculated by using ELISA data. The data revealed that all cells were more durable than 5FU to cherry laurel extracts. Also, the proliferation of the cancerous cells of the cherry laurel extracts treatment was not statistically significant, compared with that of control cells ($P > 0.05$). It is known that natural products including various metabolites exhibit a strong pharmacological activity due to interact with cell type. Therefore, the antiproliferative activity of cherry laurel extracts mostly consisting of glycosides (amygdalin, prunasin, and sambunigrin) can be conducted using other type cell lines.
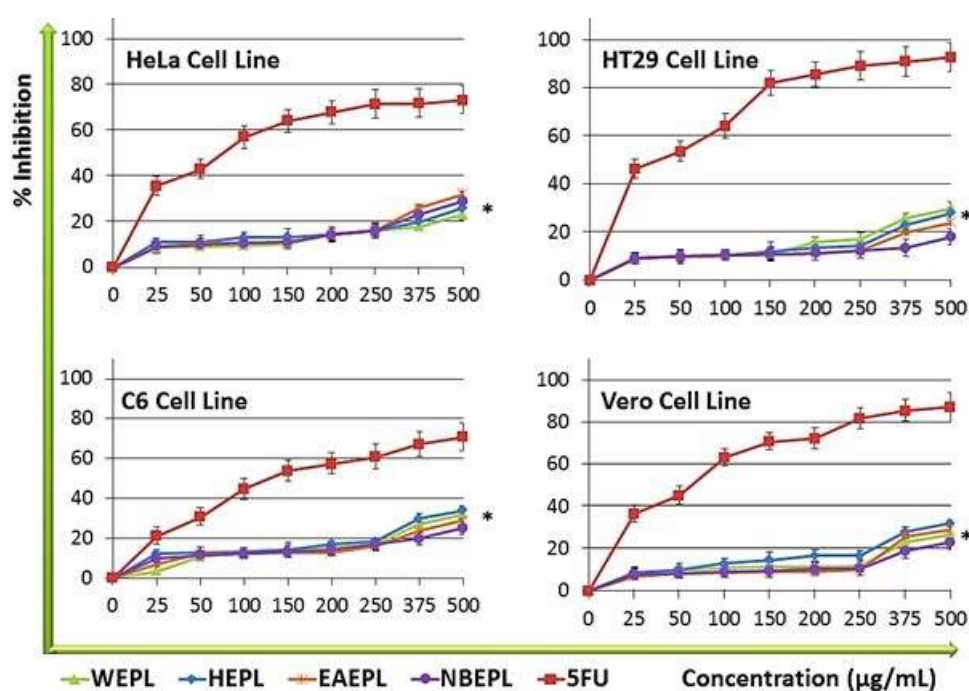
Figure 1. The Antiproliferative activity of cherry laurel extracts and positive control compound, 5FU on HeLa, HT29, C6, and Vero cell lines. Percent inhibition was noted as mean values ± SEM of three independent assays ($P < 0.05$). Each experiment was repeated at least three times for each cell line. *$P < 0.05$ in comparison with the control.

Cytotoxic activity of the *Prunus laurocerasus* extracts

The cytotoxic activity of cherry laurel extracts on HeLa, HT29, C6, and Vero cell lines were tested using an LDH cytotoxicity assay kit and were determined by treating cells with varying concentrations of the cherry laurel extracts (25, 50, 100, 150, 200, 250, 375, and 500 µg/mL), which showed concentration-dependent collapse of cell membrane. The findings of % cytotoxicity delineate that treatment of cells with higher concentrations of cherry laurel extracts resulted in significant corruption of cell membrane integrity, but its low concentrations did not same effect on the cell membrane (Figure 2). The cell line showed no cytotoxic situations in response to cherry laurel extract treatment up to 375

µg/mL, which confirms that cherry laurel extracts have no cytotoxicity in cells, but it exhibits slightly antiproliferative activity at 375 µg/mL and higher concentrations (Figure 2). Therefore, it is suggested that cherry laurel extracts may have a cytostatic potential towards the cells. Cherry Laurel contains flavonoids like kaempferol and quercetin, and caffeic and coumaric acid along with hydrocyanic acid. Quercetin is known to regulate the expression of apoptosis-related genes and to inhibit lymphocyte tyrosine kinase activity (16-18). Quercetin has also been shown to exhibit strong antiproliferative effects towards hepatocarcinoma *in vivo* experiments (19).
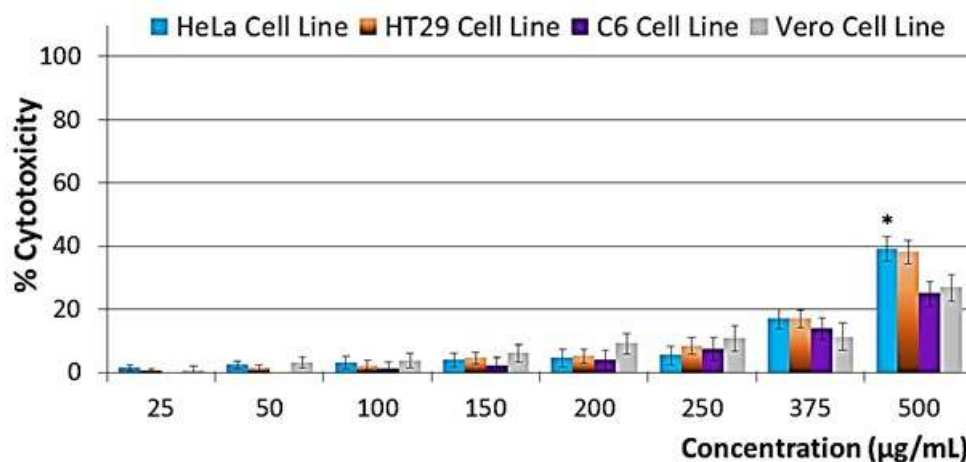
Figure 2. Cytotoxic activity of cherry laurel extracts on HeLa, HT29, C6, and Vero cell lines. Percent cytotoxicity was noted as mean values ± SDs of three independent assays. *P < 0.05 in comparison with the control.

In a clinical trial, quercetin exhibited outstanding antitumor activity with safely i.v. usage (18). According to National Cancer Institute (20), however, laetrile (amygdalin) has displayed poor anticancer effect in animal experiments and no anticancer effect in clinical phase trials. Laetrile is not approved by FDA because of its side effects like hepatic damage, difficulty of walking, fever, coma, and death which are commonly dangerous. As demonstrated in above mentioned similar studies, cherry laurel extracts acting as an adjuvant agent in cancer treatment.

Morphological assessment of the cytotoxic activity of the Prunus laurocerasus extracts

The effect of the cherry laurel fruit extracts on the morphology of the cells were visualized by digital camera attached inverted microscope (Leica IL10, Germany). Picture shows inverted microscopic images of the morphology of treated cell lines with different concentrations of cherry laurel fruit extracts as compared to respective controls. The morphology of cherry laurel fruit extracts-treated cells at merely high concentration (>375 µg/mL) changed from a cell rounding to floating cells, an indication of cell death. The cherry laurel fruit extracts were not able to inhibit growth of the cells in the culture at low and medium dosages. The control groups displayed integrity confluent growth with

normal proliferating cells. Similar to control cells, the majority of the treated cells was kept astrocyte-like or fibroblast-like appearance. Generally, at 375 µg/mL and higher doses, the numbers of cells seem to be less and separate from one another and they look small. Treatment with cherry laurel fruit extracts also delineated slightly degradations on the cells, as the cell growth affected and cellular morphology was similar to that of apoptotic situations only at high concentrations. However, the numbers of cells in low and medium concentrations of cherry laurel fruit extracts have not reduced and structurally, they look similar untreated cells.
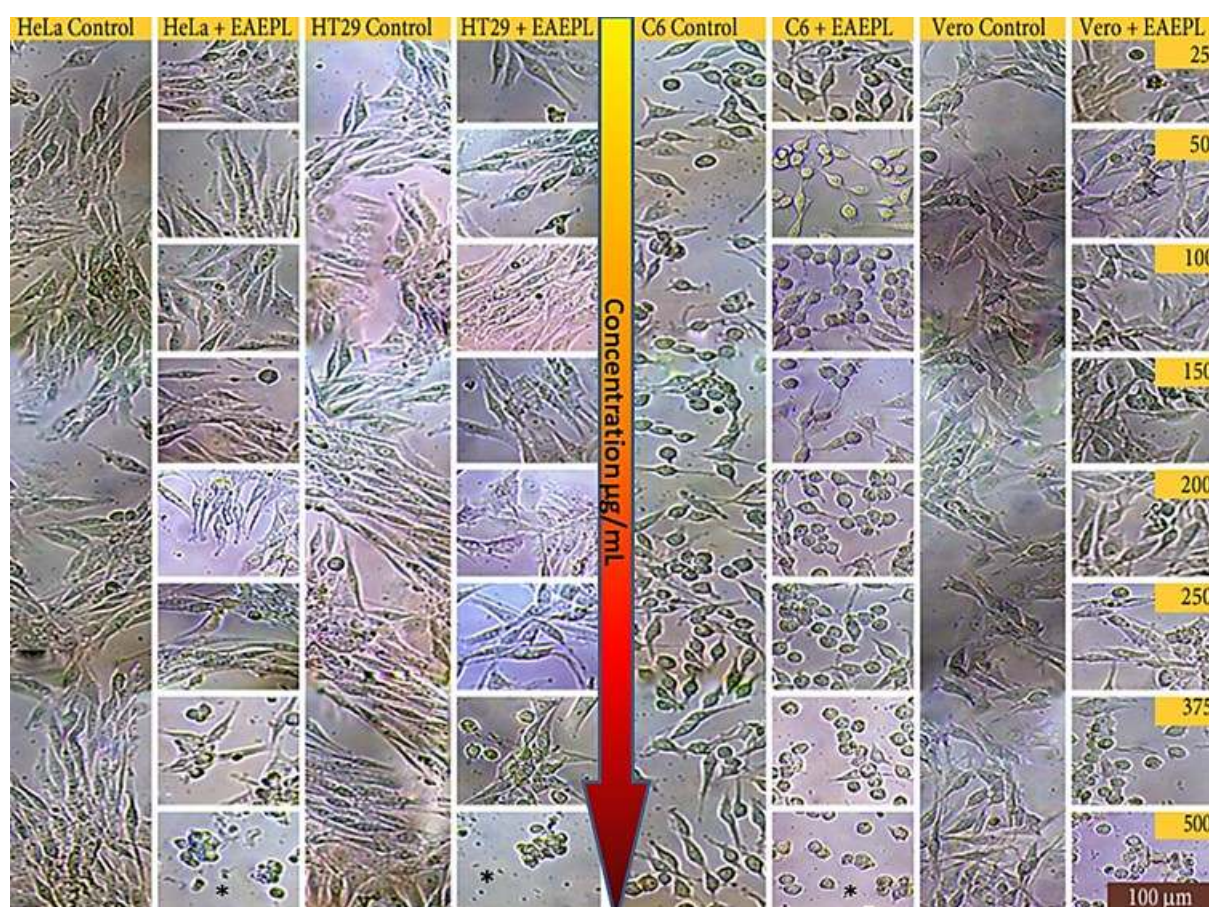
Figure 3. Effect of cherry laurel extracts on the morphology of HeLa, HT29, C6 and Vero cells. DMSO treated cells as controls. Asterisks point to the exposed surfaces from which cells have removed. All scales 100 µm.

Fatty acid analysis

Linoleic acid (18:2), palmitic acid (16:0) and oleic acid (18:1) were detected as fatty acids of hexane extract by GC-MS analysis. The human body cannot synthesize linoleic and oleic acids, both of which play an important role in the life. leading to regulate the blood homeostasis, the immune and inflammation response. In a similar study, main fatty acids constituents of cherry laurel were reported as linoleic, oleic, palmitic and stearic acid (21) which may be attributed to its pharmacological effects. Main ethereal

oils (0.5%) of Cherry Laurel were noted as the benzaldehyde, benzyl alcohol, and hydrocyanic acid (22). Plant oil originated seed or fruit has been used as a healing agent for various diseases. The protective biological activity of cherry laurel extracts is possibly attributed to its high linoleic acid, palmitic acid, and oleic acid contents. It is speculated that these fatty acids may protect DNA, RNA and other macromolecules by modulating oxidative damage in cells (23). On the other hand, these fatty acids use their receptors such as G-protein receptors to exhibit its immunomodulatory effect. However, we should be considered that palmitic acid is generally cytotoxic to cells, whereas oleic acid and linoleic acid are cytoprotective in some certain concentrations in cells (23).

CONCLUSION

In this study, we have displayed biological effects of cherry laurel fruit extracts against HT29, HeLa, C6 and Vero cell lines. The fatty acid-rich bioactive components of cherry laurel fruit extracts that is responsible for the chemoprotective effect. We found that, cherry laurel fruit extracts exhibited considerable protective activity against cell lines at even the highest concentration. Overall, we speculate that cherry laurel fruit extracts could be an important natural source of adjuvant chemotherapeutic formulary.

ACKNOWLEDGMENTS

AUTHOR CONTRIBUTIONS

Conceived and designed the experiments: AA RE. Performed the experiments: AA BY. Analyzed the data: AA RE ŞT. Contributed reagents/materials/analysis tools: AA BY.

REFERENCES

1. Elgorashi E. Screening of medicinal plants used in South African traditional medicine for genotoxic effects. Toxicol. Lett. 2003; 143, 195–207. doi:10.1016/S0378-4274(03)00176-0

2. Sithranga Boopathy N, Kathiresan K. Anticancer Drugs from Marine Flora: An Overview. J. Oncol. 2010; 1–18. doi:10.1155/2010/214186

3. Lee CC, Houghton P. Cytotoxicity of plants from Malaysia and Thailand used traditionally to treat cancer. J. Ethnopharmacol. 2005; 100, 237–243. doi: 10.1016/j.jep.2005.01.064

4. Itharat A, Houghton PJ, Eno-Amooquaye E, Burke P, Sampson JH, Raman A. In vitro cytotoxic activity of Thai medicinal plants used traditionally to treat cancer. J. Ethnopharmacol. 2004; 90, 33–38. doi: 10.1016/j.jep.2003.09.014

5. Elmastas M, Genc N, Demirtas I, Aksit H, Aboul-Enien HY. Isolation and Identification of Functional Components in Seed of Cherry Laurel (Laurocerasus officinalis Roem.) and Investigation of Their Antioxidant Capacity. J. Biol. Act. Prod. from Nat. 2013; 3, 115–120. doi:10.1080/22311866.2013.817736

6. Karabegović IT, Stojičević SS, Veličković DT, Todorović ZB, Nikolić NČ, Lazić ML. The effect of different extraction techniques on the composition and antioxidant activity of cherry laurel (Prunus laurocerasus) leaf and fruit extracts. Ind. Crops Prod. 2014; 54, 142–148. doi:10.1016/j.indcrop.2013.12.047

7. Türkan K, Kasim T, Bircan E, Murat K. DNA damage protecting activity and in vitro antioxidant potential of the methanol extract of Cherry (Prunus avium L). J. Med. Plants Res. 2014; 8, 715–726. doi:10.5897/JMPR2013.5350

8. Akkol EK, Kırmızıbekmez H, Kuçukboyacı N, Goren AC, Yesilada E. Isolation of active constituents from cherry laurel (Laurocerasus officinalis Roem.) leaves through bioassay-guided procedures. J. Ethnopharmacol. 2012; 139, 527–532. doi: 10.1016/j.jep.2011.11.043

9. Alasalvar C, Al-Farsi M, Shahidi F. Compositional characteristics and antioxidant components of cherry laurel varieties and pekmez. J. Food Sci. 2005; 70(1), S47–S52. doi: 10.1111/j.1365-2621.2005.tb09064.x

10. Ayaz FA, Kadioglu A, Reunanen M, Var M. Phenolic acid and fatty acid composition in the fruits of Laurocerasus officinalis Roem. and its cultivars. J. Food Compos. Anal. 1997; 10(4), 350–357. doi:10.1006/jfca.1997.0550

11. Karahalil FY, Sahin H. Phenolic composition and antioxidant capacity of cherry laurel (Laurocerasus officinalis Roem.) sampled from Trabzon region, Turkey. Afr. J. Biotechnol. 2011; 10(72), 16293–16299. doi: 10.5897/AJB11.1929

12. Kolayli S, Kuçuk M, Duran C, Candan F, Dinçer B. Chemical and antioxidant properties of Laurocerasus officinalis Roem. (cherry laurel) fruit grown in the Black Sea region. J. Agric. Food Chem. 2003; 51(25), 7489–7494. doi: 10.1021/jf0344486

13. Sahan Y, Cansev A, Celik G, Cinar A. Determination of various chemical properties, total phenolic contents, antioxidant capacity and organic acids in Laurocerasus officinalis fruits. Acta Hortic. 2012; 939, 359–366. doi: 10.17660/ActaHortic.2012.939.47

14. Porstmann T, Ternynck T, Avrameas S. Quantitation of 5-bromo-2-deoxyuridine incorporation into DNA: an enzyme immunoassay for the assessment of the lymphoid cell proliferative response. J Immunol Methods 1985; 82, 169-79. doi:10.1016/0022-1759(85)90236-4.

15. Weerapreeyakul N, Nonpunya A, Barusrux S, Thitimetharoch T, Sripanidkulchai B. Evaluation of the anticancer potential of six herbs against a hepatoma cell line. Chin. Med. 2012; 7, 15. doi: 10.1186/1749-8546-7-15

16. Zheng S-Y. Anticancer effect and apoptosis induction by quercetin in the human lung cancer cell line A-549. Mol. Med. Rep. 2011; 3, 822-6. doi: 10.3892/mmr.2011.726

17. Niu G, Yin S, Xie S, Li Y, Nie D, Ma L, Wang X, Wu Y. Quercetin induces apoptosis by activating caspase-3 and regulating Bcl-2 and cyclooxygenase-2 pathways in human HL-60 cells. Acta Biochim. Biophys. Sin. (Shanghai). 2011; 43, 30–37. doi: 10.1093/abbs/gmq107

18. Ferry DR, Smith A, Malkhandi J, Fyfe DW, DeTakats PG, Anderson D, Baker J, Kerr J. Phase I clinical trial of the flavonoid quercetin: pharmacokinetics and evidence for in vivo tyrosine kinase inhibition. Clin. Cancer Res. 1996; 2, 659–68. PMID: 9816216

19. Mandal AK, Das S, Mitra M, Chakrabarti RN, Chatterjee M, Das N. Vesicular flavonoid in combating diethylnitrosamine induced hepatocarcinoma in rat model. J Exp Ther Oncol 2008; 7, 123-133. PMID: 18771086

20. C.T.E.B.PDQ Integrative, Alternative, *Laetrile/Amygdalin (PDQ®): Health Professional Version*. 2002.

21. Halilova H, Ercisli S. Several Physico-Chemical Characteristics of Cherry Laurel (Laurocerasos Officinalis Roem.) Fruits. Biotechnol. Biotechnol. Equip. 2010; 24, 1970–1973. doi: 10.2478/V10133-010-0059-6

22. Stanisavljević IT, Lazić ML, Veljković VB, Stojičević SS, Veličković DT, Ristić MS. Kinetics of Hydrodistillation and Chemical Composition of Essential Oil from Cherry Laurel (Prunus laurocerasus L. var. serbica Pančić) Leaves. J. Essent. Oil Res. 2010; 22, 564–567. doi: 10.1080/10412905.2010.9700401

23. Herbal medicine: biomolecular and clinical aspects / editors, Iris F.F. Benzie and Sissi Wachtel-Galor. 2nd ed. Boca Raton: FL 33487-2742, CRC Press/Taylor & Francis Group; 2011. ISBN: 978-1-4398-0713-2.

Türkçe Öz ve Anahtar Kelimeler

Taflan Ağacının Antiproliferatif Etkisi

Ali Aydın, Ramazan Erenler, Bülent Yılmaz, Şaban Tekin

Öz: Taflan ağacı (*Prunus laurocerasus)* meyveleri fenolik ve flavonoid içerikler barındırmakta olup taze, kurutulmuş veya marmelat şeklinde tüketilirken yaprakları siyanojenik glikozidler içerir ve Anadolu folklorik tıbbında iyi bilinen iyileştirici etkilere sahiptir. Burada, taflan ağacı meyveleri suda 2 saat kaynatılmış, heksan, EtOAc ve BuOH ile ayrı ayrı ekstrakte edilmiştir. Ekstraktların antiproliferatif etkisi HeLa (İnsan Rahim Boynu Kanseri), HT29 (İnsan Kolorektal Adenokarsinoma), C6 (Sıçan Beyin Tümör Hücreleri) ve Vero (Afrika Yeşil Maymun Böbreği) hücre çizgileri üzerinde incelenmiştir. Bütün ekstraktlar yüksek derişimde çeşitli kanser hücre çizgilerinde hafif antiproliferatif etki göstermiştir. Taflan ağacı meyvesinin ekstraktlarının hücre zarını parçalama yeteneğini değerlendirdik. Sonuçlara göre taflan ağacı meyvesi sadece yüksek derişimlerde tümör hücre çizgilerinde hücre zarını biraz parçaladığı görülmektedir. Bu çalışmanın sonuçları taflan ağacı meyvesinin ekstraktlarının kanser hücreleri için antikanser araç olarak etkinliğini desteklememektedir, ancak şu andaki kemoterapötik araçlara potansiyel destek tedavisi yaparak hücre zehirliliğini düşürecek şekilde kullanılabieceğini göstermektedir. Heksan ekstraktında GC-MS analizi ile yağ asitleri bulunmuştur ve ana ürünler linoleik asit, palmitik asit ve oleik asit içermektedir.

Anahtar kelimeler: Taflan ağacı,, Laetrile, Antikanser aktivitesi, Sitotoksik aktivite.

Electrochemical Decolorization of Reactive Violet 5 Textile Dye using Pt/Ir Electrodes

Bahadır K. Körbahti* and Kezban Meltem Turan

Faculty of Engineering, Chemical Engineering Department, Mersin University, Çiftlikköy 33343 Mersin, Turkey

Abstract: Electrochemical decolorization of textile dyeing wastewater containing Reactive Violet 5 (RV5) were investigated at Pt/Ir electrodes in the presence of 75% NaCl + 25% Na_2CO_3 (w/w) supporting electrolyte mixture in a batch electrochemical reactor. Experimental parameters were operated in the range of 300-1500 mg/L textile dye concentration, 4-20 g/L 75% NaCl + 25% Na_2CO_3 electrolyte concentration, 5-15 mA/cm^2 current density, and 20-60°C reaction temperature in 15 min electrolysis time. Reactive Violet 5 decolorization increased with increasing current density and electrolyte concentration, and decreasing the textile dye concentration. Although a slight increase obtained in color removal efficiency, the temperature did not show much significant effect on decolorization. Depending on electrochemical reaction conditions, Reactive Violet 5 textile dye decolorization were obtained between 42.8-100%.

INTRODUCTION

Main processes in textile industry are singeing, desizing, sizing, bleaching, scouring, mercerization, dyeing, and finishing (1–3). Approximately 160 lb of water is required to produce 1 lb of textile product. Therefore, large amounts of wastewater are produced in textile manufacturing industry.

The application of color to the textile material is called dyeing and it may take place at any stage in the textile manufacturing process (2). In batch dyeing process, an amount of textile substrate is loaded into a dyeing machine and brings to the equilibrium with dyeing solution. In continuous dyeing processes, textile products are fed continuously into a dye solution at various speeds (2). Reactive and direct dyes are used for cotton, and disperse dyes are used for polyester in common. Dye molecules enter the fibers from the dye solution in a period of time depending on type of fabric and textile dye (2,4). The dye percentage in a bath that fixes to the textile fibers is called dye fixation. Direct and reactive dyes have a fixation rate of 90-95% and 60-90%, respectively (2,4). Dye fixation occurs more rapidly in continuous dying process than batch dyeing (2). Salt, auxiliary chemicals, and temperature controlled dye bath conditions enhance and optimize the fixation efficiency of the dyeing process (2). Typical cotton dyeing processes use sodium chloride and sodium carbonate as common salts (4).

The main source of dyeing wastewater is rinsing processes and spent dye bath which typically contains auxiliary chemicals, salt and residual dye (4). Textile wastewater is a hard-to-treat one due to its strong color, large amount of suspended solids, high chemical oxygen demand (COD), variable pH, salt content, and high temperature. Wastewater from textile processes that can cause damage if not treated before discharging to the environment (3). The major problems in the dyeing process are decolorization, removal of pollutants, salt elimination, and water-use reduction (4).

Electrochemical oxidation is a promising wastewater treatment method and replacing conventional processes in order to treat wastewater from industrial processes which are not easily biodegradable (4). Electrochemical technologies are novel treatment technologies for the elimination of broad-range of organic pollutants from water and wastewater including various types of textile dyes (5–8). Several advantages include easy operation and handling, automation, high efficiency, simple equipment, safety, operations under ambient temperature and pressure conditions. They can be applied to various types of effluents with chemical oxygen demand (COD) ranging from 0.1 g/L to about 100 g/L (5–8).

The strategies of electrochemical technologies include the treatment of effluents and wastes, and also the development of new processes or combined methods with less harmful effects (5–8). Electrolysis reactions involve electrical charges moving between the electrolyte and the electrodes. The process depends on the use of direct electric current for the chemical changes in non-spontaneous oxidation/reduction reactions.

In the literature, the electrochemical treatment have been tested for textile dye degradation with a large variety of electrodes including iron, aluminum, boron-doped diamond (BDD), carbon, graphite, doped and undoped PbO_2, mixed metal oxides of Ti, Ru, Ir, Sn and Sb, doped-SnO_2, Ti/Pt, Pt/Ir and Pt, carbonaceous electrodes, dimensionally stable anodes (DSA), and three-dimensional electrodes (5,6). The studies have utilized electrochemical systems for the treatment of synthetic and real textile dyeing wastewaters by three electrode cells with two or one compartments and divided or undivided two electrode cells or tank reactors equipped with monopolar and bipolar electrodes in batch and continuous modes (5,6). The influence of pH, pollutant concentration, current density, temperature, supporting electrolyte type and concentration, stirring rate and flowrate was investigated as main parameters for optimizing the degradation conditions (5–8).

In this study, the electrochemical decolorization of Reactive Violet 5 (RV5) textile dye was investigated using Pt/Ir electrodes. The effects of process variables such as electrolyte concentration, current density, initial dye concentration and reaction temperature on textile dye removal were analyzed.

MATERIALS AND METHODS

Chemicals and Materials

Reactive Violet 5 (RV5) textile dye (Sigma Aldrich) (Figure 1), Na_2CO_3 and NaCl (Merck) were purchased as extra pure grade. Textile dyeing wastewater was prepared synthetically using double distilled water, which was obtained using ultrapure water system (Millipore Simplicity® UV) and water still (GFL-2008) with the resistivity of 18.2 MΩ·cm@25°C, TOC < 5 ppb.
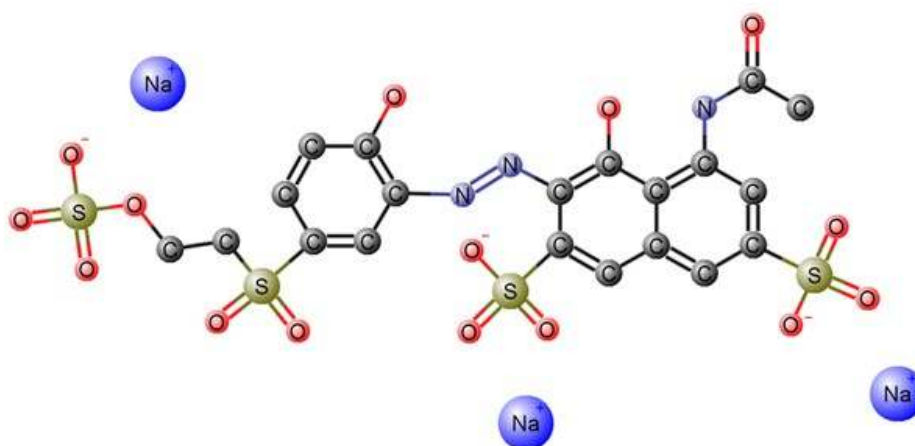
Figure 1. Molecular structure of Reactive Violet 5 textile dye ($C_{20}H_{16}N_3Na_3O_{15}S_4$).

Experimental

Electrochemical reactor (DURAN® glass) used in this study has a heating and cooling jackets (Rettberg, Germany) as shown in Figure 2. Iron cathodes and Pt/Ir anodes were used as four pairs with 5 mm anode/cathode spacing. Total electrode surface area was 172 cm^2. Pt/Ir anodes (Dr. Wieland, Germany) were in spiral shape with 90% Pt and 10% Ir composition (w=150 mm, $\phi_{internal}$=10 mm, ϕ_{wire}=1.10 mm). Iron electrodes were in cylindrical shape (ϕ=12.0 mm) and purchased from local sources. Pt/Ir and iron electrodes were used as received without further preparation and treatment. Batch electrochemical system was equipped with programmable DC power supply (Goodwill PST-3201), thermostat (Lauda RE 630 S), mechanical mixer (Heidolph RZR 2021), and peristaltic pump (Cole Parmer Masterflex® RZ-77924-60). The reaction medium was mixed at 500 rpm. Influence of experimental parameters were operated as textile dye concentration, 300-1500 mg/L; electrolyte concentration, 4-20 g/L; current density, 5-15 mA/cm^2; and reaction temperature, 20-60°C in 15 min electrolysis time.
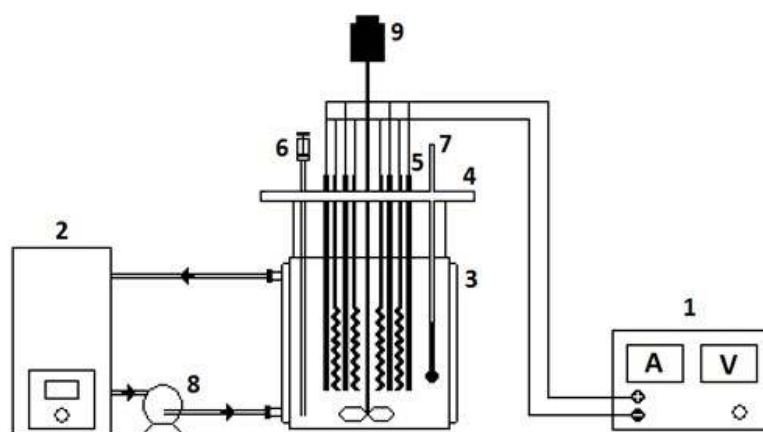
Figure 2. Batch electrochemical reactor system (1. programmable DC power supply, 2. heating/cooling tank, 3. batch electrochemical reactor, 4. reactor lid, 5. electrodes, 6. sampling cell, 7. thermometer, 8. heating/cooling pump, 9. mechanical mixer).

Samples in 10 mL volume were withdrawn from the reaction medium at 5 min time intervals for the analysis. Decolorization yield was analyzed using UNICO 4802 model UV/Vis double beam spectrophotometer at 520 nm wavelength.

RESULTS AND DISCUSSION

Textile dye concentration, current density, electrolyte (75% NaCl+25% Na_2CO_3) concentration and reaction temperature parameters were investigated on electrochemical decolorization efficiency of Reactive Violet 5 (RV5) textile dye using Pt/Ir anodes. In this study, 75% NaCl+25% Na_2CO_3 (w/w) mixture was used as a supporting electrolyte in order to increase the ionic conductivity of the reaction medium which are also main components in real textile industry wastewater (1).

Experimental results were analyzed using Design-Expert® 10 software. Reactive Violet 5 textile dye decolorization were obtained between 59.7-98.7% depending on electrochemical reaction conditions as shown in Table 1. In the study, complete decolorization was also achieved over 15 min electrolysis time.

Table 1. Influence of process parameters in electrochemical decolorization of textile dyeing wastewater containing Reactive Violet 5 (RV5) using Pt/Ir electrodes

Parameter	Reaction Conditions	Decolorization (%)
Textile dye concentration	300-1500 mg/L (Electrolyte=12 g/L, J=10 mA/cm^2, T=40°C, t=15 min)	59.7 - 98.7
Electrolyte concentration	4-20 g/L (RV5=900 mg/L, J=10 mA/cm^2, T=40°C, t=15 min)	73.3 - 95.0
Current density	5-15 mA/cm^2 (RV5=900 mg/L, Electrolyte=12 g/L, T=40°C, t=15 min)	65.0 - 96.7
Reaction temperature	20-60°C (RV5=900 mg/L, Electrolyte=12 g/L, J=10 mA/cm^2, t=15 min)	95.1 - 97.1

In electrochemical treatment processes, organic pollutants could be removed from wastewater by indirect and direct mechanisms (5–7,9,10). Indirect oxidation occurs in the liquid bulk phase by the mediated oxidants, and direct oxidation at the anode surface (5–7,9,10). Most electrochemical processes are based on indirect oxidation because direct oxidation of organic pollutants are very slow on inert anodes due to limiting reactions and reaction kinetics (8,11).

Hydroxyl radicals are produced by the anodic discharge of water in indirect electrochemical oxidation of organic pollutants at Pt/Ir anodes. Hydroxyl radicals adsorb on the anode surface [S], and oxidize the organic material (12,13). This reaction could also occur in acidic medium at high current densities (13). Oxidation process continues by the formation of hydroxyl radicals with anodic discharge of water molecules (12,13).

$$H_2O + S \rightarrow S\left[OH^\bullet\right] + H^+ + e^- \qquad\qquad \text{(Eq. 1)}$$

$$R + S\left[OH^\bullet\right] \rightarrow S + RO + H^+ + e^- \qquad\qquad \text{(Eq. 2)}$$

Chlorohydroxyl radicals are also produce with the presence of chloride ions, and adsorb on the active sites of the anode surface [S], and then oxidize the organic material (12,13).

$$H_2O + S + Cl^- \rightarrow S\left[ClOH^\bullet\right] + H^+ + 2e^- \qquad\qquad \text{(Eq. 3)}$$

$$R + S\left[ClOH^\bullet\right] \rightarrow S + RO + H^+ + 2e^- \qquad\qquad \text{(Eq. 4)}$$

Therefore, electrochemical oxidation of textile dyeing wastewater results in decolorization with the formation of chlorohydroxyl and hydroxyl radicals. The reactions can also yield O_2, H_2O_2, and Cl_2 (12,13).

$$H_2O + S[OH^{\bullet}] \rightarrow S + O_2 + 3H^+ + 3e^- \qquad \text{(Eq. 5)}$$

$$H_2O + S[OH^{\bullet}] \rightarrow S + H_2O_2 + H^+ + e^- \qquad \text{(Eq. 6)}$$

$$H_2O + S[ClOH^{\bullet}] + Cl^- \rightarrow Cl_2 + S + O_2 + 3H^+ + 4e^- \qquad \text{(Eq. 7)}$$
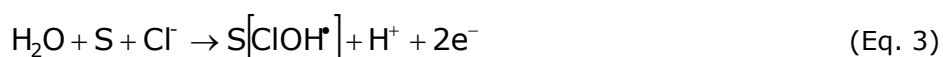
Indirect oxidation also occurs with the formation of HOCl/OCl⁻ redox mediators by the presence of NaCl which provides the anodic evolution of Cl₂ (12–16). The percentage distribution of HOCl/OCl⁻ depends on the solution pH (16). Chloride-chlorine-hypochlorite-chloride cycle occurs in neutral to moderate pH solutions which maintain the initial concentration of chlorides stable (13).

$$2Cl^- \rightarrow Cl_2 + 2e^- \qquad \text{(Eq. 8)}$$

$$Cl_2 + H_2O \Leftrightarrow HOCl + H^+ + Cl^- \qquad \text{(Eq. 9)}$$

$$HOCl \Leftrightarrow H^+ + OCl^- \qquad \text{(Eq. 10)}$$

$$6OCl^- + 3H_2O \rightarrow 2ClO_3^- + 4Cl^- + 6H^+ + \tfrac{3}{2}O_2 + 6e^- \qquad \text{(Eq. 11)}$$

$$OCl^- + H_2O + 2e^- \rightarrow Cl^- + 2OH^- \qquad \text{(Eq. 12)}$$
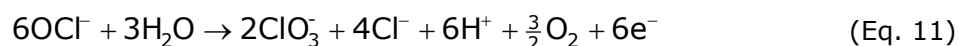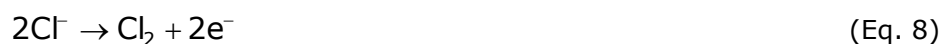
The effect of textile dye concentration on decolorization efficiency, pH, and cell voltage can be shown in Figures 3-5. The decrease in Reactive Violet 5 concentration resulted in increased decolorization rates and removal efficiency. The rate of degradation could be related to the formation of OH radicals and HOCl/OCl⁻ redox reagents.
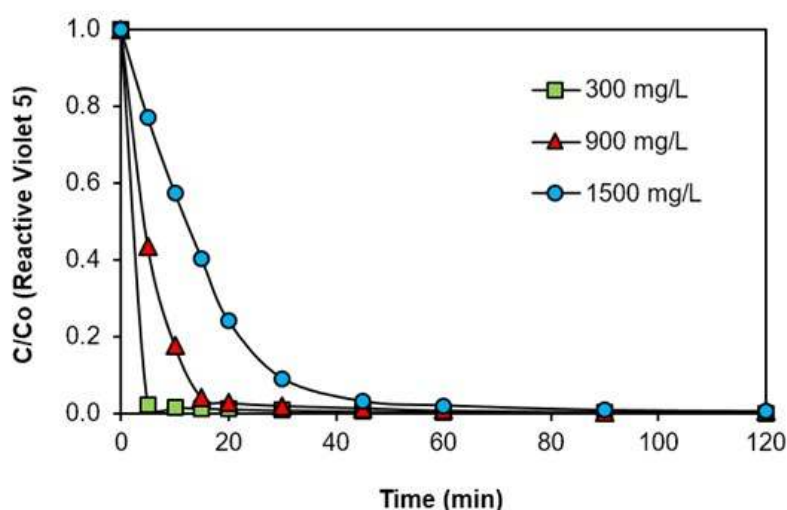
Figure 3. Effect of textile dye concentration on decolorization efficiency (Electrolyte=12 g/L, J=10 mA/cm², T=40°C).

It can be seen from Figure 3 that decolorization of RV5 dye exponentially decreases with time and almost disappears after 60 minutes resulting in complete decolorization of the solution. This exponential decrease of textile dye decolorization can be described by Equation (13):

$$-\frac{dC_{dye}}{dt} = kC_{dye}$$
(Eq. 13)

Several studies in the literature indicated that textile dye degradation reaction follows pseudo first order kinetics. Generally, first-order kinetics is appropriate for the entire concentration range and several studies were reasonably well fitted to this kinetic model (5,6,17–25). In our study, the rate constants were obtained for pseudo first order reaction as 12.7×10^{-3} s^{-1}, 3.1×10^{-3} s^{-1} and 1.2×10^{-3} s^{-1} for 300 mg/L, 900 mg/L, and 1500 mg/L RV5 dye, respectively. Reaction rate constants decreased and reaction rate increased as the initial concentration of the textile dye increased. It is generally noted that the degradation rate increases with the increase in dye concentration (17). The rate of degradation relates to the probability of OH radicals formation on the electrode surface and production of oxidizing redox reagents. As the initial concentrations of the dye increase the probability of reaction between dye molecules and oxidizing species also increases leading to an enhancement in the decolorization rate (17,23–25). In this study, reaction rate constants were obtained in a good agreement with the data previously reported in the literature for the electrochemical treatment of various types of textile dyes (5).

The pH of the reaction medium was changed between 10 and 11.5 as shown in Figure 4, which was observed in most of the runs and was most likely due to hydrolysis, ionization and $HOCl/OCl^-$ consumption reactions, and production of hydroxyl ions and oxygen evolution reaction as well (4,26). The effect of alkaline medium was also investigated in the literature for electrochemical and photocatalytic oxidation processes (5,17,21). Konstantinou and Albanis (23) reported the difficultness of the interpretation of pH effects on the efficiency of dye degradation process due to its multiple roles. The authors stated that in alkaline solution OH radicals are easier to be generated by oxidizing more hydroxide ions. Saquib and Muneer (17) indicated that the efficiency of degradation rate for the decomposition of textile dye was better at pH 3.5 and 11, whereas it was lower at pH values 5.8 and 9. In contrast, the degradation rate for the mineralization of the dye was found to decrease with the increase in pH from 3.5 to 9 and further increase in pH leads to increase in the efficiency of the degradation rate for TiO_2-mediated photocatalytic degradation of a triphenylmethane dye. Gonçalves et al. (21) obtained complete decolorization in photochemical treatment of azo dye solutions with TiO_2 catalyst after an irradiation period of 20 hours at an optimum pH 13. The authors indicated that the decolorization efficiency was lower both at pH 11 (70%) and pH 14 (55%) (21). Neppolian et al. (24) indicated that acidic pH has not

shown much influence on the percentage degradation of dye whereas the presence of hydroxyl ions in alkaline medium (pH > 10) enhances the degradation efficiency for TiO_2 assisted degradation of Reactive Blue 4 textile dye.
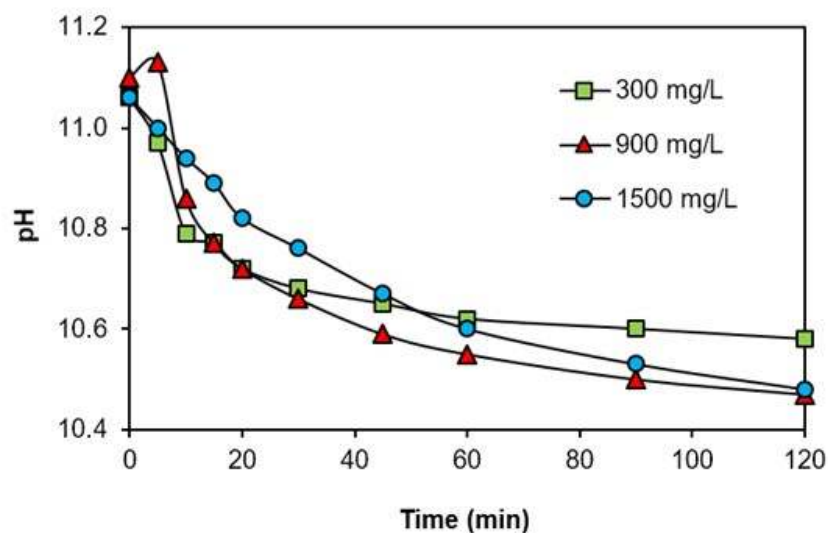
Figure 4. Effect of textile dye concentration on pH change (Electrolyte=12 g/L, J=10 mA/cm^2, T=40°C).

In this study, the cell voltage was changed between 2-3% with changing initial RV5 concentration as shown in Figure 5. It can be assumed that there were no mass transfer limitations depending on pollutant concentration and increasing dye concentration did not show significant effect on cell voltage. The runs were conducted at constant current and therefore cell voltage was variable to maintain the constant current density. As a general trend cell voltage raised about 20-25% from its initial value during the electrochemical reaction. This behavior could be attributed to the consumption of electrolyte that decreased the ionic conductivity. Ionic conductivity of the reaction medium is a very important parameter in electrochemical cells. If the concentration of electrolytes changes in the solution, then the charge difference changes. Increasing electrolyte strength decreases the solution resistance. A decrease in electrolyte concentration decreases ionic conductivity of the reaction medium that results in increase of electrical resistance and cell voltage as well (4,27–29).
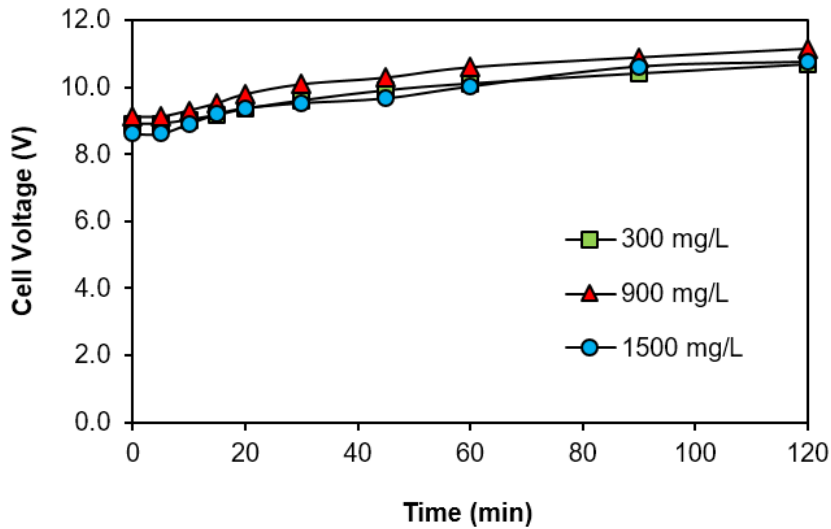
Figure 5. Effect of textile dye concentration on cell voltage (Electrolyte=12 g/L, J=10 mA/cm^2, T=40°C).

Figures 6-8 shows the effect of process parameters on textile dye decolorization that was obtained by the quadratic model in Equation 14 using Design-Expert® 10. Equation 14 evaluated with regression coefficients of R^2 and R^2_{adj} as 0.919 and 0.849, respectively, and signal/noise ratio value as 16.573 ($\geq$4) indicating that the model is adequate and can be used for the mathematical analysis. In Equation 14, x_1, x_2, x_3, and x_4 are Reactive Violet 5 concentration (mg/L), 75% NaCl + 25% Na$_2$CO$_3$ electrolyte concentration (w/w) (g/L), current density (mA/cm^2), and reaction temperature (°C), respectively.

$$
\begin{aligned}
\text{Decolorization (\%)} = &-0.088883x_1 + 3.11857x_2 + 3.59660x_3 - 1.85973x_4 \\
&+ 1.94681 \times 10^{-3}x_1x_2 + 7.11715 \times 10^{-3}x_1x_3 + 1.39549 \times 10^{-4}x_1x_4 - 0.28736x_2x_3 \\
&+ 0.052851x_2x_4 + 0.11345x_3x_4 - 2.43265 \times 10^{-5}x_1^2 - 0.12276x_2^2 - 0.38817x_3^2 \\
&+ 7.76927 \times 10^{-5}x_4^2 + 123.34789
\end{aligned}
$$

$$(14)$$

In Figure 6, dye decolorization was obtained as 42.8-100.0% between 300-1500 mg/L Reactive Violet 5 concentration and 4-20 g/L 75% NaCl+25% Na$_2$CO$_3$ (w/w) electrolyte mixture. Increase in Reactive Violet 5 concentration decreased the decolorization efficiency as shown in Figure 6. Textile dye decolorization obtained with the degradation of azo group in the dye molecule by formation of HOCl/OCl$^-$ redox reagents and weakly adsorbed hydroxyl and chlorohydroxyl radicals at the anode surface. In Figure 6, higher than 95% decolorization was achieved below 915 mg/L initial textile dye concentration. It can be concluded that mass transfer limitations have

predominant effect at low pollutant concentrations (7). Increasing electrolyte concentration increased the decolorization efficiency as shown in Figures 6 and 7. In Figure 6, higher than 95% decolorization was achieved between 14.5-18.8 g/L electrolyte concentration. Increasing NaCl concentration increased the decolorization efficiency by generation of HOCl/OCl⁻ redox reagents (4).
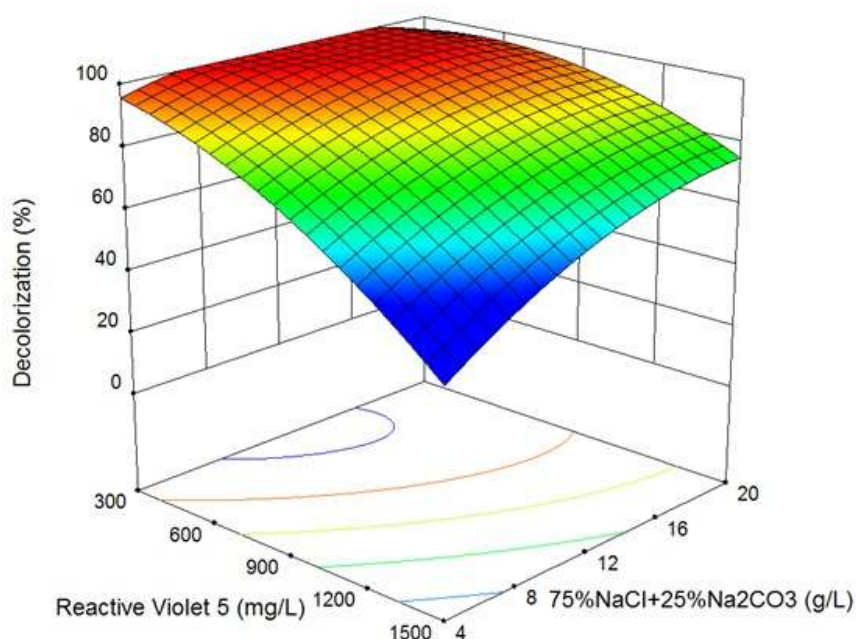
Figure 6. Effect of textile dye concentration and electrolyte concentration on electrochemical decolorization of Reactive Violet 5 textile dye using Pt/Ir electrodes (J=10 mA/cm^2, T=40°C, t=15 min).

In Figure 7, dye decolorization was obtained as 56.2-100% between 5-15 mA/cm^2 current density and 4-20 g/L 75% NaCl+25% Na$_2$CO$_3$ (w/w) electrolyte mixture. Increasing current density increased the decolorization efficiency as shown in Figures 7 and 8. In Figure 7, higher than 95% decolorization was achieved between 14.5-18.8 g/L electrolyte concentration. Increasing NaCl concentration increased the decolorization efficiency by generation of HOCl/OCl⁻ redox reagents (4). Degradation efficiency increased with increasing current density that resulted in formation of OH radicals at Pt/Ir anode, and increased formation rate of HOCl/OCl⁻ oxidants in the bulk phase. It is very well known that current density is one of the effective parameters for controlling the mass transfer and reaction rate in electrochemical processes (4). Although increasing current density increases electrochemical oxidation efficiency, applied current may be consumed by secondary reactions at high cell potentials (10,30). Therefore, optimum current density was determined as 12.8 mA/cm^2 for the highest electrochemical decolorization efficiency.
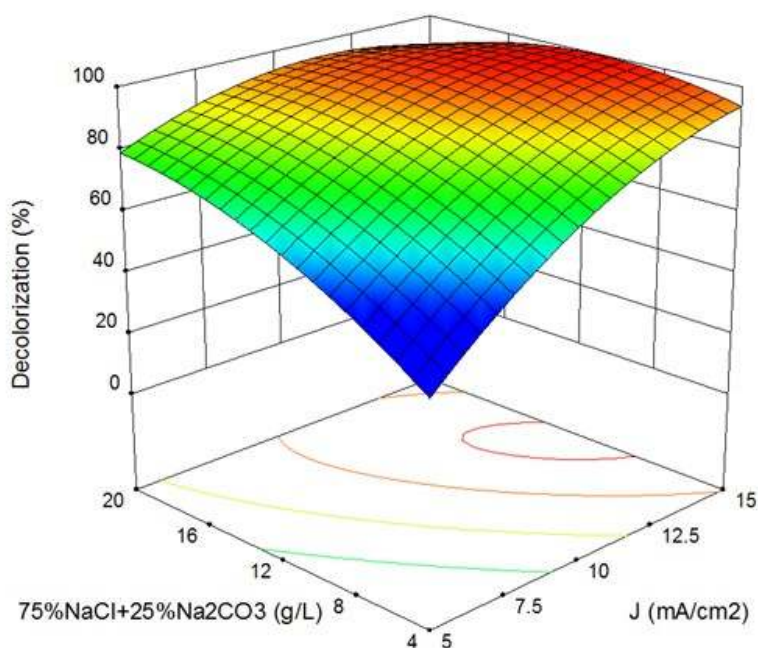
Figure 7. Effect of electrolyte concentration and current density on electrochemical decolorization of Reactive Violet 5 textile dye using Pt/Ir electrodes (RV5=900 mg/L, T=40°C, t=15 min).

Dye decolorization was obtained as 62.3-100% between 5-15 mA/cm^2 current density and 20-60°C reaction temperature in Figure 8. In Figure 8, higher than 95% decolorization was achieved above 10.2 mA/cm^2 current density and 30°C reaction temperature. Therefore, optimum reaction temperature was determined in the mid of the experimental conditions as 40°C.
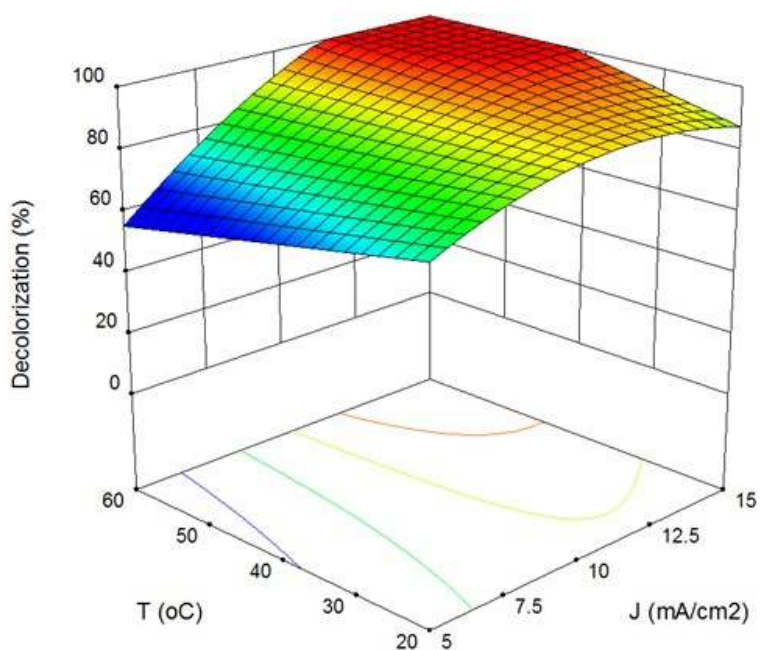
Figure 8. Effect of current density and reaction temperature on electrochemical decolorization of Reactive Violet 5 textile dye using Pt/Ir electrodes (RV5=900 mg/L, Electrolyte=12 g/L, t=15 min).

The optimum operating region was determined for the highest electrochemical decolorization efficiency of Reactive Violet 5 textile dye using Pt/Ir electrodes in Figure 9. The shaded region in Figure 9 shows the decolorization efficiency of higher than 95% for Reactive Violet 5 concentration and 75% NaCl+25% Na_2CO_3 electrolyte mixture at optimum operating values of 40°C reaction temperature and 12.8 mA/cm^2 current density. The optimum operating region was found to be applicable for the electrochemical treatment of industrial textile wastewater.
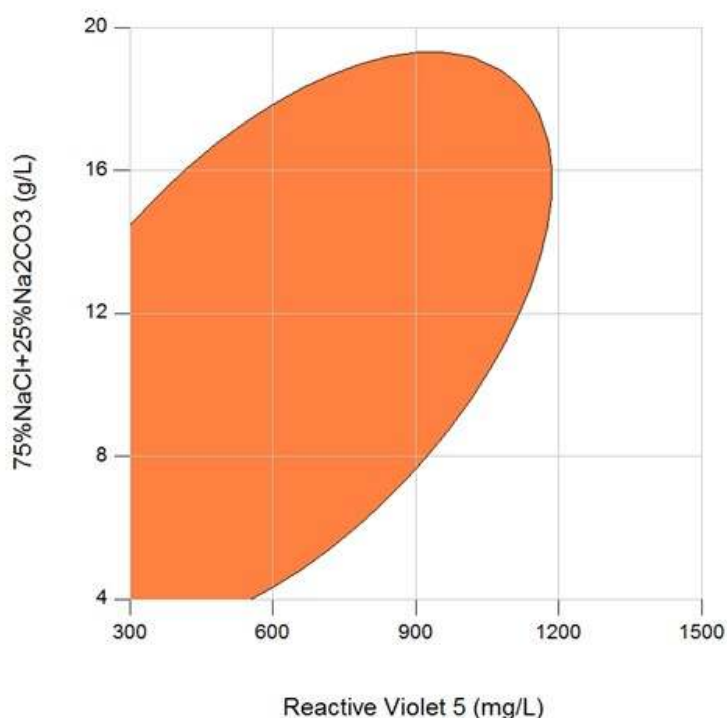
Figure 9. Optimum operating region for electrochemical decolorization of Reactive Violet 5 textile dye using Pt/Ir electrodes (J=12.8 mA/cm^2, T=40°C, t=15 min).

CONCLUSIONS

Electrochemical textile dye decolorization were investigated using Pt/Ir anodes in the presence of 75% NaCl+25% Na$_2$CO$_3$ supporting electrolyte mixture. Reactive Violet 5 decolorization increased with increasing current density and electrolyte concentration, and decreasing the textile dye concentration. Although a slight increase obtained in color removal efficiency, the temperature was not show much significant effect on decolorization. Reactive Violet 5 textile dye decolorization were obtained between 42.8-100% depending on electrochemical reaction conditions in 15 min reaction time without any further treatment. The optimum operating region at higher than 95% decolorization efficiency was determined for the Reactive Violet 5 textile dye. It can be concluded that Reactive Violet 5 textile dye decolorization obtained with the degradation of azo group in the dye molecule by the formation of redox reagents and weakly adsorbed hydroxyl and chlorohydroxyl radicals at the anode surface. Experimental findings showed that electrochemical oxidation could be an alternative for the decolorization of textile wastewater effluent.

REFERENCES

[1] Körbahti BK, Tanyolaç A. Electrochemical treatment of simulated textile wastewater with industrial components and Levafix Blue CA reactive dye: Optimization through response surface methodology. Journal of Hazardous Materials. 2008;151(2-3):422–31. DOI: 10.1016/j.jhazmat.2007.06.010.

[2] US EPA. EPA Office of Compliance Sector Notebook Project : Profile of the Textile Industry. 1997. EPA310R97009. URL: http:// nepis.epa.gov/Exe/ZyPURL.cgi?Dockey=50000HE9.TXT.

[3] US EPA. Best Management Practices for Pollution Prevention in the Textile Industry. 1996. EPA625R96004. URL: http:// nepis.epa.gov/Exe/ZyPURL.cgi?Dockey=30004Q2U.TXT.

[4] Körbahti BK. Response surface optimization of electrochemical treatment of textile dye wastewater. Journal of Hazardous Materials. 2007;145(1-2):277–86. DOI: 10.1016/j.jhazmat.2006.11.031.

[5] Brillas E, Martínez-Huitle CA. Decontamination of wastewaters containing synthetic organic dyes by electrochemical methods. An updated review. Applied Catalysis B: Environmental. 2015. p. 603–43. DOI: 10.1016/j.apcatb.2014.11.016.

[6] Panizza M, Cerisola G. Direct And Mediated Anodic Oxidation of Organic Pollutants. Chemical Reviews. 2009;109(12):6541–69. DOI: 10.1021/cr9001319.

[7] Comninellis C, Chen G. Electrochemistry for the environment. Springer; 2010. ISBN: 9780387369228.

[8] Rajeshwar K, Ibanez JG. Environmental Electrochemistry. Academic Press; 1997. ISBN: 9780123887320.

[9] Körbahti BK, Artut K. Electrochemical oil/water demulsification and purification of bilge water using Pt/Ir electrodes. Desalination. 2010;258(1-3):219–28. DOI: 10.1016/j.desal.2010.03.008.

[10]   Körbahti BK, Taşyürek S. Electrochemical oxidation of ampicillin antibiotic at boron-doped diamond electrodes and process optimization using response surface methodology. Environmental Science and Pollution Research. 2015;22(5):3265–78. DOI: 10.1007/s11356-014-3101-7.

[11]   Tarr MA. Chemical Degradation Methods for Wastes and Pollutants. CRC Press; 2003. ISBN: 9780824743079.

[12]   Vlyssides AG, Israilides CJ, Loizidou M, Karvouni G, Mourafeti V. Electrochemical treatment of vinasse from beet molasses. Water Science and Technology. 1997;36(2-3):271–8. DOI: 10.1016/S0273-1223(97)00398-3.

[13]   Israilides C, Vlyssides A, Mourafeti V, Karvouni G. Olive oil wastewater treatment with the use of an electrolysis system. Bioresource Technology. 1997;61(2):163–70. DOI: 10.1016/S0960-8524(97)00023-0.

[14]   Do J-S, Yeh W-C. Paired electrooxidative degradation of phenol with in situ electrogenerated hydrogen peroxide and hypochlorite. Journal of Applied Electrochemistry. 1996;26(6):673–8. DOI: 10.1007/BF00253467.

[15]   Lin SH, Shyu CT, Sun MC. Saline wastewater treatment by electrochemical method. Water Research. 1998;32(4):1059–66. DOI: 10.1016/S0043-1354(97)00327-8.

[16]   Tchobanoglous G, Burton FL, Stensel HD. Wastewater Engineering: Treatment and Reuse. McGraw-Hill, 2004. ISBN: 9780071241403.

[17]   Saquib M, Muneer M. TiO$_2$/mediated photocatalytic degradation of a triphenylmethane dye (gentian violet), in aqueous suspensions. Dyes and Pigments. 2003;56(1):37–49. DOI: 10.1016/S0143-7208(02)00101-8.

[18]   Augugliaro V, Baiocchi C, Prevot AB, García-López E, Loddo V, Malato S, *et al*. Azo-dyes photocatalytic degradation in aqueous suspension of TiO$_2$ under solar irradiation. Chemosphere. 2002;49(10):1223–30. DOI: 10.1016/S0045-6535(02)00489-7.

[19]   Stylidi M, Kondarides DI, Verykios XE. Pathways of solar light-induced photocatalytic degradation of azo dyes in aqueous TiO$_2$ suspensions. Applied Catalysis B: Environmental. 2003;40(4):271–86. DOI: 10.1016/S0926-3373(02)00163-7.

[20]   Epling GA, Lin C. Photoassisted bleaching of dyes utilizing TiO$_2$ and visible light. Chemosphere. 2002;46(4):561–70. DOI: 10.1016/S0045-6535(01)00173-4.

[21]   Gonçalves MST, Oliveira-Campos AMF, Pinto EMMS, Plasência PMS, Queiroz MJRP. Photochemical treatment of solutions of azo dyes containing TiO$_2$. Chemosphere. 1999;39(5):781–6. DOI: 10.1016/S0045-6535(99)00013-2.

[22]   Brillas E, Sirés I, Oturan MA. Electro-fenton process and related electrochemical technologies based on fenton's reaction chemistry. Chemical Reviews. 2009;109(12):6570–631. DOI: 10.1021/cr900136g.

[23]   Konstantinou IK, Albanis TA. TiO$_2$-assisted photocatalytic degradation of azo dyes in aqueous solution: Kinetic and mechanistic investigations: A review. Applied Catalysis B: Environmental. 2004;49(1):1–14. DOI: 10.1016/j.apcatb.2003.11.010.

[24]   Neppolian B, Choi HC, Sakthivel S, Arabindoo B, Murugesan V. Solar light induced and TiO$_2$ assisted degradation of textile dye Reactive Blue 4. Chemosphere. 2002;46(8):1173–81. DOI: 10.1016/S0045-6535(01)00284-3.

[25]   Dutta K, Mukhopadhyay S, Bhattacharjee S, Chaudhuri B. Chemical oxidation of methylene blue using a Fenton-like reaction. Journal of Hazardous Materials. 2001;84(1):57–71. DOI: 10.1016/S0304-3894(01)00202-3.

[26]   Körbahti BK, Tanyolaç A. Continuous electrochemical treatment of simulated industrial textile wastewater from industrial components in a tubular reactor. Journal of Hazardous Materials. 2009;170(2-3):771–8. DOI: 10.1016/j.jhazmat.2009.05.032.

[27]   Petrovic M, Milijkovic M, Bojic A, Dordjevic D, Stepanovic J, Stamenkovic M. The Influence of the Background Electrolyte Concentration on the Removal of Crystal Violet by Electrochemical Oxidation on the Platinum Anode. Advanced technologies. 2013;2(1):41-4. URL: http://www.tf.ni.ac.rs/casopis/sveska1vol2/c36.pdf.

[28]   İrdemez Ş, Tosunoglu NDV. The effects of supporting electrolyte type and concentration on the phosphate removal from wastewater by electrocoagulation with aluminum plate electrodes. Iğdır University Journal of the Institute of Science and Technology. 2011;1(2):35-40. URL: http://dergipark.ulakbim.gov.tr/igdirfbed/article/viewFile/5000093666/5000087209.

[29]   Dalvand A, Gholami M, Joneidi A, Mahmoodi NM. Dye Removal, Energy Consumption and Operating Cost of Electrocoagulation of Textile Wastewater as a Clean Process. CLEAN - Soil, Air, Water. 2011;39 (7):665–72. DOI: 10.1002/clen.201000233.

[30]   Shen ZM, Wu D, Yang J, Yuan T, Wang WH, Jia JP. Methods to improve electrochemical treatment effect of dye wastewater. Journal of Hazardous Materials. 2006;131(1-3):90–7. DOI: 10.1016/j.jhazmat.2005.09.010.

Pt/Ir Elektrotları Kullanarak Reaktif Viyole 5 Tekstil Boyasının Renginin Elektrokimyasal Olarak Giderilmesi

Bahadır K. Körbahti* ve Kezban Meltem Turan

Öz: Reaktif Viyole 5 (RV5) içeren tekstil boyama atık sularının elektrokimyasal olarak renginin giderilmesi, Pt/Ir elektrotlarda %75 NaCl + %25 Na_2CO_3 (w/w) destek elektrolit karışımında kesikli bir elektrokimyasal reaktörde incelenmiştir. Deneysel parametreler 300-1500 mg/L tekstil boyarmadde derişiminde, 4-20 g %75 NaCl + %25 Na_2CO_3 elektrolit derişiminde, 5-15 mA/cm^2 akım yoğunluğunda ve 20-60 °C tepkime sıcaklığında ve 15 dakika elektroliz zamanı içinde yürütülmüştür. Reaktif Viyole 5'in renginin giderilmesi artan akım yoğunluğu ve elektrolit derişimi ile artarken tekstil boyarmadde derişiminin azalması ile de artmaktadır. Renk giderme etkinliğinde hafif bir artışa rağmen, sıcaklığın renk giderme üzerinde belirgin bir etkisinin olmadığı saptanmıştır. Elektrokimyasal tepkime koşullarına dayanarak, Reaktif Viyole 5 tekstil boyarmadde renk gidermesi %42,8-100 arasında değişmiştir.

Anahtar kelimeler: Renk giderme, Elektrokimyasal Atık Su Terbiyesi, Pt/Ir Elektrotlar, Reaktif Viyole 5, Tekstil Boyarmaddesi.

Co-Pyrolysis of Göynük Oil Shale with Polypropylene and Structural Characterizatıon of Pyrolysis Liquid

Pınar Acar Bozkurt[1],*, Nagehan Merve Kutlu[1], Muammer Canel[1]

[1]Ankara University, 06100, Ankara, Turkey.

Abstract: This study is based on the purpose of obtaining high yields of liquid product by subjecting the oil shale sample taken from one of our country's important oil shale deposits and polypropylene (PP) mixtures to co-pyrolysis process. In this study, the oil shale sample and the polypropylene were firstly subjected to pyrolysis process, and then the mixture obtained by mixing of these at certain ratios was subjected to pyrolysis process. Pyrolysis experiments were performed at three different mixture ratios of 33%, 50% and 67% PP in the mixture, and in the temperature range of 600 – 800 °C. The gas, liquid, and solid product yields obtained as a result of the experiments were calculated, and the effect of PP which was added to oil shale and the changed pyrolysis temperature on the yield of liquid product was examined. As a result of the experiments, the highest liquid product yield was achieved in the mixture ratio containing 67% PP at 800 °C. Various catalysts were added to the medium in which the highest liquid product yield was achieved, and the effect of catalysts on the liquid product yield obtained from pyrolysis was examined. The structure of the obtained liquid products was investigated by various spectroscopic methods such as GC-MS and FTIR, and the effects of experimental conditions on the structure of the liquid product were analyzed. Consequently, a noticeable synergistic effect was observed in the yield of the liquid product which was obtained as a result of the co-pyrolysis of PP and oil shale, and this effect further increased with the catalyst added to the medium. The results in this study also showed that co-pyrolysis of oil shale with PP could be an environmentally friendly method for the conversion of hazardous waste into valuable chemicals and fuels.

Keywords: Co-pyrolysis, oil shale, polypropylene, characterization.

INTRODUCTION

The increasing energy and petroleum need has pushed researchers towards studies related to sustainable energy technologies. On the other hand, a rapid decrease in energy resources such as petrol and natural gas has made making use of asphaltite, oil shales, and especially coal as the potential energy and chemical raw material resources of the future a current issue again. Oil shales take the second place in terms of reserve compared to other resources such as petrol, coal and natural gas [1].

Oil shale is defined as a sedimentary rock which contains an organic substance called kerogen, a fine-grained, lamellar structure [2]. Kerogen has a high hydrogen/carbon ratio that provides superior potential use as a liquid fuel source than coal or heavy oil. Oil shale is usually used as a fuel, solvent, and chemical resource after a thermal conversion process [3, 4].

Oil shale is the second largest fossil fuel after lignite in Turkey and has a significant value in the country's economy [5]. Göynük and Seyitömer oil shales have the largest share in the distribution of oil shale deposits according to reserve status. Since the kerogen in the oil shale structure is rich in hydrogen, the ratio of giving a distillable liquid and gas yield is greater than coal when it is subjected to heat treatment. However, it is not possible to make use of these resources by burning them as in the coal. Because during burning, some portion of the rapid decay products occurring in the organic structure at temperatures reaching up to 450 °C are released with combustion gases without finding an opportunity to burn. Therefore, making use of it by burning is not approved in terms of environmental pollution. Based on this aspect, pyrolysis method can be used in making use of oil shales which are the most important fossil resources that can be considered after coal. Pyrolysis process can be defined as the conversion process of oil shales into liquid and gas products by subjecting to thermal degradation in an inert medium.

In the studies carried out in recent years, it has been determined that the liquid and gas product yield obtained by subjecting coals through mixing with polymers to processes such as co-pyrolysis, extraction, and gasification is higher than the products obtained by singly subjecting both coal and polymers to these processes, and the distribution of products has far more superior characteristics in the co-pyrolysis process in terms of quality [6-8]. During the co-pyrolysis of coal with polymers, radicals formed at high temperatures are saturated with

hydrogen, released from the polymers, increasing the liquid yield [9]. Thus, it was revealed that a synergistic effect appeared during the co-pyrolysis of polymers with coal, and the polymers served as a hydrogen source [10, 11].

In the co-pyrolysis process, plastic wastes are the main polymer sources to be processed with coal. All over the world, plastics are the indispensable material of the future which are used as an alternative material instead of materials such as glass, metal, rubber, wood, inorganic substances, or together with these materials. The fact that it is economic and easily applicable is rapidly increasing the plastic consumption compared to other materials. The increasing use of plastics leads to an increase in plastic wastes, as well; and this situation emerges as a major environmental problem that needs to be solved. Plastic wastes are disposed by waste burial and waste incineration or utilized by using various recycling techniques. Pyrolysis, one of the methods of recycling plastics, is the most advantageous method from many aspects. Plastic wastes are converted into energy and chemical raw materials by pyrolysis.

Plastics are named in several ways depending on the type of the polymer used in production. Some types of plastic which are commonly used can be listed as polyethylene (PE), polypropylene (PP), polystyrene (PS), polyethylene terephthalate (PET), polyamide (PA), polyester, polyvinyl chloride (PVC), and polyurethane. When the plastic demands of 2010 in the world and Turkey are analyzed, it is seen that PE and PP have the largest share [12, 13].

In this study, the effect of co-pyrolysis of Göynük oil shale with polypropylene waste was investigated with the aim of understanding its effect of liquid formation and fuel or raw material characteristics. In the experiments, the oil shale and polypropylene mixtures were subjected to pyrolysis process at different temperatures, and the gas, liquid and solid (residual coke) yields obtained at each temperature were determined. The effect of experimental conditions and catalysts on yields was investigated by using different catalysts such as bentonite, zeolite, and red mud under optimum conditions specified. This study is significant in terms of use co-pyrolysis of oil shale and PP with catalyst to obtain the liquid products with high heating value. An attempt to investigate the structure of the obtained liquid products was made by various spectroscopic methods such as GC-MS and FTIR.

MATERIALS AND METHODS

Oil shale sample was obtained from Bolu-Göynük located in Turkey. Pretreatments of samples were carried out before the experiments. The samples were ground to obtain the desired particle size of 1-2 mm and were subsequently dried at 105°C for 24 h. Polypropylene (PP) was provided from the Özuğur-Akçim Plastic Company (Izmir, Turkey). Elemental analysis and higher heating value (HHV) of the oil shale and PP were performed with an elemental analyzer (LECO 932 CHNS elemental analyzer) and bomb calorimeter (Parr 6200 calorimeter). The characteristics of the samples are given in Table 1.

Table 1. Main characteristics of the oil shale and PP.

	Elemental Composition, wt%, daf				Calorific value (MJ/kg)
	C	H	N	O	
Oil shale	57.50	3.50	0.70	38.30	5.90
PP	75.90	5.40	-	18.70	39.50

Characterization of products

GC–MS analysis for liquid samples (tar) were performed using an AGILENT 6890 Model gas chromatograph coupled to a HP 5973 mass selective quadrupole detector using a 50 m ×0.32 mm × 0.52 mm capillary column. Chromatographic peaks were identified by means of NIST mass spectral data library and from their retention times using standard compound when available. The percentages of the peaks were calculated from the TIC (total ion chromatogram) peak area. FTIR spectra of the liquid samples as KBr disks of the samples were recorded by a MATTSON 1000 Model FTIR spectrometer.

Pyrolysis procedure

All pyrolysis experiments were performed in a fixed bed pyrolysis system shown schematically in Figure 1 [7]. Oil shale and PP were firstly pyrolyzed, then oil shale and PP mixtures in weight percent of 33% (wt), 50%(wt) and of 67% (wt) of polymer were co-pyrolyzed at temperatures between 600°C and 800°C. Oil shale and PP were mixed together in weight percent of 33 wt% (6.66 g of oil shale and 3.33 g of PP), 50 wt % (5 g of oil shale and 5 g of PP), and 67 wt % (3.33 g of oil shale and 6.66 g of PP) of PP. In order to evaluate the effect of catalyst on product yield, different amounts of catalysts were added to 67 wt% oil shale / PP mixture and these mixtures are pyrolyzed.

The catalysts used are red mud, zeolite, and bentonite. The red mud is supplied by Seydisehir Aluminum Company, Turkey. It is filtered and then dried at 110 °C. Linde type A-zeolite is supplied by CWK Chemiewerk Köstritz Company, Germany. Zeolite is activated by heating for 2 h at 200°C and then drying for 2 h at 500 °C. Bentonite from the Kütahya region, Turkey, is used in the experiments. Bentonite is activated by heating for 6 h at 97°C in a H_2SO_4 solution (40 wt%). The specific surface area of red mud, zeolite, and bentonite are 16 m^2g^{-1}, 300 m^2g^{-1}, and 134 m^2g^{-1}, respectively.
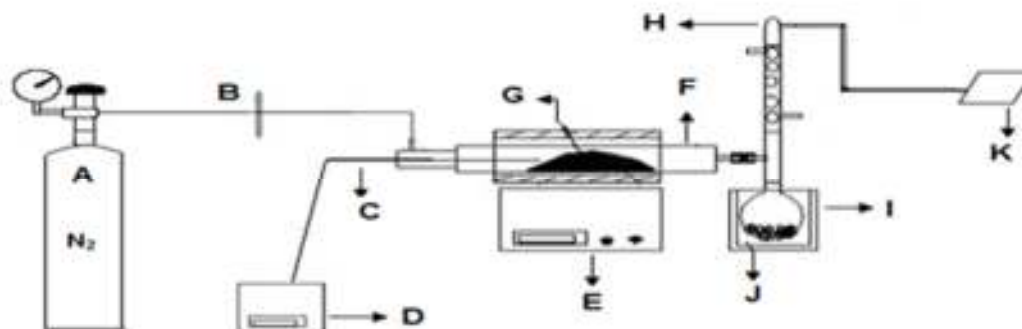
Figure 1. The schematic diagram of the experimental set-up for the co-pyrolysis. (A) nitrogen bottle, (B) float flowmeter, (C) thermocouple, (D) the temperature controller, (E) tube furnace, (F) reactor, (G) sample, (H) condenser, (I) cooling unit, (J) liquid collecting vessel, (K) gas collecting vessel.

In a typical run, the sample was placed in a stainless steel reactor. The reactor was heated by an electrical furnace in which the temperature was measured by a thermocouple inside the reactor. The air of the reactor was removed with nitrogen flow of 30 mL min^{-1} and reactor was heated to a desired temperature with a heating rate of 10 °C min^{-1}. The outlet of the reactor is connected to a round-bottomed flask with a reflux condenser where condensation of the pyrolyzate occurred. The reaction products are classified into three groups: gas, liquid hydrocarbons (tar) and residual coke. The yield of tar collected in the round-bottomed flask, and the yield of residual coke as the char remaining inside the reactor after the experiment were calculated. The gas products collected by a receiver vessel connected to the end of the reflux condenser.

RESULTS and DISCUSSION

Product yields

It is known that temperature has a significant effect on the yield of pyrolysis products [14-16]. The changes in product yields with temperature (600 °C, 700 °C and 800 °C) during the co-pyrolysis of PP and oil shale are given in Figure 2.
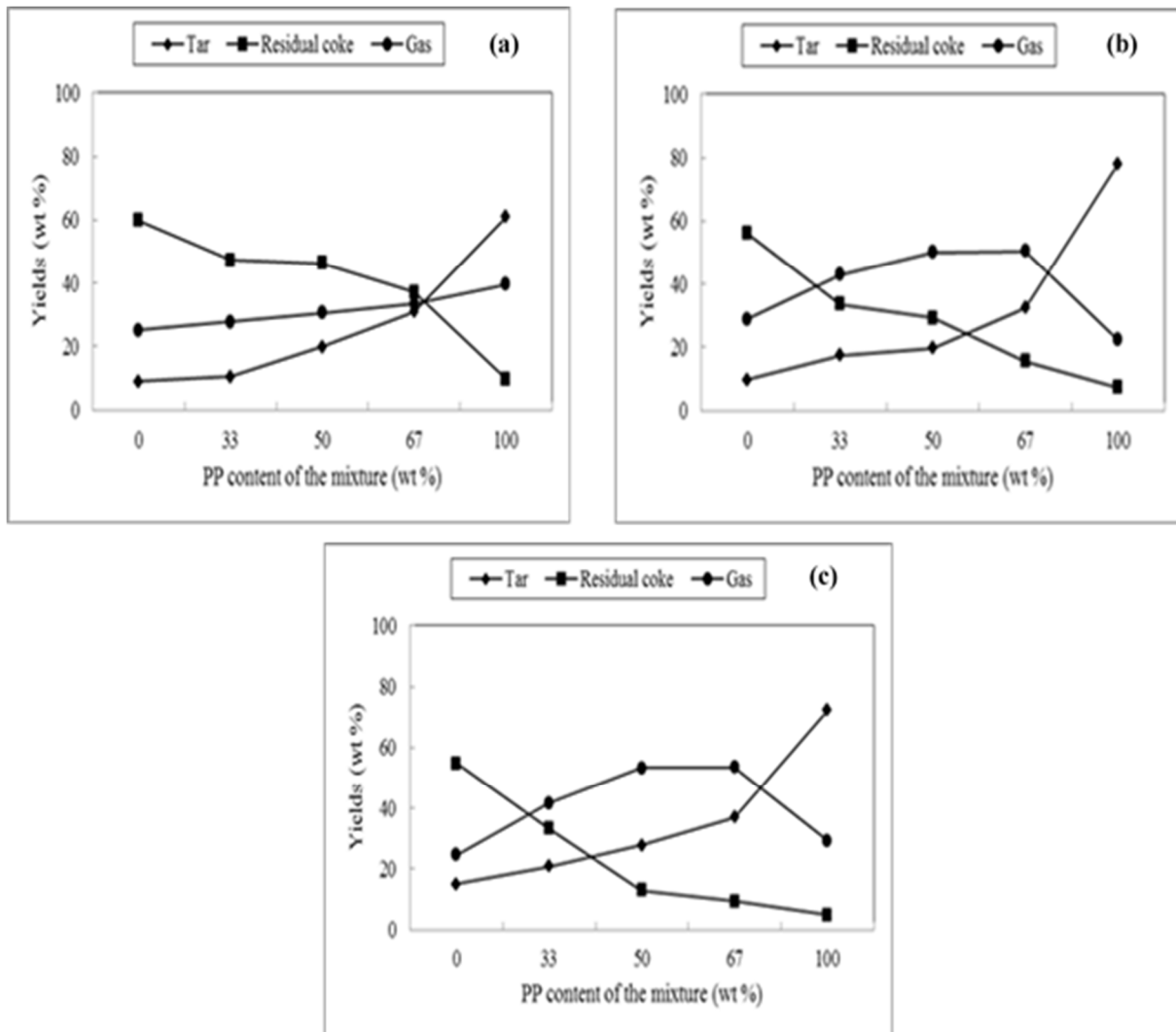
Figure 2. Effect of weight percentage of PP in the mixtures on product yields at a temperature of: (a) 600°C, (b) 700°C, and (c) 800°C.

As seen in the figure, the highest liquid yield was found to be 36.5% at the mixture ratio of 67% and at 800°C. The use of sweeping gas in the pyrolysis processes provides an inert atmosphere and helps to prevent secondary cracking reactions by removing the hydrocarbon vapors formed in during pyrolysis, and leads to an increase in the yield of the liquid product [17]. In pyrolysis processes performed at different mixture ratios and temperatures, a

decrease was observed in the yield of the solid product although an increase was observed in the yields of liquid and gas products. This situation can be explained by the fact that the bonds in the structure of samples are easily broken along with the effect of increasing temperature, and this affects the pyrolysis yield positively.

According to the co-pyrolysis results, higher ratios of liquid and gas product yields were obtained when compared to the values of oil shale yields. It is considered that an increase was observed in the liquid yield by bringing free radicals that formed during pyrolysis into steady state and by reducing the crosslinks in the structure of the polymer and oil shale. The crosslinks in the both of sample mixtures structures can be broken by effect of the increasing temperature. However, the amount of hydrogen in the oil shale structure is not sufficient to stabilize the radicals. Therefore, hydrogen should be directly provided to pyrolysis medium or the oil shale should be co-pyrolyzed with the compounds containing abundant hydrogen in their structure [18, 19]. The main reason for choosing PP as the second component in the co-pyrolysis process is the fact that it is an environmental waste and contains sufficient hydrogen to saturate the free radicals formed during the pyrolysis of the oil shale.

Conversion values (%) obtained by the addition of increasing PP ratios in the oil shale during the co-pyrolysis process and the changing with temperature are given in Figure 3. As it is seen in the figure, the conversion values also increase with increasing PP content of the mixture and temperature. This is because, as it was explained previously, the bonds in the oil shale structure are broken with increasing the temperature. These radicals are stabilized by the hydrogen provided from polypropylene. As a consequence, the liquid product yield was increased, and the gas product yield was also increased by the disintegration of the products into smaller molecular products with the temperature increase.
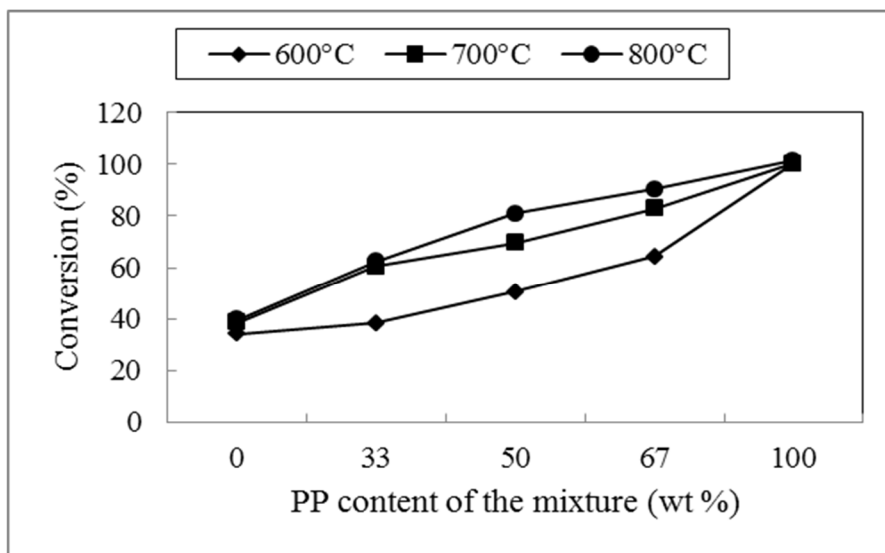
Figure 3. The effect of the percentage conversion of the PP content in the mixture**.**

Catalyst effect

It is known that various catalysts have an effect on the rate of some complex reactions in the pyrolysis process. In this study, the effects of three different catalysts selected on the co-pyrolysis of oil shale-PP mixture were examined. The red mud obtained during the production of aluminum; bentonite which is abundant in our country and zeolite which is applied in various heterogeneous reactions were selected as the catalysts. The co-pyrolysis experiments with catalyst were carried out at the mixture ratio of 67% at 800°C in which the liquid product yield was the highest. The red mud, bentonite, and zeolite were separately added to mixtures at the ratios of 0.5%, 2%, and 4% by mass to further improve the liquid product yield. The change of the liquid, gas, and solid product yields with catalytic pyrolysis is shown in Figure 4.

Any significant changes have been found when red mud is used as a catalyst (Figure 4). The surface area of red mud is smaller compared to other catalysts and therefore it does not interact sufficiently with the products during pyrolysis process. Although zeolite catalyst caused a decrease in the gas product yield, it did not cause a considerable change in the liquid product's yield. The solid product yield also increased. This is because more aromatic hydrocarbons are formed in zeolite which has greater pore opening, and the amount of residual coke increases because aromatic compounds are inclined to coke formation with hydrogen transfer and cyclization reactions [20]. It is seen that the highest liquid product yield was obtained in the pyrolysis experiments with 4% bentonite was used as a catalyst. The reason of increasing of liquid products is the catalytic effect of metal oxides in the structure of bentonite and the large pore structure of bentonite.
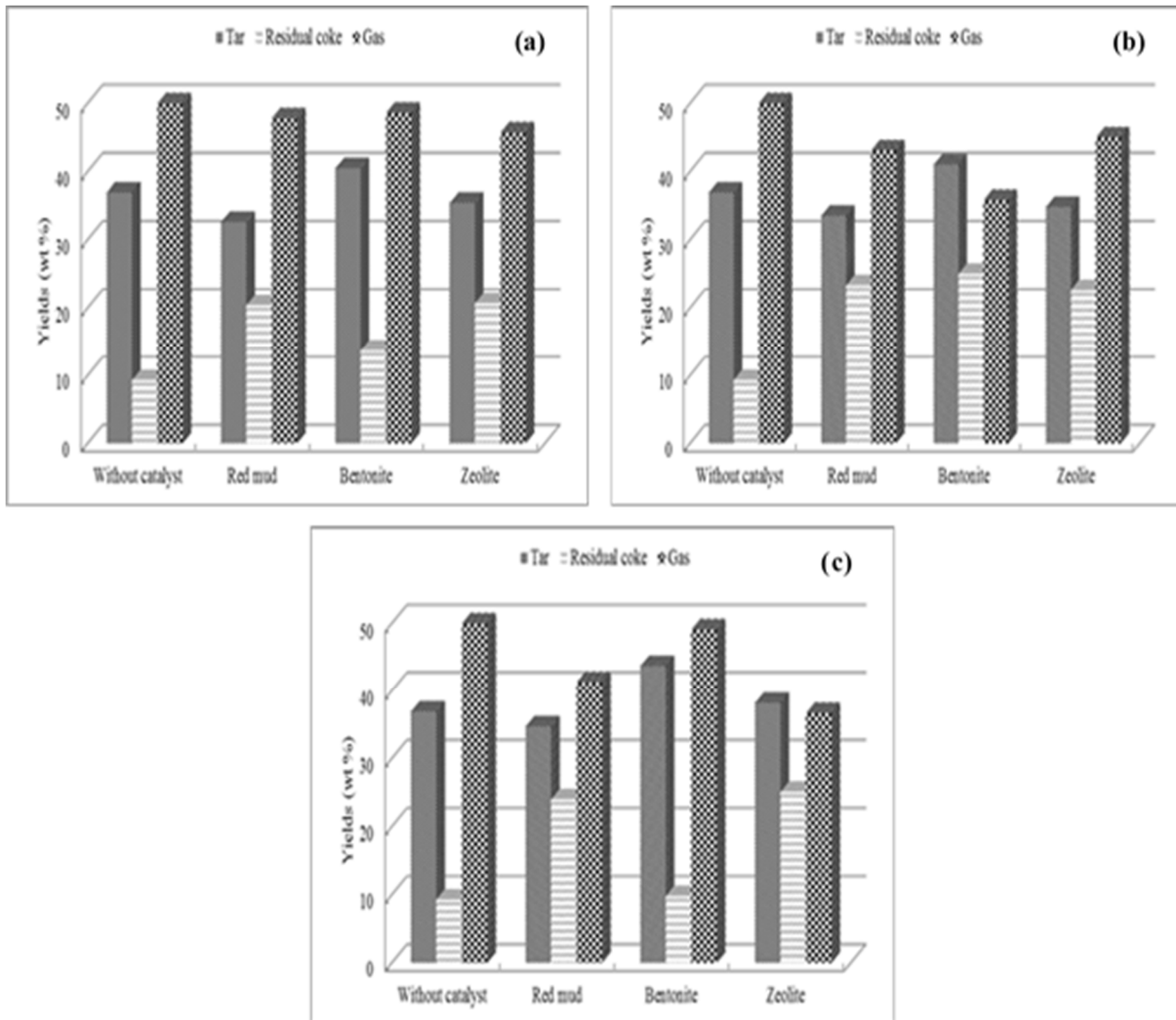
Figure 4. Effect of weight percentage of different catalyst on the yields at a temperature of 800°C and 67 wt% PP in the mixture a) 0.5 wt %, catalyst, b) 2 wt %, catalyst, c) 4 wt %, catalyst.

Characterization of pyrolysis liquid

The liquid products which were obtained from the separate pyrolysis of oil shale and PP at 800°C, the pyrolysis of 67% mixture at the same temperature, and the pyrolysis made with the addition of 4% bentonite under these conditions were given in Table 2. The substances detected in the GC-MS analysis are given as % peak area in the total chromatogram. GC-MS chromatograms of these products are shown in Figure S1-S4. During the pyrolysis process, the organic structure lost their H atoms and alkane radicals were directly converted into alkene radicals. In the pyrolysis process performed at 800°C and at the mixture ratio of 67%, alkene content is decreased when compared to the pyrolysis of oil shale and PP. This can be explained by the fact that the bonds are easily broken with increasing temperature, and consequently, free H radicals' concentration in the medium reacts with alkenes and converted to alkanes [21]. The phenol and phenol derivatives which are formed in significant amounts in the oil

shale pyrolysis are not formed in the pyrolysis of oil shale and PP mixtures. The formation of phenol and its derivatives lead to a decrease in liquid and gaseous products. This is an undesired event in the pyrolysis process [22]. When polypropylene is added to oil shale, phenolic structures converted to cyclohexene structure as a result of the ring hydrogenation. This conversion is due to the hydrogen content in the PP structure. PP plays a role as the hydrogen donor for the oil shale under the experimental conditions studied. Although the addition of bentonite catalyst to co-pyrolysis medium under optimum conditions leads to an increase in the amount of alkane in the liquid product content, and it leads to a decrease in the amount of alkene.

Figure 5 shows the FTIR spectrum for the liquid products obtained from the pyrolysis processes. In the spectrum of PP, the peaks observed between 2850-2956 cm^{-1} indicate the presence of aliphatic hydrocarbon compounds in the structure. In the spectrum of oil shale, the peaks observed around 3000 cm^{-1} and at 732 cm^{-1} indicate the presence of aromatic hydrocarbon groups. When GC-MS results are considered, especially the presence of the excessive amounts of phenol and benzene derivatives in the structure of oil shale supports this situation. In the spectrum obtained from the co-pyrolysis of oil shale and PP mixture, it was observed that the aromatic groups were decreased but the aliphatic groups were increased. This also means that polypropylene served as the hydrogenation medium in the co-pyrolysis process [23]. The C-H stretching observed in the range of 2950–2850 cm^{-1} and 1460-1370 cm^{-1} in the spectrum indicates that this liquid has more aliphatic structures. When GC-MS results are considered, it is seen that liquid products of the mixture are rich in alkane and alkene compounds. In the spectrum obtained with the catalyst, the peak range of 2925-2957 cm^{-1} indicates the aliphatic C-H stretching and the functional groups including $-CH_3$, $-CH_2$ and $-CH$. The catalysts caused an increase the amount of aromatic hydrocarbon by saturating the functional groups with hydrogen. The increase of the peak at 1265 cm^{-1} and the increased peak group at 2950 cm^{-1} indicate increasing aliphatic hydrocarbon compounds.

HHV is one of the important parameters in determining the energy content of a fuel. The elemental analysis results showed that PP was better materials for producing fuels because of its high carbon and hydrogen contents and low oxygen content (Table 1). Therefore, the addition of PP in the pyrolysis oil shale is expected to improve the calorific value of the liquid product. In present study, obtained liquid products from different mixture ratio at 800°C had HHV of 40.1 MJ/kg for the mixture ratio of 33%, 40.8 MJ/kg for the mixture ratio of 50% and 41.3 MJ/kg for the mixture ratio of 67%. HHV values of liquid products showed their potential as an alternative of conventional diesel. As shown in these results, the addition of PP in oil shale pyrolysis obviously contributed to the increase in HHV value of the liquid products.

Table 2. GC-MS analysis results of the tars (% of total chromatogram).

Compound name	PP 800°C	Oil shale 800°C	67 wt % Oil shale / PP	
			800°C	4 wt % bentonite 800°C
ethylbenzene	-	0.22	-	-
1,3dimethyl benzene	-	1.06	1.05	1.85
1,2,3trimethyl benzene	-	0.80	-	0.40
1,2,3 trimethyl cyclohexane	4.20	0.81	-	3.72
2,4 diethyl-1-methyl cyclohexane	-	2.24	-	1.74
1,2 dimethyl-3-methyl cyclohexane	19.82	9.17	3.69	-
1,1,3,5 tetramethyl cyclohexane	4.02	30.75	5.47	1.69
1,2,4,5 tetramethyl cyclohexane	4.28	-	4.35	1.47
1,2,4 trimethyl cyclohexane	2.53	-	1.43	3.98
1 ethyl-2-propyl cyclohexane	3.87	-	4.84	1.76
4,8-nonane dimethyl-1,7-nonadien	-	-	-	1.23
n-decane	-	0.32	-	-
4-methyl-2-decene	0.48	-	0.58	-
dodecane	-	1.29	-	-
tetradecane	-	0.67	-	-
n-dodecene	-	-	-	0.63
7-methyl-6-tridecene	3.38	-	0.73	-
pentadecane	-	0.34	-	-
hexadecane	-	0.43	-	-
heptadecane	-	0.26	-	-
nonadecane	-	-	0.32	-
1,1,2-trimethyl cyclodecane	-	1.07	-	-
4 methyl decane	0.50	-	-	0.70
octadecane	0.71	0.23	0.51	-
1 methyl-3-propyl cyclo octane	7.26	-	2.64	7.42

Table 2 (Continued)

3 methyl-2-pentene	0.66	-	1.16	1.37
1,2,4,4-tetramethyl cyclopentene	-	-	0.18	-
3,3 dimethyl-1-hexene	0.33	-	0.12	-
3,3,5 trimethyl-1-hexene	-	-	0.47	1.39
2-methyl--3-heptene	3.80	-	6.41	1.89
2,4dimethyl--1-heptene	7.09	-	11.40	10.70
eicosane	-	2.13	0.18	1.51
heneicosane	-	0.34	-	-
docosane	0.23	0.38	-	-
tetracosane	-	0.29	-	-
pentacosane	0.12	0.43	-	-
hexacosane	-	0.34	-	-
heptacosane	-	0.52	-	0.35
octacosane	-	0.38	-	-
nonacosane	-	0.55	-	-
Triallysilane	12.44	9.09	14.36	9.52
Indene	-	-	0.29	-
biphenyl	-	-	0.36	-
phenol	-	5.17	-	-
4 methyl phenol	-	4.18	-	-
2,4dimethyl phenol	-	0.96	-	-
3 ethyl phenol	-	0.83	-	-
naphthalene	0.29	0.26	1.63	1.50
2 methyl naphthalene	-	0.48	0.64	1.26
2,3 dimethly thiophene	-	0.53	-	-
octadecanamide	-	3.18	-	-
benzoic acid	-	-	0.63	1.47
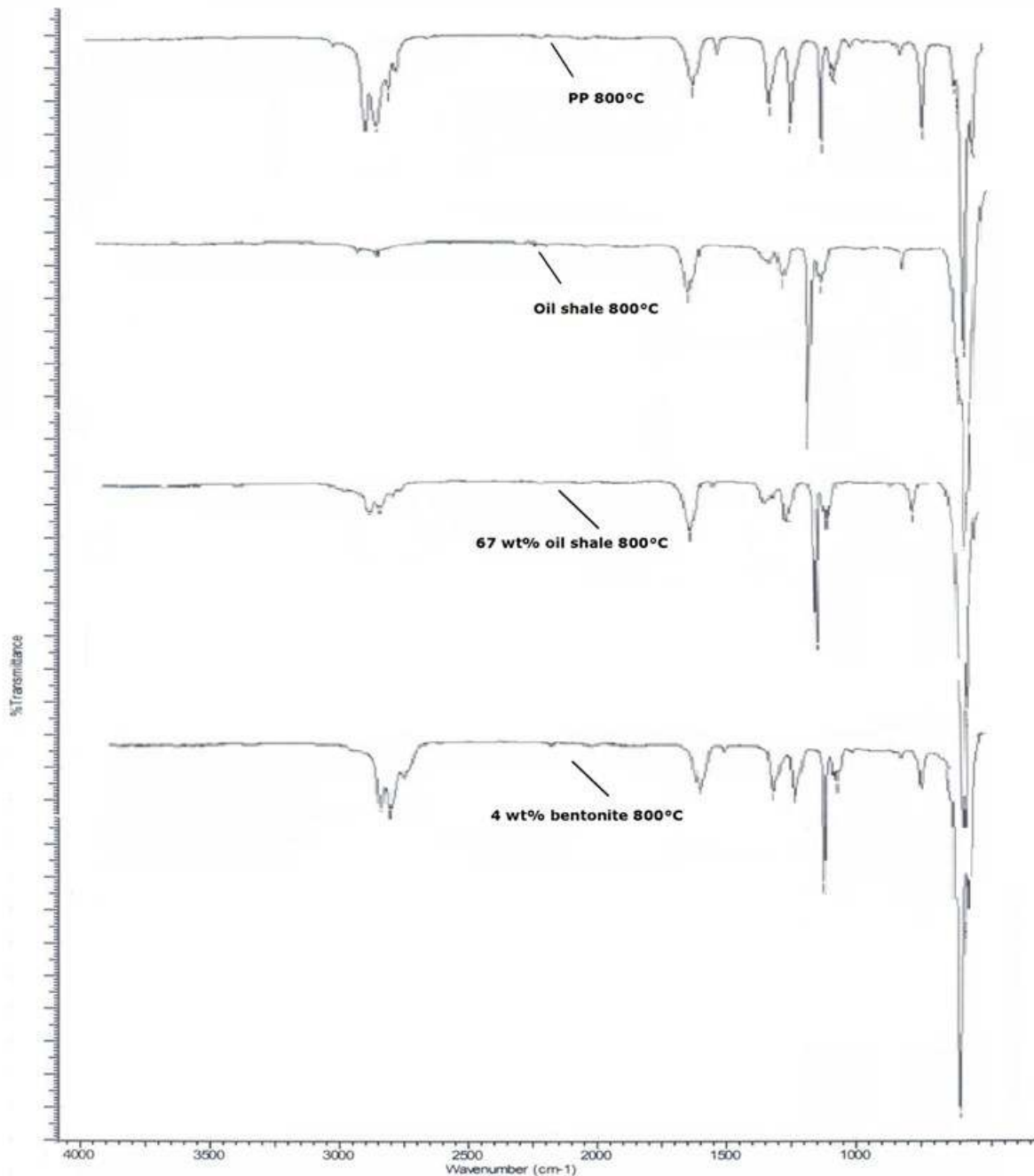
Figure 5. FTIR spectra of the tars.

CONCLUSIONS

The aim of the study is co-pyrolysis of a Turkish oil shale with PP. The conversion of oil shale and PP mixture into liquid product and other valuable chemicals using pyrolysis process is getting significant attention both as waste management and alternative energy technology.

- As a result of the experiments, precious liquid products could be obtained and the use of polypropylene as a raw material to achieve liquid products.

259

- In the co-pyrolysis processes, the liquid products were obtained at higher yields than the pyrolysis of the oil shale alone. During the co-pyrolysis process, PP acted as a hydrogen source, and saturated the free radicals formed as a result of breaking the crosslinks and made positive contributions to the liquid product yield by creating a positive synergistic effect.

- In the co-pyrolysis process, although the alkene structures in the liquid product decreased, the alkane structures gradually increased. This situation indicated that the hydrogen which is released in the presence of PP caused to convert alkanes into alkenes.

- The catalysts such as bentonite, zeolite, and red mud were added to the medium to further increase the liquid product yield at the mixture ratio of 67% and this mixture is pyrolyzed at temperature of 800 °C. Bentonite caused to increase the liquid product yield better than the other catalysts.

- GC-MS spectra showed that the obtained liquid products were similar to fossil-based liquid fuels, and also different types of chemicals were obtained.

- FTIR spectra showed that the aliphatic groups are predominant in all liquid products. This situation is supported in all spectra with the stretching and bending vibrations of C-H bond.

REFERENCES

[1] Taciuk W. Does oil shale have a significant future? Oil Shale. 2013;30:1–5. DOI: 10.3176/oil.2013.1.01.

[2] Toraman Ö Y, Uçurum M. Alternative Fossil Based Energy Resource: Oil Shale. Tübav Science Journal. 2009;2:37-46.URL: dergipark.ulakbim.gov.tr /tubav/article/download/ 1013000023/ 1013000058.

[3] Martins M, Salvador S, Thovert J. F., Debenest G. Co-current combustion of oil shale Part 1: characterization of the solid and gaseous products. Fuel. 2010 July;89:144-151. DOI: 10.1016/j.fuel.2009.06.036.

[4] Wang S, Jiang X, Han X, Tong J. Investigation of Chinese oil shale resources comprehensive utilization performance. Energy. 2012 April;42:224-232. DOI: 10.1016/j.energy.2012.03.066.

[5] Altun N E, Hıçyılmaz C, Hwang J Y, Bağcı A S, Kök M V, Oil shales in the world and Turkey; reserves, current situation and future prospects: a review. Oil Shale. 2006 May;23:211-227. URL: http://www.kirj.ee/public/oilshale/oil-2006-3-2.pdf.

[6] Sınağ A, Sungur M, Canel M. Effect of experimental conditions on the yields during the copyrolysis of Mustafa Kemal Paşa (MKP) lignite (Turkey) with low-density polyethylene. Energy & Fuels. 2006 May; 20: 1609-1613. DOI: 10.1021/ef060108l.

[7] Bozkurt P A, Tosun O, Canel M. The synergistic effect of co-pyrolysis of oil shale and low density polyethylene mixtures and characterization of pyrolysis liquid. Journal of the Energy Institute. In press, DOI: 10.1016/j.joei.2016.04.007.

[8] Espina S M, Alvarez R, Diez M A, Casal M D. Coal and plastic waste co-pyrolysis by thermal analysis–mass spectrometry. Fuel Processing Technology. 2015 October;137:351-358. DOI: 10.1016/j.fuproc.2015.03.024.

[9] Hayashi J, Mizuta H, Kusakabe K, Morooka S. Flash copyrolysis of coal and polyolefin. Energy Fuels. 1994 August;8:1353–1359. URL: http://pubs.acs.org/doi/pdf/10.1021/ef00048a026.

[10] Meesri C, Moghtaderi B. Lack of synergetic effects in the pyrolytic characteristics of woody biomass/coal blends under low and high heating rate regimes. Biomass and Bioenergy. 2002 July:23:55–66. DOI: 10.1016/S0961-9534(02)00034-X.

[11] Suelves I, Lazaro M J, Moliner R. Synergetic effects in the co-pyrolysis of Samcacoal and a model aliphatic compound studied by analytical pyrolysis. Journal of Analytical and Applied Pyrolysis. 2002 December;65:197–206. DOI: 10.1016/S0165-2370(01)00194-2.

[12] Ergün N. Turkey 10th development plan (2014-2018) in the plastics sector general assessment draft projection, PAGEV, 2013;4-5. URL: http://www.pagev.org.tr/ admin/PICS/dosyalar/Turkiye_10__Kalkinma_Plani_(_20142018_)_Projeksiyonunda_Plastik_Sektoru_Ge nel_Degerlendirmesi_Taslagi__2_.pdf.

[13] Plastics Europe. Plastics–the facts 2013 an analysis of European latest plastics production, demand and waste data. PlasticsEurope. 2013;6-31. URL: http://www.plasticseurope.org/ documents/document/20131014095824final_plastics_the_facts_2013_published_october2013.pdf.

[14] Kaminsky W, Predel M, Sadiki A. Feedstock recycling of polymers by pyrolysis in a fluidized bed. Polymer Degradation and Stability. 2004 September;85:1045–1050. DOI: 10.1016/j.polymdegradstab.2003.05.002.

[15] Onay O, Koca H. Determination of synergetic effect in co-pyrolysis of lignite and waste tyre. Fuel. 2015 June;150:169–174. DOI: 10.1016/j.fuel.2015.02.041.

[16] Serrano D P, Aguado J, Escola J M, Garagorri E. Conversion of low density polyethylene into petrochemical feedstocks using a continuous screw kiln reactor. Journal of Analytical and Applied Pyrolysis. 2001 April;58–59:789–801. DOI: 10.1016/S0165-2370(00)00153-4.

[17] Önal E. 2007. Pyrolysis different biomass and copyrolysis of them with syntetic polymers: Identification of product properties Anadolu University Graduate School of Sciences Chemical Engineering Program, Doctoral thesis, 30-42.

[18] Cit I, Sınag A, Tekes A T, Acar P, Mısırlıoglu Z, Canel M. Effect of polymers on lignite pyrolysis. Journal of Analytical and Applied Pyrolysis. 2007 August;80:195–202. DOI: 10.1016/j.jaap.2007.02.006.

[19] Ballice L. Classification of volatile products evolved from the temperature programmed co-pyrolysis of Turkish oil shales with atactic polypropylene (APP). Energy & Fuels. 2001 March;15: 659–665. DOI: 10.1021/ef0002041.

[20] Boxiong S, Chunfei W, Cai L, Binbin G, Rui W. Pyrolysis of waste tyres: The influence of USY catalyst/tyre ratio on products. Journal of Analytical and Applied Pyrolysis. 2007 March;78:243-249. DOI: 10.1016/j.jaap.2006.07.004.

[21] Dominguez A, Blanco C G, Barriocanal C, Alvarez R, Diez M A. Gas chromatographic study of the volatile products from co-pyrolysis of coal and polyethylene wastes. Journal of Chromatography A. 2011 May;918:135–144. DOI: 10.1016/S0021-9673(01)00736-1.

[22] Dorrestijn E, Laarhoven L J J, Arends I W C E, Mulder P. The occurrence and reactivity of phenoxyl linkages in lignin and low rank coal. Journal of Analytical and Applied Pyrolysis. 2000 March;54:153-192. DOI: 10.1016/S0165-2370(99)00082-0.

[23] Acar P, Sınağ A, Mısırlıoğlu Z, Canel M. Pyrolysis of scrap tyre with lignite. Energy Sources, Part A: Recovery, Utilization, and Environmental Effects. 2012 December;34:287-295. DOI: 10.1080/15567030903586063.

Göynük Bitümlü Şistinin Polipiren ile Birlikte Pirolizi ve Piroliz Sıvısının Yapısal Karakterizasyonu

Pınar Acar Bozkurt*, **Nagehan Merve Kutlu, Muammer Canel**

Öz: Bu çalışma, ülkemizin önemli bitümlü şist yataklarının birinden alınan bitümlü şist numunesi ile polipropilen (PP) karışımlarının birlikte piroliz işlemine tabi tutularak yüksek verimde sıvı ürün elde edilmesi amacına dayanmaktadır. Çalışmada öncelikle bitümlü şist numunesi ve polipropilen ayrı ayrı, daha sonra da bunların belli oranlarda karıştırılmasıyla elde edilen karışım piroliz işlemine tabi tutulmuştur. Piroliz deneyleri karışım içerisinde %33, %50 ve %67 PP olacak şekilde üç farklı karışım oranında ve 600 – 800 °C sıcaklık aralığında gerçekleştirilmiştir. Deneyler sonucunda elde edilen gaz, sıvı ve katı ürün verimleri hesaplanarak bitümlü şiste eklenen PP'nin ve değişen piroliz sıcaklığının sıvı ürün verimi üzerine etkisi incelenmiştir. Deneyler sonucunda 800 °C'de ve %67 PP içeren karışım oranında en yüksek sıvı ürün verime ulaşılmıştır. En yüksek sıvı veriminin elde edildiği şartlarda ortama çeşitli katalizörler ilave edilmiş ve katalizörlerin pirolizden elde edilen sıvı ürün verimine etkisi incelenmiştir. Deneyler sonucunda elde edilen sıvı ürünlerin yapısı GC-MS ve FTIR gibi çeşitli spektroskopik yöntemler ile aydınlatılmış ve deney koşullarının sıvı ürün yapısı üzerindeki etkileri incelenmiştir. Sonuç olarak PP ve bitümlü şistin birlikte pirolizi sonucu elde edilen sıvı ürün veriminde fark edilir sinerjik etki gözlenmiş ve bu etki, ortama eklenen katalizör ile daha da artmıştır. Çalışmadan elde edilen sonuçlar PP ve bitümlü şistin birlikte piroliz işleminin tehlikeli atıkların değerli kimyasallar ve yakıtlara dönüşümü için çevre dostu bir yöntem olabileceğini göstermiştir.

Anahtar Kelimeler: Birlikte piroliz, bitümlü şist, polipropilen, karakterizasyon.

Photocatalytic Activities of Ag⁺ Doped ZIF-8 and ZIF-L Crystals

Hüsnü Arda Yurtsever[a1], Melis Yağmur Akgünlü[a], Tuğçe Kurt[a], Ali Semih Yurttas[a],

Berna Topuz[a*]

Ankara University, 06100, Ankara, Turkey

Abstract: Zeolitic imidazolate framework (ZIF) based metal organic framework (MOF) photocatalytsts were prepared and the effect of silver (Ag⁺) doping on the photocatalytic activity of ZIF-8 and ZIF-L crystals was investigated. Ag⁺ doped ZIF-8 and ZIF-L crystals were prepared and their activities in the photocatalytic removal of methylene blue (MB) dye under UV irradiation were determined for the first time in the literature. Doped ZIF-8 and ZIF-L crystals showed better photocatalytic activities compared to the undoped crystals. Almost 100% of MB was removed with 5 mole% Ag⁺ doped ZIF-8 in 40 min. The magnitude of the calculated 2ⁿᵈ order reaction rate constants changed in the order of 5%>10%>2%>1%>undoped ZIF-8. The photocatalytic activity decreased beyond 5 mole% doping level since Ag⁺ ions may have segregated due to a possible solid state solubility limit of Ag⁺ ions in the crystal lattice of ZIF-8. ZIF-L crystals possessed a lower photocatalytic activities compared to ZIF-8 crystals.

Keywords: Photocatalysis; metal-organic framework; ZIF-8; ZIF-L, doping.

---

[1] Current Address: Adana Science and Technology University, Adana, Turkey.

INTRODUCTION

Photocatalysis is expected to contribute to the solution of environmental problems such as water and air pollution in the near future. The design of photocatalysts with high electron-hole generation rates, high surface areas and high light absorption capacities is crucial in producing sustainable and cost-effective photocatalytic processes. Titania, zirconia, copper oxide, zinc oxide, and iron oxide are widely used photocatalysts which have good light absorption capacities with moderate surface areas depending on the synthesis conditions. Intense research and advances in nanoscience and nanotechnology improved the preparation techniques and expanded the application area of nanostructured photocatalytic materials. Fujishima and Honda conducted the pioneering studies in 1970s to produce renewable energy via photocatalytic processes by using solar energy (1, 2). Since then many photocatalytic materials were prepared to be used in various photocatalytic processes. There are many examples in the literature and there is a huge variety of photocatalytic materials to be used in many different photocatalytic processes (3).

In the last decade, metal organic frameworks (MOFs) have been used in photocatalytic applications due to their very high surface areas up to 3000s of m^2/g, tunable ligand/metal clusters, and adequate light absorption capacities. MOFs are the porous crystalline hybrid materials with well-ordered pores and cavities which are mostly used in adsorption, catalysis, and separation processes where the molecular sieving and the preferential adsorption is important. Their use in photocatalysis is promising since they have high porosity and surface areas compared to oxide photocatalytic materials prepared at high temperatures. However, thermal and chemical stability of MOFs during the photocatalytic reaction is still an important issue.

Since MOFs contain organic linker with inorganic subunits they can show semiconducting properties with tunable band gap. Diversity on the metal ions and the organic linkers, and easily controlled synthesis steps make MOF materials with tailorable capacity to absorb light. Although these desirable properties open exciting opportunities to use them in photocatalytic applications, comprehensive studies on the use of MOF crystals in photocatalytic processes has not been explored widely.

Zeolitic imidazole frameworks (ZIFs) are the sub-family of MOFs, which can be synthesized by solvothermal/hydrothermal, and microwave assisted reactions at temperatures in the 298-423 K range. ZIF-8 and ZIF-L are the topologically isomorphs of

zeolites with tetrahedrally coordinated zinc metal and imidazole rings (4, 5) and they can be easily synthesized in aqueous medium at room temperature. ZIF-8 has SOD topology exhibiting 3D structure with cages 11.6 Å in diameter, which are accessible through 3.4 Å windows. Leaf-shaped 2D ZIF-L crystals have the same building units with those for ZIF-8 and have cushion-shaped cavity with dimensions of 9.4 Å x 7.0 Å x 5.3 Å (6). These materials have high surface area and high CO_2 adsorption capacities. These properties make them promising photocatalytic materials to be used in artificial photosynthesis (CO_2 photoreduction).

Photocatalytic removal of methylene blue (MB) dye was performed successfully under UV light irradiation with pure ZIF-8 nanocrystals by Jing *et al.* (7). They reported ~85% degration of MB with undoped ZIF-8 crystals under UV light irradiation. After 3.5 h, the conversion of MB was reported as 50% for polyoxometalate (POM) based MOF type photocatalyst (8).

Studies on photocatalytic applications have shown that combining ZIF-8 with semiconductors having different band structures or introducing impurity levels can increase light absorption capability, decrease the recombination rate of electron-hole pairs; hence increase the photocatalytic activity.

The photocatalytic activities of TiO_2, Zn_2GeO_4, and ZnO were increased by the incorporation of a ZIF-8 layer (10-12). Benzyl alcohol was oxidized with Au nanoparticles encapsulated ZIF-8 nanocrystals (13) under visible light. Ag^+/AgCl was synthesized on ZIF-8 nanocrystals with different weight ratios and their photocatalytic activities in the removal of RhB dye were evaluated (14). Ni substitute ZIF-8 photocatalysts were prepared for alcohol sensing and photocatalytic removal of methylene blue activities of the prepared photocatalysts were evaluated under visible light illumination (15). Studies on Ag^+ doped ZIF-8 and ZIF-L including their photocatalytic performances are currently limited to the best of our knowledge.

In this study, Ag^+ doped ZIF-8 nanocrystals with different Ag^+ contents were prepared and their photocatalytic activities under UV light irradiation towards methylene blue dye removal were evaluated. Doped and undoped ZIF-L crystals were also prepared and their activities were compared with those of ZIF-8 crystals for the first time in the literature.

MATERIALS AND METHODS

Materials

Zinc nitrate hexahydrate (98%, Aldrich), silver nitrate (99+%, Alfa Aesar), 2-methylimidazole (Hmim, 99%, Aldrich) and methanol (≥99.9%, Aldrich) were used as received without any further purification. DI water (18.2 MΩ cm) was also used in the synthesis of ZIF-L crystals.

Synthesis of Undoped/Doped ZIF 8 and ZIF-L Crystals

Undoped ZIF-8 crystals were synthesized as reported before (16). Methanol (47.52 g) solutions of $Zn(NO_3)_2.6H_2O$ (1.286 g) and Hmim (2.811 g) were prepared separately and then mixed by dropwise addition of the Hmim solution to the Zn^{2+} solution. The synthesis solutions were stirred at room temperature for 1.5 h. The crystals were separated by centrifugation (8000 rpm, 15 min) and washed with methanol (3 × 30 mL). The obtained white powders were dried at 80ºC overnight before characterization and photocatalytic experiments. Doped ZIF-8 crystals were synthesized by following the same route. $AgNO_3$ was added to the Zn^{2+} containing solution for the preparation of Ag^+ doped ZIF-8 crystals. $AgNO_3$ amount was calculated by keeping the total metal amount as 1 mol. The Metal:Hmim:MeOH molar ratios were 1:8:700 for the undoped/doped ZIF-8 crystals.

Undoped ZIF-L crystals were synthesized as described elsewhere (5,6). Aqueous (50 mL) solutions of $Zn(NO_3)_2.6H_2O$ (0.662 g) and Hmim (1.642 g) were mixed by the dropwise addition of the Zn^{2+} solution to the Hmim solution. The mixture was stirred at room temperature for 4 h and then subjected to centrifugation at 10000 rpm for 20 min (5). The obtained white powder was washed with water three times. The final powder product was stored in an oven at 105 °C. Doped ZIF-L crystals were synthesized by following the same route. $AgNO_3$ was added to the Zn^{2+} containing solution for the preparation of Ag doped ZIF-L crystals which was the same as in the synthesis of doped ZIF-8 crystals. The Metal:Hmim:H_2O molar ratios were 1:8:2241 for the undoped/doped ZIF-L crystals.

Characterization of ZIF-8 and ZIF-L Crystals

The prepared ZIF-8 and ZIF-L crystals were characterized by using X-Ray Diffraction (XRD, Rigaku Ultima-IV) equipment with monochromated high-intensity (λ=1.54 Å) CuKα radiation. The scanning step size and time were 0.02 (º) and 411.2 (s), respectively, in

the 5 and 80º 2theta range. Morphology and particle sizes were characterized by Scanning Electron Microscopy (SEM, QUANTA 400F) in the 20-50 kx magnification range.

Photocatalytic Removal of Methylene Blue

Photocatalytic experiments were conducted by using a home-made inner-irradiated photoreactor. The prepared powders (0.05 g) were dispersed in 10 ppm, 60 mL methylene blue solution. The suspensions were kept in an ultrasonic bath for 5 min to provide well dispersion. A 9W UV lamp was used as the irradiation source. Samples were withdrawn from the suspension by using a syringe with 10-minute time intervals. The samples were centrifuged and analyzed with a UV-Vis Spectrophotometer (Shimadzu UV-1600). The spectra of the samples were recorded in the 300-800 nm range and 664 nm (maximum absorption wavelength for methylene blue) was selected for the calculation of dye concentration. Methylene blue removal (%) was calculated by using the relation, MB removal % = $100-(C/C_0)*100$, where C is the concentration of the sample and C_0 is the initial methylene blue concentration. The data were fitted to second order reaction rate expression, $1/C_0-1/C = -k*t$, where k is the second order reaction rate constant and t is time.

RESULTS AND DISCUSSION

Characterization of ZIF-8 and ZIF-L Crystals

XRD patterns of undoped/10% Ag^+ doped ZIF-8 and ZIF-L crystals are given in Figure 1 along with the reference simulated XRD patterns (4, 5). The peak positions belonging to the prepared crystals coincide with reference peak positions as shown in the figure, which also showed that ZIF-8 and ZIF-L crystals were successfully synthesized. Although random orientation was observed for the powder samples, XRD patterns of both undoped and 10% Ag^+ doped ZIF-L exhibit intensity ratios different than that of the reference. Since ZIF-L has a 2-D layer network along the *ab* plane stacking along the *c* direction (6), packing of 2-D morphology may affect the orientation for the powder. The results given in Figure 1 also show that the presence of Ag^+ ion in the synthesis medium did not cause any framework change during the crystallization. The relative crystallinities have decreased upon addition of Ag^+ ion to the both structures. There were no peaks of impurity phases other than ZIF-8 phase in the XRD pattern of 10 mole % Ag^+ doped ZIF-8 and ZIF-L. This indicated that no Ag^+ phases were formed during the synthesis. Ag^+

ions may substitute Zn^{2+} ions, accommodate in the interstitial voids of ZIF-8 lattice or segregate as small clusters with the sizes which are out of XRD detection limit.
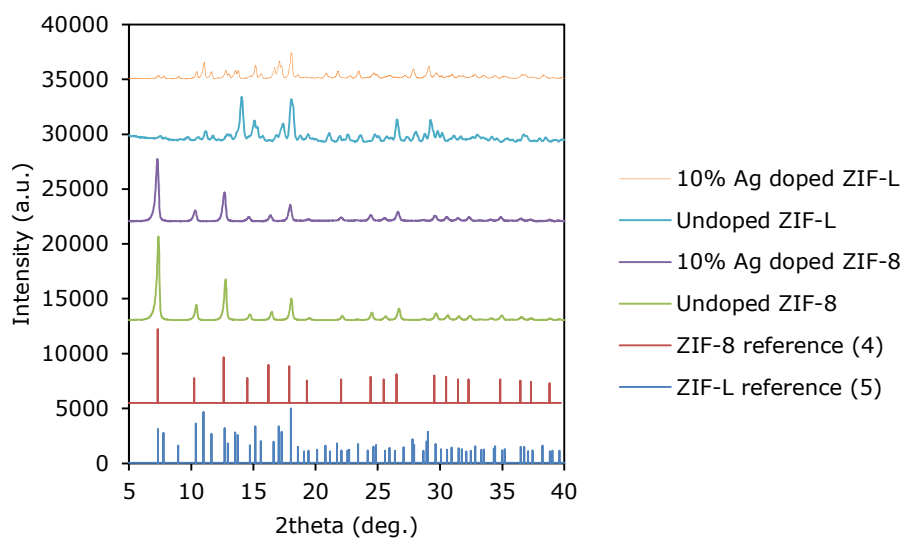
Figure 1. XRD patterns of the prepared crystals.

SEM images of undoped/10% Ag^+ doped ZIF-8 and ZIF-L crystals are shown in Figures 2 and 3, respectively. The size of the synthesized ZIF-8 crystals was estimated as ~60 nm for undoped ZIF-8 crystals and the size slightly decreased with Ag^+ doping and the SEM images also indicated that individual undoped/doped ZIF-8 crystals were successfully synthesized. The SEM images of ZIF-L crystals indicated that 2-dimensional crystals (5 μm x 2 μm) with a thickness of ~100 nm were successfully synthesized (Figure 3a). The dimensions of the doped ZIF-L crystals were estimated to be 3 μm x 1 μm with the same thickness. SEM-EDX analysis of the 10% Ag^+ doped ZIF-8 and ZIF-L crystals were also performed. SEM-EDX indicated that silver clusters were not formed at relatively high doping levels (10%) and Ag^+ ions were well dispersed in the crystalline structure (data not shown here).
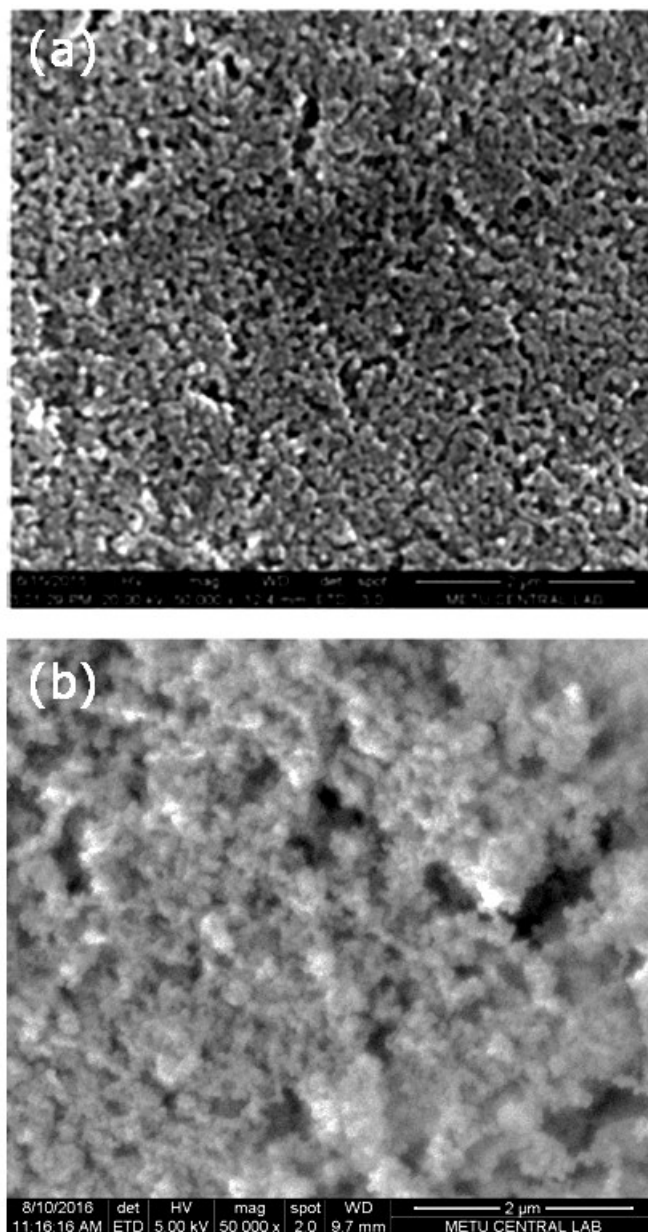
Figure 2. SEM images of (a) undoped and (b) 10% Ag$^+$ doped ZIF-8 crystals.
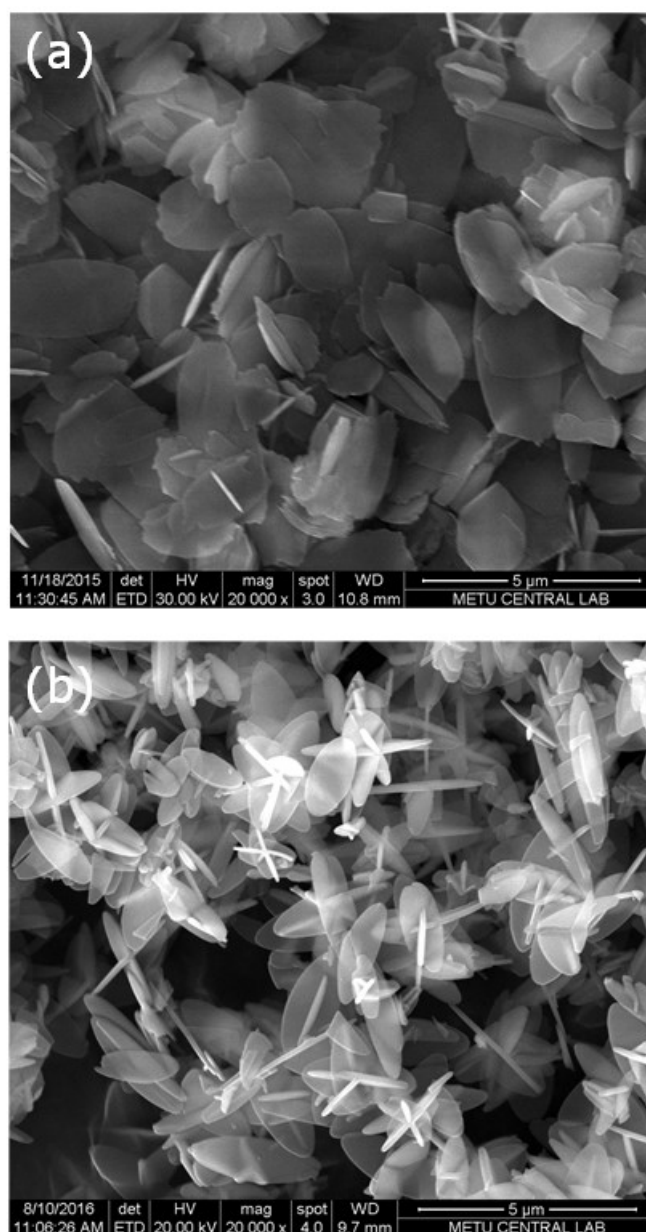
Figure 3. SEM images of (a) undoped and (b) 10% Ag$^+$ doped ZIF-L crystals.

Photocatalytic Removal of Methylene Blue

The photocatalytic activities of the prepared ZIF-8 and ZIF-L crystals in the removal of methylene blue under UV irradiation were determined. 4% MB was photocatalytically decomposed without ZIF-8/ZIF-L catalyst upon UV-light irradiation for 40 min. Time-dependent MB removal (%) and the plots of $1/C-1/C_0$ vs time obtained with ZIF-8 crystals are given in Figures 4 and 5. Methylene blue was nearly 100% removed in 40 min with 5 mole % Ag$^+$ doped ZIF-8. In comparison with the previously reported

performances, 5%-Ag$^+$ doped ZIF-8 exhibited better photocatalytic activity towards MB (7-9).

Undoped and 1 mole% Ag$^+$ doped ZIF-8 crystals showed the lowest activities towards the photocatalytic removal of methylene blue (Figure 4). Ag$^+$ doping increased the photocatalytic activity of ZIF-8 for all doping levels. Doping may have increased the light absorption capability and decrease the recombination rate of electron-hole pairs which may lead to an increase in the photocatalytic activity of ZIF-8. The photocatalytic activity decreased beyond a certain doping level (5%) since Ag$^+$ ions may have segregated due to a possible solid state solubility limit of Ag$^+$ ions in the crystal lattice of ZIF-8. It is possible for Ag$^+$ ions to substitute for the Zn^{2+} ions in the lattice or accommodate in the interstitials. Segregation, hence, would block the reactive surface of ZIF-8, which results in a decrease in the photocatalytic activity.

The photocatalytic removal of methylene blue kinetics was best fitted to 2nd order reaction rate expression. The plots of 1/C-1/C$_0$ vs time are given in Figure 5. The magnitude of the calculated 2nd order reaction rate constants changes in the following order: %5>10%>2%>1%>undoped ZIF-8 (Table 1). A pseudo-first-order kinetics was reported for MB degradation over the ZIF-8 undoped photocatalyst (7). Differences in kinetics for MB removal might be due to the smaller particle size of ZIF-8 (60 nm) which may affect the adsorption rate of MB.
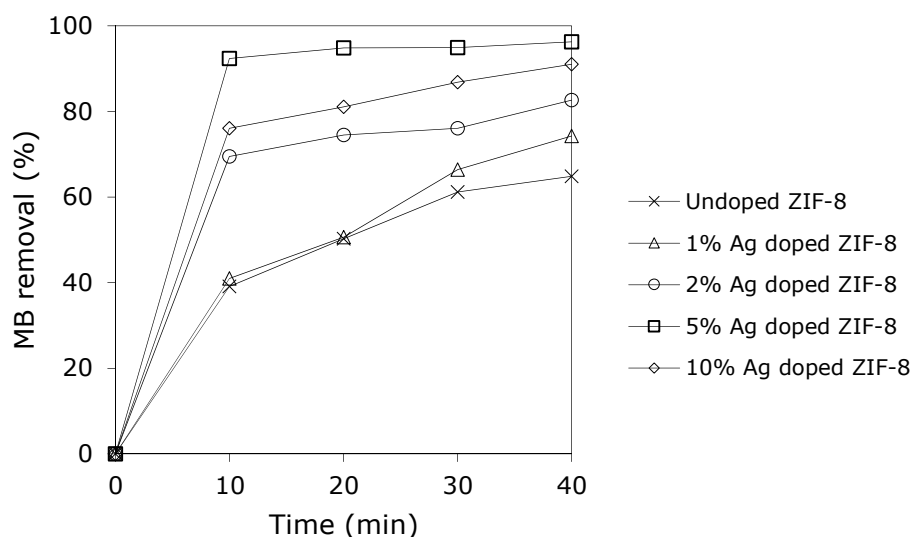
Figure 4. Time dependent MB removal (%) of undoped/doped ZIF-8 crystals.
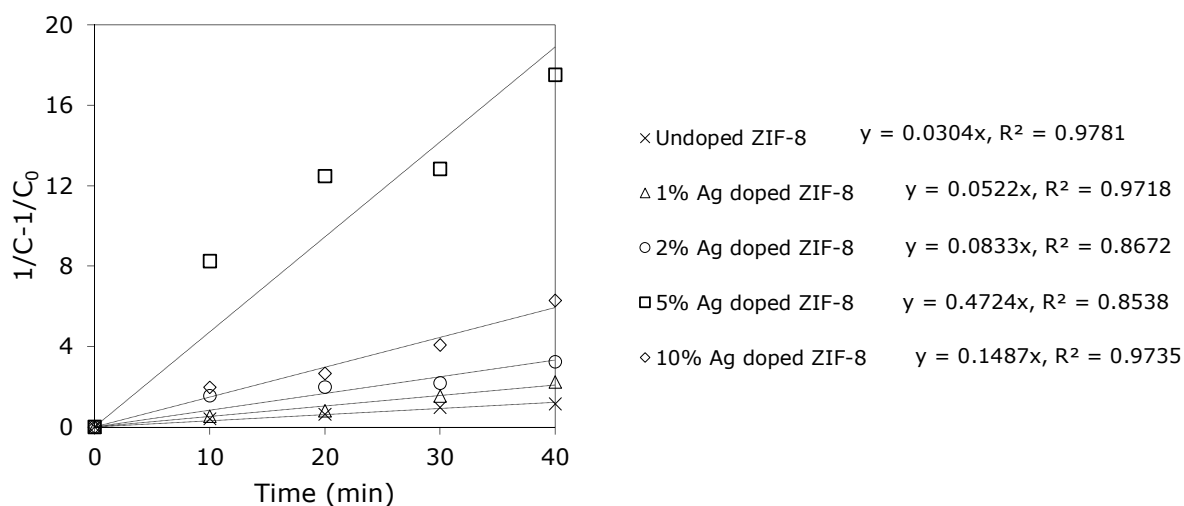
Figure 5. Reaction kinetics of undoped/doped ZIF-8 crystals.

The photocatalytic activities of the undoped/5 mole% Ag^+ doped ZIF-L crystals were also determined. Time dependent MB removal (%) and the plots of $1/C-1/C_0$ vs time obtained with undoped/doped ZIF-L (and the corresponding values for ZIF-8 for comparison) are given in Figures 6 and 7, respectively. Methylene blue removal activities of ZIF-L crystals were very low when compared to those of ZIF-8 crystals. ZIF-L and ZIF-8 are both composed of Zn metal center and imidazole linker in their structures but differ in crystal morphology. Compared to ZIF-8, ZIF-L has a lower porosity and surface area (N_2 adsorption at 77K) (6). Therefore, the significantly lower surface area of ZIF-L could be the reason for low photocatalytic activities. Ag^+ doped ZIF-L crystals possessed slightly higher photocatalytic activity compared to the undoped ZIF-L crystals. Ag^+ doping may increase the light absorption capability and decrease the recombination rate of electron-hole pairs, hence increase the photocatalytic activity of ZIF-L crystals.
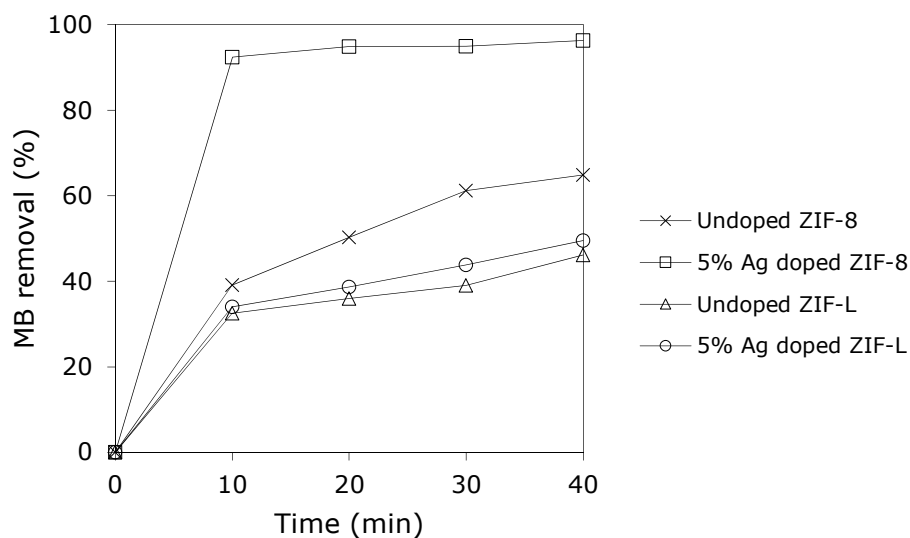
Figure 6. Time dependent MB removal (%) of undoped/doped ZIF-8 and ZIF-L crystals.
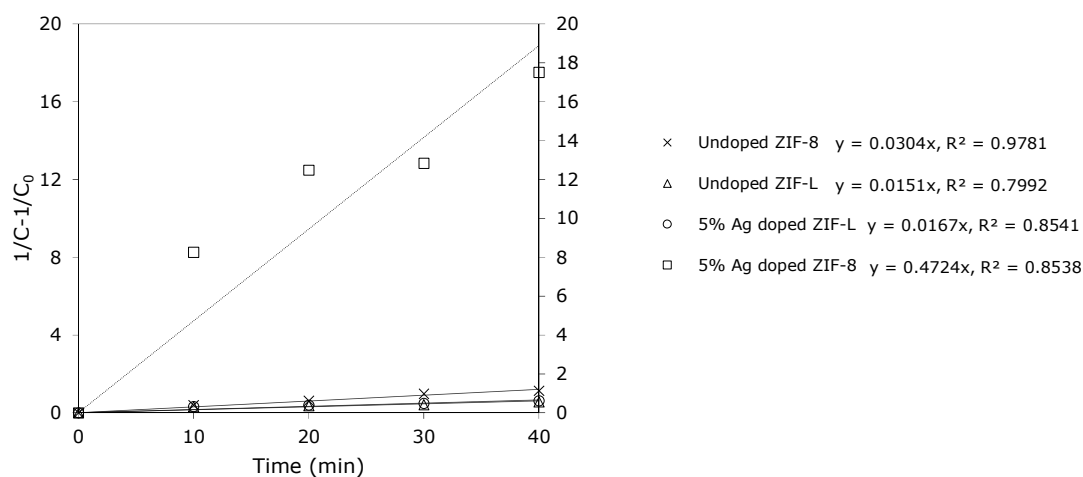
Figure 7. Reaction kinetics of undoped/doped ZIF-8 and ZIF-L crystals.

UV-Vis absorption spectra of the MB solution during the reaction under UV irradiation in the presence of 5%-Ag$^+$ ZIF-8 and 5%-Ag$^+$ ZIF-L are given in Figure 8(a), and Figure 8(b), respectively. The results shown in this figure, indicated that both crystals exhibit different behavior towards photocatalytic decomposition of MB. MB concentration decreased dramatically within 10 min in the presence of 5%-Ag$^+$ ZIF-8. However, the absorbance of MB decreased gradually with the increase of irradiation time, and 49% of MB was removed after 40 min under UV irradiation in the presence of 5%-Ag$^+$ ZIF-L.
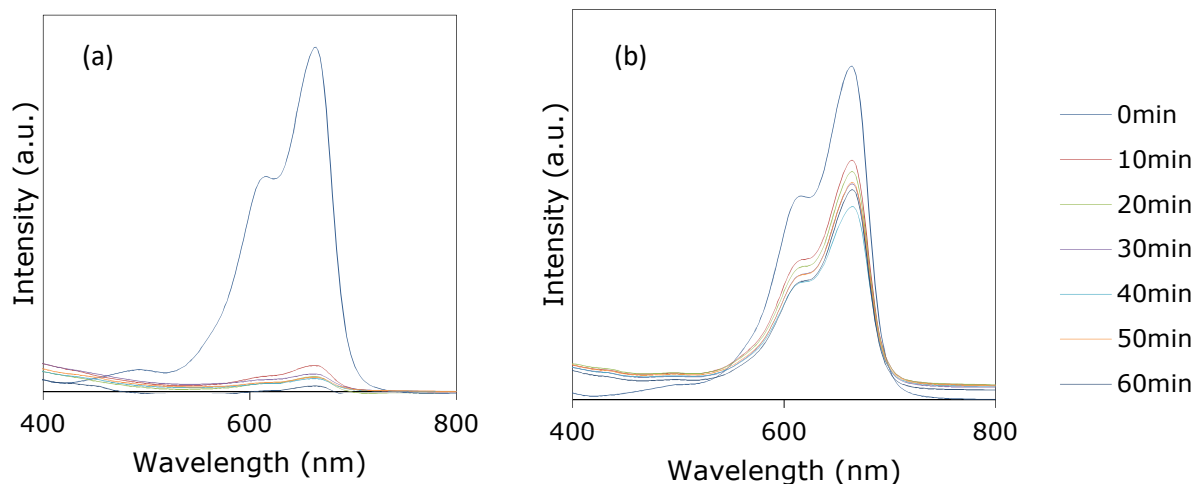
Figure 8. UV-Vis absorption spectra of the MB solution during the reaction under UV irradiation in the presence of (a) 5%-Ag^{2+} ZIF-8, (b) 5%-Ag^{2+} ZIF-L.

MB adsorption experiments (without UV light) were also conducted in order to determine whether the MB removal was achieved by adsorption or photocatalysis. MB removal % of the prepared photocatalysts by adsorption and photocatalysis in 40 minutes are given in Figure 9. The results have shown that the prepared undoped/doped ZIF-8 and ZIF-L crystals are photocatalytically active materials. MB adsorption was determined to be the highest for 2% Ag$^+$ doped ZIF-8 crystals. These results also supported that 5% Ag$^+$ doped ZIF-8 crystals have the highest photocatalytic activity since the photocatalytic removal % and adsorption % difference is more compared to the other crystals. Reusability test was conducted with 5% Ag$^+$ doped ZIF-L crystals. MB removal % slightly decreased from 49% to 42% in the second run.
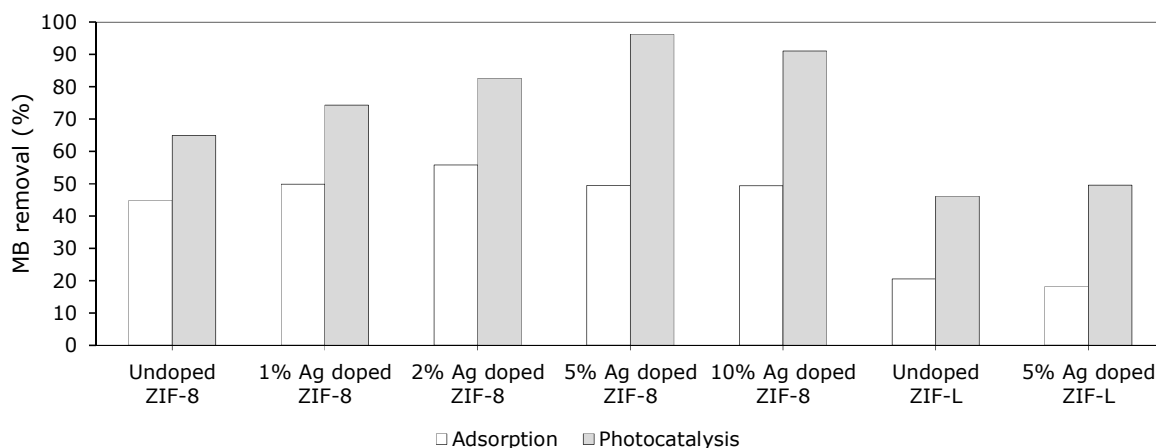
Figure 9. MB removal by adsorption and photocatalysis.

Table 1. Calculated 2nd order reaction rate constants.

Photocatalyst	2nd order reaction rate constant (1/ppm.min)
Undoped ZIF-8	0.0304
1% Ag+ doped ZIF-8	0.0522
2% Ag+ doped ZIF-8	0.0833
5% Ag+ doped ZIF-8	0.4724
10% Ag+ doped ZIF-8	0.1487
Undoped ZIF-L	0.0151
5% Ag+ doped ZIF-L	0.0167
10% Ag+ doped ZIF-L	0.0196

Overall, we report that Ag^+ doping in certain amount into the ZIF-8 and ZIF-L crystals facilitated the MB removal under UV-light irradiation. This allowed almost complete removal of MB for ZIF-8 crystals. These findings may contribute to the development of simple, environmentally friendly, and highly efficient photocatalyst for degradation of MB. Further research on influence of parameters on degradation kinetics and detailed characterization of these promising photocatalyst may significantly develop our understanding of photocatalytic mechanism towards MB degradation.

ACKNOWLEDGMENTS

REFERENCES

1.   Fujishima A, Honda K. Electrochemical Photolysis of Water at a Semiconductor Electrode. Nature. 1972;238(5358):37-8: DOI: 10.1038/238037a0.

2.   Inoue T, Fujishima A, Konishi S, Honda K. Photoelectrocatalytic reduction of carbon dioxide in aqueous suspensions of semiconductor powders. Nature. 1979;277(5698):637-8: DOI: 10.1038/277637a0.

3.   Hoffmann MR, Martin ST, Choi W, Bahnemann DW. Environmental Applications of Semiconductor Photocatalysis. Chemical Reviews. 1995;95(1):69-96: DOI: 10.1021/cr00033a004.

4.   Schejn A, Aboulaich A, Balan L, Falk V, Lalevee J, Medjahdi G, et al. Cu^{2+}-doped zeolitic imidazolate frameworks (ZIF-8): efficient and stable catalysts for cycloadditions and condensation reactions. Catalysis Science & Technology. 2015;5(3):1829-39: DOI: 10.1039/C4CY01505C.

5.   Zhong Z, Yao J, Chen R, Low Z, He M, Liu JZ, et al. Oriented two-dimensional zeolitic imidazolate framework-L membranes and their gas permeation properties. Journal of Materials Chemistry A. 2015;3(30):15715-22: DOI: 10.1039/C5TA03707G.

6.   Chen R, Yao J, Gu Q, Smeets S, Baerlocher C, Gu H, Zhu D, Morris W, Yaghi O, Wang H. A two-dimensional zeolitic imidazolate framework with a cushion-shaped cavity for CO_2 adsorption. Chem. Commun. 2013;49:9500-02: DOI: 10.1039/C3CC44342F.

7.   Jing H-P, Wang C-C, Zhang Y-W, Wang P, Li R. Photocatalytic degradation of methylene blue in ZIF-8. RSC Advances. 2014;4(97):54454-62: DOI: 10.1039/C4RA08820D.

8.   Wang X, Han N, Lin H, Luan J, Tian A, Liu D. A novel 3D metal–organic framework constructed from monosubstituted Keggin chains and metal–carboxylate chains. Inorg. Hem. Commun. 2014;42:10-14: DOI: 10.1016/j.inoche.2014.01.012.

9.   Yu B, Wang F, Dong W, Hou J, Lu P, Gong J. Self-template synthesis of core–shell ZnO@ZIF-8 nanospheres and the photocatalysis under UV irradiation. Matter. Letters. 2015;156:50-53: DOI: 10.1016/j.matlet.2015.04.142.

10.   Wee LH, Janssens N, Sree SP, Wiktor C, Gobechiya E, Fischer RA, et al. Local transformation of ZIF-8 powders and coatings into ZnO nanorods for photocatalytic application. Nanoscale. 2014;6(4):2056-60: DOI: 10.1039/C3NR05289C.

11.   Liu Q, Low Z-X, Li L, Razmjou A, Wang K, Yao J, et al. ZIF-8/Zn_2GeO_4 nanorods with an enhanced CO_2 adsorption property in an aqueous medium for photocatalytic synthesis of liquid fuel. Journal of Materials Chemistry A. 2013;1(38):11563-69: DOI: 10.1039/C3TA12433A.

12.   Isimjan TT, Kazemian H, Rohani S, Ray AK. Photocatalytic activities of Pt/ZIF-8 loaded highly ordered TiO_2 nanotubes. Journal of Materials Chemistry. 2010;20(45):10241-245: DOI: 10.1039/C0JM02152K.

13.   Chen L, Peng Y, Wang H, Gu Z, Duan C. Synthesis of Au@ZIF-8 single- or multi-core-shell structures for photocatalysis. Chemical Communications (Camb). 2014;50(63):8651-54: DOI: 10.1039/C4CC02818J.

14.   Gao S-T, Liu W-H, Shang N-Z, Feng C, Wu Q-H, Wang Z, et al. Integration of a plasmonic semiconductor with a metal–organic framework: a case of Ag/AgCl@ZIF-8 with enhanced visible light photocatalytic activity. RSC Advances. 2014;4(106):61736-42: DOI: 10.1039/C4RA11364K.

15.   Li R, Ren X, Ma H, Feng X, Lin Z, Li X, et al. Nickel-substituted zeolitic imidazolate frameworks for time-resolved alcohol sensing and photocatalysis under visible light. Journal of Materials Chemistry A. 2014;2(16):5724-29: DOI: 10.1039/C3TA15058E.

16. Demir NK, Topuz B, Yilmaz L, Kalipcilar H. Synthesis of ZIF-8 from recycled mother liquors. Microp. Mesoporus. Mat. 2014;198:291

Ag⁺ Doplanmış ZIF-8 ve ZIF-L Kristallerinin Fotokatalitik Aktiviteleri

Hüsnü Arda Yurtsever, Melis Yağmur Akgünlü, Tuğçe Kurt, Ali Semih Yurttas,

Berna Topuz*

Öz: Zeolitik imidazolat yapısı (ZIF) esaslı metal organik yapı (MOF) fotokatalizörleri hazırlanmış ve ZIF-8 ile ZIF-L kristallerinin fotokatalitik aktivitelerine gümüş (Ag⁺) doplamanın etkisi incelenmiştir. Ag⁺ doplanmış ZIF-8 ve ZIF-L kristalleri hazırlanmış ve literatürde ilk kez UV ışıması altında metilen mavisinin (MB) fotokatalitik giderilmesinde kullanılmıştır. Doplanmış ZIF-8 ve ZIF-L kristalleri doplanmamış kristallerle karşılaştırıldığında daha iyi fotokatalitik aktivite göstermiştir. 40 dakika içinde 5 mol % Ag⁺ ile doplanmış ZIF-8 ile neredeyse %100 MB giderilmiştir. Hesaplanan ikinci mertebe tepkime hız sabitlerinin büyüklüğü %5 > %10 > %2 > %1 > doplanmamış ZIF-8 sırasında değişmiştir. Fotokatalitik aktivite 5 mol % doplama seviyesinden sonra düşmüştür, çünkü Ag⁺ iyonları, ZIF-8 örgüsü içinde belli bir katı hal çözünme sınırına ulaşmış olabilir. ZIF-L kristalleri ZIF-8 kristallerine oranla daha düşük fotokatalitik aktivite göstermiştir.

Anahtar kelimeler: Fotokataliz, metal organik yapı, ZIF-8, ZIF-L, doplama.

Gönderme: 4 Temmuz 2016. **Düzeltme:** 28 Temmuz 2016. **Kabul:** 01 Eylül 2016.

Effect of the Sizing Compound on the Electropolymerization of Pyrrole and the Impedance of Carbon Fiber Coated with Polypyrrole

Hacer DOLAS[1], Digdem GIRAY[1] and A.Sezai SARAC[2]*

[1] Harran University, Chemistry Department and Vocational School of Hilvan, Sanliurfa, TURKEY.

[2] İstanbul Technical University, Chemistry Department and Polymer & Science Technology, Maslak- İstanbul, TURKEY.

Abstract: Carbon Fiber (CF) is used as a strengthening material in resin composites having high performance in most industrial areas due to the fact that it has mechanical properties such as low weight, high durability, and toughness. The mechanical performances of composite materials depend on the features of fiber and matrix which composed them. The one of methods which improves the features of fiber surface is the coating on fiber surface with thin film. When the fiber was coated with electropolymer, the mechanical durability of the composite was increased. In this study, carbon fibers were electrochemically coated with polypyrrole (PPy) in the presence of sizing compound (SC) based on epoxy. During the process, it was investigated that how current, obtained coating weights and impedance data, especially capacitance, changed by the amount of SC. For this reason, different amounts of SC (%0; % 0.18; %1.8 v/v) was added into the electrolyte solution (0.1 M NaClO$_4$-ACN) including 0.1 M Pyrrole (Py). Coating process was carried out by using Constant Potential or Cyclic Voltammetry Techniques. Other techniques for investigations were gravimetrical analysis, electrochemical impedance spectroscopy, Fourier Transform Infrared Spectroscopy (FT-IR) and Light Microscopy. At the end of the coating, the weight of coating and specific capacitance (Csp) values were 0.8 mg/g and 114 µF for % 0 of SC 10 mg/g and 57 µF for %0.18 of SC and 1.73 mg/g and 166 µF for %1.8 of SC, respectively. As a result, the coating weight and capacitance data (especially, Csp,) of carbon fiber coated with PPy were inversely changed with the amount of SC added into electrolyte.

INTRODUCTION

Carbon Fiber (CF) is used as a strengthening material in resin composites having high performance which is mostly used in the fields of industry, space, and textile due to having mechanical properties such as low weight, high durability, and strength [1-4]. The mechanical properties of composite materials are based on the properties of fiber and matrix which constitute it. Developing these properties is possible the control of intermediate surface formed between fiber and matrix. Intermediate surface plays an important role for controlling the mechanical properties such as the shearing inter layers and impact resistance of composite. A strong and durable intermediate surface can effectively transfer the load from matrix to fiber. Fiber/matrix interaction depends on chemical bonds formed from interaction between active groups existing in matrix resin and polar group such as hydroxyl and carboxyl on the surface of fiber [5-7]. Various methods were developed for raising the wettability of and functional group number on fiber surface [8-11]. Methods such as the electrochemical oxidizing [12-14], the oxidizing in acidic medium using nitric or phosphoric acid [15-19], plasma [20-22], and radiation [23, 24] were used for developing the performance of intermediate surface between fiber and matrix. Another method is coating with thin polymer film [25-27]. The film thickness and functionality of the formed coating can control with electrochemical coating method using method parameters (current density, potential, monomer concentration, and temperature, *etc*.) [28-33]. It is well known that while CF is obtained, it is sized with various adding (sizing) compounds. Also, the effect of sizing compound (SC) on the surface roughness, surface reactive group number, and wettability of the fiber were investigated [34]. When CFs based on polyacrylonitrile (Poly(AN), PAN) was treated with J4 and A436 emulsion type sizing compound, it was observed the decreasing on the average surface roughness (Ra) [35]. Acidic filling materials demonstrate more interaction durability with epoxy matrix [36]. It is considered that Ra decreased because of the filling of hollow between strains on surface of the fiber [37]. As CF was sized by electropolymerization, the mechanical strength of composite was increased. The impact, bend and shear strength of phenolic resin-based composite respectively were 44%, 68% and 87% when CF was reinforced with m-phenylenediamine. During mechanical test, composite including unsized CF possessed holes due to getting out the CF [38]. This behavior is caused that unsized CF surface does not carry convenient groups to hold on to matrix. This problem could be decreased when CFs are sized by electropolymerization. As a result, electropolymerization is a convenient method for CF sizing process [38].CF were electropolymerized with monomers including groups such as –OH, –NH$_2$ or –COOH by using Cyclic Voltammetry (CV) or Chronoamperometry to develop surface features. At the end of this process, CFs were sized [38].CF was electrochemically coated with polyethylendioxythiophene (PolyEDOT) [39], PolyAN [40, 41], Polypyrrole (PolyPy) [42],

and their derivatives (43, 44). The capacitivity and roughness of CF were increased by using this method [45]. Also it was reported that Poly(Py) contribute to the strength of composite [42]. Electrochemical Impedance Spectroscopy (EIS) was used as a spectroscopic technique to analyze electrochemical process occurring at the electrolyte/electrode interface and to investigate the charge transfer, ion diffusion and capacitor behavior of conducting polymer modified electrodes [46-48]. In the literature, the capacitive features of carbon fiber (CF) electrodes modified by conducting polymer such as poly(N-methyl pyrrole) [45], polythiophene and poly(N-methylpyrrole) [49], N-pyrrole, N-phenylpyrrole, and 1[4-methoxyphenyl]-1H-pyrrole homopolymers [50], poly(3-dodecylthiophene) [48], poly(3-methylthiophene) [51], poly(thiophene-imidazole) [52], were characterized by EIS. It was signed that the value of impedance for the electrode coated poly(3-methylthiophene) was affected with the morphology of coating and also the morphology was affected with the present electrolyte [51]. In this study, we aimed to investigate how SC affects on and the electropolymerization of Py and the impedance data of PolyPy coated CF. For this reason, CFs was electrocoated with polypyrrole (PolyPy) conducting polymer by using constant or cyclic potential in the presence of epoxy based sizing compound (SC) in electrolyte solution. The coating thickness (as weight) and capacitive features of obtained coated CF and the current flown through system were investigated.

EXPERIMENTAL

In this study, we used CFs that were coated electrochemically with Py monomer (0.1 M) by using Constant Potential (1.5 V) in three electrode system, Ag wire (calibrated with 0.1 M ferrocene) as reference electrode, Pt wire as counter electrode and CF (0.003 ± 0.0005 g and 6 cm) as the working electrode. Electrolyte solution contained different amounts (0%; 0.18% and 1.8%) of epoxy based SC (Chemetylen AK-2 (SANYO Chemical Industries, Ltd.) in 0.1 M sodium perchlorate (0.1 M $NaClO_4$)-acetonitrile (ACN) [48-50].

The Constant Potential Electropolymerization (CPE) of Fibers
The aim of this part was to investigate the effect of SC on current which is flown in the circuit, so to follow the change of weight of coating with amount of SC in the electrolyte solution. During 60 min, the current flown through the system was recorded in CPE. Obtained data vs. time were given in Table 1.

Table 1: Obtained from CPE the current-time data. ($NaClO_4$/ACN; 0.003 g CF; 1.5 V)

Current/µA	18	17.94	17.65	17.65	17.21	17.14	17.21	17	17	16.6
Time/min.	0.1	3.52	9.86	16.1	28	33	41	47	58	60

In the first experiment, SC was not added into the electrolyte to see the difference of SC. Other experiments were carried out by adding 0.18% (w/v) and 1.8% (w/v) of SC to compare and find the convenient amount of SC. Obtained data were given Table 2 and Table 3.

Table 2: Obtained from CPE the current-time data. (SC: 0.18%; NaClO$_4$/ACN; 0.003 g CF; 1.5 V)

Current/µA	10.9	11.28	12	13.09	13.59	13.52	13.45	13.67	13.74	13.59	13.59
Time/min.	1.71	5.88	9.86	17	27	32	40	46	50	54	60

When the amount of SC was 0%, current changing was not observed during process, at 60 min and its value was about 17 µA. This current value was recorded as 13 µA for 0.18% of SC. This result pointed to the finding that the SC decreased current value. However, the current increased during the process and the weight of coating reached 10 mg/g for 0.18% SC. It was, however, 0.8 mg/g for 0% SC.

Table 3: Obtained from CPE the current-time data. (SC: 1.8%; NaClO$_4$/ACN; 0.003 g CF; 1.5 V)

Current/µA	10.7	0.6	0.4	0.42	0.49	0.49	0.42	0.63	0.7	0.63	0.63
Time/min.	0.1	4.07	9.6	14	19	28	36	45	53	57	60

According to Table 3, in these conditions the current passed from circuit was 10.7 µA within the first minute. Then the value decreased to 0.4 µA. The weighed amount of coating was 1.73 mg/g. As a result, the coating came true in the first minute. The amount of SC promoted the coating. It was however seen that the excess amount of SC was inhibited the current passing. When coating weight was 0.8 mg/g for 0% SC, it was 10 mg/g for 0.18% SC. Surprisingly, while the weight was decreased to 1.73 mg/g, the current was decreased 0.63 µA for 1.8% SC. When compared with 0.18% SC, the reason of this decrease was thought that the current passing and coating were blocked by the excessive amount of SC.

Gravimetric Analysis

To see how the adding of various amount of SC in electrolyte solution affected on the amount of coating, after CPE, CFs coated with PolyPy were weighted by using a five-digit analytical balance. The obtained data were given in Table 4.

Table 4: The amount of coating as compared the different amount of SC. (0.003 gr CF; 1.5 V)

SC (%)	0	0.18	1.8
Weight (mg/g)	0.8	10	1.73

According to obtained data, as SC was added in electrolyte solution during electrocoating, a decrease in the coating amount was observed. When SC amount was 0.18%, coating amount was 10 mg/g. This increasing was attributed to including into the structure of coating. But it was determined that the increasing in the amount was inhibited, while the amount of SC added in electrolyte solution was more than 0.18%, the increasing of coating amount was inhibited. Also, this increase was supported with the current rise (Table 2 and 3). Depended on these results, it is concluded that the current and SC amount were important parameters on the controlling of the thickness or amount of coating.

Structural Analysis (FTIR-ATR)

In the data, FT-IR peaks were investigated to understand whether if SC was included into the structure of the coating. The FT-IR spectra of CF coated with PPy in the presence of the various ratios of SC were compared in Figure 1. When we look at the figure, it was considered that the characteristic peaks of CF were covered with coating (PolyPy) and the characteristic peaks of coating were seen in the spectrum. The peak of PPy was seen in 3800-3600 cm^{-1}, and the ones of SC in 2900-2800cm^{-1}. The related peak assignments were given in Table 5.

Table 5. The FTIR-ATR peak assignments.

Peak (cm^{-1})	Peak Type
3748	N-H stretching[53]
2872, 1682, 1711	SC
1537, 1452,	PolyPy ring vib.[53]
1312, 1089, 1072, 1040 and 889	=CH band vib. of PPy[53]
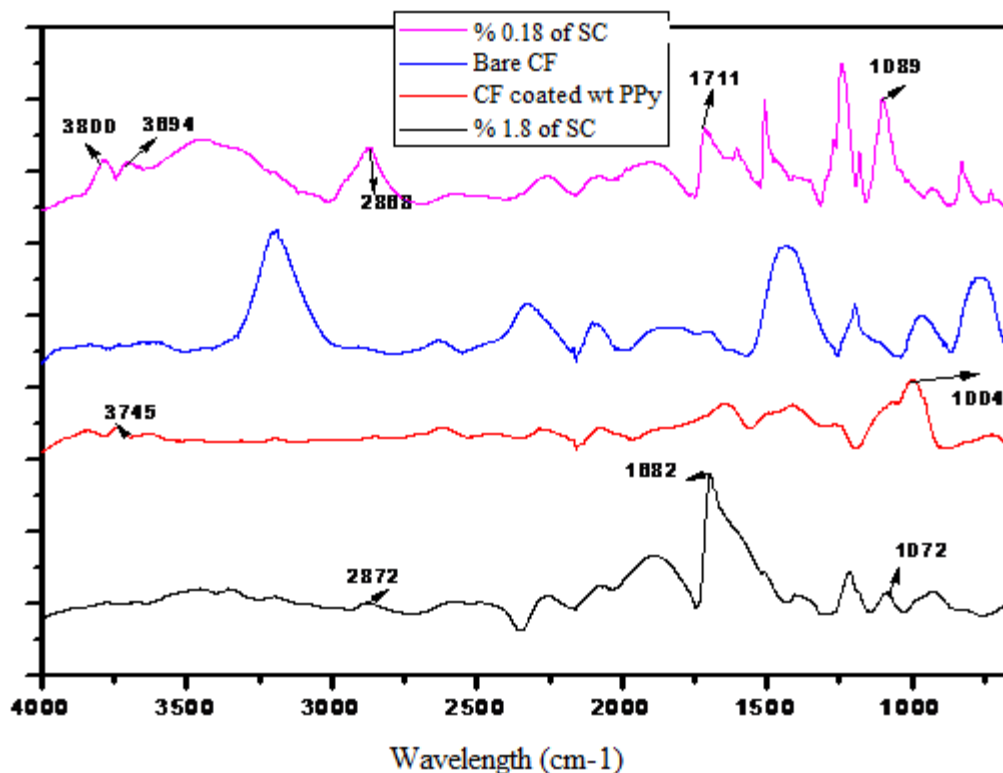
Figure 1. The FTIR-ATR spectra of CF coated with PolyPy in presence of SC (0.18%; 1.8%).

Peaks at 1452 and 1537cm^{-1} were assigned to Py ring vibration. The ones at 1312 and 1040 cm^{-1} were presented as the =C-H band vibrations. The N-H stretching vibration was observed at 3745 cm^{-1}. The peaks at 1178, 1089, 1072 and 889 cm^{-1} were characteristic peaks of =C-H out of plane vibration, demonstrating the polymerization of Py [53]. It was considered that the peaks at 2872, 1682 and 1711 cm^{-1} belonged to SC.

The Cyclic Voltammetry-Induced Electropolymerization of Fibers:

To investigate the effect of SC on the impedance values (or capacitance values), it was required to prepare CFs thin layer coated with PolyPy. For this reason, cyclic voltammetry technique was used. A three-electrode system consisted of Ag wire as a reference electrode, Pt wire as a counter electrode, and single CF as a working electrode like CPE. SC was added in 0.1 M Py including electrolyte solution (NaClO$_4$-ACN) in various ratios, which were 0%; 0.18% and 1.8%. So, obtained CV graphs were given in Figure 2.

a. NaClO$_4$/ACN 0% SC

b. NaClO$_4$/ACN 0.18% SC

c. NaClO₄/ACN

1.8% SC
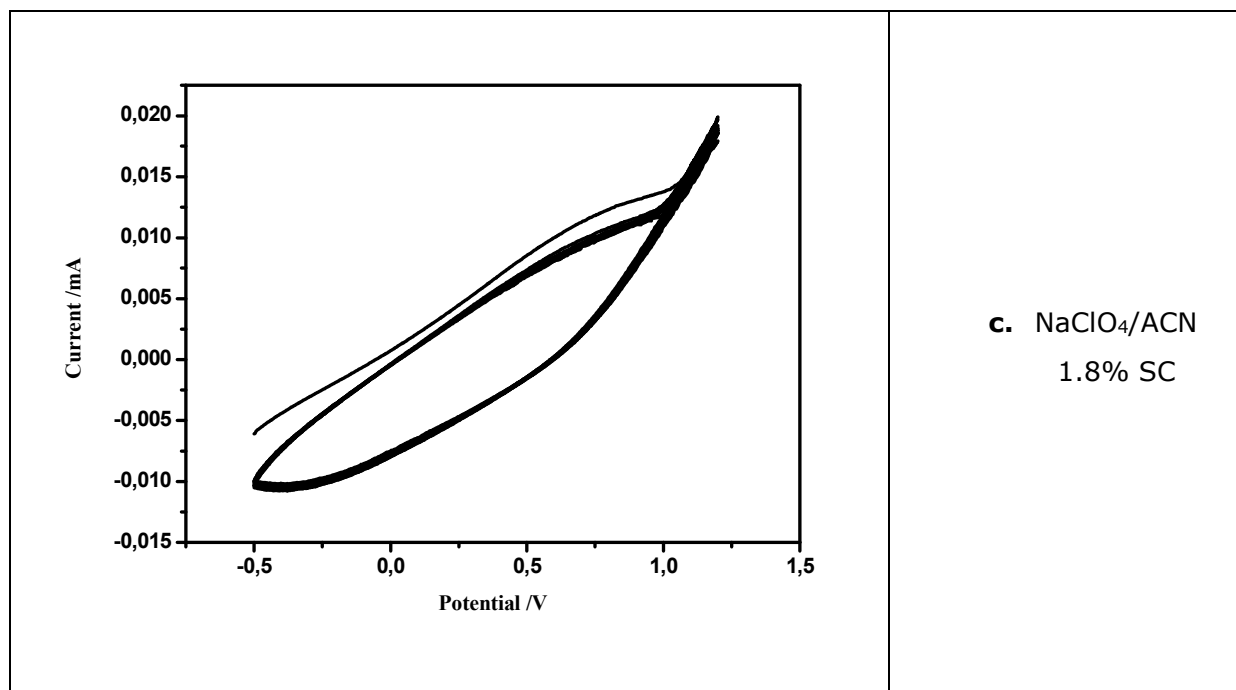
Figure 2. The CVs showing the effect of SC on polymerization of Py in NaClO₄-ACN including various ratios of SC.

It was seen clearly that adding SC affected the shape of CV. Py was oxidized at 0.9 V and current value was 0.04 mA (Figure 2a). As SC was added in electropolymerization medium, the value was decreased at 0.005 mA for %0.18 SC and 0.02 mA for 1.8% SC. It was thought that the cause of raising value at 1.8% SC might be due to the increasing amount of SC. To determine the electrical properties and if the mechanism of polymerization reaction is controlled by diffusion or not, it is required that CFs coated with PolyPy are investigated under CV conditions. Used electrolyte solution cannot include the monomer (here Py). For this reason, various scan rates were applied to CF coated with PPy and obtained CV graph, which were monomer-free graphs. The current responses to the scan rate from the polymer, oxidation (ox.) and reduction (red.) of the polymer peak current potentials and oxidation and reduction of the polymer peak current values were obtained from the graphs. Figure 3 illustrated scan rate vs. oxidation-reduction peak current values.

a. NaClO$_4$/ACN 0% SC

b. NaClO$_4$/ACN 0.18% SC
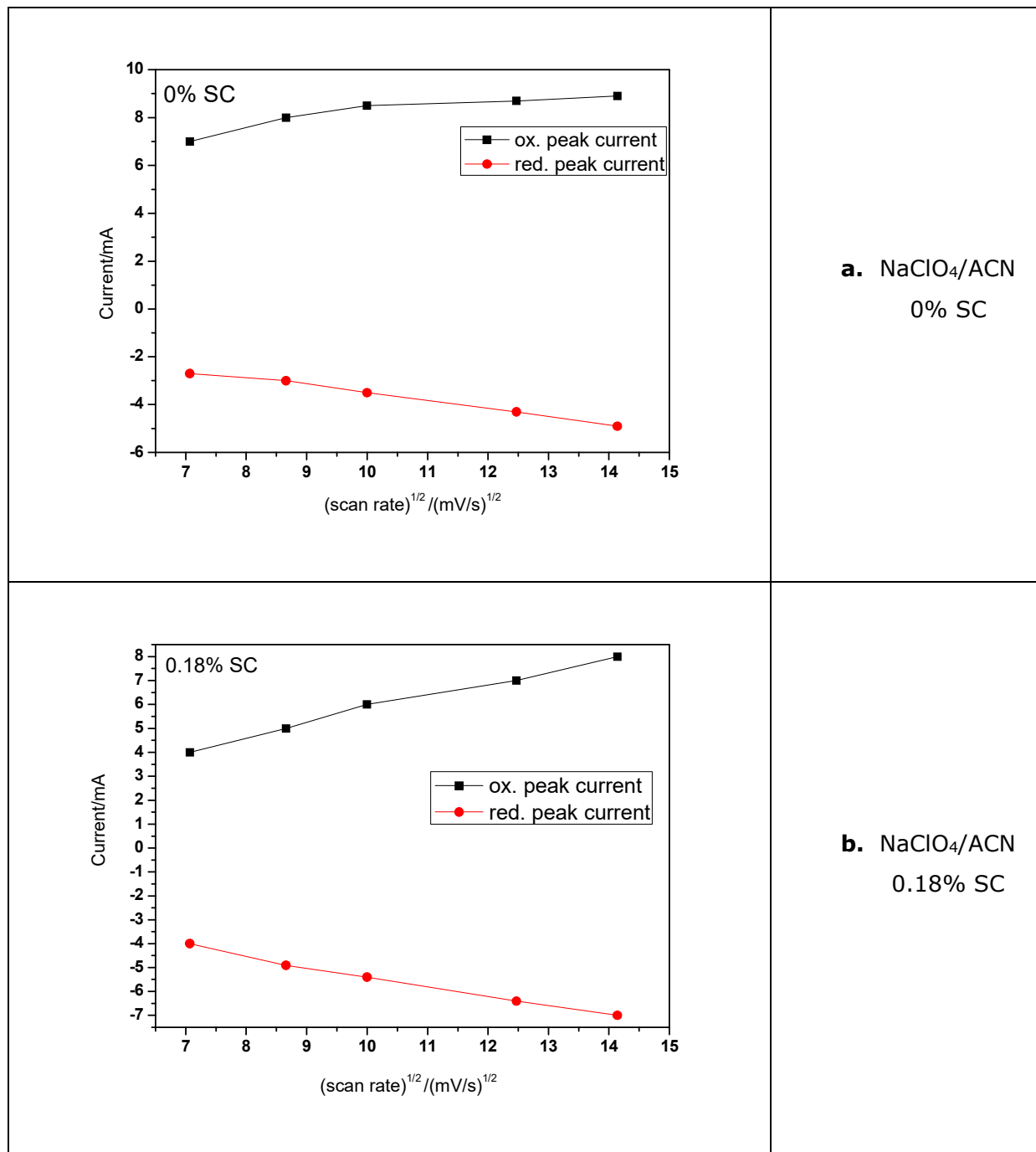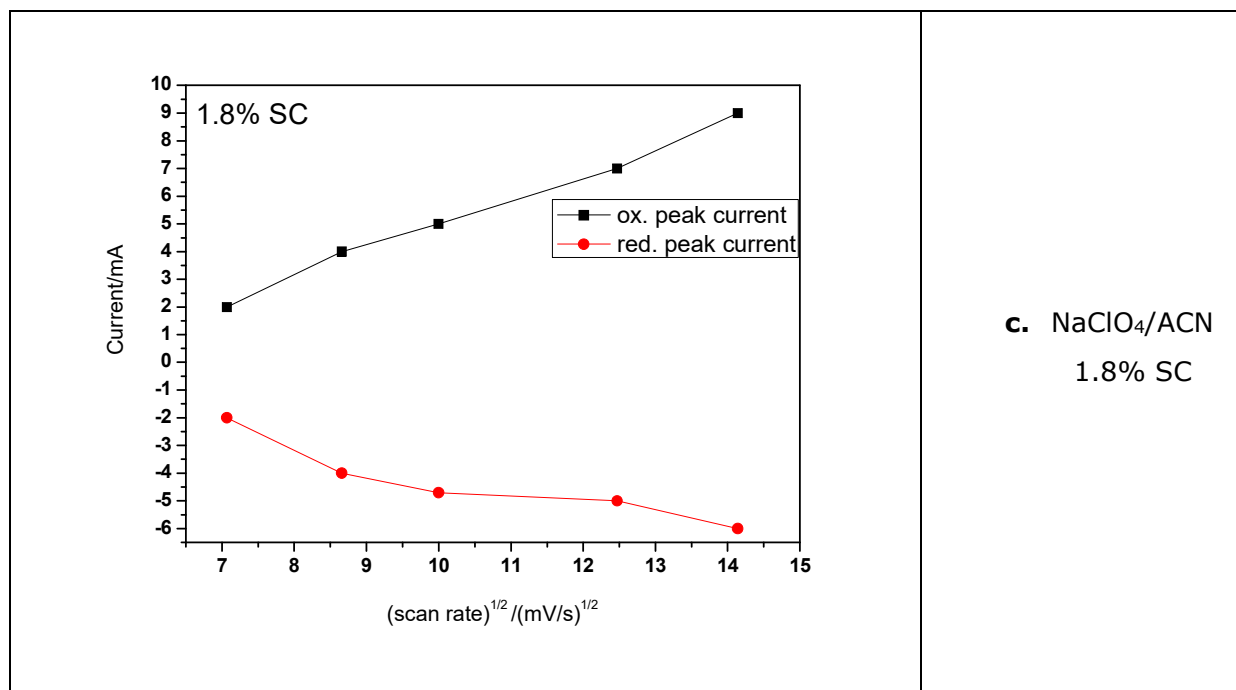
Figure 3. The monomer-free graphs of CFs coated with PPy in different conditions.

As the curve obtained from this data is approximated to a linear form, it could be concluded that the mechanism of polymerization reaction was controlled by diffusion. It can however be seen clearly that this control was destroyed by using of 1.8% SC in electrolyte medium.

The Electrochemical Impedance Analysis of Coated Fibers

To show and compare the effect of SC on electrochemical impedance, namely capacitance, the CFs obtained from related experiments were used. The measurements were taken in $NaClO_4$-ACN solution by using Electrochemical Impedance Spectroscopy (EIS). Figure 4 illustrated EIS graphs (Nyquist, Bode-Phase, Bode-Magnitude, and admittance).

a. Nyquist graph

b. Bode-Phase graph

| | **c.** Bode-Magnitude graph |
| | **d.** Admittance graph |
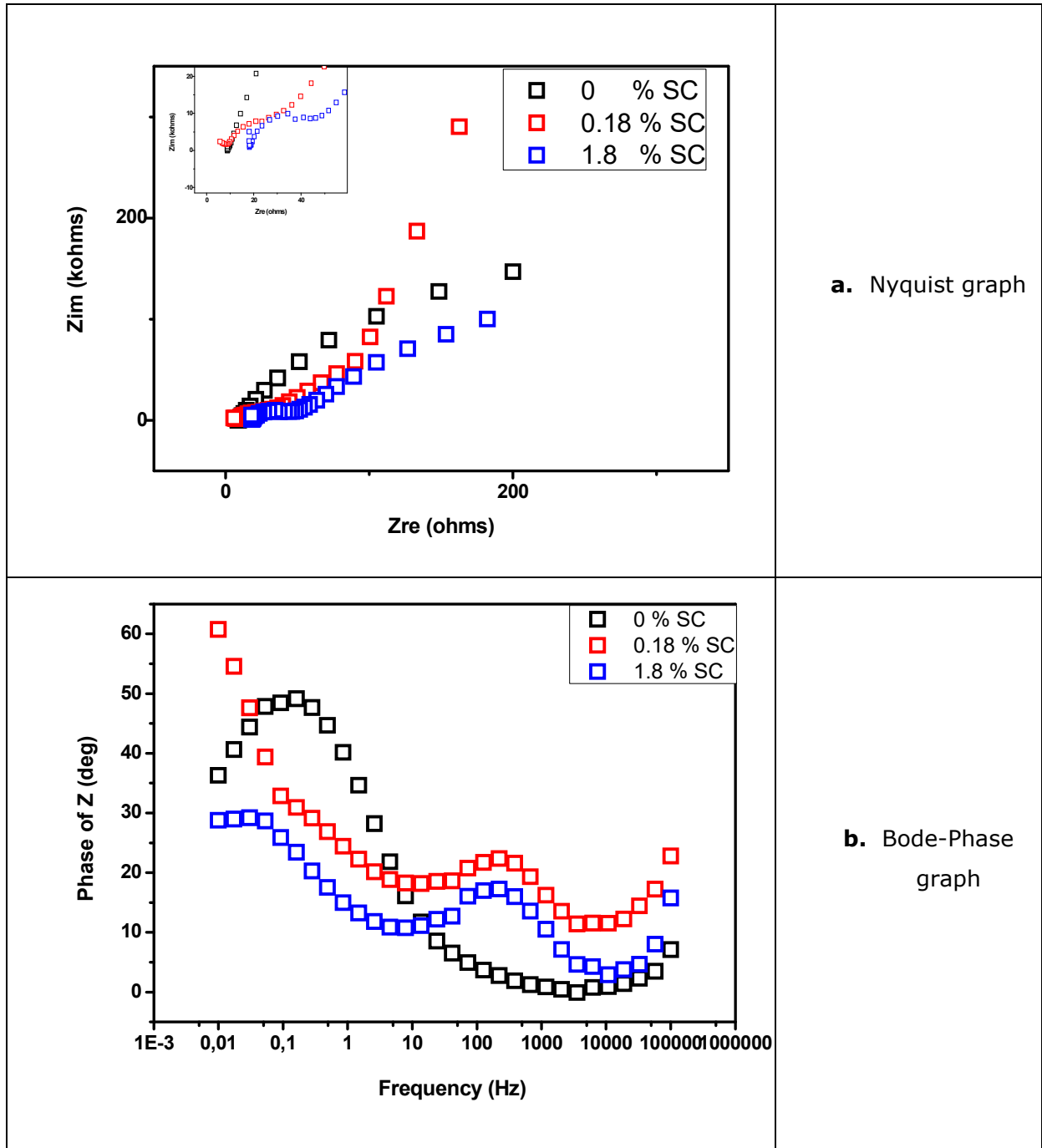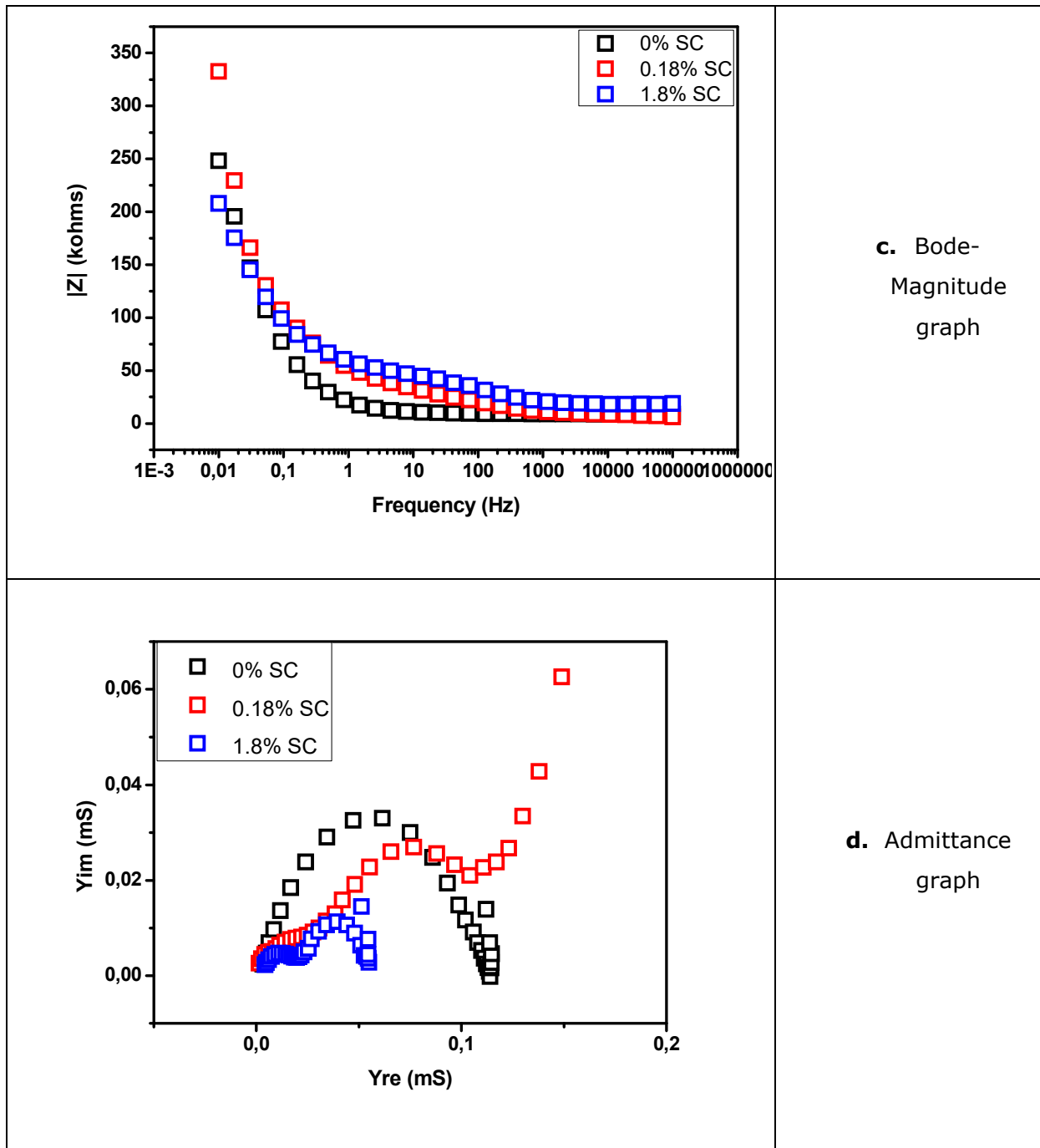
Figure 4. The EIS graphs of CFs coated with PPy in different conditions.

Different Capacitance values were obtained from these impedance graphs [54]. One of them was specific capacitance (C_{sp}) calculated from Nyquist graph by using Z_{im} at lowest frequency. The other was Double Layer Capacitance (C_{dl}) calculated from Bode-Magnitude graph by using IZI at 1 Hz. Calculated C_{sp} and C_{dl} values were 114 µF and 45 µF ; 57 µF and 19 µF; 166 µF and 17 µF for 0%; 0.18%; 1.8% of SC, respectively. Phase angle and admittance values were changed as 36° and 32 µS; 61° and 26 µS; 29° and 11 µS for 0%; 0.18%; 1.8% of SC, respectively.

In the light of this information, values obtained from these impedance graphs were given in Table 5. According to the values C_{sp} value was changed by adding SC in electrolyte solution. This change was shaped bell curve reversely, but the changing of the coating weight was shaped bell curve.

Table 5. The changing of Csp and coating weight vs. the ratio of SC.

SC (%)	0	0.18	1.8
Csp (µF)	114	57	166
Weight (mg/g)	0.8	10	1.73

Light Microscopic Images

CF was coated with PolyPy in the presence of various ratios (0%, 0.18%, and 1.8%) of SC in the electrolyte. CF was used as brush (in CPE technique) or single (in CV technique) form. The images captured from light microscopy of CFs coated with PolyPy were shown in Figure 5. Single CF was illustrated in Fig.5a, brush CF in Fig.5b and the comparison of coated and uncoated of CFs in Fig5c. As seen in the figure, the coatings were homogenous.

c)
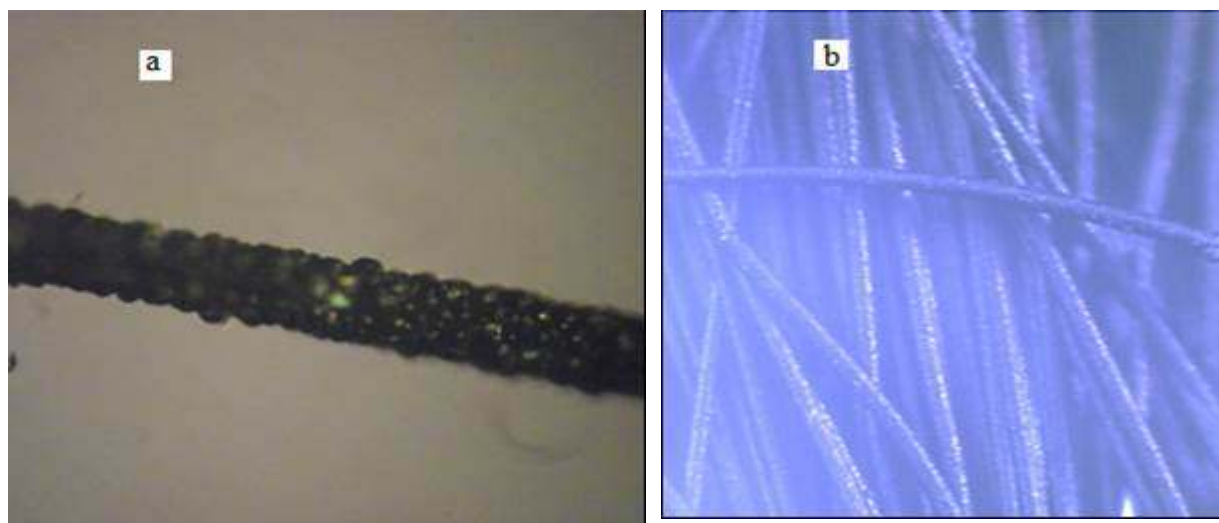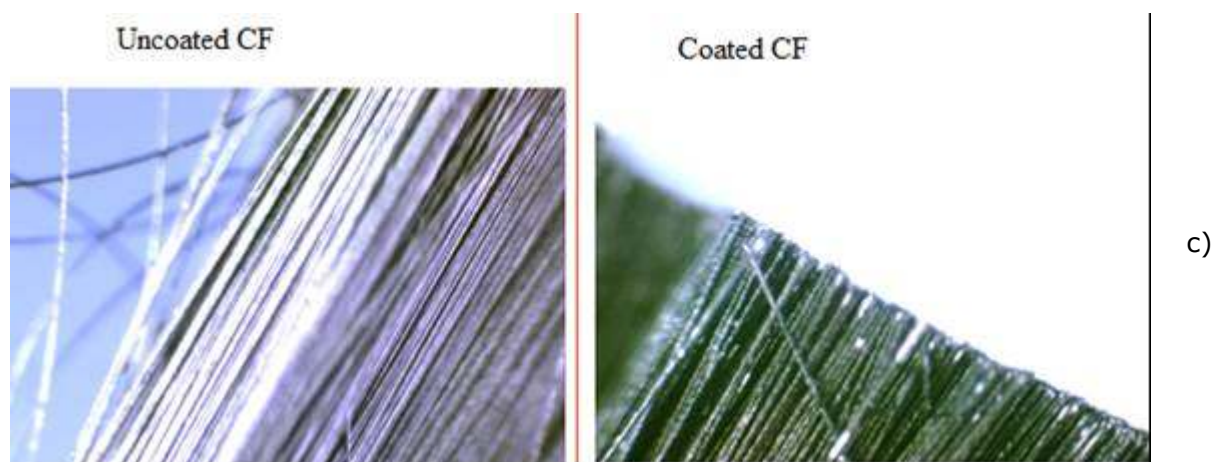
Figure 5. The images of light microscopy of Single CF (a), brush CF (b) and the comparison of uncoated and coated CFs (c).

DISCUSSIONS

In this study, it was proved that SC presented in electrolyte affected to the electropolymerization of Py, the weight of coating, the electrical, impedance, and capacitance properties of CF coated with PPy by using convenient techniques (CPE, Analytical Balance, CV, EIS and Light Microscopy). As a result, the weights and the capacitance values of CFs coated with PolyPy in conditions such as 0.1 M NaClO$_4$-ACN electrolyte solution including 0.1M Py and various ratios of epoxy based SC (0%; 0.18% and 1.8%) was changed with the SC ratios.

REFERENCES

1. Guo H, Huang Y, Liu L, Shi X. Effect of epoxy coatings on carbon fibers during manufacture of carbon fiber reinforced resin matrix composites. Materials & Design. 2010;31(3):1186-90.

2. Rezaei F, Yunus R, Ibrahim NA. Effect of fiber length on thermomechanical properties of short carbon fiber reinforced polypropylene composites. Materials & Design. 2009;30(2):260-3.

3. Bai Y, Wang Z, Feng L. Interface properties of carbon fiber/epoxy resin composite improved by supercritical water and oxygen in supercritical water. Materials & Design. 2010;31(3):1613-6.

4. Montes-Morán MA, Gauthier W, Martínez-Alonso A, Tascón JMD. Mechanical properties of high-strength carbon fibres. Validation of an end-effect model for describing experimental data. Carbon. 2004;42(7):1275-8.

5. Park S-J, Jang Y-S. Interfacial Characteristics and Fracture Toughness of Electrolytically Ni-Plated Carbon Fiber-Reinforced Phenolic Resin Matrix Composites. Journal of Colloid and Interface Science. 2001;237(1):91-7.

6. Choi MH, Jeon BH, Chung IJ. The effect of coupling agent on electrical and mechanical properties of carbon fiber/phenolic resin composites. Polymer. 2000;41(9):3243-52.

7. Park S-J, Kim M-H, Lee J-R, Choi S. Effect of Fiber–Polymer Interactions on Fracture Toughness Behavior of Carbon Fiber-Reinforced Epoxy Matrix Composites. Journal of Colloid and Interface Science. 2000;228(2):287-91.

8. Zielke U, Hüttinger KJ, Hoffman WP. Surface-oxidized carbon fibers: I. Surface structure and chemistry. Carbon. 1996;34(8):983-98.

9. Pittman Jr CU, He GR, Wu B, Gardner SD. Chemical modification of carbon fiber surfaces by nitric acid oxidation followed by reaction with tetraethylenepentamine. Carbon. 1997;35(3):317-31.

10. Hughes JDH. The carbon fibre/epoxy interface—A review. Composites Science and Technology. 1991;41(1):13-45.

11. Yuan H, Wang C, Zhang S, Lin X. Effect of surface modification on carbon fiber and its reinforced phenolic matrix composite. Applied Surface Science. 2012;259:288-93.

12. Yue ZR, Jiang W, Wang L, Gardner SD, Pittman Jr CU. Surface characterization of electrochemically oxidized carbon fibers. Carbon. 1999;37(11):1785-96.

13. Gulyás J, Földes E, Lázár A, Pukánszky B. Electrochemical oxidation of carbon fibres: surface chemistry and adhesion. Composites Part A: Applied Science and Manufacturing. 2001;32(3–4):353-60.

14. Severini F, Formaro L, Pegoraro M, Posca L. Chemical modification of carbon fiber surfaces. Carbon. 2002;40(5):735-41.

15. Seo M-K, Park S-J. Surface characteristics of carbon fibers modified by direct oxyfluorination. Journal of Colloid and Interface Science. 2009;330(1):237-42.

16. Li J. Interfacial studies on the O3 modified carbon fiber-reinforced polyamide 6 composites. Applied Surface Science. 2008;255(5, Part 2):2822-4.

17. Zhang X, Pei X, Zhang J, Wang Q. Effects of carbon fiber surface treatment on the friction and wear behavior of 2D woven carbon fabric/phenolic composites. Colloids and Surfaces A: Physicochemical and Engineering Aspects. 2009;339(1–3):7-12.

18. Fjeldly A, Olsen T, Rysjedal JH, Berg JE. Influence of the fiber surface treatment and hot–wet environment on the mechanical behavior of carbon/epoxy composites. Composites Part A: Applied Science and Manufacturing. 2001;32(3–4):373-8.

19. Ramanathan T, Bismarck A, Schulz E, Subramanian K. Investigation of the influence of acidic and basic surface groups on carbon fibres on the interfacial shear strength in an epoxy matrix by means of single-fibre pull-out test. Composites Science and Technology. 2001;61(4):599-605.

20. Montes-Morán MA, Martínez-Alonso A, Tascón JMD, Young RJ. Effects of plasma oxidation on the surface and interfacial properties of ultra-high modulus carbon fibres. Composites Part A: Applied Science and Manufacturing. 2001;32(3–4):361-71.

21. Dilsiz N, Erinç NK, Bayramli E, akovali G. Surface energy and mechanical properties of plasma-modified carbon fibers. Carbon. 1995;33(6):853-8.

22. Bubert H, Ai X, Haiber S, Heintze M, Brüser V, Pasch E, et al. Basic analytical investigation of plasma-chemically modified carbon fibers. Spectrochimica Acta Part B: Atomic Spectroscopy. 2002;57(10):1601-10.

23. Li J, Huang Y, Xu Z, Wang Z. High-energy radiation technique treat on the surface of carbon fiber. Materials Chemistry and Physics. 2005;94(2–3):315-21.

24. Xu Z, Huang Y, Zhang C, Liu L, Zhang Y, Wang L. Effect of γ-ray irradiation grafting on the carbon fibers and interfacial adhesion of epoxy composites. Composites Science and Technology. 2007;67(15–16):3261-70.

25. Saraç AS, Bardavit Y. Electrografting of copolymer of poly[N-vinylcarbazole-co-styrene] and poly[N-vinylcarbazole-co-acrylonitrile] onto carbon fiber: cyclovoltammetric (CV), spectroscopic (UV-Vis, FT-IR-ATR), and morphological study (SEM). Progress in Organic Coatings. 2004;49(2):85-94.

26. Blackketter DM, Upadhyaya D, King TR, King JA. Evaluation of fiber surfaces treatment and sizing on the shear and transverse tensile strengths of carbon fiber-reinforced thermoset and thermoplastic matrix composites. Polymer Composites. 1993;14(5):430-6.

27. Yumitori S, Wang D, Jones FR. Third International Conference on Interfacial Phenomena in Composite MaterialsThe role of sizing resins in carbon fibre-reinforced polyethersulfone (PES). Composites. 1994;25(7):698-705.

28. Lu W, Smela E, Adams P, Zuccarello G, Mattes BR. Development of Solid-in-Hollow Electrochemical Linear Actuators Using Highly Conductive Polyaniline. Chemistry of Materials. 2004;16(9):1615-21.

29. Fukuhara T, Akiyama Y, Yoneda N, Tada T, Hara S. Effective synthesis of difluorocyclohexadienones by electrochemical oxidation of phenols. Tetrahedron Letters. 2002;43(37):6583-5.

30. Matsushita M, Kuramitz H, Tanaka S. Electrochemical Oxidation for Low Concentration of Aniline in Neutral pH Medium: Application to the Removal of Aniline Based on the Electrochemical Polymerization on a Carbon Fiber. Environmental Science & Technology. 2005;39(10):3805-10.

31. Cao H, Huang Y, Zhang Z, Sun J. Uniform modification of carbon fibers surface in 3-D fabrics using intermittent electrochemical treatment. Composites Science and Technology. 2005;65(11–12):1655-62.

32. Han S, Briseno AL, Shi X, Mah DA, Zhou F. Polyelectrolyte-Coated Nanosphere Lithographic Patterning of Surfaces: Fabrication and Characterization of Electropolymerized Thin Polyaniline Honeycomb Films. The Journal of Physical Chemistry B. 2002;106(25):6465-72.

33. Kumru ME, Springer J, Saraç AS, Bismarck A. Electrografting of thiophene, carbazole, pyrrole and their copolymers onto carbon fibers: electrokinetic measurements, surface composition and morphology. Synthetic Metals. 2001;123(3):391-401.

34. Luo Y, Zhao Y, Duan Y, Du S. Surface and wettability property analysis of CCF300 carbon fibers with different sizing or without sizing. Materials & Design. 2011;32(2):941-6.

35. Kim TH, Vijayalakshmi S, Son SJ, Ryu SK, Kim JD. A Combined Study of Preparation and Characterization of Carbon Molecular Sieves (CMS) for Carbon Dioxide Adsorption from Coals of Different Origin. J Ind Eng Chem. 2003;9(5):481-7.

36. Park S-J, Kim B-J. Roles of acidic functional groups of carbon fiber surfaces in enhancing interfacial adhesion behavior. Materials Science and Engineering: A. 2005;408(1–2):269-73.

37. Dilsiz N, Wightman JP. Surface analysis of unsized and sized carbon fibers. Carbon. 1999;37(7):1105-14.

38. Li J, Fan Q, Chen Z-h, Huang K-b, Cheng Y-l. Effect of electropolymer sizing of carbon fiber on mechanical properties of phenolic resin composites. Transactions of Nonferrous Metals Society of China. 2006;16, Supplement 2:s457-s61.

39. Satici MT, Sarac AS. Synthesis and Characterization of Poly(Acrylonitrile-co-Vinylacetate)/Fe2O3@PEDOT Core-Shell Nanocapsules and Nanofibers. International Journal of Polymeric Materials and Polymeric Biomaterials. 2015;64(11):597-609.

40. Sarac AS, Ates M, Kilic B. Electrochemical impedance spectroscopic study of polyaniline on platinum, glassy carbon and carbon fiber microelectrodes. Int J Electrochem Sci. 2008;3(7):777-86.

41. Sipahi M, Parlak EA, Gul A, Ekinci E, Yardim MF, Sarac AS. Electrochemical impedance study of polyaniline electrocoated porous carbon foam. Progress in Organic Coatings. 2008;62(1):96-104.

42. Sönmez G, Saraç AS. Structural study of pyrrole-EDOT copolymers on carbon fiber micro-electrodes. Synthetic metals. 2003;135:459-60.

43. Sezgin S, Ates M, Parlak EA, Sarac AS. Scan rate effect of 1-(4-methoxyphenyl)-1H-pyrrole electro-coated on carbon fiber: characterization via cyclic voltammetry, FTIR-ATR and electrochemical impedance spectroscopy. Int J Electrochem Sci. 2012;7:1093-106.

44. Sarac AS, Gencturk A, Gilsing H-D, Schulz B, Turhan CM. Effect of Electrolyte on the Electropolymerization of 2,2-Dibutyl-3,4-Propylenedioxythiophene on Carbon Fiber Microelectrodes. Journal of Nanoscience and Nanotechnology. 2009;9(5):2877-86.

45. Sarac AS, Sezgin S, Ates M, Turhan CM, Parlak EA, Irfanoglu B. Electrochemical impedance spectroscopy of poly(N-methyl pyrrole) on carbon fiber microelectrodes and morphology. Progress in Organic Coatings. 2008;62(3):331-5.

46. Popkirov GS, Barsoukov E, Schindler RN. Investigation of conducting polymer electrodes by impedance spectroscopy during electropolymerization under galvanostatic conditions. Journal of Electroanalytical Chemistry. 1997;425(1–2):209-16.

47. Deslouis C, Musiani MM, Tribollet B, Vorotyntsev MA. Comparison of the AC Impedance of Conducting Polymer Films Studied as Electrode-Supported and Freestanding Membranes. Journal of The Electrochemical Society. 1995;142(6):1902-8.

48. Dolas H, Sarac AS. Electrosynthesis of Poly(3-dodecyl thiophene) in Acetonitrile with Boron Trifluoride Diethyl Etherate: The Effect of the Electrolyte on Electrochemical Impedance and Morphology. Journal of The Electrochemical Society. 2011;159(1):D1-D8.

49. Sarac AS, Geyik H, Parlak EA, Serantoni M. Electrochemical composite formation of thiophene and N-methylpyrrole polymers on carbon fiber microelectrodes: Morphology, characterization by surface spectroscopy, and electrochemical impedance spectroscopy. Progress in Organic Coatings. 2007;59(1):28-36.

50. Sarac AS, Sezgin S, Ates M, Turhan CM. Electrochemical impedance spectroscopy and morphological analyses of pyrrole, phenylpyrrole and methoxyphenylpyrrole on carbon fiber microelectrodes. Surface and Coatings Technology. 2008;202(16):3997-4005.

51. Dolas H, Sarac AS. An impedance-morphology study on poly(3-methylthiophene) coated electrode obtained in boron trifluoride diethyl etherate–acetonitrile. Synthetic Metals. 2014;195:44-53.

52. Dolas H, Sezer E, Sarac AS. Synthesis, Characterization and Electrochemical Polymerization of a Comonomer Bearing Thiophene and Imidazole: The Comparison of Impedance Behavior on Different Surfaces. ECS Journal of Solid State Science and Technology. 2016;5(5):P211-P7.

53. Vishnuvardhan TK, Kulkarni VR, Basavaraja C, Raghavendra SC. Synthesis, characterization and a.c. conductivity of polypyrrole/Y2O3 composites. Bulletin of Materials Science. 2006;29(1):77-83.

54. Macdonald DD. Reflections on the history of electrochemical impedance spectroscopy. Electrochimica Acta. 2006;51(8–9):1376-88.

Türkçe Öz ve Anahtar Kelimeler

Pirolün Elektropolimerleşmesi Üzerine Boyutlandırıcı Bileşiğin Etkisi ve Polipirol ile Kaplanmış Karbon Lifinin İmpedansı

Hacer DOLAS, Digdem GIRAY and A.Sezai SARAC

Öz: Karbon Lifi (CF), düşük ağırlık, yüksek dayanırlık ve sertlik gibi mekanik özelliklerinden ötürü pek çok endüstri alanında yüksek performansa sahip reçine kompozitlerinde kuvvetlendirici malzeme olarak kullanılmaktadır. Kompozit malzemelerin mekanik performansları, onu oluşturan lif ve matrisin özelliklerine dayanır. Lif yüzeyinin özelliklerine etkide bulunan yöntemlerden biri, lif yüzeyinin ince filmle kaplanmasıdır. Lif elektropolimer ile kaplandığı zaman, kompozitin mekanik dayanıklılığı artmıştır. Bu çalışmada, karbon lifleri polipirol (PPy) ile elektrokimyasal olarak kaplanmış olup ortamda epoksi esaslı boyutlandırıcı bileşik (SC) vardır. Süreç boyunca SC'nin miktarı ile akımın, elde edilen kaplama ağırlıklarının ve impedans verisinin, özellikle kapasitansın, nasıl değiştiği incelenmiştir. Bu sebeple, farklı miktarda SC (%0, %0,18, %1,8 v/v) elektrolit çözeltisi olan ve 0,1 M pirol (Py) içeren 0,1 M $NaClO_4$-ACN'ye ilave edilmiştir. Kaplama işlemi Sabit Potansiyel veya Döngülü Voltammetri teknikleri ile yürütülmüştür. Diğer inceleme teknikleri gravimetrik analiz, elektrokimyasal impedans spektroskopisi, Fourier Transform İnfrared Spektroskopisi (FT-IR) ve Işık Mikroskopisidir. Kaplamanın sonunda, kaplamanın ağırlığı ve özgül kapasitansı (Csp), %0 SC için 0,8 mg/g ve 114 µF, %0,18 SC için 10 mg/g ve 57 µF ve %1,8 SC için 1,73 mg/g ve 166 µF olarak bulunmuştur. Sonuç olarak, PPy ile kaplanmış karbon lifinin kaplanma ağırlığı ve kapasitans verisi (özellikle Csp), elektrolite ilave edilmiş SC'nin miktarı ile ters orantılı olarak değişmiştir.

Anahtar kelimeler: Elektropolimerleşme, Boyutlandırma, İmpedans ve Kapasitans.

Preparation of TiO$_2$/Perlite Composites by Using 2$^{3-1}$ Fractional Factorial Design

Dilek DURANOĞLU*

Yıldız Technical University, Chemical Engineering Department, Davutpasa Campus,

Esenler 34210, Istanbul, Turkey

*Dilek Duranoğlu, E-mail: dilekdur@gmail.com; dduran@yildiz.edu.tr

Abstract: Successive impregnation and calcination processes were performed in order to produce TiO$_2$/perlite composites. 2$^{3-1}$ fractional factorial design was first applied to optimize the production conditions of TiO$_2$/perlite photocatalysts. Seven TiO$_2$/perlite composites (including three central point experiments) were produced by manipulating three process parameters (amount of TiO$_2$ used in impregnation process, particle size of perlite and calcination temperature). Prepared TiO$_2$/perlite photocatalysts were characterized by X-Ray Diffraction Spectrometry and SEM. XRD patterns indicated that anatase was the main crystalline phase for all produced samples. Degradation capacities of produced TiO$_2$/perlite composites were investigated in methylene blue degradation process. The linear models of TiO$_2$ loading (%) and methylene blue degradation (%) of TiO$_2$/perlite composites were developed by regression analysis of the experimental data. As a result of analysis of variance, it was found that developed models were statistically significant with the p-value of 0.0040 and 0.0003, for TiO$_2$ loading (%) and methylene blue degradation (%), respectively. According to the coefficient of determination (0.9821 and 0.9970 for the models of TiO$_2$ loading and methylene blue degradation, respectively) and error analysis, developed models fit well to the experimental data. Effect of process parameters was investigated by using response surface plots. Amount of TiO$_2$ and particle size were found as the most effective parameters on both TiO$_2$ loading (%) and degradation efficiency (%). Calcination temperature did not affect TiO$_2$ loading but methylene blue degradation capacity.

Keywords: 2$^{3-1}$ factorial design, photocatalyst, TiO$_2$, perlite.

INTRODUCTION

TiO$_2$ is considered the most suitable photocatalyst due to its higher degradation capacity against to the numerous organic pollutants. However, TiO$_2$ nanoparticles require very expensive microfiltration processes for separating them from water after their use in water treatment. This problem can be solved by attaching nanoparticles onto a support material [1]. However, photocatalytic efficiency of TiO$_2$ may decrease by immobilizing it on a support material due to the different reasons like properties of support material and production conditions.

Expanded perlite, a kind of glassy volcanic rock, can be used as photocatalyst support due to its high silicon content, porous structure, and be found easily in low-cost in nature. Moreover, comparing to other porous materials like activated carbon, zeolite, and clays, lower density and higher light transparency make perlite a promising photocatalyst support. TiO$_2$ can be strongly attached to the perlite surface with Ti-O-Si bonds effectively, hence, stable photocatalysts could be developed. Expanded perlite, has been widely used as photocatalyst support in recently published works in order to photocatalytic degradation of different pollutant like ammonia [2,3], sulfamethoxazole [4], ethylbenzene [5], phenol [6,7], and furfural [8]. None of them investigated the effect of preparation conditions onto degradation efficiency by any experimental design approach. In the literature of photocatalysis and photocatalytic degradation, experimental design techniques have been just focused on the optimization of degradation process conditions [9, 10] except a few [11, 12]. However, systematic investigation of optimum preparation conditions is very important to develop effective photocatalysts. Applying experimental design techniques would have great significance in designing and developing high performance photocatalysts for environmental remediation [11].

By means of experimental design methods, higher amount of information can be obtained by performing less amount of experiments. There are many types of experimental design techniques such factorial design (Full and Fractional Factorial Design), response surface methodology (Central Composite Design, Box-Behnken Design, Doehlert Design), Plackett-Burman Design, Mixture Design, Taguchi Design, *etc* [13]. In a Full Factorial Design, coefficient of linear interactions, two-term and three-term interactions can be examined [14]. However, full factorial experiments cannot always be conducted because of economy, time, or other constraints [15]. Especially, in case of material development, by considering

the cost of raw materials and characterization, conducting Fractional Factorial Design would be more efficient. Moreover, Fractional Factorial Design gives enough information if there is only main effects, and a small number of low order interactions are important [16].

2^{3-1} Fractional Factorial Design matrix is subtracted from the matrix of 2^3 Full Factorial Design [13]. 2^3 Full Factorial Design requires eight experiments and mathematical model of it is given below:

$$Y = b_0 + b_1X_1 + b_2X_2 + b_3X_3 + b_{12}X_1X_2 + b_{13}X_1X_3 + b_{23}X_2X_3 + b_{123}X_1X_2X_3 \quad \text{(Eq. 1)}$$

However, in 2^{3-1} Fractional Factorial Design, only four experiments are performed. Two-term interactions are reduced according to following relations:

$$X_1 = X_2X_3 \; ; \; X_2 = X_1X_3 \; ; \; X_3 = X_1X_2 \; ; \; I = 1 = X_1X_2X_3 \quad \text{(Eq. 2)}$$

Consequently, mathematical model for 2^{3-1} Fractional Factorial Design is given as follows:

$$Y = \beta_0 + \beta_1X_1 + \beta_2X_2 + \beta_3X_3 \quad \text{(Eq. 3)}$$

Where $\beta_0 = b_0 + b_{123}$, $\beta_1 = b_1 + b_{23}$, $\beta_2 = b_2 + b_{13}$, $\beta_3 = b_3 + b_{12}$.

Variation of each parameters involves the effect of two-term interactions of other two parameters.

In order to carry out as possible as less amount of experiment, 2^{3-1} Fractional Factorial Design was chosen for investigation of preparation conditions on ultimate TiO_2/perlite composites and methylene blue degradation efficiency. Amount of TiO_2, particle size of perlite and calcination temperature were chosen as independent process variables; both TiO_2 loading percentage and methylene blue degradation percentage were investigated as responses.

MATERIALS and METHODS

Titanium dioxide (Degussa P-25®), as photocatalyst, was supplied from Evonik Company. The ratio of anatase:rutile phases in Degussa P-25 is about 3:1 [17]. Expanded perlite, as photocatalyst support, was obtained from TAŞPER Perlit Company, Turkey. Methylene blue (Sigma-Aldrich, >99%) was used as received and dissolved in distilled water in order to obtain the desired concentration.

Preparation and characterization of perlite supported photocatalyst: After sieving desired particle size, expanded perlite was rinsed with distilled water under 5 mL/min air flow till no powder remains in the filtrate. Typical procedure given in [6], with some changes, was applied in order to prepare TiO_2/perlite composites. According to that, a determined amount of TiO_2 (Degussa P-25), then, 5 mL of diluted nitric acid (at pH 3.3), was added into 50mL absolute ethanol in an ultrasonic bath. Then, 5 g of prepared perlite was added to the mixture while stirring in a shaker at 130 rpm, successively, the mixture was kept in ultrasonic bath for 15 minutes to disperse possible agglomerated titanium dioxide powders. After impregnation in an oven at 120°C for 12 hours, the mixture was calcined at high temperature for 1 hour. Once again, TiO_2/perlite composites were washed in distilled water with the assistance of air bubbling for few minutes in order to remove titania powders which had not been precipitated on perlite surface. After filtration and drying, TiO_2/perlite composites were weighed, then used in photocatalytic degradation experiments.

TiO_2/perlite composites were investigated by Scanning Electron Microscopy (SEM, CamScan Apollo 300). Samples were attached onto stubs by using double-sided carbon tape, and, in order to obtain high resolution images, they were coated with gold powders using an automated sputter coater. The crystalline structures of TiO_2/perlite composites were determined via X-ray diffractometer. XRD measurement was performed on Philips Panalytical X'Pert Pro X-ray diffractometer using Cu K-alpha radiation. TiO_2/perlite composites were ground to have fine powders before analysis. Crystalline structure of prepared samples has been determined by using software of the instrument.

2^{3-1} Fractional Factorial Design: TiO$_2$/perlite composites were prepared according to the experimental design matrix given in Table 1. 2^{3-1} fractional factorial experimental design was applied in order to investigate the effects of the selected parameters (amount of TiO$_2$, particle size of perlite and calcination temperature) on both TiO$_2$ loading and methylene blue degradation efficiency. Levels of selected parameters and responses for 2^{3-1} fractional factorial design can be seen in Table 2.

Table 1. 2^{3-1} Fractional Factorial Experimental Design Matrix with central points.

Sample No	X_1	X_2	X_3
PT1	+1	+1	+1
PT2	+1	-1	-1
PT3	-1	-1	+1
PT4	-1	+1	-1
PT5	0	0	0
PT6	0	0	0
PT7	0	0	0

Table 2. Factors and levels of 2^{3-1} fractional factorial design.

	Independent variables	Levels		
		Low (-1)	Middle (0)	High (+1)
X_1	Amount of TiO$_2$ (g)	0.25	0.75	1.25
X_2	Mean particle size of perlite (mm)	1.5	2.5	3.5
X_3	Calcination temperature (°C)	300	450	600
	Dependent variables	Constraints		
		Low	High	Goal
R_1	TiO$_2$ loading (%)	0	100	Maximize
R_2	MB Degradation (%)	0	100	Maximize

Statistical analysis: The statistical significance of variables was evaluated using the analysis of variance (ANOVA). Model fitting was evaluated by coefficient of determination (R^2) and error analysis. Design Expert 10.0 software package was used for evaluating model fitting and statistical significance of the developed model.

Photocatalytic degradation study: 500 mL pyrex glass reactor was equipped with 2x6W UV lamps (365nm) and was used for methylene blue degradation experiments (Figure 2). The photoreactor was covered with aluminum foil to block transition of external light to the reactor. The temperature of the reaction medium was kept constant at 20 °C by using cooling water recycling. Air flow (12 L/h) was fed into the reactor and flow rate was controlled by a flowmeter. In order to complete adsorption-desorption equilibrium, the reactor was kept in dark in the first 30 min, and then, air flow and UV source was turned on. The sample was collected from the reactor periodically, and methylene blue

concentrations were determined at 664 nm by using an Analytic Jena Specord 200 Plus UV Spectrophotometer. Experimental studies were carried with 4 g of PT samples in 500 mL methylene blue solution (initial conc: 20 ppm) and, the mixture was stirred at 500 rpm using a magnetic stirrer throughout the process.
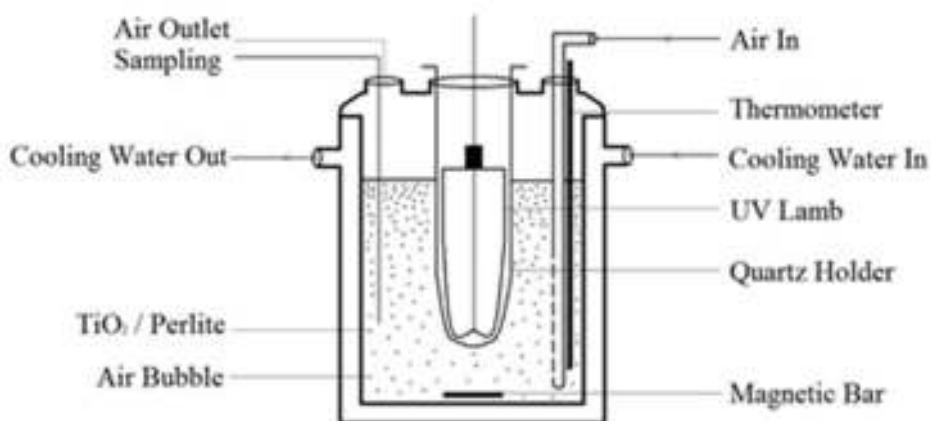
Figure 2. Experimental setup for photocatalytic degradation.

RESULTS and DISCUSSION

Characteristics of prepared TiO$_2$/perlite composites: SEM images of prepared samples can be seen in Figure 3. Although during the preparation of both PT1 and PT2 the same amount of TiO$_2$ was used, the amount of loaded TiO$_2$ onto perlite is much more in case of PT2 sample, which has the smaller particle size. Hence, it can be concluded that not only Ti/Perlite ratio is very important for impregnation process but also particle size is very effective.

| Perlite | PT1 | PT2 |

PT3	PT4	PT5
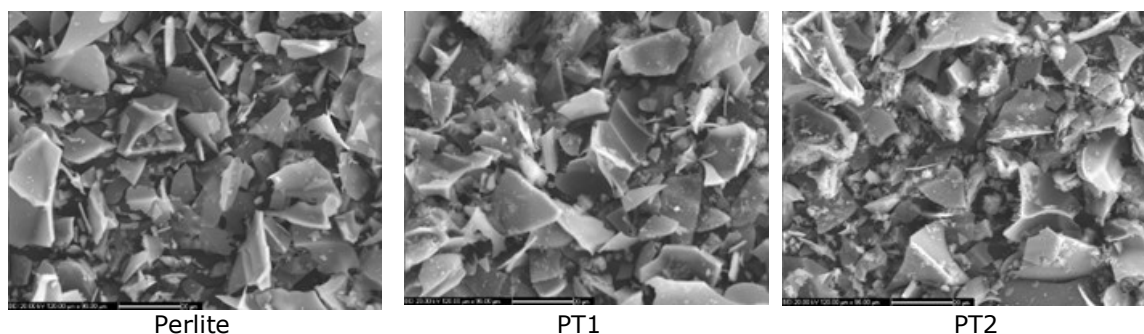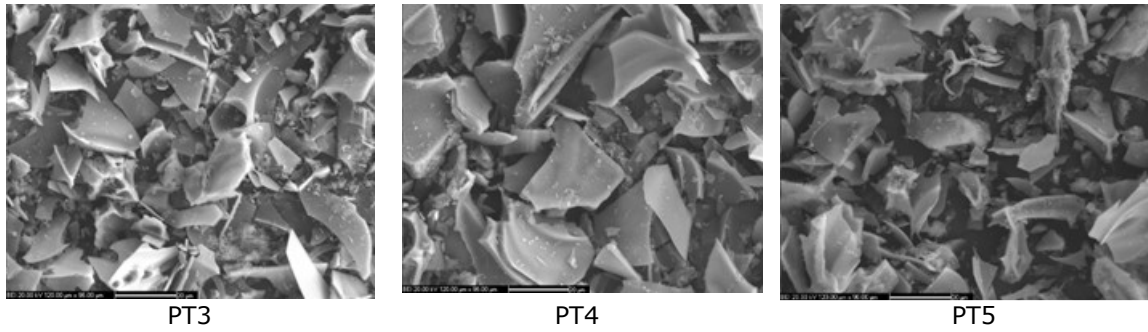
Figure 3. SEM images of perlite and TiO$_2$/perlite composites (x1000).

An X-ray diffractometer was used in order to examine the crystalline structure of TiO$_2$/perlite composites. As known that crystalline structure is mainly affected by calcination temperature, XRD patterns of TiO$_2$/perlite composites, which were calcined at different temperatures, and pure TiO$_2$ were given in Figure 4. Anatase diffraction peaks, which match well with the PDF table (01-084-1285), was observed for all samples, beside, the XRD pattern of PT2 sample, which was calcined at 300 °C, show also rutile diffraction peaks that match well with the PDF table (01-088-1175). As a conclusion, XRD patterns indicate anatase as the main crystalline TiO$_2$ phase, and rutile crystalline phase in the precursor TiO$_2$ was converted to the anatase at 450ºC and 600ºC of further calcination.
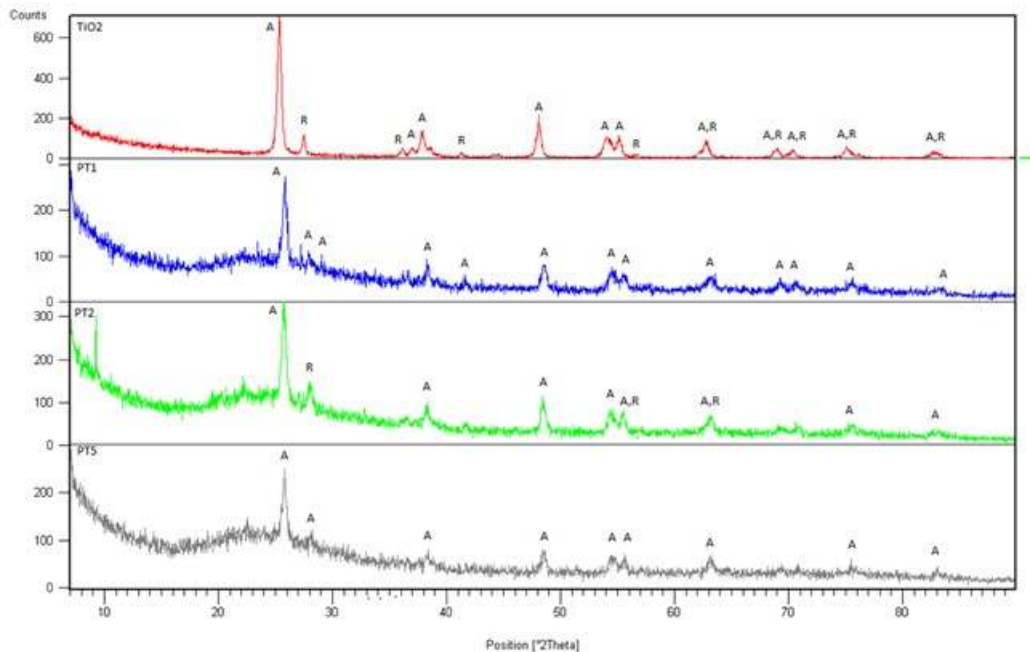
Figure 4. XRD patterns of TiO$_2$ (Degussa P25) and TiO$_2$/perlite composites (calcination temperature for PT1, PT2 and PT5 were 600, 300 and 450ºC, respectively).

Photocatalytic degradation of methylene blue: Photocatalytic degradation of methylene blue by TiO$_2$/perlite composites can be seen in Figure 5. At the first 30 minutes, all samples adsorbed different amounts of methylene blue (%13-%44) depending on their preparation conditions. Among the PT samples, the best photocatalytic efficiency was obtained with PT2 sample, which has a high amount of TiO$_2$ and low particle size of perlite. PT3 and PT4, which has low amount of TiO$_2$ during preparation, showed the worst degradation capacity, even though they had relatively high adsorption capacity. It can be concluded that amount of TiO$_2$ is the most effective parameter in order to increase photocatalytic degradation efficiency of composites.
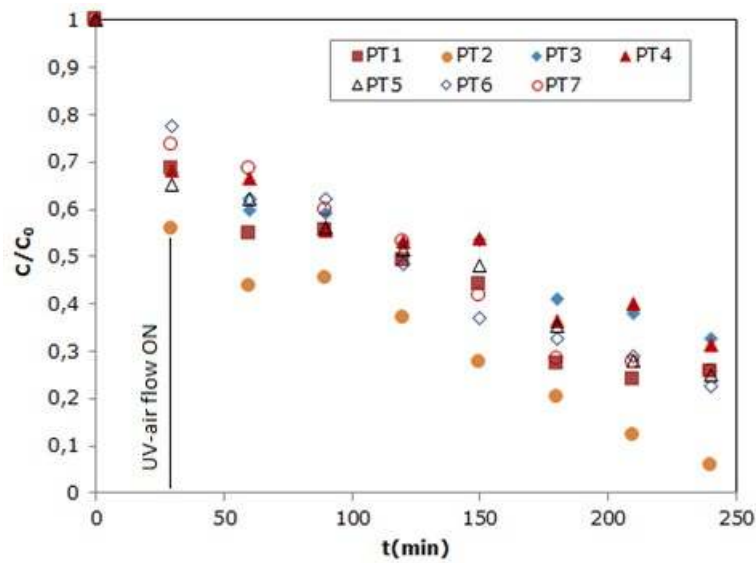
Figure 6. Photocatalytic degradation of methylene blue.

Experimental design approach, model fitting, and statistical analysis: 2$^{3-1}$ factorial design matrix with response values obtained from the experimental studies was given in Table 3. TiO$_2$ loading (R1) and methylene blue degradation (R2) values were determined by using Eq.4 and Eq.5, respectively.

$$TiO_2 \text{ loading } (\%) = [\frac{\text{Amount of TiO2 loaded on perlite (g)}}{\text{Amount of TiO2 (g)}}] * 100 \qquad (4)$$

$$MB \text{ degradation } (\%) = \left(1 - \frac{MB \text{ concentration at } 210min \, (\frac{mg}{L})}{initial \text{ MB concentration } (\frac{mg}{L})}\right) * 100 \qquad (5)$$

TiO$_2$ loading values were found between 14% and 55%, while methylene blue degradation varied between 60.1% and 87.7%, at the studied conditions (Table 3). Increasing amount of TiO$_2$ loaded on perlite surface did not increase degradation capacity at the same level.

8

This can be explained with the agglomeration of TiO_2 particles on perlite surface in case of higher loading (Figure 3). In addition, it should be kept in mind that the other parameters like particle size of perlite particles and calcination temperature also affect degradation capacity.

In order to create a relationship between synthetic parameters and responses (TiO₂ loading, MB degradation), experimental data were transferred into Design Expert (10.0) and linear regression model for both TiO_2 loading (R1) and MB degradation (R2) were developed as in Eq. 6 and 7, respectively. Significant factors contributing to the regression model can be identified by analyzing the coefficients. According to the coefficients, it is clear that X_1 (amount of TiO₂) and X_2 (particle size of perlite), respectively, are the main factors for both responses. Coefficient of particle size are almost the same magnitude for both responses, but amount of TiO_2 is more effective for TiO_2 loading than degradation capacity, as expected. Calcination temperature (X_3) did not affect TiO₂ loading, whereas there is a significant relation between calcination temperature and methylene blue degradation, due to the different crystalline structure of the samples calcined at different temperature (Figure 4). By looking at the coefficient of X_3 in Eq.7, it can be concluded that increasing calcination temperature resulted in a decrease of MB degradation. Ramli and coworkers [18] had also observed the same trend on their work related to photodegradation of diisopropanolamine by Cu/TiO_2. They indicated that calcination temperature was the least significant variable among the others (calcination time and amount of Cu).

$$R1 = 36 + 17.50X_1 - 3.00X_2 + 1.33 \times 10^{-5}X_3 \qquad \text{(Eq. 6)}$$

$$R2 = 71.53 + 10.40X_1 - 3.40X_2 - 2.5X_3 \qquad \text{(Eq. 7)}$$

Predicted data in Table 3 were obtained by using developed models (Eq.6-7) for both responses. Fitting of model to the experimental data was examined with error analysis. Error values of models were measured by using Eq. 8. As can be seen from Table 3, error values are between 2.70-10.71% and 0.15-1.42% for TiO_2 loading and MB degradation, respectively. Consequently, it can be concluded that the developed models fit experimental data, very well.

$$\text{Error \%} = \left| \frac{\text{observed data} - \text{predicted data}}{\text{observed data}} \right| * 100 \qquad \text{(Eq. 8)}$$

Significance of the developed models was examined with ANOVA (Table 4). According to ANOVA results, the model F-values were determined as 42.42 and 337.20 for R1 and R2, respectively, indicating that both models were significant. There is only a 0.44% and 0.03%

chance error in both models, respectively. p-values less than 0.500, indicate that parameters are significant in 95% confidence level.

The correctness and goodness of the models were checked by the coefficient of determination values. The R^2 values were found as 0.9821 and 0.9970 for both models, respectively.

Table 3. Design matrix, independent, dependent variables, error analysis.

	Independent variables			Dependent variables					
	X_1	X_2	X_3	R1 (TiO$_2$ loading,%)			R2 (MB degradation,%)		
				Observed	Predicted	Error	Observed	Predicted	Error
PT1	+1	+1	+1	49	50.5	3.06	75.9	76.03	0.17
PT2	+1	-1	-1	55	56.5	2.73	87.7	87.83	0.15
PT3	-1	-1	+1	20	21.5	7.50	61.9	62.03	0.21
PT4	-1	+1	-1	14	15.5	10.71	60.1	60.23	1.42
PT5	0	0	0	39	36.0	7.69	71.9	71.53	0.51
PT6	0	0	0	37	36.0	2.70	70.8	71.53	1.03
PT7	0	0	0	38	36.0	5.26	72.4	71.53	1.20

Table 4. Analysis of variance (ANOVA) of developed models for both responses.

	Source	Sum of Squares	df	Mean Square	F Value	p-value Prob > F
R1 (TiO$_2$ loading,%)	Model	1261.00	3	420.33	54.83	0.0040
	X_1	1225.00	1	1225.00	159.78	0.0011
	X_2	36.00	1	36.00	4.70	0.1188
	X_3	0.0000133	1	0.000	0.000	1.0000
	Residual	23.00	3	7.67		
	Lack of Fit	21.00	1	21.00	21.00	0.0445
	Pure Error	2.00	2	1.00		
	Cor Total	1284.00	6			
R2 (MB degradation,%)	Model	503.88	3	167.96	337.20	0.0003
	X_1	432.64	1	432.64	868.59	< 0.0001
	X_2	46.24	1	46.24	92.83	0.0024
	X_3	25.00	1	25.00	50.19	0.0058
	Residual	1.49	3	0.50		
	Lack of Fit	0.15	1	0.15	0.23	0.6787
	Pure Error	1.34	2	0.67		
	Cor Total	505.37	6			

Effects of process parameters: Response surface plots, obtained by using Statistica 8.0, were used to evaluate the effects of process parameters on both TiO_2 loading and MB degradation. In order to evaluate the effect of each parameter on the responses, the obtained regression surfaces were plotted as function of two process variables (Figure 6).

Linear effects of particle size and amount of TiO_2, and also their interactions can be seen in Figure 6a and 6d. Increasing amount of TiO_2 caused a significant increase on both TiO_2 loading and MB degradation. Particle size of perlite was also effective on both responses; smaller particle size resulted in higher loading and degradation capacity. Due to the higher surface area of small size particles, more amount of TiO_2 was impregnated on the perlite surface, hence, higher degradation capacity was obtained.

Linear effects of calcination temperature and amount of TiO_2, and also their interactions can be seen in Figure 6b and 6e. Calcination temperature (X_3) did not affect TiO_2 loading, whereas methylene blue degradation was negatively affected by increasing temperature. This result can be explained with the crystalline structure of TiO_2 on perlite surface. Lower temperature resulted in both anatase and rutile phase (Figure 4) crystalline structure that it is similar to the commercial one (Degussa P-25). As can be seen from Figure 6f, smaller particle size and lower temperature gives higher degradation capacity.

a   b   C
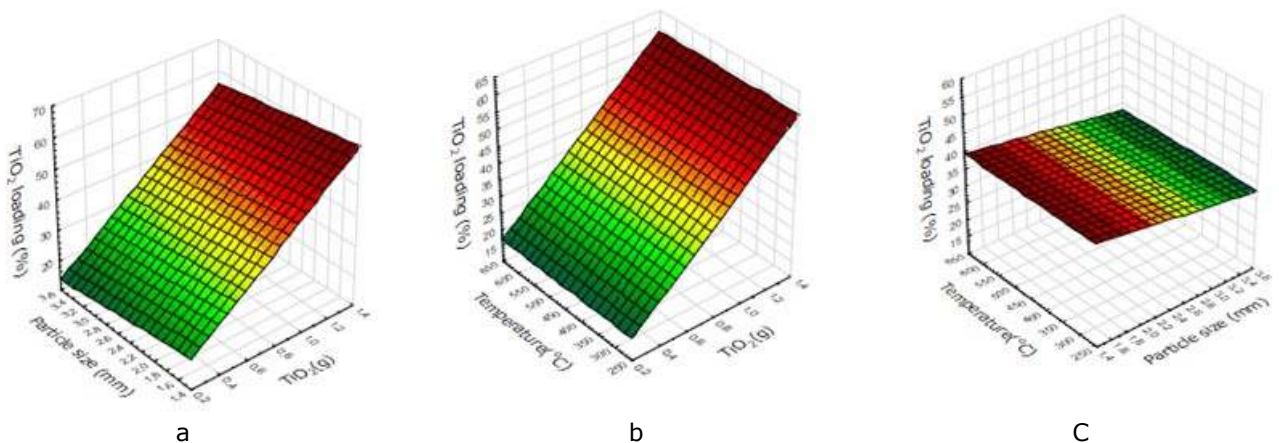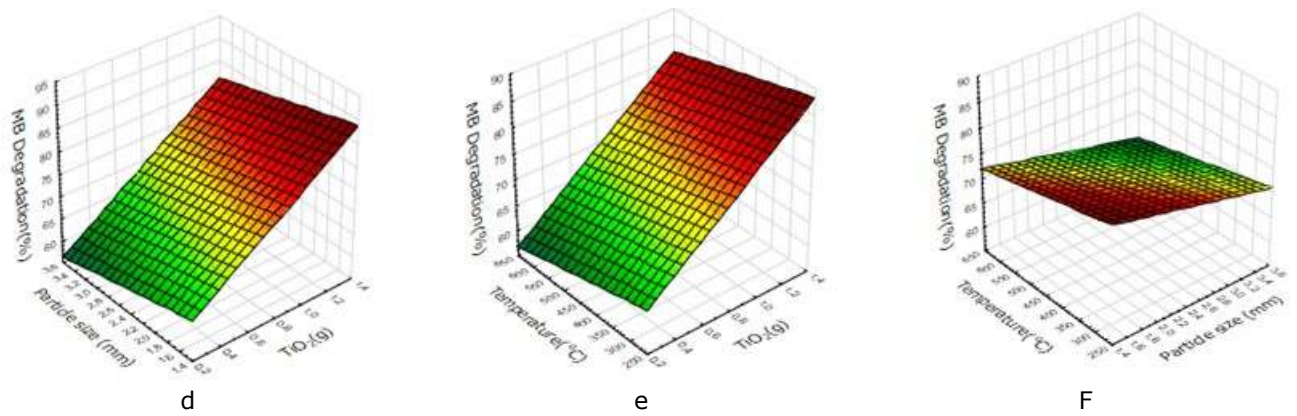
Figure 6. Response surface plots.

CONCLUSION

Experimental design method was effectively used in order to prepare higher performance TiO$_2$/perlite photocatalysts for methylene blue degradation. Effects of TiO$_2$ amount, particle size of perlite, and calcination temperature on both TiO$_2$ loading (%) and methylene blue degradation (%) were investigated by applying 2$^{3-1}$ Fractional Factorial Design. The linear models of TiO$_2$ loading (%) and methylene blue degradation (%) of TiO$_2$/perlite composites were developed by regression analysis of the experimental data. Amount of TiO$_2$ and particle size were found as the most effective parameters on both TiO$_2$ loading (%) and degradation efficiency (%). Optimum solution for the highest methylene blue degradation (%86.94) was obtained via Design Expert Software with 1.143 g of TiO$_2$, 1.5 mm of perlite particle size and 300 °C of calcination temperature.

As a conclusion, experimental design methods can be effectively used in order to prepare photocatalysts with higher capacity for degradation of target pollutant.

ACKNOWLEDGEMENT

REFERENCES

[1] Shan AY, Ghazi TIM, Rashid SA. Immobilization of titanium dioxide onto supporting materials in heterogeneous photocatalysis: A review. Applied Catalysis A: Gen. 2010; 389: 1-8. DOI:10.1016/j.apcata.2010.08.053.

[2] Shavisi Y, Sharifnia S, Hosseini SB, Khadivia MA. Application of TiO_2/perlite photocatalysis for degradation of ammonia in wastewater. Journal of Industrial and Engineering Chemistry 2014; 20(1):278-283. DOI:10.1016/j.jiec.2013.03.037.

[3] Y. Shavisi Y, Sharifnia s, Zendehzaban, M, Mirghavami ML, Kakehazar S. Application of solar light for degradation of ammonia in petrochemical wastewater by a floating TiO_2/LECA photocatalyst. Journal of Industrial and Engineering Chemistry 2014; 20(5): Pages 2806-2813. DOI:10.1016/j.jiec.2013.11.011.

[4] Długosz M, Zmudzki P, Kwiecien A, Szczubiałka K, Krzek J, Nowakowska M. Photocatalytic degradation of sulfamethoxazole in aqueous solution using a floating TiO_2-expanded perlite photocatalyst. Journal of Hazardous Materials 2015;298:146-153. DOI:10.1016/j.jhazmat.2015.05.016.

[5] Hinojosa-Reyes M, Arriaga S, Diaz-Torres LA, Rodríguez-González V. Gas-phase photocatalytic decomposition of ethylbenzene over perlite granules coated with indium doped TiO_2. Chemical Engineering Journal 2013;224:106-113. DOI:10.1016/j.cej.2013.01.066.

[6] Hosseini SN, Borghei SM, Vossoughi V, TaghaviniA N. Immobilization of TiO_2 on perlite granules for photocatalytic degradation of phenol, Appl. Catal. B: Environ. 2007;74;53-62. DOI:10.1016/j.apcatb.2006.12.015.

[7] Jafarzadeh NK, Sharifnia S, Hosseini SN, Rahimpour F. Statistical optimization of process conditions for photocatalytic degradation of phenol with immobilization of nano TiO_2 on perlite granules. Korean Journal of Chemical Engineering 2011;28(2):531-538. DOI:10.1007/s11814-010-0355-8.

[8] Faramarzpour M, Vossoughi M, Borghei M. Photocatalytic degradation of furfural by titania nanoparticles in a floating-bed photoreactor. Chemical Engineering Journal 2009;146:79-85. DOI:10.1016/j.cej.2008.05.033.

[9] Sakkas VA, Islam MdA, Stalikas C, Albanis TA. Photocatalytic degradation using design of experiments: A review and example of the Congo red degradation. Journal of Hazardous Materials 2010;175:33-44. DOI:10.1016/j.jhazmat.2009.10.050.

[10] Jiang W, Joens JA, Dionysiou DD, O'Shea DE. Optimization of photocatalytic performance of TiO_2 coated glass microspheres using response surface methodology and the application for degradation of dimethyl phthalate . Journal of Photochemistry and Photobiology A: Chemistry 2013;262:7-13. DOI:10.1016/j.jphotochem.2013.04.008.

[11] Chen J, Li G, Huang Y, Zhang H, Zhao H. An T. Optimization synthesis of carbon nanotubes-anatase TiO_2 composite photocatalyst by response surface methodology for photocatalytic degradation of gaseous styrene. Applied Catalysis B: Environmental 2012;123-124:69-77. DOI:10.1016/j.apcatb.2012.04.020.

[12] Alijani S, Vaez M, Moghaddam AZ. Optimization of synthesis parameters in photodegradation of acid red 73 using TiO_2 nanoparticles prepared by the modified sol-gel method. International Journal of Environmental Science and Development 2014;5(1):108-113. DOI:10.7763/IJESD.2014.V5.460.

[13] Lundstedt T, Seifert E, Abramo L, Thelin B, Nyström A, Pettersen J, Bergman R. Experimental design and optimization. Chemometrics and Intelligent Laboratory Systems 1998;42(1):3-40. DOI:10.1016/S0169-7439(98)00065-3.

[14] Leardi, R. Experimental design in chemistry: a tutorial. Analytica chimica acta 2009;652 (1):161-172. DOI:10.1016/j.aca.2009.06.015.

[15] Mason RL, Gunst RF, Hess JL, Statistical Design and Analysis of Experiments (Second Edition). John Wiley & Sons, Inc. 2003. Hoboken, New Jersey.

[16] Cox DR, Reid N. The Theory of the Design of Experiments. CRC Press. 2000. Boca Raton, Florida.

[17] Ohno T, Sarukawa K, Tokieda K, Matsumura M. Morphology of a TiO_2 photocatalyst (Degussa, P-25) consisting of anatase and rutile crystalline phases. Journal of Catalysis 2001;203:82-86. DOI:10.1006/jcat.2001.3316.

[18] Ramli RM, Kait CF, Omar AA. Optimization of Cu/TiO_2 Preparation Variables using Response Surface Method for Photodegradation of Diisopropanolamine. Applied Mechanics and Materials 2014;699: 124-130. DOI:10.4028/www.scientific.net/AMM.699.124.

Six Coordination Compounds: Mode of Cytotoxic Action and Biological Evaluation

Ali Aydın*[1], Şengül Aslan Korkmaz[2]

[1] Faculty of Art and Science, Department of Molecular Biology and Genetics, Gaziosmanpaşa University, 60240, Tokat, Turkey

[2] Faculty of Engineering, Department of Bioengineering, Tunceli University, 62000, Tunceli, Turkey

Abstract: This study describes the biological and anticancer properties of coordination compounds given in the text. FT-IR spectra, magnetic properties, thermal analyses and crystal structures of six cyanido-complexes derivatives with $[M^{II}(CN)_4]^{2-}$ (M^{II}= Ni and Pd) and $[Co(CN)_6]^{3-}$ anions and *N,N-bishydeten* (*N,N*-bis(2-hydroxyethyl)ethylenediamine) as a capping ligand have been reported previously. Here, we have investigated the pharmacological properties of these complexes denoted as [Ni(*N-bishydeten*)Ni(CN)$_4$] (***C1***), [Zn$_2$(*N-bishydeten*)$_2$Ni(CN)$_4$] (***C2***), [Ni(*N-bishydeten*)Pd(CN)$_4$] (***C3***), [Cd(*N-bishydeten*)$_2$][Pd(CN)$_4$] (***C4***), [Ni$_2$(*N-bishydeten*)$_2$Co(CN)$_6$].3H$_2$O (***C5***) and K[Cd(*N-bishydeten*)Co(CN)$_6$].$^3/_2$H$_2$O (***C6***), tested for their anti-proliferative activity against human cervical cancer (HeLa), human colon cancer (HT29), rat glioma (C6) and African green monkey kidney (Vero) cell lines. The DNA/BSA binding affinities of these compounds were also elucidated by spectroscopic titrations, displacement experiments, and electrophoresis measurements. Studies on cancerous cells revealed that ***C1***, ***C2***, ***C4*** and ***C6*** have exhibited the significant antitumor activity and inhibited tumor progression during testing cell lines and showed high solubility in the solvent. The results of absorbance and emission spectra data have revealed that the complexes interact with the DNA via groove binding mode of interaction. Overall, these compounds have been found to demonstrate effective anti-proliferative activity against the cancer cell lines, indicating that they are a potent candidate for preclinical or clinical studies.

Keywords: Coordination compounds, Anticancer activity, Cytotoxic activity, Apoptosis, DNA binding.

*Corresponding author. E-mail: aliaydin.bio@gmail.com; ali.aydin4409@gop.edu.tr. Tel: +90-356-2521616. Fax: +90-356-2521585.

INTRODUCTION

Today, cancer is becoming a more life-threatening endemic disease throughout the world and new effective drugs are the main necessity. In the Middle East, cancer ranks the second most common cause of death, following cardiovascular diseases [1]. According to the IARC (International Agency for Research on Cancer), a substantive increase to 19.3 million new cancer cases per year by 2025 were predicted with deaths reaching to the number of 12 million [1]. Developing countries especially suffer from the burden of cancer incidence, morbidity, and mortality [1]. Efforts to reduce the economic burden caused due to the cancer on individuals, families and the healthcare system will increase [1]. Research efforts on the development of novel anticancer agents play an important role in the current treatment process for cancer. These investigations are focused on the goal to find effective drugs without side effects or drug resistance [2-7]. It is known that the metal complexes including copper, gold, germanium, iron, rhenium, rhodium, ruthenium, silver, tin, and titanium have shown anticancer activity. However, none of the compounds have demonstrated sufficient effectiveness to pursue past phase II or past phase III clinical trials except for cis-platin and its certain derivatives such as carboplatin, oxaliplatin, nedaplatin and satraplatin [8]. Only carboplatin is FDA-approved among them. Co^{II}, Ni^{II}, Pd^{II} or Zn^{II} have been used to obtain metal complexes in medicinal studies [9-10]. Nickel plays important roles in the biological functions of various enzymes in systems including electron transport system, together with zinc, sulfur, and iron to form a cluster. Zinc plays ubiquitous biological roles by coordinating amino acid side chains of the specific enzymes in signal transduction and gene expression metabolism. Cobalt is an essential component of vitamin B_{12} that has a vital role in the normal functioning of the nervous system. Palladium is a metal with low toxicity and is like platinum. It is a component of cis-platin, which is an anticancer drug. Nickel, zinc, cobalt and palladium complexes have also shown DNA binding capacity and anti-proliferative activity [11-15]. However, metal complex of cyanido and *N-bishydeten* (*N,N*-bis(2-hydroxyethyl)-ethylenediamine) ligands have not been explored in terms of their chemical and chemotherapeutic usage. Our work in this area was concentrated on the use of these ligands to form **C1-C6** compounds and test their activities against colon, cervix and glioma cancer. Korkmaz *et al.* [16-18] have explored the Ni^{II} and Zn^{II} metal ions with a capping ligand *N,N-bishydeten*. The *in vitro* biological activity of the metal complexes was estimated using the ELISA BrdU cell proliferation assay (CPA) and Lactate Dehydrogenase (LDH) cytotoxicity assay against the cancer cell lines HT29, HeLa, C6, and Vero. The morphology of cells was investigated using phase-contrast microscopy. These complexes have also been studied to determine the extent of their physicochemical properties regarding DNA/BSA binding, and inhibition of restriction in the endonucleases activity features. The interaction of these compounds with DNA/BSA is a significant property in the determination of the mechanisms of compounds because DNA/BSA is a significant chemotherapeutic target for many current anticancer agents. According to the

present literature, this is the first study investigating the biological activities of the *N-bishydeten* based complexes.

MATERIALS and METHODS

Materials

NiCl$_2$.6H$_2$O, ZnCl$_2$, KCN, K$_2$[Ni(CN)$_4$], K$_3$[Co(CN)$_6$] and *N,N*-bis(2-hydroxyethyl)-ethylenediamine (*N,N-bishydeten*) were obtained commercially (Merck, Germany) and used without further purification.

Synthesis of C1-C6

In our previous studies, we have reported the synthesis and characteristic properties of *C1-C6* coordination compounds [16-18]. These compounds were synthesized according to the procedure published before. The procedure is based on brick-and-mortar method. In this method, Ni^{II} and Zn^{II} metal cations were coordinated with suitable ligand(s) to form the brick and with [M^{II}(CN)$_4$]$^{2-}$ (M^{II}= Ni and Pd) and [Co(CN)$_6$]$^{3-}$ anions to form the mortar.

Cell culture

The anticancer potential of these complexes was investigated on cancerous HT29 (ATCC$^®$ HTB-38™), HeLa (ATCC$^®$ CCL-2™), C6 (ATCC$^®$ CCL-107™) and no tumorigenic Vero cells (ATCC$^®$ CCL-81™). The cell lines were cultured in a cell medium (Dulbecco's modified eagle's) enriched with 10% (v/v) fetal bovine serum and 2% (v/v) Penicillin-Streptomycin (10,000 U/mL). First, the old medium was removed out of the flask while cells had reached approximately 80% confluence. Next, cells were taken from the flasks surface using 4-5 mL of trypsin-EDTA solution and then subjected to centrifugation. Following, the cell pellet was suspended with 4 mL of DMEM working solution and was counted to obtain a final concentration of 5×10^4 cells/mL, and inoculated into wells (100 µL cells/well).

Cell proliferation assay (CPA)

A cell suspension containing approximately 5×10^3 cells in 100 µL was seeded in the 96-well culture plates. The complexes and cis-platin were dissolved in sterile DMSO (max 0.5% of DMSO) at final concentrations of 0.05, 0.1, 0.2, 0.3, 0.4, 0.5, 0.75, and 1.00 mg/mL. The final volume of the wells was set to 200 µL using DMEM working solution. Cells were incubated with tested complexes at 37°C with 5% CO$_2$ for overnight. Cell proliferation assay was analyzed using ELISA BrdU methods as described previously [7].

Calculation of IC50 and percent inhibition

IC50 value is a concentration value at which half of the cells are inhibited *in vitro*. The half maximal inhibitory concentrations (IC50) of the test and control compounds were calculated using XLfit5® or Microsoft Excel® spreadsheet and represented in µM at 95% confidence intervals. The proliferation assay results were expressed as the percent inhibition according to the following formula:

$$\% \ inhibition = \left[1 - \left(\frac{Absorbance \ of \ treatments}{Absorbance \ of \ DMSO}\right) \times 100\right]$$

Cytotoxic activity assay

The cytotoxicity of the compounds and cis-platin was determined on HeLa, C6, HT29, and Vero cells through a Lactate Dehydrogenase Assay Kit according to the instruction given by manufacturer. Approximately 5×10^3 cells in 100 µL were placed in 96-well plate as triplicates and treated with IC50 (µg/mL) concentrations of test compounds at 37°C under 5% CO_2 atmosphere for 24 h. LDH activity was obtained at 492 - 630 nm absorbance wavelength using a microplate reader.

Cell imaging

Cells were plated in 96-well plate at a density of 5000 cells per well and allowed 24 h incubation. IC50 values of the test compounds were administered and morphology changes of the cells were screened via phase contrast microscopy every 6 h for 24 h. Images of control and test compound-treated cells were photographed at the end of the process using a digital camera attached on inverted microscope.

DNA/BSA binding and gel electrophoresis studies

The binding constants (Kb) and the interaction of the compounds with Calf thymus-DNA (CT-DNA) were examined using the UV spectrophotometry. A CT-DNA solution was prepared by dissolving 2.5 mg of CT-DNA in 10.0 mL of Tris–HCl buffer and it was used immediately after it was prepared. The concentration of CT-DNA was determined spectrophotometrically with the aid of ℰ value of 6600 M^{-1} cm^{-1} at 260 nm. After dissolving the CT-DNA fibers in Tris–HCl buffer, the purity of this solution was checked through the absorbance ratio of A260/A280. The DNA was pure enough to use with respect to the result A260/A280 ratio of 1.83 obtained for the CT-DNA solution in the buffer. These compounds dissolved in DMSO were re-diluted with Tris–HCl buffer to obtain the concentration of 25 µM. Test compounds in the solutions were incubated with CT-DNA solution at 20°C for about 30 min before measurements. The UV absorption spectra data were obtained without any change on the concentrations of both compounds with increasing the CT–DNA concentrations (0-100 µM). Absorption spectra were recorded using 1-cm-path quartz cuvettes at room temperature [19].

To evaluate the interaction of the compounds with BSA, a UV spectrophotometer was used. A solution of BSA was prepared by dissolving 2.5 mg BSA in 10.0 mL in Tris–HCl buffer and it was used immediately after it was prepared. The UV wavelength scans of the BSA solutions (0-100 µM) with a fixed concentration of the complexes (25 µM) were screened in the wavelength range of 250-320 nm.

The restriction on enzyme inhibition assay was conducted to determine the both specific and nonspecific binding and enzyme inhibition by the complexes. These complexes (25 µM) were added to reaction tubes containing supercoiled pTOLT (10 µM) plasmid DNA, and restriction enzymes KpnI and BamHI (2 units) in Tris–HCl/NaCl buffer (50/18 mM, pH 7.2) and incubated at 37 °C for 4 h. The digestion products were observed by using 1.5% (wt/vol) agarose gel with ethidium bromide.

Statistical analysis

The statistical significance of differences was determined through one-way analysis of variance (one-way ANOVA) tests. Post hoc analyses of group differences were performed using the Tukey test, and the levels of probability were noted. The SPSS® software for Windows was used for the statistical analyses. The results are reported as the mean values ± SEM of three independent assays, and the differences between groups were regarded as significant at $P < 0.05$.

RESULTS and DISCUSSION

FT-IR Spectra

In the FT-IR spectra of the *C1-C6* compounds, absorption bands arising from all characteristic functional groups of the *N-bishydeten* ligand (υOH and υNH$_2$, υCH$_2$, δNH$_2$, δCH$_2$, υC-N and υCO) vibrations were observed (Figure 1). Also, Figure 1 exhibits various characteristic absorption bands that confirm the presence of the *N,N-bishydeten* ligand, which coordinates to the metal centers via its NH$_2$ and OH groups. The tentative assignments of the recorded wavenumbers of the *C1-C6* compounds are in good agreement with the FT-IR spectra of the compounds synthesized and characterized in our previous studies [16-18].
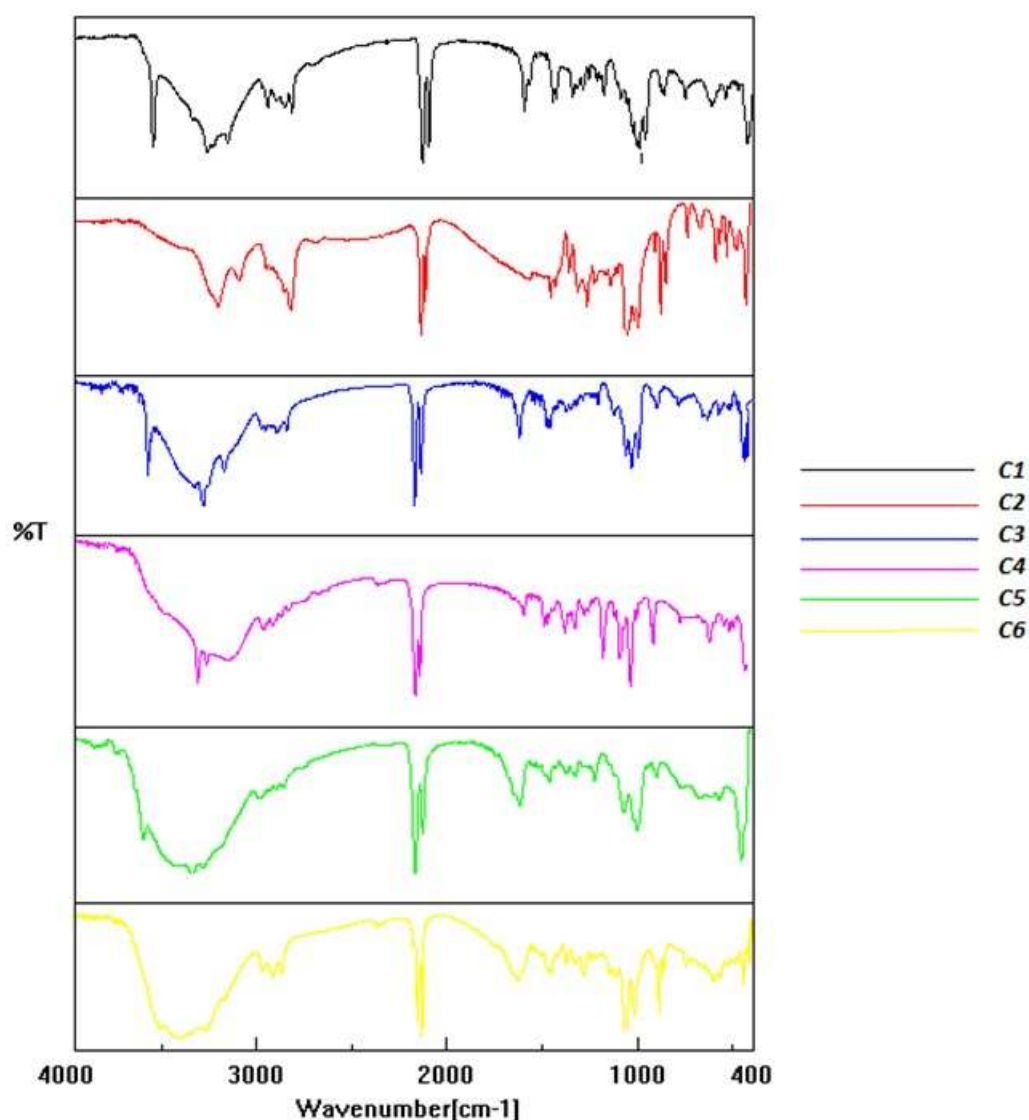
Figure 1. The FT-IR spectra of *C1-C6* compounds.

Anti-proliferative effects of the complexes against HT29, HeLa, C6 and Vero cells

We firstly studied the *in vitro* anti-proliferative effects of six compounds using ELISA BrdU assay against three cancer cell lines (HT29, HeLa, and C6) and one non-cancerous cell line, namely Vero. The cis-platin, an anticancer drug, was used as a reference compound. The data obtained using the ELISA BrdU assay, % inhibition data of the compounds was shown in Figure 2. IC50 values to be used in subsequent studies were calculated by XLfit 5 software and available in Table 1. Tumor specificity information was obtained by dividing the sum of the IC50 values obtained from the normal cells (Vero) to the sum of the IC50 values of the cancerous cells (HT29, HeLa, and C6) and given in Table 1. According to these information, the specificities of these compounds are not ideal because of poor selectivity. According to the Figure 1, in cis-platin case, each coordination polymer poorly inhibited the proliferation of cells as compared to the control compounds ($P < 0.05$). However, the compounds *C2* and *C6* have showed relatively strong anti-proliferative activity to the cells while the compounds *C1* and *C4* *have done slightly* low. A gradient obtained from the percent inhibition values of these coordination polymers can be seen

318

for complexes in order of activity starting with the highest in activity: **C2 > C6 > C4 > C1 > C3 ≈ C5** (Fig. 2).
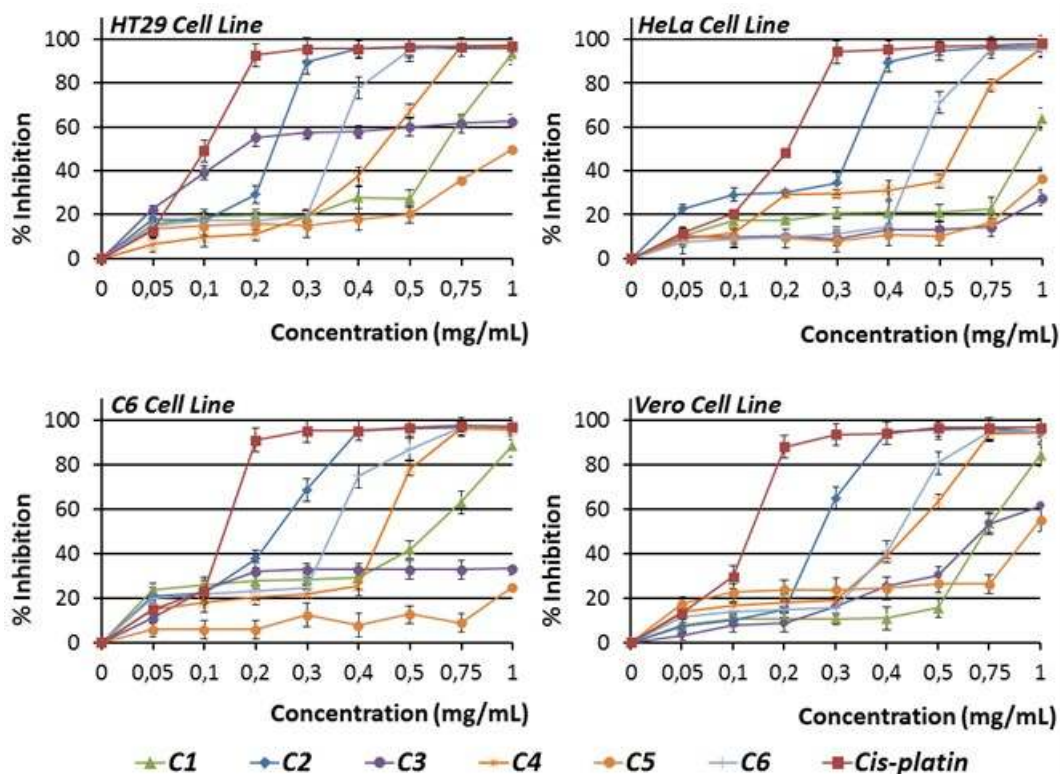
Figure 2. Effects of **C1-C6** on the proliferation of cell lines. Percent inhibition was reported as mean values ± SEM of three independent assays (P < 0.05).

The results of the cell proliferation assay have showed that the coordination compounds have less anti-proliferative effect than that of cis-platin (Fig. 2) on the cell lines indicating that their anticancer potential should be improved further.

Table 1. IC50 values for *C1-C6* compounds and Cis-platin.

Complex	IC50 (mM)				Tumor specificity		
	HeLa	HT29	C6	Vero	HeLa	HT29	C6
C1	-*	1.60±0.04	1.49±0.05	2.11±0.07	-	1.32	1.42
C2	0.54±0.03	0.46±0.02	0.46±0.02	0.58±0.03	1.07	1.26	1.26
C3	-	1.07±0.04	-	1.87±0.06	-	1.75	-
C4	1.23±0.05	1.11±0.04	1.06±0.04	1.11±0.05	0.90	1.00	1.05
C5	-	-	-	-	-	-	-
C6	0.68±0.03	0.52±0.03	0.51±0.02	0.62±0.03	0.91	1,19	1.22
Cisplatin	0.80±0.03	0.40±0.02	0.57±0.03	0.57±0.03	0,71	1.43	1.00

* not available.

Cytotoxic activity of the complexes on HT29, HeLa, C6 and Vero cells
The results obtained for the LDH assay are expressed in terms of percent cytotoxicity values and presented in Figure 3. Findings showed that the test compounds possess approximately percent nonselective toxicity values from 40% to 85% against the cells investigated.
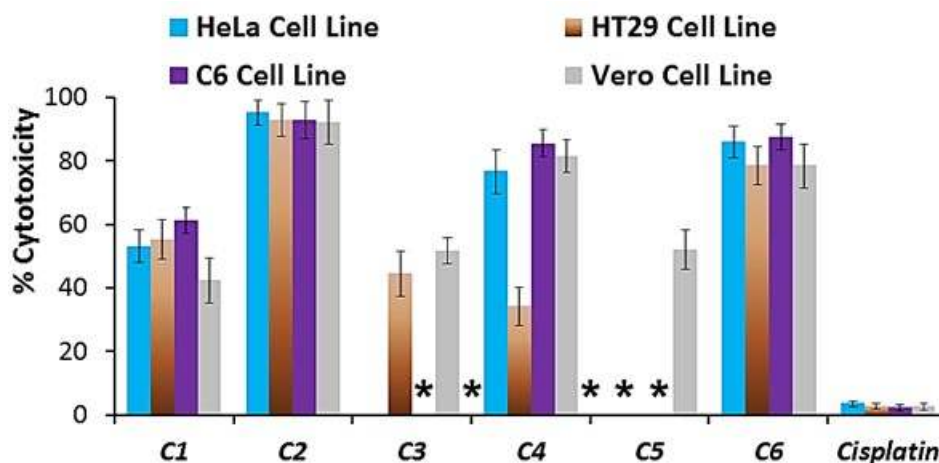
Figure 3. Cytotoxic activity of ***C1-C6*** *compounds* on HeLa, HT29, C6 and Vero cells. Data are presented as the percent cytotoxicity of cells with respect to the control cells where only DMSO in cell culture media was administered. Cells were tested for 24 h. The percent cytotoxicity values of test compounds were ranged from 40% to 85%, and percent cytotoxicity value of cis-platin was approximately 5%. The test compounds were the most cytotoxic (P < 0.05) against all cell lines tested. The percent cytotoxicity values were reported as mean values ± SDs of three independent assays. * Not available.

According to another result, the cytotoxicity of each coordination polymer was significantly higher than that of cis-platin, at their IC50 concentrations against any of the four cell lines. This means that a safety usage concentration of the test compounds does not exist in the tested cells. It is suggested that these compounds may have cytostatic potential similar to cytotoxicity *i.e.*, these coordination polymers are promising candidates for potential anticancer therapy for cancerous diseases. In our study, a variety of novel metal complexes were synthesized with the hopes of developing a useful drug candidate to use in cancer treatments.

The effect of test compounds on the morphology of HT29, HeLa, C6 and Vero cells
To determine the effect these complexes on the morphology of HeLa, HT29, C6 and Vero cells in culture, phase contrast pictures were taken for cell cultures analyzed. The pictures given above indicate that all the compounds tested possess considerable effects such as disruption of membrane integrity on the morphology of the cells. As shown in Figure 4, obvious morphological dose-dependent changes were observed in treated cells as compared to those of the untreated cells. The compounds clearly showed characteristic apoptotic changes in the surface morphology.
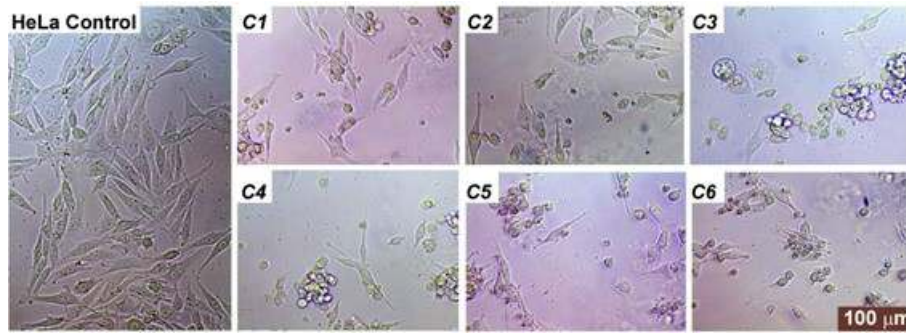
(**A**)
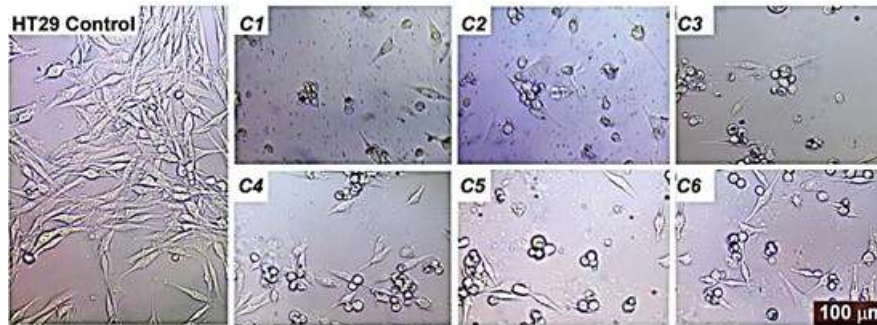
(**B**)
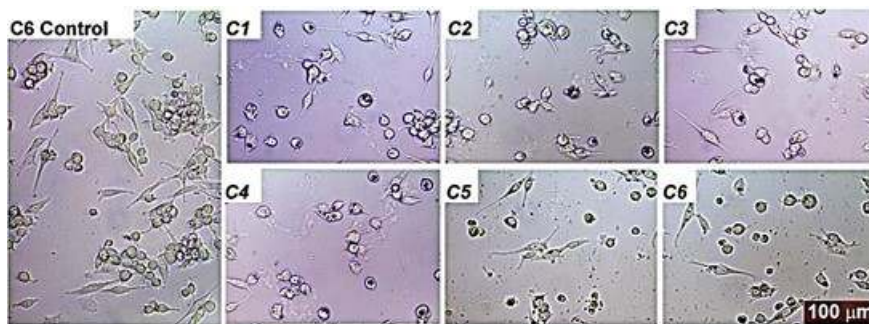
(**C**)
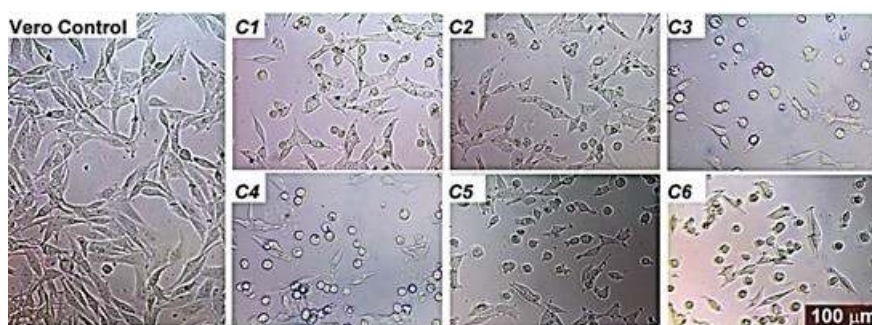
(**D**)

Figure 4. The effect of **C1**-**C6** compounds on the morphology of HeLa (**A**), HT29 (**B**), C6 (**C**), and Vero (**D**) cells. Exponentially growing cells were incubated with IC50 concentrations of test compounds at 37°C overnight and visualized by digital camera attached on an inverted microscope (Leica IL10, Germany).

These changes observed as rounding up, shrinking, and detaching from the well surface indicate that the cells were undergoing apoptosis which is a necessity for anticancer agents (Fig. 4) [20, 21]. The findings indicate that these morphological alterations are unlike necrotic situations

which are usually characterized by cell swelling and eventual cell lysis. These results were somewhat similar with those of the previous studies by Korkmaz *et al.* [4], Aydın *et al.*, [2, 6]. Thus, based on the observations in the literature, the appearance of cell lines treated with test compounds has indicated the anti-proliferative but high cytotoxic effect of these complexes clearly.

DNA/BSA binding and gel electrophoresis studies

Complex–DNA interactions can be investigated by comparing the UV–Vis absorption spectra of the free complex with that of complex–DNA adducts. The binding constant (K) of the complexes-DNA interaction can be determined according to Benesi–Hildebrand equation, $A_0/A-A_0 = \mathcal{E}_G/\mathcal{E}_{H-G}-\mathcal{E}_G+\mathcal{E}_G/\mathcal{E}_{H-G}-\mathcal{E}_G \times 1/K[DNA]$, where K is the binding constant, A_0 and A are the absorbance values of the complexes and their adducts with DNA, respectively, and $\mathcal{E}_G$ and $\mathcal{E}_{H-G}$ are the absorption coefficients of the complexes and the complex–DNA adducts, respectively. The binding constant can be obtained from the ratio of intercept to slope of $A_0/(A - A_0)$ vs. $1/[DNA]$ plot. Figure 5A describes the interaction of the complexes with CT-DNA. According to Benesi–Hildebrand equation, the data obtained from the plot of $A_0/(A-A_0)$ vs. $1/[DNA]$ yielded the binding constant (K) seen in Table 2. With the increase in CT-DNA concentration resulted in hyperchromic effect, a strong interaction between these complexes and DNA can be explained. This hyperchromic effect on the spectra of the complex-DNA adduct might be indication of the groove binding.

Table 2. The binding constants (K_b)

Complex	UV titration (x 10^3 M^{-1})
C1	1.7
C2	5.9
C3	0.79
C4	9.4
C5	2.0
C6	0.75

The interaction of these complexes with BSA can be determined via comparison of UV–Visible absorption spectra of the free metal complex and the complex–BSA adduct. The absorption spectra of the BSA solutions (0-100 µM) in the absence and presence of the complexes (25 µM) are shown in Figure 5B. The complexes have caused an increase in the absorbance of BSA and exhibited a blue shift indicating the Van der Waals interaction or hydrogen bonds through interaction with BSA. Isosbestic points near 265 - 266 nm were observed for the *C3*, *C5,* and *C6* compounds (Fig. 5B).
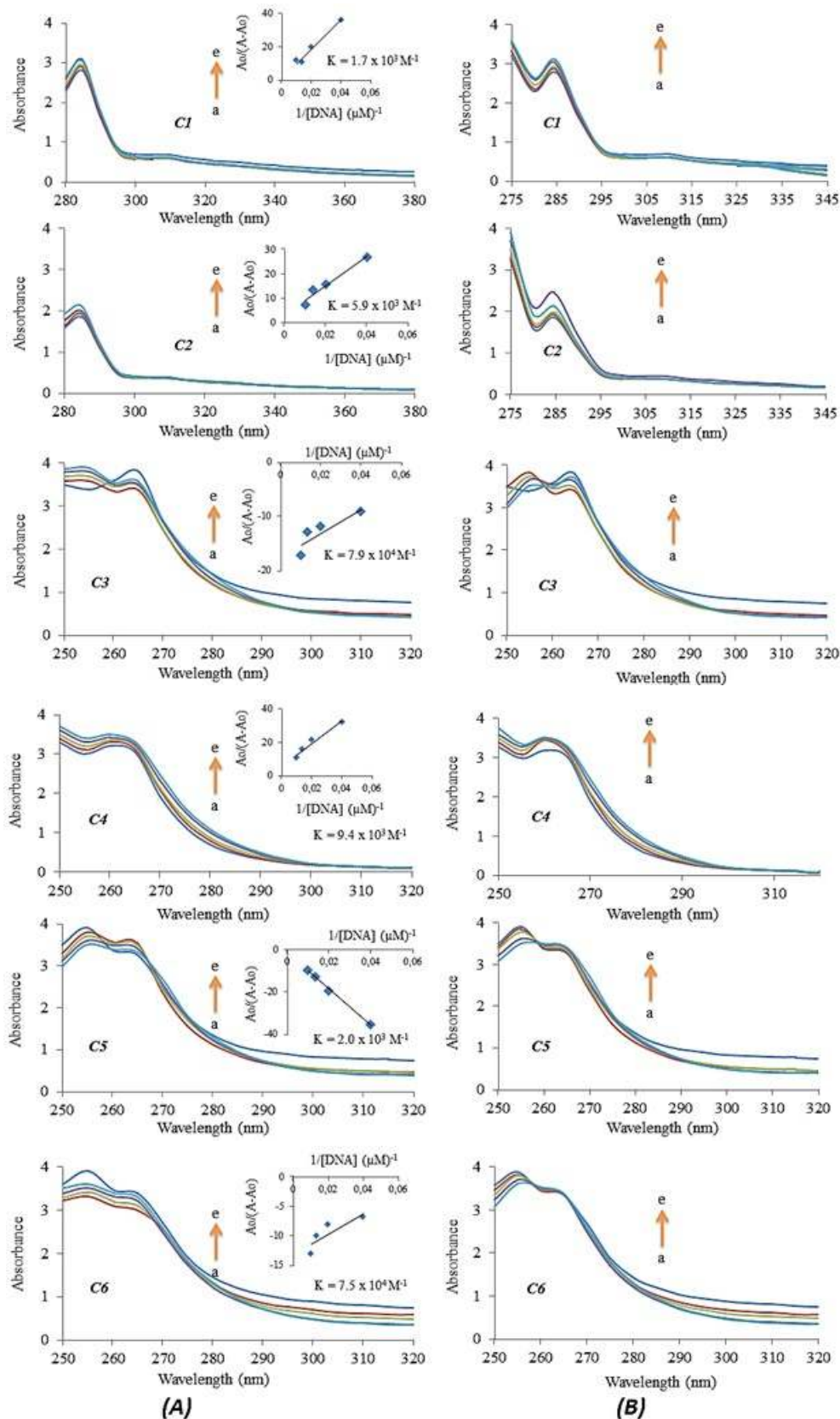
Figure 5. (**A**) UV–Visible absorption spectra of the complexes (25 µM) in the absence (a) and presence (b-e) of CT-DNA (0-100 µM) in Tris–HCl buffer. Note: The direction of arrow demonstrates the increasing concentrations of DNA. Inset is the plot of $A_0/(A-A_0)$ vs. $1/[DNA]$ to find the binding constant of the complex – DNA adduct. (**B**) Absorption spectra of the complexes (25 µM) in the absence (a) and presence (b-e) of BSA (0-100 µM) in Tris–HCl buffer. Note: The direction of arrow demonstrates the increasing concentrations of BSA.

After *Kpn*I and *Bam*HI digestion of pTOLT plasmid DNA (patented plasmid vector, US 7348408 B2), digestion products were identified by two DNA bands in the absence of the complexes (Lane 7), whereas in the presence of the **C1**, **C3** and **C5** compounds have produced three bands (Lanes 2, 4, and 6) and the **C2**, **C4** and **C6** compounds have displayed four bands of DNA fragments seen near the well at the top of the lanes (Lanes 1, 3, and 5) (Fig. 6). In the presence of the complexes, DNA digestion was incomplete and new bands were observed. Treatment of *Kpn*I and *Bam*HI with the complexes inhibits partly the restriction endonucleases activity of these enzymes, and therefore more bands were seen on the gel. The results indicated that the complexes probably bound to pTOLT plasmid DNA or to these enzymes, and thus this situation has resulted in inhibition of *Kpn*I and *Bam*HI enzyme activity to a certain degree.
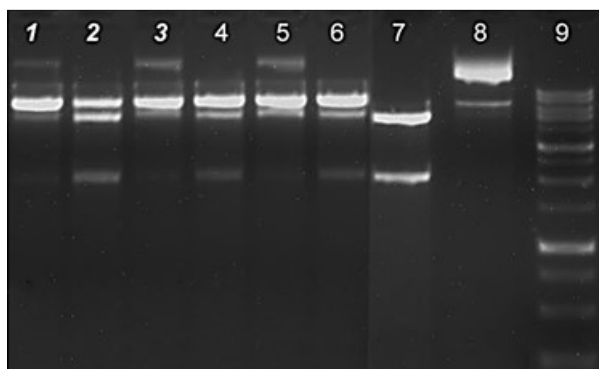
Figure 6. Inhibition of *Kpn*I and *Bam*HI restriction endonucleases activity. At the end of 4 h at 37°C digestion of the 14μL with 10 U *Kpn*I and *Bam*HI, these digestion products were resolved with 1.5% agarose gel containing ethidium bromide. Lanes 1-6: enzyme + DNA + **C1**-**C6**, Lane 7: Positive control (enzyme + DNA), Lane 8: Negative control (plasmid DNA + water); lane 9: DNA marker (1Kb).

The goal of this study is to find new metal complexes active *in vivo* and possess lowered toxicity and resistance factors as compared to current chemotherapeutic drugs. In conclusion, *in vitro* anticancer activity of [Ni(*N-bishydeten*)Ni(CN)$_4$] (**C1**), [Zn$_2$(*N-bishydeten*)$_2$Ni(CN)$_4$] (**C2**), [Ni(*N-bishydeten*)Pd(CN)$_4$] (**C3**), [Cd(*N-bishydeten*)$_2$][Pd(CN)$_4$] (**C4**), [Ni$_2$(*N-bishydeten*)$_2$Co(CN)$_6$].3H$_2$O (**C5**) and K[Cd(*N-bishydeten*)Co(CN)$_6$].1.5H$_2$O (**C6**) coordination compounds were investigated and determined. The binding of the complexes to CT-DNA and BSA resulted in significant changes in spectral characteristics. The complexes have showed hyperchromic absorption spectra and interacted directly with CT-DNA through a groove binding mode. The complexes have the tendency to possess Van der Waals contacts or hydrogen bonds during interaction with BSA. The complexes caused partial inhibition of *Kpn*I and *Bam*HI restriction endonucleases activity indicating that the complexes could interact with CT-DNA or these enzymes or both. On the contrary, **C5** and **C3** compounds were nearly ineffective against all four cell lines. All remaining metal complexes have showed impressive anticancer activity against all cancer cells tested. However, in a preliminary *in vitro* study, these metal complexes appear to be nonselective against HT29, HeLa, C6 and Vero cells. These preliminary results are important because they indicate that these complexes have affected normal Vero cells. For these reasons, we believe that these complexes need to be developed by making a more rational

design. Therefore, they may be a future replacement to the chemotherapeutic drugs in the clinical usage. As a conclusion, it seems substantial to continue to improve these chemical complex compounds to further help the problem of cancer.

ACKNOWLEDGMENTS

AUTHOR CONTRIBUTIONS

AA and SAK designed and performed experiments, analyzed the data, and wrote the paper.

REFERENCES

1. World Cancer Report 2014. http://www.iarc.fr/en/publications/books/wcr/wcr-order.php (accessed 16.04.16).

2. Aydın A, Korkmaz N, Tekin Ş, Karadağ A. Anticancer activities and mechanism of action of 2 novel metal complexes, $C_{16}H_{34}N_8O_5Ag_2Cd$ and $C_{11}H_{16}N_7O_2Ag_3Ni$. Turk J. Biol. 2014; 38,948-955. http://doi.org/10.3906/biy-1405-68.

3. Karadağ A, Aydın A, Özdemir A, Tekin Ş. Anti-proliferative and cytotoxic activities of a new cyanido coordination compound on several cancer cell lines. J. Biotechnol. 2014; 185, 105. http://doi.org/10.1016/j.jbiotec.2014.07.358.

4. Korkmaz N, Karadağ A, Aydın A, Yanar Y, Karaman İ, Tekin Ş. Synthesis and characterization of two novel dicyanidoargentate(I) complexes containing N-(2-hydroxyethyl)ethylenediamine exhibiting significant biological activity. New J. Chem. 2014; 38, 4760-4773. http://doi.org/10.1039/C4NJ00851K.

5. Tekin S, Aydın A, Dede S, Karadağ A. Anti-proliferative activity of a new coordination compound containing AuI(CN)2 in some cancer cell lines. J. Biotechnol. 2014; 185, 28-29. http://doi.org/10.1016/j.jbiotec.2014.07.096.

6. Aydın A, Karadağ A, Tekin Ş, Korkmaz N, Özdemir A. Two new coordination polymers containing dicyanidoargentate(I) and dicyanidoaurate(I): synthesis and characterization, and a detailed in vitro investigation of their anticancer activities on some cancer cell lines. Turk J. Chem. 2015; 39, 532-549. http://doi.org/10.3906/kim-1412-13.

7. Karadağ A, Aydın A, Dede S, Tekin Ş, Yanar Y, Çadırcı BH, Soylu MS, Andaç Ö. Five Novel Dicyanidoaurate(I)-Based Complexes Exhibiting Significant Biological activities: Synthesis, Characterization and Three Crystal Structures. New J. Chem. 2015; 39, 8136-8152. http://doi.org/10.1039/C5NJ01108F.

8. Dabrowiak JC. Metals in Medicine. John Wiley & Sons, 2009. 1st Edition, 321 p, West Sussex, UK. ISBN: 978-0-470-68196-1.

9. Osowole AA, Akpan EJ. Synthesis, Spectroscopic Characterisation, In-Vitro Anticancer and Antimicrobial Activities of Some Metal(II) Complexes of 3-{4, 6-Dimethoxy Pyrimidinyl} Iminomethyl Naphthalen-2-ol. European Journal of Applied Sciences 2012; 4(1), 14-20.

10. Abd-Elzaher MM, Labib AA, Mousa HA, Moustafa SA, Ali MM, El-Rashedy AA. Synthesis, anticancer activity and molecular docking study of Schiff base complexes containing thiazole moiety. Beni-Suef Univ. J. Basic Appl. Sci. 2016; 5(1), 85–96. DOI: 10.1016/j.bjbas.2016.01.001.

11. Tan KW, Seng HL, Lim FS, Cheah SC, Ng CH, Koo KS, Mustafa MR, Ng SW, Maah MJ. Towards a selective cytotoxic agent for prostate cancer: Interaction of zinc complexes of polyhydroxybenzaldehyde thiosemicarbazones with topoisomerase I. Polyhedron 2012; 38, 275–284. DOI: 10.1016/j.poly.2012.03.014.

12. Kapdi AR, Fairlamb IJS. Anti-cancer palladium complexes: a focus on PdX_2L_2, palladacycles and related complexes. Chem. Soc. Rev. 2014; 43, 4751. http://dx.doi.org/10.1039/c4cs00063c.

13. Angelè-Martìnez C, Goodman C, Brumaghim J. Metal-mediated DNA damage and cell death: mechanisms, detection methods, and cellular consequences. Metallomics 2014; 6, 1358. http://doi.org/10.1039/c4mt00057a.

14. Vignesh G, Senthilkumar R, Paul P, Periasamy VS, Akbarsha MA, Arunachalam S. Protein binding and biological evaluation of a polymer-anchored cobalt(III) complex containing a 2,20-bipyridine ligand. RSC Adv. 2014; 4, 57483. http://doi.org/10.1039/c4ra10377g.

15. Pages BJ, Ang DL, Wright EP, Aldrich-Wright JR. Metal complex interactions with DNA. Dalton Trans. 2015; 44, 3505. http://dx.doi.org/10.1039/c4dt02700k.

16. Karadağ A, Aslan Korkmaz Ş, Andaç Ö, Yerli Y, Topcu Y. Cyano-complexes and salts with tetracyanonickellate[II] and N,N-bis(2-hydroxyethyl)-ethylenediamine: synthesis, IR spectra, magnetic properties, thermal analyses, and crystal structures. Journal of Coordination Chemistry. 2012; 65, 10, 1685-1699. http://dx.doi.org/10.1080/00958972.2012.678337.

17. Aslan Korkmaz Ş, Karadağ A, Korkmaz N, Andaç Ö, Gürbüz N, Özdemir İ, Topkaya R. Five complexes containing N,N-bis(2-hydroxyethyl)-ethylenediamine with tetracyanidopalladate(II): synthesis, crystal structures, thermal, magnetic, and catalytic properties. Journal of Coordination Chemistry. 2013; 66, 17, 3072-3091. http://dx.doi.org/10.1080/00958972.2013.820827.

18. Aslan Korkmaz Ş, Karadağ A, Yerli Y, Soylu MS. Synthesis and characterization of new heterometallic cyanido complexes based on $[Co(CN)_6]^{3-}$ building blocks: crystal structure of $[Cu_2(N-bishydeten)_2Co(CN)_6].3H_2O$ having a strong antiferromagnetic exchange. New J. Chem. 2014; 38, 5402-5410. http://dx.doi.org/10.1039/c4nj00737a.

19. Sirajuddin M, Ali S, Badshah A. Drug–DNA interactions and their study by UV–Visible, fluorescence spectroscopies and cyclic voltammetry. J. Photochem. Photobiol. B 2013; 124, 1-19. http://dx.doi.org/10.1016/j.jphotobiol.2013.03.013.

20. Dabrowiak JC. Metals in Medicine. John Wiley & Sons, 2009. 1st Edition, 321 p, West Sussex, UK. ISBN: 0-470-68196-1.

21. Gielen M, Tiekink ERT. Metallotherapeutic Drugs and Metal-Based Diagnostic Agents: The Use of Metals in Medicine. John Wiley & Sons press, 2005. 644 p, West Sussex, UK. ISBN: 0-470-86403-6.

Altı Koordinasyon Bileşiği: Sitotoksik Etki Modu ve Biyolojik Değerlendirme

Ali Aydın, Şengül Aslan Korkmaz

Öz: Bu çalışma metinde verilmiş koordinasyon bileşiklerinin biyolojik ve antikanser özelliklerini anlatmaktadır. Altı adet siyanido kompleks türevinin FT-IR spektrumları, manyetik özellikleri, termal analizler ve kristal yapıları verilmiştir, burada $[M^{II}(CN)_4]^{2-}$ (M^{II} = Ni ve Pd) ve $[Co(CN)_6]^{3-}$ olup "şapka" ligand olarak *N,N*-bishydeten (*N,N*-bis(2-hidroksietil)etilendiamin) olarak daha önce çalışılmıştır. Bu çalışmada, söz konusu komplekslerin (**C1**-**C6**) farmakolojik özellikleri incelenmiş ve insan rahim ağzı kanseri (HeLa), insan kalınbağırsak kanseri (HT29), sıçan glioma (C6) ve Afrika yeşil maymun böbrek (Vero) hücre soylarına karşı anti-proliferatif aktiviteleri incelenmiştir. **C1**-**C6** komplekslerinin açılımı şöyledir: $[Ni(N\text{-bishydeten})Ni(CN)_4]$ (**C1**), $[Zn_2(N\text{-bishydeten})_2Ni(CN)_4]$ (**C2**), $[Ni(N\text{-bishydeten})Pd(CN)_4]$ (**C3**), $[Cd(N\text{-bishydeten})_2][Pd(CN)_4]$ (**C4**), $[Ni_2(N\text{-bishydeten})_2Co(CN)_6].3H_2O$ (**C5**) and $K[Cd(N\text{-bishydeten})Co(CN)_6].H_2O$ (**C6**). Bu bileşiklerin DNA/BSA bağlanma istekleri de spektroskopik titrasyonlar, yer değiştirme deneyleri ve elektroforez ölçümleri ile ortaya konmuştur. Kanserli hücreler üzerindeki çalışmalar **C1, C2, C4** ve **C6** bileşiklerinin belirgin antitümör aktivitesini göstermiş ve test edilen hücre soylarında tümör gelişimini azaltmıştır. Bu bileşiklerin çözücü içindeki çözünürlüğü de son derece yüksektir. Absorbans ve emisyon spektrum sonuçları, komplekslerin DNA ile groove-bağlanma etkileşimi gösterdiğini ortaya çıkarmıştır. Bütün bunların sonucunda, söz konusu bileşiklerin kanser hücre soylarına karşı etkili anti-proliferatif aktivite gösterdiği bulunmuştur, dolayısı ile pre-klinik veya klinik çalışmalar için potansiyel adaylar olarak gösterilebilir.

Anahtar Kelimeler: Koordinasyon bileşikleri, Antikanser aktivitesi, Sitotoksik aktivite, Apoptoz, DNA bağlanması.

Gönderme: 26 Haziran 2016. **Düzeltme:** 06 Ağustos 2016. **Kabul:** 06 Eylül 2016.

Fish Skin-Isolated Collagen Cryogels for Tissue Engineering Applications: Purification, Synthesis, and Characterization

Zeynep Çetinkaya[1], Didem Demir[1], Nimet Bölgen Karagülle[1,*]

[1]Mersin University, Engineering Faculty, Chemical Engineering Department, 33343, Mersin, Turkey

Abstract: Tissue engineering aims regenerating damaged tissues by using porous scaffolds, cells, and bioactive agents. The scaffolds are produced from a variety of natural and synthetic polymers. Collagen is a natural polymer widely used for scaffold production because of its being the most important component of the connective tissue and biocompatibility. Cryogelation is a relatively simple technique compared to other scaffold production methods, which enables to produce interconnected porous matrices from the frozen reaction mixtures of polymers or monomeric precursors. Considering these, in this study, collagen was isolated from fish skin which is a non-commercial waste material, and scaffolds were produced from this collagen by cryogelation method. Pore morphology and protein structure of collagen was proven by SEM and UV-Vis analysis, respectively. Iso-electrical point of the protein was determined by zeta potential analysis. Amide A, Amide B, Amide I, Amide II and Amide III characteristic peaks of collagen was demonstrated by FTIR analysis. The yield of isolated protein was 14.53% and 2.42% for acid-soluble and pepsin-soluble collagen, respectively. Scaffolds were produced by crosslinking isolated acid soluble collagen with glutaraldehyde at cryogenic conditions. With FTIR analysis, C=N bond which belongs to the reaction between glutaraldehyde and collagen was found to be at 1655 cm^{-1}. It was demonstrated by SEM analysis that collagen and glutaraldeyhde concentration had significant effects on the pore morphology, diameter, and wall thickness of the cryogels, which in turn changed the swelling ratio and degradation profiles of the scaffolds. In this study, synthesis and characterization results of a fish skin isolated collagen cryogel scaffold that may be potentially used in the regeneration of damaged tissues are presented.

Keywords: Tissue engineering, collagen, isolation of collagen, scaffold, cryogel.

INTRODUCTION

Tissue engineering is a discipline which aims to regenerate damaged tissues by using porous scaffolds and cells. Porous scaffolds that are produced from various polymers are used in regeneration of various organs and tissues. Interconnected pore structure of the scaffolds supports cell attachment, homogeneous cell distribution, differentiation, and proliferation [1]. Many natural polymers such as collagen have shown potential to be used in the fabrication of tissue engineering scaffolds [2]. Collagen is a natural polymer which is present in the extracellular matrix. Because of its being the most important component of extracellular matrix, and its biocompatibility and biodegradability, collagen is widely used in the preparation of tissue engineering scaffolds [3]. In recent years, researchers are searching for alternative natural sources of collagen and improved technologies for collagen isolation. Fish skin is a potential source of collagen. Therefore, skin collagen from several fish species have been extracted and characterized recently. Examples of those species are Baltic cod (*Gadus morhua*) [4], silvertip shark (*Carcharhinus albimarginatus*) [5], deep-sea redfish (*Sebastes mentella*) [6], striped catfish (*Pangasianodon hypophthalmus*) [7] and carp (*Catla catla* and *Cirrhinus mrigala*) [8]. Cryogelation is a rather simple scaffold production technique compared to other techniques. Cryogels produced by this technique have interconnected macropores that allow diffusion of nutrients and wastes as well as mass transport of nano- and microparticles, microorganisms and cells [9].

The aim of this study is extraction and characterization of acid-soluble collagen (ASC) and pepsin-soluble collagen (PSC) from the skin of shark fish and fabrication and characterization of collagen cryogel scaffolds for tissue engineering applications. Extracted collagens (ASC and PSC) were characterized by fourier transform infrared spectroscopy (FTIR), ultraviolet visible spectroscopy (UV-Vis), scanning electron microscopy (SEM) and Zeta potential analysis. Cryogels were synthesized by using ASC as the natural polymer and glutaraldehyde as the crosslinker. The chemical structure, swelling ratio, degradation profile, pore morphology, and pore size of collagen cryogels were demonstrated.

MATERIALS AND METHODS

Chemicals

KOH, NaOH, acetic acid (Glacial), and pepsin (from porcine gastric stomach mucosa) were purchased from Sigma Aldrich, USA. NaCl powder was obtained from Emsure, Germany. Butyl alcohol was obtained from Laba Chemie, India. Spectra/Por (12-14.000 Da, Cellulose) dialysis membrane was purchased from Spectrum Laboratories, USA. A cheese cloth used in filtration process was obtained from a local market in Gaziantep, Turkey. Distilled water was used in all experimental steps.

Isolation of collagen

ASC and PSC were isolated by using the method demonstrated by Benjakul *et al.*, with some modifications [10].

Fish skin preparation

Shark skin was a gift from a local fish market in Mersin, Turkey. The skin was washed with cold distilled water and then cut into small pieces (approximately 0.5 x 0.5 cm^2) by a pair of scissors. 50 grams of shark skin was treated with 0.1 M NaOH solution at 4 °C for 6 hours with continously stirring at 250 rpm in order to remove the non-collagenous compounds. The solution was replaced every two hours.

Isolation of ASC

After separating the non-collagenous proteins, the skin samples were mixed with 10% (v/v) butyl alcohol solution at a ratio of 1:10 (w/v) and continiously stirred for 48 hours at 4 °C to remove fat. The solution was replaced every 12 hours. After washing with cold water, fat-free skin was treated with 0.5 M acetic acid solution (skin/solution ratio was 1:15, w/v) for 24 hours and the extract was filtered by using the cheese cloth. The residue was re-extracted with 0.5 M acetic acid solution. Filtrates, which were very viscous, were combined. The filtrate was stirred for 24 hours, after addition of NaCl

powder to a final concentration of 2.6 M. The resultant precipitate was collected by centrifuging at 6000 rpm for 30 minutes and dissolved in a minimum volume of 0.5 M acetic acid solution, and dialyzed against 50 volumes of 0.1 M acetic acid solution for 24 hours at 4°C. It was then dialyzed against 50 volumes of distilled water for 24 hours. The dialyzate was freeze-dried by using a lyophilizer. The ASC was obtained.

Isolation of PSC

The remaining skin after ASC filtration was mixed with 0.5 M acetic acid solution [ratio of solid/solution 1:15 (w/v)] at 250 rpm for 24 hours after adding pepsin from porcine gastric stomach mucosa (20 units/g residue). The PSC was obtained followed by the same steps (filtration, centrifugation, dialysis and lyophilization) which were used in the isolation of ASC.

Characterization of isolated collagen

FTIR analysis

The obtained ASC and PSC samples were analyzed by FTIR. FTIR spectra in the range of 400- 4000 cm^{-1} with automatic signal gain were collected in 32 scans at a resolution of 4 cm^{-1}.

UV-Vis Analysis

The ultraviolet spectra were recorded by using a UV-Vis (Specord 210 Plus, Analytik Jena, Germany). 1 mg of collagen (ASC or PSC) was dissolved in 2 mL of 0.5 M acetic acid solution and centrifuged at 5000 rpm for 10 minutes. The measurement was done in the wavelength range of 200-420 nm.

ζ - Potential Analysis

The zeta potential of ASC and PSC solutions was measured by zeta potential analyzer (Zeta sizer, Malvern, UK) [10]. The samples were mixed with 0.5 M acetic acid solution to a final concentration of 0.05% (w/v) and stirred at 4 °C until they were completely

dissolved. The ζ-potential of ASC and PSC solutions at different pH values (2, 3, 4, 5, 6) were recorded.

SEM Analysis

The surface morphology of platinium coated ASC, PSC and cryogel samples was examined by SEM (Supro 55, Zeiss, Germany). The avarage pore sizes of the samples were calculated after measuring the size of ten pores.

Cryogel synthesis

Cryogels were prepared by using ASC as the polymer and glutaraldehyde as the crosslinker. The calculated amount of collagen was dissolved in distilled water at three different concentrations (3.0 - 6.0 - 8.0; w/v). The prepared collagen solutions were mixed with varying concentrations (0.5 - 1.0 - 2.0% ; v/v) of aqeous glutaraldehyde solution (25%; v/v) and then poured into plastic syringes (2 mL). The solution was immediately immersed in cryostat, incubated at -12 °C for 2 hours and then placed in the freezer (at -16°C) for 24 hours. After the crosslinking reaction was completed, the frozen samples were thawed at room temperature and washed with distilled water until the unreacted ingredients were removed. The prepeared cryogels were then dried overnight at room temperature. Schematic illustration of collagen isolation and cryogel production is demonstrated in Figure 1. The effect of collagen and glutaraldehyde concentration on the properties of the cryogels was evaluated. When the collagen concentration changed, the glutaraldehyde concentration was kept constant at 0.5% (Table 1). And when the glutaraldehyde concentration changed the collagen ratio was kept constant at 8% (Table 2).

Figure 1. Schematic illustration of collagen isolation and cryogel production.

Table 1. Cryogels synthesized with different amounts of collagen.

Concentration of Collagen (%, w/v)	Concentration of Glutaraldehyde (%, v/v)
3.0	0.5
6.0	0.5
8.0	0.5

Table 2. Cryogels synthesized with different amounts of glutaraldehyde.

Concentration of Collagen (%, w/v)	Concentration of Glutaraldehyde (%, v/v)
8.0	0.5
8.0	1.0
8.0	2.0

Swelling ratio

The swelling behavior of collagen cryogels were determined according to a previously demonstrated method [11]. The dried cryogels were weighed (W_d). Then dried cryogels were kept in 50 mL distilled water at room temperature for 360 minutes. The excess

water on the surface of the cryogels was removed with a filter paper and the cryogels were then weighed (W_w). The ratio of swelling (SR%) was calculated using equation (1).

$$SR\% = [(W_w-W_d)/W_d]*100 \qquad\qquad (Eq.1)$$

Degradation studies

Collagen cryogels were incubated at 37°C in 10 mL of distilled water at static conditions to measure their degradation rate. The samples were taken out from incubation after 42 days, dried at room temparature and weighed. The weight loss of samples were obtained according to equation (2):

$$Weight\ Loss\% =[(W_0-W_t)/W_0]*100 \qquad\qquad (Eq.2)$$

where W_0 and W_t are the weights of cryogels' initial dry weight and dry weight after degradation, respectively.

RESULTS AND DISCUSSION

Yield of ASC and PSC

The yields of ASC and PSC calculated directly based on the initial weight of skin were 14.53% and 2.42%, respectively. The following analyses were conducted in order to characterize the properties of the collagen.

FTIR analysis of collagen

The FTIR spectras of ASC and PSC were shown in Figure 2 and depicted in Table 3. According to Wang et al. [12] the Amide A band of ASC and PSC occurs at wavenumbers of 3314.82 cm^{-1} and 3315.81 cm^{-1}, respectively, were associated with NH stretch coupled with hydrogen bond. Amide B band of those collagens at 2940.72 cm^{-1} and 2940.80 cm^{-1}, respectively, corresponds to asymmetrical stretch vibration of CH_2 [10]. Amide I, Amide II, and Amide III bands of ASC were found at 1652.10, 1550.21 and 1238.64 cm^{-1}, respectively. Those bands of PSC were found at 1658.30, 1552.90 and 1239.16 cm^{-1}. Amide I band that occurs in the range of 1600 - 1700 cm^{-1} shows the existence of stretching vibration of C=O or hydrogen bond coupled with COO- group. The result of

Amide II and Amide III bands were presumed that there were stretching N-H bending vibrations and C - H stretching.

Region	ASC	PSC
Amide A	3314.82	3315.81
Amide B	2940.72	2940.81
Amide I	1652.11	1658.32
Amide II	1550.21	1552.91
Amide III	1238.64	1239.16
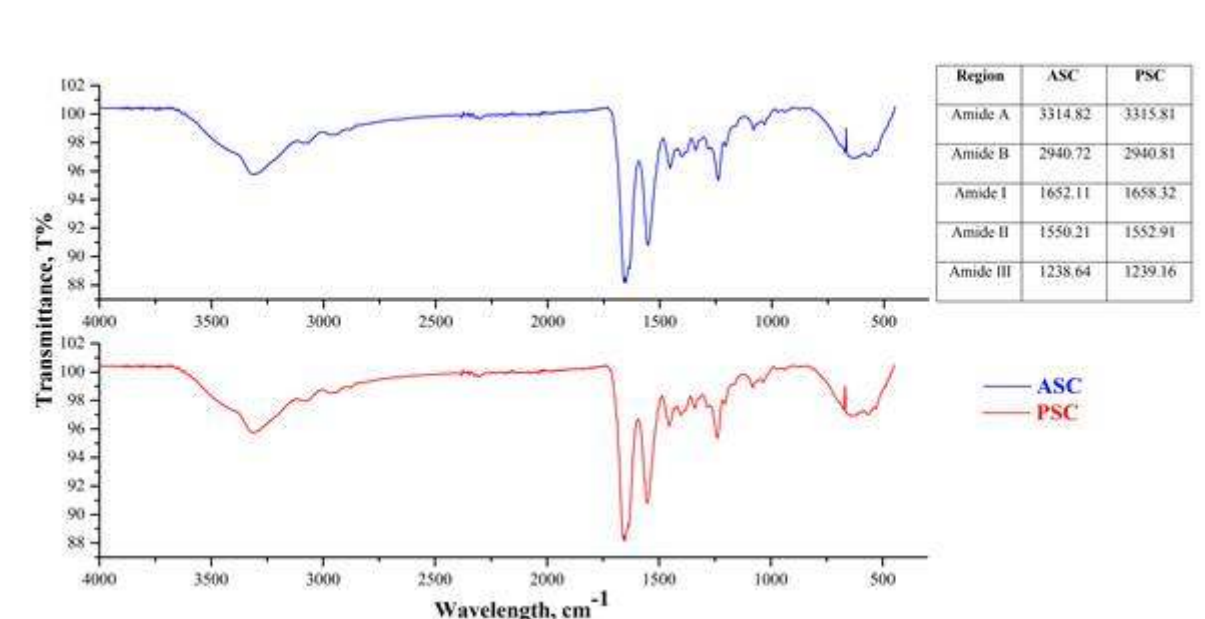
Figure 2. FTIR spectra of ASC and PSC.

Table 3. FTIR spectras peak wave numbers and assigments for ASC and PSC.

Region	Peak Wave Number (cm^{-1})		Assigment	References
	ASC	PSC		
Amide A	3314.82	3315.81	NH stretch coupled with hydrogen bond	Wang et al. [13]
Amide B	2940.72	2940.80	Asymmetrical stretch of CH$_2$	Benjakul et al. [10]
Amide I	1652.10	1658.30	Stretching vibration of C=O or hydrogen coupled with COO$^-$	Zhang et al. [14]
Amide II	1550.21	1552.90	Vibration of NH bending	Benjakul et al. [10]
Amide III	1238.64	1239.16	C-H stretching	Kittiphattanabawon et al. [15]

UV-Vis analysis

The maximum absorptions of ASC and PSC, were determined at the wavelengths of 230 - 240 nm region, as shown in Figure 3. This result is in agreement with the result of the

study presented by Huang *et al.* Moreover the absorbances at near 280 nm is related to the tyrosine in collagen [16].
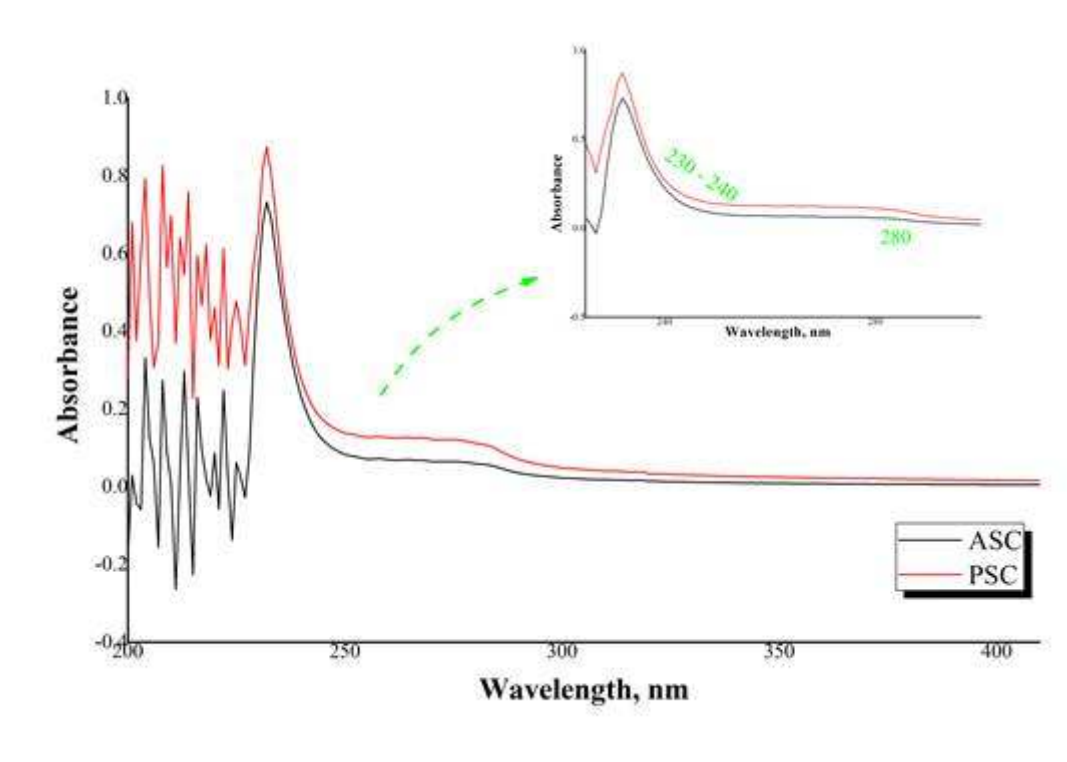
Figure 3. UV - Vis spectra of ASC and PSC.

ζ - Potential analysis

The zeta potential values of ASC and PSC solutions at different pH values (2, 3, 4, 5 and 6) were determined as shown in Figure 4. The zeta potential was zero at pH 4.8 for ASC and 5.9 for PSC. This result can be explained by the balance between positive and negative charges as reported by Bonner [17]. According to Vojdani, a protein in an aqueous system (like collagen in acetic acid solution) has a zero net charge at its isoelectric point [18]. However, the differences of surface charges of ASC and PSC might be explained by their various amino acid compositions.
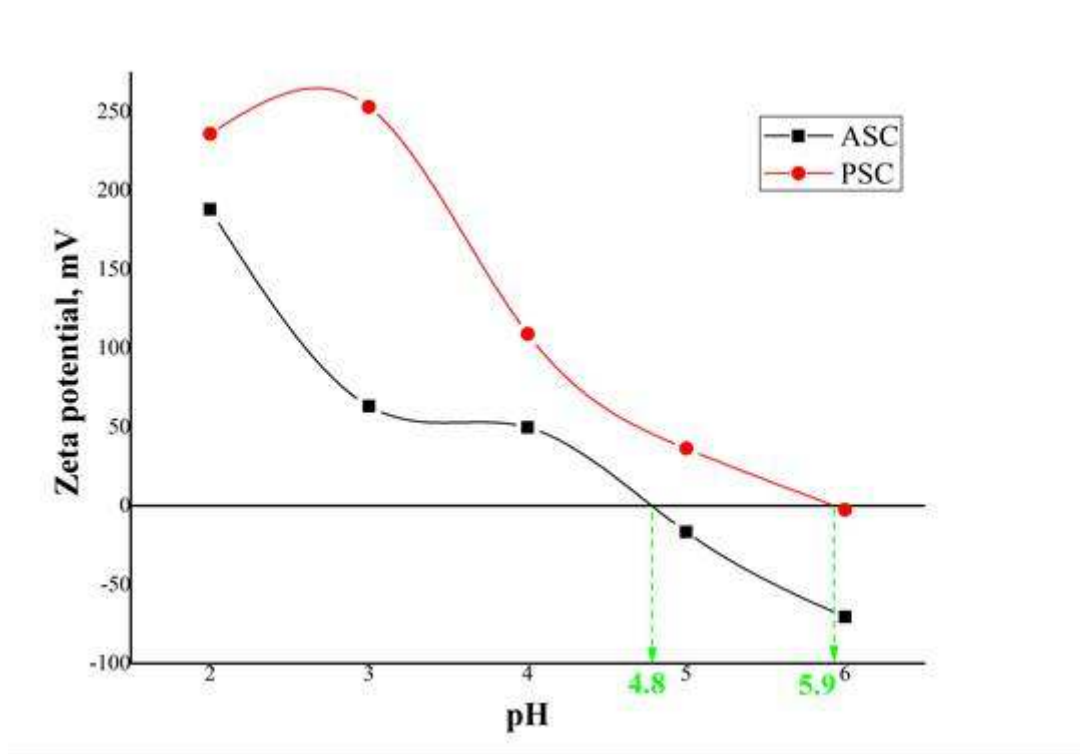
Figure 4. The zeta potential of ASC and PSC solutions at different pH values.

SEM analysis of collagen

The pore morphology of the lyophilized collagens (ASC and PSC) were quite similar when compared to each other. The average pore sizes of ASC and PSC samples were 61.071 ± 27.51 and 50.308 ± 22.89 µm (Figure 5).
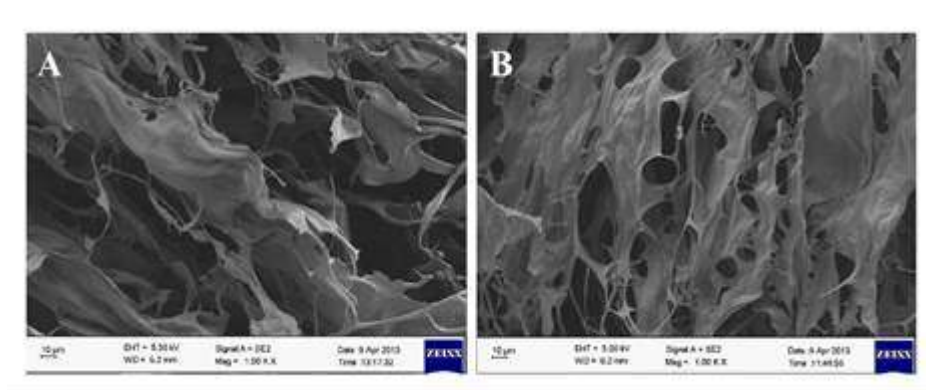
Figure 5. SEM images of ASC (A) and PSC (B) (at 1000x magnification).

Synthesis and characterization of cryogels

FTIR analysis

The chemical structure of the cryogels were analyzed by FTIR and the resulting spectra were demonstrated in Figures 6 and 7. The Amide B bands which belong to the asymmetrical stretch of CH_2 at near by 2400 cm^{-1} disappeared in FTIR of crosslinked collagen cryogels, compared to uncrosslinked collagen which may be due to the hindrance of the peak by glutaraldehyde crosslinking of collagen. The appearance of the peak at 1630 - 1648 cm^{-1} represents stretching vibrations of C=N in Schiff's base formed by the crosslinking reaction between the amide group of collagen and the aldehyde group of glutaraldehyde [7,19]. In addition, the peak at 2929 cm^{-1} of C-H streching are related to the aldehyde group of glutaraldeyde.
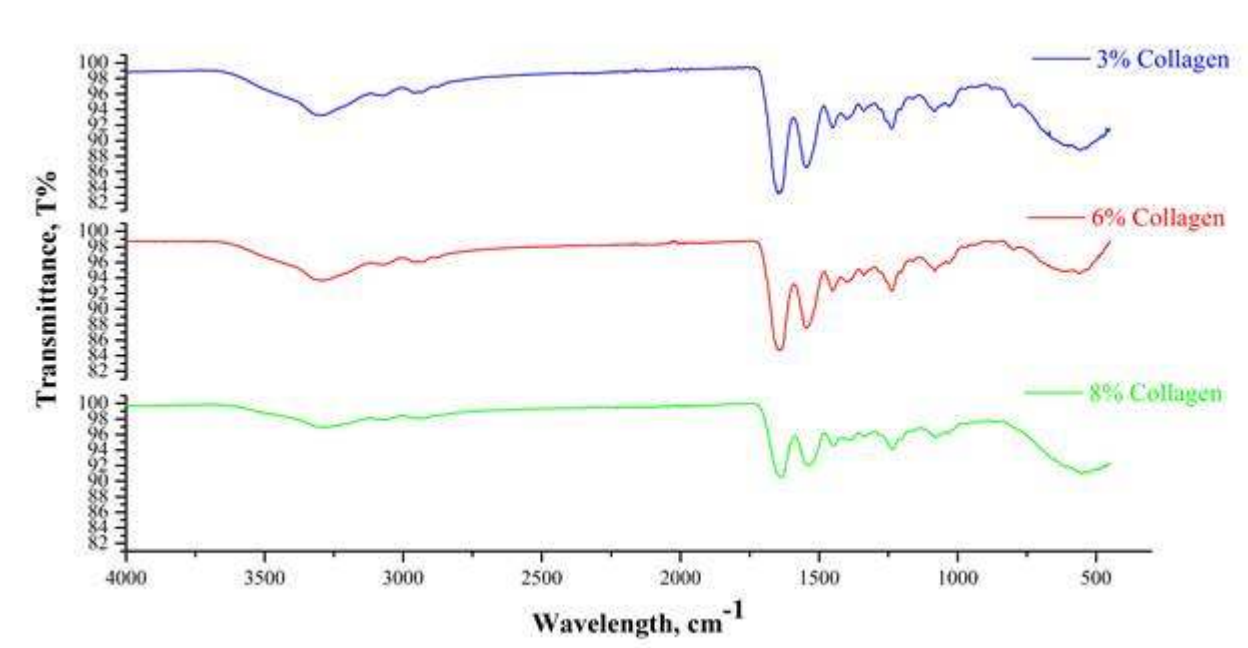
Figure 6. FTIR spectrum of cryogels prepared at different collagen concentrations while the glutaraldehyde concentration was kept constant at 0.5% (v/v).
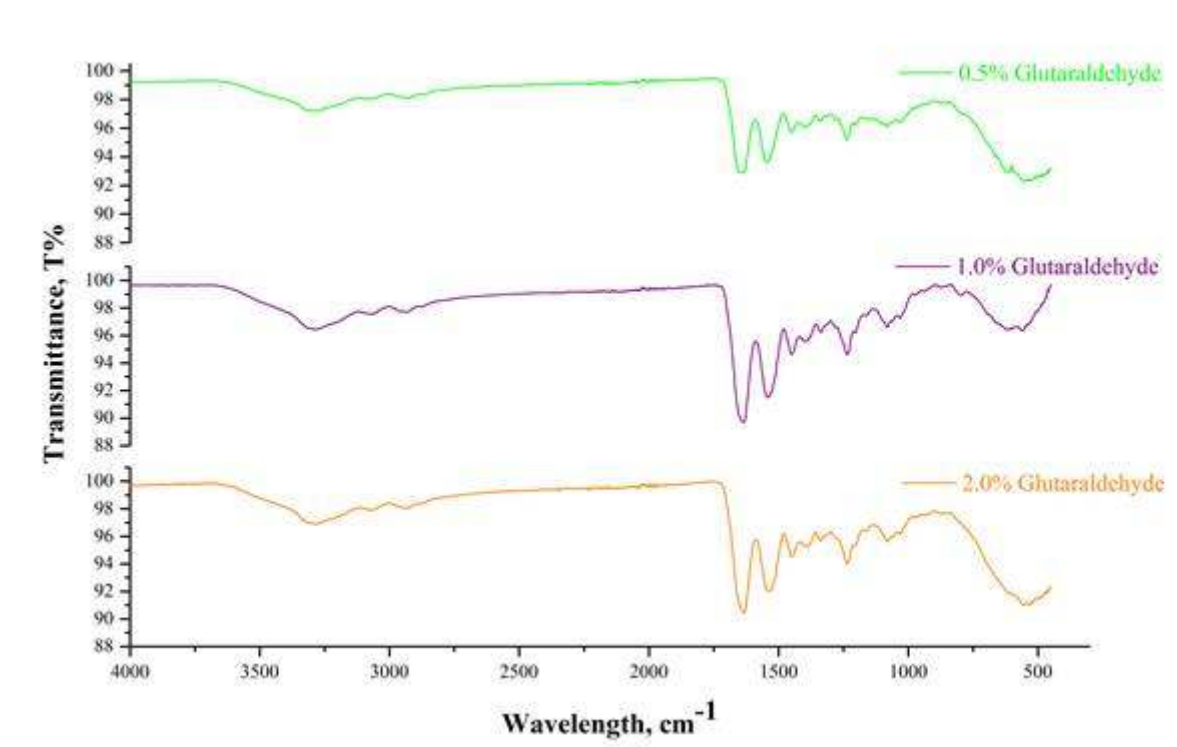
Figure 7. FTIR spectrum of cryogels prepared at different glutaraldehyde concentrations while the collagen concentration was kept constant at 8.0% (w/v).

SEM analysis

Cryogels were prepared with different ratios of collagen and glutaraldehyde, and the effect of those parameters (polymer and crosslinker concentration) on the final properties of the cryogel scaffolds were evaluated. Porosity and pore sizes are considered as important parameters in the design of scaffolds for tissue engineering applications. The adequate pore structure and pore size allow adhesion, migration, and differentation of cells and new tissue formation [20]. In this study, the morphological structure of collagen cryogels were examined by SEM analysis to assess the effects of polymer and crosslinking agent on the morphology. The results demonstrated that the cryogels exhibited interconnected porous morphology as shown in Figures 8 and 9. The pore sizes of the cryogels prepared with 3.0, 6.0 and 8.0% (w/v) concentration of collagen were 123.302 ± 35.08, 145.79 ± 49.37 ve 217.4 ± 63.96 µm, respectively. It was observed that the pore size increased with increasing the collagen concentration. In addition to this, increasing the amount of collagen from 3.0 to 6.0 and to 8.0% (w/v) increased the wall thickness of prepared cryogels from 0.96 ± 0.06 to 1.38 ± 0.09 and to 1.71 ± 0.09 µm, respectively.
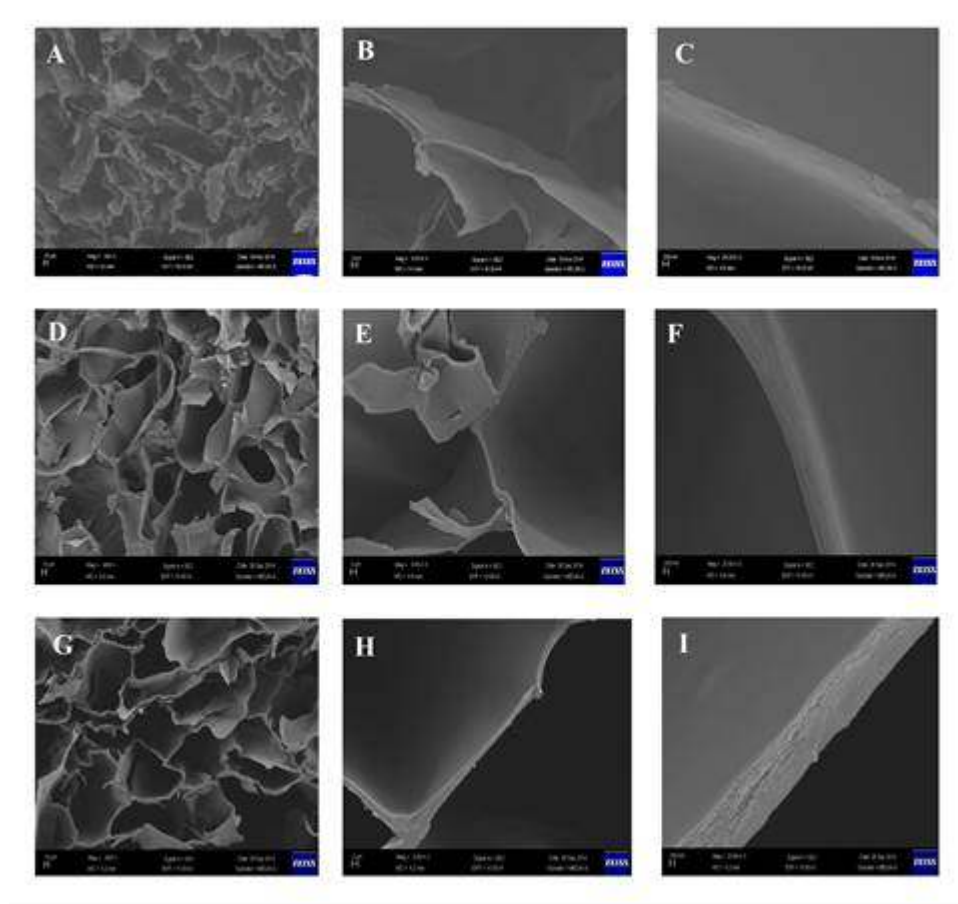
Figure 8. SEM images of the cryogels' porous structure and pore walls. The collagen concentration was changed while the crosslinker ratio was kept constant at 0.5% (v/v). Collagen concentration (w/v): (A) 3.0 %, (D) 6.0%, (G) 8.0%. Magnification: x400 in A,D,G ; x3000 in B,E,H ; x25000 in C,F,I.

The pore sizes of the cryogels prepared with 0.5, 1.0 and 2.0% (v/v) concentration of glutaraldehyde were 217.4 ± 63.96, 180.88 ± 73.31, and 157.21 ± 32.05 µm, respectively. It was observed that the pore size decreased with increasing the crosslinker concentration. Increasing the amount of crosslinker from 0.5 to 1.0 and to 2.0% (v/v), the wall thickness of prepared cryogels changed from 1.72 ± 0.09 to 0.07 ± 0.03 and to 1.61 ± 0.04 µm, respectively.
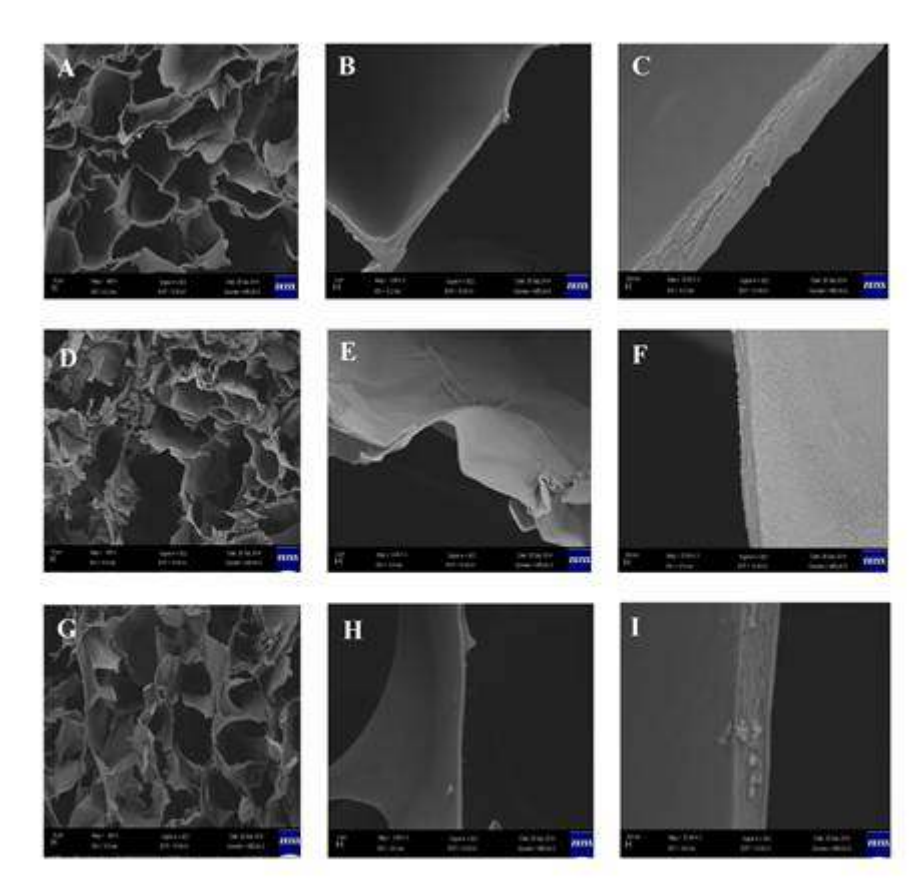
Figure 9. SEM images of the cryogels' porous structure and pore walls. The glutaraldehyde concentration was changed while the collagen ratio was kept constant at 8.0% (w/v). Glutaraldehyde concentration (v/v): (A) 0.5%, (D) 1.0%, (G) 2.0%. Magnification: x400 in A,D,G ; x3000 in B,E,H ; x25000 in C,F,I.

Swelling ratio analysis

The swelling ratios of cryogels are presented in Figure 10. All samples exhibited a swelling behavior and have the ability to retain more water than its own dry weight. It is observed that when the concentration of collagen increased from 3.0 to 6.0 and to 8.0% (w/v) swelling ratio of cryogels decreased from 4292.38 ± 446.68 to 2664.89 ± 227.85 and to $2036.27 \pm 51.95\%$, respectively, at 360 min (Figure 10A). A more rigid structure was formed as collagen concentration increased and higher wall thickness caused less water uptake, therefore the swelling ratio was decreased. As seen in Figure 10B, at 360. minute as the crosslinker ratio was increased the swelling ratio was decreased.

Figure 10C demonstrates the cryogel's flexible behavior after swelling (a representative image). It was possible to squeeze and relax the scaffold easily after it swells the water, which showed the mechanical stability and elasticity of the cryogel.
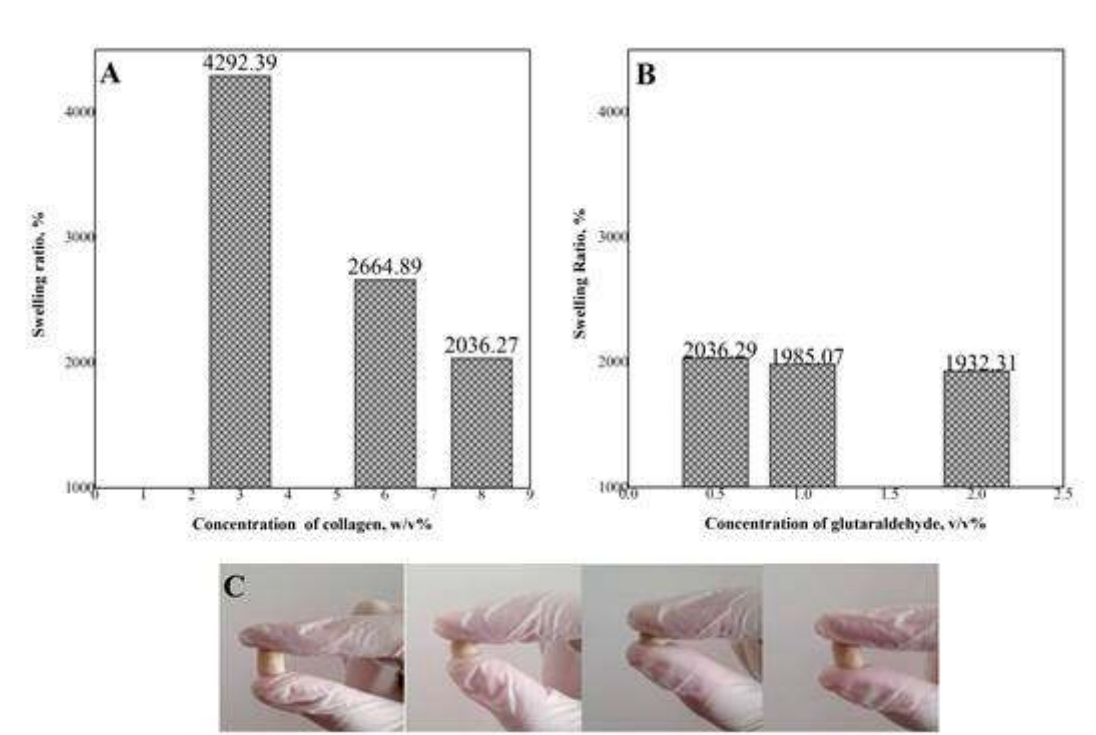
Figure 6. Swelling behavior of collagen cryogels: A) prepared at different collagen concentrations, B) prepared at different glutaraldehyde concentrations, C) cryogel's flexible structure after swelling.

In vitro degradation studies

The degradation of a scaffold is an important point in the design of a tissue engineering application [21]. For determination of how far collagen cryogel scaffolds can withstand to support tissue formation or restoration of damaged or diseased tissues, the weight loss of the collagen cryogels was demonstrated (Figure 11A and B) by the *in vitro* degradation test during 42 days and the images of cryogels before and after degradation process are shown in Figure 11C.

At the end of 42 days, as the collagen and glutaraldehyde concentration decreased, the degradation rate increased. The results were related to the results of swelling ratio studies. As the swelling ratio increased more water was uptaken by the scaffolds, which resulted in a faster degradation rate of the scaffold.
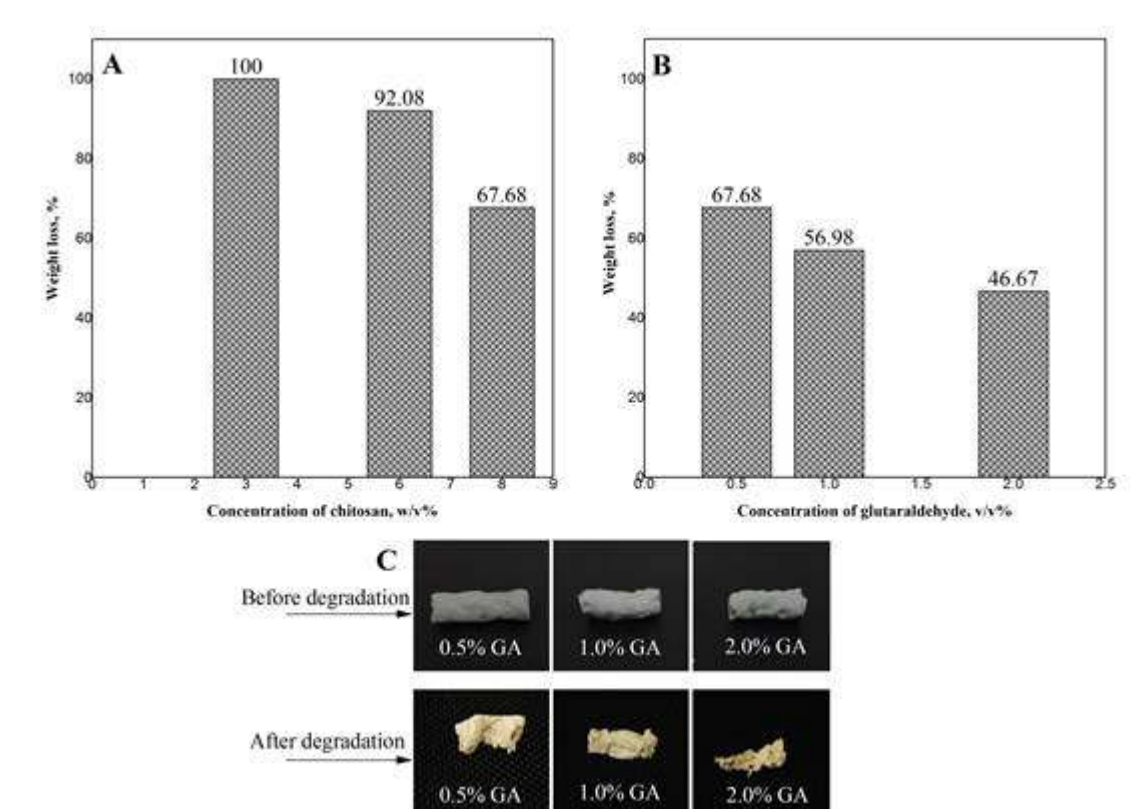
Figure 7. Degradation profiles of collagen cryogels: A) prepared at different collagen concentrations, B) prepared at different glutaraldehyde concentrations, C) cryogel images before and after degradation process.

CONCLUSION

In this study, acid-soluble collagen (ASC) with a yield of 14.53% and pepsin-soluble collagen (PSC) with a yield of 2.42% were successfully isolated from fish skin which is a waste material of the fish industry and characterized on the basis of SEM, UV-Vis, Zeta potentital and FTIR analysis. The cryogel scaffolds were produced from isolated collagen by applying the cryogelation technique which is a very unique technique in the design of a qualified scaffold with an interconnected porous structure that allows the three dimensional tissue growth and the diffusion of nutrients and wastes during tissue regeneration. Using different amounts of collagen and glutaraldehyde in the recipes resulted in properties of the scaffold such as having interconnected porosity, mechanical stability, spongy and elastic structure. Tailoring these properties of the cryogels with their swelling ability and degradation behavior would enable to design novel scaffolds for use in various applications in tissue engineering field. This study demonstrated extraction

of collagen and synthesizing cryogels from this collagen. For future tissue engineering applications, *in vitro* and *in vivo* biocompatiblity experiments would be performed.

ACKNOWLEDGEMENTS

REFERENCES

1. Sidi AB, Thomas MB, Philippe R. Advances in the design of macroporous polymer scaffolds for potential applications in dentistry. 2013 Dec;43(6):251-61. DOI: 10.5051/jpis.2013.43.6.251

2. Bhat S, Tripathi A, Kumar A. Supermacroprous chitosan–agarose–gelatin cryogels: in vitro characterization and in vivo assessment for cartilage tissue engineering. Journal of the Royal Society Interface. 2011 Apr;8:540-54. DOI: 10.1098/rsif.2010.0455

3. Martíneza A, Blancoa MD, Davidenkob N, Cameronb RE. Tailoring chitosan/collagen scaffolds for tissue engineering: Effect of composition and different crosslinking agents on scaffold properties. Carbohydrate Polymers. 2015 May;132:606-19. DOI: 10.1016/j.carbpol.2015.06.084

4. Sadowska M, Koodziejska I, Niecikowska C. Isolation of collagen from the skins of Baltic cod (Gadus morhua). Food Chemistry. 2003 Aug; 81:257-62. DOI: 10.1016/S0308-8146(02)00420-X

5. Elango J, Bin B, Yongshi B, Yu Z, Qingbo Z, Wenhui W. Type II Collagen and Gelatin from Silvertip Shark (Carcharhinus albimarginatus) Cartilage: Isolation, Purification, Physicochemical and Antioxidant Properties. Marine Drugs. 2014 June;12:3852-73. DOI:10.3390/md12073852.

6. Wang L, An X, Xın Z, Zhao L, Hu Q, Isolation and Characterization of Collagen from the Skin of Deep-Sea Redfish (Sebastes mentella). Journal of Food Science. 2007 Oct;72(8):450-55. DOI: 10.1111/j.1750-3841.2007.00478.x.

7. Singh P, Benjakul S, Maqsood S, Kishimura H. Isolation and characterisation of collagen extracted from the skin of striped catfish (Pangasianodon hypophthalmus). Food Chemistry. 2011 Jan;124:97-105. DOI: 10.1016/j.foodchem.2010.05.111.

8. Shahid M. Isolation and characterization of collagen from fish waste material- skin, scales and fins of Catla catla and Cirrhinus mrigala. Journal of Food Science and Technology. 2015 July;52(7):4296-305. DOI 10.1007/s13197-014-1520-6.

9. Lozinsky V, Galaev I. Y, Plieva FM, Savina IN, Jungvid H, Mattiasson B. Polymeric cryogels as promising materials of biotechnological interest. TRENDS in Biotechnology. 2003 Oct;21(10):445-51. DOI:10.1016/j.tibtech.2003.08.002.

10. Benjakul S, Thiansilakul Y, Visessanguan W, Roytrakul S, Kishimura H, Prodprand T, Meesaned J. Extraction and characterisation of pepsin-solubilised collagens from the skin of bigeye snapper (Priacanthus tayenus and Priacanthusmacracanthus). Journal of the Science of Food and Agriculture. 2010 Sept;90:132-38. DOI 10.1002/jsfa.3795.

11. Kemençe N, Bölgen N. Journal of Tissue Engineering and Regenerative Medicine. 2013. DOI: 10.1002/term.1813.

12. Wang B, Wang Y-W, Chi C-F, Luo H-Y, Deng S-G, Ma J-Y. Isolation and Characterization of Collagen and Antioxidant Collagen Peptides from Scales of Croceine Croaker (Pseudosciaena crocea). Marine Drugs. 2013 Nov;11:4641-661. DOI: 10.3390/md11114641

13. Wang L, An X, Yang F, Xin Z, Zhao L, Hu Q. Isolation and characterisation of collagens from the skin, scale and bone of deep-sea redfish (Sebastes mentella). Food Chemistry. 2008 May;108(2): 616–23. DOI:10.1016/j.foodchem.2007.11.017.

14. Zhang M, WenTao L, GuoYing L. Isolation and characterisation of collagens from the skin of largefin longbarbel catfish (Mystus macropterus). Food Chemistry. 2009 Aug; 115(3):826-31. DOI: 10.1016/j.foodchem.2009.01.006.

15. Kittiphattanabawon P, Benjakul S, Visessanguan W, Shahidi F. Isolation and properties of acid- and pepsin-soluble collagen from the skin of blacktip shark (Carcharhinus limbatus). European Food Research and Technology. 2010 Jan;230:475–483. DOI: 10.1007/s00217-009-1191-0.

16. Huang Y-R, Shiau C-Y, Chen H-H, Huang B-C. Isolation and characterization of acid and pepsin-solubilized collagens from the skin of balloon fish (Diodon holocanthus). Food Hydrocolloids. 2011 Febr;25:1507-13. DOI:10.1016/j.foodhyd.2011.02.011.

17. Bonner P. L. R. Protein Purification (The Basics). Biochemistry and Molecular Biology Education. 2008;36(2):170. DOI: 10.1002/bmb.20150.

18. Vojdani F. Solubility. In Methods of Testing Protein Functionality. G.M. Hall ed. Blackie Academic and Professional. London. U.K. 1996; 11-46. ISBN: 0 7514 0053 X

19. Zhang M, Liu W, Li G. Isolation and characterisation of collagens from the skin of largefin longbarbel catfish (Mystus macropterus). Food Chemistry. 2009 Aug;115:826-31. DOI: 10.1016/j.foodchem.2009.01.006

20. Song E, Kim S. Y, Chunc T, Byunc H-J, Leea YM. Collagen scaffolds derived from a marine source and their biocompatibility. Biomaterials. 2006 May;27(15):2951-61. DOI:10.1016/j.biomaterials.2006.01.015.

21. Dhandayuthapani B, Yoshida Y, Maekawa T, Kumar D. S, Polymeric Scaffolds in Tissue Engineering Application: A Review. International Journal of Polymer Science, 2011 July;2011:1-19. DOI:10.1155/2011/290602.

Doku Mühendisliği Uygulamaları için Balık Derisinden İzole Edilmiş Kolajenden Üretilen Kriyojeller: Saflaştırma, Sentez ve Karakterizasyon

Zeynep Çetinkaya, Didem Demir, Nimet Bölgen Karagülle

Öz: Doku mühendisliği gözenekli doku iskeleleri, hücreler ve biyoaktif araçlar kullanmak suretiyle zarar görmüş dokuları yenilemeyi hedefler. Doku iskeleleri bir çok doğal ve sentetik polimerden üretilir. Kolajen, bağ dokunun en önemli bileşeni olması ve biyouyumluluğu sebebiyle doku iskelesi üretiminde geniş bir kullanım alanına sahip olan bir doğal polimerdir. Kriyojelleşme, diğer yapı iskelesi üretimi yöntemlerine göre nispeten daha basit bir teknik olup polimer karışımı veya monomerik öncül maddeleri içeren donmuş tepkime karışımlarından birbiri ile bağlantılı gözenekli matrisler üretme olanağı sunar. Bunlar dikkate alındığında, bu çalışmada, kolajen balık derisi gibi ticari olmayan bir atık malzemeden izole edilmiş ve bu kolajenden kriyojelleşme yöntemiyle doku iskeleleri üretilmiştir. Kolajenin gözenek morfolojisi ve protein yapısı sırasıyla SEM ve UV-Vis analizi ile doğrulanmıştır. Proteinin izoelektrik noktası zeta potansiyel analizi ile belirlenmiştir. Kolajenin Amid A, Amid B, Amid I, Amid II ve Amid III karakteristik pikleri, FTIR analizi ile gösterilmiştir. İzole edilmiş proteinin verimi asitte çözünen ve pepsinde çözünen kolajen için sırasıyla %14,53 ve %2,42 olarak bulunmuştur. Doku iskeleleri izole edilmiş asitte çözünür kolajenin, kriyojenik koşullar altında, glutaraldehitle çapraz bağlanması ile üretilmiştir. FTIR analizi ile, glutaraldehit ile kolajen arasındaki tepkimeden oluşan C=N bağının konumu 1655 cm^{-1} olarak bulunmuştur. SEM analizi ile, kolajen ve glutaraldehit derişiminin kriyojellerin gözeneklerinin morfolojisi, çapı ve duvar kalınlığı üzerine belirgin etkide bulunduğu gösterilmiştir, bu etkiler doku iskelelerinin şişme oranını ve bozunma profillerini değiştirmiştir. Bu çalışmada, hasar görmüş dokuların yenilenmesinde potansiyel olarak kullanılabilecek, balık derisinden izole edilmiş kolajen kriyojel doku iskelesinin sentezi ve karakterizasyon sonuçları sunulmuştur.

Anahtar kelimeler: Doku mühendisliği, kolajen, kolajenin izolasyonu, doku iskelesi, kriyojel.

(This article was presented to the 28th National Chemistry Congress and submitted to JOTCSA as a full manuscript)

Anticancer Activity of *Papaver somniferum* L.

Döne Aslı Güler[1], Ali Aydın[1], Mesut Koyuncu[2], İskender Parmaksız[1], Şaban Tekin[1]*

[1] Faculty of Art and Science, Department of Molecular Biology and Genetics, Gaziosmanpaşa University, 60240, Tokat, Turkey

[2] Faculty of Art and Science, Department of Biology, Gaziosmanpaşa University, 60240, Tokat, Turkey

Abstract: This work describes the pharmacological activity of extracts of *Papaver somniferum* L., a poppy species. *P. somniferum* L. products are still considered as a unique source of drug for many diseases. The present study was designed to determine antiproliferative and cytotoxic effects of *P. somniferum* L. extracts on HeLa (Human Cervix Carcinoma), HT29 (Human Colorectal Adenocarcinoma), C6 (Rat Brain Tumor Cells), and Vero (African Green Monkey Kidney) cell lines. Alkaloid-rich extracts of *P. somniferum* L. exhibited antiproliferative effects on various cancer cell lines, especially at high concentrations. We assessed the ability of extracts of *P. somniferum* L. to give harm to the membrane of the cells. Results indicated that *P. somniferum* L. extracts destroy cellular membrane in tumor cell lines at high concentrations. Remarkably, the LDH test results disclosed that cytotoxicity of *P. somniferum* L. on cells was low at middle concentrations. This may indicate its cytostatic potential. The results of this study support the efficacy of *P. somniferum* L. extracts as an anticancer agent.

INTRODUCTION

Cervical and colon cancers are the most common form of human cancer in the world. There were over two million new cases of cervical and colon cancer diagnosed in 2012 [1]. Therefore, cancer is increasingly becoming a global burden on individuals and social health systems. However, complex pharmacological studies encompassing several disciplines showed that the natural products lead to a significantly decreased death rate, including cancer. This was mainly due to the protective or healing effects of natural products such as fruits, vegetables and spices [2, 3]. Almost every time when the diverse biological activities of natural products are studied intensively; the significant bioactive molecules of herbs and spices display antioxidant, antiinflammatory, immunomodulatory, anticarcinogenic, antithrombotic, and anticoagulant effects [4-6]. Especially the antitumor activity of natural products has recently attracted considerable attention by synthetic chemists. There have also been a variety of studies addressing chemotherapeutic usage for the adjuvant therapy. Natural products were shown to boost the antiproliferative effect of some clinic chemotherapeutics in certain cancer cells [7, 8]. *P. somniferum* L. (the opium poppy) belongs to the family *Papaveraceae* and is widely used for medicinal purposes because it contains various alkaloids such as morphine, noscapine, narcotine, codeine, papaverine, and others [9-11]. Current studies show that alkaloids obtained from *Papaver* species could not only be used as analgesic or sedative but also in other areas such as cancer treatment [12]. *P. somniferum* L. alkaloids that show promise in cancer treatment include noscapine, which interacts with α-tubulin and has anticancer and antiangiogenetic properties [13, 14]; codeinone, an oxidative product of codeine which has apoptotic effects through fragmentation of DNA [15]; morphine, which shows anticancer activities by inhibiting NF-κB; and (-)-3-acetyl-6β-(acetylthio)-N-(cyclopropyl-methyl)-normorphine (KT-90), a derivative of morphine [16]. To the best of our knowledge, pharmacological effects of *P. somniferum* L. extracts on HT29, HeLa, C6 cancer cell lines and Vero normal cell lines have not been investigated in detail. In the present work, extracts of *P. somniferum* L. from Turkey (Ofis 8 variety produced by Afyonkarahisar Agricultural Enterprise) was investigated for its antiproliferative and cytotoxic activities against HT29, HeLa, C6 and Vero cells. We conducted in-depth analysis of the inhibitory effect on proliferation, cytotoxicity and morphology.

MATERIALS and METHODS

Preparation of extracts

A Turkish poppy (*Papaver somniferum* L.) cultivar, namely Ofis 98, was used in this study. The stem, leaf, capsule and root parts of the plant material were dried at shade and then extracted (each of 10 g) with hexane, ethyl acetate, and methanol (each of 150 mL) for 1 day. The solvents were dried to yield the hexane, ethyl acetate, and methanolic extracts (Table 1).

Table 1. *Papaver somniferum* L. extracts

Solvent system/*P. somniferum* L. *parts*	Root	Stem	Leaf	Capsule
Hexane	*HPSR*	*HPSS*	*HPSL*	*HPSC*
Methanol	*MPSR*	*MPSS*	*MPSL*	*MPSC*
Ethyl acetate	*EPSR*	*EPSS*	*EPSL*	*EPSC*

Preparation of cell culture

The anticancer potential of *Papaver somniferum* L. extracts was investigated on cancerous HT29 (ATCC® HTB-38™), HeLa (ATCC® CCL-2™), and C6 cells (ATCC® CCL-107™) and nontumorigenic Vero cells (ATCC® CCL-81™). The cell lines were cultured in a cell medium (Dulbecco's modified eagle's) enriched with 10% (v/v) fetal bovine serum and 2% (v/v) Penicillin-Streptomycin (10,000 U/mL). First, old medium was removed out of the flask while cells had reached approximately 80% confluence. Next, cells were taken from the flasks surface using 4-5 mL of trypsin-EDTA solution and neutralized by the addition of at least 15 mL supplemented DMEM and then subjected to centrifugation. Following, the cellular pellet was suspended with 4 mL of DMEM working solution and was counted to obtain a final concentration of 5×10^4 cells/mL, and inoculated into wells (100 µL cells/well).

Cell proliferation assay (CPA)

A cell suspension containing approximately 5×10^3 cells in 100 µL was seeded into the wells of 96-well culture plates. The cells were treated with *Papaver somniferum* L. extracts and control drug, 5-fluorouracil (5FU), dissolved in sterile DMSO (max 0.5% of DMSO) at final concentrations of 25, 50, 100, 150, 200, 250, 375, and 500 µg/mL at 37 °C with 5% CO_2 overnight. The final volume of the wells was set to 200 µL by medium. Cell proliferation assay was evaluated by ELISA BrdU methods as described previously [17].

Calculation of IC50 and % inhibition

IC50 value is a concentration that inhibits half of the cells in vitro. The half maximal inhibitory concentration (IC50) of the *Papaver somniferum* L. *extracts* and control compounds was calculated using XLfit5® or Microsoft Excel® spreadsheet and represent in µM at 95% confidence intervals. The proliferation assay results were expressed as the percent inhibition according to the following formula: % Inhibition = [1 - (Absorbance of Treatments / Absorbance of DMSO) x 100].

Cytotoxic activity assay

The cytotoxicity of the *Papaver somniferum* L. *extracts* and 5 fluorouracil on HeLa, C6, HT29, and Vero cells was determined through a Lactate Dehydrogenase Assay Kit according to the manufacturer's instructions (Roche, LDH Cytotoxicity Detection Kit). Approximately 5×10^3 cells in 100 µL were placed into 96-well plates as triplicates and treated with IC50 (µg/mL) concentrations of *Papaver somniferum* L. extracts at 37°C with 5% CO_2 for 24 h. LDH activity was obtained by determining absorbance at 492 - 630 nm using a microplate reader. The

cytotoxicity assay's results were noted as the percent cytotoxicity according to the following formula: % Cytotoxicity = [(Experimental Value - Low Control / High Control - Low Control) x 100].

Cell imaging

Cells were plated in 96-well plates at a density of 5.000 cells per well and allowed 24 h. IC50 values of the *Papaver somniferum* L. extracts were administered and morphology alters of the cells were screened by phase contrast microscopy for 24 h every 6 h. Images of control and *Papaver somniferum* L. extracts treated cells were photographed at the end of the process using a digital camera attached to an inverted microscope.

RESULTS AND DISCUSSION

Antiproliferative effect of the *Papaver somniferum* L. extracts

The inhibitory effects of stem, capsule, root, and leaf extracts of the opium poppy on cancer cell lines were determined according to anticancer activity tests performed by using ELISA BrdU cell proliferation kit.

Table 2. IC50 (µg/mL) values of ethyl acetate (EPSR, EPSS, EPSL, and EPSC), hexane (HPSR, HPSS, HPSL, and HPSC), and methanol (MPSR, MPSS, MPSL, and MPSC) root, stem, leave and capsule extracts, respectively, of *Papaver somniferum* and positive control compound, 5FU on HeLa, HT29, C6, and Vero cell lines.

IC50 (µg/mL)	HT29	HeLa	C6	Vero
EPSR	225.62	120.52	170.60	113.98
HPSR	186.17	226.01	218.57	201.39
MPSR	128.90	118.76	203.49	170.30
5FU	91.23	82.16	94.21	88.74
EPSS	174.72	130.70	176.71	153.92
HPSS	219.97	209.60	271.50	190.82
MPSS	247.37	210.25	261.31	210.62
5FU	88.24	83.80	95.09	84.57
EPSL	195.17	264.40	146.69	134.34
HPSL	189.58	131.61	378.70	289.96
MPSL	212.95	174.62	155.38	143.25
5FU	84.26	86.54	91.44	85.71
EPSC	325.04	271.83	299.93	350.20
HPSC	348.79	290.18	323.67	376.11
MPSC	371.85	301.06	318.25	390.64
5FU	87.06	82.37	83.79	85.43

5-fluorouracil (5-FU) was used as a positive control for anticancer activity. Stem, root, and leaf extracts displayed significantly more anticancer activity than capsule extracts (Figure 1-2). IC50 values were determined by XLfit5 software using ELISA data (Table 2).
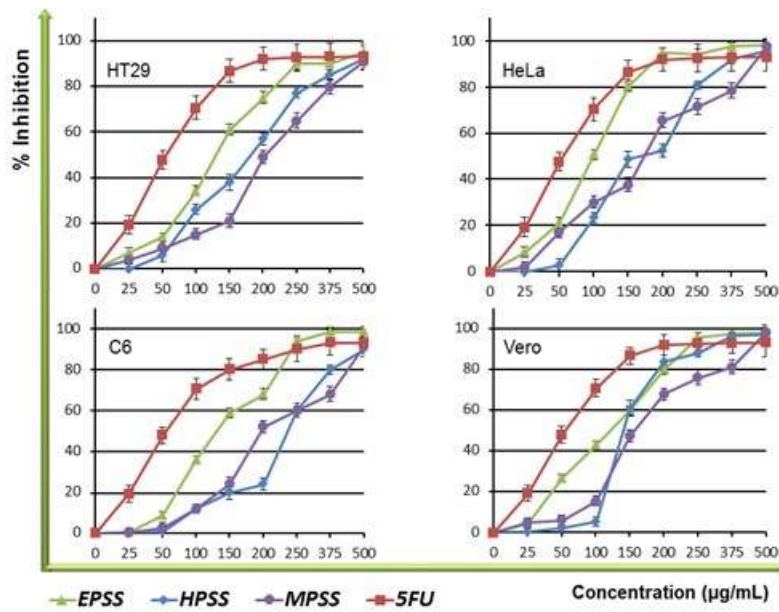
(A)
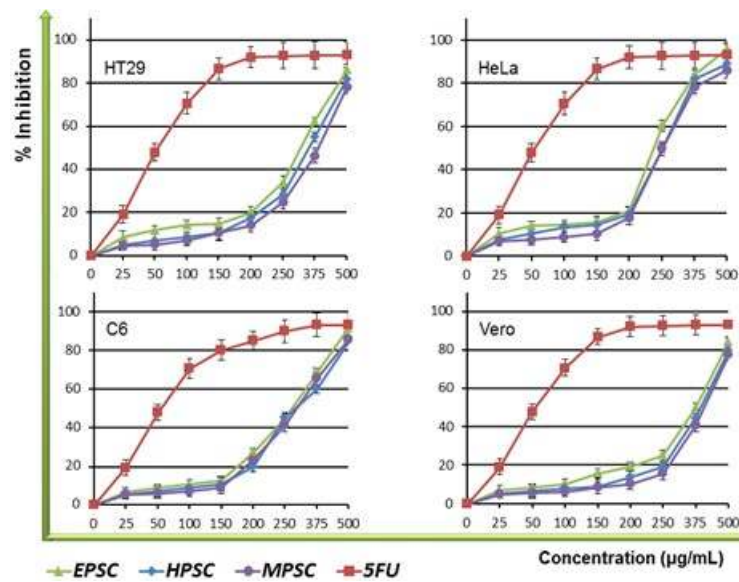
(B)

Figure 1. Antiproliferative effects of ethyl acetate (EPSS, EPSC), hexane (HPSS, HPSC), and methanolic (MPSS, MPSC) opium stem extracts (**A**) and opium capsule extracts (**B**), respectively, and positive control 5FU on HeLa, HT29, C6 and Vero cell lines. Cell proliferation measurement was carried out with BrdU cell ELISA kit. Inhibition percentage was reported as ± SEM value of three independent measurements (P < 0.05). Each experiment was triplicated for each cell line and r^2=0.85 to 0.97.
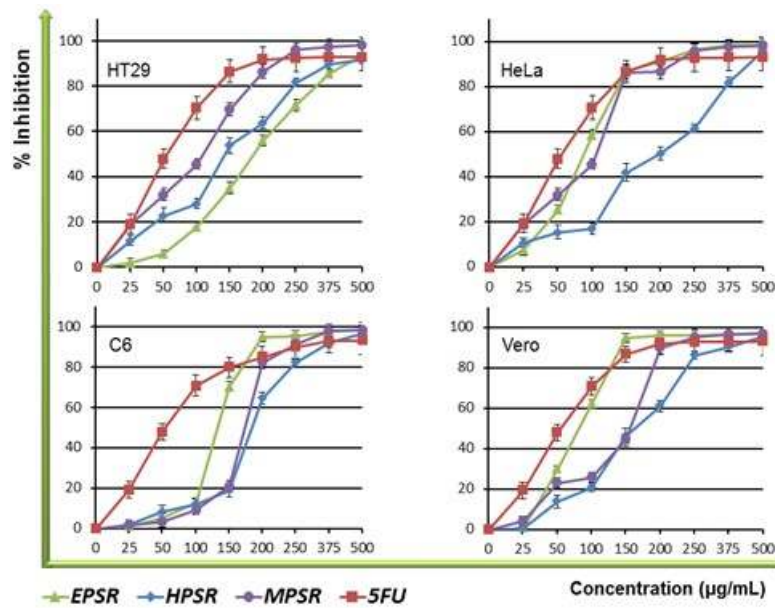
(A)
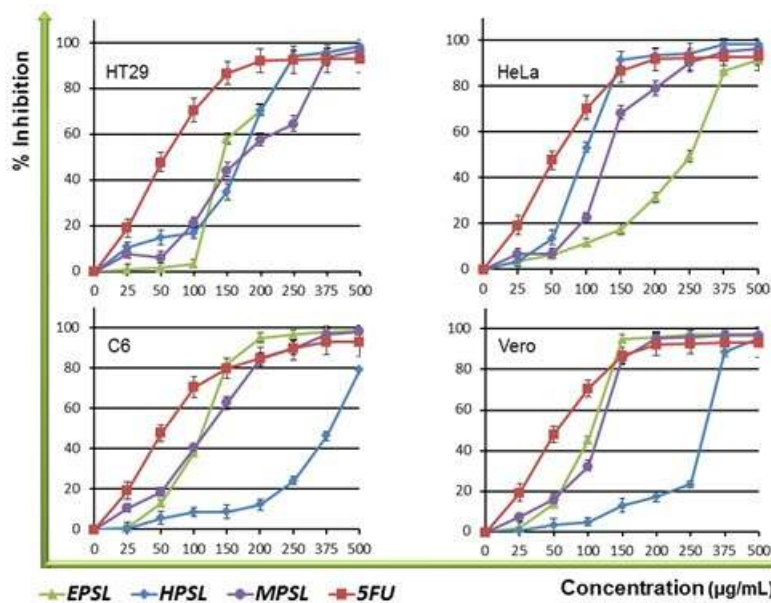
(B)

Figure 2. Antiproliferative effects of ethyl acetate (EPSR, EPSL), hexane (HPSR, HPSL), and methanolic (MPSR, MPSL) opium root extracts (**A**) and opium leave extracts (**B**), respectively, and positive control 5FU on HeLa, HT29, C6 and Vero cell lines. Cell proliferation measurement was carried out with BrdU cell ELISA kit. Inhibition percentage was reported as ± SEM value of three independent measurements (P < 0.05). Each experiment was triplicated for each cell line and r^2=0.85 to 0.97.

Data showed that cell lines were resistant to extracts up to at least 5FU. In addition, there was statistically significant difference (P < 0.05) among cancer cell lines compared to Vero cell

lines. According to IC50 values in Table 1, opium stem ethyl acetate extract (EPSS) displayed very strong anticancer activity on all cell lines. Opium stem hexane extract (HPSS) was effective only on Vero (190.82 µg/mL) cell line. Opium capsule extracts (EPSC, HPSC, MPSC) showed the least anticancer activity but low cytotoxicity. It is interesting to note that opium capsule displayed the lowest anticancer activity against the cells. The pharmacological activity of opium poppy is due to the major bioactive compounds such as morphine, codeine, tebaine, noscapine, papaverine and the capsule had the highest content of these bioactive compounds. However, one of them, noscapine, was responsible for their anticancer activity [18, 19]. Opium root ethyl acetate extract (EPSR) had anticancer activity on HeLa (120.52 µg/mL), C6 (170.60 µg/mL) and Vero (113.98 µg/mL) cell lines. Opium root hexane extract (HPSR) was effective only on HT29 (186.17 µg/mL) cell line, whereas the opium root methanol extract (MPSR) had quite a strong effect on both HT29 (128.90 µg/mL) and HeLa (118.76 µg/mL) cell lines. Opium leaf ethyl acetate extract (EPSL) showed highest anticancer activity on HT29 (195.17 µg/mL), C6 (146.69 µg/mL) and Vero (134.34 µg/mL) cell lines, while opium leaf methanolic extract (MPSL) had high anticancer activity on HeLa (174.62 µg/mL), C6 (155.38 µg/mL) and Vero (143.25 µg/mL) cell lines. Opium leaf hexane extract (HPSL) was effective only on HT29 (189.58 µg/mL) and HeLa (131.61 µg/mL) cell lines.

Cytotoxic activity of the *Papaver somniferum* L. extracts

Cytotoxic activities of various concentrations of opium plant extracts (25, 50, 100, 150, 200, 250, 375, and 500 µg/mL) on HeLa, HT29, C6 and Vero cell lines were measured using the LDH cytotoxicity kit. It was determined that there was cell membrane damage on high concentrations. Cytotoxicity results showed that only membranes of cells treated with high concentrations sustained significant damage and the same effect was not observed in lower concentrations (Figure 3-6). Figure 3 shows that opium stem hexane and methanol extracts (HPSS, MPSS) were not cytotoxic against HeLa, HT29 and Vero cells, but may induce necrosis against C6 cells. Probably, opium stem ethyl acetate extract (EPSS) was necrotic against all cells at 150 µg/mL or above concentrations. However, there is a significant application opportunity below that dose (Figure 3). Opium capsule ethyl acetate extract (EPSC) showed therapeutic promise at 200 µg/mL and below doses. Opium capsule hexane extract (HPSC) was safe for HT29 cell line at 250 µg/mL, but was quite toxic for C6 cells. The opium capsule methanolic extract (MPSC) at 250 µg/mL was likely not cytotoxic for HeLa, HT29 and Vero cell lines but was cytostatic (Figure 4). Opium root ethyl acetate extract (EPSR) had a cytotoxic effect on HeLa, HT29 and Vero cells at 150 µg/mL and above doses, but was cytotoxic at 50 µg/mL for C6 cell line. Opium root hexane and methanolic extract (HPSR, MPSR) were cytostatic at 100 µg/mL and below. It is possible that, they were necrotic for C6 cells at 150 µg/mL while necrotic for HeLa, HT29 and Vero cells at 200 µg/mL (Figure 5).
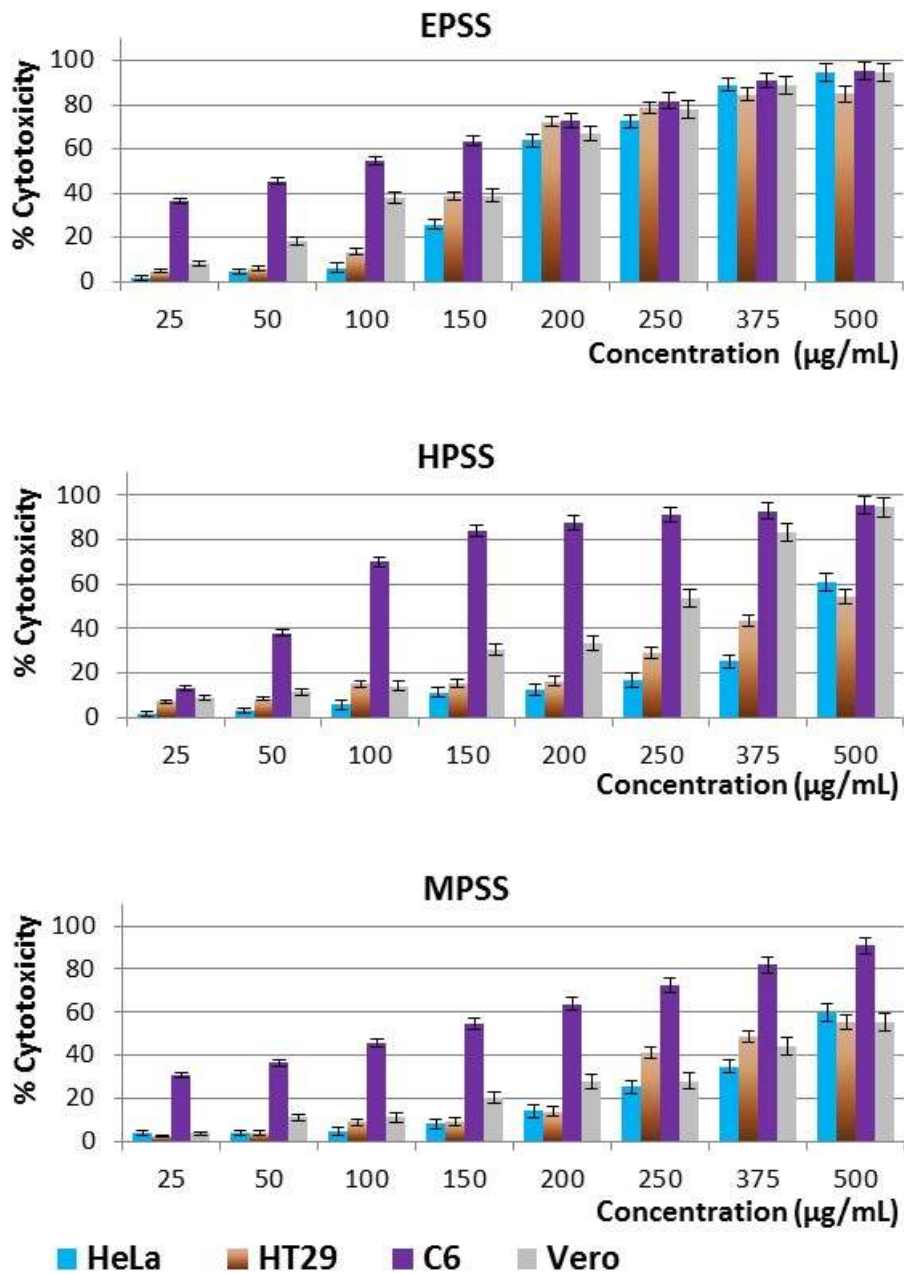
Figure 3. Cytotoxic effects of opium stem extracts on HeLa, HT29, C6 and Vero cell lines. Cell lines were incubated with extracts of varying concentrations for 24 hrs and cytotoxicity was determined using the LDH cytotoxicity kit. Inhibition percentage was reported as ± SEM value of three independent measurements (P < 0.05).
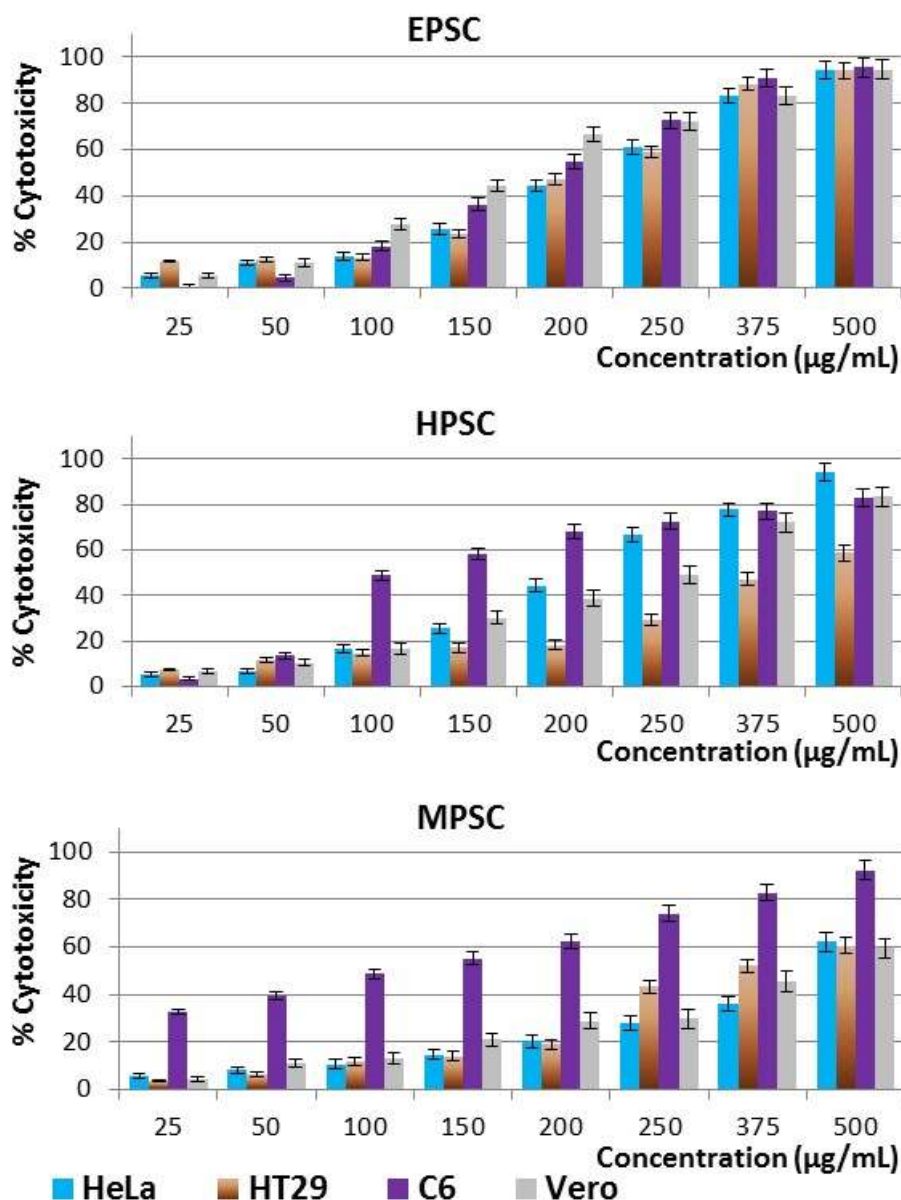
Figure 4. The cytotoxic effects of opium capsule extracts on HeLa, HT29, C6 and Vero cell lines. Cell lines were incubated with extracts of varying concentrations for 24 h and cytotoxicity was determined using the LDH cytotoxicity kit. Inhibition percentage was reported as ± SEM value of three independent measurements (P < 0.05).

It is known that the alkaloid contents of the opium poppy are very highly dynamic due to growth stages, environmental conditions and locations, plant diseases by fungi or bacteria, and parts and ages of plants. Our results showed that the opium extracts had high antiproliferative effects but caused toxic affects towards the cells (Figure 3-6). So it is not possible to evaluate opium extracts as a medical purpose. However, in the future, high noscapine (anticancer agent) and total antioxidant and phenolic content (protective agents) lines of opium poppy will be likely developed commercially to eliminate the alkaloid induced toxic effects.
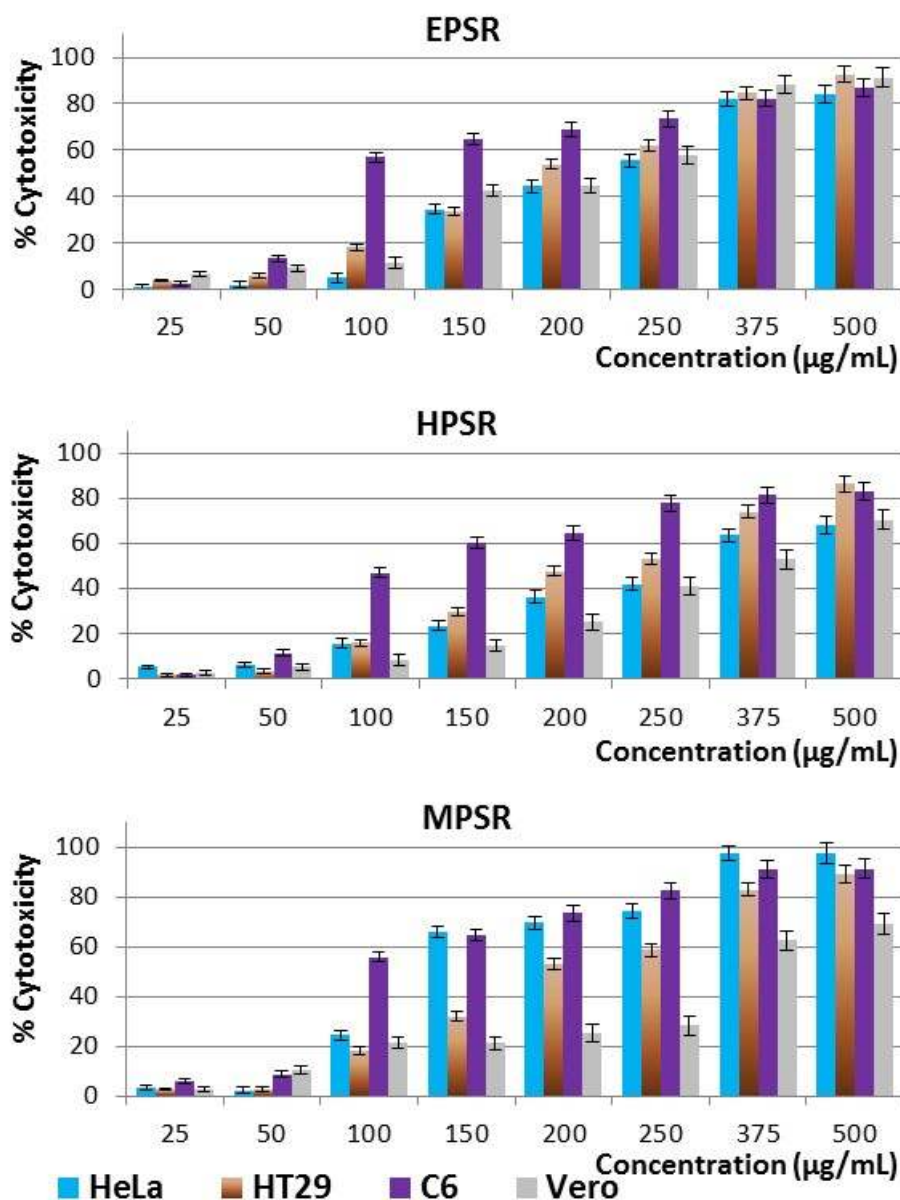
Figure 5. The cytotoxic effects of opium root extracts on HeLa, HT29, C6 and Vero cell lines. Cell lines were incubated with extracts of varying concentrations for 24 h and cytotoxicity was determined using the LDH cytotoxicity kit. Inhibition percentage was reported as ± SEM value of three independent measurements (P < 0.05).

Opium leaf ethyl acetate and methanolic extracts (EPSL, MPSL) were cytotoxic generally at 200 µg/mL and above concentrations, whereas the opium leaf hexane extract (HPSL) was safe up to 375 µg/mL. C6 cell line was the most effected from leaf extracts (50-150 µg/mL) while Vero and HT29 cell lines were the least effected (Figure 6). The fact that opium extracts displayed not very high cytotoxic activities while showing quite high antiproliferative properties indicates that these extracts could be used for further studies such as bioactivity-guided isolation and identification of active metabolites, preclinical and nonclinical studies.
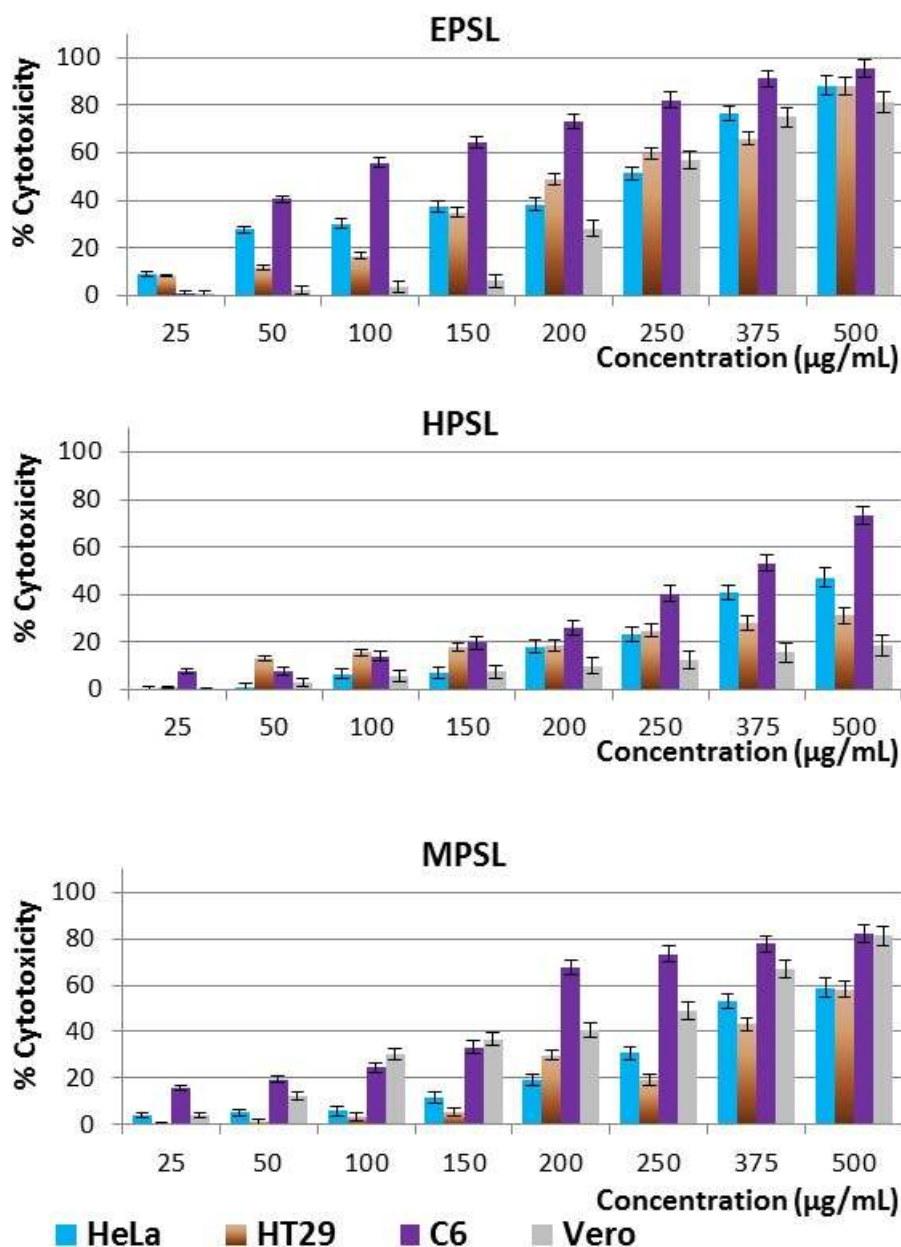
Figure 6. ***The c***ytotoxic effects of opium leaf extracts on HeLa, HT29, C6 and Vero cell lines. Cell lines were incubated with extracts of varying concentrations for 24 h and cytotoxicity was determined using LDH the cytotoxicity kit. Inhibition percentage was reported as ± SEM value of three independent measurements (P < 0.05).

Morphological assessment of the cytotoxic activity of the *Papaver somniferum* L. extracts

Effects of opium extracts on cell morphology were determined with a phase-contrast microscope with a digital camera attachment. The images show phase-contrast pictures of cell morphologies treated with various opium extracts compared to negative controls. Cell morphologies treated with opium extracts especially at high concentrations (>375 μg/mL) include cell rounding, mixing of cells with medium and then floating (indicates that the cells are dead), cytoplasmic bubbles, contraction, abnormal globular structures and apoptotic particles. Opium extracts could not inhibit cell growth at low concentrations (<75 μg/mL). At

these concentrations, normally growing cells and control cells display a confluent image with intact membrane integrity (Figure 7). Similar to control cells, a big majority of cells treated with opium extracts kept their starry or normal fibroblast looks. In general, 250 µg/mL and above doses caused separation of cells, smaller looking cells and decreasing cell numbers. In cells treated with opium extracts, medium and high concentrations resulted in cell morphologies similar to apoptosis and cellular damage seen in affected growth (Figure 7).
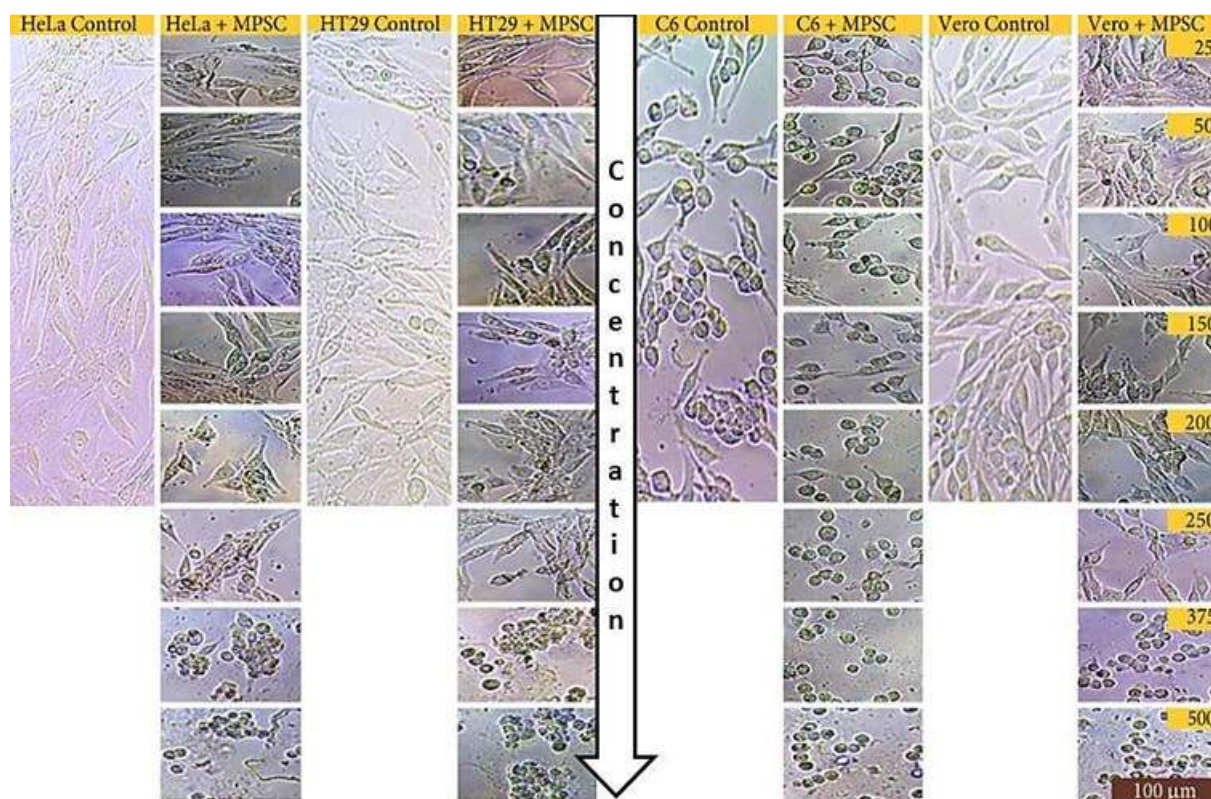
Figure 7. Effects of opium capsule's methanolic extracts on the morphologies of HeLa, HT29, C6 and Vero cell lines. Exponentially growing cells were incubated overnight with various concentrations of opium extracts at 37 °C. Control cells were treated with only DMSO. All measurements were 100 µm.

In this study, we have evaluated the biological activity of *P. somniferum* L. extracts. The findings showed that these extracts can inhibit cell proliferation and thus may create a new opportunity for the treatment of cancer diseases. Similar to other reports using various methods [18, 19], *P. somniferum* L. extracts generally exhibited the outstanding antiproliferative effect. Necrosis is an unprogrammed cell death and is the undesirable increased LDH leakage of plasma membrane. Hence, LDH assay results may imply that opium extracts show a low necrotic effect on the cells at therapeutic concentrations. Our findings showed that opium extracts caused high antiproliferative and low cytotoxic activities towards cell lines at IC50 concentrations; indicating they have significant potential as a useful medicine. Previous studies reported that these extracts have a similar effect with current chemotherapeutics in various cell lines [20, 21]. These extracts induced decrease in cell growth in culture through causing cell shrinkage and changing their astrocyte-like and

fibroblast-like structures to globular shape. Results show that different extraction methods applied to different plant parts yield different antiproliferative and cytotoxic effects on cells. However, it is possible to say that the extract containing the most effective metabolites in general is methanol extract. If the extraction method is disregarded, then the plant part with the most active ingredients is roots, while capsule contains the least active substances. The extract HPSL, EPSC and HPSC showed a potent antiproliferative activity and low cytotoxic effects against HeLa cancer cells, compared with that of Vero normal cells. However, the effects could differ depending on the cancer cell line, due to metabolic differences. In addition, growth conditions, maturity levels, and presence of various stresses may affect the amount and content of alkaloids and therefore the pharmacological potency of Papaver species [22-29]. Results of the present study exhibit extensive similarities with the results of similar studies in terms of statistics [30-32]. Other possible effects of these extracts are currently being investigated in our laboratory. Overall, we have demonstrated that these extracts may be used as chemotherapeutic and potentially valuable pharmacological agents.

ACKNOWLEDGMENTS

AUTHOR CONTRIBUTIONS

Conceived and designed the experiments: DAG AA IP. Performed the experiments: AA DAG. Analyzed the data: AA IP MK ŞT. Contributed reagents/materials/analysis tools: AA IP.

REFERENCES

1. World Cancer Report 2014. URL: http://www.iarc.fr/en/publications/books/wcr/wcr-order.php (accessed 16.04.16).

2. Elgorashi E. Screening of medicinal plants used in South African traditional medicine for genotoxic effects. Toxicol. Lett. 2003; 143, 195–207. doi:10.1016/S0378-4274(03)00176-0.

3. Fennell CW, Lindsey KL, McGaw LJ, Sparg SG, Stafford GI, Elgorashi EE, Grace OM, van Staden J. Assessing African medicinal plants for efficacy and safety: pharmacological screening and toxicology. J. Ethnopharmacol. 2004; 94, 205–217. doi:10.1016/j.jep.2004.05.012.

4. Sithranga Boopathy N, Kathiresan K. Anticancer Drugs from Marine Flora: An Overview. J. Oncol. 2010; 1–18. doi:10.1155/2010/214186.

5. Weerapreeyakul N, Nonpunya A, Barusrux S, Thitimetharoch T, Sripanidkulchai B. Evaluation of the anticancer potential of six herbs against a hepatoma cell line Chin. Med. 2012; 7, 15. doi:10.1186/1749-8546-7-15.

6. Lee CC, Houghton P. Cytotoxicity of plants from Malaysia and Thailand used traditionally to treat cancer. J. Ethnopharmacol. 2005; 100, 237–243. doi:10.1016/j.jep.2005.01.064.

7. Berrington D, Lall N. Anticancer Activity of Certain Herbs and Spices on the Cervical Epithelial Carcinoma (HeLa) Cell Line. Evidence-Based Complement. Altern. Med. 2012; 1–11. doi: 10.1155/2012/564927.

8. Itharat A, Houghton PJ, Eno-Amooquaye E, Burke P, Sampson JH, Raman A. In vitro cytotoxic activity of Thai medicinal plants used traditionally to treat cancer. J. Ethnopharmacol. 2004; 90, 33–38. doi: 10.1016/j.jep.2003.09.014.

9. Gürkök T, Parmaksız İ, Boztepe G, Kaymak E. Alkaloid biosynthesis Mechanism in Opium Poppy (*Papaver somniferum* L.). Electronic Journal of BioTechnology 2010; 1(2) 31-45. URL: http://teknolojikarastirmalar.com/pdf/tr/05_2010_1_2_89_569.pdf.

10 Parmaksiz I, Özcan S. Morphological, chemical and molecular analyses of Turkish Papaver accessions (Sect. Oxytona). Turk J. Bot. 2011; 35, 1-16. doi:10.3906/bot-1003-39.

11. Gürkök T, Kaymak E, Boztepe G, Koyuncu M, Parmaksız İ. Molecular characterization of the genus Papaver section Oxytona using ISSR markers. Turk J. Bot. 2013; 37:644-650. doi:10.3906/bot-1208-16.

12. Chen X, Dang T-TT, Facchini PJ. Noscapine comes of age. Phytochemistry 2015; 111, 7–13. doi: 10.1016/j.phytochem.2014.09.008.

13. Priyadarshani A, Chuttani K, Mittal G, Bhatnagar A. Radiolabeling, biodistribution and gamma scintigraphy of noscapine hydrochloride in normal and polycystic ovary induced rats. J. Ovarian Res. 2010; 3, 10. doi: 10.1186/1757-2215-3-10.

14. Mahmoudian M, Rahimi-Moghaddam P. The anti-cancer activity of noscapine: a review. Recent Pat. Anticancer. Drug Discov. 2009; 4, 92–7. doi:10.2174/157489209787002524.

15. Takeuchi R, Hoshijima H, Onuki N, Nagasaka H, Chowdhury SA, Kawase M, Sakagami H. Effect of anticancer agents on codeinone-induced apoptosis in human cancer cell lines. Anticancer Res. 2005; 25, 4037–41. PMID: 16309196.

16. Sueoka E, Sueoka N, Kai Y, Okabe S, Suganuma M, Kanematsu K, Yamamoto T, Fujiki H. Anticancer activity of morphine and its synthetic derivative, KT-90, mediated through apoptosis and inhibition of NF-kappaB activation. Biochem. Biophys. Res. Commun. 1998; 252, 566–70. doi:10.1006/bbrc.1998.9695.

17. Porstmann T, Ternynck T, Avrameas S. Quantitation of 5-bromo-2-deoxyuridine incorporation into DNA: an enzyme immunoassay for the assessment of the lymphoid cell proliferative response. J Immunol Methods 1985; 82(1): 169-79. doi:10.1016/0022-1759(85)90236-4.

18. Segal MS, Goldstein MM, Attinger EO. The use of noscapine (narcotine) as an antitussive agent. CHEST Journal. 1957; 32(3), 305-9. PMID: 13461774.

19. Joshi HC, Zhou J. Noscapine and analogues as potential chemotherapeutic agents. Drug News Perspect. 2000;13(9), 543-6. PMID: 12879125.

20. Anderson JT, Ting AE, Boozer S, Brunden KR, Danzig J, Dent T. Discovery of S-phase arresting agents derived from noscapine. J. Med. Chem. 2005; 48, 2756–2758. doi: 10.1021/jm0494220.

21. Aneja R, Vangapandu SN, Lopus M, Chandra R, Panda D, Joshi HC. Development of a novel nitro-derivative of noscapine for the potential treatment of drug-resistant ovarian cancer and T-cell lymphoma. Mol. Pharmacol. 2006; 69, 1801–1809. doi: 10.1124/mol.105.021899.

22. Boke H, Ozhuner E, Turktas M, Iskender I, Sebahattin O, Unver T. Regulation of the alkaloid biosynthesis by miRNA in opium poppy. Plant Biotech. 2015; 1-12. doi: 10.1111/pbi.12346. doi: 10.1111/pbi.12346.

23. Gurkok T, Turktas M, Parmaksiz I, Unver T. Transcriptome Profiling of Alkaloid Biosynthesis in Elicitor Induced Opium Poppy. Plant Mol. Biol. Report. 2015; 33, 673–688. doi:10.1007/s11105-014-0772-7.

24. Gümüşçü A, Arslan N, Sarıhan EO. Evaluation of selected poppy (Papaver somniferum L.) lines by their morphine and other alkaloids contents. Eur. Food Res. Technol. 2008; 226, 1213–1220. doi:10.1007/s00217-007-0739-0.

25. Dittbrenner LA, Mock H-P, Börner A, Lohwasser U. Variability of alkaloid content in Papaver somniferum. Journal of Applied Botany and Food Quality 2009; 82, 103-107. URL: http://pub.jki.bund.de/index.php/JABFQ/article/view/2087.

26. Krist S, Stuebiger G, Unterweger H, Bandion F, Buchbauer G. Analysis of Volatile Compounds and Triglycerides of Seed Oils Extracted from Different Poppy Varieties (Papaver somniferum L.). J. Agric. Food Chem. 2005; 53, 8310-8316, Oct. 2005. doi: 10.1021/jf0580869.

27. Musa Özcan M, Atalay Ç. Determination of seed and oil properties of some poppy (Papaver somniferum L.) varieties. Grasas y Aceites. 2006; 57. doi:10.3989/gya.2006.v57.i2.33.

28. Stranska I, Skalicky M, Novak J, Matyasova E, Hejnak V. Analysis of selected poppy (Papaver somniferum L.) cultivars: Pharmaceutically important alkaloids. Ind. Crops Prod. 2013; 41, 120-126. Doi:10.1016/j.indcrop.2012.04.018.

29. Choe S, Lee E, Jin G, Lee YH, Kim SY, Choi H, Chung H, Hwang BY, Kim S. Genetic and chemical components analysis of Papaver setigerum naturalized in Korea. Forensic Sci. Int. 2012; 222, 387-393. doi:10.1016/j.forsciint.2012.08.002.

30. Facchini PJ, De Luca V. Opium poppy and Madagascar periwinkle: model non-model systems to investigate alkaloid biosynthesis in plants. Plant J. 2008; 54, 763–784. doi:10.1111/j.1365-313X.2008.03438.x.

31. Alagöz Y, Gürkök T, Parmaksız İ, Ünver T. Identification and sequence analysis of alkaloid biosynthesisgenes in Papaver section Oxytona. TURKISH J. Biol. 2016; 40, 174–183. doi:10.3906/biy-1505-22.

32. Gurkok T, Ozhuner E, Parmaksiz I, Özcan S, Turktas M, İpek A, Demirtas I, Okay S, Unver T. Functional Characterization of 4'OMT and 7OMT Genes in BIA Biosynthesis. Front. Plant Sci. 2016; 7. doi:10.3389/fpls.2016.00098.

Papaver somniferum L.'nin Antikanser Aktivitesi

Döne Aslı Güler, Ali Aydın, Mesut Koyuncu, İskender Parmaksız[*], Şaban Tekin

Öz: Bu çalışmada *Papaver somniferum* L. (bir haşhaş türü) ekstraktlarının farmakolojik aktivitesi tarif edilmektedir. *P. somniferum* L. ürünleri hâlâ pek çok hastalık için benzersiz bir ilaç kaynağı olarak düşünülmektedir. Bu çalışmada *P. somniferum* L. ekstraktlarının HeLa (İnsan Rahim Ağzı Kanseri), HT29 (İnsan Kolorektal Adenokarsinoma), C6 (Sıçan Beyni Tümör Hücreleri) ve Vero (Afrika Yeşil Maymun Böbreği) hücre dizilerinde sitotoksik etkisi ve antiproliferatif etkisinin belirlenmesi için tasarımlar yapılmıştır. Alkaloidçe zengin *P. somniferum* L. ekstraktları çeşitli kanser hücre dizilerinde, özellikle yüksek derişimlerde antiproliferatif etkiler göstermiştir. Hücre zarlarına zarar vermek için *P. somniferum* L. ekstraktlarının yeteneklerini inceledik. Sonuçlara göre *P. somniferum* L. ekstraktları yüksek derişimde tümör hücre dizilerinde hücre zarını yok etmektedir. Dikkat çekici şekilde, LDH test sonuçları *P. somniferum* L.'nin hücreler üzerindeki sitotoksisitesinin orta düzey derişimlerde düşük olduğu bulunmuştur. Bu da ekstraktların sitostatik potansiyelini gösteriyor olabilir. Bu çalışmanın sonuçları *P. somniferum* L. ekstraktlarının antikanser araç olarak etkinliğini desteklemektedir.

Anahtar kelimeler: *Papaver somniferum* L.*, HT29, HeLa, Antikanser aktivitesi, Sitotoksik aktivite.

RESEARCH ARTICLE

Determination of the Trace Element Levels in Hair of Smokers and Non-Smokers by ICP-MS

Elif VARHAN ORAL

Dicle University, Faculty of Pharmacy, Department of Analytical Chemistry, TR-21280 Diyarbakir, Turkey

Abstract: For at least 50 years, determination of the trace element levels in human hair has been used to assess environmental and vocational exposure to toxic elements. As compared to other biological matrices (*e.g.* blood, urine), human hair is stable and therefore useful as a matrix. In this study, analyses of toxic and essential trace elements, such as Cd, Pb, Cu, and Fe were done in hair samples which we collected from male smokers (10 people) and non-smokers (10 people) who live in Diyarbakır, Turkey and concentrations in hair samples were compared. Hair samples were washed by a standard procedure proposed by the International Atomic Energy Agency. Then the samples were dried for 16 h at 110°C in an oven. Solubilization procedure was carried out by nitric acid-hydrogen peroxide mixture (3:1) in closed vessels in a microwave oven. Trace element analyses were carried out by using inductively coupled plasma-mass spectrometry (ICP-MS) technique. In this study, while concentrations of Cd, Pb, and Fe elements were found to be considerably higher in smokers than non-smokers, similar results were observed in Cu concentrations. The accuracy of the method was evaluated by applying spike method to samples. There was a good agreement between added and found analyte content. Analytical recovery values were determined between 91.2% and 104.6%. The values of R were found to be higher than 0.99.

Keywords: Human Hair, Smokers, Non-smokers, Trace Element, ICP-MS.

*Corresponding author. E-mail: evarhan@dicle.edu.tr.

INTRODUCTION

In recent years, the increasing environmental and vocational awareness of toxic elements has been seen. Being exposed to heavy metals can cause to poisoning and this fact can reveal significant threats to the human health and all living organisms (1). The heavy metals are accumulated inside cells that can cause several pathological changes, affection or death in the case of excessive poisoning (1).

Effect of environmental pollution on human health can be explained with some biological markers such as tooth, hair, and fingernail. Analyzing the hair samples taken from human ensured us the helpful information in order to analyze the changes in our bodies and it became successful in various applications. Analyzing the trace metals on hair samples has some advantages in comparison with the analyzing carried out by using blood or urine samples. The simplicity of matrix, presence of high concentration of trace elements, being collected, stored, and treated easily can be counted in the scope of mentioned advances of analyzing the trace metals on hair samples (2). Furthermore, precious information regarding our medical condition, the implementation of certain drugs and diagnosis about various diseases can be provided by the hair analysis. Thus, human hair analyzing became a significant method for understanding any of quantitative alterations about the certain elements within the human body (2).

The heavy metals are absorbed by tobacco supposedly from the soil as the natural environment of it and from the fertilizers, or pesticides which are used to protect the plant. The alternative environmental effects that can create an impact on the removal of toxic elements by using the plant of tobacco that contains some substances as pH of the soil, and contaminated irrigated water and sewage sludge that is used as fertilizer. Smoking the tobacco takes 87 kinds of organic carcinogens to the lungs as well as the toxic elements that can be parted during the smoke phase of combustion. Some metals [cadmium (Cd), nickel (Ni), and lead (Pb)] easily mix with blood stream and can accumulate within the body of particular organs as the kidney and liver (3). There can be mentioned some studies which were notified on the great diversities about the toxic elements in the compositions of commercial tobacco products where smoking-related troubles have been tried to be connected with toxic elements arisen from the burning of tobacco (3, 4).

Many different techniques such as graphite furnace atomic absorption spectrometry (GF-AAS) (5), flame atomic absorption spectrometry (F-AAS) (6), inductively coupled plasma optical emission spectrometry (ICP-OES) (7, 8), inductively coupled plasma mass spectrometry ICP-MS (9, 10) and X-ray fluorescence spectrometry (XRF) (11) are used in determining the levels of trace elements. ICP-MS, being one of these techniques, is used effectively and widely because of its high sensitivity, accuracy, wide dynamic range in determining of multiple elements at trace levels.

The aim of this study was evaluating the trace toxic and nutrient elements concentrations in the hair of human groups consist of smokers and non-smokers living in urban parts of the city of Diyarbakır. Ten (10) smoker and ten (10) non-smoker male individuals were chosen as referents in order to perform a comparative study. Trace elements levels were determined by ICP-MS, prior to microwave acid digestion. The precision and accuracy of the method was evaluated by applying spike method to solutions.

MATERIALS and METHODS

Instrument

Agilent 7700X model ICP-MS was used for finding the trace elements within the hair samples. The operating conditions for this device are shown in Table 1. The solubilization procedure of hair samples before the analysis was carried out in Milestone Start D brand microwave oven which has the PTFE vessels.

Reagents and Solution

18.2 MΩ deionized water was used in all experiments and also nitric acid (Merck) and hydrogen peroxide (Merck) were used in the procedure of solubilization. All used reagents were analytical grade. ^{6}Li, ^{45}Sc, ^{72}Ge, ^{115}In, and ^{209}Bi in the concentration of 100 mg/L were used as mix internal standard (Matrix: %10 HNO_3, Agilent technologies) in ICP-MS measurements. The calibration graphs were prepared by diluting in the concentration range of 0-100 μg/L from the standard of mix about 10 mg/L for the metals.

Sample Collection

The hair samples were collected from the male individuals live initially in the city center of Diyarbakır. Totally 20 healthy individuals consist of 10 smoker individuals and 10 non-smoker individuals from the volunteers informed about the research were added to the research randomly. The hair samples (approximately 1 g) were taken from the points in nape which are near scalp area by cutting with steel scissors. Hair samples were washed with acetone/water (1:3) according to the International Atomic Energy Agency to remove external contamination (12). The washed samples were dried in an oven at 110 °C about 16 hours.

Table 1: Optimum operating conditions of ICP-MS for analyzing the samples.

Instrument parameter	Condition
RF power	1550 W
RF frequency	27.12 MHz
RF Matching	1.80 V
Carrier gas (inner)	1.1 L/min
Makeup Gas	0.9 L/min
Plasma gas	Ar X50S 5.0
Plasma gas flow (Ar)	15 L/min
Nebulizer pump	0.1 rps
Sample intake	0.5 mL/min
Spray chamber temperature	2 °C
Resolution m/z	244 amu
Background	<5 cps (9 amu)
Short-term stability	<3% RSD
Long-term stability	<4% RSD/2 h
Isotopes measured	^{111}Cd, ^{208}Pb, ^{56}Fe, ^{63}Cu

Analytical Methods

The amount about 0.2 g from each of dried hair samples was weighed and concentrated nitric acid (6 mL) and hydrogen peroxide (2 mL) at analytical purity were added (3:1 ratio) and it was made soluble in the microwave oven system. Afterwards, it was taken to the volumetric containers and last volumes of it were completed until 15 mL with deionized water. The samples were stored in refrigerator until the measurement was carried out. The trace elements measurements were carried out with the method of ICP-MS.

Method Validation

Known amounts of the analytes were spiked to the solutions in order to evaluate the accuracy of the method. The results are given in Table 2. Good agreement was obtained between added and found analyte contents using the recommended procedure and recovery values were between 91.2 and 104.6 percent, which is within expected ICP-MS performance.

Table 2: Spike recovery values for Cd, Pb, Fe and Cu

Elements	Added (µg/L)	Found (µg/L)	Recovery (%)
Cd	50.0	45.6 ± 1.37	91.2
Pb	50.0	47.5± 1.42	95.0
Fe	50.0	51.3± 2.05	102.6
Cu	50.0	52.3± 2.61	104.6

[mean ± SD, n=3]

Analytical Figures of Merit

The quantitation of the analytes was performed by using the calibration curve method for each analyte, the calibration curves were prepared from the standard solutions of the analytes. The correlation coefficients were obtained at least 0.9993. The limits of detection (LOD=3s) and limits of quantification (LOQ=10s) for four metals were also calculated by analyzing 3 blank solutions. The linear range of calibration graph drawn under the optimized conditions functioning for four elements and values of R, LOQ and LOD are shown in Table 3.

Table 3: Parameters of merit for ICP-MS.

Elements	Linear range (µg/kg)	Regression	R^2	LOD (µg/kg)	LOQ (µg/kg)
Cd	0-100	y= 0.0344 x + 0.0280	0.9993	0.0103	0.0310
Cu	0-100	y= 0.0662 x + 0.1028	0.9999	1.0200	3.0600
Fe	0-100	y= 0.3359 x + 4.6289	0.9999	2.3108	6.9324
Pb	0-100	y= 0.1861 x + 0.2314	0.9996	0.0832	0.2777

R=Correlation coefficient , LOD= Limit of detection, LOQ=Limit of quantification

RESULTS and DISCUSSION

The metal analysis results of smokers and non-smokers hair samples are given in Figure 1-4.
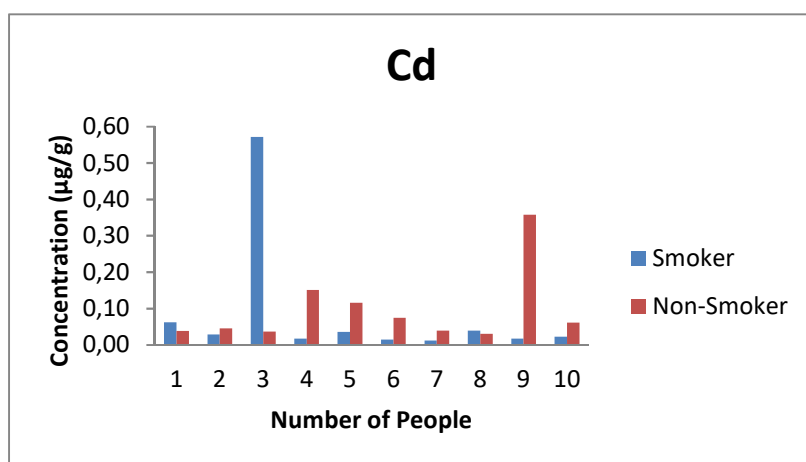
Figure 1: Cd concentrations of smokers and non-smokers.
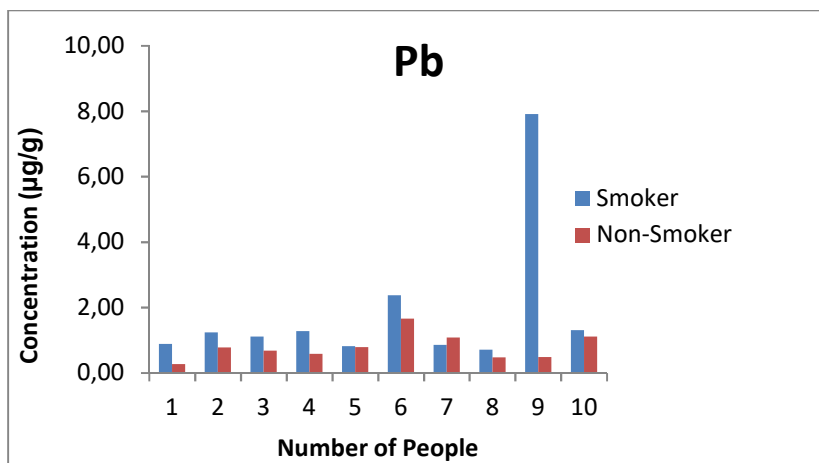
Figure 2: Pb concentrations of smokers and non-smokers.
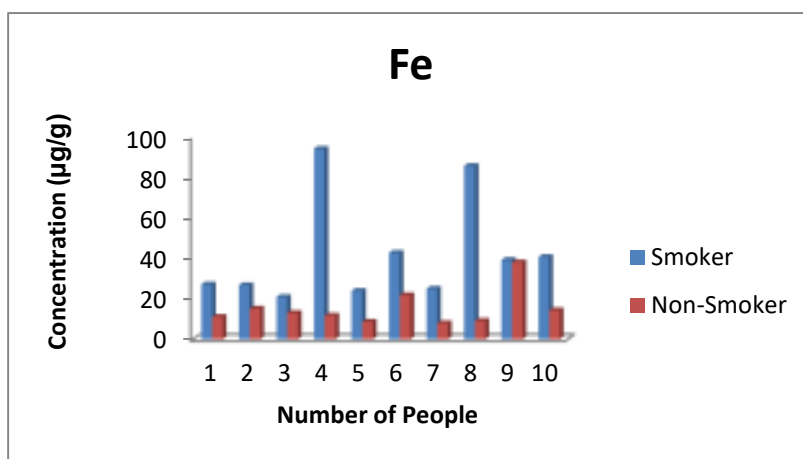
Figure 3: Fe concentrations of smokers and non-smokers**.**
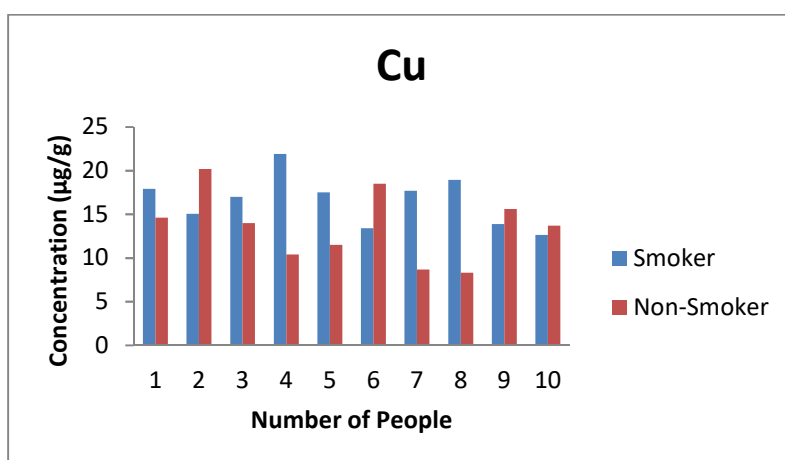
Figure 4: Cu concentrations of smokers and non-smokers.

Mean values of the metal analysis of smokers and non-smokers hair samples are given in Table 4.

Table 4: Comparisons between smokers and non-smokers in relation to levels Cd, Pb, Fe and Cu in hair samples.

Individuals	n	Cd (µg/g)	Pb (µg/g)	Fe (µg/g)	Cu (µg/g)
Smokers	10	0.140 ± 0.04	1.85 ± 0.05	42.59± 1.28	16.59± 0.49
Non-Smokers	10	0.037±0.001	0.79 ± 0.01	15.07 ± 0.45	13.55± 0.41

Analyzed metals content [mean ± SD, n=3]

Cadmium is one of very scarce metals within the soil as in the atmosphere. Cadmium enters the body through respiration and digestion. 15-30% of cadmium taken through respiration is absorbed. One of the most important cadmium sources is cigarette, in a single of which there is 1-2 µg of cadmium. 10% of this amount (0.1-0.2 µg) is taken through inhalation. Besides, cadmium is also present in the inhaled environmental atmosphere (13). Cadmium is able to affect kidney, lung, and gastrointestinal system. Long-term low-dose Cd exposure leads to bone loss. Low birth weight, skeletal abnormalities, behavioral and learning problems were observed in animals exposed to Cd during the prenatal period. It was observed in animal testing that Cd exposure during pregnancy period affected mostly the nervous system (14, 15). Hair is one of the tissues, where heavy metals such as cadmium are removed out of the body (16, 17). The differences were found significant while the cadmium levels in collected hair samples were compared between smokers and non-smokers in this study. Mean Cd levels of male smokers (0.140 µg/g) were found to be nearly 4 times higher than those of non-smokers (0.037 µg/g) as seen in Table 4. Sukumar and Subramanian found that the amount of Cd (1.7 µg/g) in the hair samples of smokers was higher than that of non-smokers (0.5 µg/ g) (18). Özden *et al*. found Cd level of hair high in children whose schools are near the main street and live in centrally heated houses. Furthermore, as the number of smokers in the house increases, they stated that the rate of determination of Cd level in hair increased, too (19). It was emphasized that the external environment activities, the season and the Cd amount in potable water are important exogenic sources determining the Cd level of hair (14, 20).

Lead is an element existing naturally in nature. An important part of lead in the body is taken by means of foods. Potable water, old houses, and smoking may lead to exposure

to toxic lead. While the lead enters into the body, it mixes with blood stream and starts entering into bone tissues, soft tissues, and the brain (21, 22). Exposure to excessive lead reveals itself with lead poisoning. As symptoms, diagnosis is established with weakness, tiredness, stomachache, anaemia, and sensitiveness. Lead poisoning affects functions of central nervous system in children more (22). It was found in this study that the mean level of Pb (1.85 µg/g) accumulating in hair of smokers was 2.5 times more than mean level of Pb (0.79 µg/g) in hair of non-smokers (Table 4). Many studies, by supporting our study, show that Pb amount in hair samples of smokers is higher than that of non-smokers (19, 23, 24). In a study done on smoker mothers by Serdar *et al*. they expressed that there was a significant connection between smoking levels of mothers and concentrations of toxic element (especially Pb) in hair. Furthermore, it is found in the same study that although mothers said they did not smoke around their children, Pb amount in hair of their children was in high concentrations (23). In another study done on school children between the ages 11-13 by Özden *et al*. They determined higher levels of Pb in hair as the number of smokers in the house increased (25). When Mortada *et al*. compared levels of Pb in hair of smokers and non-smokers between the ages 25-35 in Egypt; they found the level of Pb in the hair of smokers significantly high (26).

Iron is an essential trace element which exists in especially the structure of red blood cells in the human organism and is important in terms of being a functional part of hemoglobin. Besides, iron is a vital mineral present in the myoglobin of muscles, the cytochrome, peroxidase, and catalase systems. Iron has important tasks in terms of biochemical reactions especially in terms of respiratory system (22).

Copper is an important element nutritionally and in terms of toxicity (23). The copper is the basic component of hair, skin flexible parts, bone and some internal organs as well as being important in terms of bodily functions. Copper, which is present by average 50-120 mg in adult people, is essential element of reactions of amino acids, fatty acids and vitamins in metabolism under normal conditions. Copper, which exists in the structure of many enzymes and proteins, takes on a task of activator for iron to carry out its functions. In the event of copper deficiency, abnormalities, anemia, bone problems, and nervous system disorders were detected in animals (27).

Metals tied to enzymes such as Cu and Fe exist in tissues with high rates (28). In this study, these elements were also found in high concentrations in hair samples as seen in

Table 4. When Fe and Cu levels were compared while the mean Fe level (42.59 µg/g) of smokers was found to be approximately 3 times higher than non-smokers (15.07 µg/g), the mean Cu level (16.59 µg/g) of smokers was found to be similar to that (13.55 µg/g) of non-smokers. In the study of Serdar *et al.,* by supporting our study, Fe amount was found high in hair of children who live in smoking houses (23). Samanta *et al.* found Fe amount in hair samples as 69.50 µg/g and Cu amount as 14.76 µg/g in their study (28) . Szynkowska *et al*. found Cu level as 10.23 µg/g in hair samples of smokers and as 9.40 µg/g in those of non-smokers in the study in 2015 (1); Sukumar and Subramanian found Cu level as 13.8 µg/g in hair samples of smokers and as 14.8 µg/g in those of non-smokers in the study in 2007 (18).

CONCLUSIONS

In this study, while the concentrations of toxic trace elements (Cd, Pb) and essential element (Fe) were found to be considerably higher in smokers than non-smokers, Cu which is nutritionally and toxicologically important element concentration was found similar. Applying spike method to samples assured the accuracy of the method. Good agreement was obtained between added and found analyte contents using the recommended procedure. Recovery values were between 91.2% and 104.6%, thus it is possible to conclude that no analyte loss and no contamination were occured during the whole procedure. The value of R to be bigger than 0.99 was evaluated as " the linearity of acceptability". The analyte contents in the hair samples were clearly higher than the detection limits observed.

REFERENCES

1.   Szynkowska MI, Marcinek M, Pawlaczyk A, Albińska J. Human hair analysis in relation to similar environmental and occupational exposure. Environmental Toxicology and Pharmacology. 2015;40(2):402-8. DOI: 10.1016/j.etap.2015.07.005.

2.   Szynkowska M, Pawlaczyk A, Wojciechowska E, Sypniewski S, Paryjczak T. Human hair as a biomarker in assessing exposure to toxic metals. Pol J Environ Stud. 2009;18:1151-61. URL: http://www.pjoes.com/pdf/18.6/1151-1161.pdf.

3.   Afridi HI, Kazi TG, Brabazon D, Naher S. Interaction between zinc, cadmium, and lead in scalp hair samples of Pakistani and Irish smokers rheumatoid arthritis subjects in relation to controls. Biological Trace Element Research. 2012;148(2):139-47. DOI: 10.1007/s12011-012-9352-6.

4.   Witte KK, Clark AL, Cleland JG. Chronic heart failure and micronutrients. Journal of the American College of Cardiology. 2001;37(7):1765-74. DOI: 10.1016/S0735-1097(01)01227-X.

5.   Kalny P, Fijałek Z, Daszczuk A, Ostapczuk P. Determination of selected microelements in polish herbs and their infusions. Science of the Total Environment. 2007;381(1):99-104. DOI: 10.1016/j.scitotenv.2007.03.026.

6.   Maiga A, Diallo D, Bye R, Paulsen BS. Determination of some toxic and essential metal ions in medicinal and edible plants from Mali. Journal of Agricultural and Food Chemistry. 2005;53(6):2316-21. DOI: 10.1021/jf040436o.

7.   Başgel S, Erdemoğlu S. Determination of mineral and trace elements in some medicinal herbs and their infusions consumed in Turkey. Science of the Total Environment. 2006;359(1):82-9. DOI: 10.1007/BF02167998.

8.   Malik J, Szakova J, Drabek O, Balik J, Kokoska L. Determination of certain micro and macroelements in plant stimulants and their infusions. Food Chemistry. 2008;111(2):520-5.7. DOI: 10.1016/j.foodchem.2008.04.009.

9.   Nookabkaew S, Rangkadilok N, Satayavivad J. Determination of trace elements in herbal tea products and their infusions consumed in Thailand. Journal of Agricultural and Food Chemistry. 2006;54(18):6939-44. DOI: 10.1021/jf060571w.

10.   Raman P, Patino LC, Nair MG. Evaluation of metal and microbial contamination in botanical supplements. Journal of Agricultural and Food Chemistry. 2004;52(26):7822-7. DOI: 10.1021/jf049150+.

11.   Bumbálová A, Komová M, Dejmková E. Identification of elements in plant drugs and their water infusion using X-ray fluorescence analysis. Journal of radioanalytical and nuclear chemistry. 1992;166(1):55-62. DOI: 10.1007/BF02167998.

12.   Deppisch LM, Centeno JA, Gemmel DJ, Torres NL. Andrew Jackson's exposure to mercury and lead: poisoned president? Jama. 1999;282(6):569-71. DOI: 10.1001/jama.282.6.569.

13.   Cogun HY, Firat O. Sigara İçen ve İçmeyenlerin Saç ve Tırnaklarında Kadmiyum Düzeyleri. Ekoloji. 2013;22(89):84-8. DOI: 10.5053/ekoloji.2013.8910.

14.   Örün E, Yalçın SS. Kurşun, Civa, Kadmiyum: Çocuk Sağlığına Etkileri ve Temasın Belirlenmesinde Saç Örneklerinin Kullanımı. Ankara Üniversitesi Çevrebilim Dergisi. 2011; 3(2): 73-81. URL: http://dergiler.ankara.edu.tr/dergiler/47/1665/17771.pdf.

15.   Ali M, Murthy R, Chandra S. Developmental and longterm neurobehavioral toxicity of low level in-utero cadmium exposure in rats. Neurobehavioral Toxicology & Teratology. 1986;8(5):463-8. URL: http://psycnet.apa.org/psycinfo/1988-03688-001.

16.   Diez S, Montuori P, Querol X, Bayona JM. Total mercury in the hair of children by combustion atomic absorption spectrometry (Comb-AAS). Journal of analytical toxicology. 2007;31(3):144-9. DOI: 10.1093/jat/31.3.144.

17.   Rodrigues JL, Batista BL, Nunes JA, Passos CJ, Barbosa F. Evaluation of the use of human hair for biomonitoring the deficiency of essential and exposure to toxic elements. Science of the Total Environment. 2008;405(1):370-6. DOI: 10.1016/j.scitotenv.2008.06.002.

18.   Sukumar A, Subramanian R. Relative element levels in the paired samples of scalp hair and fingernails of patients from New Delhi. Science of the Total Environment. 2007;372(2):474-9. DOI: 10.1016/j.scitotenv.2006.10.020.

19.   Özden T, Kılıc A, Toparlak D, Gökçay G, Saner G. Blood lead levels in school children. Indoor and Built Environment. 2004;13(2):149-54. DOI: 10.1177/1420326X04038838.

20.   Seifert B, Becker K, Helm D, Krause C, Schulz C, Seiwert M. The German Environmental Survey 1990/1992 (GerES II): reference concentrations of selected environmental pollutants in blood, urine, hair, house dust, drinking water and indoor air. Journal of Exposure Analysis & Environmental Epidemiology. 2000;10(6 Pt 1):552-565. DOI: 10.1038/sj.jea.7500111.

21.   Demir N, Göktürk T, Akçay O. Bazı Kozmetik Ürünlerde Ağır Metal (Pb, Cd) Tayini. SDU Journal of Science (E-Journal). 2014;9(2):194-200. URL: http://dergipark.ulakbim.gov.tr/sdufen/article/download/1089005098/1089004056.

22.   Güler Ç, Çobanoğlu Z. Kimyasallar ve Çevre. Ankara, Sağlık Bakanlığı. 1997. URL: http://www.acilafet.org/upload/dosyalar/kimyasallarvecevre.pdf.

23.   Serdar MA, Akin BS, Razi C, Akin O, Tokgoz S, Kenar L, Aykut O. The correlation between smoking status of family members and concentrations of toxic trace elements in the hair of children. Biological Trace Element Research. 2012;148(1):11-7. DOI: 10.1007/s12011-012-9337-5.

24.   Wolfsperger M, Hauser G, Gößler W, Schlagenhaufen C. Heavy metals in human hair samples from Austria and Italy: influence of sex and smoking habits. Science of the Total Environment. 1994;156(3):235-42. DOI: 10.1016/0048-9697(94)90190-2.

25.   Özden TA, Gökçay G, Ertem HV, Süoğlu ÖD, Kılıç A, Sökücü S, Saner G. Elevated hair levels of cadmium and lead in school children exposed to smoking and in highways near schools. Clinical biochemistry. 2007;40(1):52-6. DOI: 10.1016/j.clinbiochem.2006.07.006.

26.   Mortada WI, Sobh MA, El-Defrawy MM. The exposure to cadmium, lead and mercury from smoking and its impact on renal integrity. Medical Science Monitor. 2004;10(3):CR112-CR6.

27.   Kartal G, Güven A, Kahvecioğlu Ö, Timur S, Metalurji İ. Metallerin Çevresel Etkileri-II. Metalurji Dergisi. 2004;137:46-51.

28.   Samanta G, Sharma R, Roychowdhury T, Chakraborti D. Arsenic and other elements in hair, nails, and skin-scales of arsenic victims in West Bengal, India. Science of the Total Environment. 2004;326(1):33-47. DOI: 10.1016/j.scitotenv.2003.12.006.

RESEARCH ARTICLE

Türkçe Öz ve Anahtar Kelimeler
Sigara İçen ve İçmeyen Kişilerde Eser Element Seviyelerinin ICP-MS ile Belirlenmesi

Öz: En az 50 yıldır, insan saçındaki eser element seviyelerinin belirlenmesi çevresel ve mesleki anlamda zehirli elementlere maruziyetin değerlendirilmesi için kullanılmaktadır. Diğer biyolojik matrislere (örneğin kan, idrar) nazaran, insan saçı kararlıdır ve bu nedenle de bir matris olarak faydalıdır. Bu çalışmada Diyarbakır ilinde yaşayan, sigara içen (10 kişi) ve içmeyen (10 kişi) erkeklerden topladığımız saç örneklerinde Cd, Pb, Cu ve Fe gibi toksik ve besleyici eser elementlerin analizleri yapıldı ve saç örneklerindeki konsantrasyonları karşılaştırıldı. Saç örnekleri, Uluslararası Atom Enerjisi Kurumu tarafından önerilen standart prosedüre göre yıkandı ve 16 saat 110 °C' de etüvde kurutuldu. Çözünürleştirme işlemi, nitrik asit-hidrojen peroksit karışımı (3:1) ile kapalı tüplerde mikrodalga fırında gerçekleştirildi. Eser element analizleri ICP-MS tayin tekniği ile gerçekleştirildi. Çalışmada Cd, Pb, Fe elementlerinin konsantrasyonları sigara içen kişilerde içmeyenlere oranla önemli derecede yüksek bulunurken, Cu konsantrasyonunda benzer sonuçlar gözlendi. Örnek numunelere spike yöntemi uygulanarak metodun doğruluğu ve kesinliği kontrol edildi. Eklenen ve bulunan analit içerikleri arasında iyi bir ilişki bulundu. Analitik geri kazanım sonuçları % 91.2 ile % 104.6 arasında belirlendi. R değerleri 0.99'dan büyük bulundu.

Anahtar Kelimeler: İnsan Saçı , Sigara İçen Kişiler, Sigara İçmeyen Kişiler, Eser Element, ICP-MS**.**

Gönderme: 19 Temmuz 2016. **Düzeltme:** 09 Ağustos 2016. **Kabul:** 03 Eylül 2016.

Theoretical and Spectroscopic Studies of (*E*)-3-Benzyl-4-((4-Isopropylbenzylidene)-Amino)-1-(Morpholinomethyl)-1*H*-1,2,4-triazol-5(4*H*)-one Molecule

Gül Kotan[1*], Haydar Yüksek[2]

[1]Vocational School, Kafkas University, 36100, Kars, Turkey.
[2]Department of Chemistry, Kafkas University, 36100, Kars, Turkey.

Abstract: In this study, (*E*)-3-benzyl-4-((4-isopropylbenzylidene)-amino)-1-(morpholinomethyl)-1*H*-1,2,4-triazol-5(4*H*)-one (**1**) was synthesized by the reaction of 3-benzyl-4-(4-isopropylbenzylidenamino)-4,5-dihydro-1*H*-1,2,4-triazol-5-one with morpholine and formaldehyde. The structure of compound **1** was determined by FT-IR, ^{1}H-NMR, ^{13}C-NMR spectral data. Then, the synthesized compound **1** was optimized by using the B3LYP/6-31G (d,p) and HF/6-31G (d,p) basis sets. ^{1}H-NMR and ^{13}C-NMR isotropic shift values, IR absorption frequencies, bond angles, bond lengths, HOMO-LUMO energy, electronegativity, and Mulliken charges were calculated theoretically by using the program package Gaussian G09W. In addition, IR, ^{1}H-NMR, ^{13}C-NMR theoretical spectral data were compared with certain experimental data.

INTRODUCTION

Mannich bases have applications the field of medicinal chemistry, the product synthetic polymers, the petroleum industry, as products used in water treatment, cosmetics, the dyes industry, *etc* [1]. On the other hand, quantum chemical calculation methods have widely been used to theoretically predict the structural, spectroscopic, thermodynamic, and electronic properties of molecular systems. The quantum chemical calculation methods provide support for experimental structural and spectroscopic studies [2–7].

In this study, (*E*)-3-benzyl-4-((4-isopropylbenzylidene)-amino)-1-(morpholinomethyl)-1*H*-1,2,4-triazol-5(4*H*)-one (**1**) molecule, which was obtained from the reaction of 3-benzyl-4-(4-isopropylbenzylidenamino)-4,5-dihydro-1*H*-1,2,4-triazol-5-one   with morpholine and formaldehyde (**Scheme 1**). The compound **1** was optimized by using the B3LYP/6-31G (d,p) and HF/6-31G (d,p) basis sets [8,9]. This optimized structure was used to research the other different theoretical properties of the main compound.^{1}H-NMR and ^{13}C-NMR isotropic shift values were calculated by the method of GIAO using the program package Gaussian G09W [9]. Experimental and theoretical values were inserted into the graphic according to equitation δ exp=a+b. δ calc. The standard error values were found via SigmaPlot program with regression coefficient of a and b constants. Then, they were compared with certain experimental data, which are shown to be accurate. The veda4f program was used in defining IR data calculated theoretically [10]. IR absorption frequencies of analyzed molecule were calculated by two methods. Infrared spectra were composed by using the data obtained from both methods. IR absorption frequencies were multiplied by the appropriate adjustment factors B3LYP / 631G(d,p) 0.9688 and HF/631G (d, p) 0.9059 [11]. Furthermore, bond angles, bond lengths, the highest occupied molecular orbital (HOMO) energies, the lowest unoccupied molecular orbital (LUMO) energies, electronegativity and Mulliken charges of this compound was found.
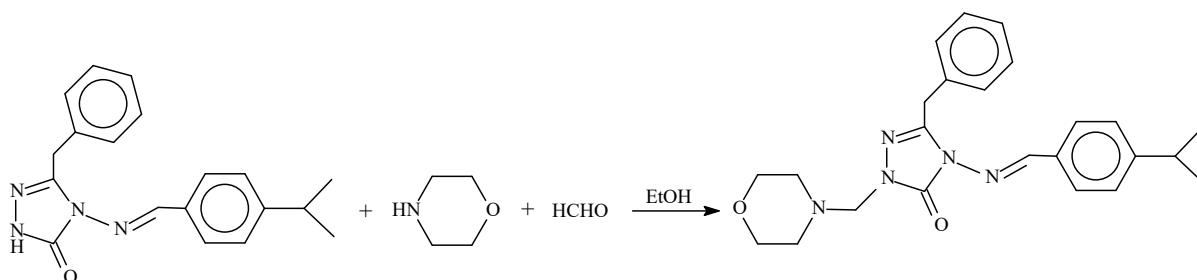
Scheme 1

MATERIALS AND METHODS

Experimental: The synthesis of *((E)-3-benzyl-4-((4-isopropylbenzylidene)-amino)-1-(morpholinomethyl)-1H-1,2,4-triazol-5(4H)-one* (1): 3-Benzyl-4-(4-ethylbenzylidenamino)-4,5-dihydro-1*H*-1,2,4-triazole-5-one (5 mmol) was dissolved in

absolute ethanol and to this solution were added formaldehyde (%37, 10 mmol) and morpholine (6 mmol). The reaction mixture was refluxed for 4 hours. The mixture was left at room temperature overnight. Then, the mixture was cooled in the -18 ^{0}C refrigerator. The solid formed was obtained by filtration, washed with cold ethanol and recrystallized from ethanol. Melting points were checked on WRS-2A Microprocessor Melting-Point Apparatus. The FTIR spectra were measured on an Alpha-P Bruker FT-IR Spectrometer. ^{1}H- and ^{13}C-NMR spectra were recorded in deuteriated dimethyl sulfoxide with TMS as internal standard on a Bruker 400 MHz spectrometer, respectively. Yield 89%; m.p: 120 ^{0}C; FTIR (KBr, cm^{-1}): 1692 (C=O), 1602, 1586 (C=N), 835 (1,4-disubstituted benzenoid ring), 731 and 696 (monosubstitued benzenoid ring) cm^{-1}. ^{1}H-NMR (400 MHz, DMSO) δ (ppm): 1.22 (d, 6H, 2C$\underline{H}_3$; J=6.80 Hz), 2.58-2.60 (m, 4H, C$\underline{H}_2$NC$\underline{H}_2$), 2.95 (heptet, 1H, C$\underline{H}$(CH$_3$)$_2$; J=6.80 Hz), 4.09 (s, 2H, C$\underline{H}_2$Ph), 4.57 (s, 2H, NC$\underline{H}_2$N), 3.55-3.58 (m, 4H, C$\underline{H}_2$OC$\underline{H}_2$), 7.21-7.25 (m, 1H, ArH), 7.30-7.35(m, 4H, ArH), 7.37 (d, 2H, ArH; J=8.40 Hz), 7.72 (d, 2H, ArH; J=8.40 Hz), 9.62 (s, 1H, N=C$\underline{H}$), ^{13}C-NMR: δ 23.53 (2CH$_3$), 30.92 ($\underline{C}$H$_2$Ph), 33.45 ($\underline{C}$H(CH$_3$)$_2$), 49.99 ($\underline{C}$H$_2$N$\underline{C}$H$_2$), 66.03(N$\underline{C}$H$_2$N + $\underline{C}$H$_2$O$\underline{C}$H$_2$), [126.77, 126.99 (2C), 127.89(2C), 128.49(2C), 128.67(2C), 131.01, 135.65, 144.91] (ArC), 150.30 (Triazole C$_3$), 152.39 (N=$\underline{C}$H), 154.21(Triazole C$_5$).

Methods: The quantum chemical calculations were carried out with density functional theory (DFT) and Hartree-Fock (HF) methods using 6-31G (d,p) basis set at the Gaussian 09W program package on a computing system [9]. Firstly, the compound **1** was optimized by using the B3LYP/6-31G (d,p) and HF/6-31G (d,p) basis sets [8,9]. Thus, the most stable geometric conformer of compound **1** was obtained. Then, ^{1}H-NMR and ^{13}C-NMR isotropic shift values were calculated with method of GIAO. The veda4f program was used in defining IR data [10]. Otherwise, bond angles, bond lengths, the HOMO-LUMO energy, electronegativity and Mulliken charges of compound were calculated theoretically on the computer.

Theoretical Calculations
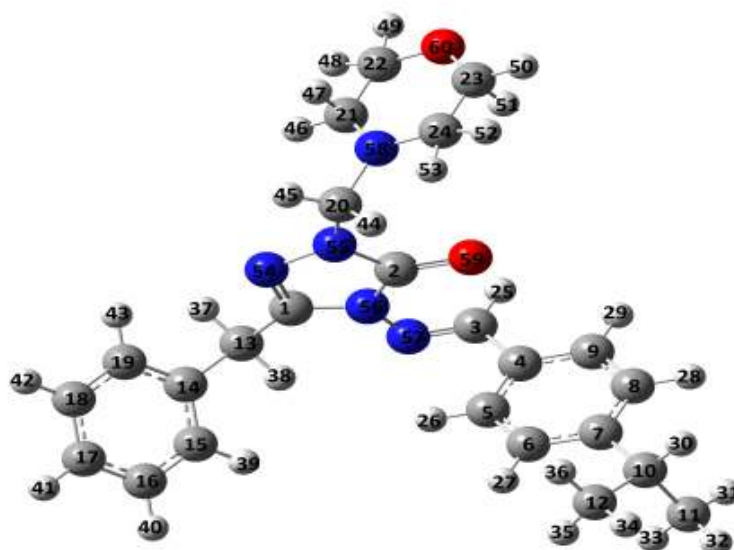
Figure 1. Optimized geometry of the molecule **1**.

Table 1. The calculated and experimental ^{13}C and ^1H-NMR/NMR DMSO(B3LYP/ HF 6-31G(d,p)) isotropic chemical shifts of the molecule (δ/ppm)

No	Exp.	B3LYP	Diff.	B3LYP/ DMSO	Diff./ DMSO	HF	Diff.	HF/ DMSO	Diff./ DMSO
C1	144,91	149,46	150,46	-4,55	-5,55	144,48	146,67	0,43	-1,76
C2	154,21	152,26	152,86	1,95	1,35	147,15	147,68	7,06	6,53
C3	152,39	154,54	155,44	-2,15	-3,05	148,87	149,88	3,52	2,51
C4	131,01	137,23	136,10	-6,22	-5,09	126,57	125,53	4,44	5,48
C5	127,89	128,23	127,64	-0,34	0,25	123,30	122,85	4,59	5,04
C6	126,99	128,62	129,24	-1,63	-2,25	123,38	123,44	3,61	3,55
C7	150,30	154,39	156,54	-4,09	-6,24	148,11	149,77	2,19	0,53
C8	126,99	131,66	132,17	-4,67	-5,18	120,69	121,07	6,30	5,92
C9	127,89	136,06	136,44	-8,17	-8,55	130,22	130,63	-2,33	-2,74
C10	33,45	47,66	47,50	-14,21	-14,05	29,47	29,23	3,98	4,22
C11	23,53	33,10	32,44	-9,57	-8,91	20,27	19,81	3,26	3,72
C12	23,53	32,90	32,66	-9,37	-9,13	20,27	19,81	3,26	3,72
C13	30,92	42,49	42,18	-11,57	-11,26	27,94	27,49	2,98	3,43
C14	135,65	140,47	140,64	-4,82	-4,99	130,02	130,35	5,63	5,30
C15	128,67	132,30	132,42	-3,63	-3,75	126,49	126,42	2,18	2,25
C16	128,49	131,27	131,74	-2,78	-3,25	124,57	124,81	3,92	3,68
C17	126,77	129,55	129,82	-2,78	-3,05	123,26	123,53	3,51	3,24
C18	128,49	131,38	131,47	-2,89	-2,98	124,62	124,86	3,87	3,63
C19	128,67	130,71	130,57	-2,04	-1,90	126,45	126,39	2,22	2,28
C20	66,03	74,30	74,05	-8,27	-8,02	56,28	56,12	9,75	9,91
C21	49,99	58,50	58,28	-8,51	-8,29	41,27	40,95	8,72	9,04
C22	66,03	73,89	73,73	-7,86	-7,70	55,76	55,61	10,27	10,42
C23	66,03	74,50	74,40	-8,47	-8,37	55,65	55,48	10,38	10,55
C24	49,99	59,16	58,86	-9,17	-8,87	40,74	40,48	9,25	9,51
H25	9,62	10,99	10,93	-1,37	-1,31	10,31	10,27	-0,69	-0,65
H26	7,72	9,14	9,16	-1,42	-1,44	8,89	8,95	-1,17	-1,23
H27	7,37	8,35	8,56	-0,98	-1,19	7,75	7,95	-0,38	-0,58
H28	7,37	8,01	8,20	-0,64	-0,83	7,90	8,11	-0,53	-0,74
H29	7,72	8,07	8,21	-0,35	-0,49	8,06	8,25	-0,34	-0,53
H30	2,95	3,58	3,72	-0,63	-0,77	2,76	2,92	0,19	0,03
H31	1,22	2,89	2,05	-1,67	-0,83	1,48	1,41	-0,26	-0,19
H32	1,22	2,11	2,19	-0,89	-0,97	1,49	1,56	-0,27	-0,34
H33	1,22	2,14	2,20	-0,92	-0,98	1,55	1,61	-0,33	-0,39
H34	1,22	2,06	2,01	-0,84	-0,79	1,49	1,42	-0,27	-0,20

H35	1,22	2,12	2,17	-0,90	-0,95	1,50	1,61	-0,28	-0,39
H36	1,22	2,09	2,16	-0,87	-0,94	1,48	1,56	-0,26	-0,34
H37	4,09	4,64	4,76	-0,55	-0,67	4,04	4,22	0,05	-0,13
H38	4,09	4,64	4,80	-0,55	-0,71	4,00	4,19	0,09	-0,10
H39	7,34	8,37	8,56	-1,03	-1,22	7,86	8,06	-0,52	-0,72
H40	7,32	8,25	8,43	-0,93	-1,11	7,92	8,11	-0,60	-0,79
H41	7,23	8,11	8,28	-0,88	-1,05	7,87	8,06	-0,64	-0,83
H42	7,32	8,20	8,34	-0,88	-1,02	7,94	8,12	-0,62	-0,80
H43	7,34	8,40	8,42	-1,06	-1,08	7,92	8,11	-0,58	-0,77
H44	4,57	4,63	4,79	-0,06	-0,22	3,93	4,04	0,64	0,53
H45	4,57	5,23	5,27	-0,66	-0,70	4,62	4,67	-0,05	-0,10
H46	2,59	3,81	3,80	-1,22	-1,21	2,52	2,46	0,07	0,13
H47	2,59	3,13	3,23	-0,54	-0,64	2,06	2,19	0,53	0,40
H48	3,56	4,34	4,57	-0,78	-1,01	3,55	3,65	0,01	-0,09
H49	3,56	4,48	4,35	-0,92	-0,79	3,29	3,30	0,27	0,26
H50	3,56	4,51	4,61	-0,95	-1,05	3,38	3,46	0,18	0,10
H51	3,56	4,51	4,49	-0,95	-0,93	3,64	3,72	-0,08	-0,16
H52	2,59	3,33	3,46	-0,74	-0,87	2,46	2,49	0,13	0,10
H53	2,59	3,27	3,37	-0,68	-0,78	2,45	2,46	0,14	0,13

The relation between R^2 values of the compound 1

B3LYP/631G(d,p): [13]C: 0.9977, [1]H: 0.9853; HF/631G(d,p): [13]C: 0.9960, [1]H: 0.9867, B3LYP/631G(d,p) (DMSO): [13]C: 0.9974, [1]H: 0.9921; HF/631G(d,p) (DMSO): [13]C: 0.9954, [1]H: 0.9874. There were such relationships between R^2 values of the compound. Found standard error rate and a, b constants regression values were calculated according to formula exp =a +b. δ calc Eq. These values for compound were shown in Table 2.

Table 2. The correlation data for chemical shifts of the molecule.

	[13]C				[1]H			
	R^2	S. error	a	b	R^2	S. error	a	b
DFT	0.9977	2.2456	1.0745	-13.6269	0.9853	0.3195	0.9766	-0.7337
HF	0.9960	2.9582	0.9715	7.4501	0.9867	0.3035	0.9070	0.2378
	[13]C (DMSO)				[1]H(DMSO)			
	R^2	S. error	a	b	R^2	S. error	a	b
DFT	0.9974	2.4004	1.0650	-12.7398	0.9921	0.2346	0.9610	-0.7073
HF	0.9954	3.0914	0.9629	8.1616	0.9874	0.2953	0.8937	0.2124
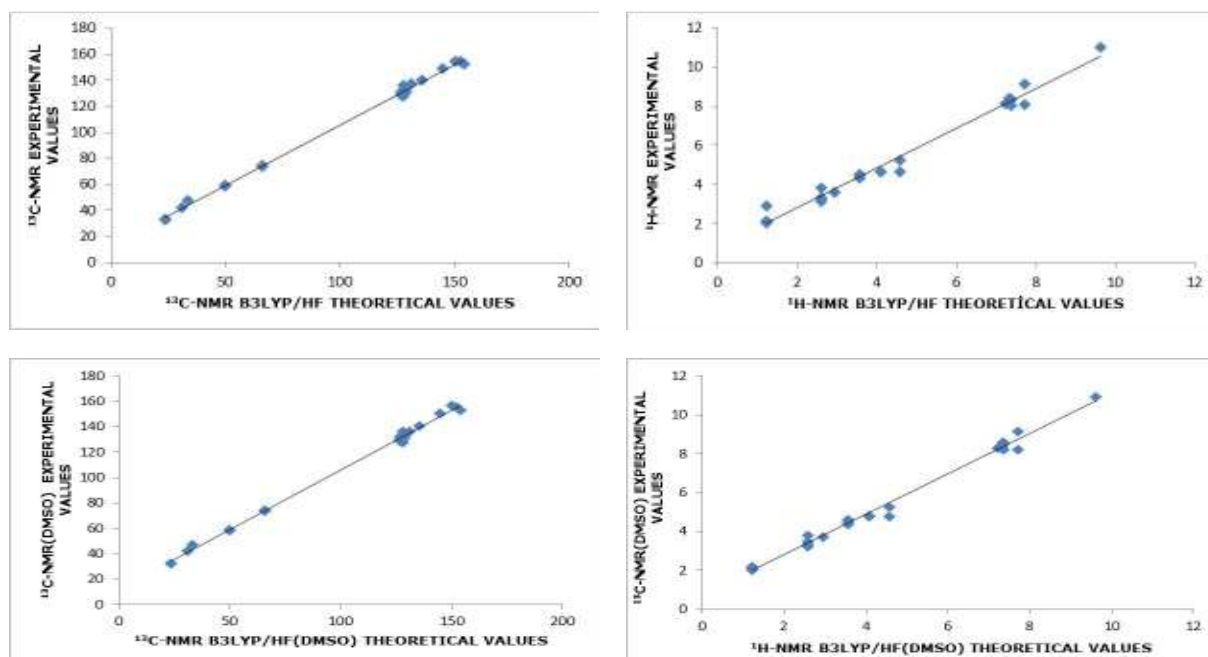
Figure 2. The correlation graphs for chemical shifts of the molecule.

Vibration frequency of the compound

Theoretical IR values were calculated with the Veda 4f program and scalar values were obtained. Negative frequencies were not found in the data. This shows that the structure of the compound is stable. IR spectra were drawn with obtained values according to HF and DFT method (Figure 3). Theoretical IR values were compared with the experimental counterparts. The result of this comparison were found to correspond to each other. Experimental carbonyl peak (C=O) was found in 1692 cm^{-1} and theoretical (C=O) peak was found in 1735 cm^{-1}.

Table 3. The calculated frequencies values of the molecule.

Vibration Types	Experimental	Scaled dft	Scaled hf
τ HCOC(16)	626	602	560
τ ONNC(12)	696	670	623
τ HCCC(11)	731	704	685
τ HCCC(50)	835	819	764
ν NC(10)	1586	1419	1423
ν NC(32)	1602	1614	1519
ν OC(76)	1692	1735	1635
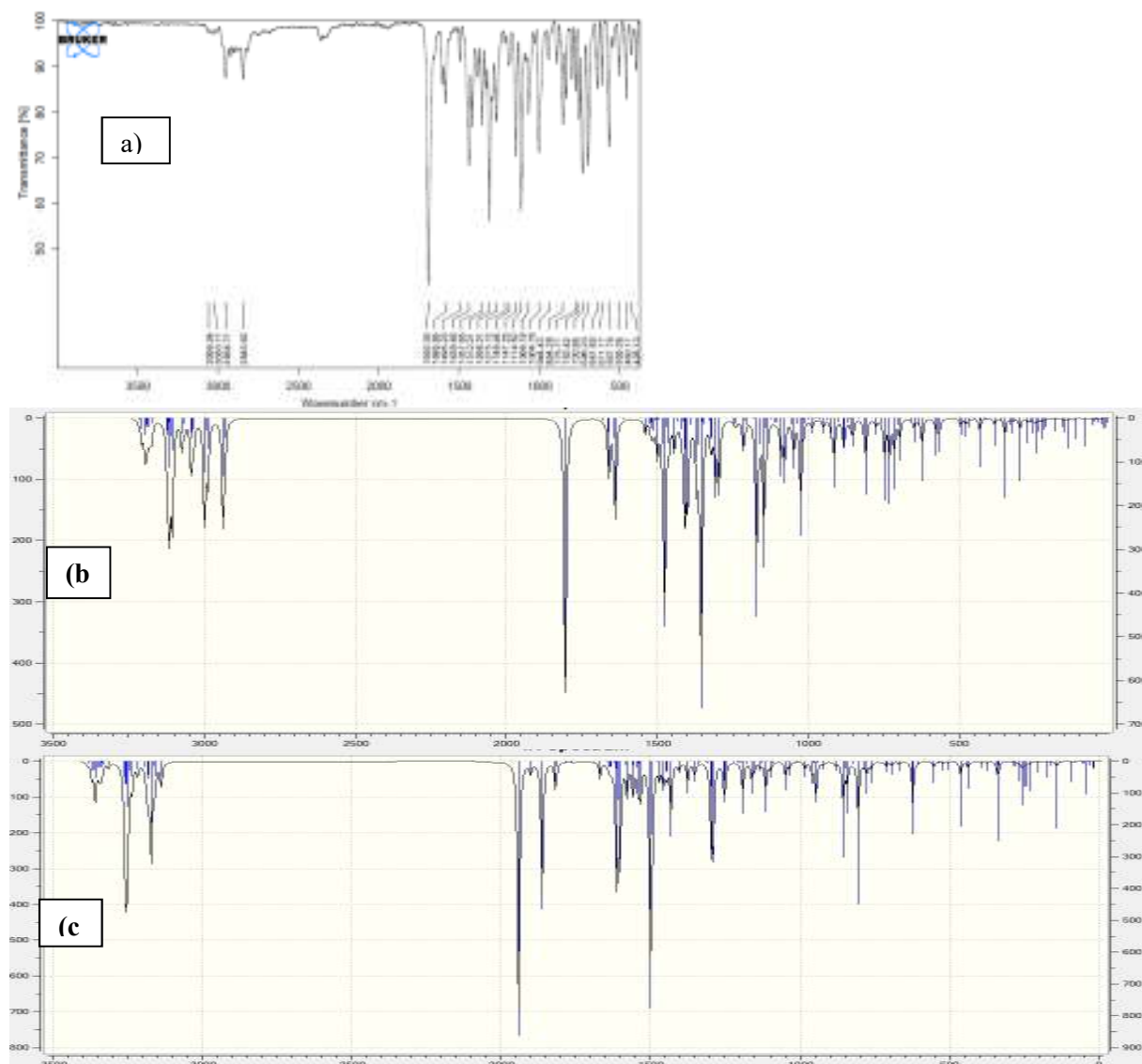
Figure 3. Experimental **(a)** and theoretical IR spectra and simulation with DFT/B3LYP/6-31G(d,p)**(b)** and HF/B3LYP/6-31G(d,p)**(c)** levels of the molecule.

Table 4. Calculated bond angles B3LYP/HF 6-31G(d,p) of the molecule.

	Bond Angles	B3LYP	HF		Bond Angles	B3LYP	HF
1	N(54)-C(1)-N(56)	111.37	111.11	**45**	C(7)-C(8)-C(9)	121.17	120.89
2	N(54)-N(55)-C(2)	113.24	112.51	**46**	C(8)-C(9)-H(29)	119.87	119.46
3	N(54)-N(55)-C(20)	122.00	121.29	**47**	C(8)-C(9)-C(4)	120.67	120.86
4	C(20)-N(55)-C(2)	124.58	126.14	**48**	C(7)-C(10)-C(11)	111.84	111.87
5	N(55)-C(2)-O(59)	129.07	128.82	**49**	C(7)-C(10)-C(12)	111.79	111.87
6	O(59)-C(2)-N(56)	128.87	128.35	**50**	C(7)-C(10)-H(30)	106.97	106.92
7	C(2)-N(56)-N(57)	130.61	131.01	**51**	H(30)-C(10)-C(11)	107.43	107.31
8	C(1)-N(56)-N(57)	121.23	121.10	**52**	C(10)-C(11)-H(31)	111.27	111.47
9	N(56)-C(1)-C(13)	124.00	121.98	**53**	C(10)-C(11)-H(32)	110.55	110.44
10	N(54)-C(1)-C(13)	124.60	126.89	**54**	C(10)-C(11)-H(33)	111.32	111.11
11	C(1)-C(13)-H(37)	106.28	107.85	**55**	C(10)-C(12)-H(34)	110.58	110.44
12	C(1)-C(13)-H(38)	109.06	107.90	**56**	C(10)-C(12)-H(35)	111.28	111.47
13	H(37)-C(13)-H(38)	107.85	105.83	**57**	C(10)-C(12)-H(36)	111.26	111.11
14	H(37)-C(13)-C(14)	109.96	110.59	**58**	H(34)-C(12)-H(35)	107.65	107.69
15	H(38)-C(13)-C(14)	109.53	110.62	**59**	H(34)-C(12)-H(36)	108.17	108.13
16	C(13)-C(14)-C(15)	120.63	120.62	**60**	H(35)-C(12)-H(36)	107.73	107.84
17	C(13)-C(14)-C(19)	120.46	120.57	**61**	H(31)-C(11)-H(32)	108.17	108.13
18	C(14)-C(15)-H(39)	119.43	119.68	**62**	H(31)-C(11)-H(33)	107.76	107.84

19	C(14)-C(15)-C(16)	120.66	120.69	**63**	H(32)-C(11)-H(33)	107.60	107.69
20	H(39)-C(15)-C(16)	119.89	119.62	**64**	N(55)-C(20)-H(44)	106.24	106.00
21	C(15)-C(16)-C(17)	120.09	120.10	**65**	N(55)-C(20)-H(45)	106.58	106.44
22	C(15)-C(16)-H(40)	119.76	119.78	**66**	N(55)-C(20)-N(58)	113.05	116.83
23	H(40)-C(16)-C(17)	120.13	120.10	**67**	C(20)-N(58)-C(24)	112.57	115.07
24	C(16)-C(17)-H(41)	120.20	120.19	**68**	C(20)-N(58)-C(21)	113.26	115.52
25	H(41)-C(17)-C(18)	120.19	120.19	**69**	N(58)-C(21)-H(46)	109.17	112.00
26	C(16)-C(17)-C(18)	119.60	119.61	**70**	N(58)-C(21)-H(47)	111.31	109.23
27	C(17)-C(18)-H(42)	120.06	120.11	**71**	H(46)-C(21)-H(47)	107.63	107.60
28	C(17)-C(18)-C(19)	120.20	120.10	**72**	H(46)-C(21)-C(22)	110.13	109.78
29	H(42)-C(18)-C(19)	119.73	119.78	**73**	H(47)-C(21)-C(22)	109.12	109.32
30	C(18)-C(19)-H(43	120.10	119.62	**74**	C(21)-C(22)-H(48)	109.41	109.60
31	N(55)-N(54)-C(1)	105.17	105.65	**75**	C(21)-C(22)-H(49)	110.58	110.63
32	N(56)-N(57)-C(3)	118.60	119.77	**76**	H(48)-C(22)-H(49)	108.70	108.61
33	N(57)-C(3)-H(25)	121.93	122.12	**77**	C(21)-C(22)-O(60)	111.33	110.95
34	H(25)-C(3)-C(4)	117.88	117.33	**78**	H(48)-C(22)-O(60)	106.54	106.93
35	C(3)-C(4)-C(5)	122.70	122.78	**79**	H(49)-C(22)-O(60)	110.19	110.04
36	C(3)-C(4)-C(9)	118.82	118.64	**80**	C(22)-O(60)-C(23)	110.78	112.39
37	C(4)-C(5)-C(6)	120.45	120.31	**81**	O(60)-C(23)-H(50)	106.61	106.94
38	C(4)-C(5)-H(26)	118.87	119.47	**82**	O(60)-C(23)-H(51)	110.27	110.04
39	H(26)-C(5)-C(6)	120.66	120.21	**83**	H(50)-C(23)-H(51)	108.78	108.60
40	C(5)-C(6)-H(27)	118.99	119.14	**84**	O(60)-C(23)-C(24)	111.35	111.00
41	C(5)-C(6)-C(7)	121.37	121.46	**85**	H(52)-C(24)-N(58)	109.00	109.34
42	H(27)-C(6)-C(7)	119.62	119.39	**86**	H(53)-C(24)-N(58)	112.21	111.83
43	C(6)-C(7)-C(8)	117.85	117.89	**87**	C(23)-C(24)-N(58)	109.27	109.00
44	C(7)-C(8)-H(28)	119.37	120.15	**88**	H(52)-C(24)-H(53)	107.98	107.62

Table 5. The calculated bond lengths B3LYP/HF 6-31G(d,p) of the molecule.

	Bond Lengths	B3LYP	HF		Bond Lengths	B3LYP	HF
1	C(1)-C(13)	1.49	1.49	**32**	C(8)-C(9)	1.39	1.38
2	C(1)-N(54)	1.30	1.26	**33**	C(9)-H(29)	1.08	1.07
3	C(1)-N(56)	1.38	1.38	**34**	C(4)-C(9)	1.40	1.38
4	N(54)-N(55)	1.39	1.37	**35**	C(7)-C(10)	1.52	1.52
5	N(55)-C(2)	1.37	1.34	**36**	C(10)-H(30)	1.10	1.09
6	C(2)-N(56)	1.41	1.38	**37**	C(10)-C(11)	1.54	1.53
7	C(2)-O(59)	1.22	1.20	**38**	C(11)-H(31)	1.09	1.09
8	N(56)-N(57)	1.37	1.36	**39**	C(11)-H(32)	1.10	1.08
9	C(13)-H(37)	1.09	1.08	**40**	C(11)-H(33)	1.09	1.08
10	C(13)-H(38)	1.09	1.08	**41**	C(10)-C(12)	1.54	1.53
11	C(13)-C(14)	1.52	1.51	**42**	C(12)-H(34)	1.09	1.08
12	C(14)-C(15)	1.40	1.39	**43**	C(12)-H(35)	1.09	1.08
13	C(15)-H(39)	1.09	1.08	**44**	C(12)-H(36)	1.09	1.08
14	C(15)-C(16)	1.39	1.38	**45**	N(55)-C(20)	1.44	1.42
15	C(15)-H(40)	1.09	1.07	**46**	C(20)-H(44)	1.09	1.08
16	C(16)-C(17)	1.39	1.38	**47**	C(20)-H(45)	1.10	1.08
17	C(17)-H(41)	1.09	1.07	**48**	C(20)-N(58)	1.45	1.42
18	C(17)-C(18)	1.39	1.38	**49**	N(58)-C(24)	1.46	1.45
19	C(18)-H(42)	1.09	1.07	**50**	C(21)-H(46)	1.09	1.09
20	C(18)-C(19)	1.39	1.38	**51**	C(21)-H(47)	1.10	1.08
21	C(19)-H(43)	1.08	1.08	**52**	C(21)-C(22)	1.52	1.51
22	N(57)-C(3)	1.29	1.26	**53**	C(22)-H(48)	1.09	1.08
23	C(3)-H(25)	1.09	1.07	**54**	C(22)-H(49)	1.10	1.09
24	C(3)-C(4)	1.46	1.47	**55**	C(22)-O(60)	1.42	1.40
25	C(4)-C(5)	1.40	1.39	**56**	O(60)-C(23)	1.42	1.40
26	C(5)-H(26)	1.08	1.07	**57**	C(23)-H(50)	1.09	1.09
27	C(5)-C(6)	1.39	1.38	**58**	C(23)-H(51)	1.10	1.08
28	C(6)-H(27)	1.09	1.07	**59**	C(23)-C(24)	1.52	1.52
29	C(6)-C(7)	1.40	1.39	**60**	C(24)-H(52)	1.09	1.08
30	C(7)-C(8)	1.39	1.39	**61**	C(24)-H(53)	1.10	1.09
31	C(8)-H(28)	1.08	1.07	**62**	C(24)-N(58)	1.46	1.45

E_HOMO (B3LYP) : -0.21472 Hartree

E_HOMO (HF) : -0.30768 Hartree

E_LUMO (B3LYP) : -0.05370 Hartree

E_LUMO (HF) : 0.08899 Hartree
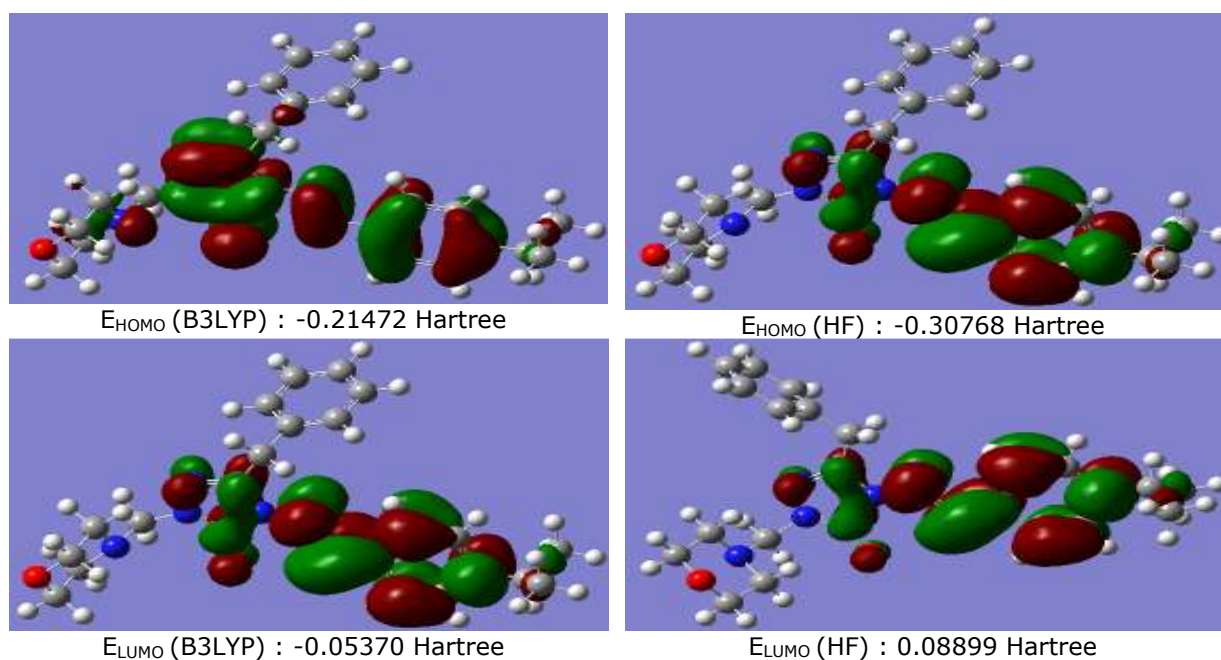
Figure 4. HOMO-LUMO energy calculated with DFT/B3LYP/6-31G(d,p) and HF/B3LYP/6-31G(d,p) levels of the molecule.

Table 6. The calculated Mulliken charge data with B3LYP/HF 6-31G(d,p) of the molecule

	DFT	HF		DFT	HF		DFT	HF
C1	0.541	0.611	C21	-0.048	-0.028	H41	0.085	0.149
C2	0.846	1.100	C22	0.052	0.110	H42	0.087	0.151
C3	0.112	0.181	C23	0.054	0.118	H43	0.098	0.149
C4	0.083	-0.086	C24	-0.045	-0.033	H44	0.138	0.155
C5	-0.101	-0.111	H25	0.157	0.227	H45	0.105	0.167
C6	-0.127	-0.176	H26	0.106	0.177	H46	0.123	0.120
C7	0.151	0.022	H27	0.083	0.150	H47	0.082	0.123
C8	-0.144	-0.156	H28	0.084	0.152	H48	0.092	0.122
C9	-0.122	-0.144	H29	0.094	0.164	H49	0.102	0.102
C10	-0.130	-0.154	H30	0.091	0.124	H50	0.101	0.103
C11	-0.305	-0.314	H31	0.110	0.122	H51	0.095	0.124
C12	-0.305	-0.314	H32	0.102	0.114	H52	0.084	0.135
C13	-0.287	-0.272	H33	0.103	0.110	H53	0.108	0.108
C14	0.126	0.002	H34	0.102	0.114	N54	-0.350	-0.334
C15	-0.123	-0.141	H35	0.104	0.118	N55	-0.388	0.592
C16	-0.085	-0.145	H36	0.110	0.122	N56	-0.436	-0.641
C17	-0.085	-0.151	H37	0.130	0.168	N57	-0.322	-0.333
C18	-0.084	-0.145	H38	0.141	0.167	N58	-0.425	-0.624
C19	-0.115	-0.141	H39	0.082	0.140	O59	-0.550	-0.679
C20	0.121	0.192	H40	0.085	0.150	O60	-0.485	-0.641

RESULTS AND DISCUSSION

In this work, geometric parameters and spectroscopic parameters such as IR, ^{1}H-NMR and ^{13}C-NMR spectra of (E)-3-benzyl-4-((4-isopropylbenzylidene)-amino)-1-(morpholinomethyl)-1H-1,2,4-triazol-5(4H)-one were calculated by density functional theory (DFT) and Hartree-Fock (HF) methods with the 631G(d,p) basis set. Obtained spectroscopic parameters were compared with experimental data. The chemical shifts in the calculated ^{1}H-NMR and ^{13}C-NMR and IR vibrational frequencies were found to be

compatible with the experimental data. Theoretical and experimental carbon and proton chemical shifts ratios between according to a, b, and R^2 values, a linear correlation were observed. Furthermore, IR vibrational frequencies for experimental carbonyl peak (C=O) in 1692 cm^{-1} and theoretically (C=O) peak in 1735 cm^{-1} were observed. The negative frequency in the IR data was not found. This result shows that the structure of compound was shown to be stable. In addition, the minimum-energy geometry structure in obtained optimization results was determined bond lengths of the molecule. The bond length of the molecule investigated theoretically to see the agreement with experimental data of the molecule C-C bond lengths and the C-H bond of length in the benzene ring in the literature was found to be registered in accordance with the data. Finally, bond angles, the HOMO-LUMO energy, electronegativity and Mulliken charges are calculated theoretically by using the B3LYP/6-31G (d,p) and HF/6-31G (d,p) basis sets.

REFERENCES

1.   Tramontini M, Angiolini L. Mannich Bases: Chemistry and Uses. CRC Press; 1994. 289 p.

2.   Yüksek H, Gürsoy O, Cakmak I, Alkan M. Synthesis and GIAO NMR calculations for some new 4,5-dihydro-1H-1,2,4-triazol-5-one derivatives: comparison of theoretical and experimental 1H and 13C chemical shifts. Magn Reson Chem. 2005;43(May):585–7. DOI: 10.1002/mrc.1591. .

3.   Yüksek H, Cakmak I, Sadi S, Alkan M, Baykara H. Synthesis and GIAO NMR Calculations for Some Novel 4-Heteroarylidenamino-4,5-dihydro-1H-1,2,4-triazol-5-one Derivatives: Comparison of Theoretical and Experimental 1Hand 13C- Chemical Shifts. Int J Mol Sci. 2005;6(6):219–29. doi:10.3390/i6060219.

4.   Yüksek H, Alkan M, Bahçeci Ş, Cakmak I, Ocak Z, Baykara H, et al. Synthesis, determination of pKa values and GIAO NMR calculations of some new 3-alkyl-4-(p-methoxybenzoylamino)-4,5-dihydro-1H-1,2,4-triazol-5-ones. J Mol Struct. 2008;873(1-3):142–8. DOI: 10.1016/j.molstruc.2007.03.016.

5.   Yüksek H, Alkan M, Cakmak I, Ocak Z, Bahçeci S, Calapoglu M, et al. Preparation, GIAO NMR calculations and acidic properties of some novel 4,5-dihydro-1H-1,2,4-triazol-5-one derivatives with their antioxidant activities. Int J Mol Sci. 2008 Jan 8;9(1):12–32. PMCID: PMC2635600.

6.   Gökce H, Bahçeli S, Akyildirim O, Yüksek H, Kol ÖG. The Syntheses, Molecular Structures, Spectroscopic Properties (IR, Micro– Raman, NMR and UV–vis) and DFT Calculations of Antioxidant 3– alkyl–4–[3–methoxy–4–(4–methylbenzoxy)benzylidenamino]–4,5–dihydro– 1H–1,2,4–triazol–5–one Molecules. Lett Org Chem. 2013;10:395–441. DOI: 10.2174/15701786113109990001.

7.   Gökce H, Akyildirim O, Bahçeli S, Yüksek H, Kol ÖG. The 1-acetyl-3-methyl-4-[3-methoxy-4-(4-methylbenzoxy)benzylidenamino]-4,5- dihydro-1H-1,2,4-triazol-5-one molecule investigated by a joint spectroscopic and quantum chemical calculations. J Mol Struct. 2014;1056-1057(1):273–84. DOI: 10.1016/j.molstruc.2013.10.044.

8.   Frisch MJ, Trucks GW, Schlegel GE, Scuseria GE, Robb MA, Cheeseman JR, et al. Gaussian 09. Wallingford CT: Gaussian, Inc.; 2009.

9.   Wolinski K, Hinton JF, Pulay P. Efficient Implementation of the Gauge-Independent Atomic Orbital Method for NMR Chemical Shift Calculations. J Am Chem Soc [Internet]. 1990 Nov;112(d):8251–60. DO:10.1021/ja00179a005.

10.   Jamroz MH. Vibrational Energy Distribution Analysis VEDA 4. Warsaw; 2010.

11.   Merrick JP, Moran D, Radom L. An evaluation of harmonic vibrational frequency scale factors. J Phys Chem A. American Chemical Society; 2007;111(45):11683–700. DOI: 10.1021/jp073974n.

Theoretical and Spectroscopic Studies of (*E*)-3-Benzyl-4-((4-Isopropylbenzylidene)-Amino)-1-(Morpholinomethyl)-1*H*-1,2,4-triazol-5(4*H*)-one Molecule

Gül Kotan, Haydar Yüksek

Öz: Bu çalışmada, (*E*)-3-benzil-4-((4-izopropilbenziliden)-amino)—(morfolinometil)-1*H*-1,2,4-triazol-5(4*H*)-on (**1**) bileşiği, 3-benzil-4-(4-izopropilbenzilidenamino)-4,5-dihidro-1*H*-1,2,4-triazol-5-on ile morfolin ve formaldehit arasındaki tepkimeden elde edilmiştir. **1** bileşiğinin yapısı FT-IR, ^{1}H-NMR, ^{13}C-NMR spektral verileriyle aydınlatılmıştır. Bunun ardından, sentezlenen **1** bileşiği B3LYP/6-31G (d,p) ve HF/6-31G (d,p) baz setleri kullanılarak en iyi duruma getirilmiştir. ^{1}H-NMR ve ^{13}C-NMR izotropik kayma değerleri, IR soğurma frekansları, bağ açıları, bağ uzunlukları, HOMO-LUMO enerjisi, elektronegatiflik ve Mulliken yükleri teorik olarak Gaussian G09W programı ile hesaplanmıştır. Buna ilave olarak, IR, ^{1}H-NMR ve ^{13}C-NMR teorik spektrumları deneysel verilerle karşılaştırılmıştır.

Anahtar kelimeler: Mannich bazları, HOMO-LUMO enerjisi, B3LYP 631G(d,p), HF 631G(d,p), Gaussian 09W.

Gönderme: 01 Temmuz 2016. **Düzeltme:** 19 Eylül 2016. **Kabul:** 20 Eylül 2016.

Oxovanadium(IV)-Containing N_2O_2 Chelate Complex; Crystal Structure Determination and DFT

Berat İlhan Ceylan*[1]

[1]University of Istanbul, Engineering Faculty, Department of Chemistry, 34320, Istanbul, Turkey

Abstract: The stable oxovanadium(IV) complex was obtained by template condensation of 2-hydroxynaphthaldehyde S-methylthiosemicarbazone and salicylaldehyde in the presence of $VOSO_4$. The structure of VO(II)-centered metal complex was confirmed by elemental analysis and was characterized by single crystal X-ray diffraction technique and the optimized geometry of the crystal structure was calculated by density functional theory (DFT/B3LYP) with LANL2DZ basis set. Theoretical data were compared with experimental data. The complex crystal is in the form of dark green-colored small sticks. The experimental data of the monoclinic crystalline structure belonging P 21/n space group was compared to those obtained with DFT-B3LYP-LANL2DZ. It was seen that experimental and theoretical values are in a good agreement.

Keywords: Oxovanadium(IV) complexes; thiosemicarbazones; template reaction; crystal structure; DFT.

INTRODUCTION

Thiosemicarbazone compounds have long been known to show biological activities like antibacterial, antifungal, antimalarial, antitumor, antiviral, antitubercular, and anti-HIV activities. In general, biological activities of thiosemicarbazones have been shown to change depending on the metal complex infrastructure in which they are bound to. An important notice in the structure-activity relationship is that complexation not only enhances the strength of the bioactive ligands but also the metal center plays a role in the process (1, 2).

Thiosemicarbazone compounds have the thione-thiol tautomerism (Scheme 1). Studies about metal complexes of the S-alkylated thiosemicarbazones have shown that the molecular geometries of S-alkylthiosemicarbazones and coordinated metal bonding type change and terminal nitrogen (N4) atom takes place in the coordination process instead of the sulfur atom whose donor property has been diminished significantly (3-5).
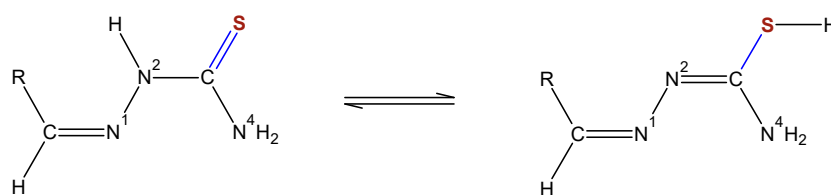
Scheme 1. Tautomerism of thiosemicarbazones.

The antitumor and insulin-mimetic properties of vanadium-bearing complexes have increased the number of publications in the literature (6, 7). Vanadium thiosemicarbazone complexes have long been known to have potential anticancer activity toward renal tumor cells *in vitro*. In a study, some oxovanadium(IV) complexes were reported to employ DNA interaction through the intercalative mode and can cleave the plasmid pBR322 DNA efficiently (8). The chemical structures include V(IV) and V(V) species; therefore the reaction-based parameters like ligand structure, type of the solvent, and pH value of the medium have an effect on the actual structures: The species might be one or more of the following: $[VO]^{2+}$, $[VO]^{3+}$, $[VO_2]^+$, $[V_2O_3]^{n+}$ (n = 2, 3, 4), and $[V_2O_4]^{2+}$ (9).

Nitrogen-fixing bacteria must acquire molybdenum or vanadium in order to form the nitrogenase structure. Since Mo and V are important metal ions, they were investigated in the acquisition mechanism by *Azotobacter vinelandii* and several siderophores (10).

Physicochemical characterization of vanadium complexes can be studied by researching the inorganic pharmacology of them. Oxovanadium(IV) complexes were synthesized containing ONS, N_2O, N_2O_2, and S_2O_2 donor ligands (11). Administration of vanadium (IV) oxide-ligand complexes to the diabetic rats rendered them diabetic, which has had a significant effect over diabetes mellitus by regenerating the B cells of the pancreas (12).
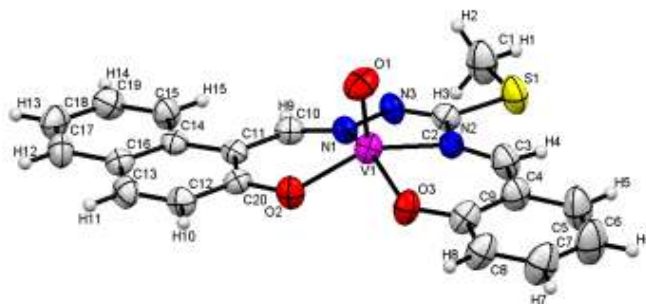
Figure 1. Crystal structure of the oxovanadium(IV) template.

In our previous study, the oxovanadium(IV) complex was synthesized and characterized by electronic, Fourier-transform infrared, ^{1}H-NMR, and electron paramagnetic resonance spectra (11). Here, the molecular and crystal structures of the oxovanadium(IV) complex were investigated by single crystal diffraction technique and the obtained experimental data of the crystal structure was compared to DFT-B3LYP-LANL2DZ results.

EXPERIMENTAL SECTION

Synthesis

The oxovanadium(IV) complex (Scheme 2) was isolated by template condensation of 2-hydroxynaphthaldehyde S-methylthiosemicarbazone and salicylaldehyde in the presence of $VOSO_4$ (11). The structure of VO(II)-centered metal complex was confirmed by elemental analysis.
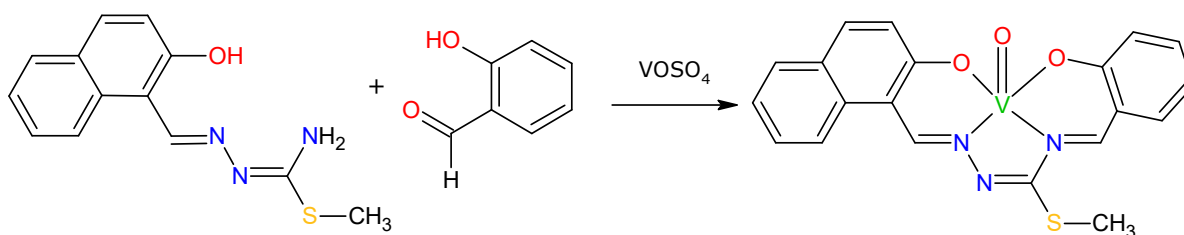
Scheme 2. Formation of the vanadium template complex.

Crystalline Structure Determination and Refinement

A single crystal of compound with dimensions 0.010 x 0.200 x 0.400 mm was grown by slow evaporation of the ethanolic solution. Crystals were mounted on a cryoloop and attached to a goniometer head on a Bruker D8 VENTURE diffractometer equipped with PHOTON100 detector using graphite monochromated Mo-Kα radiation (λ = 0.71073 Å) and 1.0° Φ-rotation frames. Crystal parameters and refinement results of the complexes are summarized in Table 1. The structure of the complex has been solved by intrinsic method SHELXS-1997 (13) and refined SHELXL-2014/7 (14, 15). ORTEP drawings with the atom numbering schemes are given in Figure 1. Selected bond lengths and bond and torsion angles of compound are given in Tables 2-3.

RESULTS AND DISCUSSION

Template condensation resulted in a thiosemicarbazidato ligand having four functional donor atoms. The VO(II) center has a square pyramidal environment consisted of N1, N2 (azomethine nitrogen) and O2, O3 (deprotonated oxygen) atoms of the thiosemicarbazidato backbone. The square pyramide is distorted because of relatively shorter V-O bond distances compared to V-N bond distances in Table 2.

The optimized geometries of the monomeric and dimeric structures of the template complex were obtained at the DFT/B3LYP method combined with the LANL2DZ basis set by using Gaussian 09 software in order to determine the change in the geometric structure of the synthesized complexes (16). By comparing the theoretical values with the experimental ones, vanadium centered bond distances, vanadium-centered angles, selected torsion angles, and selected bond lengths were presented in Tables 2-3. Although the theoretical values of bond distances and angles are slightly larger, all of the data obtained both methods were seen to be harmonious with each other.

Optimized geometric parameters are found to be nearly the same as those of experimental in solid state by X-ray single diffraction. The reason for the minor discrepancies are due to approximations, basis set incompleteness, and that the molecule is assumed to be isolated in gas phase in the theoretical calculation.

Table 1. Crystal data and structure refinement details for compound.

CCDC number	1506865
Chemical formula	C20H15N3O3SV
Crystal habit	Dark green rod
Crystal size (mm)	0.01 x 0.20 x 0.40 mm
Formula weight (g/mol)	428.35
Temperature (K)	299
Wavelength (Å)	0.71073
Crystal system	monoclinic
Space group	P 21/n
Unit cell parameters	
a, b, c (Å)	8.7158(8) , 12.2954(11), 17.0263(15)
γ, ß, V (Å)	90°, 97.593(2)°, 90°
Cell volume (Å^3)	1808.6(3)
Z	4
Density (g/cm^3)	1.573
Absorption coefficient (mm^{-1})	0.692
F000	876
Index ranges	-10<=h<=10, -14<=k<=14, -20<=l<=20
Reflections collected	49049
Independent reflections	3374
Rint	0.1473
Data reflections / parameters	3374 / 254
Goodness of fit indicator	1.074
Final R indices [I>2σ(I)]	R1 = 0.0640, wR2 = 0.1009
Δρmax , Δρmin (e/Å3)	0.314, -0.260

Table 2. Selected bond lengths of compound (Å).

Experimental	Calculated
1.583(3)	1.600
1.923(3)	1.934
1.917(3)	1.928
2.030(3)	2.037
2.047(3)	2.082
1.750(4)	1.831
1.797(5)	1.885
1.322(4)	1.329
1.300(5)	1.327
1.300(5)	1.330
1.408(4)	1.419
1.306(5)	1.334
1.403(5)	1.411
1.279(5)	1.310

Table 3. Selected angular values and torsion angles of compound (°).

	Experimental	Calculated
O1-V1-O3	108.64(14)	109.20
O1-V1-O2	109.01(14)	109.90
O3-V1-O2	91.12(12)	91.50
O1-V1-N1	105.51(14)	105.10
O3-V1-N1	144.88(13)	143.60
O2-V1-N1	85.35(12)	86.30
O1-V1-N2	107.04(15)	106.10
O3-V1-N2	87.75(13)	86.30
O2-V1-N2	142.25(13)	143.70
N1-V1-N2	74.57(13)	76.50
C20-O2-V1	129.6(2)	131.80
C9-O3-V1	131.0(3)	133.30
C10-N1-V1	127.8(3)	129.1
N3-N1-V1	118.3(2)	116.30
C3-N2-V1	125.2(3)	125.90
C2-N2-V1	113.4(3)	111.1
V1-O2-C20-C11	27.85	18.27
V1-O3-C9-C4	−15.38	-20.50
V1-N2-C3-C4	9.39	11.06
V1-N1-C10-C11	-6.86	-10.12
O2-C20-C11-C10	-0.59	-1.96
N1-N3-C2-N2	-0.20	0.79
O3-C9-C4-C3	-5.40	3.89
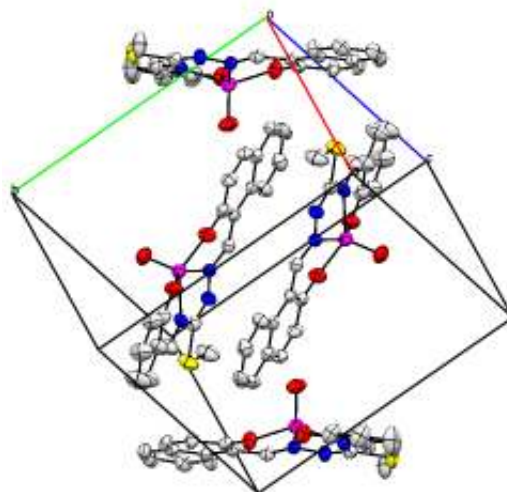
Figure 2. Molecular packing of the complex.

ACKNOWLEDGMENTS

REFERENCES

1.   Pahontu E, Julea F, Rosu T, Purcarea V, Chumakov Y, Petrenco P, et al. Antibacterial, antifungal and in vitro antileukaemia activity of metal complexes with thiosemicarbazones. Journal of Cellular and Molecular Medicine. 2015; 19(4): 865–78. DOI: 10.1111/jcmm.12508.

2.   Da S. Maia PI, Pavan FR, Leite CQF, Lemos SS, de Sousa GF, Batista AA, et al. Vanadium complexes with thiosemicarbazones: Synthesis, characterization, crystal structures and anti-Mycobacterium tuberculosis activity. Polyhedron. 2009; 28(2): 398–406.
DOI: 10.1016/j.poly.2008.11.017.

3.   Ülküseven B. Studies of the S-Ethylthiosemicarbazones with Cu(I), Zn(II), Cd(II), Hg(II) Chloride Salts. Synthesis and Reactivity in Inorganic, Metal-Organic, and Nano-Metal Chemistry. 1995; 25(9): 1549–60. DOI: 10.1016/j.poly.2008.11.017.

4.   Bourosh P, Gerbeleu N, Revenko M, Simonov Y, Belskii V, Byrotosu N. Preparation and crystal structure of salicylaldehyde S-methyl-4-phenylthiosemicarbazone (H2L) and its copper complex [Cu(HL)H2O] NO3. Russ J Inorg Chem. 1987; 32:1446–50.

5.   Lewis NA, Liu F, Seymour L, Magnusen A, Erves TR, Arca JF, et al. Synthesis, Characterisation, and Preliminary In Vitro Studies of Vanadium(IV) Complexes with a Schiff Base and Thiosemicarbazones as Mixed Ligands. European Journal of Inorganic Chemistry. 2012; 4: 664–77. DOI: 10.1002/ejic.201100898.

6.   Noblıa P, Vieites M, Torre M.H, Costa-Filho A.J, Cerecetto H, Gonzalez M, Laura Lavaggi M, Adachi Y, Sakurai H, Gambino D. Journal of Inorganic Biochemistry. 2006; 100: 281–87. DOI :10.1016/j.jinorgbio.2005.11.012.

7.   Sanna D, Ugone V, Pisano L, Serra M, Micera M, Garribba E, Journal of Inorganic Biochemistry. 2015; 153: 167–77. DOI:10.1016/j.jinorgbio.2015.07.018.

8.   Ying P, Zeng P, Lu J, Chen H, Liao X, Yang N. New Oxidovanadium Complexes Incorporating Thiosemicarbazones and 1, 10-Phenanthroline Derivatives as DNA Cleavage, Potential Anticancer Agents, and Hydroxyl Radical Scavenger. Chemical Biology & Drug Design. 2015; 86(4): 926–37. DOI: 10.1111/cbdd.12535.

9.   Rubčić M, Milić D, Horvat G, Đilović I, Galić N, Tomišić V, et al. Vanadium-induced formation of thiadiazole and thiazoline compounds. Mononuclear and dinuclear oxovanadium(v) complexes with open-chain and cyclized thiosemicarbazone ligands. Dalton Transactions. 2009; 44: 9914. DOI: 10.1039/b913653c.

10.   Springer SD, Butler A. Microbial ligand coordination: Consideration of biological significance. Coordination Chemistry Reviews. 2016; 306: 628–35.
DOI: 10.1016/j.ccr.2015.03.013.

11.   Ilhan-Ceylan B, Tuzun E, Kurt Y, Acikgoz M, Kahraman S, Atun G, et al. Oxovanadium(IV) complexes based on S -alkyl-thiosemicarbazidato ligands. Synthesis, characterization, electrochemical, and antioxidant studies. Journal of Sulfur Chemistry. 2015; 36(4): 434–49. DOI: 10.1080/17415993.2015.1050396.

12.   Yanardag R, Demirci TB, Ülküseven B, Bolkent S, Tunali S, Bolkent S. Synthesis, characterization and antidiabetic properties of N1-2,4-dihydroxybenzylidene-N4-2-hydroxybenzylidene-S-methyl-thiosemicarbazidato-oxovanadium(IV).European Journal of Medicinal Chemistry. 2009; 44(2): 818–26. DOI: 10.1016/j.ejmech.2008.04.023.

13.   Sheldrick G. SHELXS-97, Program for Crystal Structure Solution, Univ. Göttingen, Germany. 1997

14.   Sheldrick G. SHELXL2014/1 Programs for the Solution and Refinement of Crystal Structures. University of Göttingen; 2014.

15.   Sheldrick GM. A short history of SHELX. Acta Crystallographica Section A Foundations of Crystallography. 2008; 64(1): 112–22.

16.   M.J. Frisch, G.W. Trucks, H.B. Schlegel, G. Scuseria, M. Robb, J. Cheeseman, G. Scalmani, V. Barone, B. Mennucci, G. Petersson. Gaussian 09, Revision A. 02, Gaussian, Inc., Wallingford, CT, 2009; 200.

Türkçe Öz ve Anahtar Kelimeler
Oksovanadyum(IV) İçeren N₂O₂ Kelat Kompleksleri; Kristal Yapı Tayini ve DFT

Berat İlhan Ceylan

Öz: Kararlı oksovanadyum(IV) kompleksi, 2-hidroksinaftaldehit S-metiltiyosemikarbazon ve salisilaldehidin $VOSO_4$ varlığındaki template kondensasyonu ile elde edilmiştir. VO^{2+}-merkezli metal kompleksinin yapısı elementel analiz ile doğrulanmış ve X-ışını saçılması tekniği ile karakterize edilmiştir, kristal yapının optimize geometrisi yoğunluk fonksiyonel teorisi (DFT/B3LYP) LANL2DZ baz seti kullanılarak hesaplanmıştır. Teorik veriler deneysel verilerle karşılaştırılmıştır. Kompleks kristali, koyu yeşil renkli küçük çubuklar halinde elde edilmiştir. P 21/n uzay grubuna bağlı olan monoklinik kristal yapısına ait deneysel veriler DFT-B3LYP-LANL2DZ ile elde edilenlerle karşılaştırılmıştır. Deneysel ve teorik değerlerin iyi bir uyum içinde olduğu bulunmuştur.

Anahtar kelimeler: Oksovanadyum(IV) kompleksleri; tiyosemikarbazonlar; template tepkimesi; kristal yapısı; DFT.

RESEARCH ARTICLE

Misens Device as a New Automated Biosensing Platform Based on Real-Time Electrochemical Profiling (REP)

Yildiz Uludag*

Bioelectronics Devices and Systems Group - UEKAE - BILGEM - The Scientific and

Technological Research Council of Turkey (TUBITAK), 41470 Gebze/Kocaeli, Turkey.

Abstract: In various fields like health, environmental control, food security, and military defense, there is an increasing demand for on-site detection, fast identification, and urgent response which bring about the necessity to employ laboratory detection procedures on standalone automatic devices. In response to that, TUBITAK BILGEM's Bioelectronic Devices and Systems Group has been developing portable and fully automated biosensor devices using optical and electrochemical biosensor detection techniques. Here we describe a new integrated and fully automated lab-on-a-chip based biosensor device 'MiSens'. The key features of the MiSens include a new electrode array, an integrated microfluidic system, and real-time amperometric measurements during the flow of enzyme substrate. While simple protocols can be controlled from the LCD display on the device, other main device control procedures can be run wireless by a tablet/PC using the MiCont™ software developed by the team. For the device, a new plug and play type sensor chip docking station has been designed that with one move it enables the formation of a ~ 7-10 µL capacity flow cell on the electrode array with the necessary microfluidic and electronic connections. The MiSens device has been developed by our multi-disciplinary team by integrating and automatising the earlier developed sensing platform REP™ (Real-time Electrochemical Profiling). The performance of the MiSens device has been tested using cyclic voltammetry and amperometry tests and the results were compared with an of the shelf potentiostat.

*Corresponding author. E-mail: Yildiz.uludag@tubitak.gov.tr, Tel: 0 262 648 1910.

INTRODUCTION

Biosensors are analytical devices that comprise a biological recognition element, a suitable transducer, and an appropriate data processing system (1-3). While one of the main application of the biosensors are in the research and development for biomolecule interaction analysis or drug discovery, it is also possible to design biosensors for end users in order to perform analytical measurements for environmental monitoring, quality assurance in agriculture/food and medical diagnostics (4). The number of biosensor-related articles has exceeded 9000 / year; search on the term "biosensor*'' for 2015 yields 9226 articles, using the Web of Knowledge, 8 times more than that of the year 2000. Compared with the numerous publications and patents available since the early 1990's, the commercialisation of the miniaturised biosensor devices for end users has significantly lagged behind the research output. (2, 5). However, in recent years due to the advances in microelectronics, nanotechnology, bioengineering, and especially the microfluidic technologies, new on-site or point-of-care biosensor devices started to appear in the diagnostics market indicating a significant change (6). Currently, testing for *in vitro* diagnostics is typically performed in centralised laboratories using large automated analysers in hospitals (7, 8). Similarly, tests for environmental monitoring and quality control of food/agriculture products typically performed in centralised laboratories using expensive laboratory equipment and trained personnel (2, 9-12). To eliminate sample transportation, to reduce the time spent between the sample acquisition to the results and hence for a rapid response to an emergency, fully automated on-site testing devices are promising tools. Portable biosensor devices connected through the *Internet of Things* may change the way we perform the analytic measurements not only in healthcare but also for other application areas of the biosensors. Therefore, for on-site testing, a biosensing platform needs to be able to work automatically with minimum user interference. The tasks that need to be automated may include sample preparation, separation, detection, waste collection, and data analysis. While it is reasonably easy to manipulate fluids using the bench top biosensor devices using automated pipetting and robotic arms, for portable devices that deals with microlitres or smaller amounts of liquids it constitutes a challenge. Recent advances in microfluidics have enabled the miniaturisation of the devices and multiplex testing of a range of analytes (13-15). Advanced micro fabrication techniques have facilitated integration of sensing functionalities with microfluidics on the same biochip enabling automated systems (14). To address the need in automated and on-site testing of analytes, a new electrochemical biosensor device has been developed by TUBITAK

BILGEM that relies of Real-time Electrochemical Profiling (REP^{TM}) and novel electrode array based biochips.

MATERIALS AND METHODS

Materials

Phosphate buffered saline (PBS, 0.01 M phosphate buffer, 0.0027 M potassium chloride and 0.137 M sodium chloride, pH 7.4) tablets, mercaptoundecanoic acid (MUDA), spectrophotometric grade ethanol, horseradish peroxidase (HRP), 3,3',5,5'-tetramethylbenzidine (TMB) ready to use reagent (includes H_2O_2), potassium ferrocyanide ($K_4[Fe(CN)_6]$) and KCl were purchased from Sigma-Aldrich (Poole, UK).

Electrochemical Analysis

An integrated and fully automated electrochemical biosensor has been designed and fabricated (MiSens^{TM} V01; Figure 1-A) by BİLGEM-Bioelectronic Devices and System Development Group. MiSens device is controlled wireless using a tablet/PC with the developed MiCont^{TM} software (TUBİTAK-BİLGEM, Kocaeli, Turkey). Cyclic voltammetry (CV) tests were performed using 1 mM potassium ferrocyanide solution in 1 M KCl. The MiSens biosensor chip includes an electrode array that is fabricated on a 10 x 20 mm glass slide. Each array consist of 8 working electrodes (d = 1 mm) with shared Au counter and quasi-reference electrodes (**Error! Reference source not found.**-B) (16). The design of the electrodes was formed on the glass slide by means of a Fine Metal Mask made of a laser cut patterned stainless steel and Au metal was deposited on the wafer using an electron beam evaporator (Torr EB-4P, New Windsor, US). Before the application of Au (200 nm), a 20 nm Ti layer is applied on to the wafer as an intermediary adhesive layer to increase the adhesion between the Au and the glass. For easy handling of the sensor chip, a holder has been designed and fabricated from poly(methyl methacrylate) (PMMA) (Figure 1-B).
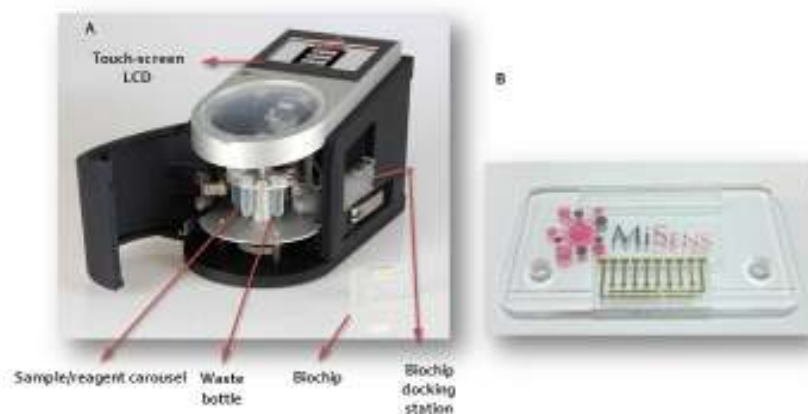
Figure 1. Fully integrated and automated MiSens biosensor device (A) and its biochip (working electrode diameter 1 mm) (B).

For comparison purposes, the tests has been replicated using an off-the-shelf screen printed electrodes (SPE) (Dropsens, Oviedo, Spain) . Using the SPEs, cyclic voltammetry and amperometric measurements were performed with a MicroStat 8000 Electrochemical Analyser with the general purpose electrochemical software Dropview 1.4 (Dropsens, Oviedo, Spain). The electrochemical analyser and the purpose built shielded cables enable simultaneous electrochemical measurements of 8 electrodes. Cyclic voltammetry (CV) tests were performed using 1 mM potassium ferrocyanide solution in 1 M KCl.

Biochip Surface Modification

Surface modification of the SPE and MiSens biochips with a self-assembled monolayer (SAM) has been achieved by plasma cleaning of the arrays and later immersing in an ethanolic solution of 2 mM MUDA for overnight. Later, the electrode arrays were rinsed with ethanol and water. After drying with nitrogen stream, the arrays were vacuum-packed and stored at +4ºC till use.

Enzymatic Assay

For the MiSens assay, enzyme assays were performed by mixing HRP enzyme and TMB substrate, then injecting 150 µL of this solution to the biochip at 55 µL/min. The real-time

amperometric measurements were recorded by the MiCont[TM] software (TUBITAK BILGEM) for analysis. The chronoamperometric responses obtained at -0.1 V potential at the 150 s of the measurements were used as assay response. For the SPE assays, 50 μL of the enzyme-substrate solution has been dropped on the inidividual electrodes and the amperometric signal has been recorded using the Dropview 1.4 software. The chronoamperometric responses obtained at -0.1 V potential at the 90 s of the measurements were used as assay response. For the MiSens assays, 8 data points, for the SPE assays, 3 data points were used to obtain the mean and standard deviation of the results. The limit of detection (LOD) was calculated as the signal obtained from the assays that is equivalent to 3 times the standard deviation of the signals obtained from the blank standards.

RESULTS AND DISCUSSION

Device Integration

The MiSens device has been developed by TUBITAK BILGEM's multi-disciplinary team by integrating and automatising the earlier developed sensing platform REP[TM] (17). The key features of this platform include a new biochip (18), an integrated microfluidic system and real-time amperometric measurements during the flow of enzyme substrate. In earlier studies, an electrode array has been developed that utilises shared reference and counter electrodes to minimise the size of the sensor. Later, a new plug and play type sensor chip docking station has been designed. With one move, the chip docking station enables the formation of a ~ 7 μL capacity flow cell on the electrode array with the necessary microfluidic and electronic connections. The mechanical parts of the MiSens device include biochip docking station, a pump, microfluidic tubing connected sample pick up needle, sample/reagent carousel, and a waste bottle. The electronic parts of the device include an LCD display, multiplexed potentiostat, a digital control circuit and wired/wireless communication interface. MiCont[TM] software enables user to create a list of assay steps that forms the test protocol of the MiSens device (Figure 2). The user can save and re-use the protocol created when needed. During data acquisition, the MiCont software shows the electrochemical measurements real time.

Figure 2. The MiCont™ software developed by the team that enables fast and easy assay protocol formation prior to automated assay run.

Sensor Surface Characterization

To investigate the electrochemical behaviour of the designed electrode arrays, cyclic voltammetry technique has been utilised and voltammograms were recorded for a model electroactive species, potassium ferricyanide (19, 20). Application of alkanethiols on a gold electrode surface forms a self-assembled monolayer and hence insulates the electrode surface (21, 22). By comparing the cyclic voltammograms of a bare gold electrode and SAM coated gold electrode, it is possible to investigate the coverage of the monolayer. Cyclic voltammograms of bare Au and SAM coated MiSens biochip and SPE were obtained using $K_4[Fe(CN)_6]$ as the electroactive marker. As it could be seen from the Figure 3A-C, the oxidation and reduction peaks of $K_4[Fe(CN)_6]$ was visible and there was a larger redox area between positive and negative potential sweeps when cyclic voltammetry performed on bare gold surfaces. Whereas, the redox area between positive and negative potential sweeps of the SAM coated sensor chips were smaller in SPE, and non-existed in MiSens biochip. The SPE surface is formed using an ink containing Au and polymer, this surface shows a rough surface characteristic. While rough surface results in a larger electroactive area, the existence of polymer rather than pure Au results in lower coverage of SAM layer as seen from the cyclic voltammogram. However, MiSens biochips are made using pure Au that is sputtered on a flat glass slide. This surface is not as rough as the SPE, however as the electrode is formed using pure Au, the SAM coverage of the surface is higher as seen from the cyclic voltammogram (Figure 3B).

The surface coverage (θ) of the SAM can be calculated by comparing the charge (Q) during reduction/oxidation of cyclic voltammetry at a monolayer covered electrode with respect to a bare gold electrode (Equation 1) (23, 24).

$$\theta = 1 - (Q_{SAM}/ Q_{bare\ gold}) \qquad\qquad \text{(Eq. 1)}$$

The surface coverage of the SAM-coated MiSens biochip and the screen printed electrode has been calculated using Equation 1 as 0.96 ± 0.03 and 0.54 ± 0.06, respectively.
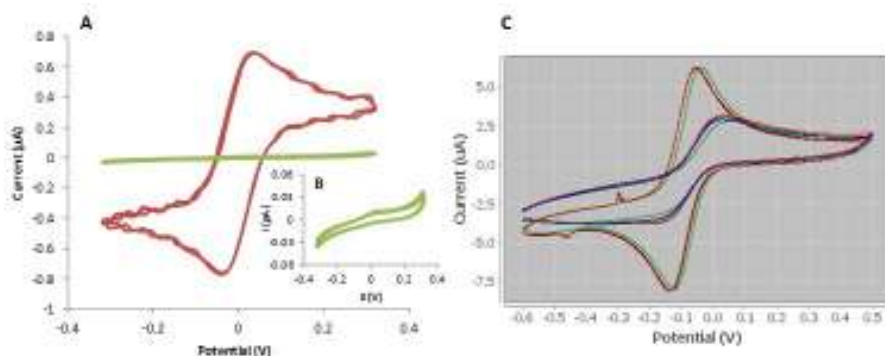
Figure 3. Cyclic voltammetry has been performed with 1 mM K$_4$[Fe(CN)$_6$] / KCl at 100 mV/s can rate, using bare and MUDA coated MiSens biochips (A, B) and SPE (C).

Enzymatic activity measurement of HRP

Horseradish peroxidase (HRP) is an enzyme label widely used in immunoassays. The enzymatic activity of HRP and its substrate TMB (3,3',5,5'-tetramethylbenzidine) can be determined by measuring the absorbance in the visible region, by fluorescence or by electrochemistry (25). During the enzyme-linked immunosorbent assay (ELISA), after the addition of the TMB substrate on to the enzyme-bound microwell plate, the reaction is allowed to take place around 15 minutes before stopping the reaction and measuring the colour formation by a spectrophotometer. The aim of 15 minutes reaction is to increase the colour formation and hence obtain a reasonable optical detection signal. As the electrochemical measurements are more sensitive than the optical detection, 15 minutes reaction may not be needed for the measurement. During the Real-time Electrochemical Profiling (REP) assay, the HRP and TMB mixture is injected on to the electrode arrays of the MiSens biochip and a real-time amperometric signal is obtained at -0.1V potential (Figure 4).
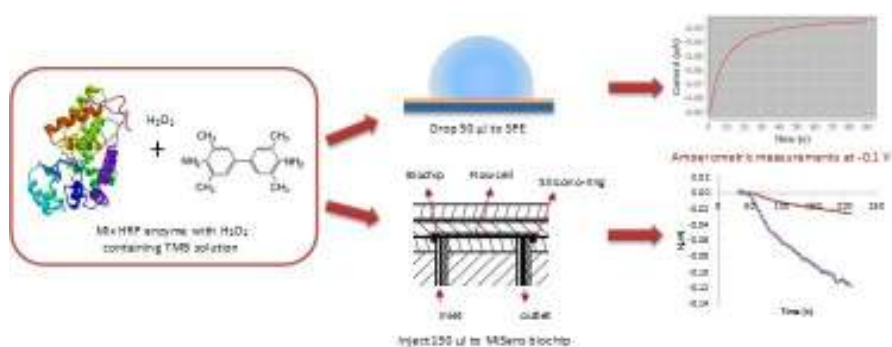
Figure 4. The chemical reaction of TMB in the presence of the HRP enzyme has been measured as an amperometeric signal using both SPE and MiSens biochip.

For the HRP enzymatic activity measurement assays, initially plasma cleaned bare Au SPE and MiSens biochips were coated with a SAM layer. The Au surface of the electrodes were coated with a self assembled monolayer (MUDA) to prevent the adsorbance of HRP on the electrode array surface and also to mimick a recognition element (antibody, DNA etc) immobilised electrode, in other words an electrode with a reduced electrochemically active area. Later, the enzyme assays were performed by mixing varying concentrations of HRP with a fixed concentration of TMB reagent, then injecting to the flow cell containing electrode arrays for MiSens, or dropping the solution on to the SPE surface. Later the chronoamperometric responses obtained at -0.1 V potential has been analysed (See Figure 4). In Figure 5, the raw data obtained from the enzyme assay using Misens biochips and device is shown. In Figure 6-A, the amperometric signals obtained from both SPE and MiSens biochip are compared. As seen from this figure, the results obtained from both SPE and MiSens biochips were comparable to each other with coefficient of determination of 1.0 and 0.98, respectively. Although similar amperometric results have been obtained from both sensor chips, as the electroactive area of both chips differ, a considerable difference was observed when current density is calculated. As MiSens biochips have 1 mm diameter with respect to 4 mm diameter of SPE chips, the current density of MiSens biochips are 14.4 times higher than the SPE (Figure 6-B,

Table 1).
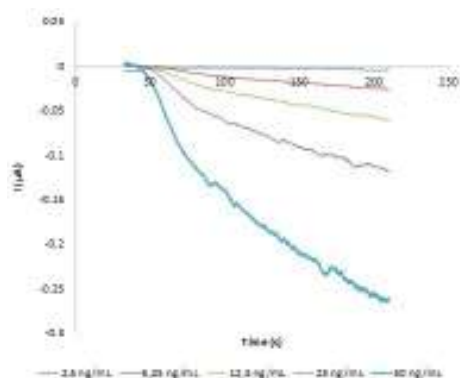
Figure 5. Enzymatic activity measurement assays were performed by mixing varying concentrations (2.5 - 50 ng/mL) of horseradish peroxidase (HRP) and TMB reagent, then injecting to the SAM coated electrodes in a flow cell for chronoamperometric measurements. The current measurements were taken at -0.1 V potential. The plot shows the raw data obtained from the MiSens device.
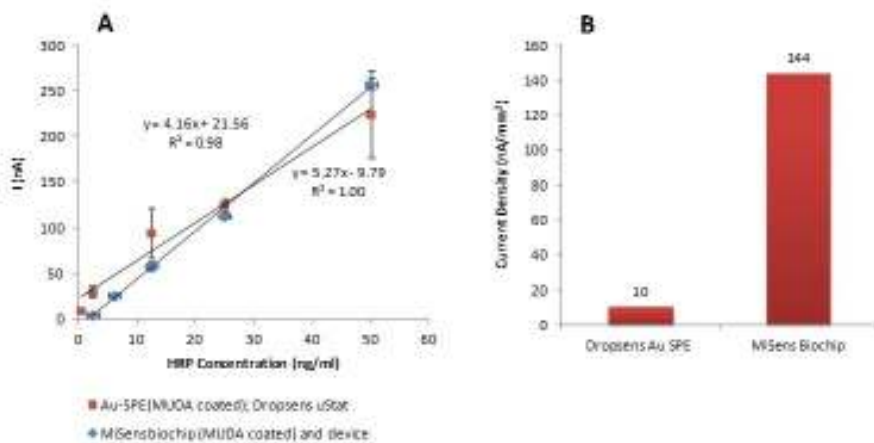
Figure 6. A) The amperometric response from the enzymatic reaction of HRP and TMB has been plotted with respect to HRP concentration for MiSens and SPE electrodes. B) The current response obtained from the chronoamperometry results after the addition of 25 ng/mL HRP and TMB reagent were used to assess the current density on MiSens biochip and Au SPE.

411

412
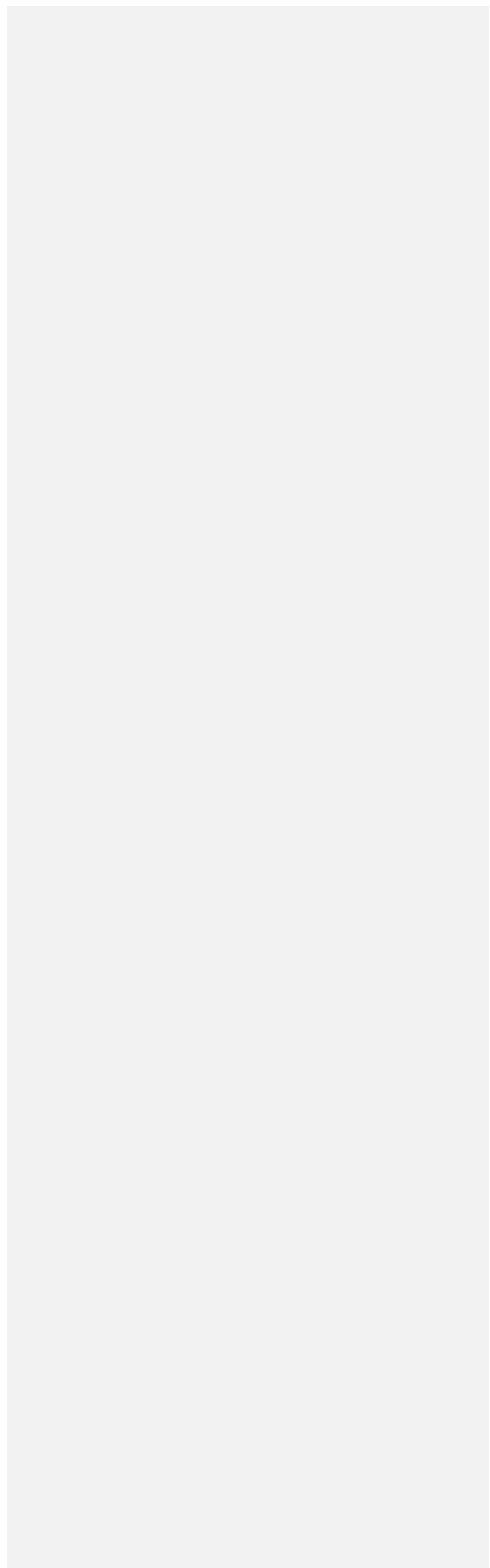
Table 1. The curreny density results for SPE and MiSens biochip.

MUDA-coated	Response for 25 ng/mL HRP (nA)	Area (mm²)*	Current density (nA/mm²)
Dropsens Au SPE (d = 4 mm)	125	12.56	9.98
MiSens Biochip (Au) (d = 1 mm)	113	0.79	143.75

*The area calculation does not take into account the roughness of the SPE chip. If that is also considered, the current density of the SPE chip will further decrease. The MiSens chip is produced by sputtering Au on a glass slide surface, hence its roughness is minimal with respect to the SPE chips.

The HRP and substrate reaction incubation time have direct effect to the detection limit of the assay and usually ranges from a few minutes to an hour. While in almost all studies minimum 15 minutes of HRP reaction time is allowed, in the current study the aim was to minimise the assay time since the biosensor device MiSens has been designed for on-site or point of care detection. As can be seen from Table 2, even without any incubation, a detection limit of 3.4×10^{-11} M has been achieved for the HRP enzyme activity using the MiSens biosensor device. Here, we have shown that MiSens device can be used as a flow injection analysis system for the detection of HRP enzymatic activity, hence an indication that it can be utilised as an electrochemical ELISA reader. In addition to that the easily programmable automated flow injection system of the device enables the injection of multiple analytes to the sensor surface in the required order hence immunoassays can be performed on the electrode surface directly with ease (26).

Table 2. HRP enzyme activity measurements using different electrochemical setups.

1 System	2 Electrode type	3 Electrode diameter	4 Microfluidics	5 Incubation before measurement	6 Detection Limit 7 (HRP Concentration)	8 Reference
MiSens biochip & device	Au electrode	1 mm	Automated flow injection analysis	None	3.4×10^{-11} M	Current work
SPE & Potentiostat	Au SPE	4 mm	x	None	1.1×10^{-11} M	Current work
Disk electrode and potentiostat	Glassy carbon electrode	3 mm	Flow injection analysis	30 min	2.6×10^{-12} M	(27)
Disk electrode and potentiostat	Glassy carbon disk working electrode	3 mm	Flow injection analysis	15 min	8.5×10^{-14} M	(25)
SPE & potentiostat	Carbon SPE	4 mm	Flow injection analysis	30 min	2×10^{-14} M	(28)

CONCLUSIONS

The recent advances in electronics, bioengineering and lab-on-a-chip technologies results in the development of new generation bioanalytics devices for out-of-the-laboratory and on-site testing. By combining the device development capabilities of BILGEM TUBITAK with bioengineering and nanotechnology, the BILGEM Bioelectronics group has developed a new fully automated electrochemical biosensor device, MiSens and biochips. The performance of this new electrochemical device and biochips have been compared to a commercial potentiostat with its SPE chips. The results show that the smaller footprint of the MiSens biochip (d=1 mm) and integrated microfluidics enables similar amperometric responses to the HRP-TMB enzymatic assay with respect to the SPE (d=4 mm). However, when the current obtained with respect to the sensor surface area is compared, the current density of the MiSens chips has been found 14.4 times higher, showing the effectiveness of the biochip design and the microfluidic system. The fully automated format of the MiSens device and its microfluidic system enables electrochemical measurements to be performed with ease, hence provides a very effective tool for research and development of new biosensing assays. In the future, MiSens device has also a potential to be used for on-site testing of environmental / food toxins, and for biodefense.

ACKNOWLEDGMENTS

REFERENCES

1. Lowe C. An introduction to the concepts and technology of biosensors. Biosensors. 1985;1(1):3–16.

2. D'Orazio P. Biosensors in clinical chemistry-2011 update. Clinica Chimica Acta. 2011;412(19-20):1749-61. DOI: 10.1016/j.cca.2011.06.025.

3. Keusgen M. Biosensors: new approaches in drug discovery. Naturwissenschaften. 2002;89(10):433-44. DOI: 10.1007/s00114-002-0358-3.

Commented [BA1]: Please provide DOI names for journal articles. If a DOI name could not be found, present an URL instead. For books, please provide ISBN numbers. http://scholar.google.com and http://books.google.com are at your service.

Commented [BA2]: Please find the DOI names and add them to the end of each reference. If a DOI could not be found, add an URL instead. For books, please provide the ISBN numbers.

4. Turner APF. Biosensors: sense and sensibility. Chemical Society Reviews. 2013:3184-96. DOI: 10.1039/C3CS35528D.

5. Luong JHT, Male KB, Glennon JD. Biosensor technology: Technology push versus market pull. Biotechnology Advances. 2008;26(5):492-500. DOI: 10.1016/j.biotechadv.2008.05.007.

6. Tothill IE. Biosensors for cancer markers diagnosis. Seminars in Cell & Developmental Biology. 2009;20(1):55-62. DOI: 10.1016/j.semcdb.2009.01.015.

7. Healy DA, Hayes CJ, Leonard P, McKenna L, O'Kennedy R. Biosensor developments: application to prostate-specific antigen detection. Trends in Biotechnology. 2007;25(3):125-31. DOI: 10.1016/j.tibtech.2007.01.004.

8. Wu J, Fu Z, Yan F, Ju H. Biomedical and clinical applications of immunoassays and immunosensors for tumor markers. Trac-Trends in Analytical Chemistry. 2007;26(7):679-88. DOI: 10.1016/j.trac.2007.05.007.

9. Li Y, Liu X, Lin Z. Recent developments and applications of surface plasmon resonance biosensors for the detection of mycotoxins in foodstuffs. Food Chemistry. 2012;132(3):1549-54. DOI: 10.1016/j.foodchem.2011.10.109.

10. Svabenska E, Kovar D, Krajicek V, Pribyl J, Skladal P. Electrochemical Biosensor for Detection of Bioagents. International Journal of Electrochemical Science. 2011;6(12):5968-79. URL: http://www.electrochemsci.org/papers/vol6/6125968.pdf.

11. Piliarik M, Parova L, Homola J. High-throughput SPR sensor for food safety. Biosensors & Bioelectronics. 2009;24(5):1399-404. DOI: 10.1016/j.bios.2008.08.012.

12. Mascini M, Tombelli S. Biosensors for biomarkers in medical diagnostics. Biomarkers. 2008;13(7-8):637-57. DOI: 10.1080/13547500802645905.

13. Eicher D, Merten CA. Microfluidic devices for diagnostic applications. Expert Review of Molecular Diagnostics. 2011;11(5):505-19. DOI: 10.1586/erm.11.25

14. Gervais L, de Rooij N, Delamarche E. Microfluidic Chips for Point-of-Care Immunodiagnostics. Advanced Materials. 2011;23(24):H151-H76. DOI: 10.1002/adma.201100464.

15. Trietsch SJ, Hankemeier T, van der Linden HJ. Lab-on-a-chip technologies for massive parallel data generation in the life sciences: A review. Chemometrics and Intelligent Laboratory Systems. 2011;108(1):64-75. DOI: 10.1016/j.chemolab.2011.03.005.

16. Uludag Y, Sagiroglu M, Ersoy A, Edis A, Budak S, Demiralp A, inventors. An electrochemical sensor array and apparatus, PCT/IB2015/0524792015. URL: https://patents.google.com/patent/WO2015155665A1/en?q=%22An+electrochemical+sensor+arr ay+and+apparatus%22.

17. Olcer Z, Esen E, Muhammad T, Ersoy A, Budak S, Uludag Y. Fast and sensitive detection of mycotoxins in wheat using microfluidics based Real-time Electrochemical Profiling. Biosensors & Bioelectronics. 2014;62:163-9. DOI: 10.1016/j.bios.2014.06.025.

18. Uludag Y, Olcer Z, Samil Sagiroglu M. Design and characterisation of a thin-film electrode array with shared reference/counter electrodes for electrochemical detection. Biosensors and Bioelectronics. 2014;57(0):85-90. DOI: 10.1016/j.bios.2014.01.048.

19. García-Raya D, Madueño R, Sevilla JM, Blázquez M, Pineda T. Electrochemical characterization of a 1,8-octanedithiol self-assembled monolayer (ODT-SAM) on a Au(1 1 1) single crystal electrode. Electrochimica Acta. 2008;53(27):8026-33. DOI: 10.1016/j.electacta.2008.06.017.

20. Cavallini M, Bracali M, Aloisi G, Guidelli R. Electrochemical STM investigation of 1,8-octanedithiol self-assembled monolayers on Ag(111) in aqueous solution. Langmuir. 1999;15(8):3003-6. DOI: 10.1021/la9815392.

21. Campuzano S, Pedrero M, Montemayor C, Fatas E, Pingarron JM. Characterization of alkanethiol-self-assembled monolayers-modified gold electrodes by electrochemical impedance spectroscopy. Journal of Electroanalytical Chemistry. 2006;586(1):112-21. DOI: 10.1016/j.jelechem.2005.09.007.

22. Senaratne W, Andruzzi L, Ober CK. Self-assembled monolayers and polymer brushes in biotechnology: Current applications and future perspectives. Biomacromolecules. 2005;6(5):2427-48. DOI: 10.1021/bm050180a.

23. Campuzano S, Pedrero M, Montemayor C, Fatás E, Pingarrón JM. Characterization of alkanethiol-self-assembled monolayers-modified gold electrodes by electrochemical impedance spectroscopy. Journal of Electroanalytical Chemistry. 2006;586(1):112-21. DOI: 10.1016/j.jelechem.2005.09.007.

24. Yang YJ, Khoo SB. Fabrication of self-assembled monolayer of 8-mercaptoquinoline on polycrystalline gold electrode and its selective catalysis for the reduction of metal ions and the oxidation of biomolecules. Sensors and Actuators B-Chemical. 2004;97(2-3):221-30. DOI: 10.1016/j.snb.2003.08.019.

25. Volpe G, Compagnone D, Draisci R, Palleschi G. 3,3 ',5,5 '-tetramethylbenzidine as electrochemical substrate for horseradish peroxidase based enzyme immunoassays. A comparative study. Analyst. 1998;123(6):1303-7. DOI: 10.1039/A800255J.

26. Uludag Y, Esen E, Kokturk G, Ozer H, Muhammad T, Olcer Z, et al. Lab-on-a-chip based biosensor for the real-time detection of aflatoxin. Talanta. 2016;160:381-8. DOI: 10.1016/j.talanta.2016.07.060.

27. DelCarlo M, Mascini M. Enzyme immunoassay with amperometric flow-injection analysis using horseradish peroxidase as a label. Application to the determination of polychlorinated biphenyls. Analytica Chimica Acta. 1996;336(1-3):167-74. DOI: 10.1016/S0003-2670(96)00377-7.

28. Fanjul-Bolado P, González-Garcıa MaB, Costa-Garcıa An. Voltammetric determination of alkaline phosphatase and horseradish peroxidase activity using 3-indoxyl phosphate as substrate: Application to enzyme immunoassay. Talanta. 2004;64(2):452-7. DOI: 10.1016/j.talanta.2004.03.003.

(This article was presented to the 28th National Chemistry Congress and submitted to JOTCSA as a full manuscript)

Design of a Novel Conducting Composite Supported by Platinum Nanoparticles for Hydrogen Production from Water

Didem BALUN KAYAN[1]*, Merve İLHAN[1], Derya KOÇAK[1]

[1]University of Aksaray, Science and Arts Faculty, Chemistry Department, 68100, Aksaray, Turkey.

Abstract: Because of the decrease in fossil fuel resources and the continuous increase in energy demands, clean energy requirements have become extremely important for future energy generation systems. Hydrogen is well known as an efficient and environmentally friendly energy carrier. Highly catalytic active and low-cost electrocatalysts for hydrogen production are key issues for sustainable energy technologies. Here we report an aluminum electrode modified with polypyrrole (PPy)-chitosan (Chi) composite film decorated with Pt nanoparticles for hydrogen production from water. Hydrogen evolution reaction (HER) is examined by cyclic voltammetry (CV), Tafel polarization curves and electrochemical impedance spectroscopy (EIS) in 0.5 M H_2SO_4. The structural properties of the modified surface analyses were investigated by scanning electron microscopy (SEM). The stability tests also performed for aluminum electrode coated with PPy-Chi/Pt composite film.

INTRODUCTION

Increasing energy requirements due to industrial and population growth has rendered the fossil fuels insufficient. Hydrogen seems to be an ideal energy carrier as a carbon-free fuel due to its high energy density. The generation of molecular hydrogen by the electrolysis of water is an important part of clean energy technologies [1-5].

Water dissociates into H^+ ions and OH^- ions; the H^+ ions are attracted to the cathode and are reduced to a hydrogen atom ($H^+ + e- \rightarrow H$). This is highly unstable and immediately reacts with another hydrogen atom to produce H_2, molecular hydrogen gas.

A practical and sustainable way to produce hydrogen is by the electrolysis of water, but this has one disadvantage due to an over-potential occurring in the electrochemical system, which increases the cost of the method. Although some noble metals, such as Pt, Au and Rh, are known as good hydrogen evolving catalysts in acidic solutions, the high cost of these metals limits their large-scale application. Therefore, cost-effective materials for the electrochemical production of hydrogen are a central area of the research into renewable energy. In addition to being low-cost, it is a challenge to develop highly active catalysts that are stable for long periods. From this point of the view, due to the fact that it is electrochemically active, low-cost, and commercially available aluminum electrode is an appropriate material for hydrogen production as in many other electrocatalytic applications [6, 7].

Conducting polymers incorporating metal nanoparticles modified on various electrode materials have been widely used for electrocatalytic processes [8, 9]. The porous structure, and consequently high surface area, of conducting polymers has led to their use as supporting materials for the development of new electrocatalytic materials. The surface of thin films of the conducting polymers/composites can be a supporting material for metal nanoparticles, provides a much larger effective surface area than bare metal electrodes due to their rough surfaces [10].

On the other hand, chitosan is a natural biopolymer that has attracted great attention in recent decades, both in science and various areas of everyday life due to its interesting properties, such as excellent film forming ability, high mechanical strength, cheapness, and susceptibility to chemical modifications [11, 12].

Herein we present a method for the fabrication of an efficient catalyst for electrocatalytic hydrogen production from water by modifying a low-cost and low-technology aluminum electrode. The modification was performed by co-deposition of polypyrrole using the abundant natural biopolymer chitosan as the raw material. Then we used this porous

surface for the electrodeposition of platinum metal particles at the nano-scale, which exhibit high catalytic activity in hydrogen evolution. Using this efficient catalyst at the nano-scale considerably reduced the amount of Pt in the catalyst, resulting in the low cost of the prepared catalyst. The performances of both PPy-Chi and PPy-Chi/Pt were examined by electrochemical techniques.

MATERIALS AND METHODS

Aluminum rod (99.99%) with a 3 mm diameter was used as the working electrode. The outside of the rod was isolated with epoxy resin leaving only a geometric area of 0.07065 cm^2. Electrochemical measurements were performed in a standard electrochemical cell containing a Pt wire as an auxiliary electrode and Ag/AgCl as a reference electrode. All purchased reagents were of analytical grade and came from commercial sources. Medium molecular weight chitosan was used with a 75-85% deacetylation degree. Pyrrole was distilled under vacuum before use. Prior to modification, the surface of the aluminum electrode was polished with emery paper (180 to 2500 grit) and rinsed with distilled water. Polypyrrole-chitosan was deposited on the aluminum from 0.3 M oxalic acid solution containing 0.1 M pyrrole and 0.01 g of chitosan in a final volume of 10 mL, by chronopotentiometry at a constant current density of 2.5 $mAcm^{-2}$. All electrochemical measurements were performed using a potentiostat/galvanostat (Gamry Interface 1000) and software (Gamry Framework and GamryEchem Analyst).

The PPy-Chi modified electrode was immersed in a 0.5 M H_2SO_4 aqueous solution for five minutes to remove any surplus from its surface and was washed with double distilled water. For comparison, the electrochemical deposition of PPy was performed under the same conditions, but in a chitosan-free solution. The electrochemical measurements showed that the optimum film thickness is obtained after 15 minutes. The electrodeposition of the Pt nanoparticles was achieved on the PPy-Chi modified electrode by cyclic voltammetry from 0.5 M H_2SO_4 aqueous solution containing 3 mM H_2PtCl_6 (hexachloroplatinic acid) in a potential range of -0.25 V and +0.65 V with 50 mV s^{-1} scan rate for two cycles. After washing the modified electrodes with 0.5 M H_2SO_4 solution, they were ready to be used in the electrochemical measurements. The electrode setup is illustrated in Fig. 1.
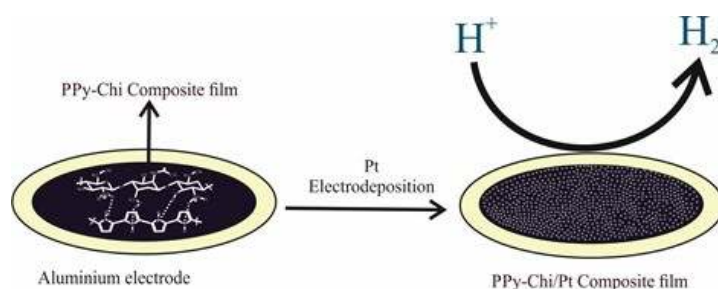
Figure 1. Schematic illustration of experimental setup.

Spectrometric measurements of impedance were performed in a frequency range of 0.1 Hz to 100 kHz. The amplitude of the applied sine wave potential was 10 mV with the direct current potential set at -1.0V. The EIS was obtained in 0.5 M H_2SO_4 solution and plotted in the form of complex planar diagrams (Nyquist plots). A FEIQuanta 250 FEGScanning Electron Microscope (SEM) was used for the morphological analyses.

RESULTS AND DISCUSSION

Morphological analyses were performed by SEM before performing electrochemical analyses (Figure 2). Polypyrrole coating displays a typically cauliflower-like image (Figure 2a), the structure shows a more compact image in the case of PPy-Chi (b). The homogenous distribution of Pt particles (c) and their enlarged images (d) show that the Pt particles electrodeposited on PPy-Chi composite film in nano-scale.
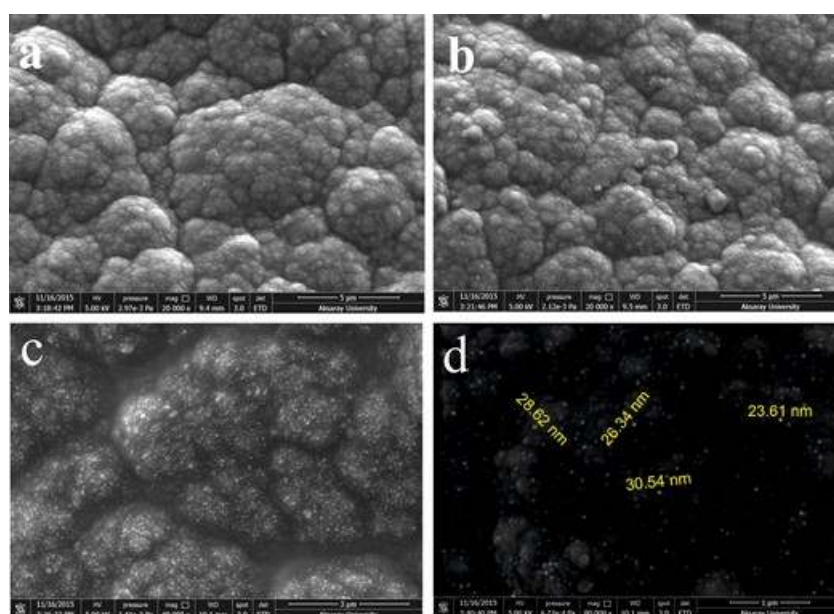
Figure 2. SEM images of a) PPy film, b) PPy-Chitosan composite film, c) PPy-Chitosan/Pt and d) Enlarged image of c).

Voltammetric studies of the aluminum electrode coated with PPy film, PPy-Chi and PPy-Chi/Pt composite films are shown in Figure 3. Cyclic voltammetry was performed in the potential range between -0.6 to -1.5 V with a scan rate of 20 mVs^{-1}.
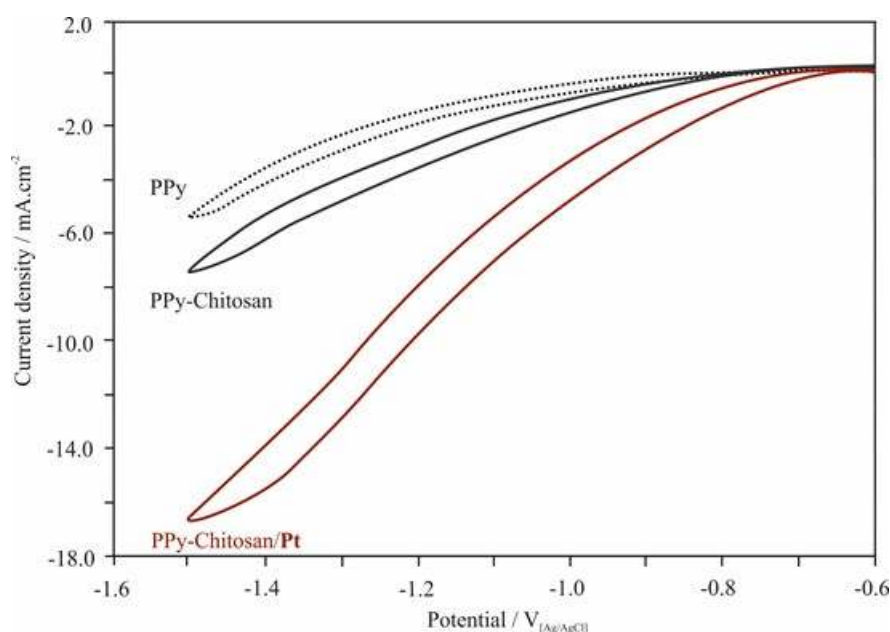
Figure 3. Cyclic voltammograms of PPy film, PPy-Chitosan and PPy-Chitosan/Pt composite films coated on the aluminum electrode.

The current density for the hydrogen evolution was increased by loading chitosan in the PPy film. Chitosan contributes to the polypyrrole chains via hydrogen bonds, leading to a formation of a conductive composite film [13, 14] which has a more compact structure. A more compact film increases the ability of the electron transfer [15] and leads to an increase in the current density for the HER. After the electrochemical deposition of Pt nanoparticles on to the PPy-Chi surface, the current density obtained for the HER increased significantly. The enhanced current density for the HER of the PPy-Chi/Pt catalyst compared with the Pt-free composite can be explained by the well-known catalytic activity of the Pt.

To obtain further insight into the HER on aluminium coated electrode, the Tafel extrapolation curves were also developed for PPy film, PPy-Chi and PPy-Chi/Pt composite films (Figure 4).
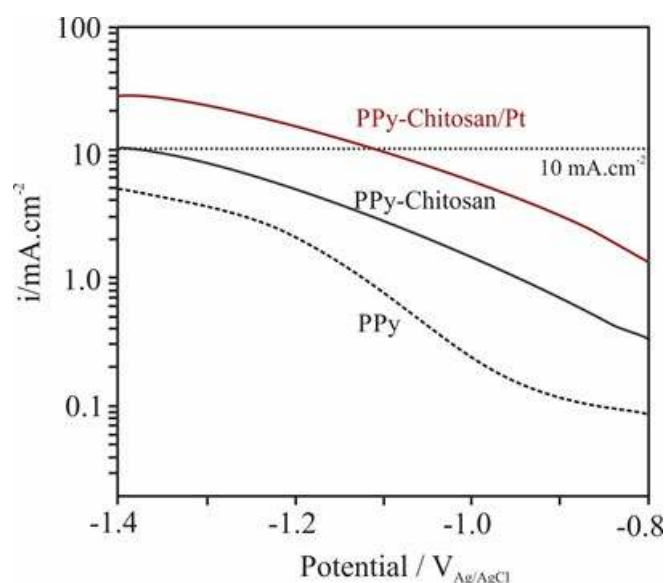
Figure 4. Tafel polarization curves of PPy film, PPy-Chitosan, and PPy-Chitosan/Pt composite films coated on the aluminum electrode.

The obtained current densities were higher for PPy-Chi than the PPy film, consistent with the cyclic voltammetric results and the current densities increased noticeably after Pt electrodeposition. The data of Figure 4 may be considered more quantitatively by examining several kinetic parameters. Table 1 summarizes Tafel parameters for HER on prepared electrodes. The linear region of Tafel plots were fitted into the Tafel equation [16, 17];

$$\eta = a + b \log j \qquad (Eq.\ 1)$$

where η(mV) represents the applied over-potential, b (mV/dec) is the Tafel slope and j (mA/cm^2) is the resulting current density, and a (mV) is the intercept related to the exchange current density j_0(mA/cm^2).

Table 1. The electrochemical parameters calculated from Tafel polarization curves for PPy film, PPy-Chitosan and PPy-Chitosan/Pt composite films coated on the aluminum electrode.

Film	-b/mV dec^{-1}	i_o/mA cm^{-2}	i/ mA cm^{-2} (η= -1.2V)	-η/V (10 mA cm^{-2})
PPy	234	0.21	0.64	1.70
PPy-Chitosan	192	0.54	2.45	1.37
PPy-Chitosan/**Pt**	141	2.44	8.14	1.12

In general, a smaller Tafel slope and related higher current density is desired because it corresponds to less energy loss. The resulting Tafel slopes of PPy film, PPy-Chi and PPy-Chi/Pt are respectively 234, 192 and 141 mV/dec. The smaller Tafel slope for PPy-Chi/Pt compared to PPy-Chi composite film explained by the fact that the catalytic activity of the Pt nanoparticles on hydrogen evolution. There was also an increase about 5 times in the obtained exchange current density in the case of Pt nanoparticles.

A more practical parameter is the over-potential at a given current density. Aluminum electrode modified with PPy-Chi/Pt exhibited a lower over-potential of -1.12 V, at a fixed current density of -10 mAcm^{-2}. Another important parameter calculated from the Tafel results is the resulting current density at a fixed applied potential (energy input). The obtained current density at a chosen applied potential (-1.2 V) for PPy-Chi/Pt increased more than that of PPy-Chi composite film (Table 1).

Electrochemical impedance spectroscopy is a very powerful technique for studying the interface properties of the modified electrodes. The Nyquist plot of impedance spectra include a semicircle which corresponds to the electron-transfer limited process [18]. The diameter of the semicircle is equal to the electron-transfer resistance at the electrode surface and it can be used to describe the interface properties of the electrode. Figure 5 exhibits the Nyquist plots of the impedance spectroscopy of the PPy, PPy-Chi and PPy-Chi/Pt coated aluminum electrodes.
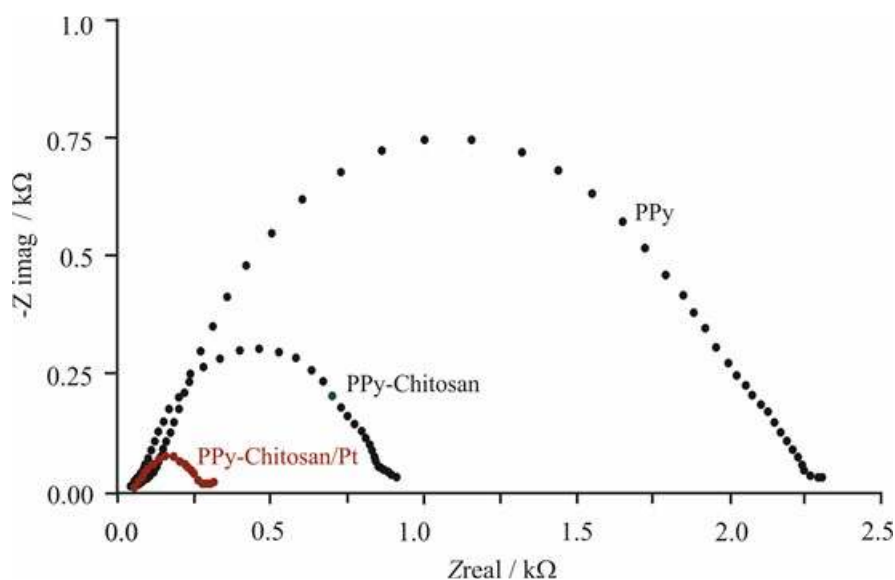
Figure 5. Electrochemical impedance spectrum (Nyquist diagrams) of PPy film, PPy-Chitosan and PPy-Chitosan/Pt composite films coated on the aluminum electrode.

The smaller charge transfer resistance, which indicates the catalytic performance of the catalyst. By the electrodeposition of the Pt nanoparticles on the PPy-Chi composite film the charge transfer resistance decreased from $\approx$0.85 kΩ to $\approx$0.25 kΩ.

In addition to the high electrocatalytic activity, the stability of an electrocatalyst is also important to accept it as an efficient material [19]. For this reason, the stability tests were carried out for PPy-Chi/Pt coating on hydrogen production (Figure 6).
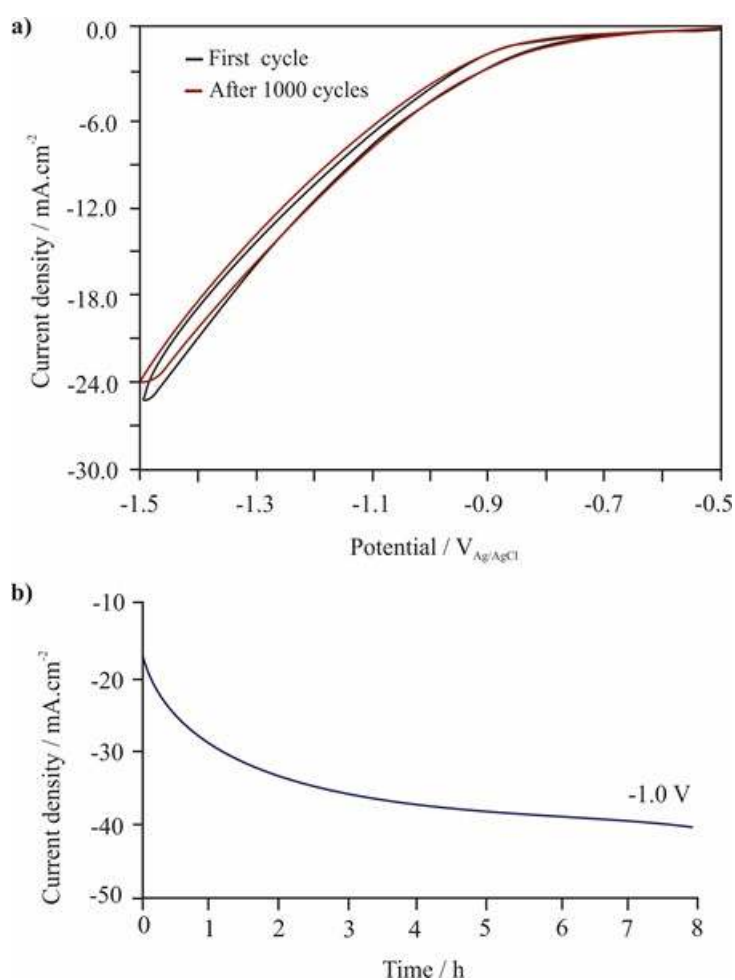
Figure 6. a) CVs of the PPy-Chi/Pt in 0.5 M H_2SO_4 at 1st cycle and 1000th cycle at a scan rate ν=100 mVs^{-1}. b) Chronoamperogram of the PPy-Chi/Pt in 0.5M H_2SO_4 at applied potential -1.0 V.

A remarkable durability obtained for over 1000 cycles in the potential range between -0.5 and -1.5 V at 100 mV/s sweep rate and constant potential measurements for 8 hours.

In conclusion, we have demonstrated the electrocatalytic activity of the aluminum electrode modified by PPy-Chi/Pt composite film for the production of hydrogen from water electrolysis. The aluminum electrode was easily modified by co-electrodeposition of polypyrrole and chitosan at a constant current density of 2.5 mAcm^{-2}. The insertion of chitosan to the polypyrrole chains provided a more compact film which increased the

electron transfer to the H^+ to produce H_2. Then the electrodeposition of Pt particles was achieved on this porous surface at nano-scale to benefit both from its well-known high catalytic activity and to reduce the amount of this precious metal to prepare a low-cost electrocatalyst.

ACKNOWLEDGMENTS

REFERENCES

[1] Hassan S, Suzuki M, Abd El-Moneim A. New MnO2/carbon nanowalls composite electrode for supercapacitor application. J. Power Sources 2014;246:68-73. DOI: 10.1016/j.jpowsour.2013.10.097.

[2] Hao P, Zhao Z. Leng Y, Tian J, Sang Y, Boughton R.I, Wong C.P, Liu H, Yang B. Graphene-based nitrogen self-doped hierarchical porous carbon aerogels derived from chitosan for high performance supercapacitors, Nano Energy 2015;15:9-23. DOI: 10.1016/j.nanoen.2015.02.035.

[3] Chen J, Lim B, Lee E.P, Xia Y. Shape-controlled synthesis of platinum nanocrystals for catalytic and electrocatalytic applications. Nano Today 2009;4:81-95. DOI: 10.1016/j.nantod.2008.09.002.

[4] Navarro-Flores E, Omanovic S. Hydrogen evolution on nickel incorporated in three-dimensional conducting polymer layers. J. Mol. Catal. A: Chem. 2005;242:182-194. DOI: 10.1016/j.molcata.2005.08.008.

[5] Dalla Corte D.A, Torres C, Correa P. dos S, Rieder E.S, Malfatti C. de F. The hydrogen evolution reaction on nickel-polyaniline composite electrodes. Int. J. Hydrogen Energy 2012;37:3025-3032. DOI: 10.1016/j.ijhydene.2011.11.037.

[6] Alexis D, Omanovic S. Ni and Ni Mo hydrogen evolution electrocatalysts electrodeposited in a polyaniline matrix. J. Power Sources 2006;158(1):464-76. DOI: 10.1016/j.jpowsour.2005.09.007.

[7] Tuomi S, Guil-Lopez R, Kallio T. Molybdenum carbide nanoparticles as a catalyst for the hydrogen evolution reaction and the effect of pH. J Catal 2016;334:102-109. DOI: 10.1016/j.jcat.2015.11.018.

[8] Yuvaraj AL,Santhanaraj D. A systematic study on electrolytic production of hydrogen gas by using graphite as electrode. Materials Research 2014;17(1):83-87. URL**:** http://www.scielo.br/scielo.php?pid=S1516-14392013005000153&script=sci_arttext&tlng=pt **.**

[9] Flores EN, Omanovic S. Hydrogen evolution on nickel incorporated in three-dimensional conducting polymer layers. J Mol Catal A: Chem 2005;242:182-194. DOI: 10.1016/j.molcata.2005.08.008.

[10] Niu L. Li Q, Wei F, Wu S, Liu P, Cao X. Electrocatalytic behaviour of Ptmodified polyaniline electrode for methanol electrooxidation: Effect of Pt deposition modes.J. Electroanal. Chem. 2005;578:331-337. DOI: 10.1016/j.jelechem.2005.01.014.

[11] Yavuz A.G, Uygun A, Bhethanabotla VR. Substituted polyaniline/chitosan composites: Synthesis and characterization. Carbohydr Polym 2009;75:448–453. DOI: 10.1016/j.carbpol.2008.08.005.

[12] Marroquina J.B, Rheea K.Y, Park S.J. Chitosan nanocomposite films: Enhanced electrical conductivity, thermal stability, and mechanical properties. Carbohydr Polym 2013;92:1783-1791. DOI: 10.1016/j.carbpol.2012.11.042.

[13] Silva R.C, Sarmento M.V, Nogueira A.R.F, Tonholo J, Mortimer R.J, Faez R, Ribeiro A.S. Enhancing the electrochromic response of polyaniline films by the preparation of hybrid materials based on polyaniline, chitosan and organically modified clay. RSC Adv 2014;4:14948–14955. DOI: 10.1039/c3ra47474g.

[14] Varghese J.G, Kittur A.A, Rachipudi P.S, Kariduraganavar M.Y. Synthesis, characterization and pervaporation performance of chitosan-g-polyaniline membranes for the dehydration of isopropanol. J Membr Sci 2010;364:111-121. DOI: 10.1016/j.memsci.2010.08.007.

[15] Gök A, Omastova M, Yavuz A.G. Synthesis and characterization of polythiophenes prepared in the presence of surfactants. Synth Met 2007;157:23–29. DOI: 10.1016/j.synthmet.2006.11.012.

[16] Kayan D.B, Koçak D, İlhan M. The activity of PAni-Chitosan composite filmdecorated with Pt nanoparticles for electrocatalytichydrogen generation. Int. J. Hydrogen Energy 2016; 41:10522-10529. DOI: 10.1016/j.ijhydene.2016.05.024.

[17] Zheng Y, Jiao Y, Zhu Y, Li LH, Han Y, Chen Y, Du A, Jaroniec M, Qiao SZ. Hydrogen evolution by a metal-free electrocatalyst. Nature Commun 2014; 5:3783:1-8. DOI:10.1038/ncomms4783.

[18] Kayan D.B, Köleli F. Dinitrogen reduction on a polypyrrole coated Pt electrode under high-pressure conditions: electrochemical impedance spectroscopy studies. Turk J Chem 2015;39:648-659. DOI:10.3906/kim-1501-80.

[19] Winther-Jensen B.B, Fraser K, Ong C, Forsyth M, MacFarlane D.R. Conducting polymer composite materials for hydrogen generation. Adv. Mater. 2010;2:1727–1730. DOI: 10.1002/adma.200902934.

Investigation of Essential Oil Composition, Polyphenol Content, and Antioxidant Activity of *Myrtus communis* L. from Turkey

Belma Hasdemir[1]*, Hasniye Yaşa[1], Hülya Çelik Onar[1] and Ayşe Sergüzel Yusufoğlu[1]

[1]Department of Chemistry, Faculty of Engineering, Istanbul University, 34320 Avcılar, Istanbul, Turkey.

Abstract: In this study, it is aimed to investigate the chemical composition of the essential oil, polyphenol content, and antioxidant activity of *Myrtus communis* L. from Turkey. The plant, *Myrtus communis* L., was collected from Yalova, in the Marmara region of Turkey. The essential oil was prepared with 0.5% by hydrodistillation of its leaves in a Clevenger-type apparatus. The chemical composition of the essential oil was analyzed by GC and GC–MS, using two columns with stationary phases of different polarity (polar ZB-WaxMS/apolar ZB-5MS). On both columns, monoterpenes were determined to be the dominant compounds. The myrtenyl acetate, α-pinene, 1,8-cineole, linalool, and limonene were the remarkable substances. As polyphenolic compounds, the flavanoids and anthocyanidins in leaves and berries were detected by HPLC. The antioxidant activity was studied with DPPH, Cuprac and Folin–Ciocalteu methods.

Keywords: *Myrtus communis* L.; anthocyanidins; flavonoids; essential oils; antioxidant activity.

INTRODUCTION

Myrtus communis L., growing in several regions all over the world (1-3) is found in pine forests and all coastal zones in Turkey. Myrtle (*Myrtus communis* L.) is called as "hambeles", "mersin" or "murt" in Turkish.

Myrtus communis L., expecially its leaves and berries, is traditionaly used in folk medicine as antiseptic, antidiaretic, antibacterial, disinfectant drug, hypoglycaemic, and stomachic (4-6). The essential oils from leaves of this plant also have a private role in treatment of lung diseases (7), perfumery, beverages, candies, ice cream and bakery products (8-9) and show antimicrobial (10), antibacterial (11), and antioxidant activities (12-14). Isolation of some compounds from the leaves (15-16), the essential oil (10,17) and berries (18) has been reported in the literature. Some researchers indicated that the chemical composition of *Myrtus communis* L. essential oils showed a difference depending on the harvesting time, origin, and extraction method (12,19-21). Fatty acid composition of the plant from Erzurum and Muğla region in Turkey was determined in addition to nutritional and physical properties of myrtle fruits from Mersin in the previous studies (22-23).

The human body has a complex system and free radicals produced from biochemical reactions in our body are responsible for chronic diseases. The antioxidant substances can prevent the damaging effects of these radicals to quench them and detoxify the organism (24). The studies in this field emphasize the importance of antioxidant nutrients for protection diseases.

According to the literature, there is no study based on the antioxidant activity of the essential oil and polyphenolic contents of Turkish *Myrtus communis* L. leaves and berries.

This work aims at analyzing the components of the essential oil of *Myrtus communis* L. leaves, determining as the anthocyanidin and flavonoid compounds and evaluating the antioxidant properties of methanolic extracts of *Myrtus communis* L. leaves and berries.

MATERIALS AND METHODS

Reagents and Standards

HPLC grade methanol, acetonitrile, trifluoroacetic acid and Folin - Ciocalteau reagent were purchased from Merck. Anthocyanidin standards of (delphinidin, peonidin, pelargonidin, malvidin, cyanidin chloride) and flavonoids (myricetin, quercetin, p-coumaric acid) and DPPH (1,1-diphenyl-2-picrylhydrazyl), NDGA (Nordihydroguiaretic acid), ascorbic acid, pryrocatechol were obtained from Sigma-Aldrich.

Standard stock solutions (1 mg mL^{-1} in methanol) of each of anthocyanidin and flavonoid **(1-8)** were prepared (Figure 1a and 1b).

Plant Material

Leaves and berries of *Myrtus communis* L. from Yalova region of Turkey were dried, powdered, and stored at -20°C.

Hydrodistillation

The leaves of plant were hydrodistilled for 2h with a simple Clevenger- type apparatus. Yield of the oil was 0.5% based on dry plant weight.

GC/MS Analysis of the Essential Oils

Thermo Finnigan trace DSQ GC-instrument (FID) combined with MS system was used to analyze the chemical components. The capillary columns, ZB-WaxMS (polyethylene glycol, 60 m × 0.25 mm i.d., 0.25 µm film thickness) and ZB-5MS (5% polysilarylene, 95% polydimethyl siloxane, 30 m × 0.25 mm i.d., 0.25 µm film thickness) were used. Operating conditions were chosen as injection temperature 250 °C, helium carrier gas flow (1,5 mL min^{-1}), split flow: 10 mL min^{-1}. Temperature programming 30-100 °C (2 °C min^{-1}) (5 min)-240 °C at 5 °C min^{-1}, hold 30 min.

The results were determined by looking at the retention indices in the literature (10,12,17,25-26) and comparing with their MS spectra.

Qualitative Analysis of Phenolic Compounds by HPLC

Preparation of *Myrtus communis* L. Extracts for HPLC Analysis: Dried leaves and berries (1 g) were extracted in flasks immersed into an ultrasonic bath firstly with 70% MeOH (15 mL) for 45 min, then 5 mL of the same solvent for second 45 min and minimum 5 mL more of the solvent for last 15 min were added, the total extraction time was 105 min (27). The plant extracts were filtered with a GF/PET 1.0 / 0.45 µm microfiber, and analyzed (Figures 2 and 3).

HPLC / UV-vis Analysis

The HPLC equipment employed in this study was a Shimadzu / DGU-20 A_5 HPLC apparatus fitted with intertsil O DS-3 C_{18} column (4,6 × 150 mm, 5 µm particle size) according to the procedure described by literature (13). The elution program was used in the reversed- phase HPLC analysis.

Compounds **1-7** could be detected between 350 and 520 nm, characteristics for flavonoids and anthocyanidin, respectively, according to the chromatographic conditions described in the literature above. The chromatograms can be seen in Figures 2-5.

Hydrolysis of plant extracts have been done according to the literature (27). These extracts were also analyzed (Figures 4, 5a and 5b).

In addition, all flavonoids and anthocyanidins were identified from their spectroscopic properties and their range of retention times.

Antioxidant Activity

DPPH Radical Scavenging Activity: The DPPH radical scavenging activity of the *Myrtus communis* L. extracts were defined by the procedure of Brand-Williams *et al.*(28). An appropriate dilution series (20 to 100 µg mL^{-1}) were made for each methanolic extract in methanol, afterwards 0.1 mL of each sample was mixed with 3.9 mL of a 6 × 10^{-5} M methanolic solution of DPPH. The mixture was flattered fiercely and left in the darkness at room temperature (30 min) and then the absorbance was read at 517 nm against methanol. The equation given below represents the calculation of capability to scavenge the DPPH radical.

$$\text{DPPH radical scavenging activity } (\%) = (A_0 - A_1 / A_0) \times 100 \qquad \text{(Eq.1)}$$

A_0 and A_1 is the absorbance of control (without sample) and test sample, respectively.

Determination of Total Phenolic Contents

Determination of total phenolic content in *Myrtus communis* L. extracts was predicted using Folin - Ciocalteau method (29). The measured wavelength with maximum absorbance in a spectrophotometer was 760 nm. The total phenolic compound amount in the extract was calculated as mg of pyrocatechol equivalent from the calibration curve and as mg pyrocatechol equivalents per mg of extract.

CUPRAC Method

The proposed Cuprac method by Apak (30) was applied as follows: 1 mL of 1.0×10^{-2} M copper(II) chloride, 1 mL of 7.5×10^{-3} M neocuproine solution and 1 mL of 1 M ammonium acetate buffer at pH 7.0, x mL sample solution and (1- x) mL distilled water (total volume: 4.0 mL) were added to a test tube and mixed well. This mixture was stoppered and let stand at room temperature (30 min). The absorbance was recorded at 450 nm against a reagent blank.

RESULTS AND DISCUSSION

Yield and Chemical Composition of *Myrtus communis* L. Essential Oil

The essential oil of the plant leaves was prepared by hydrodistillation in a Clevenger-type apparatus in 0.5%. The plant collected from Yalova, Turkey was analyzed qualitatively and quantitatively via GC and GC / MS on two different columns, on a polar column ZB-Wax MS and on a apolar column ZB-5MS (Table 1). The Relative Retention Indices (RRI) for all the compounds were calculated using a homologous series of n-alkanes. All components were identified by comparing their relative retention indices and also their mass spectras with the literature data.

Thirty one and eighteen compounds were identified on the polar column and on the apolar column, respectively. The major components were myrtenyl acetate (22.26 %), α-pinene (15.51%), linalool (14.91%), 1,8-cineole (14.30%) and limonene (13.63%) on

ZB-Wax MS. On the ZB-5MS, the main components were myrtenyl acetate (21.42%), 1,8-cineole (16.78%), linalool (15.66%), limonene (15.59%) and α-pinene (15.07%).

HPLC / UV-vis Analysis of *Myrtus communis* L. Leaves and Berries Extracts

Myrtus communis L. leaves and berries were extracted according to the literature (27) for HPLC analysis. The hydrolysis of flavonoid glycosides in plant extracts to their parent aglycone was also identified using standarts (quercetin and kaempferol).

Figures 1a and 1b show the chromatogram of synthetic mixture flavonoids and anthocyanidins, respectively. The chromatogram of 70% methanolic extract of *Myrtus communis* L. leaves and the chromatogram of the same extract after 4h hydrolysis are given in Figures 2 and 4, respectively. When Figure 3 represents the chromatogram of 70% methanolic extract of *Myrtus communis* L. berries, Figures 5a and 5b give the chromatogram of the same extract after 4h hydrolysis.

P.coumaric acid, myricetin, and quercetin in the *Myrtus communis* L. leaves and berries, cyanidin, malvidin, pelargonidin, and peonidin in the *Myrtus communis* L. berries have been specified according to their retention times and the spectral characteristics of their peaks against those of standards.

Major peak in the flavonoid chromatogram was identified as myricetin **2** and minor peaks were characterized as compounds **1** and **3**, respectively, p.coumaric acid and quercetin at 350 nm (Figures 4 and 5a).

Major peak in the anthocyanidin chromatogram corresponded to compound **5** was defined as cyanidin and minor peaks were obtained as compounds **6**, **7** and **8**, respectively, malvidin, pelargonidin and peonidin at 520 nm (Figure 5b).

DPPH Assay

DPPH assay is an antioxidant method based on a color change of the solution from violet to yellow upon reduction and this method supplies an easy and rapid way to determine antioxidants by spectrometry.

Figure 6 shows the concentration-inhibition(%) curves for the DPPH radical scavenging activity of the methanolic extracts from *Myrtus communis* L. leaves and berries and standards. The scavenging activity of these extracts from *Myrtus communis* L. berries and leaves, tocopherol, ascorbic acid, butylated hydroxyanisole (BHA), nordihydroguiaretic acid (NDGA) on DPPH radicals increased between 20-100 µg mL^{-1} and were 82.20 ± 1.237, 95.09 ± 0.305, 95.71 ± 0.3010, 96.93 ± 0.178, 94.48 ± 0.352, 96.63 ± 0.178 at a concentration of 100 µg mL^{-1}, respectively. Methanolic extract of leaves, BHA, tocopherol, ascorbic acid and NDGA displayed similar DPPH scavenging activities, while the effective DPPH scavenging activity of methanolic extract of berries was quite low (Figure 6).

Total Phenolic Contents

Phenols are good scavengers because of having hydroxyl groups of components found in plants. These antioxidants also exhibit different biological activities like antiatherosclerotic, antiinflammatory, and anticarcinogenic effects (31).

The results of total phenolic content for the methanolic extracts from *Myrtus communis* L. berries and leaves, expressed as pryrocatechol equivalents, are presented in Table 2. Methanolic extract of leaves contains more phenolic compounds than the berry extract.

CUPRAC Method

The reducing power of antioxidant compounds was determined by the CUPRAC assay, which is a useful method and Cu^{2+} is reduced to Cu$^+$ with antioxidants in the presence of neocuproin. In this method, a higher absorbance means a higher cupric ion reduction ability. The method is also cheap, and is suitable for a lot of antioxidants (32).

The cupric ion (Cu^{2+}) reducing abilities of the methanolic extracts from *Myrtus communis* L. leaves and berries are given in Table 3. Methanolic extract of leaves exhibited more reducing capacity than that of berries.

CONCLUSION

The chemical composition of *Myrtus communis* L. essential oil could be divided into subgroups according to the relative ratio of α-pinene and myrtenyl acetate or α-pinene and 1,8-cineole (19). Myrtenyl acetate content is high (22.26-21.42%) as Spanish, Moroccon, Portuguese, French, Albanian and Yugoslavian myrtle oils (20,33-34) in the essential oil of *Myrtus communis* L. leaves from Yalova region, Turkey.

Phenolic compounds, flavonoids and anthocyanidins of *Myrtus communis* L. leaves and berries were determined qualitatively by HPLC method at 350 nm and 520 nm. The major component of flavonoids in leaves and berries was myricetin. The main compound of anthocyanidins in berries was cyanidin. However, the anthocyanidins have not been detected in the leaves.

The findings of this study demonstrated that methanolic extracts of *Myrtus communis* L. leaves and berries possess antioxidant activity. The antioxidant activity of these extracts is similar to standarts of BHA, tocopherol, ascorbic acid and NDGA.

The plant, *Myrtus communis* L. from Turkey together with its leaves and the berries is a rich antioxidant source due to its essential oil composition (Table 1) and flavonoid content (Figures 4, 5a and 5b) and can be used in food, pharmaceutical, cosmetic industries and against diseases with its good antioxidant ability tested in this study.

ACKNOWLEDGMENTS

REFERENCES

1. Akgül A. Spice science and technology; Ankara: Turkish Association of Food Technologists. 1993 Publ.No.15.

2. Davis PH. Flora of Turkey and the East Aegean Islands; Edinburgh:Univercity Press. 1982 Vol.4: 172.

3. Benabid A. Project GEF-RIF (Protection et qestion participatives des ecosystemes forestieres du Rif). 1997 BDRA:Paris.

4. Bravo L. Polyphenols:chemistry, dictary sources, metabolism and nutritional significance. Nutrition Reviews. 1998 56: 317-333. DOI: 10.1111/j.1753-4887.1998.tb01670.x.

5. Elfellah MS, Akhter MH, Khan MT. Anti-hyperglycaemic effect of an extract of Myrtus communis in streptozotocin-induced diabetes in mice. Journal of Ethnopharmacology. 1984 11:275- 281. DOI: 10.1016/0378-8741(84)90073-4.

6. Twaij HAA, Elisha EE, Khalid RM, Analgesic Studies on Some Iraqi Medicinal Plants Part II. J.of Crude Drug Research. 1989 27: 109-112. DOI: 10.3109/13880208909053947.

7. Gauthier R, Agoumi A, Gourai M. Acrivite d'extrait de Myrtus communis contre pediculs humanus capitis. Plante Medicinales et Phytotherapie. 1989 23: 95-108.

8. Baytop T. Treatment with plants in Turkey; Istanbul, Turkey: Istanbul Univ. (in Turkish), 1984 Publ.No.3255. ISBN 975-420-021-1.

9. Akgül A, Bayrak A. The essential oil yield and composition of myrtle plant (Myrtus communis L.) leaves. Doğa Türk Tarım ve Ormancılık Dergisi. 1989 13: 143-147.

10. Yadegarinia D, Gachkar L, Rezaei M, Taghizadeh M, Alipoor Astaneh Sh, Rasooli I. Biochemical activities of Iranian Mentha piperita L.and Myrtus communis L. essential oils. Phytochemistry. 2006 67: 1249-1255. DOI**:** 10.1016/j.phytochem.2006.04.025.

11. Hayder N, Kilani S, Abdelwahed A, Mahmoud A, Meftahi K, Benchibani J. *et.al*. Antimutagenic activity of aqueous extracts and essential oil isolated from Myrtus communis. Pharmazie. 2003 58: 25-27.

12. Chryssavgi G, Vassiliki P, Athanasios M, Kibouris T, Michael K. Essential oil composition of Pistacia lentiscus L. and Myrtus communis L. Evaluation of antioxidant capacity of methanolic extracts. Food Chemistry. 2008 107: 1120-1130. DOI.10.1016/j.foodchem.2007.09.036

13. Montoro P, Tuberoso CI, Piacente S, Perrone A, Feo VD, Cabras P, Pizza C. Stability and antioxidant activity of polyphenols in extracts of Myrtus communis L. berries used for the preparation of myrtle liqueur. J. of Pharmaceutical and Biomedical Analysis. 2006 41: 1614-1619. DOI.10.1016/j.jpba.2006.02.018

14. Romani A, Coinu R, Carta S, Pinelli P, Galardi C, Vincieri FF. et al. Evaluation of antioxidant effect of different extracts of Myrtus comminus L. Free Radical Research. 2004 38: 97-103. DOI.10.1080/10715760310001625609

15. Pichon-Prum N, Raynaud J, Debourchieu L, Joseph MJ. Sur la presence d'un heteroside acyle de la quercetine dans les feuilles de Myrtus communis L. (Myrtaceae). Pharmazie. 1989 44: 508-509.

16. Pichon-Prum, N., Joseph, M.J., Raynoud, J. (1993). Myricetine-3-β-D-(6''-o-galloyl-galactoside) de Myrtus communis L (Myrtaceae). Plantes Méd Phytothér. 26: 86-92.

17. Mimica-Dukić N, Bugarin D, Grbović S, Mitić-Ćulafić D, Vuković-Gačić B, Orčić D, Jovin E, Couladis M. Essential Oil of Myrtus communis L. as a Potential antioxidant and antimutagenic agents. Molecules. 2010 15: 2759-2770. DOI:10.3390/molecules15042759

18. Martin T, Villaescusa L, De Sotto M, Lucia A, Diaz AM. Determination of anthocyanic pigments in Myrtus communis L. berries. Fitoterapia. 1990 61: 85.

19. Farah A, Afifi A, Fechtal M, Chhen A, Satrani B, Talbi M, Chaouch A. Fractional distillation effect on the chemical composition of Moroccan myrtle   (Myrtus communis L.) essential oils. Flavour and Fragrance Journal. 2006 21: 351-354. DOI: 10.1002/ffj.1651

20. Özek T, Demirci B, Başer KHC. Chemical Composition of Turkish Myrtle Oil. Journal of Essential Oil Research. 2000 12: 541-544. DOI: 10.1080/10412905.2000.9712154.

21. Nassar MI, Aboutabl el-SA, Ahmed RF, El-Khrisy ED, Ibrahim, KM, Sleem AA. Secondary metabolites and bioactivities of Myritus communis. Pharmacognosy Research. 2010 2: 325-329. DOI. 10.4103/0974-8490.75449.

22. Cakir A. Essential oil and fatty acid composition of the fruits of Hippophae rhamnoides L. (Sea Buckthorn) and Myrtus communis L. from Turkey. Biochemical Systematics and Ecology. 2004 32: 809-816. DOI: 10.1016/j.bse.2003.11.010.

23. Cevat A, Özcan MM. Determination of nutritional and physical properties of myrtle (Myrtus communis L.) fruits growing wild in Turkey. Journal of Food Engineering. 2007 79: 453-458. DOI: 10.1016/j.jfoodeng.2006.02.008.

24. Ebrahimzadeh MA, Nabavi SF, Nabavi SM. Essential oil composition and antioxidant activity of Pterrocarya fraxinifolia. Pakistan Journal of Biological Sciences. 2009 12: 957-963. URL: https://www.researchgate.net/profile/Mohammad_Ebrahimzadeh/publication/26882991_Essential_oil_Composition_and_Antioxidant_Activity_of_Pterocarya_fraxinifolia/links/00b4951e924e3e0db1000000.pdf.

25. Wannes WA, Mhamdi B, Marzouk B. Variations in essential oil and fatty acid composition during Myrtus communis var. italica fruit maturation. Food Chemistry. 2009 112: 621-626. DOI.10.1016/j.foodchem.2008.06.018.

26. Adams RP. Identification of Essential Oil Components by Gas Chromatography/Mass Spectrometry. Allured Publishing Corporation, Carol Stream, 2007 4th Ed. ISBN: 1932633219.

27. Yıldız L, Başkan KS, Tütem E, Apak R. Combined HPLC-CUPRAC (cupric ion reducing antioxidant capacity) assay of parsley, celery leaves, and netle. Talanta. 2008 77: 304-313. DOI:10.1016/j.talanta.2008.06.028.

28. Brand-Williams W, Cuvelier ME, Berset C. Use of a free radical method to evaluate antioxidant activity. LWT-Food Sci. Technol. 1995 28: 25-30. DOI: 10.1016/S0023-6438(95)80008-5.

29. Slinkard K, Singleton VL. Total phenols analysis: automation and comparison with manual methods. Am.J.Enol.Viticult. 1977 28: 49-55. URL: http://www.ajevonline.org/content/28/1/49.

30. Apak R, Güçlü K, Özyürek M, Karademir SE. Novel Total Antioxidant Capacity Index for Dietary Polyphenols and Vitamins C and E, Using Their Cupric Ion Reducing Capability in the Presence of Neocuproine: CUPRAC Method. J. Agric. Food Chem. 2004 52: 7970-7981. DOI. 10.1021/jf048741x.

31. Onar HÇ, Yusufoglu A, Turker G, Yanardag R. Elastase, tyrosinase and lipoxygenase inhibition and antioxidant activity of an aqueous extract from Epilobium angustifolium L. leaves. Journal of Medicinal Plants Research. 2012 6: 716-726. DOI: 10.5897/JMPR11.1127.

32. Karaman Ş, Tütem E, Başkan KS, Apak R. Conparison of total antioxidant capacity and phenolic composition of some apple juice with combined HPLC-CUPRAC assay. Food Chemistry. 2010 120: 1201-1209. DOI: 10.1016/j.foodchem.2009.11.065.

33. Boelens MH, Jimenes R. The Chemical Composition of Spanish Myrtle Leaf Oils. Journal essential oil research. 1991 3: 173-177. DOI: 10.1080/10412905.1991.9700498.

34. Boelens MH, Jimenes R. Changes in Monoterpene Content Accompanying Development of Cymbopogon winterianus Jowitt Leaves. Journal essential oil research. 1992 4: 349-353. DOI: 10.1080/10412905.1992.9698084.

Türkçe Öz ve Anahtar Kelimeler
Türkiye'den *Myrtus communis* L.'nin Esansiyel Yağ Bileşimi, Polifenol İçeriği ve Antioksidan Aktivitesinin İncelenmesi

Belma Hasdemir, Hasniye Yaşa, Hülya Çelik Onar ve Ayşe Sergüzel Yusufoğlu

Öz: Bu çalışmada, Türkiye'den toplanmış *Myrtus communis* L.'nin esansiyel yağının kimyasal bileşimi, polifenol içeriği ve antioksidan aktivitesinin incelenmesi amaçlanmıştır. Bitki Türkiye'nin Marmara bölgesinde yer alan Yalova ilinden toplanmıştır. Esansiyel yağ, Clevenger tipi cihazda yaprakların hidrodestilasyonu ile %0,5 verimle hazırlanmıştır. Esansiyel yağın kimyasal bileşimi GC ve GC-MS ile analiz edilmiştir, farklı polariteye sahip durağan fazlar içeren iki kolon kullanılmıştır (polar ZB-WaxMS/apolar ZM-5MS). Her iki kolonda da monoterpenlerin baskın olduğu görülmüştür. Mirtenil asetat, α-pinen, 1,8-sineol, linalool ve limonenin belirgin bileşikler olduğu tespit edilmiştir. Polifenolik bileşikler olarak, yapraklarda ve tanelerde flavanoidlerin ve antosiyanidinlerin varlığı HPLC ile tespit edilmiştir. Antioksidan aktivitesi DPPH, Cuprac ve Folin-Ciocalteau yöntemleriyle çalışılmıştır.

Anahtar kelimeler: *Myrtus communis* L.; antosiyanidin; flavanoidler; esansiyel yağlar; antioksidan aktivitesi.

Sunulma: 22 Ağustos 2016. **Düzeltme:** 03 Eylül 2016. **Kabul:** 28 Eylül 2016.

A Novel Acrylonitrile Derivative Having Photovoltaic Performance

Çiğdem Yörür-Göreci[1*],Mehmet Kazici[2], Sinem Bozar[2], Zulal Demir[1], Abdullah Toraman[1], Fatih Ongul[2], Abid Ali[2], Serap Güneş[2]

[1]Yildiz Technical University, Faculty of Arts and Sciences, Department of Chemistry, 34210 Istanbul, Turkey

[2]Yildiz Technical University, Faculty of Arts and Sciences, Department of Physics, 34210 Istanbul, Turkey

Abstract: A new acrylonitrile derivative, *2-(4-bromophenyl)-3-{5-[2-cyano-2-phenylethenyl]furan-2-yl}acrylonitrile (***BPCPFA, 3***)* which is a potential material for application in organic solar cells, was synthesized by a three-step reaction. The structures of the molecules synthesized in these steps were characterized by using various spectral analyses. **BPCPFA** was investigated as an electron acceptor molecule in next generation organic solar cells. Theoretical prediction and experimental studies for photovoltaic performance were also performed. Based on these results, it is concluded that **BPCPFA** with extended conjugated system has good and promising photovoltaic performance with V_{oc} value as 0.96 V.

INTRODUCTION

Organic photovoltaics (OPVs) are an encouraging field to produce energy as a renewable energy source. The simple processing, cost-effective fabrication, and device flexibility of organic solar cells make them superior as compared to the inorganic solar cells. Recently, the most popular and efficient way of fabricating organic solar cells is to use the bulk heterojunction concept in which an electron donor and an acceptor is blended in a solution and cast as a film from this solution. The development of bulk heterojunction organic solar cells has shown a fascinating increase in the power conversion efficiency [1-4].

Despite all this increase, their power conversion efficiency is still low as compared to inorganic solar cells. The most efficient organic solar cells make use of small organic molecules and conjugated polymers in their structure. Most of the small molecules and conjugated polymers used in photovoltaics are mostly p-type (donor) materials [5, 6]. In this area, the number of materials exhibiting n-type (acceptor) properties is very restricted and among acceptor type molecules the most well-known molecules are fullerenes. For example [6, 6]-phenyl C_{61} butyric acid methyl ester (PCBM) is a fullerene derivative which has excellent acceptor characteristics. Unfortunately, PCBM also has some disadvantages such as air degradation and cost intensive synthesis [7, 8]. The need for new acceptor materials for organic photovoltaics is growing rapidly. Consequently, the importance of these materials increases dramatically day by day.

We have synthesized a novel acceptor organic molecule which contains furan ring with electron-withdrawing cyano groups **(BPCPFA)** and investigated its photovoltaic properties. Until recently, various organic small molecules have been synthesized for solar cells. However, most of these molecules have commonly triphenylamine-based structure and are often symmetric [9]. The molecular structure containing heterocyclic system of these type diarylacrylonitriles has been synthesized to investigate their capacity in solar cells as acceptor elsewhere [7, 10-13].

In this study, photovoltaic properties of a new compound was thoroughly investigated. We achieved comparably a higher V_{oc} as compared to the reference device employing P3HT (poly(3-hexylthiophene-2,5-diyl)) and PCBM blends.

MATERIALS AND METHODS

All reactions were carried out under nitrogen atmosphere. The solvents were purchased from Merck and dried by standard methods (using anhydrous CaO and distillation). The reagents were used without further purification from commercial suppliers.

The FT-IR spectra were collected on a Perkin Elmer, Spectrum One Bv 5.0 spectrometer. ^{1}H NMR and ^{13}C NMR spectra were recorded on a Varian Unity Inova Spectrometer (500 MHz) using $CDCl_3$. The LC-MS spectra were measured on an Agilent 1200 Infinity HPLC with Agilent 6460 spectrometer.

Melting points of synthesized compounds were determined with Gallenkamp melting point apparatus in open capillaries.

As substrates, ITO (indium tin oxide) glass sheets of 1.5 cm x 1.5 cm, from Kintec Company, Hong kong which has a sheet resistance < 12 $\Omega.cm^{-2}$ were used. The ITO was patterned by etching with an acidic mixture of $HCl:HNO_3:H_2O$ (4.6:0.4:5) for 30 min. The part of the substrate which forms the contact was covered with a scotch tape to prevent etching. The tape was removed after etching and the substrate was then cleaned using distilled water, acetone and isopropanol in an ultrasonic bath, respectively as described elsewhere [7].

The active layer with 1:0.5 wt ratio was prepared by blending 10 mg of P3HT and 5 mg of compound **3** (**BPCPFA**) in 1 mL of chlorobenzene (CB) and also blends for active layer with 1:1 wt ratio was prepared by dissolving 10 mg of P3HT and 10 mg of **3 (BPCPFA)** in 1 mL of chlorobenzene (CB).

For the organic bulk heterojunction solar cells, poly(3,4-ethylenedioxythiophene)–poly(styrenesulfonate) (PEDOT:PSS) was deposited on to the ITO coated glass substrate by spin coating at 2000 rpm in air. The PEDOT:PSS layers were annealed in a furnace at 150 °C for 4 minutes. Active layers of P3HT:CPCPFA were spin-coated onto PEDOT:PSS films at 800 rpm in a glovebox. For some of the devices, thermal annealing of the active layer was done on a hot plate at 120 °C for 3 minutes. Finally, 100 nm Al was thermally evaporated as top contact.

All current–voltage (I–V) characteristics of the PV devices were measured (using a Keithley 2400) under nitrogen in a dry glove box just after production. Abet solar simulator, simulating AM1.5 conditions, was used as the excitation source with an input power of 100 mW/cm^2 white-light illumination.

The power conversion efficiencies of the organic solar cells were calculated according to the following equation:

$$\eta_{AM\ 1.5}\ (\%) = \left(\frac{P_{out}}{P_{In}}\right) x\ 100 = \frac{FF\ V_{oc}\ J_{sc}}{P_{in}}\ x\ 100 \qquad \text{(Eq. 1)}$$

The percentage efficiency, ηAM 1.5, is given by the ratio of the power output (P_{out}), to the power input from the solar simulator (P_{in}, 100mW/cm^2). The output power of a solar cell under illumination is the product of the fill factor (FF), the open-circuit voltage V_{oc} (V) and the current density under short circuit conditions J_{sc} (mA/cm^2). The fill factor is obtained using the following equation:

$$FF = \frac{V_{mpp}\ J_{mpp}}{V_{oc}\ J_{sc}} \qquad \text{(Eq. 2)}$$

where the maximum power point of the product of the voltage and the current density (V_{mpp} and J_{mpp}) is divided by the product of the open-circuit voltage and the short circuit current.

The current–voltage curves (*J–V*) of the photovoltaic devices were created by a Keithley 2400 under nitrogen atmosphere.

Synthesis

The compound **3 (BPCPFA)** studied in this paper was prepared via a three-step procedure (Scheme 1).

The nitrile derivatives (**1-3)** were obtained by the reaction of appropriate starting materials and characterized by using FT-IR, ^{1}H NMR, ^{13}C NMR, and LC-MS spectral data. All data supported the structures of target molecules (Figure 1-4, *see SI*).
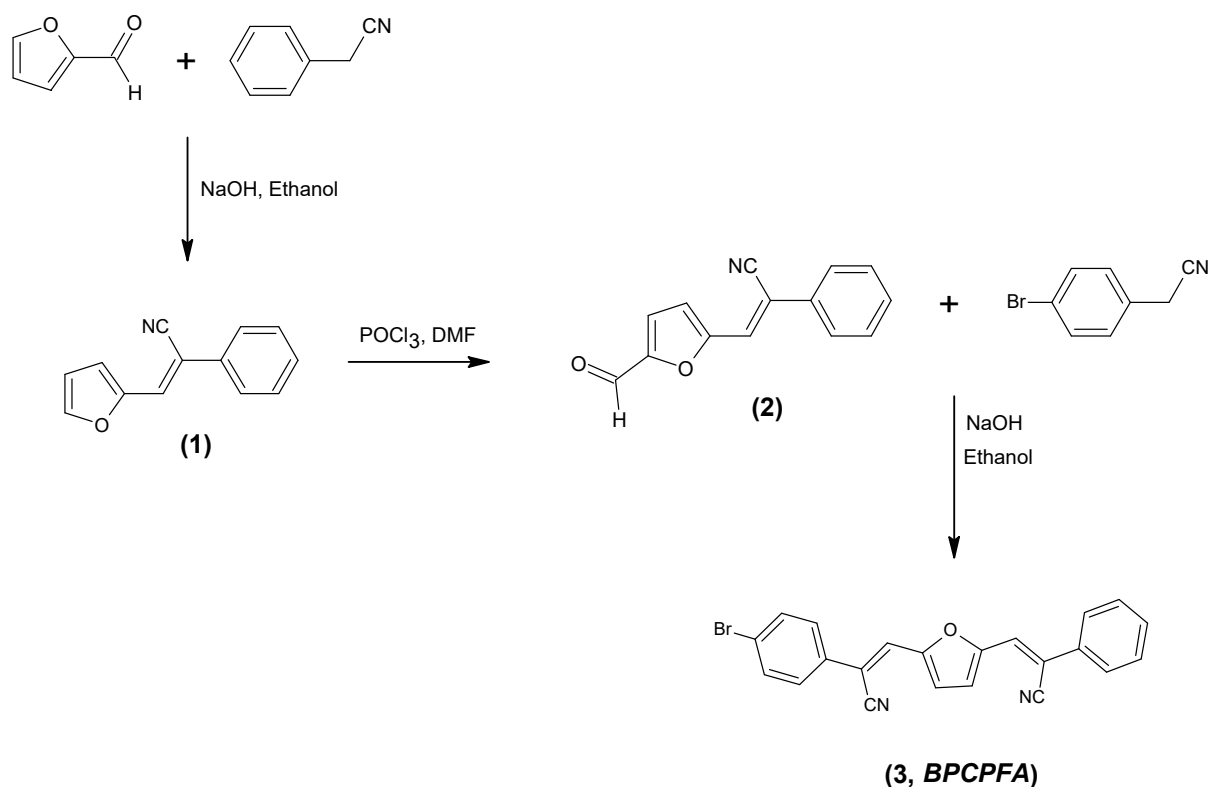
Scheme 1. Synthesis of compounds (**1-3)**.

Synthesis of 2-phenyl-3-(furan-2-yl)acrylonitrile (1) [7]

Furan-2-carbaldehyde (1 mmol) and phenylacetonitrile (1 mmol) were dissolved in dry ethanol (10 mL). After that, sodium hydroxide (0.1 mmol) was added and stirred for 5 min at room temperature under nitrogen atmosphere. The precipitated yellow solid was filtered, washed with ethanol, and recrystallized in CHCl$_3$ to give pure product **1** as light yellow crystals [14]. Yield: 97%, mp 86-88 °C. FT-IR (ATR) v, 3098, 3057, 3045, 2214, 1683, 1595 cm^{-1}; ^{1}H NMR (500 MHz, CDCl$_3$): δ (ppm) 6.55 (m, 1H, furan), 7.32 (brd, *J*= 7.0 Hz, 1H, furan), 7.53 (brs, 1H, =CH), 7.58 (brd, *J*= 3.2 Hz, 1H, furan), 7.64 (m, 3H,

ArH), 8.12 (d, *J*= 8.0 Hz, 2H, ArH); ^{13}C NMR (125 MHz, CDCl$_3$) δ (ppm) 112, 120, 128, 129, 130, 134, 144, 147, 148, 163, 172. LC-MS m/z: 196 [M]$^+$ (calculated for C$_{13}$H$_9$NO, 195.22).

Synthesis of 2-phenyl-3-(5-formylfuran-2-yl)acrylonitrile (2) [7]

The freshly distilled DMF (3 eq) and POCl$_3$ (5 eq) was stirred for 30 min at 0°C, under nitrogen. Compound **1** (0.5 g, 1.49 mmol) in CH$_2$Cl$_2$ (5 mL) was added to the mixture and stirred for 12 h at room temperature [15]. The obtained solid was collected by filtration and purified by column chromatography on silica gel using ethyl acetate/hexane (5:1). A dark yellow solid of compound **2** was obtained. Yield: 83%, mp 127-129 °C. FT-IR (ATR) v, 3098, 3062, 3032, 2222, 1667, 1596 cm^{-1}; ^{1}H NMR (500 MHz, CDCl$_3$): δ (ppm) 7.38 (d, *J*= 7.0 Hz, 1H, furan), 7.47 (brd, *J*= 3.2 Hz, 1H, furan), 7.49 (m, 3H, ArH), 7.50 (brs, 1H, =CH), 7.67 (d, *J*= 8.0 Hz, 2H, ArH), 9.73 (s, 1H, -CHO); ^{13}C NMR (125 MHz, CDCl$_3$) δ (ppm) 113, 115, 117, 122, 126, 129, 130, 132, 133, 152, 154, 178. LC-MS m/z: 224 [M]$^+$ (calculated for C$_{14}$H$_9$NO$_2$, 223.23).

2-(4-Bromophenyl)-3-{5-[2-cyano-2-phenylethenyl]furan-2-yl}acrylonitrile (3, BPCPFA)

The compound **3 (BPCPFA)** synthesized from compound **2** and 4-bromophenylacetonitrile starting materials according to the same procedure with compound **1** [7, 15]. Light-orange solid. Yield: 97%, mp 159-161°C. FT-IR (ATR) v, 3088, 3051, 3029, 2209, 1675, 1596 cm^{-1}; ^{1}H NMR (500 MHz, CDCl$_3$): δ (ppm) 7.42 (s, 2H, 2 x -C=CH), 7.43-7.49 (m, 5H, ArH), 7.55-7.62 (m, 4H, ArH), 7.69 (d, *J*= 7.2 Hz, 2H, ArH). ^{13}C-NMR (125 MHz, CDCl$_3$): δ (ppm) 109, 111, 117, 118, 126, 127, 129, 130, 136, 152. LC-MS m/z: 402 [M]$^+$ (calculated for C$_{22}$H$_{13}$BrN$_2$O, 401.25).

RESULTS AND DISCUSSION

Theoretical calculation of HOMO-LUMO

HOMO and LUMO energies of the compound **3** have been calculated. The calculations were saved using Gaussian 09 W software [16] by DFT/B3LYP method with 6-31 G(d) basis set. Optimized molecular structure and energy of the **BPCPFA** are given in Figure 5.
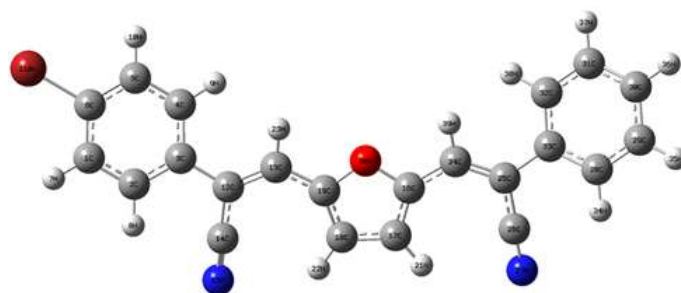
E= -98.032 KeV

Figure 5. Optimized molecular structure and energy of **BPCPFA**.

HOMO-LUMO energies are crucial in order to explain the chemical reactivity and stability of molecule. Determination of the HOMO-LUMO level alignment between the donor and acceptor is crucial to designate whether there will be an efficient charge transfer or not [17, 18]. The HOMO-LUMO energy gap of **BPCPFA** is shown in Figure 6. HOMO-LUMO energy band for new compound **3** is 2.83 eV, so it is possible that charge transfer interaction may easily occur in the molecule.
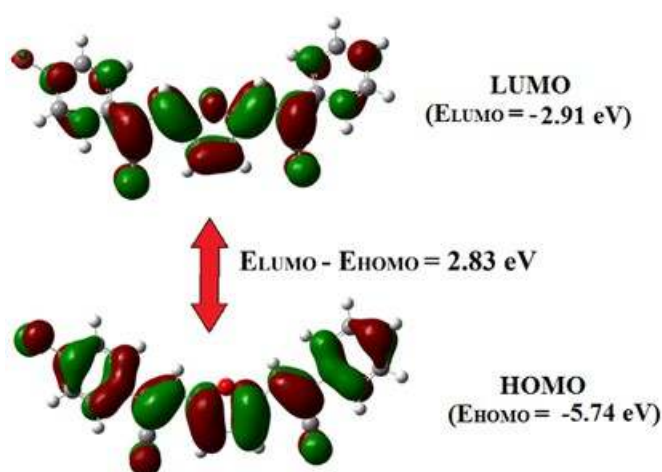
Figure 6. HOMO-LUMO energy diagrams for compound **3**, **BPCPFA.**

The theoretical HOMO-LUMO levels of P3HT are -4.32 eV and -2.3 eV, whereas the values of PCBM are -5.66 eV and -3.02 eV, respectively [19]. In calculations performed for **BPCPFA**, the HOMO and LUMO energies were calculated to be -5.74 eV and -2.91 eV. It can be concluded that since the LUMO level of P3HT lies above the **BPCPFA**, and there is an energy difference of 0.61 eV between their LUMOs which is more than 0.3 eV, a charge transfer can be possible between P3HT and **BPCPFA**. Therefore, P3HT was

evaluated as a donor whereas **BPCPFA** was generated as an acceptor in the organic solar cells.

Photovoltaic Studies

Photovoltaic performance of the devices employing active layers of P3HT:BPCPFA with different weight ratios (1:0.5 and 1:1 wt) have been studied. A reference device in which no BPCPFA employed was also studied to understand whether BPCPFA has an acceptor role in the device. As can be seen from Figure 7a, devices comprising of 1:0.5 wt donor acceptor ratio showed a short-circuit current density (J_{sc}) of 0.124 mA/cm^2, an open-circuit voltage (V_{oc}) of 960 mV and a fill factor (FF) of 0.24 was calculated which led to a power conversion efficiency (PCE) of 0.029 %.

We achieved a J_{sc} of 0.206 mA/cm^2 and a V_{oc} of 958 mV, and an FF of 0.26 which led to a PCE of 0.051 % for the devices containing of 1:1 wt donor acceptor ratio (Figure 7b).

There is an ongoing debate on the nature of the open-circuit voltage in literature, however V_{OC} value is known to be proportional to the difference between the HOMO of the donor and the LUMO of the acceptor. In the best case, we achieved a V_{OC} of 0.960 V.

V_{OC} value can be calculated by the following equation [20, 21]:

$$V_{OC} = (1/e)[(E_{donor}HOMO) - (E_{acceptor}LUMO)] - 0.3 \text{ V} \qquad \text{(Eq. 3)}$$

Figure 7c displays the *J-V* curves of the reference P3HT device (J_{sc} = 0.017 mA/cm^2, V_{OC} =105 mV and FF = 0.28).
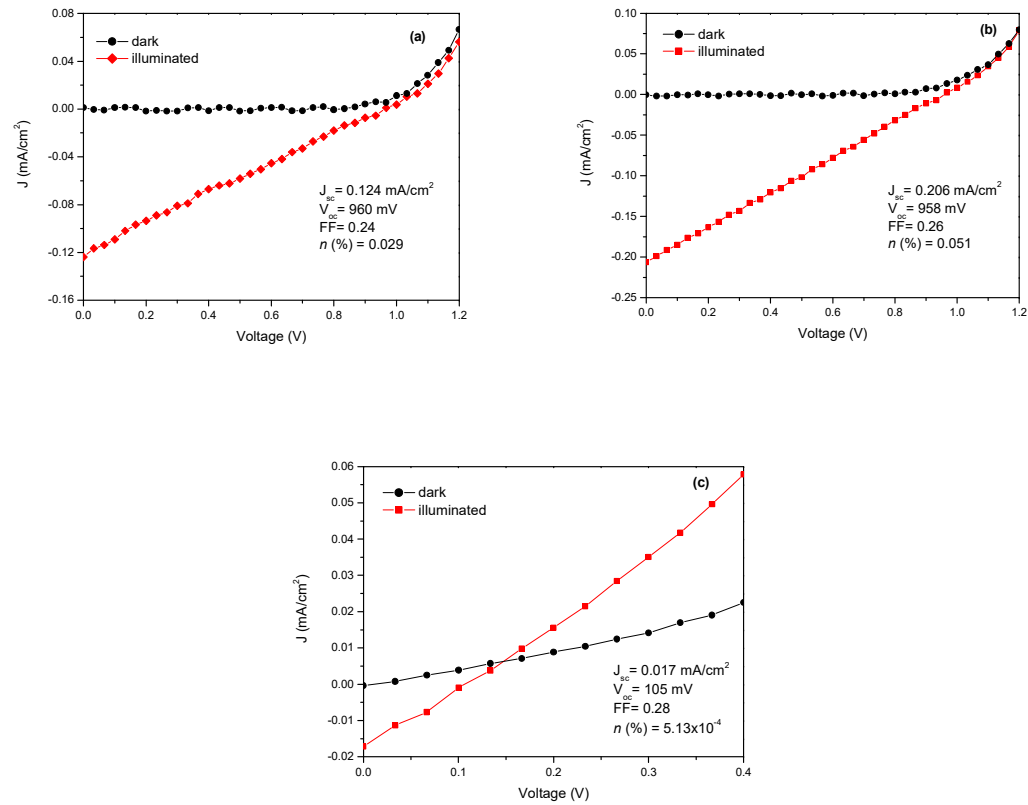
Figure 7. *J–V* curves of (a) devices with active layers of 1:0.5 donor–acceptor ratio, (b) 1:1 donor–acceptor ratio, (c) *J–V* curves of a reference device.

Briefly, the performance of the device created by using **BPCPFA** is approximately 7 times more than the performance of created by using P3HT reference.

CONCLUSIONS

In conclusion, a new diarylacrylonitrile derivative **(BPCPFA)** was used as an electron acceptor in organic solar cells and its synthetic and device performance characteristics were fully investigated. The photovoltaic performance of this compound was investigated using both theoretical and experimental techniques. The acceptor type molecules for photovoltaic use are off great interest. Polymer or small molecule acceptors have several advantages such as good absorption in the visible region and a higher LUMO energy level than PCBM, which in turn leads to a high open-circuit voltage (V_{OC}). We achieved a V_{OC} of 960 mV, which is higher than that of the conventional bulk heterojunction organic solar cells comprising of P3HT and PCBM.

The offset of HOMO and LUMO levels between donor and the acceptor is very important to get efficient charge transfer. The offset of HOMO-LUMO energy levels should be almost 0.3 eV. The theoretical HOMO-LUMO energy levels of **BPCPFA** are very close to that of PCBM which is most used as an electron acceptor materials in organic photovoltaics.

Based on all the data of our study, further studies will be carried on by changing the device parameters and molecular structure.

ACKNOWLEDGEMENT

REFERENCES

1. Bloking JT, Han X, Higgs AT, Kastrop JP, Pandey L, Norton JE, Risko C, Chen CE, Brédas JL, McGehee MD, Sellinger A. Solution-processed organic solar cells with power conversion efficiencies of 2.5% using benzothiadiazole/imide-based acceptors. Chemistry of Materials. 2011;23:5484–90. DOI: 10.1021/cm203111k.

2. Gunes S, Neugebauer H, Sariciftci NS. Conjugated polymer-based organic solar cells. Chemical Reviews. 2007;107: 1324–38. DOI:10.1021/cr050149z.

3. Brabec CJ, Gowrisanker S, Halls JJM, Laird D, Jia S, Williams SP. Polymer-fullerene bulk-heterojunction solar cells. Advanced Materials. 2010;22:3839–56. DOI:10.1002/adma.200903697.

4. Linac Y and Zhan X. Non-fullerene acceptors for organic photovoltaics: an emerging horizon. Materials Horizons. 2014;1: 470-88. DOI: 10.1039/c4mh00042k.

5. Babu DD, Gachumale SR, Anandan S, Adhikari AV. New D-π-A type indole based chromogens for DSSC: design, synthesis and performance studies. Dyes and Pigments. 2015;112:183–91. DOI:10.1016/j.dyepig.2014.07.006.

6. Liang Y, Xu Z, Xia J, Tsai ST, Wu Y, Li G, Ray C, Yu L. For the bright future-bulk heterojunction polymer solar cells with power conversion efficiency of 7.4%. Advanced Energy Materials. 2010;22:135–38. DOI: 10.1002/adma.200903528.

7. Kazici M, Bozar S, Aydin-Yuksel S, Ongul F, Gokce H, Gunes S, Yorur-Goreci C. Nanotechnology theoretical and experimental investigations of a 2-(4-chlorophenyl)-3-{[5-(2-cyano-2- phenylethenyl)]furan-2-yl}acrylonitrile molecule as a potential acceptor in organic solar cells. Nanotechnology. 2016;27:234003(9pp). DOI:10.1088/0957-4484/27/23/234003.

8. Eftaiha AF, Sun JP, Hill IG, Welch GC. Recent advances of non-fullerene, small molecular acceptors for solution processed bulk heterojunction solar cells. Journal of Materials Chemistry A. 2014;2:1201–13. DOI: 10.1039/C3TA14236A.

9. Yue Y, Kang, J, Yu M. The synthesis and photophysical properties of novel triphenylamine derivatives containing α, ß-diarylacrylonitrile. Dyes and Pigments. 2009;83:72-80. doi:10.1016/j.dyepig.2009.03.014.

10. Mishra A and Bäuerle P. Small molecule organic semiconductors on the move: promises for future solar energy technology. Angewandte Chemie International Edition. 2012;51: 2020–67. DOI:10.1002/anie.201102326.

11. Lu SL, Yang MJ, Bai FL. Synthesis, electrochemical, and optical properties of a novel PPV/PPE block-copolymer. Macromolecular Rapid Communications. 2004;25:968-71. DOI:10.1002/marc.200400004.

12. Xu Y, Zhang H, Li F, Shen F, Wang H, Li X, Yu Y, Ma Y. Supramolecular interaction-induced self-assembly of organic molecules into ultra-long tubular crystals with wave guiding and amplified spontaneous emission. Journal of Materials Chemistry. 2012;22:1592–97. DOI: 10.1039/C1JM14815J.

13. Nagamatsu S, Oku S, Kuramoto K, Moriguchi T, Takashima W, Okauchi T, Hayase S. Long-term air stable n-channel organic thin-film transistors using 2,5-difluoro-1,4-phenylene-bis{2-[4-(trifluoromethyl)phenyl]acrylonitrie}. Applied Materials and Interfaces. 2014;6:3847–52. DOI: 10.1021/am.404549e.

14. Ying A, Wang L, Qiu F, Hu H, Yang J. Magnetic nanoparticle supported amine: an efficient and environmental benign catalyst for versatile Knoevenagel condensation under ultrasound irradiation. Comptes Rendus Chimie. 2015;18:223–32. DOI:10.1016/j.crci.2014.05.012.

15. Yang C, Chen H, Chuang Y, Wu C, Chen C, Liao S, Wang T. Characteristic of triphenylamine-based dyes with multiple acceptors in application of dye-sentized solar cells. Journal of Power Sources. 2009;188: 627-34. DOI:10.1016/j.powsour.2008.12.026.

16. Becke AD. Density functional thermochemistry: III. The role of exact exchange. Journal of Chemical Physics. 1993;98:5648–52. DOI:10.1063/1.464913.

17. Karthighaa S, Kalainathana S, Raob KUM, Hamadac F, Yamadad M, Kondoe Y. Synthesis, growth, structural, optical, luminescence, surface and HOMO-LUMO analysis of 2-[2-(4-cholro-phenyl)-vinyl]-1-methylquinolinium naphthalene-2-sulfonate organic single crystals grown by a slow evaporation technique. Journal of Crystal Growth. 2016;436 :113-24. DOI:10.1016/j.jcrysgro.2015.11.028.

18. Kim BG, Xiao M, Chen C, Ie Y, Coir EW, Hashemi H, Aso Y, Green PF, Kieffer J, Kim J. Energy level modulation of HOMO-LUMO, and band-gap in conjugated polymers for organic photovoltaic applications. Advanced Functional Materials. 2013;23:439–45. DOI: 10.1002/adfm.201201385.
19. Xie XH, Shen W, He RX, Li M. A density functional study of furofuran polymers as potential materials for polymer solar cells. Bulletin Korean Chemical Society. 2013;34: 2995–04. DOI: 10.5012/bkcs.2013.34.10.2995.

20. Scharber MC. On the efficiency limit of conjugated polymer: fullerene-based bulk heterojunction solar cells. Advanced Materials. 2016;28 :1994–01. DOI: 10.1002/adma.201504914.

21. Elumalai NK and Ashraf U. Open circuit voltage of organic solar cells: an in-depth review. Energy and Environmental Science. 2016;9:391-10. DOI: 10.1039/c5ee02871j.

Fotovoltaik Performans Gösteren Yeni bir Akrilonitril Türevi

Çiğdem Yörür-Göreci[*],Mehmet Kazici, Sinem Bozar, Zulal Demir, Abdullah Toraman, Fatih Ongul, Abid Ali, Serap Güneş

Öz: Yeni bir akrilonitril türevi olan 2-(4-bromofenil)-3-{5-[2-siyano-2-feniletenil]furan-2-il}akrilonitril (**BPCPFA, 3**) bileşiğinin organik güneş pillerinde uygulanma potansiyeli vardır ve üç kademeli bir tepkimeyle sentez edilmiştir. Bu adımlar sırasında sentezlenen moleküllerin yapıları çeşitli spektral analizler kullanılarak karakterize edilmiştir. **BPCPFA** yeni nesil organik güneş pillerinde elektron alıcı molekül olarak incelenmiştir. Teorik tahminler ve fotovoltaik performans için deneysel çalışmalar da yürütülmüştür. Bu sonuçlara dayanarak, **BPCPFA**'nın uzamış konjuge sistemiyle iyi ve ümit vaat eden bir fotovoltaik performans (V_{oc} = 0,96 V) gösterdiği sonucuna varılmıştır.

Anahtar kelimeler: Konjuge sistemler; nitriller; organik güneş pilleri; fotovoltaikler.

Sunulma: 15 Temmuz 2016. **Düzeltme:** 19 Eylül 2016. **Kabul:** 30 Eylül 2016.

RESEARCH ARTICLE

Influence of Aluminum Concentration on the Electrical and Optical Properties of ZnO Thin Films

Ebru Gungor* and Tayyar Gungor

Mehmet Akif Ersoy University, 15030 Burdur, Turkey

Abstract: Al:ZnO (AZO) thin films having with different Al concentrations were deposited on glass substrates by a sol-gel technique. The effects of Al doping on the structural, optical, and electrical properties of Al:ZnO were investigated using with XRD, optical transmittance, and sheet resistance measurements. The concentration of zinc acetate was 0.1 M. Al content in the starting solution was varied from 0 to 20% as the molarity range. Optical transmittance spectra of the films in the form of Film/Glass were used to determine the film thickness and optical band gaps. The optical transmissions of Al:ZnO thin films were higher than 80% in the visible and near infrared region. The optical band gaps of Al:ZnO films decrease with increase of Al content. In order to obtain the average sheet resistance of the films the current and voltage through the probes have been measured for five different position by four-point probe method. The results showed that the sheet resistances of Al:ZnO thin films increased with the Al concentration. Considering the film thickness and geometric factor, the electrical resistivity values were computed. It was observed that the sheet resistance of AZO films up to 10% molarity of Al in the starting solution increased.

INTRODUCTION

ZnO and ZnO-related compounds are suitable for many different applications, such as opto-electrodes, surface acoustic wave devices (SAW), and sensor materials. In order to meet these demands, various dopants such as group III-A elements of the periodic table (B, Al, Ga, In) can be used. These elements have been used to increase the electron density for conductivity of ZnO films [1, 2]. Considering these elements' cost, nontoxic natures, good electrical conductivity, and availability in nature, Al comes to the forefront [3, 4]. It is possible to coat the substrate surface with the Al material using different growth techniques such as sputtering, metal organic vapor deposition (MOCVD), pulsed laser deposition, and ultrasonic spray pyrolysis technique (USP). The USP technique, among the various deposition techniques, is quite simple and the required setup is economic and flexible for process modifications such as large area coating for industrial applications. Dopant-induced optical band gap shift observed in Al doped ZnO thin films prepared by USP technique. The blue shift in the optical band gap of Al:ZnO films for low Al concentrations is observed [5]. However, the optical band gap energy was decreased by doping process, which was finding in photoluminescence spectrum of Al doped ZnO film [6]. As seen there is a conflict about the optical band gap shifting for the Al-doped ZnO prepared by USP.

In this study, undoped and Al-doped ZnO polycrystalline thin films were fabricated on glass substrates by using USP system. The effects of Al doping on structural, optical, and electrical properties of ZnO thin films were investigated by the X-ray diffraction, optical transmittance, and sheet resistance measurements at room temperature.

MATERIALS AND METHODS

Experimental details

Undoped ZnO and Al-doped ZnO (labeled as Al:ZnO or AZO) thin films were deposited on to ultrasonically cleaned glass substrates using the ultrasonic spray pyrolysis (USP) technique. With conventional USP technique, the substrates were fixed and precursor solution was sprayed over a hot substrate. The substrate temperature was kept at 400 $^{\circ}$C. The salts of zinc acetate dehydrate ($CH_3COO)_2.2H_2O$, 99.9%-Merck) and Al chloride hexahydrate ($AlCl_3.6H_2O$, 99.9%-Merck) as the metal sources which were dissolved in methanol. In order to produce a clear and homogeneous solution, monoethanolamine

(MEA) was added into the precursor solution which was stirred at 60 °C at a moderate speed for 1 h. In the starting solutions, Al contents were changed from 2% to %20 according to Zn salt's molarity and the films were labeled as AZO1-AZO20 (Table 1). Zn content (0.1 M) was held constant. The solution flow rate was held constant at 5 mL/min. Nozzle (100 kHz oscillator frequency) used in this study was in a downward vertical configuration. A more detailed description of the USP system were reported in previous papers [7]. X-ray diffraction (XRD) patterns were collected with a D-Max X-ray diffractometer (Rigaku International Corp. Japan) with $CuK_{\alpha1}$ (λ=1.5405Å) to obtain the structural information of the films. The optical measurements of the Al:ZnO thin films were carried out at room temperature using T70 Model Spectrophotometer (PG Instrument) in the wavelength range 300–900 nm. The sheet resistance of thin films was determined using 4-point probe method.

Table 1. Calculated film thickness t (nm), refractive index n for 390nm and 700nm wavelengths, and E_g (eV) optical band gap values of the AZO thin films vs the molarity of Al in the starting solutions.

Sample	Molarity of Al (M)	t (nm)	n (390nm)	n (700nm)	E_g (eV)
ZO	0.00	602	2.22	2.00	3.23
AZO2	0.02	104	2.00	1.67	3.32
AZO3	0.03	118	2.19	2.00	3.30
AZO4	0.04	88	2.21	1.88	3.32
AZO5	0.05	81	2.47	1.88	3.32
AZO10	0.10	104	2.05	1.55	3.32
AZO20	0.20	220	1.74	1.48	3.35

RESULTS AND DISCUSSION

Structural characterization

The X-ray patterns for Al:ZnO thin films at room temperature and reference peak positions are presented in Fig. 1. All the films were polycrystalline with a structure that belongs to the hexagonal wurtzite type that of ZnO. It was observed that the (002) peak indicating a strong orientation along the c-axis for undoped ZnO film. For Al with 2% molarity doped ZnO film, (200) and (101) as well as (110) and (103) peaks were observed. It was difficult to detect (101), (110), and (103) peaks for the increasing Al concentration. When a small amount of Al was introduced into the ZnO film, Al was

ionized into Al^{3+} and substitute for Zn^{2+} sites. The intensity of the (002) peak decreases and corresponding peak position moves to the lower angles up to 10% molarity of Al. Zn and Al have different ion size such as 0.074 nm and 0.054 nm, respectively. This can cause a stress which affects to shift the peak position and change the peak characteristics (Fig 2). In the XRD patterns, it was observed that the full width half maxima values decreased. The reason of this is the increase of the crystallinity of films.
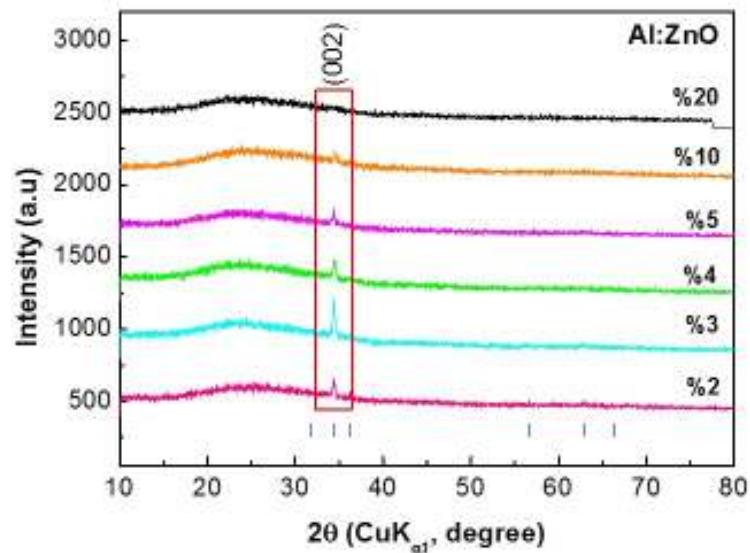
Figure 1. XRD patterns of AZO and undoped ZnO films. "|"indicates the reference peaks for ZnO (JCPDS file no. 03-065-3411).
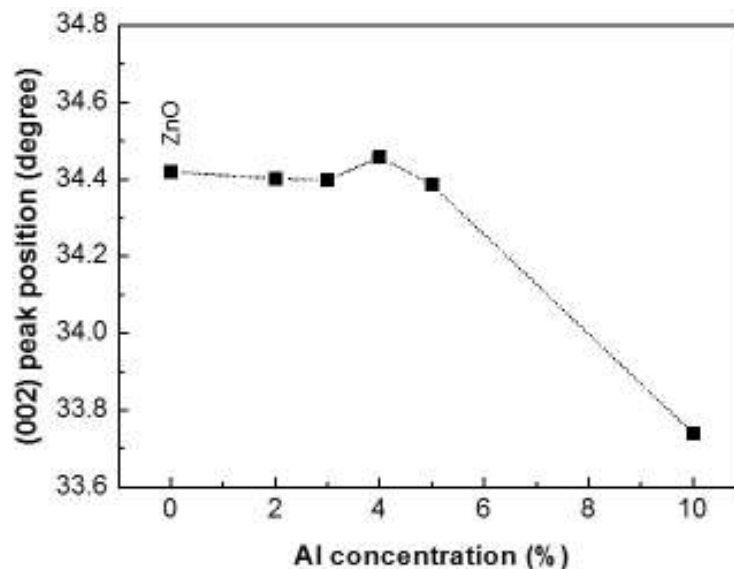
Figure 2. (002) peak position as a function of Al doping concentration.

Optical characterization

The optical transmission spectra $T(\lambda)$ of ZnO and Al-doped ZnO thin film samples are shown in Fig 3. The optical transmission spectra were used to determination of the optical constants of the thin films. In cases where the refractive index does not change very fast with wavelength, and considering the thin film thickness, interference fringes could not be seen in the optical transmission spectrum. In this cases, one of the iterative method such as *pointwise unconstrained minimization algorithm (PUMA)* [8] that can be used as an alternative to the classical method developed by Swanepoel [9]. There is excellent agreement between the experimental spectra and theoretical spectra for all the samples and one of the experimental and theoretical optical transmission spectra for the Al:ZnO thin film are shown in Fig. 4. Calculated film thickness and refractive index for 390 nm and 700nm are given in Table 1. The effects of Al doping into the ZnO lattice is clearly observed in the optical transmission spectra. The results showed that the optical transmittance of Al:ZnO samples in the range of 550-1100 nm wavelength region increases with the Al concentration except for the samples containing 2% and 3%. As it is observed in the structural characterization of the films, the (002) peak intensity and its angular position changes clearly are seen in the XRD pattern for the Al concentration higher than 3%. This can be associated with a refractive index, which is an important parameter.

The decrease of the refractive index that is indicating the optical transmission increases. This result is clearly observed in the optical transmission spectrum. It requires attention to calculate the band gap value using traditional methods. If the transmittance rapidly decreases in the UV region this means that absorption increases. Then the optical band gap of the film can be calculated using the Tauc relation. After Al-doped in ZnO film two different behaviors at low wavelengths in the optical transmission spectrum can be observed. In this case, the optical band gaps of the thin films can be determined using this wavelength with the relation, $E_g(eV) = 1240.8/\lambda_{inf}$. Where λ_{inf} is the defined as the inflexion wavelength where the second derivative of the transmission curve is zero [10]. The optical band gap (E_g) was estimated from the second derivative of the $T(\lambda)$ (Table 1). It is observed that E_g in the undoped ZnO thin film is 3.23 eV which is lower than value of bulk ZnO (3.37 eV). The change in the band gap value was observed in the AZO films prepared up to 10% molarity of Al. Then the band gap increased with doping over 10% molarity of Al. For Al doped ZnO film (AZO20) which prepared with the 20% molarity of Al in the starting solution, the band gap was observed as a value of 3.35 eV. Similar type of E_g behavior have been reported for Al doped ZnO thin film that deposited by USP technique [11].
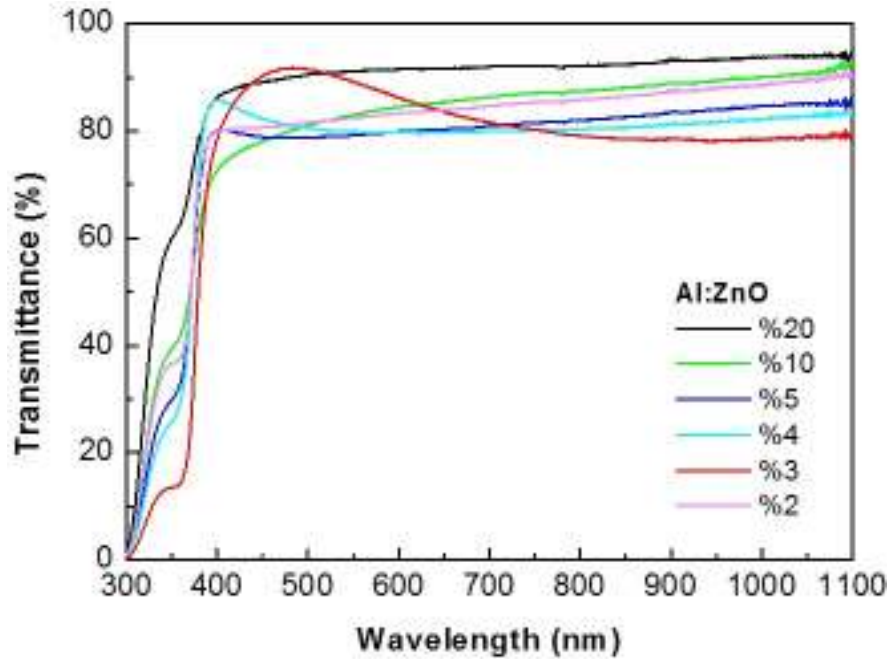
Figure 3. Optical transmittance spectra of Al:ZnO films.
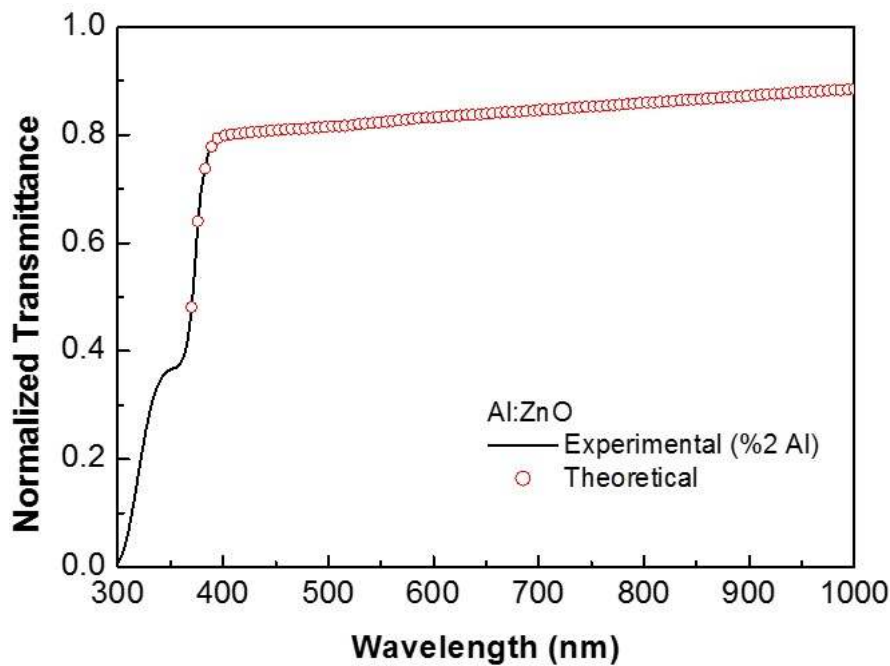
Figure 4. Experimental optical transmittance spectrum (solid line) for 2% Al molarity in starting solution for AZO2 sample: Also the theoretical optical transmission spectrum ("o″ symbol) obtained using PUMA are shown for comparison.

Electrical characterization

In order to obtain the conductivity of the films, the resistance was determined by four-point probe method. The current and voltage through the probes have been measured for five different positions. Then the average sheet resistance obtained (R_{Sheet}=GF*V/I).

Where *GF* is the geometric factor related with sample width and inter-electrode spacing. Considering the thin film thickness and geometric factor, the electrical resistivity/conductivity was computed. The results showed that while the sheet resistance of Al:ZnO thin film increases with the Al concentration (Fig 5) conductivity decreases with the Al concentration (Fig 6). The decrease in optical conductivity can be explained as increasing optical transmittance due to the low absorbance (α) of Al:ZnO thin films at low photon energies region using the relation [12] $\sigma = \alpha n c / 4\pi$, where *c* is the speed of light. In addition, the increase of Al concentration can cause some kind of neutral defect. Because of this case these neutralize Al atoms cannot contribute free electrons for the higher doping concentrations.
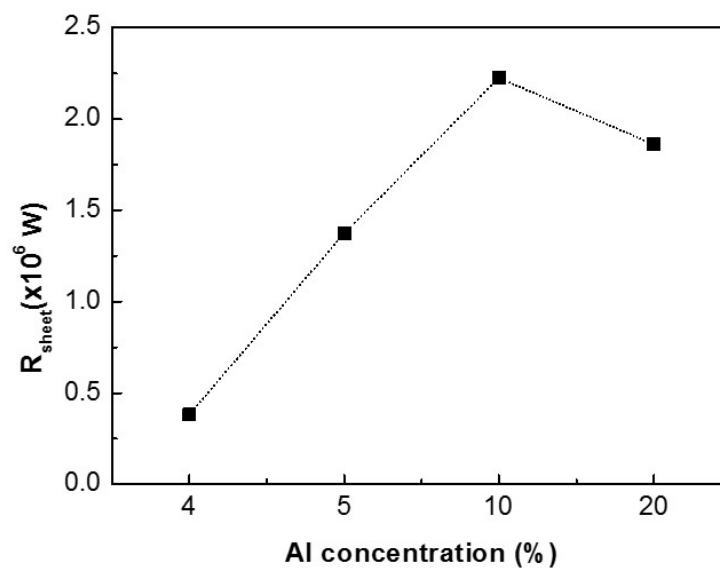
Figure 5. The sheet resistance as a function of Al concentration (%) in the starting solution of AZO films.
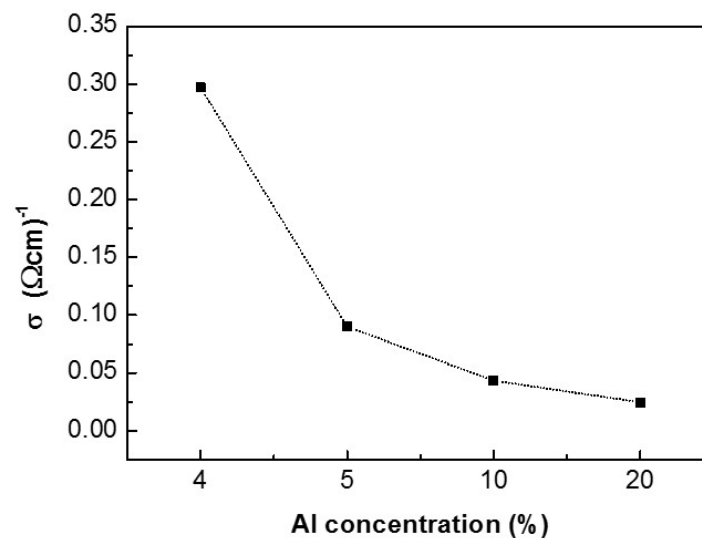
Figure 6. Electrical conductivity vs Al concentration (%) in the starting solution of AZO films.

CONCLUSION

In this study Al:ZnO thin films having with Al at different concentrations were deposited on glass substrates by ultrasonic spray pyrolysis technique. The effect of doping on the crystalline structure was studied by the X-ray diffraction measurement. The wurtzite structure with preferred orientations of (0 0 2) retained for the Al:ZnO films. Optical transmittance spectrum of the films in the form of film/glass was used to determine the film thickness and optical band gaps. The refractive index values decrease when Al concentration increased which makes the increase in the transmittance for the doped films. The optical transmission of Al:ZnO/Glass samples was higher than 80% in the visible and near infrared region. After Al-doped in ZnO film, the shoulder observed at lower wavelengths in the transmission spectrum with increasing amounts of Al, is a sign that the band gap increases. The optical band gap energy obtained from second derivative of the transmission curve was increased by Al doping. So, the sheet resistance of Al:ZnO/Glass samples increases with the Al concentration. Considering the film thickness and geometric factor, the electrical conductivity was computed and the results showed that the low Al concentration values had more important role for the electrical properties of AZO films. In other words, the increasing of the Al content will be effective on the neutral defects of semiconductor structure. Structural changes has been proved by XRD measurements for the ZnO films including the more Al concentration. This case means that the electrical conductivity decreases when Al doping is high.

ACKNOWLEDGMENTS

REFERENCES

[1] Minami T, Sato H, Nanto H, Takata S, Highly Conductive and Transparent Silicon Doped Zinc Oxide Thin Films Prepared by RF Magnetron Sputtering. Jpn J Appl Phys. 1986;25:9-L776. http://stacks.iop.org/1347-4065/25/i=9A/a=L776.

[2] Kobayashi K, Maeda T, Matsushima S, Okada G, Mechanism of Photoinduced Charge Transfer of Cu-Doped ZnO Film in Strong Electric Field. J Mater Sci. 1992;32:9R-3854. http://stacks.iop.org/1347-4065/32/i=9R/a=3854.

[3] Li Q. H, Zhu D, Liu W, Liu Y, Ma X. C, Optical properties of Al-doped ZnO thin films by ellipsometry. Appl. Surface Sci. 2008, 254, 2922-2926. DOI:10.1016/j.apsusc.2007.09.104.

[4] Kim H, Horwitz J. S, Kushto G. P, Kafa Z. H, Chrisey D. B, Indium tin oxide thin films grown on flexible plastic substrates by pulsed-laser deposition for organic light-emitting diodes. Appl. Phys. Lett. 2001; 79: 284-286. DOI: 10.1063/1.1350595.

[5] Hung-Chun H, Basheer L. T, Kuznetsov V. L, Egdell R. G, Jacobs R. M. J, Pepper M, and Edwards P.P, Dopant-induced bandgap shift in Al-doped ZnO thin films prepared by spray pyrolysis. J. Appl. Phys. 2012;112:083708. DOI:/10.1063/1.4759208.

[6] Sivasankar G, Ramajothi J, Aluminium Doped Zinc Oxide (ZnO) Thin Film Fabricated for Semiconductor by Spray Pyrolysis Technique. International Journal of ChemTech Research. 2015; 8:11: 497-501. http://sphinxsai.com/2015/ch_vol8_no11/2/(497-501)V8N11CT.pdf.

[7] Gungor E, Gungor T, Effect of the substrate movement on the optical properties of ZnO thin films deposited by ultrasonic spray pyrolysis, Advances in Materials Science and Engineering. 2012;1-7 Article ID 594971. DOI: 10.1155/2012/594971.

[8] Birgin E. G, Chambouleyron I, and Martinez J. M, Estimation of optical constants of thin films using unconstrained optimization. Journal of Computational Physics. 1999; 151: 862-888.

[9] Swanepoel R, Determination of the thickness and optical constants of amorphous silicon Journal of Physics E: Scientific Instruments. 1983; 16:12: 1214-1222. DOI:10.1088/0022-3735/16/12/023

[10] E. Gungor, T. Gungor, D. Caliskan, A, Ceylan, and E. Ozbay, Applied Surface Science, 318, 309–313 (2014). DOI:10.1016/j.apsusc.2014.06.132.

[11] Lee J. H, Park B. O, Characteristics of Al-doped ZnO thin films obtained by ultrasonic spray pyrolysis: effects of Al doping and an annealing treatment. Materials Science and Engineering: B 2004 15 February 2004; 106:3, 242–245. DOI:10.1016/j.mseb.2003.09.040.

[12] Pankove J. I, Optical processes in semiconductors, (Dover Publications, Inc. NewYork, 1975) p. 91.

Türkçe Öz ve Anahtar Kelimeler
ZnO İnce Filmlerinin Elektriksel ve Optik Özellikleri Üzerine Alüminyum Derişiminin Etkisi

Ebru Gungor ve Tayyar Gungor

Öz: Al:ZnO ince filmleri, farklı Al derişimlerine sahip olacak şekilde, bir sol-jel tekniği kullanılarak cam substratlar üzerine kaplanmıştır. Al aşılamasının Al:ZnO'nun yapısal, optik ve elektrik özelliklerine etkileri XRD, optik geçirgenlik ve tabaka direnç ölçümleri ile incelenmiştir. Çinko asetatın derişimi 0,1 M olarak belirlenmiştir. İlk çözeltideki Al içeriği molarite aralığı bakımından %0 ile 20 arasında tutulmuştur. Film/Cam biçimindeki filmlerin optik geçirgenlik spektrumları, film kalınlığı ve optik bant aralığını bulmak için kullanılmıştır. Al:ZnO ince filmlerinin optik geçirgenlikleri görünür ve yakın kızılötesi bölgede %80'den daha yüksektir. Al:ZnO filmlerinin optik bant aralığı, Al içeriğinin artmasıyla azalmaktadır. Filmlerin ortalama tabaka direncini elde etmek için, dört noktalı prob yöntemi ile beş farklı konumdan akım ve gerilim değerleri ölçülmüştür. Sonuçlara göre Al:ZnO ince filmlerinin tabaka dirençleri Al derişimi ile artmaktadır. Film kalınlığı ve geometric faktörler düşünüldüğünde, elektriksel direnç değerleri hesaplanmıştır. AZO filmlerinin, başlangıç çözeltisinde %10 Al molaritesine kadar olan kısmında tabaka direncinin yükseldiği gözlenmiştir.

Anahtar kelimeler: Alüminyum aşılı çinko oksit; ince film; ultrasonik püskürtme pirolizi tekniği; elektriksel karakterizasyon; optik sabitler.

Sunulma: 09 Temmuz 2016. **Düzeltme:** 23 Eylül 2016. **Kabul:** 03 Ekim 2016.

The Graphene Oxide Effect on the Optical Properties of NIPA-GO Composites

Gülşen Akın Evingür[1*]

[1]Piri Reis University, 34940, İstanbul, Turkey

Abstract: Poly (N-isopropylacrylamide) (NIPA)-Graphene oxide (GO) composites were polymerized radically with various contents of GO solution. The gelation process was performed by Steady State Fluorescence Spectroscopy. The results of gelation were modelled by Percolation and Classical Model, respectively. Our results show that the critical exponent of gel fraction that agrees with percolation model till 25 µL content of the GO solution. On the other hand, the optical energy band gap of the NIPA-GO composite was decided by using UV spectrophotometry from the absorbance measurement in the range of 200-800 nm. The effect of graphene oxide dopant on the gap has been examined for NIPA-GO composites. In conclusion, their gelation process and optical energy band gap behavior were investigated and correlated to the GO content in the composites.

Keywords: Graphene oxide; NIPA; gelation; optical band gap.

*Corresponding author. E-mail: gulsen.evingur@pirireis.edu.tr, Tel:+90 216 581 00 50 (Ext.1363) and Fax: +90 216 581 00 51.

INTRODUCTION

Graphene oxide (GO) is a carbon-based material in two dimensions (2D) and has hydrophilic oxygenated functional groups including hydroxyl (-OH), epoxy (-C-O-C-), carbonyl (-C=O), and carboxyl (-COOH) groups (1). These groups also enable GO to be functionalized through covalent approaches (2). GO shows some heterogeneous optical transition and nonlinear dynamics because of its characteristic hybrid structure, in which the sp^2 carbon nanoislands are isolated by the sp^3 carbon matrix (3). In parallel with developments from the basic scientific perspective, many applications of GO have been proposed and are currently being explored. Thus, it can be used as a super capacitor, gas sensor, drug delivery system, and nano-electronic device (2-4), and also presents the behavior of high strength, and thermal stability (5).

Poly (N-isopropylacrylamide) (NIPA) is well known as a temperature-sensitive gel (6) which is chosen and studied for various technological applications. NIPA structures with graphene oxide was prepared by click chemistry and RAFT polymerization (7). The swelling of stimuli-responsive polymers grafted of graphene oxide was performed for controlled drug release by changing temperature (8). And also, pH effect on the polyvinyl alcohol- graphene oxide was studied for the release performance (9). GO in the PVA-GO network behaves as a crosslinker and the network in the acid can be performed as a pH controlled drug. As a thermoresponsive hydrogel, NIPA contained graphene was prepared by frontal polymerization (10). The rheological and swelling properties were mentioned by SEM and Raman spectroscopy. On the other hand, NIPA grafted various graphene contents were produced to investigate the effect of thermoresponsive properties (11). When the temperature increases, the morphological properties were changed between 33 and 40 °C. NIPA in aqueous solution was grafted by graphene oxide to be characterized by rheological experiments (12). The study includes the comparison of the behavior of PNI-GO and PNI-RGO (Reduced graphene oxide) composites. NIPA- GO (GPNM) hybrids were designed for both hydrophilic and hydrophobic drugs in aqueous medium, and investigated the origin of the enhanced fluorescence property (13). Previously, we studied the gelation of polyacrylamide (PAAm)-NIPA (14), PAAm-kC (kappa-carrageenan) (15), PAAm-MWCNT (multiwalled carbon nanotubes) (16), PAAm-GO (17). The universality of them was modelled by using Classical and Percolation theory.

In this article, graphene oxide (GO) has been used to prepare poly(N-isopropylacrylamide) (NIPA)-GO composites with improvement to the universality on the gelation of the composite by a free radical copolymerization with various GO contents in the range between 0-35 μL. Steady-State Fluorescence Spectroscopy was performed for the gelation process of NIPA-GO composites. The gelation and its weight average degree of polymerization were monitored and tested as a function of GO contents. The critical exponent, β near the percolation threshold was calculated. And also, optical energy band gap was calculated from absorption spectrum fitting method (ASF).

MATERIALS AND METHODS

NIPA- GO composites were designed by using 1 M NIPA (N-isopropylacrylamide) with changing amounts of GO (Graphene Oxide) respectively; 0, 5, 15, 25, 30, and 35 μL were used at room temperature. GO was purchased from Graphenea (Spain). Its concentration is 4 mg/mL and is dispersed in 250 mL of water. The purity of commercial GO is higher than 95% (wt). The absorbance and SEM images of GO are given in Figure 1(a) and (b), respectively (18). The composite was copolymerized radically including 0.011 g of NIPA, 0.020 g of N, N'–methylenebisacrylamide (BIS, Merck), 0.016 g of ammonium persulfate (APS, Merck), and 6 μL of tetramethylethylenediamine (TEMED, Merck) were dissolved in 10 mL of distilled water (pH 6.5). The chemicals are given in Figure 2. GO was added to the solution just before the addition of TEMED. A Perkin-Elmer model LS-55 spectrometer, and UV spectrophotometry was performed in the gelation process. During the gelation experiment, the composite for each sample was at 90° position and was excited by 340 nm and the behavior of scattering at 340 nm, emission at 427 nm and 512 nm of light intensities were monitored as a function of time, and also optical band gap measurement by UV spectrophotometry was performed for each concentration.
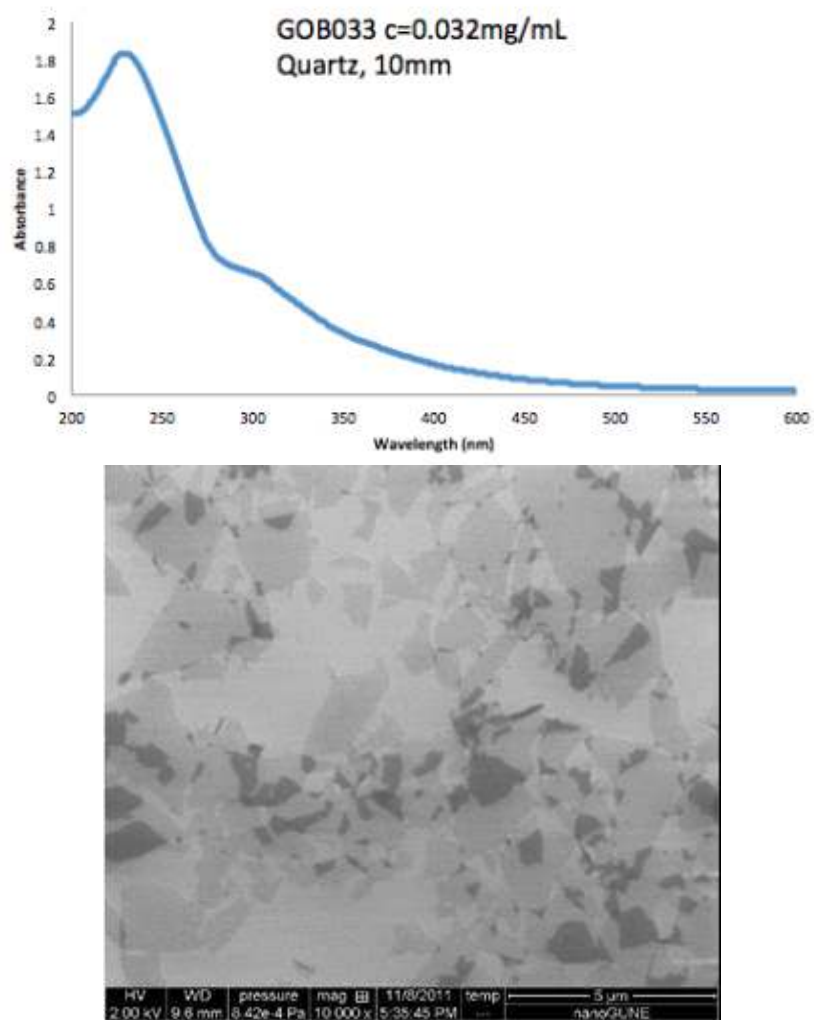
Figure 1. (Top) Absorbance of GO and (bottom) SEM images of GO (16).

N-isopropylacrylamide (NIPA)

Graphene Oxide(GO) (16)

ammonium persulfate (APS)

N, N' –methylenebisacrylamide (BIS)

Tetramethylethylenediamine (TEMED)
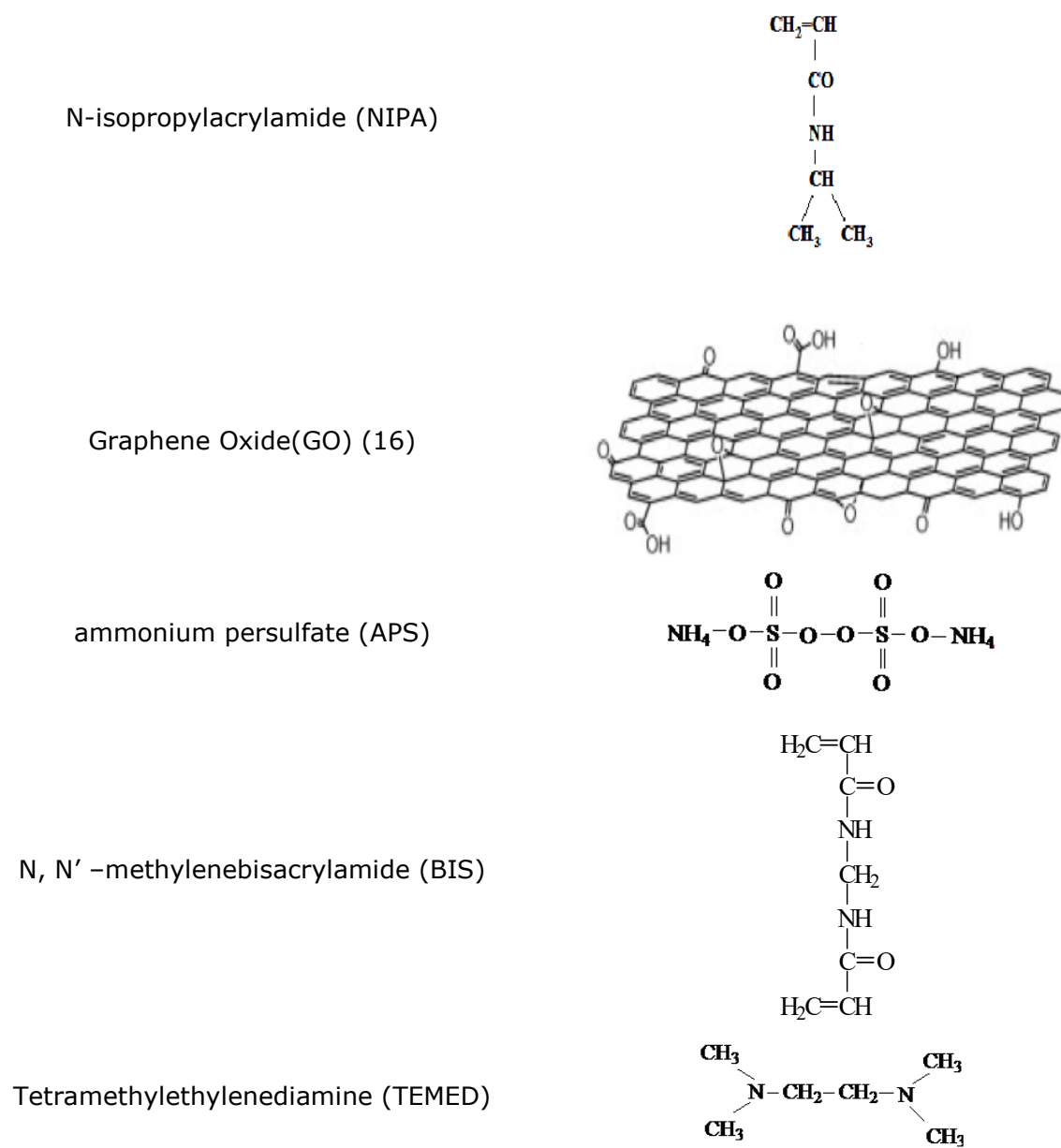
Figure 2. Chemicals of the composite in the experiment.

RESULTS AND DISCUSSION

The fluorescence spectra of the behavior of pyranine in the composite by changing time for 15 µL GO content are shown in Figure 3(a). At the beginning of the gelation, the wavelength at 512 nm-peak is at the maximum, which shows the free pyranine in the composite.

During the gelation process, the wavelengths behave to increase to the 427 nm-peak, and decrease to the 512 nm-peak, and also the short wavelength at 380 nm shifting through 427 nm which gives the information about the interaction between the monomer, GO and pyranine as defined in the previous studies (14-17, 19). Because pyranine is a fluorescent probe and its photophysical properties are well characterized and can be bound to polymeric structure because of having three functional groups (20). While polymerization, its three functional groups can bind to the polymeric system.

Since the wavelengths shift from 380 nm to 427 nm as shown in Figure 3(b) because of the binding of SO_3^- groups on pyranine to protonated amide groups on the NIPA electrostatically and binding -OH groups in pyranine to a vinyl group on the NIPA covalently, NIPA polymer chains grow (21).
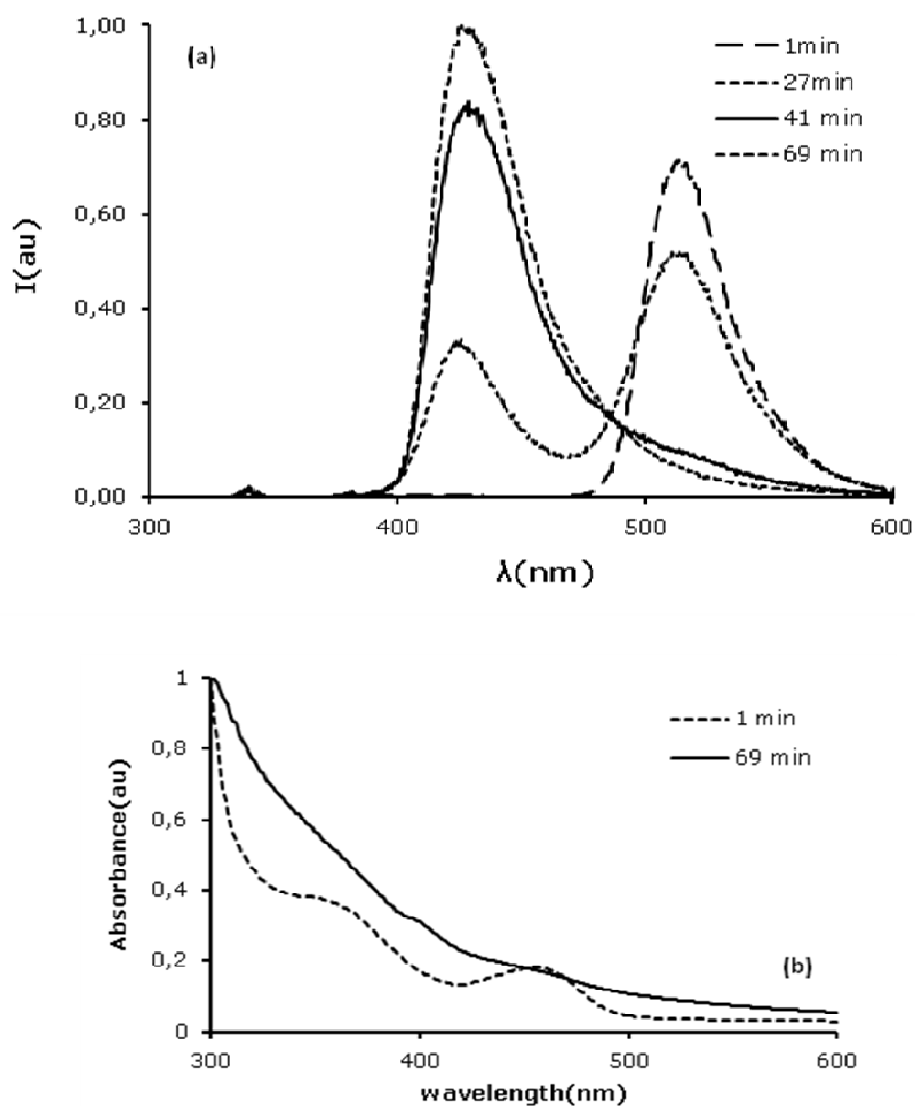
Figure 3. (a) The fluorescence and **(b)** absorbance spectra of the NIPA- 15 µL of GO composites for a given reaction time during the gelation process, respectively.

Figure 4 shows the behavior of the free pyranines referring to I_{free} at 512nm peak in the composite versus time for 15 µL and 30 µL of GO contents, respectively. As seen in Figure 4, the intensity of the free pyranines at 512 nm first decreased and then increased until some point, and then descended at the end of the reaction for GO contents.
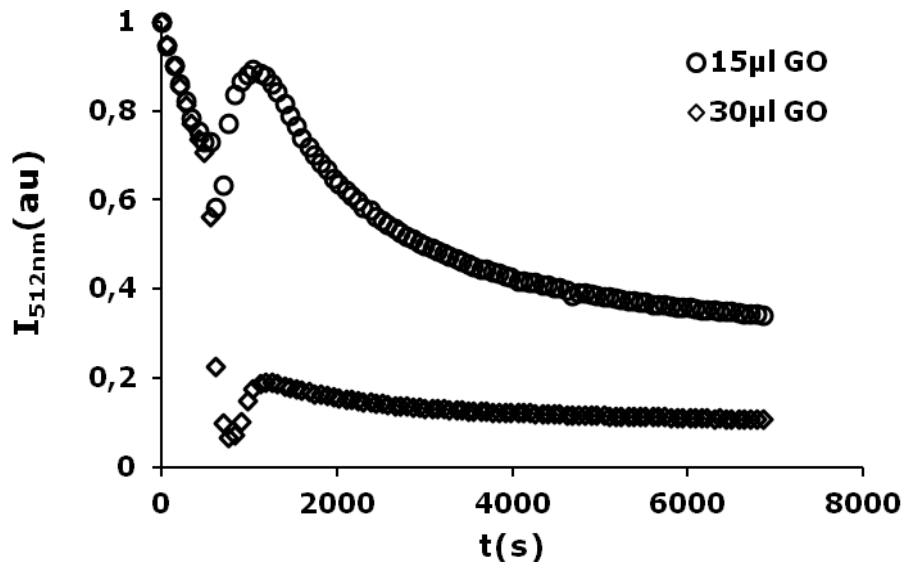
Figure 4 The intensity at 512 nm variations of free pyranine for 15 µL and 30 µL of GO contents, versus gelation time, respectively.

Figure 5 presents the behavior of bonded pyranine at 427 nm peak with respect to the time for 15 µL and 30 µL of GO contents. When I_{cross} refers for bonding between pyranine and monomers of NIPA shifting from 380 to 427 nm, the polymerization has been realized. Thus, the fluorescence spectra were monitored in the large periods of time in Figure 5. These data are used to decide the critical behavior of the gelation as shown in Figure 6.
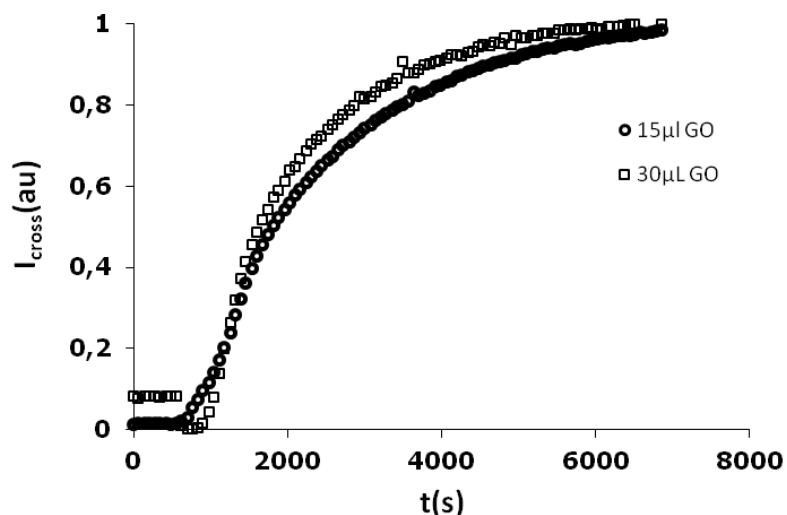
Figure 5. The fluorescence intensities at 427 nm variations of the pyranine, bonded to the NIPA for 15 µL and 30 µL of GO contents versus gelation time, respectively.

The assumption of gelation theory is given by the conversion factor, *p*, which decides the behavior of gelation process by changing temperature, concentration of monomers, and time (22-24). When the temperature and concentration are kept constant, then *p* will be directly proportional to the reaction time, *t*. This proportionality can be assumed that in the critical region. Therefore, $|p - p_c|$ is linearly proportional to $|t - t_c|$ (25- 26).

The fluorescence intensities in Figure 3 give the information about the weight average degree of polymerization and the growing gel fraction for below and above the gel point, respectively. It can be proven by using a Stauffer type argument under the assumption that the monomers occupy the sites of an imaginary periodic lattice (22-24). Therefore, the fluorescence intensity, I', measures the weight average degree of polymers or average cluster size below t_c as given in Eq.1.

$$I' \propto DP_w = C^+ \left(t_c - t\right)^{-\gamma} \qquad t < t_c \qquad \text{(Eq. 1)}$$

On the other hand, if the intensity from finite clusters distributed through the infinite network I_{ct} (in Eq.2) is subtracted from the maximum fluorescence intensity,

$$I_{ct} \propto DP_w = C^- \left(t_c - t\right)^{-\gamma'} \qquad t > t_c \qquad \text{(Eq. 2)}$$

Then, the corrected intensity I_{ms} measures only the gel fraction G, the fraction of the monomers that belong to the macroscopic network above t_c as given in Eq.3.

$$I' - I_{ct} \propto G = B\left(t - t_c\right)^{\beta} \qquad t > t_c \qquad \text{(Eq. 3)}$$

C^+, C^-, and B are the critical amplitudes in Equations 1-3. The ratio C^-/C^+ has different values for mean-field versus percolation as discussed by Stauffer (22) and Aharony (27). The estimated values for C^-/C^+ are given in Table 1.

Table 1. The ratio C^-/C^+ values by Stauffer (22) and Aharony (27).

	Classical		Percolation		
		Direct ε expansion	$\gamma_{εexp}$=1.840 and $\beta_{εexp}$ = 0.52	γ =1.7 and β = 0.4	Series and Montecarlo
C^-/C^+	1	1/2.7	1/3.5	1/4.3	1/10
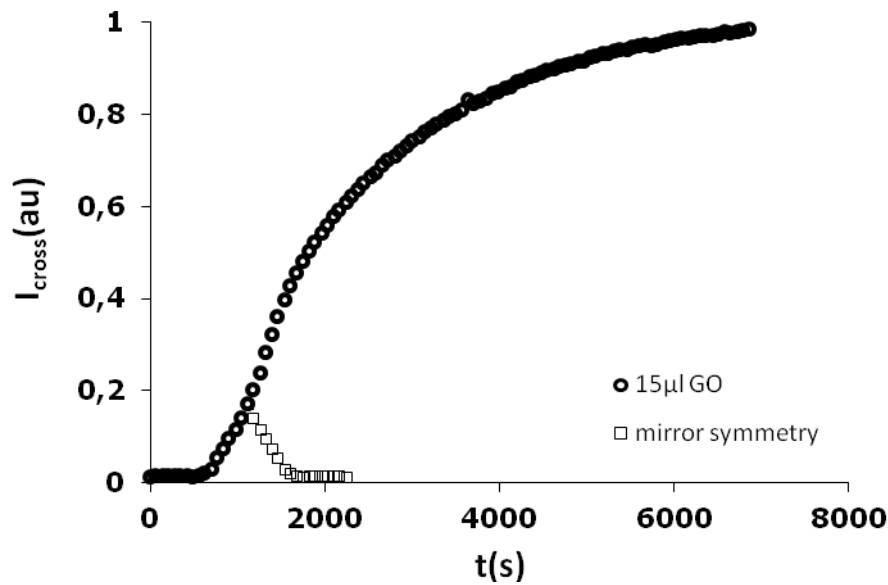
Figure 6. Intensity at 427 nm versus during gelation of the composite gel of NIPA−15 μL of GO. The curve depicted by squares represents the mirror symmetry I_{ms} of the intensity according to the axis perpendicular to time axis at $t = t_c$.

To determine the intensity I_{ct} in Eqs. 2 and 3, we first choose the parts of the intensity-time curves up to the gel points, then the mirror symmetry I_{ms} of these parts according to the axis perpendicular to the time axis at the gel point were multiplied by the ratio C^-/C^+, so that $I_{ct} = \dfrac{C^-}{C^+} I_{ms}$. Thus, the intensity from the clusters above the gel point is calculated as $I_{ct} = (C^-/C^+) I_{ms}$. $I'-I_{ct}$ monitors the growing gel fraction for $t > t_c$. The intensity from the lower part of the symmetry axis monitors the average cluster size for $t < t_c$. Figure 6 shows that I_{ms} and the fluorescence intensity at 427 nm. Using Eq. 3, and the values for t_c summarized in Table 2. β exponents as a function of various GO contents for 1 M NIPA were calculated as a given in Table 2.

Figure 7 shows the log-log plots of the intensity versus time data above the gel point for 15 μL GO, where the slope produced the gel fraction exponent, β values for $C^-/C^+ = 0.1$ which are listed in Table 2 for changing GO in the NIPA-GO composites, respectively.

The inline annotation on the plot reads:
$$y = 0,4027x + 0,9191$$
$$R^2 = 0,997$$
$$C^-/C^+ = 0.1$$

Axis labels: vertical axis "log I", horizontal axis "logIt-t_cI".
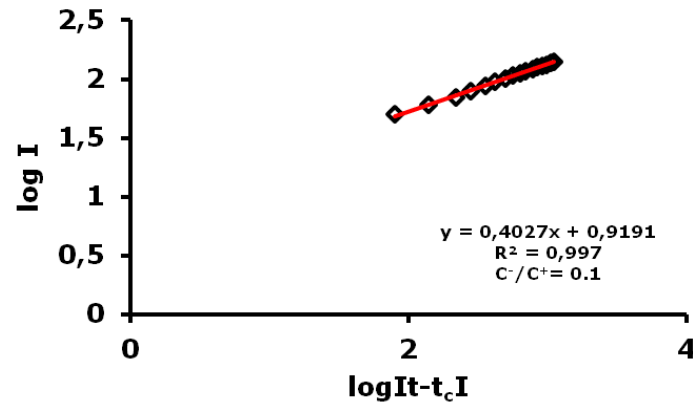
Figure 7. Double logarithmic plot of the intensity I versus time curves above t_c for 15 µL of GO contents. The β exponent was determined from the slope of the straight line (where $C^-/C^+=0.1$).

Table 2. Experimental measured parameters for NIPA-GO composites.

NIPA	GO(µL)	t_c(s)	β	E_g(eV)
	0	620	0.98	1,02
	5	700	0.55	2,37
1M	15	1180	0.44	2,90
	25	1280	0.56	2,91
	30	980	0.94	2,93
	35	1040	0.85	3,04

As given in Table 2, the gel fraction exponent,β, was agreed with the percolation for below 30 µL of GO content. On the other hand, the classical result was observed above 30 µL of GO content.

On the other hand, optical energy band gap is another important optical parameter of the composites doped by nanomaterials. The gap of the composite can be estimated for utilization of this composite in applications such as optical sensors, solar cells etc. The resulting absorbance spectrum obtained on NIPA- 15 µL of GO composite between 400-700 nm is shown in Figure 8.
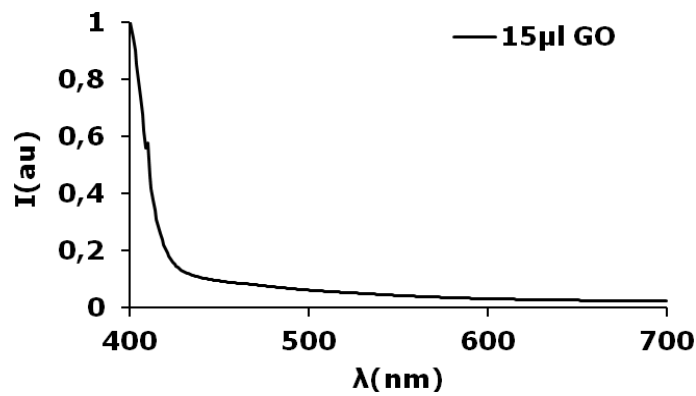
Figure 8. The absorbance of composite of NIPA- 15 µL of GO between 400- 700 nm.

Figure 9 shows that optical energy band gap was calculated from the absorption spectrum fitting method (ASF) (28-29) of NIPA - 5 µL and 15 µL of GO composites, respectively. The spectral data recorded showed the strong cut off wavelength, where the absorbance value is minimum. The optical energy band gap was decided from Eq. 4, and are given in Table II.

$$E_g = \frac{hc}{\lambda}$$ (Eq. 4)

where h is Planck's constant (Joules.sec), and c is the speed of light (m/s), λ is cut-off wavelength (m), and 1 eV=1.6*10^{-19} Joules as a conversion factor, respectively.
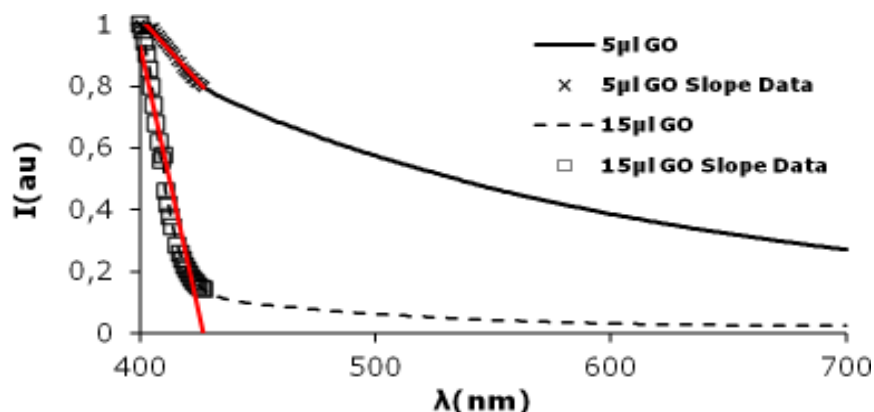
Figure 9. Optical energy band gap was calculated from the absorbance graph of NIPA - 5 µL and 15 µL of GO composite, respectively.

CONCLUSION

In this work, NIPA-GO composite was obtained by free radical copolymerization. The gelation and optical energy band gap were performed by Fluorescence and UV spectrophotometry, respectively. Firstly, the critical exponents, β for C_-/C_+= 0.1 were calculated from percolation and classical theory. The copolymerization kinetics obey the percolation picture for below 30 μL of GO content, and agree with classical theory above 30 μL of GO content. Lastly, the absorption spectrum fitting method (ASF) was mentioned to estimate the optical energy band gap for the composite. The optical energy band gap of the composite increases with increasing GO content and the composite behaves as a semiconductor. Thus, it was found that even small amounts of GO strongly influence the optical behavior of the NIPA-GO composite.

REFERENCES

1. Huang Y, Zeng M, Ren J, Wang J, Fan L, Xu Q, Preparation and swelling properties of graphene oxide/poly(acrylic acid-co-acrylamide) super-absorbent hydrogel nanocomposites. Colloids and Surfaces A: Physicochemical and Engineering Aspects, 2012 May; 401: 97- 106. DOI:10.1016/j.colsurfa.2012.03.031.

2. Shen J, Yan B, Li T, Long Y, Li N, Ye M, Study on graphene-oxide- bades polyacrylamide composite hydrogels. Composites: Part A, 2012 September; 43: 1476- 1481.DOI: 10.1016/j.compositesa.2012.04.006.

3. Song W, He C, Dong Y, Zhang W, Gao Y, Wu Y, Chen Z, The effects of central metals on the photophysical and nonlinear optical properties of reduced grapheme oxide- metal (II) phthalocyanine hybrids. Physical Chemistry Chemical Physics, 2015 February; 17: 7149- 7157. DOI: 10.1039/C4CP05963H.

4. Wang J, Liu C, Shuai Y, Cui X, Nie L, Controlled release of anticancer drug using graphene oxide as a drug-binding effector in konjac glucomannan/sodium alginate hydrogels, Colloids and Surfaces B: Biointerfaces, 2014 January; 113: 223- 229. DOI:10.1016/j.colsurfb.2013.09.009.

5. Zhang L, Wang Z, Xu C, Li Y, Gao J, Wang W, Lui Y, High strength graphene oxide/polyvinyl alcohol composite hydrogels. Journal Material Chemistry, 2011 April; 2: 10399- 10406. DOI: 10.1039/C0JM04043F.

6. Dušek K, Editor, Coexistence of Phases and the Nature of First- Order Phase Transition in Poly- N- isopropylacrylamide Gels. Hirotsu S: Advanced Polymer Science, Springer Berlin Heidelberg; 1993. 110: 1- 26 p. ISBN: 978-3-540-56970-1.

7. Yang Y, Song X, Yuan L, Li M, Liu J, Ji R, Zhao H, Synthesis of PNIPAM polymer brushes on reduced graphene oxide based on click chemistry and RAFT polymerization. Journal of Polymer Science, Polymer Chemistry, 2012 October; 50: 329- 337. DOI: 10. 1002/pola.25036.

8. Zhu S, Li J, Chen Y, Chen Z, Chen C, Li Y, Cui Z, Zhang D, Grafting of graphene oxide with stimuli-responsive polymers by using ATRP for drug release, Journal of Nanoparticle Research, 2012 September; 14: 1132- 42. DOI: 10.1007/s11051-012-1132-x.

9. Bai H, Li C, Wang X, Shi G, A pH-sensitive graphene oxide composite hydrogel. Chemistry Communication, 2010 February; 46: 2376-78, DOI: 10.1039/C000051E.

10. Alzari V, Nuvoli D, Scognamillo S, Piccinini M, Gioffredi E,   Malucelli G, Marceddu S, Sechi M,   Sanna V, Mariani A, Graphene-containing thermoresponsive nanocomposite hydrogels of poly(N-isopropylacrylamide) prepared by frontal polymerization, Journal of Materials Chemistry, 2011 April; 21: 8727-33, DOI: 10.1039/C1JM11076D.

11. Dong J, Weng J, Dai L, The effect of graphene on the lower critical solution temperature of poly (N-isopropylacrylamide). Carbon, 2013 February; 52: 326- 36, doi:10.1016/j.carbon.2012.09.034.

12. GhavamiNejad A,   Hashmi S,   Joh H, Lee S,   Lee Y, Vatankhah-Varnoosfaderani M, Stadler F.J, Network formation in graphene oxide composites with surface grafted PNIPAM chains in aqueous solution characterized by rheological experiments, Physical Chemistry Chemical Physics, 2014 March; 16: 8675- 85, DOI: 10.1039/C3CP55092C.

13. Kundu A, Nandi S, Das P, Nandi AK, Fluorescent Graphene Oxide via Polymer Grafting: An Efficient Nanocarrier for Both Hydrophilic and Hydrophobic Drugs, ACS Applied Materials and Interfaces, 2015 January; 7(6):3512- 23. DOI: 10. 1021/am507110r.

14. Evingur GA, Aktas DK, Pekcan Ö, Steady state fluorescence technique for studying phase transitions in PAAm- PNIPA mixture, Phase Transitions, 2009 January; 82(1): 53–65. DOI: 10.1080/01411590802296294.

15. Aktas DK, Evingur GA, Pekcan Ö, Universal behavior of gel formation from acrylamide-carrageenan mixture around the gel point: A fluorescence study, Journal Biomolecular Structure and Dynamics, 2006 March, 24(1), 83–90, DOI:10.1080/07391102.2006.10507102.

16. Aktas DK, Evingur GA, Pekcan Ö, Critical exponents of gelation and conductivity in Polyacrylamide gels doped by multiwalled carbon nanotubes, Composite Interfaces, 2012 April; 17: 301–318, DOI:10.1163/092764410X495243

17. Evingur GA, Pekcan Ö, PAAm- GO Composites: Optical and mechanical properties with various GO contents, 46th IUPAC World Polymer Congress (Macro 2016) 17-21 July 2016, İstanbul-Turkey.

18. http://www.graphenea.com/. Visited on 10th August 2016

19. Evingur GA, Tezcan F, Erim FB, Pekcan Ö, Monitoring the gelation of polyacrylamide–sodium alginate composite by fluorescence technique, Phase Transitions, 2012 December; 85(6): 530-541, DOI: 10.1080/01411594.2011.629363.

20. Ashokkumar M, Grieser F, Sonophotoluminescence: pyranine emission induced by ultrasound, Chemical Communication, 1998; 5: 561- 62. DOI: 10.1039/A708708J.

21. Yılmaz Y, Uysal N, Gelir A, Güney O, Aktaş DK, Göğebakan S, Öner A, Elucidation of multiple- point interactions of pyranine fluoroprobe during the gelation. Spectrochimica Acta Part A: Molecular and Biomolecular Spectroscopy, 2009 March, 72: 332- 38, DOI:10.1016/j.saa.2008.09.012.

22. Stauffer D, Coniglio A, Adam M, Gelation and Critical Phenomena, Advances in Polymer Science, 1982, 44: 103- 158, DOI: 10.1007/3-540-11471-8_4.

23. Stauffer D, Introduction to Percolation Theory, Taylor and Francis, London; 2 edition; 1994 July. ISBN-10: 0748402535.

24. de Gennes PG, Scaling Concepts in Polymer Physics, Cornell University Press, Ithaca; 1979 November. ISBN-10: 080141203X.

25. Yılmaz Y, Erzan A, Pekcan Ö, Critical exponents and fractal dimension at the sol- gel phase transition via in situ fluorescence experiments, Physical Review E, 1998; 58: 7487- 7491, DOI: 10.1103/PhysRevE.58.7487.

26. Yılmaz Y, Erzan A, Pekcan Ö, Slow Release percolate near glass transition, The European Physical Journal E, 2002; 9: 135- 141, DOI: 10.1140/epje/i2002-10069-1.

27. Aharony A, Universal critical amplitude ratios for percolation, Physical Review B, 1980; 22: 400-414. DOI: 10.1103/PhysRevB.22.400

28. Ghobadi N,Band gap determination using absorption spectrum fitting procedure, International Nano Letters, 2013 December; 3:2, DOI: 10.1186/2228-5326-3-2.

29. Dharma J, Simple Method of Measuring the Band Gap Energy Value of TiO2 in the Powder Form using a UV/Vis/NIR Spectrometer, Perkin Elmer Application note, PerkinElmer, Inc. Shelton, CT USA, 1-4.

NIPA-GO Kompozitlerinin Optik Özellikleri Üzerine Grafen Oksidin Etkisi

Gülşen Akın Evingür

Öz: Poli(N-izopropilakrilamid) (NIPA)-Grafen oksit (GO) kompozitleri çeşitli GO çözeltileri içeriği ile radikal olarak polimerleştirilmiştir. Jelleşme süreci Durgun Hal Floresans Spektroskopisi ile gerçekleştirilmiştir. Jelleşme sonuçları sırasıyla sızma ve klasik modelle açıklanmıştır. Sonuçlarımıza göre GO çözeltisinin 25 µL içeriğine kadar sızma modeline uyan jel kısmının kritik bir örneği ortaya konmuştur. Diğer taraftan, NIPA-GO kompozitinin optik enerji bant aralığı, 200-800 nm aralığında soğurma ölçümlerinden UV spektrofotometrisi ile tespit edilmiştir. Grafen oksit katkısının enerji aralığı üzerindeki etkisi NIPA-GO kompozitleri için incelenmiştir. Sonuç olarak, kompozit malzemelerin jelleşme süreci ve optik enerji aralığı davranışı incelenmiş ve kompozitlerdeki GO içeriği ile ilişkilendirilmiştir.

(This article was presented to the 28th National Chemistry Congress and submitted to JOTCSA as a full manuscript)

In Vitro Studies on Pesticide-Induced Oxidative DNA Damage

Özlem DEMİRCİ[1], Bircan ÇEKEN TOPTANCI[2] and Murat KIZIL[2]

[1]University of Dicle, Faculty of Science, Biology Department, 21280, Diyarbakır, Turkey

[2]University of Dicle, Faculty of Science, Chemistry Department, 21280, Diyarbakır, Turkey

Abstract: Pesticides are among the most extensively used chemicals in the world today and they are also among the most hazardous compounds for the human. This study was designed to use the plasmid relaxation assay to describe the association of markers of DNA damage with pesticide exposure. The DNA damage activity of fluoxastrobin and imazamox were checked on pBluescript M13+ plasmid DNA (3.2 kb) in the absence and presence of Cu(II) ions. It has been found that the fluoxastrobin and imazamox can cleavage plasmid DNA in the absence and presence of Cu(II) ions. DNA cleavage was found to be concentration- and time-dependent. In conclusion, the present study showed that fluoxastrobin and imazamox can damage DNA, which warrants for further investigations to correctly evaluate the hazards of exposure to these chemicals.

Keywords: DNA damage; Genotoxicity; Fluoxastrobin; Imazamox.

*Corresponding author. E-mail: ozdem22@gmail.com.

INTRODUCTION

Though extreme anthropogenic activities bring about innumerable accumulation of xenobiotics in biosphere (1, 2), especially pesticides are designed specifically to kill the organisms. Therefore, they are one of the most dangerous chemical compounds (3). Pesticides have to comply with a demand: a high degree of toxicity for only target organisms, but synthetic pesticides are quite inadequate in this respect (4). Pesticides consist of a heterogeneous class of chemicals, developed for the purpose of controlling pests, requisite in modern agriculture, but numerous studies available in the literature are with regard to their genotoxicity (5).

The primary risk factor is the genotoxic potential for long-term effects such as carcinogenic and reproductive toxicology. Most of the pesticides have been tried in a wide range of mutagenicity assays covering gene mutation, DNA damage and chromosomal alteration (6).

Fluoxastrobin is a new strobilurin-type fungicide and it has a broad spectrum of activity against many fungal diseases. It is known that Fluoxastrobin has been registered for foliar utilization on corn vegetables, peanuts, and tuberous, fruiting vegetables, leaf petiole vegetables, and turf, as well as peanut.

Imazamox is a widely used herbicide in the imidazolinone herbicide family and inhibits the acetolactate synthase enzyme, which is critical for the synthesis of the amino acids valine, leucine, and isoleucine in plants.

In field crops, imazamox is effective against a large variety of grass and broadleaf weeds, including downy brome, red rice, shattercanech, jointed goatgrass, wild mustards, common ragweed, common lambsquarters, and others. Pesticides tend to accumulate in the environment and organisms.

It was reported that the amount of pesticide utilized was approximately 2.4 million tons in both 2006 and 2007, with herbicides calculating for the largest part of the total use, followed by other pesticides, fungicides, and insecticides (7). Distinct agriculture applications practised in agricultural areas of the extensive farming inside of hothouses (most especially close the seaboard) and another hand conventional agriculture, which accounts for a heterogeneous type of pesticide use (8).

Pesticides can be connected to each groove of the DNA double helix with various non-covalent interactions. For example; pesticides can be linked in the wall/surface of each groove of DNA with hydrophobic interaction, specific hydrogen bonds or van der Waals interactions.

Experimental input demonstrated that numerous pesticides had mutagenic qualities causing genetical chromosomal alteration, DNA damage, or mutation (9).

Pesticides exposure caused increasing incidence of cancer, endocrine disorders, neurodegenerative disorders, birth defects, reproductive disorders, Parkinson, Alzheimer, diabetes, cardiovascular diseases, chronic nephropathies, and chronic respiratory disease (10).

However, few *in vitro* studies focusing on effects of pesticides on DNA damage have been performed. A study of the genotoxicity of chemicals, such as fluoxastrobin and imazamox is important because of their possible consequences on human health and their relation with cancer and other diseases. Therefore, the aim of present study was to determine the effect of fluoxastrobin and imazamox on plasmid DNA in the absence and presence of ions Cu(II) ions.

MATERIALS AND METHODS

Chemicals

Fluoxastrobin, Imazamox, acetone, agarose, bromophenol blue, copper(II) chloride, sodium chloride, ethylenediaminetetraacetic acid (EDTA), glacial acetic acid, and trisma base were purchased from Sigma-Aldrich (St Louis, MO) and ethidium bromide was obtained from Amresco LLC (Solon, OH). Plasmid miniprep kit was obtained from Qiagene (Valencia, CA).

Purification of Plasmid DNA

Genejet plasmid mini preparation kit was used to isolate the pBluescript M13+ plasmid DNA. U.V spectroscopy was used to checked the purity of plasmid DNA. DNA concentration is estimated by measuring the absorbance at 260 nm. (A_{260} = 1.0 for 50 µg/mL).

DNA Damage with Fluoxastrobin and Imazamox

This study was designed to use the plasmid relaxation assay to describe the association of markers of DNA damage with pesticide exposure (11). DNA cleavege activity of fluoxastrobin and imazamox were checked in the absence and presence of Cu(II) ions on pBluescript M13+ plasmid DNA (3.2 kb) by agarose gel electrophoresis according to Çeken (12).

0.5-mL Eppendorf tubes which were covered with aluminum foil were used for the reactions and for protecting the samples from light. All reactions were performed in a volume of 10 μL, containing 200 ng of pBluescript M13+ plasmid DNA at room temperature, in phosphate buffer (pH 7.4; 14.29 mM NaCl, 7.14 mM phosphate). Fluoxastrobin and Imazamox (50, 100, 150, 200, 250 μg/mL) were added in the absence and presence of (II) at a final concentration of 100 μM. Electrophoresis was performed in the presence of ethidium bromide (10 mg/mL), at 60 V for 90 minutes.

In this experiment, we take advantage of the fact that double-stranded plasmid DNA molecules generally exhibit three conformations that reflect the integrity of the DNA: Supercoiled (sc), open circular (oc), and linear (l).

Densitometric analysis

Gel documentation system was used for scanning to the gel (Gel-Doc-XR; BioRad).

RESULTS AND DISCUSSION

In order to assess whether prolonged exposure to pesticides in the presence of metal ions could lead to an increase in genetic damage, plasmid DNA exposed to pesticides were evaluated using plasmid relaxation assay.

Excessive use of pesticides in agricultural or domestic areas results in environmental contamination. Though pesticides have significant contributions for the elimination of the harmful effects of pests on plant, animal, and human, they have toxic effects on the non-target organism.

It has been clearly demonstrated that pesticidal toxicity alters a variety of physiological functions. Additionally, evidence has shown that pesticide exposure can promote the risk of neurodegenerative diseases and cancer.

Recent evidence also suggests that the pesticides which act as endocrine disruptors have the ability to cause diverse side effect regarded to developmental toxicity and reproductive.

Therefore, it is now evident that research towards understanding how pesticides effect the progression and development of disease will cause to further improvements in public health.

In the literature, chlorpyrifos, methyl parathion, and malathion were investigated for their DNA damage activities (13, 14). However, there is no study with new generation pesticides. Therefore, in this study we used the plasmid relaxation assay to describe the association of markers of DNA damage with fluoxastrobin and imazamox exposure. Plasmid relaxation assay is a cheap and fast method to explain the toxic effect of pesticide. Oxidative damage to DNA is one of the most important mechanisms in the initiation of cancer such damage is sometimes caused by pesticides.

This study is the first to investigate the role of metal ion (copper) in the observed toxic action of pesticides. It is known that copper has the ability to capable of mediating the action of several phenolic compounds producing reactive oxygen and other radicals (15). Since copper exists in the nucleus and is closely associated with chromosomes and DNA bases, in this study we have investigated whether the activation of pesticides such as fluoxastrobin and imazamox by copper can induce strand breaks in DNA. Copper salts have been used extensively as fungicides for a long time so that it is very important to investigate the effects of the combination of copper with other pesticides (16).

The role of fluoxastrobin and imazamox DNA damage was evaluated, and the exposure time is presented in Figure 1-4. As shown in Figures 1 and 3, fluoxastrobin at concentrations between 50-250 μg/mL has no significant effect on cleavage of plasmid DNA in the absence and presence of Cu(II) ions (Figure 1, lane 2-6; Fig 3, lane 3-7). On the other hand, at the concentration between 50-250 μg/mL imazamox can effectively promote cleavage of plasmid DNA in the absence and presence of Cu(II) ions (Figure 2, lane 2-6; Fig 4, lane 3-7).

In the presence of 100 µM concentration of Cu(II), imazamox (50-250 µg/mL) induced extensive DNA strand breaks as indicated by disappearance of supercoiled (sc) form and the formation of open circular (oc) and linear form (l).

Copper is widely distributed in nature and is an essential element. Acute poisoning occurs most frequently from the ingestion of copper sulfate or other copper salts, and hepatic necrosis is characteristic of copper poisoning. The redox properties of copper and iron complexes of adriamycin, bleomycin, and thiosemicarbazones have been investigated by electron spin resonance spectroscopy (ESR) (17).

A common property of these metal complexes is their ability to be readily reduced by thiol compounds and oxidized by iron or reduced species of iron to produce free radicals. Copper is also a common cofactor for many enzymes including oxidases and oxygenases (18). Similar to iron, copper acts as a catalyst in the formation of reactive oxygen species and catalyzes peroxidation of membrane lipids (19). The metal ions present in some pesticides and fertilizers (20) may interfere with DNA repair and produce reactive oxygen species (ROS), leading to oxidative damage (6). The pesticide-metal ion-DNA associations might contribute to genotoxicity.

The individual and the combined toxicity of pesticides and metals were studied by Bhuvaneshwari *et al.* (2012). They observed that pesticides, metal ions, and a mixture of them caused DNA damage and this damage inducts mutation in the GADD45β gene (21).

The cleavage of DNA was found to depend on both the concentration of pesticide and the reaction time (24-48 h). Our results indicate that both pesticides used in this study have the ability to damage plasmid DNA in the absence and the presence of metal ions. Therefore, further detailed evaluation of genotoxicity is thus required.
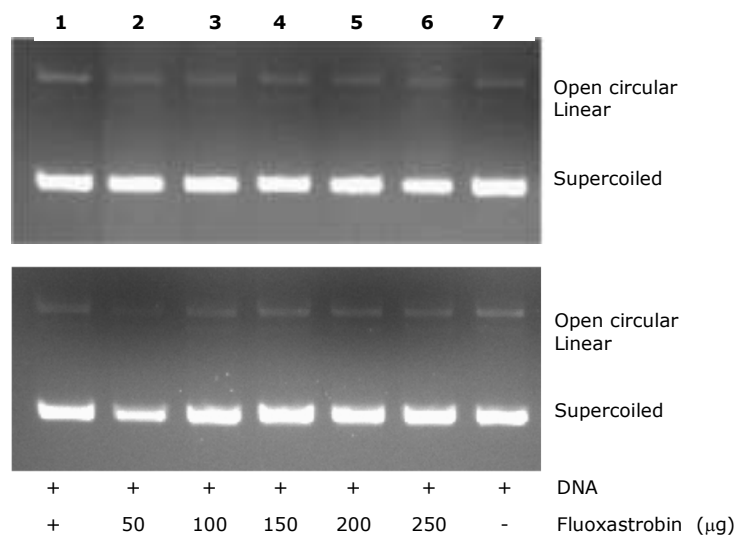
Figure 1. Gel electrophoresis diagram showing the cleavage of pBluescript M13+ plasmid DNA (3.2 kb) fluoxastrobin in the dark at different exposure times (A: 24h, B: 48 h).
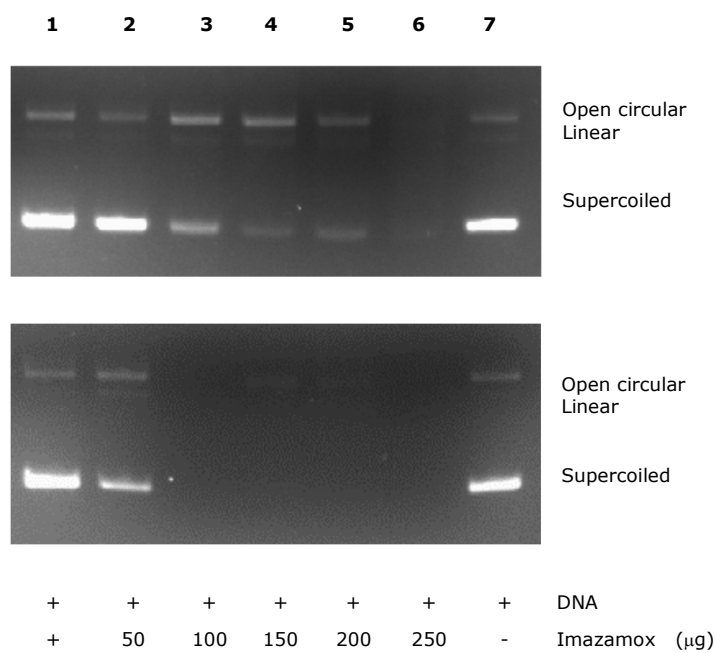
Figure 2. Gel electrophoresis diagram showing cleavage of pBluescript M13+ plasmid DNA (3.2 kb) by imazamox in the dark at different exposure times (A: 24h, B: 48 h).

485
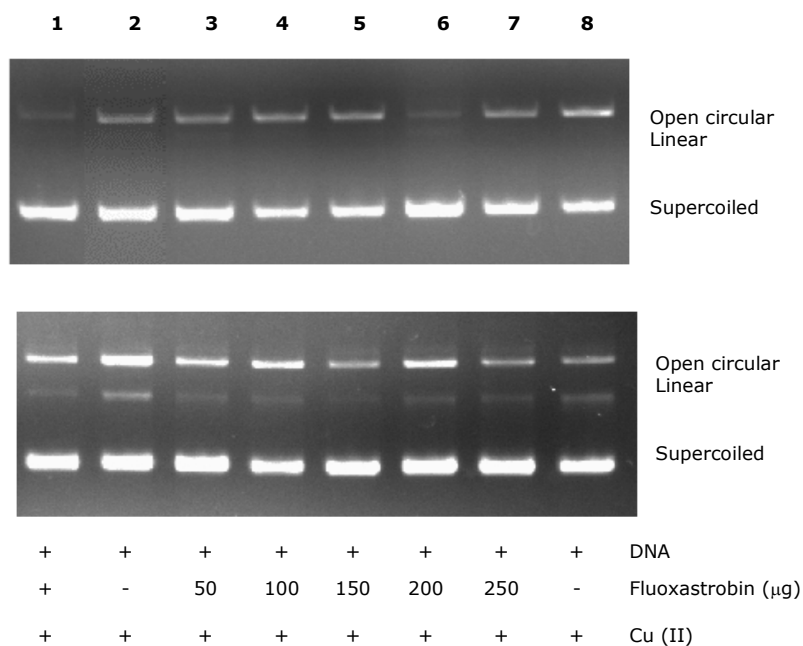
Figure 3. Gel electrophoresis diagram showing cleavage of pBluescript M13+ plasmid DNA (3.2 kb) by fluoxastrobin in the presence of $CuCl_2$ in the dark at different exposure times (A: 24h, B: 48 h).
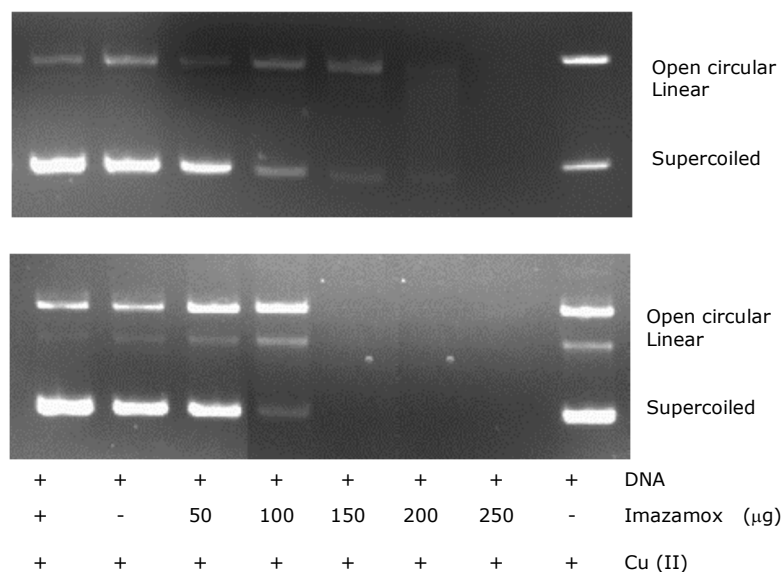
Figure 4. Gel electrophoresis diagram showing cleavage of pBluescript M13+ plasmid DNA (3.2 kb) by imazamox in the presence of $CuCl_2$ in dark at different exposure times (A: 24h, B: 48 h).

REFERENCES

1.   Fernández-Alba AR, Guil H, López GD, Chisti Y. Comparative evaluation of the effects of pesticides in acute toxicity luminescence bioassays. Analytica Chimica Acta. 2002;451:195–202. DOI: 10.1016/S0003-2670(01)01422-2.

2.   Vrankovic J, Labus-Blagojevic S, Csanyi B, Makovinska J, Cvetkovic O, Gacic Z, et al. Antioxidant enzymes and GST activity in natural populations of Holandriana holandrii from the Bosna River. Turkish Journal of Biology. 2012;36:477-85. DOI: 10.3906/biy-1111-43.

3.   Hanazato T. Pesticide effects on freshwater zooplankton: an ecological perspective. Environmental Pollution. 2001;112:1-10. DOI: 10.1016/S0269-7491(00)00110-X.

4.   Lioi MB, Scarfı MR, Santoro A, Barbieri R, Zeni O, Di Berardino D, et al. Genotoxicity and oxidative stress induced by pesticide exposure in bovine lymphocyte cultures in vitro. Mutation Research/Genetic Toxicology and Environmental Mutagenesis. 1998 403 13-20. DOI: 10.1016/S0027-5107(98)00010-4.

5.   Fragiorge EJ, Rezende AAAd, Graf U, Spanó MA. Comparative genotoxicity evaluation of imidazolinone herbicides in somatic cells of Drosophila melanogaster. Food and Chemical Toxicology. 2008;46(1):393-401. DOI: 10.1016/j.fct.2007.08.022.

6.   Bolognesi C. Genotoxicity of pesticides: a review of human biomonitoring studies. Mutation Research/Reviews in Mutation Research. 2003;543(3):251-72. DOI: 10.1016/S1383-5742(03)00015-2.

7.   Grube A, Donaldson D, Kiely T, Wu L. U.S. EPA Pesticide Market Estimates: 2006-2007. Office of Pesticide Programs. Washington, DC 2011. URL: https://www.epa.gov/sites/production/files/2015-10/documents/market_estimates2007.pdf.

8.   Parrón T, Requena M, Hernández AF, Alarcón R. Association between environmental exposure to pesticides and neurodegenerative diseases. Toxicology and Applied Pharmacology. 2011 256:379-85. DOI: 10.1016/j.taap.2011.05.006.

9.   Bolognesi C, Morasso G. Genotoxicity of pesticides: potential risk for consumers. Trends in Food Science & Technology 2000;11:182-7. DOI: 10.1016/S0924-2244(00)00060-1.

10.   Mostafalou S, Abdollahi M. Pesticides and human chronic diseases: Evidences, mechanisms, and perspectives. Toxicology and Applied Pharmacology. 2013;268(2):157-77. 10.1016/j.taap.2013.01.025.

11.   Çeken B, Kízíl M. Synthesis and DNA-cleaving activity of a series of substituted arenediazonium ions. Russian Journal of Bioorganic Chemistry. 2008;34(4):488-98. DOI: 10.2307/3752354.

12.   Toptancı BÇ. (+)-Duocarmycin Antibiyotiği Analoglarının Sentezlenmesi ve DNA Üzerine Etkilerinin Araştırılması. Dicle University, Science Faculty, Chemistry Department. [PhD Thesis]. 2013.

13.   Bagchi D, Bagchi M, Hassoun E, Stohs S. In vitro and in vivo generation of reactive oxygen species, DNA damage and lactate dehydrogenase leakage by selected pesticides. Toxicology. 1995;104(1):129-40. DOI: 10.1016/0300-483X(95)03156-A.

14.   Ojha A, Yaduvanshi SK, Pant SC, Lomash V, Srivastava N. Evaluation of DNA damage and cytotoxicity induced by three commonly used organophosphate pesticides individually and in mixture, in rat tissues. Environmental Toxicology. 2013;28(10):543-52. DOI: 10.1002/tox.20748.

15.   Nazeem S, Azmi AS, Hanif S, Kumar KS. Reactive Oxygen-Dependent DNA Damage Resulting from the Oxidation of Plumbagin by a Copper-redox Cycle Mechanism: Implications for its Anticancer Properties. Austral-Asian Journal of Cancer. 2008;7:65-72. URL: http://cancerres.aacrjournals.org/content/54/7 Supplement/1895s.short.

16.   Chester F. The copper salts as fungicides. The Journal of Mycology. 1890:21-4. DOI: 10.2307/3752354.

17.   Antholine WE, Kalyanaraman B, Petering DH. ESR of copper and iron complexes with antitumor and cytotoxic properties. Environmental Health Perspectives. 1985;64:19. URL: https://www.ncbi.nlm.nih.gov/pmc/articles/PMC1568621/.

18.   Gutteridge J. Tissue damage by oxy-radicals: the possible involvement of iron and copper complexes. Medical biology. 1983;62(2):101-4. URL: http://europepmc.org/abstract/med/6471925.

19.   Chan PC, Peller OG, Kesner L. Copper (II)-catalyzed lipid peroxidation in liposomes and erythrocyte membranes. Lipids. 1982;17(5):331-7. DOI: 10.1007/BF02535190.

20.   Zoffoli HJO, do Amaral-Sobrinho NMB, Zonta E, Luisi MV, Marcon G, Tolón-Becerra A. Inputs of heavy metals due to agrochemical use in tobacco fields in Brazil's Southern Region. Environmental Monitoring and Assessment. 2013;185(3):2423-37. DOI: 10.1007/s10661-012-2721-y.

21.   Bhuvaneshwari R, Babu Rajendran R, Kumar K. Induction of DNA Damage and GADD45β gene Mutation in Zebra fish (Danio rerio) due to Environmentally Relevant Concentrations of Organochlorine Pesticides & Heavy Metals. International Journal of Environmental Research. 2012;7(1):219-24. URL: https://ijer.ut.ac.ir/article_600_7.html.

Türkçe Öz ve Anahtar Kelimeler

Pestisit-Kaynaklı Oksidatif DNA Hasarı üzerine *in vitro* Çalışmalar

Özlem DEMİRCİ, Bircan ÇEKEN TOPTANCI ve Murat KIZIL

Öz: Pestisitler dünyada bugün en çok miktarda kullanılan kimyasallar arasında olup insanlar için en zararlı bileşikleri oluşturmaktadır. Bu çalışma, pestiside maruz kalmakla beraber DNA hasarını gösteren işaretlerin toplamını tarif etmek üzere plazmid gevşeme çalışmasını kullanmaktadır. Fluoksastrobin ve imazamox pestisitlerinin DNA hasar aktivitesi pBluescript M13+ plazmid DNA (3,2 kb) incelemesi Cu(II) iyonlarının varlığında ve yokluğunda incelenmiştir. Fluoksastrobin ve imazamox'un plazmid DNA'sını Cu(II) iyonlarının varlığında ve yokluğunda parçalayabildiği bulunmuştur. DNA parçalanmasının derişime ve zamana bağlı olduğu bulunmuştur. Sonuç olarak, bu çalışma fluoksastrobin ve imazamox'un DNA'yı tahrip edebildiğini göstermiştir, bu da söz konusu kimyasalların maruziyetleri için zararlı etkinin doğru bir şekilde değerlendirilmesi için daha fazla çalışma yapılması gerektiğini göstermektedir.

Anahtar kelimeler: DNA hasarı; Genotoksisite; Fluoksastrobin; Imazamox.

Gönderilme: 17 Temmuz 2016. **Düzeltme:** 09 Eylül 2016. **Kabul:** 06 Ekim 2016.

Interrelation among Serum Lithium Levels, Bone Metabolism, and Some Biochemical Parameters in Pre- and Post-Menopausal Women

Ruken Esra Demirdogen*[1], Fatih Mehmet Emen[2], Derya Kilic[2], Gokturk Avsar[3], Tuncay Yesilkaynak[4], Tunay Askar[5]

[1]Cankiri Karatekin University, Faculty of Science, Department of Chemistry, 18100, Cankiri, Turkey. [2]Mehmet Akif Ersoy University, Faculty of Science, Department of Chemistry, 15100, Burdur, Turkey. [3]Mersin University, Faculty of Science, Department of Chemistry, 33342, Mersin, Turkey. [4]Afsin Vocational High School, Sütcü İmam University, TR46500, Kahramanmaras, Turkey. [5]Cankiri Karatekin University, Health High School, Department of nutrition and dietetics, 18100, Cankiri, Turkey,

Abstract: The target of this study is to determine the interrelation among serum Li level on bone metabolism (Ca, P, Parathormone, and Vitamin-D), sex and metabolic hormones (estrogen, FSH, LH and TSH), and some biochemical parameters in premenopausal and postmenopausal women. The study is carried out with 10 women, 5 of which is in the premenopausal period. The serum Li levels, bone metabolism indicators (*i.e.*, ALP, Ca, P, Mg, Cu, and Zn) and some biochemical parameters such as serum triglyceride, alkalene phosphatase, total cholesterol, HDL, LDL, and cholesterol levels were determined. The estrogen blood level of women in menopause period was found to be lower than that of women in pre-menopause period ($p<0.01$) and the FSH level was found to be higher ($p<0.01$). In the lipid profile, the triglyceride level in the post-menopause period was found to be low ($p<0.05$) and HDL ($p<0.001$), LDL ($p<0.001$) and the cholesterol levels were found to be high ($p<0.001$). The alkalene phosphatase ($p<0.001$) and Vitamin-D levels ($p<0.001$) were found to decrease. When the mineral levels were investigated, no meaningful difference was observed in the serum magnesium and copper levels while zinc ($p<0.01$) and phosphorus ($p<0.005$) levels were observed to increase, the calcium levels ($p<0.05$) decreased and Li levels considerably decreased ($p<0.0001$). According to the results obtained it was determined for the first time that Li deficiency can be related with menopause and the related diseases and thus Li therapy can be used in developing new treatment protocols of menopause as an alternative method.

Keywords: Bone metabolism, menopause, osteoporosis, serum Li level.

INTRODUCTION

Menopause can be defined as decrease of hormones periodically secreted from the ovaries and full-stop of menstrual bleeding which is a natural consequence of aging. In the period when women try to adapt themselves from a period, when they are physiologically stimulated with estrogen and progesterone, to a period, when they are deprived of these hormones and decrease in estrogen levels, serious complications such as cardiovascular diseases, cancer, bone loss and osteoporosis arise [1].

Osteoporosis is a disease which leads to bone fractures due to decrease in the bone density. In osteoporosis, bones become sensitive due to decrease in bone mass caused by factors related with genetics, hormonal, environmental and diet and bone loss occurs in the endostal region of the skeleton [2]. One of the main reasons of osteoporosis is the deficiency in estrogen. Estrogen is necessary for the normal maintenance of the bone matrix and for incorporation of calcium in the matrix. Moreover, estrogen increases absorption and excretion of calcium and inhibits bone resorption [3].

Today modern menopausal treatment is focused on developing therapy models which would eliminate the symptoms suffered during menopause period with the least side effects. Studies have shown that there is a relation between lithium and sex hormones and it affects these hormones [4]. In another study it was reported that lithium antagonizes the effects of estrogen [5]. Moreover it was shown that lithium affects the wnt path which plays an important role on development and differentiation of bone tissues and hair follicles. In an increased number of studies, it was shown that wnts are key regulators on osteogenic differentiation of mesenchyme stem cells and on bone formation. For example, while a change in the wnt signalization path can cause osteoporosis and osteopenia inactivating mutation of wnt inhibitors lead to hyperostotic skeleton formation and thus an increase in bone mineral density. Lithium blocks the wnt antagonist and decreases fracture risk of the patient [6]. It was shown that lithium can be related with hyperparathyroidism which is a risk factor for osteoporosis. However, the data regarding the relationship between lithium and bone mass is contradictory. Lithium can cause hypercalcemia and paratyroid function disorder [7]. Moreover, the therapeutic effect of lithium can be observed in a very narrow window and the concentrations above this level can cause poisoning or can be lethal. For instance, while its concentration in the plasma and in the serum is above 1.5 mmol.L^{-1} poisoning can happen when its concentration in the serum is above 2-2.5 mmol.L^{-1} and when its concentration in the serum is above 3.5 mmol.L^{-1} in the serum it can be lethal. On the other hand, it is known that lithium therapy is successful only when lithium concentration in the plasma is above 0.050 mmol.L^{-1}, and is in the range 0.5-1.5 M in the blood and 0.3-1.3 mM in the serum [8,

9].

Therefore, in order to provide optimum benefit from therapeutic effect of lithium, its accurate, sensitive, selective, and reliable detection in blood, blood plasma, serum, and saliva is of great importance.

Studies have shown that the toxic effect of lithium does not only depend on the amount of lithium administered but also other parameters such as sodium intake affect the mechanism. Therefore, in this study both determination of serum lithium levels in women in pre-menopause and menopause periods and also the relation among lithium levels, bone metabolism (Ca, P, Parathormone, Vitamin-D), sex and metabolic hormones (estrogen, FSH, LH, TSH) and some biochemical parameters were targeted for evaluating efficacy of lithium as a therapeutic agent in treatment of osteoporosis.

MATERIAL AND METHODS

This study is made on volunteering women who had visited Çankırı Karatekin Hospital Outpatient Polyclinics of Gynecology and Obstetrics. The study was carried out with two groups each of which were consisted of 5 female subjects. The first group (Pre-menopause Group) was under the age 45 and had regular periods (menstrual cycle) and who was determined not to be in the menopause period by the doctor and the second group (Post-menopause Group) comprised of women, who were above the age 55 and did not have their periods and they were clinically diagnosed by the doctor to be in the menopausal period. The volunteer subjects were none-smokers and did not have any systemic diseases such as renal failure, diabetes mellitus, heart diseases and who did not use any kind of estrogen preparative before. The subjects, who were included in the control group, were included in this group according to the diagnosis of the doctor and had estrogen value above 30 pg/mL. The subjects with estrogen value below 20 pg/mL were included in the menopausal group. Ethical board permission was obtained from Kirikkale University Faculty of Medicine and each patient was asked to offer their consent via "informed consent form".

10 mL venous blood was taken from the subjects participating in the study into serum tubes and tubes containing anticoagulant for the biochemical analysis. The venous blood samples were centrifuged at 3000 rpm for 10 min.s and the sera were separated from the blood samples. Serum samples were placed in Eppendorf tubes and were kept at -80 ºC until they were analyzed.

Water used in the experiments was purified with a MilliQPLUS 185 system (Millipore, St Quentin-en-Yvelines, France). Suprapur nitric acid 65 % and Triton X-100 were obtained from Merck (Darmstadt, Germany). Rhodium standard for ICP TraceCERT®, 1000 mg/L Rh in hydrochloric acid was obtained from Sigma Aldrich.

Serum Ca, P, Zn, Cu, Mg, triglyceride, total cholesterol, HDL, LDL, ALP, FSH, estrogen, and Vitamin D levels were determined via commercial kits in the auto-analyzer. Serum lithium concentrations were determined by ICP-MS Thermo Elemental X7CCT series and PlasmaLab1 software without a dynamic reaction cell. Plasma torch argon purity was higher than 99.9 %.

Blood plasma samples (0.4 mL each) were diluted with purified water, acid, triton X100, and butanol and Rhodium was used as internal standard. The Li measurements showed linearity (from limit of detection to 25 ng/mL or to 250 ng/mL) with a correlation coefficient > 0.99. and also the intra-assay and inter-assay inaccuracy, which was measured as the variation coefficient, was < 5 and 10% respectively.

The data obtained in the study were evaluated via the statistical package program (SPSS 11.5 for Windows Standard Version) and were expressed as mean ± standard deviations. Normalization tests of the data obtained were made and in order for to determine the statistical differences among the groups one way variance analysis (ANOVA) and Duncan test were used as post-test.

RESULTS AND DISCUSSION

The serum estrogen and FSH values, according to which the menopause diagnosis is made, are presented in Table 1.

Table 1. Serum mineral, lipid, and hormone values of the female subjects.

Parameters	Pre-Menopausal Group	Post-Menopausal Group
Li (µg/dL)	22,6±0,40	7,58±0,21***
Ca (g/dL)	9,84±0,65	9,59±1,04*
P (g/mL)	4,16±0,74	4,46±0,81*
Zn (g/dL)	100±24,1	110±28,4**
Cu	123±18,8	122±16,7*
Mg (g/dL)	1,82±0,138	1,94±0,18
HDL (mg/dL)	38,5±7,78	43,7±8,93***
LDL (mg/dL)	128±46,1	146±45,0**
Triglyceride (mg/dL)	156±104	151±96,5*
Alkalene phosphatase (U/L)	195±66,7	231±86,7**
Cholesterol (mg/dL)	197±43,2	224±51,1**
Vitamin D (25-OHD)	12,7±3,81	5,67±1,41***
Estradiol (pmol/L)	220,3 ± 59,7	88.2 ± 16,2***
FSH (IU/L)	19.7 ± 10.2	71.5 ± 15.8**
LH (IU/L)	8.65 ± 6.21	35.02 ± 7.13**

* sign indicates the statistical differences among the groups when p<0.05.

** sign indicates the statistical differences among the groups when p<0.01.

*** sign indicates the statistical differences among the groups when p<0.001.

In the study, it was determined that the estrogen level of women in the menopausal period is lower than that of the women in the pre-menopausal period (p<0.01) while the FSH level was found to be higher (p<0.01). In the lipid profile, while the triglyceride level was found to be low in the post- menopausal period (p<0.05), the HDL (p<0.001), LDL (p<0.001) and the cholesterol levels (p<0.001) were found to be high. Alkalene phosphatase (p<0.001) and Vitamin D levels (p<0.001) were found to decrease in the post-menopausal period. When the mineral levels were investigated, it was observed that there was no significant change in serum magnesium and copper levels, but zinc (p<0.01) and phosphorus levels (p<0.005) increased, and calcium level (p<0.05) decreased. However, serum lithium level (p<0.0001) considerably decreased.

Considerable physiological changes happen in the bodily functions of women in the period when sex hormones (estrogen and progesterone) are diminished and disappear and as a result of this they become prone to various diseases. Menopause causes important changes to take place in the metabolism and in the lipid profile. Since the protective effects of estrogen diminish in the post-menopausal period the risk to osteoporosis and coronary diseases increase. Today modern menopause treatment works on therapeutic models which would eliminate the symptoms in this period with the least side effect. This study is important with regard to establishing basis for understanding the effect of lithium on treatment of symptoms of menopause (*i.e.*, osteoporosis and coronary diseases).

The target of this study is to determine lithium levels in women in the pre- and post-menopausal periods and to investigate the relation among lithium level, bone metabolism (Ca, P,

Parathormone, Vitamin D), sex and metabolic hormones (estrogen, FSH, LH, TSH) and some biochemical parameters to understand the efficacy of lithium as a therapeutic agent in treatment of osteoporosis.

Although the lipid profile plays an effective role in menopause, it was shown that triglyceride level causes bone density to decrease in the post-menopausal women. However, it is known that the lipid profile alone cannot be effective on bone density, but estrogen level and the period of menopause would play important roles [10]. Also in our study, the HDL (p<0.001), LDL (p<0.01), and cholesterol (p<0.01) levels of women in menopausal period were found to increase as compared to the values of women in the pre-menopausal period. Considerable decrease was observed in the estrogen level (p<0.001) while the FSH (p<0.01) and LH levels (p<0.01) increased. Since the follicles in the ovaries of women in the menopause period are drained decrease in estrogen and progesterone hormone levels and as a consequence of this increase in the levels of luteinizing hormone (LH) and follicle stimulating hormone (FSH) is a part of the natural process. If the blood FSH level is > 30 mIU/mL and the menstrual period had not occurred for one year the subject can be diagnosed with menopause [10].

When the lipid profile was investigated in the post-menopause period the blood triglyceride level (p<0.05) was found to be low but the HDL (p<0.001), LDL (p<0.001) and cholesterol levels (p<0.001) were found to be high. It is known that cholesterol level of osteoporosis patients is high [11].

The latest studies have shown that in the menopausal period, total cholesterol and LDL cholesterol (p<0.001) levels increase. It was shown that although triglyceride level is high in women in the post-menopausal period, HDL level decreases (p<0.001). Thus, it is shown that menopause decreases total and LDL cholesterol levels via decreasing HDL cholesterol and it changes the triglyceride level is high the lipid profile [12]. High LDL values show that the protective effects of HDL decreases. It is shown that hyperlipidemia contributes to osteoporosis and the basis of this process is lipid oxidation. The oxidized lipids are inhibited *in vitro* osteoblastic differentiation [13]. Moreover, the *in vivo* studies showed that diets rich in fat and cholesterol decreases bone mineral density and increases alkalene phosphatase level (p<0.001). The increase in the alkalene phosphatase level, which is frequently seen in the menopausal period, shows the increase in the activity in the bone cells and thus the increase in the risk of bone loss [14, 15]. The decrease in level of estrogen hormone, which plays and important role in Vitamin D to be active, during menopausal period can cause serious problems regarding bodily functions in which Vitamin D acts as a mediator [16]. In our study, it was observed that Vitamin D level (p<0.001) decreases in the post-menopausal period. However, Vitamin-D and calcium levels and supplementation play critical

role in prevention of osteoporosis and in formation of healthy bone structure [16].

Some minerals (Zn, Cu), hormones (estrogen) and Vitamin D are important factors affecting ligaments and bone matrix [17]. It is known that, in the fight with osteoporosis, calcium and Vitamin-D are the first strategic factors [18]. In the study it was observed that Vitamin D level (p<0.0001) was considerably low in subjects in the menopausal period. Moreover, serum estrogen level (p<0.001) of women in post-menopausal period was found to be lower, but their FSH and LH levels were higher and serum calcium level (p<0.05) was also lower than those in pre-menopausal period. Regarding bone health these values indicate the risk of osteoporosis. Bone minerals are consisted of calcium phosphate. Therefore, regarding bone health, phosphorus is as important as calcium [20]. The typical adult diet contains phosphorus in abundance. It was observed that phosphorus level (p<0.5) in women in the menopausal period, who participated in our study, did not change much. This shows that the women who participated in this study do not take such supplementations. In the study made against the common view, the main cause of osteoporosis is not the deficiency in estrogen and calcium but the deficiency in the micronutrients [20]. Low serum ALP level which indicated weak bone formation is a sign of low serum zinc level [21]. In our study we found that in women in menopausal period serum ALP level (p<0.01) and thus zinc level (p<0.01) were found to be high. High zinc level causes copper level (p<0.5) to be low. Studies made indicate that low copper level can cause osteoporosis, anemia, and neurodegenerative disorders [21]. It was observed that serum copper level (p<0.05) was lower in women in menopausal period than those in pre-menopausal period. This indicates risk of osteoporosis in the patients in the menopause period who participated in our study.

There is a positive correlation between magnesium level and bone mineral density. It is mentioned that serum magnesium level in women, who had osteoporosis, was lower than those who had osteopenia and who did not have osteoporosis or osteopenia [22]. No important difference was observed in serum magnesium levels of women who were in menopausal period and who were not in menopausal period.

In most of the studies made, lithium was found to be related with sex hormones and affected these hormones. It was found that lithium therapy cause induced proliferative and morphogenetic changes induced by estradiol in the uterus. In another study, it was mentioned that lithium antagonizes the effects of estrogen [23]. Therefore, it is expected that women in menopausal period have low lithium levels. In this study, we obtained the data supporting this view and when serum mineral levels of women in menopausal period were compared with those who were not in menopausal period, it was observed that serum lithium level (p<0.0001) of women in pre-menopausal period was much lower than all other mineral levels. Therefore, findings of our study

indicate that finding serum lithium levels to be much lower in subjects in the menopausal period compared to those who are not in menopausal period is an indicator for the possibility of using lithium to antagonize the effects of estrogen encountered in osteoporosis and thus lithium can be used as an effective therapeutic agent.

As a result, in this study, together with hormonal changes in menopause, changes are observed in the mineral levels and lithium level was found to be considerably lower in women in menopausal period. Along with this, Vitamin D level was also found to be lower and all these were risk factors for osteoporosis. However, this also indicated that lipid profile alone would not play a role. Lithium deficiency was found to be related with menopause, and in relation with this, with osteoporosis. These results indicate that lithium therapy can be considered as an effective alternative method for treatment of menopause and of osteoporosis related with menopause which is a very risky period for women as they become prone to various diseases in this period.

ACKNOWLEDGMENTS

REFERENCES

1. Marslı M S. Whitehead MI. Management of the Menopause, Bulletin, 1992, 487.426. URL: http://bmb.oxfordjournals.org/content/48/2/426.short

2. Black DM, Rosen CF. Postmenopausal Osteoporosis. N Engl J Med 2016 Jan;374:254-262. DOI: 10.1056/NEJMcp1513724

3. Civitelli R, Agnusdei D, Nardi P, Zacchei F, Avioli LV, Gennari C. Effects of one-year treatment with estrogens on bone mass, intestinal calcium absorption, and 25-hydroxyvitamin D-1 alpha-hydroxylase reserve in postmenopausal osteoporosis. Calcif Tissue Int. 1988 Feb;42(2):77-86. URL: http://www.ncbi.nlm.nih.gov/pubmed/3127028

4. Valquiria A. Coronado Dorce, Joao Palermo-Neto, Lithium Effects on Estrogen-Induced Supersensitivity in Rats, Brain Research Bulletin, 1992 Aug;29(2):239-241. URL: http://www.ncbi.nlm.nih.gov/pubmed/1525677.

5. Wagner E R, Zhu G, Zhang B-Q, Luo Q, Shi Q, Huang E, Gao Y, Gao J L, Kim S H, Rastegar F, Yang K, He B C, Chen L, Zuo G W, Bi Y, Su Y, Luo J, Luo X, Huang J, Deng Z L, Reid R R, Luu H H, Haydon R C, He T C. The Therapeutic Potential of the wnt Signaling Pathway in Bone Disorders, Current Mol. Pharm. 2011 Ju;4(1):14-25.URL: http://www.ncbi.nlm.nih.gov/pubmed/20825362

6. Swiecicka A, Malige M. Lithium-Induced Hypercalcemia and Parathyroid Dysfunction, *Endocrine Abstracts*. 2010; 21: P90. URL: http://www.endocrine-abstracts.org/ea/0021/ea0021p90.htm

7. Thase M E, Sachs G S. Bipolar depression: pharmacotherapy and related therapeutic strategies, Biol. Psychiatry. 2000 Sep: 48(6):558-572.URL: http://www.ncbi.nlm.nih.gov/pubmed/11018227.

8. Da Silva C.M. L., V.G.K. Almeida, R.J. Casella, Determination of lithium in pharmaceutical formulations used in the treatment of bipolar disorder by flow injection analysis with spectrophotometric detection. Talanta. 2007 Nov; 73(4): 613-620. DOI: 10.1016/j.talanta.2007.04.019.

9. Begic Z, Balic D, Rizvanovic M. The Association Between Lipid Profile and Bone Density in Postmenopausal Women. Med Arh. 2012;66(6):378-381. URL: http://www.ncbi.nlm.nih.gov/pubmed/23409515.

10. Santoro N, Epperson CN, Mathews SB. Menopausal Symptoms and Their Management. Endocrinol Metab Clin North Am. 2015 Sep;44(3):497–515. DOI: 10.1016/j.ecl.2015.05.001

11. Parhami F, Garfinkel A, Demer LL. Role of lipids in osteoporosis. Arterioscler Thromb Vasc Biol. 2000 Nov;20(11):2346-8.URL: http://www.ncbi.nlm.nih.gov/pubmed/11073836.

12. Saha KR, Rahman MM, Paul AR, Das S, Haque S, Jafrin W, Mia AR. Changes in lipid profile of postmenopausal women. Mymensingh Med J. 2013 Oct;22(4):706-11. URL: http://www.ncbi.nlm.nih.gov/pubmed/24292300.

13. Parhami F, Jackson SM, Tintut Y, Le V, Balucan JP, Territo MC, Demer LL. Atherogenic diet and minimally oxidized low-density lipoprotein inhibit osteogenic and promote adipogenic differentiation of marrow stromal cells. J. Bone Miner Res. 1999;14:2067-2078. DOI: 10.1359/jbmr.1999.14.12.2067.

14. Parhami F, Tintut Y, Beamer WG, Gharavi N, Goodman W, Demer LL. Atherogenic high fat diet reduces bone mineralization in mice. J Bone Miner Res. 2001;16:182-188. DOI: 10.1359/jbmr.2001.16.1.182.

15. Crilly RG, Jones MM, Horsman A, Nordin BE, Rise in plasma alkaline phosphatase at the menopause. Clin Sci (Lond). 1980 Apr;58(4):341-2. URL: http://www.ncbi.nlm.nih.gov/pubmed/7379460.

16. Sunyecz JA, The use of calcium and vitamin D in the management of osteoporosis. Ther Clin Risk Manag. 2008 Aug;4(4):827–836.URL: http://www.ncbi.nlm.nih.gov/pmc/articles/PMC2621390/

17. McLaren-Howard J, Grant ECG, Davies S. Hormone Replacement Therapy and Osteoporosis: Bone Enzymes and Nutrient Imbalances. J Nutr Environ Med. 1998 Jul;8:129-138. DOI: 10.1080/13590849862168.

18. Heaney RP. Phosphorus Nutrition and the Treatment of Osteoporosis. 2004 Jan;79(1):91–97. DOI: 10.4065/79.1.91

19. McLaren-Howard J, Grant ECG, Davies S. Hormone Replacement Therapy and Osteoporosis: Bone Enzymes and Nutrient Imbalances. J Nutr Environ Med, 1998 Jul;8:129-138. DOI. 10.1080/13590849862168.

20. Takeda E, Yamamoto H, Yamanaka-Okumura H, Taketani Y. Dietary phosphorus in bone health and quality of life. Nutr Rev. 2012 Jun;70(6):311-21. DOI: 10.1111/j.1753-4887.2012.00473.x.

21. Osredkar J, Sustar N. Copper and Zinc, Biological Role and Significance of Copper/Zinc Imbalance. Journal of Clinical Toxicology. 201 Dec;S3:001. doi:10.4172/2161- 0495.S3-001. URL: http://www.omicsonline.org/copper-and-zinc-biological-role-and-significance-of-copper-zincimbalance-2161-0495.S3-001.php?aid=3055

22. Mutlu M, Argun M, Kilic E, Saraymen R, Yazar S. Magnesium, zinc and copper status in osteoporotic, osteopenic and normal post-menopausal women. J Int Med Res 2007;35:692-5. DOI: 10.11138/ccmbm/2015.12.1.018

23. Valquiria A. Coronado Dorce, Joao Palermo-Neto, Lithium Effects on Estrogen-Induced Supersensitivity in Rats, Brain Research Bulletin, 1992, 29 (2): 239-241. DOI:10.1016/0361-9230(92)90032-S.

Türkçe Öz ve Anahtar Kelimeler

Menopoz Öncesi ve Sonrası Kadınlarda Serum Lityum Seviyeleri, Kemik Metabolizması ve Bazı Biyokimyasal Parametreler Arasındaki İlişkiler

Ruken Esra Demirdogen, Fatih Mehmet Emen, Derya Kilic, Gokturk Avsar, Tuncay Yesilkaynak, Tunay Askar

Öz: Bu çalışmanın hedefi, premenopozal ve postmenopozal kadınlarda serum Li seviyesinin kemik metabolizması (Ca, P, Parathormon ve D vitamini), cinsiyet ve metabolik hormonlar (estrojen, FSH, LH ve TSH) ve bazı biyokimyasal parametrelerin arasındaki ilişkiyi belirlemektir. Çalışma 10 kadın üzerinde yürütülmüştür, bunlardan 5'i menopoz öncesi periyotta bulunmaktadır. Serum Li seviyeleri, kemik metabolizması göstergeleri (örneğin ALP, Ca, P, Mg, Cu, Zn) ve serum trigliserit, alkalen fosfataz, total kolesterol, HDL, LDL ve kolesterol seviyeleri gibi bazı biyokimyasal parametreler belirlenmiştir. Menopoz periyodunda bulunan kadınların estrojen kan seviyeleri pre-menopozal periyottaki kadınlara göre daha düşük çıkmıştır (p < 0,01) ve FSH seviyeleri ise daha yüksek bulunmuştur (p < 0,01). Lipid profilinde, menopoz sonrası dönemdeki trigliserit seviyeleri düşük çıkmıştır (p < 0,05) ve HDL (p < 0,001), LDL (p < 0,001) ve kolesterol seviyeleri ise yüksekir (p < 0,001). Alkalen fosfataz (p < 0,001) ve D vitamini seviyeleri (p < 0,001) azalmaktadır. Mineral seviyeleri incelendiğinde, serumdaki magnezyum ve bakır seviyelerinde anlamlı bir değişme gözlenmezken çinko (p < 0,01) ve fosfor (p < 0,005) seviyelerinin yükseldiği, kalsiyum seviyelerinin (p < 0,05) azaldığı ve Li seviyelerinin de ciddi biçimde azaldığı (p < 0,0001) görülmüştür. Elde edilen sonuçlara göre, ilk kez Li azlığının menopoz ve bununla ilgili hastalıklarla ilişkili olabileceği ve bu sebeple Li terapisinin alternatif bir yöntem olmak üzere menopoz için yeni tedavi protokollerinin geliştirilmesinde kullanılabileceği bulunmuştur.

Anahtar kelimeler: Kemik metabolizması; menopoz; osteoporoz; serum Li düzeyi.

Sunulma: 05 Temmuz 2016. **Kabul:** 25 Ağustos 2016.

(This article was presented to the 28th National Chemistry Congress and submitted to JOTCSA as a full manuscript)

Nitroaromatic Compound Sensing Application of Hexa-Armed Dansyl End-Capped Poly(ε-Caprolactone) Star Polymer With Phosphazene Core

Merve Dandan Doganci[1]*, Sümeyra Bayir[2], Erdinc Doganci[1], Mesut Gorur[3], Faruk Yilmaz[2]*

[1]*Department of Chemistry and Chemical Processing Tech., Kocaeli University, Kocaeli, Turkey*
[2]*Department of Chemistry, Gebze Technical University, Kocaeli, Turkey*

[3]*Department of Chemistry, Istanbul Medeniyet University, Istanbul, Turkey*

Abstract: Hexa-armed dansyl end-capped poly(ε-caprolactone) star polymer with phosphazene core (**N_3P_3-(PCL-Dansyl)$_6$**) was prepared in a two-step synthetic procedure including ring opening polymerization (ROP) of ε-caprolactone (ε-CL) and esterification reactions. The obtained fluorescence-active polymer was employed as a fluorescent probe towards certain nitroaromatic compounds (2,4,6-trinitrotoluene (TNT), 2,4-dinitrotoluene, 2,6-dinitrotoluene, 2-nitrotoluene, 3-nitrotoluene, 2,4,6-trinitrophenol (picric acid), 2,4-dinitrophenol, 4-nitrophenol, and 1,2-dinitrobenzene). Fluorescence intensity of **N_3P_3-(PCL-Dansyl)$_6$** was decreased gradually upon the addition of nitroaromatic compounds and the highest quenching efficiency was found to be 100% with TNT. Besides, **N_3P_3-(PCL-Dansyl)$_6$** gave exceptionally selective response toward nitroaromatic compounds, even in the presence of toxic metal cations such as Pb^{2+}, Co^{2+}, Hg^{2+}, Mn^{2+}, Cd^{2+} and Zn^{2+}.

INTRODUCTION

Nitroaromatics are organic molecules which contain one or more nitro groups (NO_2) attached to the aromatic ring. These compounds are registered as environmentally hazardous materials by U.S. Environmental Protection Agency [1, 2]. Among them, 2,4,6-trinitrotoluene (TNT) and nitrophenols, such as 4-nitrophenol (4-NP), and picric acid (2,4,6-trinitrophenol, PA), are important pollution sources. TNT is best known as an explosive material for military and terrorist activities, industrial, and mining applications [3-5]. When it enters the environment, a small amount of it is enough to cause health problems such as headaches, anemia, and skin irritation. Picric acid is another explosive material which is even stronger than TNT. Since it is highly soluble in water, it can easily contaminate water and environment [6]. Meanwhile, 4-NP is one of the highly hazardous and toxic phenols which are used in the production of various analgesics, pesticides, dyes and processing of leather [2]. Besides their toxicities to humans, animals, and plants, and they give an undesirable taste and odor to drinking water, even in very low concentration [7-9]. Decontamination of wastewaters from these pollutants is very difficult since they are usually resistant to microbial degradation [9, 10]. Therefore, accurate, rapid and selective detection of nitroaromatics is very crucial in many areas, such as environmental science, public security, and forensics.

Different methods have been reported for detection of trace amounts of nitroaromatic compounds [9-13]. Among them, fluorescence spectroscopic method has many advantages related to sensitivity, selectivity, and response time [11-14]. Therefore, fluorescence chemosensors were used for the detection of various analytes such as cations, anions, nitroaromatics, biological entities, *etc*. [15-18]. Dansyl-based polymers have been employed as fluorescent probes due to strong fluorescence and relatively long emission wavelength of dansyl unit in the visible region as well as its structural flexibility for derivatization [18-21]. Gorur *et al*. synthesized hexa-armed dansyl end-functional poly(ε-caprolactone) (PCL) star polymer with phosphazene core for the selective fluorescence detection of Pb^{2+} cation [18]. Murariu *et al.* prepared optically active dansyl-labeled copolyacrylates for sensitive and selective detection of transition metal ions. They showed that the dansyl side-functional copolymers selectively responded the presence of Fe^{2+} cations [22]. Dansyl-containing polymers were mainly used for the fluorescent detection of ionic species. They were rarely used as fluorescence probes against nitroaromatic compounds. Buruiana *et al.* synthesized two acrylic copolymers containing dansyl groups by free radical polymerization to be used in fluorescence detection of Cu^{2+}, Fe^{2+}, Ni^{2+} metal ions as well as some of nitroaromatic compounds (picric acid, p-nitrotoluene, nitrobenzene, *etc*.) in organic medium. They concluded that the fluorescence

emission of the polymer films were quenched by nitrobenzene vapors and the nitroaromatic compounds had a higher degree of fluorescence quenching [23]. To the best of our knowledge, there is no other report in the literature that uses dansyl-based fluorescent polymers for detection of nitroaromatic compounds.

Star- shaped polymers consist of several linear chains connected to a central core and have many advantages due to their compact molecular shapes, highly branched structures and unique rheological properties [24-34]. They are highly soluble in organic solvents, have smaller hydrodynamic volume and radius of gyration, resulting in their lower solution and melt viscosities with respect to linear polymers with similar molecular weights [32]. Besides, star polymers demonstrate less chain entanglements than the linear ones [27, 32]. There are two main approaches to synthesize star polymers: divergent (core-first) and convergent (arm-first). In the divergent method, the polymerization starts from multifunctional initiators and the number of arms of the star polymer is determined by the number of initiating functional groups on the initiator [26, 28-32]. On the other hand, the convergent method requires the preparation of polymer arms with suitable functional groups and followed by a coupling or terminating reaction with a multifunctional core compound [26, 30, 33, 34].

In one of our previous studies, we prepared dansyl end-functional PCL star polymer with a phosphazene core (N_3P_3-(PCL-Dansyl)$_6$, see Scheme 1) via ring opening polymerization (ROP) of ε-caprolactone (ε-CL) and esterification reactions. Then, N_3P_3-(PCL-Dansyl)$_6$ was used as fluorescent chemical probe for the detection of transition metal cations [18]. In this report, the same star polymer was employed as fluorescent chemical sensing agent for the determination of nitroaromatic compounds. Chemical structures of the obtained polymers were confirmed by FTIR and ^{1}H-NMR spectroscopic techniques.
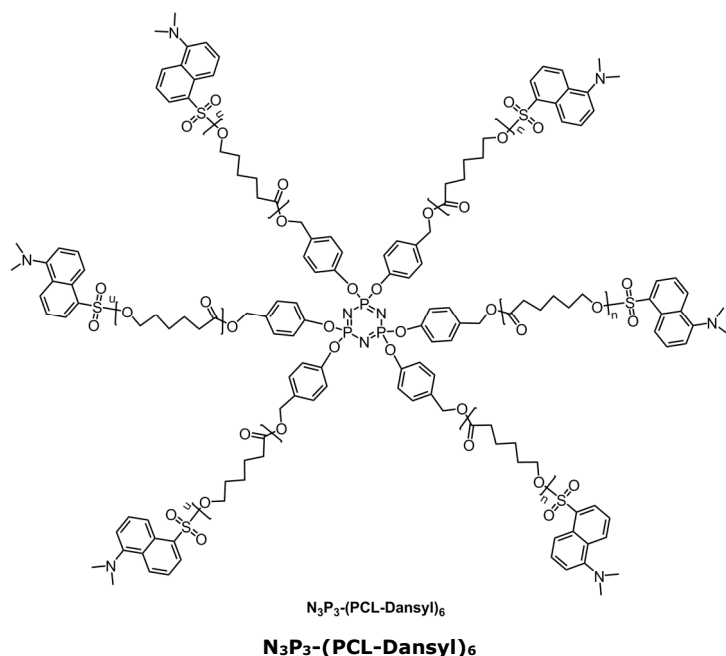
N₃P₃-(PCL-Dansyl)₆

Scheme 1: Hexa-armed dansyl end-capped poly(ε-caprolactone) star polymer with phosphazene core (**N₃P₃-(PCL-Dansyl)₆**).

MATERIALS AND METHODS

Materials. All chemicals used were of analytical grade or of the highest purity available. 2,4,6-trinitrotoluene (1 mg/mL TNT solution), 2,4-dinitrotoluene (2,4-DNT, 97%), 2,6-dinitrotoluene (2,6-DNT, 98%), 2-nitrotoluene (2-NT, ≥99%), 3-nitrotoluene (3-NT, 99%), 2,4,6-trinitrophenol (picric acid, PA, ≥98%), 2,4-dinitrophenol (2,4-DNP, ≥98%), 4-nitrophenol (4-NP, ≥99%), 1,2-dinitrobenzene (1,2-DNB, ≥99%) were all purchased from Sigma-Aldrich. The molecular structures of nitroaromatic compounds used in the present study are given in Scheme 2. Tetrahydrofuran (THF) used as solvent was purchased from Sigma-Aldrich.

Instrumentation. ¹H- and ³¹P-NMR, FTIR spectroscopy techniques were used for characterization of the synthesized polymer. ¹H and ³¹P-NMR spectra were measured on a Varian ᵁᴺᴵᵀʸ INOVA 500 MHz (202 MHz for ³¹P) spectrometer in CDCl₃ and d₆-DMSO solutions at 25 ºC. ATR-FTIR spectra were obtained on Perkin-Elmer Spectrum Two™ spectrometer equipped with Perkin Elmer UATR Two diamond ATR accessory and the results were uncorrected. The molecular weight of the polymers was characterized by

Agilent 1260 Infinity GPC/SEC Instruments. Thermal properties of the obtained polymers were analyzed by Perkin Elmer DSC 8500 double-furnace differential scanning calorimeter and Perkin Elmer STA 6000 simultaneous thermal analyzer, respectively. UV-Vis and fluorescence spectra were measured using quartz cuvettes (1 cm path length) on Shimadzu UV-2600 and Agilent Cary Eclipse spectrophotometers, respectively.

Synthesis of dansyl end-capped poly(ε-caprolactone) star polymer with phosphazene core (N$_3$P$_3$-(PCL-Dansyl)$_6$). **N$_3$P$_3$-(PCL-Dansyl)$_6$** was prepared according to the method reported in the literature [18]. Details are given in Supporting Information.

Nitroaromatic sensing applications of dansyl end-capped PCL star polymer via fluorescence spectroscopy. Nitroaromatic sensing applications of **N$_3$P$_3$-(PCL-Dansyl)$_6$** were performed via fluorescence spectroscopy. Fluorescence emission spectra were obtained with Agilent Cary Eclipse spectrophotometers with an excitation wavelength 328 nm in THF solutions. Firstly, definite amounts of **N$_3$P$_3$-(PCL-Dansyl)$_6$** were dissolved in THF at room temperature. Then, the fluorescent responses of star PCL polymer upon the addition of prescribed amount of targeted nitroaromatics were measured.

RESULTS AND DISCUSSION

The dansyl end-capped PCL star polymer with phosphazene core (**N$_3$P$_3$-(PCL-Dansyl)$_6$**) was successfully synthesized in a two-step synthetic procedure reported in the literature (see Supporting Information for the detailed description) [18]. The dansyl fluorophore had strong fluorescence emission in the visible region with high quantum yields [18, 35]. It consists of two main parts in its molecular structure. Dimethylamino moiety works as the electron donor while sulfonic acid group acts as the acceptor. Because of these characteristics, dansyl fluorophore was widely used as fluorescent probe for the detection of various materials [18-22] or as a label for bio-imaging [36, 37].
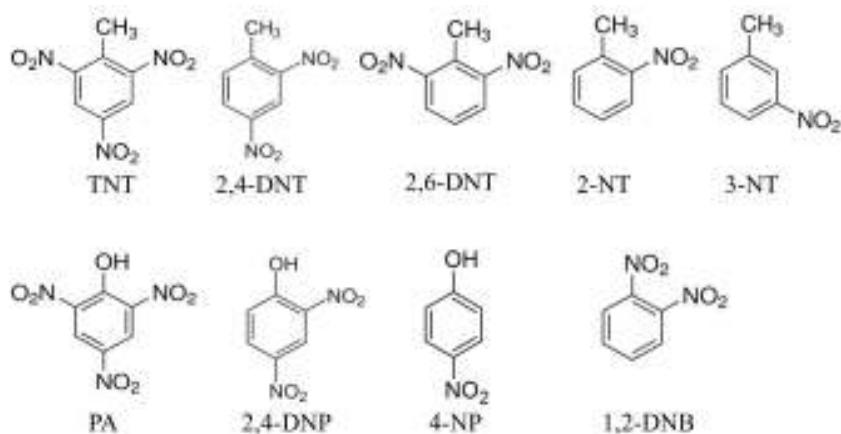
Scheme 2. The molecular structures of nitroaromatic compounds used in the present study.

The binding behavior and recognition characteristics of the dansyl end-capped PCL star polymer toward several nitroaromatic compounds were determined via fluorescence spectrophotometric measurements using 1-cm path length cuvettes. The solutions were prepared fresh in THF solution and the analysis performed at 328 nm excitation wavelengths at room temperature. The fluorescence emission spectra of dansyl end-capped PCL star polymer with phosphazene core upon addition of 50 equivalent of nitroaromatic compounds are given in Figure 1. It can be seen from the figure that all nitroaromatic compounds in this study quenched fluorescence emission of dansyl fluorophore efficiently. The highest quenching efficiency was observed for TNT and 4-NP. The photographs of the 1.27×10^{-5} M bare **N$_3$P$_3$-(PCL-Dansyl)$_6$** solutions and with 50 equivalent of 4-NP, 2,4-DNP, PA, and TNT under daylight and UV-light (λ_{ext}-365 nm) were given in Figure 2. As seen in the figure, upon the addition of 50 equivalent of TNT, fluorescence emission of the dansyl unit were quenched completely.
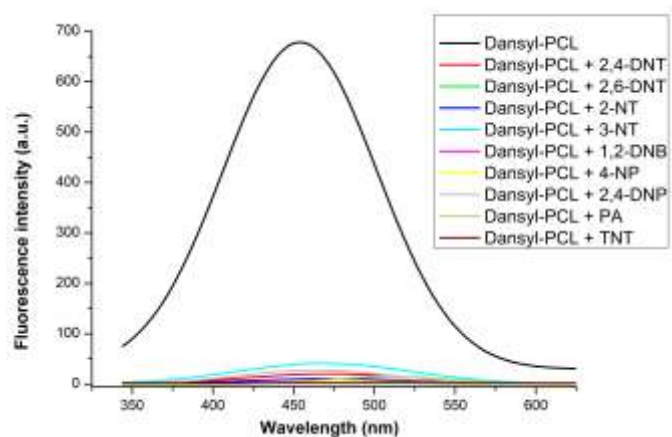
Figure 1. The fluorescent emission spectra (λ_{ex}= 328 nm) of **N$_3$P$_3$-(PCL-Dansyl)$_6$** (1.27×10^{-5} M) in THF upon addition of 50 eq. of different nitroaromatic compounds.
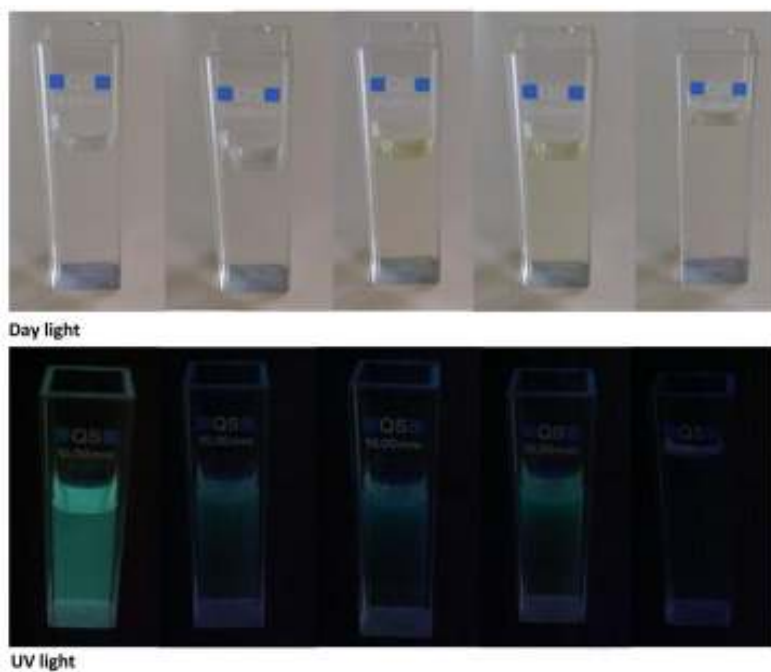
Figure 2. Photograph of **N$_3$P$_3$-(PCL-Dansyl)$_6$** (1.27×10^{-5} M) with 50 eq of 4-NP, 2,4-DNP, PA, and TNT (from left to right) under day light and UV light (λ_{ext}-365 nm).

The evolution of fluorescence emission spectra of dansyl end-capped PCL upon titration with 4-NP at different equivalent ratios are given in Figure 3. The fluorescence intensity was found to decrease significantly as a function of concentration.
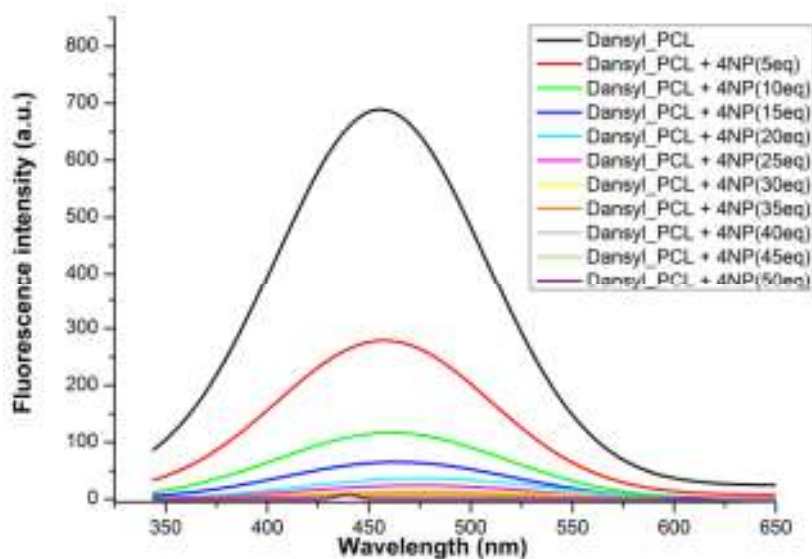
Figure 3. Fluorescence emission spectra of **N₃P₃-(PCL-Dansyl)₆** (1.27×10^{-5} M) in THF in the presence of 4-NP at 5, 10, 15, 20, 25, 30, 35, 40, 45, and 50 equivalent ratios.

Quenching efficiency ratios (QE) were calculated using equation 1:

$$QE = \left(\frac{(I_0 - I)}{I_0}\right) x 100$$ (Eq. 1)

where, I_o is the fluorescence intensity without nitroaromatic compounds and I is the fluorescence intensity observed in the presence of the nitroaromatic compounds. The highest quenching efficiency was obtained for TNT as 100% and for 4-NP as 99.37%. It can be said that nitrophenols had high quenching values. The sensing performance was found to be selective toward nitroaromatic compounds, even in the presence of toxic metal cations such as Pb^{2+}, Co^{2+}, Hg^{2+}, Mn^{2+}, Cd^{2+} and Zn^{2+} as seen from Figure 4.
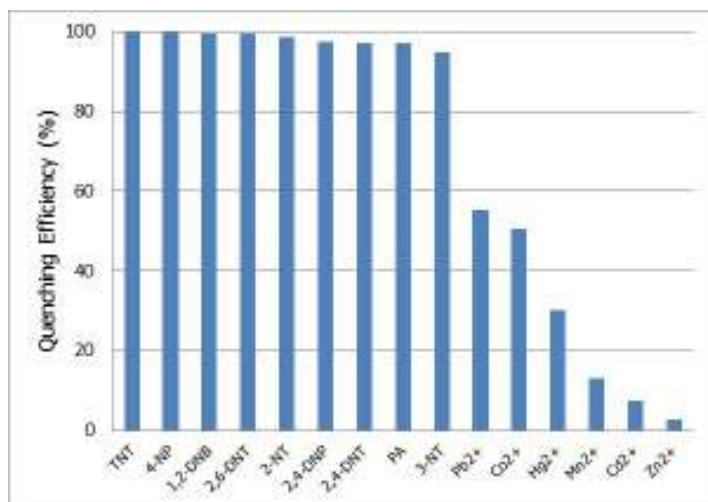
Figure 4. Quenching efficiency ratios for fluorescent emission intensities of **N₃P₃-(PCL-Dansyl)₆** upon addition of 50 eq. nitroaromatic compounds and metal cations.

CONCLUSION

The dansyl end-capped poly(ε-caprolactone) star polymer with phosphazene core (**N₃P₃-(PCL-Dansyl)₆**) could serve as an alternative nitroaromatic compund sensor due to the strong sensitivity, selectivity, and synthetic simplicity. The fluorescent intensity of **N₃P₃-(PCL-Dansyl)₆** was decreased gradually upon the addition of nitroaromatic compounds and the highest quenching efficiency was found to be 100% with TNT. The sensing performance was found to be selective toward nitroaromatic compounds, even in the presence of toxic metal cations such as Pb^{2+}, Co^{2+}, Hg^{2+}, Mn^{2+}, Cd^{2+} and Zn^{2+}.

REFERENCES

[1] Ju K-S, Parales RE. Nitroaromatic Compounds, from Synthesis to Biodegradation. Microbiology and Molecular Biology Reviews. 2010, 74 (2): 250-72. DOI: 10.1128/mmbr.00006-10.

[2] Yang X, Wang J, Su D, Xia Q, Chai F, Wang C, Qu F. Fluorescent detection of TNT and 4-nitrophenol by BSA Au nanoclusters. Dalton Transactions. 2014, 43 (26): 10057-63. DOI: 10.1039/C4DT00490F.

[3] Dasary SSR, Senapati D, Singh AK, Anjaneyulu Y, Yu H, Ray PC. Highly Sensitive and Selective Dynamic Light-Scattering Assay for TNT Detection Using p-ATP Attached Gold Nanoparticle. ACS Applied Materials & Interfaces. 2010, 2 (12): 3455-60. DOI: 10.1021/am1005139.

[4] Shanmugaraju S, Joshi SA, Mukherjee PS. Fluorescence and visual sensing of nitroaromatic explosives using electron rich discrete fluorophores. Journal of Materials Chemistry. 2011, 21 (25): 9130-8. DOI: 10.1039/C1JM10406C.

[5] Agency for Toxic Substances and Disease Registry (ATSDR). 1995. Toxicological profile for 2,4,6-Trinitrotoluene (TNT). Atlanta, GA: U.S. Department of Health and Human Services, Public Health Service.

[6] Roy B, Bar AK, Gole B, Mukherjee PS. Fluorescent Tris-Imidazolium Sensors for Picric Acid Explosive. The Journal of Organic Chemistry. 2013, 78 (3): 1306-10. DOI: 10.1021/jo302585a.

[7] Niaz A, Fischer J, Barek J, Yosypchuk B, Sirajuddin, Bhanger MI. Voltammetric Determination of 4-Nitrophenol Using a Novel Type of Silver Amalgam Paste Electrode. Electroanalysis. 2009, 21 (16): 1786-91. DOI: 10.1002/elan.200904622.

[8] Pedrosa VdA, Codognoto L, Avaca LA. Electroanalytical determination of 4-nitrophenol by square wave voltammetry on diamond electrodes. Journal of the Brazilian Chemical Society. 2003, 14: 530-5.

[9] Hu S, Xu C, Wang G, Cui D. Voltammetric determination of 4-nitrophenol at a sodium montmorillonite-anthraquinone chemically modified glassy carbon electrode. Talanta. 2001, 54 (1): 115-23. DOI: http://dx.doi.org/10.1016/S0039-9140(00)00658-5.

[10] Lipczynska-Kochany E. Degradation of aqueous nitrophenols and nitrobenzene by means of the Fenton reaction. Chemosphere. 1991, 22 (5): 529-36. DOI: http://dx.doi.org/10.1016/0045-6535(91)90064-K.

[11] Alizadeh T, Ganjali MR, Norouzi P, Zare M, Zeraatkar A. A novel high selective and sensitive para-nitrophenol voltammetric sensor, based on a molecularly imprinted polymer–carbon paste electrode. Talanta. 2009, 79 (5): 1197-203. DOI: http://dx.doi.org/10.1016/j.talanta.2009.02.051.

[12] Chen J-C, Shih J-L, Liu C-H, Kuo M-Y, Zen J-M. Disposable Electrochemical Sensor for Determination of Nitroaromatic Compounds by a Single-Run Approach. Analytical Chemistry. 2006, 78 (11): 3752-7. DOI: 10.1021/ac060002n.

[13] Nie H, Zhao Y, Zhang M, Ma Y, Baumgarten M, Mullen K. Detection of TNT explosives with a new fluorescent conjugated polycarbazole polymer. Chemical Communications. 2011, 47 (4): 1234-6. DOI: 10.1039/C0CC03659E.

[14] Sun X, Wang Y, Lei Y. Fluorescence based explosive detection: from mechanisms to sensory materials. Chemical Society Reviews. 2015, 44 (22): 8019-61. DOI: 10.1039/C5CS00496A.

[15] Ojida A, Takashima I, Kohira T, Nonaka H, Hamachi I. Turn-On Fluorescence Sensing of Nucleoside Polyphosphates Using a Xanthene-Based Zn(II) Complex Chemosensor. Journal of the American Chemical Society. 2008, 130 (36): 12095-101. DOI: 10.1021/ja803262w.

[16] Li D, Li H, Liu M, Chen J, Ding J, Huang X, Wu H. A Novel D-π-A Conjugated Polymer Chemosensor Based on Benzo[c][1,2,5]selenadiazole for Highly Selective and Sensitive Recognition of Mercury (II) Ions. Macromolecular Chemistry and Physics. 2014, 215 (1): 82-9. DOI: 10.1002/macp.201300542.

[17] Liu Y, Miao Q, Zhang S, Huang X, Zheng L, Cheng Y. A Fluorescent Chemosensor for Transition-Metal Ions Based on Optically Active Polybinaphthyl and 2,2'-Bipyridine. Macromolecular Chemistry and Physics. 2008, 209 (7): 685-94. DOI: 10.1002/macp.200700460.

[18] Gorur M, Doganci E, Yilmaz F, Isci U. Synthesis, characterization, and Pb2+ ion sensing application of hexa-armed dansyl end-capped poly(ε-caprolactone) star polymer with phosphazene core. Journal of Applied Polymer Science. 2015, 132 (32): n/a-n/a. DOI: 10.1002/app.42380.

[19] Silva AJC, Silva Jr JG, Alves Jr S, Tonholo J, Ribeiro AS. Dansyl-based fluorescent films prepared by chemical and electrochemical methods: cyclic voltammetry, afm and spectrofluorimetry characterization. Journal of the Brazilian Chemical Society. 2011, 22: 1808-15.

[20] Wanichacheva N, Watpathomsub S, Lee VS, Grudpan K. Synthesis of a Novel Fluorescent Sensor Bearing Dansyl Fluorophores for the Highly Selective Detection of Mercury (II) Ions. Molecules. 2010, 15 (3): 1798.

[21] Wanichacheva N, Kumsorn P, Sangsuwan R, Kamkaew A, Lee VS, Grudpan K. A new fluorescent sensor bearing three dansyl fluorophores for highly sensitive and selective detection of mercury(II) ions. Tetrahedron Letters. 2011, 52 (46): 6133-6. DOI: http://dx.doi.org/10.1016/j.tetlet.2011.09.033.

[22] Murariu M, Buruiana EC. Synthesis and characterization of new optically active poly(acrylamide/methacrylurea-co-vinyl acetate) copolymers with dansyl units. Designed Monomers and Polymers. 2015, 18 (2): 118-28. DOI: 10.1080/15685551.2014.971391.

[23] Buruiana EC, Chibac AL, Buruiana T. Polyacrylates containing dansyl semicarbazide units sensitive for some structures in solution and film. Journal of Photochemistry and Photobiology A: Chemistry. 2010, 213 (2–3): 107-13. DOI: http://dx.doi.org/10.1016/j.jphotochem.2010.05.008.

[24] Hadjichristidis N. Synthesis of miktoarm star (μ-star) polymers. Journal of Polymer Science Part A: Polymer Chemistry. 1999, 37 (7): 857-71. DOI: 10.1002/(SICI)1099-0518(19990401)37:7<857::AID-POLA1>3.0.CO;2-P.

[25] Lapienis G. Star-shaped polymers having PEO arms. Progress in Polymer Science. 2009, 34 (9): 852-92. DOI: http://dx.doi.org/10.1016/j.progpolymsci.2009.04.006.

[26] Ren JM, McKenzie TG, Fu Q, Wong EHH, Xu J, An Z, Shanmugam S, Davis TP, Boyer C, Qiao GG. Star Polymers. Chemical Reviews. 2016, 116 (12): 6743-836. DOI: 10.1021/acs.chemrev.6b00008.

[27] Aydin M, Uyar T, Tasdelen MA, Yagci Y. Polymer/clay nanocomposites through multiple hydrogen-bonding interactions. Journal of Polymer Science Part A: Polymer Chemistry. 2015, 53 (5): 650-8. DOI: 10.1002/pola.27487.

[28] Gorur M, Yilmaz F, Kilic A, Demirci A, Ozdemir Y, Kosemen A, Eren San S. Synthesis, characterization, electrochromic properties, and electrochromic device application of a novel star polymer consisting of thiophene end-capped poly(ε-caprolactone) arms emanating from a hexafunctional cyclotriphosphazene core. Journal of Polymer Science Part A: Polymer Chemistry. 2010, 48 (16): 3668-82. DOI: 10.1002/pola.24151.

[29] Gorur M, Yilmaz F, Kilic A, Sahin ZM, Demirci A. Synthesis of pyrene end-capped A6 dendrimer and star polymer with phosphazene core via "click chemistry". Journal of Polymer Science Part A: Polymer Chemistry. 2011, 49 (14): 3193-206. DOI: 10.1002/pola.24756.

[30] Doganci E, Gorur M, Uyanik C, Yilmaz F. Synthesis of AB3-type miktoarm star polymers with steroid core via a combination of "Click" chemistry and ring opening polymerization techniques. Journal of Polymer Science Part A: Polymer Chemistry. 2014, 52 (23): 3390-9. DOI: 10.1002/pola.27406.

[31] Doganci E, Tasdelen MA, Yilmaz F. Synthesis of Miktoarm Star-Shaped Polymers with POSS Core via a Combination of CuAAC Click Chemistry, ATRP, and ROP Techniques. Macromolecular Chemistry and Physics. 2015, 216 (17): 1823-30. DOI: 10.1002/macp.201500199.

[32] Eren O, Gorur M, Keskin B, Yilmaz F. Synthesis and characterization of ferrocene end-capped poly(ε-caprolactone)s by a combination of ring-opening polymerization and "click" chemistry techniques. Reactive and Functional Polymers. 2013, 73 (1): 244-53. DOI: http://dx.doi.org/10.1016/j.reactfunctpolym.2012.10.009.

[33] Wu Z-M, Liang H, Lu J, Deng W-L. Miktoarm star copolymers via combination of RAFT arm-first technique and aldehyde–aminooxy click reaction. Journal of Polymer Science Part A: Polymer Chemistry. 2010, 48 (15): 3323-30. DOI: 10.1002/pola.24116.

[34] Rele SM, Cui W, Wang L, Hou S, Barr-Zarse G, Tatton D, Gnanou Y, Esko JD, Chaikof EL. Dendrimer-like PEO Glycopolymers Exhibit Anti-Inflammatory Properties. Journal of the American Chemical Society. 2005, 127 (29): 10132-3. DOI: 10.1021/ja0511974.

[35] de Almeida AKA, Dias JMM, Silva AJC, Navarro M, Junior SA, Tonholo J, Ribeiro AS. Synthesis and characterization of a dansyl-based fluorescent conjugated polymer. Synthetic Metals. 2013, 171: 45-50. DOI: http://dx.doi.org/10.1016/j.synthmet.2013.03.015.

[36] Tang M, Huang J, Weng X, Yang L, Liu M, Zhou M, Wang X, Gao J, Yi W, Zeng W, Sun L, Cao Y. Evaluation of a dansyl-based amino acid DNSBA as an imaging probe for apoptosis detection. Apoptosis. 2015, 20 (3): 410-20. DOI: 10.1007/s10495-014-1075-z.

[37] Zeng W, Miao W, Kabalka G, Puil ML, Biggerstaff J, Townsend D. Design, synthesis, and biological evaluation of a dansyled amino acid derivative as an imaging agent for apoptosis. Tetrahedron Letters. 2008, 49 (45): 6429-32. DOI: http://dx.doi.org/10.1016/j.tetlet.2008.08.091.

Türkçe Özet ve Anahtar Kelimeler

Fosfazen Çekirdeği İçeren Altı Kollu Dansil Uçlu Poli(ε-Kaprolakton) Yıldız Polimerinin Nitroaromatik Bileşikleri Sensör Uygulaması

Merve Dandan Doganci, Sümeyra Bayir, Erdinc Doganci, Mesut Gorur, Faruk Yilmaz

Öz: Altı kollu, dansil uçlu ve fosfazen çekirdekli poli(ε-kaprolakton) yıldız polimeri (**N₃P₃-(PCL-Dansil)₆**) iki adımlı sentez prosedürü ile hazırlanmıştır. Yürütülen adımlar ε-kaprolaktonun (ε-CL) halka açılması ve esterleştirme tepkimelerini içermektedir. Elde edilen floresans aktif polimer belli nitroaromatik bileşiklerin (2,4,6-trinitrotoluen, TNT; 2,4-dinitrotoluen; 2,6-dinitrotoluen; 2-nitrotoluen; 3-nitrotoluen; 2,4,6-trinitrofenol, pikrik asit; 2,4-dinitrofenol; 4-nitrofenol ve 1,2-dinitrobenzen) sensöründe floresan prob olarak kullanılmıştır. **N₃P₃-(PCL-Dansil)₆** polimerinin floresans şiddeti nitroaromatik bileşiklerin ilavesiyle yavaş yavaş azalmaktadır ve en yüksek sönümleme etkinliği TNT ile %100 oranında sağlanmıştır. Bunun yanında, ortamda Pb^{2+}, Co^{2+}, Hg^{2+}, Mn^{2+}, Cd^{2+} ve Zn^{2+} gibi zehirli metal katyonları varlığında olduğu gibi, **N₃P₃-(PCL-Dansil)** nitroaromatik bileşiklere karşı da çok seçici tepki vermektedir.

Anahtar kelimeler: Nitroaromatik bileşikler; dansil fonksiyonlu yıldız polimer; floresans spektroskopisi.
Gönderilme: 22 Temmuz 2016. **Kabul:** 26 Ağustos 2016.

Synthesis of Novel Fluoroquinolone-Triazole Hybrid Compounds as Antimicrobial Agents

Serap Başoğlu Özdemir

Karadeniz Technical University, Department of Chemistry, 61080, Trabzon, Turkey

Abstract: The hydrazide compound (**2**) was synthesized starting from 1-(2-fluorophenyl)piperazine via two steps. The reaction of compound (**2**) with different alkyl(aryl)isothiocyanates afforded the corresponding compounds (**3a-c**)*.* 1,3-Thiazolidine derivatives (**4a-c**) were synthesized from the treatment of (**3a-c**) with ethyl bromoacetate. Mannich bases (**6a-d**) were synthesized with the treatment of (**5a-c)** with various suitable amines in the presence of formaldehyde. Compound (**3**) derivatives were converted to 1,2,4-triazole as the starting material of fluoroquinolone analogues (**11a-c**). Finally, synthesized compounds were examined their biological properties and some of these showed potent activity.

INTRODUCTION

Nowadays, bacterial strength towards used antibiotics has become a major worldwide problem [1]. Although new strategies have been developed for control and treatment of microbial infections, biological strength proceeds to be one of primary anxiety to the community welfare and academic society around the world. Due to the re-emergence of microbial threats with increased antibacterial resistance, high safety profile with novel and more active antibacterial agents are required [2]. 1,2,4-Triazole moiety is recognized to be a sophisticated molecule which is mainly used in the design of possible bioactive form. Its derived functions possess medicinal important activities [3-10]. Several drugs have fungicidal activity like fluconazole, consisting of 1,2,4-triazole nucleus [11].

Quinolones are mostly used in the fight against serious hospital-acquired and community-acquired infections. Therefore, quinolones became an important class of antibacterial agents [12]. These agents possess excellent safety profile, favorable pharmacokinetic characteristics, and broad antibacterial spectrum, respectively. In this way, they are well tolerated with against genitourinary infections and common respiratory tract pathogens [13].

Over the years, heterocyclic compounds have been attracted scientific attention because of their diverse biological activities [14]. Among them, 4-thiazolidinones are the derivatives of thiazole have been indicated to own a varied range of biological properties containing antitubercular, anti-inflammatory, antitumor, antihistaminic, antibacterial, and anticonvulsant activities [15]. In recent years, to overcome the drug resistance problem, the concept of hybrid molecules, which contain two or more pharmacophore groups binding together covalently in one molecular framework, has been introduced in the medicinal chemistry field. These compounds that are obtained by molecular hybridization of several pharmacophore groups, act by inhibiting two or more conventional targets simultaneously, and this multiple target strategy has resulted in the development of a number of bioactive hybrid molecules [1]. Mannich reaction involves condensation of a compound with active hydrogens with suitable amine and formaldehyde [16].

Mannich base functional group can increase the lipophilicity of essential amines and amides, which results in the increase of absorption through bio-membranes [17]. Lipophilic properties of fluoroquinolones affect their ability to cross bacterial membranes [18]. In light of these considerations, we reported here the synthesis and investigation of 1,2,4-triazoles fused fluoroquinolone or Mannich bases as hybrid molecules own biological properties.

MATERIALS AND METHODS

Chemistry

Used chemicals were purchased from Fluka Chemie AG Buchs (Switzerland). Melting points were measured in open capillaries on a Büchi B-540 device. Reactions were determined by thin-layer chromatography (TLC) on silica gel 60 F254 aluminum sheets. FT-IR spectra were recorded using a *Perkin Elmer* 1600 series FT IR spectrometer. ^{1}H NMR and ^{13}C NMR spectra were recorded in DMSO-d_6 on a *BRUKER AVENE II* 400 MHz (^{1}H) NMR Spectrometer. The chemical shifts are given in ppm relative to Me$_4$Si as an internal reference, *J* values are given in Hz. The elemental analysis was checked on *a Costech Elemental Combustion System* CHNS-O elemental device. All the compounds displayed C, H and N analysis within ±0.4% of the technical rates. The mass spectra were registered on a *Quattro GC-MS* (70 eV) apparatus. CEM Discovery monomode synthesis reactor was used for microwave synthesis.

EXPERIMENTAL SECTION

Ethyl [4-(2-fluorophenyl)piperazin-1-yl]acetate (1)

To the mixture of 1-(2-fluorophenyl)piperazine (10 mmol) and triethylamine (15 mmol) in dry tetrahydrofuran, ethyl bromoacetate (10 mmol) was added at 0–5 °C. Then, the reaction mixture was taken to room temperature and stirred for additional 24 h. The precipitated salt was removed by filtration and the solvent was evaporated. The oily mass was purified with ethyl acetate. Yield 97%, mp 36-38°C. ^{1}H NMR (DMSO-d_6, δ ppm): 1.20 (t, 3H, CH$_3$, *J*= 6.8 Hz), 2.68 (brs, 4H, 2CH$_2$), 3.01 (brs, 4H, 2CH$_2$), 3.40 (s, 2H, CH$_2$), 4.10 (q, 2H, CH$_2$, *J*= 7.2 Hz), 6.94-7.04 (m, 2H, arH), 7.05-7.13 (m, 2H, arH). ^{13}C NMR (DMSO-d_6, δ ppm): 14.57 (CH$_3$), 50.44 (CH$_2$), 50.47 (CH$_2$), 52.43 (2CH$_2$), 58.79 (CH$_2$), 60.33 (CH$_2$), arC: [116.23 and 116.44 (d, CH, *J*= 21.0 Hz), 119.67 and 119.70 (d, CH, *J*= 3.0 Hz), 122.70 and 122.78 (d, CH, *J*= 8.0 Hz), 125.22 and 125.26 (d, CH, *J*= 4.0 Hz), 140.24 and 140.32 (d, C, *J*= 8.0 Hz), 154.19 and 156.62 (d, C, J_{C-F}= 243.0 Hz)], 170.28 (C=O). FT IR (v_{max}, cm^{-1}): 3066 (Aromatic CH), 2982 (Aliphatic CH), 1745 (C=O). EI MS *m/z* (%): 267.01 ([M+1]$^+$, 40), 256.98 (55), 125.82 (100). Anal. Calcd. for C$_{14}$H$_{19}$FN$_2$O$_2$ (266.31); C, 63.14; H, 7.19; N, 10.52%. Found: C, 63.21; H, 7.08; N, 10.55%.

2-[4-(2-Fluorophenyl)piperazin-1-yl]acetohydrazide (2)

Hydrazine hydrate (2.5 mmol) was added to the solution of compound **1** (1 mmol) in ethanol and the mixture was irradiated in monomode microwave reactor in closed vessel at 125 °C for 20 min. After evaporation, a solid was obtained. This was purified with

ethyl acetate. Yield 95%, mp 84-86°C. ^{1}H NMR (DMSO-d_6, δ ppm): 2.58 (brs, 4H, 2CH$_2$), 3.01 (brs, 4H, 2CH$_2$), 3.68 (brs, 2H, CH$_2$), 4.25 (s, 2H, NH$_2$), 6.94-6.96 (m, 1H, arH), 7.02 (d, 1H, arH, J= 8.0 Hz), 7.07-7.13 (m, 2H, arH), 8.94 (s, 1H, NH). ^{13}C NMR (DMSO-d_6, δ ppm): 50.40 (CH$_2$), 50.43 (CH$_2$), 53.25 (2CH$_2$), 60.26 (CH$_2$), arC: [116.25 and 116.46 (d, CH, J= 21.0 Hz), 119.62 and 119.65 (d, CH, J= 3.0 Hz), 122.65 and 122.73 (d, CH, J= 8.0 Hz), 125.24 and 125.27 (d, CH, J= 3.0 Hz), 140.27 and 140.35 (d, C, J= 8.0 Hz), 154.17 and 156.60 (d, C, J_{C-F}= 243.0 Hz)], 168.63 (C=O). FT IR (v_{max}, cm^{-1}): 3256 and 3225 (NH$_2$), 3174 (NH), 3037 (Aromatic CH), 2819 (Aliphatic CH), 1692 (C=O). EI MS m/z (%): 252.80 ([M]$^+$, 60), 225.09 (32), 180.23 (100). Anal. Calcd for C$_{12}$H$_{17}$FN$_4$O (252.29); C, 57.13; H, 6.79; N, 22.21%. Found: C, 57.23; H, 6.69; N, 22.09%.

General procedure for preparation of compounds 3a–c

The corresponding alkyl(aryl)isothiocyanate (1 mmol) was added to the solution of compound **2** (1 mmol) in ethanol and the reaction was irradiated in monomode microwave reactor in closed vessel at 150°C for 10 min. After evaporation, a solid appeared. This solid was purified with acetone:diethyl ether (1:2 v/v).

2-{[4-(2-Fluorophenyl)piperazin-1-yl]acetyl}-*N*-phenylhydrazine carbothioamide (3a)

Yield: 80%, mp 183-185°C. ^{1}H NMR (DMSO-d_6, δ ppm): 2.68 (brs, 4H, 2CH$_2$), 3.05 (brs, 4H, 2CH$_2$), 3.14 (s, 2H, CH$_2$), 6.95-7.11 (m, 5H, arH), 7.12-7.35 (m, 2H, arH), 7.43 (brs, 2H, arH), 9.59 (brs, 2H, 2NH), 9.90 (brs, 1H, NH). ^{13}C NMR (DMSO-d_6, δ ppm): 50.42 (CH$_2$), 53.28 (2CH$_2$), 60.22 (2CH$_2$), arC: [116.28 and 116.48 (d, CH, J= 20.0 Hz), 119.69 (2CH), 122.68 and 122.76 (d, CH, J= 8.0 Hz), 125.30 (2CH), 128.60 (3CH), 140.36 (C), 140.94 and 141.03 (d, C, J= 9.0 Hz), 154.19 and 156.62 (d, C, J_{C-F}= 243.0 Hz)], 161.21 (C=O), 181.24 (C=S). FT IR (v_{max}, cm^{-1}): 3223 (2NH), 3120 (NH), 3065 (Aromatic CH), 2945 (Aliphatic CH), 1670 (C=O), 1237 (C=S). EI MS m/z (%): 410.45 ([M+Na]$^+$, 17), 401.23 (43), 321.00 (56), 126.90 (100). Anal. Calcd. for C$_{19}$H$_{22}$FN$_5$OS (387.47); C, 58.90; H, 5.72; N, 18.07%. Found: C, 58.70; H, 5.92; N, 18.37%.

N-ethyl-2-{[4-(2-fluorophenyl)piperazin-1-yl]acetyl}hydrazinecarbothioamide (3b)

Yield: 95%, mp 156-157°C. ^{1}H NMR (DMSO-d_6, δ ppm): 1.06 (t, 3H, CH$_3$, J= 8.0 Hz), 2.64 (brs, 4H, 2CH$_2$), 3.03 (brs, 4H, 2CH$_2$), 3.08 (s, 2H, CH$_2$), 3.44 (q, 2H, CH$_2$, J= 6.4 Hz), 6.93-7.08 (m, 1H, arH), 7.10-7.12 (m, 1H, arH), 7.14 (s, 2H, arH), 7.85 (s, 1H, NH), 9.13 (s, 1H, NH), 9.65 (brs, 1H, NH). ^{13}C NMR (DMSO-d_6, δ ppm): 14.91 (CH$_3$), 50.37 (CH$_2$), 50.39 (CH$_2$), 53.26 (2CH$_2$), 60.16 (2CH$_2$), arC: [116.26 and 116.47 (d, CH,

J= 21.0 Hz), 119.64 and 119.67 (d, CH, J= 3.0 Hz), 122.65 and 122.73 (d, CH, J= 8.0 Hz), 125.26 and 125.29 (d, CH, J= 3.0 Hz), 140.27 and 140.36 (d, C, J= 9.0 Hz), 154.19 and 156.62 (d, C, J_{C-F}= 243.0 Hz)], 169.32 (C=O), 181.75 (C=S). FT IR (v_{max}, cm^{-1}): 3211 (2NH), 3152 (NH), 3078 (Aromatic CH), 2955 (Aliphatic CH), 1667 (C=O), 1235 (C=S). EI MS m/z (%): 340.34 ([M+1]$^+$, 55), 158.09 (100). Anal. Calcd. for $C_{15}H_{22}FN_5OS$ (339.43); C, 53.08; H, 6.53; N, 20.63%. Found: C, 53.23; H, 6.66; N, 20.87%.

N-benzyl-2-{[4-(2-fluorophenyl)piperazin-1-yl]acetyl}hydrazinecarbothioamide (3c)

Yield: 97%, mp 191-192°C. ^{1}H NMR (DMSO-d_6, δ ppm): 2.64 (brs, 4H, 2CH$_2$), 3.09 (brs, 2H, CH$_2$), 3.36 (s, 4H, 2CH$_2$), 4.73 (d, 2H, CH$_2$, J= 5.6 Hz), 6.95-7.14 (m, 4H, arH), 7.22-7.30 (m, 5H, arH), 8.40 (brs, 1H, NH), 9.33 (s, 1H, NH), 9.77 (s, 1H, NH). ^{13}C NMR (DMSO-d_6, δ ppm): 47.16 (CH$_2$), 50.35 (CH$_2$), 50.38 (CH$_2$), 53.26 (2CH$_2$), 60.17 (CH$_2$), arC: [116.27 and 116.48 (d, CH, J= 21.0 Hz), 119.64 and 119.66 (d, CH, J= 2.0 Hz), 122.66 and 122.74 (d, CH, J= 8.0 Hz), 125.26 and 125.30 (d, CH, J= 4.0 Hz), 127.07 (2CH), 127.47 (CH), 128.50 (2CH), 139.73 (C), 140.27 and 140.35 (d, C, J= 8.0 Hz), 154.18 and 156.61 (d, C, J_{C-F}= 243.0 Hz)], 168.63 (C=O), 180.21 (C=S). FT IR (v_{max}, cm^{-1}): 3221 (2NH), 3174 (NH), 3065 (Aromatic CH), 2918 (Aliphatic CH), 1666 (C=O), 1232 (C=S). EI MS m/z (%): 402.43 ([M+1]$^+$, 17), 190.25 (100). Anal. Calcd. for $C_{20}H_{24}FN_5OS$ (401.50); C, 59.83; H, 6.03; N, 17.44%. Found: C, 60.00; H, 6.23; N, 18.00%.

General procedure for preparation of compounds 4a-c

Ethyl bromoacetate (1 mmol) and dried sodium acetate (5 mmol) were added to the solution of compound **3a-c** (1 mmol) in ethanol and the medium was irradiated in monomode microwave reactor in closed vessel at 150°C for 45 min. With removal of solvent with evaporation, an oily mass occurred, then it was purified with ethanol:water (1:3).

2-[4-(2-Fluorophenyl)piperazin-1-yl]-*N*'-[(4-oxo-3-phenyl-1,3-thiazolidin-2-ylidene]acetohydrazide (4a)

Yield: 60%, mp 150-151°C. ^{1}H NMR (DMSO-d_6, δ ppm): 2.38 (brs, 4H, 2CH$_2$), 2.81 (brs, 4H, 2CH$_2$), 3.41 (s, 4H, 2CH$_2$), 6.95 (d, 2H, arH, J= 8.0 Hz), 7.07 (t, 2H, arH, J= 8.0 Hz), 7.44-7.54 (m, 5H, arH), 9.05 (brs, 1H, NH). ^{13}C NMR (DMSO-d_6, δ ppm): 33.19 (CH$_2$), 40.59 (CH$_2$), 45.92 (2CH$_2$), 50.58 (CH$_2$), 60.39 (CH$_2$), arC: [116.28 and 116.48 (d, 2CH, J= 20.0 Hz), 119.60 (2CH), 122.75 and 122.83 (d, 2CH, J= 8.0 Hz), 127.99 (CH), 128.29 (2CH), 136.30 (C), 140.21 and 140.28 (d, C, J= 7.0 Hz), 154.56 and 156.60 (d, C, J_{C-F}= 204.0 Hz)], 158.56 (C=N), 165.59 (C=O), 171.99 (C=O). FT IR (v_{max}, cm^{-1}): 3277 (NH), 3071 (Aromatic CH), 2919 (Aliphatic CH), 1728 (2C=O), 1499 (C=N).

EI MS *m/z* (%): 450.01 ([M+Na]$^+$, 23), 232.21 (100). Anal. Calcd. for $C_{21}H_{22}FN_5O_2S$ (427.50); C, 59.00; H, 5.19; N, 16.38%. Found: C, 59.23; H, 5.00; N, 16.46%.

N'-[3-ethyl-4-oxo-1,3-thiazolidin-2-ylidene]-2-[4-(2-fluorophenyl)piperazin-1-yl]acetohydrazide (4b)

Yield: 55%, mp 164-165°C. ^{1}H NMR (DMSO-d_6, δ ppm): 1.14 (t, 3H, CH$_3$, *J*= 7.2 Hz), 2.67 (brs, 2H, CH$_2$), 3.05 (brs, 2H, CH$_2$), 3.13 (s, 2H, CH$_2$), 3.36 (brs, 4H, 2CH$_2$), 3.68 (d, 2H, CH$_2$, *J*=7.2 Hz), 4.04 (s, 2H, CH$_2$), 6.95-7.12 (m, 4H, arH), 10.05 (brs, 1H, NH). ^{13}C NMR (DMSO-d_6, δ ppm): 12.56 (CH$_3$), 32.21 (CH$_2$), 37.96 (CH$_2$), 50.60 (CH$_2$), 50.63 (CH$_2$), 53.19 (2CH$_2$), 60.19 (CH$_2$), arC: [116.28 and 116.49 (d, 2CH, *J*= 21.0 Hz), 119.67 and 119.70 (d, 2CH, *J*= 3.0 Hz), 122.74 and 122.82 (d, C, *J*= 8.0 Hz), 154.19 and 156.61 (d, C, J_{C-F}=242.0 Hz)], 158.38 (C=N), 165.47 (C=O), 171.54 (C=O). FT IR (v_{max}, cm^{-1}): 3197 (NH), 3073 (Aromatic CH), 2979 (Aliphatic CH), 1713 (C=O), 1692 (C=O), 1497 (C=N). EI MS *m/z* (%): 379.98 ([M]$^+$, 11), 301.12 (45), 204.26 (56), 128.80 (100). Anal. Calcd. for $C_{17}H_{22}FN_5O_2S$ (379.45); C, 53.81; H, 5.84; N, 18.46%. Found: C, 54.00; H, 5.99; N, 18.59%.

N'-[3-benzyl-4-oxo-1,3-thiazolidin-2-ylidene]-2-[4-(2-fluorophenyl)piperazin-1-yl]acetohydrazide (4c)

Yield: 45%, mp 198-199°C. ^{1}H NMR (DMSO-d_6, δ ppm): 2.66 (brs, 2H, CH$_2$), 3.04 (brs, 2H, CH$_2$), 3.12 (brs, 2H, CH$_2$), 3.39 (s, 4H, 2CH$_2$), 4.14 (s, 2H, CH$_2$), 4.84 (s, 2H, CH$_2$), 6.95-7.05 (m, 2H, arH), 7.08-7.12 (m, 2H, arH), 7.32-7.36 (m, 5H, arH), 10.12 (brs, 1H, NH). ^{13}C NMR (DMSO-d_6, δ ppm): 33.17 (CH$_2$), 40.54 (CH$_2$), 45.92 (CH$_2$), 50.58 (CH$_2$), 53.17 (2CH$_2$), 60.37 (CH$_2$), arC: [116.28 and 116.49 (d, 2CH, *J*= 21.0 Hz), 119.66 (CH), 122.75 and 122.83 (d, 2CH, *J*= 8.0 Hz), 127.98 (CH), 128.24 (2CH), 128.85 (CH), 136.29 (C), 140.20 and 140.28 (d, C, *J*= 8.0 Hz), 154.56 and 156.60 (d, C, J_{C-F}= 204.0 Hz)], 158.46 (C=N), 165.52 (C=O), 171.90 (C=O). FT IR (v_{max}, cm^{-1}): 3198 (NH), 3066 (Aromatic CH), 2828 (Aliphatic CH), 1720 (C=O), 1689 (C=O), 1496 (C=N). EI MS *m/z* (%): 442.09 ([M+1]$^+$, 19), 376.20 (21), 305.75 (100), 231.67 (60), 104.30 (21). Anal. Calcd. for $C_{22}H_{24}FN_5O_2S$ (441.52); C, 59.85; H, 5.48; N, 15.86%. Found: C, 60.00; H, 5.34; N, 15.89%.

General procedure for preparation of compounds 5a–c

Compounds **3a-c** (1 mmol) and 20 mL of 2 N NaOH in water was irradiated in monomode microwave reactor in closed vessel at 150 °C for 15 min. Then, the reaction mixture was cooled to room temperature and acidified to pH 4 with 37% HCl. The resulting solid was filtered off, and purified with dimethyl sulfoxide-water (1:4).

5-{[4-(2-Fluorophenyl)piperazin-1-yl]methyl}-4-phenyl-4H-1,2,4-triazole-3-thiol (5a)

Yield: 87%, mp 179-180°C. ^{1}H NMR (DMSO-d_6, δ ppm): 2.38 (s, 2H, CH$_2$), 2.81 (brs, 4H, 2CH$_2$), 3.41 (brs, 4H, 2CH$_2$), 6.95 (d, 2H, arH, J= 7.6 Hz), 7.05-7.08 (m, 2H, arH), 7.44-7.54 (m, 5H, arH), 13.90 (s, 1H, SH). ^{13}C NMR (DMSO-d_6, δ ppm): 50.33 (CH$_2$), 52.03 (2CH$_2$), 52.42 (2CH$_2$), arC: [116.24 and 116.45 (d, CH, J= 21.0 Hz), 119.60 and 119.63 (d, CH, J= 3.0 Hz), 122.73 and 122.81 (d, CH, J= 8.0 Hz), 125.21 and 125.24 (d, CH, J= 3.0 Hz), 128.70 (CH), 129.37 (2CH), 129.61 (2CH), 134.51 (C), 140.06 and 140.14 (d, C, J= 8.0 Hz), 154.10 and 156.53 (d, C, J_{C-F}= 243.0 Hz)], 149.62 (triazole C-3), 168.68 (triazole C-5). FT IR (v_{max}, cm^{-1}): 3035 (Aromatic CH), 2942 (Aliphatic CH), 1499 (C=N). EI MS m/z (%): 369.56 ([M]$^+$, 23), 200.76 (100). Anal. Calcd. for C$_{19}$H$_{20}$FN$_5$S (369.46); C, 61.77; H, 5.46; N, 18.96%. Found: C, 61.56; H, 5.66; N, 18.99%.

4-Ethyl-5-{[4-(2-fluorophenyl)piperazin-1-yl]methyl}-4H-1,2,4-triazole-3-thiol (5b)

Yield: 75%, mp 171-172°C. ^{1}H NMR (DMSO-d_6, δ ppm): 1.26 (brs, 3H, CH$_3$), 2.50 (brs, 2H, CH$_2$), 3.03 (brs, 4H, 2CH$_2$), 3.38 (s, 2H, CH$_2$), 3.64 (brs, 2H, CH$_2$), 4.07 (brs, 2H, CH$_2$), 6.98-7.12 (m, 4H, arH), 13.69 (brs, 1H, SH). ^{13}C NMR (DMSO-d_6, δ ppm): 13.82 (CH$_3$), 52.62 (5CH$_2$), arC: [116.34 and 116.54 (d, CH, J= 20.0 Hz), 119.81 (CH), 123.15 (CH), 125.29 and 125.32 (d, CH, J= 3.0 Hz), 141.26 (C), 154.15 and 156.58 (d, C, J_{C-F}= 243.0 Hz)], 167.73 (triazole C-3 and triazole C-5). FT IR (v_{max}, cm^{-1}): 3083 (Aromatic CH), 2927 (Aliphatic CH), 1497 (C=N). EI MS m/z (%): 321.48 ([M]$^+$, 47), 301.40 (31), 276.21 (100). Anal. Calcd. for C$_{15}$H$_{20}$FN$_5$S (321.42); C, 56.05; H, 6.27; N, 21.79%. Found: C, 56.15; H, 6.35; N, 21.90%.

4-Benzyl-5-{[4-(2-fluorophenyl)piperazin-1-yl]methyl}-4H-1,2,4-triazole-3-thiol (5c)

Yield: 67%, mp 228-230°C. ^{1}H NMR (DMSO-d_6, δ ppm): 2.50 (brs, 4H, 2CH$_2$), 2.83 (s, 2H, CH$_2$), 3.43 (brs, 4H, 2CH$_2$), 5.41 (s, 2H, CH$_2$), 6.99 (s, 2H, arH), 7.09-7.12 (m, 2H, arH), 7.25-7.36 (m, 5H, arH), 13.97 (s, 1H, SH). ^{13}C NMR (DMSO-d_6, δ ppm): 47.75 (3CH$_2$), 52.30 (3CH$_2$), arC: [116.37 and 116.57 (d, CH, J= 20.0 Hz), 119.80 (CH), 125.35 (CH), 127.46 (CH), 128.21 (2CH), 129.02 (CH), 129.39 (2CH), 136.31 (2C), 154.11 and 156.54 (d, C, J_{C-F}= 243.0 Hz)], 157.78 (triazole C-3) 168.58 (triazole C-5). FT IR (v_{max}, cm^{-1}): 3091 (Aromatic CH), 2925 (Aliphatic CH), 1498 (C=N). EI MS m/z (%): 383.50 ([M]$^+$, 21), 326.45 (36), 280.40 (78), 225.60 (21), 170.00 (100). Anal. Calcd. for C$_{20}$H$_{22}$FN$_5$S (383.49); C, 62.64; H, 5.78; N, 18.26%. Found: C, 62.70; H, 5.88; N, 18.32%.

General procedure for preparation of compounds 6a-d

To the solution of **5a-c** (10 mmol) in dimethylformamide, a suitable amine (10 mmol) and formaldehyde (50 mmol) was added and the mixture was stirred at room temperature for 24 h. Then water was added to the reaction. The solid precipitated was filtered off and purified with dimethyl sulfoxide:water (1:3).

4-Benzyl-5-{[4-(2-fluorophenyl)piperazin-1-yl]methyl}-2-[(4-methylpiperazin-1-yl)methyl]-2,4-dihydro-3*H*-1,2,4-triazole-3-thione (6a)

Yield: 60%, mp 72-73°C. ^{1}H NMR (DMSO-d_6, δ ppm): 2.30 (brs, 2H, CH$_2$), 2.45 (brs, 7H, CH$_3$+2CH$_2$), 2.76 (brs, 8H, 4CH$_2$), 3.46 (brs, 2H, CH$_2$), 3.52 (s, 2H, CH$_2$), 5.35 (s, 2H, CH$_2$), 5.38 (s, 2H, CH$_2$), 6.93 (s, 2H, arH), 7.08 (d, 2H, arH, J=4.8 Hz), 7.26-7.32 (m, 5H, arH). ^{13}C NMR (DMSO-d_6, δ ppm): 40.90 (CH$_3$), 46.75 (2CH$_2$), 47.74 (CH$_2$), 47.81 (CH$_2$), 50.04 (CH$_2$), 50.23 (CH$_2$), 52.31 (CH$_2$), 52.47 (CH$_2$), 54.98 (CH$_2$), 69.11 (CH$_2$), 71.03 (CH$_2$), arC: [116.24 and 116.45 (d, CH, J= 21.0 Hz), 119.59 (CH), 122.75 and 122.83 (d, CH, J= 8.0 Hz), 125.23 (CH), 125.26 (CH), 127.42 (CH), 127.79 (CH), 127.79 (CH), 128.87 (CH), 140.10 and 140.17 (d, C, J= 7.0 Hz), 148.38 (C), 154.16 and 156.59 (d, C, J_{C-F}= 243.0 Hz)], 149.57 (triazole C-3), 168.72 (triazole C-5). FT IR (v_{max}, cm^{-1}): 3033 (Aromatic CH), 2919 (Aliphatic CH), 1498 (C=N), 1238 (C=S). EI MS *m/z* (%): 496.43 ([M+1]$^+$, 31), 345.90 (76), 301.24 (40), 278.65 (35), 201.10 (100). Anal. Calcd. for C$_{26}$H$_{34}$FN$_7$S (495.66); C, 63.00; H, 6.91; N, 19.78%. Found: C, 62.87; H, 7.09; N, 19.79%.

4-Benzyl-5-{[4-(2-fluorophenyl)piperazin-1-yl]methyl}-2-[(4-phenylpiperazin-1-yl)methyl]-2,4-dihydro-3H-1,2,4-triazole-3-thione (6b)

Yield: 56%, mp 65-67°C. ^{1}H NMR (DMSO-d_6, δ ppm): 2.43-2.50 (m, 6H, 3CH$_2$), 2.76 (brs, 6H, 3CH$_2$), 3.35 (brs, 6H, 3CH$_2$), 3.46 (s, 2H, CH$_2$), 5.36 (d, 2H, CH$_2$, J= 7.2 Hz), 6.90-6.95 (m, 4H, arH), 7.06-7.09 (m, 3H, arH), 7.25-7.27 (m, 4H, arH), 7.33 (d, 3H, arH, J= 7.2 Hz). ^{13}C NMR (DMSO-d_6, δ ppm): 46.75 (CH$_2$), 47.74 (CH$_2$), 48.67 (CH$_2$), 50.05 (CH$_2$), 50.27 (CH$_2$), 52.30 (CH$_2$), 52.46 (CH$_2$), 52.65 (CH$_2$), 52.68 (CH$_2$), 69.07 (CH$_2$), 71.02 (CH$_2$), arC: [116.25 and 116.45 (d, CH, J= 20.0 Hz), 122.83 (CH), 125.24 and 125.27 (d, CH, J= 3.0 Hz), 127.19 (2CH), 127.41 (2CH), 127.79 (CH), 127.79 (2CH), 128.87 (2CH), 129.34 (2CH), 140.11 and 140.19 (d, C, J= 8.0 Hz), 148.71 (C), 151.32 (C), 154.16 and 156.59 (d, C, J_{C-F}= 243.0 Hz)], 149.59 (triazole C-3), 168.54 (triazole C-5). FT IR (v_{max}, cm^{-1}): 3092 (Aromatic CH), 2919 (Aliphatic CH), 1498 (C=N), 1238 (C=S). EI MS *m/z* (%): 557.74 ([M+1]$^+$, 34), 501.23 (43), 456.78 (35), 301.80 (75), 250.54 (100), 125.12 (51). Anal. Calcd. for C$_{31}$H$_{36}$FN$_7$S (557.73); C, 66.76; H, 6.51; N, 17.58%. Found: C, 66.79; H, 6.65; N, 17.60%.

1-Ethyl-6-fluoro-7-{4-[(3-{[4-(2-fluorophenyl)piperazin-1-yl]methyl}-4-phenyl-5-thioxo-4,5-dihydro-1*H*-1,2,4-triazol-1-yl)methyl]piperazin-1-yl}-4-oxo-1,4-dihydroquinoline-3-carboxylic acid (6c)

Yield: 70%, mp 213-215°C. ^{1}H NMR (DMSO-d_6, δ ppm): 1.41 (t, 3H, CH$_3$, *J*= 6.4 Hz), 2.40 (brs, 4H, 2CH$_2$), 2.78 (brs, 6H, 3CH$_2$), 2.99 (s, 2H, CH$_2$), 3.34 (brs, 6H, 3CH$_2$), 4.57 (q, 2H, CH$_2$, *J*= 6.8 Hz), 5.21 (s, 2H, CH$_2$), 6.90-6.96 (m, 3H, arH), 7.03-7.08 (m, 2H, arH), 7.50-7.54 (m, 5H, arH), 7.87 (d, 1H, arH, *J*= 13.6 Hz), 8.92 (s, 1H, quinolone CH), 15.32 (s, 1H, OH). ^{13}C NMR (DMSO-d_6, δ ppm): 14.73 (CH$_3$), 49.23 (2CH$_2$), 49.58 (2CH$_2$), 49.99 (2CH$_2$), 50.17 (CH$_2$), 51.89 (CH$_2$), 52.38 (CH$_2$), 68.97 (CH$_2$), 70.98 (CH$_2$), 107.50 (C), arC: [106.46 (CH), 111.54 and 111.77 (d, CH, *J*= 23.0 Hz), 115.57 and 115.77 (d, 2CH, *J*= 20.0 Hz), 117.48 and 117.55 (d, 2CH, *J*= 7.0 Hz), 119.79 (C), 128.60 (2CH), 129.45 (2CH), 129.79 (CH), 134.80 and 134.95 (d, C, *J*= 15.0 Hz), 137.66 (C), 145.77 (C), 148.23 and 148.46 (d, C, *J*= 23.0 Hz), 152.05 and 154.53 (d, C, J_{C-F}= 248.0 Hz), 155.27 and 157.61 (d, C, J_{C-F}= 234.0 Hz], 148.99 (CH), 162.79 (triazole C-3), 169.75 (triazole C-5), 175.73 (C=O), 176.58 (C=O). FT IR (v_{max}, cm^{-1}): 3450 (OH), 3068 (Aromatic CH), 2920 (Aliphatic CH), 1719 (2C=O), 1497 (C=N), 1241 (C=S). EI MS *m/z* (%): 718.25 ([M+H$_2$O]$^+$, 34), 521.00 (65), 431.09 (67), 340.01 (23), 309.90 (67), 295.24 (100), 123.67 (32). Anal. Calcd. for C$_{36}$H$_{38}$F$_2$N$_8$O$_3$S (700.80); C, 61.70; H, 5.47; N, 15.99%. Found: C, 61.90; H, 5.32; N, 16.16%.

1-Cyclopropyl-6-fluoro-7-{4-[(3-{[4-(2-fluorophenyl)piperazin-1-yl]methyl}-4-phenyl-5-thioxo-4,5-dihydro-1*H*-1,2,4-triazol-1-yl)methyl]piperazin-1-yl}-4-oxo-1,4-dihydroquinoline-3-carboxylic acid (6d)

Yield: 79%, mp 225-226°C. ^{1}H NMR (DMSO-d_6, δ ppm): 1.17 (brs, 2H, CH$_2$), 1.33 (brs, 2H, CH$_2$), 2.40 (brs, 4H, 2CH$_2$), 2.79 (brs, 4H, 2CH$_2$), 3.00 (s, 2H, CH$_2$), 3.34 (brs, 6H, 3CH$_2$), 3.47 (s, 2H, CH$_2$), 3.81 (brs, 1H, CH), 5.21 (s, 2H, CH$_2$), 6.92 (d, 2H, arH, *J*= 8.4 Hz), 7.04-7.07 (m, 2H, arH), 7.51-7.56 (m, 6H, arH), 7.87 (d, 1H, arH, *J*= 13.2 Hz), 8.64 (s, 1H, quinolone CH), 15.19 (s, 1H, OH). ^{13}C NMR (DMSO-d_6, δ ppm): 8.08 (2CH$_2$), 36.27 (CH), 49.21 (2CH$_2$), 49.80 (2CH$_2$), 50.09 (2CH$_2$), 51.83 (2CH$_2$), 52.38 (CH$_2$), 68.95 (CH$_2$), 107.01 (C), arC: [107.21 (CH), 111.30 (CH), 115.55 and 115.77 (d, 2CH, *J*= 22.0 Hz), 117.28 and 117.49 (d, 2CH, *J*= 21.0 Hz), 119.12 (C), 128.75 (CH), 129.43 (2CH), 129.78 (2CH), 134.95 and 135.11 (d, C, *J*= 16.0 Hz), 139.62 (2C), 148.13 and 148.35 (d, C, *J*= 22.0 Hz), 152.20 and 155.27 (d, c, J_{C-F}= 307.0 Hz), 157.61 and 162.76 (d, C, J_{C-F}= 514.0 Hz], 148.49 (CH), 166.39 (triazole C-3), 169.79 (triazole C-5), 173.27 (C=O), 176.88 (C=O). FT IR (v_{max}, cm^{-1}): 3277 (OH), 3071 (Aromatic CH), 2919 (Aliphatic CH), 1728 (2C=O), 1499 (C=N), 1257 (C=S). EI MS *m/z* (%): 712.00 ([M]$^+$, 10), 651.00 (67), 550.34 (89), 210.50 (100). Anal. Calcd. for C$_{37}$H$_{38}$F$_2$N$_8$O$_3$S (712.81); C, 62.34; H, 5.37; N, 15.72%. Found: C, 62.50; H, 5.41; N, 16.00%.

Diethyl {[(3-chloro-4-fluorophenyl)amino]methylene}malonate (7)

The synthesis of this compound was achieved according to published procedure [19]. Yield: 94%, mp 58°C. ^{1}H NMR (300 MHz, CDCl$_3$) δ: 1.3-1.4 (m, 6H, 2CH$_3$ of OCH$_2$CH$_3$), 4.2-4.3 (m, 4H, 2CH$_2$ of OCH$_2$CH$_3$), 6.9-7.2 (m, 3H, ArH), 8.3 (d, 1H, Vinylic, J_{H-H}= 13 Hz), 10.9 (d, 1H, NH, J_{H-H}= 13 Hz). IR (KBr, cm^{-1}): 1722, 1658, 1622. ESI MS *m/z*: 338 [M+Na]$^+$. Anal. Calcd. for C$_{14}$H$_{15}$ClFNO$_4$: C, 53.26; H, 4.79; N, 4.44: found: C, 53.27: H, 4.74: N, 4.43%.

Ethyl 7-chloro-6-fluoro-4-oxo-1,4-dihydroquinoline-3-carboxylate (8)

The cyclization of **7** (1 mmol) that was published previously [19] was achieved by irradiation with diphenyl ether (12 mL) in monomode microwave reactor in closed vessel at 240°C for 5 min. A white solid occurred by cooling the reaction. Then this solid was washed with ethyl acetate and purified with dimethylformamide. Yield: 75%, mp>290°C. ^{1}H NMR (DMSO-d_6, δ ppm): 1.28 (brs, 3H, CH$_3$), 4.21 (brs, 2H, CH$_2$), 7.63 (s, 1H, ArH), 7.74 (s, 1H, ArH) 8.48 (s, 1H, quinolone CH), 12.37 (brs, 1H, NH). FT IR (ν$_{max}$, cm^{-1}): 3103 (NH), 3095 (Aromatic CH), 2987 (Aliphatic CH), 1698 (2C=O).

Ethyl 7-chloro-1-ethyl-6-fluoro-4-oxo-1,4-dihydroquinoline-3-carboxylate (9)

To obtain compound **9** that was published previously [19], the solution of compound **8** (1 mmol) in dimethylformamide, ethyl bromide (5 mmol) and K$_2$CO$_3$ (2 mmol) was added. The reaction was irradiated in monomode microwave reactor in closed vessel at 75 °C for 20 min. A solid was appeared by evaporating the solvent. This solid was washed with water and purified with dimethylformamide:water (1:3). Yield 90%, mp 134-135°C. ^{1}H NMR (DMSO-d_6, δ ppm): 1.28 (t, 3H, CH$_3$, *J*=8.0 Hz), 1.35 (t, 3H, CH$_3$, *J*=8.0 Hz), 4.22 (q, 2H, CH$_2$, *J*=3.6 Hz), 4.42 (q, 2H, CH$_2$, *J*=7.2 Hz), 8.03 (d, 1H, ArH, *J*=9.6 Hz), 8.18 (d, 1H, ArH, *J*= 6.0 Hz), 8.70 (s, 1H, quinolone CH). ^{13}C NMR (DMSO-d_6, δ ppm): 14.74 (CH$_3$), 14.81 (CH$_3$), 48.78 (CH$_2$), 60.37 (CH$_2$), 110.45 (C), arC: [112.90 and 113.13 (d, CH, *J*=23.0 Hz), 120.52 (CH), 125.91 and 126.11 (d, C, *J*= 20.0 Hz), 129.13 and 129.19 (d, C, *J*= 6.0 Hz), 136.18 (C), 153.59 and 156.04 (d, C, J_{C-F}= 245.0 Hz)], 149.93 (CH), 164.75 (C=O), 171.86 (C=O). FT IR (ν$_{max}$, cm^{-1}): 3073 (Aromatic CH), 2918 (Aliphatic CH), 1716 (C=O), 1688 (C=O). EI MS *m/z* (%): 320.04 ([M+Na]$^+$, 25), 125.14 (100). Anal. Calcd. for C$_{14}$H$_{13}$ClFNO$_3$ (297.70); C, 56.48; H, 4.40; N, 4.70%. Found: C, 56.70; H, 4.44; N, 5.00%.

7-Chloro-1-ethyl-6-fluoro-4-oxo-1,4-dihydroquinoline-3-carboxylic acid (10)

The compound **9** (10 mmol) was refluxed with 2 N NaOH (100 mL) for 2 h [19]. Then, the resulting solution was cooled to room temperature and acidified with acetic acid. The

precipitate solid was filtered off, washed with water, and purified with dimethyl sulfoxide-water (1:4). Yield: 90%, mp>300°C. ^{1}H NMR (DMSO-d_6, δ ppm): 1.39 (t, 3H, CH$_3$, J=7.2 Hz), 4.61 (q, 2H, CH$_2$, J=7.2 Hz), 8.15 (d, 1H, ArH, J=8.8 Hz), 8.42 (d, 1H, ArH, J= 6.0 Hz), 9.05 (s, 1H, quinolone CH), 14.96 (brs, 1H, OH). FT IR (v_{max}, cm^{-1}): 3057 (Aromatic CH), 1715 (2C=O).

General procedure for the preparation of compounds 11a-c

The mixture of compound **10** (1 mmol), triethylamine (3 mmol) and compounds **5a-c** (1.1mmol) in dimethylformamide was irradiated in monomode microwave reactor in closed vessel at 80°C for 15 min. After evaporation of the solvent, a solid was formed, which was washed with water and recrystallized with dimethylsulfoxide: water (1:3).

1-Ethyl-6-fluoro-7-[(5-{[4-(2-fluorophenyl)piperazin-1-yl]methyl}-4-phenyl-4H-1,2,4-triazol-3-yl)thio]-4-oxo-1,4-dihydroquinoline-3-carboxylic acid (11a)

Yield 70%, mp 200-201°C. ^{1}H NMR (DMSO-d_6, δ ppm): 1.39 (brs, 3H, CH$_3$), 2.39 (brs, 4H, 2CH$_2$), 2.80 (brs, 4H, 2CH$_2$), 3.35 (s, 2H, CH$_2$), 4.60 (brs, 2H, CH$_2$), 6.92 (s, 2H, arH), 7.05 (s, 2H, arH), 7.47 (s, 3H, arH), 7.52 (s, 2H, arH), 8.13 (brs, 1H, arH), 8.41 (s, 1H, arH), 9.05 (s, 1H, quinolone CH), 14.74 (brs, 1H, OH). ^{13}C NMR (DMSO-d_6, δ ppm): 14.25 (CH$_3$), 50.25 (CH$_2$), 51.25 (2CH$_2$), 54.26 (2CH$_2$), 55.80 (CH$_2$), 107.56 (C), arC: [115.23 and 115.34 (d, CH, J= 11.0 Hz), 116.45 and 116.67 (d, CH, J= 22.0 Hz), 119.20 and 119.28 (d, C, J= 8.0 Hz), 121.20 and 121.38 (d, 2CH, J= 18.0 Hz), 124.26 and 124.34 (d, 2CH, J= 8.0 Hz), 128.23 (2CH), 129.90 (CH), 132.18 (2CH), 136.67 and 136.74 (d, C, J= 7.0 Hz), 138.90 (2C), 141.56 (C), 152.78 and 156.10 (d, C, J_{C-F}= 332.0 Hz), 159.12 and 162.90 (d, C, J_{C-F}= 378.0 Hz)], 148.55 (CH), 155.25 (triazole C-3), 161.67 (triazole C-5), 170.09 (C=O), 172.34 (C=O). FT IR (v_{max}, cm^{-1}): 3456 (OH), 3057 (Aromatic CH), 2919 (Aliphatic CH), 1714 (2C=O), 1499 (C=N). EI MS m/z (%): 625.14 ([M+Na]$^+$, 18), 447.54 (90), 392.35 (100), 292.18 (91). Anal. Calcd. for C$_{31}$H$_{28}$F$_2$N$_6$O$_3$S (602.65); C, 61.78; H, 4.68; N, 13.95%. Found: C, 61.65; H, 4.72; N, 14.09%.

1-Ethyl-7-[(4-ethyl-5-{[4-(2-fluorophenyl)piperazin-1-yl]methyl}-4H-1,2,4-triazol-3-yl)thio]-6-fluoro-4-oxo-1,4-dihydroquinoline-3-carboxylic acid (11b)

Yield: 65%, mp 183-185°C. ^{1}H NMR (DMSO-d_6, δ ppm): 1.30 (brs, 3H, CH$_3$), 1.39 (brs, 3H, CH$_3$), 2.58 (brs, 4H, 2CH$_2$), 2.99 (brs, 4H, 2CH$_2$), 3.35 (s, 2H, CH$_2$), 3.64 (s, 2H, CH$_2$), 4.03 (s, 2H, CH$_2$), 7.08 (s, 4H, arH), 8.16 (brs, 1H, arH), 8.42 (brs, 1H, arH), 9.06 (s, 1H, quinolone CH), 13.63 (s, 1H, OH). ^{13}C NMR (DMSO-d_6, δ ppm): 13.78 (CH$_3$), 14.00 (CH$_3$), 50.15 (2CH$_2$), 51.95 (CH$_2$), 53.26 (2CH$_2$), 55.81 (2CH$_2$), 107.59 (C), arC: [115.33 and 115.44 (d, CH, J= 11.0 Hz), 116.47 and 116.67 (d, CH, J= 20.0 Hz), 119.28 and 119.36 (d, C, J= 8.0 Hz), 121.20 and 121.37 (d, 2CH, J= 17.0 Hz), 124.26 and

124.39 (d, 2CH, J= 15.0 Hz), 136.08 and 136.14 (d, C, J= 6.0 Hz), 137.90 (C), 141.66 (C), 152.80 and 156.12 (d, C, J_{C-F}= 332.0 Hz), 160.12 and 162.90 (d, C, J_{C-F}= 278.0 Hz)], 148.55 (CH), 155.95 (triazole C-3), 161.60 (triazole C-5), 170.89 (C=O), 172.33 (C=O). FT IR (v_{max}, cm^{-1}): 3400 (OH), 3093 (Aromatic CH), 2917 (Aliphatic CH), 1714 (2C=O), 1499 (C=N). EI MS *m/z* (%): 591.37 (100), 577.35 ([M+Na]$^+$, 18), 563.46 (46). Anal. Calcd. for $C_{27}H_{28}F_2N_6O_3S$ (554.61); C, 58.47; H, 5.09; N, 15.15%. Found: C, 58.61; H, 5.19; N, 15.32%.

7-[(4-Benzyl-5-{[4-(2-fluorophenyl)piperazin-1-yl]methyl}-4*H*-1,2,4-triazol-3-yl)thio]-1-ethyl-6-fluoro-4-oxo-1,4-dihydroquinoline-3-carboxylic acid (11c)

Yield: 57% mp 184-186°C. ^{1}H NMR (DMSO-d_6, δ ppm): 1.39 (s, 3H, CH$_3$), 2.44 (brs, 4H, 2CH$_2$), 2.76 (brs, 4H, 2CH$_2$), 3.46 (brs, 2H, CH$_2$), 4.61 (s, 2H, CH$_2$), 5.33 (s, 2H, CH$_2$), 6.92 (d, 2H, arH, J= 8.8 Hz), 7.08 (s, 2H, arH), 7.26-7.33 (m, 5H, arH), 8.21 (d, 1H, arH, J= 8.0 Hz), 8.44 (s, 1H, arH), 9.08 (s, 1H, quinolone CH), 13.44 (s, 1H, OH). ^{13}C NMR (DMSO-d_6, δ ppm): 14.23 (CH$_3$), 49.25 (CH$_2$), 50.35 (2CH$_2$), 51.26 (2CH$_2$), 53.80 (2CH$_2$), 107.50 (C), arC: [115.26 and 115.33 (d, CH, J= 7.0 Hz), 116.55 and 116.77 (d, CH, J= 22.0 Hz), 119.20 and 119.29 (d, C, J= 9.0 Hz), 121.25 and 121.38 (d, 2CH, J= 13.0 Hz), 124.27 and 124.34 (d, 2CH, J= 7.0 Hz), 128.20 (2CH), 129.99 (CH), 132.48 (2CH), 136.57 and 136.64 (d, C, J= 7.0 Hz), 138.75 (2C), 141.50 (C), 152.78 and 156.10 (d, C, J_{C-F}= 332.0 Hz), 158.00 and 162.20 (d, C, J_{C-F}= 420.0 Hz)], 148.78 (CH), 155.29 (triazole C-3), 161.97 (triazole C-5), 170.19 (C=O), 172.84 (C=O). FT IR (v_{max}, cm^{-1}): 3400 (OH), 3092 (Aromatic CH), 2918 (Aliphatic CH), 1718 (2C=O), 1498 (C=N). EI MS *m/z* (%): 655.39 ([M+K]$^+$, 46), 653.37 (100). Anal. Calcd. for $C_{32}H_{30}F_2N_6O_3S$ (616.68); C, 62.32; H, 4.90; N, 13.63%. Found: C, 62.40; H, 5.12; N, 13.87%.

Antimicrobial Activity Assessment

The test microorganisms were purchased from the Hifzissihha Institute of Refik Saydam (Ankara, Turkey). All the newly synthesized compounds were weighed and dissolved in hexane for preparing the extract stock solution of 20.000 microgram/milliliter (µg/mL). The antimicrobial effects of the substances were tested quantitatively in respective broth media by using double microdilution and the minimal inhibition concentration (MIC) values (µg/mL) were determined. The antibacterial and antifungal assays were performed in Mueller-Hinton broth (MH) (Difco, Detroit, MI) at pH.7.3 and buffered Yeast Nitrogen Base (Difco, Detroit, MI) at pH 7.0, respectively. The micro dilution test plates were incubated for 18-24 h at 35 °C. Brain Heart Infusion broth (BHI) (Difco, Detriot, MI) was used for *M. smegmatis*, and incubated for 48-72 h at 35 °C [22]. Ampicillin (10 µg) and fluconazole (5µg) were used as standard antibacterial and antifungal drugs, respectively. Dimethylsulfoxide with dilution of 1:10 was used as solvent control.

RESULTS AND DISCUSSION

The new Mannich base derivatives **6a-d** and novel fluoroquinolone analogues **11a-c** described herein were synthesized and examined in terms of biological activity as shown in Schemes 1 and 2, respectively. Newly compounds were obtained according to the synthetic route summarized in Scheme 1. Firstly, compound **1** was obtained from the treatment of ethyl bromoacetate with 1-(2-fluorophenyl)piperazine provided commercially. FT-IR spectrum of compound **1** indicated absorption band at 1745 cm^{-1} belonging the carbonyl function.

In ^{1}H NMR spectra, it was noticed that the protons of ethyl group peaks at 1.20 and 4.10 ppm. With the conversion of compound **1** to hydrazide (**2**), the signals of ester function were not observed in the ^{1}H and ^{13}C NMR spectrum. Additional peaks are due to the presence of −NHNH$_2$ and were indicated at 4.25 and 8.94 ppm. Moreover, in the FT-IR spectrum, absorption bands were registered at 3256 and 3225 cm^{-1} as a broad peak typical for this structure. Reaction of compound **2** with suitable isothiocyanates phenyl-, ethyl- and benzyl isothiocyanates respectively generated the corresponding carbonothioylhydrazino derivatives **3a-c**, which behave as suitable intermediates in the reactions leading to the formation of nitrogen- and/or sulfur-containing compounds having biological activity. The reaction was investigated in ethanol at microwave irradiated conditions. The FT-IR spectra of derivatives **3a-c** showed an absorption band at 1237, 1235 and 1232 cm^{-1} which can be attributed to -C=S function. The synthesis of (1,3-thiazoline-2-ylidene) acetohydrazide derivatives (**4a-c**) was carried out by the condensation of **3a-c** with ethyl bromoacetate and dried sodium acetate in ethanol by refluxing. ^{1}H NMR spectrum of **4a-c** showed signal at between 3.41-4.14 ppm which can be attributed to thiazolidinone nucleus. In addition, signals of −CH$_2$ groups resulting from thiazolidinone ring resonated at 33.19 (for **4a**), 32.21 (for **4b**), 33.17 (for **4c**) ppm in the ^{13}C NMR spectrum. Another evidence for the compounds, **4a-c** showed the molecular ion peak, suggesting the assigned structure. The basic reaction of **3a-c** yielded 1,2,4-triazole (**5a-c**) which can be considered as important tools for further condensation reactions leading to the formation of novel bioactive molecules (Scheme 1). The reaction was carried out in water, which is not a toxic solvent, under microwave conditions.
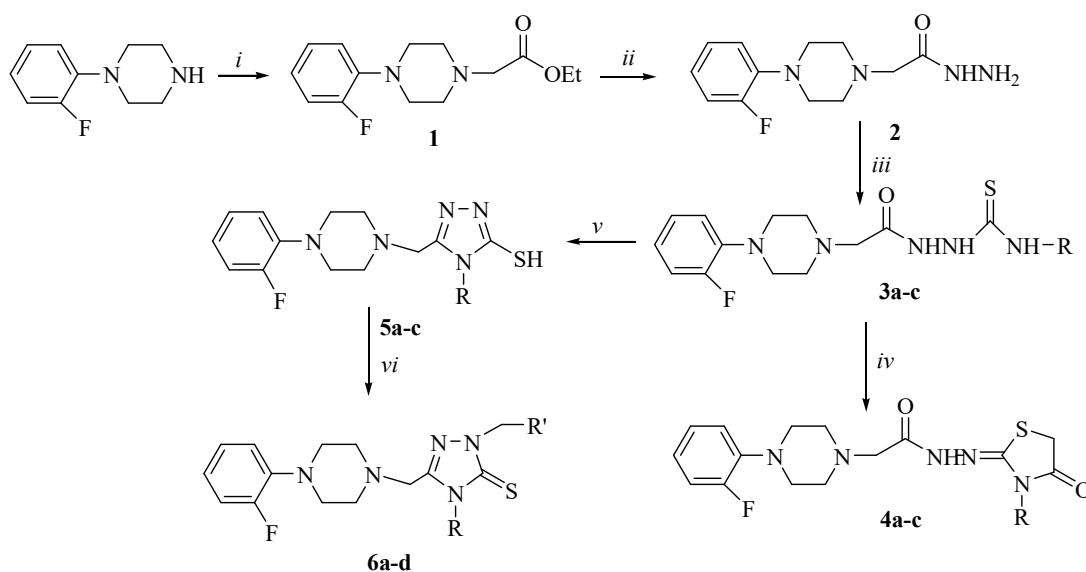
3a, **4a**, **5a**: R= -C₆H₅; **3b**, **4b**, **5b**: R= -CH₂CH₃; **3c**, **4c**, **5c**: R= - CH₂C₆H₅
6a: R= - CH₂C₆H₅; **R'**= methyl piperazine; **6c**: R= -C₆H₅; **R'**= norloxacin
6b: R= - CH₂C₆H₅; **R'**= phenyl piperazine; **6d**: R= -C₆H₅; **R'**= ciprofloxacin

Scheme 1. Reagents and conditions: *i*: BrCH₂COOEt, Et₃N, THF, rt; *ii*: H₂NNH₂.H₂O, MW; *iii*: suitable alkyl(aryl)isothiocyanate, EtOH, MW; *iv*: BrCH₂COOEt, NaOAc, MW; *v*: NaOH, MW; *vi*: HCHO, suitable amine, DMF, rt.

In the ¹H NMR spectrum of **5a-c**, the SH signals were observed at 13.90 ppm (for **5a**), 13.69 (for **5b**) 13.97 (for **5c**) as a proof of cyclization. In the ¹³C NMR spectrum, triazole C-3 and C-5 carbon atoms of compounds **5a-c** resonated at 149.62-157.78 ppm (triazole C-3) and 167.73-168.68 ppm (triazole C-5), respectively consistent with literature findings [20, 21]. The mass spectrum of compounds showed peaks according to their molecular formula.

The preparation of compound (**7**) was obtained with the reaction of 3-chloro-4-fluoroaniline with diethylethoxymethylene malonate according to published procedure [19]. Then compound **7** was converted to (**8**) by cyclization with diphenyl ether. The reaction was carried out by microwave irradiation. With the use of MW conditions, higher yield was assessed; however, the important effect of MW irradiation was on reaction time. The complete conversion of the compound **7** in best yield was observed after microwave irradiation at 240 °C for 5 min. Compounds **8-10** were published in the literature [19]. Subsequently, compound **8** was alkylated with ethyl bromide using K₂CO₃ in dimethylformamide to give the corresponding compound (**9**). As different from compound **8**, ¹H and ¹³C NMR spectrum of **9** showed extra peaks owing to ethyl group at the belonging chemical shift values, while the signal originated from any amino group was not recorded. In addition, mass spectrum and elemental analysis results confirm with the structure. Compound **10** was synthesized by the treatment of compound **9** with NaOH under reflux conditions [19]. In the ¹H NMR spectrum of compound **10**, the -OH

peak was recorded 14.96 ppm while the peaks belonging to ester group were not seen in the ^{1}H NMR spectrum.

The new fluoroquinolones **11a-c** described herein were synthesized as shown in Scheme 2.
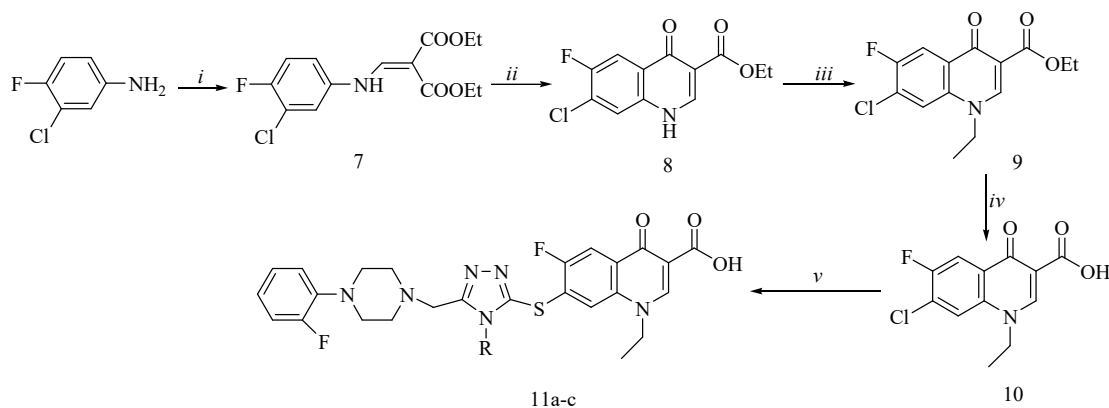
11a: R= -C$_6$H$_5$; **11b**: R= -CH$_2$CH$_3$; **11c**: R= -CH$_2$C$_6$H$_5$

Scheme 2: Reagents and conditions: *i*: diethyl ethoxymethylenemalonate, 100°C, reflux; *ii*: diphenyl ether, MW, 240°C for 5 min; *iii*: ethyl bromide, K$_2$CO$_3$, DMF, MW, 75°C for 20 min; *iv*: 2N NaOH, reflux; *v*: Et$_3$N, compounds 5a-c, DMF, MW, 80°C, 15 min.

To obtain new fluoroquinolone-triazole hybrid compounds, compound **10** was subjected to react with compounds **5a-c** in the presence of triethylamine. This reaction was achieved under microwave conditions. The best MW condition in terms of yields and product stability was assessed at 80°C, 15 min in dimethylformamide. In ^{1}H NMR spectrum of these compounds, additional signals derived from fluorophenyl ring and piperazine nucleus appeared at the related regions. Additionally, all the other aromatic and aliphatic carbons also appeared at the appropriate chemical shift regions. Mass spectrum of **11a-c** was showed [M+Na]$^+$ and [M+K]$^+$ ion peaks suitable their molecular formula.

Antimicrobial activity

Newly synthesized compounds were screened for their biological properties and the results were illustrated in Table 1. This reveals that the most compounds own well activities against to test microorganisms with the mic values varying between 0.24-500 µg/mL. Compounds **3a,** and **3b** showed medium activity towards *Enterococcus faecalis* (Ef), with the mic values 250 µg/mL while, compound **3c** showed slight antifungal activity on *Candida albicans* (Ca) and *Saccharomyces cerevisiae* (Sc). Compounds **4a-c** displayed moderate activity on *Mycobacterium smegmatis* (Ms). The compounds carrying an 1,2,4-triazole moiety (**5a-c**) showed moderate activity on Ms with the mic value 62.50-125

µg/mL and slight activity towards Ca with mics 62.5-500 µg/mL. Moreover, the conversion of compounds **5a-c** to compounds **6a-d**, which can be regarded as Mannich bases, resulted in a remarkable increase in the antimicrobial activity. Among these, the better activity was observed for compounds **6c** and **6d** carrying a fluoroquinolone unit. According to Table 1, it is more attractive to speculate the observation that the excellent antimicrobial activity results were observed for compounds **11a-c** which triazole-fluoroquinolone hybrid compounds on the test microorganisms, except Ca and Sc with the mic values between 0.24-1.9 µg/mL. In fact, the activity of these compounds was better than reference drugs, as shown table 1.

Table 1. Antimicrobial activity of the synthesized compounds (µg/mL).

Comp.No	Ec	Yp	Pa	Sa	Ef	Bc	Ms	Ca	Sc
				Microorganisms and Minimal Inhibition Concentration					
3a	-	-	-	-	250	-	62.5	500	-
3b	-	-	-	-	250	-	62.5	500	-
3c	-	-	-	-	-	-	-	125	62.5
4a	-	-	-	-	-	62.5	31.3	125	-
4b	-	-	-	-	-	-	125	500	-
4c	-	-	-	-	-	-	250	500	-
5a	-	-	-	-	-	-	62.5	500	125
5b	-	-	-	-	-	-	125	250	-
5c	-	-	-	125	-	-	62.5	62.5	-
6a	31.3	62.5	62.5	-	-	-	-	500	-
6b	31.3	-	-	-	-	-	-	125	250
6c	<3,9	<3,9	<3,9	<3,9	<3,9	<3,9	125	-	-
6d	<0,24	<0,24	<0,24	<0,24	<0,24	<0,24	<0,24	-	-
11a	<0.26	<0,26	<0.26	<0.26	<0.26	<0.26	<0.26	-	-
11b	<1,9	<1,9	<1,9	<1,9	<1,9	<1,9	<1,9	-	-
11c	<0,24	<0,24	<0,24	<0,24	<0,24	<0,24	<0,24	-	-
Amp.	10	18	>128	10	35	15			
Strep.							4		
Flu.								<8	<8

Ec: Escherichia coli ATCC 25922, Yp: Yersinia pseudotuberculosis ATCC 911, Pa: Pseudomonas aeruginosa ATCC 43288, Sa: Staphylococcus aureus ATCC 25923, Ef: Enterococcus faecalis ATCC 29212, Bc: Bacillus cereus 702 Roma, Ms: M. smegmatis ATCC607, Ca: Candida albicans ATCC 60193, Sc: Saccharomyces cerevisiae RSKK 251, Amp.: Ampicillin, Strep.: Streptomycin, Flu.: Fluconazole, (—): no activity.

CONCLUSION

This study reports the synthesis of novel hybrid compounds including fluoroquinolone and Mannich base derivatives starting from 1-(2-fluorophenyl)piperazine. The antimicrobial activity studies were examined. The results show that 1,2,4-triazole attached to

fluoroquinolones (**11a-c**) displayed excellent activity against to test microorganism except *Candida albicans* and *Saccharomyces cerevisiae*.

ACKNOWLEDGEMENTS

REFERENCES

1. Panda Siva S, Liaqat S, Girgis SA, Samir A, Hall D, Katritzky AR. Novel antibacterial active quinolone–fluoroquinolone conjugates and 2D-QSAR studies. Bioorganic & Medicinal Chemistry Letters. 2015; (25): 3816–3821. DOI: 10.1016/j.bmcl.2015.07.077.

2. Mentese MY, Bayrak H, Uygun Y, Mermer A, Ulker S, Karaoglu SA, Demirbas N. Microwave assisted synthesis of some hybrid molecules derived from norfloxacin and investigation of their biological activities, European Journal of Medicinal Chemistry. 2013; (67): 230-242. DOI: 10.1016/j.ejmech.2013.06.045.

3. Bayrak H, Demirbas A, Karaoglu SA, Demirbas N. Synthesis of some new 1,2,4-triazoles, their Mannich and Schiff bases and evaluation of their antimicrobial activities. Eur. J. Med. Chem. 2009; (44): 1057-1066. DOI: 10.1016/j.ejmech.2008.06.019.

4. Ulusoy-Guzeldemirci N, Kuçukbasmacı O. Synthesis and antimicrobial activity evaluation of new 1,2,4-triazoles and 1,3,4-thiadiazoles bearing imidazo2,1-bthiazole moiety. Eur. J. Med. Chem. 2010; (45): 63-68. DOI: 10.1016/j.ejmech.2009.09.024.

5. Bayrak H, Demirbas A, Demirbas N, Karaoglu SA. Synthesis of some new 1,2,4-triazoles starting from isonicotinic acid hydrazide and evaluation of their antimicrobial activities. Eur. J. Med. Chem. 2009; (44): 4362-4366. DOI: 10.1016/j.ejmech.2009.05.022.

6. Tozkoparan B, Küpeli E, Yesilada E, Ertan M. Preparation of 5-aryl-3-alkylthio-l,2,4-triazoles and corresponding sulfones with antiinflammatorial analgesic activity. Bioorg. Med. Chem. 2007; (15): 1808-1814. DOI: 10.1016/j.bmc.2006.11.029.

7. Stefanska J, Szulczyk D, Koziol AE, Miroslawc B, Kedziersk E, Fidecka S, Busonera B, Sanna G, Giliberti G, Colla PL, Struga M, Disubstituted thiourea derivatives and their activity on CNS: synthesis and biological evaluation. Eur.J. Med. Chem. 2012; (55): 205-213. DOI: 10.1016/j.ejmech.2012.07.020.

8. Kumar GVS, Rajendraprasad Y, Mallikarjuna BP, Chandrashekar SM, Kistayya C, Synthesis of some novel 2-substituted-5-isopropylthiazoleclubbed 1,2,4-triazole and 1,3,4-oxadiazoles as potential antimicrobial and antitubercular agents. Eur. J. Med. Chem. 2010; (45): 2063-2074. DOI: 10.1016/j.ejmech.2010.01.045.

9. Küçükgüzel I, Tatar E, Küçükgüzel SG, Rollas S, Clercq ED. Synthesis of some novel thiourea derivatives obtained from 5-(4-aminophenoxy)methyl-4-alkyl/aryl-2,4-dihydro-3H-1,2,4-triazole-3-thiones and evaluation as antiviral/anti-HIV and anti-tuberculosis agents. Eur. J. Med. Chem. 2008; (43): 381-392. DOI: 10.1016/j.ejmech.2007.04.010.

10. Rashid M, Husain A, Siddiqui AA, Mishra R. Benzimidazole clubbed with triazolo-thiadiazoles and triazolo-thiadiazines: new anticancer agents. Eur. J.Med. Chem. 2013; (62): 785-798. DOI: 10.1016/j.ejmech.2012.07.011.

11. Johnsona E, Espinel-Ingroff A, Szekelya A, Hockeyc H, Troked P. Activity of voriconazole, itraconazole, fluconazole and amphotericin B in vitro against 1763 yeasts from 472 patients in the

voriconazole phase III clinical studies. Int. J. Antimicrob. Agents 2008; (32): 511-514. DOI: 10.1016/j.ijantimicag.2008.05.023.

12. Guo Q, Feng LS, Liu ML, Zhang YB, Chai Y, Lv K, Guo HY, Han LY. Synthesis and in vitro antibacterial activity of fluoroquinolone derivatives containing 3-(N0-alkoxycarbamimidoyl)-4-(alkoxyimino) pyrrolidines. European Journal of Medicinal Chemistry. 2010; (45): 5498-5506. DOI: 10.1016/j.ejmech.2010.08.050.

13. Cui SF, Ren Y, Zhang SL, Peng XM, Damu GLV, Geng RX, Zhou CE. Synthesis and biological evaluation of a class of quinolone triazoles as potential antimicrobial agents and their interactions with calf thymus DNA. Bioorganic & Medicinal Chemistry Letters. 2013; (23): 3267–3272. DOI: 10.1016/j.bmcl.2013.03.118.

14. Kaur K, Kumar V, Gupta GK. Trifluoromethylpyrazoles as anti-inflammatory and antibacterial agents. Journal of Fluorine Chemistry. 2015; (178): 306–326. DOI: 10.1016/j.jfluchem.2015.08.015.

15. Rahim F, Zaman K, Ullah H, Taha M, Wadood A, Javed MT, Rehman W, Ashraf M, Uddin R, Uddin I, Asghar H, Khan AA, Khan KM. Synthesis of 4-thiazolidinone analogs as potent in vitro anti-urease agents. Bioorganic Chemistry. 2015; (63): 123–131. DOI: 10.1016/j.bioorg.2015.10.005.

16. Bala S, Sharma N, Kajal A, Kamboj S and Saini V. Mannich Bases: An Important Pharmacophore in Present Scenario. International Journal of Medicinal Chemistry. 2014; DOI: 10.1155/2014/191072.

17. Oloyede GK, Willie IE, Adeeko OO. Synthesis of Mannich bases: 2-(3-Phenylaminopropionyloxy)-benzoic acid and 3-Phenylamino-1-(2,4,6-trimethoxy-phenyl)-propan-1-one, their toxicity, ionization constant, antimicrobial and antioxidant activities. Food Chemistry. 2014; (165): 515–521. DOI: 10.1016/j.foodchem.2014.05.119.

18. Abuo-Rahma G.A.A, Sarhan H.A, Gad G.F.M. Design, synthesis, antibacterial activity and hysicochemical parameters of novel N-4-piperazinyl derivatives of norfloxacin. Bioorg. Med. Chem. 2009; (17): 3879-3886.DOI: 10.1016/j.bmc.2009.04.027.

19. Dixit S. K, Yadev N, Kumar S, Good L, Awasthi K, Synthesis and antibacterial activity of novel fluoroquinolone analogs, Medicinal Chem Research 2014; (23): 5237-5249. DOI: 10.1007/s00044-014-1049-2.

20. Basoglu S, Yolal M, Demirbas A, Bektas H, Abbasoglu R, Demirbas N. Synthesis of linezolid-like molecules and evaluation of their antimicrobial activities. Turk. J. Chem. 2012; (36): 37–53. URL: http://journals.tubitak.gov.tr/chem/issues/kim-12-36-1/kim-36-1-3-1105-54.pdf.

21. Demirci S, Demirbas A, Ulker S, Alpay-Karaoglu S, and Demirbas N. Synthesis of Some Heterofunctionalized Penicillanic Acid Derivatives and Investigation of Their Biological Activities. Arch. Pharm. Chem. Life Sci. 2014; (347): 200–220. DOI: 10.1002/ardp.201300280.

22. Willanova, P. A. National Committee for Clinical Laboratory Standard, NCCLS Document M7-A3, 1993; 13.

Türkçe Öz ve Anahtar Kelimeler
Antimikrobiyal Araçlar Olarak Yeni Florokinolin-Triazol Hibrit Bileşiklerinin Sentezi

Serap Başoğlu Özdemir

Öz: Hidrazid bileşiği (**2**) 1-(2-florofenil)piperazin bileşiğinden iki kademede sentezlenmiştir. Bileşik (**2**)'nin farklı alkil (aril) izotiyosiyanatlarla muamele edilmesi ile (**3a-c**) bileşikleri elde edilmiştir. 1,3-Tiyazolidin türevleri (**4a-c**), (**3a-c**) bileşiklerinin etil bromoasetat ile reaksiyonundan sentezlenmiştir. Mannich bazları (**6a-d**), (**5a-c**) bileşiklerinin formaldehit varlığında çeşitli uygun aminlerle tepkimeye sokulmasıyla elde edilmiştir. Bileşik (**3**) türevleri, florokinolon analogları (**11a-c**) için başlangıç bileşiği olması amacıyla 1,2,4-triazol halkalarına dönüştürülmüştür. Son olarak, sentezlenmiş bileşiklerin biyolojik özellikleri incelenmiş ve bunların bazıları kuvvetli etki göstermiştir.

Anahtar kelimeler: Florokinolin; 1,2,4-triazol; mannich bazı; biyolojik özellikler.
Sunulma: 23 Haziran 2016. **Kabul:** 07 Ekim 2016.

534

Determination of Cocaine and Benzoylecgonine in Biological Matrices by HPLC and LC-MS/MS

Zinar Pinar Gumus[1*], Veysel Umut Celenk[2], Emine Güler[1,4], Bilal Demir[4], Hakan Coskunol[1,3], Suna Timur[1,4]

[1]University of Ege, Institute on Drug Abuse, Toxicology and Pharmaceutical Sciences, 35040, İzmir, Turkey
[2]University of Ege, Faculty of Science, Department of Chemistry, 35100, İzmir, Turkey.
[3] University of Ege, Faculty of Medicine, Department of Psychiatry, 35040, İzmir, Turkey
[4] University of Ege, Faculty of Science, Department of Biochemistry, 35100, İzmir, Turkey.

Abstract: Cocaine is a powerfully addictive illicit drug. Cocaine abuse and addiction continue to increase in the world. Most analytical tests for the detection of cocaine use include the analysis of the metabolite, benzoylecgonine, in the urine. Benzoylecgonine is a major urinary metabolite of cocaine. Generally, the most common biologic matrices used for the analysis of cocaine contain the urine and blood however saliva was also added as a matrix in this study. Practical, quick, reliable, precise and accurate, reproducible analytical methods have been developed and validated for cocaine and benzoylecgonine. In addition, these chromatographic techniques were used as both initial test and confirmatory. The validated chromatographic method was successfully applied to the analysis of cocaine and benzoylecgonine compounds in synthetic matrix. Confirmation analyses were made by LC-MS/MS to support reliability of HPLC results. As a result of this study, it can be claimed that HPLC could be a good alternative for the analyses of various biological matrices in forensic studies.

INTRODUCTION

Cocaine is a strongly addictive stimulant drug made from the leaves of the coca plant. Cocaine is directly affected the central nervous system (CNS) [1]. Cocaine was labelled as the drug of the 1980s and 1990s because of its widespread popularity and use during that period. However, cocaine is not a new drug. Actually, it is one of the oldest known psychoactive substances [2]. Cocaine consist in illicit samples as the cocaine salt or as the cocaine base. The use of illicit drugs has negative effect on the health of drug users in addition to this drugs have been affected economic and social costs to the community [3]. Cocaine has a lot of health effects, which are constriction of blood vessels, increase of bodily temperature, heart rate, blood pressure, abdominal pain, nausea, headaches, restlessness, and anxiety [4,5]. Injecting cocaine can do strong allergic reactions and increased risk for HIV, hepatitis C, and other blood-spread diseases [1]. According to United Nations Office on Drugs and Crime (UNODC) World Drug Report, it is estimated that one-twentieth of people between the ages of 15 and 64 used illicit drugs within the last year [6]. In addition, there are 14.9 million cocaine users according to the last European Monitoring Centre for Drugs and Drug Addiction (EMCDDA) annual report [7].

The most common form of illicit cocaine is the white crystalline, highly water soluble powder. Cocaine metabolites such as norcocaine, benzoylecgonine (BE) and ecgonine methylester, *etc.*, contribute to the toxicity of cocaine (metabolite). The major metabolic pathways of cocaine metabolism involve 1) human carboxylesterase-1 (hCE-1)–mediated and spontaneous chemical hydrolysis of cocaine to BE and 2) pseudocholinesterase–2 and human carboxylesterase-2 (hCE-2)-mediated hydrolysis of cocaine to ecgonine methyl ester [8]. BE is a major urinary metabolite of cocaine.

Among the worldwide addiction problems, cocaine addiction is a frequent and severe public health problem; therefore, quick, easy, and reliable methods are required to determine of cocaine and BE in the biological matrix for medical and toxicology laboratories [9]. Most chromatographic methods for the detection of cocaine use involve the analysis of the metabolite, BE, in the biological matrix such as urine, serum and saliva. Liquid chromatography is a very powerful tool increasingly used in analytical laboratories [10]. Cocaine and its metabolite BE can be separated by using chromatographic methods from other analytes and impurities. Therefore, liquid chromatographic techniques were used in this study for better determination of cocaine and also chromatographic techniques are very specific, minimizes false positives and false negatives, very sensitive, detects low levels of drug, and quantitative testing methods [11-13]. Cut off concentrations of cocaine and BE were identified by Substance Abuse and Mental Health Services Administration (SAMSHA) as 150 ng/mL and 100 ng/mL for initial test and confirmatory test, respectively [14]. Generally, the most common biologic samples used for the analysis of

cocaine involve the blood and urine however saliva was also added as a matrix in this study. Practical, quick, reliable, precise and accurate, reproducible analytical methods have been developed and validated for cocaine and benzoylecgonine. In addition, these chromatographic techniques were used both initial test and confirmatory test for forensic toxicology. After analytical method validation, its application to biological samples was tested by using synthetic urine, serum and saliva. Confirmation analyses were made by LC-MS/MS to support reliability of HPLC results.

MATERIALS AND METHODS

Standards, samples, chemicals, and reagents All chemicals and reagents was obtained from Merck, Sigma Aldrich and LabScan. Ultrapure water was produced by purification system Milli-Q from Millipore Corporation. The analytical standard of cocaine and benzoylecgonine were obtained from Cerillant.

Standard solutions

Stock solutions of cocaine and benzoylecgonine were prepared separately in methanol at concentrations of 100 μg/mL. All stock solutions were stored at -20 ˚C. Different concentrations of working solutions for liquid chromatography analysis were diluted from this solution with methanol.

Sample preparation

Synthetic urine, saliva, and serum samples were prepared according to the Wilsenach *et al.,* Gal *et al.,* and Bahadir *et al.* and the compositions of synthetic urine, saliva, and serum solutions are given in supplementary material SM-1 [15-17]. The synthetic biological matrices were spiked with standard solutions of Cocaine and BE and then filtered before injection into the chromatographic system. The samples were prepared freshly prior to chromatographic analyses. Cocaine or BE spiked samples were injected to the chromatography system without needing any extraction procedures.

HPLC-DAD instrumentation and conditions

The chromatographic separation and analysis of cocaine and BE were carried out using HPLC (Agilent) combined DAD detector and the elution of the compounds in the chromatogram was

performed by an Eclipse XDB-C18 column (5.0 µm particle size, 4.6x150 mm). Instrument parameters was given in Table 1 for the Cocaine and BE analyses.

Table 1. HPLC instrument conditions of cocaine and BE

HPLC Instrument Conditions	COCAINE	BE
Mobile Phase	Isocratic; (A) pH 6.0 phosphate buffer (B) acetonitrile (40:60, v:v)	Isocratic; (A) 0.2% (v/v) aqueous phosphoric acid and (B) acetonitrile (80:20, v:v)
Wavelength	235 nm	225 nm
Column Temperature	40 °C	35 °C
Flow rate	1.0 mL/min	1.0 mL/min
Injection Volume	20 µL	20 µL

LC-MS/MS instrumentation and conditions

The LC-MS/MS system consisted of a Waters Acquity UPLC instrument using an Acquity UPLC BEH C18 column (1.7 µm, 50 mm x 2.1 mm i.d.). The UPLC was connected to Waters TQD Mass Spectrometer. Tandem mass spectrometer was equipped with an electrospray ionization (ESI) and operated in positive-ion mode. The scanned data was collected in single ion monitoring mode (SIM). Nitrogen and argon were used as cone and collision gases, respectively. LC-MS/MS instrument parameters for the analysis of Cocaine and BE were shown in Table 2.

Table 2. LC-MS/MS instrument conditions of Cocaine and BE

LC-MS/MS Instrument Conditions	COCAINE	BE
Mobile Phase	A) Water contains 0.1 % Acetic Acid B) Acetonitrile contains 0.1 % Acetic Acid	A) Water contains 0.1 % Acetic Acid B) Acetonitrile contains 0.1 % Acetic Acid
Cone Voltage (V)	35	30
Collision Voltage (V)	25	30
Parent Ion/Daughter Ions (m/z)	304/150, 182*	290.3/105.3, 168.3*
Dwell Time (s)	0.01	0.01
Column Temperature (°C)	50	50
Desolvation Gas Temp. (°C)	350	350
Gas Flow Rate (L/h)	500L/h	500L/h
Flow rate (mL/min)	0.400	0.400
Injection Volume (µL)	5	5

*Daughter ions were used as determinant ions. The others were used as control ions.

The Masslynx software version 4.1 was used in controlling the instruments, peak integration and calculation.

Validation of the chromatographic methods

The validation of the analytical procedures was carried out according to the International Conference on Harmonization Guidelines (ICH Q2B, validation of analytical procedures, methodology) [18]. According to these guidelines, the key parameters to assurance the acceptability of the performance of an analytical method are as follows: Linearity, sensitivity (limit of detection (LOD) and limit of quantification (LOQ)), precision and accuracy, selectivity.

RESULTS AND DISCUSSION

Several mobile phase systems were tested for developing liquid chromatographic method for determination of Cocaine and BE. Mobile phase and related chromatographic conditions were chosen considering the smooth baseline, and peak response.

Linearity of the analytical methods

The linearity was studied through the external standardization method. To conduct this study, working standard solutions were prepared at five level of concentration for LC-MS/MS analyses and six levels of concentration for HPLC analyses with triplicate injections. The calibration curves were designed to investigate the correlation between the peak area (y) and the injection concentration (x; ng/mL) of analytes. The linearity was expressed in terms of the correlation coefficient (R^2). The results showed a good correlation between the peak areas and the concentration of chromatographic injections, with R^2. The concentrations ranges, linear regression equations, correlation coefficient and retention times of analytes were given in Table 3.

Table 3. Linear regression equation, calibration curve and retention times of the analytical method.

HPLC method	COCAINE	BE
Linear Ranges (ng/mL)	1.0 – 100	50.0 - 7500
Linear Regression Equation	y=0.3453x-0.0154	y=0.0241x-0.0192
Correlation Coefficient	0.9999	0.9999
Retention Time (min)	2.09	2.67
LC-MS/MS method	**COCAINE**	**BE**
Linear Ranges (ng/mL)	0.25 - 5.0	1.0 - 25
Linear Regression Equation	y=854.18x+7.9587	y=91128x-275.52
Correlation Coefficient	1.00	1.00
Retention Time (min)	1.65	0.90

Both HPLC and LC/MS/MS methods have good correlation coefficient values in terms of linearity. Blank chromatograms for matrices could be seen in SM-3. HPLC chromatograms of cocaine and BE were shown in Figures 1 and 2.
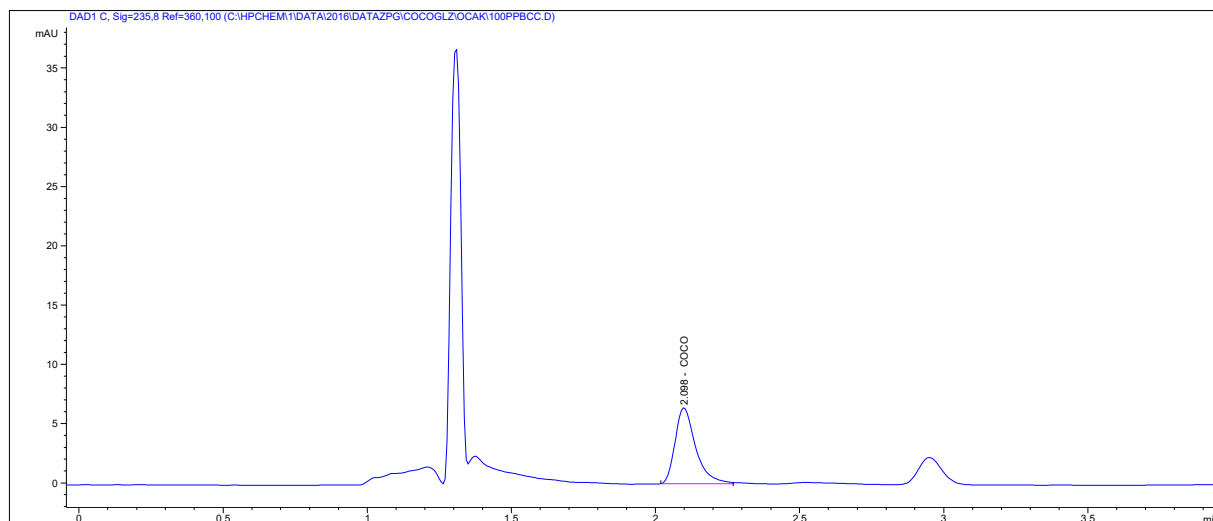
Figure 1. HPLC chromatogram of cocaine.
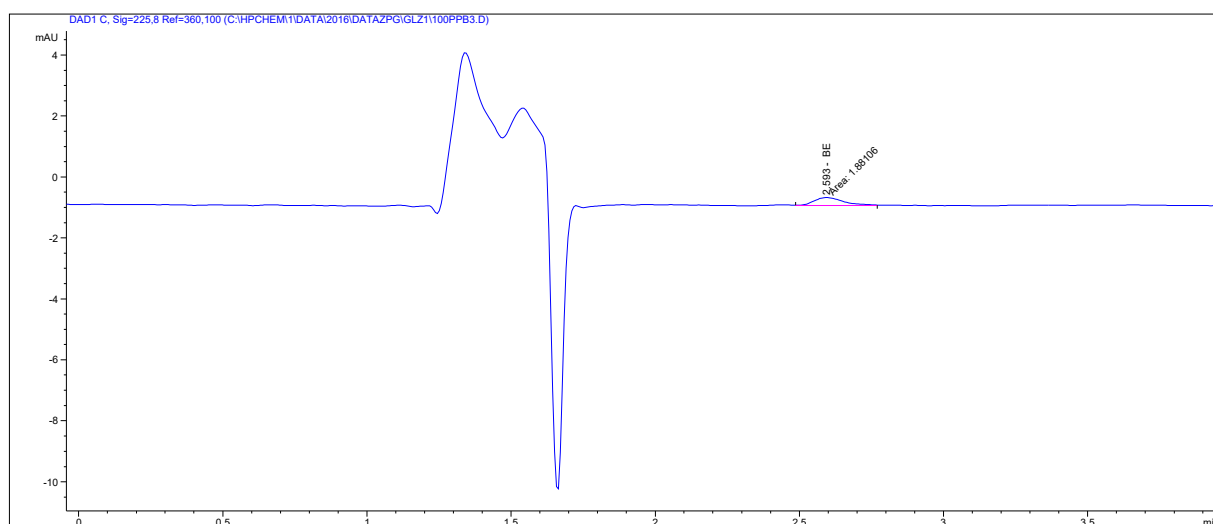
Figure 2. HPLC chromatogram of BE.

m/z 182 and m/z 150 ions chromatogram of cocaine was shown as in Figures 3 and 4.
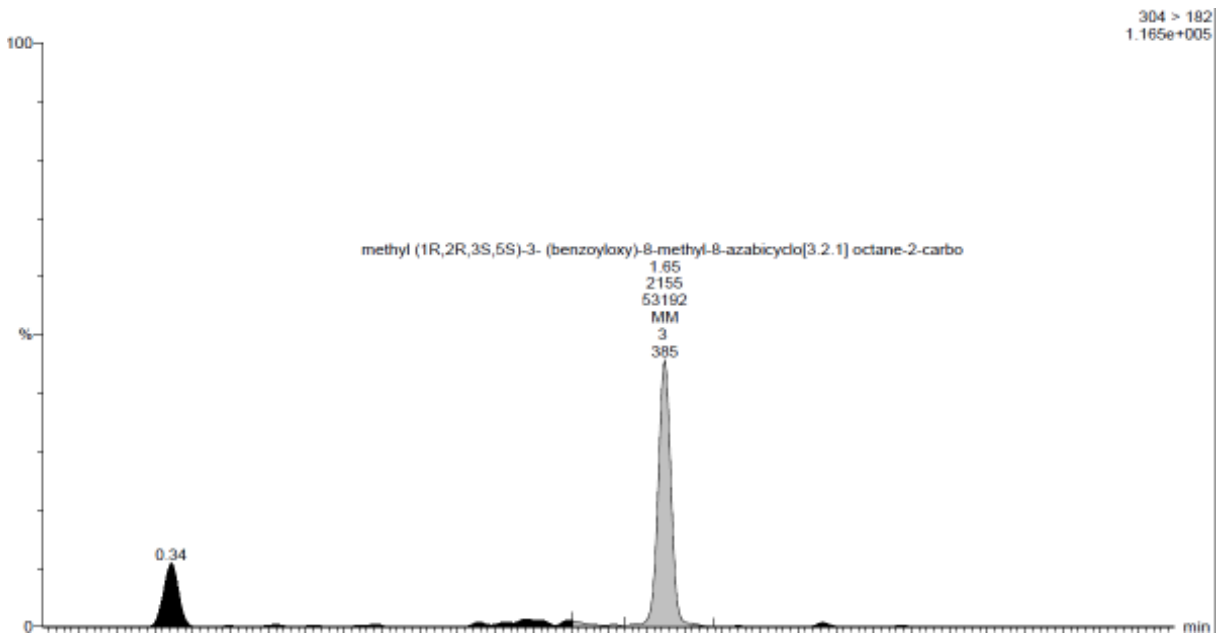
Figure 3. LC-MS/MS chromatogram of cocaine for determinant ion m/z 182.
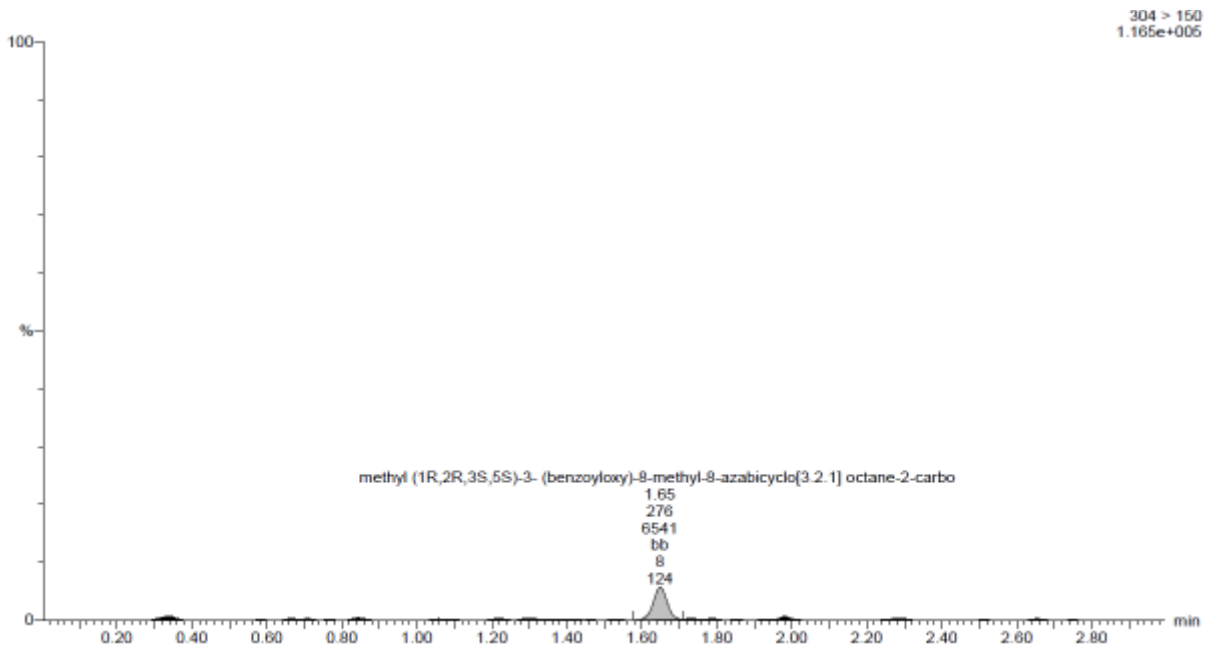
Figure 4. LC-MS/MS chromatogram of cocaine for control ion m/z 150.

m/z 168.3 and m/z 105.3 ions chromatogram of BE was shown as in Figure 5 and 6.

290.3 > 168.3
8.649e+007

3-Benzoyloxy-8-methyl-8-azabicyclo[3.2.1]octane-4-carboxylic acid
0.90
232013
12667566
MM
3
9381
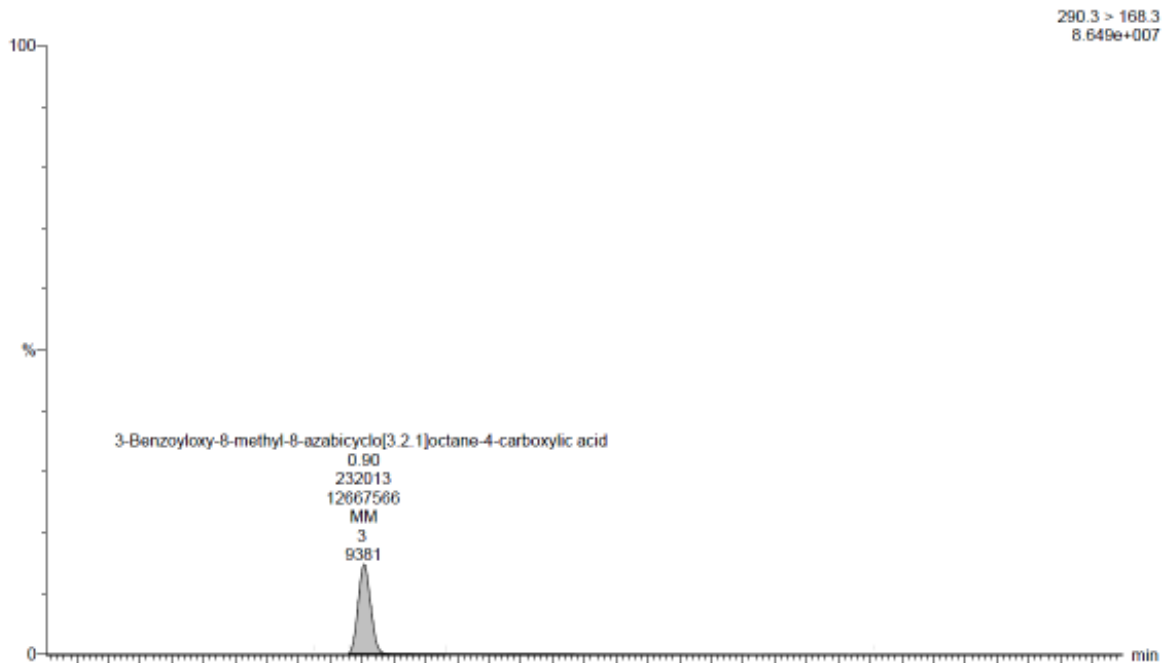
Figure 5. LC-MS/MS chromatogram of BE for determinant ion m/z 168.3.

290.3 > 105.3
8.649e+007

3-Benzoyloxy-8-methyl-8-azabicyclo[3.2.1]octane-4-carboxylic acid
0.90
80314
3373604
bb
3
7657
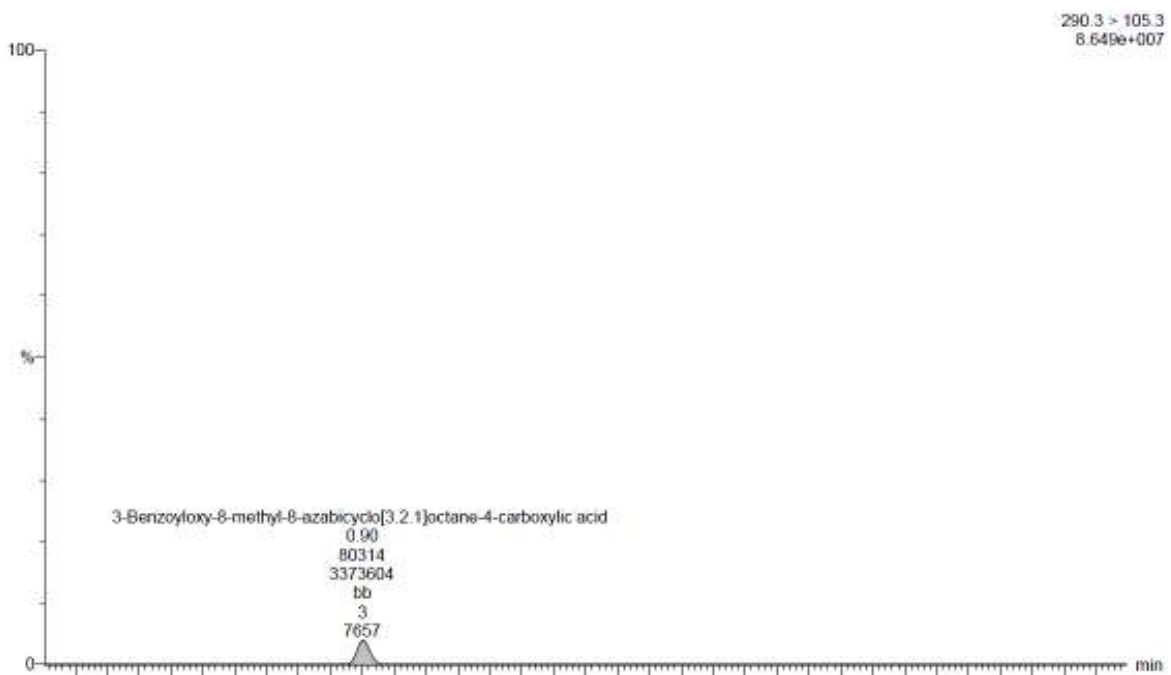
Figure 6. LC-MS/MS chromatogram of BE for control ion m/z 105.3.

Limits of detection (LOD) and quantification (LOQ)

The limit of detection (LOD) and the limit of quantification (LOQ) for Cocaine and BE were analysed to evaluate the sensitivity of the methods. LOD and LOQ of the HPLC and LC-MS/MS

methods were estimated from the signal-to-noise ratio of about 3:1 and 10:1, respectively. LOD and LOQ values of Cocaine and BE were given in Table 4 for HPLC and LC-MS/MS methods.

Table 4. LOD and LOQ values of methods for COCAINE and BE.

HPLC method	COCAINE	BE
LOD (ng/mL)	0.55	4.62
LOQ (ng/mL)	1.82	15.38
LC-MS/MS method	**COCAINE**	**BE**
LOD (ng/mL)	0.03	0.69
LOQ (ng/mL)	0.10	2.33

Since these values are lower than SAMSHAs' cut off values, these chromatographic methods could be used to determine COCAINE and BE in the synthetic biological matrices successfully according to LOD and LOQ values.

Precision of analytical methods

The precision was evaluated using measurements of the injection repeatability of analytes. The repeatability was investigated using working standard solutions prepared at appropriate concentration levels. Cocaine and BE concentrations were 10 ng/mL; 1.0 ng/mL and 500 ng/mL and 5.0 ng/mL for HPLC and LC-MS/MS, respectively. Peak areas and retention times were identified. The results were expressed as the Relative Standard Deviation of measurements (RSD%).at six replicate injections as described in Table 5.

Table 5. Precision of HPLC and LC-MS/MS method.

HPLC method	Cocaine (Area)	BE (Area)	Cocaine (RT)	BE (RT)
Mean	3.382	13.817	2.098	2.673
SD	0.064	0.147	0.003	0.008
RSD %	0.100	1.065	0.162	0.305
LC-MS/MS	**Cocaine (Area)**	**BE (Area)**	**Cocaine (RT)**	**BE (RT)**
Mean	868024	454252686	1.65	0.90
SD	1190	1917980	0.00	0.00
RSD %	0.137	0.422	0.00	0.00

According to RSD values of repeatability, these methods indicated good precision and RSD values which were under the 2%.

Accuracy of analytical methods

The accuracy of the methods was evaluated on the basis of the spiked matrix recovery for each standard substance. The accuracy was expressed as the percentage of the amount recovered in the spiked sample compared to the standard concentrations.

A certain amount of Cocaine and BE standards was added to synthetic serum, saliva and urine samples and then analysed using the developed HPLC and LC-MS/MS methods. The recovery of each added standard substance was calculated by the following formula: recovery% = [(Cm – Cs)/(Ca)] X 100, where Cm is the measured amount of the samples; Cs and Ca represent the mean value of the detected Cocaine and BE in synthetic biological samples and added standard substances, respectively.

Percent recovery values of Cocaine and BE were shown in Table 6 and Table 7 for HPLC and LC-MS/MS methods in synthetic biological matrices.

Table 6. Recovery of HPLC method for urine, saliva, serum.

Added COCAINE (ng/mL)	Recovery (%) (Urine)	Recovery (%) (Saliva)	Recovery (%) (Serum)
1	80.46	42.48	71.69
1	83.38	36.63	83.38
1	77.53	39.56	77.53
5	96.72	38.29	82.12
5	93.80	39.46	87.37
5	95.55	40.05	85.62
10	97.44	40.47	92.18
10	100.36	39.01	89.26
10	97.15	43.10	84.88
Added BE (ng/mL)	**Recovery (%) (Urine)**	**Recovery (%) (Saliva)**	**Recovery (%) (Serum)**
100	91.26	99.89	97.9
100	90.24	98.37	102.9
100	94.30	96.34	98.9
500	92.16	102.41	100.4
500	95.21	99.57	99.06
500	95.41	98.05	97.94
1000	91.21	95.52	99.58
1000	96.08	98.11	100.09
1000	99.84	93.44	99.94

Table 7. Recovery of LC-MS/MS method for urine, saliva, serum.

Added Cocaine (ng/mL)	Recovery (%) (Urine)	Recovery (%) (Saliva)	Recovery (%) (Serum)
0.3	85.2	50.7	94.7
0.3	90.7	47.1	93.4
0.3	90.3	55.0	97.6
0.75	97.1	51.8	107.6
0.75	103.6	59.1	102.8
0.75	102.2	52.5	106.7
1.50	91.1	78.5	101.4
1.50	92.1	73.3	103.1
1.50	101.4	85.2	100.1
Added BE (ng/mL)	**Recovery (%) (Urine)**	**Recovery (%) (Saliva)**	**Recovery (%) (Serum)**
1.00	101.7	102.7	99.2
1.00	96.7	100.4	99.0
1.00	98.2	100.5	98.9
2.50	91.9	101.0	101.3
2.50	92.0	103.5	98.4
2.50	92.0	102.3	97.2
5.00	80.5	100.5	82.4
5.00	82.7	102.9	79.1
5.00	82.1	101.7	80.7

The recoveries of the cocaine ranges were not appropriate in saliva but the others were shown good accuracy for LC-MS/MS method. The RSDs were less than 8.0%, thus representing the good reliability and accuracy of the method as it can be seen SM-2. In addition, some ruggedness and robustness method validation parameters were given in SM-2 for proposed method.

Selectivity of the analytical methods

Solvents, saliva and urine solutions which are used during analysis were injected under same instrument conditions and any peak was monitored at the same retention time with Cocaine and BE. This shows that suitability of HPLC and LC-MS/MS methods in terms of selectivity and there are no interferences from solvents and solution.

CONCLUSION

As a result of this study, it can be claimed that liquid chromatographic techniques could be a good alternative for the analyses of various biological matrices in forensic studies. Practical, quick, precise, and accurate, reproducible analytical methods have been developed and validated for cocaine and BE. Reliable of HPLC method was shown by using LC-MS/MS method as a confirmation analysis. Also the matrices and concentrations were determined by HPLC instrument could be used, where necessary, according to SAMSHA cut off values. In the future studies, extraction procedure would be experienced to increase recovery of saliva matrix.

ACKNOWLEDGMENTS

REFERENCES

1. National Institute on Drug Abuse (NIH), Research Report Series, 2013, Cocaine, www.drugabuse.gov

2. National Institute on Drug Abuse (NIH), Drug Facts,2013, Cocaine, www.drugabuse.gov

3. Guler E., Bozokalfa G., Demir B., Gumus ZP., Guler B., Aldemir E., Timur S., Coskunol H., 'An Aptamer Folding based Sensory Platform' Decorated with Nanoparticles for Simple Cocaine Testing, Drug Testing and Analysis 2016 Jun, doi: 10.1002/dta.1992

4. Donald G. Barceloux Robert B. Palmer (Editor), Medical Toxicology of Drug Abuse, Synthesized Chemicals and Psychoactive Plants, 2012, Wiley, 805-885 p. ISBN: 978-0-471-72760-6

5. Mackey-Bojack S., Kioss J., Apple F. Cocaine, cocaine metabolite, and ethanol concentrations in postmortem blood and vitreous humor. J. Anal. Toxicol. 2000 Jan/Feb, 24, 59-65. URL: http://jat.oxfordjournals.org/content/24/1/59.long

6. United Nations Office on Drugs and Crime. World Drug Report. United Nations, New York, 2015. https://www.unodc.org/documents/wdr2015/World_Drug_Report_2015.pdf

7. European Monitoring Centre for Drugs and Drug Addiction. European drug report 2014: Trends and developments. Publications Office of the European Union, Luxembourg, 2014. http://www.emcdda.europa.eu/system/files/publications/963/TDAT14001ENN.pdf

8. Kolbrich EA., Barnes AJ., Gorelick DA., Boyd SJ., Cone EJ., and Huesfis MA. Major and Minor Metabolites of Cocaine in Human Plasma following Controlled Subcutaneous Cocaine Administration, J. Anal. Toxicol, 2006 Oct, 30, 501-510. URL: http://jat.oxfordjournals.org/content/30/8/501.long

9. Cone EJ, Tsadik A, Oyler J, Darwin WD. Cocaine metabolism and urinary excretion after different routes of administration. Therapeutic Drug Monitoring 1998 Oct; 20(5), 556 – 560. URL: http://journals.lww.com/drug-monitoring/Abstract/1998/10000/Cocaine_Metabolism_and_Urinary_Excretion_After.19.aspx.

10. Bozokalfa, G, Akbulut, H; Demir, B, Guler, E, Gumus, ZP, Odaci Demirkol, D, Aldemir, E, Yamada, S, Endo, T, Coskunol, H, Timur, S, Yagci, Y. A polypeptide functional surface for the aptamer immobilization: Electrochemical cocaine bio-sensing, Analytical Chemistry, 2016 Mar, 88(7), 4161–4167. DOI: http://dx.doi.org/10.1021/acs.analchem.6b00760

11. Hiemke C. Baumann P. Bergemann N. Conca A. Dietmaier O. Egberts K. et al. The AGNP Consensus Guidelines for Therapeutic Drug Monitoring in Psychiatry: Update 2011, Pharmacopsychiatry, 2011, 44 (06), 195-235. DOI: 10.1055/s-0031-1286287

12. Urine drug testing in the management of chronic pain. URL: https://www.drugabuse.gov/sites/default/files/files/UrineDrugTesting.pdf.

13. Gourlay DL Heit HA. Caplan, YH. Urine Drug Testing in Clinical Practice. 2010, 1-24. URL: http://www.pharmacomgroup.com/udt/udt5.pdf

14. Analytes and Their Cutoffs, 2010, URL: http://www.samhsa.gov/sites/default/files/workplace/2010GuidelinesAnalytesCutoffs.pdf

15. Wilsenach, JA.; Schuurbiers, CAH.; Van Loosdrecht, MCM. Phosphate and Potassium Recovery from Source Seperated Urine through Struvite Preparation. Water Research. 2007, 41, 458−466. DOI: http://dx.doi.org/10.1016/j.watres.2006.10.014.

16. Gal, JY.; Fovet, Y.; Adib-Yadzi, M. About a Synthetic Saliva for in vitro Studies. Talanta 2001 Mar, 53 (6), 1103−1115. DOI: http://dx.doi.org/10.1016/S0039-9140(00)00618-4.

17. Bahadır EB., Sezgintürk MK., A comparative study of short chain and long chain mercapto acids used in biosensor fabrication: A VEGF-R1-based immunosensor as a model system. Artificial Cells, Nanomedicine, and Biotechnology, 2016, 44(2), 462-470. DOI: 10.3109/21691401.2014.962743

18. 18.ICH, International Conference on Harmonization Guidelines (ICH Q2B, validation of analytical procedures, methodology). http://www.ich.org/products/guidelines/quality/quality-single/article/validation-of-analytical-procedures-text-and-methodology.html

Biyolojik Ortamlarda Kokain ve Benzoilekgoninin HPLC ve LC–MS/MS ile Analizi

Öz: Yasadışı ve bağımlılık yapan bir kimyasal olan kokainin kötüye kullanımı ve bu ilaca olan bağımlılık dünya çapında artmaya devam etmektedir. Birçok analitik test kokainin idrardaki ana metaboliti olan benzoilekgoninin idrar içersinde analizine yöneliktir. Bu çalışmada kokainin idarar ve kandaki analizinin yanısıra tükürükte de analizi gerçekleştirilmiştir. Kokain ve benzoilekgonin için pratik, hızlı, güvenilir, kesin, doğru ve tekrarüretilebilir metotlar geliştirilmiş ve valide edilmiştir. Ayrıca, bu kromatografik teknikler hem başlangıç hem de doğrulayıcı testler olarak uygulanmıştır. Valide edilmiş olan kromatografik metotlar sentetik ortamlar içerisindeki kokain ve benzoilekgonin bileşiklerine başarılı bir şekilde uygulanmıştır. Doğrulama analizleri HPLC sonuçlarını desteklemek amacıyla LC-MS/MS cihazında yapılmıştır. Sonuç olarak, birçok matriks için uygulanan adli çalışmalarda HPLC'nin iyi bir alternatif olduğu gösterilmiştir.

Anahtar Kelimeler: Kokain; Benzoilekgonin; HPLC; LC-MS/MS.

Biosorption of Methylene Blue from Aqueous Solutions by Iron Oxide-Coated *Cystoseira barbata*

Yeliz Özüdoğru[1], Melek Merdivan[2], Tolga Göksan[1]

[1]Çanakkale Onsekiz Mart University, Faculty of Marine Sciences and Technology, Çanakkale, Turkey

[2]Dokuz Eylül University, Faculty of Sciences, Department of Chemistry, İzmir, Turkey

Abstract: In this study, *Cystoseira barbata* was coated with iron oxide (Fe_3O_4) to obtain a magnetic biomaterial and used as a sorbent material for the removal of methylene blue from aqueous solution. This biosorbent was characterized by Scanning Electron Microscopy (SEM) and Fourier Transform Infrared spectroscopy (FTIR). Methylene blue adsorption capacity of this material was investigated as function of pH, contact time, initial methylene blue concentration and temperature. The equilibrium data was analyzed with Langmuir and Freundlich isotherms. The results showed that the maximum adsorption capacities were achieved in 300 min at pH 2 and reached to 5.74 and 1.08 mg/g at 25 ºC and 45 ºC respectively.

Keywords: Methylene blue, biosorption, *C. barbata,* iron oxide-coating.

INTRODUCTION

Industrial and environmental pollutants mostly cause water pollution [1] and one of the most important pollutants is coloring agents. The synthetic dyes are in general toxic and can cause serious environmental problems [2, 3]. Dyes are mainly used in textile, plastics, tanneries, pharmaceuticals, leather, paint, and electroplating industries [4]. For example, methylene blue (MB), a common type of colorants, are usually used to dye cotton, wool and other materials [1, 5]. Several methods such as biosorption, chromatography, membrane separation, and ion exchange have been tested for the removal of dyes since they have destructive effect on aquatic life and human body [6-8]. The use of magnetic separation in biosorption process has increased in the last decades [9, 10]. This procedure might be problematic on biomass separation. Magnetic sorbents, following the adsorption procedure, simplify the separation of sample solutions from sorbents and no centrifugation is needed. Therefore, magnetic separation method, which is simple, fast, energy efficient and low cost, was used in the study [11-12].

Many kinds of adsorbents such as fruit peels, potato plant wastes and dried algae have been tested for the removal of the pollutants [13, 14]. In addition, tremendous developments have occurred in nanoparticle technology in the past decade. Magnetic nanoparticles, which generally consist of magnetic elements such as iron, nickel, and cobalt [15], have potential applications in some fields such as biotechnology/biomedicine and environmental remediation [12]. Magnetite (Fe_3O_4) is a common compound used for the synthesis of magnetic nanoparticles [16], especially for that of algae [10]. Algae have been shown to be proper biosorbents because of the functional groups such as amino, carboxyl, hydroxyl, and sulfate on the cell wall [17]. Brown algae are the renewable biomass used in many parts of the world [3]. *Cystoseira barbata*, a brown alga, has air vesicles and the biomass can be used in different areas such as food, medical, and pharmacological applications [18].

The aim of this work is to inquire the potential of iron-coated *C. barbata* for the removal of MB from aqueous solution. The effects of pH, contact time, concentration of MB solution and temperature were investigated on the biosorption of the alga. The data were fit to Langmuir and Freundlich isotherm models. SEM and FTIR analyses were utilized to compare the surfaces of raw and iron-oxide coated *C. barbata*.

MATERIALS AND METHODS

Biomass: Brown alga *Cystoseira barbata* (Stackhouse) C. Agardh was collected from the Dardanos Campus of Çanakkale Onsekiz Mart University. The biomass was rinsed to remove some impurities and dried in an oven at 60 °C until constant weight was reached. Dried biomass was ground and sieved.

Iron Oxide-Coated Biomass

The method proposed by Pokhrel and Viraraghavan (2008) was used for the preparation of magnetic biosorbent. A solution of 80 mL of 2 M $Fe(NO_3)_3.9H_2O$ was prepared and 1 mL of 10 M NaOH was added into this solution and mixed. The autoclaved *C. barbata* (20 g) and the mixture was poured into the porcelain pot, homogenized and kept at 80ºC for 3 h. The oven temperature was then increased to 110 ºC for 24 h. The prepared biosorbent powder was sieved to same particle size. The magnetic *C. barbata* was labeled as "Mag-*C. barbata*" in this study*.*

Reagents and Equipment

All chemicals used were of analytical grade (Merck). All the solutions were prepared with distilled water. For biosorption experiments, stock methylene blue (MB) solution (1000 mg/L) was used and different concentrations of MB (5, 10, 20, 50, 100, 150, 200, 250, 300, 350, 400, 450 and 500 mg/L) were prepared from stock solution using distilled water. The MB concentration in the solution was measured with a spectrophotometer (Rayleigh Vis-7220 G). The pH of aqueous solutions was adjusted using 0.1 M HCl or 0.1 M NaOH. The samples were filtered through Millipore Millex-HV hydrophilic PVDF 0.45 µm syringe filter. A Wise Bath WSB-30 model shaker was used for the adsorption experiments.

Biosorption Experiments

Batch adsorption technique was used to assess the adsorption of MB from the aqueous solution. Mag-*C. barbata* (100 mg) was put into a 50 mL falcon tube and treated with 10 mL of a MB solution. All the biosorption experiments were carried out using 10 mL aqueous MB solutions. The test solutions were shaken at 250 rpm at room temperature for 60 min, centrifuged at 3000 rpm and the supernatants were filtered through the

syringe filter. The adsorbed amount of MB was calculated following the spectrophotometric measurement of supernatant at 665 nm.

Determination of Optimum pH

Five pH values (2, 3, 5, 7 and 9) were tested in the trials. Accordingly, 100 mg dried Mag-*C. barbata* was put into the Falcon tubes filled with 10 mg/L MB solutions at different pH values. The tubes were shaken at room temperature for 60 min at 250 rpm. After adsorption step, sorbents easily came together by means of a magnet kept from outside of the tube and supernatant is simply taken out by a syringe. The absorbance value of the supernatant was measured with the spectrophotometer and the amount of adsorbed methylene blue was calculated.

The percentage of MB removal (*R*) from the aqueous solution was calculated as follows:

$$\% \ R = \frac{(C_o - C_s)}{C_o} \times 100 \tag{Eq. 1}$$

Where C_o is the initial MB concentration (mg/L) and C_s is the adsorbed MB concentration (mg/L).

Determination of Optimum Contact Time: Mag-*C. barbata* (100 mg) was added into 10 mL of MB (10 mg/L) solution and the pH was adjusted to 2. Falcon tubes were shaken at room temperature for different time intervals (10, 25, 45, 60, 80, 100, 150, 200, 300 and 400 min). Samples were centrifuged, filtered, and the absorbance of the supernatant was measured with the spectrophotometer. The amount of MB uptake, qt (mg/g), at each interval was calculated using the following equation:

$$q_t = \frac{(C_o - C_e)}{M} \times V \tag{Eq. 2}$$

Where C_o is the initial MB concentration (mg/L), C_e is the concentration of MB solution at a given time (mg/L), *V* is the volume of metal solution (L) and *M* is the mass of biosorbent (g) (dry weight).

Adsorption Isotherms: A 10 mL MB test solutions (pH 2) were prepared at different concentrations (5, 10, 20, 50, 75, 100, 150, 200 and 300 mg/L) and added into the Falcon tubes each containing 100 mg Mag-*C. barbata*. The test solution was shaken for

200 min at 25°C and 45°C. The amount of MB concentration was calculated using Eq. (2). In Eq. (2), q_t is substituted with q_e.

Characterization of Biomass: FTIR spectra were obtained using Perkin-Elmer FTIR Spectrometer (Spectrum BX-II). The biomass was dried at 60°C to the constant weight; 1 mg of *C. barbata* was then pelleted with 100 mg KBr. FTIR analysis was studied in the range 400-4000 cm^{-1} for the characterization of biomass.

Morphological features of algal biosorbent particles before and after the adsorption of MB were obtained using the Scanning Electron Microscope (Jeol JSM 7100F) at accelerating voltages of 10 kV attached to an X-ray energy dispersive spectrometer (EDX). Before the scanning process, all samples were dried and coated with gold to enhance electron conductivity. In this study, SEM micrographs were taken at different magnifications.

RESULTS AND DISCUSSION

Determination of Optimum pH

Algal cell surfaces have several functional groups such as amino, carboxyl, and phosphate groups. The biosorption mechanism depends on these functional groups on the surface of the cell wall and the solution pH is important in the process [19]. The effect of pH was studied in the pH range of 2-9 at room temperature. The effect of the pH values on biosorption were shown in Figure 1. It was found that the removal percentage decreased by the increase in pH from 2 to 5, remained stable at pH 5 and 7, and then started to increase again until pH 9. However, the pH was in general not so important on the biosorption of MB by Mag-*C. barbata*. The maximal removal was 40.61% at pH 2. The surface of the algae is negatively charged and the strength of the negative charge is higher on acidic zone. Under normal conditions, the strength of the negative charge of adsorbent decreases in lower pH values, which also results in a reduction on the adsorption potential of positively charged ions. When the non-magnetic algae are treated with iron, an electrostatic interaction takes place between positive (Fe^{2+}) and negative (algal surface) charges. In the case of algae magnetized with iron, however, Van der Waals interaction takes place. In our opinion, the type of the

interaction was the main reason as to why the adsorption capacity of the magnetic algae was independent from the pH changes.
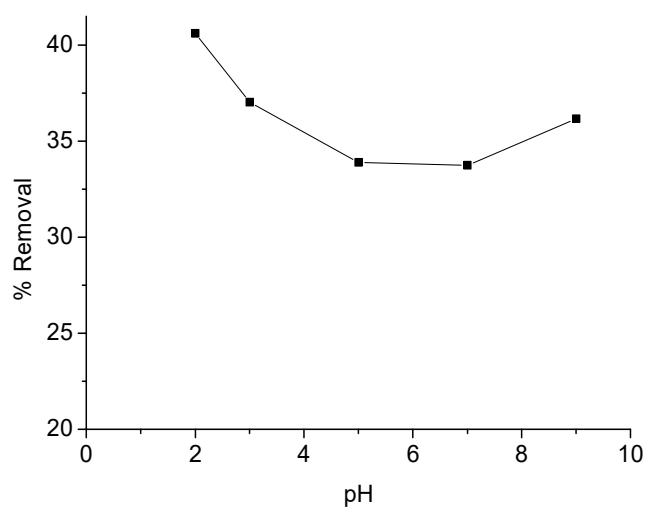
Figure 1. Effect of pH on the biosorption of MB.

Determination of Optimum Contact Time

The effect of contact time for MB biosorption onto Mag-*C.barbata* was studied at two different temperatures (Figure 2). The results showed that the q_t value increased in parallel to the rise in temperature. The adsorption reached to equilibrium within 300 min at both temperatures. The biosorption capacity became stable at 0.57 and 0.71 mg/g for the temperatures 25 ºC and 45 ºC, respectively.
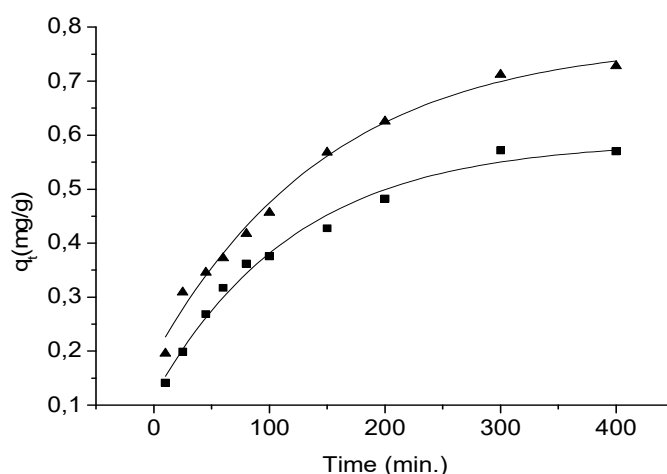
Figure 2. Effect of contact time on the biosorption of MB at 25 ºC (■) and 45 ºC (▲).

Adsorption Isotherms

Several isothermal models are used to determine the relationship between q_e and C_e. In the study, the equilibrium data were analyzed with Langmuir and Freundlich isotherms at different temperatures. The monolayer of the adsorbate on the adsorbent surface was predicted with the Langmuir model while the multi-layer adsorption isotherm, the Freundlich model, was applied to the heterogeneous surfaces. The Langmuir was shown below [20]:

$$\frac{C_e}{q_e} = \frac{1}{q_m a_L} + \frac{C_e}{q_m}$$

(Eq. 3)

Where q_e is the amount of adsorbent (mg/g), C_e is the equilibrium concentration of the MB solution (mg/L), q_m is the maximum adsorption capacity and a_L is the Langmuir constant related to the energy of adsorption.

A linear form of the Freundlich equation was shown below [21]:

$$log\ q_e = log\ K_f + 1/\ n\ log\ C_e$$

(Eq. 4)

Where K_f (mg/g) is related to adsorption capacity and n is an empirical parameter that varies with degree of heterogeneity.

Fig. 3 shows the adsorption isotherm used to characterize the interaction between MB and algal biomass. According to the results, MB amount adsorbed by *C. barbata* increased in higher solution concentrations. The maximum adsorption capacities of *C. barbata* were 5.74 and 1.08 mg/g at 25 ℃ and 45 ℃, respectively. In this study, Freundlich isotherm model showed a better fit than the Langmuir isotherm model at 25 ℃ ($R_F^2 = 0.989$), while Langmuir isotherm model showed a better fit than the Freundlich isotherm model at 45 ℃ ($R_L^2 = 0.999$) (Table 1).
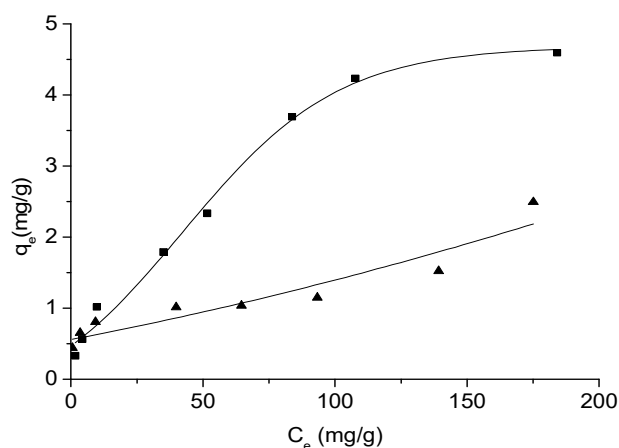
Figure 3. Sorption isothermal curves for biosorption of MB at 25⁰C (■) and 45⁰C (▲).

Table 1. A comparison of Langmuir and Freundlich isotherm models for MB by Mag-*C.barbata* at different temperature.

Temperature (⁰C)	Langmuir isotherm model			Freundlich isotherm model		
	q_m (mg/g)	a_L	R_L^2	n_f	K_f (mg/g)	R_F^2
25	5.74	0.02	0.981	0.26	1.79	0.989
45	1.08	0.08	0.999	0.55	6.30	0.922

Characterization of Biomass

FTIR: FTIR spectroscopy is largely used to characterize the mechanism of binding on algal surfaces with the help of the hydroxyl, carboxylic acid, amine, amino, sulfonyl, and phosphate functional groups found in the structure of algae [8, 22, 23]. The FTIR analysis was carried out to identify the functional groups on unloaded *C. barbata* and Mag-*C. barbata* (Fig. 4). The functional groups of MB adsorbed Mag-*C. barbata* were also examined. It has been observed that Fe_3O_4 was connected to carboxyl groups of biomass since the peak at 2926 cm⁻¹ (Figure 4a) was not observed after Fe_3O_4 loading (Fig. 4b). The peaks at 2325 cm⁻¹ and 2058 cm⁻¹ also disappeared when MB was loaded onto Mag-*C. barbata* (Fig. 4c). In general, the peak areas were changed by both Fe_3O_4 and MB loading. The functional groups of biomass were also given in Table 2. Similar results were also reported for the biosorption of different colorant agency [9, 15, 24-26].

SEM: SEM is used as a useful tool to examine the surface structure of the biosorbent. In this study, the surface microstructures of *C. barbata* samples were analyzed by the SEM technique while the existence of iron was analyzed by the EDX technique. Figure 5 shows SEM images of *C. barbata* (a), Mag-*C. barbata* (b) and MB loaded Mag-*C. barbata* (c). Structure of *C. barbata* indicated the presence of rough flat surfaces. After coating with

iron oxide, the surface of magnetic algae began to shine and the layered structure looked like a sponge (Figure 5b). After MB adsorption, MB possibly attached onto this porous surface (Figure 5c) and the surface of magnetized algae appeared roughed and more porous in comparison to the raw sample. Furthermore, the iron was detected as a signal in the EDX spectrum (Figure 5d).
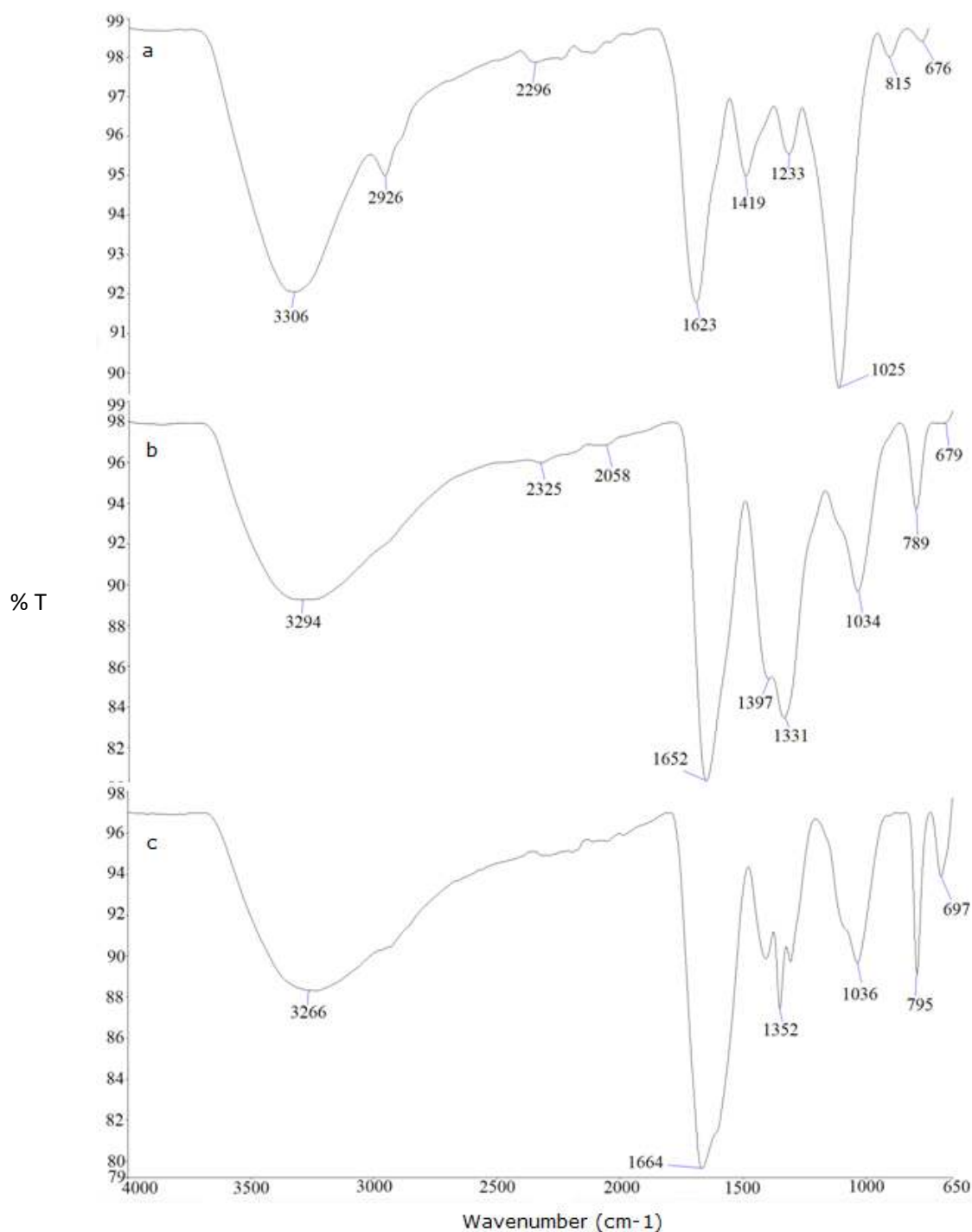
Fig.4. FTIR spectra of *C. barbata* unloaded (a), Mag-*C. barbata* unloaded (b) and Mag-*C. barbata* loaded with MB (c).

Table 2. Functional groups observed in FTIR of *C. barbata*

Functional group	Wavenumber (cm^{-1})		
	Unloaded	Mag- *C. barbata*	Mag- *C. barbata* loaded with MB
-OH and – NH stretching	3306	3294	3266
-CH stretching	2926	-	-
- OH bond	2296	2325	-
C≡C bond	-	2058	-
C = O groups in amide	1623	1652	1664
C-O stretching	1419	1397	1352
C-O carboxyl	1233	1331	-
S=O stretching	1025	1034	1036
S-O stretching	815	789	795

(a)   (b)   (b)

(c)   (c)   (d)
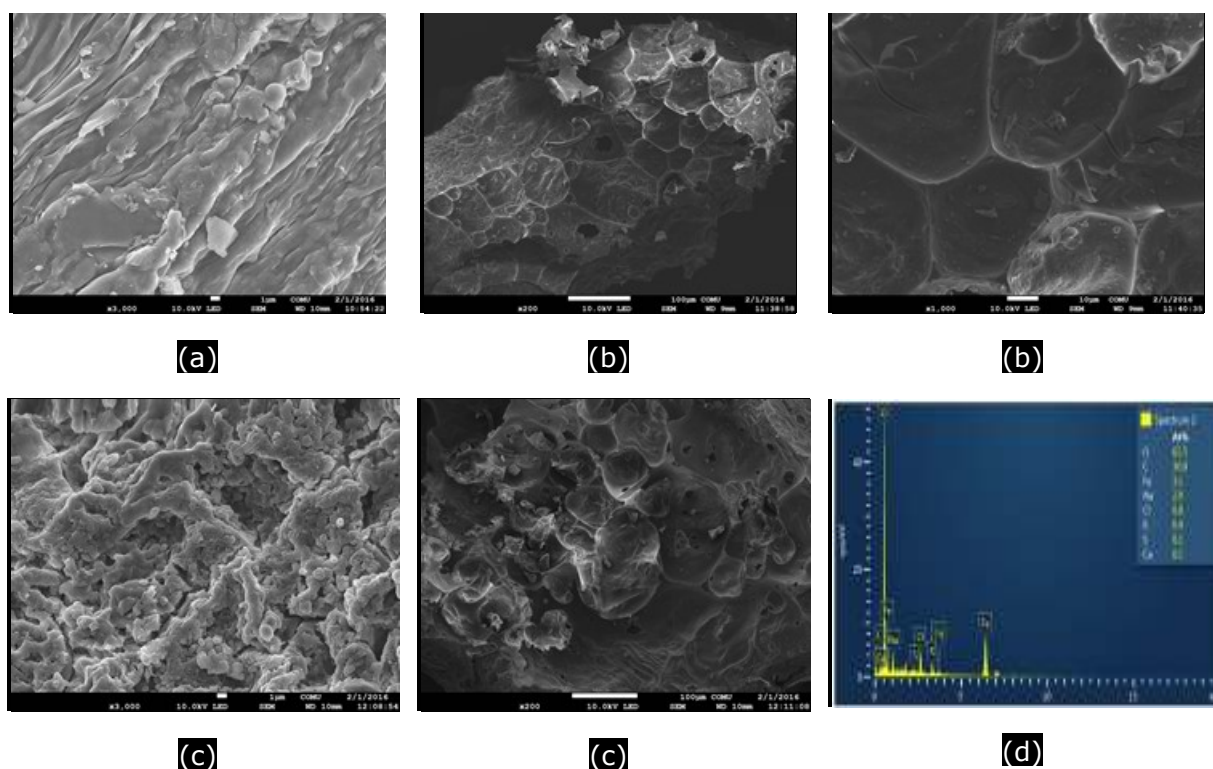
Fig.5. SEM images of *C. barbata*, unloaded (a), Mag-*C. barbata* (b), Mag-*C. barbata* loaded with MB (c), EDX images of Mag-*C. barbata* (d).

CONCLUSION

The removal of MB from aqueous solution was investigated with iron oxide-coated *C. barbata*. Effect of pH, contact time, initial MB concentrations and temperature were studied. The results showed that the pH value was not so effective on adsorption of MB. The biosorption reaction reached equilibrium within the first 300 min. Active sites of *C.*

barbata surface decreased by the rising temperature. The maximum adsorption capacities (q_m) were 5.74 and 1.08 mg/g at 25 ºC and 45 ºC, respectively. Freundlich isothermal model showed a better fit than the Langmuir isothermal model at 25 ºC, while Langmuir isothermal model showed a better fit at 45 ºC. The FTIR analyses and SEM images before and after biosorption of MB onto Mag-*C. barbata* showed the binding of several functional groups during biosorption. According to the results, Mag-*C. barbata* can be used as an alternative low-cost material for the removal of MB from aqueous solution.

ACKNOWLEDGEMENTS

REFERENCES

[1] El Jamal MM, Ncibi MC. Biosorption of Methylene Blue by Chaetophora Elegans Algae: Kinetics, Equilibrium and Thermodynamic Studies. Acta Chimica Slovenica**.** 2012**;** 59 (1): 24-31.

[2] Ergene A, Ada K, Tan S, Katırcıoglu H. Removal of remazol brilliant blue R dye from aqueous solutions by adsorption onto immobilized *Scenedesmus quadricauda*: equilibrium and kinetic modeling studies. Desalination. 2009; 249: 1308-1314. DOI:10.1016/j.desal.2009.06.027.

[3] Daneshvar E, Kousha M, Sohrabi MS, Khataee A, Converti A. Biosorption of three acid dyes by the brown macroalga *Stoechospermum marginatum*: Isotherm, kinetic and thermodynamic studies. Chemical Engineering Journal. 2012; (195-196): 297-306. DOI: 10.1016/j.cej.2012.04.074.

[4] Nagarani N, Vahitha H, Kumaraguru AK. Comparative studies on the removal of textile effluents by various eco-friendly adsorbent strategies. Toxicological & Environmental Chemistry. 2012; 94(7): 1259-1271. DOI: 10.1080/02772248.2012.702860.

 [5] Kushwaha AK, Gupta N, Chattopadhyaya MC. Removal of cationic methylene blue and malachite green dyes from aqueous solution by waste materials of *Daucus carota*. Journal of Saudi Chemical Society. 2014; 18 (3): 200-207. DOI: 10.1016/j.jscs.2011.06.011.

[6] Riazi M, Keshtkar AR, Moosavian MA. Batch and continuous fixed-bed column biosorption of thorium(IV) from aqueous solutions: equilibrium and dynamic modeling. Journal of Radioanalytical and Nuclear Chemistry. 2014; 301 (2): 493-503. DOI: 10.1007/s10967-014-3129-7.

[7] Kratochvil D, Volesky, B. Biosorption of Cu from ferruginous wastewater by algal biomass. Water Research. 1998; 32(9): 2760-2768. DOI:10.1016/S0043-1354(98)00015-3.

[8] Pavasant P, Apiratikul R, Sungkhum V, Suthiparinyanont P, Wattanachira S, Marhaba TF. Biosorption of Cu^{2+}, Cd^{2+}, Pb^{2+}, and Zn^{2+} using dried marine green macroalga *Caulerpa lentillifera.* Bioresource Technology. 2006; 97(18): 2321-2329. DOI:10.1016/j.biortech.2005.10.032.

[9] Akar T, Balk YY, Tuna O, Akar ST. Characterization and application of plant-based magnetic biomaterial for batch and fixed-bed mode sequestration of lead from synthetic and real effluents. Ecological Engineering. 2013; 61 (A): 251-257. DOI: 10.1016/j.ecoleng.2013.09.062.

[10] Cerff M, Morweiser M, Dillschneider R, Michel A, Menzel K, Posten C. Harvesting fresh water and marine algae by magnetic separation: screening of separation parameters and high gradient magnetic filtration. Bioresource Technology. 2012; 118: 289–295. DOI: 10.1016/j.biortech.2012.05.020.

[11] Xu L, Guo C, Wang F, Zheng S, Liu CZ. A simple and rapid harvesting method for microalgae by in situ magnetic separation. Bioresource Technlogy. 2011; 102: 10047-10051. DOI:10.1016/j.biortech.2011.08.021.

[12] Liu J, Qiao SZ, Hong Hu Q, Qing (Max) Lu G. Magnetic Nanocomposites with Mesoporous Structures: Synthesis and Applications. Nano Small Mico. 2011; 7 (4): 425-443**.**

[13] Khataee AR, Vafaei F, Jannatkhah M. Biosorption of three textile dyes from contaminated water by filamentous green algal *Spirogyra* sp.: Kinetic, isotherm and thermodynamic studies. International Biodeterioration & Biodegradation. 2013; 83: 33-40. DOI: 10.1016/j.ibiod.2013.04.004.

[14] Peng X, Luan Z, Zhang H. Montmorillonite-Cu(II)/Fe(III) oxides magnetic material as adsorbent for removal of humic acid and its thermal regeneration. Chemosphere. 2013; 63(2): 300–306. DOI: 10.1016/j.chemosphere.2005.07.019.

[15] Mahdavi M, Namvar F, Bin Ahmad M, Mohamad R. Green biosynthesis and characterization of magnetic iron oxide (Fe_3O_4) nanoparticles using seaweed (*Sargassum muticum*) aqueous extract. Molecules. 2013; *18:* 5954-5964. DOI: 10.3390/molecules18055954.

[16] Silva VAJ, Andrade PL, Silva MPC, Bustamante DA, Valladares LDLS, Albino Aguiar, J. Synthesis and characterization of Fe_3O_4 nanoparticles coated with fucan polysaccharides. Journal of Magnetism and Magnetic Materials. 2013; 343: 138-143. 10.1016/j.jmmm.2013.04.062

[17] Abd-El-Kareem M, Taha H. Decolorization of malachite green and methylene blue by two microalgal species. International Journal of Chemical and Environmental Engineering. 2013; 3 (5): 297-302.

[18] Irkin LC, Erdugan H. Çanakkale Boğazı'nda yayılış gösteren *Cytoseira barbata* (Stackhouse) C. Agardh'ın kimyasal kompozisyonunun mevsimsel olarak incelenmesi. Ege Journal of Fisheries Aquatic Science. 2014; 31 (4): 209-213.

[19] Tüzün İ, Bayramoğlu G, Yalçın E, Başaran G, Çelik G, Arıca MY. Equilibrium and kinetic studies on biosorption of Hg(II), Cd(II) and Pb(II) ions onto microalgae *Chlamydomonas reinhardtii*. Journal of Environmental Management. 2005; 77 (2): 85-92. i:10.1016/j.jenvman.2005.01.028.

[20] Langmuir I. The adsorption of gases on plane surfaces of glass, mica and platinum. Journal of American Chemical Society. 1918; 40 (9): 1361-1403. DOI: 10.1021/ja02242a004.

[21] Freundlich H. Over the adsorption in solution. The Journal of Physical Chemistry. 1906; 57: 385.

[22] Dahri MK, Rahimi Kooh MR, Lim LBL. Application of *Casuarina equisetifolia* needle for the removal of methylene blue and malachite green dyes from aqueous solution. Alexandria Engineering Journal. 2015; 54 (4): 1253-1263. DOI: 10.1016/j.aej.2015.07.005

[23] Lim LBL, Priyantha N, Tennakoon DTB, Ing CH, Bandara C. Sorption Characteristics of peat of Darussalam I: Preliminary characterization and equilibrium studies of methylene blue- peat interactions. Ceylon Journal of Science (Physical Sciences). 2013; 17 (1): 41-51.

[24] Vijayaraghavan J, Bhagavathi Pushpa T, Sardhar Basha SJ, Jegan J. Isotherm, kinetics and mechanistic studies of methylene blue biosorption onto red seaweed *Gracilaria Corticata*. Desalination of Water Treatment. 2016; 57 (29): 13540- 13548. DOI: 10.1080/19443994.2015.1060174.

[25] Ing CH, Zehra T, Lim LBL, Priyanta, N, Tennakoon DTB. Sorption characteristics of peat of Brunei Darussalam. Environmental Earth Science. 2014; 72 (7): 2263-2277. DOI: 10.1007/s12665-014-3135-7.

[26] Marungrueng K, Pavasant P. High performance biosorbent (*Caulerpa lentillifera*) for basic dye removal. Biorescource Technology. 2007; 98: 1567-1572. DOI:10.1016/j.biortech.2006.06.010

Türkçe Öz ve Anahtar Kelimeler

Demir Oksitle Kaplanmış *Cystoseira barbata* tarafından Sulu Çözeltilerden Metilen Mavisinin Biyosorpsiyonu

Yeliz Özüdoğru, Melek Merdivan, Tolga Göksan

Öz: Bu çalışmada, *Cystoseira barbata* demir oksitle (Fe_3O_4) kaplanmış ve manyetik bir biyomalzeme elde edilmiştir, bu malzeme sulu çözeltiden metilen mavisini gidermek için sorbent olarak kullanılmıştır. Bu biyosorbent Taramalı Elektron Mikroskopisi (SEM) ve Fourier Dönüşüm Kızılötesi Spektroskopisi (FTIR) ile karakterize edilmiştir. Bu malzemenin metilen mavisi adsorpsiyon kapasitesi pH, temas süresi, ilk metilen mavisi derişimi ve sıcaklığa bağlı olarak incelenmiştir. Denge verisi Langmuir ve Freundlich izotermleri ile analiz edilmiştir. Sonuçlara göre, maksimum adsorpsiyon kapasiteleri 300 dakikada ve pH 2'de elde edilmiş olup 25 °C ve 45 °C için sırası ile 5,74 ve 1,08 mg/g olarak elde edilmiştir.

Anahtar kelimeler: Metilen mavisi, biyosorpsiyon, *C. barbata,* demir oksit kaplaması.

Sunulma: 11 Temmuz 2016. **Düzeltme:** 01 Eylül 2016. **Kabul:** 05 Ekim 2016.

Synthesis, Characterization, and Chemosensing Application of Poly(Methyl Methacrylate-*co*-Hydroxyethyl Methacrylate) with Dansyl Side Group

Erdinc Doganci[a]*, Mesut Gorur[b]*

[a]*Department of Chemistry and Chemical Processing Tech., Kocaeli University, 41380 Kocaeli, Turkey*
[b]*Department of Chemistry, Istanbul Medeniyet University, 34700 Istanbul, Turkey*

Abstract: A novel dansyl side-functional polymer (**P2**) was prepared and employed as the metal cation sensing chemical probe. The synthesis of **P2** was performed via consecutive free radical polymerization and esterification reactions. **P2** showed characteristic UV-Vis and fluorescence emission bands for the dansyl unit. The fluorescence emission intensity of **P2** gradually decreased as the concentrations of the added metal ions were increased. The highest quenching efficiencies (QE) were observed for Pb^{2+} (84.56%) and Co^{2+} (83.69%). Besides, the responses of **P2** to the addition of Pb^{2+} cation were quite linear up to 50 equivalent. The presence of Cd^{2+}, Hg^{2+}, Mn^{2+}, and Zn^{2+} cations did not pose significant interferences. Thus, **P2** is a potential candidate for the fluorescence chemical sensor for Pb^{2+} cation.

*Corresponding authors. e-mails: edoganci@kocaeli.edu.tr (E.D.) and mesut.gorur@medeniyet.edu.tr (M.G.). Tel: +90 262 349 43 51-349 43 52 (185) (E.D.) and +90 216 280 34 50 (3450) (M.G.). Fax: +90 262 349 39 97 (E.D.) and +90 216 280 34 04 (M.G.)

INTRODUCTION

Heavy metal pollution in natural water or soil environments has attracted a worldwide attention because of their severe effects to human health and the environment [1, 2]. While certain heavy metals, including iron, copper, manganese, and zinc, are essential nutrients in small quantities to have a healthy life, some others (Hg^{2+}, Pb^{2+}, As^{3+}, Cu^{2+}, Cd^{2+}, Ni^{2+}, and Cr^{3+}) are highly toxic and carcinogenic for human health [3-6]. Recently, accumulation of heavy metals in rivers, lakes, and seas due to increasing industrial, agricultural, mining, and transportation activities resulted in serious environmental pollution and threatened biolife, particularly in developing countries [7-9]. Contrary to organic contaminants, since they are not biodegradable; they recirculate and accumulate in the environment [7, 10]. Besides, heavy metal ions have great tendencies to produce complexes with nitrogen, sulfur, or oxygen containing biologically important ligands. Consequently, molecular structures of proteins change, hydrogen bonds break, or enzymes are inhibited [3, 11]. The toxic heavy metals affect various tissues and organs, including central nervous system, kidneys, liver, skin, bones, and teeth [4-6]. Therefore, maximum contamination levels for various metal cations in drinking water have been set by different organizations [3, 12]. World Health Organization (WHO) defined the maximum acceptable contamination level for Hg^{2+}, Pb^{2+}, and other toxic metal ions as 10 µg L^{-1} [13].

There is urgent requirement for simple, sensitive, selective, and inexpensive determination of metal cations for various applications, including environmental monitoring, industrial process management, food quality control, and chemical threat detection [13, 14]. In this respect, fluorescence spectroscopy is a robust method with its simplicity, low detection limit, sensitivity, selectivity, and fast response among the others [15-17]. Dansyl group, consisting of dimethylamino and naphthalene sulfonyl as donor and acceptor parts, respectively, is one of the most attractive fluorophores and has been extensively used in a wide variety of optical sensing applications since it has intense fluorescence emissions in the visible region with high quantum yields and it can be easily attached to various structures in a covalent way [18-20]. Additionally, being one of the smallest available fluorophores, its emission spectrum is sensitive to chemical environment, such as pH and polarity [21]. Thus, dansyl-containing small molecular compounds, dendrimers, or polymers were used as fluorescent probes against metal cations, anions, biological materials, and nitro aromatic compounds [19, 20, 22-25]. Zhou *et al.* synthesized a dansyl-based fluorescence probe for selective determination of Hg^{2+} in complicated environment samples [26]. Jisha *et al.* repaired dansyl-naphthalimide dyads for fluorescence ratiometric selective recognition of Cu^{2+} ions [27].

Liu *et al.* synthesized calix[4]arene compounds having two dansyl units and employed them in enantioselective sensing of amino acid anions [28]. Yin *et al.* produced thermo-responsive microgels, based on dansyl-containing poly(N-isopropylacrylamide) (PNIPAM), for the selective fluorescent detection of Cu^{2+} cations [29]. Murariu and Buruiana prepared dansyl-labelled poly(acrylamide/methacrylurea-*co*-vinyl acetate) copolymers for the fluorescent sensing studies towards some organic acids (1-S-camphorsulfonic acid and p-toluenesulfonic acid) and cations (H^+, Cu^{2+}, Hg^{2+}, and Fe^{2+}) [30]. Recently, we have synthesized dansyl end-functional phosphazene-cored poly(ε-caprolactone) star polymer and employed as a selective fluorescent probe for the detection of Pb^{2+}[1].

With this background information in mind, we are reporting herein the synthesis and characterization of novel poly(methyl methacrylate)-*co*-poly(2-hydroxyethyl methacrylate) copolymer with dansyl side groups ((poly(MMA-*co*-HEMA-DNS), **P2**). To the best of our knowledge, this is the first report on the synthesis and optical chemosensing application of dansyl-functional PMMA-*co*-PHEMA copolymer which were obtained via free radical polymerization (FRP) of MMA and HEMA monomers and esterification. Dansyl group was selected as a fluorophore for the preparation of the polymeric chemosensing agent due to its intense emissions, sensitivity to its microenvironments, and strong absorption in the near UV and structural flexibility for derivatization [31-33]. The structural characterizations of **P1** and **P2** polymers were performed using by FT-IR and ^{1}H NMR spectroscopies. The thermal properties of the obtained polymers were confirmed via differential scanning calorimetry (DSC) and thermogravimetric analysis (TGA). Then, the sensing capacity of the polymers was investigated by fluorescence spectroscopy with quenching studies using Pb^{2+}, Hg^{2+}, Co^{2+}, Cd^{2+}, Mn^{2+}, and Zn^{2+} metal ions in the analytic media.

EXPERIMENTAL

Materials
Methyl methacrylate (MMA, Alfa Aesar, 99%) and 2-hydroxyethyl methacrylate (HEMA, Aldrich, 98%) were passed through a column of alumina for the removal of stabilizers and then stored under argon. Triethylamine (TEA, Fluka, ≥99.5%) was dried over CaH_2 and stored over 3 Å molecular sieves. Benzoyl peroxide (BPO, Aldrich, 98%) was recrystallized from methanol and dried before use. Tetrahydrofuran (THF, Merck, 99.8%) was freshly dried over Na/benzophenone ketyl and freshly distilled under argon atmosphere before use. Dansyl chloride (Alfa Aesar, 97≥%), methylene chloride (DCM, Sigma-Aldrich, 98≥%), diethyl ether (Aldrich, ≥99%), n-hexane (Sigma-Aldrich, ≥95%), cadmium chloride (Alfa Aesar, 99.0%), lead(II) nitrate (Alfa Aesar, 99%), manganese(II)

chloride (Alfa Aesar, 97%), cobalt(II) chloride hexahydrate (Alfa Aesar, 98%), zinc chloride (Aldrich, 98%), and mercury(II) chloride (Alfa Aesar, 98≥%) were used as received.

Instrumentation

^{1}H NMR spectra were measured in CDCl$_3$ solutions on a Varian UNITY INOVA 500 MHz spectrometer using solvent residue as the internal reference (7.26 ppm for chloroform) at 25°C. FT-IR spectra were obtained via the attenuated total reflectance (ATR) method on a Perkin–Elmer Paragon 1000 spectrometer equipped with PIKE MIRacle^{TM} diamond ATR attachment at wavenumbers ranging from 600 to 4500 cm^{-1}. Gel permeation chromatography (GPC) measurements were recorded on an Agilent GPC instrument (Model 1100) having a Waters Styragel column (HR 5E), a refractive index detector, and a pump. THF was used as the eluent at a flow rate of 0.3 mL min^{-1} at 24 °C. Average molecular weights and molecular weight distributions were estimated based on a calibration curve drawn using linear polystyrene (PS) polymers as monodisperse standards. Differential scanning calorimetry (DSC) experiments were performed on a DSC 4000 (PerkinElmer) under a protective nitrogen flow (10 mL min^{-1}) from 25 to 220 °C to determine glass transition temperatures (T_g) of the polymers. Thermal stabilities of the obtained polymers were investigated using a Mettler Toledo TGA/SDTA 851 thermogravimetric analyzer from room temperature to 700 °C at a heating rate of 10 °C min^{-1} under a nitrogen flow. UV-Vis spectroscopy measurements of the samples were recorded at room temperature on a Shimadzu UV-2600 spectrophotometer and fluorescence emission spectra of the samples were obtained on an Agilent Cary Eclipse spectrophotometer. Quartz cuvettes (1 cm path length) were used both UV-Vis and fluorescence spectra.

Synthesis of methyl methacrylate-*co*-2-hydroxyethyl methacrylate copolymer, poly(MMA-*co*-HEMA) (P1)

Poly(MMA-*co*-HEMA) (**P1**) was synthesized according to the literature method with minor modifications [42]. HEMA (0.97 g, 7.431 mmol), MMA (4.46 g, 44.586 mmol), and BPO (0.03 g, 0.124 mmol) were added to a 25-mL one-necked round-bottomed flask equipped with a magnetic stirrer under argon atmosphere. The mixture was deoxygenated by purging gently with argon and the reaction was carried out at 80°C for 2 h. The reaction was quenched by dipping the flask into a salt-ice mixture, the crude product was dissolved in 10 mL DCM, and precipitated into cold hexane. The precipitation procedure was performed once more, **P1** was isolated by filtration, and dried at room temperature *in vacuo* until a constant weight was obtained.

Yield: 4.07 g (75%). $M_{n,GPC}$: 57100 g mol^{-1}; M_w/M_n: 1.84. FT-IR (cm^{-1}): 3515 (broad, OH); 2997 and 2951 (C-H); 1720 (C=O) 1476 (C-H); 1248 ((C=O)-O). ^{1}H NMR (500 MHz, CDCl$_3$, d, ppm): 0.8-1.13 (6H, s, backbone -CC*H*$_3$); 1.84 (4H, t, backbone -C*H*$_2$-); 3.59 (3H, s, -COOC*H*$_3$ of MMA); 3.84 (2H, t, -CH$_2$C*H*$_2$OH of HEMA); 4.11 (2H, t, -C*H*$_2$CH$_2$OH of HEMA).

Synthesis of dansyl side-functional poly(MMA-*co*-HEMA) copolymer (poly(MMA-*co*-HEMA-DNS), P2)

P1 (0.5 g, contains 0.724 mmol OH units) was dissolved in dry THF (12 mL) under dry nitrogen atmosphere. After addition of TEA (0.220 g, 2.171 mmol), the reaction mixture was cooled to -15°C by an ice-salt mixture and dansyl chloride (0.976 g, 3.619 mmol) in dry THF (8 mL) was added drop-wise into the mixture via dropping funnel over 25 min. Subsequently, the cooling bath was removed and the solution was stirred for 60 h at room temperature. The salts were filtered off, the filtrate was concentrated using a rotary evaporator, and then precipitated into a cold diethyl ether twice. **P2** was isolated by filtration and dried at room temperature *in vacuo*.

Yield: 0.599 g (86.2%). $M_{n,NMR}$: 71464 g/mol; $M_{n,GPC}$: 76300 g/mol; M_w/M_n: 1.93. FTIR (cm^{-1}): 2997 (C-H), 2951 (C-H); 1720 (C=O); 1476 (C-H); 1248 ((C=O)-O). ^{1}H NMR (CDCl$_3$, δ, ppm): 0.8-1.13 (6H, s, backbone -CC*H*$_3$); 1.84 (4H, t, backbone -C*H*$_2$-); 2.88 (s, -N(C*H*$_3$)$_2$, in dansyl moiety); 3.59 (3H, s, -COOC*H*$_3$ of MMA); 3.84 (2H, t, -CH$_2$C*H*$_2$OH of HEMA); 4.11 (2H, t, -C*H*$_2$CH$_2$OH of HEMA); 8.60 ppm (1H, d, -C*H*- of dansyl moiety);8.25 ppm (2H,d, -C*H*- of dansyl moiety); 7.56 ppm (2H, q, -C*H*- of dansyl moiety); 7.24 ppm (1H, d,-C*H*- of dansyl moiety).

Fluorescence sensing application of P2 against metal cations

A definite amount of poly(MMA-*co*-HEMA-DNS) copolymer (**P2**) was dissolved in ACN:water (6:4, v/v) solvent mixture to provide the concentration of DNS group to be 2.7 10^{-5} M. Then, **P2** was titrated with prescribed amount of Cd^{2+}, Co^{2+}, Hg^{2+}, Pb^{2+}, Mn^{2+}, and Zn^{2+} cations and the fluorescent responses of **P2** were measured by fluorescence spectroscopy at room temperature.

RESULTS AND DISCUSSION

The poly(MMA-*co*-HEMA-DNS) (**P2**) copolymer was prepared via a combination of free radical polymerization (FRP) and esterification reactions (Scheme 1). Firstly, poly(MMA-*co*-HEMA) copolymer with the hydroxyl side groups (**P1**) was synthesized by FRP using MMA and hydroxyl functional HEMA monomers in the presence benzoyl peroxide as

initiator. In the final step, dansyl groups were successfully attached as side groups by esterification between dansyl chloride and hydroxyl-functional groups of **P1**, yielding **P2.**
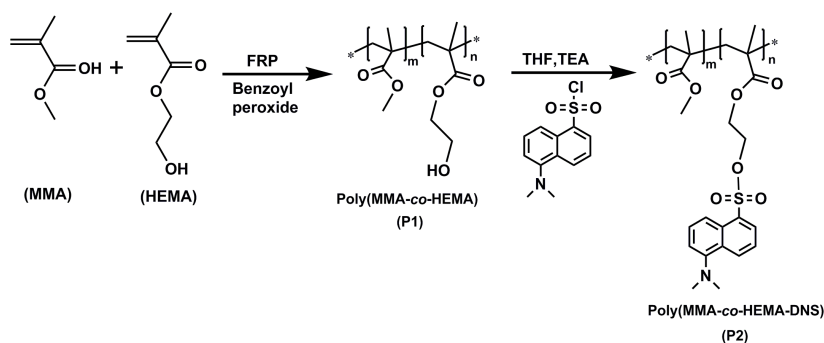
Scheme 1. General procedure for the synthesis of dansyl functional poly(MMA-co-HEMA-DNS) (**P2**).

^{1}H NMR and FT-IR spectroscopic methods were employed to characterize the structures of **P1** and **P2** polymers with hydroxyl and dansyl side group, respectively. The FT-IR spectra of the polymers are shown in Figure 1. In these spectra, the observation of strong and sharp peak at 1720 cm^{-1} was ascribed to the carbonyl groups in HEMA and MMA repeating units of both polymers. The signals between 2950 and 3000 cm^{-1} was due to asymmetric and symmetric CH stretching vibrations of the obtained polymers, respectively. In the FT-IR spectrum of **P1,** the intense broad band around 3515 cm^{-1} corresponds to the OH stretching frequencies of HEMA units. After esterification of **P1** with dansyl chloride, these signals completely disappeared in the FT-IR spectrum of **P2**, indicating the success of the reaction.
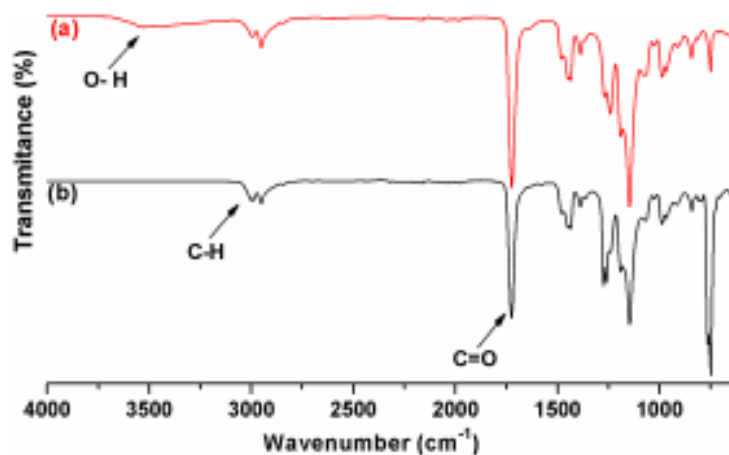
Figure 1. FTIR spectra of **(a)P1** and **(b)P2**.

The ^{1}H NMR spectra of **P1** and **P2** were given in Figure 2. The peaks between 0.8 and 1.14 ppm were attributed to the protons of H_a methyl groups in the polymer chain of **P1** and **P2**. The signals of the H_b methylene protons of the polymer skeleton were seen around 0.8 and 1.13 ppm. The peak at 3.59 ppm were assigned to H_c methyl protons in the MMA repeating units of both polymers while H_e and H_d methylene protons in the HEMA repeating units of **P1** resonated at 3.84 and 4.11 ppm, respectively [43]. The ratio of MMA and HEMA repeating units (m/n, see Scheme 1) in **P1** was calculated as 5.6 using the integration ratio between the H_c methyl protons of MMA and H_d methylene protons of HEMA repeating units. Upon esterification of **P1** with dansyl chloride, the signal of the methylene protons (H_e) next to the hydroxyl group in **P1** (Figure 2a) moved to lower magnetic fields and overlapped by H_d methylene proton signals (adjacent to the ester group in HEMA repeating unit) in the ^{1}H NMR spectrum of **P2** (Figure 2b). Besides, some new peaks also appeared in the spectrum (Figure 2b) related to the aromatic CH (δ = 8.60, 8.25, 7.56, and 7.24 ppm) and H_f methyl protons (δ = 2.88 ppm) in the DNS moiety. Overall, these data clearly showed the successful synthesis of the polymers.
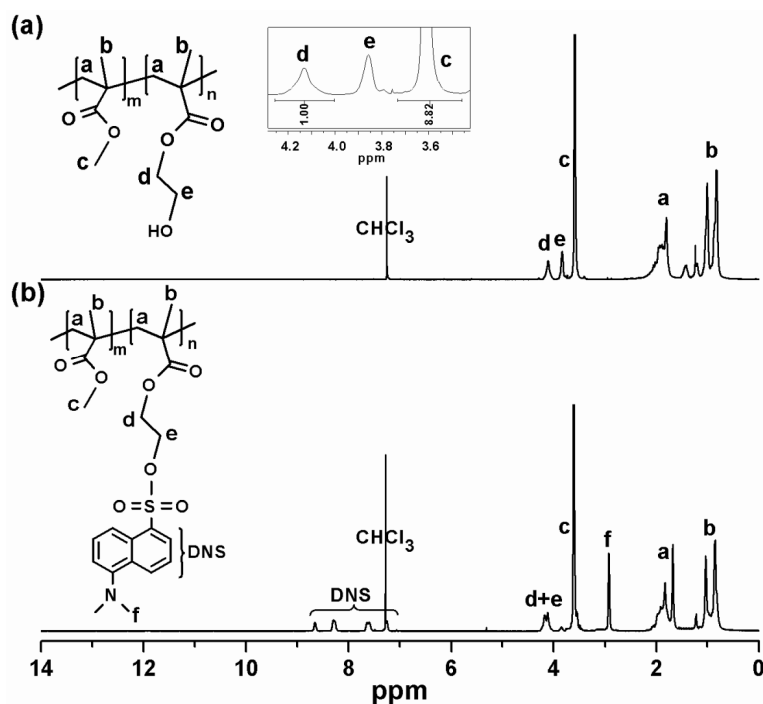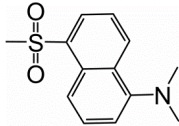
Figure 2. ^{1}H NMR spectra of **(a)P1** and **(b)P2** in CDCl$_3$ at room temperature.

Commented [BA2]: Figure 2 is missing. Please replace.

The average molecular masses of the copolymers (**P1** and **P2**) were estimated by gel permeation chromatography (GPC) based on linear polystyrene calibration standards. Related data are given in Table 1 and GPC chromatograms are presented in Figure S1 and S2 in the Supporting Information. The polymers showed symmetrical and unimodal elution peaks in these chromatograms with polydispersity values in the range of 1.84–1.93, indicating that the purified polymerization products contained only the targeted polymers. Since the hydrodynamic volumes of the obtained polymers (**P1** and **P2**) and polystyrene calibration standards are different, the average molecular weights of the polymers obtained from GPC measurements are regarded to be less reliable than those calculated from ^{1}H NMR data. In the ^{1}H NMR spectra of the polymers, initiator residue signals could not be observed due to dilution of the terminal units in the polymer chains [34]. On the other hand, the molar weights of the polymer fragment containing single OH (**P1**) or DNS (**P2**) units were calculated from the equation (m/n) x MW of MMA + MW of OH or DNS functional unit.

Table 1. Molecular weight analysis of the MMA-*co*-HEMA copolymers with different side groups.

Polymers	$M_{n,GPC}$[a]	$M_{w,GPC}$[a]	M_w/M_n[a]	Side Group
P1	57100	105100	1.84	$-OH$
P2	76300	147300	1.93	

[a]Determined by GPC with linear polystyrene standards.THF was used as eluent (RI detector)

Since PMMA and PHEMA are amorphous in nature [44, 45], glass transition temperature (T_g) of the polymers with different side-functional groups were investigated by differential scanning calorimetry (DSC) experiments. The related thermograms of polymers in the second heating runs were presented in Figure 3 and the data were briefly given in Table 2. In these thermograms, T_g of **P1** and **P2** were observed at 121 and 117 °C, respectively. The slight decrease in the T_g values of the polymers can be attributed to the presence of bulky DNS side groups, decreasing molecular packing in **P2**.
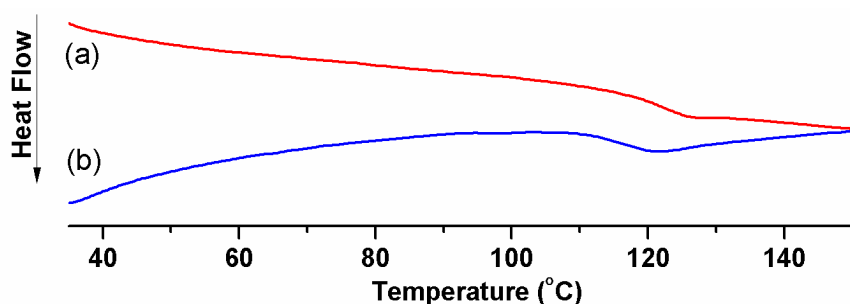
Figure 3. DSC curves of **(a)**P1 and **(b)**P2 in the second heating runs.

Commented [BA3]: Figure 3 is missing. Please replace.

Thermal stabilities of the hydroxyl (**P1**) and dansyl (**P2**) side-functional polymers were determined by termogravimetric analysis (TGA) experiments under nitrogen flow with a heating rate of 10°C min^{-1} from room temperature to 700 °C. Figure 4 demonstrates the percent remaining weight versus temperature curves of the polymers whereas data related to $T_{d, onset}$, $T_{d, max}$, and char yield are summarized in Table 2. Hydroxyl functional groups are known to be thermally labile [35]. Upon esterification of hydroxyl side-functional polymer (**P1**) with dansyl chloride, there observed a significant increase in $T_{d, onset}$, $T_{d, max}$, percent char yield values of the obtained DNS-functional polymer (**P2**).

Table 2. Thermal properties of the polymers.

Entry	T_g (ºC)[a]	$T_{d,\,onset}$ (ºC)[b]	$T_{d,\,max}$ (ºC)[c]	Char Yield(%)[d]
P1	121	243	315	3.49
P2	117	268	387	6.87

[a]T_g is the glass transition temperature determined by DSC experiments in the second heating run. [b]$T_{d,onset}$, [c]$T_{d,max}$, and [d]Char yield were determined by TGA experiments at 700 °C under a argon atmosphere. [b]$T_{d,onset}$, [c]$T_{d,max}$, and [d]Char yield are the onset decomposition temperature of the polymers, the temperature corresponding to the maximum rate of weight loss, and the percent of mass remaining in TGA experiments, respectively.
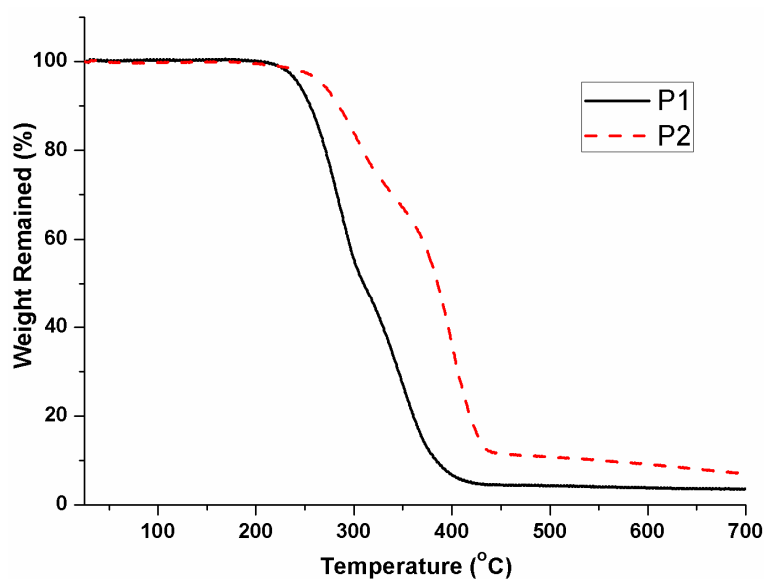
Figure 4. TGA curves of **P1** and **P2.**

The presence of DNS side-groups in the chemical structure of **P2** was further proved by absorbance and fluorescence emission spectra. In the UV-Vis spectrum of **P2** (containing 2.7×10^{-5} M DNS) taken in ACN:water (6:4) solvent system at room temperature, there was seen a very strong absorption around 200 nm, a shoulder peak at 254 nm, and comparatively weak band with a maximum of 344 nm (Figure 5). The position of band maxima and the relative peak strengths are in accordance with the literature [1, 36]. The fluorescence emission spectrum of **P2** was taken in the same experimental conditions and depicts a broad band with a maximum at 530 nm (Figure 5). This band is called as Band A and ascribed to twisted intramolecular charge transfer (TICT) emission due to charge transfer between dimethyl amino donor and naphthalene sulfonyl acceptor groups of the dansyl fluorophore [37].
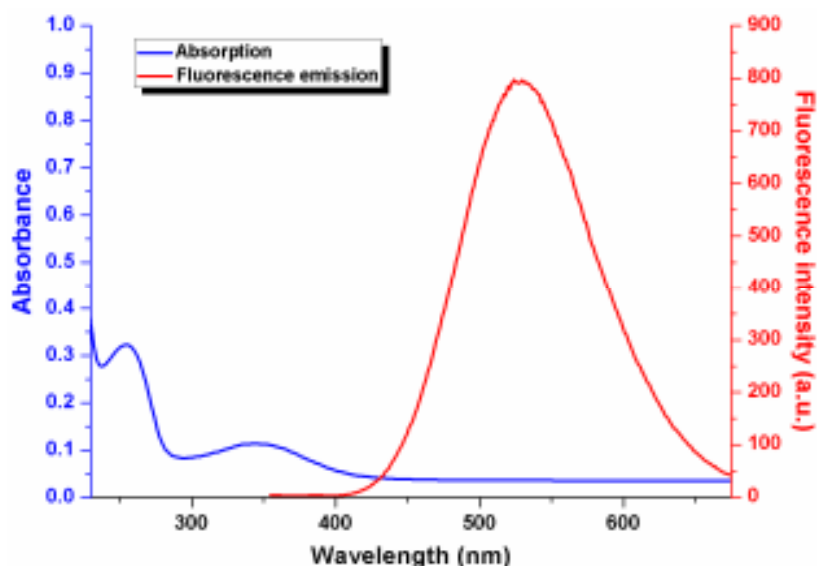
Figure 5. Absorbance and fluorescence emission spectra (λ_{ex} =344 nm) of **P2** in ACN:water (6:4). The concentration of DNS units was 2.7 10^{-5} M.

The binding and recognition behavior of the dansyl side-functional polymer (**P2**) towards different metal cations were investigated via fluorescence measurements. Metal cation sensing experiments were conducted in ACN:water (6:4) solvent system at 344 nm excitation wavelength at room temperature and the obtained spectra were given in Figure 6. In these spectra, dansyl fluorophore of **P2** gave a very strong emission spectrum in the absence of any metal cations due to intramolecular charge transfer (ICT) from nitrogen atom of the dimethylamino group to naphthalene moiety [37]. When **P2** was titrated with 100 equivalents of Cd^{2+}, Co^{2+}, Hg^{2+}, Pb^{2+}, Mn^{2+}, and Zn^{2+} cations, ICT emission of **P2** was quenched remarkably with slight blue-shifting of the band maxima. The quenching of the emission intensity of **P2** was attributed to electron transfer from the excited DNS to nearby metal cations. Quenching efficiency ratios (QE) of the metal cations were calculated from the equation: QE=$((I_0-I)/I_0)$ x 100. The obtained results were demonstrated in Figure 7. The highest QEs among the studied metal cations were observed for Pb^{2+} (84.56%) and Co^{2+} (83.69%). As seen from Figure 8, the interferences resulting from other cations are not significant. Besides, dansyl fluorophore of **P2** gave very linear responses to the addition of Pb^{2+} cation up to 50 eq with R^2 value of 0.99 (Figure 9). These results indicate that **P2** could be employed as Pb^{2+} sensing fluorescence chemical probe.

575
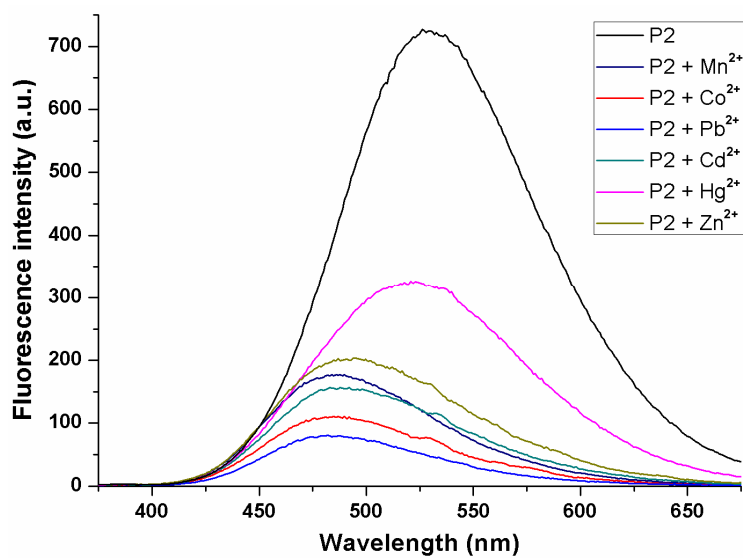
Figure 6. Fluorescence spectral response of **P2** solution (containing 2.7 10^{-5} M DNS) in ACN:water (6 : 4, v/v) upon addition of 100 eq. of Cd^{2+}, Co^{2+}, Hg^{2+}, Pb^{2+}, Mn^{2+}, and Zn^{2+} cations.
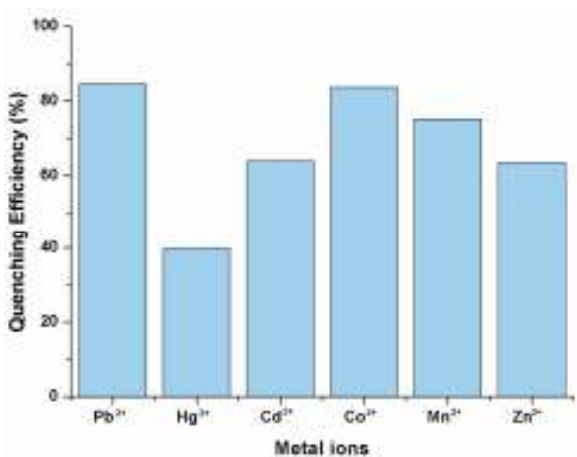
Figure 7. Responses of the dansyl-modified polymer (**P2**) upon addition of 100 eq. targeted metal ions.

576
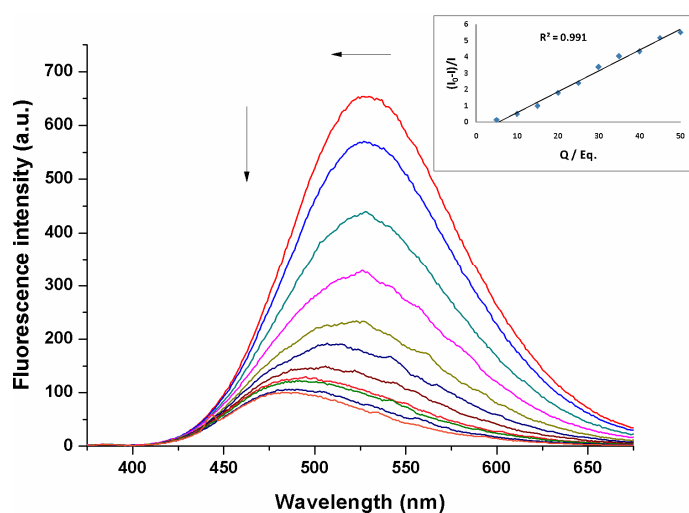
Figure 8. Fluorescence emission spectra of **P2** (2.7 10^{-5} M) in ACN :water (6:4) in the presence of Pb^{2+} cation at 10, 20, 30, 40, 50, 60, 70, 80, 90, and 100 equivalent ratios.

Commented [BA7]: Please change "Wavelenght" in the figure.

CONCLUSION

The dansyl side-functional polymer (**P2**) was synthesized via free radical polymerization of MMA and HEMA monomers and esterification of the obtained polymer (**P1**) with dansyl chloride. The FT-IR, ^{1}H NMR, UV-Vis, and fluorescence spectral data confirm the successful synthesis of the polymers. Then, **P2** was employed as fluorescence sensor probe for various metal cations. Fluorescence emissions of **P2** were effectively quenched upon addition of metal cations. The highest QEs were observed for Pb^{2+} (84.56%) and Co^{2+} (83.69%). Besides, **P2** gave highly linear response to the addition of Pb^{2+} up to 50 equivalent. Interferences resulting from the presence of Cd^{2+}, Hg^{2+}, Mn^{2+}, and Zn^{2+} cations are not significant. Therefore, **P2** has the potential to be used as a fluorescent-active chemical probe for the determination of Pb^{2+} cation.

ACKNOWLEDGMENTS

REFERENCES

1. Gorur M, Doganci E, Yilmaz F, Isci U. Synthesis, characterization, and Pb^{2+} ion sensing application of hexa-armed dansyl end-capped poly(ε-caprolactone) star polymer with phosphazene core. Journal of Applied Polymer Science. 2015, 132(32). DOI: 10.1002/app.42380.

2. Long F, Zhu A, Shi H, Wang H, Liu J. Rapid on-site/in-situ detection of heavy metal ions in environmental water using a structure-switching DNA optical biosensor. Scientific Reports. 2013, 3: 2308. DOI: 10.1038/srep02308.

3. Aragay G, Pons J, Merkoçi A. Recent Trends in Macro-, Micro-, and Nanomaterial-Based Tools and Strategies for Heavy-Metal Detection. Chemical Reviews. 2011, 111(5): 3433-58. DOI: 10.1021/cr100383r.

4. Rizescu C-Z, Stoian E-V, Poinescu A-A, Teodorescu S, Heavy metals in suspended powders from steelmaking. Proceedings of the 3rd WSEAS international conference on Engineering mechanics, structures, engineering geology, World Scientific and Engineering Academy and Society (WSEAS): Corfu Island, Greece. 2010: 48-50.

5. Bitto A, Pizzino G, Irrera N, Galfo F, Squadrito F. Epigenetic Modifications Due to Heavy Metals Exposure in Children Living in Polluted Areas. Current Genomics. 2014, 15(6): 464-8. DOI: 10.2174/1389202915066150106153336.

6. Sharma B, Singh S, Siddiqi NJ. Biomedical Implications of Heavy Metals Induced Imbalances in Redox Systems. BioMed Research International. 2014, 2014: 640754. DOI: 10.1155/2014/640754.

7. Fu F, Wang Q. Removal of heavy metal ions from wastewaters: A review. Journal of Environmental Management. 2011, 92(3): 407-18. DOI: 10.1016/j.jenvman.2010.11.011.

8. Tchounwou PB, Yedjou CG, Patlolla AK, Sutton DJ. Heavy Metals Toxicity and the Environment. EXS. 2012, 101: 133-64. DOI: 10.1007/978-3-7643-8340-4_6.

9. Huang M, Zhou S, Sun B, Zhao Q. Heavy metals in wheat grain: Assessment of potential health risk for inhabitants in Kunshan, China. Science of The Total Environment. 2008, 405(1–3): 54-61. DOI: 10.1016/j.scitotenv.2008.07.004.

10. Li Z, Ge Y, Wan L. Fabrication of a green porous lignin-based sphere for the removal of lead ions from aqueous media. Journal of Hazardous Materials. 2015, 285: 77-83. DOI: 10.1016/j.jhazmat.2014.11.033.

11. Fu J, Wang X, Li J, Ding Y, Chen L. Synthesis of multi-ion imprinted polymers based on dithizone chelation for simultaneous removal of Hg^{2+}, Cd^{2+}, Ni^{2+} and Cu^{2+} from aqueous solutions. RSC Advances. 2016, 6(50): 44087-95. DOI: 10.1039/C6RA07785D.

12. Chen J, Tong P, Lin Y, Lu W, He Y, Lu M, Zhang L, Chen G. Highly sensitive fluorescent sensor for mercury based on hyperbranched rolling circle amplification. Analyst. 2015, 140(3): 907-11. DOI: 10.1039/C4AN01769B.

13. Sedghi R, Heidari B, Behbahani M. Synthesis, characterization and application of poly(acrylamide-co-methylenbisacrylamide) nanocomposite as a colorimetric chemosensor for visual detection of trace levels of Hg and Pb ions. Journal of Hazardous Materials. 2015, 285: 109-16. DOI: 10.1016/j.jhazmat.2014.11.049.

14. Azzazy H, Shahat A, Hassan MAH, Chemosensors, compositions and uses thereof. T.A.U.O. US 20150369746 A1 Cairo, 2014. URL: https://www.google.com/patents/US20150369746.

15. Ojida A, Takashima I, Kohira T, Nonaka H, Hamachi I. Turn-On Fluorescence Sensing of Nucleoside Polyphosphates Using a Xanthene-Based Zn(II) Complex Chemosensor. Journal of the American Chemical Society. 2008, 130(36): 12095-101. DOI: 10.1021/ja803262w.

16. Güney O, Cebeci FÇ. Molecularly imprinted fluorescent polymers as chemosensors for the detection of mercury ions in aqueous media. Journal of Applied Polymer Science. 2010, 117(4): 2373-9. DOI: 10.1002/app.32077.

17. Jeong Y, Yoon J. Recent progress on fluorescent chemosensors for metal ions. Inorganica Chimica Acta. 2012, 381: 2-14. DOI: 10.1016/j.ica.2011.09.011.

18. Chen Q-Y, Chen C-F. A new Hg2+-selective fluorescent sensor based on a dansyl amide-armed calix[4]-aza-crown. Tetrahedron Letters. 2005, 46(1): 165-8. DOI: 10.1016/j.tetlet.2004.10.169.

19. Silva AJC, Silva Jr JG, Alves Jr S, Tonholo J, Ribeiro AS. Dansyl-based fluorescent films prepared by chemical and electrochemical methods: cyclic voltammetry, afm and spectrofluorimetry characterization. Journal of the Brazilian Chemical Society. 2011, 22: 1808-15. DOI: 10.1590/S0103-50532011000900025.

20. Parola AJ, Lima JC, Pina F, Pina J, Melo JSd, Soriano C, García-España E, Aucejo R, Alarcón J. Synthesis and photophysical properties of dansyl-based polyamine ligands and their Zn(II) complexes. Inorganica Chimica Acta. 2007, 360(3): 1200-8. DOI: 10.1016/j.ica.2006.11.006.

21. Tharmaraj V, Pitchumani K. An acyclic, dansyl based colorimetric and fluorescent chemosensor for Hg(II) via twisted intramolecular charge transfer (TICT). Analytica Chimica Acta. 2012, 751: 171-5. DOI: 10.1016/j.aca.2012.09.016.

22. Talanova GG, Talanov VS. Dansyl-containing fluorogenic calixarenes as optical chemosensors of hazardous metal ions: a mini-review. Supramolecular Chemistry. 2010, 22(11-12): 838-52. DOI: 10.1080/10610278.2010.514612.

23. Horie K, Yamada S, Machida S, Takahashi S, Isono Y, Kawaguchi H. Dansyl Fluorescence and Local Structure of Dansyl-Labeled Core-Shell and Core-Hair Type Microspheres in Solution. Macromolecular Chemistry and Physics. 2003, 204(1): 131-8. DOI: 10.1002/macp.200290064.

24. González-Benito J, Mikeš F, Baselga J, Lemetyinemm H. Fluorescence method using labeled chromophores to study the curing kinetics of a polyurethane system. Journal of Applied Polymer Science. 2002, 86(12): 2992-3000. DOI: 10.1002/app.11281.

25. Buruiana EC, Chibac AL, Buruiana T. Polyacrylates containing dansyl semicarbazide units sensitive for some structures in solution and film. Journal of Photochemistry and Photobiology A: Chemistry. 2010, 213(2–3): 107-13. DOI: 10.1016/j.jphotochem.2010.05.008.

26. Zhou S, Zhou Z-Q, Zhao X-X, Xiao Y-H, Xi G, Liu J-T, Zhao B-X. A dansyl based fluorescence chemosensor for Hg^{2+} and its application in the complicated environment samples. Spectrochimica Acta Part A: Molecular and Biomolecular Spectroscopy. 2015, 148: 348-54. DOI: 10.1016/j.saa.2015.03.126.

27. Jisha VS, Thomas AJ, Ramaiah D. Fluorescence Ratiometric Selective Recognition of Cu^{2+} Ions by Dansyl−Naphthalimide Dyads. The Journal of Organic Chemistry. 2009, 74(17): 6667-73. DOI: 10.1021/jo901164w.

28. Liu S-Y, He Y-B, Qing G-y, Xu K-X, Qin H-J. Fluorescent sensors for amino acid anions based on calix[4]arenes bearing two dansyl groups. Tetrahedron: Asymmetry. 2005, 16(8): 1527-34. DOI: 10.1016/j.tetasy.2005.02.032.

29. Yin J, Guan X, Wang D, Liu S. Metal-Chelating and Dansyl-Labeled Poly(N-isopropylacrylamide) Microgels as Fluorescent Cu^{2+} Sensors with Thermo-Enhanced Detection Sensitivity. Langmuir. 2009, 25(19): 11367-74. DOI: 10.1021/la901377h.

30. Murariu M, Buruiana EC. Synthesis and characterization of new optically active poly(acrylamide/methacrylurea-co-vinyl acetate) copolymers with dansyl units. Designed Monomers and Polymers. 2015, 18(2): 118-28. DOI: 10.1080/15685551.2014.971391.

31. Joshi BP, Park J, Lee WI, Lee K-H. Ratiometric and turn-on monitoring for heavy and transition metal ions in aqueous solution with a fluorescent peptide sensor. Talanta. 2009, 78(3): 903-9. DOI: 10.1016/j.talanta.2008.12.062.

32. Wanichacheva N, Watpathomsub S, Lee VS, Grudpan K. Synthesis of a Novel Fluorescent Sensor Bearing Dansyl Fluorophores for the Highly Selective Detection of Mercury (II) Ions. Molecules. 2010, 15(3): 1798. DOI: 10.3390/molecules15031798.

33. Beck MT, Nagypal L, Chemistry of Complex Equilibria. 1990, NewYork: Halsted Press. ISBN: 9780131730632.

34. Senthamizhan A, Celebioglu A, Bayir S, Gorur M, Doganci E, Yilmaz F, Uyar T. Highly Fluorescent Pyrene-Functional Polystyrene Copolymer Nanofibers for Enhanced Sensing Performance of TNT. ACS Applied Materials & Interfaces. 2015, 7(38): 21038-46. DOI: 10.1021/acsami.5b07184.

35. Hasegawa S, Takeshita H, Yoshii F, Sasaki T, Makuuchi K, Nishimoto S. Thermal degradation behavior of gamma-irradiated acetyloxy end-capped poly(oxymethylene). Polymer. 2000, 41(1): 111-20. DOI: 10.1016/S0032-3861(99)00131-7.

36. Flink S, C. J. M. van Veggel F, N. Reinhoudt D. A self-assembled monolayer of a fluorescent guest for the screening of host molecules. Chemical Communications. 1999(21): 2229-30. DOI: 10.1039/A906563F.

37. Ding L, Fang Y, Jiang L, Gao L, Yin X. Twisted intra-molecular electron transfer phenomenon of dansyl immobilized on chitosan film and its sensing property to the composition of ethanol–water mixtures. Thin Solid Films. 2005, 478(1–2): 318-25. DOI: 10.1016/j.tsf.2004.07.013.

RESEARCH ARTICLE

Türkçe Öz ve Anahtar Kelimeler

Dansil Yan Grubuna Sahip Poli(Metil Metakrilat-ko-Hidroksietil Metakrilat) Polimerinin Sentezi, Karakterizasyonu ve Kemo-hissetme Uygulaması

Erdinc Doganci, Mesut Gorur

Öz: Yeni bir dansil yan grubuna sahip polimer (**P2**) hazırlanmış ve metal katyon hissedici kimyasal prob olarak kullanılmıştır. **P2**'nin sentezi art arda gelen serbest radikal polimerizasyonu ve esterleştirme ile gerçekleştirilmiştir. **P2**, dansil grubuna ait karakteristik UV-Vis ve floresans emisyon bantları göstermektedir. **P2**'nin floresans emisyon şiddeti, ilave edilen metal iyonlarının derişimi artırıldıkça azalmaktadır. En yüksek söndürme etkinliği (QE) Pb^{2+} için (%84,56) ve Co^{2+} için (%83,69) elde edilmiştir. Bunun yanında, **P2**'nin Pb^{2+} ilavesine verdiği cevaplar 50 eşdeğere kadar oldukça doğrusal bir şekilde gitmektedir. Cd^{2+}, Hg^{2+}, Mn^{2+} ve Zn^{2+} katyonlarının varlığı belirgin bir girişim etkisine neden olmamaktadır. Bu sebeple, **P2**'nin Pb^{2+} katyonu için potansiyel bir floresans kimyasal sensör olarak kullanılabileceği anlaşılmaktadır.

Anahtar kelimeler: Dansil grubu; metal iyon sensörü; metil metakrilat; 2-hidroksietil metakrilat; bütülmüş molekül içi yük iletimi.

RESEARCH ARTICLE

Preparation of a Human Skin-Mimicking Gels for *In Vitro* Measurements of the Dual-Band Medical Implant Antenna

Erdinc Doganci[1]*, Mustafa Hikmet Bilgehan Ucar[2]*, Adnan Sondas[2]

[1]Department of Chemistry and Chemical Processing Tech., Kocaeli University, Kocaeli, Turkey
[2]Department of Information Systems Engineering, Faculty of Technology, Kocaeli University, Kocaeli, Turkey

Abstract: The purposes of this study are to design a small size implantable antenna and to present a complementary recipe for a human skin-mimicking material for *in vitro* testing of implantable antennas operating at MICS (Medical Implant Communications Service, 402–405 MHz) and ISM (Industrial, Scientific and Medical, 2.4 GHz–2.48 GHz) bands. Approximate electrical properties of human tissues at MICS and ISM bands were obtained by mixing deionized water, sucrose, sodium chloride (NaCl), and poly(acrylic acid) (PAA or Carbomer) with different content percentages. To test the antenna *in vitro*, skin mimicking gels were made that to show electrical properties real skin tissue (relative permittivity (ε_r) and conductivity (σ)) for the operation frequencies of ISM and MICS bands. For the antenna performance evaluations the measurements of the antenna (return loss (S_{11})) have been performed by placing in to the skin mimicking gels. The measurements were taken in the 1 GHz - 5 GHz frequency band. The measurement and simulation results are quite good agreement except some discrepancy in S_{11} levels and frequency bands.

Keywords: Skin-mimicking gel; carbomer; implantable antennas; MICS-band; ISM-band.

*Corresponding authors. edoganci@kocaeli.edu.tr; Tel: +90 262 349 43 (E.D.) and mhbucar@kocaeli.edu.tr; Tel: +90 262 303 22 61 (M.H.B.U.).

INTRODUCTION

Recently, wireless telemetric systems have attracted much attention because of the needs for enable early detection of diseases and continuous monitoring of physiological parameters such as oxygen level, sucrose level, heart rate, blood pressure, and bodily temperature in medical technology (1-5). Antennas are crucial parts of these telemetric systems because they supply communication between the patient and the external environment. Implantable antennas have recently been getting extensive interest in several wireless data telemetry applications such as cardiac pacemakers, brain pacemakers, nerve signal recorders, artificial eyes, cochlear implants, implantable drug pumps, and glucose sensors with the developments in telecommunications and telemedicine (5-8). However, designing antennas for implantable telemetric systems is a quite challenging problem for researchers because of impedance matching, biocompatibility, low power requirements, antenna miniaturization, and high losses in the tissue. These factors play a vital role in the design for overall system reliability (9-14). In addition, the body tissue temperature and placing the antenna inside a biological tissue can be added significant complexity to the problem. Because the antenna resides in the human body consisting of many loss media with a very high permittivity such as skin, muscle, blood, and bone. The human body has electrical properties (such as relative permittivity and conductivity) that are frequency dependent (15-17). For this reason, antenna placed in the human body is designed as based on electrical properties of the human tissue.

Commonly, antenna engineers developed their antenna designs according to the specifications (such as operating bands, size, *etc*.) in simulators, and here we use Computer Simulation Technology (CST) Microwave Studio. After obtaining the optimum antenna design, it should be measured via testing devices using the Vector Network Analyzer (VNA) to observe radiation parameters [S_{11}, Antenna Gain (*G*) and Directivity (*D*)]. The most critical antenna parameter is the S_{11} both in simulation and measurement. In the S_{11} measurements, the VNA transmits a small amount of power to your antenna and measures how much power is reflected back ($S_{11}=10 \log_{10} (P_i/P_r)$ (in decibels; dB), here P_i, P_r stand for incident and delivered power, respectively) to the VNA, hence it is known as the reflection coefficient. For example if the $S_{11}=0$ dB, then all the power (100%) is reflected from the antenna and nothing is radiated, or if the $S_{11}=-10$ dB, then ~30% is reflected from the antenna and 70% is radiated at the designed frequency band. In the antenna radiation considerations, it is desired that almost the entire power fed to the antenna should be radiated at the resonant (operation) frequency. In this context, in the antenna's S_{11} performance evaluations, $|S_{11}|<-10$ dB standard (with 50Ω system impedance) is sufficient [18].

Moreover, measurement set up should be same as the simulations. The numeric analysis of the implant antennas is executed in a tissue medium which has electrical properties of the skin (ε_s, σ_s). In this context, to provide realistic measurement set up, there are two possible ways to create the medium which the implant antenna operates. One uses real tissue (*in vivo*), the other uses skin-mimicking gels (*in vitro*). *In vivo* measurement is not practical during the design process and it also needs some ethical permission from the Food and Drug Administration (FDA). Conversely, *in vitro* measurement is crucial to verify the proper of these antennas. Hence we used skin-mimicking gels (*in vitro*) in antenna measurements. *In vitro* testing of these antennas requires the development of materials that can mimic the electrical properties of the human skin. Recently, an implantable dual-band antenna operating at MICS and ISM bands was designed and fabricated for in body wireless data telemetry [13].

The aim of this study is to propose a complementary for human tissue gels that mimic both relative dielectric constant (ε_r) and conductivity (σ) of the human tissue at both MICS and ISM bands in the light of recent studies. Sucrose, NaCl, deionized water, and carbomer were used to formulate the desired gels. The gels were prepared via mixing different percentages of different biocompatible chemicals for tissue samples in the literature (13, 17, 19). In the literature, agarose, a polysaccharide polymer material, was widely used to ensure the formation of gel of the mixture and in our study we used carbomer instead of agarose for this aim. Carbomer is a generic name for homopolymer of acrylic acid having high molecular weight, which is cross-linked, or bonded, with any of several polyalcohol allyl ethers. In our study, we have focused on the use of these polymers due to very good mucoadhesive properties. Carbomer, which is a type of anionic polymer, is water-soluble at neutral pH. It is well known as anionic polyelectrolyte that the side chains of PAA would lose their protons and obtain negative ions. It is recognized as a binder when placed in water due to its ability to absorb water and swell into many times their original size and weight. Carbomers are frequently used as thickening, dispersing, suspending, and emulsifying agents in paints, pharmaceuticals, cosmetics, and personal care products including skin, hair, nail, makeup products, as well as dentifrices [20]. Also, due to obtainable biocompatible matrices for medical applications, these polymers are convenient such as gels for skin care or skin disease treatment products. Recently, for the development of polymeric matrices, investigations aimed towards the clarification of the conformational changes of the polymeric gel during neutralization, light irradiation, and embedment of gold nanoparticles [21, 22]. To the best of our knowledge, this is the first report on the implantable antenna application of a human skin mimicking gel containing carbomer as polymer to solidify the liquid blend to simplify measurements. These gels were created by adding Carbomer in the liquid solution and waiting

the blend until a clear solution forms overnight. Thus, they will not be dissolved in one-another during *in vitro* testing. There was a very good agreement between the electrical properties of the proposed material and the human skin at ISM and MICS bands.

MATERIALS AND METHODS

Materials

Carbomer (Rheocare C Plus, commercial, BASF), Sodium chloride (NaCl, Aldrich, ≥99%), water (deionized, Sigma-Aldrich) and sucrose (commercial) were used as received.

Physical Measurements

Numeric analysis of the proposed antenna design and the skin mimicking gels were carried out using CST Microwave Studio simulation software which is a well-known electromagnetic (EM) simulator based on Finite Integration Technique (FIT) in the time domain. Also return loss (S_{11}) measurements of the implant antennas in the proposed skin mimicking gel medium were carried out using Rohde & Schwarz ZVB8 Vector Network Analyzer (VNA).

Preparation of Human Skin-Mimicking Gel

Table 1 shows the amount and percentages of content of gels used to build the proposed complementary recipes for human skin-mimicking materials for the MICS and ISM bands. Firstly, sucrose, deionized water and NaCl (only MICS band) were added to an 80-mL beaker equipped with a magnetic stirrer and stirred for 20 minutes. These human skin-mimicking gels were formed by adding dry carbomer in liquid solution. A clear solution was obtained by heating the mixture at 80 °C for 1 h and then the mixtures were solidified by cooling to room temperature to simplify measurements. The individually prepared human skin-mimicking gels for MICS and bands ISM are shown in Figure 1a and Figure 1b, respectively.

Table 1. Suggested ingredients for human skin tissue.

Frequency	Ingredients (%)
ISM	Sucrose 53%, Deionized water 47%, Carbomer for 0.5 g in 40 mL solution
MICS	Sucrose 56.18%, NaCl 2.33%, Deionized water 41.49%, Carbomer for 0.5 g in 40 mL solution
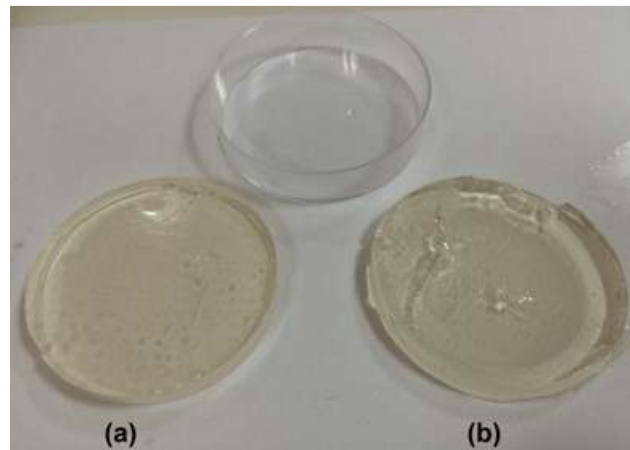
Figure 1. The individually prepared human skin-mimicking gels according to suggestions listed in Table 1 for the concerned frequency bands of (a) MICS, (b) ISM gel form view.

Design of Microstrip Implantable Antenna

The microstrip implantable antenna which is shown in Figure 2 was designed using concentric square split-ring elements with inserting a metallic pad between the rings. Also note that the antenna is excited via SMA type coaxial connector.
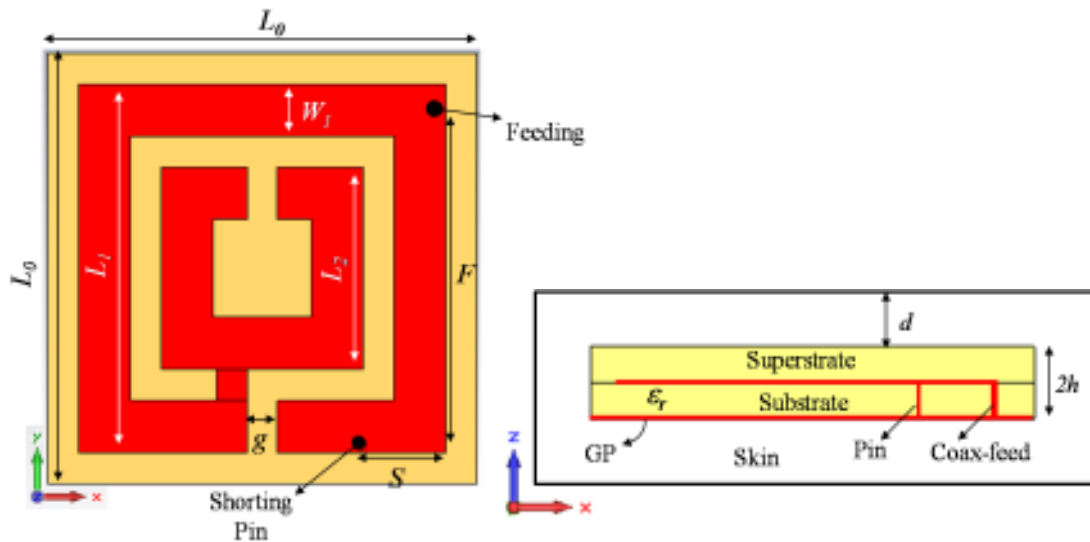
Figure 2. The proposed microstrip implantable antenna design: (L_0=14, L_1=12, W_1=1.7, g=1, S=2.8, F=11.2, h=1.27 (all in mm), ε_r=10.2).

The radiating elements were placed on a ground backed thin substrate (Rogers RO3210) with a thickness of h=1.27 mm and electrical properties of ε_r=10.2 and tan δ=0.003. Besides, the outer ring element and the ground plane were connected each other by means of shorting-pin with a radius of 0.2 mm. The radiating element is sandwiched between two substrate layers to prevent the connection between tissue and the metallic elements. The proposed antenna located in the tissue covers the two bands, namely MICS (402 – 405 MHz) and ISM (2.4 – 2.48 GHz) bands. We also note that numerical analysis of the proposed implantable antenna design and the skin mimicking gels were carried out using CST Microwave Studio simulation software which based on finite Integration technique in the time domain.

The simulated return loss (S_{11}) characteristic of the implant antenna is given in Figure 3. As can be seen, the antenna provides an impedance bandwidth of 30 MHz (392-422 MHz) and 300 MHz (2.25-2.55 GHz) covering the MICS and ISM standards respectively. Note that S_{11} ≤-10 dB standard with 50Ω system impedance is considered.
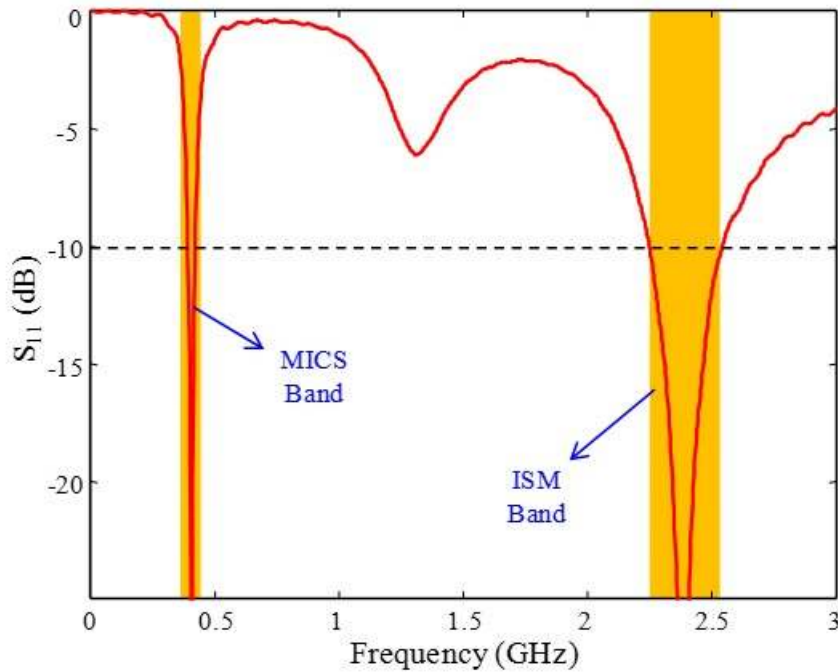
Figure 3. The simulated return loss characteristics of the implantable antenna design.

RESULTS AND DISCUSSIONS

Characterization of Human Skin-Mimicking Gel

The numeric analysis of the implant antennas is realized in a tissue medium which has electrical properties of human skin (ε_s, σ_s). In this context, we used human skin-mimicking gels which are significant for *in vitro* testing of implantable systems to provide realistic measurement for the fabricated antenna. For *in vitro* testing of dual band implantable systems, characterizations of human tissue-mimicking gels examine the interaction between tissues and electromagnetic waves. For preparation of these gels, many recipes have been proposed in the literature and used in SAR measurements, cardiac pacemakers, microwave imaging systems, implantable antennas, and ultrasound measurements (23-29). The characterization of skin-mimicking materials must be made for *in vitro* measurements because the implanted antenna must work through the human skin. To create human skin-mimicking gels we used materials which are usually made of low toxic, edible, and easily obtainable substances such as sucrose (sucrose), salt (NaCl), carbomer, and deionized water. Sucrose is used to lower the dielectric constant of water whereas salt is used to increase the conductivity of the mixture. ε_r decreases significantly as sucrose concentration increases in the mixture. Besides, there is only a small increase in σ as the sucrose concentration increases and also an increase in NaCl content concentration decreases ε_r and significantly increases σ [30, 31]. Carbomer has been used as a gelling agent. To see the practical performance of the antenna, the gels were prepared by

mixing different content percentages of different chemicals for human tissue samples suggested in the references [32, 33].

Results of the Measurement

We fabricated the antenna design and located in two different skin mimicking gel at MICS and ISM bands for the purpose of realistic antenna measurement. The fabricated antenna and the measurement set up are given in Figure 4. As seen, the fabricated antenna is located in the gel and the return loss measurements were carried out using Rohde & Schwarz ZVB8 VNA.

(a)

(b)   (c)
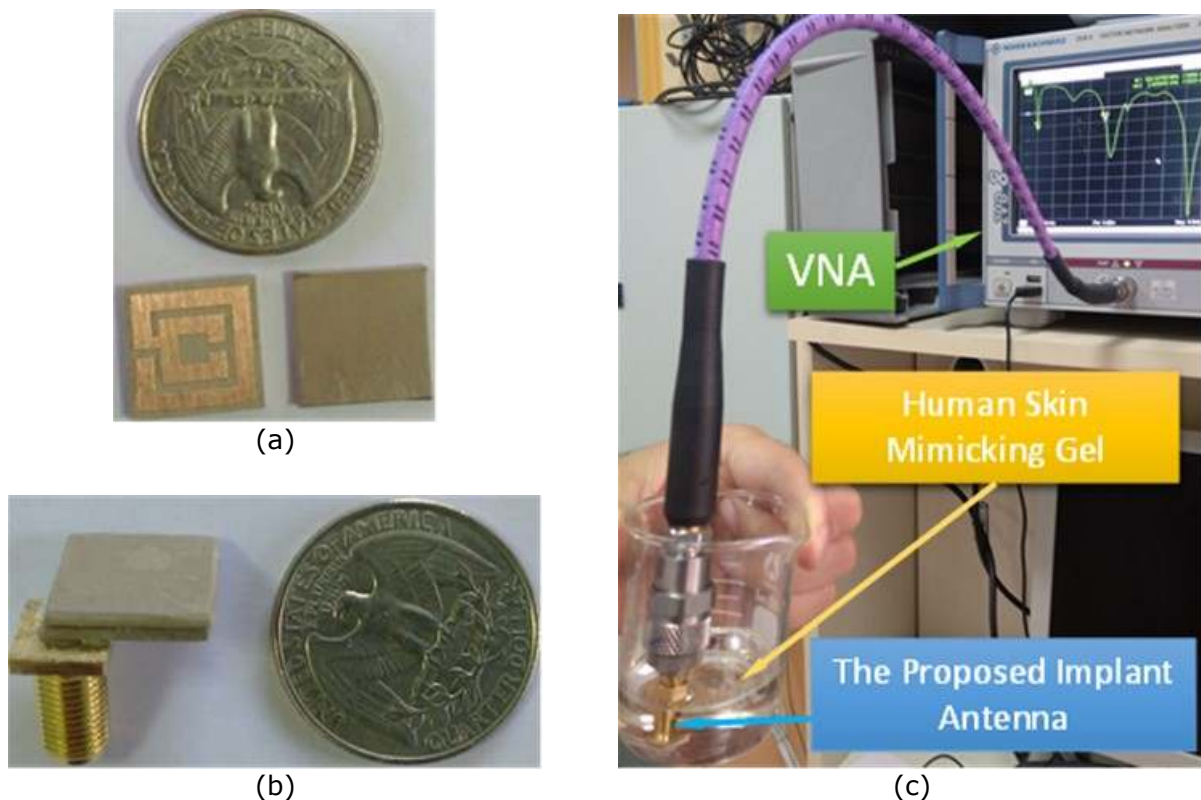
Figure 4. (a) The fabricated layers (b) perspective view of the implant antenna design and (c) the S_{11} measurement set up.

The measured and the simulated return loss characteristics of the implant antenna are displayed in Figure 5. As seen in the figure, the measurement and simulation results agree quite well except some frequency and S_{11} level differences mainly due to fabrication, material tolerances, and unknown electrical properties of skin-mimicking gel. Of importance is that for the realistic antenna measurements individually prepared gels for the MICS and ISM operation bands are sufficient. On the other hand, those results show the estimated dual-band (MICS and ISM bands) performance.
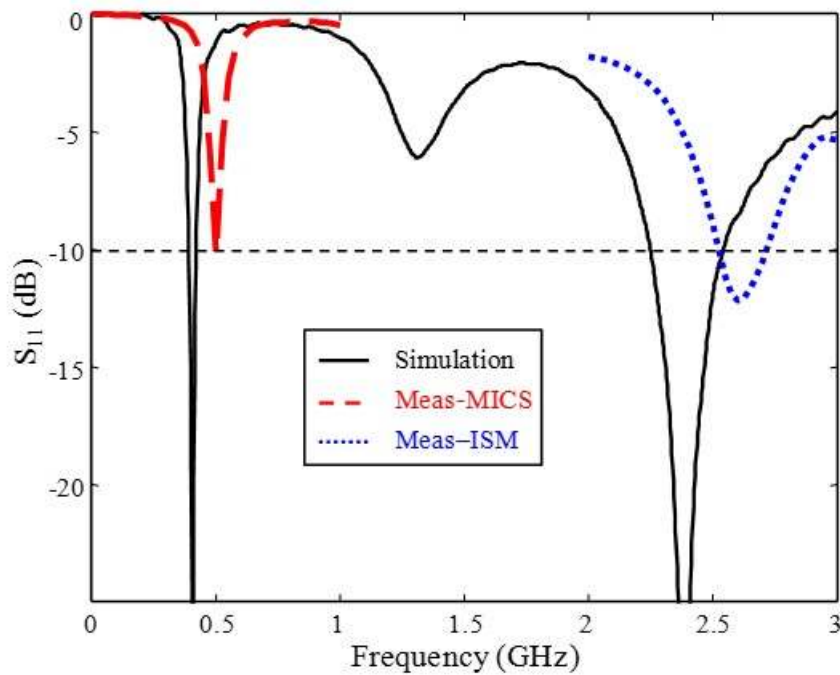
Figure 5. The return loss (S_{11}) characteristics of the antenna: simulation versus measurement.

CONCLUSION

In this study, we prepared two different human skin-mimicking gels and designed a small size dual band implantable micro-strip antenna for medical applications covering ISM and MICS bands in the light of recent studies. We developed gels to mimic the electrical properties of real human skin tissue and used these gels for *in vitro* testing of the proposed dual-band implantable antenna. The recipe for the skin mimicking gels is composed of carbomer, sucrose, NaCl, and deionized water at several percentages. We note that numerical analysis of the proposed antenna carried out using CST Microwave Studio software. It has been shown that the measurement and simulation results agree with each other except for some discrepancy in S_{11} levels and frequency bands. These differences mainly due to antenna fabrication, material tolerances and unknown electrical properties of skin-mimicking gel. Currently, we are working to acquire perfect complementary recipe using alternative materials instead of sucrose, carbomer, agarose, *etc*. to match both the ε_r and σ of human skin for the ISM and MICS bands.

ACKNOWLEDGMENTS

REFERENCES

[1] Asili M, Green R, Seran S, Topsakal E. A small implantable antenna for medradio and ISM bands. IEEE Antennas and Wireless Propagation Letters. 2012, 11: 1683-1685. DOI:10.1109/LAWP.2013.2241723.

[2] Beach RD, Conlan RW, Godwin MC, Moussy F. Towards a miniature implantable in vivo telemetry monitoring system dynamically configurable as a potentiostat or galvanostat for two- and three-electrode biosensors. IEEE Trans. Instr. Meas. 2005, 54 (1): 61-72. DOI:10.1109/TIM.2004.839757.

[3] Beach RD, Kuster FV, Moussy F. Subminiature implantable potentiostat and modified commercial telemetry device for remote glucose monitoring. IEEE Trans. Instr. Meas. 1999, 48 (6): 1239–1245. DOI:10.1109/19.816143.

[4] Yilmaz T, Karacolak T, Topsakal E. Characterization and testing of a skin mimicking material for implantable antennas operating at ISM band (2.4 GHz-2.48 GHz). IEEE Antennas and Wireless Propagation Letters. 2008, 7: 418-420. DOI:10.1109/LAWP.2008.2001736.

[5] Furse CM. Design of an antenna for pacemaker communication. Microw. RF. 2000, 39 (3): 73-76. URL: http://www.eng.utah.edu/~cfurse/Publications/Micorwaves%20and%20RF%20paper.pdf.

[6] Cavuoto J. Neural engineering's image problem. IEEE Spectr. 2004, 41 (4): 32-37. DOI: 10.1109/MSPEC.2004.1279191.

[7] Schuster JW, Luebbers RJ. An FDTD algorithm for transient propagation in biological tissue with a Cole-Cole dispersion relation. Antennas and Propagation Society International Symposium, IEEE.1998, 4: 1988-1991. DOI:10.1109/APS.1998.701597.

[8] Weir RF, Troyk PR, DeMichele G, Kuiken T. Implantable myoelectric sensors (IMES) for upper-extremity prosthesis control-preliminary work. Engineering in Medicine and Biology Society, Proceedings of the 25th Annual International Conference of the IEEE, 2003, 2: 1562-1565. DOI:10.1109/IEMBS.2003.1279658.

[9] Budinger TF. Biomonitoring with wireless communications. Annual Review of Biomedical Engineering. 2003, 5 (1): 383-412. DOI: 10.1146/annurev.bioeng.5.040202.121653.

[10] Gosalia K, Humayun MS, Lazzi G. Impedance matching and implementation of planar space-filling dipoles as intraocular implanted antennas in a retinal prosthesis. IEEE Transactions on Antennas and Propagation. 2005, 53 (8): 2365-2373. DOI:10.1109/TAP.2005.852514.

[11] Jaehoon K, Rahmat-Samii Y. Implanted antennas inside a human body: simulations, designs, and characterizations. IEEE Transactions on Microwave Theory and Techniques. 2004, 52 (8): 1934-1943. DOI:10.1109/TMTT.2004.832018.

[12] Karacolak T, Cooper R, Topsakal E. Electrical properties of rat skin and design of implantable antennas for medical wireless telemetry. IEEE Transactions on Antennas and Propagation. 2009, 57 (9): 2806-2812. DOI:10.1109/TAP.2009.2027197.

[13] Karacolak T, Hood AZ, Topsakal E. Design of a dual-band implantable antenna and development of skin mimicking gels for continuous glucose monitoring. IEEE Transactions on Microwave Theory and Techniques. 2008, 56 (4): 1001-1008. DOI:10.1109/TMTT.2008.919373.

[14] Soontornpipit P, Furse CM, You Chung C. Design of implantable microstrip antenna for communication with medical implants. IEEE Transactions on Microwave Theory and Techniques. 2004, 52 (8): 1944-1951. DOI:10.1109/TMTT.2004.831976.

[15] Karacolak T. Implantable antennas for wireless data telemetry: Design, simulation, and measurement techniques. Electrical and Computer Engineering, Mississippi State University, Mississippi State, Mississippi, 2009:1-123. ISBN: 9781109516692.

[16] Topsakal E. Antennas for medical applications: Ongoing research and future challenges. Electromagnetics in Advanced Applications, 2009. ICEAA '09. International Conference on, 2009: 890-893.DOI:10.1109/ICEAA.2009.5297319.

[17] Zengin F, Akkaya E, Turetken B, San SE. Design and realization of ultra wide-band implant antenna for biotelemetry systems. General Assembly and Scientific Symposium, 2011 XXXth URSI, 2011: 1-4. DOI:10.1109/URSIGASS.2011.6051320.

[18] Bird TS. Definition and misuse of return loss. IEEE Antennas and Propagation Magazine. 2009, 51 (2): 166-167. DOI: 10.1109/MAP.2009.5162049.

[19] Yilmaz T, Characterization of tissue mimicking materials for testing of implantable and on body antennas. Electrical engineering, Mississippi State University, Mississippi, 2009: 1-69. URL: http://gradworks.umi.com/14/67/1467229.html.

[20] Orwoll RA, Yong CS. Poly(acrylic acid). J.E. Mark (Ed.) Polymer Data Handbook. Oxford University Press, Inc., Oxford, England, 1999: 252–253. ISBN: 978-0195107890.

[21] Todica M, Pop CV, Stefan R, Nagy M, Garabagiu S. Spectroscopic investigation of some poly (acrylic acid) gels with embedded gold nanoparticles. Studia Universitatis Babes-Bolyai, Chemia. 2015, 60 (1): 19-28. URL: http://chem.ubbcluj.ro/~studiachemia/issues/chemia2006_2015/Chemia2015_1.pdf.

[22] Todica M, Stefan R, Pop CV, Papuc I, Stan O, Olar EL. UV-VIS and fluorescence investigation of some poly(acrylic) gels. Studia Universitatis Babes-Bolyai, Chemia. 2015, 60(1):7-17.URL: http://chem.ubbcluj.ro/~studiachemia/issues/chemia2006_2015/Chemia2015_1.pdf.

[23] Ballen M, Kanda M, Chou CK, Q. Balzano. Formulation and characterization of tissue simulating liquids used for SAR measurement. Proc. 23rd Annu. Bioelectromagn. Soc. Meeting. 2001, 14 (3): 80.

[24] Chou CK, Chen GW, Guy AW, Luk KH. Formulas for preparing phantom muscle tissue and various radio frequencies. Bioelectromagn. 1984, 5: 435-441. DOI:10.1002/bem.2250050408.

[25] Fukunaga K, Watanabe S, Yamanaka Y. Dielectric properties of tissue equivalent liquids and their effects on specific absoption rate. IEEE Trans. Electromagnetic Compatibility. 2004, 46 (1): 126-129. DOI:10.1109/TEMC.2004.823624.

[26] Lazebnik M, Madsen EL, Frank GR, Hagness SC. Tissue-mimicking phantom materials for narrowband and ultrawideband microwave applications. Phys.Med. Biol. 2005, 50: 4245–4258. DOI:10.1088/0031-9155/50/18/001.

[27] Peyman A, Gabriel C. Tissue equivalent liquids for SAR measurement at microwave frequencies. Proc. 24th Annu. Bioelectromagn. Soc. Meeting. 2002, P-53: 184–185.

[28] Stuchly SS. Specific absorption rate distributions in a heterogeneous model of the human body at radio frequencies. Nat. Tech. Inform. Ser. PB 87-201 356/AS. 1987, 89. URL: https://nepis.epa.gov/Exe/ZyPDF.cgi/2000TRUE.PDF?Dockey=2000TRUE.PDF.

[29] Stuchly SS, Kraszewski A, Stuchly MA, Hartsgrove G, Spiegel RJ. RF energy deposition in a heterogeneous model of man:Far-field exposures. IEEE Trans. Biomed. Eng. 1987, BME-34 (12): 951–957. DOI:10.1109/TBME.1987.325934.

[30] Kumar SA, Shanmuganantham T. Design and analysis of implantable CPW fed bowtie antenna for ISM band applications. AEU - International Journal of Electronics and Communications. 2014, 68 (2): 158-165. DOI:10.1016/j.aeue.2013.08.003.

[31] Xia W, Saito K, Takahashi M, Ito K. Performances of an implanted cavity slot antenna embedded in the human arm. IEEE Transactions on Antennas and Propagation. 2009, 57 (4): 894-899. DOI:10.1109/TAP.2009.2014579.

[32] Karacolak T, Topsakal E. Electrical properties of nude rat skin and design of implantable antennas for wireless data telemetry. Microwave Symposium Digest, IEEE MTT-S International. 2008, 907-910. DOI:10.1109/MWSYM.2008.4632980.

[33] Kiourti A, Nikita KS. Miniature scalp-implantable antennas for telemetry in the mics and ism bands: design, safety considerations and link budget analysis. IEEE Transactions on Antennas and Propagation. 2012, 60 (8): 3568-3575. DOI:10.1109/TAP.2012.2201078.

Çift Bantlı Medikal İmplant Antenin *In Vitro* Ölçümleri için İnsan Derisini Taklit Eden Jellerin Hazırlanması

Erdinc Doganci, Mustafa Hikmet Bilgehan Ucar, Adnan Sondas

Öz: Bu çalışmanın amaçları küçük boyutlu ve vücuda yerleştirilebilir bir anteni tasarlamak ve MICS (Medikal İmplant Haberleşme Servisi, 402-405 MHz) ve ISM (Endüstriyel, Bilimsel ve Medikal, 2,4 GHz-2,48 GHz) bantlarında çalışan, vücuda yerleştirilebilir antenlerin *in vitro* testi için insanda deriyi taklit eden bir malzeme oluşturan bir reçete sunmaktır. MICS ve ISM bantlarında insan dokusunun yaklaşık elektriksel özellikleri deiyonize su, sakkaroz, sodyum klorür (NaCl) ve poli(akrilik asit) (PAA veya carbomer) içeriği farklı yüzdelerde karıştırılarak incelenmiştir. Anteni *in vitro*'da denemek için, deriyi taklit eden jeller yapılmıştır, böylece gerçek deri dokusunun elektriksel özellikleri taklit edilmiştir (relatif permittivite (ε_r) ve kondüktivite (σ)). Çalışma ISM ve MICS bantlarının çalışma frekanslarında yürütülmüştür. Anten performansı değerlendirmesi için, anten deri taklit eden jellerin içine yerleştirilerek ölçümler (geri dönüş kaybı (S_{11})) yapılmıştır. Ölçümler 1 GHz – 5 GHz frekans bandında alınmıştır. Ölçüm ve simülasyon sonuçları çok iyi uyum göstermektedir, yalnızca S_{11} seviyeleri ve frekans bantlarında bir miktar uyumsuzluk görülmüştür.

Anahtar kelimeler: Deriyi taklit eden jel; carbomer; vücuda yerleştirilebilir antenler; MICS-bandı; ISM-bandı.

(This article was presented to the 28th National Chemistry Congress and submitted to JOTCSA as a full manuscript)

Selective Gas-Phase Oxidation of Monochlorotoluenes over Modified Oxovanadium Systems Supported on Al₂O₃ and SiO₂

Arif Javanshir Efendi, Elmir Magsad Babayev, Fakhriyya Mashallah Nasiri, Bilqeyis Adil Ismayilova , Firuza Alasgar Yunisova

Institute of Catalysis and Inorganic Chemistry named after M.Nagiev, NAS of Azerbaijan, Baku, Azerbaijan

Abstract: V-Mo-O/SiO₂ materials were prepared by the impregnation techniques and characterized by Scanning Electron Microscopy (SEM), FT-IR, Thermal analysis, N₂ adsorption/desorption and X-ray powder diffraction (XRD) to determine the phase structure and loadings of vanadium species. This material was tested for solvent-free catalytic oxidation of monochlorotoluene under chosen conditions. The results show that V-Mo-O/SiO₂ is an effective catalyst, exhibiting a conversion of monochlorotoluene and selectivity on monochloromaleic anhydride 75–85%, 24–32% respectively. Furthermore, the catalyst can be easily recovered and reused for 20-25 hours without a significant loss in its activity and selectivity. The oxidation rate and direction determined by the temperature (315-450 °C), proportions between the reagents (1:1–1:15 mol/L), bond dissociation energies, the effects of active components of catalyst, and contact time.

INTRODUCTION

Catalytic systems based on vanadium oxides which are supported on different types of supporting agents are one of the most studied ones, because of their wide range of applicability in the petrochemical industry, especially in alkyl aromatic hydrocarbons and its chlorosubstituted derivatives' conversion. Oxovanadium systems modified by Mo, Sr, Bi, Cu, Cr, and Co were prepared by co-precipitation, impregnation, and mechanical-chemical shifting for carrying out heterogeneous oxidation reactions of alkylaromatic chlorohydrocarbons, and the systems supported on carriers Al_2O_3, SiO_2, TiO_2, pumice, and coal showed higher performance among the received systems [1–4]. Depending on the specific oxide support vanadia catalysts may show different catalytic activity and selectivity due to the nature and the surface area of the support as well as the vanadium content, all of which are key factors in the formation of surface species [5–7]. Apart from this, vanadium oxide has also been explored for various other applications including pseudo-capacitors and cathode material in various conversion reactions. Notably, vanadium has displayed excellent catalytic activities in all forms, whether it has been employed as a supported active phase or in the form of mixed oxides prepared in combination with other ions; it displayed efficient catalytic properties as an oxidation catalyst [8, 9]. However, the zeal for finding a better performing catalyst for the selective oxidation of toluene and its chlorinated derivations still is an ongoing process.

In this respect, the present work is aimed at preparation and textural, structural and acid characterization as well as catalytic behavior in the gas phase selective oxidation of mono-CT of vanadium systems with different V_2O_5 loading, supported Al_2O_3 and SiO_2. Catalytic systems were prepared co-precipitation and they characterized by FT-IR, X-ray diffraction, N_2 adsorption/desorption, thermal analysis, and SEM. The effect of heat treatment and phase formation of the synthesized catalytic systems on their activity in the oxidation reactions was studied.

MATERIALS AND METHODS

The systems were mainly received by diluting vanadate or phosphate in oxalate or hydrochloric acid. The solution was evaporated for a short time and permeated on SiO_2 or Al_2O_3 and subsequently desiccated in air at 180–230 °C for an hour, further step being calcination in the fume cupboard at 270–380 °C for two hours, and lastly, calcination for an hour at 500 °C. Before the reaction the reagents were heated above than 100 °C, and then oxidation process was carried out. Kinetic regularities of heterogeneous catalytic oxidation of chlorinated alkyl aromatic hydrocarbons studied [2,3]. Probable scheme of mechanism, kinetics and mathematical models of the oxidation processes were proposed. The influence of

initial, intermediate products and reaction yields on the kinetics of oxidation reactions were revealed.

Phase identification and quantification: Phase properties (cell parameters, crystallite size, and lattice strain), are offered by the crystal structure of synthesized catalytic systems, determined by the Bruker manufactured (Germany) D2 Phase X-ray powder diffraction analyzer.

Surface area (S_{BET}, m^2/g) and pore size (cumulative volume VΣ, cm^3/g; diameter d, Å) information of catalytic systems were obtained from the adsorption-desorption isotherm of nitrogen at its liquid temperature (-196 ^{0}C), using a Gas Adsorption Surface Porosimeter (Thermo Scientific, Italy). Prior to the measurements, all samples were degassed to 0.1 Pa. Brunauer–Emmett–Teller (BET) surface areas were calculated assuming a cross-sectional as 0.164 nm^2 for nitrogen molecule.

Thermogravimetric analyses were carried out using NETZSCH STA 449F3 (Germany). Temperature was programmed from 25 °C to 900 °C at a heating rate of 10 °C min^{-1}. The weight of the nanopowder obtained was 0.6 g.

SEM and elemental analysis were carried out. This was used to determine the morphology of system and its elemental composition. Element analysis of the catalyst precursor components was performed on TruSpec Micro analyzer of Horiba company.

Selective oxidation mono–CT was carried out in a continuous flow fixed-bed reactor at an atmospheric pressure and in the temperature range of 370–480 °C. Chlorotoluenes were fed by means of a micro-feeder at 0.8 mL/h and the ratio CT/air (O_2) =1:20. The catalyst was pre-treated at the reaction temperature for 1 h in a F_{air} = 25 cm^3/min. An analysis of reagent and product composition was carried out using Agilent 7820A (Agilent Technologies, USA) Gas Chromatography equipped a flame ionization detector (FID) and HP5 column.

The values of CT oxidation rate, r_{CT}, were obtained from conversion (X) values, according to the equation, $r_{CT}=XF/W\times100$, where W is catalyst weight, and F is feed rate of CT (mol/h).

RESULTS AND DISCUSSION

Characterization of Catalysts

The morphology and particle size of the synthesized catalysts were characterized using SEM. The SEM micrographs of the pre-calcined (300 ^{0}C) catalyst V-Mo-O/SiO_2, where V:Mo=1:1– 1:5, are shown in Figure 1. It was observed that the morphology of the synthesized catalysts

is not well defined, and the surface appears to be rugged without any obvious phase separation. The stoichiometric amount of elements was confirmed from the elemental analysis and found to be approximately in agreement with calculated value. The result of elemental analysis is given in Table 1. There is insignificant amount of calcium and sodium in the system which probably does not influence catalytic behavior in the system, as seen from Table 1.
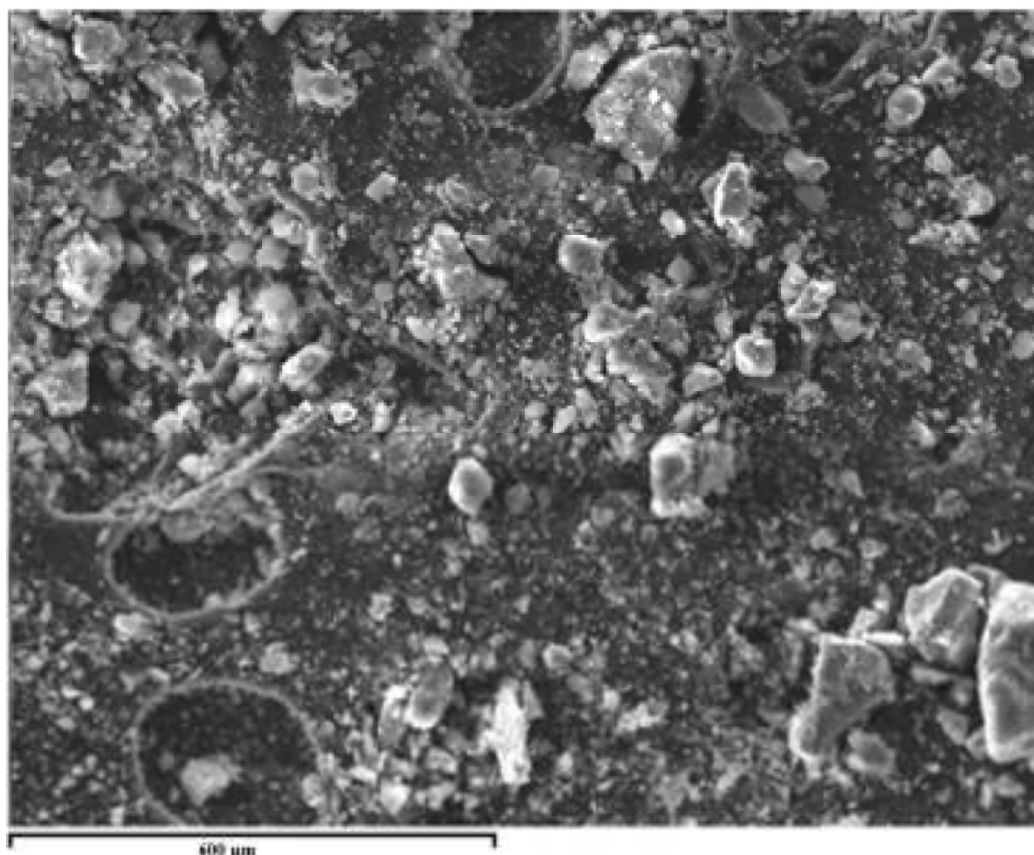
Figure 1. SEM of the catalysts V-Mo-O/SiO$_2$ at 300 °C.

Table 1. Elemental characterization of VMoO/SiO$_2$ (V:Mo=1:2).

Element	Weight %	Atom %	Comp %	Formula
Na K	0.43	0.39	0.58	Na$_2$O
Si K	28.62	21.26	61.23	SiO$_2$
Mo K	9.59	6.46	21.97	MoO
Ca K	0.21	0.11	0.30	CaO
V K	8.92	3.66	15.93	V$_2$O$_5$
O	52.23	68.12		
Total	100.00			

Figure 2 shows X-ray diffraction patterns of mixed oxides of phosphorus silica, with different ratio of vanadium oxide pre-calcined at 300 °C. Both oxovanadium (33.3%), and vanadium pentoxide (28.3 %) in the catalytic system were found, and vanadium is included of the monoclinic structure.
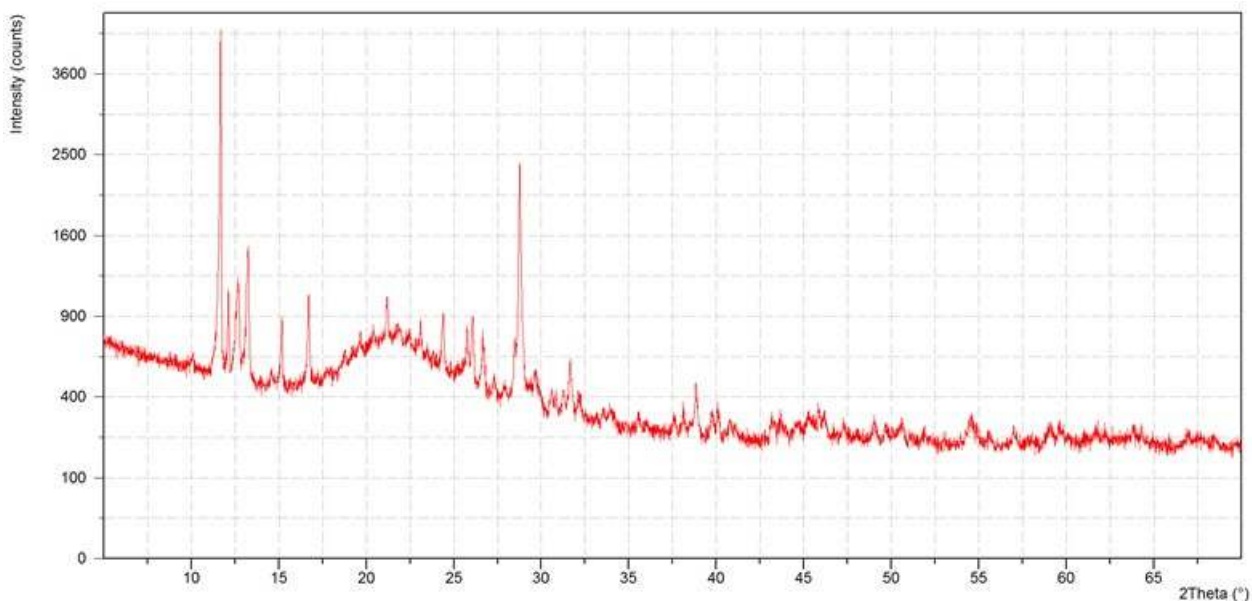
Fig.2. XRD patterns of V-Mo-O/SiO$_2$ (V:P=1:2) calcined at 300 ^{0}C.

The thermal stability of the synthesized catalyst with different % loading of vanadium oxide systems were studied using TGA analysis. Temperature was programmed from 25 °C to 900 °C at a heating rate of 10 °C min^{-1}. It was observed that almost all synthesized catalysts are thermally stable, yielding a maximum loss of weight of 31.97 % at 895 °C the catalyst; VMoO/SiO$_2$ (V:P=1:5) was the least stable while VMoO/SiO$_2$ (V:P=1:2) was the most thermally stable catalyst with a least weight loss % just 18.4 % at the same temperature among the synthesized systems. A graphical illustration is given in Figure 3.
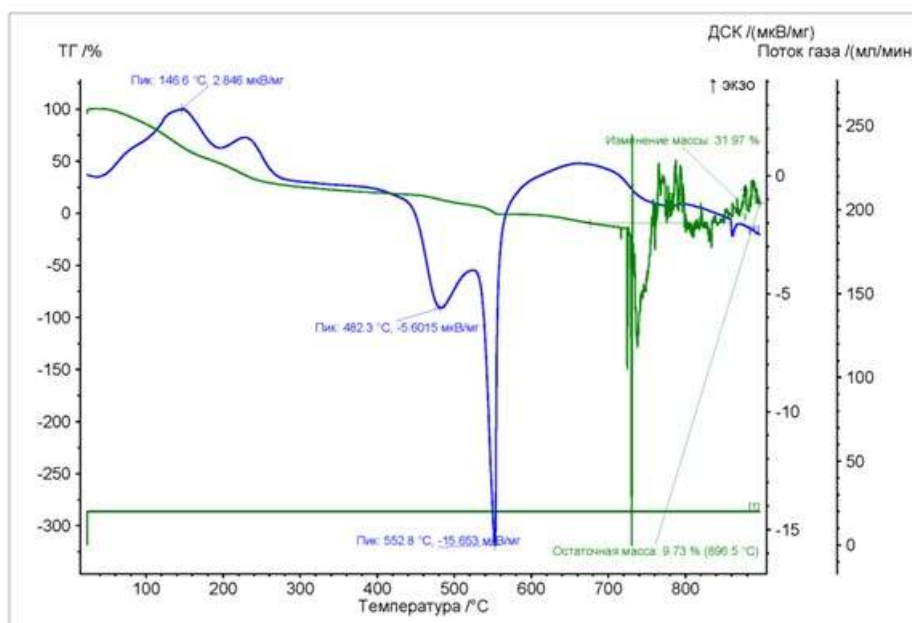
Figure 3. TGA curves of the synthesized catalyst V-Mo-O/SiO$_2$.

The surface and porous properties of the attained catalytic systems were studied and a plot for V-Mo-O/SiO$_2$ system was shown in Figure 4. The values for surface area, porous radius, and radius/diameter are respectively, 12 m^2/g, 0,7mL/g, 344 A$^°$ for V-Mo/Si system.
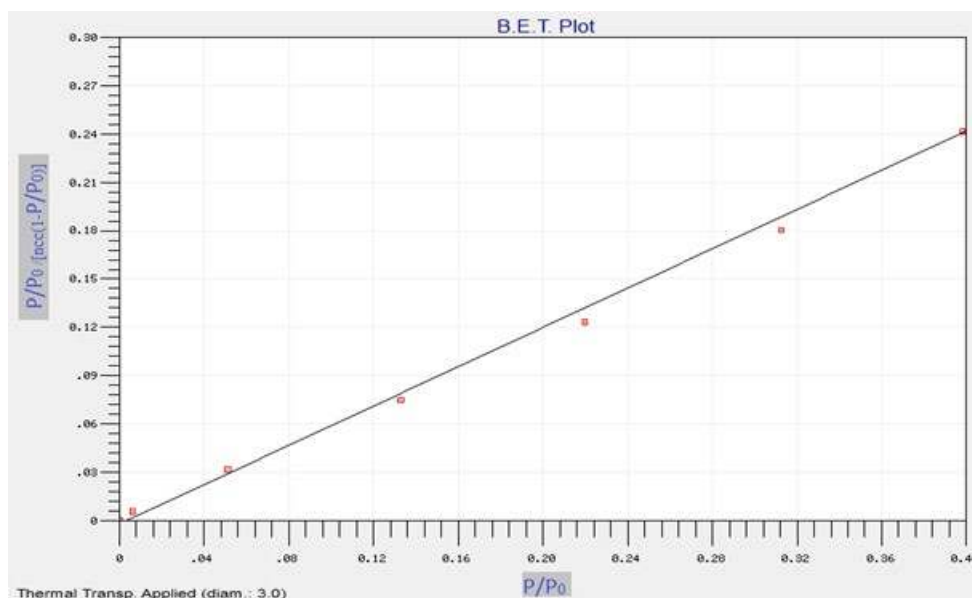
Figure 1: B.E.T plot of V-Mo-O system based on SiO$_2$

Catalytic test

It is defined that chlorotoluenes (CT) form π- and σ-complexes while adsorption on a surface of heterogeneous catalysts (V-Mo-O/SiO$_2$, *etc*.) which turns into maleates and desorption yields maleic anhydride (MA) and its chloro derivatives. Oxidation process of CT takes place on the redox mechanism and a series-parallel pattern was revealed [3, 8]. The reaction scheme for the p-chlorotoluene showed below in Scheme 2.
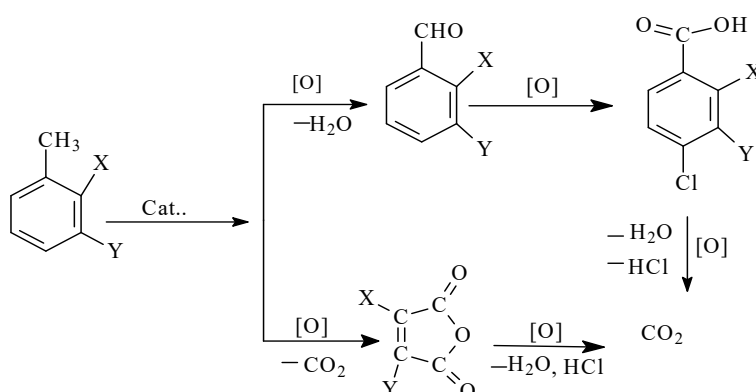
Scheme 2: Conversion of chlorotoluenes to maleic anhydrides and chlorobenzoic acids.
Note: X=H, Y=Cl or X=Cl, Y=H.

The oxidation processes of chlorinated alkyl aromatic hydrocarbons investigated both on a fixed bed and fluid-bed layer of catalyst. Although the process of heterogeneous catalytic

oxidation of chlorotoluenes took place with a higher conversion in a fixed bed but it showed higher selectivity fluid-bed layer of the catalyst. We also determined that when vanadium/ phosphorus/oxide system (V-Mo/Si *etc.*) was deactivated both on a fixed bed and fluid-bed layer of catalyst, but deactivation rate and time was almost twice lower on the fluid-bed layer of catalyst.

An effect of active components of these catalysts on the oxidation reaction was also studied. CT performs 75–92% conversion at a V:Mo=1:2–1:3 ratios, the yields of chloromaleic anhydride (CMA) was 24-32%. The yield of chlorobenzaldehyde begins to increase at V:P=1:4–1:5 ratios. According to the obtained results usage of the catalytic systems based on V: P=1:2–1:3 are considered purposeful for further researches.

Although the oxidation reaction begins from 350 °C, we determined that the yields of main products are negligible. By increasing temperature both the conversion of the CT and yield of CMA begins to enhance, and at 420 °C temperature it shows the maximum (24–32%), and simultaneously, yields of maleic anhydride (MA), chlorobenzaldehyde and chlorobenzoic acid (CB acid) decreases. By the further rise of temperature CT conversion continues to increase, but also yields of the main products at its maximum begin to decrease and this happens by way of their exposing deep oxidation process that verified by increasing of CO_2 yield as it is seen from the reaction scheme.

CONCLUSION

In conclusion, it has been determined that oxovanadium systems modified with molybdenum or phosphorus, and supported on SiO_2 and Al_2O_3 (V-Mo-O/SiO_2) are the most active and selective catalytic systems in the gas phase selective partial oxidation of chlorotoluenes. The catalysts show excellent recyclability and reusability. The optimum reaction condition for the activity and selectivity for received catalysts was designated. Consequently, the p-chloro-substituted substrate, p-chlorotoluene, is much more reactive than the m-chloro-substituted counterpart.

REFERENCES

1. Əfəndi A.C.,Salehli N.F., Məlikova İ.H., Manafov M.R., Əliyeva T.S., Şahtaxtinski T,N. o-Dixlorbenzolun oksid katalizatorları üzərində oksidləşmə reaksiyalarının tədqiqi. //Azərb. kim. J.2004. № 3. P.13–17.

2. Babayev E.M., Afandi A.C., Aykhan N., Ismayilova B.A. // Oxidation reactions of chloro benzene and chloro toluene in the presence of oxide catalysts. Baku World Forum of Young Scientists 2014. Collection of abstracts. 2014. P. 143–145.

3. Reddy BM, Rao KN, Reddy GK, Bharali P. Characterization and catalytic activity of V2O5/Al2O3-TiO2 for selective oxidation of 4-methylanisole. Journal of Molecular Catalysis A: Chemical. 2006 Jul;253(1–2):44–51. DOI: 10.1016/j.molcata.2006.03.016.

4. Babayev E.M., Efendi A.C., Yunisova F.A., Aykan N.F. Catalytic Activity of Oxovanadium Catalysts Supported SiO2 or Al2O3 in the Selective Oxidation of p- Chlorotoluene // J.Environ Sci. Comput. Eng. Technol. 2016. V. 5. No. 2. P. 017–022.

5. Yang SC, Wang JQ. Catalytic Oxidation of o-chlorotoluene to o-chlorobenzaldehyde by Vanadium Doped Anatase Mesoporous TiO<sub>2</sub> Advanced Materials Research. 2013 Sep;781–784:182–5. DOI: 10.4028/www.scientific.net/AMR.781-784.182.

6. Martra G, Arena F, Coluccia S, Frusteri F, Parmaliana A. Factors controlling the selectivity of V2O5 supported catalysts in the oxidative dehydrogenation of propane. Catalysis Today. 2000 Dec;63(2–4):197–207. DOI: 10.1016/S0920-5861(00)00460-0.

7. Ferreira M., Volpe M. A combined theoretical and experimental study of supported vanadium oxide catalysts. Journal of Molecular Catalysis A: Chemical. 2002 Jun;184(1–2):349–60. DOI: 10.1016/S1381-1169(02)00026-2.

8. Wachs IE, Chen Y, Jehng J-M, Briand LE, Tanaka T. Molecular structure and reactivity of the Group V metal oxides. Catalysis Today. 2003 Feb;78(1–4):13–24. DOI: 10.1016/S0920-5861(02)00337-1.

9. Zhou W-F, Chen L, Xie J, Au C-T, Yin S-F. Efficient synthesis of p-chlorobenzaldehyde through liquid-phase oxidation of p-chlorotoluene using manganese-containing ZSM-5 as catalyst. RSC Adv. 2015;5(91):74162–9. DOI: 10.1039/C5RA16206H.

Al$_2$O$_3$ ve SiO$_2$ üzerinde Desteklenmiş Modifiye Oksovanadyum Sistemleri Üzerinden Monoklorotoluenlerin Seçimli Gaz Faz Yükseltgenmesi

Arif Javanshir Efendi, Elmir Magsad Babayev, Fakhriyya Mashallah Nasiri, Bilqeyis Adil Ismayilova , Firuza Alasgar Yunisova

Öz: V-Mo-O/SiO$_2$ malzemeleri emprenye teknikleri ile hazırlanmış ve Taramalı Elektron Mikroskopisi (SEM), FT-IR, Termal Analiz, N$_2$ adsorpsiyonu/desorpsiyonu ve X-ışını toz saçılması (XRD) yöntemleri ile faz yapısı ve vanadyum türlerinin yüklenme miktarı belirlenmeye çalışılmıştır. Hazırlanan malzeme, seçilen koşullar altında, çözücüsüz ortamda monoklorotoluenin katalitik yükseltgenmesinde test edilmiştir. Sonuçlara göre V-Mo-O/SiO$_2$ etkili bir katalizördür, monoklorotoluenin dönüşümü %75-85, monokloromaleik anhidrit üzerindeki seçimliliği de %24-32 oranındadır. Bunun yanı sıra, katalizör kolayca geri kazanılabilmekte ve aktivite ile seçimlilikte belirgin bir kayıp olmaksızın 20-25 saat boyunca kullanılabilmektedir. Yükseltgenme hızı ve yönü sıcaklık (315-450 °C), reaktifler arasındaki oran (1:1-1:15 mol/L), bağ ayrışma enerjileri, katalizörün aktif bileşenlerinin etkisi ve temas süresi ile belirlenmektedir.

Hydroxyethyl Methacrylate-based Nanocomposite Hydrogels with Tunable Pore Architecture

Erhan Bat[1],*

[1]Middle East Technical University, 06800, Ankara, Turkey.

Abstract: Hydroxyethyl methacrylate (HEMA)-based hydrogels have found increasing numbers of applications in areas such as chromatographic separations, controlled drug release, biosensing, and membrane separations. In all these applications, the pore size and pore interconnectivity are crucial for successful application of these materials as they determine the rate of diffusion through the matrix. 2-Hydroxyethyl methacrylate is a water-soluble monomer but its polymer, polyHEMA, is not. Therefore, during polymerization of HEMA in aqueous media, a porous structure is obtained as a result of phase separation. Pore size and interconnectivity in these hydrogels is a function of several variables such as monomer concentration, cross-linker concentration, temperature, *etc*. In this study, we investigated the effect of monomer concentration, graphene oxide addition or clay addition on hydrogel pore size, pore interconnectivity, water uptake, and thermal properties. PolyHEMA hydrogels were prepared by redox initiated free radical polymerization of the monomer using ethylene glycol dimethacrylate as a cross-linker. As a nanofiller, a synthetic hectorite Laponite® XLG and graphene oxide were used. Graphene oxide was prepared by the Tour Method. Pore morphology of the pristine HEMA based hydrogels and nanocomposite hydrogels were studied by scanning electron microscopy. The formed hydrogels were found to be highly elastic and flexible. A dramatic change in the pore structure and size was observed in the range between 22 to 24 wt/vol monomer at 0.5 % of cross-linker. In this range, the hydrogel morphology changes from typical cauliflower architecture to continuous hydrogel with dispersed water droplets forming the pores where the pores are submicron in size and show an interconnected structure. Such controlled pore structure is highly important when these hydrogels are used for solute diffusion or when there's flow through monolithic hydrogels. These robust hydrogels may be useful in separation and biomedical applications.

Keywords: Hydrogels; hydroxyethyl methacrylate; porous polymers; nanocomposites.

INTRODUCTION

Recently, porous polymers have found numerous applications in a wide range of fields [1]. The major advantage of porous polymers is their high surface area for adsorption and release of compounds which is highly desired in materials for separation, gas storage, controlled drug release, catalysis, and sensors. Macroporous polymer networks, formed as a result of phase separation during network formation, is an important class of such porous polymers [2]. Several monomers have been utilized to obtain macroporous polymer networks [2, 3]. Among these are hydroxyethyl methacrylate, glycidyl methacrylate, ethyleneglycol dimethacrylate (crosslinker), N,N-methylene bisacrylamide (crosslinker), divinyl benzene (crosslinker), styrene, and methacrylic acid.

HEMA is a water-soluble monomer. Its polymer poly(hydroxyethyl methacrylate) is hydrophilic but not water-soluble for degree of polymerizations above 40 [4]. Therefore, phase separation during polymerization of hydroxyethyl methacrylate has been widely utilized to obtain macroporous polymers for different applications. Several attempts have been made to control the pore architecture of HEMA based hydrogels. In some approaches hydrophobic porogens such as cyclohexane, dodecanol [5, 6], polyacrylonitrile fibers [7], surfactants [8], or NaCl as a phase separation enhancer [9] were used. Hydroxyethyl methacrylate based hydrogels are highly hydrophilic and biocompatible. These characteristics have enabled their use in biomedical field for applications such as contact lenses, drug delivery [10-12], and tissue engineering [13-16]. Owing to their high surface area, HEMA based hydrogels have found application also in environmental remediation such as removal of dyes from industrial waste waters [17, 18], and in separation [19].

For successful application of macroporous polymers in all of the aforementioned fields, a tunable pore size, interconnected pore structure, and thermal stability are important parameters. Herein, we set out to explore the characteristics of HEMA based hydrogels at the borderline between macrosyneresis and microsyneresis. In this transition zone, seldomly encountered pore structures were observed. The effects of monomer composition and addition of nanofillers such as clay and graphene oxide on the pore architecture, water uptake, and thermal properties of hydroxyethyl methacrylate based hydrogels have been investigated. A range of monomer compositions where a highly ordered micron to submicron range porous hydrogels were obtained.

MATERIALS AND METHODS

Materials: Sodium persulfate (SPS), N,N,N',N'-tetramethylethylenediamine (TEMED), ethylene glycol dimethacrylate (EGDMA), and 2-hydroxyethyl methacrylate (HEMA), were obtained from Sigma-Aldrich and used as received. Laponite® XLG was kindly supplied by BYK Additives and instruments. Graphite flakes with an average lateral size of 40 μm were kindly supplied by Asbury Carbons. Graphene oxide was obtained from flake graphite by the Tour Method [20].

Hydrogel Synthesis: Poly(hydroxyethyl methacrylate-co-ethylene glycol dimethacrylate) (Poly(HEMA)) hydrogels were synthesized by redox initiated radical polymerization at room temperature. SPS and TEMED were used as a redox initiator pair. As a crosslinker and solvent, EGDMA and MilliQ water were respectively used. For the synthesis of hydrogels, predetermined amounts of monomer, crosslinker, and solvent were placed in glass vials sealed with a rubber septum. The dissolved oxygen was removed from the solution by passing argon through this solution for 15 min. After adding the initiators (2.5 mg SPS and 2.5 μL TEMED), the reaction mixture was drawn into a syringe the reaction was allowed to proceed for 18 h at room temperature under argon. Hydrogels prepared in this way were named H20-H28 where the numbers next to the letter H indicate the volume percentage of hydroxyethyl methacrylate monomer in the solution. Nanocomposite hydrogels were prepared by adding predetermined amounts of Laponite® XLG or graphene oxide into MilliQ water to be used in polymerization.

Swelling Studies: Disk-shaped specimens with a diameter of 9 mm and a height of 3 mm (n=3) were cut from the prepared hydrogels and placed in glass vials containing 2 mL H_2O for four days. Water in the vials was refreshed twice a day. After four days of incubation in water at room temperature, water on the samples was carefully removed with a tissue and wet masses of the samples were recorded. Dry masses were recorded after freeze drying the samples for at least 48 h. Swelling percentage was calculated by the following formula:

$$\text{Swelling Percentage} = [(m_{wet}-m_{dry})/m_{dry}]*100 \qquad \text{(Eq. 1)}$$

Where m_{wet} is the mass of the swollen hydrogel sample and m_{dry} is the mass of the freeze-dried hydrogel sample.

Characterization: Pore structure of the formed hydrogels was investigated by scanning electron microscopy (SEM) using FEI Nova NanoSEM 430 field emission electron microscope with an accelerating voltage of 10 kV. Hydrogel samples were freeze-dried and snap frozen in liquid nitrogen before being cut with a scalpel for cross-sectional analysis. Samples were sputter-coated with a thin layer of gold before visualization with SEM.

Thermal characterization of freeze-dried hydrogel samples was done using thermal gravimetric analysis (TGA) and differential scanning calorimetry (DSC). TGA analysis was performed from room temperature up to 800 °C, under a nitrogen atmosphere, using a Shimadzu DTG-60H thermal analyzer (Columbia, MD, USA) with a scanning rate of 10 °C/min. Differential scanning calorimetry measurements were carried out under nitrogen atmosphere by using DSC-60 Shimadzu differential scanning calorimeter to assess the effect of hydrogel composition on glass transition temperature of the freeze dried samples. Samples were cut from freeze dried gel samples and scanned from 25 to 200 °C at a heating rate of 10 °C min^{-1}. Glass transition temperature was calculated from the second scan of the samples.

RESULTS AND DISCUSSION

Several porous hydrogels were prepared by redox-initiated free radical polymerization using HEMA as the monomer, EGDMA as the crosslinker, and SPS-TEMED as the redox pair. Volume percentage of HEMA in these hydrogels ranged from 20 vol% to 28 vol% and named as H20-H28 depending on the monomer content. In all the hydrogels, the amount of crosslinker was kept at 0.5 mol% with respect to HEMA. In the preliminary experiments it was seen that increasing the amount of crosslinker leads to smaller particles forming the hydrogel (not shown). For HEMA based hydrogels (without filler), only monomer concentration was varied. The obtained hydrogels showed high flexibility and elasticity (Figure S1). To prepare the nonocomposite hydrogels, with respect to HEMA either 1.0 wt. % Laponite® XLG or 1.0 wt. % graphene oxide (GO) were added to the water used for polymerization. A schematic representation of the network model can be seen in Scheme 1. Nanocomposites containing Laponite® XLG clay and graphene oxide (GO) were named as H24C-H28C and H24GO-H28GO, respectively where numbers indicate the monomer concentration.
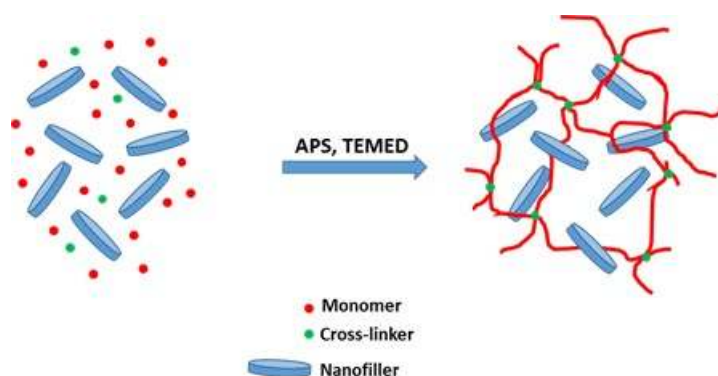
Scheme 1. A schematic representation of nanocomposite hydrogels.

Equilibrium swelling studies showed that HEMA based hydrogels are able to take up water roughly two to three and a half times their weight. Percentage swelling values for HEMA based hydrogels ranged from 204.3±2.3 to 344.6±8.7. With increasing HEMA concentration, percentage swelling values decreased. Addition of Laponite® XLG did not seem to have a dramatic effect on water uptake of the hydrogels. Percentage swelling values ranged from 223.7±1.7 to 314.2±1.3. Addition of graphene oxide did have a large influence on polymerization and water uptake behavior. Graphene oxide-containing gels did not have a homogeneous structure. This could have two probable causes: Firstly, graphene oxide has an unsaturated structure that could lead to grafting of growing chains and alter crosslinked structure, hydrophobicity which might eventually influence pore formation by phase separation. Secondly, high viscosity of graphene oxide solution might influence polymerization and phase separation kinetics. The swelling percentage values of nanocomposite gels containing GO ranges from 177±18.7 to 281.1±54.8. Decreased swelling ratios compared to HEMA based hydrogels (column I) suggest that GO has indeed took part in crosslinking reactions and increased standard deviation values indicate non-homogeneous character of GO containing nanocomposite gels.

Table 1. Equilibrium percentage swelling values of hydroxyethyl methacrylate based hydrogels in MilliQ water. (Numbers are given as arithmetic average of three samples ± standard deviation)

Hydrogel	Percetage Swelling	Hydrogel	Percentage Swelling	Hydrogel	Percentage Swelling
H20	344.6±8.7				
H22	323.9±6.3				
H24	320.4±1.3	H24C	314.2±1.3	H24GO	177.7±18.7
H25	297.3±1.4	H25C	296.4±2.3	H25GO	281.1±54.8
H26	270.5±1.4	H26C	271.7±2.0	H26GO	185.5±8.3
H28	204.3±2.3	H28C	223.7±1.7	H28GO	201.6±5.9

Hydroxyethyl methacrylate is a water-soluble monomer whereas the crosslinker EGDMA is not water-soluble at all. In the presence of HEMA, however, the crosslinker molecule could be dispersed in the aqueous polymerization medium. Upon polymerization, formed water insoluble polyHEMA phase separated and initially transparent solution became turbid and eventually white. This phase separation during hydrogel formation leads to a porous structure. To investigate the pore structure of the formed hydrogels, Cross-sections of freeze dried samples were sputter coated with gold and visualized with SEM. Figure 1 shows the effect of monomer content on pore structure of HEMA based hydrogels. When the monomer concentration is less than 24 vol%, HEMA and EGDMA form microparticles that separate out of the polymerization solution and eventually these formed microparticles fuse to form a cauliflower like structure typically seen in hydrogels used as chromatographic media. Upon increasing the monomer content to 24 vol% a transition from macrosyneresis to microsyneresis is observed [2]. For these hydrogels, the polymer forms a continuous network while trapping the solvent molecules inside the gel. When the HEMA concentration was between 24 to 28 vol%, hydrogels with highly ordered pore structure with interconnected pores were obtained. The pore sizes decreased from a few micrometers to submicron range as the HEMA content increased from 24 to 28 vol%. Such porous hydrogels with interconnected pores and tunable pore size could be highly useful in chromatography, adsorption, and controlled drug delivery applications.
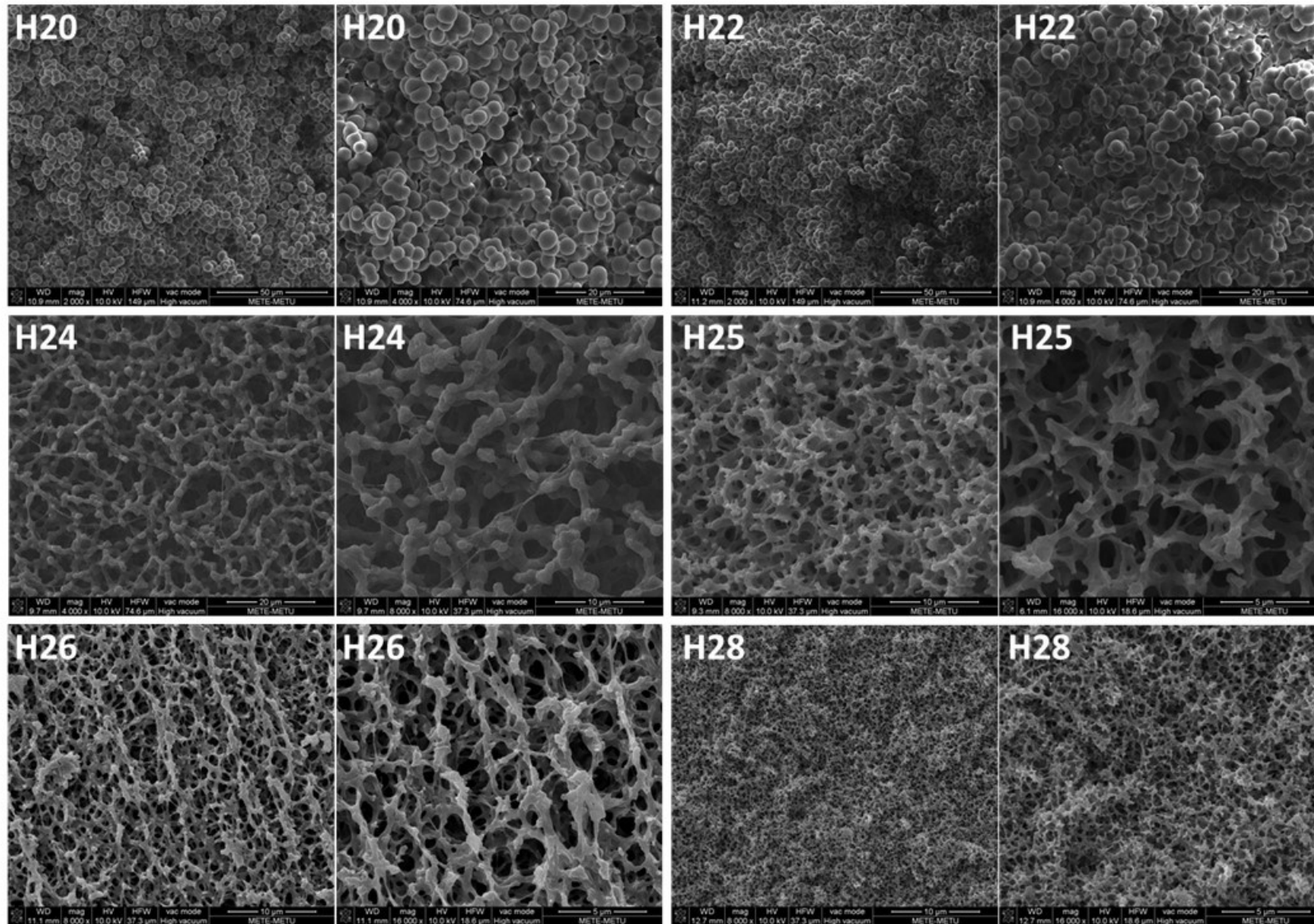
Figure 1. SEM micrographs showing the microstructure of the HEMA based hydrogels containing different amounts of HEMA.

Clays offer very rich interaction possibilities with many molecules such as proteins and dyes, *etc*. Clay containing hydrogels could have increased drug loading capacity and dye adsorption capacity. Therefore, it was intended to prepare clay containing hydrogels using a synthetic hectorite Laponite® XLG. The microstructure of these hydrogels were assessed using SEM. In Figure 2, it can be seen that highly porous nanocomposite hydrogels with regular pore structure have been obtained when 1 wt% Laponite® XLG was used as a filler. Again pore sizes ranged from microns to submicron range depending on HEMA content. Figure 2 shows that randomly distributed large pores are visible at low magnifications when Laponite® XLG is used as a filler. Addition of clay leads to formation of less ordered areas within the hydrogel. For hydrogels containing 28 % HEMA, addition of clay seems to have a dramatic effect on the porous structure. H28C seems to have much less ordered but much larger pores compared to H28. As the clay, monomer and the polymer are hydrophilic, formation of intercalated or exfoliated structures may be expected for clay containing HEMA hydrogels. In XRD analysis the characteristic peak of Laponite® XLG could not be seen at 2Θ values higher than 2 degrees. This indicates that the clay is most probably exfoliated in the hydrophilic matrix.

Pore structure of graphene oxide-containing gels are given in Figure 3. When GO is added as a filler, pore structure seems to vary from one region to another as can be seen in the insets. This could be due to macroscopically observed non-homogeneous character of GO containing hydrogels. In these hydrogels, interestingly both fused microparticle shaped structures (indicating macrosyneresis) and continuous structures (indicating microsyneresis) were visible. These observations also point that the polymerization conditions were not the same at different part of the gel. SEM micrographs (H25GO, H28 inset) also reveal coating of GO surface with HEMA indicating grafting of the polymer onto GO surface.
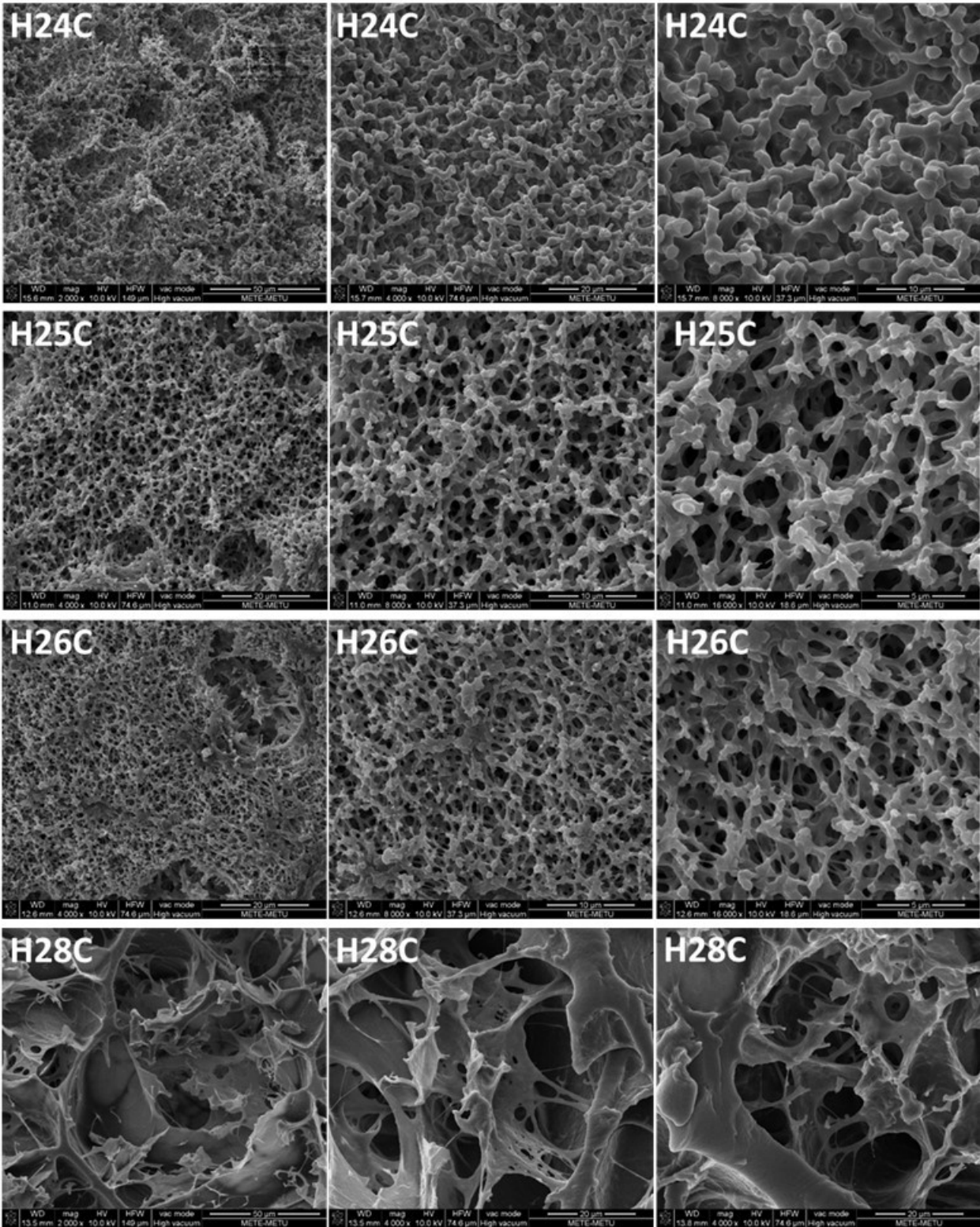
Figure 2. SEM micrographs showing the microstructure of the HEMA-based hydrogels containing different amounts of HEMA and 1wt % Laponite® XLG clay (with respect to HEMA).
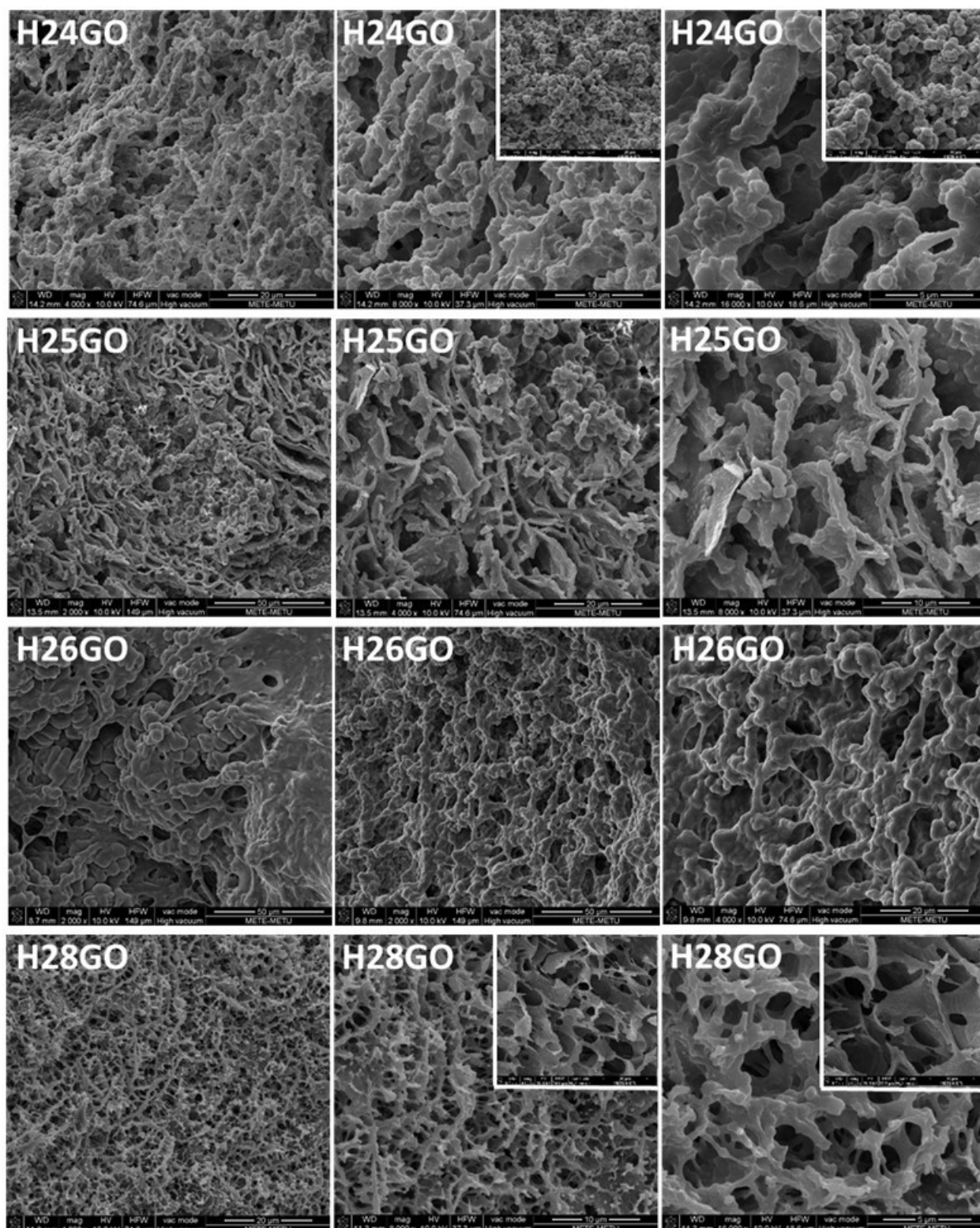
Figure 3. SEM micrographs showing the microstructure of the HEMA-based hydrogels containing different amounts of HEMA and 1 wt % graphene oxide (with respect to HEMA).

In thermal gravimetric analysis of HEMA based hydrogels, a slight decrease in mass was observed at temperatures below 100 °C (Figure 4). This could be attributed to adsorbed water. No other significant mass loss is observed till the onset of thermal degradation which indicates that almost all monomers have participated in the polymerization reaction. The onset of degradation temperature seemed to increase with increasing monomer concentration. The values ranged from 256 °C to 378 °C for networks containing 20 vol% and 28 vol% monomer, respectively. The glass transition temperatures of dry HEMA-based networks were very close to each other. The values ranged from 109 °C to 113 °C. Figure 5 shows the thermal behavior of nanocomposite hydrogels containing 1 wt% Laponite. Addition of Laponite seemed to have an adverse effect on thermal stability of the networks. The values for onset of degradation temperature ranged from 254 °C to 363 °C for Laponite-containing networks. The glass transition temperatures of dry nanocomposite networks were very close to those of pristine HEMA based networks (not shown). The values for Laponite containing networks ranged from 111 °C to 114 °C. Graphene oxide containing networks showed very similar thermal behavior with onset of degradation temperatures ranging from 332 °C to 357 °C. Glass transition temperatures of graphene oxide containing dry nanocomposite networks were lower than that of Laponite containing or pristine HEMA based networks. The values ranged from 103 °C to 106 °C.
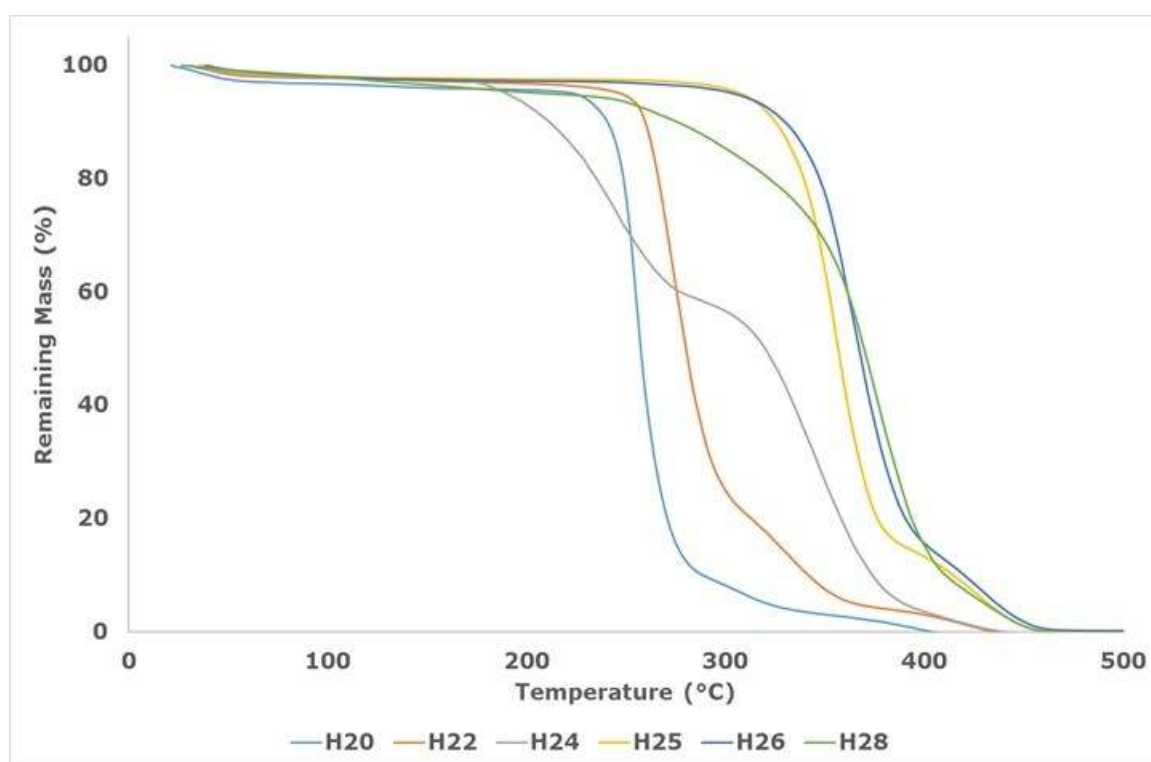
Figure 4. TGA thermograms of dry HEMA based hydrogels with monomer concentrations of 20 vol% to 28 vol%.
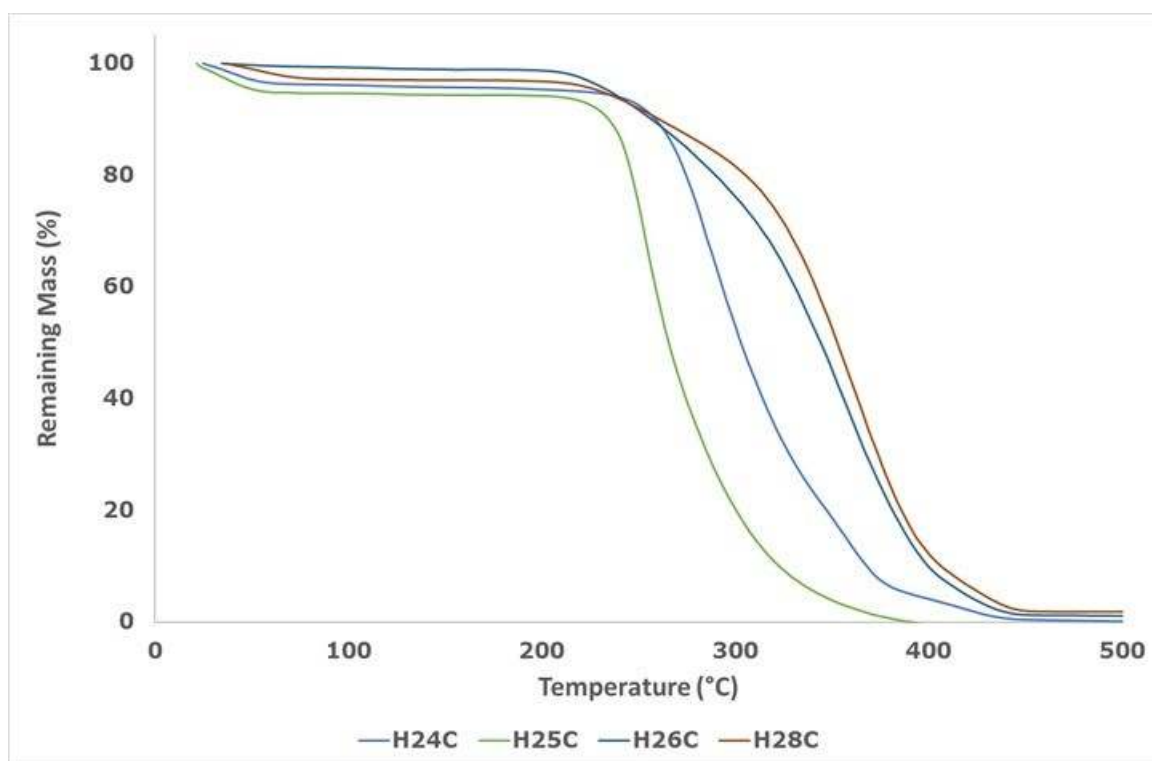
Figure 5. TGA thermograms of dry nanocomposite hydrogels containing 1 wt % Laponite XLG with monomer concentrations of 24 vol % to 28 vol %.
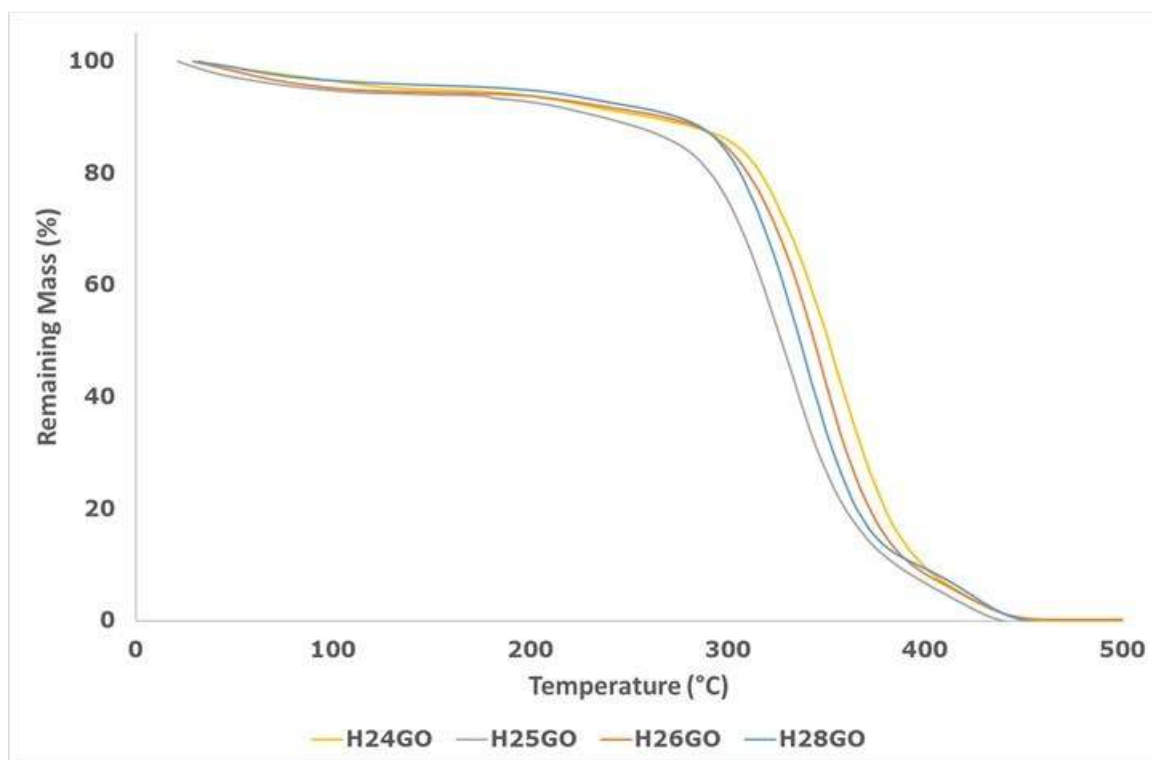
Figure 6. TGA thermograms of dry nanocomposite hydrogels containing 1 wt % graphene oxide with monomer concentrations of 24 vol % to 28 vol %.

CONCLUSION

HEMA based hydrogels without additives or with nanofillers were prepared by redox-initiated free radical polymerization. As a nanofiller, a synthetic hectorite Laponite® XLG and graphene oxide were used. A transition from macrosyneresis to microsyneresis is observed when the monomer concentration was increased from 22 to 24 vol%. This leads to a profound change in the pore structure of the prepared HEMA-based hydrogels. At lower monomer concentrations, polymer microparticles fuse to form a macroporous structure whereas in the case of higher monomer concentrations, a continuous macroporous structure with micron to submicron highly interconnected pores is obtained. Laponite® XLG containing gels seemed to have more regular pores compared to graphene oxide-containing gels. The suitability of these porous materials as separation materials or biomedical materials should be assessed in future research.

ACKNOWLEDGMENTS

REFERENCES

1.   Wu D, Xu F, Sun B, Fu R, He H, Matyjaszewski K. Design and Preparation of Porous Polymers. Chemical Reviews. 2012;112(7):3959-4015. DOI: 10.1021/cr200440z.

2.   Okay O. Macroporous copolymer networks. Progress in Polymer Science. 2000;25(6):711-79. http://dx.doi.org/10.1016/S0079-6700(00)00015-0.

3.   Benes MJ, Horak D, Svec F. Methacrylate-based chromatographic media. Journal of Separation Science. 2005;28(15):1855-75. DOI: 10.1002/jssc.200500186.

4.   Khutoryanskaya OV, Mayeva ZA, Mun GA, Khutoryanskiy VV. Designing Temperature-Responsive Biocompatible Copolymers and Hydrogels Based on 2-Hydroxyethyl(meth)acrylates. Biomacromolecules. 2008;9(12):3353-61. DOI: 10.1021/bm8006242.

5.   Hradil J, Horak D. Characterization of pore structure of PHEMA-based slabs. Reactive & Functional Polymers. 2005;62(1):1-9. http://dx.doi.org/10.1016/j.reactfunctpolym.2004.08.007.

6.   Vianna-Soares CD, Kim CJ, Borenstein MR. Manufacture of porous cross-linked HEMA spheres for size exclusion packing material. Journal of Porous Materials. 2003;10(2):123-30. DOI: 10.1023/A:1026083713349.

7.   Vidaurre A, Cortazar IC, Meseguer JM. Water sorption properties of poly(ethyl acrylate-co-hydroxyethyl methacrylate) macroporous hydrogels. Macromolecular Symposia. 2003;200:283-90. DOI: 10.1002/masy.200351030.

8.   Antonietti M, Caruso RA, Goltner CG, Weissenberger MC. Morphology variation of porous polymer gels by polymerization in lyotropic surfactant phases. Macromolecules. 1999;32(5):1383-9. DOI: 10.1021/ma9812478.

9.   Liu Q, Hedberg EL, Liu ZW, Bahulekar R, Meszlenyi RK, Mikos AG. Preparation of macroporous poly(2-hydroxyethyl methacrylate) hydrogels by enhanced phase separation. Biomaterials. 2000;21(21):2163-9. http://dx.doi.org/10.1016/S0142-9612(00)00137-X.

10.   Kumar A, Tyagi P, Singh H, Kumar Y, Lahiri SS. Synthesis and characterization of a porous poly(hydroxyethylmethacrylate-co-ethylene glycol dimethacrylate)-based hydrogel device for the implantable delivery of insulin. Journal of Applied Polymer Science. 2012;126(3):894-905. DOI: 10.1002/app.36531.

11.   Dziubla TD, Torjman MC, Joseph JI, Murphy-Tatum M, Lowman AM. Evaluation of porous networks of poly(2-hydroxyethyl methacrylate) as interfacial drug delivery devices. Biomaterials. 2001;22(21):2893-9. http://dx.doi.org/10.1016/S0142-9612(01)00035-7.

12.   Galperin A, Smith K, Geisler NS, Bryers JD, Ratner BD. Precision-Porous PolyHEMA-Based Scaffold as an Antibiotic-Releasing Insert for a Scleral Bandage. Acs Biomaterials-Science & Engineering. 2015;1(7):593-600. DOI: 10.1021/acsbiomaterials.5b00133.

13.   Horak D, Kroupava J, Slouf M, Dvorak P. Poly(2-hydroxyethyl methacrylate)-based slabs as a mouse embryonic stem cell support. Biomaterials. 2004;25(22):5249-60. DOI: 10.1016/j.biomaterials.2003.12.031.

14.   Horak D, Hlidkova H, Hradil J, Lapcikova M, Slouf M. Superporous poly(2-hydroxyethyl methacrylate) based scaffolds: Preparation and characterization. Polymer. 2008;49(8):2046-54. DOI: 10.1016/j.polymer.2008.02.041.

15.   Arslantunali D, Budak G, Hasirci V. Multiwalled CNT-pHEMA composite conduit for peripheral nerve repair. Journal of Biomedical Materials Research Part A. 2014;102(3):828-41. DOI: 10.1002/jbm.a.34727.

16.   Studenovska H, Slouf M, Rypacek F. Poly(HEMA) hydrogels with controlled pore architecture for tissue regeneration applications. Journal of Materials Science-Materials in Medicine. 2008;19(2):615-21. DOI: 10.1007/s10856-007-3217-0.

17.   Dalaran M, Emik S, Guclu G, Iyim TB, Ozgumus S. Removal of acidic dye from aqueous solutions using poly(DMAEMA-AMPS-HEMA) terpolymer/MMT nanocomposite hydrogels. Polymer Bulletin. 2009;63(2):159-71. DOI: 10.1007/s00289-009-0077-4.

18.   Gupta VK, Tyagi I, Agarwal S, Sadegh H, Shahryari-ghoshekandi R, Yari M, et al. Experimental study of surfaces of hydrogel polymers HEMA, HEMA-EEMA-MA, and PVA as adsorbent for removal of azo dyes from liquid phase. Journal of Molecular Liquids. 2015;206:129-36. DOI: 10.1016/j.molliq.2015.02.015.

19.   Andac M, Galaev IY, Denizli A. Molecularly imprinted poly(hydroxyethyl methacrylate) based cryogel for albumin depletion from human serum. Colloids and Surfaces B-Biointerfaces. 2013;109:259-65. DOI: 10.1016/j.colsurfb.2013.03.054.

20.   Marcano DC, Kosynkin DV, Berlin JM, Sinitskii A, Sun ZZ, Slesarev A, et al. Improved Synthesis of Graphene Oxide. Acs Nano. 2010;4(8):4806-14. DOI: 10.1021/nn1006368.

Türkçe Öz ve Anahtar Kelimeler

Ayarlanabilir Gözenek Yapısı ile Hidroksietil Metakrilat Esaslı Nanokompozit Hidrojeller

Öz: Hidroksietil metakrilat (HEMA) esaslı hidrojeller, kromatografik ayırmalar, kontrollü ilaç salımı, biyo-hissetme ve membran ayırmaları gibi alanlarda geniş uygulama alanı bulmaktadırlar. Bu uygulamaların hepsinde, gözenek boyutu ve gözeneksel bağlanabilirlik özellikleir malzemenin başarılı uygulaması için hayati önem taşımaktadır, çünkü bunlar matriks boyunca diffüzyonu belirlemektedir. 2-Hidroksietil metakrilat suda çözünen bir monomer iken polimeri olan poliHEMA suda çözünmez. Bu sebeple, HEMA'nın sulu ortamda polimerizasyonu sırasında faz ayrımının bir sonucu olarak gözenekli bir yapı elde edilir. Gözenek boyut uve bu hidrojeller içindeki bağlanabilirlik monomer konsantrasyonu, çapraz bağlayıcı konsantrasyonu, sıcaklık ve benzeri pek çok değişkenin bir fonksiyonudur. Bu çalışmada, monomer konsantrasyonu, grafen oksit veya kil ilavesinin hidrojel gözenek boyutuna etkisi, gözeneksel bağlanabilirlik, su alımı ve termal özelliklerin etkisi incelenmiştir. PoliHEMA hidrojelleri redoksla başlatılan, monomerin serbest radikal polimerizasyonu kullanılarak ve çapraz bağlayıcı olarak etilen glikol dimetakrilat seçerek hazırlanmıştır. Nano-dogu maddesi olarak, sentetik hektorit Laponit ® XLG ve grafen oksit kullanılmıştır. Grafen oksit Tour Yöntemi ile hazırlanıştır. Saf HEMA esaslı hidrojellerin ve nanokompozit hidrojellerin gözenek morfolojisi taramalı elektron mikroskobu ile çalışılmıştır. Oluşan hidrojellerin son derece elastik ve esnek olduğu bulunmuştur. 22 ile 24 ağırlık/hacim monomerin %0,5 çapraz bağlayıcı ile beraber kullanıldığı zaman gözenek yapısı ve boyutunda dramatik bir değişme olduğu gözlenmiştir. Bu aralıkta, hidrojel morfolojisi tipik karnabahar görünümünden ayrılmış su damlacıklarının gözenekleri oluşturduğu sürekli hidrojel yapısına geçilmiştir; gözenekler mikron altı seviyede olup birbirine bağlıdır. Bu şekilde kontrollü gözenek yapısı, bu hidrojeller çözünen maddenin diffüzyonunda kullanılacağı zaman veya monolitik hidrojeller boyunca akış olduğu zaman son derece önemlidir. Bu sağlam hidrojeller ayırma ve biyomedikal uygulamalarda faydalı olabilir.

Anahtar kelimeler: Hidrojeller; hidroksietil metakrilat; gözenekli polimerler; nanokompozitler.

Demirci Gültekin et al., JOTCSA. 2016; 3(3): 623-636.

RESEARCH ARTICLE

Synthesis of Copper Nanoparticles Using a Different Method: Determination of Their Antioxidant and Antimicrobial Activity

Demet DEMİRCİ GÜLTEKİN[1*], Azize ALAYLI GÜNGÖR[2,3], Hicran ÖNEM[3], Aynur BABAGİL[3], Hayrunnisa NADAROĞLU[3,4]

[1]Ataturk University, Aşkale Vocational Collage, Department of Metallurgical Program, 25500, Aşkale, Erzurum, TURKEY
[2]Ataturk University, Erzurum Vocational Collage, Department of Chemical Technology, 25240 Erzurum, TURKEY
[3]Ataturk University, Faculty of Engineering, Department of Nano-Science and Nano-Engineering, 25240 Erzurum, TURKEY
[4]Ataturk University, Erzurum Vocational Collage, Department of Food Technology, 25240 Erzurum, TURKEY

Abstract: The aim of this study was to obtain copper oxide nanoparticles (CuO NPs) through a method of green synthesis that involves using peroxidase enzymes that are partly purified from fig leaves (*Ficus carica*). CuO NPs were successfully synthesized using the green synthesis method in the experiments performed. Ultraviolet–visible (UV–Vis) spectrophotometry of the characteristics of the acquired CuO NPs was performed with scanning electron microscopy (SEM) and X-ray diffraction (XRD). The optimum activation temperature for green synthesis was observed to be in 30 min, pH: 8, at 25 °C and in the concentration of 1 mM $CuCl_2$. By using peroxidase enzymes with green synthesis, it was found that the results of the SEM and XRD measurements that acquired the CuO NPs were in the size of 50-120 nm. Afterwards, the antioxidant and antibacterial activities of these nanoparticles were measured, and it was understood from the obtained results that CuO NPs have both antioxidant and antimicrobial activities.

*Corresponding author. E-mail: dedemirci@yahoo.com.

INTRODUCTION

Nowadays, the subject of nanotechnology encompasses many fields, including the environment, water treatment, chemical production, containers and converters of solar power, antimicrobial agents, textiles, dyes, health, and even defense [1-3]. The research indicates that nanotechnology is engaging even more with these fields as time passes.

The characteristics of a material can change significantly when that material is nano-sized. The differences in the characteristics of the substance are the result of quantum size effects. Metal nanoparticles, in particular, show very different optical, thermal, chemical, and conductivity characteristics compared to normal metal particles. Nano-sized metals and metal oxides are able to be used in many areas because of the characteristics they assume.

Green synthesis has become one of the most preferred applications in various fields, including chemistry, because of its eco-friendly approach. With the application of green synthesis to nanochemistry, another area of study had emerged that has gained increasing value: Green nano synthesis. Green nano synthesis allows for a nano material to be synthesized in a way that is friendly to both humans and to the environment. In this synthetic method, toxic chemicals that are damaging to nature are avoided and, instead, less-harmful substitutes are used. The reaction environment used in green nano synthesis can be a tissue, cell, organism, extract, enzyme, carbohydrate, lipid, or protein produced from a lipid. Three of these types of green synthesis environments are commonly used. The first of these is enzymes, which are able to catalyze a wide range of chemical reactions, resulting in their use in green nano synthesis in recent years. In addition, microorganisms (such as bacteria, yeast and mold) and plant and animal extracts are commonly used to synthesize nanoparticles in green synthesis. These three reaction environments are most common because they allow for eco-friendly, non-toxic, cost-efficient and mild conditions [6-9]. These are not, however, the only reaction environments used in green synthesis. The synthesis of silver nanoparticles (AgNPs) has been achieved by some research groups using *Nephelium lappaceum* L. and *Plectranthus amboinicus* leaf extracts. Another research group has synthesized gold nanoparticles (Au NPs) using a plant extracts in a similar way [3-4].

Copper nanoparticles, which have been a focus of interest since the end of 20th century due to their catalytic, optical, and electrical features, are widely used in the electricity sector because of their conductivity features; in chemistry, they are used as a lubricator and catalyst [10-12]. Since the copper (II) oxide nanoparticle (CuO NP) is semi-conductive, it is often used in catalysts, gas sensors, and photovoltaic cells. Due to its electronic and magnetic characteristics, CuO has been used as one of the basic components of high temperature superconductive substances, causing it to become very widely used [13]. Etefagh *et al.* designed a sensor founded on

nanoparticles and nanolayers of CuO. CuO NPs were produced using the sol–gel technique, and their nanolayers were prepared using spray pyrolysis [14]. Phiwdang's research group investigated the effect of starting precursors on structural properties of CuO nanostructures synthesized via the precipitation technique [15]. Khashan *et al.* discovered the consequence of altering the ablation time and laser energy on produced CuO NPs using laser ablation in liquid. The antibacterial activity of these CuO NPs with or without amoxicillin on cultures of gram-negative and gram-positive bacteria was also presented [16].

Recently, fig extracts have become another preferred reaction environment for green nano synthesis. For instance, Hu (2015) achieved a synthesis of tin dioxide (SnO_2) using the extract obtained from fig leaves, applying the synthesized compound to the electrochemical detection of mercuric Hg(II) [3]. In another field, Singh and Bhakat studied the nano technological applications of gold and silver nanoparticles after synthesizing both with the leaves and bark of a fig tree [6].

Peroxidases are known as (EC.1.11.1.7) oxidoreductases. Usually, there is an iron porphyrin ring on their structures, and they catalyze redox reactions such as electron transfer and oxygen exits from a donor such as hydrogen peroxide (H_2O_2). The peroxidase enzyme (POX) has been purified so far in plants such as turnips, soy beans, tomatoes, potatoes, carrots, wheat, pears, apricots, bananas, dates, and strawberries [17].

In this study, we used POX that has been partly purified from the leaves of a fig plant. CuO NPs were synthesized using the purified enzymes. The characterization of the obtained CuO NPs was performed using an ultraviolet–visible (UV–VIS) spectrophotometer, X-ray diffraction (XRD), scanning electron microscopy (SEM) and Fourier transform infrared spectroscopy (FTIR). The antioxidant and antimicrobial features of the obtained CuO NPs were discovered.

EXPERIMENTAL SECTION

Chemicals and Reagents
Copper(II) chloride ($CuCl_2$), 2,2'-azino-bis (3-ethylbenzthiazol-6-sulfonic acid) (ABTS), neocuproine (2,9-dimethyl-1,10-phenanthroline), riboflavin, methionine, nitroblue tetrazolium (NBT), 1,1-diphenyl-2-picryl-hydrazyl (DPPH), 3-(2-pyridyl)-5,6-bis (4-phenyl-sulfonic acid) - 1,2,4-triazine (ferrozine), α-tocopherol, linoleic acid, gallic acid, quercetin, Folin-Ciocalteu and trichloroacetic acid (TCA) was purchased from Sigma-Aldrich GmbH (Sternhe I Germany). All other chemicals were obtained from Merck.

Preparation of Plant Samples
The fig plant (*Ficus carica*) used in the study was collected from Sakarya, Turkey, and it was identified with the help of taxonomists. The plant was cut into small (50 g) pieces. The pieces

were thoroughly shattered to form a homogeneous mixture in a blender, along with a 250 mL, 10 mM sodium phosphate buffer (pH:6.0). The mixture was centrifuged at 5000 g for 10 min, and the supernatant was used for enzyme purification [18].

Partial Purification of the POX with Ammonium Sulfate Precipitation

The upper solution of the fig plant in sodium phosphate buffer was saturated from 60% to 80% with ammonium sulfate; then, the POX was precipitated by being centrifuged at 7000 g for 30 min. The obtained precipitate was dissolved in the 5 mL, 10 mM sodium phosphate buffer (pH:6.0) and was incubated at 4°C for further analysis [18].

POX Activity Test

The peroxidase activity assay was measured using a substrate of 1 mM 2, 2'-azino-bis(3-ethylbenzthiazoline-sulfonic acid) diammonium salt (ABST) prepared in a 0,1 M phosphate buffer (pH:6.0). The changes in absorbance were monitored at 412 nm using a UV–Vis spectrophotometer at 1-min intervals for 3 min [18].

Synthesis of CuO NPs

An amount of 300 μg/mL of purified POX from the fig plant was added to a sample of copper-(II) chloride solution ($CuCl_2$) (2.9 mL, 10 mM) and incubated in a closed space for 4 hours. The solution became blue in color and was cloudy, indicating the presence of CuO NPs. Then, water was removed with the help of an evaporator, and the synthesized CuO NPs were dried at 70°C for 24 hours [18].

Characterization of CuO NPs

Synthesized CuO NPs were characterized by being scanned with a UV–VIS spectrophotometer (PG Instrument T80 UV-VIS spectrophotometer, UK) at a range of 200–1000 nm. Determination of the topography of the CuO NPs was performed using a scanning electron microscope (Sigma 300, SEM Zeiss, Germany). In addition, XRD analysis (PANalytical, Empyrean, Netherlands) was performed at DAYTAM (Eastern Anatolian High Technology Applications and Research Center) to determine the size of the CuO NPs.

Optimization of Green Synthesis Reaction Medium

Optimum contact time: To determine the optimum contact time, samples were spectrophotometrically measured between 0 and 240 min at 3-min intervals.

Determination of optimum pH: Synthesis of the CuO NPs was performed at pH 2–3, an acetate buffer at pH 4–6, a phosphate buffer at pH 7–8, and a carbonate buffer at pH 9–11. The values of absorbance were measured by UV–Vis spectrophotometer. The pH was adjusted using 0,1 N HCl and 0,1 N NaOH.

Determination of optimum temperature: Synthesis of the CuO NPs was carried out separately from 10 °C to 90 °C, respectively, and the changes in absorbance in the samples was measured by UV–VIS spectrophotometer.

Determination of optimum concentration of metal ion: Synthesis of the CuO NPs was performed using a copper(II) chloride solution at 0.5 mM, 1 mM, 3 mM, 5 mM and 7 mM, and the absorbance of the samples was measured by a UV–Vis spectrophotometer (350 nm).

Antimicrobial Activity of Copper Nanoparticles

Antagonistic activity of the synthesized CuO NPs was determined against *Pediococcus acidilactici.* A sterile Potato Dextrose Agar (PDA-Oxoid) nutrient medium was prepared and sterilized overnight. The bacterium was studied in three replications, and the average inhibition zone created by the bio-agent was identified with the help of the values obtained [19-20]. In addition, the minimum inhibitory concentration (MIC), defined as the lowest concentration of material that inhibits the growth of a bacterium, was determined as based on batch cultures containing varying concentrations of CuO NPs.

RESULTS AND DISCUSSION

Synthesis of copper nanoparticles

300 μg/mL of purified peroxidase enzyme was added in sample of copper(II) chloride solution CuCl$_2$, (10 mM) and incubated in a closed space for 3 hours. The solution was becoming blue to intense blue, which indicates the presence of copper nanoparticles. Then, water was removed with the help of an evaporator and copper nanoparticles were synthesized and they were dried at 65 °C for 48 hours (Figure 1) [21].
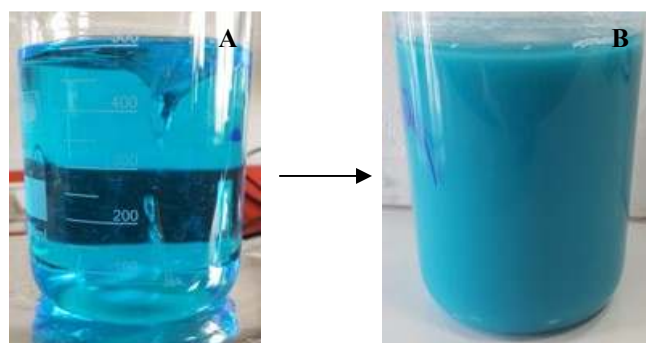
Figure 1. Reaction of green synthesis of copper nanoparticules (A): Before reaction, (B) After reaction.

Chemical properties of CuO NPs synthesis

Contact time was determined to be 30 min., optimum pH was determined as 8.0, optimum temperature was 25 °C, and metal ion concentration was determined as 1 mM for the purpose of optimization of synthesized CuO nanoparticles using a UV-Vis spectrophotometer at 350 nm.

XRD studies

Copper nanoparticles' XRD which was produced in its peroxidase enzyme catalyst and its crystallographic analysis are given in Figure 2. Characteristic peaks which belong to XRD spectrum in its at 2θ= 19.86°, 24.55°, 58.71°, 75.22° that can be indexed at (111), (200), (220) facets which agree with the values reported for face centered cubic (fcc) copper nanocrystals (Figure 2).
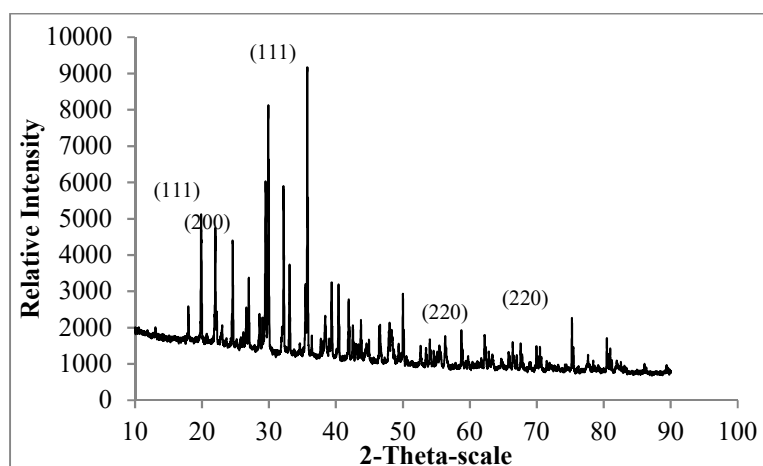
Figure 2. X-ray diffraction pattern of the synthesis of copper nanoparticles using peroxidase enzyme from Fig (*Ficus Carica*).

Surface characterization of CuO NPs

Chemical and mineralogical compositions of synthesized green copper NPs were determined by scanning electron microscopy (SEM), which was used to examine the surface of the adsorbent. Images of CuO NPs were magnified 10000 times by Zeiss, Active area 10 mm^2, (Figure 3). It was observed from figure that most of the CuO NPs were spherical in shape. Figure 3 showed a well dispersed CuO NPs had identified in the sizes range 50-120 nm. In CuO nano particles, which were synthesized by using many plant extracts were identified as mostly in spherical from and between 5-200 nm in sizes [21].
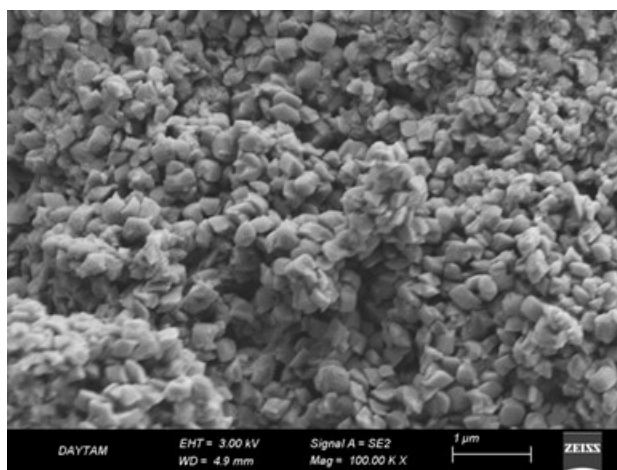
Figure 3. SEM image of the synthesized copper nanoparticles.

Antioxidant activity of CuO NPs

The Fe^{3+}- Fe^{2+} reducing (FRAP) activity: In Fe^{3+}- Fe^{2+} reducing method, antioxidants give electron and show activity. It is found that the potential of synthesized copper NPs to reduce ferric ions (Fe^{3+}) to ferrous ions (Fe^{2+}) directly increase in directly proportional with concentration. The reduction was monitored by measuring the change of absorbance at 593 nm. (Figure 4).
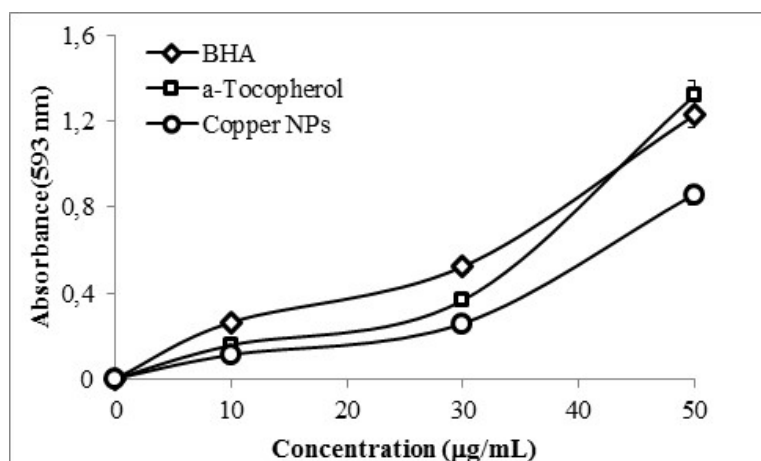
Figure 4. The Fe^{3+}- Fe^{2+} reducing activity of different concentrations (10-30 µg/mL) of water extracts, alcohol extracts, α–tocopherol, and BHA.

The Cu^{2+}- Cu^+ reducing activity

Another method to determine reducing capacity is CUPRAC method. Cupric ions (Cu^{2+}) reducing capacity of copper NPs is determined with spectrophotometric method having different concentrations (10-30 µg/mL) of copper NPs. Reducing capacity of (Cu^{2+}) by synthesized copper NPs are compared with BHT and α-tocopherol as standard antioxidants and were shown in Figure

5. In 50 µg/mL concentration of copper NPs, capacity of reducing highest cupric ions to (Cu^{2+}) cuprous ions (Cu^+) is found to be BHA $> \alpha$-tocopherol $>$ copper NP when compared with standards.
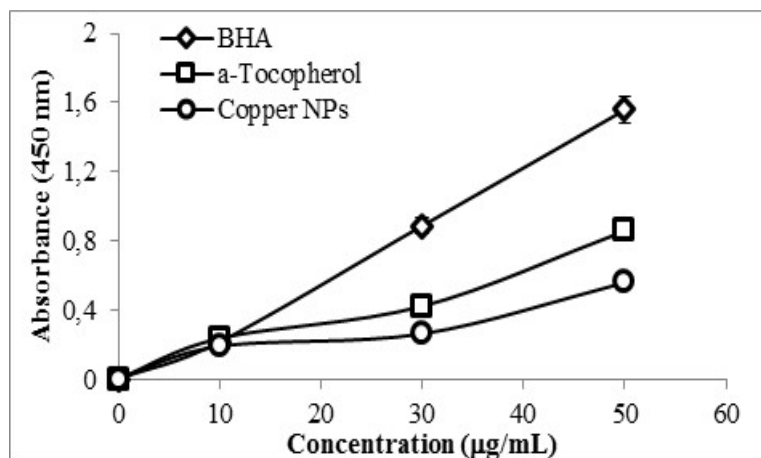
Figure 5. The Cu^{2+}- Cu^+ reducing activity of Copper NPs, BHA and α-tocopherol at different concentrations (10-50 µg/mL).

Superoxide anion radical scavenging activity

One of free radicals, superoxide radical is the easiest and most formed oxygen radical by environmental factors and enzymatic and non-enzymatic reactions in the organism. Superoxide anion radicals cause lipid peroxidation. These radicals cause lipid peroxidation and connected deterioration in membrane structure [22]. Besides, superoxide anion radicals can reduce Fe^{3+} ions to Fe^{2+}. Fe^{2+} ions react with Fenton and use hydrogen peroxide to create OH radicals which are very reactive and cause much structural deterioration. Therefore it is necessary to scavenge superoxide anion radicals in the medium. Standard antioxidant materials' activity to scavenge superoxide anion radical in 50 µg/mL concentration is found to be respectively **BHA > α-Tocopherol > Copper NPs**. These values respectively are 72.3 ± 0.5 > 56.4 ± 1.1 > 48.3± 1.03. When findings are compared with standards, it is observed that copper NPs scavenged superoxide radicals effectively (Figure 6).
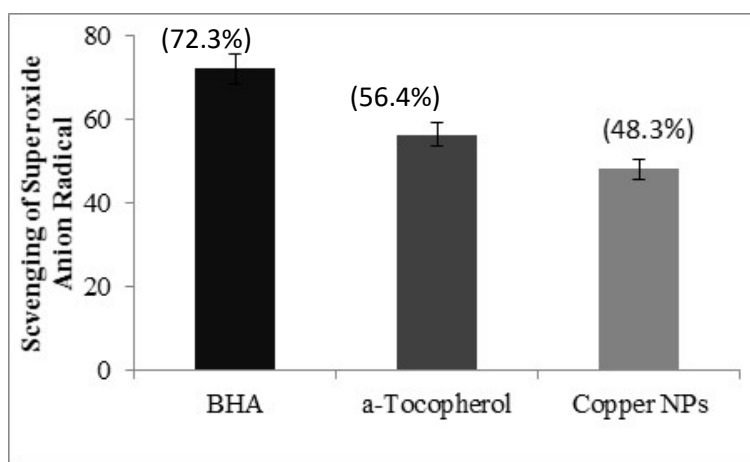
Figure 6. The activity of superoxide anion scavenging of Copper NPs, BHA and α-tocopherol at different concentrations (50 µg/mL)

The ABTS•+ scavenging activity

ABTS•+ radical is a colored compound which gives absorbance at 734 nm. ABTS•+ radical reacts with antioxidant materials and transfers electron and transforms to non-radical ABTS material. Related material is shown below:

$$ABTS^{+\bullet} + A \rightarrow ABTS + A^{+\bullet}$$
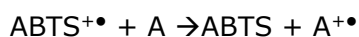
The study used spectrophotometric measurement and followed reducing of absorbance value at 734 nm and calculate ABTS•+ radical scavenging activity. ABTS•+ scavenging activity is frequently used in radical scavenging activities of liquid mixtures, drinks, extracts and pure materials [23]. Firstly, standard plot is formed to determine scavenging activity of copper NPs produced with green synthesis and standard antioxidant compounds like BHA and α-tocopherol used in study, and ABTS•+ scavenging activities are calculated in all samples using standard plot. ABTS•+ scavenging activity of copper NPs is compared with standard BHA and α-tocopherol. According to findings, at 50 µg/mL concentration, BHA achieved 73.7%, α-tocopherol achieved 79.7% and copper NPs achieved 85.4% ABTS•+ radical scavenging activity (Figure 7). It was found in this study that copper NPs scavenge ABTS•+ radical better than standard antioxidants.
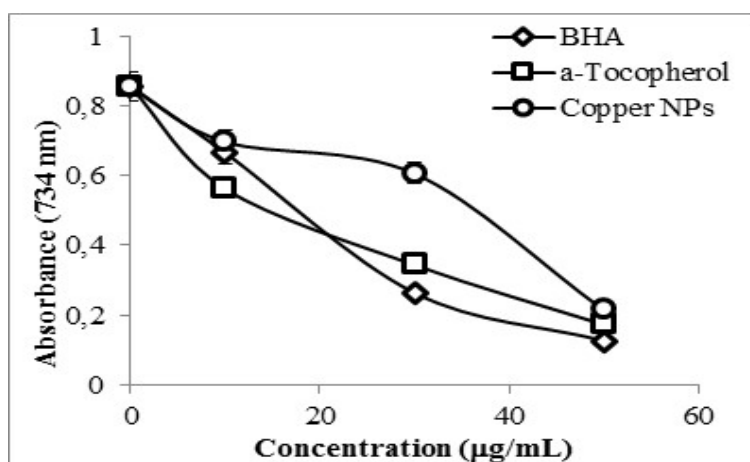
Figure 7. The activity of ABTS radical scavenging of CuO NPs, BHA and α-tocopherol at different concentrations (10-50 µg/mL).

Antimicrobial activity of CuO NPs

In the studies, antibacterial features of CuO NPs which were formed with green synthesis method are determined using spread and culture method which is a simple and fast method on nutrient agar. For this purpose, *Pediococcus acidilactici* bacteria is applied on agar surface with spread culture method and it is seen that bacteria growth is avoided around disk and diameter of created inhibition is 16.5 mm. The minimum inhibitory concentration (MIC) value was found Cu NPs (10 µg/mL) using batch method for *Pediococcus acidilactici.* It is understood that copper NPs connect to cell wall of bacteria, damages its structure and cancels its development [24].

CONCLUSION

As a result of our examinations, we understood that peroxidase enzyme can be partly purified from fig leaves (*Ficus carica*) to be used in reaction medium for green synthesis. CuO NPs were characterized using analysis of UV-Vis spectrophotometry, SEM, and XRD. The analysis revealed that the synthesis of CuO NPs and was achieved quantity, direction, and morphology characterization. Manufactured CuO NPs are considered to have been an extensive range of applications in the nanotechnology, the catalyst, pharmaceutical and medical industries. In addition, the experiments showed that CuO NPs have both antimicrobial and antioxidant features. CuO NPs which are acquired with green nano synthesis can be produced more economically and in adequate conditions nontoxic effects on the environment. Besides, examination of electrical and chemical features of acquired CuO NPs can indicate their usage in different areas.

REFERENCES

1. Hutchison JE. Greener Nanoscience: A Proactive Approach to Advancing Applications and Reducing Implications of Nanotechnology. ACS Nano. 2008 Mar;2(3):395–402. DOI: 10.1021/nn800131j.

2. Sharma VR, Yngard RA, Lin L. Silver Nanoparticles: Green Synthesis and Their Antimicrobial Activities. Adv. Colloid. Interface Sci. 2009 Jan 30;145(1-2):83-96. DOI: 10.1016/j.cis.2008.09.002.

3. Junjie H. Biosynthesis of SnO2 Nanoparticles by Fig (*Ficus Carica*) Leaf Extract for Electrochemically Determining Hg(II) in Water Samples Int. J. Electrochem. Sci. 2015 Nov;10:10668–10676. URL: http://www.electrochemsci.org/papers/vol10/101210668.pdf

4. Liu FK. Analysis and Applications of Nanoparticles in the Separation Sciences: a Case of Gold Nanoparticles. Journal of Chromatography A. 2009 Dec;1216(52):9034–9047. DOI: 10.1016/j.chroma.2009.07.026.

5. Singh DJ, Upadhya MK, Nandelwal NK. Green Synthesis Of Silver Nanoparticles Using *Argemonemexicana* Leaf Extract And Evaluation Of Their Antimicrobial Activities. Digest Journal of Nanomaterials and Biostructures. 2010 July-Sept;5:483-489.   URL: http://www.chalcogen.ro/483_Singh.pdf

6. Prasoon PS, Chittaranjan B. Green Synthesis of Gold Nanoparticles and Silver Nanoparticles from Leaves and Bark of Ficus Carica for Nanotechnological Applications. International Journal of Scientific and Research Publications. 2012 May;2(5):1-4. URL: http://citeseerx.ist.psu.edu/viewdoc/download?doi=10.1.1.387.6161&rep=rep1&type=pdf.

7. Konishi Y, Ohno K, Saitoh N, Nomura T, Nagamine S, Hishida H, Takahashi Y, Uruga T. Bioreductive deposition of Platinum Nanoparticles on the Bacterium *Shewanella algae.* J. Biotechnol. 2007 Jun;*128(3)*:648-653. DOI:10.1016/j.jbiotec.2006.11.014.

8. Das SK, Dickinson CF, Lafir DF, Broughamand EM. Synthesis, Characterization and Catalytic Activity of Gold Nanoparticles Biosynthesized with *Rhizopus Oryzae* Protein Extract Green Chemistry. 2012 Feb;14:1322-1334. DOI:10.1039/c2gc16676c.

9. Abdul Salam HR, Sivarajand R, Venckatesh R. Green Synthesis and Characterization of Zinc Oxide Nanoparticles from *Ocimum Basilicum L. Var. Purpurascens Benth.-Lamiaceae* Leaf Extract. Materials Letters. 2014 Sept 131(15): 16-18.URL: http://dx.doi.org/10.1016/j.matlet.2014.05.033.

10. Park BK, Jeong S, Kim D, Moon J, Lim S, Kim JS. Synthesis and Size Control of Monodisperse Copper Nanoparticles by Polyol Method. Journal of Colloids and Interface Science. 2007 Mar; 311(2):417-424. DOI: 10.1016/j.jcis.2007.03.039.

11. Han WK, Choi JW, Hwang GH, Hong SJ, Lee JS, Kang SG. Fabrication of Cu Nano Particles by Direct Electrochemical Reduction from Cuo Nano Particles. Applied Surface Science. 2006 Feb;252(8):2832-2838. URL: http://dx.doi.org/10.1016/j.apsusc.2005.04.049.

12. Zhu HT, Zhang CY, Yin YS. Rapid Synthesis of Copper Nanoparticles by Sodium Hypophosphite Reduction ın Ethylene Glycol under Microwave İrradiation. Journal of Crystal Growth. 2004 Oct;270(3-4):722-728. URL: http://dx.doi.org/10.1016/j.jcrysgro.2004.07.008.

13. Tetsuya K, Oka T, Nagano M, Ishiwata Y, Zheng XG. Synthesis and Application of Stable Copper Oxide Nanoparticle Suspensions for Nanoparticulate Film Fabrication. J. Am. Ceram. Soc. 2007 Jun; 90(1):107–110. DOI: 10.1111/j.1551-2916.2006.01402.x.

14. Etefagh R, Azhir E, Shahtahmasebi N. Synthesis of Cuo Nanoparticles and Fabrication of Nanostructural Layer Biosensors for Detecting *Aspergillus niger* Fungi. Scientia Iranica. 2013 Jun; 20(3):1055–1058. URL: http://dx.doi.org/10.1016/j.scient.2013.05.015.

15. Phiwdang K, Suphankij S, Mekprasart W, Pecharapa W. Synthesis of CuO Nanoparticles by Precipitation Method Using Different Precursors. Energy Procedia. 2013 June;34:740-745. URL: http://dx.doi.org/10.1016/j.egypro.2013.06.808.

16. Khashan KS, Sulaiman GM, Abdulameer FA. Synthesis and Antibacterial Activity of CuO Nanoparticles Suspension Induced by Laser Ablation in Liquid. Arab J Sci Eng. 2016 Jun 41:301–310. DOI: 10.1007/s13369-015-1733-7.

17. Cicek S, Gungor AA, Adiguzel A, Nadaroglu H. Biochemical Evaluation and Green Synthesis of Nano Silver Using Peroxidase from Euphorbia (*Euphorbia amygdaloides*) and Its Antibacterial Activity. Journal of Chemistry. 2015 Agust;Article ID:486948,1-7. URL: http: //dx.doi.org/10.1155/2015/486948.

18. Gungor AA. Use of Different Plant Derived Peroxidases for the Removal of Phenol from Water. Asian Journal of Chemistry. 2011 Jun;23(8):3710-3712. URL: http://www.asianjournalofchemistry.co.in/User/ViewFreeArticle.aspx?ArticleID=23_8_96.

19. Sharma S, Manhar AK, Bora PJ, Dolui KS, Mandal M. Plasmonic Bulk Heterojunction Photovoltaic Devices Based on Poly (9-Vinylcarbazole)/Gold Nanocomposites: Effect of Aspect Ratio of Gold Nanorod. Journal of Materials Science: Materials in Electronics. 2015;Jul26(7):5465-5474. DOI: 10.1007/s10854-015-3103-3.

20. Abdel-Aziz MS, Shaheen MS, El-Nekeety AA, Abdel-Wahhab MA. Antioxidant and Antibacterial Activity of Silver Nanoparticles Biosynthesized Using *Chenopodium Murale* Leaf Extract. Journal of Saudi Chemical Society. 2014 Sept; 18(4): 356–363. URL: http://dx.doi.org/10.1016/j.jscs.2013.09.011.

21. Nasrollahzadeh M, Sajadi SM, Vartooni AR. Green synthesis of palladium nanoparticles using *Hippophae rhamnoides Linn* leaf extract and their catalytic activity for the Suzuki–Miyaura coupling in water. Journal of Molecular Catalysis A: Chemical. 2015 Jun;396:297–303. URL: http://dx.doi.org/10.1016/j.molcata.2014.10.019.

22. Halliwell B. Establishing the Significance and Optimal Intake of Dietary Antioxidants: The Biomarker Concept. Nutr Rev. 1999 Apr; 57(4):104–113. URL: https://www.ncbi.nlm.nih.gov/pubmed/10228347.

23. Miller NJ, Sampson J, Candeias LP, Bramley PM. Catherine A. Rice-Evans Antioxidant activities of Carotenes and Xanthophylls. FEBS Letters. 1996 Apr;384(3):240–242. DOI: 10.1016/0014-5793(96)00323-7.

24. Ruparelia JP, Chatterjee AK, Duttagupta SP, Mukherji S. Strain Specificity in Antimicrobial Activity of Silver and Copper Nanoparticles. Acta Biomaterialia. 2008 May;4(3):707-716. URL: https://dx.doi.org/10.1016/j.actbio.2007.11.006.

Synthesis of Copper Nanoparticles Using a Different Method: Determination of Their Antioxidant and Antimicrobial Activity

Demet DEMİRCİ GÜLTEKİN, Azize ALAYLI GÜNGÖR, Hicran ÖNEM, Aynur BABAGİL, Hayrunnisa NADAROĞLU

Öz: Bu çalışmanın amacı, kısmen incir yapraklarından (*Ficus carica*) saflaştırılmış peroksidaz enzimlerini kullanarak yeşil bir sentez yöntemi üzerinden bakır oksit nanoparçacıklar (CuO NPler) elde etmektir. CuO NPler, gerçekleştirilen deneylerde yeşil sentez yöntemi ile başarı ile sentezlenmiştir. Elde edilen CuO NPlerin morötesi-görünür (UV-Vis) spektrofotometri ile karakteristik özellikleri, ayrıca taramalı elektron mikroskopisi (SEM) ve X-ışını saçılması (XRD) yapılmıştır. Yeşil sentez için en uygun aktifleşme sıcaklığı 30 dakikada gözlenmiştir, pH 8'dir, sıcaklık 25 °C'dir ve 1 mM $CuCl_2$ kullanılmıştır. Peroksidaz enzimlerinin yeşil sentezde kullanılması ve SEM ve XRD ölçümlerinin sonuçlarına göre CuO NPlerin boyutlarının 50-120 nm arasında olduğu bulunmuştur. Bunun dışında, bu nanoparçacıkların antioksidan ve antibakteriyel özellikleri ölçülmüş ve CuO NPlerinin antioksidan ve antimikrobiyal aktiviteye sahip olduğu bulunmuştur.

Anahtar kelimeler: Bakır nanoparçacıklar; yeşil sentez; peroksidaz.

Sunulma: 22 Temmuz 2016. **Düzeltme:** 24 Eylül 2016. **Kabul:** 20 Ekim 2016.

Thermal, Mechanical and Water Resistance Properties of LDPE/Starch Bio-Based Polymer Blends for Food Packing Applications

Hale Berber Yamak[1,*]

[1]Yildiz Technical University, Department of Metallurgical and Materials Engineering, 34220, Istanbul, Turkey

Abstract: In this study, low density polyethylene (LDPE) was melt-blended with starch using twin screw extruder to form biodegradable polymer blends. The LDPE/starch blend films used in food packing were obtained by hot pressing of the granules produced by extrusion process. The starch content was varied from 0 to 40 wt% of LDPE. To provide fine starch dispersion, glycerol and zinc stearate were used as plasticizer and compatibilizer, respectively. The effect of starch content on the properties of LDPE film was investigated. A good dispersion was achieved for low starch contents (10 and 20 wt%), but agglomeration of the starch particles occurred in the presence of high amounts of starch (>20 wt%). The addition of starch to LDPE reduced the tensile strength, elongation at break, crystallinity, and water resistance of LDPE. This decline in the LDPE properties was dramatic when the starch content was increased to 30 wt% in the blend. In addition, silver nanoparticles as antibacterial agent were incorporated to the biodegradable LDPE blends where LDPE/starch weight ratio of 60/40. The effects of these nanoparticles on morphological, mechanical, thermal and water resistance properties of the LDPE/starch biodegradable blends were investigated. It was observed that the incorporation of nanoparticles to the LDPE/starch blend was completely changed the morphology of the film, and accordingly, the mechanical, thermal, and water resistance properties were varied depending on the silver nanoparticle content in LDPE/starch blend film. Moreover, antibacterial activities of the nanocomposite films against gram-negative bacteria (*E. coli*) and gram-positive bacteria (*S. aureus*) were determined by measuring the inhibition zone around each film. However, the nanocomposite films did not show any antibacterial activities in the presence of silver nanoparticles as an antibacterial agent.

Keywords: Biodegradable materials; low density polyethylene; starch; food packing.

*Corresponding author. E-mail: hberber@yildiz.edu.tr.

INTRODUCTION

The use of plastics as a packaging material has continuously increased worldwide due to their excellent physicochemical, mechanical and barrier properties, ease of processing, lightweight nature, low cost, and versatility. More than 40% of the plastics are used for packaging and almost half of them are used for food packaging in the form of films, sheets, bottles, cups, tubs, and trays, *etc.* [1, 2]. However, these petroleum-based plastics are not biodegradable and totally recyclable, and cause serious environmental and economic problems related to the increasing volume of plastic waste and the consumption of non-renewable resources arising from plastic production [1-3]. For these reasons, there has been an increasing interest for making and use of environmentally friendly biodegradable food packing material instead of synthetic polymers [4, 5]. Although biopolymers obtained from renewable natural resources such as cellulose, starch, chitosan, and proteins are preferred for the preparation of biodegradable packaging materials [1, 4-7], their weak mechanical properties and poor barrier properties have strongly limited the use of these polymers for food packing applications [2, 8, 9]. In addition, they are not convenient for industrial processes via extrusion, melt mixing or other thermal processes because of their difficult processes. They are not thermoplastic materials and can be degraded before melting [1, 8]. Therefore, manufacturing a product using 100% renewable resources seems impossible in the near future.

To obtain biodegradable polymers with desired properties, one of the most useful routes is blending of natural biopolymers with synthetic commercial polymers. The obtained biodegradable polymer can be decomposable and/or compostable when there is a sufficient amount of biopolymer in the blend, and also the microorganisms in waste disposal environment consume the biopolymer [3, 10]. Here, the biopolymer is not only consumed but also the degradation rate of the synthetic polymer increases as a result of the enhancing of chain oxidation reactions [8]. Thus, the use of these biodegradable blends in daily life can reduce the volume of plastic waste and the use of petroleum-based plastic materials.

Among the petroleum-based plastics, low density polyethylene (LDPE) is the most extensively used packing material. Because of its hydrophobicity, high molecular weight, and absence of functional groups susceptible to microorganisms, it is hard to degrade under normal composting conditions, and the ever-increasing waste of this plastic constitutes a major environmental risk [3, 11]. The melt blending of LDPE with a biopolymer such as starch makes it biodegradable [3, 12-15]. Starch is a biopolymer derived from renewable resources such as corn, wheat, rice, and potato, and has a renovated interest to form biodegradable plastics due

to its lower price, wider availability, higher purity, non-toxicity, and very favorable environmental profile. It is composed of two types of molecules, linear amylose and branched amylopectin, and also has hydrophilic character and strong intermolecular hydrogen bonding, which cause its thermal decomposition temperature is lower than the melting temperature [4, 5]. Although, these properties make the starch unfavorable for use in the thermal processes of hydrophobic LDPE, it can possess thermoplastic character after some pretreatment involving gelatinization [15] and/or plasticization, which allow to disrupt the intermolecular hydrogen bonding and to progressively destroy the crystallinity [16, 17]. The materials used to plasticize the starch such as glycerol, sorbitol, urea, and water not only allow the thermal processing, but also improve the compatibility of starch with LDPE, enhance the mechanical properties of the starch based blend films and the biodegradability rate [17-21]. However, the addition of such plasticizers could not sufficient to completely eliminate the weaknesses in dispersion, gloss, transparency, and mechanical properties such as tensile strength and tear strength, and gas barrier properties [22, 23]. To overcome these problems caused by incompatibility in LDPE/starch blends, there have been various approaches including modification of starch such as stearic acid-grafted starch, adipate starch, acetylated starch and phthalate starch [24-26], the use of a compatibilizer, which have reactive groups such as maleic anhydride, maleate esters, glycidyl methacrylate and hydroxyl [8, 13, 22, 27] and the use of a crosslinking agent [18, 28].

In addition to the improvement of compatibility, physical appearance, and mechanical and barrier properties of the biodegradable food packing films, the incorporation of other additives into the films to enhance functional properties such as being antibacterial and antioxidant and the color is also extremely important for the quality of packing films and/or packed food. The antibacterial agents can make a longer shelf life and increase the food safety by delaying or preventing the growth of microorganisms on the food packing film surface [7]. Among these agents, silver nanoparticles (AgNPs) have strong antibacterial activity and broad-spectrum toxicity to microorganism as well as the unique catalytic, optic, and electronic properties, and thermal stability [29-32]. They can be incorporated into a wide range of packing materials from petroleum-based plastics such as polyethylene, polypropylene, polystyrene and nylon to biodegradable polymers such as chitosan, starch, and other synthetic biopolymers [33-35].

The object of this study was to produce the low density polyethylene (LDPE) based biodegradable films as food packing material. LDPE, used in blown film extrusion processes, was melt-blended with starch biopolymer. Glycerol and zinc stearate were used as plasticizer and compatibilizer, respectively to provide the fine dispersion of starch in LDPE matrix, and

also AgNPs were used as an antibacterial agent for gaining antibacterial properties to the LDPE/starch biodegradable blends. The structure of LDPE/starch blends was studied by FTIR. The effects of starch and AgNPs contents on the morphology, mechanical properties and crystallinity degree of the biodegradable films were investigated by SEM, mechanical test and DSC analyses. The water resistances of the films were analyzed by water absorption test and contact angle measurements. The antibacterial analyses of the AgNPs incorporated LDPE/starch blends were done by agar diffusion method. The antibacterial activities were evaluated whether the formation of clear zone around the samples as an indication of inhibition of the bacterial species.

MATERIALS AND METHODS

Chemicals

Film-grade low density polyethylene pellets (LDPE; Petilen F2-12), with a density of 0.920 g/cm^3 and a melt flow index (MFI) of 2.0 g/10 min (190 ^{o}C/2.16 kg; ASTM D1238), was supplied by PETKIM Petrochemical Co., Turkey. The soluble potato starch and pure glycerol (87% purity) were purchased from Merck, Turkey. Zinc stearate used as compatibilizer was a product of Melos Co., Turkey. Silver nanoparticles (AgNPs) within nano-sized zeolite, which were produced by ion exchange route, (AgZ; NKZFT89654) were used as antibacterial agent and supplied by Yıldız Kolor, Turkey. The weight ratio of silver to zeolite, Ag/zeolite was 1/2 and Ag average particle size was less than 20 nm. All ingredients were used without further purification.

Preparation of LDPE/Starch Blend Films

Starch was dried in an air-circulating oven at 100 °C for 2 h. Just prior to the extrusion process, starch and glycerol in a constant weight ratio of 70:30 were manually mixed. The mixture in polyethylene bag was left overnight under atmospheric conditions to allow the starch granules to swell. Then, the milled LDPE and zinc stearate were added to this bag and the whole was again mixed thoroughly. To prepare the LDPE/starch blends, the mixture was fed into a co-rotating twin screw extruder with a screw diameter of 22 mm and an L/D ratio of 40 (Coperion Company, China). The barrel temperature profile along the extruder was in a range of 70-180 ^{o}C (from feed zone to die), and the screw speed was kept constant at 250 rpm while the material feed rate was 18 rpm. The starch contents in the blends were varied from 0 to 40 wt% (relative to LDPE), and also zinc stearate was used at a constant amount of 3 wt% based on the total polymer consisting of LDPE and starch for all samples. The chemical

structures of components used in the preparation of LDPE/starch blends were given in Scheme 1. After the extrusion process, the films were formed from the LDPE/starch blend samples obtained as granules. Firstly, the neat LDPE granules and the blend samples were melted using two-roll mills (LabTech Engineering Co. Inc., Thailand) at 140 °C and 35 rpm rotate speed, and then 4 grams of melted samples were hot-pressed at 140 °C under 16 MPa for 15 s into plates using LabTech hydraulic laboratory press. The thickness of films was 250 μm.
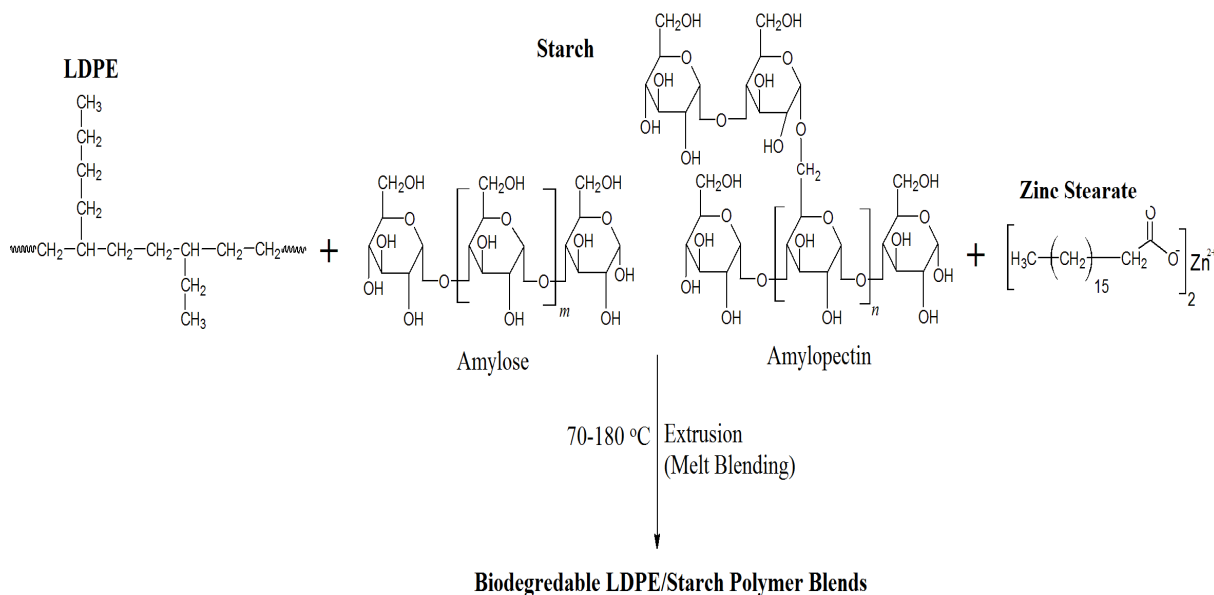
Scheme 1. Preparation of LDPE/starch blends.

Preparation of LDPE/Starch-AgNPs Nanocomposite Films

The starch was plasticized with glycerol in a constant weight ratio of 70:30. Then, the silver nanoparticles, AgNPs within nano-sized zeolite were melt-blended with the mixture consisting of pure milled LDPE, plasticized starch, and zinc stearate by using a co-rotating twin screw extruder. The concentrations of silver nanoparticles in total polymer matrix formed by LDPE and starch were ranged from 100 ppm to 300 ppm while the weight ratio of LDPE to starch, LDPE/starch was kept constant at 60/40 for all the nanocomposites. After the extrusion processes, the nanocomposite films with the thickness of 250 μm were formed from the obtained granules. To produce the nanocomposite films, the same process conditions were applied from beginning to end as those applied for LDPE/starch blend samples, as described in detail above.

Characterization Methods

FTIR analyses of the blends were carried out by using IR-Prestige 21 FTIR Spectrometer (Shimadzu, Japan) in ATR (Attenuated Total Reflection) mode. The wavenumber range, scan number for per sample and wave resolution were 4000–750 cm^{-1}, 16 and 4 cm^{-1}, respectively.

Scanning Electron Microscopy, SEM (Zeiss EVO® LS 10) was used to investigate the surface morphology of the film samples which were coated with thin carbon film before the analyses. Mechanical properties were analyzed using a Devotrans tensile testing machine (model GPG; No. 161072 CKS; Devotrans, Turkey) equipped with a 10 kN load cell. The test cross speed was 100 mm/min. The results were obtained from an average of three tests for each sample. Differential Scanning Calorimetry (DSC) analyses of the films were done using a Perkin Elmer Pyris 6 type DSC under N_2 atmosphere. The samples weighted 5-7 mg were heated from 25 to 200 °C at a heating rate of 10 °C/min and kept isothermally at 200 °C for 1 min. Then, they were cooled down to 25 °C and reheated to 200 °C at a rate of 10 °C/min. Melting and crystallization data of the samples were obtained from second heating and first cooling scans, respectively. The antibacterial activity of the silver nanoparticles incorporated LDPE/starch films was tested by agar diffusion method. *Escherichia coli* (Gram negative) and *Staphylococcus aureus* (Gram positive) were used as two common bacterial pathogens. They were grown in Petri dishes with agar as the culture medium, and then disc-shaped film samples were placed on the surface and incubated at for 24h at 37 °C. The antibacterial activity results were examined by the formation of clear zone around the samples as an indication of inhibition of the bacterial species. The surface wettability of the films was investigated by measuring the contact angle of water drop with 5 µL volume on the film surface using a KSV Instruments Cam 200 contact angle meter at room temperature. The final contact angle value for each sample was obtained from an average of five measurements. Water absorption test of the films were performed according to gravimetric methods. Before testing, the film samples were dried in an air circulating oven at 80 °C for 24 hours and then their initial weights (w_i) were recorded. These dry samples were immersed in water and kept at ambient conditions until constant weight was reached. The final weights (w_f) were recorded again, and the water absorption percentage of the samples (w_{ab}) was calculated from the following equation:

$$W_{ab} = \frac{W_f - W_i}{W_i} x \ 100\%$$ **(Eq. 1)**

RESULTS AND DISCUSSION

LDPE/starch blends in different weight ratios (100/0, 90/10, 80/20, 70/30 and 60/40) were prepared by a continuous single-step extrusion process using a co-rotating twin screw extruder. Starch was pretreated with glycerol for the plasticization before the process. To provide a fine dispersion of starch in LDPE matrix, zinc stearate was used as compatibilizer in the extrusion processes. The biodegradable films with homogenous appearance were obtained. Following this step, AgNPs within zeolite were incorporated to the LDPE/starch blend with weight ratio of 60/40 by melt-blended method. The nanocomposite films with homogenous

appearance were also obtained in three different AgNPs concentrations including 100, 200 and 300 ppm (relative to total polymer amount). Sample codes are given in Table 1.

Table 1. Sample codes of the LDPE/starch blends and the LDPE/starch-AgNP nanocomposites.

Sample Code	LDPE/Starch (by weight)	AgNPs* (ppm)
LDPE	100/0	-
90/10	90/10	-
80/20	80/20	-
70/30	70/30	-
60/40	60/40	-
100ppm	60/40	100
200ppm	60/40	200
300ppm	60/40	300

* Based on total polymer amount consisting of LDPE and starch.

FTIR Analysis

Figure 1 shows FTIR spectra of the pure LDPE and starch, and the obtained LDPE/starch blends with different starch contents. For the pure LDPE, the characteristic strong peaks at 2914 cm^{-1} and 2847 cm^{-1} correspond to asymmetric and symmetric C-H stretching vibrations, respectively. The sharp peak at 1462 cm^{-1} and the double peaks at 729-719 cm^{-1} also indicate the C-H bending and C-C rocking deformation vibrations, respectively [36]. On the other hand, two broad and strong peaks at region of 3600-3000 cm^{-1} and 1050-950 characterize the starch, and they are respectively attributed to O-H and C-O stretching vibrations, respectively. The weak broad band around 1640 cm^{-1} corresponds to O-H bending. In the FTIR spectra of LDPE/starch blends, all characteristic peaks belonging to both LDPE and starch were observed. The intensities of the characteristic starch peaks were increased by increasing starch content in the blend. For the blends, the values of starch peaks were slightly shifted to left and also their peak width were narrower, compared with starch. These changes in the starch peaks indicates that there were new physical interactions between starch molecules and other components such as glycerol and zinc stearate instead of the intermolecular interactions between starch molecules. Moreover, the new peak appeared around 1740 cm^{-1}, which is attributed to C=O stretching vibration. This belongs to ester bond of the zinc stearate, showing the incorporation of zinc stearate to the blend structure.
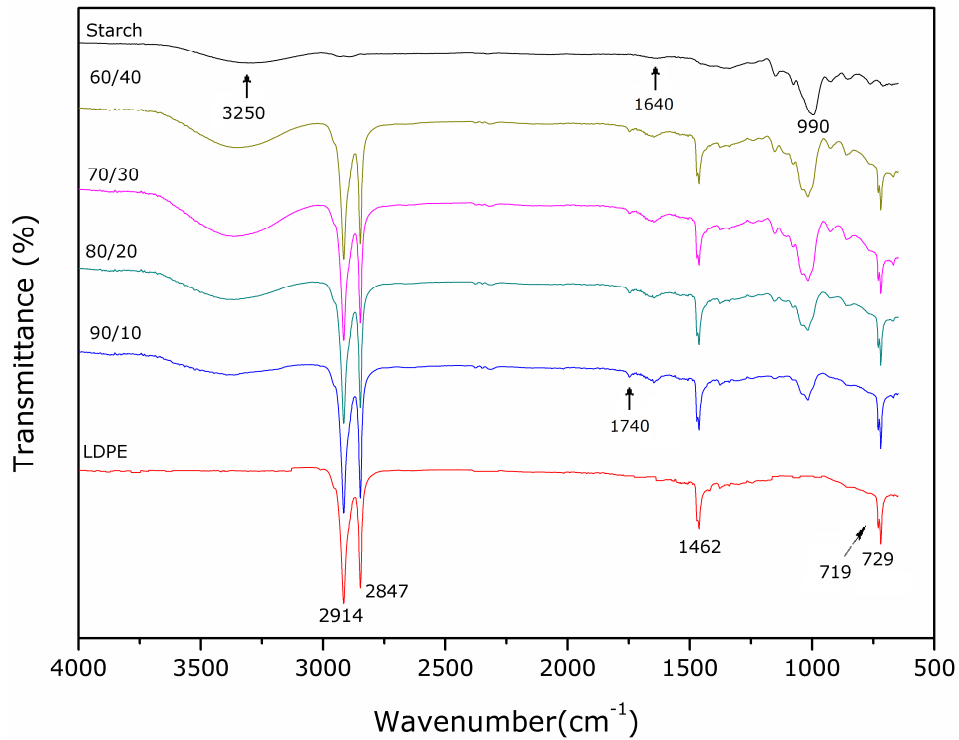
Figure 1. FTIR spectra of LDPE, starch and LDPE/starch blends.

SEM Analysis

The dispersion of starch in LDPE matrix was examined by SEM analysis. SEM micrographs of the pure LDPE and LDPE/starch blends with different starch content are given in Figure 2 (a-e). LDPE film had a smooth surface and showed a uniform continuous matrix. By the addition of starch particles into the LDPE matrix, the different surface morphologies were observed depending on the amount of starch. As seen in Figure 2(b) and (c), the LDPE/starch blends containing 10 and 20 wt% starch exhibited a good dispersion of starch particles, any phase separation between LDPE and starch did not appear, and starch particles were embedded in the matrix. This indicated that the use of glycerol as a plasticizer and zinc stearate as a compatibilizer reduced the interfacial energy between the starch and LDPE phases and made them more compatible in these weight ratios [24].

However, the finer distribution of starch particles decreased with increasing starch content in the blends, and more a small amount of particle agglomeration was observed on the sample surface when the starch content was increased to 30 wt%, as seen in Figure 2(d). The micrograph for the sample containing 40 wt% starch, given in Figure 2(e) presented a rougher surface and separate larger agglomerated starch particles, and also few surface holes formed by removal of loosely embedded starch particles were detected, corresponding to

incompatibility of starch and LDPE. This incompatibility can occur as a result of the weakened interfacial adhesion between LDPE and starch with increased hydrophilic starch content in hydrophobic LDPE, and also the decreased compatibilizing effect of zinc stearate for these two separate phases [24, 26, 37].
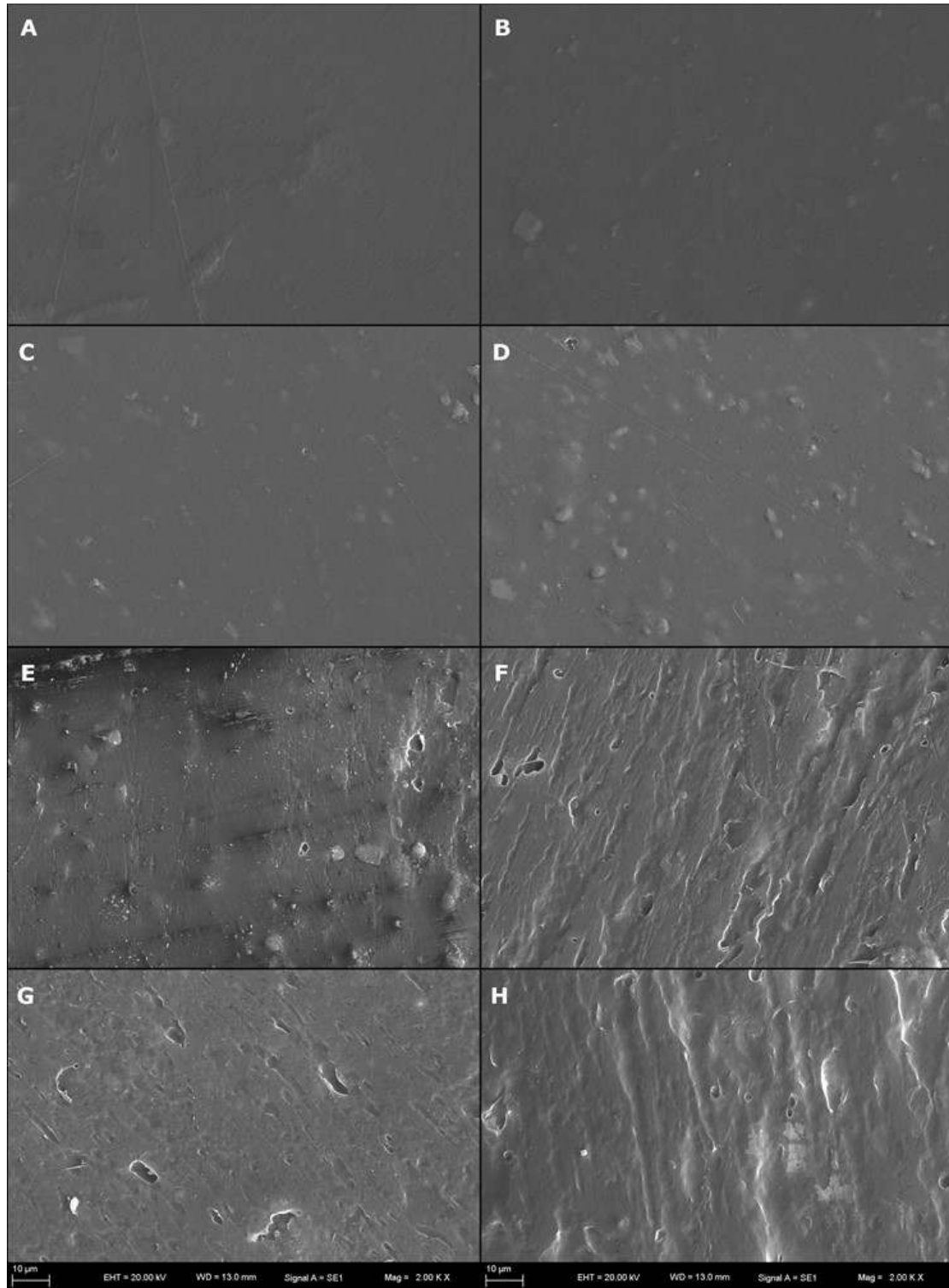
Figure 2. SEM micrographs of the pure LDPE (A), LDPE/starch blends; 90/10(B), 80/20(C), 70/30 (D) and 60/40 (D), and LDPE/starch-AgNP nanocomposites; 100 ppm(F), 200 ppm(G) and 300 ppm(H), (magnification of 2000x).

645

In addition, AgNPs incorporating LDPE/starch nanocomposites showed a different surface morphology from the LDPE/starch blends, (Figure 2(f-h)). The nanocomposites were prepared by melt-mixing of silver nanoparticles within nano-sized zeolite and polymer matrix consisting of LDPE and starch in a constant weight ratio of 60/40. The amount of silver nanoparticles was varied from 100 ppm to 300 ppm (relative to the total polymer matrix). Although the agglomerated starch particles disappeared, the surface roughness, deep cracks and voids were observed, as seen Figure 2 (f-h). These images revealed that the AgNPs in zeolite prevented the agglomeration of starch particles in LDPE, compared to AgNPs-free LDPE/starch blend in Figure 2 (e). However, an extreme surface roughness, deep cracks and voids, which were appeared by the incorporation of AgNPs in zeolite as a third phase into the blend, indicate the formation of non-uniform and discontinuous structures, phase separations and inhomogeneous surfaces. Also, the surface voids and deep cracks were varied with increasing concentration of AgNPs in the nanocomposites.

Mechanical Properties

The tensile properties of pure LDPE, LDPE/starch blend and LDPE/starch-AgNP nanocomposite films are presented in Table 2. It was obviously seen that the tensile properties of LDPE were significantly affected by the presence of starch and its content, as expected. The results are agreement with other studies on LDPE/starch blends [37-40]. The tensile strength of LDPE was found to be 17.1 MPa and decreased to 7.3 MPa with the increase of starch content to 40 wt% in LDPE. The percentage elongation at break also decreased from 815% (LDPE) to 640, 360, 36 and 24% when the weight ratio of starch in LDPE was increased to 10, 20, 30 and 40%, respectively, and there was even a dramatic decrease over 30 wt% of starch content, as seen in Table 2. These obtained results are consistent with the surface morphologies of the LDPE/starch blend films (Figure 2 (a-e)).

The mechanical properties of starch-based polymer blends are influenced by the dispersion of starch in the main polymer, because the dispersion primarily determines the microstructure of the blend [41]. By the incorporation of starch into the LDPE, a polar discontinuous phase forms in a nonpolar continuous phase of the LDPE [38]. If there are no interfacial strong interactions such as hydrogen bonds between these two phases having different polarities, the interfacial tension between the phases does not decrease sufficiently, so a weak interfacial adhesion and incompatibility occur, which lead to a mechanical rupture at the blend interface. This results in a decrease of the tensile strength and elongation at break, and an increase of fragility [25, 28, 37]. In addition, the significant drop in the elongation at break, which was observed for the samples with higher starch contents, could be due to the agglomeration of starch particles in

the blend. For the agglomerated large starch particles, particle-particle interactions are more dominant instead of particle-LDPE matrix interactions. This causes a greater phase separation, the poorer tensile properties, and especially the fractures at lower values of elongation [10, 26, 37].

Table 2. The tensile properties of LDPE/starch blend and LDPE/starch-AgNP nanocomposite films.

Sample	Tensile Strength (mPa)	Elongation at Break (%)
LDPE	17.1	813
90/10	12.8	640
80/20	8.3	360
70/30	7.5	36
60/40	7.3	24
100ppm	5.7	36
200ppm	5.5	22
300ppm	6.2	13

On the other hand, the addition of AgNPs within zeolite to the LDPE/starch blend consisting of 60/40 weight ratio showed variety in both mechanical properties depending on the nanoparticle concentration, as seen in Table 2. Although the agglomerated starch particles were not seen on SEM micrographs of the nanocomposite films, the obtained poor mechanical properties could be due to the intense roughness and presence of voids and cracks observed on the film surfaces, as seen in Figure 2 (f-h). The incorporation of silver nanoparticles within nano-sized zeolite as a rigid third phase into the polymer blend has created the new filler-filler and/or filler-matrix interactions between LDPE matrix, starch particles and silver-doped zeolites, which prevents the formation of homogeneous and fine dispersed phases. This can explain the weaker mechanical properties of the obtained nanocomposite structures compared to the pure LDPE and LDPE/starch blends [37, 38].

DSC Analysis

Table 3 shows the DSC data including peak melting temperature (T_m), peak crystallization temperature (T_c), melting and crystallization enthalpies (ΔH_m and ΔH_c), and percent crystallinity (X_c) of all resulting samples. Melting and crystallization curves obtained from second heating and first cooling cycles of the LDPE/starch blends and LDPE/starch-AgNP nanocomposites are given in Figure 3(a-b) and Figure 4 (a-b), respectively. X_c of LDPE phase was calculated using the following equation:

$$X_c = (\Delta H_m - \Delta H_c)/\Delta H_m^o \; x \; 100 \qquad \textbf{(Eq. 2)}$$

where $\Delta H^o{}_m$, the heat of melting for 100% crystalline PE was taken to be 293 J g^{-1} [42].

Table 3. DSC data of the pure LDPE, LDPE/starch blends and LDPE/starch-AgNP nanocomposites.

Sample	T_m (ºC)	T_c (ºC)	ΔH_m (J/g)	ΔH_c (J/g)	X_c (%)
LDPE	111.13	96.72	83.072	-78.680	55.21
90/10	111.45	98.83	80.728	-70.719	51.69
80/20	111.14	99.05	79.759	-56.557	46.52
70/30	111.21	99.08	67.181	-48.935	39.63
60/40	111.37	99.08	65.404	-45.255	37.77
100 ppm	110.37	97.90	58.803	-41.933	34.38
200 ppm	111.04	98.10	59.713	-42.714	34.96
300 ppm	110.35	98.11	57.302	-36.988	32.18
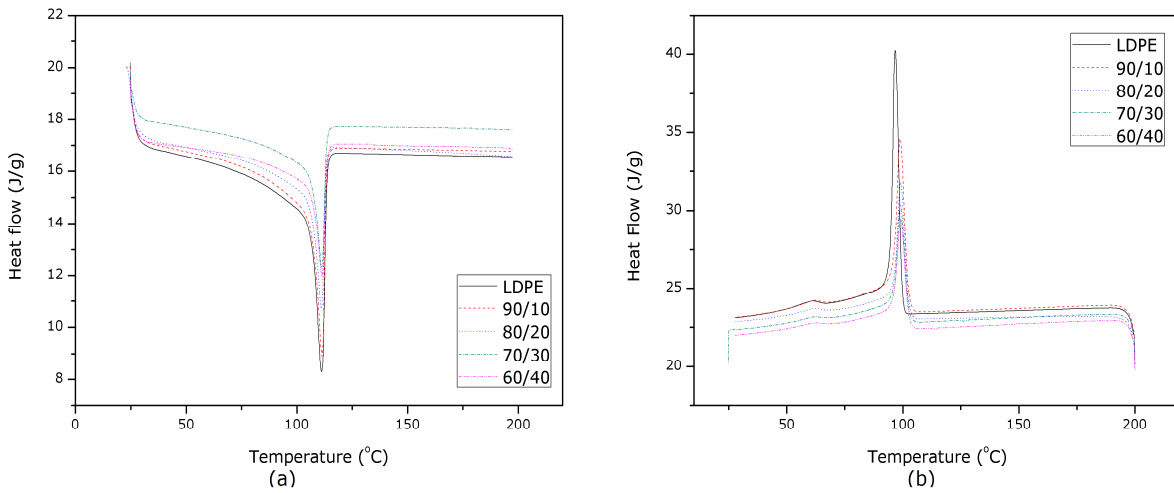
Figure 3. Melting (a) and crystallization (b) curves of LDPE/starch blends.
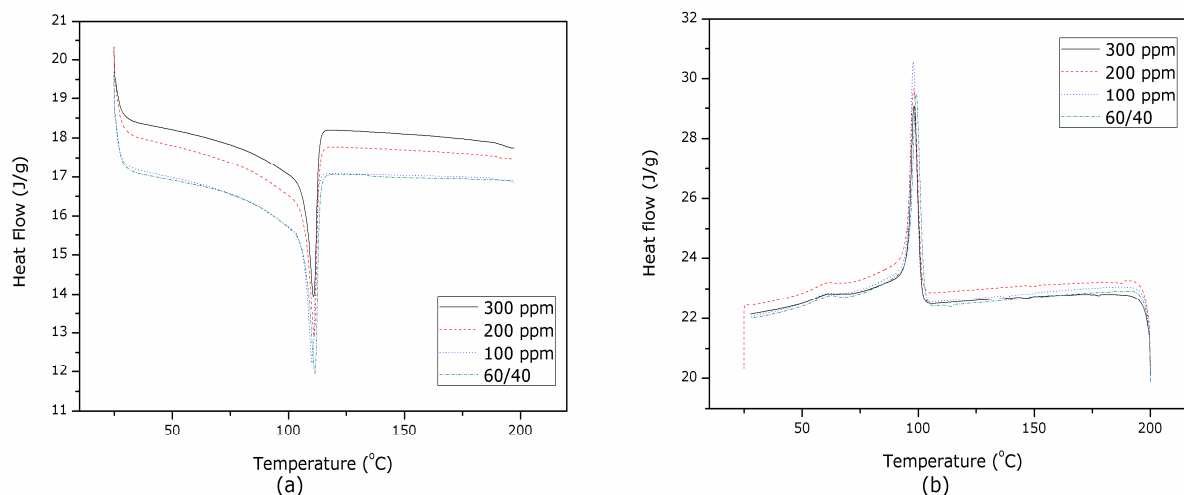
Figure 4. Melting (a) and crystallization (b) curves of LDPE/starch-AgNP nanocomposites.

The DSC curves of LDPE/starch blends and LDPE/starch-AgNP nanocomposites showed the same behavior with the pure LDPE. Any other endothermic peaks were not observed in the thermograms for these samples. These results indicate that there was no any degradation in the thermal properties of LDPE by the addition of starch and AgNPs, and the obtained films were compatible under these combinations [43]. There were also no significant differences between the T_m of the LDPE/starch blends; their values were very close to that of LDPE. However, T_c of the pure LDPE increased with the addition of starch, and this value was slightly shifted to higher values by increasing starch contents, as seen Figure 3 (b). The incorporation of AgNPs into the LDPE/starch blend with weight ratio of 60/40 caused a slight decrease in both temperatures, Figure 4 (a-b). In addition, the crystallinity degree decreased markedly with increasing content of starch in the blend, and also with the addition of AgNPs. This decrease was even in the blend appearing agglomeration. The % crystallinity reduced up to 37.77% at 60/40, LDPE/starch composition, and continued to fall up to 32.12% by the increasing amount of AgNPs to 300 ppm in the LDPE/starch blend. This linear decrease with the increase in the amount of starch and AgNPs arises from the inhibition of close packing of the LDPE chains due to the incorporation of starch and AgNPs in the blends. Moreover, this result was attributed that glycerol and zinc stearate used as plasticizer and compatibilizer generated the interactions between starch and LDPE, and also between AgNPs within zeolite and these polymers during the extrusion process.

Water Resistance Analyses

Water resistances of the obtained films were investigated with two methods composed of contact angle and water absorption measurements. The measured water contact angle values

including the right and left sides of the drop and the average contact angle of the films as a function of starch and AgNPs contents are given in Table 4. The images of water drops on these films are also given in Figure 5. The contact angle measurements give information about the degree of hydrophobicity/hydrophilicity of film surfaces. If the contact angle value of the water drop on the surface of a film sample is higher, it means that the film surface has a more hydrophobic character and is more resistant against water. This value is significantly influenced by the chemical composition of the film surface [14, 44]. The average contact angle value was found to be 107.67° for the pure LDPE film. Then, this value started to decrease by the addition of starch to the LDPE and fell to 91.53° for the blend containing the highest amount of starch (as LDPE/starch=60/40). This phenomenon indicated that the addition of hydrophilic starch into the hydrophobic LDPE polymer matrix made significant changes in the physicochemical characteristics of film surfaces. As expected, hydrophilic character of the film surfaces increased with the increasing starch contents. On the other hand, a higher difference between the contact angle values of the right and left sides of the water drop was observed for the blends with high starch content. This difference is explained by the inhomogeneous surfaces formed due to the agglomeration of starch particles.

Table 4. The water contact angles and water absorption values of the obtained films.

Sample	Q_L (°)	Q_R (°)	$Q_{average}$ (°)	W_{ab} (%)
LDPE	107.72	107.62	107.67	0.00
90/10	101.08	101.63	96.53	2.75
80/20	94.58	94.27	94.43	7.11
70/30	91.78	92.83	92.31	11.58
60/40	90.43	92.62	91.53	12.89
100ppm	95.93	97.97	96.95	12.71
200ppm	99.43	100.16	99.80	12.51
300ppm	101.20	104.14	102.67	12.08

The incorporation of the AgNPs within zeolite to the LDPE/starch blend with weight ratio of 60/40 completely changed the surface of the LDPE/starch film. The average contact angle values showed an increase with the presence of AgNPs in the polymer matrix. The value increased to 102.67° when the AgNPs content rose to 300 ppm. These results indicate the formation of more hydrophobic LDPE-rich surfaces as a result of phase separation and non-uniform composite structure during extrusion. It was also detected big differences between the contact angle values of the right and left sides of the water drop, which was caused by the

excessive surface roughness of these films. The contact angle measurements were consistent with the SEM analysis results.

The water absorption percentages of the films are given in Table 4. There was no water absorption for the pure LDPE, and then the absorption increased to 12.81 % by the increasing ratio of hydrophilic starch to 40 wt% in the hydrophobic LDPE polymer. The incorporation of the AgNPs into the LDPE/starch blend made no significant changes in the water absorption percentages of the nanocomposites.
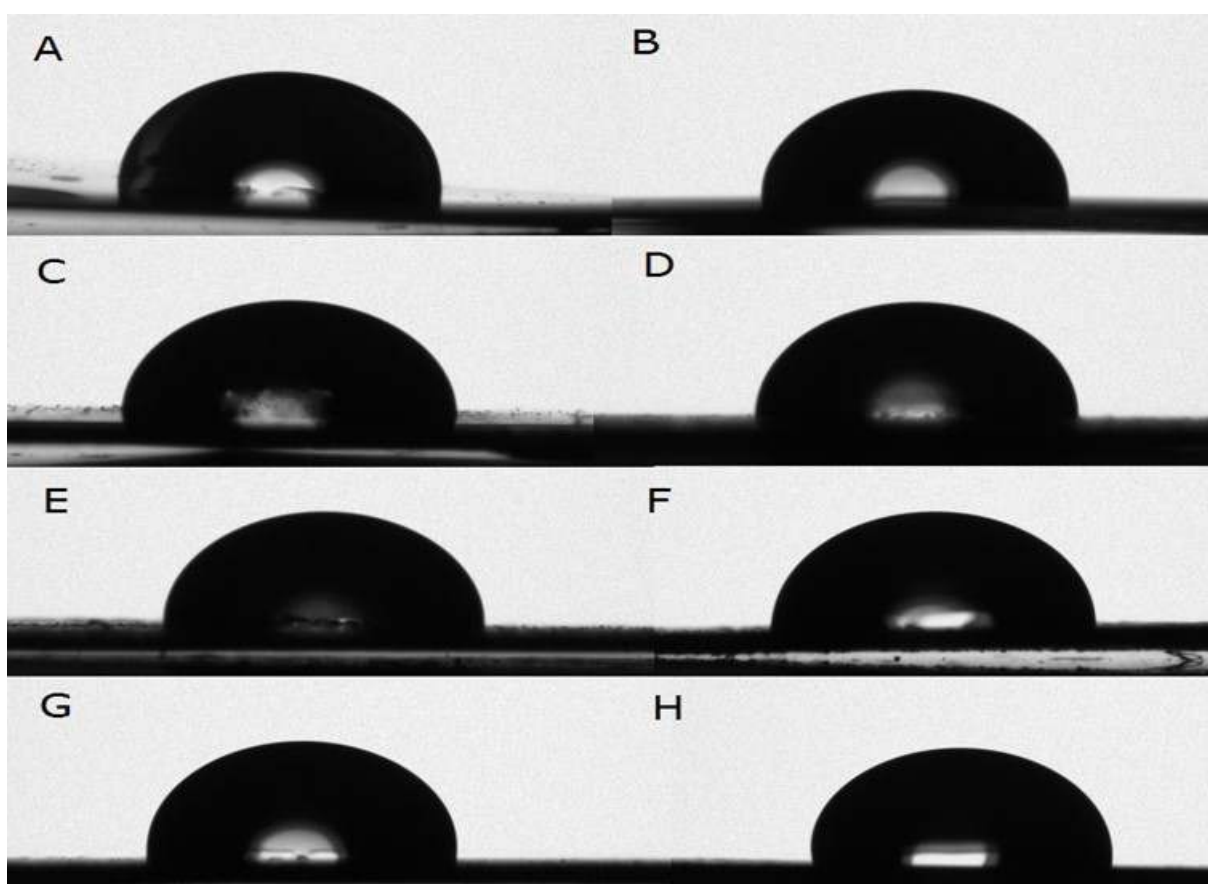
Figure 5. The images of water drops on the pure LDPE (A), LDPE/starch blend; 90/10(B), 80/20(C), 70/30 (D) and 60/40 (D), and LDPE/starch-AgNP nanocomposites; 100 ppm(F), 200 ppm(G) and 300 ppm(H) films.

Antibacterial Activity

The AgNPs within zeolite were incorporated to the LDPE/starch biodegradable polymer blends by extrusion method. The antibacterial activities of the obtained films with AgNPs were investigated by agar diffusion method. Figure 6 shows the AgNPs incorporated nanocomposite

films in the Petri dishes containing grown bacterial species, *Escherichia coli* (Gram negative) and *Staphylococcus aureus* (Gram positive). The formation of any clear zone around the samples, as an indication of inhibition of the bacterial species, was not osbserved. This zone forms when the diffusion of antibacterial agent in agar occurs. As seen in Figure 6, the creation of no clear zone in all samples consisting of AgNPs as antibacterial agent indicated that any diffusion of AgNPS from the sample to the agar medium with bacterial species did not occur. This may have arisen as a result of the chemical composition of the polymer mixture and/or the applying methods for the production of nanocomposites and their films.
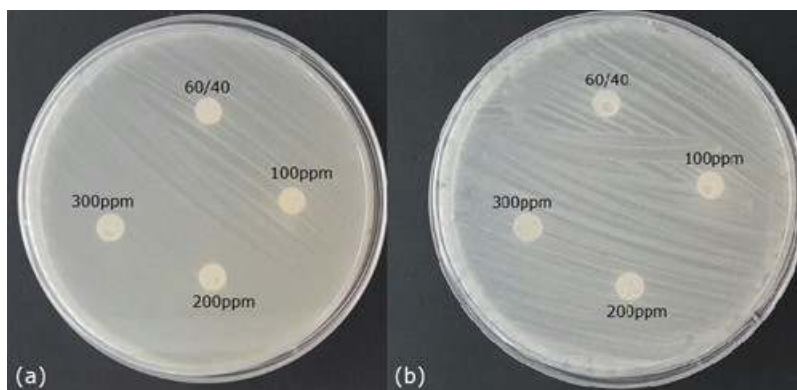
Figure 6. Appearance of AgNPs incorporated LDPE/starch nanocomposite films against *E. coli* (a) and *S. aureus* (b).

CONCLUSION

The biodegradable polymer blends were produced by melt blending of synthetic LDPE and the starch biopolymer for the food packing applications. The effects of starch content on the film properties were investigated in detail. The compatible films were obtained for low starch concentrations while the agglomerations of the starch particles in the blend occurred for higher concentrations of starch. The tensile properties and crystallinity degree of the LDPE decreased with the increasing content of starch in the blend. The water resistance of the hydrophobic LDPE was dropped by the addition of starch to this polymer. The incorporation of AgNPs within zeolite used as antibacterial agent caused the phase separation in the nanocomposite and the obtaining an inhomogeneous and discontinuous composite structure. The tensile properties and crystallinity decreased by this incorporation. In addition, it was not observed any antibacterial activities in these nanocomposite films where AgNPs were used as an antibacterial agent.

REFERENCES

1.		Rhim J-W, Park H-M, Ha C-S. Bio-nanocomposites for food packaging applications. Prog Polym Sci. 2013;38:1629-52. DOI: 10.1016/j.progpolymsci.2013.05.008.

2.		Siracusa V, Rocculi P, Romani S, Rosa MD. Biodegradable polymers for food packaging: a review. Trends Food Sci Tech. 2008;19:634-43. DOI: 10.1016/j.tifs.2008.07.003.

3.		Shah AA, Hasan F, Hameed A, Ahmed S. Biological degradation of plastics: A comprehensive review. Biotechnol Adv. 2008;26:246-65. DOI: 10.1016/j.biotechadv.2007.12.005.

4.		Halley PJ. 6 - Themoplastic starch biodegradable polymers A2 - Smith, Ray. Biodegradable Polymers for Industrial Applications. Woodhead Publishing; 2005. 140-62 p. ISBN: 978-1-85573-934-5.

5.		Platt DK. Biodegredable Polymers Market Report: Rapra Technology; 2007. 11-7 p. ISBN: 1-85957-519-6.

6.		Bastioli C. Handbook of Biodegradable Polymers Rapra Technology Limited; 2005. 257 p. ISBN: 1-85957-389-4.

7.		Wihodo M, Moraru CI. Physical and chemical methods used to enhance the structure and mechanical properties of protein films: A review. J Food Eng. 2013;114:292-302. DOI: 10.1016/j.jfoodeng.2012.08.021.

8.		Inceoglu F, Menceloglu YZ. Transparent low-density polyethylene/starch nanocomposite films. J Appl Polym Sci. 2013;129:1907-14. DOI: 10.1002/app.38811.

9.		Guilbert S, Cuq B, Gontard N. Recent innovations in edible and/or biodegradable packaging materials. Food Addit Contam Part A-Chem. 1997;14:741-51. DOI: 10.1080/02652039709374585.

10.		Chandra R, Rustgi R. Biodegradable polymers. Prog Polym Sci. 1998;23:1273-335. DOI: 10.1016/S0079-6700(97)00039-7.

11.		Chiellini E, Corti A, Swift G. Biodegradation of thermally-oxidized, fragmented low-density polyethylenes. Polym Degrad Stab. 2003;81:341-51. DOI: 10.1016/s0141-3910(03)00105-8.

12.		Pedroso AG, Rosa DS. Mechanical, thermal and morphological characterization of recycled LDPE/corn starch blends. Carbohydr Polym. 2005;59:1-9. DOI: 10.1016/j.carbpol.2004.08.018.

13.		Pedroso AG, Rosa DS. Effects of the compatibilizer PE-g-GMA on the mechanical, thermal and morphological properties of virgin and reprocessed LDPE/corn starch blends. Polym Adv Technol. 2005;16:310-7. DOI: 10.1002/pat.581.

14.		Peres AM, Pires RR, Orefice RL. Evaluation of the effect of reprocessing on the structure and properties of low density polyethylene/thermoplastic starch blends. Carbohydr Polym. 2016;136:210-5. DOI: 10.1016/j.carbpol.2015.09.047.

15.		Psomiadou E, Arvanitoyannis I, Biliaderis CG, Ogawa H, Kawasaki N. Biodegradable films made from low density polyethylene (LDPE), wheat starch and soluble starch for food packaging applications. Part 2. Carbohydr Polym. 1997;33:227-42. DOI: 10.1016/S0144-8617(97)00032-5.

16.		Róz ALD, Carvalho AJF, Gandini A, Curvelo AAS. The effect of plasticizers on thermoplastic starch compositions obtained by melt processing. Carbohydr Polym. 2006;63:417-24. DOI: 10.1016/j.carbpol.2005.09.017.

17.		Griffin GJL. Environmentally Degradable PolymersStarch polymer blends. Polym Degrad Stab. 1994;45:241-7. DOI: 10.1016/0141-3910(94)90141-4.

18.		Garg S, Jana AK. Studies on the properties and characteristics of starch-LDPE blend films using cross-linked, glycerol modified, cross-linked and glycerol modified starch. Eur Polym J. 2007;43:3976-87. DOI: 10.1016/j.eurpolymj.2007.06.030.

19.   Wang YJ, Liu W, Sun Z. Effects of glycerol and PE-g-MA on morphology, thermal and tensile properties of LDPE and rice starch blends. J Appl Polym Sci. 2004;92:344-50. DOI: 10.1002/app.20015.

20.   Yang JH, Yu JG, Ma XF. Study on the properties of ethylenebisformamide and sorbitol plasticized corn starch (ESPTPS). Carbohydr Polym. 2006;66:110-6. DOI: 10.1016/j.carbpol.2006.02.029.

21.   Ma XF, Yu JG, Wan JJ. Urea and ethanolamine as a mixed plasticizer for thermoplastic starch. Carbohydr Polym. 2006;64:267-73. DOI: 10.1016/j.carbpol.2005.11.042.

22.   Sabetzadeh M, Bagheri R, Masoomi M. Effect of corn starch content in thermoplastic starch/low-density polyethylene blends on their mechanical and flow properties. J Appl Polym Sci. 2012;126:E63-E9. DOI: 10.1002/app.36329.

23.   Fabra MJ, López-Rubio A, Ambrosio-Martín J, Lagaron JM. Improving the barrier properties of thermoplastic corn starch-based films containing bacterial cellulose nanowhiskers by means of PHA electrospun coatings of interest in food packaging. Food Hydrocolloids. 2016;61:261-8. DOI: 10.1016/j.foodhyd.2016.05.025.

24.   Khanoonkon N, Yoksan R, Ogale AA. Morphological characteristics of stearic acid-grafted starch-compatibilized linear low density polyethylene/thermoplastic starch blown film. Eur Polym J. 2016;76:266-77. DOI: 10.1016/j.eurpolymj.2016.02.001.

25.   Nakamura EM, Cordi L, Almeida GSG, Duran N, Mei LHI. Study and development of LDPE/starch partially biodegradable compounds. J Mater Process Technol. 2005;162–163:236-41. DOI: 10.1016/j.jmatprotec.2005.02.007.

26.   Thakore IM, Desai S, Sarawade BD, Devi S. Studies on biodegradability, morphology and thermo-mechanical properties of LDPE/modified starch blends. Eur Polym J. 2001;37:151-60. DOI: 10.1016/S0014-3057(00)00086-0.

27.   Girija BG, Sailaja RRN. Low-density polyethylene/plasticized tapioca starch blends with the low-density polyethylene functionalized with maleate ester: Mechanical and thermal properties. J Appl Polym Sci. 2006;101:1109-20. DOI: 10.1002/app.24025.

28.   Hoque ME, Ye TJ, Yong LC, Mohd Dahlan K. Sago Starch-Mixed Low-Density Polyethylene Biodegradable Polymer: Synthesis and Characterization. Journal of Materials. 2013;2013:7. DOI: 10.1155/2013/365380.

29.   Carlson C, Hussain SM, Schrand AM, K. Braydich-Stolle L, Hess KL, Jones RL, et al. Unique Cellular Interaction of Silver Nanoparticles: Size-Dependent Generation of Reactive Oxygen Species. The Journal of Physical Chemistry B. 2008;112:13608-19. DOI: 10.1021/jp712087m.

30.   Dallas P, Sharma VK, Zboril R. Silver polymeric nanocomposites as advanced antimicrobial agents: Classification, synthetic paths, applications, and perspectives. Adv Colloid Interface Sci. 2011;166:119-35. DOI: 10.1016/j.cis.2011.05.008.

31.   Russell AD, Hugo WB. 7 Antimicrobial Activity and Action of Silver. Ellis GP, Luscombe DK, editors. Progress in Medicinal Chemistry. Elsevier; 1994. 351-70 p. ISBN: 0079-6468.

32.   Azeredo HMCd. Nanocomposites for food packaging applications. Food Res Int. 2009;42:1240-53. DOI: 10.1016/j.foodres.2009.03.019.

33.   Cheviron P, Gouanvé F, Espuche E. Effect of silver nanoparticles' generation routes on the morphology, oxygen, and water transport properties of starch nanocomposite films. J Nanopart Res. 2015;17:1-16. DOI: 10.1007/s11051-015-3173-4.

34.   Jokar M, Rahman RA, Ibrahim NA, Abdullah LC, Tan CP. Melt Production and Antimicrobial Efficiency of Low-Density Polyethylene (LDPE)-Silver Nanocomposite Film. Food Bioprocess Technol. 2012;5:719-28. DOI: 10.1007/s11947-010-0329-1.

35.   Appendini P, Hotchkiss JH. Review of antimicrobial food packaging. Innov Food Sci Emerg. 2002;3:113-26. DOI: 10.1016/S1466-8564(02)00012-7.

36.   Alkan U, Kilic M, Karabul Y, Yamak HB, Okutan M, Icelli O. Electrical and Mechanical Properties of LDPE/PANI Composites. J Nanoelectron Optoelectron. 2016;11:343-8. DOI: 10.1166/jno.2016.1889.

37.   Beg MDH, Kormin S, Bijarimi M, Zaman HU. Preparation and Characterization of Low-Density Polyethylene/Thermoplastic Starch Composites. Adv Polym Tech. 2016;35:n/a-n/a. DOI: 10.1002/adv.21521.

38.   Oromiehie AR, Lari TT, Rabiee A. Physical and thermal mechanical properties of corn starch/LDPE composites. J Appl Polym Sci. 2013;127:1128-34. DOI: 10.1002/app.37877.

39.   Gupta AP, Sharma M, Kumar V. Preparation and characterization of potato starch based low density polyethylene/low density polyethylene grafted maleic anhydride biodegradable polymer composite. Polym-Plast Technol Eng. 2008;47:953-9. DOI: 10.1080/03602550802274597.

40.   Gupta AP, Sharma M. Characterization of Biodegradable Packaging Films Derived from Potato Starch and LDPE Grafted with Maleic Anhydride–LDPE Composition. Part-II. J Polym Environ. 2010;18:492-9. DOI: 10.1007/s10924-010-0214-z.

41.   Wang H, Zeng CC, Elkovitch M, Lee LJ, Koelling KW. Processing and properties of polymeric nano-composites. Polym Eng Sci. 2001;41:2036-46. DOI: 10.1002/pen.10899.

42.   Wunderlich B, Czornyj G. A Study of Equilibrium Melting of Polyethylene. Macromolecules. 1977;10:906-13. DOI: 10.1021/ma60059a006.

43.   Gupta AP, Kumar V, Sharma M. Formulation and Characterization of Biodegradable Packaging Film Derived from Potato Starch & LDPE Grafted with Maleic Anhydride—LDPE Composition. J Polym Environ. 2010;18:484-91. DOI: 10.1007/s10924-010-0213-0.

44.   Yamak HB, Yildirim H. Improvement of film properties of vinyl acetate based emulsion polymers by using different types of maleic acid diesters. Prog Org Coat. 2013;76:1874-8. DOI: 10.1016/j.porgcoat.2013.05.032.

Türkçe Öz ve Anahtar Kelimeler

Gıda Ambalaj Uygulamaları İçin LDPE/Nişasta Biyo-Polimer Karışımlarının Isıl, Mekanik ve Su Direnç Özellikleri

Öz: Bu çalışmada, biyo-bozunur polimer karışımları oluşturmak için; düşük yoğunluklu polietilen (LDPE) nişasta ile çift vidalı ekstruder kullanarak eriyik halinde harmanlandı. Gıda ambalajlamada kullanılan LDPE/nişasta karışım filmleri, ekstrüzyon sürecinde üretilen granüllerin sıcak preslenmesiyle elde edildi. Karışımlardaki nişasta içeriği, LDPE'nin ağırlıkça %0-40'ı olacak şekilde değiştitirildi. Karışım içerisinde iyi bir nişasta dağılımı sağlamak için; gliserol ve çinko stearat sırası ile plastikleştirici ve uyumlaştırıcı olarak kullanıldı. LDPE filminin özellikleri üzerine nişasta içeriğinin etkisi incelendi. Düşük nişasta içeriklerinde (ağırlıkça %10 ve 20) iyi bir dağılım elde edildi, ancak daha yüksek içeriklerde (%20'den büyük) nişasta taneciklerinin topaklanması meydana geldi. Nişastanın LDPE'ye ilave edilmesi; LDPE'nin gerilme mukavemetini, kopmadaki uzamasını, kristallilik derecesini ve suya karşı direncini düşürdü. LDPE'nin özelliklerindeki bu düşme, nişasta içeriği %30'a artırıldığında ise dramatik bir şekilde gözlendi. Buna ek olarak, antibakteriyel katkı maddesi olarak gümüş nanotanecikleri LDPE/nişasta ağırlıkça oranının 60/40 olarak sabit tutulduğu biyo-bozunur LDPE karışımlarına ilave edildi. Bu nanotaneciklerin LDPE/nişasta biyo-bozunur karışımlarının morfolojik, mekanik, ısıl ve su direnci özellikleri üzerine etkisi incelendi. LDPE/nişasta karışımlarına nanotaneciklerin ilavesinin LDPE/nişasta filminin morfolojisini tamamen değiştirdiği gözlendi ve LDPE/nişasta karışım filminin mekanik, ısıl ve su direnci özellikleri, içindeki gümüş nanotaneciklerinin miktarına bağlı olarak değişti. Ayrıca, nanokompozit filmlerin gram negatif (E. coli) ve gram pozitif (S. aureus) bakterilerine karşı antibakteriyel aktiviteleri her film etrafındaki inhibisyon bölgesinin ölçülmesiyle belirlendi. Ancak, nanokompozit filmler antibakteriyel katkı maddesi olarak gümüş nanotanecikleri içermesine rağmen hiç bir antibakteriyel aktivite göstermedi.

Anahtar kelimeler: Biyo-bozunur malzemeler; düşük yoğunluklu polietilen; nişasta; gıda ambalajı.

Gönderme: 04 Temmuz 2016. **Düzeltme:** 09 Ekim 2016. **Kabul:** 31 Ekim 2016.

Theoretical Studies on the Thermodynamic Properties and Detonation Properties of Cyclotrimethylene Trinitramine (RDX) with Aluminum and Boron Metals

Nilgün ŞEN[1]*, Bayram YÜKSEL[2]
[1] Police Academy, Institute of Forensic Sciences, 06570, Anıttepe, Ankara, Turkey
[2] Ankara Criminal Police Laboratory, 06830, Gölbaşı, Ankara, Turkey

Abstract: The B3LYP/6-311++G(2df,2p) density functional theory (DFT) method was used to investigate the molecular geometry and thermodynamic properties of RDX and RDX derivatives containing Al and B metals. The detonation velocity (D) and detonation pressure (P), estimated by using Kamlet–Jacobs and literature equations, respectively. Total energies (E_t), frontier orbital energy (E_{HOMO}, E_{LUMO}), energy gap ($\Delta E_{LUMO-HOMO}$) and theoretical molecular density (ρ) were calculated with Spartan 14 software package program. It was shown that the presence of aluminum and boron atoms affects the good thermal stabilities. The results suggest that the composite RDX-Al, RDX-B derivatives have further detonation performance and higher density than RDX. RDX-Al derivatives appeared to be superior to RDX-B mixtures in terms of these parameters. These results provide information on the molecular design of new energetic materials.

Cite this: Şen N, Yüksel B. Theoretical Studies on the Thermodynamic Properties and Detonation Properties of Cyclotrimethylene Trinitramine (RDX) with Aluminum and Boron Metals. JOTCSA. 2016;3(3):657–68.

*Corresponding author: E-mail: nilgunsen2001@yahoo.com.

INTRODUCTION

The studies on high-energy density compounds have been increasing recently due to their superior explosive performances [1–4]. Organic chemists and material scientists have been continuing research efforts to meet industrial and military requirements in order to develop new energetic materials with good thermal stability, higher performance, insensitivity, and economically and environmentally friendliness [5–8]. Detonation performance, good thermal stability, low impact, high pressure and density are all known to be important major parameters in explosives. Therefore, the objective of this study is to find the molecules with better detonation performance and thermal stability.

(RDX) ($C_3N_6O_6H_6$) is a significant energetic material which is used as propellants and explosives. In the literature, there are numerous studies on RDX explosives focusing on their detonation performance and thermal stability [9–12]. Since there are limited studies on the explosives with composite RDX-Al and RDX-B derivatives including their thermodynamic properties, this study is expected to contribute to fill this gap in the literature. Figure 1 presents the calculated substances and their chemical structures.

The metal additives used in explosives for civil and military purposes since the beginning of the 21st century, have been employed to strengthen the detonation characteristic of high explosives [13-14]. It has been discovered that compositions of high explosives with aluminum, boron or beryllium cause enrichment explosion heat and strength in demolition effect [15].

A (RDX)   B   C

D   E
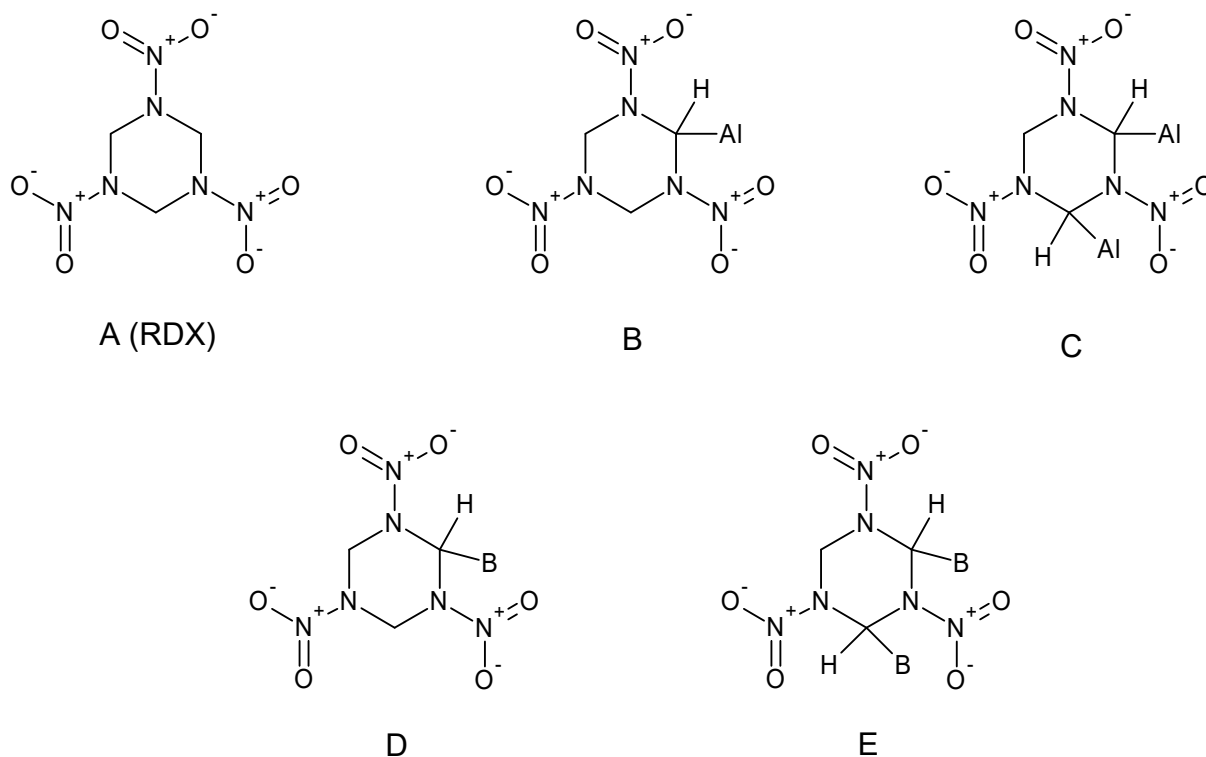
Figure 1. Chemical structures of calculated RDX derivatives.

The aluminized explosives are an energetic material widely used in the defense industry since the 20th century in various formulations (*e.g*. Ammonal, Tritonal, aluminized plastic bonded explosives, *etc*). There is presently an increased interest to discover more detonation characteristics of aluminized explosives [16]. Reaction temperature and reaction time increase when Al is added into the explosives [17]. When the metal participates in the reaction zone, aluminized explosives exhibit eigenvalue detonation behavior since the aluminum unreacted or partially reacted at the initial point in the reaction zone [18-19]. The properties of explosives containing boron have not been widely investigated though these materials have significant impact [20-21]. Boron flames at 2067 ºC, and its boiling temperature is 3865 ºC. It appears that it is stronger than steel, harder than corundum, and lighter than aluminum. Unlike aluminum, boron's oxidizing products are gases, not solids. In addition, the boron powders of sub-micrometer size particle are easily available, and the boron particles are not coated by the oxide film. A positive effect of boron on the explosion heat exceeds even that of aluminum [22].

To the best of our knowledge, there have been no precedents on a theoretical study about thermodynamic features and detonation velocities of additive metals (Al and B) RDX type plastic explosive mixtures so far. In this study, novel additive metals including RDX derivatives were examined comparatively.

MATERIALS AND METHODS

Computational methods

In the present study, quantum chemical calculations were carried out by using Spartan 14 software program at 298.15 K and under vacuum [23]. The B3LYP/6-311++G(2df,2p) (DFT) method was employed for detonation performance and thermodynamic properties. AM1 geometry was used in the calculations for the initial state and the geometry optimization was carried out 5×10^5 cycles.

Detonation performance

Density: The density of RDX compounds needs the data of the molecular volume. The molecular volume was defined as inside a contour of 0.001 electrons/bohr^3 density that was evaluated by Monte-Carlo integration. In this study, all compounds' density (A, B, C, D, E) were calculated by using molecular weight, molecular volume and molecular interactive length in SPARTAN 14 software package program and the results were shown in Table 2. Calculated data in the Table 2 supplies some ideas about the characteristics features of the compounds. RDX derivative compounds with different additive metal groups have different density values. Incorporation of metal groups in explosives increase and affect detonation performance of compounds.

It seems that the density of explosive increases when Al and B metals are composited with RDX. It appears that there is more increase in density when Al is added rather than B. Table 2 shows the density comparison as follows; $\rho A < \rho B < \rho C$ and $\rho A < \rho D < \rho E$. In the literature, the explosive performances are better with the increasing density [24].

Detonation velocity: The detonation properties (*i.e.* detonation energy, velocity, pressure, and density) before synthesis, needs to be taken into consideration as it decreases the cost for synthesis and characterization of the energetic compounds. Detonation performance includes two important parameters; detonation pressure (P, GPa), and detonation velocity (D, km.s^{-1}) to calculate performance of explosive compounds. In this study, Kamlet–Jacobs empirical equations (1,2) were used to determine $C_a H_b O_c N_d$ (RDX)(A) compounds [25-26].

$$P = 1.558 \; N.M^{1/2} . Q^{1/2} . \rho^2 \qquad \text{(Eq. 1)}$$

$$D = 1.01(N.M^{1/2} . Q^{1/2})^{1/2} . (1 + 1.30 \; \rho) \qquad \text{(Eq. 2)}$$

As for the $C_aH_bO_cN_d$ type explosives, the parameters N, M, and Q were computed and each was shown in Table 1.

Table 1. Calculations of the N, M and Q are determined with the following formula [27].

	Stoichiometric Relations		
Parameter	$c \geq 2a + b/2$	$2a + b/2 > c \geq b/2$	$b/2 > c$
N	$(b + 2c + 2d)/4M_i$	$(b + 2c + 2d)/4M_i$	$(b + d)/2M_i$
M_{ave}	$4M_i/(b + 2c + 2d)$	$(56d + 88c - 8b)/$ $(b + 2c + 2d)$	$(2b + 28d + 32c)/$ $(b + d)$
$Qx10^{-3}$	$(28.9b + 94.05a +$ $0.239\Delta H^o f)/M_i$	$[28.9b + 94.05(c/2 - b/4)+$ $0.239\Delta H^o f]/M_i$	$(57.8c +$ $0.239\Delta H^o f)/M_i$
M_i molecular weight of the compound (g/mol)			

Detonation velocity of RDX molecule was calculated with Kamlet-Jacobs equations, and Equation 3 was used in the calculation for the detonation velocity (D, km.s^{-1}) of B, C, D, and E compounds [28]. These results point out that the following simple equation can provide the suitable pathway for predicting D [28]:

$$D\,(km.s^{-1}) = y_1 + y_2 a + y_3 b + y_4 c + y_5 d + \sum_{i=6} y_{iSSPi} \qquad \text{(Eq. 3)}$$

Velocity values obtained for RDX were placed into Equation 3 because of existing special and structural variants (SSPi). Due to the fact that the co-efficients a, b, c, d have a linear relation with detonation velocity, the equation becomes linear, too. Based on these results for different a, b, c, d obtained by Spartan 14 software package program, y_i coefficients were found out by regression method by means of Mathematica 8 [29]. After that, addition of an inorganic element into the explosive molecule was performed by using y_6 coefficient. It is e=1 for one Al or one B, and it is e=2 for two Al or two B. After y_i and e parameters were found, theoretical explosive velocities were calculated for B, C, D, E compounds. Table 2 presents calculated theoretical ρ(g.cm^{-3}), D(km.sn^{-1}), and P (GPa) of the RDX derivations. As can be seen in Table 2, all RDX derivatives have good detonation properties (Q=1369.74-1473.91 J.g^{-1}, D=8.76-8.98 km.s^{-1}, P=34.32-40.28 GPa). Meanwhile, as the number of metallized groups increase, ρ, D, and P of the corresponding compounds increase. Molecule C was calculated as having the highest D, ρ and P values among RDX derivative compounds.

Table 2. Predicted densities and detonation properties of RDX, RDX derivatives containing Al and B metals.

Molecule	Formula	φ	N	M	Q	ρ[e]	D[f]	P[g]
A	$C_3H_6N_6O_6$	6.65	0.034	27.2	1426.6	1.82	8.768	343.3
B	$C_3H_5AlN_6O_6$	5.91	0.029	284	1438.5	2.03	8.943	379.3
C	$C_3H_4Al_2N_6O_6$	5.15	0.026	29.7	1369.7	2.24	8.986	402.8
D	$C_3H_5BN_6O_6$	6.36	0.031	28.4	1456.4	1.90	8.839	357.7
E	$C_3H_4B_2N_6O_6$	6.06	0.029	29.7	1473.9	1.98	8.888	370.2

[e] g/cm^3, [f] km/s, [g]kbar

When Figure 2 and 3 are examined, it can be seen that D ($km.s^{-1}$) and ρ ($g.cm^{-3}$) linearly increase with the addition of explosive metallized groups. However, compounds having Al increase the D and ρ relatively much more than compounds having B. Aluminized explosives, in particular, had been thoroughly investigated as they were extensively employed. Hence, the results are consistent with the literature [30].
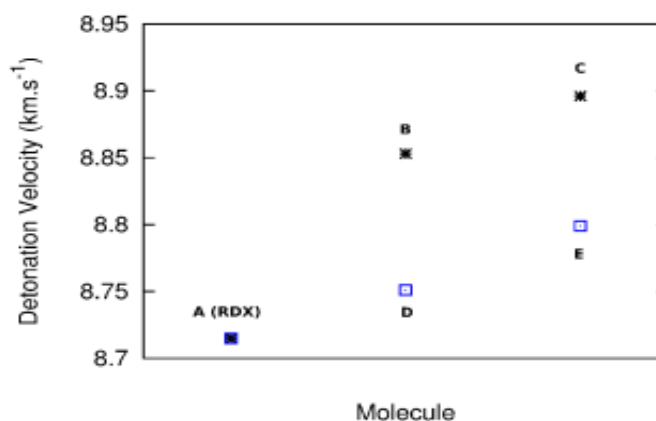
Figure 2. Prediction of detonation velocity ($km.s^{-1}$) of RDX derivatives.
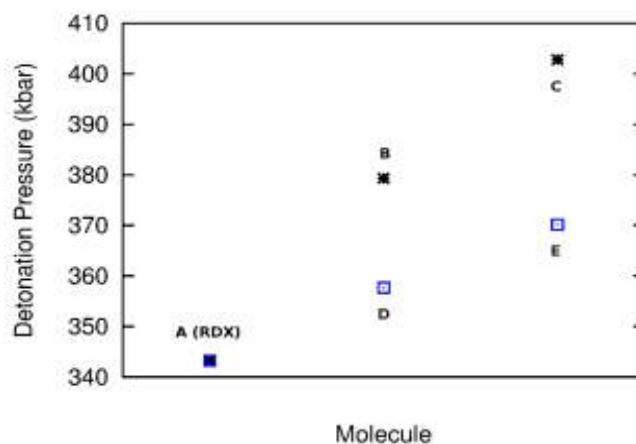
Figure 3. Prediction of detonation pressure (kbar) of RDX derivatives.

Thermal stability: Studying HOMO and LUMO demonstrates whether or not the reaction is feasible and the relative thermal stability of an individual molecule in the gas phase [1]. The higher value of energy gap (ΔE) resulting from higher energy of LUMO and lower energy of HOMO indicates that neither losing nor capturing an electron would happen on the title compound easily, so it is more stable.

Table 3 shows the zero-point energy (ZPE), HOMO and LUMO energies, energy gap $\Delta E_{LUMO-HOMO}$, total energies geometry of the optimized compounds which were calculated at the theoretical level of B3LYP/6-311++G(2df,2p). When Table 3 is considered, it is obvious that the ZPE and total energies of compounds get lower from A to E. It is known that as the molecular weight of compounds get higher, the total electronic energy values get lower. The average values of frontier orbital energy gap $\Delta E_{LUMO-HOMO}$ of A, B, C, D and E at B3LYP/6-311++G(2df,2p) levels are 5.75, 3.84, 2.15, 4.02 and 3.43 a.u., respectively. As can be seen in Figure 4, it is notable that compound C has the smallest energy gap, which indicates that this compound is the least stable among the five compounds studied, while compound A has the largest energy gap and is, therefore, the most stable of them. Thermal stability order of them are as follows:

(least stable) C<E<B<D<A (most stable)

Table 3. ZPE, E_{HOMO}, E_{LUMO} and energy gaps ($\Delta E_{LUMO-HOMO}$) for RDX derivatives.

Molecules	Weight[a]	Total Energy[b]	HOMO[b]	LUMO[b]	Energy Gap[b]	ZPE[c]
A	222.117	24426.79	-8.06	-2.31	5.75	359.54
B	248.091	31007.16	-6.59	-2.75	3.84	332.30
C	274.065	37586.68	-5.87	-3.72	2.15	302,91
D	231.92	25083.65	-7.41	-3.39	4.02	336.62
E	241.723	25739.75	-7.36	-3.93	3,43	308.62

[a] amu. [b] eV. [c] kJ/mole.
The total electronic energies were corrected for zero point energies (ZPE) taking into consideration Total energies listed in the table were included ZPE.

Inspection of Figure 5 and Table 3 reveals that the presence of Al and B metals appreciably raises the HOMO level and decreases the LUMO level compared to RDX.
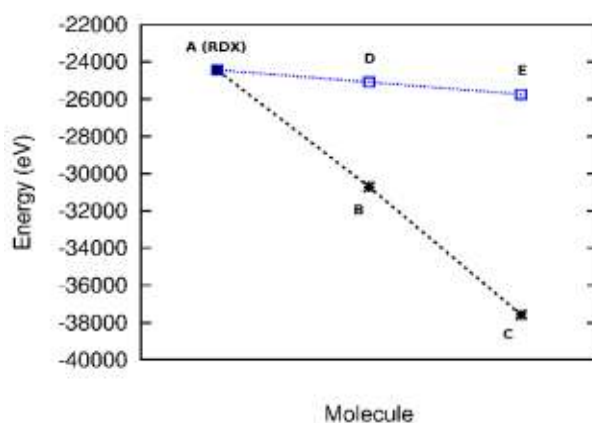
Figure 4. Calculated energy gap of all compounds.
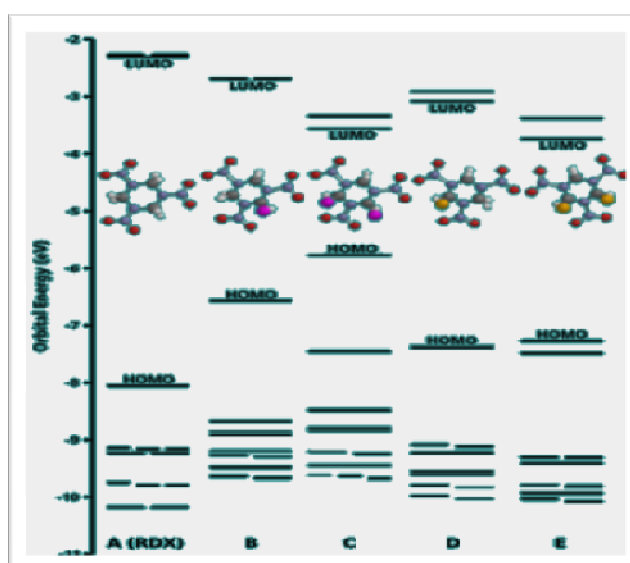
Figure 5. Molecular orbital energy spectra of the species [B3LYP/6-311++G(2df,2p), energies in eV].

RESULTS AND DISCUSSION

In this study, we have studied the detonation performance and thermal stability of RDX and RDX derivatives containing Al and B metals by the DFT- B3LYP method. As a result of our theoretical study, the following conclusions are drawn:

(1) The calculated detonation performance (D, P, ρ) are very helpful for enhancing detonation performance. Considering the detonation performance and thermal stability, additive metal groups (Al, B) can be regarded as potential candidates in high energetic materials. These results supply theoretical calculation for basic information about the molecular design of new high energetic materials and experimental synthesis.

(2) As for the RDX compounds contain metals, as number of metals increases, D, P and ρ linearly increase, however energy gap and ZPE linearly decrease.

(3) Calculated results showed that aluminum and boron metals groups can be added to explosives, as an enhancement to their performances. In addition, results indicate that aluminum is more effective than boron.

ACKNOWLEDGEMENTS

REFERENCES

1. Zhang J. Y, Du H. C., Wang F, Gong X. D, Huang Y. S. DFT studies on a high energy density cage compound 4-trinitroethyl-2,6,8,10,12-pentanitrohezaazaisowurtzitane. Journal of Physical Chemistry A. 2011;115(24):6617-6621. DOI: 10.1021/jp1118822.

2. Klapotke T. M, Piercey D. G, Stierstorfee J. The Facile Synthesis and Energetic Properties of an Energetic Furoxan Lacking Traditional "Explosophore" Moieties:(E,E)-3,4-bis (oximomethyl) furoxan (DPX1). Propellants Explos. Pyrotech. 2011; 36:160–167. DOI: 10.1002/prep.201000057.

3. Wang G. X, Gong X. D, Liu Y, Du H. C, Xu X. J, Xiao H. A theoretical investigation on the structures, densities, detonation properties and pyrolysis mechanism of the nitro derivatives of toluenes. Journal of Hazard. Materials. 2010; 177:703–710. DOI:10.1016/j.jhazmat.2009.12.088.

4. Zhang J. G, Niu X. Q, Zhang S. W, Zhang T. L, Huang H.S, Zhou Z.N. Novel potential high-nitrogen-content energetic compound: Theoretical study of diazido-tetrazole (CN_{10}). Comput.Theor. Chem. 2011; 964:291–297. DOI: 10.1016/j.comptc.2011.01.014.

5. Li X. H, Zhang R. Z, Zhang X. Z. Computational study of imidazole derivative as high energetic materials. J. Hazard. Mater. 2010; 183: 622–631. DOI:10.1016/j.jhazmat.2010.07.070.

6. Talawar M. B, Sivabalan R, Mukundan T, Muthurajan H, Sikder A.K, Gandhe B.R, Rao A.S. Environmentally compatible next generation green energetic materials (GEMs). J. Hazard. Mater. 2009;161:589–607. DOI:10.1016/j.jhazmat.2008.04.011.

7. Li X.H, Zhang R Z, Zhang X Z, Computational study of imidazole derivative as high energetic materials. J. Hazard. Mater. 2010;183: 622–631. DOI: 10.1016/j.jhazmat.2010.07.070.

8. Badgujar D.M, Talawar M.B,Asthana S.N, Mahulikar P.P. Advances in science and technology of modern energetic materials: An overview. J. Hazard. Mater. 2008;151: 289–305. DOI:10.1016/j.jhazmat.2007.10.039.

9. Zhu W. H, Zhang X. W, Wei T, Xiao H. M. Density functional theory study of structural of structural vibrational, and thermodynamic properties of crystalline 2,4- dinitrophenol, 2,4- dinitroresorcinol, and 4,6-dinitroresorcinol. J. Mol. Struct. Theochem. 2009; 895:131-137. DOI:10.1016/j.theochem.2008.10.037.

10. Kohno Y, Hiyoshi R. I, Yamaguchi Y, Matsumoto S, Koseki A, Takahashi O, Yamasaki K, Ueda K. Molecular Dynamics Studies of the Structural Change in 1,3-Diamino-2,4,6-trinitrobenzene (DATB) in the Crystalline State under High Pressure. J. Physical Chem. A. 2009; 113: 2551–2560. DOI: 10.1021/jp809240x.

11. Zhou Y, Long X. P, Shu Y. J. Theoretical studies on the heats of formation, densities, and detonation properties of substituted s-tetrazine compounds. J. Mol. Model. 2010; 16:1021–1027. DOI: 10.1007/s00894-009-0605-z.

12. Ghule V. D, Sarangapani R, Jadhav P. M, Tewari S. P. Theoretical studies on nitrogen rich energetic azoles. J. Mol. Model. 2011; 17:1507–1515. DOI: 10.1007/s00894-010-848-8.

13. Belyaev A. Combustion, Detonation, and Work of Explosion of Condensed Systems. Nauk~, Moscow. 1968;

14. Cook MA, editor. The Science of Industrial Explosives, IRECO Chemicals, Salt Lake City, Utah 1974. 15-17 p. URL: http://onlinelibrary.wiley.com/doi/10.1002/3527600515.biblio/pdf.

15. Kanel G.I, Utkin A.V, Razorenov S V. Central, Rate of the energy release in high explosives containing nano-size boron particles. European Journal of Energetic Materials. 2009; 6(1): 15-30. http://yadda.icm.edu.pl/yadda/element/bwmeta1.element.baztech-article-BAT1-0034-0021.

16. Stark JG, Wallace HG. Co-editor. Chemistry Data Book, Hodder Murray, London, 2004. 15p. ISBN 10: 071953951X.

17. Keshavarz M. H. Simple correlation for predicting detonation velocity of ideal and non-ideal explosives. J. Hazard. Mater. 2009;166: 762–769. DOI: 10.1016/j.jhazmat.2008.11.117.

18. Baker E. L, Capellos C, Stie L. l. Stable Detonation Velocities for Aluminized Explosives. Sci. Tech. Energ. Mat. 2006;67(4): 134–138. http://ci.nii.ac.jp/naid/1001753386119. Yen N.H,

19. Yen N. H and Wang L. Y. Reactive Metals in Explosives. Propellants Explos. Pyrotech. 2012; 37:143 – 155. DOI: 10.1002/prep.200900050.

20. Arnold W, Rottenkolber E. The performance of insensitive blast enhanced explosives. Insensitive Munitions and Energetic Materials Technology Symposium, Tucson, AZ,USA, May 11-14, 2009. 111 p. http://www.dtic.mil/ndia/2009insensitive/6Barnold.

21. Sezaki T, Date S, Satoh J. Study on the effects of addition of boron particles to RDX based PBX Regarding Prevention of Neumann Effect. Materials Science Forum. 2004; 465-466:195-200. DOI:10.4028/www.scientific.net/MSF.465-466.195.

22. Schaefer R. A, Nicolich S. M. Development and evaluation of new high blast explosives, Insensitive munitions and energetic materials technical symposium, San Francisco, CA, USA, November 15–17, 2004, 111 p.

23. SPARTAN 14. Wavefunction Inc. Irvine CA, USA. 2014. URL:
http://www.wavefun.com/products/spartan.html.

24. Zhao G.Z, Lu M. Theoretical studies on the structures and detonation properties of nitramine explosives containing benzene ring. J. Mol. Model. 2012; 18: 2443–2451. DOI: 10.1007/s00894-011-1267-1.

25. Kamlet M. J, Jacobs S. J. Chemistry of Detonations. I. A Simple Method for Calculating Detonation Properties of C H N O Explosives. J. Chem. Phys. 1968:48; 23-30. URL:
http://oai.dtic.mil/oai/oai?verb=getRecord&metadataPrefix=html&identifier=AD0661483.

26. Zhang XH, Yun ZH. Explosive chemistry; National Defense Industry Press, Beijing People's Republic of China; 1989.107 p. URL: http://www.nrcresearchpress.com/doi/abs/10.1139/cjc-2012-0468.

27. Qiu L, Xiao H, Gong X, Ju X, Zhu W. Theoretical studies on the structures, thermodynamic properties, detonation properties and pyrolysis mechanisms of spiro nitramines. J. Phys. Chem. 2006;110 (10):3797-3807. DOI: 10.1021/jp054169g.

28. Keshavarz M. H. Detonation velocity of pure and mixed C H N O explosives at maximum nominal density. J. Hazard. Mater .2007,141, 536–539. DOI:10.1016/j.jhazmat.2006.07.060.

29. Wolfram research Inc. Mathematica. Version 7.0. Champaign, Illinois. 2008. URL:
http://www.wolfram.com/mathematica/.

30. Akimova. L. N, Apin A. Y, Stesik L. N. Detonation of explosives containing boron and its organic derivatives. Combustion explosion and shock waves. 1972; 8:475-479.
http://link.springer.com/article/10.1007%2FBF00741190?LI=true#page-1.

Türkçe Öz ve Anahtar Kelimeler

Alüminyum ve Bor Metalleri içeren Siklotrimetilen Trinitramin (RDX) Bileşiklerinin Termodinamik ve Patlama Özellikleri Üzerine Teorik Çalışmalar

Nilgün ŞEN, Bayram YÜKSEL

Öz: B3LYP/6-311++G(2df,2p) yoğunluk fonksiyonel teorisi (DFT) yöntemi kullanılarak RDX ile Al ve B metali içeren RDX türevlerinin moleküler geometrisi ve termodinamik özellikleri incelendi. Patlama hızı (D) ve patlama basıncı (P) Kamlet-Jacobs ve literatürdeki eşitliklere göre hesaplandı. Toplam enerjiler (E_t), sınır orbital enerjisi (E_{HOMO}, E_{LUMO}), enerji aralığı ($\Delta E_{LUMO-HOMO}$) ve teorik moleküler yoğunluk (ρ) Spartan 14 program paketi ile hesaplandı. Alüminyum ve bor atomlarının varlığında iyi ısıl kararlılık elde edildiği gösterildi. Sonuçlara göre RDX-Al, RDX-B türevlerinin daha ileri patlama performansına sahip olduğu ve yoğunluklarının RDX'e göre daha yüksek olduğu bulundu. RDX-Al türevlerinin bu parametreler ışığında RDX-B türevlerine göre daha üstün olduğu gözlendi. Bu sonuçlar yeni enerjetik malzemelerin moleküler tasarımında bilgi verecektir.

Preparation and Characterization of Montmorillonite/Polycaprolactone Composite Scaffold Containing Strontium for Bone Tissue Engineering Studies

Aysel Koç Demir

Ankara University, Faculty of Science, Department of Chemistry, Tissue Engineering, Biomaterials and Nanobiotechnology Laboratory, 06100, Ankara, Turkey.

Abstract: In this study, composite scaffolds containing strontium-modified MMT and polycaprolactone (SrMMT-PCL) were prepared by using particulate leaching technique. The macrostructure and morphology of composite scaffolds were characterized by X-ray diffraction (XRD), thermogravimetric analysis (TGA), and scanning electron microscopy (SEM). The released amount of Sr^{2+} from scaffolds into cell culture medium was examined by inductive coupled plasma optical emission spectrometer (ICP-OES). The pore size distribution of scaffolds was determined by mercury intrusion porosimetry. The mechanical properties of the scaffolds were also evaluated. The results of XRD confirmed intercalation of PCL into MMT layers. TGA studies concluded that the MMT in PCL promoted the thermal degradation of the matrix. ICP results showed that Sr^{2+} was released from composite scaffolds. The majority of pore volume seems to be occupied by pores around 250-350 μm. SEM observations demonstrated the macroporous structure of the composite scaffolds obtained by using the particulate leaching method. As a result, the gained data suggest that obtained tissue-engineered scaffold has the potential to serve as a suitable template for bone tissue engineering applications.

INTRODUCTION

Every year, thousands of patients around the world suffer from bone fractures and degenerative disease. Although various treatment options are available for repairing bone defects resulting from trauma, tumors, biochemical disorders, and developmental abnormalities, using methodology have some drawbacks including donor site scarcity, inflammation, and the risk of immune rejection. Hence, researchers have begun to focus on bone tissue engineering (BTE) perspectives to find alternative solutions to address common clinical challenges.

The development of suitable three dimensional composite materials play a significant role in tissue engineering studies. An engineered scaffold in bone tissue engineering serves as a temporary artificial extracellular template to support and stimulate bone tissue regeneration via mimicking the native extracellular matrix of the native tissue (1). The scaffold should be 3D and highly porous with an interconnected pore network for cell growth and enable diffusion of nutrients and possess certain mechanical stability, have suitable surface chemistry to allow cell attachment, proliferation and differentiation (2, 3). Natural and synthetic materials, cells and growth factors are three important factors to construct the artificial tissue. Among several choices of synthetic polymers, polycaprolactone (PCL) has been widely used as implantable material in the preparation of scaffolds because of its favorable properties. It is a semicrystalline, biodegradable, hydrophobic polymer belonging to the aliphatic polyester family (4). However, its limited bioactivity and mechanical features do not suit the specific needs of BTE applications. In the recent years, clays receive special interest as reinforcement materials to create a template with improved properties. Among clay minerals, montmorillonite (MMT) offers a wide variety of advantages. MMT is a three-layered smectite group of minerals. Its structure is composed of two silica tetrahedral layers (T) sandwiched a central octahedral sheet of aluminium hydroxide (O). Undergoing to the isomorphic substitution of Al^{3+} with Si^{4+} in the tetrahedral layer and Al^{3+} with Mg^{2+} in the octahedral layer will generate negative charges (5). Excess negative charge in the layers of TOT can be balanced with exchangeable alkaline or earth alkaline cations as K^+, Na^+, Ca^{2+} naturally occurring between the layers and also with other positively charged ions like Sr^{2+}, Zn^{2+}. It has wide specific surface area, good cation-exchange capacity, high adsorption capacity and drug carrying capability for polymers (6). Furthermore, it can also serve as a reservoir for different molecules and ions (7).

It is well known that metallic ions such as strontium, calcium, magnesium, and zinc are necessary for bone growth and development. These elements are involved in the process of bone development by ensuring the activation of bone cells (osteoblasts), while inhibition of bone resorption cells (osteoclasts) via a variety of mechanisms (8). From this point, the release of these ions from materials is very important to support bone regeneration. Due to the increasing evidence for the significant role of strontium in bone formation, the incorporation of strontium

with biomaterials to improve their osteoinductive properties has become a focus of interest (9, 10).

Keeping all of these interesting facts about PCL, MMT, and Sr^{2+} in mind, we aimed to develop Sr^{2+}-containing composite scaffolds by particulate leaching method and investigate the physical properties of Sr-modified MMT-PCL scaffold to determine its feasibility for bone tissue engineering studies.

MATERIALS AND METHODS

Materials

Polycaprolactone was purchased from Aldrich company (Mn: 70,000-90,000). Montmorillonite (MMT) used in this study with a cation exchange capacity (CEC) of 102 meq/100 g was obtained from Ünye Bentonite Company. Other chemicals used were purchased from Sigma.

Preparation of Sr-modified MMT

Sr^{2+} montmorillonites were prepared by a cation exchange method. Briefly, MMT was dispersed in distilled water and mechanically stirred at room temperature for 24 h. Then, strontium chloride solution with various concentrations ranging from 1 to 4 CEC was added dropwise to MMT solution. The mixture was stirred for overnight to allow the ion exchange reactions. The resulting Sr-modified MMT was collected by centrifugation and the pellet was rinsed in distilled water several times until a negative $AgNO_3$ test was observed. The product was dried at 100°C for 2 days, grinded, and characterized by XRD and XRF to compare the structures obtained by adding Sr^{2+}.

Preparation and characterization of MMT-PCL composite scaffolds

Taking in consideration the XRD and XRF results, Sr-modified MMT was prepared as described above using twice the ratio of Sr^{2+} concentration, for the following experiments. Composite scaffolds were fabricated by particulate leaching method. Briefly, a 10 % PCL in methylene chloride freshly prepared and mixed with the required amount of modified and non-modified MMT. The mixture was homogenized first by mechanical stirring and then by ultrasonic agitation to obtain a homogeneous suspension. The obtained mixture was casted into Teflon molds packed with NaCl crystalline particles (sieved to 200–350 μm). The solvent was evaporated and the resulting MMT-PCL/salt composite was immersed in distilled lukewarm water to dissolve the porogen.

X-ray powder diffractometer (XRD) was employed to analyze the crystalline phases of PCL, MMT, MMT-PCL, and SrMMT-PCL composite structure using a monochromatic Cu-Kα radiation (D8 Advance; Bruker, Germany).

Thermal gravimetric analysis (TGA) was performed on the obtained composite material using a thermal analysis system (Shimadzu DTG-60H) under nitrogen atmosphere in the temperature range of 20-800°C.

A mercury intrusion porosimeter (Quantachrome Corporation, Poremaster 60) was used to quantify pore size distribution of the scaffolds. The pressures were applied in the low pressure setting. A contact angle of 140° and a surface tension of mercury of 480 mN/m were determined for the samples.

SEM was employed to confirm the surface/cross-sectional pore morphology of composite scaffolds by using a Gemini 1525 FEGSEM model scanning electron microscope.

The mechanical properties of PCL, MMT-PCL, and SrMMT-PCL were evaluated through compression testing on an Shimadzu AGS-X machine at a constant strain rate (2 mm/min) with a 0.7 N loading cell.

Inductive coupled plasma optical emission spectrometer (ICP-OES) (Perkin Elmer Optima 4300D) was conducted to examine the concentration of the Sr^{2+} ions released from the composite scaffolds into media. Briefly, scaffolds were weighted and soaked in cell culture media (1 mg / 1 mL) in 24-well plates, then samples were transferred into incubator to mimic cell culture condition for up to 7 days. The medium was collected at days 1, 3 and 7. The collected medium was diluted ultrapure distilled water and filtered through a 0.2 µm filter to remove suspended particles before measurement of ions in the supernatant.

RESULTS AND DISCUSSION

Characterization of Sr-modified MMT

The XRD patterns of MMT and its modified structures with different Sr^{2+} concentration were illustrated in Figure 1. The basal spacing of the MMTs was calculated by using Bragg's equation ($n.\lambda = 2d.\sin\theta$). The obtained results showed the basal distance between the layers was not changed with the introduction of the cations, but the intensity of the peaks were increased compared to non-modified MMT (Table 1). XRF was used to estimate the optimum amount of Sr^{2+} incorporated into the MMT. The amount of Sr^{2+} inserted MMT structure was found 0.0139%, 2.709%, 3.6320% and 3.531%, the non-modified MMT (Sr(0x)-MMT), Sr(1x)-MMT, Sr(2x)-MMT and Sr(4x)-MMT, respectively. The Sr content of MMT increased with increasing Sr concentration as expected, but there was no detectable difference between Sr(2x) and Sr(4x). Thus, taking the results of XRD and XRF, twice the ratio of Sr^{2+} was chosen for the modification of MMT.

Table 1. The values of 2θ and the basal spacing of nonmodified and modified MMTs.

	$2\theta_1$	$2\theta_2$	d_1	d_2
Sr(0x)-MMT	7.06	22.65	14.5	4.56
Sr(1x)-MMT	7.35	23.65	13.96	4.36
Sr(2x)-MMT	7.53	23.63	13.96	4.37
Sr(4x)-MMT	7.43	23.12	14.43	4.46
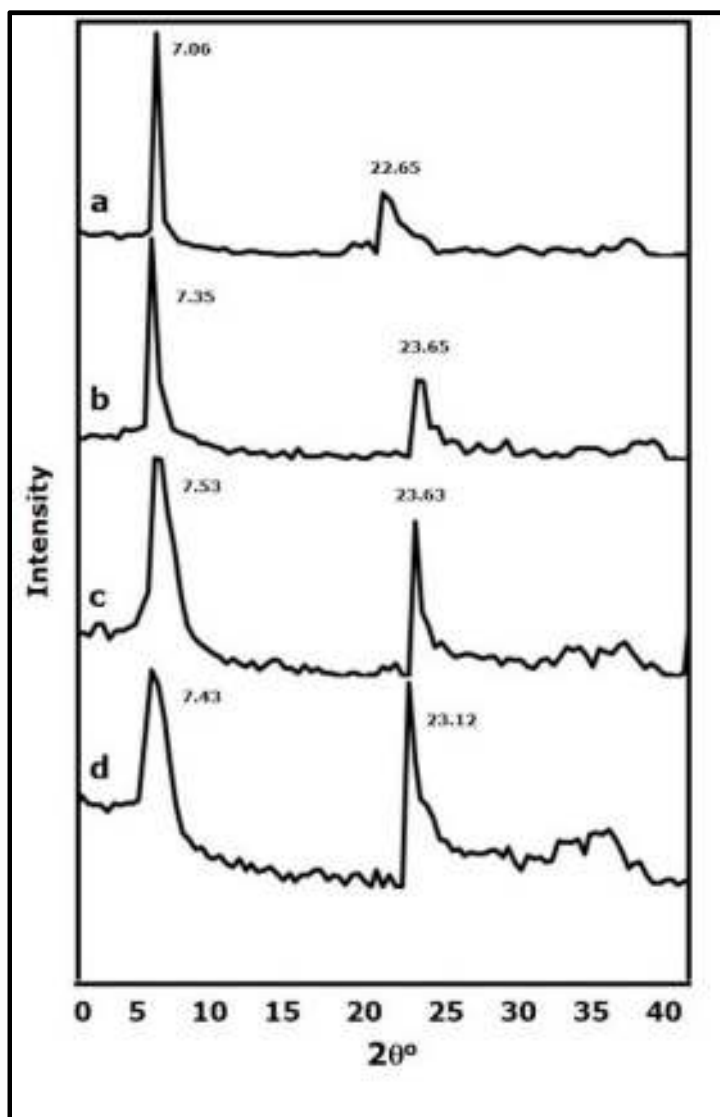
Figure 1. XRD pattern of the non-modified MMT (a), Sr(1x)-MMT (b), Sr(2x)-MMT (c), Sr(4x)-MMT (d).

Characterization of MMT-PCL composite scaffolds

The XRD patterns of PCL, MMT, and the composite scaffold were shown in Figure 2. The basal spacing of the samples was calculated by using Bragg's equation ($n.\lambda = 2d.\sin\theta$). The XRD pattern of the PCL shows a reflection peak at about $2\theta = 25.51°$ and $37.53°$. The interlayer distance

estimated from Bragg's law was 4.05 and 2.78 nm, respectively. MMT shows two main diffraction peaks around 2θ =7.53° and 23.63°. After the incorporation, the peaks of PCL and MMT moves to a lower angle. The increase of interlayer spacing for the composites was indicated the intercalation of PCL into MMT interlayers.
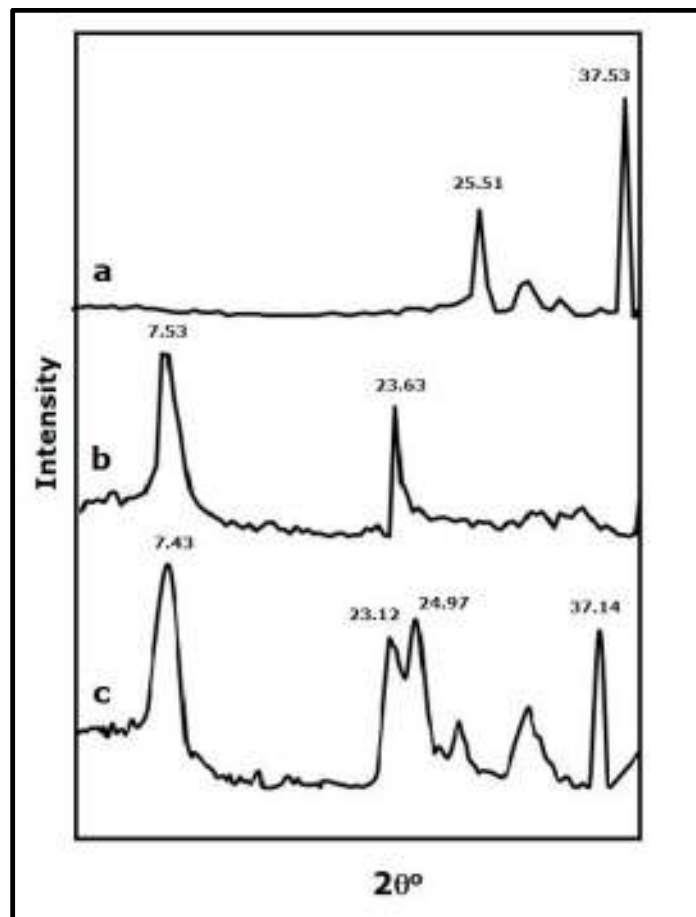
Figure 2. XRD pattern of PCL (a), SrMMT (b) and SrMMT-PCL scaffold (c).

The thermal behavior of MMT, PCL and MMT-PCL were assessed by means of thermogravimetry. The TGA curves of MMT, PCL and MMT-PCL composite scaffold were shown in Figure 3. MMT did not exhibit any significant weight loss in the range of temperature, while PCL exhibited significant weight loss after 600 °C. The degradation of PCL in PCL-MMT composite structure was observed over a range of 500-650 °C and the amount of remaining residue was 70 %, implying that MMT promoted the thermal stability of the polymeric matrix.
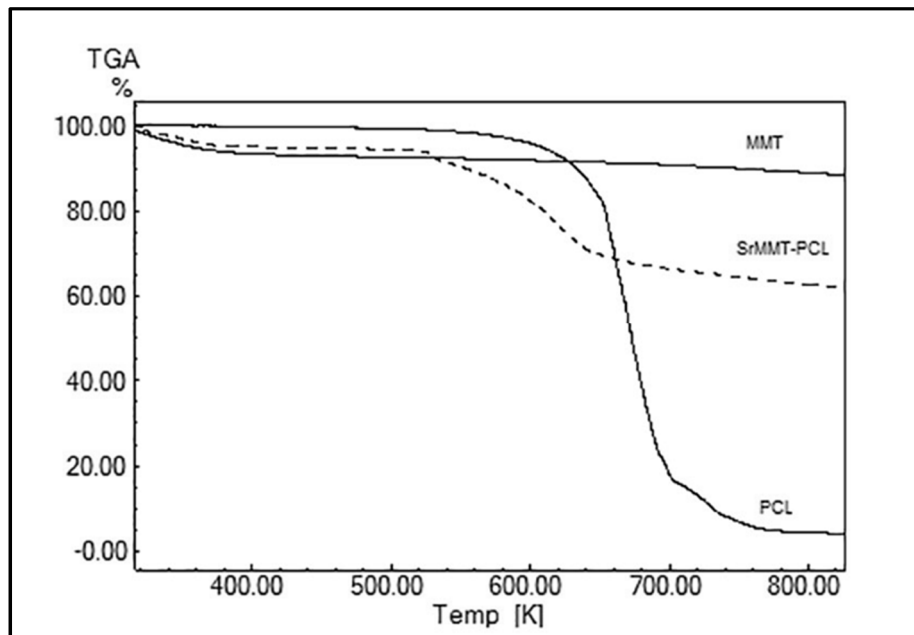
Figure 3. Thermogravimetric curves of MMT, PCL and SrMMT-PCL scaffold.

The pore size and interconnectivity of the engineered biomaterials are really vital factors for creating a suitable scaffold, because these parameters have a strong effect on cellular response such as cell attachment, proliferation, and differentiation (11). The scaffold should be highly porous with an interconnected pore structure for transportation of necessary nutrition factors and oxygen for seeded cell and maintain its mechanical stability between the scaffolds and surrounding tissue (2, 3). The pore size distribution of composite scaffolds was investigated with a mercury intrusion porosimeter. The curves of pore size distribution of PCL and MMT-PCL scaffolds were presented in Figure 4. As shown in the figure, the pore size of composite scaffold was found to vary between 50 and 250 µm. Based on previous study, scaffolds with interconnected pores and pore sizes ranges from 200 µm up to 350 µm have been generally used to support osteoblastic response of mesenchymal stem cells and this range is the convenient range for good interconnection and exchange of nutrients and waste (12).
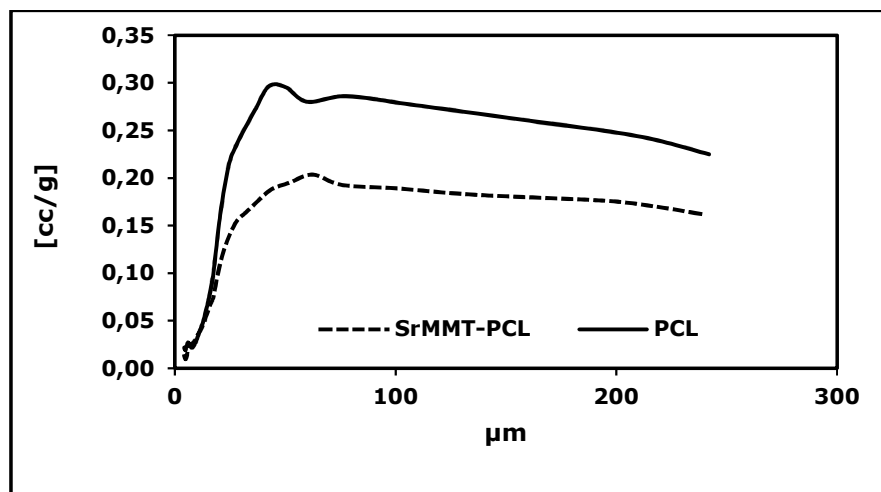
Figure 4. The size distribution of the pores of PCL and SrMMT-PCL scaffold.

The macroporous structure of the MMT-PCL scaffold obtained by using the particulate leaching method was given in Figure 5. Morphological observation by SEM indicated that the composite scaffold had a highly porous morphology with interconnected structure and MMT particles were dispersed homogeneously throughout PCL matrix. MMT particles in PCL matrix will improve cell attachment properties of scaffold via enhancing the surface area. The well-dispersed MMT also helps to improvement of mechanical and thermal properties of the composite (13-15). There was no observable difference in the structures of the non-modified and Sr-modified MMT-PCL composite scaffolds. Associated with pore size distribution data, it is possible to say that, the pore size of scaffold is adequate for viability and function of cells.
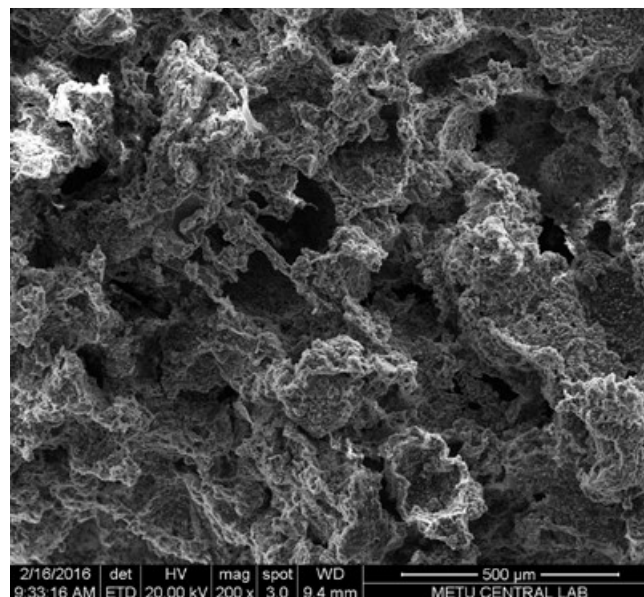
Figure 5. Representative SEM micrograph of MMT-PCL composite scaffold.

Figure 6 presents the stress-strain curves of PCL and SrMMT-PCL scaffolds. Comparison of PCL with SrMMT-PCL shows that the addition of MMT into PCL matrix appeared to lead to significant increase in the mechanical properties of PCL, suggesting that MMT has a positive effect on

improving mechanical properties of polymers due to its small particle size and its intercalation properties.
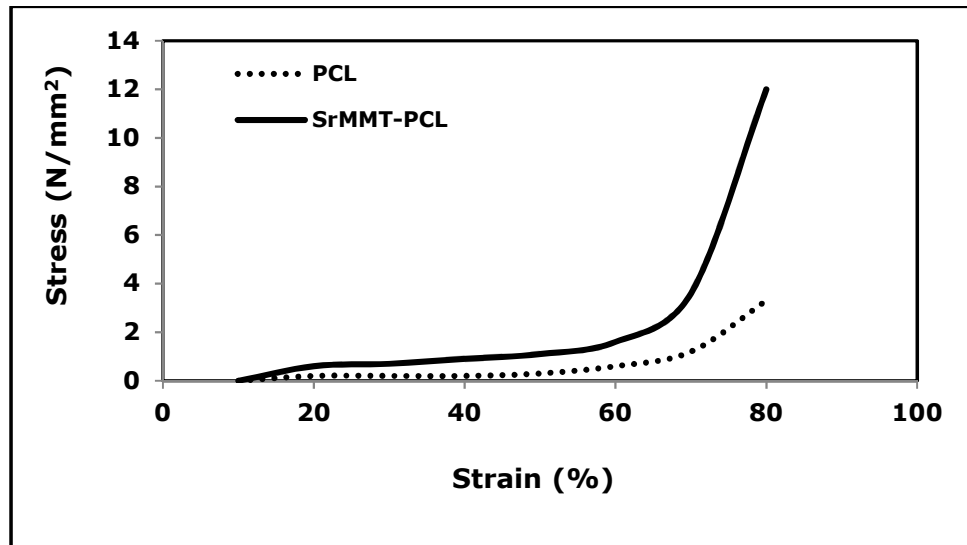
Figure 6. The stress–strain curves of PCL and SrMMT-PCL scaffolds.

Many trace metallic ions present in human body such as strontium, calcium, zinc, magnesium, and boron are known for their effects in bone metabolism (8). Increasing evidence in the literature indicates that the secretion of these therapeutic ions from engineered biomaterials facilitate bone healing process by supplying more appropriate environment to cell proliferation, differentiation and gene expression (16-17). Sr has an opposite effect on bone homeostasis. It increases the pre-osteoblast proliferation and activity, while decreasing the resorbing activity of osteoclasts. In our study, the release of Sr^{2+} from the non-modified and modified composite scaffolds was determined by using ICP-OES. The results showed that the release of Sr^{2+} was increased by the time (Figure 7). There was no Sr^{2+} release from non-modified scaffolds despite their small amount of Sr^{2+} content. Although the concentration of released Sr ions is lower than expected, it will favorably affect the replication of preosteoblast via enhancing the bioactivity of the scaffolds.
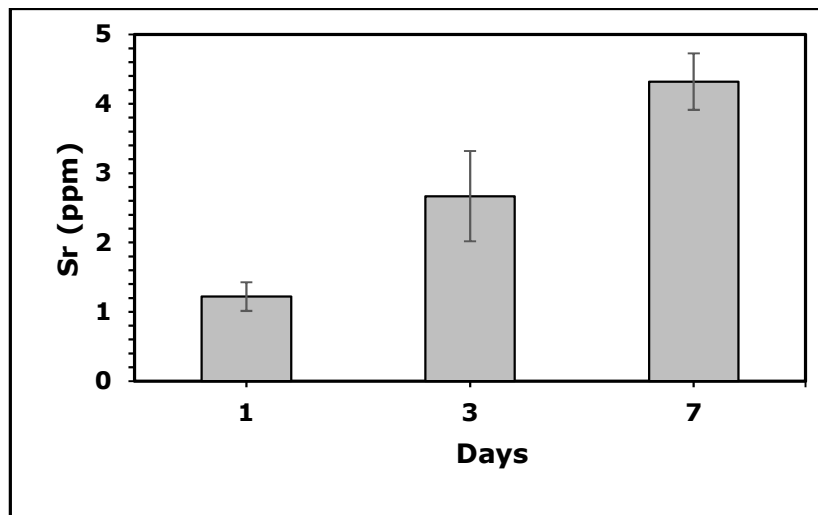
Figure 7. In vitro release of Sr from modified composite scaffolds into cell culture media.

CONCLUSIONS

The scaffold combined with PCL and Sr-modified MMT was successfully developed and characterized in this study. Interest in the use of clay minerals to develop tissue-engineered scaffold to enhance osteogenesis has been growing recently. Among clay minerals, MMT may be considered as an 'ion reserve' due to its properties. Based on this approach, MMT was modified with Sr, which has a role in bone development, afterwards modified MMT was used in fabrication of biocomposite scaffold. The findings of this study suggest that SrMMT-PCL could be a promising biomaterial for bone tissue engineering applications. The release efficiency of MMT might be improved via increasing the concentration of Sr which intercalates into MMT layers. Ongoing studies in our laboratory will perhaps shed light to the biocompatibility of the composite via conducting cell culture experiments.

ACKNOWLEDGMENTS

REFERENCES

1.   Koç A, Emin N, Elçin AE, Elçin YM. In Vitro Osteogenic Differentiation of Rat Mesenchymal Stem Cells on Mineralized PLGA Foams in Microgravity Bioreactor. Journal of Bioactive and Compatible Polymers. J Bioact Compat Pol. 2208; 23: 244-261. DOI: 10.1177/0883911508091828.

2.   Langer R and Vacanti J. Tissue Engineering, Science, 1993; 260: 920–928. DOI: 10.1126/science.8493529.

3.   Elçin YM. Stem Cells and Tissue Engineering. Biomaterials. Volume 553 of the series Advances in Experimental Medicine and Biology. 2004: 301-316. ISBN: 978-1-4757-0988-9.

4.   Iroh O. Poly(epsilon-caprolactone), edited by J. E. Mark. Oxford Press, Oxford, 1999, pp. 361–362. ISBN: 0195107896.

5.   Choudalakis G, Gotsis AD. Permeability of polymer/clay nanocomposites: A review. E Polym J. 2009; 45 :967–984. DOI:10.1016/j.eurpolymj.2009.01.027.

6.   Aguzzi C, Cerezo P, Viseras C, Caramella C. Use of clays as drug delivery systems: possibilities and limitations. Appl. Clay Sci. 2007; 36: 22–36. DOI: 10.1016/j.clay.2006.06.015.

7.   Ruiz-Hitzky E, Aranda P, Dardera M and Rytwob G. Hybrid materials based on clays for environmental and biomedical applications. J Mater Chem. 2010; 20: 9306–9321. DOI: 10.1039/c0jm00432d.

8.   Bose S, Fielding G, Tarafder S, and Bandyopadhyay A. Understanding of dopant-induced osteogenesis and angiogenesis in calcium phosphate ceramics. Trends in Biotechnol. 2013; 31: 594–605. DOI: 10.1016/j.tibtech.2013.06.005.

9.   Dahl SG, Allan P, Marie PJ, Mauras Y, Boivin G, Ammann P, et al. Incorporation and distribution of strontium in bone. Bone. 2001; 28(4): 446–453. DOI: 10.1016/S8756-3282(01)00419-7.

10.   Qiua K, Zhao XJ, Wana CX, Zhaoa CS, Chen YW. Effect of strontium ions on the growth of ROS17/2.8 cells on porous calcium polyphosphate scaffolds. Biomaterials. 2006; 27: 1277–1286. DOI: 10.1016/j.biomaterials.2005.08.006.

11.   Loh QL and Choong C. Three-dimensional scaffolds for tissue engineering applications: Role of porosity and pore size. Tissue Eng Part B Rev. 2013; 19(6): 485–502. DOI: 10.1089/ten.teb.2012.0437.

12.   Koç A, Elçin EE, Elçin YM. Ectopic osteogenic tissue formation by MC3T3-E1 cell-laden chitosan/hydroxyapatite composite scaffold. Artif Cells Nanomed Biotechnol, 2015. DOI: 10.3109/21691401.2015.1036998.

13.   Sikdar D, Katti D, Katti K and Mohanty B. Effect of organic modifiers on dynamic and static nanomechanical properties and crystallinity of intercalated clay–polycaprolactam nanocomposites J. Appl. Polym. Sci. 2007;105: 790–802. DOI: 10.1002/app.26284.

14.   Yu S, Zhao J, Chen G, Juay YK and Yong MS. The characteristics of polyamide layered-silicate nanocomposites. J Mater Process Tech. 2007; 192–193: 410–414. DOI:10.1016/j.jmatprotec.2007.04.006.

15.   Kojima Y, Usuki A, Kawasumi M, Okada A, Kurauchi T, and Kamigaito O. Synthesis of nylon 6–clay hybrid by montmorillonite intercalated with e-caprolactam. J Polym Sci A. 1993; 31: 983–986. DOI: 10.1002/pola.1993.080310418.

16.   Beattie JH, Avenell A. Trace element nutrition and bone metabolism. Nutr Res Rev 1992; 5(01):167-188. DOI: 10.1079/NRR19920013.

17.   Nielsen F. New essential trace elements for the life sciences. Biol Trace Elem Res. 1990; 26-27(1):599-611. DOI:10.1007/BF02992716.

Türkçe Öz ve Anahtar Kelimeler

Kemik Dokusu Mühendisliği Çalışmaları için Stronsiyum İçeren Montmorillonit/Polikaprolakton Kompozit İskelesinin Hazırlanması ve Karakterizasyonu

Aysel Koç Demir

Öz: Bu çalışmada, stronsiyum ile modifiye edilen MMT ve polikaprolakton içeren kompozit iskeleler partikül uzaklaştırma yöntemi kullanılarak hazırlandı (SrMMT-PCL). Kompozit iskelelerin makroyapı ve morfolojileri X-ışını kırınımı (XRD), termogravimetrik analiz (TGA) ve taramalı elektron mikroskobu (SEM) ile karakterize edildi. İskele yapılarından hücre kültürü ortamına salınan Sr^{2+} miktarı indüktif eşleşmiş plazma optik emisyon spektrometresi (ICP-OES) ile belirlendi. İskele yapılarının gözenek boyut dağılımı civa porozimetresi ile incelendi. İskele yapılarının mekanik özellikleri de değerlendirildi. XRD sonuçları PCL'nin MMT tabakaları arasına girdiğini gösterdi. TGA çalışmaları, PCL içindeki MMT'nin, matrisin ısıl bozunma sıcaklığını yükselttiğini gösterdi. ICP sonuçları, Sr^{2+} iyonunun kompozit iskele yapılarından salındığını gösterdi. Gözenek hacminin büyük kısmının 250-350 µm civarındaki gözeneklerden oluştuğu tespit edildi. SEM görüntüleri partikül uzaklaştırma yöntemi ile elde edilen kompozit iskelelerin makrogözenekli yapıda olduğunu gösterdi. Sonuç olarak, elde edilen veriler, hazırlanan doku mühendisliği iskelesinin kemik doku mühendisliği uygulamaları için uygun bir malzeme olma potansiyeline sahip olduğunu gösterdi.

682

RESEARCH ARTICLE

(This article was presented to the 28th National Chemistry Congress and submitted to JOTCSA as a full manuscript)

Synthesis, Characterization, and Investigation of the Spectroscopic Properties of Novel Peripherally 2,3,5-trimethylphenoxy Substituted Cu and Co Phthalocyanines, Computational and Experimental Studies of 4-(2,3,5-trimethylphenoxy)phthalonitrile

Nesuhi Akdemir[1]

[1]Department of Chemistry, Amasya University, İpekköy, 05200, Amasya, Turkey

Abstract: 4-(2,3,5-trimethylphenoxy)phthalonitrile (**3**) was prepared via aromatic nucleophilic substitution reaction and characterized by FT-IR, mass spectrometry, ^{1}H and ^{13}C NMR techniques. The molecular structure of compound (**3**) was optimized using Density Functional Theory (DFT/B3LYP) method with 6-311G(d,p) basis set in the ground state. The molecular geometric parameters which were obtained by X-ray single crystal diffraction method and the spectral results were compared with computed bond lengths and angles, vibrational frequencies, and ^{1}H, ^{13}C NMR chemical shifts values of compound (**3**). Also, Cu(II) and Co(II) phthalocyanines were synthesized by the treatment of dinitrile derivative with anhydrous $CuCl_2$ or $CoCl_2$ under N_2 atmosphere in dry n-pentanol at 140 °C. The new compounds have been determined by elemental analysis, FT-IR, and electronic absorption. The UV-Vis spectra of the Cu(II) and Co(II) phthalocyanines were recorded with different concentration in THF and also with different solvents as DMF, DMSO, DCM, $CHCl_3$, toluene.

Keywords: Phthalocyanines, phthalonitrile, 2,3,5-trimethylphenol, DFT.

Submitted: July 04, 2016**. Accepted:** November 02, 2016.

* Corresponding author. E-mail: nasuhi55@hotmail.com.

INTRODUCTION

Phthalocyanines (Pcs), discovered accidentally in 1907 and characterized in 1930s, are synthetic heterocyclic aromatic compounds [1]. Pcs have high thermal and chemical stability along with their unique properties such as strong visible light absorption, high molar absorption coefficients, electron transfer abilities, and the flexibility involved in the synthesis of these compounds [2]. These features promote an extensive use of these molecules primarily as dyes and pigments. A minimum amount of 80.000 tons of Pcs are produced per year just for this purpose [3]. They have been also used in other applications such as liquid crystals [4, 5], optical applications [6, 7], HIV inactivation [8, 9], electrochromism [10, 11], molecular solar cells [12, 13], chemical sensors [13, 14], semiconductors for organic field-effect transistors [16, 17], and photodynamic therapy [18, 19, 20].

These applications of the phthalocyanines can not be achieved since many unsubstituted Pcs are not soluble neither in organic solvents nor in water. The solubility can be increased by adding substituents to the periphery, nonperiphery or axial position of phthalocyanines, and designing central metal ions differently. It is well known that tetrasubstituted phthalocyanines usually present a higher solubility than octasubstituted Pc derivatives [21, 22, 23].

Our earlier studies concentrated on synthesis and characterization of metal-free and metallophthalocyanines containing tetrathiaoxa [24], dithiaoxa [25], diazadithiaoxa macrocyclic moieties [26], N-(n-octyl)mercaptoacetamide groups [22], naphthalene-amide groups [27] and 3,5-dimethoxyphenol groups [28]. The present work introduces the preparation and characterization of Cu(II) and Co(II) phthalocyanines containing 2,3,5-trimethylphenol moieties. Then UV-Vis spectra of these compounds were recorded in different solvents and different concentrations. Furthermore, molecular geometry parameters, vibrational frequencies and ^{1}H, ^{13}C NMR chemical shift values of the 4-(2,3,5-trimethylphenoxy)phthalonitrile, which was reported the crystal structure of which was reported by our group in previous paper [29], were calculated and compared with the experimental specifications.

MATERIALS AND METHODS

IR spectra was recorded on a Perkin Elmer Frontier FT-IR Spectrometer as KBr pellets. UV-Vis spectra were recorded on a Perkin Elmer Lambda 35 UV/Vis Spectrophotometer. ^{1}H-NMR and ^{13}C-NMR spectra were recorded on an Agilent 600 MHz spectrometer (Çankırı Karatekin University NMR Laboratory). Mass spectra were measured on an Ab Sciex 3200 QTrap LC-MS/MS (Amasya University-AUMAULAB). Elemental analyses were performed on a Leco

Truspect Micro Analyzer. 4-Nitrophthalonitrile was synthesized by following the procedure reported in [30]. All other reagents and solvents were of reagent-grade quality and were obtained from commercial suppliers. DMF was dried and purified as described by Armarego and Perrin [31]. The homogeneity of the products was tested by TLC (SiO$_2$).

Computational Details

The crystal structure of the compound was (**3**) reported by Akbal *et al*. [29], so the molecular geometry was taken on the coordinates obtained from the X-ray single crystal diffraction data. The geometry optimization was carried out with DFT / B3LYP (Becke's Three Parameter Hybrid Functional using the Lee, Yang, and Parr Correlation Functional) [32-34] method and 6-311G(d,p) the basis set in the ground state. All the computational process was realized over the optimized structure and the same method. The harmonic vibrational frequencies were computed and multiplied by the scale factor 0.9682 [35] to eliminate systematic errors between the experimental values and theoretical values the frequencies. ^{1}H and ^{13}C-NMR chemical shift values were calculated according to GIAO (Gauge-Independent Atomic Orbital) method [36] and with respect to TMS (tetramethylsilane) an internal standard chemical shifts as solvent CDCl$_3$. The predicted ^{1}H-NMR and ^{13}C-NMR chemical shifts were obtained from the equation δ=(ΣTMS-Σ), where δ is the chemical shift, Σ is the absolute shielding and ΣTMS is the absolute shielding of the standard (TMS), its values are 32.002 and 184.923 ppm, respectively. All the computational analysis on the structure have been performed with Gaussian 09W [37] electronic structure and GaussView 5.0 [38] graphical interface software on a Intel Core i5/3.2 GHz personal computer.

Synthesis

Synthesis of 4-(2,3,5-trimethylphenoxy)phthalonitrile (3): The compound (**3**) was synthesized according to the reported procedure [29]. FT-IR :v_{max}, cm^{-1} 3091 (Ar-CH), 2965, 2947, 2917, 2860 (CH$_3$), 2231 (CN), 1597 (C=C), 1566 (C=C), 1495, 1454, 1408, 1380, 1371, 1312, 1278 (C-O), 1244, 1199, 1162, 1133, 1088, 1069, 1022, 971, 946, 870, 856, 842, 746, 717, 726, 661. ^{1}H NMR (600 MHz, CDCl$_3$, δ, ppm) 2.00 (s, 3H, methyl), 2.30 (s, 6H, methyl), 6.64 (s, 1H, Ar-H), 6.95 (s, 1H, Ar-H), 7,15 (s, 1H, Ar-H), 7.17 (d, *J* = 1.6, 1H, Ar-H), 7.69 (d, *J* = 8.2, 1H, Ar-H). ^{13}C NMR (151 MHz, CDCl$_3$):δ, ppm 11.82 (CH$_3$), 19.96 (CH$_3$), 20.83 (CH$_3$), 108.14, 115.08, 115.49 (CN), 117.60 (CN), 118.92, 120.52, 120.64, 125.55, 128.91, 135.35, 137.24, 139.54, 151.18, 162.05. MS m/z [M+H$^+$] 262.8

General procedure for the synthesis of copper and cobalt phthalocyanines: The mixture of 4-(2,3,5-trimethylphenoxy)phthalonitrile (0.75 g, 2.88 mmol), the related anhydrous metal salt [CuCl$_2$ (0.15 g, 1,12 mmol) for compound **4**, CoCl$_2$ (0.14 g, 1.06 mmol) for compound **5**] and 0.5 mL DBU was heated at 140 °C with dry n-pentanol (10 mL) and stirred for 28 h in a nitrogen atmosphere. Then, the mixture was cooled to room temperature,

precipitated by adding methanol and filtered off. The green products were washed with hot methanol, hot ethanol, diethyl ether, and water. They were washed with methanol for 24 h in the soxhlet apparatus and dried *in vacuo*.

2(3), 9(10), 16(17), 23(24)-Tetrakis-(2,3,5-trimethylphenoxy) copper(II) phthalocyanine (4)

The product is soluble in DMF, DMSO, DCM, toluene, CHCl$_3$, and THF. Yield: 0.689 g (86%); mp> 250°C; anal. calcd. for C$_{68}$H$_{56}$N$_8$O$_4$Cu: C, 73.40; H, 5.07; N, 10.07%. Found: C, 73.45; H, 5.08; N, 10.11%. FT-IR :v_{max}, cm^{-1} 3064 (Ar-CH), 2916, 2859, 1611, 1575, 1506, 1470, 1403, 1342, 1294, 1268, 1224, 1174, 1133, 1120, 1094, 1076, 1049, 948, 970, 853, 823, 747, 666.

2(3), 9(10), 16(17), 23(24)-Tetrakis-(2,3,5-trimethylphenoxy) cobalt(II) phthalocyanine (5)

The product is soluble in DMF, DMSO, DCM, toluene, CHCl$_3$, and THF. Yield: 0.459 g (58%); mp > 250°C; anal. calcd. for C$_{68}$H$_{56}$N$_8$O$_4$Co: C, 73.70; H, 5.09; N, 10.11%. Found: C, 73.75; H, 5.10; N, 10.06%. FT-IR :v_{max}, cm^{-1} 3064 (Ar-CH), 2918, 2863, 1612, 1575, 1524, 1473, 1408, 1332, 1294, 1269, 1226, 1177, 1123, 1094, 1078, 970, 955, 855, 824, 752, 665.

RESULTS AND DISCUSSION

Synthesis and characterization

Scheme 1 shows the synthetic route to tetrakis(2,3,5-trimethylphenoxy) Cu and Co phthalocyanines. 4-(2,3,5-trimethylphenoxy)phthalonitrile (**3**) was firstly prepared by treating 4-nitrophthalonitrile (**2**) with 2,3,5-trimethylphenol in DMF using K$_2$CO$_3$ as the base for nucleophilic displacement reaction and gave high yield (74 %) [29]. Copper(II) and cobalt(II) phthalocyanines (**4** and **5**) were synthesized by the treatment of compound **3** with anhydrous CoCl$_2$ and CuCl$_2$ in n-pentanol in the presence of 0,5 mL 1,8-diazabicyclo[5.4.0]undec-7-ene (DBU) as a strong base at 140 °C for 28 h in a nitrogen atmosphere. The yields of compounds **4** and **5** were 86% and 58%, respectively.
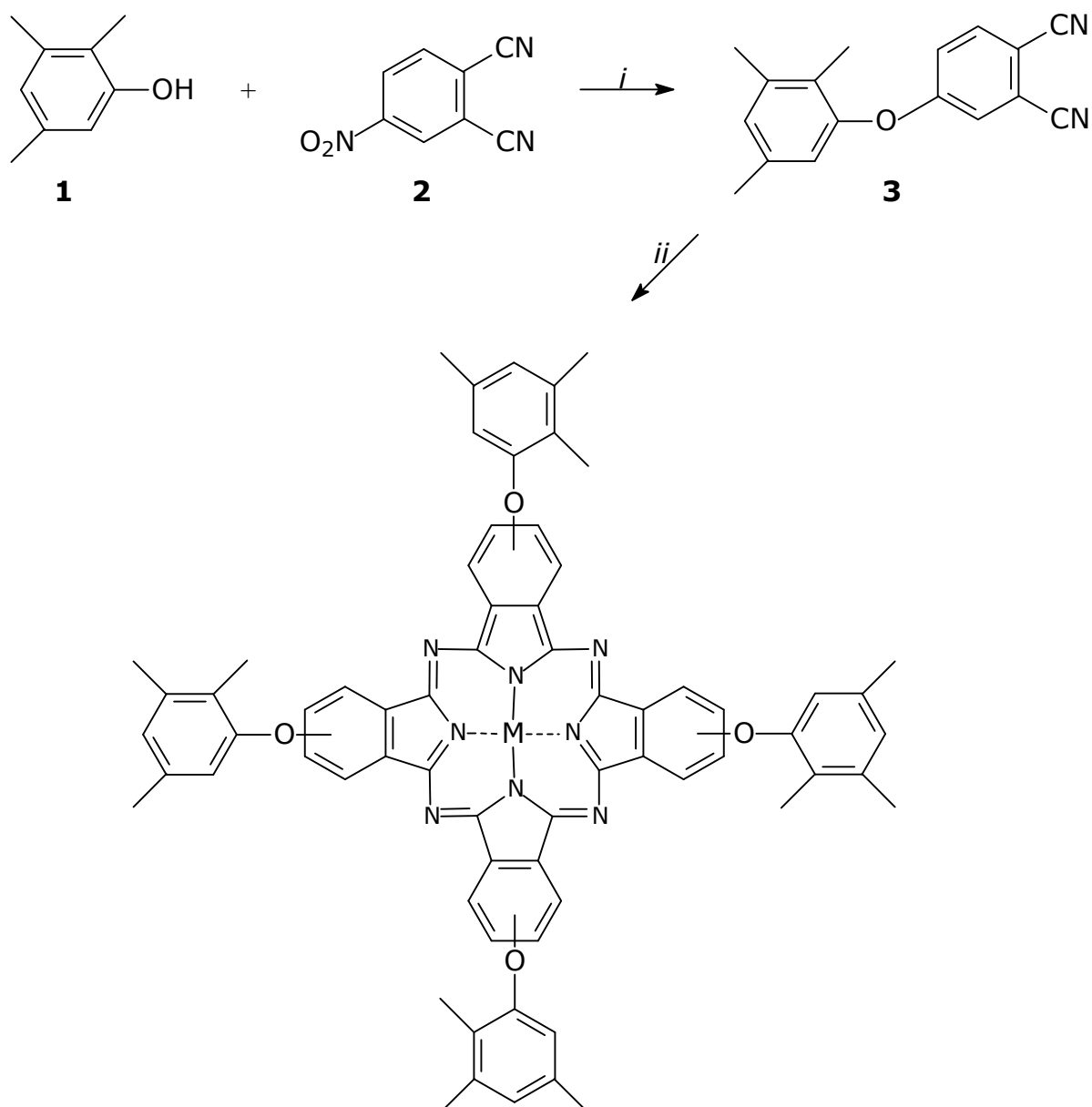
Scheme 1. Synthetic route for compounds (**4** and **5**) i: DMF, K_2CO_3, N_2, 40°C, 48h ii: n-pentanol, DBU, $CuCl_2$ or $CoCl_2$, N_2, 24h, 140°C.

The phthalocyanines showed high solubility in organic solvents such as DMF, DMSO, DCM, toluene, $CHCl_3$, and THF, but they are insoluble in methanol, ethanol, and diethyl ether. The products having been washed consequently with different solvents were obtained in sufficient purity. All new compounds were characterized by UV-Vis, FT-IR, ^{1}H NMR, ^{13}C NMR, MS spectra, and elemental analysis. All the results were in very good agreement with targeted structures.

In the FT-IR spectrum of starting compound (**3**), aromatic CH, aliphatic CH, nitrile C≡N, aromatic C=C, ether Ar-O-Ar stretching vibrations appeared at 3091, 2964, 2231, 1597, and 1278 cm^{-1}, respectively. While the strong -C≡N band appeared at 2231 cm^{-1}, this band

completely disappeared after conversion to compounds (**4** and **5**). The FT-IR spectra phthalocyanines are very similar with the exception of small stretching shifts. ^{1}H NMR and ^{13}C NMR spectra of phthalocyanines (**4** and **5**) could not be measured due to the paramagnetic cobalt(II) and copper(II) centers.

Ground state electronic absorption spectra

The phthalocyanines can be characterized by recording UV-Vis spectra. These compounds have two strong absorption regions, one of them in the UV region at *ca*. 275-400 nm (B band) and the other in the visible region at 600-700 nm (Q band) [2]. The UV-Vis spectra of the phthalocyanines (**4**, **5**) were recorded in different solvents (Figures 1 and 2). The data were presented in Table 1.
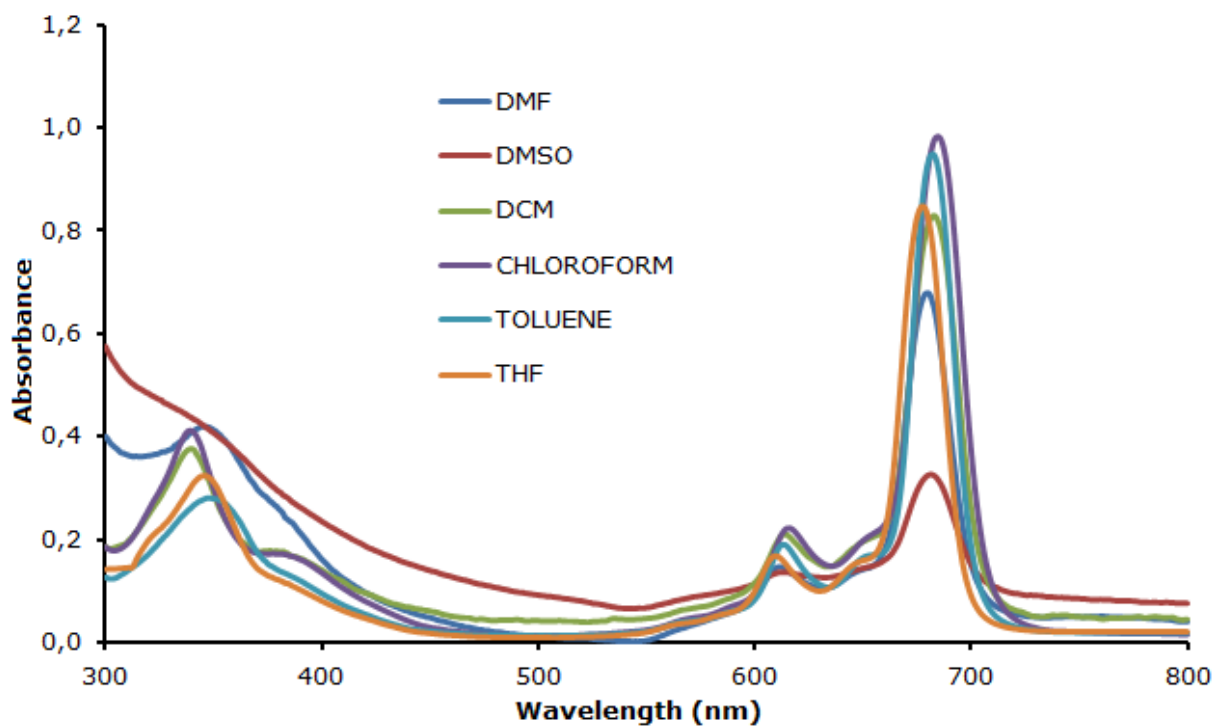
Figure 1. Absorption spectra of the compound (**4**) (CuPc) in different solvents.
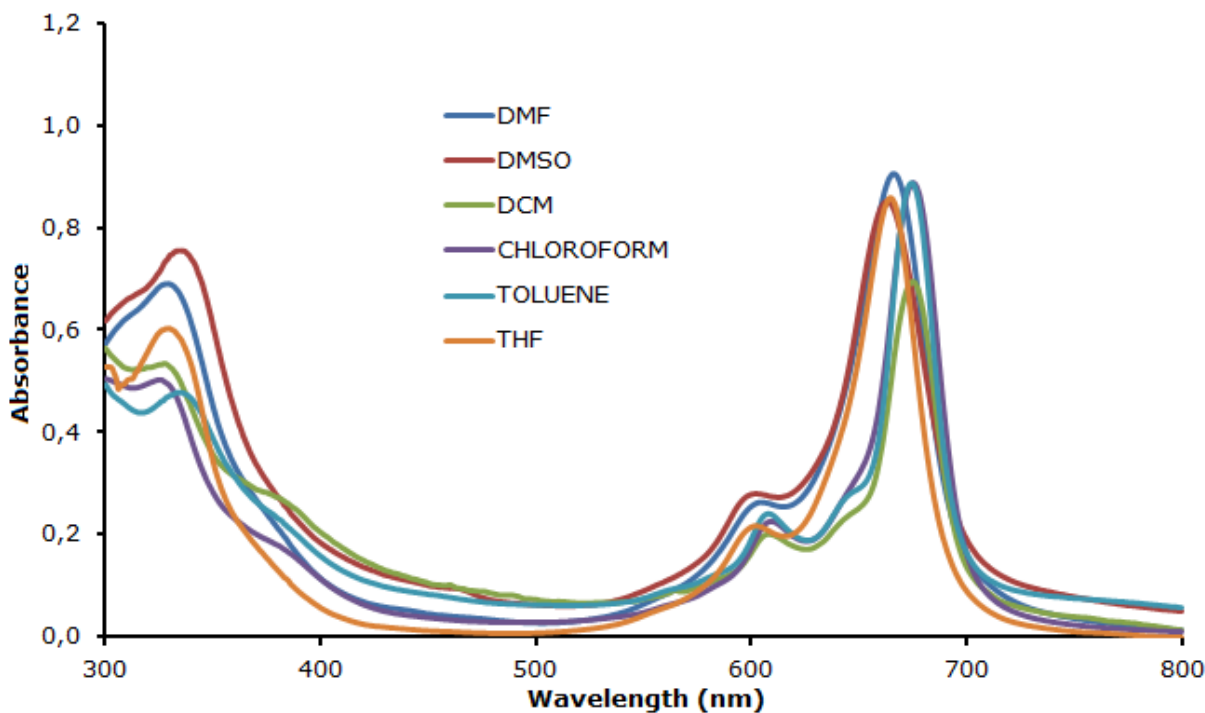
Figure 2. Absorption spectra of the compound (**5**) (CoPc) in different solvents.

The phthalocyanines (**4**, **5**) showed monomeric behavior in different solvents, evidenced by a single (narrow) Q-band at 678-685 nm for **4,** 663-675 nm for **5**, confirming non-aggregation. However compound (**4**) showed aggregation in DMSO (Figure 1). B-Band absorptions in different solvents were observed at 339-348 nm for **4** and 326-335 nm for **5**.

Figures 2 and 4 show electronic absorption spectra of Pcs (**4** and **5**) in the concentration range 2×10^{-6} - 1.20×10^{-5} M in THF. As shown in the Figures 3 and 4, the Q band increases in intensity with increasing concentration of phthalocyanines (**4** and **5**) and no new band was observed due to the aggregated species [39, 40]. Beer's law was obeyed for (**4**) and (**5**) in the concentration range 2×10^{-6} - 1.20×10^{-5} M.

Table 1. UV-Vis spectral data for phthalocyanines (**4** and **5**) in various solvents at a concentration of 1x10^{-5} M

Compound	Solvent	Q-Band		B-Band	
		λ_{max} (nm)	ε (dm^3 mol^{-1} cm^{-1})	λ_{max} (nm)	ε (dm^3 mol^{-1} cm^{-1})
4	DMF	680, 612	67880; 14690	346	41930
4	DMSO	681, 613	32630; 13620	340	43640
4	DCM	683, 614	82930; 20920	339	37480
4	CHCl$_3$	685, 616	98130; 22150	339	41080
4	Toluene	682, 613	94860; 18930	348	27980
4	THF	678, 610	84600; 16810	346	32370
5	DMF	666, 605	90500; 26370	329	69040
5	DMSO	663, 603	85070; 28070	335	75500
5	DCM	675, 608	69280; 20100	328	53310
5	CHCl$_3$	675, 609	88700; 22660	326	50320
5	Toluene	675, 608	88680; 24020	334	47740
5	THF	665, 603	85890; 21770	330	60360
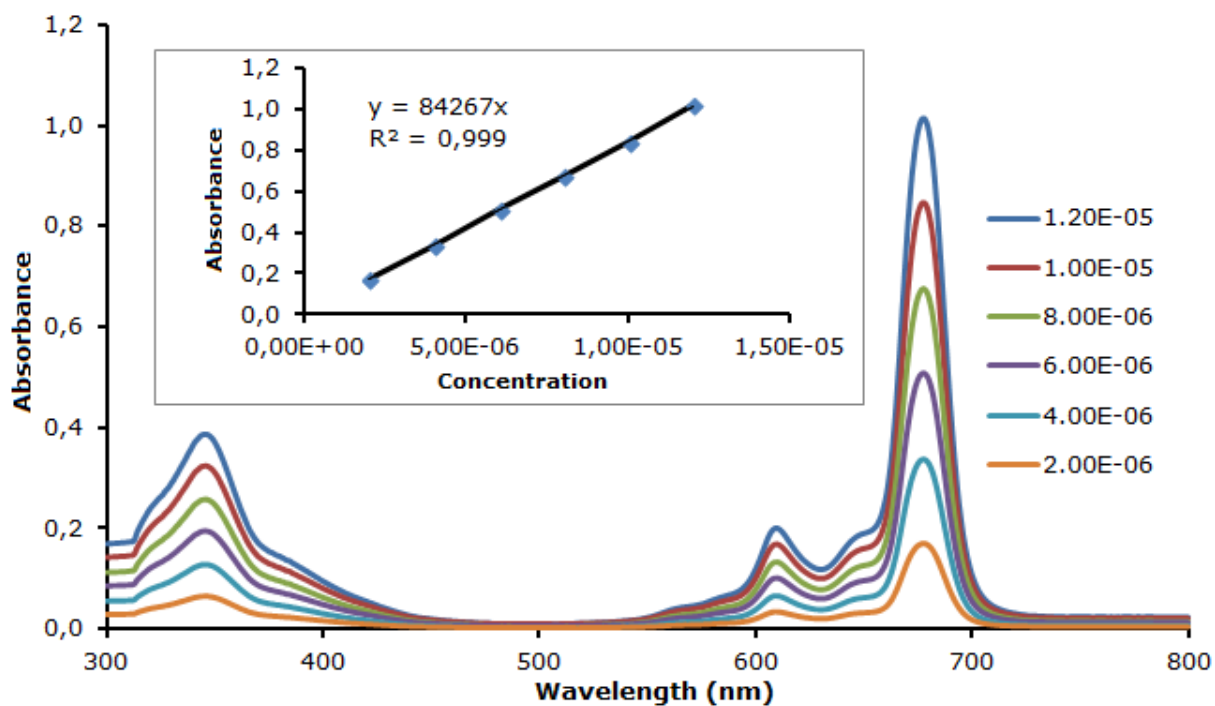
Figure 3. Absorption spectra of the compound (**4**) (CuPc) in THF at different concentrations.
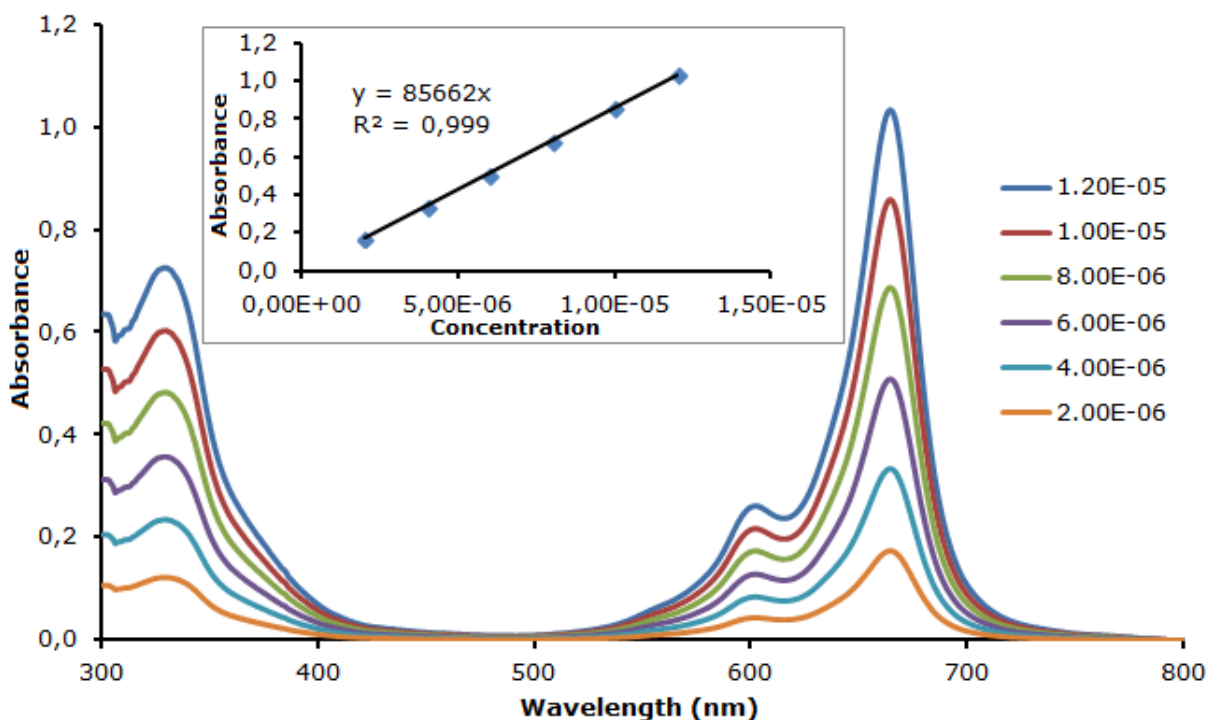
Figure 4. Absorption spectra of the compound (**5**) (CoPc) in THF at different concentrations.

Optimized Structure

The experimental geometric structure with the atom-mumbering scheme [29] and the optimized structure of the compound (**3**) are shown in Figure 5. The crystal structure of the compound (**3**) has an orthorhombic crystal system and Pbcaspace group with a=7.8929 (8) Å, b=29.415 (4) Å, c=12.4679 (14) Å, V=2894.7 (6) Å^3 and Z=8 unit cell parameters [31]. Some selected optimized structure parameters such as bond lengths and angles, torsion angles were compared with experimental values and the results were tabulated in Table 2.
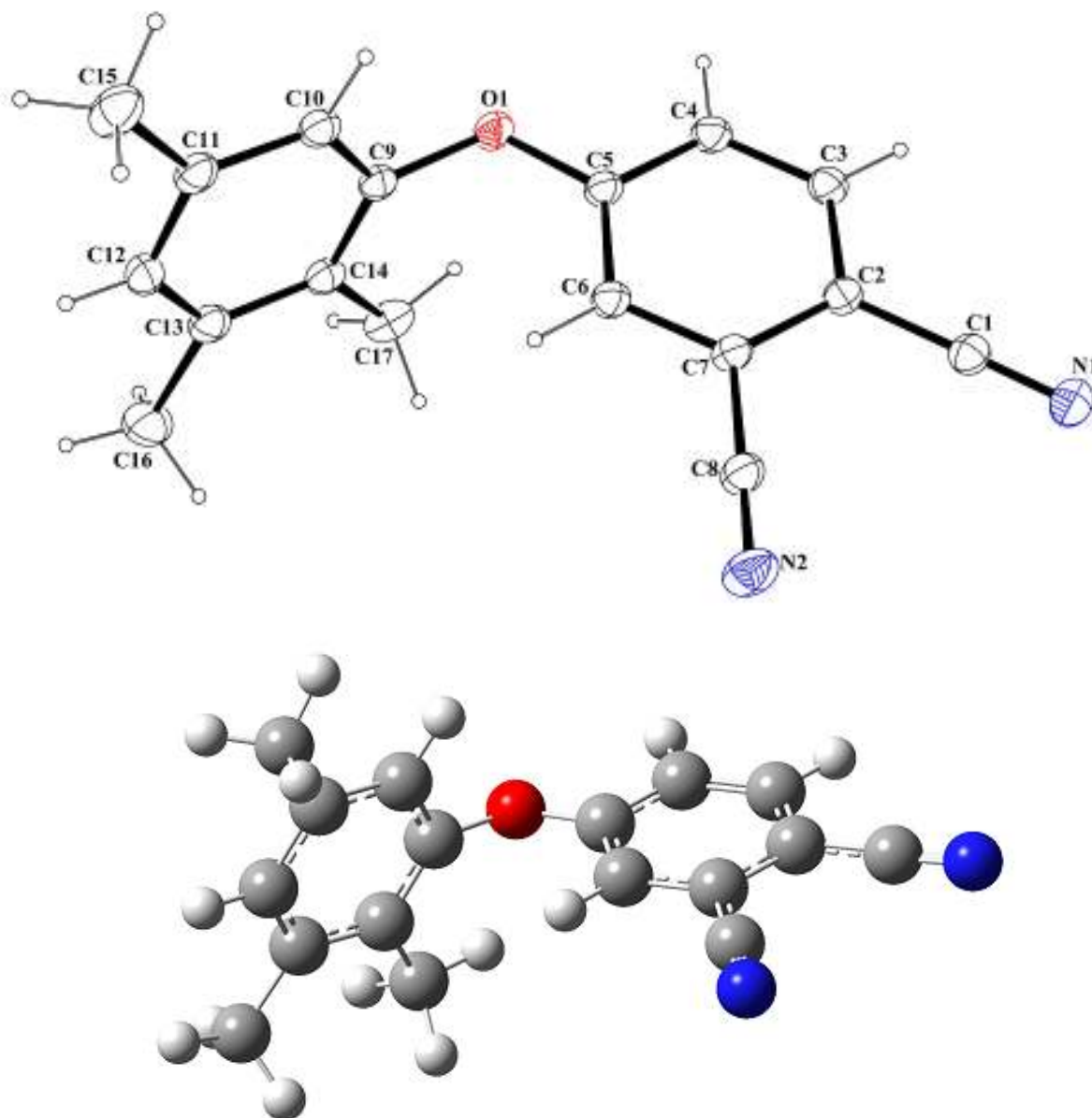
Figure 5. Top: An ORTEP-III view of the structure of the compound (**3**), showing 30% probability displacement ellipsoids and the atom-mumbering scheme [31]. **Bottom:** The optimized geometric structure of the compound (**3**) with DFT/B3LYP method and 6-311G(d,p) basis set.

Table 2. Some experimental and optimized geometrical parameters of the compound (**3**).

Parameters	Experimental Values Ref.[31]	Theoretical Values DFT/B3LYP/6-311G(d,p)
Bond lengths (Å)		
C1—N1	1.142(2)	1.155
C1—C2	1.433(3)	1.426
C7— C8	1.439(2)	1.430
C8—N2	1.134(2)	1.154
C2—C3	1.393(2)	1.402
C3—C4	1.371(2)	1.382
C5—O1	1.362(19)	1.359
C9—O1	1.410(19)	1.403
C11—C15	1.508(2)	1.509
C13—C16	1.520(3)	1.509
C14—C17	1.503(3)	1.507
Bond angles (°)		
N1—C1—C2	179.27(2)	178.42
N2—C8—C7	179.12(2)	178.50
C5—O1—C9	118.22(12)	120.05
C4—C5—O1	116.14(14)	115.99
C10—C9—O1	116.97(18)	117.99
C9—C14—C17	121.25(18)	121.60
C10—C11—C15	121.71(2)	121.27
Torsion angles (°)		
N1—C1—C2—C3	-122.21(17)	0.384
N2—C8—C7—C6	-66.13(14)	-0.030
C4—C5—O1—C9	-179.82(16)	-172.13
C10—C9—O1—C5	96.18(18)	77.32

As seen in Table 2, C1-N1, C8-N2 bond lengths are 1.142, 1.134 Å accordingly X-ray analysis data, 1.155, 1.154 Å for DFT/B3LYP/6-311G(d,p) method. These lengths were stated as 1.142 Å experimentally, 1.162 Å for 6-31G(d) [41], 1.138 experimentally, 1.146 Å for 6-31G(d,p) basis sets [42] in other DFT studies containing phthalonitrile group, and results are in agreement with typical carbon-nitrogen triple bond (about 1.16 Å). The lengths of carbon-oxygen bond which serves as a bridge between phthalonitrile and trimethylbenzene groups are 1.359 and 1.403 Å, theoretically, 1.36, 1.44 Å for 6-31G(d) basis set in another study [43]. Also N1-C1-C2, N2-C8-C7 bond angles of phthalonitrile are 178.42, 178.50° while these values are recorded 178.24, 178.51°for 6-311+G(d,p) basis set in a similar paper [44].

When the experimental values compared with theoretical values, minor discrepancy are observed between them, because compound is accepted in the gas phase during theoretical calculation process, whereas it is solid phase in the experimental analysis. Even so, correlation coefficient is 0.9984 for bond lengths, 0.9996 for bond angles and according to these values it can be said that it showed a good correlation. Also, an atom-by-atom superimposition of the structure the compound (**3**) as established by DFT/B3LYP/6-311G(d,p) and X-ray data is shown in Figure 6 and RMSE value is 0.277 Å.
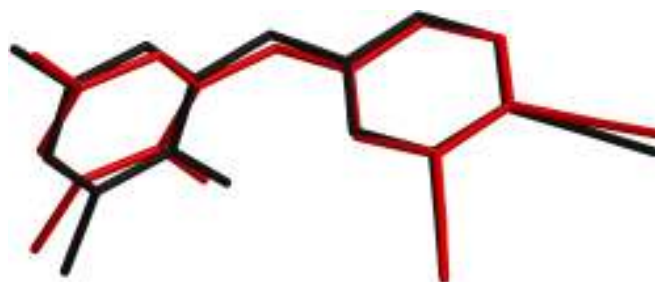
Figure 6. Atom-by-atom superimposition of the calculated structure (DFT/B3LYP76-311G(d,p) (red) on the X-ray structure (black) of the compound (**3**).

Vibrational Spectral Analysis

The scaled harmonic vibrational frequencies of the compound (**3**) were calculated with DFT/B3LYP/6-311G(d,p) basis set. The compound (**3**), which has 34 atoms and 96 fundamental vibrational frequencies, consisting of phthalonitrile and trimethylbenzene groups. The theoretical vibrational assignments in these groups were designated with Gauss View interface program [38] and compared with spectral values and the results were tabulated in Table 3. Also, the FT-IR spectrum which was plotted on the transmittance (%) against the wavenumber (cm^{-1}) is shown in Figure 7.
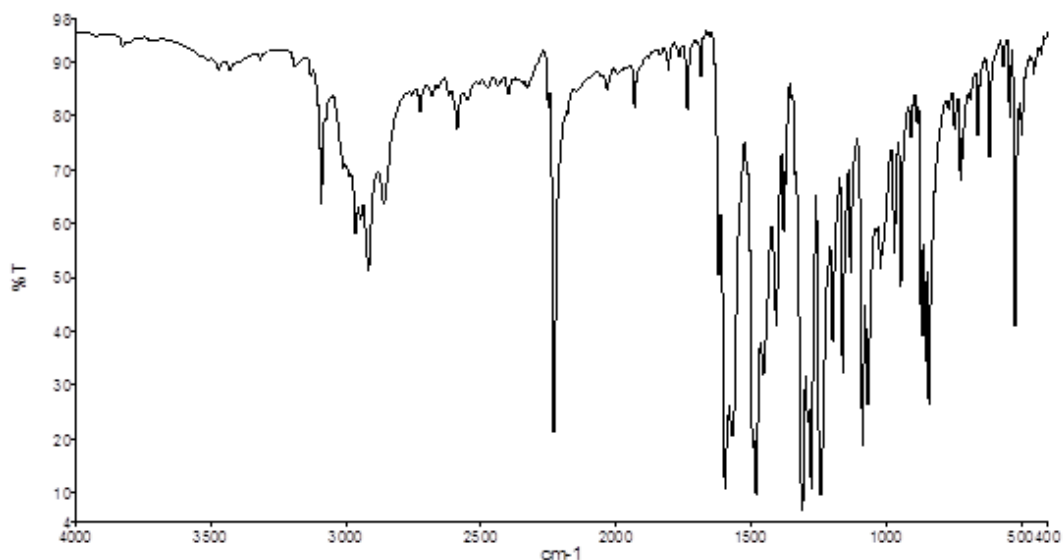
Figure 7. The FT-IR spectrum of compound (**3**).

The vibrational spectra of the compound (**3**) has some characteristic bands of the stretching vibrations such as C-H, C≡N, C=C, and C-O. The C-H are recorded at 3091.44-2860.18 cm^{-1} in the FT-IR spectrum, 3117.05-2927.15 cm^{-1} in the theoretical IR spectrum of the compound (**3**) as a result of characteristic feature C-H stretching bands are assigned at 3100-3000 cm^{-1} region in aromatic groups, at 3000-2700 cm^{-1} in aliphatic groups [45]. The asymmetric and symmetric C-H stretching vibrations modes were recorded at 3039.62-2970.46 cm^{-1} and

2931.38-2927.15 cm^{-1}, respectively. These assignments are compatible with the knowledge which defines C-H asymmetric and symmetric stretching vibrations for methyl groups occur at 3091.44 and 2860.18-2964.81 cm^{-1} [46]. In the other studies, strong C≡N stretching band, characteristic of the vibrations of phthalonitrile moiety, is observed 2234.13, 2258.71 cm^{-1} for 6-31G(d) [41], 2234.65, 2260.14 cm^{-1} for 6-31G(d) [47], 2923-2243 cm^{-1}, 2928-2264 cm^{-1} for 6-31G(d) [43] while this band is recorded at 2230.76 and 2264.60 cm^{-1} in this study, as experimental and computed values, respectively. This mode was observed about 2232-2237 cm^{-1} and 2230 cm^{-1} as experimentally in phthalonitrile groups [48, 49]. The C=C stretching modes belong to aromatic groups are appeared at 1400-1600 cm^{-1} bandwidth, and in accordance with this information these modes are recorded 1597.30, 1605.78 cm^{-1} in trimethylbenzene and 1566.41, 1584.88, experimentally and theoretically, respectively, for the compound (**3**). The C$_{Ar}$-O stretching vibration mode of the ether group is observed at 1311.58, 1278 cm^{-1} as experimental and as theoretical 1227.18 cm^{-1}, so these values are agreement with the literature that recorded about 1300-1000 cm^{-1} [50]. Some of the C-H in-plane and out-of plane bending vibrations bands and the deformation modes on the functional groups are shown in Table 3.

The selected vibrational frequencies have a good correlation with corresponding spectral values and similar studies in literature. And the correlation graphic (R^2 value is 0.9987) is shown in Figure 8.
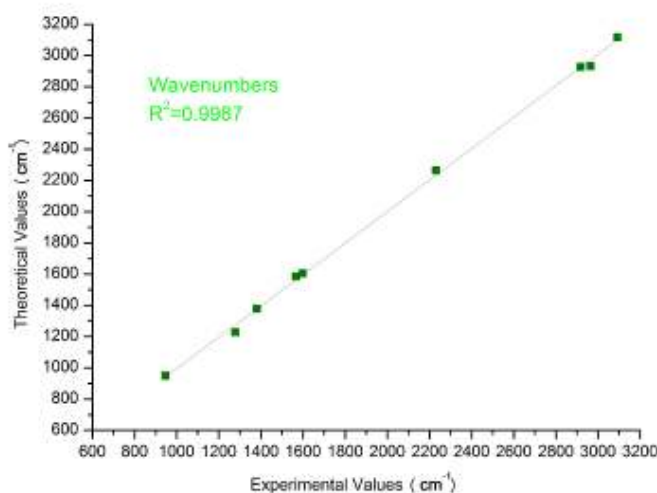
Figure 8. The correlation plot for experimental and theoretical wavenumbers of the compound (**3**).

Table 3. The comparison of the observed and calculated vibrational spectra of the compound (**3**).

Assignments	Experimental FT-IR (cm^{-1}) with KBr	Calculated (cm^{-1}) DFT/B3LYP/6-311G(d,p)
v_sC−H$_{(phthalonitrile)}$	3091.44	3117.05
v_{as}C−H$_{(phthalonitrile)}$	-	3093.85
v_sC−H$_{(trimethylbenzene)}$	-	3076.86
v_{as}C−H$_{3(trimethylbenzene)}$	-	3039.62-2970.46
v_sC−H$_{3(trimethylbenzene)}$	2964.81-2917.12	2931.38-2927.15
vC≡N	2230.76	2264.60
vC=C$_{(trimethylbenzene)}$	1597.30	1605.78
vC=C$_{(phthalonitrile)}$	1566.41	1584.88
vC−C$_{(phthalonitrile)}$	-	1543.31
γC-H$_{(phthalonitrile)}$	-	1471.73
ωC−H$_{3(trimethylbenzene)}$	1380.52	1378.05
vC−O	1278	1227.18
δC−H$_{(phthalonitrile)}$	946.20	949.40
$\theta_{(phthalonitrile)}$	-	715.40
βccc	-	561.89

Vibrational modes: v; stretching (s; symmetric, as; asymmetric), γ; rocking, ω; wagging, δ; twisting, β; deformation in-plane, θ; ring breathing.

NMR Spectral Analysis

Spectral and theoretical ^{13}C-NMR and ^{1}H-NMR chemical shift values of the compound (**3**) were recorded within the range of 162.05-11.82 ppm, 171.80-13.69 ppm and 7.69-2.00 ppm, 7.94-1.86 ppm respectively, and results are shown in Table 4.

Table 4. Experimental and theoretical ^{13}C NMR and ^1H NMR isotropic chemical shift values for the compound (**3**).

Atom	Experimental chemical shift values (ppm)	Theoretical chemical shift values (ppm)
C1	117.60	121.86
C2	108.14	113.66
C3	135.35	143.85
C4	120.52	129.19
C5	162.05	171.80
C6	120.64	125.20
C7	115.08	123.95
C8	115.49	121.50
C9	151.18	158.70
C10	118.92	125.25
C11	139.54	149.28
C12	128.91	135.14
C13	134.24	145.93
C14	125.55	135.45
C15	19.96	23.59
C16	20.83	23.32
C17	11.82	13.69
H3	7.69	7.94
H4	7.17	7.70
H6	7.15	6.69
H10	6.64	6.82
H12	6.95	7.38
H15[a]	2.30	2.35
H16[a]	2.30	2.36
H17[a]	2.00	2.11

Note: The atom numbering according to Fig.5 used in the assignment of chemical shifts. [a] Average

As it can be seen in Table 4, C5 atom has the highest chemical shift values in the downfield observed at 162.05 ppm, 171.80 ppm for as experimental, theoretical, respectively. Another the highest chemical shift value is stated as 151.18 and 158.70 ppm for C9 atom. It has less chemical shift value than C5 atom by reason of the effect of electron withdrawing substituent.

The aromatic carbon atoms have chemical shift values special to aromatic ring carbon atoms (100-150 ppm) [51] and these were recorded 108.14-115.08 ppm experimentally, 113.66-123.95 ppm theoretically for phthalonitrile ring atoms, 118.92-134.24 ppm for experimentally, and 125.25-145.93 for theoretically calculated benzene ring atoms. C1 and C8 atoms have typical triple bond with nitrogen chemical shift values, and were observed 117.60-115.49 ppm and 121.86-121.50 ppm as experimental and theoretical. sp^3 hybridized C15, C16, C17 atoms of the methyl groups have low chemical shift values in the upfield, these values confirm that information sp^3 hybridized methyl group protons are assigned at 0-30 ppm [50].

The chemical shift values belong to aromatic hydrogen atoms-H3, H4, H6, H10 and H12 atoms- are 7.69-6.95 ppm as spectral values, 7.94 and 6.82 ppm as computed values GIAO method. These resonance values are in concert with the literature [43, 52] that indicates as 6.0-8.5 ppm for aromatic protons. And the chemical shift values of the methyl protons, H15, H16 and H17, are assigned 2.30, 2.00 ppm as experimental and 2.35, 2.36, 2.11 ppm average values as theoretical.

Both spectral and theoretical chemical shift values are in agreement with literature values and with each other. The experimental ^{13}C-NMR and ^{1}H-NMR spectra are shown in Figure 9. To compare the experimental and theoretical values, the correlation coefficients and graphics were examined, R^2 value is 0.9992 for ^{13}C-NMR, 0.9849 for ^{1}H-NMR, and they are shown in Figure 10.
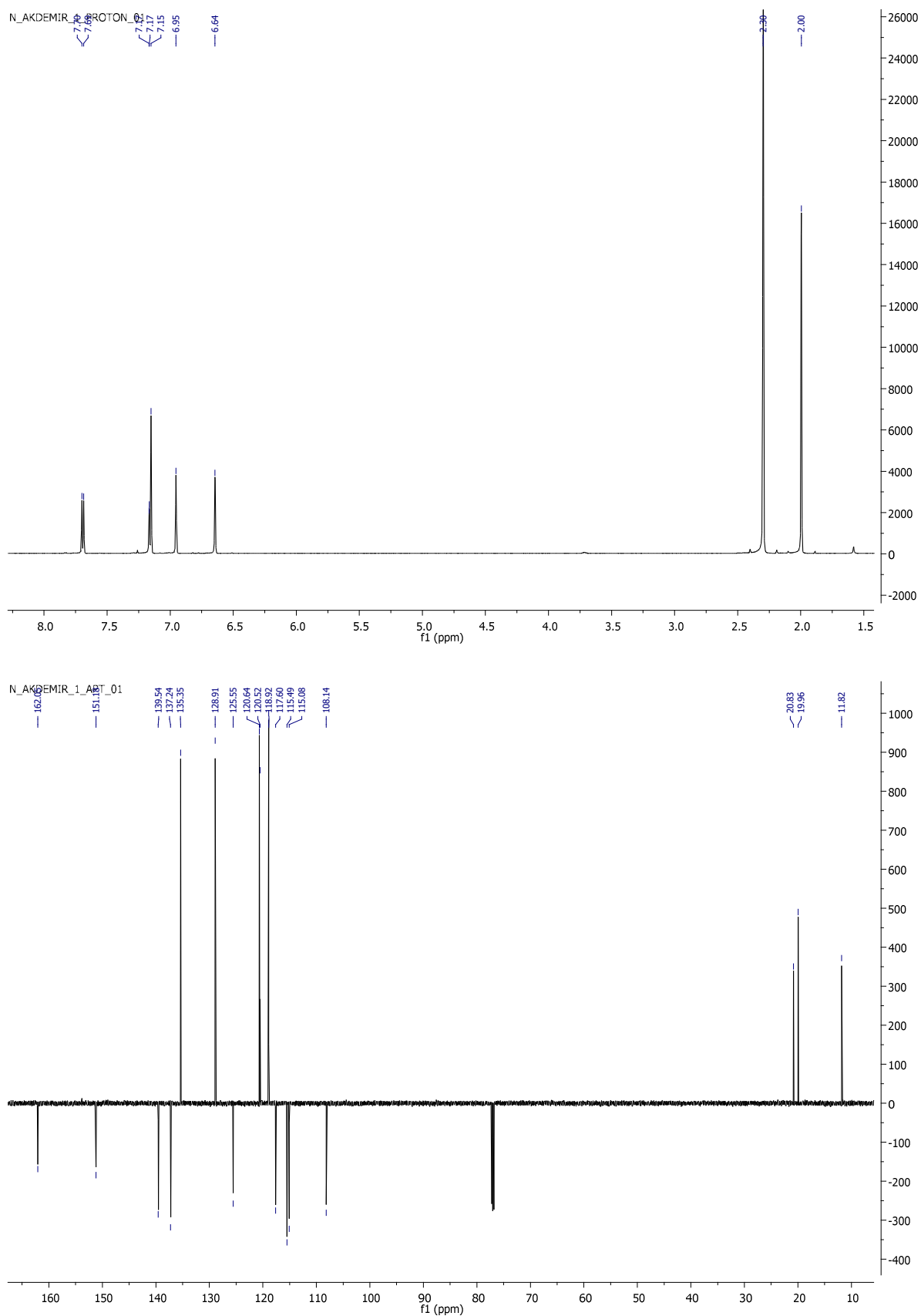
Figure 9. Top)^{1}H NMR spectrum**, bottom)**^{13}C NMR spectrum (APT) of compound (**3**)
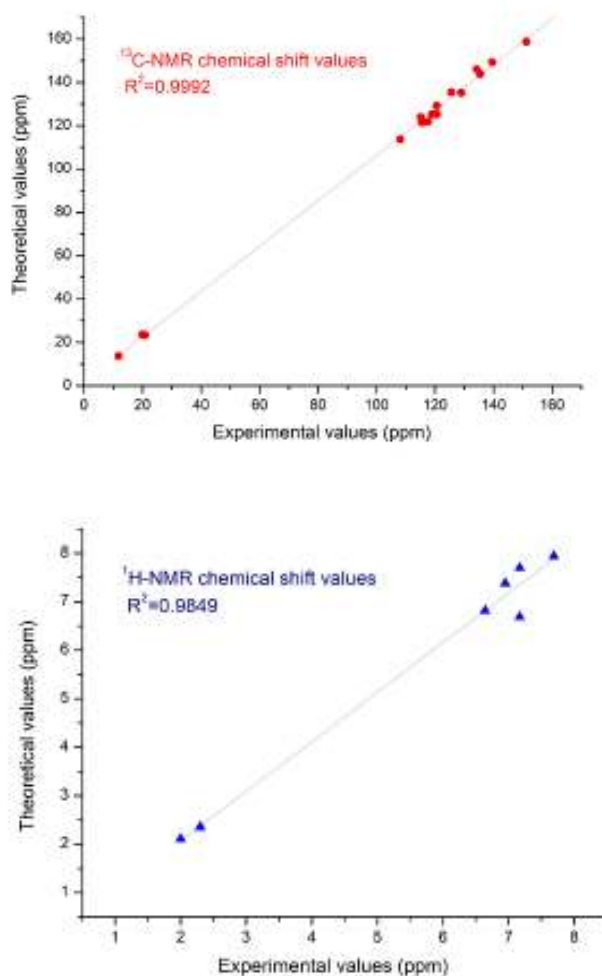
Figure 10. Correlation graphics between the experimental and theoretical Top) ^{13}C-NMR, bottom) ^{1}H-NMR chemical shift values of the compound (**3**).

CONCLUSION

Cu(II) and Co(II) phthalocyanines containing 2,3,5-trimethylphenoxy on the periphery were successfully prepared. Structures of all synthesized compounds were determined by elemental analyses, UV-Vis, ^{1}H-NMR, ^{13}C-NMR, Mass spectra, and FT-IR spectroscopy. The phthalocyanines showed excellent solubility in general organic solvents such as DCM, THF, chloroform, DMF, DMSO, and toluene. The absorption spectra of the new phthalocyanines were recorded in different solvents. The aggregation behaviors of compound (**4**) and (**5**) were investigated at different concentrations in THF. Also, computational studies on compound (**3**) were performed with DFT/B3LY/6-311G(d,p) basis set over the ground state and gas phase. So as to support that, the results of experimental were compared molecular structure parameters, vibrational frequencies, ^{1}H-NMR and ^{13}C-NMR chemical shift values. In comparison experimental with theoretical values, it is seen that most of the parameters are slightly different, as experimental results over the solid state, theoretical ones over the gas phase. And, correlation coefficients which were obtained indicate in compliance with results of both

spectral and modelling that is not only among themselves but also other phthalonitrile studies. The author hopes that these consequences will be created an infrastructure for researchers carrying out similar studies and can be used for the further analysis.

ACKNOWLEDGMENTS

REFERENCES

1. McKeown NB. Phthalocyanine Materials: Synthesis, Structure and Function. Cambridge University Press 1998. ISBN:9780521496230.

2. Leznoff CC, Lever ABP. Phthalocyanines: Properties and Applications, vols. 1-4, VCH, Weinheim, 1998. ISBN: 978-0-471-18720-2 ; ISBN: 978-0-471-18828-5; ISBN: 978-0-471-18863-6; ISBN: 978-0-471-18629-8.

3. Wöhrle D. Phthalocyanines in macromolecular phases-methods of synthesis and properties of the materials. Macromol. Rapid Comm. 2001 Feb;22:2;68-97. DOI: 10.1002/1521-3927(20010201)22:2<68::AID-MARC68>3.0.CO;2-Z.

4. Duro JA, Torre G, Barbera J, Serrano JL, Torres T. Synthesis and Liquid-Crystal Behavior of Metal-Free and Metal-Containing Phthalocyanines Substituted with Long-Chain Amide Groups. Chem. Mater. 1996 May; 8:5;1061–6. DOI: 10.1021/cm950478f.

5. Yakuphanoglu F, Durmuş M, Okutan M, Köysal O, Ahsen V. The refractive Index dispersion and theoptical constants of metal-free and nickel(II) phthalocyanines liquid crystals. Physica B: 2006 Mar;373:262–6. DOI:10.1016/j.physb.2005.11.153.

6. Xia H, Nogami M. Copper phthalocyanine bonding with gel and their optical properties. Opt. Mater. 2000 Nov;15:2;93-8. DOI:10.1016/S0925-3467(00)00024-0.

7. Makhseed S, Al-Sawah M, Samuel J, Manaa H. Synthesis, characterization and nonlinear optical properties of non aggregating hexadeca-substituted phthalocyanines. Tetrahedron Lett. 2009 Jan;50:2;165-8. DOI:10.1016/j.tetlet.2008.10.102.

8. Ben-Hur E, Otjen J, Horowitz B. Silicon Phthalocyanine Pc 4 and Red Light Causes Apoptosis in HIV-infected Cells. Photochem Photobiol. 1997 Mar;65:3;456-460. DOI: 10.1111/j.1751-1097.1997.tb08589.x.

9. Margolis-Nunno H, Ben-Hur E, Gottlieb P, Robinson R, Oetjen J, Horowitz B. Inactivation by phthalocyanine photosensitization of multiple forms of human immuno deficiency virus in red cell concentrates. Transfusion. 1996 Aug;36:8;743-750. DOI:10.1046/j.1537-2995.1996.36896374381.x.

10. Krasnov YS, Kolbasov GY, Tretyakoya IN, Tomachynska LA, Chernii YY, Volkov SV. Dynamics of redox processes and electrochromism of films of zirconium (IV) phthalocyanines without-of-plane β-dicarbonylligands. Solid State Ionics. 2009 Jun;180:14-16;928-933. DOI:10.1016/j.ssi.2009.03.019.

11. Monk PMS, Mortimer RJ, Rosseinsky DR. Electrochromism: Fundamentals and Applications. VCH, Weinheim, 2008. ISBN: 978-3-527-61536-0.

12. Ikeuchi T, Nomoto H, Masaki N, Griffith MJ, Mori S, Kimura M. Molecular engineering of zinc phthalocyanine sensitizers for efficient dye-sensitized solar cells. Chem. Commun. 2014;50:1941-3. DOI: 10.1039/C3CC47714B.

13. Kimura M, Nomoto H, Suzuki H, Ikeuchi T, Matsuzaki H, Murakami TN, Furube A, Masaki N, Griffith MJ, Mori S. Molecular Design Rule of Phthalocyanine Dyes for Highly Efficient Near-IR Performance in Dye-Sensitized Solar Cells**.** Chem Eur J. 2013 Jun;19;23;7496-7502. DOI: 10.1002/chem.201300716.

14. Basova TV, Taşaltın C, Gürek AG, Ebeoğlu MA, Öztürk ZZ, Ahsen V. Mesomorphic phthalocyanine as chemically sensitive coatings for chemical sensors. Sensors and Actuators B: Chemical. 2003 Nov;96:1-2;70-5. DOI:10.1016/S0925-4005(03)00487-8.

15. Valli L. Phthalocyanine-based Langmuir–Blodgett films as chemical sensors. Advances in Colloid and Interface Science. 2005 Nov;116:1-3;13-44. doi:10.1016/j.cis.2005.04.008.

16. Zhang Y, Cai X, Bian Y, Jiang J. Organic Semiconductors of Phthalocyanine Compounds for Field Effect Transistors (FETs). Structure and Bonding. 2009 Dec;135: 275-321.ISBN: 978-3-642-04751-0.

17. Bouvet M. Phthalocyanine-basedfield-effect transistors as gas sensors. Analytical and Bioanalytical Chemistry. 2006 Jan;384:2;366-373. ISSN:1618-2642.

18. Durmuş M, Ahsen V. Water-soluble cationic gallium(III) and indium(III) phthalocyanines for photodynamictherapy. Journal of Inorganic Biochemistry 2010 Mar;104:3;297-309. DOI:10.1016/j.jinorgbio.2009.12.011.

19. Çakır D, Çakır V, Bıyıklıoğlu Z, Durmuş M, Kantekin H. New water soluble cationic zinc phthalocyanines as potential for photodynamic therapy of cancer. J Orgonomet. Chem. 2013 Nov; 745-746:423-431. DOI:10.1016/j.jorganchem.2013.08.025.

20. Ranyuk E, Cauchon, Klarskov, Guerin B, van Lier. Phthalocyanine–Peptide Conjugates: Receptor-Targeting Bifunctional Agents for Imaging and Photodynamic Therapy**.** J. Med. Chem. 2013 Jan; 56:4;1520–1534. DOI: 10.1021/jm301311c.

21. Eberhardt W, Hanack M. Synthesis of Hexadecaalkyl-Substituted Metal Phthalocyanines. Synthesis. 1998;12:1760-4. DOI: 10.1055/s-1998-2218.

22. Akdemir N, Gümrükcüoğlu İE, Ağar E. Synthesis and Characterization of Novel Phthalocyanines Containing N-(n-Octyl)mercaptoAcetamid Substituents. Synth. React. Inorg. Met.-Org. Chem. 2005;35:10:819-824. DOI:10.1080/15533170500360297.

23. Gürel E, Pişkin M, Altun S, Odabaş Z, Durmuş M. Synthesis, characterization and investigation of the photophysical and photochemical properties of highly soluble novel metal-free, zinc(II), and indium(III) phthalocyanines substituted with 2,3,6-trimethylphenoxy moieties. Dalton Trans. 2015;44:6202-6211. DOI:10.1039/C5DT00304K.

24. Ağar E, Şaşmaz S, Akdemir N, Keskin İ. Synthesis and Characterization of New Phthalocyanines Containing Four 15-Membered Tetrathiaoxa Macrocycles. Synth. React. Inorg. Met.-Org. Chem. 1999;29:3;473-485. DOI:10.1080/00945719909349463.

25. Şaşmaz S, Ağar E, Akdemir N, Keskin İ. Synthesis and Characterization of New Phthalocyanines Containing Thio-Oxa-Ether Moieties. Dyes and Pigments. 1998 May;37:3;223-230. DOI:10.1016/S0143-7208(97)00061-2.

26. Ağar E, Şaşmaz S, Akdemir N, Keskin İ. Synthesis and Characterization of Novel Phthalocyanines Containing Four 15-Membered Oxathiadiaza Mixed-donor Macrocycles. Dalton Trans. 1997;2087-2090. DOI: 10.1039/A607349B.

27. Özil M, Ağar E, Şaşmaz S, Kahveci B, Akdemir N, Gümrükçüoğlu İE. Microwave-assisted synthesis and characterization of the monomeric phthalocyanines containing naphthalene-amide group moieties and the polymeric phthalocyanines containing oxa-azabridge. Dyes and Pigments. 2007;75:3;732-740. DOI:10.1016/j.dyepig.2006.07.026.

28. Kantar C, Akdemir N, Ağar E, Ocak N, Şaşmaz S. Microwave-assisted synthesis and characterization of differently substituted phthalocyanines containing 3,5-dimethoxyphenol and octanethiol moieties. Dyes and Pigments. 2007;76:1;7-12. DOI:10.1016/j.dyepig.2006.08.005.

29. Akbal T, Akdemir N, Ağar E, Kantar C, Erdönmez A. 4-(2,3,5-trimethylphenoxy)phthalonitrile. Acta Cryst. E 2005 Aug;E61:8;o2630-o2631. DOI: 10.1107/S1600536805022592.

30. Young JG, Onyebuagu, W. Synthesis and characterization of di-disubstitutedphthalocyanines**.** J. Org. Chem. 1990 Mar;55:7;2155-9. DOI:10.1021/jo00294a032.

31. Armarego WLF, Perrin DD., Purification of Laboratory chemicals, 6nd ed.; Elsevier: Burlington, 2009. ISBN: 978-1-85617-567-8.

32. a) Becke A.D. Density-functional exchange-energy approximation with correct asymptotic behavior. J. Chem. Phys. 1988 Sep;38:3098-3100. DOI:10.1103/PhysRevA.38.3098.
b) Becke AD. Density-Functional Thermochemistry. I. The Effect of the Exchange-Only Gradient Correction. J. Chem. Phys. 1992 Feb;96:2155-2160. DOI: 10.1063/1.462066.
c) Becke AD. Density functional thermochemistry III.The role of exact exchange. J. Chem. Phys. 1993 Apr;98:5648-5652. DOI:10.1063/1.464913.

33. Ditchfield R, Hehre WJ, Pople JA. Self-Consistent Molecular-Orbital Methods. IX. An Extended Gaussian Type Basis for Molecular Orbital Studies of Organic Molecules. J. Chem. Phys. 1971 Jan; 54:724-728. DOI:10.1063/1.1674902.

34. Lee C, Yang C.W, Parr R. Development of the Colle-Salvetti correlation-energy formula into a functional of the electron density. Phys. Rev. 1988 Jan;37:785–789. DOI:10.1103/PhysRevB.37.785.

35. Merrick J.P, Moran D, Radom L. An Evaluation of Harmonic Vibrational Frequency Scale Factors. J. Phys. Chem. A. 2007 Oct;111:11683-11700. DOI:10.1021/jp073974n.

36. a) Wolinski K, Hilton J.F, Pulay P. Efficient implementation of the gauge-independent atomic orbital method for NMR chemical shift calculations. J. Am. Chem. Soc. 1990 Nov;112:8251-8260. DOI:10.1021/ja00179a005.
b) Cheeseman J.R, Trucks G.W, Keith T.A, Frisch M.J.A comparison of models for calculating nuclear magnetic resonance shielding tensors. J Chem Phys 1996 Apr;104:5497-5509. DOI:10.1063/1.471789.

37. Gaussian 09, Revision E.01, Frisch, M. J.; Trucks, G. W.; Schlegel, H. B.; Scuseria, G. E.; Robb, M. A.; Cheeseman, J. R.; Scalmani, G.; Barone, V.; Mennucci, B.; Petersson, G. A.; Nakatsuji, H.; Caricato, M.; Li, X.; Hratchian, H. P.; Izmaylov, A. F.; Bloino, J.; Zheng, G.; Sonnenberg, J. L.; Hada, M.; Ehara, M.; Toyota, K.; Fukuda, R.; Hasegawa, J.; Ishida, M.; Nakajima, T.; Honda, Y.; Kitao, O.; Nakai, H.; Vreven, T.; Montgomery, J. A., Jr.; Peralta, J. E.; Ogliaro, F.; Bearpark, M.; Heyd, J. J.; Brothers, E.; Kudin, K. N.; Staroverov, V. N.; Kobayashi, R.; Normand, J.; Raghavachari, K.; Rendell, A.; Burant, J. C.; Iyengar, S. S.; Tomasi, J.; Cossi, M.; Rega, N.; Millam, J. M.; Klene, M.; Knox, J. E.; Cross, J. B.; Bakken, V.; Adamo, C.; Jaramillo, J.; Gomperts, R.; Stratmann, R. E.; Yazyev, O.; Austin, A. J.; Cammi, R.; Pomelli, C.; Ochterski, J. W.; Martin, R. L.; Morokuma, K.; Zakrzewski, V. G.; Voth, G. A.; Salvador, P.; Dannenberg, J. J.; Dapprich, S.; Daniels, A. D.; Farkas, Ö.; Foresman, J. B.; Ortiz, J. V.; Cioslowski, J.; Fox, D. J. Gaussian, Inc., Wallingford CT, 2009.

38. GaussView, Version 5, Dennington, Roy; Keith, Todd; Millam, John. Semichem Inc., Shawnee Mission, KS, 2009.

39. Brannon JH, Magde D. Picosecond laser photophysics. Group 3A phthalocyanines. J. Am. Chem. Soc. 1980 Jan;102:1;62-5. DOI: 10.1021/ja00521a011.

40. Ogunsipe A, Nyokong T. Photophysical and photochemical studies of sulphonated non-transition metal phthalocyanines in aqueous and non-aqueous media. J. Photochem. Photobiol. A: Chem. 2005 Jul;173:2;211-220. DOI:10.1016/j.jphotochem.2005.03.001.

41. Hasan M, Shalaby M. Synthesis, click reaction, molecular structure, spectroscopic and DFT computational studies on 3-(2,6-bis(trifluoromethyl)phenoxy)-6- (prop-2-yn-1-yloxy)phthalonitrile. J. Mol. Struc. 2016 Jun;1113:88-98. DOI:10.1016/j.molstruc.2016.01.078.

42. Tereci H, Askeroğlu İ, Akdemir N, Uçar İ, Büyükgüngör O. Combined experimental and theoretical approaches to the molecular structure of 4-(1-formylnaphthalen-2-yloxy)phthalonitrile. Spectro Chimica Acta Part A: Molecular and Biomolecular Spectroscopy. 2012 Oct;96:569–577. DOI:10.1016/j.saa.2012.07.005.

43. Akçay H. T, Bayrak R, Şahin E, Karaoğlu K, Demirbaş Ü. Experimental and computational studies on 4-(3,5-dimethyl-1H-pyrazol-1-yl)methoxyphthalonitrile and synthesis and spectroscopic characterization of its novel phthalocyanine magnesium(II) and tin(II) metal complexes. Spectro Chimica Acta Part A: Molecular and Biomolecular Spectroscopy. 2013 Oct;114:531-540. DOI:10.1016/j.saa.2013.05.042.

44. Tanak H. Molecular structure, spectroscopic and DFT computational studies on 4,5-bis(tert-butylsulfanyl)phthalonitrile. J. Mol. Struct. 2015 Nov;1090:86-92. DOI:10.1016/j.molstruc.2014.11.025.

45. Ferraro J.R, Basile L.J, Editors. Fourier Transform Infrared Spectroscopy: Applications to Chemical Systems (Vol. 1). Academic Press, USA;1978. 311p. ISBN: 978-0122541018.

46. Socrates G.Infrared and Raman Characteristic Group Frequencies: Tables and Charts, 3rd Edition. John Wiley&Sons LTD, UK; 2004. 366 p. ISBN: 978-0-470-09307-8.

47. Tanak H, Köysal Y, Işık Ş, Yaman H, Ahsen V. Experimental and Computational Approaches to the Molecular Structure of 3-(2-Mercaptopyridine)phthalonitrile. Bull. Korean Chem. Soc. 2011 Feb; 32:673-680. DOI: 10.5012/bkcs.2011.32.2.673.

48. Zhang X-F, Jia D, Song A, Liu Q. 3-(2-Nitrophenoxy)phthalonitrile. Acta Cryst. E. 2008 Feb; E64:2;356. DOI: 10.1107/S1600536807067797.

49. Halls, M.D, Aroca R, Terekhov D.S, D'Ascanio, A, Leznoff, C.C. Vibrational spectra of halophthalonitriles. Spectro Chimica Acta Part A: Molecular and Biomolecular Spectroscopy 1998 Feb, 54:2;305-317. DOI:10.1016/S1386-1425(97)00236-9.

50. Erdik E. Organik Kimyada Spektroskopik Yöntemler. Ankara, Türkiye: Gazi Kitabevi; 2008. ISBN: 975-7373-04-1.
51. Kalinowski H.O, Berger S, Braun S. Carbon-13 NMR Spectroscopy. Chichester, UK John Wiley&Sons; 1988. 792 p. ISBN: 978-0-471-91306-1.

52. Balcı M. Nükleer Manyetik Rezonans Spektroskopisi. Ankara, Türkiye: ODTÜ Yayıncılık, 2004. 452p. ISBN:975-7064-23-8**.**

Türkçe Öz ve Anahtar Kelimeler

Yeni, Periferal Konumlarda 2,3,5-Trimetilfenoksi Sübstitüe Cu ve Co Ftalosiyaninlerin Sentezi, Karakterizasyonu ve Spektroskopik Özelliklerinin İncelenmesi, 4-(2,3,5-trimetilfenoksi)ftalonitrilin Hesaplamalı ve Deneysel Çalışmaları

Nesuhi Akdemir[1]

Öz: 4-(2,3,5-trimetilfenoksi)ftalonitril (**3**) nükleofilik aromatik sübstitüsyon ile hazırlanmış ve FT-IR, kütle spektrometrisi, ^{1}H ve ^{13}C-NMR teknikleriyle karakterize edilmiştir. **3** bileşiğinin moleküler yapısı Yoğunluk Fonksiyonel Teorisi (DFT/B3LYP) yöntemiyle temel halde 6-311G(d,p) taban seti ile en uygun hale getirilmiştir. X-ışını tek kristal saçılması yöntemiyle moleküler geometrik parametreler elde edilmiştir, spektral sonuçlar hesaplanan bağ uzunlukları ve açıları, titreşim frekansları ve ^{1}H ile ^{13}C kimyasal kaymaları ile karşılaştırılmıştır. Bunun dışında, dinitril türevinin susuz CuCl$_2$ veya CoCl$_2$ ile azot atmosferinde kuru n-pentanol içinde 140 °C'de tepkimeye sokulmasıyla karşılık gelen Cu(II) ve Co(II) ftalosiyaninler elde edilmiştir. Yeni bileşikler elementel analiz, FT-IR ve elektronik soğurma spektrumu ile belirlenmiştir. Cu(II) ve Co(II) ftalosiyaninlerin UV-Vis spektrumları THF içinde farklı derişimlerde kaydedilmiş ve ayrıca başka çözücüler de (DMF, DMSO, DCM, CHCl$_3$ ve toluen) denenmiştir.

Anahtar kelimeler: Ftalosiyaninler; ftalonitril; 2,3,5-trimetilfenol; DFT.

Understanding the Behaviour of Sulphur-Centred Radicals During Polymer Self-Healing

Isa Degirmenci*[1] and Michelle L. Coote*[2]

[1] Chemical Engineering Department, Ondokuz Mayıs University, 55139, Samsun, Turkey
[2] ARC Centre of Excellence for Electromaterials Science, Research School of Chemistry, The Australian National University, Canberra, 2601, ACT, Australia

Abstract: The high-level composite *ab initio* G3(MP2)-RAD method has been used to study the self-healing mechanism of materials based on thiuram disulfides and their derivatives (S=C(Z)S–SC(Z)=S, for Z = CH_3, NEt_2, $N(Et)CH_2CH_2OH$, Ph, Bz), and the effects of these Z-substituents on their efficacy. The relative contributions of cross-over and reversible addition fragmentation chain transfer reactions were ascertained, and the likelihood of chain-breaking side reactions was assessed. To rationalize the results, the various stabilisation energies of the radicals and closed-shell species were also evaluated. The study revealed that the self-healing mechanism of thiuram disulfides follows predominantly the cross-over reaction because of the high energies of intermediate radicals in the chain transfer mechanism. Based on the study, the most effective self-healing materials are predicted to contain amines as Z-groups, while those containing benzyl and its derivatives are most likely to undergo side reactions.

Keywords: Self-Healing polymers; thiuram disulfides; Radical Stabilisation energy.

Cite this: Değirmenci İ, Coote M. Understanding the Behaviour of Sulphur-Centred Radicals During Polymer Self-Healing. JOTCSA. 2016;3(3):707–20.

DOI: To be assigned.

*Corresponding authors. Isa Degirmenci: isa.degirmenci@omu.edu.tr, Michelle L. Coote: michelle.coote@anu.edu.au.

INTRODUCTION

In recent decades, self-repairing or self-healing polymers have been developed so as to extend the working lifetime of materials [1-5]. They generally utilize non-covalent bonding networks [6, 7] or dynamic covalent bonds [8, 9] — special crosslinks that can be physically or chemically rearranged in response to external stimuli. Non-covalent bond forming systems are promising as self-repairing structures but tend to produce materials with weak mechanical strength [6, 7], whereas dynamic covalent systems tend to offer more mechanically stable polymeric materials [10]. Dynamic covalent systems utilise functional groups that are capable of reacting reversibly to form cross-links. They are designed so that the equilibrium position of the cross-linking reaction can be externally manipulated by chemical stimulation [11, 12], thermal stimulation [13-15] and photostimulation [16-18]. Photostimulation is especially promising for commercial applications as repair can occur at room temperature, is easy to handle, and targeted areas can be healed by limited exposure.

Recently, Amamoto *et al.* [16] introduced a covalently cross-linked polymer capable of undergoing visible light initiated self-healing. The photolabile groups in this system are thiuram disulfide linkages [19], which undergo S-S bond cleavage in the presence of light to produce sulphur-centred radicals that can either recombine or undergo a series of addition-fragmentation chain transfer reactions, reminiscent of the RAFT process (Scheme 1). In the latter case, the sulphur centred radical adds to the sulphur side of the S=C bond in another dithiuram linkage forming an intermediate radical that can then undergo β-scission, either to reproduce the reactants or a new "reshuffled" dithiuram linkage and a new sulphur-centred radical that can continue the process. The reshuffling of the covalent bond network can in principle occur purely by homolytic cleavage and subsequent recombination with a different sulphur-centred radical ("cross-over"), but is thought to contain significant contributions from the chain transfer processes. In particular, experimental studies in which light exposed samples are mixed with non-light exposed samples and then held in the dark demonstrate significant reshuffling over the course of several minutes, supporting not only a significant role for the radical transfer reaction but a relatively long half-life for the sulphur centred radicals [19] Earlier work by García-Con *et al.* [20] also supports a long lifetime (in excess of 2 weeks) for these types of radicals.

1-Homolitic Cleavage
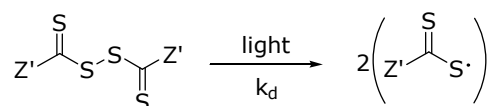
2 -Addition Reaction
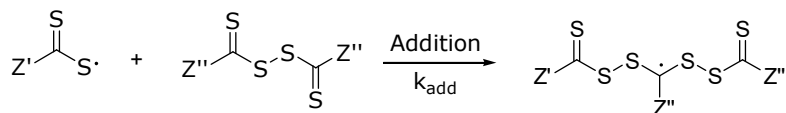
3 -Fragmentation Reaction
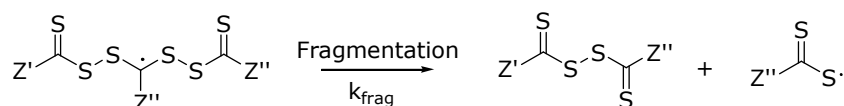
Scheme 1. Schematic representation of the reshuffling mechanism of DTS units.

Whilst these studies provide evidence for the role of chain transfer in the self-healing process, its relative extent (compared with cross-over) and its role improving the reshuffling efficiency is yet to be quantified. Understanding the mechanism of the self-healing process would be particularly useful in guiding the design of more efficient systems. Of particular interest is what role the thiocarbonyl substituent (Z in S=C(Z)S-S-R) plays in promoting cleavage and efficient reshuffling. At the same time, it is important to consider whether certain Z-groups might introduce an unwanted side reaction in which the sulphur-centred radical undergoes β-scission to produce CS_2 and Z• (Scheme 2). To address these questions in the present work, we use high-level *ab initio* molecular orbital calculations to study the key steps in the self-healing process for a variety of Z-groups, and use these in conjunction with relevant experimental data from the literature develop an *ab initio* kinetic model of the self-healing process.

Homolitic Cleavage

Side Reaction

Z=
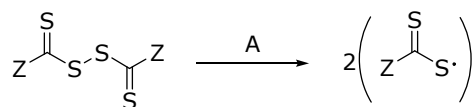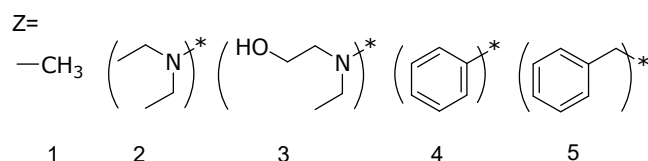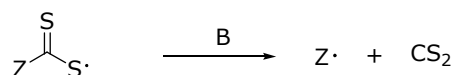
Scheme 2. Schematic representation of homolytic bond cleavage and side reactions for the special substituent.

COMPUTATIONAL METHODOLOGY

All geometry optimisations and single point energy calculations were carried out by using Gaussian 09 [21] and Molpro2009.1 [22] program packages. The recently developed DFT method (U)M06-2X/6-31G(d) level of theory [23] was chosen for the geometry optimisations and frequency calculations. Complete conformational searches were undertaken to ensure that the species were global rather than merely local minima. (U)HF and (U)MP2 methodologies at 6-31G(d) level were also tested during the transition state search for addition and fragmentation reactions. Improved energies were calculated using the high-level composite *ab initio* method G3(MP2)RAD [24] that approximates (UR)CCSD(T) calculations with a large triple-ζ basis from calculations with a double-ζ basis set, via basis-set corrections carried out at the R(O)MP2 level. A double-layer-ONIOM [25] approximation to G3(MP2)RAD in which remote substituent effects were evaluated with RMP2/GTMP2Large was used for the larger species. The accuracy of this level of theory for these types of species has been benchmarked previously [26, 27].

The electronic energies (E), geometries and vibrational frequencies (v_i) were then used to calculate the entropies (S), enthalpies (H) and Gibbs (G) free energies using the standard textbook formulae for the statistical thermodynamics of an ideal gas under the harmonic oscillator / rigid rotor approximation [28, 29] as follows.

$$G = H - TS \tag{1}$$

$$H = E + 4RT + \frac{R}{2}\sum_i \frac{hv_i}{k_B} + R\sum_i \frac{hv_i/k_B}{\exp(hv_i/k_BT)-1} \tag{2}$$

$$S = R\left(\ln\left(\left(\frac{2\pi M k_B T}{h^2}\right)^{3/2}\frac{k_B T}{P}\right)+\frac{5}{2}\right) + R\left(\ln\left(\frac{\pi^{1/2}}{\sigma_r}\frac{T^{3/2}}{(\theta_{r,x}\theta_{r,y}\theta_{r,z})^{1/2}}\right)+\frac{3}{2}\right) + R\sum_i\left(\frac{hv_i/k_BT}{\exp(hv_i/k_BT)-1}-\ln\left(1-\right.\right.$$
$$\left.\left.\exp\left(-\frac{hv_i}{k_BT}\right)\right)\right) + Rln(\omega_0) \tag{3}$$

where: k_B is the Boltzmann constant, h is Planck's constant, T is the temperature, P is the pressure, M is the molecular weight, σ_r is the rotational symmetry number, and $\theta_{r,i}$ are calculated from the i = x, y and z components of the principal moments of inertia I_i of the optimized geometries as follows:

$$\theta_{r,i} = \frac{h^2}{8\pi^2 I_i k_B} \tag{4}$$

RESULTS AND DISCUSSION

The first stage of the self-healing process is homolytic S–S cleavage of the thiuram disulphides (ZC(=S)S–S(S=)CZ), producing sulphur-centred radicals which can either trigger reshuffling or undergo an unwanted β-scission side reaction (see Scheme 2). The energetics of cleavage and β-scission as a function of the Z-group is summarised in Table 1. From these it can be seen that for the species studied, the side reaction is a relatively minor process, except where the Z-group is a benzyl moiety. In that case, the side reaction produces the highly stabilized benzyl radical [30, 31] and CS_2 and would prevent further self-healing from occurring. The other substituents resist this side reaction and are thus better suited to this application.

Table 1. Homolytic cleavage and side reaction energies at 298.15 K in kJ/mol at the G3(MP2)-RAD//M062X/6-31G(d) level of theory.

Z	Homolytic cleavage			Side reaction			
	ΔH_{rxn}	ΔG_{rxn}	$\Delta H^{\ddagger}$	$\Delta G^{\ddagger}$	ΔH_{rxn}	ΔG_{rxn}	
CH_3	189.2	130.4	128.9	125.7	76.7	35.7	
$(C_2H_5)_2N$	155.0	98.3	166.1	158.7	118.9	66.6	
$(HOC_2H_4)N(C_2H_5)$	169.9	99.6	169.1	164.5	110.4	58.0	
Ph	181.1	123.5	173.8	169.7	151.4	109.8	
Bz	209.7	141.1	88.8	87.2	32.7	-5.6	

For the homolytic cleavage reaction, the nitrogen substituted reagents have the lowest bond dissociation energies (BDEs), followed by the methyl and then the benzyl. Lower enthalpies of the homolytic cleavage reaction for thiuram disulphides can be attributed to higher stability of the molecule structure and/or lower stability of the produced radical structure. The inherent stability of the thiuram disulphide agent can be qualitatively assessed from its agent stability energy (ASE) which is defined as the energy of the following isodesmic reaction:

$$\text{(5)}$$
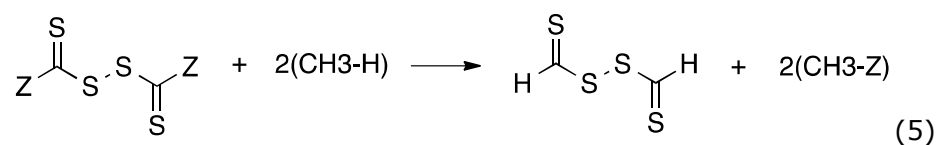
The inherent stability of the radical can be assessed from its radical stabilization energy (RSE). In this work, two methods for assessing the RSE have been considered: the standard radical stabilisation energy (RSE$_{R-H}$, eq 6) and Zavitsas's inherent RSE method (RSE$_Z$, eq 7, [32]), which was introduced as a more universal definition of radical stability:

$$RSE_{R-H} (R\bullet) = D[H-CH_3] - D[H-R] \qquad (6)$$

$$RSE_Z (R\bullet) = \tfrac{1}{2}(D[H_3C-CH_3]_{calc} - D[R-R]_{calc}) \qquad (7)$$

In order to calculate RSE$_Z$, the "strain free" R–R bond dissociation energies are calculated using Pauling's electronegativity equation [33] (see Refs [30, 31] for more details). Recently, this definition has been used successfully in various studies [30, 31, 34, 35] and has been recommended as being highly promising for comparing different classes radical on the same scale.

Table 2. Agent stability energies (ASE) and radical stabilization energies (RSE) energy values (kJ/mol) are calculated using G3(MP2)-RAD//M06-2X/6-31G(d) ΔH_{gas} values at 298.15 K

Z	ASE	RSE$_{R-H}$	RSE$_Z$
CH$_3$	73.2	113.3	96.4
(C$_2$H$_5$)$_2$N	180.4	128.9	116.0
(HOC$_2$H$_4$)N(C$_2$H$_5$)	207.2	128.9	129.7
Ph	83.8	118.3	101.1
Bz	92.8	115.4	95.7

Values of the ASE, RSE$_{R-H}$ and RSE$_Z$ are provided in Table 2, from which it is seen that the nitrogen atom highly stabilizes both the agent and resulting radical, in both cases through resonance effects with the lone-pair donor nitrogen atom. Quantitatively, the stabilization of the agent is much larger than that of the radical, which would seem to indicate that the homolytic BDE should be larger for these compounds rather than smaller. Indeed, in a normal RAFT process [36], stabilization of the agent outweighs stabilisation of the radical and deactivates these reagents towards radical addition. However, here the homolytic BDEs for the nitrogen substituted agents are low implying the opposite is actually true. The low BDEs in this case are probably due to cross conjugation, which preferentially diminishes the stabilizing effect of the lone pair nitrogens on the disulfide agents (Scheme 3), and weakens these compounds compared

to the other substituents. These interactions between substituents are not properly captured in the simplified ASE values.
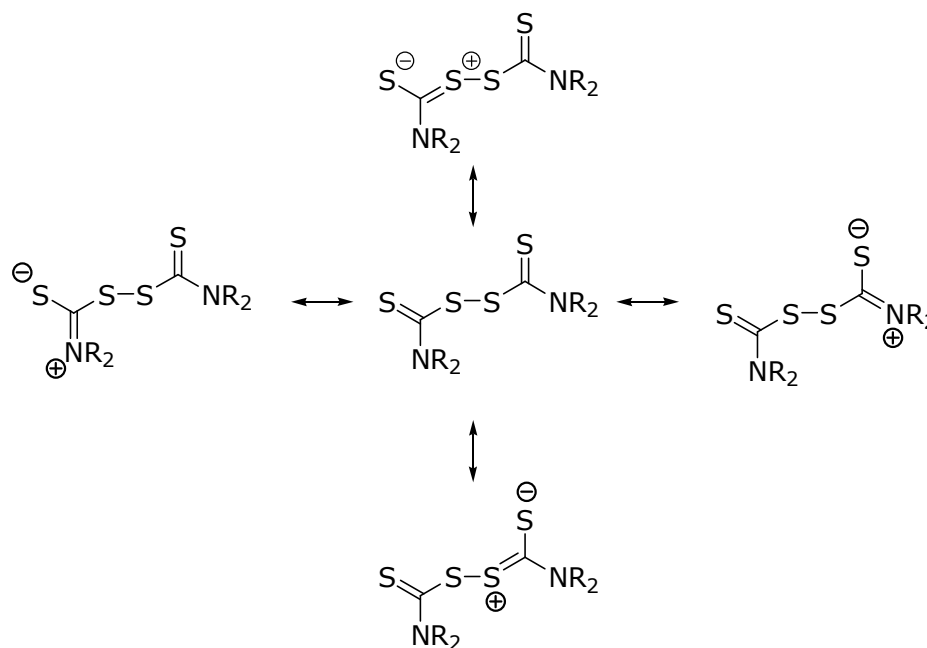
Scheme 3. Cross conjugation in nitrogen substituted agents.

The second part of the reshuffling mechanism investigation is the addition of the produced radicals to the C=S double bond of the disulphide agents dithioacetate (CH$_3$C(=S)S-SC(=S)CH$_3$) (DTA) and tetraethylthiuram disulphide ((CH$_3$CH$_2$)$_2$NC(=S)S-SC(=S)N(CH$_2$CH$_3$)$_2$) (TETD). In the first case, the reshuffling of dithioacetate (DTA) and tetraethylthiuram disulphide (TETD) were taken into account. In the second case, the reshuffling of tetraethylthiuram disulphide (TETD) and diethyl dihydroxyethyl thiuram disulphide (DEDHETD) was modelled. The reactions studied are listed in Scheme 4. Add1, Add3 (= Add5) and Add7 can be classified as self-addition reactions and Add2, Add4, Add6 and Add8 can be classified as cross addition reactions. Conformational analysis for all reactants and dormant species were performed at the M06-2X/6-31G(d) level of theory. Unfortunately, establishing the addition transition state geometries at this level of theory was problematic due to the low or non-existent reaction barriers, as established previously [35] and below. Therefore, only reaction enthalpies and the Gibbs Free energies were calculated based on M06-2X/6-31G(d) geometries (Table 3). The G3(MP2)-RAD composite method was used to improve the energetics with ONIOM procedure. Interestingly, the addition reaction is much *less* exothermic than that of the carbon-centred radical addition to C=C double bond [37]. Indeed, addition reactions 6, 7 and 8 are actually endothermic. This contrasts with our recent study of simpler prototypical examples of these reactions, where thiyl radical addition to thioketones is

strongly exothermic (by more than -50 kJ/mol) [35]. The conjugation with the sulphur substituents in the disulfides clearly deactivates the addition process in this case.
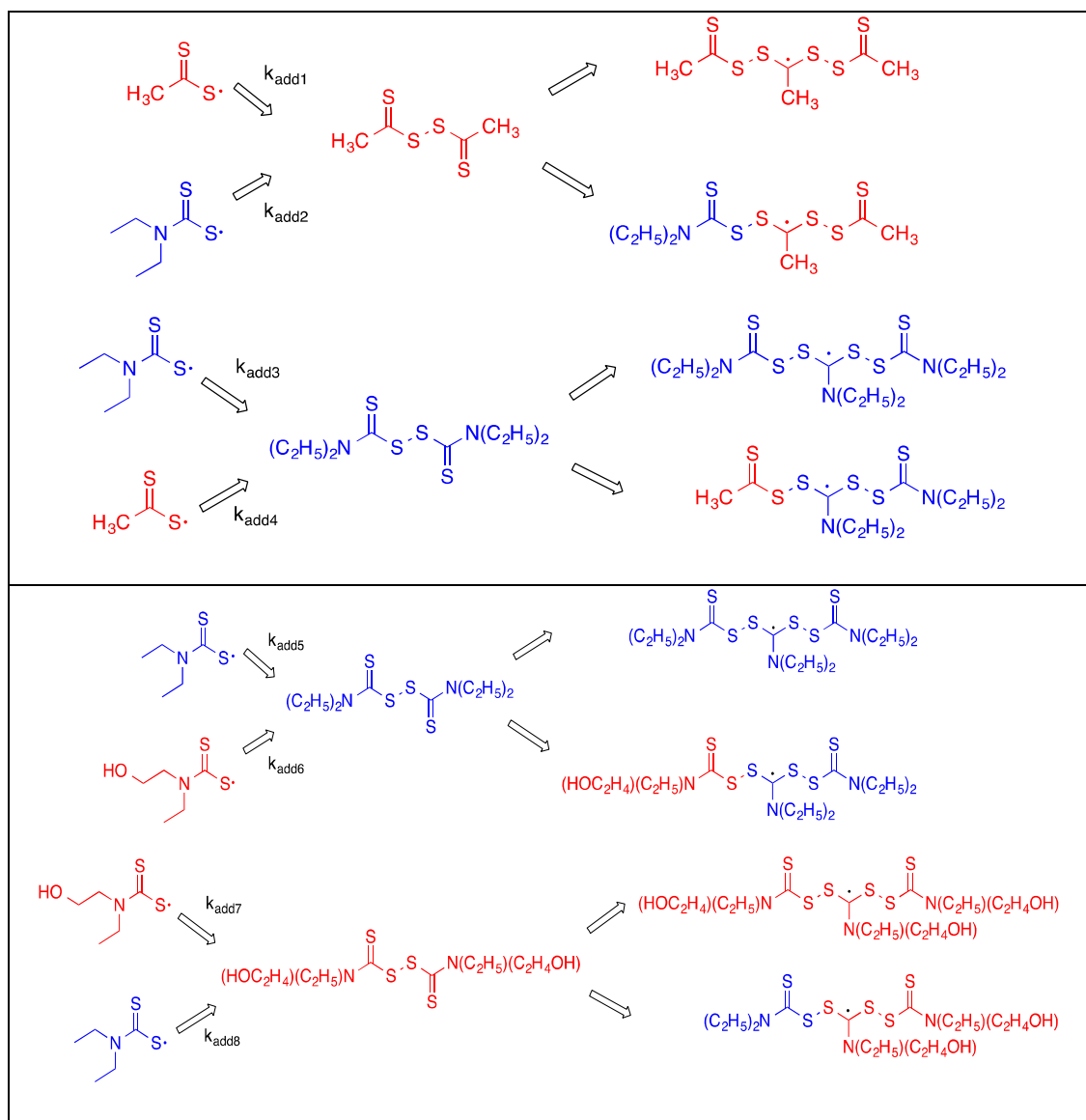
Scheme 4. Representation of the addition reactions and produced intermediates.

Table 3. Energetics (kJ/mol) and kinetics for the addition reactions in Scheme 4 at the G3(MP2)-RAD//M062X/6-31G(d) level.

Rxn #	Add1	Add2	Add3 (=Add5)	Add4	Add5 (=Add3)	Add6	Add7	Add8
ΔH_{rxn}	-40.15 (-39.82)	-27.05 (-26.19)	-23.80	-29.24	-23.80	-7.43	3.31	-6.59
ΔG_{rxn}	8.24 (8.56)	15.81 (16.68)	18.44	12.96	18.44	40.70	53.65	38.20

An ONIOM approximation to G3(MP2)-RAD in which the core is studied at G3(MP2)-RAD and outer shell is calculated MP2/G3MP2Large was used. G3(MP2)-RAD calculations for full geometries are mentioned in brackets.

Due to the difficulty of locating the transition states using M06-2X/6-31G(d), *ab initio* methods were tested for further analysis. These methods tend to overestimate reaction

barriers, whereas DFT methods tend to underestimate them, and hence it was thought that the *ab initio* methods should be better able to locate transition structures if they existed. The MP2/6-31G(d) method was used to locate the transition state geometries for the Add1 and the Add2 reactions. However, MP2 was not feasible for the other addition reactions due to the large size of the species involved. Therefore, the HF/6-31G(d) level of theory was chosen for consistently modelling all addition-fragmentation reactions (Table 4 and Figure 1). This level of theory is likely to overestimate reaction barriers and yet even here, the enthalpic barriers are either extremely low or submerged in the case of thiuram disulphide (TETD) with dithioacetate (DTA), indicating that pre-complexes probably play a role. Such submerged barriers have been noted previously for thiyl radical addition to C=S double bonds [35, 38-41] and arises because the high energy SOMO of the sulphur-centred radical is capable of the strong resonance interactions with the π* orbital of the substrate [35]. Overall there is a wide range of enthalpies depending on the Z-group, ranging from mildly exothermic to strongly endothermic, but importantly the Gibbs free energies of addition in all cases are positive, implying that addition is thermodynamically disfavoured and thus likely to be slow. When it does occur, fragmentation in either direction is expected to be fast and exergonic. Of the species studied, the lone pair donor substituted groups are again the most reactive to radical addition for the same cross-conjugation reasons outlined above.

Table 4. Energetics (kJ/mol) for the addition and fragmentation reactions in Scheme 4 at the G3(MP2)-RAD//HF/6-31G(d) level.

Rxn #	d (Å)	Addition				Fragmentation			
		ΔH_{rxn}	ΔG_{rxn}	$\Delta H^{\ddagger}$	$\Delta G^{\ddagger}$	$\Delta G^{\ddagger}$	ΔH_{rxn}	ΔG_{rxn}	$\Delta G^{\ddagger}$
Add1	2.373 2.444	-18.40 (-18.90) *-27.76*	30.00 (29.51) *24.39*	3.83 (4.38) *-9.89*	48.01 (48.57) *39.72*	18.01	18.40	- 30.00	18.01
Add2	2.390 2.468	-8.73 (-8.63) *-15.58*	34.39 (34.48) *32.89*	5.77 (9.40) *-2.45*	47.18 (50.81) *44.31*	19.26	5.66	- 35.83	19.26
Add3	2.294	21.59	63.97	-2.10	42.94	- 21.03	- 21.59	- 63.97	- 21.03
Add4	2.387	19.22	63.37	8.58	54.53	- 23.34	- 36.28	- 72.44	- 23.34
Add5	2.294	21.59	63.97	-2.10	42.94	- 21.03	- 21.59	- 63.97	- 21.03
Add6	2.293	-6.13	39.34	-38.76	12.61	- 10.51	- 45.08	- 80.88	- 10.51
Add7	2.368	-27.88	19.73	-33.17	12.96	-6.77	27.88	- 19.73	-6.77
Add8	2.362	2.66	46.68	-8.32	37.57	- 12.87	13.54	- 36.44	- 12.87

ONIOM (the core shell is studied at G3(MP2)-RAD and outer shell is calculated MP2/G3MP2Large). Where available, G3(MP2)-RAD//HF-6-31G(d) calculations for full geometries are mentioned and G3(MP2)-RAD//MP2/6-31G(d) data are provided in italics.
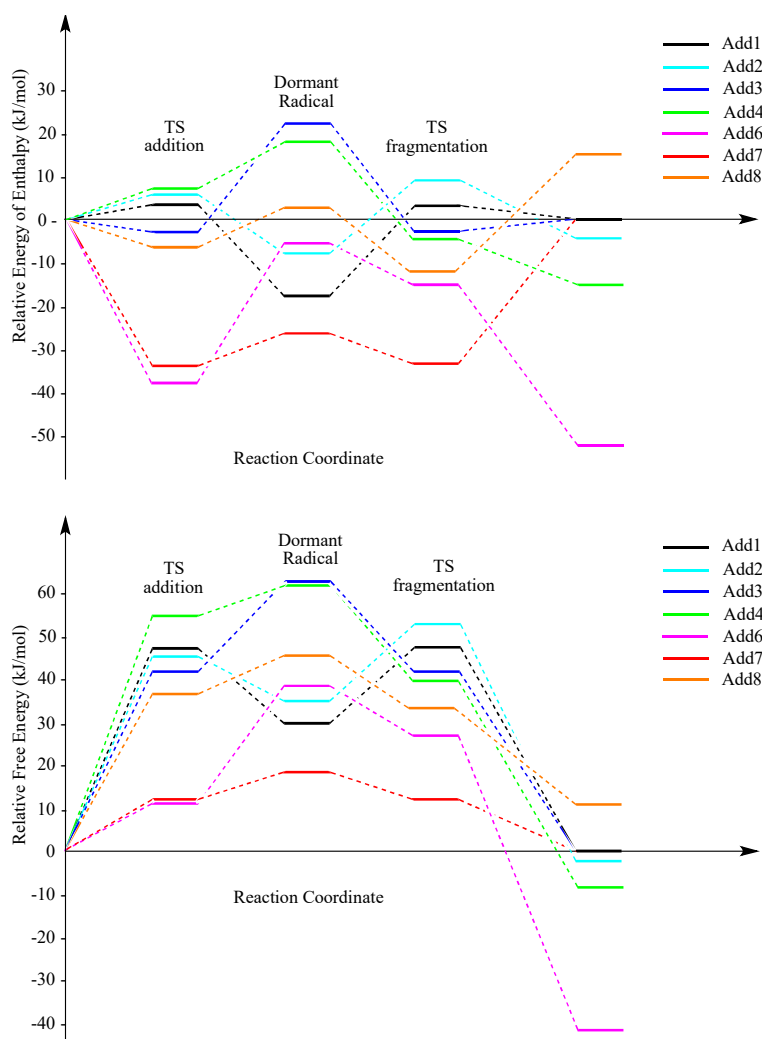
Figure 1. Relative enthalpies and free energies of reshuffling reactions at G3(MP2)-RAD//HF/6-31G(d) with ONIOM procedure.

CONCLUSION

In this study, reshuffling mechanism of thiuram disulphides has been investigated using quantum chemical tools. Among the dithiodisulphides studied, dibenzyl dithioacetate was shown be subject to side reactions which render it unsuitable for these self-healing polymer applications. The remainder of the species are generally resistant to side reactions. The most reactive compounds, both to homolytic cleavage and addition-fragmentation reactions are the nitrogen substituted species. This arises from cross-conjugation effects, and suggests that these and other lone-pair donor substituted agents are the best candidates for self-healing materials. The re-shuffling mechanism itself can in principle proceed via both direct cross-over and addition-fragmentation. The calculations herein suggest that while addition fragmentation occurs with submerged reaction barriers, the process itself is relatively unfavourable due to the instability of the

radical intermediate. Whilst full kinetic studies would be required to confirm this result, it is likely cross-over is the dominant pathway in the self-healing process.

References

1.   Caruso, M.M., et al., Mechanically-Induced Chemical Changes in Polymeric Materials. Chemical Reviews, 2009. 109(11): p. 5755-5798. DOI: 10.1021/cr9001353.

2.   Murphy, E.B. and F. Wudl, The world of smart healable materials. Progress in Polymer Science, 2010. 35(1-2): p. 223-251. DOI: 10.1016/j.progpolymsci.2009.10.006.

3.   Urban, M.W., Stratification, stimuli-responsiveness, self-healing, and signaling in polymer networks. Progress in Polymer Science, 2009. 34(8): p. 679-687. DOI: 10.1016/j.progpolymsci.2009.03.004.

4.   Wu, D.Y., S. Meure, and D. Solomon, Self-healing polymeric materials: A review of recent developments. Progress in Polymer Science, 2008. 33(5): p. 479-522. DOI: 10.1016/j.progpolymsci.2008.02.001.

5.   Kolmakov, G.V., K. Matyjaszewski, and A.C. Balazs, Harnessing Labile Bonds between Nanogel Particles to Create Self-Healing Materials. Acs Nano, 2009. 3(4): p. 885-892. DOI: 10.1021/nn900052h.

6.   Cordier, P., et al., Self-healing and thermoreversible rubber from supramolecular assembly. Nature, 2008. 451(7181): p. 977-980. DOI:10.1038/nature06669.

7.   Wang, Q., et al., High-water-content mouldable hydrogels by mixing clay and a dendritic molecular binder. Nature, 2010. 463(7279): p. 339-343. DOI:10.1038/nature08693.

8.   Rowan, S.J., et al., Dynamic covalent chemistry. Angewandte Chemie-International Edition, 2002. 41(6): p. 898-952. DOI: 10.1002/1521-3773(20020315)41:6<898::AID-ANIE898>3.0.CO;2-E.

9.   Maeda, T., H. Otsuka, and A. Takahara, Dynamic covalent polymers: Reorganizable polymers with dynamic covalent bonds. Progress in Polymer Science, 2009. 34(7): p. 581-604. DOI:10.1016/j.progpolymsci.2009.03.001.

10.   Deng, G.H., et al., Covalent Cross-Linked Polymer Gels with Reversible Sol-Gel Transition and Self-Healing Properties. Macromolecules, 2010. 43(3): p. 1191-1194. DOI: 10.1021/ma9022197.

11.   Nicolay, R., et al., Responsive Gels Based on a Dynamic Covalent Trithiocarbonate Cross-Linker. Macromolecules, 2010. 43(9): p. 4355-4361. DOI: 10.1021/ma100378r.

12.   Kamada, J., et al., Redox Responsive Behavior of Thiol/Disulfide-Functionalized Star Polymers Synthesized via Atom Transfer Radical Polymerization. Macromolecules, 2010. 43(9): p. 4133-4139. DOI: 10.1021/ma100365n.

13.   Amamoto, Y., et al., Programmed thermodynamic formation and structure analysis of star-like nanogels with core cross-linked by thermally exchangeable dynamic covalent bonds. Journal of the American Chemical Society, 2007. 129(43): p. 13298-13304. DOI: 10.1021/ja075447.

14.   Amamoto, Y., et al., Reorganizable Chemical Polymer Gels Based on Dynamic Covalent Exchange and Controlled Monomer Insertion. Macromolecules, 2009. 42(22): p. 8733-8738. DOI: 10.1021/ma901746n.

15.   Chen, X.X., et al., A thermally re-mendable cross-linked polymeric material. Science, 2002. 295(5560): p. 1698-1702. DOI: 10.1126/science.1065879.

16.   Amamoto, Y., et al., Polymers through Reshuffling of Trithiocarbonate Units. Angewandte Chemie-International Edition, 2011. 50(7): p. 1660-1663. DOI: 10.1002/ange.201003888.

17.   Ghosh, B. and M.W. Urban, Self-Repairing Oxetane-Substituted Chitosan Polyurethane Networks. Science, 2009. 323(5920): p. 1458-1460. DOI: 10.1126/science.1167391.

18.   Scott, T.F., et al., Photoinduced plasticity in cross-linked polymers. Science, 2005. 308(5728): p. 1615-1617. DOI: 10.1126/science.1110505.

19.   Amamoto, Y., et al., Self-Healing of Covalently Cross-Linked Polymers by Reshuffling Thiuram Disulfide Moieties in Air under Visible Light. Advanced Materials, 2012. 24(29): p. 3975-3980. DOI: 10.1002/adma.201201928.

20.   Garcia-Con, L.M., et al., A Sulfur-Sulfur Cross-Linked Polymer Synthesized from a Polymerizable Dithiocarbamate as a Source of Dormant Radicals. Angewandte Chemie-International Edition, 2010. 49(24): p. 4075-4078. DOI: 10.1002/anie.200906676.

21.   Frisch, M., G. Trucks, and H. Schlegel, GAUSSIAN03, Revision D. 01, Gaussian, Inc., Wallingford, CT, 2004. 90 Y. Zhao and DG Truhlar, MN-GFM 4.3. University of Minnesota, Minneapolis, 2009.

22.   H.-J. Werner, P.J.K., G. Knizia, F. R. Manby, M. Schütz, P. Celani, W. Györffy, D. Kats, T. Korona, R. Lindh, A. Mitrushenkov, G. Rauhut, K. R. Shamasundar, T. B. Adler, R. D. Amos, A. Bernhardsson, A. Berning, D. L. Cooper, M. J. O. Deegan, A. J. Dobbyn, F. Eckert, E. Goll, C. Hampel, A. Hesselmann, G. Hetzer, T. Hrenar, G. Jansen, C. Köppl, Y. Liu, A. W. Lloyd, R. A. Mata, A. J. May, S. J. McNicholas, W. Meyer, M. E. Mura, A. Nicklaß, D. P. O'Neill, P. Palmieri, D. Peng, K. Pflüger, R. Pitzer, M. Reiher, T. Shiozaki, H. Stoll, A. J. Stone, R. Tarroni, T. Thorsteinsson, M. Wang . MOLPRO 2012.1. 2015 [cited 2015; Available from: http://www.molpro.net/.

23.   Zhao, Y. and D.G. Truhlar, The M06 suite of density functionals for main group thermochemistry, thermochemical kinetics, noncovalent interactions, excited states, and transition elements: two new functionals and systematic testing of four M06-class functionals and 12 other functionals. Theoretical Chemistry Accounts, 2008. 120(1-3): p. 215-241. DOI: 10.1007/s00214-007-0310-x.

24.   Henry, D.J., M.B. Sullivan, and L. Radom, G3-RAD and G3X-RAD: Modified Gaussian-3 (G3) and Gaussian-3X (G3X) procedures for radical thermochemistry. Journal of Chemical Physics, 2003. 118(11): p. 4849-4860. DOI: 10.1063/1.1544731.

25.   Vreven, T. and K. Morokuma, Investigation of the S-0 -> S-1 excitation in bacteriorhodopsin with the ONIOM(MO : MM) hybrid method. Theoretical Chemistry Accounts, 2003. 109(3): p. 125-132. DOI 10.1007/s00214-002-0418-y.

26.   Izgorodina, E.I. and M.L. Coote, Reliable low-cost theoretical procedures for studying addition-fragmentation in RAFT polymerization. Journal of Physical Chemistry A, 2006. 110(7): p. 2486-2492. DOI: 10.1021/jp055158q.

27.   Degirmenci, I. and M.L. Coote, Effect of Substituents on the Stability of Sulfur-Centered Radicals. Journal of Physical Chemistry A, 2016. 120(37): p. 7398-7403. DOI: 10.1021/acs.jpca.6b08223.

28.   Atkins, P.W., Physical Chemistry. 4th ed. 1990, Oxford: Oxford University Press. DOI: 10.1002/bbpc.19900941026.

29.   Kroschwitz, J.I., These formulae are described in full in Coote, M. L. , in Encyclopedia of Polymer Science and Technology, Wiley, Editor. 2004: New York. p. 319-371.
        DOI: 10.1002/0471440264.pst083.

30.   Coote, M.L., C.Y. Lin, and A.A. Zavitsas, Inherent and transferable stabilization energies of carbon-and heteroatom-centred radicals on the same relative scale and their applications. Physical Chemistry Chemical Physics, 2014. 16(18): p. 8686-8696.
        DOI: 10.1039/C4CP00537F.

31.   Coote, M.L. and A.A. Zavitsas, Using inherent radical stabilization energies to predict unknown enthalpies of formation and associated bond dissociation energies of complex molecules. Tetrahedron, 2016. DOI: 10.1016/j.tet.2016.03.015.

32.   Matsunaga, N., D.W. Rogers, and A.A. Zavitsas, Pauling's electronegativity equation and a new corollary accurately predict bond dissociation enthalpies and enhance current understanding of the nature of the chemical bond. Journal of Organic Chemistry, 2003. 68(8): p. 3158-3172. DOI: 10.1021/jo020650g.

33.   Pauling, L., The nature of the chemical bond and the structure of molecules and crystals: an introduction to modern structural chemistry. Vol. 18. 1960: Cornell university press. ISBN-10: 0801403332.

34.   De Vleeschouwer, F., et al., An Intrinsic Radical Stability Scale from the Perspective of Bond Dissociation Enthalpies: A Companion to Radical Electrophilicities. Journal of Organic Chemistry, 2008. 73(22): p. 9109-9120. DOI: 10.1021/jo802018b.

35.   Degirmenci, I. and M.L. Coote, Comparison of Thiyl, Alkoxyl, and Alkyl Radical Addition to Double Bonds: The Unusual Contrasting Behavior of Sulfur and Oxygen Radical Chemistry. Journal of Physical Chemistry A, 2016. 120(10): p. 1750-1755. DOI: 10.1021/acs.jpca.6b00538.

36.   Moad, G., E. Rizzardo, and S.H. Thang, Living Radical Polymerization by the RAFT Process - A Third Update. Australian Journal of Chemistry, 2012. 65(8): p. 985-1076. DOI 10.1071/CH12295.

37.   Fischer, H. and L. Radom, Factors controlling the addition of carbon-centered radicals to alkenes-an experimental and theoretical perspective. Angewandte Chemie-International Edition, 2001. 40(8): p. 1340-1371. DOI: 10.1002/1521-3773(20010417)40:8<1340::AID-ANIE1340>3.0.CO;2-#.

38.   Greenwald, E.E., et al., A two transition state model for radical-molecule reactions: A case study of the addition of OH to C2H4. Journal of Physical Chemistry A, 2005. 109(27): p. 6031-6044. DOI: 10.1021/jp058041a.

39.   Senosiain, J.P., S.J. Klippenstein, and J.A. Miller, Reaction of ethylene with hydroxyl radicals: A theoretical study. Journal of Physical Chemistry A, 2006. 110(21): p. 6960-6970. DOI: 10.1021/jp0566820.

40.   Golden, D.M., The Reaction OH+C2H4: An Example of Rotational Channel Switching. Journal of Physical Chemistry A, 2012. 116(17): p. 4259-4266. DOI: 10.1021/jp302009t.

41.   Zhu, R.S., J. Park, and M.C. Lin, Ab initio kinetic study on the low-energy paths of the HO+C2H4 reaction. Chemical Physics Letters, 2005. 408(1-3): p. 25-30. DOI:10.1016/j.cplett.2005.03.133.

Türkçe Öz ve Anahtar Kelimeler
Polimer İyileşmesi Sırasında Kükürtlü Radikallerin Davranışını Anlamak

Isa Degirmenci, Michelle L. Coote

Öz: Yüksek seviye kompozit *ab initio* G3(MP2)-RAD yöntemi tiuram disülfürlerin ve türevlerinin (S=C(Z)S–SC(Z)=S, Z = CH$_3$, NEt$_2$, N(Et)CH$_2$CH$_2$OH, Ph, Bz) kendi kendine iyileşme mekanizmasını çalışmakta kullanılmıştır ve bu Z sübstitüentlerinin etkinlik üzerindeki etkileri çalışılmıştır. Cross-over ve tersinir katılma kısımlanma zincir iletim tepkimelerinin relatif olarak katkıları bulunmuş ve zincir kırılma yan tepkimelerinin olasılığı değerlendirilmiştir. Sonuçları rasyonelize etmek için, radikallerin ve kapalı kabuki türlerinin çeşitli kararlılaşma enerjileri değerlendirilmiştir. Çalışma, tiuram disülfidlerin kendi kendine iyileşme mekanizmasının baskın şekilde cross-over tepkimesi üzerinden gittiğini göstermektedir, çünkü zincir iletim mekanizmasında ara radikallerin enerjisi yüksektir. Çalışmaya dayanarak, en etkili kendi başına iyileşme sağlayan malzemelerin Z grubu olarak amin taşıdığı bulunmuştur; benzil ve türevlerini içeren yan grupların ise yan tepkimelere yol açtığı anlaşılmıştır.

Anahtar kelimeler: Kendi kendine iyileşen polimerler; tiuram disülfidler; radikal kararlılaşma enerjisi.

(This article was presented to the 28th National Chemistry Congress and submitted to JOTCSA as a full manuscript)

Synthesis and Characterization of Bio-Based Polyester Polyol

Tugba Yazici[1,2] and Mithat Celebi[1*]

[1]University of Yalova, Department of Polymer Engineering, 77100, Yalova, Turkey

[2]Hürkimsa Chemical Industry, Çayirova, Kocaeli, Turkey

Abstract: Polyurethanes are versatile polymeric materials and are usually synthesized by isocyanate reactions with polyols. Polyurethanes have been used in very wide applications such as rigid and flexible foams, coatings, adhesives, and elastomers because of variety of polyols and isocyanates. Usage of bio-based resources has been increased due to limited petroleum resources, environmental concerns and ensuring sustainability. Polyester polyols are based on aliphatic and aromatic dicarboxylic acids are one of the most important materials in polymer technologies. Bio-based polyester polyols from renewable resources were successfully synthesized with different molecular weight at low acid value and desired hydroxyl value. In addition, the properties of the bio-based polyester polyols were compared with petroleum-based analogues.

INTRODUCTION

Polyester polyols based on aliphatic and aromatic dicarboxylic acids are one of the most important materials in polymer technologies [1]. A large volume of plant oils is used as renewable resources to produce various chemicals which are industrially important to make soaps, cosmetic products, surfactants, lubricants, diluents, plasticizers, inks, agrochemicals, composite materials, and food industry [2]. Vegetable oils are one of the most important renewable resources in the chemical industry due to their biodegradability, availability, low-cost price, environmental acceptance, renewability, and non-toxic nature [3–8]. Vegetable oils and their derivatives have been widely used for the production of various polymers including polyols. Vegetable oil derivatives, such as fatty acids, fatty acid esters, and crude glycerol, can be obtained via hydrolysis or transesterification of vegetable oils [4]. Polyols and polyurethanes with properties comparable to those of petroleum-based analogs have been prepared from vegetable oils and their derivatives for various applications such as foams, coatings and adhesives, *etc*. [9–11].

Polyester polyols are the second most important group of oligo-polyols for the production of polyurethanes after polyether polyols. Polyester polyols have stable and specific practical applications due to some superior characteristics of the resulting polyurethanes [9]. The superior characteristics of polyester polyol based polyurethanes are explained by a better crystalline structure in the urethane segment, compared to the majority of polyether polyols which are amorphous, due to the superior secondary forces between the polyester chains and also due to a superior thermal and fire resistance, compared to polyether polyol based polyurethanes. Polyester based polyurethanes have a superior solvent resistance compared to the polyether-based polyurethanes. Polyester polyols were employed in both rigid and flexible polyurethane formulations [6, 10]. The most important segments of polyester polyol applications are those of polyurethane elastomers, flexible foams, coatings, adhesives, rigid foams, synthetic leather, and sealants [1, 12].

In this work, production of polyester polyols was carried out by using dicarboxylic acids, diols, triols, and polyol from renewable resources with the presence of a catalyst.

MATERIALS AND METHODS

Adipic acid (99% pure; Acar Kimya, Turkey), phthalic anhydride (99% pure; Acar Kimya, Turkey), terephthalic acid (99% pure; Sigma-Aldrich, Turkey), ethylene glycol (99% pure; Acar Kimya, Turkey), diethylene glycol (99% pure; Acar Kimya, Turkey), trimethylolpropane (99% pure; Sigma-Aldrich, Turkey), glycerol (99% pure; Acar Kimya, Turkey) were used. Sorbitol was kindly obtained from Sunar Mısır, Turkey.

The dicarboxylic acids which are used to production of polyester polyols in this study were listed in Table 1.

Table 1: Main properties of used dicarboxylic acids.

	Adipic Acid (AD)	**Phthalic anhydride (PA)**	**Terephthalic acid (TPA)**
Appearance (25 ºC)	White powder	White flakes	White crystals
Molecular Weight (g/mol)	146.14	148.1	166.13
pH(of a solution)	3.2 (0.1% solution)	2 (6 g/L aq. sol.)	-
Density (g/cm³)	1.360	1.53	1.522
Melting point/Boiling point (˚C)	152.1 / 337.5	131.6 / 295	300 / decompose
pH	4.43 / 5.41	-	3.51 / 4.82

Table 2: Main properties of the used glycols

	Ethylene glycol(EG)	**Diethylene glycol (DEG)**	**Trimethyl olpropane (TMP)**	**Glycerol**	**Sorbitol (ST)**
Appearance (25 ˚C)	Colorless liquid	Liquid	Colorless solid	Liquid	Crystalline solid
Functionality	2	2	3	3	6
Melting Point/Boiling Point (˚C)	-12.9 /197.3	-10.45/ 244	58 / 285	18 / 290	95 / 296
Molecular Weight (g/mol)	62.07	106.12	134.14	92.08	182.17
Density (25 ˚C g/cm³)	1.1132	1.118	1.084	1.261	1.489

Synthesis of Bio-Based Polyester Polyols

Commonly used diols and triols for production of polyester polyols were listed in Table 2. Ethylene glycol and diethylene glycol which are bifunctional alcohols (glycols) were used in the synthesis of polyesters. Trifunctional ones, glycerol and trimethylolpropane were

used. In addition, sorbitol from corn starch sources wasused in this work. Sorbitol polyol which is obtained from renewable resource contains 6 hydroxyl groups.

The direct polyesterification reaction was self-catalyzed by carboxyl groups of the acid reactants. However, due to the reduction of the concentration of these groups with increasing conversion, external catalysts were often used to maintain the rate of reaction. Stannous octoate and p-toluene sulfonic acid catalysts were used in synthesis.

The excess of diol hasinfluence in final M_W of polyester. Usually, in industry a 5-15% excess of diol is used.

The stoichiometric calculation;

$$(n+1) \ R(OH)_2 + n \ R'(COOH)_2 \longrightarrow HO[ROOCR'COO]_nROH + 2n \ H_2O \quad (Eq. \ 1)$$

The stoichiometric ratio was n mol of diacid for (n+1) mol of diol.

Experimental apparatus
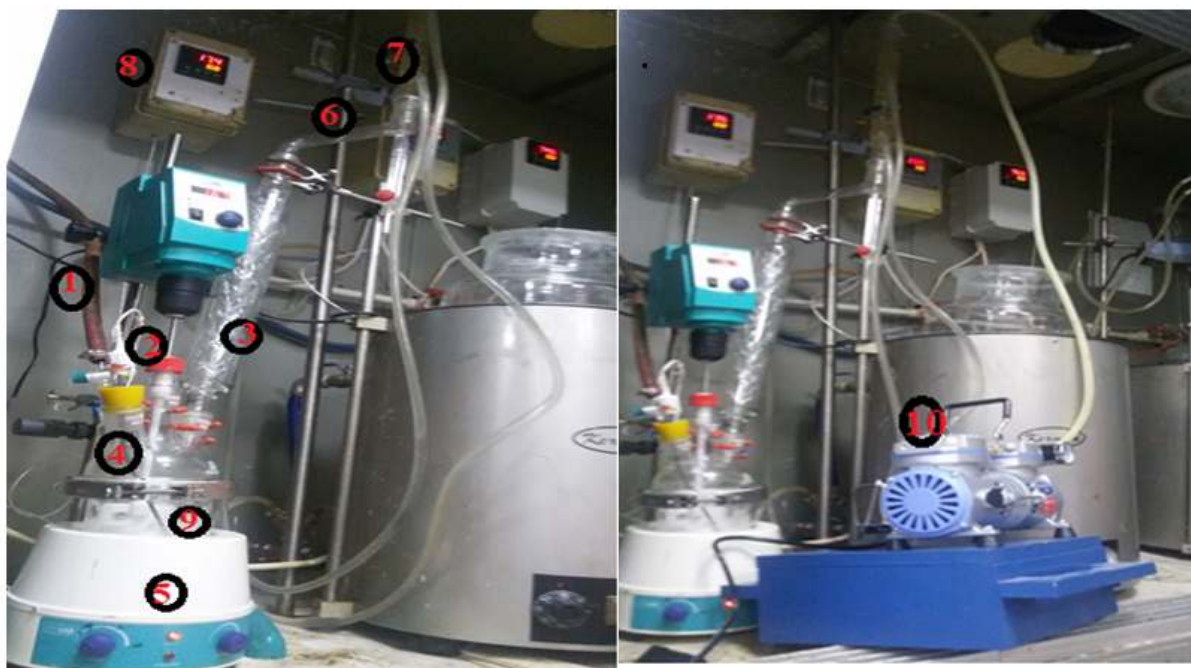
Figure 1: Set up equipment.

Set up equipment:1.Nitrogen spurge, 2.Stirrer, 3.Vigreux column, 4.Thermocouple, 5.Heating mantle, 6.Dean-Stark apparatus, 7.Condenser, 8.PID controller, 9.Three-necked round bottom flask, 10. Vacuum pump.

Polycondensation

To a three-necked reactor with a previously measured weight of dicarboxylic acid and glycol with PID controller set at 100 °C, constant stirring and under nitrogen atmosphere. The temperature was increased alternately from 140 to 220 °C (at 140-160-180-200-220 °C). The reaction was very slow at low temperatures (120-140 °C). Therefore, the reflux of water was negligible at 120-140 °C. The reflux of water was introduced at 170-180 °C. When no further reflux of water was observed, a few grams of resin (1-2 g) should be taken in order to measure the acid number by titration with 0.1 mol/L alcoholic solution of KOH. When the acid number (V_H) is lower than 3.0 mg KOH/g, the nitrogen flow should be increased. Vacuum can be applied to speed up the process. The acid number should be measured again and the synthesis is finished when V_H is lower than 1.0 mgKOH/g and hydroxyl value (V_{OH}) is required. In parallel with the acid value (V_H) analysis, hydroxyl value (V_{OH}) should be also measured. For this 2-3 g of resin should be taken and the V_{OH} was determined by titration with 0.5 mol/L alcoholic solution of KOH. The industrially used parameters to control the quality of the polyols are: appearance, color, hydroxyl number (V_H),acid number (V_{OH}), amount of water removed, -M_W Distribution, -Infrared Fourier Transform-Attenuated Total Reflectance Spectroscopy (FTIR-ATR), -viscosity and –density. Moreover, some of controlling parameters (V_H, V_{OH}, M_W) should be calculated and checked during the whole reaction process.

RESULTS AND DISCUSSION

In this work, mainly the effects of reaction time, the amount of catalyst, reaction temperature, and the type of reactants and its ratio were investigated in the synthesis of polyesters. Percentage ratio moles of dicarboxylic acids, diols, triols, and renewable glycols used to each formulation were shown in Table 3.

Table 3: Formulations of polyester polyol synthesis (mole %) in this study.

Number of Formulation	AD	TPA	PA	EG	DEG	TMP	Glycerol	Sorbitol
		ACIDS		DIOLS		TRIOLS		OTHER GLYCOLS
1.	0.63			1.26				
2.	1.00				1.92	0.08		
3.	1.00				1.98			0.02
4.		0.36	0.22		1.16			
5.		0.56			1.00		0.22	
6.		0.25	0.15		1.00		0.11	
7.		0.27	0.10		1.00	0.11		
8.		0.33	0.13		1.00		0.29	

Hydroxyl and acid numbers are indirectly proportional to polyesters' molecular weight. Table 4 represents the final acid and hydroxyl values obtained for eight syntheses.

Table 4: The results of acid value and hydroxyl value, molecular weight, amount of water distilled during process and density.

Number of formulation	Capacity of reactor (L)	V_H [mgKOH /g polyol]	V_{OH} [mgKOH /g polyol]	M_W [g/mol]	% Reflux of water	Density (g/cm³)
1.	0.5	5.25	300	367.56	5.0	1.28
2.	0.5	5.95	350	472.82	5.6	1.18
3.	0.5	7.8	380	433.99	5.2	1.16
4.	0.5	5.6	250	438.97	5.5	1.23
5.	0.5	5.96	350	346.72	4.8	1.19
6.	0.5	7.2	315	383.05	5.6	1.19
7.	0.5	7.0	350	345.71	5.1	1.18
8.	0.5	6.9	350	377.24	5.2	1.20

Figure 2 presents the typical behavior of the curves of acid number, hydroxyl number and M_W over time for a produced polyol. The M_W was calculated from the V_H and V_{OH}.
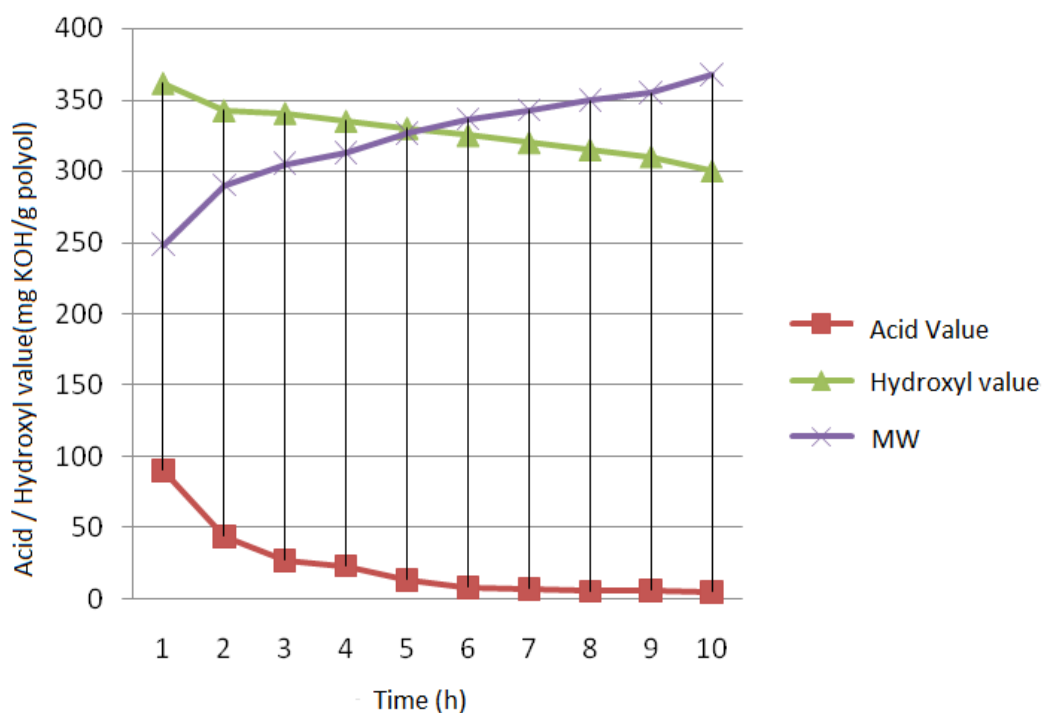
Figure 2: Number the fact of 1 formulation controlled medium values of V_H, V_{OH} and M_W over time.

FTIR spectra of polyester polyol was presented in Figure 3.
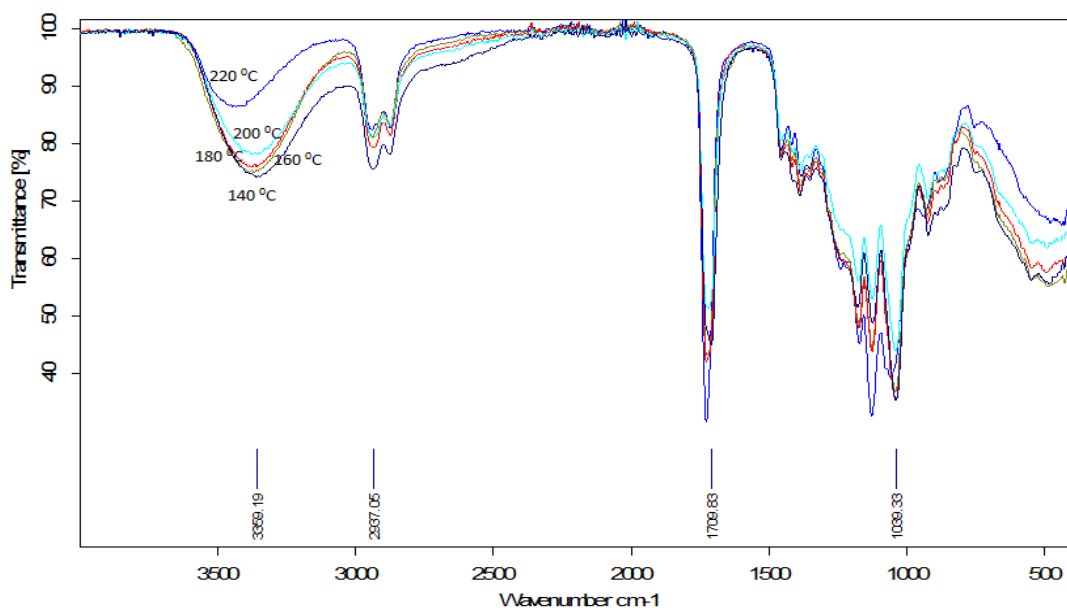
Figure 3: FTIR analysis of Number 1 formulation.

The peak at 1700 cm^{-1} corresponding to the C=O stretch that was saturated carboxylic acid peak. The peak 2937 cm^{-1} was corresponding to the C-H stretch. Also, the fact of hydroxyl band has high intensity-peak at near 3350 cm^{-1}.High hydroxyl number polyester polyol were reached for rigid polyurethane. As the reaction temperature up to 220 °C from 140 °C, the hydroxyl band formed high. This means that the reaction was completed.

The experimental part of this work involves the synthesis of saturated polyester polyols with petroleum glycols and biodegradable glycols. Sorbitol, which is a biodegradable and renewable polyol, has been produced from corn starch in Turkey. Different molecular weight polyester polyols were synthesized. However, the main goal of this study was to obtain saturated polyester polyols with high molecular weight. Polyesterification was confirmed via FTIR-ATR spectroscopy. Polyester polyols were synthesized successfully at low acid value and desired hydroxyl value.

REFERENCES

1. Ionescu, M. (2007). Chemistry and technology of polyols for polyurethanes. Polymer International (Vol. 56). DOI:10.1002/pi.2159.

2. Noreen A, Zia KM, Zuber M, Tabasum S, Zahoor AF. Bio-based polyurethane: An efficient and environment friendly coating systems: A review. Progress in Organic Coatings. 2016 Feb;91:25–32. DOI: 10.1016/j.porgcoat.2015.11.018.

3. Campanella, A., Rustoy, E., Baldessari, A., &Baltans, M. A. (2010). Lubricants from chemically modified vegetable oils. Bioresource Technology, 101(1), 245–254. DOI:10.1016/j.biortech.2009.08.035.

4. Alagi, P., & Hong, S. C. (2015). Vegetable oil-based polyols for sustainable polyurethanes. Macromolecular Research, pp. 1–8. DOI:10.1007/s13233-015-3154-6.

5. Desroches, M., Escouvois, M., Auvergne, R., Caillol, S., &Boutevin, B. (2012). From Vegetable Oils to Polyurethanes: Synthetic Routes to Polyols and Main Industrial Products. Polymer Reviews, 52(1), 38–79. DOI:10.1080/15583724.2011.640443.

6. Pfister, D. P., Xia, Y., &Larock, R. C. (2011). Recent advances in vegetable oil-based polyurethanes. Chem. Sus. Chem. DOI:10.1002/cssc.201000378.

7. Petrovic, Z. (2008). Polyurethanes from Vegetable Oils. Polymer Reviews, 48(1), 109–155. DOI:10.1080/15583720701834224.

8. Polyols, V. O. (2015). Feature Article, 23(12), 1079–1086. DOI:10.1007/s13233-015-3154-6.

9. Kadkin O, Osajda K, Kaszynski P, Barber TA. Polyester polyols: Synthesis and characterization of diethylene glycol terephthalate oligomers. Journal of Polymer Science Part A: Polymer Chemistry. 2003 Apr 15;41(8):1114–23. DOI: 10.1002/pola.10655.

10. Sonnenschein MF. Polyurethanes: science, technology, markets, and trends. Hoboken, New Jersey: Wiley; 2015. 417 p. ISBN: 978-1-118-73783-5.

11. Septevani, A. A., Evans, D. A. C., Chaleat, C., Martin, D. J., &Annamalai, P. K. (2015). A systematic study substituting polyether polyol with palm kernel oil based polyester polyol in rigid polyurethane foam. Industrial Crops and Products, 66, 16–26. DOI:10.1016/j.indcrop.2014.11.053

12. Ang, K. P., Lee, C. S., Cheng, S. F., &Chuah, C. H. (2014). Synthesis of palm oil-based polyester polyol for polyurethane adhesive production. Journal of Applied Polymer Science, 131(6). doi:10.1002/app.39967

Türkçe Öz ve Anahtar Kelimeler

Biyo-Esaslı Poliester Poliolün Sentezi ve Karakterizasyonu

Tugba Yazici ve Mithat Celebi

Öz: Poliüretanlar genellikle izosiyanatların poliollerle tepkimesi ile elde edilen çok yönlü polimerik malzemelerdir. Poliüretanlar, poliollerin ve izosiyanatların çeşitliliğinden dolayı sert ve esnek köpükler, kaplamalar, yapıştırıcılar ve elastomerler gibi çok çeşitli uygulamalarda kullanılmaktadırlar. Biyo-esaslı kaynakların kullanımı sınırlı petrol kaynakları, çevresel kaygılar ve sürdürülebilirliğin sağlanması nedeniyle artmaktadır. Alifatik ve aromatik dikarboksilli asitlere dayanan poliester polioller polimer teknolojisinde en önemli malzemelerden biridir. Yenilenebilir kaynaklardan üretilen biyo-esaslı poliester polioller, düşük asit değerinde ve istenen hidroksil değerine sahip olacak şekilde farklı moleküler ağırlıklarda başarı ile sentezlendi. Ek olarak, biyo-esaslı poliester poliolün özellikleri petrol esaslı benzerleri ile karşılaştırıldı.

Anahtar kelimeler: Poliester poliol; yenilenebilir kaynaklar; poliesterleşme.

Thermochemical Conversion Behavior of Different Biomass Feedstocks: Pyrolysis and Gasification

Işıl Işık-Gülsaç[1*], Yeliz Durak-Çetin[1], Berrin Engin[1], Parvana Gafarova-Aksoy[1], Hakan Karataş[1], Alper Sarıoğlan[1]

[1]TUBITAK Marmara Research Center, Energy Institute, P. O. Box 21, 41470, Gebze Kocaeli-TURKEY

Abstract: In this study, a bench-scale bubbling fluidized bed (BFB) gasifier and thermogravimetric analyzer (TGA) were applied for the determination of the thermochemical conversion reactivity of biomass fuels under both gasification and pyrolysis conditions. Six different biomass feedstocks, namely; straw pellet (SP), softwood pellet (WP), torrefied wood chips (TWC), pyrolysis char (PC), milled sunflower seed (MSS) and dried distillers' grains and solubles (DDGS) were investigated. TGA of biomass feedstocks were carried out under pyrolysis conditions at four different heating rates (2-15 °C/min). Raw data obtained from the experiments were used to calculate the kinetic parameters (A, E_a) of the samples by using two different models; Coats-Redfern and Isoconversional Method. TGA analysis showed that pyrolysis char was the only sample having decomposition temperature above 800 K since it was the pre-pyrolized sample before gasification. According to Derivative Thermogravimetric Analysis (DTG) profiles, two peaks and two shoulders at around 450-650 K were observed for DDGS whereas no peaks were detected for pyrolysis char as the indication of absence of volatiles/cellulosic components. It was seen that the highest devolatilization rates and devolatilization temperatures (associated mainly with cellulose decomposition) were obtained for softwood and torrefied wood samples, which had the least char yields among the other biomass feedstocks. It was seen that WP was more reactive for thermochemical conversion and less prone to agglomeration. Furthermore high ash content and agglomeration index of MSS were the potential drawbacks in front of its utilization via thermochemical conversion. During the air gasification of these feedstocks (except DDGS), the product syngas was characterized in terms of main gas composition, tar, and sulfur compounds. It was shown that the highest cold gas efficiency, carbon conversion and calorific value were obtained for the gasification of SP. On the other hand, SP had some drawbacks regarding its high agglomeration tendency and low deformation temperature. Among all feedstocks, gasification reactivity of MSS was found to be quite poor. MSS seemed to expose to pyrolization instead of gasification. WP and TWC were gasified with acceptable conversion values and efficiencies when compared with SP. It was understood that WP is the preferred choice for the thermochemical conversions.

Keywords: Thermochemical conversion; gasification; pyrolysis; syngas; biomass.

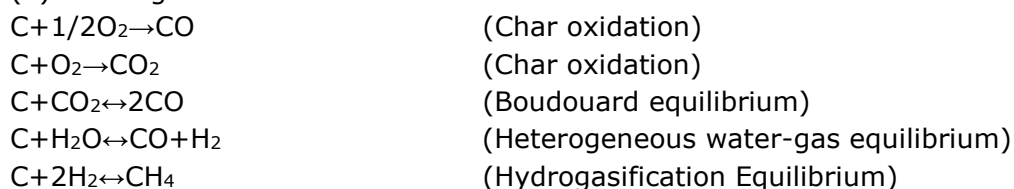*Corresponding author. E-mail: isil.gulsac@tubitak.gov.tr, tel: +902626772619.

INTRODUCTION

Biomass can be a generous source for energy, fuels, and chemicals (1, 2). Gasification is a process for converting lignocellulosic biomass and/or agricultural wastes into fuel gases (having BTU of 5-15 MJ/Nm^3) using air, air/oxygen, steam, CO_2, or their combinations as gasification agents. The syngas produced can be directly utilized as fuels for heat and electricity generation, or as feedstocks for chemical production such as methanol, ethanol, dimethyl ether, and Fischer-Tropsch oils (3). Many studies were conducted to evaluate the efficiency and performance of the biomass gasification process. Gasification characteristics of various types of biomasses were investigated such as: sugarcane residue (4), rice hulls (5), pine sawdust (6), almond (7, 8), wheat straw (9), food waste (10), and wood-based biomass (11). Lignocellulosic biomass is mainly composed of cellulose and hemicellulose (60-80% dry basis), lignin (10-25%), some extractives, minerals, and small amounts of sulfur, nitrogen, and chlorine (12). The amount of these elements varies depending on species and location (13). Three main components of lignocellulosic biomass show different decomposition profiles during pyrolysis. Hemicellulose dehydrates at 90°C and reaches a maximum decomposition rate at around 300 °C whereas cellulose begins to decompose after hemicellulose and reaches a maximum decomposition rate at 400 °C approximately. Lignin has more complex structure than hemicellulose or cellulose, its thermal decomposition occurs between 300 and 600 °C (14). A simplified mechanism for biomass gasification can be represented as follows, consisting of four overlapping aspects (15):

(1) Pyrolysis: Biomass → Char, H_2, CO, CO_2, H_2O, CH_4, C_nH_m, tars, *etc*.

(2) Tar cracking: Tar → H_2+CO+CO_2+*etc.*

(3) Heterogeneous reactions:
$C+1/2O_2 \rightarrow CO$	(Char oxidation)
$C+O_2 \rightarrow CO_2$	(Char oxidation)
$C+CO_2 \leftrightarrow 2CO$	(Boudouard equilibrium)
$C+H_2O \leftrightarrow CO+H_2$	(Heterogeneous water-gas equilibrium)
$C+2H_2 \leftrightarrow CH_4$	(Hydrogasification Equilibrium)

(4) Homogeneous reactions:
$CO+1/2O_2 \rightarrow CO_2$	
$H_2+1/2O_2 \rightarrow H_2O$	
$CO+H_2O \leftrightarrow CO_2+H_2$	(Water-gas shift)
$C_xH_y+xH_2O \leftrightarrow xCO+(x+y/2)H_2$	(Steam reforming)
$C_xH_y+xCO_2 \leftrightarrow 2xCO+ y/2\ H_2$	(Dry reforming)
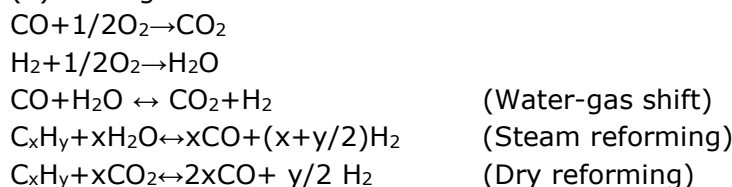
It is known that the cellulose, hemicellulose, and lignin amounts in the biomass affect gasification behavior. Yang *et al.* studied hemicellulose, cellulose, and lignin pyrolysis characteristics and reported that lignin contributed to higher H_2 yields than cellulose (16). In a study by Kumabe *et al.*, carbon conversion efficiencies for cellulose, hemicelluloses, and lignin were reported as 97.7%, 92.2%, and 52.8%, respectively (11). They also stated that the gasification products were similar for lignin and hemicelluloses, whereas cellulose produced higher amounts of CO_2

and CH_4 in the product gas. Kezhong *et al.* co-gasified Shenmu coal with pine sawdust and rice straw, and they found out that H_2 composition in syngas increased from 17.66% for pine sawdust to 21.96% for rice straw (17). Herguido *et al*. investigated the steam gasification behavior of different lignocellulosic residues. According to their results, syngas composition varied with the biomass type and gasification temperature (18). There are many factors influencing thermochemical conversion process: (a) intrinsic biomass characteristics such as moisture content, carbohydrate and ash compositions, bulk density, and particle size/shape distributions (b) thermochemical conversion system design and operation conditions like steam to biomass ratio, equivalence ratio, heating rate, temperature profile of the reactor and heat input. This first group of factors determines the reactivity of the biomass and can impact the economics of transforming biomass into value-added products. The aim of this study is to compare the thermochemical conversion reactivity of six different biomass samples, namely straw pellet, softwood pellet, torrefied wood chips, pyrolysis char, milled sunflower seed and dried distillers' grains and solubles (DDGS). For this purpose, all samples were chemically characterized to identify the samples. Then, their gasification tendencies (except DDGS) and pyrolysis behavior were investigated via using bubbling fluidized bed gasifier test unit and thermogravimetric analyzer, respectively.

MATERIALS AND METHODS

Characterization of the biomass feedstocks

The straw pellet (SP), softwood pellet (WP), torrefied wood chip (TWC), pyrolysis char (PC), milled sunflower seeds (MSS) and dried distillers' grains and solubles (DDGS) were supplied in the scope of "The European Research Infrastructure for Thermochemical Biomass Conversion (BRISK)" project funded by European Commission Seventh Framework Programme. Before analysis, the raw materials were prepared by grinding and sieving the samples below 250 μm. Proximate and ultimate analyses of the samples were conducted according to the relevant American Society for Testing and Materials (ASTM) standards. Their lower and higher heating values both on original and dry basis were measured and calculated as described in ASTM D 5865. Perkin Elmer Optima 2100 Inductively Coupled Plasma (ICP)-OES analyzer and X-Ray Fluorescence were applied to determine the inorganic content of the fuel and agglomeration indexes. Ash melting behaviors of the samples (initial deformation, softening, hemispherical, and fluid temperatures of ashes) were analyzed by LECO AF700 Ash Fusion Determinator.

Pyrolysis experiments of biomass feedstocks by TGA

Thermogravimetric analysis of biomass feedstocks have been carried out under pyrolysis conditions by using Mettler Toledo TGA 851 instrument. Experimented TGA conditions are given in Table 1. Raw data obtained from the experiments were used to calculate kinetic parameters (A, E_a) of samples by using two different models; Coats-Redfern and Isoconversional method.

Table 1: TGA conditions for the pyrolysis of the biomass feedstocks.

Initial weight. m_0	~35 mg
N_2 flow rate	40 mL/min
Fine powder sample size	<250 μm
Heating rate	2-5-10-15 °C/min
Initial-final temperature	25-850 °C

Experimental apparatus: Bubbling fluidized bed gasifier

The gasification experiments were performed in a 20 kW$_{th}$ atmospheric bubbling fluidized bed gasifier, shown in Figure 1. The gasification reactor made of AISI 310S stainless steel, with a height of 2.29 m and an inner diameter of 82 mm. Four thermocouples, T/C-1, T/C-2, T/C-3 and T/C-4, were installed to measure the temperature at the axis of the reactor. The thermocouples were of type K. Two electrical furnaces were used to heat the reactor. Two screw feeders, positioned one on top of the other, were used to feed the biomass fuel to the reactor. Nitrogen gas at ambient temperature was used to facilitate the fuel feeding. Air, as a gasification agent, was fed to the gasifier at ambient temperature by means of an air compressor. All flow rates were measured/controlled with a rotameter. The particle sizes of SP, WP, TWC, PC, MSS and DDGS were in the range of 0.5–1.0 mm. The fuel feeding rates of the feedstocks, equivalence ratios (ER) and typical operation parameters were given in Table 2. Silica sand (99.2% SiO_2, 0.5% Al_2O_3 and 0.1% Na_2O) was used as the bed material. The bed material had a mean particle size of 450 μm.
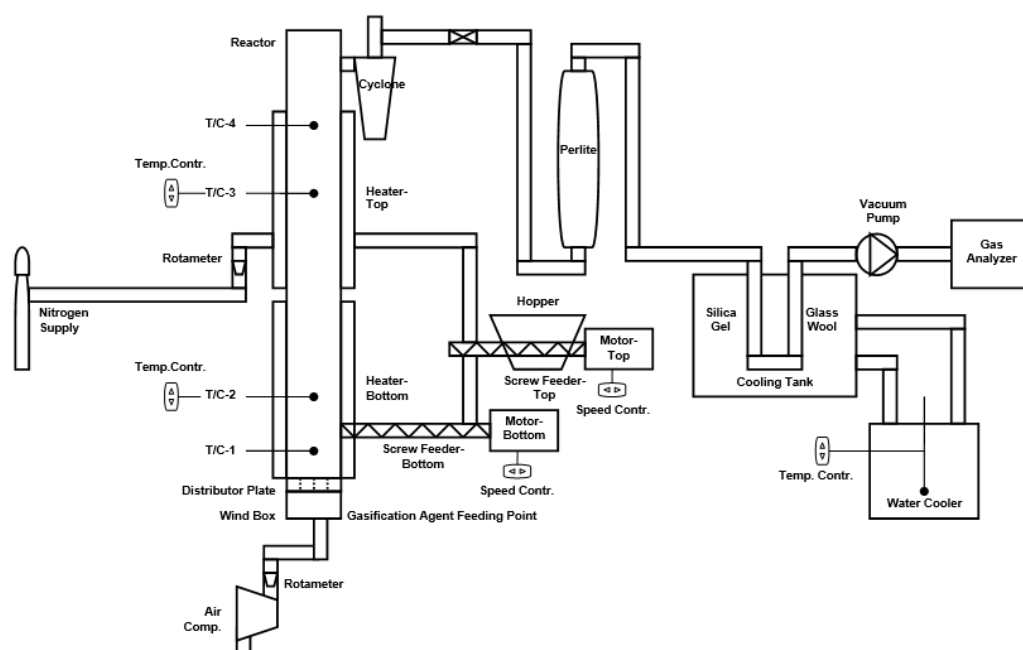
Figure 1: The schematic diagram of the bubbling fluidized bed gasifier.

Table 2: Typical operation parameters for biomass gasification experiments.

	SP	WP	TWC	PC	MSS
Reactor temperature (°C)	780	760	760	740	760
ER	0.24	0.21	0.29	0.25	0.25
Fuel feeding rate (g/h)	566	581	400	466	490

Syngas characterization

Product gas leaving the gasifier passed from the cyclone where the particulates in the product gas were captured. Two T unions were placed at the cyclone outlet. One of them was connected to a sulfur inert tube, a vacuum pump, and a Tedlar bag. This line was used for sampling of syngas and for measurement of its composition, along with the contaminants like H_2S, COS and NH_3. EPA 15 Method "Determination of hydrogen sulfide, carbonyl sulfide, and carbon disulfide emissions from stationary sources" was applied and Agilent 6890N gas chromatograph equipped with pulsed flame photometric detector was used to analyze the sulfur-based compounds. Total sulfur content of the gas samples was measured by Analytic Jena multi EA® 5000 UV Fluorescence as well.

Syngas composition (CO, CO_2, H_2, CH_4, and O_2) was measured with an ABB AO2040 online gas analyzer. CO, CO_2, and CH_4 were detected by the non-dispersive infrared absorption technique, whereas hydrogen and oxygen were analyzed with thermal conductivity and paramagnetic detectors, respectively. The N_2 component of the product gas is calculated from the balance. The amounts of C1 - C5 hydrocarbon components of the syngas were determined by gas chromatographic measurements equipped with flame ionization detector (FID), by sampling through the Tedlar bags. The second T union at the cyclone outlet was used for tar sampling. Tar compounds were collected according to the tar protocol (DS/CEN/TS 15439). Iso-propanol was used as a solvent for tar trapping. Tar compounds were analyzed by a GC-FID.

RESULTS AND DISCUSSION

Biomass Feedstock Characterization

The results of proximate and ultimate analysis together with the higher heating values of the samples are given in Table 3. As it is seen in the table, PC has the highest fixed carbon and the lowest volatile matter content amongst the others, which is the indicative of its pyrolized nature. WP and SP are seen to have nearly the same amount of moisture and fixed carbon. On the other hand, the fixed carbon content of torrefied wood chips was 8% higher than that of WP as expected due to the release of its volatile matter upon torrefaction. Regarding the ash, wood was distinguished with its low ash content while MSS and DDGS were the ash-rich samples among the others. It is known that woody samples usually contains relatively low amount of ash while straw, bark, grasses and grain have significantly higher ash contents [19].

Tables 4, 5 and 6 show the chemical analysis of the ash, ash melting temperatures and calculated agglomeration indexes for all samples, respectively. It is known that high levels of alkali/alkaline metals and chlorine content are responsible for fouling, corrosion, sintering and agglomeration during combustion and gasification processes (20). It was seen in the Tables that MSS and DDGS have higher amounts of alkali and alkaline earth metals (K, Na, Ca, *etc*.) than the others, which react with silica to form alkali and alkaline earth metal silicates with low melting temperatures.

When the fuel analysis results of the samples were compared, SP, MSS and DDGS were the samples with relatively high ash content. On the other hand, in terms of agglomeration index of (Si+P+K)/(Ca+Mg), these samples seemed to be more prone to agglomeration during thermochemical conversion as well. The lowest ash fusion temperatures of these samples supported its agglomeration tendency. This is thereof high Na_2O and K_2O contents of their ash.

Table 3: Proximate and ultimate analysis and heating values of the biomass feedstocks.

	SP	WP	TWC	PC	MSS	DDGS
PROXIMATE ANALYSIS (wt.%)						
Original Basis						
Moisture	7.40	7.52	5.58	2.16	8.42	6.88
Volatile matter	70.50	76.85	71.53	20.27	66.36	71.50
Ash	5.85	0.53	0.17	2.17	7.44	6.14
Fixed carbon	16.25	15.11	22.73	75.40	17.78	15.50
Dry Basis						
Volatile matter	76.13	83.09	75.75	20.71	72.46	76.77
Ash	6.32	0.57	0.18	2.21	8.12	6.59
Fixed carbon	17.55	16.34	24.07	77.07	19.42	16.64
ULTIMATE ANALYSIS (dry basis, wt.%)						
C	49.52	54.30	58.66	87.53	48.86	49.02
H	5.72	5.80	5.52	3.73	5.80	6.38
N	0.77	0.002	0.15	0.60	4.78	5.50
S_{total}	0.13	0.03	0.05	0.00	0.57	0.85
O (by difference)	37.54	39.30	35.44	5.93	31.87	32.11
HIGH HEATING VALUES (kcal/kg, (dry basis))						
HHV	4595	4791	5206	7937	4540	4853

Table 4: Chemical analysis of the biomass ashes measured by ICP (mg/kg, dry basis).

	SP	WP	TWC	PC	MSS	DDGS
Al	22	65	20	259.2	1028.8	70.1
Ca	1577	1415	546	3655.3	4617.0	1510.3
Fe	68	149	41	744.1	724.3	191.8
K	1635	299	180	510.9	13130.0	14421.4
Mg	216	152	100	776.1	5255.3	5487.2
Mn	6	94	51	90.8	203.8	106.5
Na	452	125	89	798.9	431.2	4347.9
P	145	76	26	162.9	6368.5	6289.3
Si	414	307	60	775.3	1127.9	589.9
Zn	0	2	4	67.4	149.4	111.9

Table 5: Ash melting temperatures of biomass feedstocks,°C.

Feedstock	IDT	ST	HT	FT
SP	955	1051	1162	1256
WP	1353	1425	1427	1438
TWC	>1500	>1500	>1500	>1500
PC	1371	1379	1391	1432
MSS	1127	1128	1162	1375
DDGS	900	900	900	1220

IDT: Initial deformation temperature, ST: Softening temperature, HT: Hemispherical temperature, FT: Fluid temperature

Table 6: Agglomeration indexes of the biomass feedstocks (mole/mole).

	SP	WP	TWC	PC	MSS	DDGS
Si/(Ca+Mg)	0.26	0.31	0.12	0.22	0.12	0.08
(Si+P+K)/(Ca+Mg)	1.27	0.51	0.43	0.37	1.75	2.25

Raveendran *et al.* reported that metals influence pyrolysis and gasification mechanism (14). Alkali metals are good catalysts for carbon-gas reactions. A number of experimental and modeling studies have been conducted to observe and predict ash behavior in gasification systems (23, 24). It was found that the order of retention in the bed for different elements is Ca > K > Mg > P (20). Therefore, the alkali metal content of the samples might have a catalytic function during combustion and gasification.

Pyrolysis experiments of biomass feedstocks with TGA

Thermal decomposition of biomass is influenced by many factors such as heating rate, temperature, pressure, residence time, moisture, composition, and particle size. In this study, all six biomass feedstocks were pyrolyzed under the conditions given in Table 1. Thermographs were taken at four different heating rates (2-15 °C/min) from 25 to 850 °C under N_2 atmosphere. The change of weight loss (TG) and derivative weight loss (DTG) profiles of these feedstocks with heating rates were plotted and evaluated. Effect of heating rate on the TG/DTG profiles for SP was given as an example in Figure 2a and 2b, respectively. The profiles for all other samples can be reached in the conference presentation proceedings (21). It was well established that thermolysis of biomass generally occurs between 200-400 °C. TGA proceeds in three stages for wood: water evaporation, active pyrolysis and passive pyrolysis according to the Gasparovic *et al.* (22). As seen in Figure 2a-b, heating rate affects TG and DTG curve positions, maximum decomposition rate, and location of maximum peaks. When heating rate increases, initial and final temperature of active and passive pyrolysis regions also increase. The maximum points of DTG curves are shifted to higher temperature. For example, the peak for passive pyrolysis region obtained from DTG profile of SP was increased from 302 to 340 °C when the heating rate was increased from 2 °C/min to 15 °C/min (Figure 2b). Nearly the same trend was observed for all feedstocks. Because the temperature intervals of hemicellulose and cellulose decomposition partially overlap each other, the hemicellulose decomposition usually appears as a shoulder instead of a well-defined peak, as was also observed by Gunnar *et al.* (23).

(a)

(b)
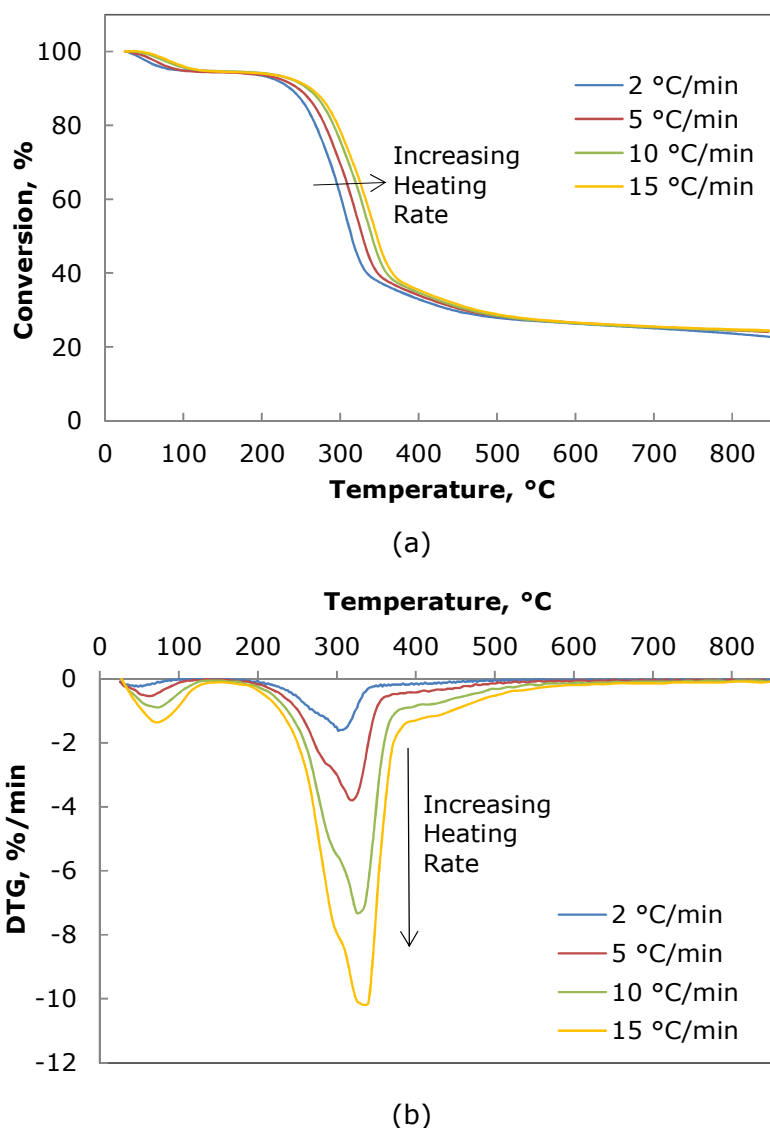
Figure 2: Pyrolysis profiles of straw pellet at different heating rates (a) Weight loss curves (b) Derivative weight loss curves.

When the TG and DTG profiles of all feedstocks were plotted on the same scale as in Figure 3a-b, respectively it was seen that the highest devolatilization rates and maximum temperatures (associated mainly with cellulose decomposition) were obtained for TWC and WP. Among all the examined samples, DTG profile of DDGS and PC differed from others. Two peaks and two shoulders at around 165-380 °C were observed for DDGS at 2°C/min while no peaks were detected there for PC as an indication of absence of volatiles/cellulosic components. During the pyrolysis process, PC lost its volatile content. So, PC has no peaks due to its high amount of fixed carbon (~77%).

(a)

(b)
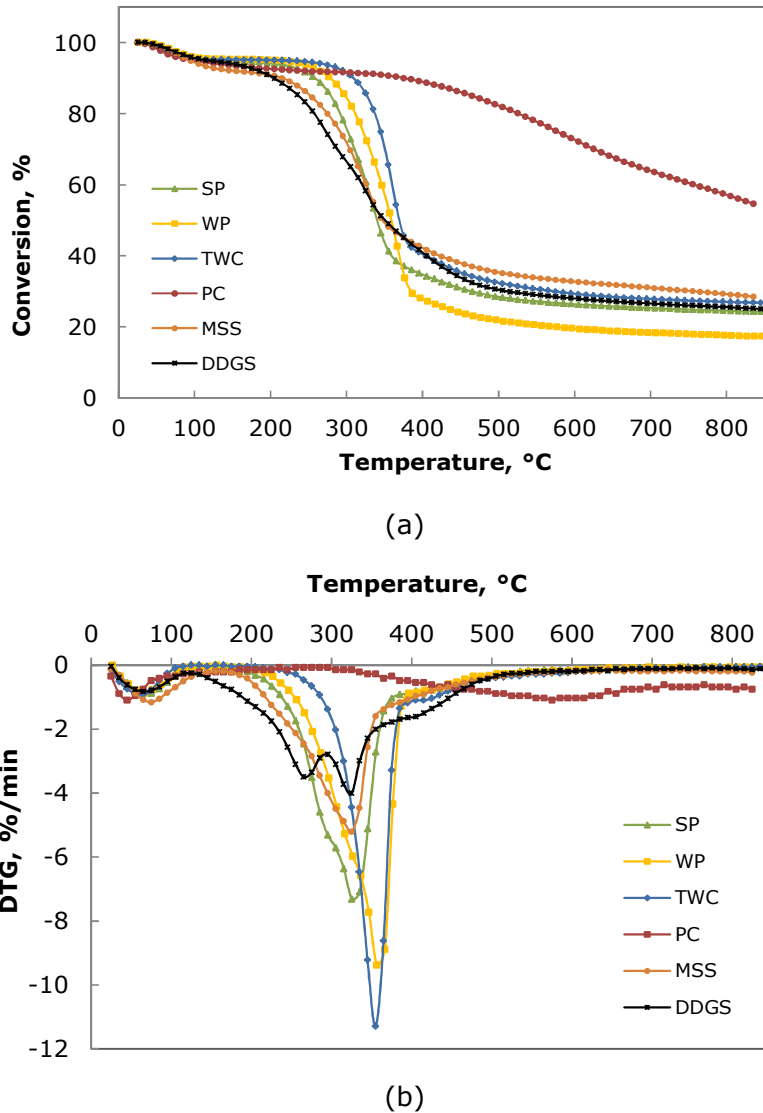
Figure 3: Pyrolysis profiles of all biomass feedstocks at 10 °C/min (a) Weight loss curves (b) Derivative weight loss curves.

There are many methods for analyzing non-isothermal solid-state kinetic data from TGA (24-25). These methods can be divided into two types: model-fitting and model-free. Model-fitting methods were widely used for solid-state reactions because of their ability to directly determine the kinetic parameters from a single TGA measurement. However, these methods suffer from several problems, such as their inability to uniquely determine the reaction model, especially for non-isothermal data. On the other hand, the model free methods require several kinetic curves to perform the analysis. Calculations from several curves at different heating rates are performed on the same value of conversion, which allows calculating the activation energy for each conversion point. In this study, the results obtained from TGA were elaborated according to Coats-Redfern (model fitting) and Isoconversional (model free) methods to calculate the kinetic parameters; namely apparent activation energy (E_a) and pre-exponential factor (A) of biomass feedstocks. It was seen that the choice on the starting and ending points of decomposition stages was determinative in model fitting methods, whereas model free methods were evaluated to be independent from the choice of the stages and gave more freedom to the user. Thus, evaluations

were progressed on the model free methods. The values obtained for pyrolysis char was questionable since the decomposition profiles were in poor quality due to its high fixed carbon content. So PC was disregarded in the evaluations. For isoconversional method, activation energies at 40% and 60-70% conversions, which can be taken as a measure of holocellulose (hemicellulose+cellulose) decomposition, were compared for other five samples (Table 6). Based on the fixed carbon and ash contents of the samples, activation energies were changed as well. In case of TWC, activation energies at 40% and 70% conversions were 189.8 and 377.3 kJ/mole, higher than those values for non-torrefied wood (WP). Similarly, SP gave activation energies changing between 197.8 kJ/mole and 202.4 kJ/mole. It was seen that the lowest activation energies were obtained for WP as an indication of its higher reactivity to thermochemical conversion.

Table 6: Activation Energies in kJ/mole at 40% and 60-70% Conversions

Conversion (%)	Activation Energy (kJ/mole)				
	SP	WP	TWC	DDGS	MSS
40	197.8	172.8	189.8	238.0	186.5
60-70	202.4	172.6	377.3	350.3	187.5

Gasification experiments in BFB gasifier

The syngas compositions obtained during the gasification study were given in Table 7. Calculated gasification yields such as cold gas efficiency, carbon conversion, gas yield and calorific values of the syngas were reported in Table 8. When the results were evaluated, it was seen that MSS produced the highest tar yield ($\sim$ 32.8 gC/Nm^3), compared with the other biomasses whilst TWC has the lowest tar amount as $\sim$ 1 gC/Nm^3. Torrefaction was considered to have an effect on decreasing the tar content. The lowest carbon conversion and cold gas efficiency were obtained with MSS and PC. This was expected for PC since it was the pre-pyrolized sample before the gasification. On the other hand, gasification reactivity of MSS was found to be quite poor. It seemed that MSS was exposed to pyrolization instead of gasification. This might be related to its lower bulk density and poor fluidization conditions inside the gasification reactor. Considerably 10 times less tar was produced during the gasification of torrefied sample (TWC) in relation to its non-torrefied counterpart (WP). Carbon conversions and cold gas efficiencies were also decreased from 69.7% and 56% to 59.1% and 53% upon torrefaction. According to X. Ku *et al.,* intensified energy density of torrefied biomass needs a longer oxidation period, therefore a gasifier for torrefied biomass requires longer gasification zones to reach the same level of conversion (26). Although this was claimed for entrained flow gasification, a similar case might be valid for bubbling bed gasification as well. The tar compounds analysis with respect to biomass feedstock types as shown in Table 9, relatively higher concentrations of lignin-degraded phenolic compounds were present in MSS. It is known that the phenol and benzene derivatives in the tar products were mainly resulted from lignin decomposition by cleavage of its ether linkages at a

higher temperature (27). Therefore, this might be the indication of relatively high lignin content of MSS compared to other samples.

Table 7: Syngas composition with respect to biomass type.

	SP	WP	TWC	PC	MSS
CO (%)	11.9	12.2	7.2	9.0	8.6
CO_2 (%)	9.4	10.0	8.6	8.4	7.2
H_2 (%)	6.53	5.9	8.2	6.2	4.0
CH_4 (%)	2.92	3.10	3.4	1.4	2.8
C_2H_6 (%)	0.4	0.1	0.01	0	na
C_2H_4 (%)	1.23	1.49	0.8	0.01	na
C_{3+} (%)	0.14	na	na	0	na
N_2 (%)	67.5	67.2	71.9	75	76.7
H_2/CO	0.87	0.48	1.14	0.69	0.47
Tar (gC/Nm^3)	~4.3	~9.4	~0.99	1.94	32.8
Total S (ppm)	242	22	17	22.3	na
H_2S (ppm)	104	34	12.7	7.5	10
COS (ppm)	19	3.9	1.2	14.5	18
Methylmercaptane (ppm)	0.8	0.4	0.7	na	na

na: not analyzed.

Table 8: Results for biomass gasification experiments.

	SP	WP	TWC	PC	MSS
Fluidization velocity (m/s)	0.41	0.43	0.43	0.24	0.17
Residence time (s)	1.22	1.17	1.17	2.11	2.95
Cold gas efficiency (%)	69	56	53	16	17.3
Carbon conversion (%)	82.2	69.7	59.1	25.9	26.7
Gas yield (Nm^3/kg fuel)	2.83	2.47	3.12	2.25	1.31
Calorific value of the syngas per Nm^3 (MJ/Nm^3)	4.40	4.25	3.50	2.33	2.51
Calorific value of the syngas per kg gasified fuel (MJ/kg fuel)	12.46	10.52	10.89	5.24	3.29

CONCLUSIONS

Determination of the thermochemical conversion reactivity of six biomass feedstocks (straw pellet (SP), softwood pellet (WP), torrefied wood chips (TWC), pyrolysis char (PC), milled sunflower seed (MSS) and dried distillers' grains and solubles (DDGS)) under both pyrolysis and gasification conditions were studied. When the feedstock analysis results were compared, WP and TWC were the samples with relatively low ash content. On the other hand, in terms of agglomeration index (Si+P+K)/(Ca+Mg), SP seemed to be more prone to agglomeration during thermochemical conversion. The lowest ash fusion temperatures of SP supported its agglomeration tendency as well. Calculated activation energies and characterization studies of biomass feedstocks were indicated that, WP was more reactive to thermochemical conversion and less prone to agglomeration. Although MSS gave comparable activation energies with the WP, its high ash content and agglomeration index were the potential drawbacks in front of its utilization via thermochemical conversion. In the scope of gasification experiments, the highest cold gas efficiency and carbon conversion were obtained for the gasification of SP. On the other hand, SP had some drawbacks such as its high agglomeration tendency and low deformation temperature. It was observed that MSS produced the highest tar yield compared with the others This might be related to its lower bulk density and poor fluidization conditions inside the gasification reactor favoring fast pyrolysis conditions instead of gasification. WP was gasified

with acceptable conversion values and efficiencies when compared with SP. When characterization results were evaluated together with the gasification studies, it was seen that WP would be the preferred fuel for an efficient and effective thermochemical conversion.

Table 9: The analysis of tar compounds for the gasification of different biomass samples

Tar Compound	Concentration (mg C/Nm^3)				
	SP	WP	TWC	PC	MSS
Benzene	2061	4648	805	1344	21499
Toluene	539	1221	137	-	7091
Xylene	41	257	2	-	2172
Ethylbenzene	10	3	9	-	794
Styrene (vinyl benzene)	3	-	-	-	-
Indene	4	8	8	-	-
Phenol	14	13	1	-	113
Napthalene	1088	1795	-	-	490
Methylnapthalene	-	33	3	-	-
Ethylnapthalene	-	12	-	-	-
Dimethylnapthalene	24	6	-	-	-
Acenapthalene	74	251	7	122	136
Fluorene	-	-	-	181	-
Diethylnapthalene	7	9	5	-	-
Antracene	348	161	4	-	78
Phenantrene	-	761	-	205	47
Pyrene	132	253	5	70	45
Total	~4345	~9433	~986	1937	32780

REFERENCES

1. Fang Z, Sato T, Smith R, Inomata H, Arai K, Kozinski J. Reaction chemistry and phase behaviour of lignin in high temperature and supercritical water. Bioresource Technology. 2008; 99: 3424-30. DOI: 10.1016/j.biortech.2007.08.008.

2. Kirubakaran V, Sivaramakrishnan V, Nalini R, Sekar T, Premalatha M, Subramanian P. A review on gasification of biomass. Renewable and Sustainable Energy Reviews. 2009; 13:179-86. DOI: 10.1016/j.rser.2007.07.001.

3. McKendry P. Energy production from biomass (part 3): gasification technologies. Bioresource Technology. 2002;83:55-63. DOI: 10.1016/S0960-8524(01)00120-1.

4. Gabra M, Pettersson E, Backman R, Kjellstrom B. Evaluation of cyclone gasifier performance for gasification of sugarcane residue-Part 1: gasification of bagasse. Biomass and Bioenergy. 2001; 21:351-69. DOI: 10.1016/S0961-9534(01)00043-5.

5. Boateng A A, Walawender W P, Fan L T, Chee C S. Fluidized-bed steam gasification of rice hull. Bioresource and Biotechnology. 1992; 40: 235-39. DOI: 10.1016/0960-8524(92)90148-Q.

6. Lv P M, Xiong Z H, Chang J, Wu C X, Chen Y, Zhu J X. An experimental study on biomass air-steam gasification in a fluidized bed. Bioresource Technology. 2004; 95: 95-101. DOI: 10.1016/j.biortech.2004.02.003.

7. Rapagna S, Jand N, Kiennemann A, Foscolo P U. Steam-gasification of biomass in a fluidized-bed of olivine particles. Biomass and Bioenergy. 2000; 19: 187-97. DOI: 10.1016/S0961-9534(00)00031-3.

8. S. Rapagna S, A. Latif A. Steam gasification of almond shells in a fluidized bed reactor: The influence of temperature and particle size on product yield and distribution. Biomass and Bioenergy. 1997; 12: 281-88. DOI: 10.1016/S0961-9534(96)00079-7.

9. Ergudenler A, Ghaly A E. Agglomeration of alumina sand in a fluidized-bed straw gasifier at elevated temperatures. Bioresource Technology. 1993; 43: 259-68. DOI: 10.1016/0960-8524(93)90039-E.

10. Ko M K, Lee W Y, Kim S B, Lee K W, Chun H S. Gasification of food waste with steam in fluidized bed. Korean Journal of Chemical Engineering. 2001; 18: 961-64. DOI: 10.1007/BF02705626.

11. Kumabe K, Hanaoka T, Fujimoto S, Minowa T, Sakanishi K. Co-gasification of woody biomass and coal with air and steam. Fuel. 2007; 86: 684-89. DOI: 10.1016/j.fuel.2006.08.026.

12. Gates B C, Huber G W, Marshall C L, Ross O N, Sirolla J, Wang Y. Catalysts for emerging energy applications. MRS Bull. 2008; 33: 429-35. DOI:http://dx.doi.org/10.1557/mrs2008.85.

13. Demirbas A. Combustion characteristics of different biomass fuels. Progress in Energy and Combustion Science. 2004; 30: 219-30. DOI: 10.1016/j.pecs.2003.10.004.

14. Raveendran K, Ganesh A, Khilar K C. Pyrolysis characteristics of biomass and biomass components. Fuel. 1996; 75: 987-98. DOI: 10.1016/0016-2361(96)00030-0.

15. Schuster G, Loffler G, Weigl K, Hofbauer H. Biomass steam gasification – an extensive parametric modeling study. Bioresources Technology. 2000; 77: 71-79. DOI: 10.1016/S0960-8524(00)00115-2.

16. Yang H, Yan R, Chen H, Lee H D, Zheng C. Characteristics of hemi-celulose, cellulose, and lignin pyrolysis. Fuel. 2007; 86: 1781-88. DOI: 10.1016/j.fuel.2006.12.013.

17. Kezhong L, Zhang R, Bi J. Experimental study on syngas production by co-gasification of coal and biomass in fluidized bed. International Journal of Hydrogen Energy. 2010; 35: 2722-26. DOI: 10.1016/j.ijhydene.2009.04.046.

18. Herguido J, Corella J, Gonzalez-Saiz J. Steam gasification of lignocellulosic residues in a fluidized bed at a small pilot scale Effect of type of feedstock. Industrial and Engineering Chemistry. 1992; 31: 1274-82. DOI: 10.1021/ie00005a006.

19. Biedermann F, Obernberger I. Ash-related Problems during Biomass Combustion and Possibilities for a Sustainable Ash utilisation. URL: http://www.bios-bioenergy.at/uploads/media/Paper-Biederman AshRelated-2005-10-11.pdf.

20. Arvelakis S, Sotiriou C, Moutsatsou A, Koukios E G. Prediction of the behaviour of biomass ash in fluidized bed combustors and gasifiers. J. Therm. Anal. Calorim. 1999; 56: 1271-78. DOI: 10.1023/A:1010189919655.

21. Durak-Çetin Y, Engin B, Sarıoğlan A. Thermogravimetric Behaviour of Different Biomass Feedstocks and Their Pyrolysis Kinetics. Papers of the 23rd European Biomass Conference held in Vienna Austria. 2015; 1236-1242.

22. Gašparovič L, Koreňová Z, Jelemenský L. Kinetic study of wood chips decomposition by TGA. Proceedings of the 36th International Conference of Slovak Society of Chemical Engineering. 2009; pag. 178.

23. Gunnar M, Grønli, Varhegyi G, Blasi C D. Thermogravimetric Analysis and Devolatilization Kinetics of Wood. Ind. Eng. Chem. Res. 2002; 41: 4201-4208. DOI: 10.1021/ie0201157.

24. Simon P. Isoconversional methods: fundamental, meaning and application. Journal of Thermal Analysis and Calorimetry. 2004;76, 1, 123-132. DOI: 10.1023/B:JTAN.0000027811.80036.6c.

25. Sbirrazzuoli N, Vincent L, Mija A, Guio N. Integral, differential and advanced isoconversional methods: Complex mechanisms and isothermal predicted conversion–time curves. Chemometrics and Intelligent Laboratory Systems. 2009;96, 2, 219-226. DOI:10.1016/j.chemolab.2009.02.002.

26. Ku X, Lin J, Yuan F. Influence of Torrefaction on Biomass Gasification Performance in a High-Temperature Entrained-Flow Reactor. Energy&Fuels 2016; 30; 4053-4064. DOI 10.1021/acs.energyfuels.6b00163.

27. Palma C F. Modelling of tar formation and evolution for biomass gasification: A review. Applied Energy. 2013; 111; 129-141. DOI 10.1016/j.apenergy.2013.04.082.

Farklı Biyokütle Hammaddelerinin Termokimyasal Dönüşüm Davranışı: Piroliz ve Gazlaştırma

Işıl Işık-Gülsaç, Yeliz Durak-Çetin, Berrin Engin, Parvana Gafarova-Aksoy, Hakan Karataş, Alper Sarıoğlan

Öz: Bu çalışmada, tezgah ölçeğinde kabarcıklı akışkan yatak (BFB) gazlaştırıcı ve termogravimetrik analizör (TGA) kullanılarak gazlaştırma ve piroliz koşulları altında biyokütle yakıtlarının termokimyasal dönüşüm reaktivitesi tespit edilmiştir. Altı farklı biyokütle hammaddesi kullanılmıştır, bunlar hasır tanesi (SP), yumuşak kereste tanesi (WP), kurutulmuş odun kıymıkları (TWC), piroliz kömürü (PC), değirmenden geçmiş ayçiçeği tanesi (MSS) ve kurutulmuş damıtıcı tanesi ve çözünürleri (DDGS) olarak verilmiştir. Biyokütle hammeddelerinin TGA'sı dört farklı ısıtma hızında (2-15 °C/dakika) pirolitik koşullarda yürütülmüştür. Deneylerden elde edilen ham veriler örneklerin kinetik parametrelerini (A, E_a) hesaplamak için kullanılmıştır, burada Coats-Redfern ve Isoconversional Yöntem kullanılmıştır. TGA analizine göre piroliz kömürü 800 K'nin üzerindeki sıcaklıklarda bozunma sonucu kalan tek üründür, çünkü gazlaştırmadan önce buna ön piroliz uygulanmıştır. Türevli Termogravimetrik Analiz (DTG) profillerine göre, 450-650 K civarındaki iki pik ve iki omuz DDGS için gözlenirken piroliz kömürü için hiç bir pik elde edilmemiştir, bu da uçucu maddelerin veya selülozik bileşenlerin yokluğu anlamına gelmektedir. Yumuşak kereste ve kurutulmuş odun parçaları için elde edilen en yüksek uçuculuk giderme hızları ve uçuculuk giderme sıcaklıkları (temel olarak selülozun bozunması ile ilgilidir) diğer biyokütle hammaddeleri içinde en düşük kömür verimlerini oluşturmaktadır. WP'nin termokimyasal dönüşüme karşı daha reaktif olduğu ve kümeleşmeye karşı daha dayanıklı olduğu görülmüştür. Bunun dışında, MSS'nin yüksek kül yüzdesi ve kümelenme indisi termokimyasal dönüşüm yoluyla kullanılmasının önünde potansiyel engeller olarak durmaktadır. Bu hammaddelerin (DDGS dışında) havayla gazlaştırması sırasında, ürün olarak elde edilen sentez gazı temel gaz bileşimi, zift ve kükürtlü bileşikler cinsinden karakterize edilmiştir. En yüksek soğuk gaz etkinliği, karbon dönüşümü ve kalorifik değerler SP'nin gazlaştırılması için elde edilmiştir. Diğer taraftan, SP'nin yüksek kümelenme eğilimi ve düşük deformasyon sıcaklığından dolayı bazı dezavantajlar getirdiği bulunmuştur. Bütün hammaddeler içinde, MSS'nin gazlaştırma reaktifliğinin oldukça düşük olduğu bulunmuştur. MSS'nin gazlaştırma yerine pirolize uğradığı görülmektedir. WP ve TWC kabul edilebilir dönüşüm değerlerinde gazlaştırılmış ve etkinlikleri SP ile karşılaştırılmıştır. WP'nin termokimyasal dönüşümlerde tercih sebebi olduğu anlaşılmıştır.

RESEARCH ARTICLE

(This article was presented to the 28th National Chemistry Congress and submitted to JOTCSA as a full manuscript)

Synthesis and Antimicrobial activities of New 1,2,4- Triazoles, Mannich Bases, Conazoles, and Fluoroquinolones

Sule CEYLAN[1*]

[1]Artvin Coruh University, 08000, Artvin, Turkey

Abstract: Triazoles are heterocyclic compounds which have been of interest in the development of novel compounds with antidepressant, anti-inflammatory, analgesic, antibacterial, antimycobacterial, antifungal, antiviral, anticancer, and other activities. In this article, a series of fluorine- and piperazine-containing some novel biologically active 1,2,4-triazole-3-one derivatives were synthesized by the Mannich reaction of triazole intermediates. The structures for novel synthesized compounds were elucidated using elemental analysis and FT IR, ^{13}C NMR, ^{1}H NMR, EI MS techniques. These compounds were investigated *in vitro* for their antimicrobial properties and several compounds have fungicidal activity against *Candida albicans* and *Saccharomyces cerevisiae*. And also some of the compounds exhibited excellent activity on *Mycobacterium smegmatis*, a nonpigmented fast-rising mycobacterium, at the concentration of <1 µg/mL is better than standard drug streptomycin.

INTRODUCTION

On account of growing number of multidrug resistant microbial pathogens, rising infectious infirmity and the cure of infectious illness still remain serious and challenging problem. For this reason, novel species of antimicrobial compounds are vitally important in fight with multidrug-resistant microbial diseases [1-5]. The most important and challenge of pharmaceutical chemistry is to design and synthesis of novel combinational chemotherapeutics constitute for coping with the antimicrobial resistance. There are two approaches for overcome multidrug-resistant bacteria. One of them is the synthesis of entirely novel compounds having unlike chemical structures than available ones, the other method is to unite two or more active groups into one compound. Thus, a single compound possessing more than one active group, each with varied form of activity, might be advantageous for the cure of bacterial diseases [6, 7]. Heterocycle- and fluorine-containing compounds play a crucial role both in the research field of organic chemistry and in a variety of practical chemistry fields, such as, material science, medicinal chemistry, and pesticide chemistry [8–12]. 1,2,4-triazole is a five-membered heterocycle, and has a broad spectrum of biological properties containing anticancer [13, 14], insecticidal [15], antifungal [16], anti-inflammatory [17], and plant growth regulating activities [18]. Moreover, one of the significant heterocycles is piperazine. Piperazine ring has different features, for example, simple building multiple ionic or hydrogen bonds appear low toxicity and functional influence. Thus it is frequently placed into various main compounds for increasing the antimicrobial activities along the applied medicine. It is mentioned that *N*-substituted piperazine structures possess a broad range of biological properties, like anticancer [20], antimicrobial [19], herbicidal activities [21], especially that compounds were frequently used as antibacterial material. Mannich bases of 1,2,4-triazole derivatives having a piperazine moiety have been determined to possess antifungicidal activity [22, 23], and some Mannich bases containing piperazine-4,5-disubstituted-1,2,4-triazole were reported to have tuberculostatic property [24]. However, there are relatively not many researches concerning the piperazine-possesing compounds about the design and enhance of pesticides. In view of these facts and as a piece of our continuing study on the synthesis of active hybrid compounds, we expected to get novel 1,2,4-triazole compounds having azole moieties and their Mannich bases as potential biodynamic agents.

RESULTS AND DISCUSSION

Chemistry

The basic purpose of this research is to synthesize and examine the antimicrobial properties of some novel hybrid compounds containing different heterocyclic moieties,

the pharmacological importance of which is well documented. The synthetic methods accepted to acquire the aimed molecules are showed in Schemes 1, 2, and 3. The structures for novel synthesized molecules were explained using physicochemical, elemental analysis, and spectral methods (FT IR, ^{1}H NMR, ^{13}C NMR and EI-MS).
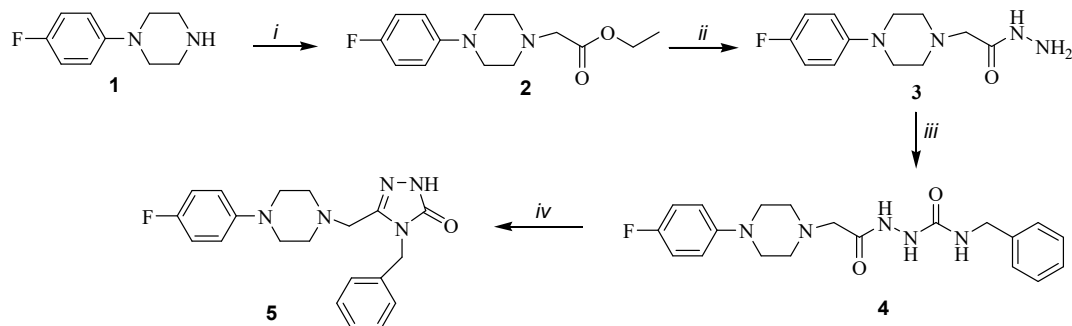
Scheme 1. Reactions and conditions. *i*: triethylamine, BrCH$_2$COOC$_2$H$_5$, THF, 24 h rt; *ii*: EtOH, H$_2$NNH$_2$, reflux, 27 h; *iii*: CH$_2$Cl$_2$, PhCH$_2$NCO, 24 h rt; *iv*: 2 N NaOH in EtOH/H$_2$O, reflux, 5 h.
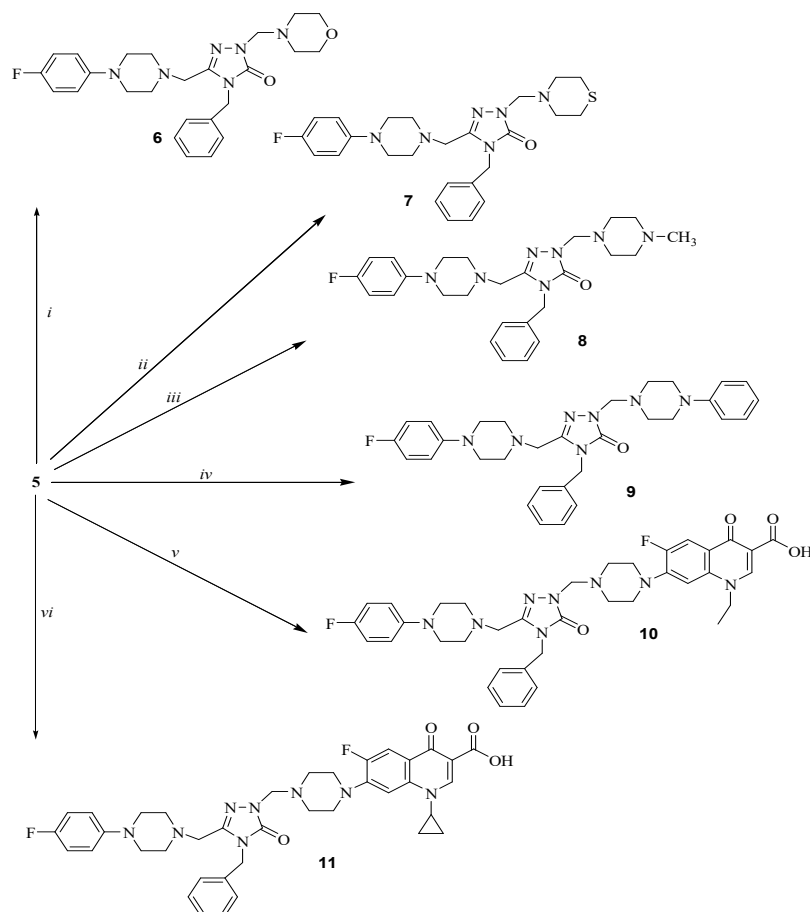
Scheme 2. Reactions and conditions. *i*: morpholine, HCHO in DMSO, 24 h rt; *ii*: thiomorpholine, HCHO in DMSO, 24 h rt; *iii*: methylpiperazine, HCHO in DMSO, 24 h rt; *iv*: 1-phenylpiperazine, HCHO in DMSO, 24 h rt; *v*: norfloxacin, HCHO in DMSO, 24 h rt; *vi*:ciprofloxacin, HCHO in DMSO, 24 h rt.
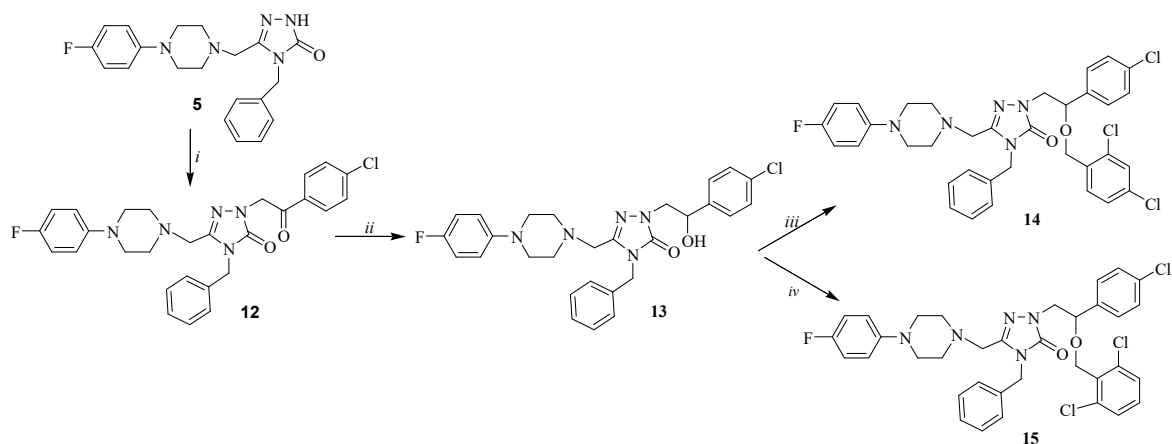
Scheme 3. Reactions and conditions. *i*: EtOH, Na, ClC6H4COCH2Br, reflux, 17 h; *ii*: EtOH, NaBH4, reflux, 15 h; *iii*: THF, NaH, 2-4-dichlorobenzyl chloride, reflux, 15 h; *iv*: THF, NaH, 2-6-dichlorobenzyl chloride reflux, 15 h.

The esterification of 1-(4-fluorophenyl)piperazine (**1**) by tetrahydrofuran and ethyl bromoacetate in the presence of triethylamine generated the corresponding ester (**2**). Then, the ester **2** was changed to the corresponding hydrazide (**3**) by the reaction with hydrazine hydrate. The ^{1}H NMR and FT-IR spectra for compound **3** showed signals pointing the presence of hydrazide group, while the signals because of the ester function were not seen in the NMR spectrum.

Compound **3** was changed to the corresponding carboxamide by the reaction with benzyl isocyanate. Compounds (**4**) was evaluated by the existence of absorption bands at 1655 cm^{-1} due to -C=O stretching in the FT-IR spectra. In the ^{13}C NMR spectra of this compound (**4**), -C=O function resonated at 158.59 ppm. The other proof for the appearance of carboxamides was the presence of three NH signals at 7.86-9.45 ppm in the ^{1}H NMR spectra as D2O-exchangeable singlets. Moreover, the signals refer to alkyl or aryl function of isothiocyanate ring were observed at the appropriate chemical shift range.

The synthesis of the triazole (**5**) was carried out by the intramolecular cyclization of compound **4** by treatment with base; we aimed to bind the 1,2,4-triazole ring to fluorophenylpiperazine nucleus, it is stated that more efficient antimicrobial molecules may be planned by combined two or more biologically active heterocyclic groups together in a single molecular structure [25-27]. In the ^{1}H NMR spectra of compound **5** the signal obtained at 9.25 ppm was described to –NH proton. The signal owing to this function was observed at 3167 cm^{-1} in the FT-IR spectra. In addition, compound **5** showed stable

[M+1]$^+$ and [M+Na]$^+$, signals in the mass spectra and also the elemental analysis data are coherent with the appointed molecules. Because of their basic purpose depicting the compound solvable in aqueous solvents when it is converted into aminium salt, Mannich bases are physiologically reactive and they have been noticed as possible biological materials [28]. Moreover, it is stated that the function connected to parent amine by Mannich reaction rises the lipophilicity of compound [29]. In view of these facts, we treated compounds **5** with several amines, namely morpholine, thiomorpholine, methylpiperazine, 1-phenylpiperazine, norfloxacine, and ciprofloxacine due to their therapeutic effect [30-32]. The successful synthesis of the alkylaminomethylation was provided by the disappearance of peak for the proton at the *N*-1 nitrogen (**5**) of the 1,2,4-triazole derivative. In addition, in the ^{1}H and ^{13}C NMR spectra of compounds **6-11** displayed additional peaks resulting from alkylaminomethyl group at the connected chemical shift ranges.

Treatment of compound **5** with 4-chlorophenacyl bromide gave compound **12** which was converted into compound **13** by reduction of the ketone functionality using sodium borohydride. The treatment of compound **13** with 2-4-dichlorobenzyl chloride or 2-6-dichlorobenzyl chloride generated the corresponding conazole derivatives **14** and **15** respectively. The structures of molecules **12-15** were confirmed using spectroscopic techniques such as FT-IR, EI-MS, ^{1}H NMR, ^{13}C NMR, and elemental analysis.

BIOLOGICAL ACTIVITY

Antimicrobial activity

All the novel synthesized molecules were investigated for their antibacterial activities but only the values of the compounds which have activities were shown in Table 1. Among the novel synthesized molecules, compounds **4, 6, 7, 10, 11, 14,** and **15** displayed moderate-slight activities against to the tested microorganisms with the mic values between <1-125 µg/mL.

Moderate activities were observed for compound **4**, a carboxamide derivative, on Gram-positive bacteria, *Mycobacterium smegmatis* (Ms), and yeast like fungi, *Candida albicans* (Ca), and *Saccharomyces cerevisiae* (Sc).

The conversion of compounds **5** to their Mannich bases resulted in an increase in the antimicrobial activity. Mannich base derivatives **6, 7, 10** and **11** were obtained to have good activity against on some of the test microorganisms. Among these, compound **6** and **7** namely a 1,2,4-triazole compound containing a thiomorpholine or a morpholine moiety have moderate antibacterial activity only against Ms, Ca and Sc with the MIC

values between of 15.6-125 mg/mL. However, Mannich compounds **10** and **11,** containing a norfloxacin or ciprofloxacin nucleus attached to 1,2,4-tirazole nucleus showed perfect antimicrobial activities on Gram-negative and Gram-positive bacteria, except Ca and Sc. Especially, 7-{4-[(4-benzyl-3-{[4-(4-fluorophenyl)piperazin-1-yl]methyl}-5-oxo-4,5-dihydro-1*H*-1,2,4-triazol-1-yl)methyl]piperazin-1-yl}-1-cyclopropyl-6-fluoro-4-oxo-1,4-dihydroquinoline-3-carboxylic   acid   compound   (**11**) exhibited good activity on Ms, a nonpigmented fast-rising mycobacterium, with the mic value <1 µg/mL is better than standard drug streptomycin or *Escherichia coli* (Ec), a Gram-negative, facultative anaerobic bacterium, with the mic value <1 µg/mL is better than standard drug ampicillin. Conazole derivative, **14** and **15**, were found to have a slight activity only against Ms with the mic values 125 µg/mL. Nevertheless, none of the compounds **2-15** exhibited activity on *Enterococcus faecalis* (Ef).

Table 1. Antimicrobial activity of the compounds (µg/mL)

Comp.No	Minimal Inhibition Concentration Values (µg/mL)								
	Ec	Yp	Pa	Sa	Ef	Bc	Ms	Ca	Sc
4	-	-	-	-	-	-	62.5	125	125
6	-	-	-	-	-	-	62.5	15.6	31.2
7	-	-	-	-	-	-	125	15.6	31.2
10	<1	<1	3.9	<1	-	<1	3.9	-	-
11	<1	<1	<1	<1	-	<1	<1	-	-
14	-	-	-	-	-	-	125	-	-
15	-	-	-	-	-	-	125	-	-
Amp.	10	32	>128	35	10	15			
Strep.							4		
Flu.								<8	<8

Ec: *E. coli* ATCC 35218, Yp: *Y. pseudotuberculosis* ATCC 911, Pa: *P. aeruginosa* ATCC 10145, Ef: *E. faecalis* ATCC 29212, Bc: *B. cereus* 709 Roma, Ms: *M. smegmatis* ATCC607, Ca: *C. albicans* ATCC 60193, *S. cerevisiae* RSKK 251, Amp.: Ampicillin, Strep.: Streptomycin, Flu.: Fluconazole, (—): no activity of test concentrations

CONCLUSIONS

This research reports the successful synthesis of some new hybrid compounds starting from 1-(4-fluorophenyl)piperazine. The antimicrobial activity investigation studies were also performed in this study. The antimicrobial investigation provides that the molecules containing norfloxacine, ciprofloxacine acid nucleus displayed excellent antibacterial activity. In addition, some of them showed inhibition properties on *Escherichia coli* (Ec) and *Mycobacterium smegmatis* (Ms) better to ampicillin or streptomycin.

EXPERIMENTAL

General

All the chemicals were bought from Fluka Chemie AG Buchs (Switzerland) and used without further purification. Melting points of the synthesized compounds were determined in open capillaries on a Büchi B-540 melting point apparatus and are uncorrected. Reactions were monitored by thin-layer chromatography (TLC) on silica gel 60 F254 aluminum sheets. The mobile phase was ethyl acetate:diethyl ether (1:1), and detection was made using UV light. FT-IR spectra were recorded using a *Perkin Elmer* 1600 series FTIR spectrometer. ^{1}H NMR and ^{13}C NMR spectra were registered in DMSO-d_6 on a *BRUKER AVENE II* 400 MHz NMR Spectrometer (400.13 MHz for ^{1}H and 100.62 MHz for ^{13}C). The chemical shifts are given in ppm relative to Me$_4$Si as an internal reference, *J* values are given in Hz. The elemental analysis was performed on *a Costech Elemental Combustion System* CHNS-O elemental analyzer. All the compounds gave C, H and N analysis within ±0.4% of the theoretical values. The Mass spectra were obtained on a *Quattro GC-MS* (70 eV) Instrument. Nalidixic acid (**1**) was provided commercially from Sigma-Aldrich.

Ethyl [4-(4- fluorophenyl)piperazine-1-yl]acetate (2)

1-(4-fluorophenyl)piperazine **1** (1.80 g, 10 mmol) in tetrahydrofuran, triethylamine (2.10 mL, 15 mmol) and ethyl bromoacetate (1.13 mL, 10 mmol) were added and the mixture was stirred at room temperature for 24 hours. After evaporating the solvent under reduced pressure, a solid appeared. The crude product was recrystallized from chloroform–petroleum ether (1:3) to yield the target compounds. Yield 90%, mp: 54-55°C. FT-IR (υ$_{max}$, cm^{-1}): 3015 (aromatic CH), 2986 (aliphatic CH), 1736 (C=O); ^{1}H NMR (DMSO-d_6, δ ppm): 1.19 (t, 3H, CH$_3$, *J*= 6.8 Hz), 2.65 (t, 4H, 2CH$_2$, *J*= 4.8 Hz), 3.06 (d, 4H, 2CH$_2$, *J*= 5.2 Hz), 3.27 (s, 2H, CH$_2$), 4.09 (q, 2H, CH$_2$, *J*= 7.2 Hz), 6.91-6.95 (m, 2H, arH), 7.00-7.05 (m, 2H, arH); ^{13}C NMR (DMSO-d_6, δ ppm): 14.58, 49.38, 52.38, 58.78, 60.33, 115.54 and 115.79, 117.59 and 117.67, 148.34 and 148.35, 155.30 and 157.64, 170.29; EI-MS *m/z* (%): 267.23 ([M+1]$^+$, 100), 193.14 (39), 188.18 (39), 160.19 (34).

Anal. Calcd. for $C_{14}H_{19}FN_2O_2$: C, 63.14; H, 7.19; N, 10.52%. Found: C, 63.30; H, 7.48; N, 10.21%

2-(4-(4-fluorophenyl)piperazine-1-yl)acetohydrazide (3)

A solution of compound **2** (2.66 g, 10 mmol) in ethanol was refluxed with hydrazine hydrate (1.21 mL, 25 mmol) for 27 h (controlled with TLC). After cooling the reaction mixture to room temperature, the mixture was kept overnight in cold. The resulting solid was collected by filtration and recrystallized from ethyl acetate–diethyl ether (1:3) to afford the desired product **3**. Yield 91%, mp: 155-156 °C.

FT-IR (u_{max}, cm^{-1}): 3295 and 3255 (NH$_2$), 3166 (NH), 3051 (aromatic CH), 2962 (aliphatic CH), 1666 (C=O); ^{1}H NMR (DMSO-d_6, δ ppm): 2.56 (t, 4H, 2CH$_2$, J= 4.8 Hz), 2.96 (s, 2H, CH$_2$), 3.08 (t, 4H, 2CH$_2$, J= 4.4 Hz), 4.28 (brs, 2H, NH$_2$), 6.91-6.95 (m, 2H, ArH), 7.00-7.05 (m, 2H, ArH), 8.94 (s, 1H, NH); ^{13}C NMR (DMSO-d_6, δ ppm): 49.31, 53.20, 60.26, 115.57 and 115.79, 117.49 and 117.57, 148.36, 155.44 and 157.58, 168.57; EI-MS m/z (%):293.30 (43), 193.18 (100), 178.16 (20), 150.13 (62), 138.11 (37); Anal. Calcd. for $C_{12}H_{17}FN_4O$: C, 57.13; H, 6.79; N, 22.21%. Found: C, 57.32; H, 6.59; N, 22.57%.

N-benzyl-2-{[4-(4-fluorophenyl)piperazin-1-yl]acetyl}hydrazinecarboxamide (4)

To a solution of corresponding compound **3** (2.52 g, 10 mmol) in dichloromethane, benzyl isocyanate (2.57 mL, 20 mmol) was added and the mixture was stirred at room temperature for 24 hours. After evaporating the solvent under reduced pressure, a solid appeared. The crude product was recrystallized from acetone–diethyl ether (1:3) to yield the target compounds. Yield 91%, mp: 195-196 °C.

FT-IR (u_{max}, cm^{-1}): 3249 (2NH), 3219 (NH), 3090 (aromatic CH), 2958 (aliphatic CH), 1655 (2C=O); ^{1}H NMR (DMSO-d_6, δ ppm): 2.63 (s, 4H, 2CH$_2$), 3.07 (s, 4H, 2CH$_2$), 3.34 (s, 2H, CH$_2$), 4.24 (d, 2H, CH$_2$, J= 8.0 Hz), 6.87 (s, 1H, NH), 6.92-6.95 (m, 2H, ArH), 7.04 (t, 2H, ArH, J= 8.0 Hz), 7.22-7.32 (m, 5H, ArH), 7.86 (s, 1H, NH), 8.97 (s, 1H, NH), 9.45 (s, 1H, NH); ^{13}C NMR (DMSO-d_6, δ ppm): 43.11, 49.22, 53.13, 60.08, 115.59 and 115.80, 117.50 and 117.57, 127.00, 127.39, 128.58, 140.95, 148.33, 155.25 and 157.59, 158.59, 169.46; EI-MS m/z (%): 430.33 (10), 408.13 ([M+Na]$^+$, 47), 386.22 ([M+1]$^+$, 62), 273.16 (15); Anal. Calcd. for $C_{20}H_{24}FN_5O_2$: C, 62.32; H, 6.28; N, 18.17%. Found: C, 62.11; H, 6.57; N, 18.56%.

5-{[4-(4-fluorophenyl)piperazin-1-yl]methyl}-4-phenyl-2,4-dihydro-3*H*-1,2,4-triazol-3-one (5)

A solution of carbothioamide **4** (3.85 g, 10 mmol) in ethanol/water (1:1) was refluxed in the presence of 2 N NaOH for 5 h (the progress of the reaction was monitored by TLC). Then, the resulting solution was cooled to room temperature and acidified to pH 7 with 37% HCl. The precipitate formed was filtered off, washed with water, and recrystallized from ethyl acetate to give the target compound **5**. Yield 70%, mp: 185-186 °C.

FT-IR (υ_{max}, cm^{-1}): 3167 (NH), 3035 (aromatic CH), 2919 (aliphatic CH), 1696 (C=O), 1511 (C=N); ^{1}H NMR (DMSO-d_6, δ ppm): 2.43 (s, 2H, CH$_2$), 2.89 (s, 2H, CH$_2$), 3.30 (s, 2H, CH$_2$), 3.34 (s, 4H, 2CH$_2$), 4.88 (s, 2H, CH$_2$), 6.87-6.89 (m, 2H, ArH), 7.02 (t, 2H, ArH, *J*= 7.2 Hz), 7.04-7.25 (m, 3H, ArH), 7.32 (t, 2H, ArH, *J*= 4.4 Hz), 9.25 (s, 1H, NH); ^{13}C NMR (DMSO-d_6, δ ppm): 44.20, 49.11, 52.65, 53.43, 115.59 and 115.80, 117.57 and 117.80, 127.53, 127.71, 128.87, 137.67, 144.75, 148.27 and 155.29, 155.97, 157.63; EI-MS *m/z* (%): 459.33 (25), 407.39 ([M+1+K]$^+$, 47), 390.25 ([M+Na]$^+$, 62), 367.10 ([M]$^+$, 70), 261.11 (10); Anal. Calcd. for C$_{20}$H$_{22}$FN$_5$O: C, 65.38; H, 6.04; N, 19.06%. Found: C, 65.11; H, 6.32; N, 19.33%.

General Synthetic Method of Compounds 6-11

To a solution of compound **5** (3.67 g, 10 mmol) in dimethyl sulfoxide (10 mL), morpholine (for **6**) (0.87 mL, 10 mmol) or thiomorpholine (for **7**) (0.94 mL, 10 mmol) or methyl piperazine (for **8**) (1.11 mL, 10 mmol) or 1-phenylpiperazine (for **9**) (1.52 mL, 10 mmol), or norfloxacin (for **10**) (3.19 g, 10 mmol) or ciprofloxacin (for **11**) (3.31 g, 10 mmol) was added in the presence of formaldehyde (37%, 3.72 mL, 50 mmol) and the mixture was stirred at room temperature for 24 hours. The resulting solution was poured into ice-cold water and a solid appeared. The crude product was recrystallized from ethanol–water (1:3) (for **6** and **7**), from ethyl acetate (for **8** and **9**), from dimethyl sulfoxide–water (1:3) (for **10** and **11**) to yield the target compounds.

4-Benzyl-5-{[4-(4-fluorophenyl)piperazin-1-yl]methyl}-2-(morpholin-4-ylmethyl)-2,4-dihydro-3*H*-1,2,4-triazol-3-one (6)

Yield 87%, mp: 102-103 °C; FT-IR (υ_{max}, cm^{-1}): 3053 (aromatic CH), 2938 (aliphatic CH), 1701 (C=O), 1508 (C=N); ^{1}H NMR (DMSO-d_6, δ ppm): 2.08 (s, 2H, CH$_2$), 2.43 (s, 4H, 2CH$_2$), 2.89 (s, 4H, 2CH$_2$), 3.34 (s, 10H, 5CH$_2$), 4.88 (s, 2H, CH$_2$), 6.86-6.89 (m, 2H, ArH), 7.02 (t, 2H, ArH, *J*= 8.8 Hz), 7.25 (d, 3H, ArH, *J*= 6.4 Hz), 7.31 (d, 2H, ArH, *J*= 6.8 Hz); ^{13}C NMR (DMSO-d_6, δ ppm): 40.60, 44.20, 49.11, 52.65, 53.43, 115.59 and 115.80, 117.58 and 117.65, 127.52, 127.71, 128.87, 137.64, 140.23, 144.77 and 148.25, 148.05, 155.98; EI-MS *m/z* (%): 490.39 ([M+1+Na]$^+$, 70), 467.61 ([M+1]$^+$,

100), 390.20 (24), 292.21(16); Anal. Calcd. for $C_{25}H_{31}FN_6O_2$: C, 64.36; H, 6.70; N, 18.01%. Found: C, 64.13; H, 6.92; N, 18.30%.

4-Benzyl-5-{[4-(4-fluorophenyl)piperazin-1-yl]methyl}-2-(thiomorpholin-4-ylmethyl)-2,4-dihydro-3*H*-1,2,4-triazol-3-one (7)

Yield 91%, mp: 118-120 °C; FT-IR ($υ_{max}$, cm^{-1}): 3052 (aromatic CH), 2820 (aliphatic CH), 1695 (C=O), 1509 (C=N); ^{1}H NMR (DMSO-d_6, δ ppm): 2.45 (s, 6H, 3CH$_2$), 2.89 (s, 6H, 3CH$_2$), 3.35 (s, 6H, 3CH$_2$), 4.92 (s, 2H, CH$_2$), 5.03 (d, 2H, CH$_2$, *J*= 7.2 Hz), 6.86-6.89 (m, 2H, ArH), 7.02 (t, 2H, ArH, J= 12.0 Hz), 7.25- 7.34 (m, 5H, ArH); ^{13}C NMR (DMSO-d_6, δ ppm): 27.59, 43.87, 44.78, 49.09, 49.60, 52.68, 53.23, 67.50, 115.59 and 115.80, 117.59 and 117.67, 127.57, 127.80, 128.56, 137.33, 143.90 and 148.23, 155.30, 154.04, 157.64; EI-MS *m/z* (%): 482.71 ([M]$^+$, 90); Anal. Calcd. for $C_{25}H_{31}FN_6OS$: C, 62.22; H, 6.47; N, 17.41%. Found: C, 62.02; H, 6.62; N, 17.29%.

4-Benzyl-5-{[4-(4-fluorophenyl)piperazin-1-yl]methyl}-2-[(4-methylpiperazin-1-yl)methyl]-2,4-dihydro-3*H*-1,2,4-triazol-3-one (8)

Yield 85%, mp: 127-128 °C; FT-IR ($υ_{max}$, cm^{-1}): 3061 (aromatic CH), 2939 (aliphatic CH), 1701 (C=O), 1508 (C=N); ^{1}H NMR (DMSO-d_6, δ ppm): 2.44 (s, 3H, CH$_3$), 2.49 (s, 4H, 2CH$_2$), 2.89 (s, 4H, 2CH$_2$), 3.34 (s, 10H, 5CH$_2$), 4.92 (s, 2H, CH$_2$), 5.02 (d, 2H, CH$_2$, *J*= 7.6 Hz), 6.86-7.00 (m, 2H, ArH), 7.00-7.05 (m, 2H, ArH), 7.23-7.27 (m, 3H, ArH), 7.32 (d, 2H, ArH, *J*= 7.2 Hz); ^{13}C NMR (DMSO-d_6, δ ppm): 43.87, 44.78, 46.20, 49.09, 49.89, 52.68, 53.23, 54.99, 66.03, 67.49, 115.59 and 115.80, 117.59 and 117.66, 127.58, 128.80, 128.92, 137.34 and 137.49, 143.89, 148.25, 154.03, 157.75; EI-MS *m/z* (%):589.26 (41), 519.60 ([M+1+K]$^+$, 25), 502.81 ([M+Na]$^+$, 16), 479.71 ([M]$^+$, 90), 376.57 (38); Anal. Calcd. for $C_{26}H_{34}FN_7O$: C, 65.11; H, 7.15; N, 20.44%. Found: C, 65.33; H, 7.01; N, 20.18%.

4-Benzyl-5-{[4-(4-fluorophenyl)piperazin-1-yl]methyl}-2-[(4-phenylpiperazin-1-yl)methyl]-2,4-dihydro-3*H*-1,2,4-triazol-3-one (9)

Yield 88%, mp: 140-141 °C; FT-IR ($υ_{max}$, cm^{-1}): 3063 (aromatic CH), 2917 (aliphatic CH), 1698 (C=O), 1512 (C=N); ^{1}H NMR (DMSO-d_6, δ ppm): 2.43 (s, 2H, CH$_2$), 2.72 (s, 4H, 2CH$_2$), 2.86 (s, 4H, 2CH$_2$), 3.13 (s, 4H, 2CH$_2$), 3.35 (s, 4H, 2CH$_2$), 4.65 (s, 2H, CH$_2$), 4.93 (s, 2H, CH$_2$), 6.76 (t, 1H, ArH, *J*= 8.0 Hz), 6.84-6.92 (m, 4H, ArH), 7.01 (t, 2H, ArH, *J*= 12.0 Hz), 7.18-7.25 (m, 5H, ArH), 7.30-7.33 (m, 2H, ArH); ^{13}C NMR (DMSO-d_6, δ ppm): 43.88, 44.82, 48.60, 49.05, 49.60, 49.97, 52.64, 53.20, 66.04, 115.57 and 115.79 , 117.54 and 117.62, 119.28, 127.39, 127.76, 128.92, 129.36, 137.46, 143.54, 148.22, 151.36 and 155.16, 155.28, 157.42; EI-MS *m/z* (%): 579.60 ([M-1+K]$^+$, 19), 564.54 ([M+Na]$^+$, 40), 560.39 ([M+1+H$_2$O]$^+$, 42), 542.77 ([M+1]$^+$, 70), 531.37 (100);

Anal. Calcd. for $C_{31}H_{36}FN_7O$: C, 68.74; H, 6.70; N, 18.10%. Found: C, 68.38; H, 6.60; N, 18.18%.

7-{4-[(4-Benzyl-3-{[4-(4-fluorophenyl)piperazin-1-yl]methyl}-5-oxo-4,5-dihydro-1*H*-1,2,4-triazol-1-yl)methyl]piperazin-1-yl}-1-ethyl-6-fluoro-4-oxo-1,4-dihydroquinoline-3-carboxylic acid (10)

Yield 84%, mp: 205-206 °C; FT-IR (u_{max}, cm^{-1}): 3391 (OH), 3090 (aromatic CH), 2946 (aliphatic CH), 1702 (2C=O), 1623 (C=O), 1508 (C=N); ^{1}H NMR (DMSO-d_6, δ ppm): 1.39 (t, 3H, CH$_3$, *J*= 7.2 Hz), 2.49 (s, 4H, 2CH$_2$), 2.80 (s, 2H, CH$_2$), 2.85 (s, 4H, 2CH$_2$), 3.34 (s, 8H, 4CH$_2$), 4.59 (d, 2H, CH$_2$, *J*= 6.8 Hz), 4.67 (s, 2H, CH$_2$), 4.93 (s, 2H, CH$_2$), 6.82-6.86 (m, 2H, ArH), 7.01 (t, 2H, ArH, *J*= 8.8 Hz), 7.18-7.30 (m, 6H, ArH), 7.92 (d, 1H, ArH, *J*= 13.2 Hz), 8.95 (s, 1H, quinolone CH), 15.36 (s, 1H, OH); ^{13}C NMR (DMSO-d_6, δ ppm): 14.79, 44.84, 49.06, 49.51, 49.77, 49.86, 52.65, 53.19, 66.01, 107.53,106.41, 111.56 and 111.79, 115.36 and 115.58, 117.54 and 117.62, 119.62 and 119.69, 127.46, 127.79, 128.90, 137.43 and 137.64, 143.65, 145.74 and 145.85, 148.19, 152.04 and 154.52, 155.29 and 157.63, 148.99, 155.19, 166.57, 176.38; EI-MS *m/z* (%):738.73 (50), 700.73 (47), 699.98 ([M+1]$^+$, 94), 698.81 ([M]$^+$,100), 675.23 ([M-Na]$^+$, 38), 589.59 (41); Anal. Calcd. for $C_{37}H_{40}F_2N_8O_4$: C, 63.60; H, 5.77; N, 16.04%. Found: C, 63.38; H, 5.81; N, 16.17%.

7-{4-[(4-Benzyl-3-{[4-(4-fluorophenyl)piperazin-1-yl]methyl}-5-oxo-4,5-dihydro-1*H*-1,2,4-triazol-1-yl)methyl]piperazin-1-yl}-1-cyclopropyl-6-fluoro-4-oxo-1,4-dihydroquinoline-3-carboxylic acid (11)

Yield 88%, mp: 258-260 °C; FT-IR (u_{max}, cm^{-1}): 3400 (OH), 3090 (aromatic CH), 2937 (aliphatic CH), 1702 (2C=O), 1627 (C=O), 1509 (C=N); ^{1}H NMR (DMSO-d_6, δ ppm): 1.13 (s, 2H, CH$_2$), 1.32 (s, 2H, CH$_2$), 2.44 (s, 2H, CH$_2$), 2.85 (s, 10H, 5CH$_2$), 3.35 (s, 6H, 3CH$_2$), 3.79 (s, 1H, CH), 4.68 (s, 2H, CH$_2$), 4.94 (s, 2H, CH$_2$), 6.84 (d, 2H, ArH, *J*= 4.0 Hz), 6.99 (t, 2H, ArH, *J*= 8.4 Hz), 7.24-7.30 (m, 5H, ArH), 7.52 (d, 1H, ArH, J= 6.0 Hz), 7.83 (d, 1H, ArH, J= 13.2 Hz), 8.61 (s, 1H, quinolone CH), 15.17 (s, 1H, OH); ^{13}C NMR (DMSO-d_6, δ ppm): 8.02, 36.26, 40.59, 44.85, 49.07, 49.75, 52.66, 53.21, 66.03, 107.17, 106.81, 111.24 and 111.47, 115.56 and 115.78, 117.53 and 117.60, 118.90 and 118.98, 127.47, 127.78, 128.98, 137.41, 139.54, 143.66, 145.43 and 145.53, 152.14 and 154.62, 155.20 and 157.62, 148.30, 155.28, 166.35, 176.73; EI-MS *m/z* (%): 765.22 (88), 711.36 ([M+1]$^+$, 67), 522.29 (47), 332.27 (76), 205.15 (82), 195.92 (100); Anal. Calcd. for $C_{38}H_{40}F_2N_8O_4$: C, 64.21; H, 5.67; N, 15.77%. Found: C, 64.38; H, 5.82; N, 15.51%.

4-Benzyl-2-[2-(4-chlorophenyl)-2-oxoethyl]-5-{[4-(4-fluorophenyl)piperazin-1-yl]methyl}-2,4-dihydro-3*H*-1,2,4-triazol-3-one (12)

Compound **3** (2.52 g, 10 mmol) was added to a solution of Na (0.23 g, 10 mmol) in ethanol. The reaction mixture was refluxed for 2 h. Then, the resulting solution was cooled to room temperature and 4-chlorophenacyl bromide (2.33 g, 10 mmol) was added to the reaction mixture. After that the mixture was refluxed for 15 h, cooled to room temperature, and after evaporating the solvent under reduced pressure, a solid appeared. The formed solid was filtered, washed with water and recrystallized from acetone–water (1:3) to afford the pure compound **12**. Yield 65%, mp: 152-153°C. FT-IR (u_{max}, cm^{-1}): 3037 (aromatic CH), 2920 (aliphatic CH), 1699 (2C=O), 1509 (C=N); ^{1}H NMR (DMSO-d_6, δ ppm): 2.43 (s, 4H, 2CH$_2$), 2.88 (s, 4H, 2CH$_2$), 3.35 (s, 4H, 2CH$_2$), 4.88 (s, 2H, CH$_2$), 6.88 (s, 2H, ArH), 7.00 (s, 2H, ArH), 7.26 (s, 5H, ArH), 7.65 (d, 2H, ArH, *J*= 8.0 Hz), 8.03 (d, 2H, ArH, *J*=4.0 Hz); ^{13}C NMR (DMSO-d_6, δ ppm): 44.19, 44.88, 49.03, 52.27, 52.54,115.60 and 115.82, 117.61 and 117.68, 127.33, 127.52, 127.77, 128.90, 130.51, 133.50, 137.33, 139.37, 148.18, 155.06 and 157.67, 155.33, 155.92, 193.16; EI-MS *m/z* (%): 543.03 ([M+Na]$^+$, 69), 521.08 ([M+1]$^+$, 100), 520.19 ([M]$^+$, 70), 503.27 (44), 490.85 (50); Anal. Calcd. for C$_{28}$H$_{27}$ClFN$_5$O$_2$: C, 64.67; H, 5.23; N, 13.47%. Found: C, 64.28; H, 5.32; N, 13.60%.

4-benzyl-2-[2-(4-chlorophenyl)-2-hydroxyethyl]-5-{[4-(4 fluorophenyl)piperazin-1-yl]methyl}-2,4-dihydro-3*H*-1,2,4-triazol-3-one (13)

To a solution of corresponding compound **10** (5.20 g, 10 mmol) in ethanol, sodium borohydride (1.11 g, 30 mmol) was added and the mixture was refluxed for 15 h. After evaporating the solvent under reduced pressure, a solid appeared. The crude product was recrystallized from acetone–water (1:3) to yield the target compounds. Yield 78%, mp: 100-101 °C. FT-IR (u_{max}, cm^{-1}): 3376 (OH), 2956 (aliphatic CH), 1692 (C=O); ^{1}H NMR (DMSO-d_6, δ ppm): 2.43 (s, 4H, 2CH$_2$), 2.88 (s, 4H, 2CH$_2$), 3.35 (s, 4H, 2CH$_2$), 4.88 (s, 2H, CH$_2$), 6.88 (s, 2H, ArH), 7.00 (s, 2H, ArH), 7.26 (s, 5H, ArH), 7.65 (d, 2H, ArH, *J*= 8.0 Hz), 8.03 (d, 2H, ArH, *J*=4.0 Hz), 10.03 (s, 1H, OH); ^{13}C NMR (DMSO-d_6, δ ppm): 44.20, 44.67, 49.03, 49.12, 52.52, 52.65, 79.21, 115.59 and 115.81, 117.55 and 117.61, 127.28, 127.53, 127.63, 128.48, 128.72, 128.75, 128.87, 132.30, 137.39 and 137.67, 141.97, 143.34, 148.25 and 154.28, 155.29, 157.73; EI-MS *m/z* (%): 523.03 ([M+1]$^+$, 100), 483.27 (34), 460.85 (16); Anal. Calcd. for C$_{28}$H$_{29}$ClFN$_5$O$_2$: C, 64.42; H, 5.60; N, 13.42%. Found: C, 64.18; H, 5.48; N, 13.75%.

General Synthetic Method of Compounds 14 and 15

To a solution of corresponding compound **13** (5.22 g, 10 mmol) in tetrahydrofuran, sodium hydride (0.24 g, 10 mmol) was added and the reaction mixture was refluxed for

7 h. Then, the resulting solution was cooled to room temperature and 2,4-dichlorobenzyl chloride (4.17 mL, 30 mmol) (for **14**) or 2,6-dichlorobenzyl chloride (4.17 mL, 30 mmol) (for **15**) was added in the presence of reaction mixture. After that the mixture was refluxed for 8 h, the mixture was cooled to room temperature. After evaporating the solvent under reduced pressure, an oily product appeared. Oily product was extracted with ethyl acetate and potassium carbonate. Then organic phase was dried and the solvent was evaporated under reduced pressure. The formed oily product recrystallized from acetone to afford the desired compounds **14** and **15**.

4-Benzyl-2-{2-(4-chlorophenyl)-2-[(2,4-dichlorobenzyl)oxy]ethyl}-5-{[4-(4-fluorophenyl) piperazin-1-yl]methyl}-2,4-dihydro-3*H*-1,2,4-triazol-3-one (14)

Yield 51%, mp: 70-71 °C; FT-IR (υ_{max}, cm^{-1}): 3085 (aromatic CH), 2927 (aliphatic CH), 1698 (C=O), 1509 (C=N), 1138 (C-O); ^{1}H NMR (DMSO-d_6, δ ppm): 2.08 (s, 4H, 2CH$_2$), 2.36 (s, 2H, CH$_2$), 2.88 (s, 2H, CH$_2$), 3.36 (s, 5H, 2CH$_2$+CH), 4.81 (s, 2H, CH$_2$), 5.00 (s, 2H, CH$_2$), 6.85-7.00 (m, 2H, ArH), 7.00-7.23 (m, 2H, ArH), 7.25-7.43 (m, 8H, ArH), 7.44-7.64 (m, 3H, ArH), 7.66-7.69 (m, 1H, ArH); ^{13}C NMR (DMSO-d_6, δ ppm): 43.35, 43.89, 44.68, 45.01, 45.96, 49.07, 49.61, 51.87, 70.21, 115.58 and 115.80, 117.58 and 117.65, 127.28, 127.37, 127.82, 128.06, 128.47, 128.75, 129.43, 130.86, 132.30, 133.34 and 133.67, 134.70, 137.29, 137.84, 141.97, 154.30 and 155.51, 148.21, 157.75; EI-MS *m/z* (%): 704.26 ([M+Na]$^+$, 10), 703.19 ([M-1+Na]$^+$, 12), 683.48 ([M+2]$^+$, 16), 681.47 ([M]$^+$,20), 674.44 (40), 673.37 (100); Anal. Calcd. for C$_{35}$H$_{33}$Cl$_3$FN$_5$O$_2$: C, 61.73; H, 4.88; N, 10.28%. Found: C, 61.58; H, 4.82; N, 10.41%.

4-Benzyl-2-{2-(4-chlorophenyl)-2-[(2,6-dichlorobenzyl)oxy]ethyl}-5-{[4-(4-fluorophenyl) piperazin-1-yl]methyl}-2,4-dihydro-3*H*-1,2,4-triazol-3-one (15)

Yield 45%, mp: 65-66 °C; FT-IR (υ_{max}, cm^{-1}): 3095 (aromatic CH), 2937 (aliphatic CH), 1701 (C=O), 1510 (C=N), 1125 (C-O); ^{1}H NMR (DMSO-d_6, δ ppm): 2.08 (s, 6H, 3CH$_2$), 2.36 (s, 2H, CH$_2$), 2.84 (s, 2H, CH$_2$), 3.24 (s, 1H, CH), 3.37 (s, 2H, CH$_2$), 4.89 (s, 4H, 2CH$_2$), 6.84-6.88 (m, 2H, ArH), 6.98-7.04 (m, 2H, ArH), 7.25-7.45 (m, 8H, ArH), 7.52-7.57 (m, 4H, ArH); ^{13}C NMR (DMSO-d_6, δ ppm): 40.61, 41.64, 49.27, 52.87, 70.11, 110.93, 111.91, 115.57 and 115.80, 117.25 and 117.32, 118.46, 118.92, 121.52 , 123.68, 127.50, 129.12, 130.05, 131.20, 136.64, 155.25 and 157.85, 152.26, 165.28; EI-MS *m/z* (%): 720.26 ([M+K]$^+$, 16), 705.19 ([M+1+Na]$^+$, 32), 681.47 ([M]$^+$,70), 670.37 (100); Anal. Calcd. for C$_{35}$H$_{33}$Cl$_3$FN$_5$O$_2$: C, 61.73; H, 4.88; N, 10.28%. Found: C, 61.95; H, 5.02; N, 10.13%.

BIOLOGICAL ACTIVITY

Antimicrobial activity
The test microorganisms were acquired from the Hifzissihha Institute of Refik Saydam (Ankara, Turkey) and were as follows: *Escherichia coli* (*E. coli*) ATCC35218, *Yersinia pseudotuberculosis (Y. pseudotuberculosis*) ATCC911, *Pseudomonas aeruginosa* (*P. aeruginosa*) ATCC43288, *Enterococcus faecalis* (*E. faecalis*) ATCC29212, *Staphylococcus aureus* (*S. aureus*) ATCC25923, *Bacillus cereus* (*B. cereus)* 709 Roma, *Mycobacterium smegmatis* (*M. smegmatis*) ATCC607, *Candida albicans* (*C. albicans*) ATCC60193 and *Saccharomyces cerevisiae* (*S. cerevisia*) RSKK 251 which are laboratory strains. All the novel synthesized molecules were weighed and dissolved in hexane to prepare extract stock solution of 20.000 microgram/milliliter (µg/mL). The antimicrobial effects of the compounds were tested quantitatively in respective broth media by using double microdilution and the minimal inhibition concentration (MIC) values (µg/mL) were determined. The antibacterial and antifungal assays were performed in Mueller-Hinton broth (MH) (Difco, Detroit, MI) at pH.7.3 and buffered Yeast Nitrogen Base (Difco, Detroit, MI) at pH 7.0, respectively. The micro dilution test plates were incubated for 18-24 h at 35 °C. Brain Heart Infusion broth (BHI) (Difco, Detriot, MI) was used for *M. smegmatis,* and incubated for 48-72 h at 35 °C [33]. Ampicillin (10 µg) and fluconazole (5 µg) were used as standard antibacterial and antifungal drugs, respectively. Dimethyl sulfoxide with dilution of 1:10 was used as solvent control.

ACKNOWLEDGMENTS

REFERENCES

1 Akbas E, Berber I, Sener A, Hasanov B. Synthesis and antibacterial activity of 4-benzoyl-1-methyl-5-phenyl-1H-pyrazole-3-carboxylic acid and derivatives. Il Farmaco. 2005;60(1):23–26. DOI: 10.1016/j.farmac.2004.09.003.

2 Rawal RK, Phabhakar YS, Kati SB, De Clercq E. 2-(Aryl)-3-furan-2-ylmethyl-thiazolidin-4-ones as selective HIV-RT inhibitors. Bioorg. Med. Chem. 2005;13:6771-6776. DOI: 10.1016/j.bmc.2005.07.063.

3 Bonde CG, Gaikwad NJ. Synthesis and preliminary evaluation of some pyrazine containing thiazolines and thiazolidinones as antimicrobial agents. Bioorg. Med. Chem. 2004;12(9):2151-2161. DOI: 10.1016/j.bmc.2004.02.024.

4 Rawal RK, Tripathi R, Kati SB, Pannecouque C, De Clercq E. Design, synthesis, and evaluation of 2-aryl-3-heteroaryl-1,3-thiazolidin-4-ones as anti-HIV agents. Bioorg. Med.Chem. 2007;15(4):1725-1731. DOI: 10.1016/j.bmc.2006.12.003.

5. Dixit PP, Patil VJ, Nair PS, Jain S, Sinha N, Arora SK. Synthesis of 1-[3-(4-benzotriazol-1/2-yl-3-fluorophenyl)- 2-oxo-oxazolidin-5-ylmethyl]-3-substituted-thiourea derivatives as antituberculosis agents. Eur. J. Med. Chem. 2006;41:423–428. DOI: 10.1016/j.ejmech.2005.12.005.

6. Hu C, Solomon VR, Cano P Lee HA. 4-aminoquinoline derivative that markedly sensitizes tumor cell killing by Akt inhibitors with a minimum cytotoxicity to non-cancer cells, Eur. J. Med. Chem. 2010;45:705-709. DOI: 10.1016/j.ejmech.2009.11.017.

7. Anderegg TR, Jones RN, Preliminary susceptibility testing guidelines for AZD2563, a long-acting oxazolidinone. Inter. J. Antimic. Agents. 2004;23:6–10. DOI: 10.1016/j.ijantimicag.2003.05.007.

8. Zhu W, Wang J, Wang S, Gu Z, Aceña JL, Izawa K, Liu H, Soloshonok VA. Recent advances in the trifluoromethylation methodology and new CF3-containing drugs. J. Fluorine Chem. 2014;167:37–54. DOI: 10.1016/j.jfluchem.2014.06.026.

9. Wang J, Sánchez-Roselló M, Aceña JL, del Pozo C, Sorochinsky AE, Fustero S, Soloshonok VA, Liu H. Fluorine in pharmaceutical industry: fluorine-containing drugs introduced to the market in the last decade (2001-2011). Chem. Rev. 2014;114(4):2432–2506. DOI: 10.1021/cr4002879.

10. Abdel-Megeed MF, Badr BE, Azaam MM, El-Hiti GA. Synthesis and Antimicrobial Activities of Diphenyl(Arylamino)(1-Phenyl-3-(Pyridin-2-Yl)-1H-Pyrazol-4-Yl)Methylphosphonates. Phosphorus Sulfur Silicon Relat. Elem. 2012;187:1462–1468. DOI: 10.1080/10426507.2012.690117.

11. Corr MJ, O'Hagan D. Fluorosugars: An improved synthesis of the 2,3,4-trideoxy-2,3,4-trifluoro hexose analogue of D-glucose. J. Fluorine Chem. 2013;155:72-77. DOI: 10.1016/j.jfluchem.2013.06.003.

12. Kirk KL. Fluorine in medicinal chemistry: Recent therapeutic applications of fluorinated small molecules. J. Fluorine Chem. 2006;127(8): 1013–1029. DOI: 10.1016/j.jfluchem.2006.06.007.

13. Li QH, Zhang G, Ding Y, et al. Synthesis and anti-tumor activities of novel triazole Schiff-base derivatives, J. Southwest Univ. Natl. Sci. Ed. 2014;40:826-832. DOI: 10.3969/j.issn.1003-4271.2014.06.05

14. Yuguo Z, Wei X, Qingqing G, Ping L, Zhenchao W, Kai Y. Synthesis and Antitumor Activity of 5, 6-2H-[1, 2, 4]-Triazolo [3, 4-b][1, 3, 4] thiadiazine Derivatives. CHINESE JOURNAL OF ORGANIC CHEMISTRY. 2011;31(6):912–916. URL: http://sioc-journal.cn/Jwk_yjhx/EN/abstract/abstract340136.shtml.

15. Yin K, Jiang L, Zhou H, Huang Y, Xiang J. Synthesis and insecticidal activity of 2-perfluoroalkyl-substituted or glucopyranosyl-substituted 2, 4-dihydro-1, 2, 4-triazole-3-thione Schiff base. Chinese journal of organic chemistry. 2008;28(6):1016–1023. URL: http://sioc-journal.cn/Jwk_yjhx/EN/abstract/abstract336787.shtml.

16. Feng ZX, Zhang WN, Zhou YJ, et al. Synthesis and antifungal activities of 1-[2- (N-methyl-N-substituted-benzyl)amino-2-(4-tert-butylphenyl)ethyl]-1H-1,2,4- triazoles, Chem. J. Chin. Univ. 2000;21:1221–1226. URL: http://en.cnki.com.cn/Article_en/CJFDTOTAL-GDXH200008015.htm.

17. Xu JY, Zeng Y, Jiang B, et al. Synthesis, anti-inflammatory activities and SAR studies of 1,5-diaryl substituted-1,2,4-triazoles, Chin. J. Med. Chem. 2008;18:321–328

18. Zhao XY, Gong YX, Zhang ZW, et al. Synthesis and plant growth regulating activity of N-5-(3-carboxy-1,2,4-triazolyl)-N0 -aroyl urea, Chin. J. Appl. Chem. 2003;20:594–596.

19. Jiang DH, Huang M. Design and synthesis of thieno[3,2-d]pyrimidine derivatives containing a piperazine unit as anticancer agents, Chem. Reag. 2012;34:797– 799. URL: http://en.cnki.com.cn/Article_en/CJFDTOTAL-HXSJ201209012.htm.

20. Wu Q, Wang ZC, Wei X, Xue W. Synthesis and antibacterial activities of 1- substituted-4-[5-(4-substitutedphenyl)-1,3,4-thiadiazol-2-sulfonyl]piperazine derivatives, Chin. J. Synth. Chem. 2014;22:429–434. DOI: 10.3969/j.issn.1005-1511.2014.04.001.

21. Li GY, Ysn SG, Jiang S, et al. Synthesis of piperazine derivatives containing pyridinemethyl/thiazolemethyl and their biological activities, Chin. J. Org. Chem. 2008;28:2001–2006. URL: http://sioc-journal.cn/Jwk_yjhx/EN/Y2008/V28/I11/2001.

22. Sahooa S, Pranesh PK, Mahendra KCB, et al. Synthesis and Biological Activity of Certain Mannich Bases Derivatives from 1, 2, 4-Triazoles, Iranian Journal of Pharmaceutical Sciences.   2013;9(4):51-60. URL:http://www.ijps.ir/article_10248_b02d56dcd5b30e0eabfb136e9369ef80.pdf.

23. Wang Y, Xu K, Bai G, et al. Synthesis and antifungal activity of novel triazole compounds containing piperazine moiety, Molecules. 2014;19:1133-11340. DOI:10.3390/molecules190811333.

24. Foks H, Janowiec M, Zwolska Z, Augustynowicz-Kopec´ E. Synthesis and tuberculostatic activity of some 2-piperazinmethylene derivatives 1,2,4-triazole-3- thiones, Phosphorus Sulfur Silicon Relat. Elem. 2005;180:537–543. DOI: 10.1080/104265090517280.

25. Kouznetsov VV, Gomez-Barrio A. Recent developments in the design and synthesis of hybrid molecules basedon aminoquinoline ring and their antiplasmodial evaluation. Eur. J. Med. Chem. 2009;44(8):3091-3113. DOI: doi:10.1016/j.ejmech.2009.02.024.

26. Basoglu S, Demirbas A, Ulker S, Karaoglu SA, Demirbas N. Design, Synthesis And Biological Activities Of Some 7-Aminocephalosporanic Acid Derivatives. Eur. J. Med. Chem. 2013;69:622-631. URL: http://dx.doi.org/10.1016/j.ejmech.2013.07.040.

27. Bayrak H, Demirbas A, Karaoglu SA, Demirbas N. Synthesis of some new 1, 2, 4-triazoles, their Mannich and Schiff bases and evaluation of their antimicrobial activities. Eur. J. Med. Chem. 2009;44(3):1057-1066. DOI: 10.1016/j.ejmech.2008.06.019.

28. Zhao YJ, Wei W, Su ZG, Ma GH. Poly(ethylene glycol) prodrug for anthracyclines via N-Mannich base linker: Design, synthesis and biological evaluation. Int. J. Pharm. 2009;379(1):90–99. DOI: 10.1016/j.ijpharm.2009.06.013.

29. Gayniyat K, Wilie IE, Oluwakemi O. Synthesis of Mannich bases: 2-(3-Phenylaminopropionyloxy)-benzoic acid and 3-Phenylamino-1-(2, 4, 6-trimethoxy-phenyl)-propan-1- one, their toxicity, ionization constant, antimicrobial and antioxidant activities. Food Chem. 2014;165:515-521. DOI: 10.1016/j.foodchem.2014.05.119.

30. Fekner T, Baldwin JE, Adlington RM, Fardeau S, Jones TW, Prout CK, Schofield CJ. Syntheses of (6S)-cephalosporins from 6-aminopenicillanic acid. Tetrahedron. 2000;56: 6053–6074. URL: http://dx.doi.org/10.1016/s0040-4020(00)00486-5.

31. Dassonville-Klimpt A, Audic N, Sasaki A, Pillon M, Baudrin E, Mullié C, Sonnet P. Synthesis and antibacterial activity of catecholate–ciprofloxacin conjugates. Bioorg. Med. Chem. 2014;22:4049–4060. DOI: 10.1016/j.bmc.2014.05.067.

32. Foroumadi A, Oboudiat M, Emami S, Karimollah A, Saghaee L, Moshafi MH, Shafiee A. Synthesis and antibacterial activity of N-[2-[5- (methylthio)thiophen-2-yl]-2-oxoethyl] and N-[2-[5-(methylthio)thiophen- 2-yl]-2-(oxyimino) ethyl]piperazinyl quinolone derivatives. Bioorg. Med. Chem. 2006;14:3421-3427. DOI: 10.1016/j.bmc.2005.12.058.

33. National Committee for Clinical Laboratory Standards. Methods for dilution antimicrobial susceptibility tests for bacteria that grow aerobically. 3rd ed., approved standard. Villanova (PA): National Committee for Clinical Laboratory Standards, 1993; NCCLS document no. M7-A3;13(25):1-32.

Yeni 1,2,4-Triazoller, Mannich Bazları, Konazoller ve Florokinolinlerin Sentezi ve Antimikrobiyal Aktivitesi

Sule CEYLAN[1*]

Öz: Triazoller antidepresan, antienflamatuar, analjezik, antibakteriyel, antimikobakteriyel, antifungal, antiviral, antikanser ve diğer aktivitelere sahpi olan yeni bileşiklerin geliştirilmesinde ilgi çeken heterosiklik bileşiklerdir. Bu makalede, bir seri florlu ve piperazinli yeni biyolojik aktif 1,2,4-triazol-3-on türevleri triazol öncül maddelerinin Mannich reaksiyonuyla sentez edilmiştir. Sentezlenmiş yeni bileşiklerin yapıları elementel analiz, FT-IR, ^{13}C NMR, ^{1}H NMR ve EI MS teknikleriyle aydınlatılmıştır. Bu bileşikler *in vitro*'da antimikrobiyal özellikleri açısından incelenmiştir ve pek çok bileşiğin *Candida albicans* ve *Saccharomyces cerevisiae*'ye karşı fungusidal aktivitesi olduğu bulunmuştur. Bazı bileşikler ise *Mycobacterium smegmatis* (pigmentsiz, hızlı yükselen bir mikobakteri) üzerinde mükemmel bir aktivite göstermişlerdir, uygulama konsantrasyonu <1 µg/mL olup standart ilaç olan streptomisin'den daha iyidir.

Anahtar kelimeler: 1,2,4-triazol, piperazin, konazol, mannich bazı, biyolojik aktivite.

Sunulma: 22 Haziran 2016. **Düzeltme**: 23 Temmuz 2016. **Kabul**: 23 Eylül 2016

(This article was presented to the 28th National Chemistry Congress and submitted to JOTCSA as a full manuscript)

Synthesis and Characterization of Cellulose-Based Bio-Polymer Aerogel Isolated from Waste of Blueberry Tree (*Vaccinium myrtillus*)

Mehmet KAYA[*]

[*] *Recep Tayyip Erdoğan University, Faculty of Arts and Sciences, Department of Chemistry 53100, Rize, Türkiye.*

Abstract: Cellulose aerogel (CA) with a highly porous structure is environmentally friendly, thermally stable, and flame retardant. These properties in material worlds have attracted large interest as a potentially industrial material. In this paper, cellulose aerogel with flame retardant feature was produced from pruned branches and bushes of blueberry wastes (PBW). Firstly, cellulose raw material was obtained from these wastes and then, cellulose aerogel was prepared via freeze-drying, followed by cellulose hydrogel production. The work showed that a three dimensional network aerogel structure was prepared from NaOH/Urea as scaffold solution. The present cellulose aerogel has excellent flame retardant property, which can extinguish within 140 s. By the way, it was inferred that thermal stability performance of cellulose aerogel could be an efficient potential thermal insulating material. Besides, this process is sustainable, easily available at low cost, and suitable for industrial applications.

INTRODUCTION

Today, composite materials take an important place in the industrial area due to their variety and advantages (1-3). Some materials are inadequate to meet some physical and/or chemical properties required in the fields of application. When these materials are supported by another type of materials in various amounts, composite structures providing the required properties are obtained, which is a method commonly used nowadays. In recent years, people's interest in polymeric composite originating from cellulose obtained from vegetable wastes has gradually increased because of its gripping properties (4, 5). An important reason why cellulose products are preferred is that it provides composite materials with some advantages such as high strength and thermal insulation (6). Being organic substances, cellulosic waste materials also bio-degrade in a short while and they do not have any disadvantages except their unaesthetic effects on the environment. Utilizing cellulosic waste materials and recycling them as new useful composite materials play a crucial role in contributing to the national economy. In addition, it decreases energy costs and consequently provides added value in regions where there are limited energy sources. Recently, aerogels from cellulosic wastes have great interest, because they have their own perfect feature (7). These kind of aerogels, which are among the lightest solid and a new third-generation materials, are one of the finest insulation materials available (8, 9). Traditional aerogels are mainly made of silica, which is not environmentally-friendly. In contrast, cellulose is a major component of wood, the most abundant, low cost naturally occurring polymer of glucose and attracts a lot of interest for producing novel aerogel materials. In addition to thin films, sponges and fibers, functional materials with high added value, such as cellulose nanocrystals, nanofibers, hydrogels and aerogels can be made from cellulose (10-13). Cellulose based aerogels have several unique features such as super absorbent and heat insulating. In this regard, when the variety of sources is taken into consideration, it is aimed to use PBW found abundantly in the Eastern Black Sea region, especially in Rize, as an economic value in Turkey. With this study, a new product which is biopolymer, eco-credential, biodegradable, low-cost, and flame-retardant was achieved using cellulose as a raw material obtained from wastes of the pruned blueberry tree, which is one of the important herbal products in the mentioned region. In addition to the structural and thermal characteristics, flame retardation, and surface properties of CA biopolymer materials obtained from the study were determined with the help of the scanning electron microscope (SEM), Fourier transform infrared spectroscopy (FT-IR), thermal analysis (TG-DTG/DTA), X-ray diffraction (XRD), Brunauer-Emmett-Teller (BET) surface area measurement techniques (pore size, volume, type, and surface areas), and flame retardant measurements.

EXPERIMENTAL SECTION

Materials

All chemicals (urea, sodium hydroxide, and ethanol) were of analytical grade and purchased from Merck. All the solutions were prepared with deionized (DI) water. The isolation of cellulose fibers from PBW was performed by a way of an environmental friendly process for cellulose extraction and bleaching .

Cellulose production from PBW

The PBW was washed with DI water for a few times and filtrated using a cloth strainer to remove impurities such as water soluble sand, soil *etc*. Alkaline treatment was carried out in NaOH solution of 4 wt% at 80°C for three times. Alkaline treated fibers were subjected to $NaClO_2$ or H_2O_2 bleaching of 1.7 wt% in acetic acid buffer at 80°C for 4 times. The resulting fibers were strained and rinsed with DI water and cloth strainer until it reached neutrality. Afterwards, the PBW sawdust powder was oven-dried at 105°C.

Acid Treatment

Bleached PBW product was hydrolyzed in pre-heated H_2SO_4 (64 wt%) (14). The high concentration of acid was removed through centrifugation at 10.000 rpm for 10 min and repeated until the solution was turbid. The resulting cellulose suspension was filtered using glass filter or cellulose membrane in DI water until the suspension reached a pH of 5.

Production of Cellulose Aerogels

Cellulose fibers (2 wt %) were dispersed into a sodium hydroxide/urea solution (1.9 wt %/10 wt %) by sonicating for 6 min. Then the solution was placed in a freezer for more than 24 h for gelation to take place. After the solution had been frozen, it was then thawed at room temperature, followed by immersion into ethanol (99 vol %) for coagulation (3 h). The specimen's thickness was controlled around 1 cm with a diameter of 3.8 cm using a beaker as a mold. After coagulation, solvent exchange was carried out by immersing the gel in DI water for 2 days. Freeze-drying was carried out for the sample for 2 days at −98 °C with a freeze-dryer after pre-freezing the sample at −18 °C for 12 h (15).

## RESULTS and DISCUSSIONS

SEM Analysis

The structural and morphological characteristics of CA were displayed by SEM and are shown in Figures 1-3. It is clear that the CA has a largely homogeneous porous structure consisting of microfibrillar networks (Figure 3). The pore structure results from the sublimation of frozen

water during the freeze-drying process (16). This property is coherent with those of nitrogen adsorption data, and seems to be reasoned by crystal formation during the relatively slow freezing process, which would have caused to press out fibrils to form the film-like structure (17). According to the aforesaid findings, the CA with a homogeneous microporous structure can be fabricated via *in situ* templated synthesis of sample in the cellulose gel framework (16).
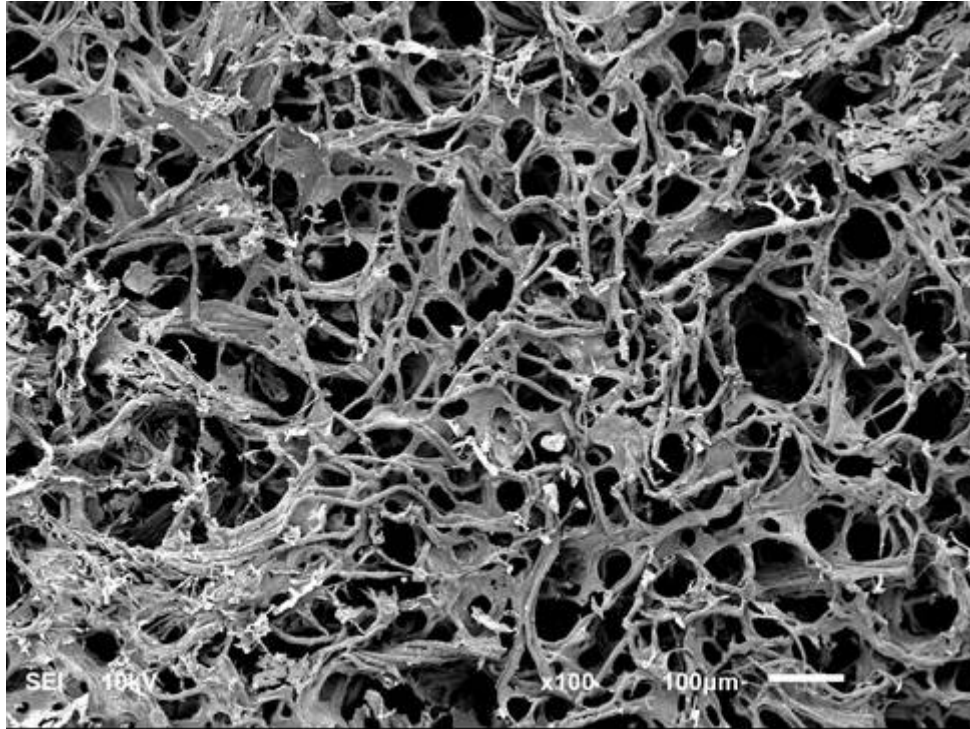
Figure 1. SEM image x100 of CA
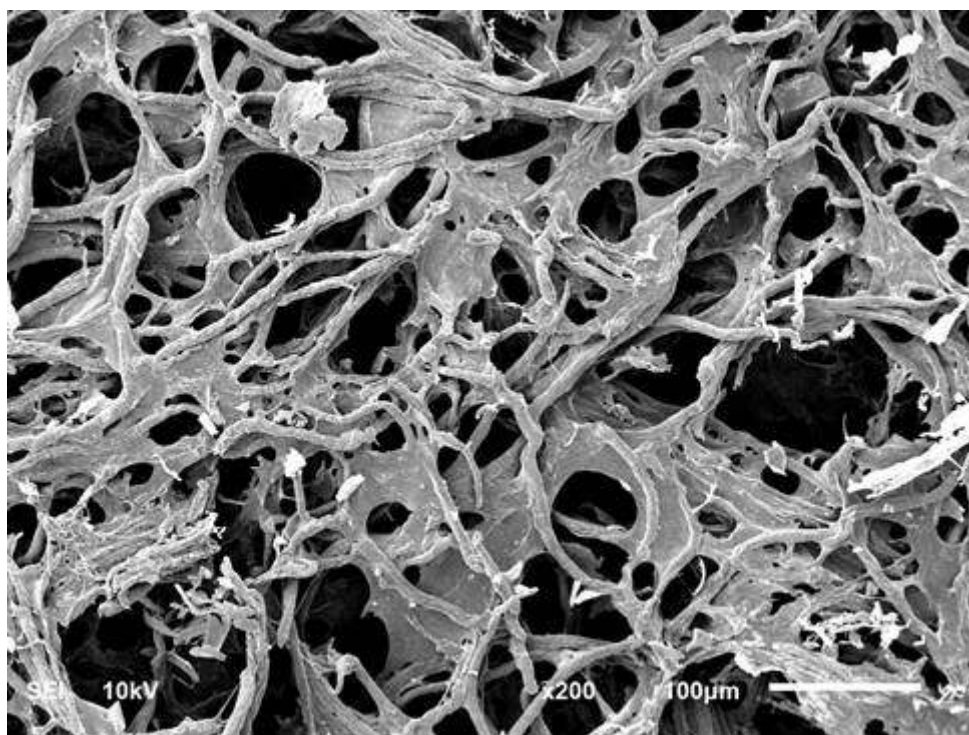
Figure 2. SEM image x200 of CA.
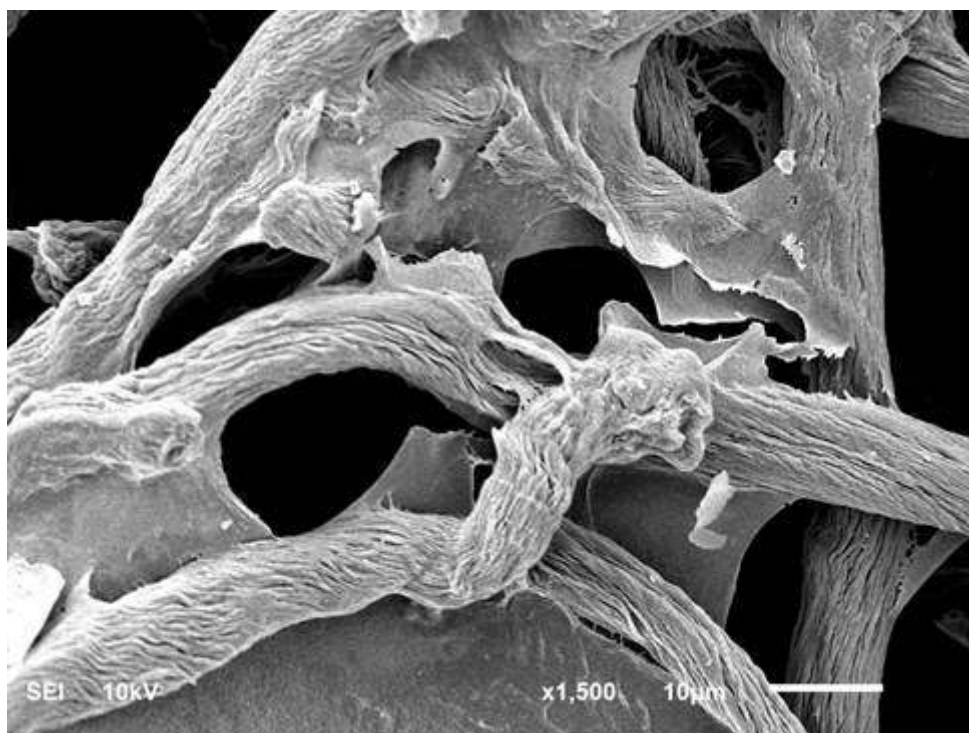
Figure. 3. SEM image x1500 of CA.

FT-IR Analysis

The FT-IR signal pertaining to the characteristic functional groups are shown in Figure 4. It can be observed that the several components of the CA are most likely consisted of alkene, esters, aromatics, ketone and alcohol, with different oxygen-containing functional groups observed,

e.g., OH (3450–3300 cm^{-1}), C=O (1775–11680 cm^{-1}), C–O–C (1162 cm^{-1}), and C–O–(H) (1050 cm^{-1}) (18).
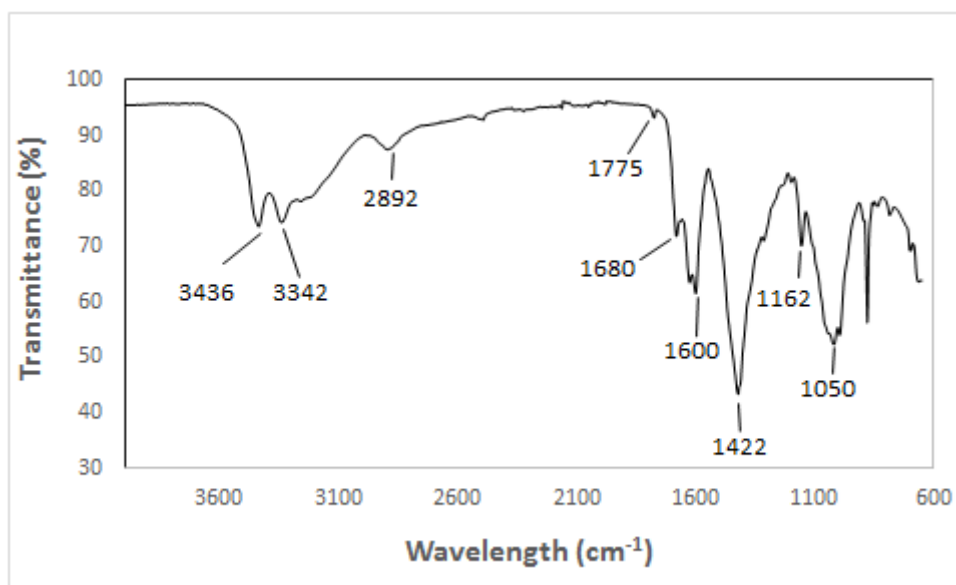
Figure 4. FT-IR Spectrum of CA.

Thermal Analysis

Considering industrial applications of heat insulating materials, the thermal behavior of the CA was investigated by TGA analysis. As demonstrated in Figure 5, a gradual weight loss occurs up to about 500 degrees. The weight loss at a temperature range of 0°C-200°C can be attributed the loss of moisture in both surface and inner moisture evaporation in porous structure where removal of water is more difficult relatively (18). The stage of weight loss around 300−500 °C can be ascribed to the depolymerization of cellulose with generation of CO_2 and volatile hydrocarbons (16). Finally, it appeared that the CA has high thermal stability (weight loss only 60 % at about 350°C).
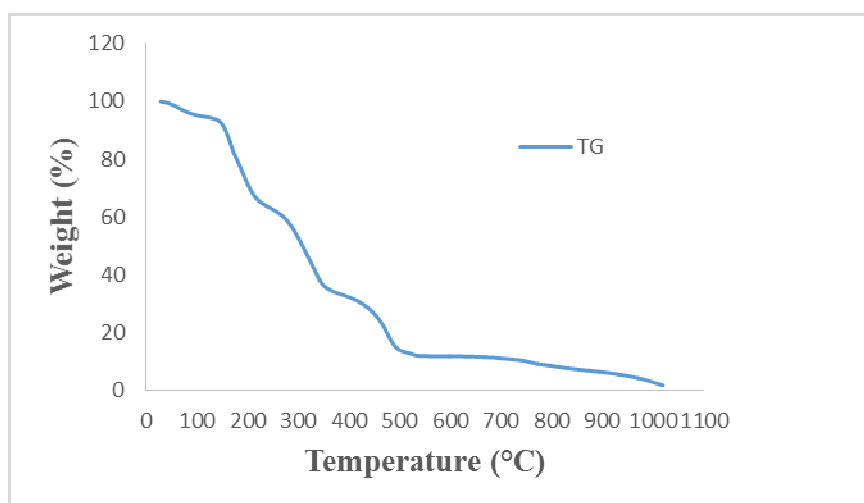

Figure 5. Thermal Stability of CA.

XRD Analysis

XRD spectrum for CA was performed on a Rigaku DMAX-3C automated diffractometer using Ni filtered CuK-beta radiation (40 kV and 30 mA). Diffractograms were recorded from 5° to 40° at a scan rate of 3°/min. Figure 6 displayed a crystal structure of cellulose with typical diffraction peaks for the plane (200) at $2\theta = 22.20°$ and (110) at $2\theta = 19.8°$. Crystallinity index (CrI) was calculated from the intensity of the 200 peak (I_{200}, $2\theta = 22.2°$) and the intensity minimum between 200 and 110 (Iam, $2\theta = 19.8°$) peaks using the empirical equation (8):

$$CrI = \{(I_{200}-I_{am})/I_{200}S \times 100 = 76.52\ \%$$ (Eq. 1)

It was observed that the cellulose aerogel had a higher crystallinity (76.52%) than that of the raw amorphous woody material, probably because of the remotion of hemicellulose and lignin. This result also reveals that amorphous and crystalline cellulose regions are considerably divided.
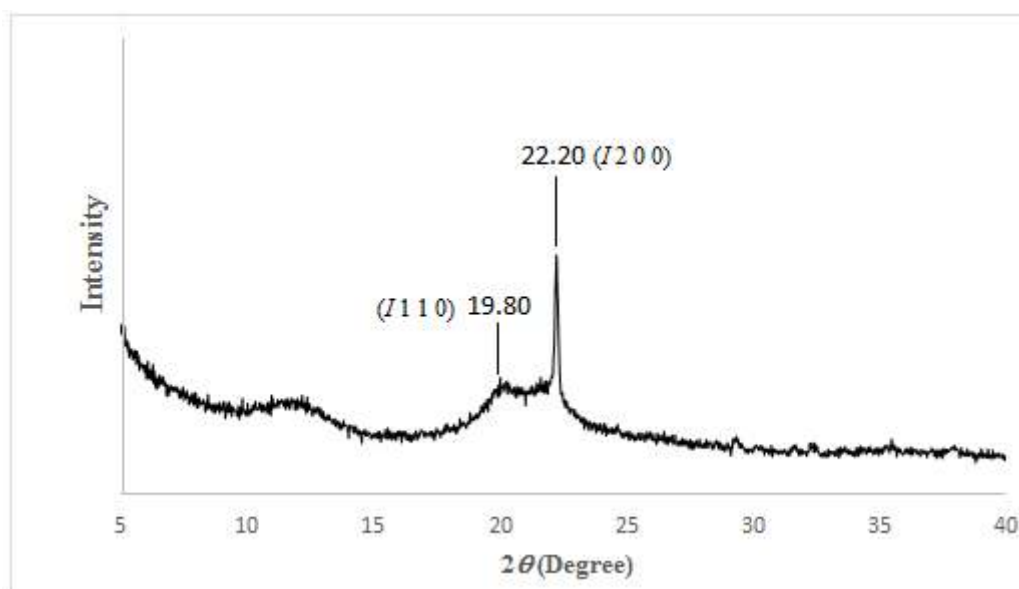

Figure 6. XRD Spectrum of CA.

BET Specific Surface Area

The pore features of the CA involving the total pore volume, average pore diameter, and specific surface area (from N_2 adsorption measurements) are shown in Table 1. The results showed the CA with the total pore volume and average pore diameter as 0.25 cm^3/g and 4.30 nm, respectively. The nitrogen adsorption at 77 K on CA resembles the type II isotherms (according to IUPAC classification), which are typical for physical adsorption on microporous and non-porous or macroporous solids (Figure 7). The characteristic features of these isotherms are the reversible part at relatively lower pressures and the hysteresis loop at relatively higher pressures (19). To examine the porous structure of the aerogel, nitrogen

adsorption and desorption isotherm techniques were performed. Figure 7 exhibits the adsorption and desorption isotherms, which show a hysteresis typical of a porous system. According to BET analysis, a specific surface area of 42.25 m^2 g^{-1} is recorded for the CA.

Table 1. Specific Surface Area and Porosity.

Sample	Specific surface area (m^2g^{-1})	Average pore diameter (nm)	Total pore volume (cm^3/g^{-1})
CA	42.25	4.30	0.25
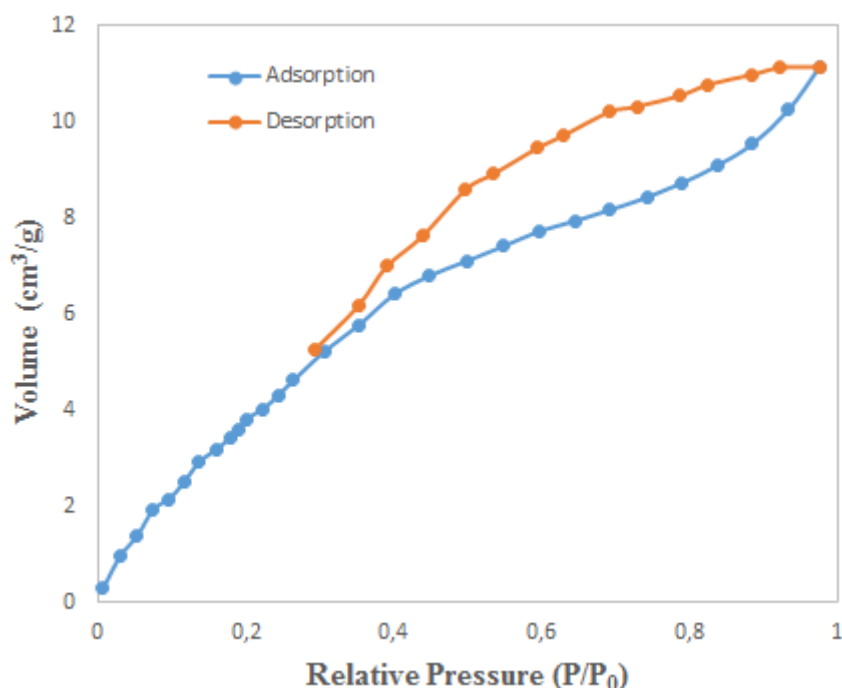
Figure 7. Nitrogen Adsorption-Desorption Isotherm.

Flame Retardant Characteristic of CA

Due to the investigation, the flame retardant performance of the CA produced in this work, the aerogel was emblazed and the burning velocity was calculated. At this stage, it was observed that the CA was ignited slowly, and burned only the part of 25 percent burned after 33 s of combustion (see the video in Supporting Information). However, the neat cellulose aerogel was quickly ignited (about 10 s) and burned completely after 10 s of combustion in the literature (16). The photo in Figure 8 demonstrates the remains of the CA after 34. The combustion velocity of the aerogel decreases from 4 to 3.71 mm s^{-1} (Figure 8). Besides, when the CA with the length of 40 mm was ignited, flame propagation apparently slowed, and then the flame gradually became smaller and finally extinguished within about 140 s. The results indicate that the CA is a highly an efficient flame retardant.
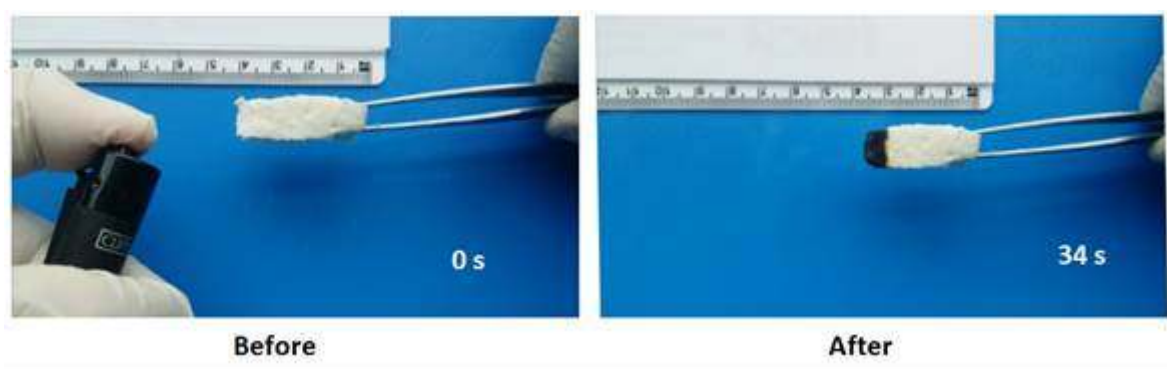
Figure 8. Flame Retardant Study.

CONCLUSIONS

The cellulose aerogel with a highy porous structure was produced from pruned branches and bushes of blueberries via *in situ* converting cellulose hydrogel scaffold to aerogel. This work is an efficient, environmentally friendly, and low cost process and the bio-polymer material is an effective flame retardant, porous, and potential super absorbent (next studies). It was concluded that the prepared cellulose aerogel has extremely porous networks and perfect flame retardant performance. Besides, the cellulose aerogel has good crystallinity feature and thermal stability. This environmentally friendly and low cost work will offer insight into the new opportunities for the use of inexpensive waste-derived cellulose to fabricate several materials. It has a major potential application in the future of "green" materials chemistry and it may be appropriate for industrial scale production.

REFERENCES

1. Nishino T, Matsuda I, Hirao K. All-cellulose composite. Macromolecules. 2004;37(20):7683-7.

2. Dormanns JW, Schuermann J, Mussig J, Duchemin BJC, Staiger MP. Solvent infusion processing of all-cellulose composite laminates using an aqueous NaOH/urea solvent system. Compos Part a-Appl S. 2016;82:130-40.

3. Yang J, Zhang EW, Li XF, Zhang YT, Qu J, Yu ZZ. Cellulose/graphene aerogel supported phase change composites with high thermal conductivity and good shape stability for thermal energy storage. Carbon. 2016;98:50-7.

4. Ahmadi M, Madadlou A, Sabouri AA. Isolation of micro- and nano-crystalline cellulose particles and fabrication of crystalline particles-loaded whey protein cold-set gel. Food Chem. 2015;174:97-103.

5. Awal A, Sain M, Chowdhury M. Preparation of cellulose-based nano-composite fibers by electrospinning and understanding the effect of processing parameters. Compos Part B-Eng. 2011;42(5):1220-5.

6. Duong HM, Nguyen ST. Nanocellulose aerogels as thermal insulation materials. In: Pacheco Torgal F, Buratti C, Kalaiselvam S, Granqvist C-G, Ivanov V, editors. Nano and Biotech Based Materials for Energy Building Efficiency. Cham: Springer International Publishing; 2016. p. 411-27.

7. Postek MT, Vladar A, Dagata J, Farkas N, Ming B, Wagner R, et al. Development of the metrology and imaging of cellulose nanocrystals. Meas Sci Technol. 2011;22(2).

8. Seantier B, Bendahou D, Bendahou A, Grohens Y, Kaddami H. Multi-scale cellulose based new bio-aerogel composites with thermal super-insulating and tunable mechanical properties. Carbohyd Polym. 2016;138:335-48.

9. Kobayashi Y, Saito T, Isogai A. Aerogels with 3D ordered nanofiber skeletons of liquid-crystalline nanocellulose derivatives as tough and transparent insulators. Angew Chem Int Edit. 2014;53(39):10394-7.

10. Liu J, Cheng F, Grenman H, Spoljaric S, Seppala J, Eriksson JE, et al. Development of nanocellulose scaffolds with tunable structures to support 3D cell culture. Carbohyd Polym. 2016;148:259-71.

11. Shen XP, Shamshina JL, Berton P, Bandomir J, Wang H, Gurau G, et al. Comparison of hydrogels prepared with ionic-liquid-isolated vs commercial chitin and cellulose. Acs Sustain Chem Eng. 2016;4(2):471-80.

12. Kwon GJ, Kim DY, Hwang JH, Kang JH. Structural properties and adsorption capacity of holocellulose aerogels synthesized from an alkali hydroxide-urea solution. J Korean Phys Soc. 2014;64(10):1470-3.

13. Wang ZG, Liu SL, Matsumoto Y, Kuga S. Cellulose gel and aerogel from LiCl/DMSO solution. Cellulose. 2012;19(2):393-9.

14. Beck-Candanedo S, Roman M, Gray DG. Effect of reaction conditions on the properties and behavior of wood cellulose nanocrystal suspensions. Biomacromolecules. 2005;6(2):1048-54.

15. Nguyen ST, Feng JD, Le NT, Le ATT, Hoang N, Tan VBC, et al. Cellulose aerogel from paper waste for crude oil spill cleaning. Ind Eng Chem Res. 2013;52(51):18386-91.

16. Han YY, Zhang XX, Wu XD, Lu CH. Flame Retardant, Heat insulating cellulose aerogels from waste cotton fabrics by in situ formation of magnesium hydroxide nanoparticles in cellulose gel nanostructures. Acs Sustain Chem Eng. 2015;3(8):1853-9.

17. Jin H, Nishiyama Y, Wada M, Kuga S. Nanofibrillar cellulose aerogels. Colloid Surface A. 2004;240(1-3):63-7.

18. Poletto M, Ornaghi HL, Zattera AJ. Native Cellulose: structure, characterization and thermal properties. Materials. 2014;7(9):6105-19.

19. Zhang SQ, Wang J, Shen J, Deng ZS, Lai ZQ, Zhou B, et al. The investigation of the adsorption character of carbon aerogels. Nanostruct Mater. 1999;11(3):375-81.

Türkçe Öz ve Anahtar Kelimeler

Yabanmersini Ağacı Atıklarından (Vaccinium myrtillus) Selüloz Esaslı Biyo-Polimer Aerojelinin Sentezi ve Karakterizasyonu

Mehmet KAYA

Öz: Selüloz aerojeli (CA) çok gözenekli bir yapıya sahiptir ve çevreyle dosttur, ısıl olarak kararlıdır ve alev geciktirici özelliği vardır. Malzeme dünyasında bu özellikler çok ilgi çekmekte olup potansiyel olarak endüstriyel bir malzeme çıkmasına da yol açabilir. Bu çalışmada, alev geciktirici özelliğine sahip selüloz aerojeli, yabanmersini ağacı atıklarından budanmış dal ve çalılarından üretilmiştir. Öncelikle selüloz ham maddesi elde edilmiş ve daha sonra selüloz hidrojel üretilmiştir. Ardından dondurarak kurutma ile selüloz aerojel oluşturulmuştur. Çalışmada, yapı iskelesi çözeltisi olarak NaOH/Üreden oluşan üç boyutlu ağ sistemine sahip aerojelin üretilmesi anlatılmıştır. Elde edilen selüloz aerojelin mükemmel alev geciktirici özelliği bulunmaktadır ve 140 saniye içinde sönüm sağlanmaktadır. Bunun dışında, selüloz aerojelin ısıl kararlılık özelliğinin mükemmel bir ısıl yalıtkan olabileceği düşünülmektedir. Son olarak, süreç sürdürülebilir özelliğe sahiptir, düşük maliyetle kolaylıkla elde edilebilir ve endüstriyel uygulamalar için uygundur.